INTERNATIONAL WORKSHOP ON RICHTMYER-MESHKOV AND RAYLEIGH-TAYLOR MIXING

(Second International Workshop on the Physics of Compressible Turbulent Mixing)

Pleasanton, California, U.S.A.
November 16 and 17, 1989

International Exchange on RM and RT Mixing

Here is a collection of the papers presented at the November 89 meeting. As promised, copies of the presentation materials have been used unless a more formal paper was made available. In order to expedite the dissemination of the information, no editing has been done.

A list of attendees, and the pictures taken on Friday are also included. Dr. Vasilenko had a few suggestions concerning the topics which we may want to address before the next meeting, so I have included his comments as well.

Much has been accomplished during our meeting, and I look forward to more gatherings of the same kind. As you know the French scientists have offered to host the next meeting, and December 1990 was suggested as a possible time frame. You may want to contact them, if you have any special suggestions or requests.

To those of you who attended the APS Palo Alto Meeting, I would like to express my regrets at not having seen you there as well. Because of the sudden death of a very close friend's daughter, a delightful twenty one year old girl which we considered as our niece, we flew to Los Angeles on Saturday to be with her family and did not return to the Bay Area until Wednesday.

Thank you all for participating in the Workshop.

Sincerely,

Viviane Rupert,
Chairman, 1989 Workshop on
RM and RT Mixing

1. Michael Wehner
2. John Lilley
3. John Molitoris
4. Neil Hoffman
5. John Hawley
6. Nick Stearman
7. William Varnum
8. Gene Burke
9. Arkady Polyonov
10. Gregory D'Alessio
11. Bradford Sturtevant
12. Doug Rotman
13. Steve Haan
14. William Noh
15. John Bolstad
16. John Bell
17. Rick Rauenzahn
18. Liang Chern
19. Claude Cavailler
20. James Glimm
21. George Kramer
22. Jean Francois Haas
23. Norman Zabusky
24. Michel Legrand
25. Timothy Clark
26. Alexei Vasilenko
27. Timothy Goldsack
28. Robert Benjamin
29. Gerry Puckett
30. Peter Eltgroth
31. Riccardo Bonazza
32. Neil Cowperthwaite
33. William Powers
34. Patrick Spitz
35. Karnig Mikaelian
36. Coralie Kahle
37. Lawrence Cloutman
38. Paul Thompson
39. Viviane Rupert
40. Ned Dairiki
41. Xiaolin Li
42. Xiad Yang
43. Jevgenii Meshkov
44. Jacob Grun
45. David Youngs
46. Didier Besnard
47. Jose Redondo
48. Lazhar Houas
49. Brian Hankin
50. Alan Smith
51. W. Patrick Crowley
52. Jon Bryan

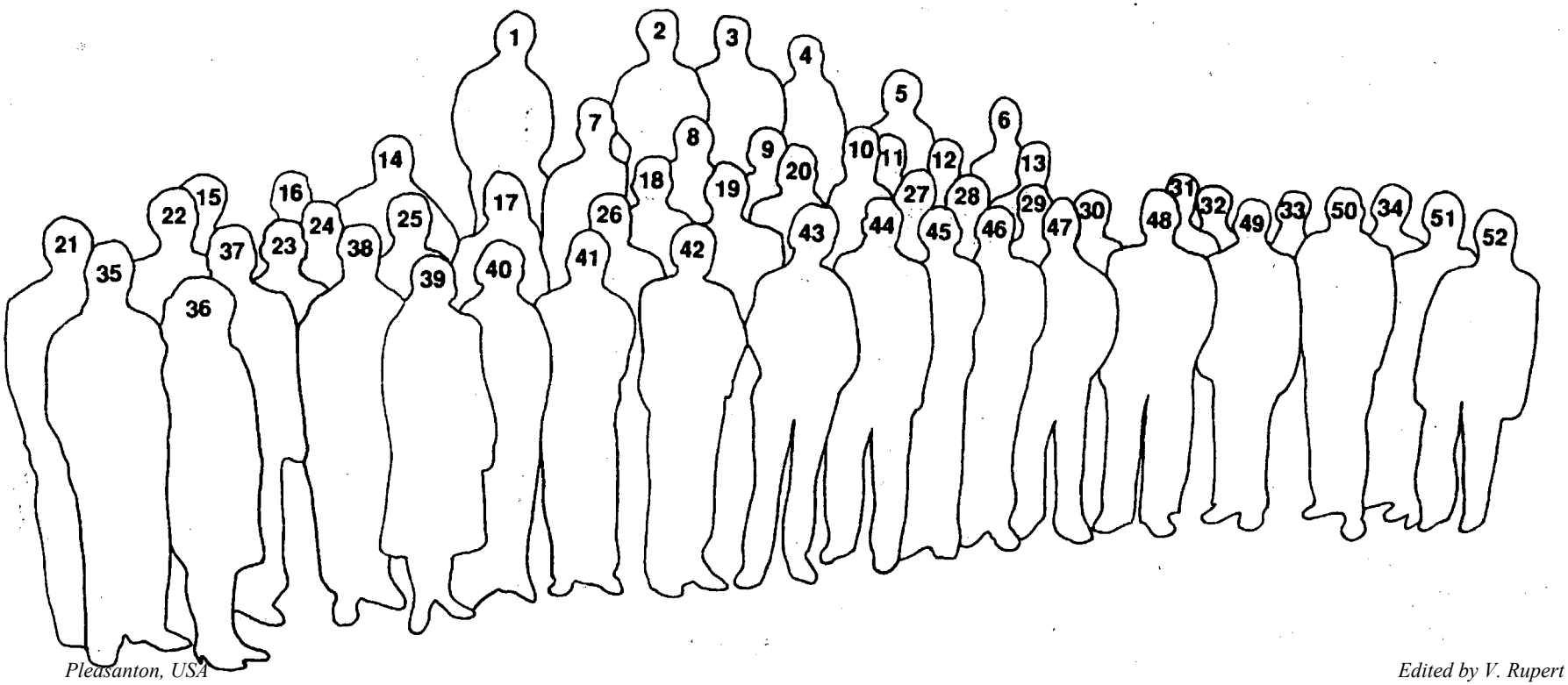

Pleasanton, USA

Edited by V. Rupert

Table of Content:

ATTENDEES & ADDRESSES FOR THE INTERNATIONAL EXCHANGE ON RM & RT MIXING CONFERENCE

Dr. Gregory D'Alessio
U.S. Department of Energy
Office of WRD&T
DP-243 GTN
Washington, D.C. 20545

Dr. John Bell
Lawrence Livermore National Laboratory
P.O. Box 808, L-316
Livermore, CA 94550

Dr. Robert F. Benjamin
Los Alamos National Laboratory
P.O. Box 1663, M/S J970
Los Alamos, NM 87545

Dr. Didier C. Besnard
Centre d'Etudes de Limeil-Valenton
Department MA/MCN
94195 Villeneuve St. George Cedex
FRANCE

Dr. John H. Bolstad
Lawrence Livermore National Laboratory
P.O. Box 808, L-16
Livermore, CA 94550

Mr. Riccardo Bonazza
California Institute of Technology
M/S 301-46
Pasadena, CA 91125

Dr. Jon Bryan
Lawrence Livermore National Laboratory
P.O. Box 808, L-22
Livermore, CA 94550

Dr. Alfred Buckingham
Lawrence Livermore National Laboratory
P.O. Box 808, L-16
Livermore, CA 94550

Dr. Eugene Burke
Lawrence Livermore National Laboratory
P.O. Box 808, L-22
Livermore, CA 94550

Dr. Claude Cavailler
C.E.A./Centre d'Etudes de Vaujours
B. P. No. 7
77181 Coutry
FRANCE

Dr. I. Liang Chern
Argonne National Laboratory
Math & Computer Science Department
9700 So. Cass Avenue
Argonne, IL 60439
(708) 972-7232 / FAX # (708) 972-5986

Dr. Randy Christensen
Lawrence Livermore National Laboratory
P.O. Box 808, L-35
Livermore, CA 94550

Dr. Timothy Clark
Los Alamos National Laboratory
P.O. Box 1663
M/S B216
Los Alamos, NM 87545

Dr. Larry Cloutman
Lawrence Livermore National Laboratory
P.O. Box 808, L-35
Livermore, CA 94550

Dr. Jeffrey Colvin
Los Alamos National Laboratory
P.O. Box 1663, M/S E531
Los Alamos, NM 87545

Dr. Neil Cowperthwaite
AWE
Aldermaston, Reading RG7 4PR
ENGLAND

Dr. W. Patrick Crowley
Lawrence Livermore National Laboratory
P.O. Box 808, L-16
Livermore, CA 94550

Dr. Ned Dairiki
Lawrence Livermore National Laboratory
P.O. Box 808, L-298
Livermore, CA 94550

Dr. William Dannevik
Lawrence Livermore National Laboratory
P.O. Box 808, L-16
Livermore, CA 94550

Dr. William Dunlop
Lawrence Livermore National Laboratory
P.O. Box 808, L-13
Livermore, CA 94550

Dr. Pete Eltgroth
Lawrence Livermore National Laboratory
P.O. Box 808, L-298
Livermore, CA 94550

Dr. Patrick Spitz
Centre D'Etudes De Limeil Valenton
94195 Villeneuve-Saint-Georges Cedex
FRANCE

Professor James Glimm
State University of New York
at Stonybrook
Department of Applied Mathematics and Statistics
Stonybrook, NY 11796
516-632-8355/FAX 516-632-8490

Dr. Timothy Goldsack / AWE
Lawrence Livermore National Laboratory
P.O. Box 808, L-473
Livermore, CA 94550

Dr. Jakob Grun
Code 4784
Naval Research Laboratory
Washington, D.C. 20375

Dr. Steve Haan
Lawrence Livermore National Laboratory
P.O. Box 808, L-477
Livermore, CA 94550

Dr. Jean-Francois Haas
Centre d'Etudes de Limeil-Valenton
94195 Villeneuve St. George Cedex
FRANCE

Dr. Brian C. Hankin
AWE
Aldermaston, Reading RG7 4PR
ENGLAND

Professor John Hawley
Leander McCormick Observatory
University of Virginia
P.O. Box 3818, University Station
Charlottesville, VA 22903-0818

Dr. Neil Hoffman
Los Alamos National Laboratory
P.O. Box 1663, M/S B-216
Los Alamos, NM 87545

Dr. Lazhar Houas
Universite de Provence
Centre Saint-Jerome
S.E.T.T.
Milieux Hors d'Equilibre
13397 Marseille Cedex 13
FRANCE

Dr. Robert Janssen
Los Alamos National Laboratory
P. O. Box 1663, M/S 664
Los Alamos, NM 87545

Mrs. Coralie Kahle
Lawrence Livermore National Laboratory
P.O. Box 808, L-23
Livermore, CA 94550
Dr. Rupert's Secretary
(415) 422-0217

Dr. Robert Kerr, 6110
National Center for Atmospheric Research
P.O. Box 3000
Boulder, CO 80307-3000
(303) 497-8727 / FAX 303-497-8701

Dr. George Kramer
Lawrence Livermore National Laboratory
P.O. Box 808, L-22
Livermore, CA 94550

Dr. James LeBlanc
Lawrence Livermore National Laboratory
P.O. Box 808, L-35
Livermore, CA 94550

Dr. Michel Legrand
C.E.A./Centre d'Etudes de Vauours
B. P. No. 7
77187 Country
FRANCE

Dr. Cecil Leith
Lawrence Livermore National Laboratory
P.O. Box 808, L-16
Livermore, CA 94550

Dr. Xiaolin Li
Department of Applied Math
New Jersey Institute of Technology
Newark, NJ 07102
201-596-3485/FAX 201-565-0586

Professor John R. Lilley
Los Alamos National Laboratory
P.O. Box 1663, M/S F664
Los Alamos, NM 87545

Professor Daniel Meiron
Department of Applied Mathematics
California Institute of Technology
Pasadena, CA 91125

Dr. Jevgenii Meshkov
109180, Moscow, Staromonetnii Per, 26
State Executive Committee for Atomic Energy
USSR

Dr. Karnig Mikaelian
Lawrence Livermore National Laboratory
P.O. Box 808, L-471
Livermore, CA 94550

Dr. John Molitoris
Lawrence Livermore National Laboratory
P.O. Box 808, L-321
Livermore, CA 94550

Professor Neuvazhaev
State University of Chelyabinsk
454136 Chelyabinsk
Molodogvardeytzev St. 70B
USSR

Dr. William Noh
Lawrence Livermore National Laboratory
P.O. Box 808, L-321
Livermore, CA 94550

Dr. Stephen M. Pollaine
Lawrence Livermore National Laboratory
P.O. Box 808, L-477
Livermore, CA 94550

Professor Arkady V. Polyonov
All Union Scientific Research
Institute of Technical Physics
45470 Chelyabinsk
USSR

Dr. William Powers
Los Alamos National Laboratory
P. O. Box 1663, M/S K723
Los Alamos, NM 87545

Dr. Gerry Puckett
Lawrence Livermore National Laboratory
P.O. Box 808, L-298
Livermore, CA 94550

Dr. Rick M. Rauenzahn
Orgn. T-3, MS/B216
Los Alamos National Laboratory
P.O. Box 1663
Los Alamos, NM 87545

Dr. Jose M. Redondo
D.A.M.T.P. Cambridge University
Silver Street, Cambridge
C83 9EW
UNITED KINGDOM

Dr. Douglas Rotman
Lawrence Livermore National Laboratory
P.O. Box 808, L-321
Livermore, CA 94550

Dr. Viviane C. Rupert
Lawrence Livermore National Laboratory
P.O. Box 808, L-22
Livermore, CA 94550

Dr. Alan J. Spero
Lawrence Livermore National Laboratory
P.O. Box 808, L-22
Livermore, CA 94550

Dr. Philip Saffman
Department of Applied Mathematics
California Institute of Technology
Pasadena, CA 91125

Dr. Alan V. Smith
AWE, Foulness
Southend-on-Sea
Essex SS3 9XE
UNITED KINGDOM

Dr. Nick Stearman
AWE, Foulness
Southend-on-Sea
Essex SS3 9XE
UNITED KINGDOM

Dr. Peter Stry
Lawrence Livermore National Laboratory
P.O. Box 808, L-22
Livermore, CA 94550

Dr. Bradford Sturtevant
California Institute of Technology
M/S 301-46
Pasadena, CA 91125

Dr. Paul H. Thompson
AWE
Aldermaston, Reading RG7 4PR
ENGLAND

Dr. Robert Tipton
Lawrence Livermore National Laboratory
P.O. Box 808, L-35
Livermore, CA 94550

Dr. William Varnum
Los Alamos National Laboratory
P.O. Box 1663, M/S E531
Los Alamos, NM 87545

Dr. Alexei Vasilenko
All Union Scientific Research
Institute of Technical Physics
45470 Chelyabinsk
USSR

Dr. James Viecelli
Lawrence Livermore National Laboratory
P.O. Box 808, L-321
Livermore, CA 94550

Dr. Michael Wehner
Lawrence Livermore National Laboratory
P.O. Box 808, L-35
Livermore, CA 94550

Dr. ~~Xiad~~ XIAOLONG Yang
Rutgers University
Department of Mechanical & Aerospace
Engineering
P.O. Box 909
Piscataway, NJ 08855-0909

Dr. David L. Youngs
Atomic Weapons Research Establishment
Aldermaston, Reading RG7 4PR
ENGLAND

Dr. Ronald Zabowski
Lawrence Livermore National Laboratory
P.O. Box 808, L-389
Livermore, CA 94550

Professor Norman Zabusky
Rutgers University
Department of Mechanical & Aerospace
Engineering
P.O. Box 909
Piscataway, NJ 08855-0909

Mikhail V. Nikitin
26 Staromonetny
109180, Moscow
USSR

I believe that two problems are important at present :

1. Causes of results disagreements of turbulent mixing experiments, performed with liquid and gaseous media. And is it possible to explain this difference by gas compressibility?
2. Experimental procedure of the turbulent mixing of different densities gases in the most pure form -without membrane or barrier.

The aim is to proof the experimental confidence of experiments with and membranes, initially separating the gases.

A Vasilenko

C. Leith

Rayleigh-Taylor mixing

Single-scale

Classical linear instability

bubbles and spikes

Layzer eqn for $A = 1$

boundary integral or vortex methods in 2D

Kelvin-Helmholtz instability for $A < 1$ → singularity

Boussinesq limit $A \to 0$ with $gA = 1$

RT multi-scale

Youngs' similarity: $h \sim gAt^2$

Coherent bubbles and spikes
(two fluid models)
vs.
Turbulence

Demixing

Transition

Initial length scale

imposed

selected by
surface tension

Richtmyer-Meshkov mixing

Single-scale
like RT

Multi-scale

no simple similarity law

first shock passage
how much turbulence
is produced ?

second shock passage
how does the shock interact
with a layer of turbulence
and random density fluctuations

simpler questions
shock / homogeneous turbulence
shock / density fluctuations

sound wave / turbulence
sound wave / density fluct.

	Shock width	Viscosity coef
Molecular:	$\delta = \ell$	$\nu = c\ell$
	$\delta = \frac{\nu}{c}$	
Artificial:	$\delta_{art} = \Delta x$	$\nu_{art} = c\Delta x$
		$\approx (\Delta u)(\Delta x)$
Turbulence:	$\delta_{eddy} = \frac{\nu_{eddy}}{c}$	$\nu_{eddy} = \bar{u} L$

Ratio: $$\frac{\delta_{eddy}}{\delta_{art}} = \frac{\nu_{eddy}}{\nu_{art}} = \frac{\bar{u} L}{c \Delta x}$$

1D, 2D AND 3D CALCULATIONS OF SHOCK TUBE MIXING EXPERIMENTS

N Cowperthwaite

AWE Aldermaston

1-D LAGRANGIAN CALCULATIONS

(a) Passive Mix Model
(D L Youngs)

(b) Dynamic Mix Model
(D L Youngs, Physica 12D (1988) 270)

2-D CALCULATIONS

PETRA - Semi-Lagrangian hydrocode
with interface tracking

3-D CALCULATIONS

NUTMEG - 3D version of PETRA

PASSIVE MIX MODEL EQUATIONS

$$(\rho_1 + \rho_2)(1 + E_1)\frac{d^2h_1}{dt^2} = (\rho_1 - \rho_2)(1 - E_1)\,g_1 - \frac{C_D f_1 \rho_1}{R}\,\frac{dh_1}{dt}\left|\frac{dh_1}{dt}\right|$$

$$(\rho_1 + \rho_2)(1 + E_2)\frac{d^2h_2}{dt^2} = (\rho_1 - \rho_2)(1 - E_2)\,g_2 - \frac{C_D f_2 \rho_2}{R}\,\frac{dh_2}{dt}\left|\frac{dh_2}{dt}\right|$$

Where $E_1 = \exp - \left[\frac{4\beta_1 h_1}{\lambda_o}\right]$

$E_2 = \exp - \left[\frac{4\beta_1 h_2}{\lambda_o}\right]$

$R = \max\left[\min(h_1, h_2),\ \frac{C_D \lambda_o}{2\beta_1}\right]$

$f_1 = \frac{\rho_1 + \rho_2}{\rho_1}$

$f_2 = f_1\left[\frac{\rho_1}{\rho_2}\right]^{0.49}$

$\beta_1 = 3.83171$ First zero of the Bessel function J_1

$C_D = {}^{11}/_{3}$ Chosen to fit the rocket rig expts.

INITIAL CONDITIONS FOR THE DYNAMIC MIX MODEL

1. VOLUME FRACTIONS

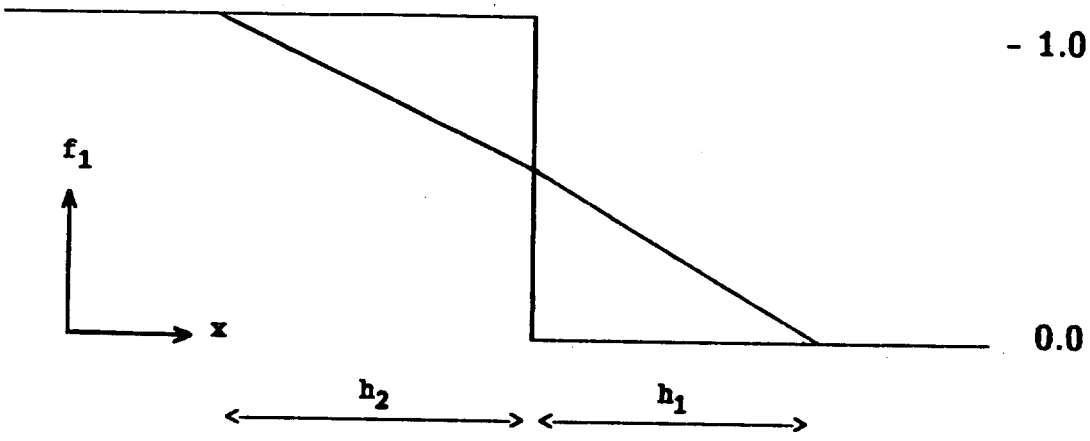

For volume conservation

$$f_1(x_o) = \frac{h_2}{h_1 + h_2}$$

$$f_2(x_o) = \frac{h_1}{h_1 + h_2}$$

2. FLUID VELOCITIES

$$u_1 = \bar{u} + f_2 V$$

$$u_2 = \bar{u} - f_1 V$$

If V varies linearly to give the correct end values then

$$V_{(x)} = \frac{\dot{h}_2 (h_1 - x + x_o) + \dot{h}_1 (h_2 + x - x_o)}{h_1 + h_2}$$

$\left[h_1, h_2, \dot{h}_1, \dot{h}_2 \text{ taken from PMM}\right]$

Initial Conditions for DMM (continued)

3. INITIAL LENGTH SCALE
(used in drag and turbulent diffusion equations)

$$L_o = \max\left[\min(h_1,h_2),\ \frac{C_D\lambda_o}{2\beta_1}\right]$$

Throughout mix region, ie for

$$-h_2 \leq x - x_o \leq h_1$$

$L_o = 0$ elsewhere

4. TURBULENT KINETIC ENERGY

$$K_o(x) = 4u^2 f_1(x) f_2(x)$$

(Quadratic if $h_1 = h_2$)

$$u = \min(\dot{h}_1, \dot{h}_2)$$

ANDRONOV TEST PROBLEM

(Sov. Phys. JETP, Vol. 44, p424 (1976))

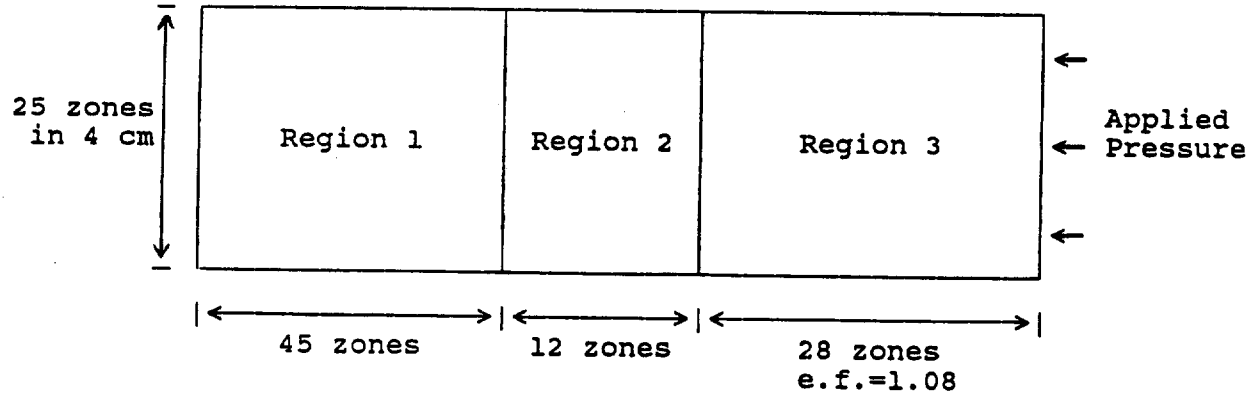

Problem start time = 200.0 microseconds

REGION 1: Helium
length = 16.9 cm
rho = 0.0001664 g/cm
E = 0.009665465 Mbcc/g
P = 1 atmosphere

REGION 2: Air
length = 3.6755068 cm
rho = 0.001184 g/cm
E = 0.002139464 Mbcc/g
P = 1 atmosphere

REGION 3: Air
length = 19.4244932 cm
rho = 0.001794572 g/cc
E = 0.002547822 Mbcc/g
vel = 0.015309605 cm/musec

Pressure behind shock = 1.8289 bar (12 psi above atmospheric)
giving a Mach no of 1.3

Problem used for comparison of

1D Passive mix model
1D Dynamic mix model
2D PETRA calculation
3D NUTMEG calculation

Ideal gas equations of state used with ratios of specific heats

1.63 for helium
1.40 for air

3D PERTURBATION IS OF THE FORM

$$x(y,z) = \sum_{m,n} a \cos(k_y y) \cos(k_z z)$$

where $k_y = \frac{m\pi}{ymax}$, $k_z = \frac{n\pi}{zmax}$

since

$$2 \cos(k_y y) \cos(k_z z) = \cos(k_y y + k_z z) + \cos(k_y y - k_z z)$$

each term represents two sinusoidal corragations of equal magnitude, with slopes in opposite directions in the y-z plane

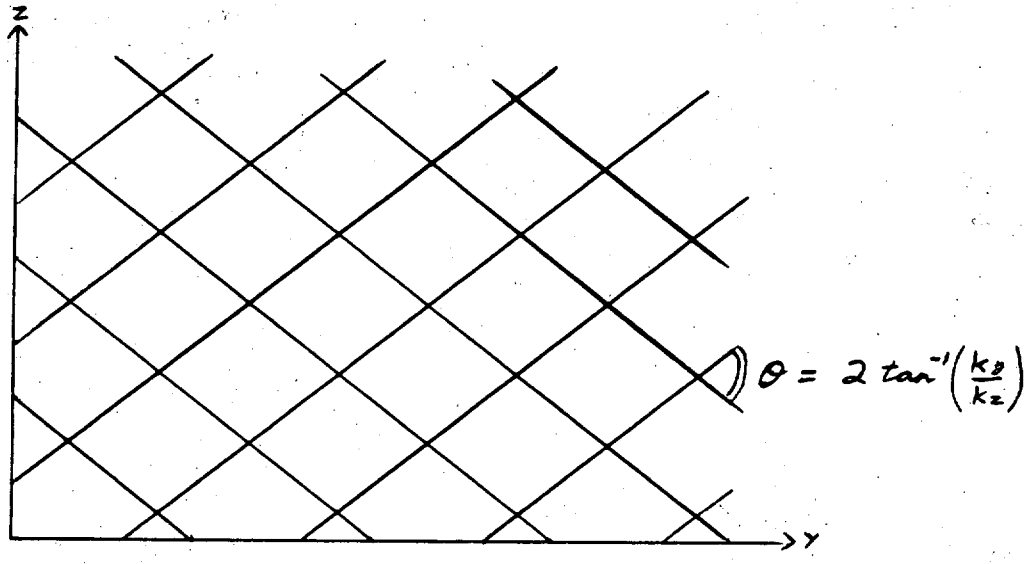

For the problems considered here the minimum wavelength was 1.0 cm ($2 \leq m,n \leq 8$) and the perturbation was normalised to give a root mean squared amplitude of 0.01 cm.

For the passive mix model the initial amplitude was twice the rms amplitude in the PETRA and PERSEUS calculations ie 0.02 cm, since this is supposed to represent a peak value.

1D FIN[illegible]ONED PETRA SIMULATION SHOWI[illegible] THE POSITION OF THE IN[illegible]RFACE AND ITS INTERACTION WITH SHOCKS.

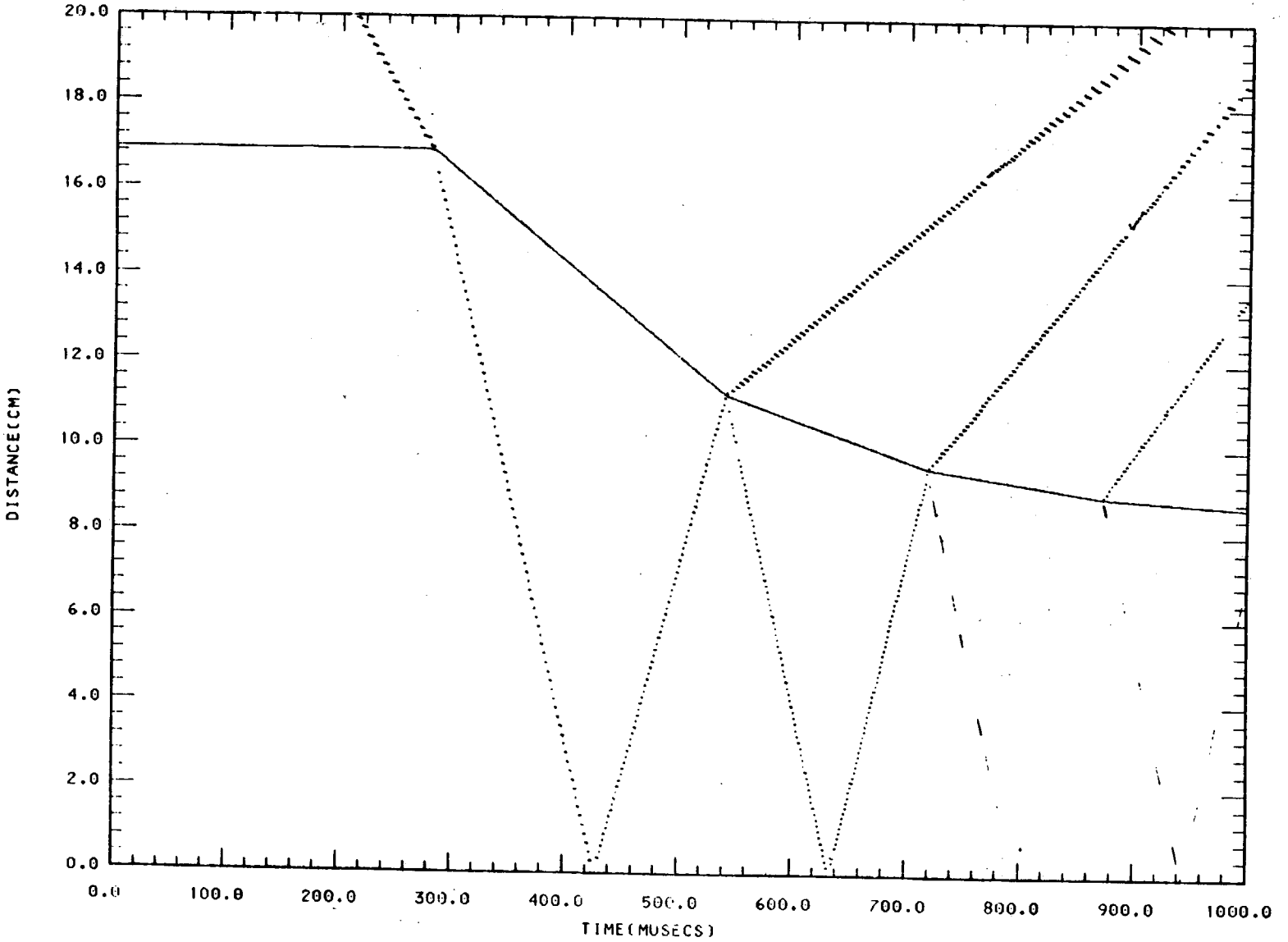

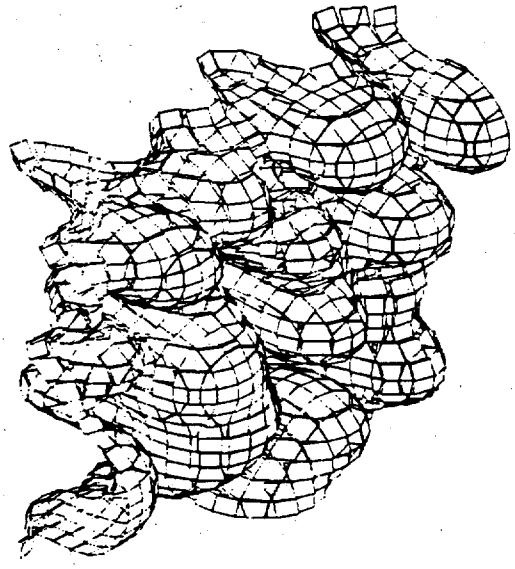

$t = 500\,\mu s$

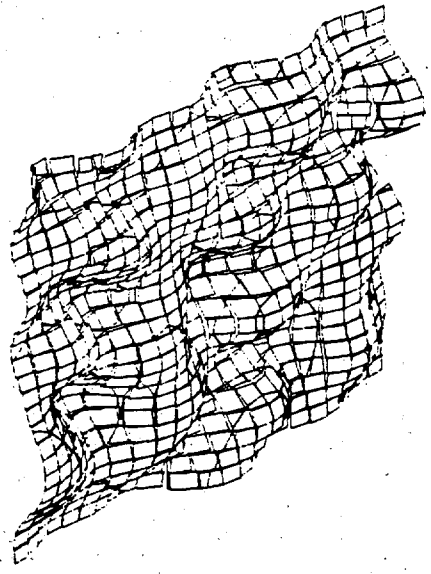

$t = 600\,\mu s$

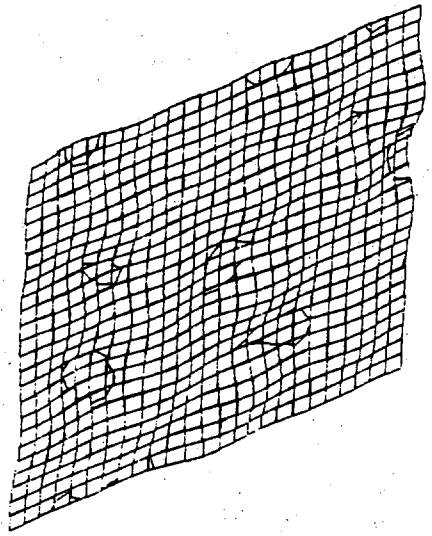

$t = 400\,\mu s$

INTERFACE PLOTS FROM 2D AND 3D CALCULATIONS AT T = 200.0 MICROSECONDS

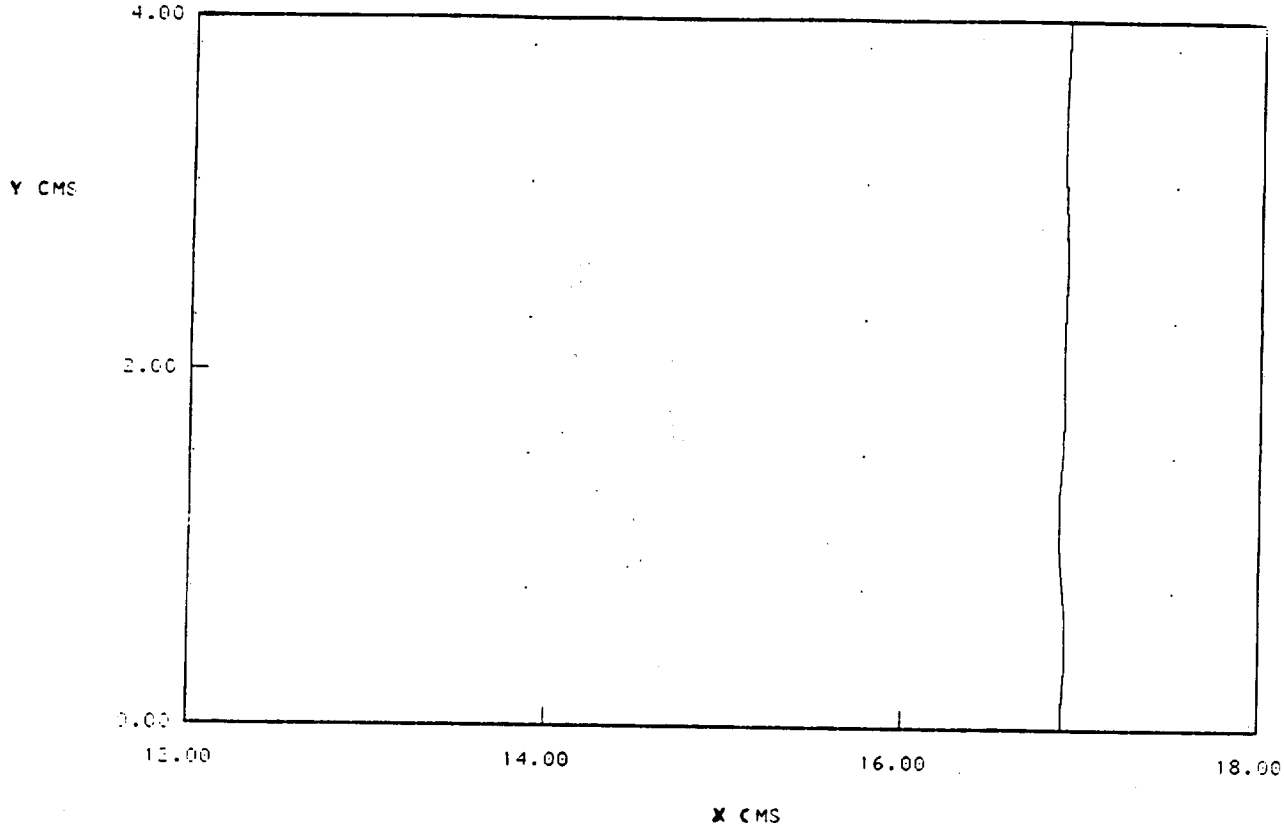

INTERFACE PLOTS FROM 2D AND 3D CALCULATIONS AT T = 400.0 MICROSECONDS

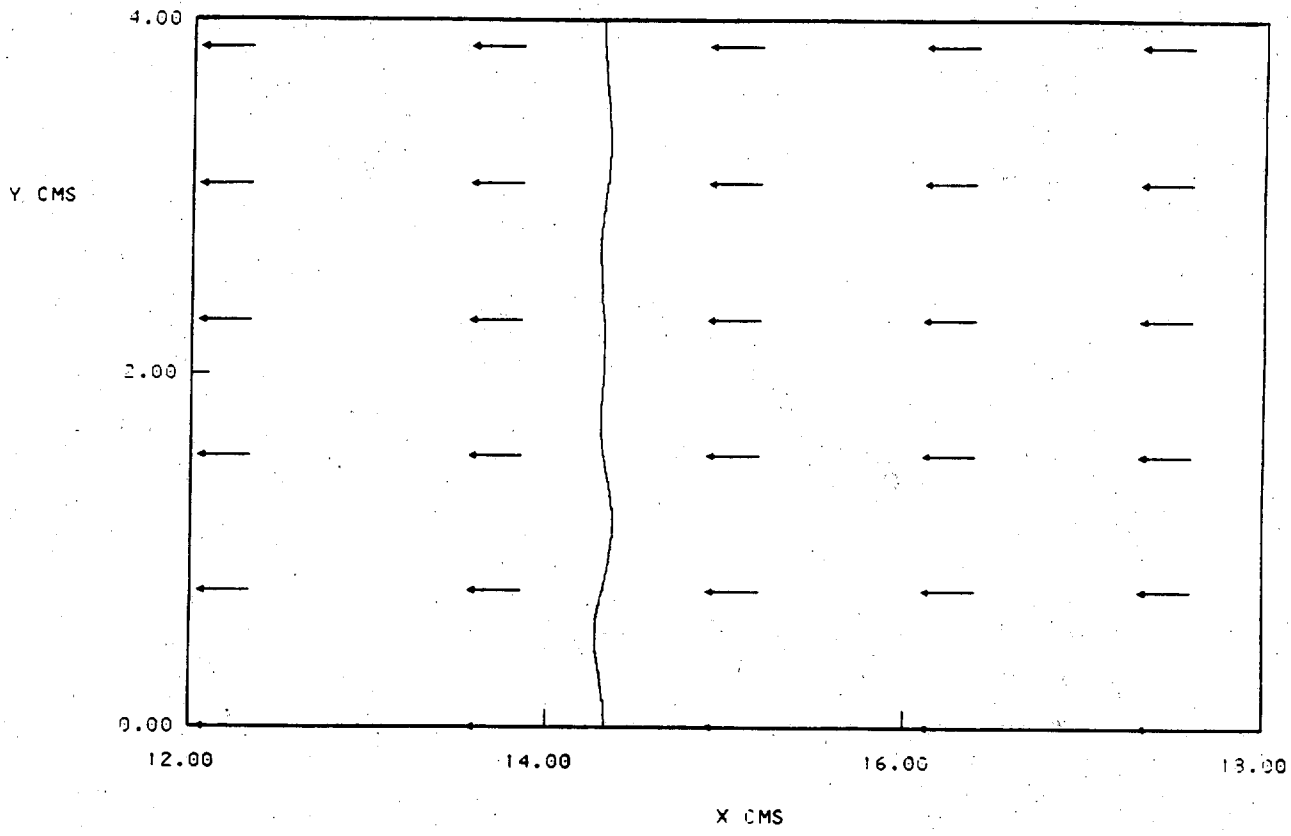

INTERFACE PLOTS FROM 2D AND 3D CALCULATIONS AT T = 600.0 MICROSECONDS

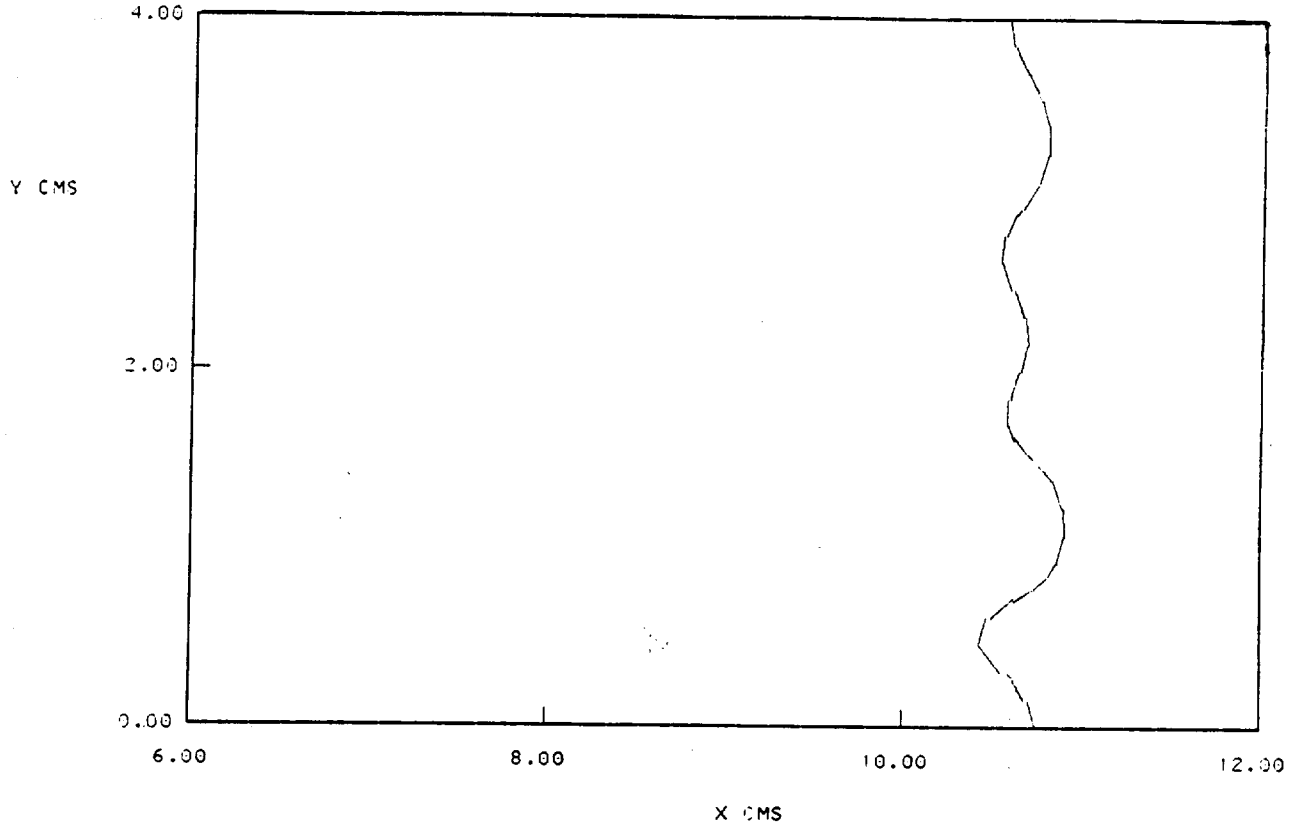

INTERFACE PLOTS FROM 2D AND 3D CALCULATIONS AT T = 800.0 MICROSECONDS

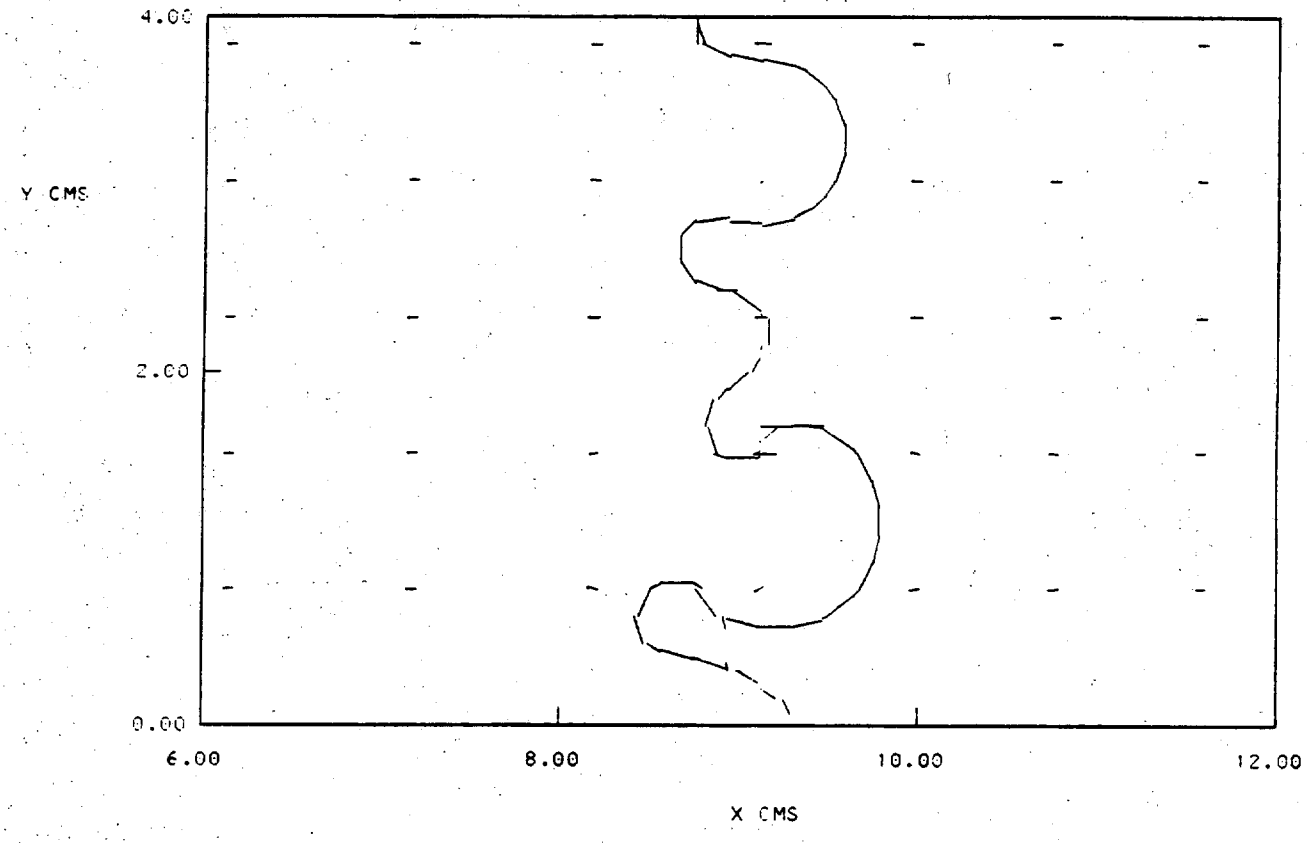

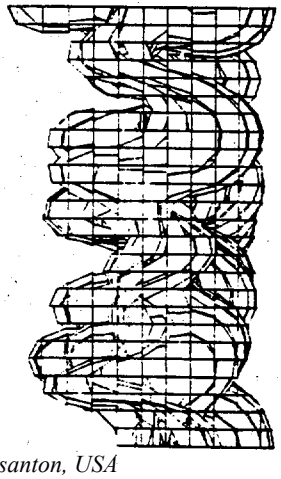

INTERFACE PLOT AND DENSITY CONTOURS FROM 2D CALCULATION AT T = 1000.0 MICROSECONDS

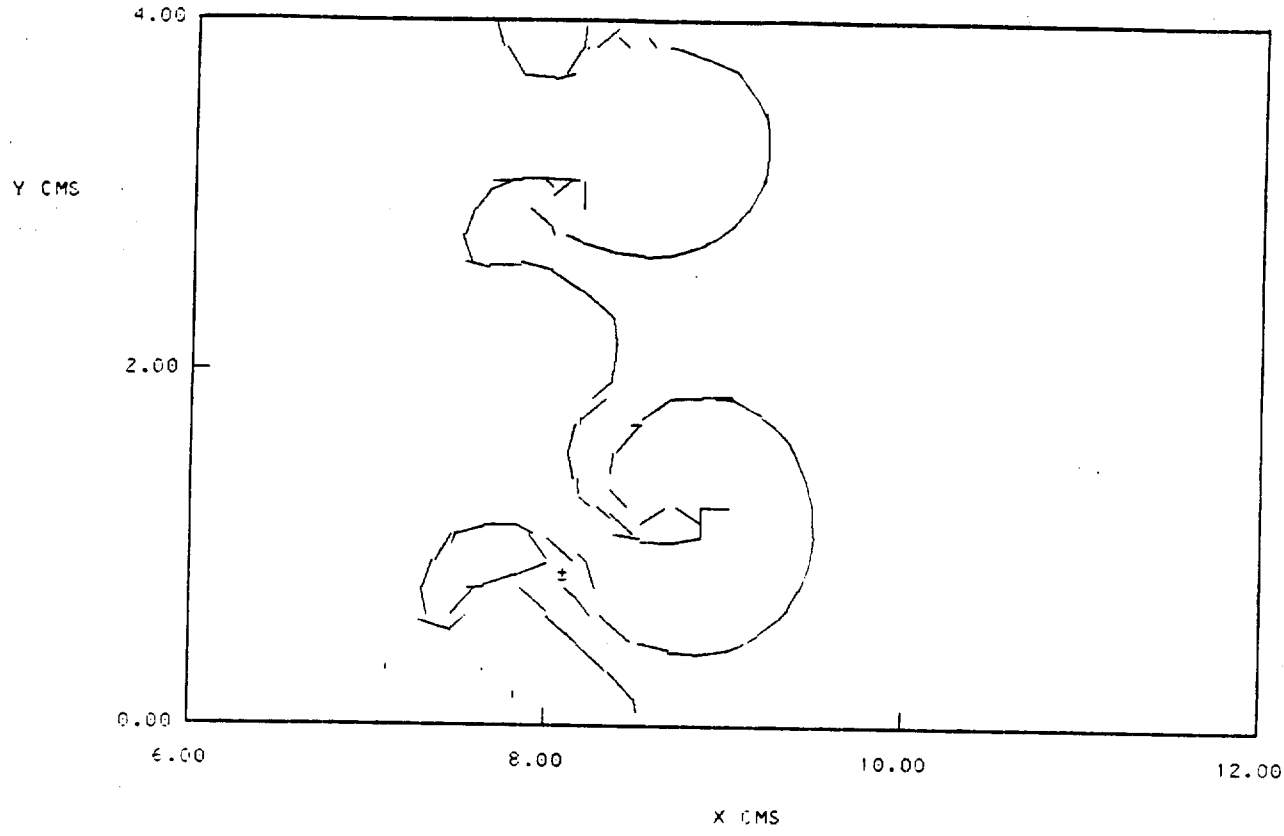

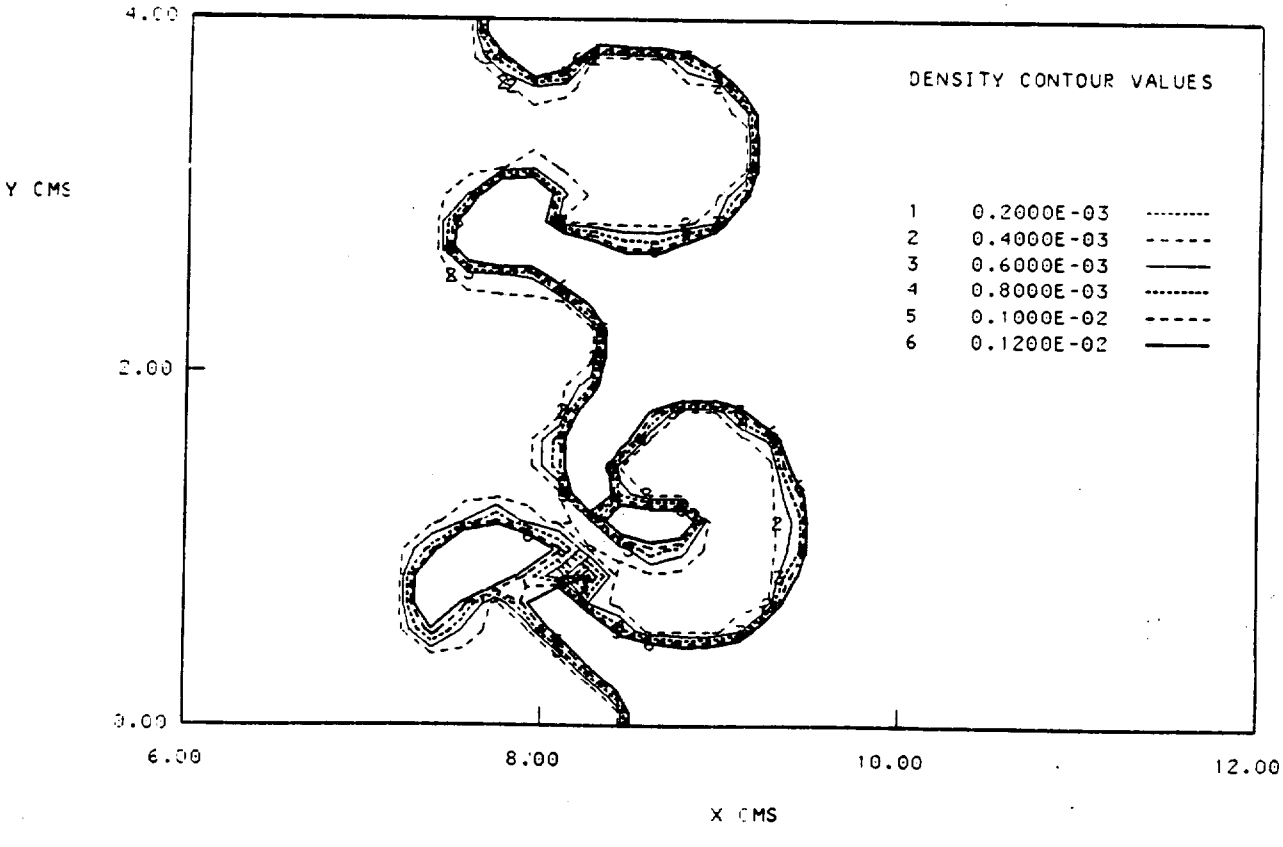

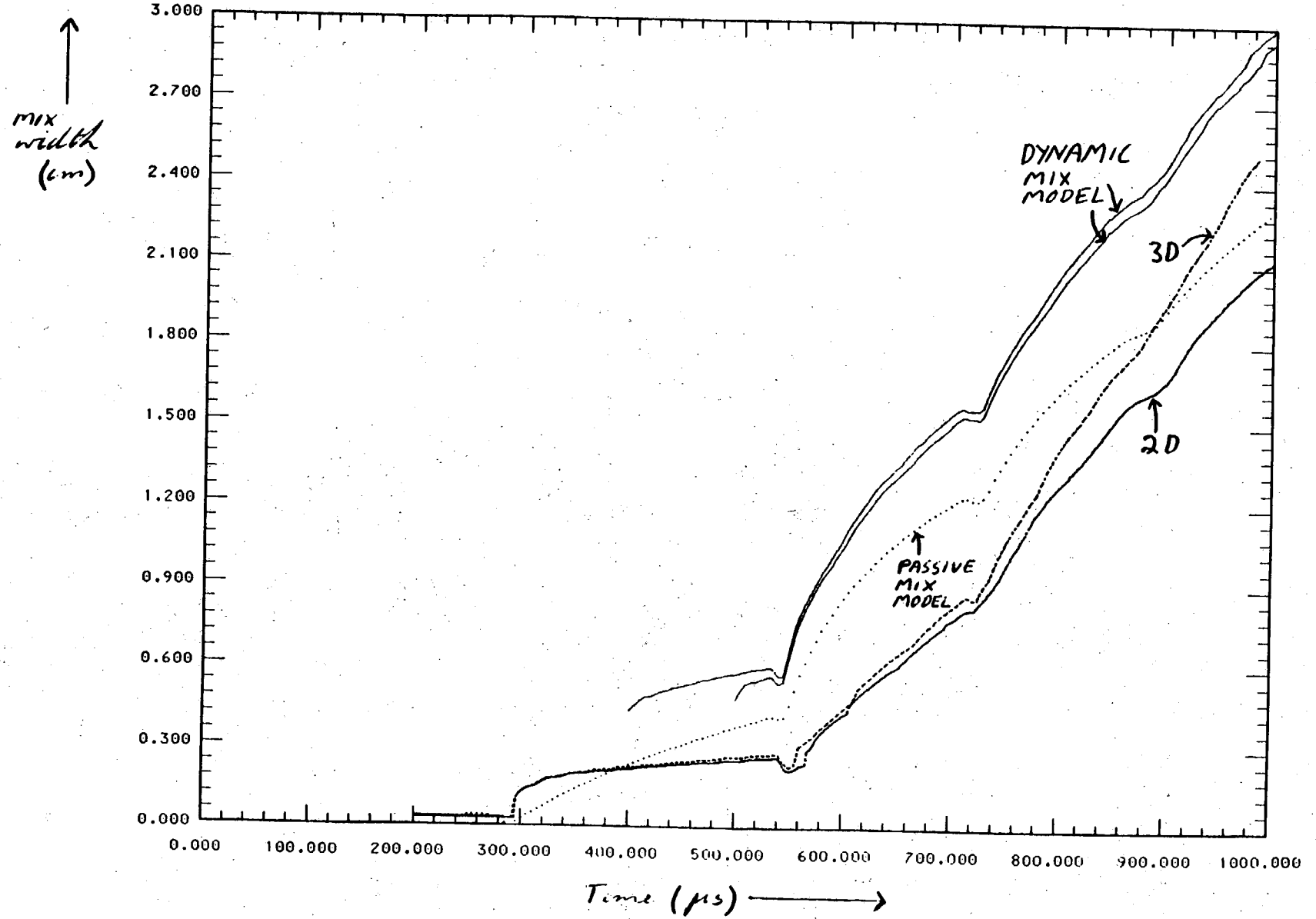
mix width (cm)
3.000
2.700
2.400
2.100
1.800
1.500
1.200
0.900
0.600
0.300
0.000
0.000
100.000
200.000
300.000
400.000
500.000
600.000
700.000
800.000
900.000
1000.000
Time (μs)
DYNAMIC MIX MODEL
3D
2D
PASSIVE MIX MODEL

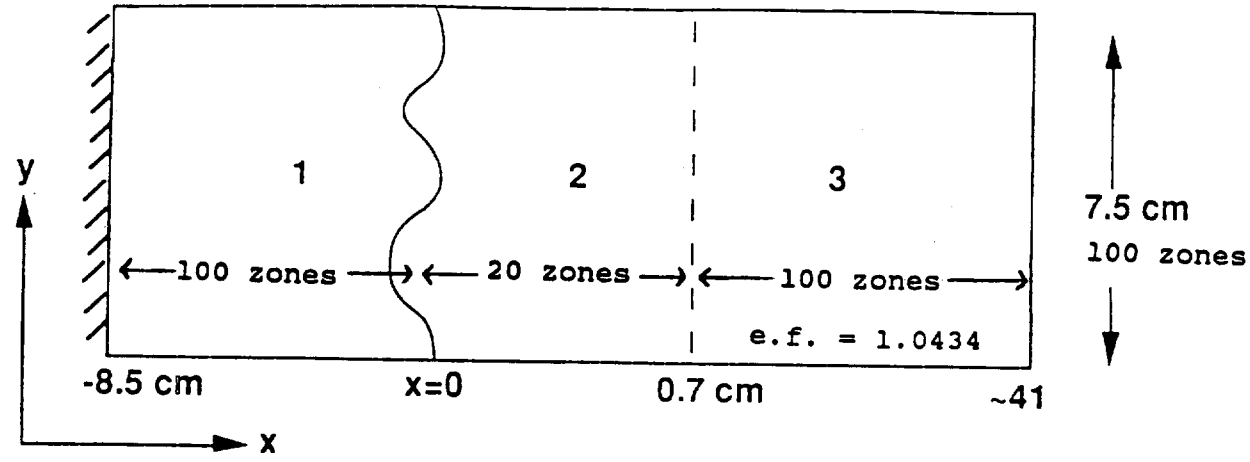

REGION 1: HELIUM AT REST
Density = 0.0001694 g/cm^3
Pressure - 1.013 bar
γ = 1.67

REGION 2: AIR AT REST
Density = 0.001225 g/cm^3
Pressure = 1.013 bar
γ = 1.4

REGION 3: SHOCKED AIR, VELOCITY = 12.29 cm/ms MACH # = 1.24
Density = 0.0017285 g/cm3
Pressure = 1.6482 bar
γ = 1.4

TEST PROBLEM 2 AIR/SF6 SHOCK TUBE

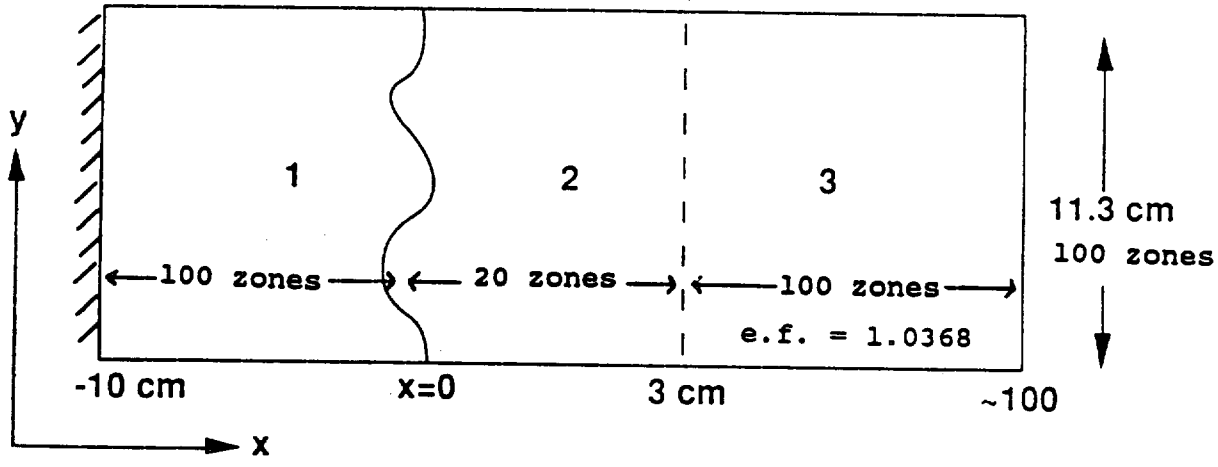

REGION 1: SF6 AT REST
Density = 0.006187 g/cm^3
Pressure = 1.013 bar
γ = 1.06

REGION 2: AIR AT REST
Density = 0.001225 g/cm^3
Pressure = 1.013 bar
γ = 1.4

REGION 3: SHOCKED AIR, VELOCITY = 15.95 cm/ms MACH # = 1.32
Density = 0.001900 g/cm3
Pressure = 1.8993 bar

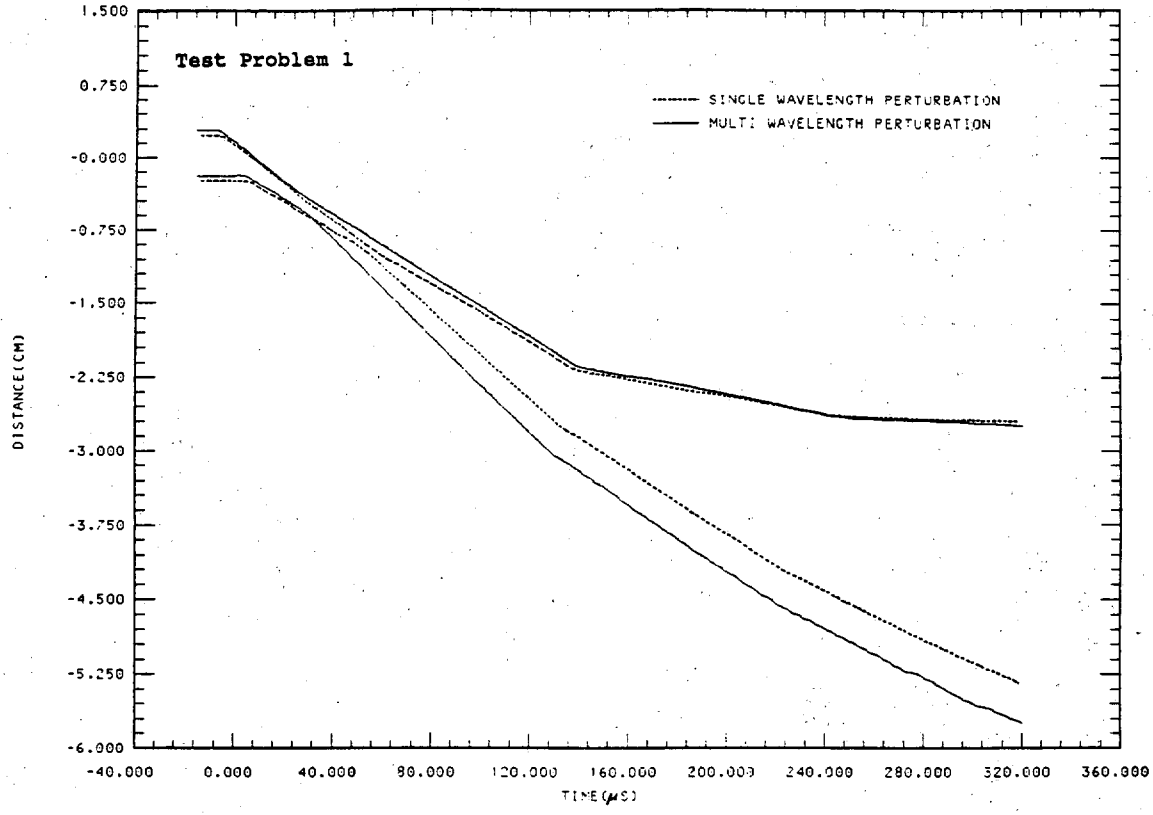
Test Problem 1
SINGLE WAVELENGTH PERTURBATION
MULTI WAVELENGTH PERTURBATION
DISTANCE(CM)
1.500
0.750
-0.000
-0.750
-1.500
-2.250
-3.000
-3.750
-4.500
-5.250
-6.000
-40.000
0.000
40.000
80.000
120.000
160.000
200.000
240.000
280.000
320.000
360.000
TIME(μS)

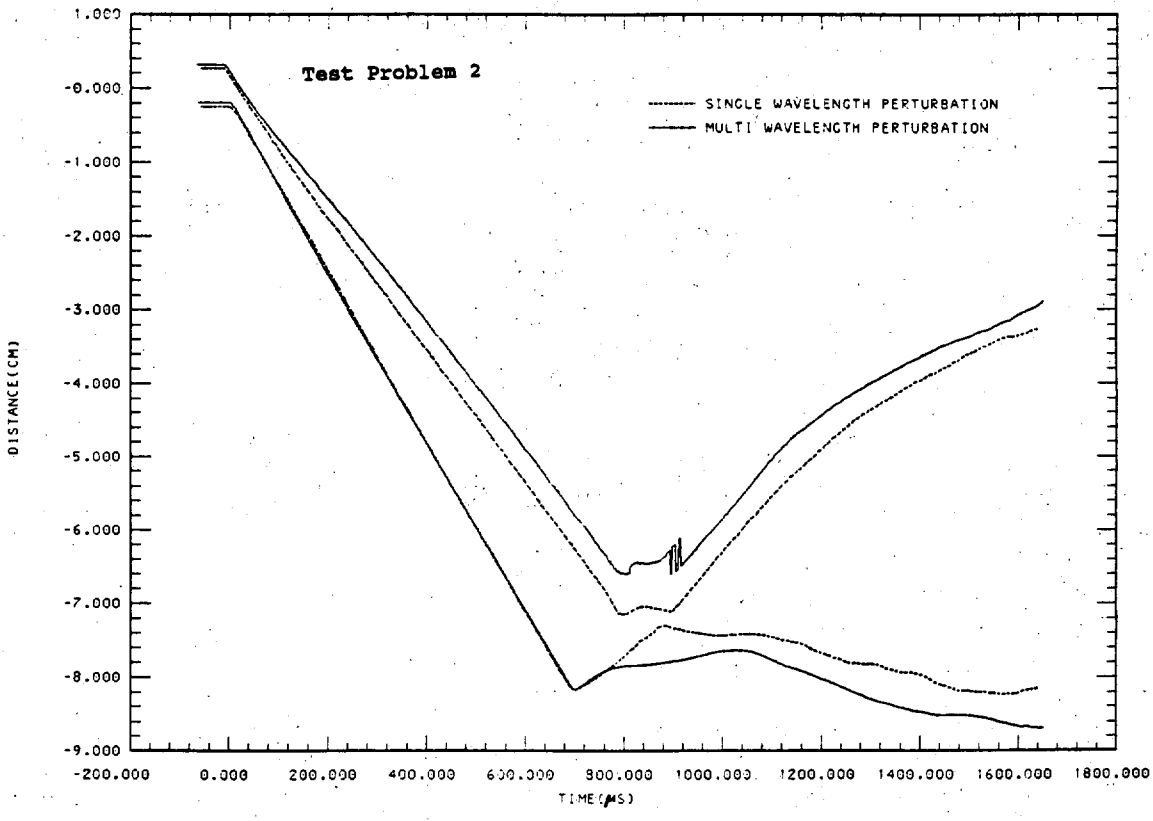
Test Problem 2
SINGLE WAVELENGTH PERTURBATION
MULTI WAVELENGTH PERTURBATION
DISTANCE(CM)
1.000
-0.000
-1.000
-2.000
-3.000
-4.000
-5.000
-6.000
-7.000
-8.000
-9.000
-200.000
0.000
200.000
400.000
600.000
800.000
1000.000
1200.000
1400.000
1600.000
1800.000
TIME(μS)

TEST PROBLEM 1 AIR/HELIUM SHOCK TUBE SINGLE WAVELENGTH

T = 20 microseconds log density contours

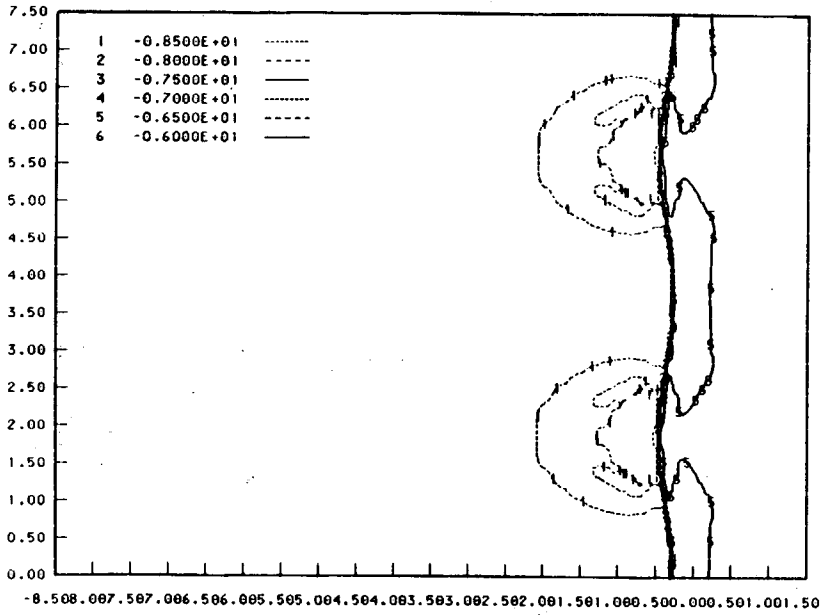

T = 120 microseconds log density contours

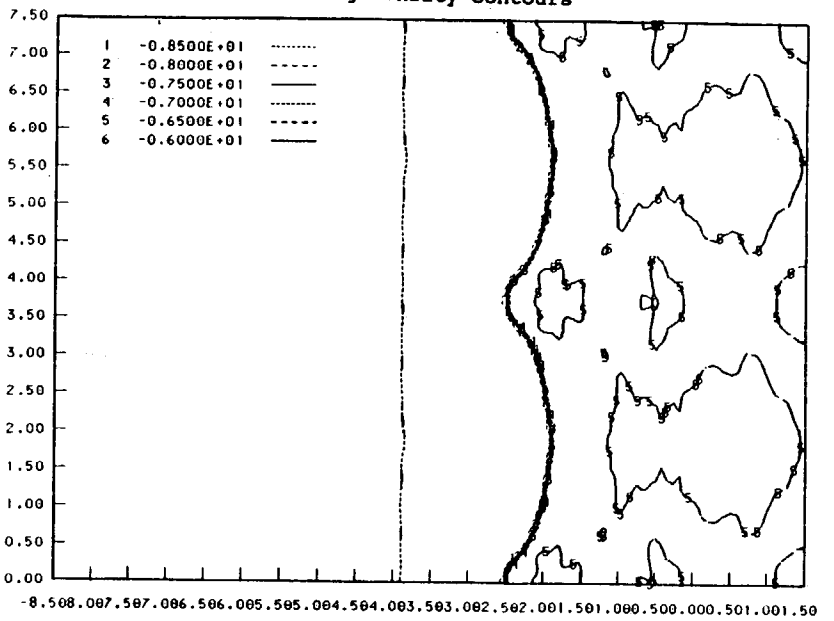

T = 220 microseconds interface plot

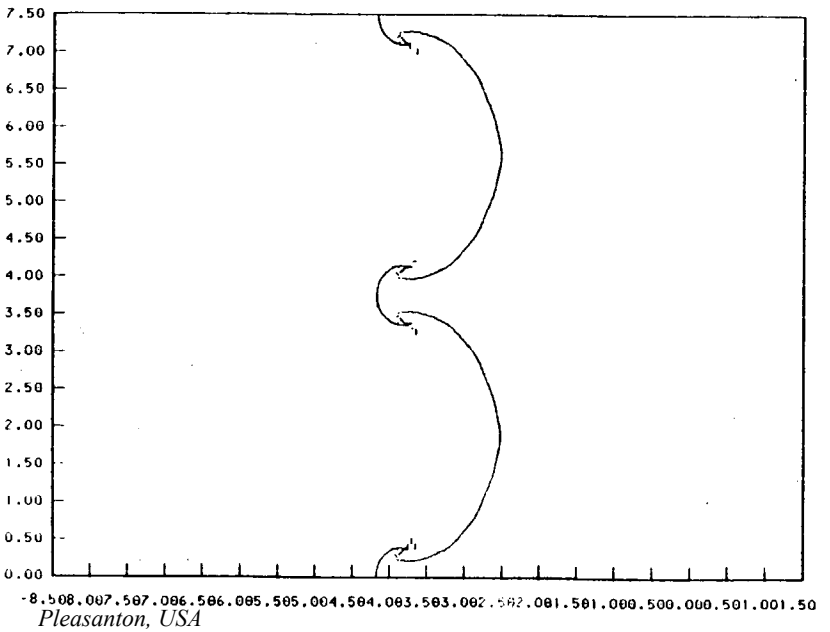

T = 320 microseconds interface plot

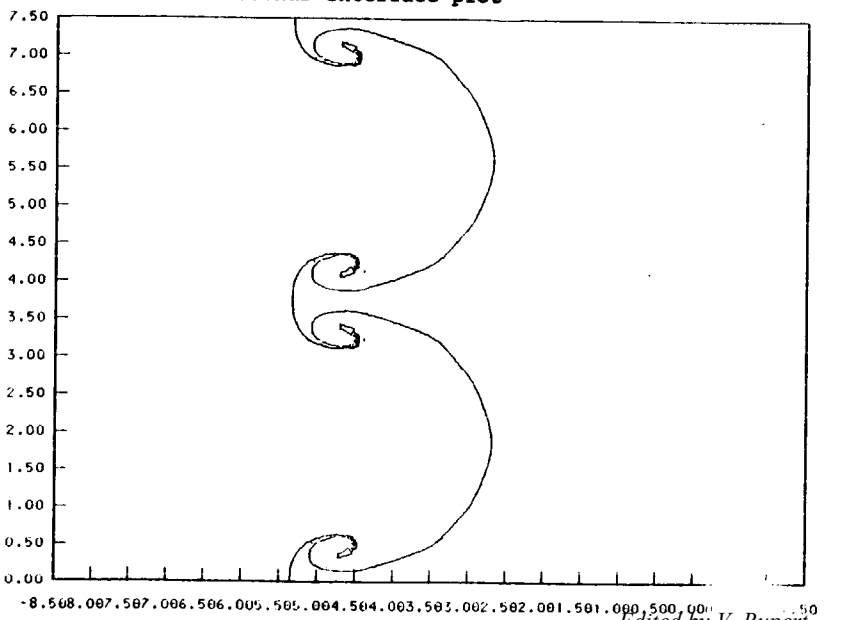

TEST PROBLEM 1 AIR/HELIUM SHOCK TUBE MULTI WAVELENGTH

T = 20 microseconds log density contours

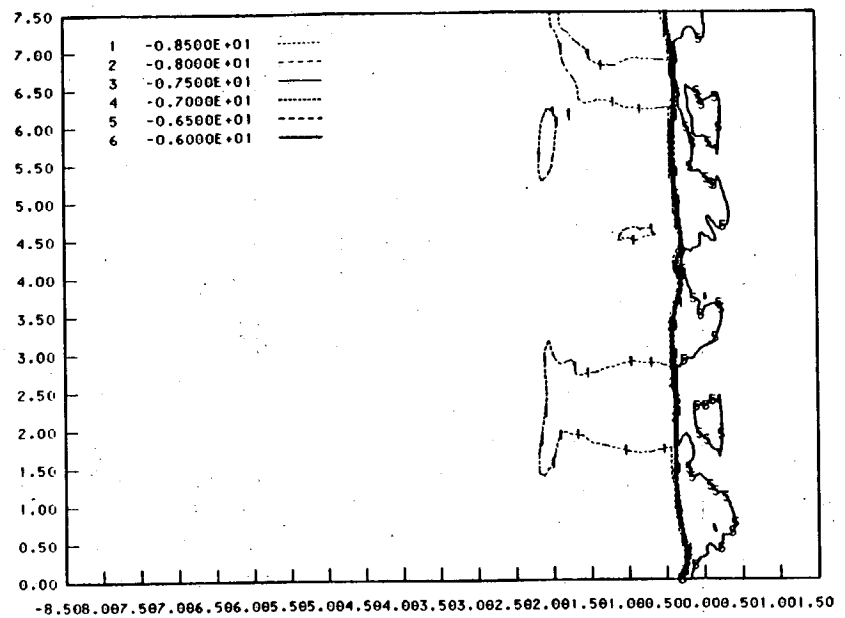

T = 120 microseconds log density contours

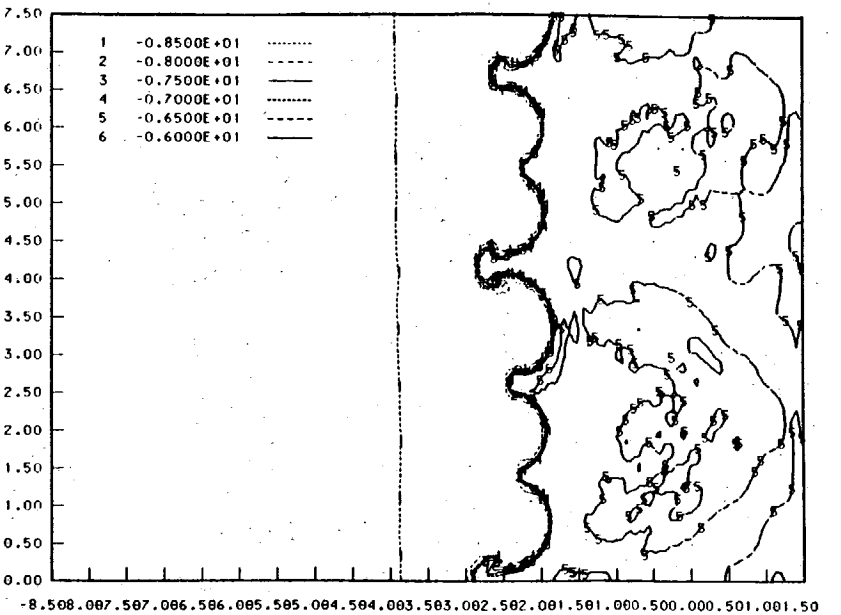

T = 220 microseconds interface plot

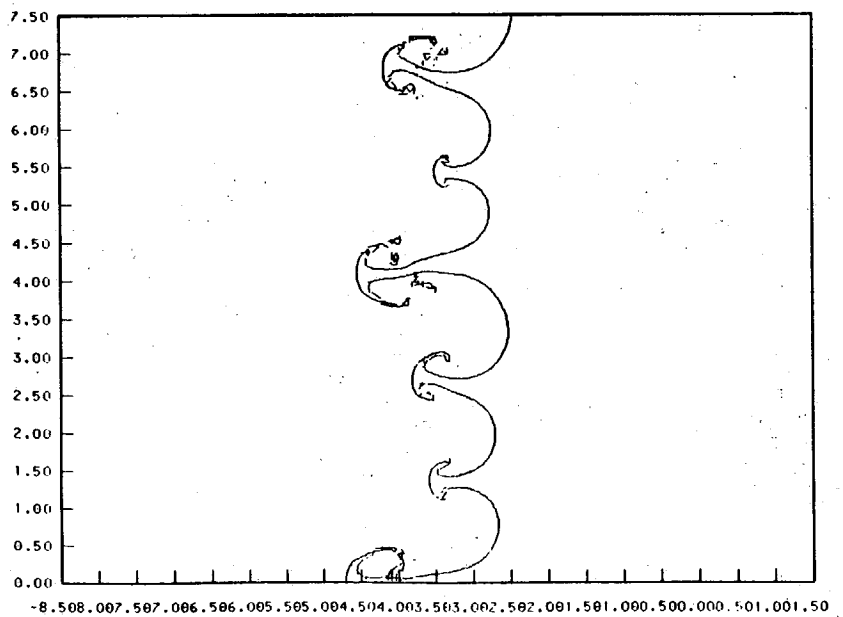

T = 320 microseconds interface plot

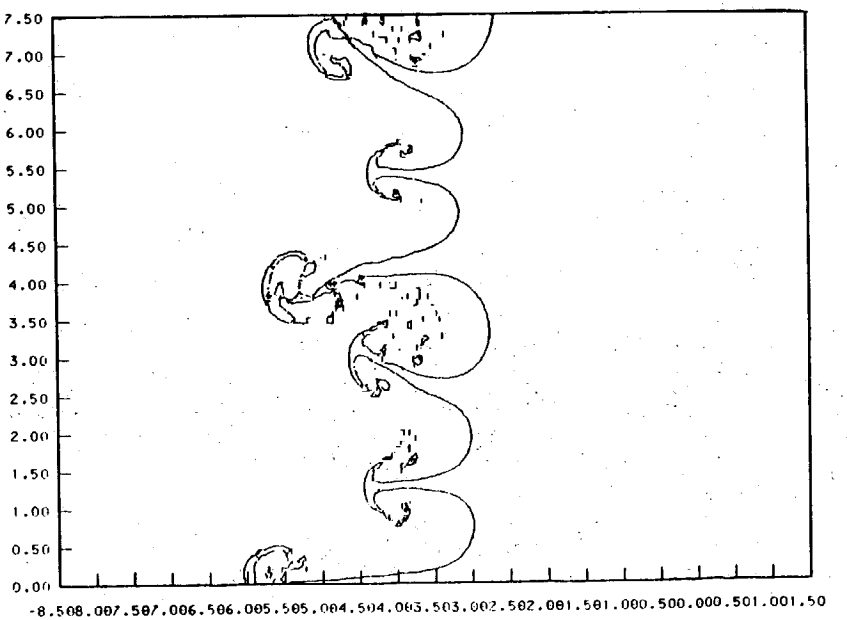

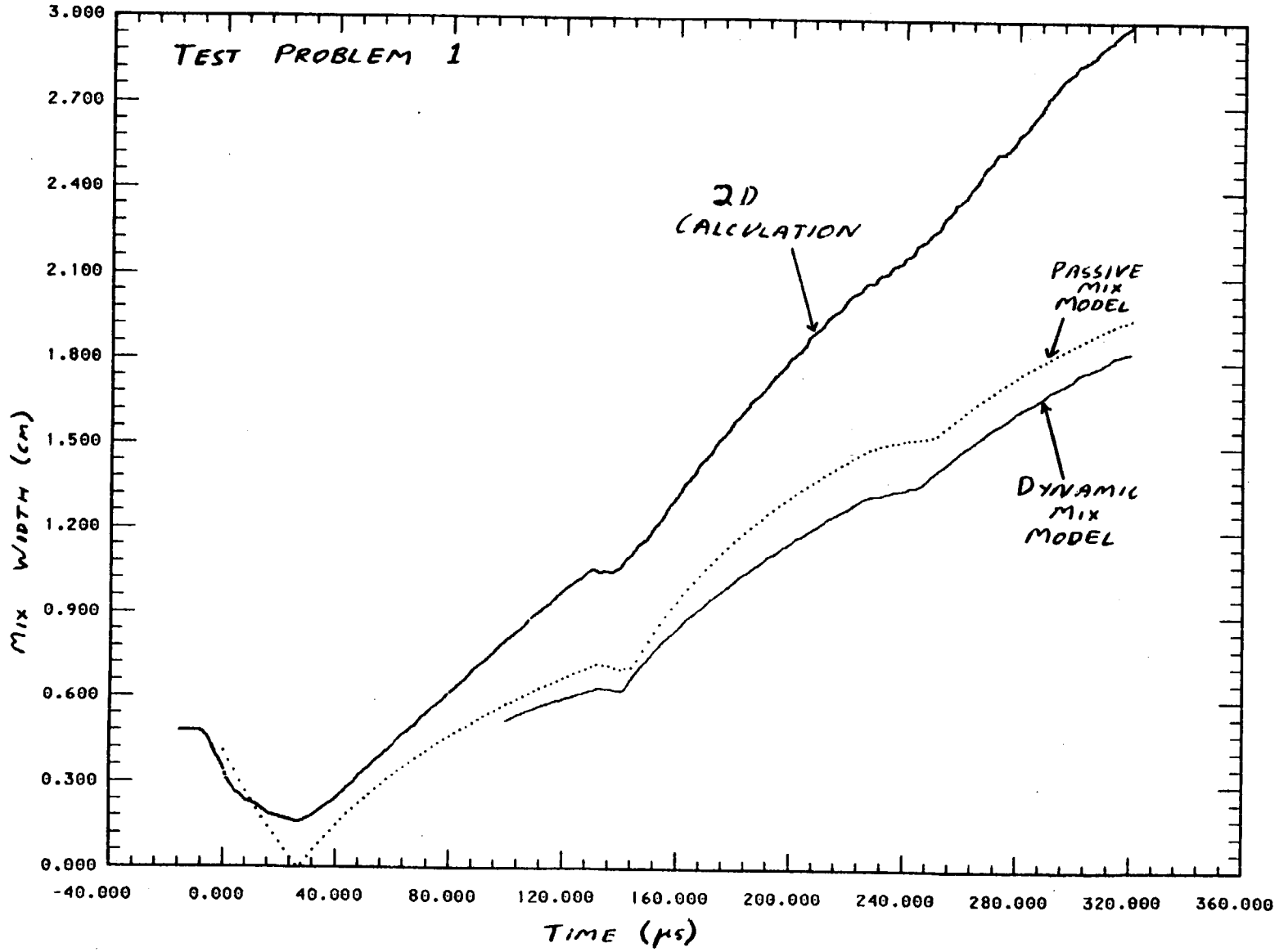
TEST PROBLEM 1
2D CALCULATION
PASSIVE MIX MODEL
DYNAMIC MIX MODEL
MIX WIDTH (cm)
TIME (μs)
3.000
2.700
2.400
2.100
1.800
1.500
1.200
0.900
0.600
0.300
0.000
-40.000
0.000
40.000
80.000
120.000
160.000
200.000
240.000
280.000
320.000
360.000

TEST PROBLEM 2 AIR/SF6 SHOCK TUBE SINGLE WAVELENGTH

T = 300 microseconds log density contours

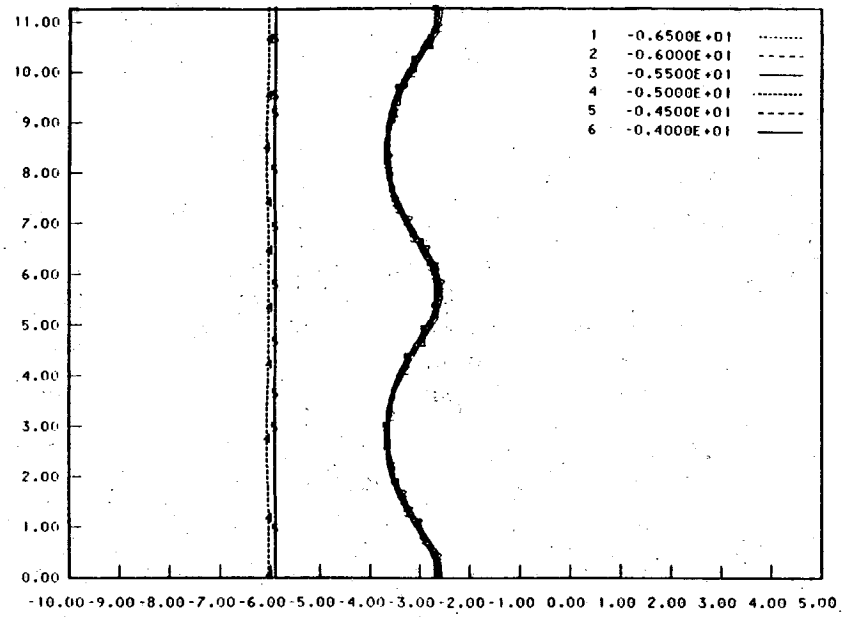

T = 700 microseconds log density contours

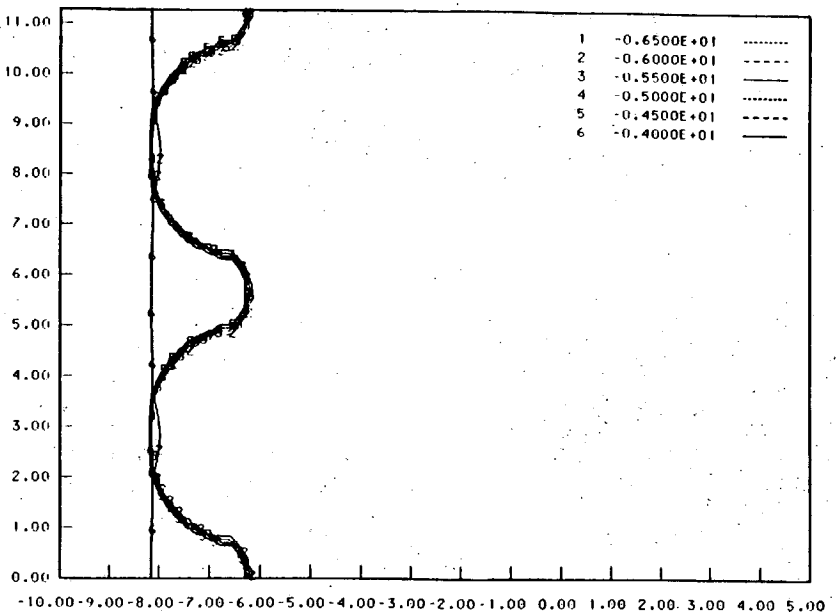

T = 1100 microseconds interface plot

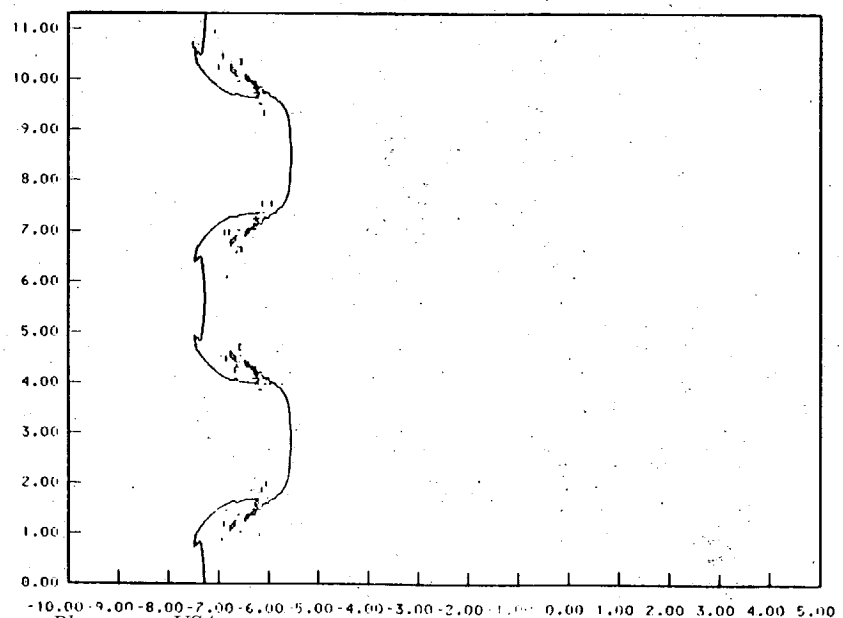

T = 1650 microseconds interface plot

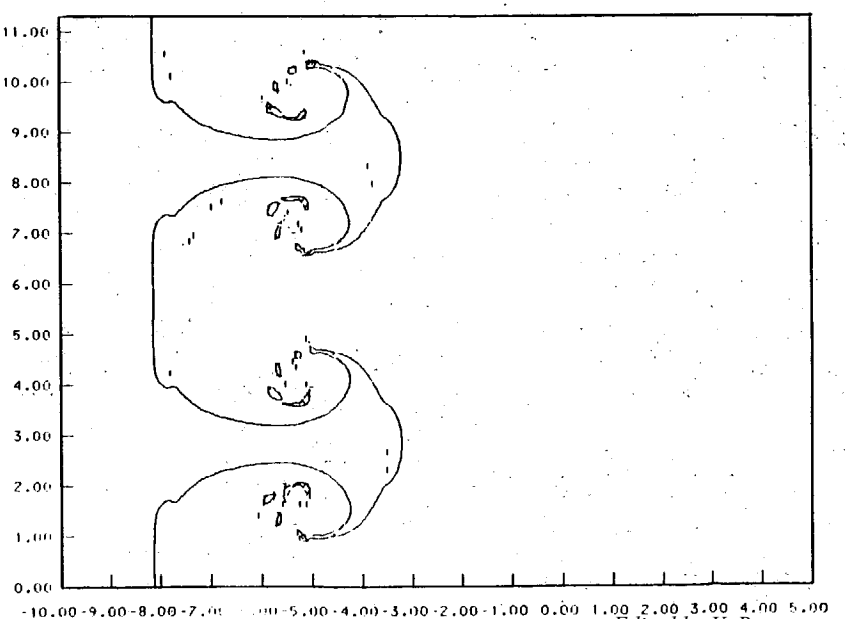

TEST PROBLEM 2 AIR/SF6 SHOCK TUBE MULTI WAVELENGTH

T = 300 microseconds log density contours

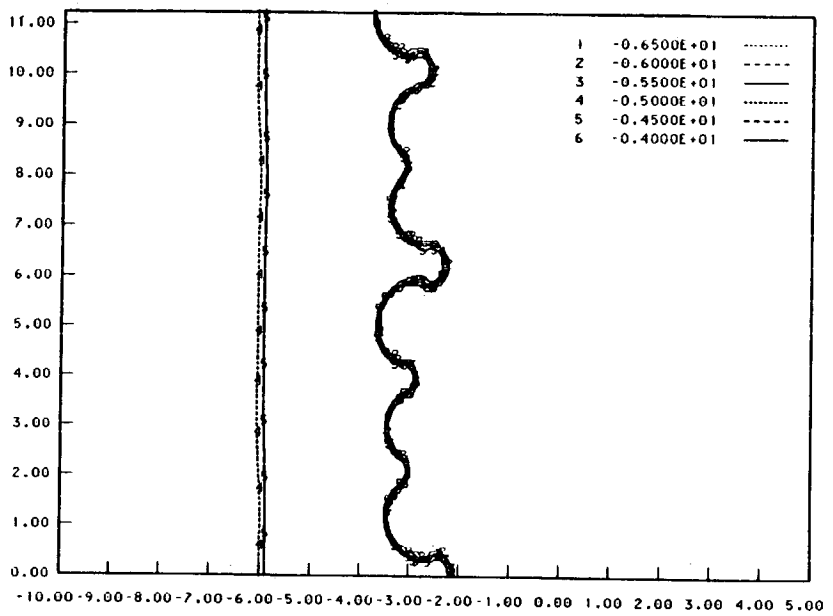

T = 700 microseconds log density contours

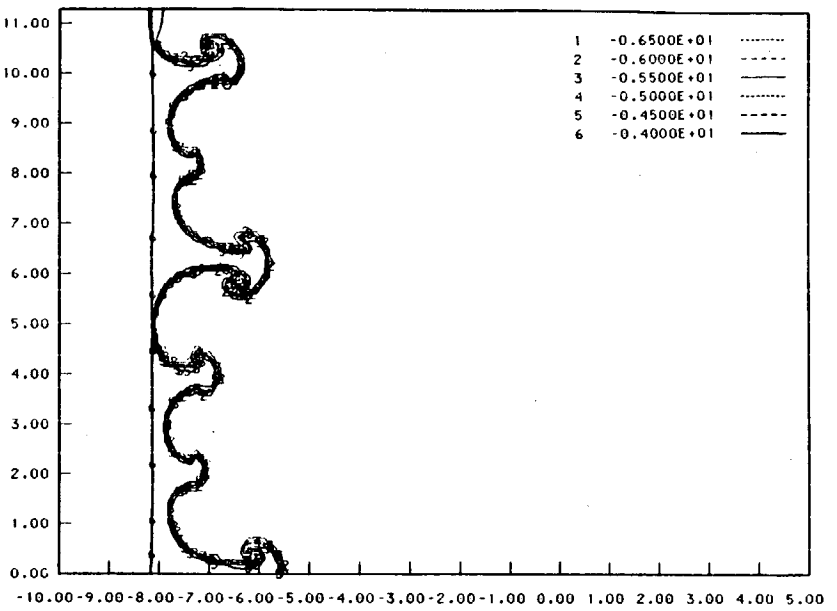

T = 1100 microseconds interface plot

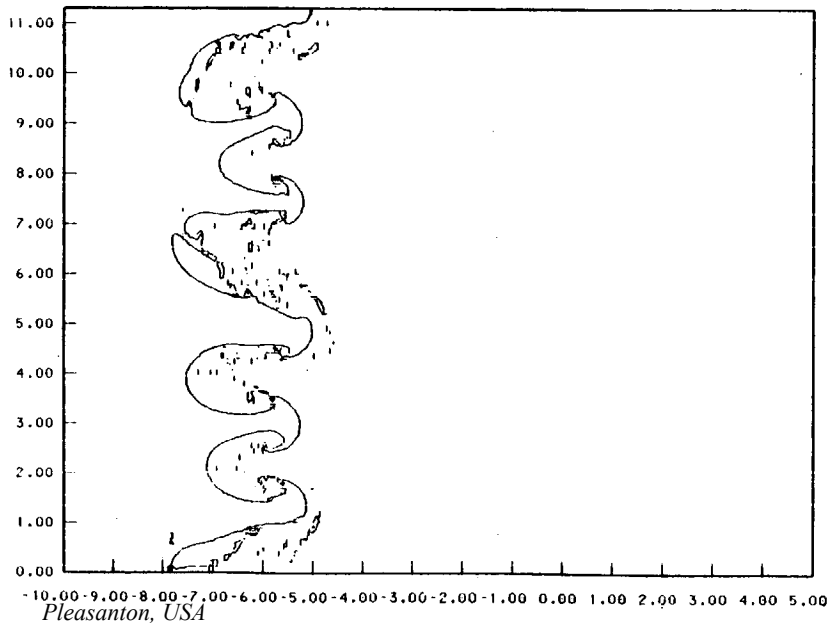

T = 1650 microseconds interface plot

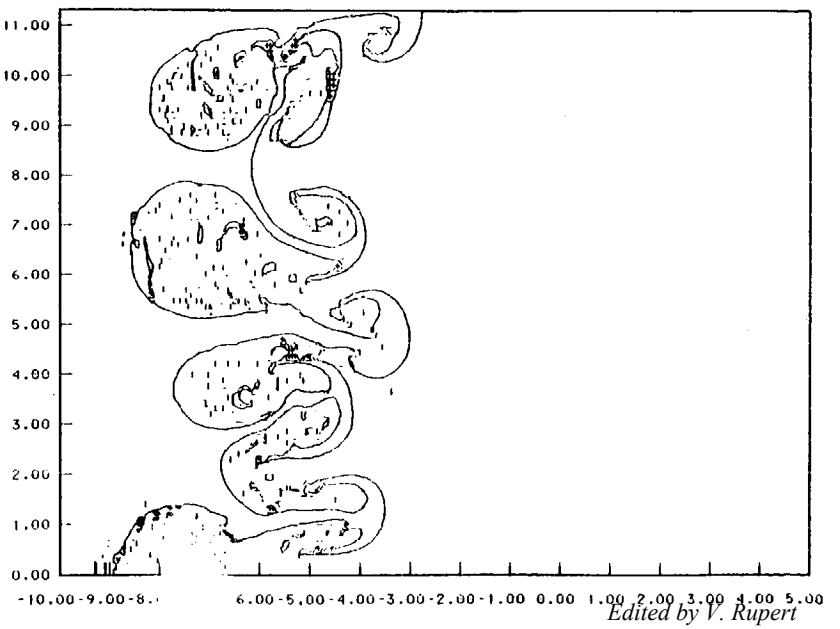

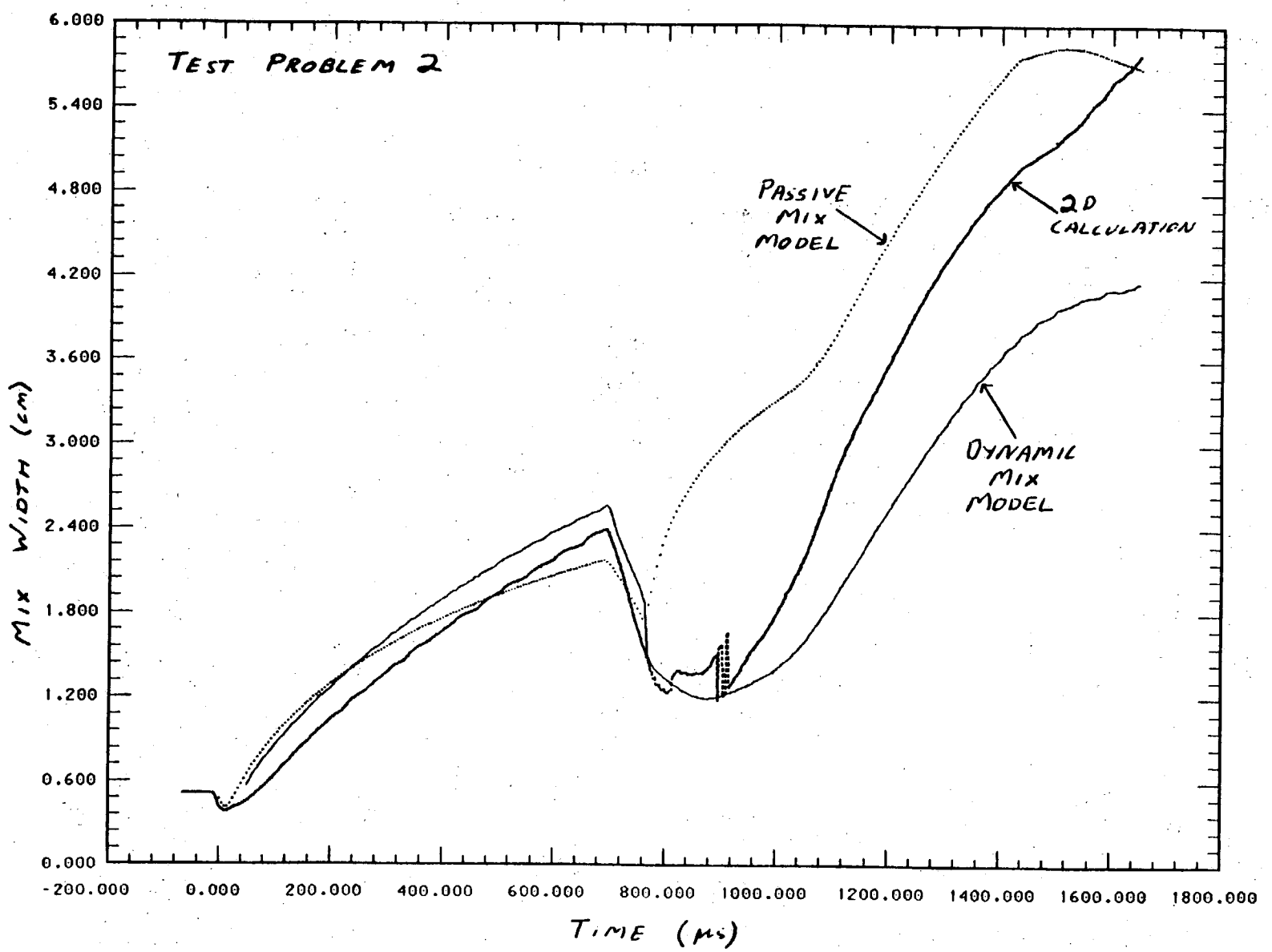
TEST PROBLEM 2
PASSIVE MIX MODEL
2D CALCULATION
DYNAMIC MIX MODEL
MIX WIDTH (cm)
TIME (μs)
6.000
5.400
4.800
4.200
3.600
3.000
2.400
1.800
1.200
0.600
0.000
-200.000
0.000
200.000
400.000
600.000
800.000
1000.000
1200.000
1400.000
1600.000
1800.000

FOULNESS SHOCK TUBE CALCULATION

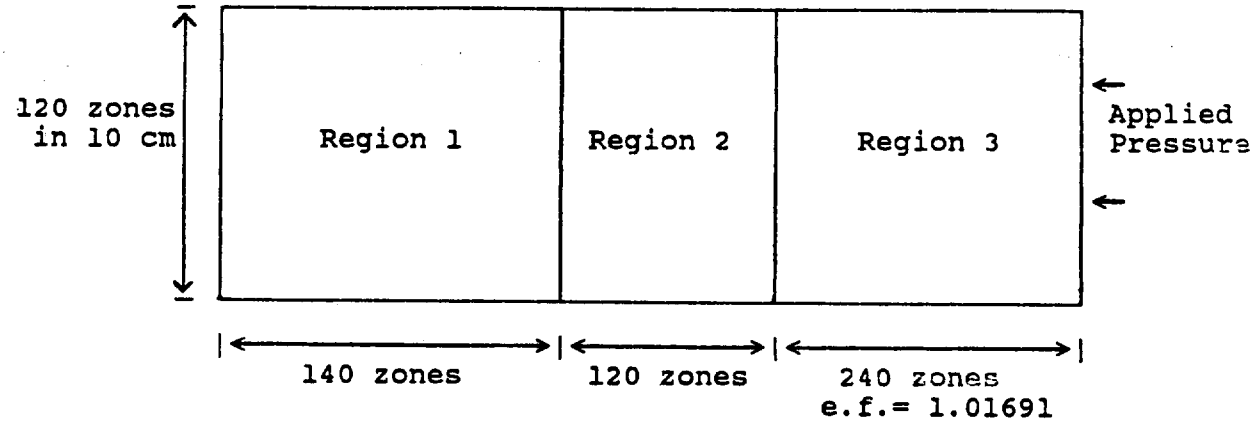

Problem start time = -100.0 microseconds
=> shock passes interface at t = 0

Region 1: Helium
length = 14.0 cm
rho = 0.000166064 g/cm^3
E = 0.009814537 Mbcc/g
P = 1.0268 bar

Region 2: Air
length = 4.4802918 cm
rho = 0.001195230 g/cm^3
E = 0.002142348 Mbcc/g
P = 1.0268 bar

Region 3: Air
length = 81.5197082 cm
rho = 0.001793373 g/cm^3
E = 0.002540525 Mbcc/g
vel = 0.014943101 cm/musec

Pressure behind shock = 1.8270 bar (11.606 psi above ambiant)
giving a Mach no of 1.2914

Ideal gas equations of state used with ratios of specific heats

1.630 for helium
1.401 for air

Interface perturbation consist of a wavelength of 1.0 cm and an amplitude of 0.05 cm superimposed on a random Fourier series of 30 wavelengths with an rms amplitude of 0.01 cm.

FOULNESS SHOCK TUBE CALCULATION

Interface plot and vorticity contours at t = 0 microseconds

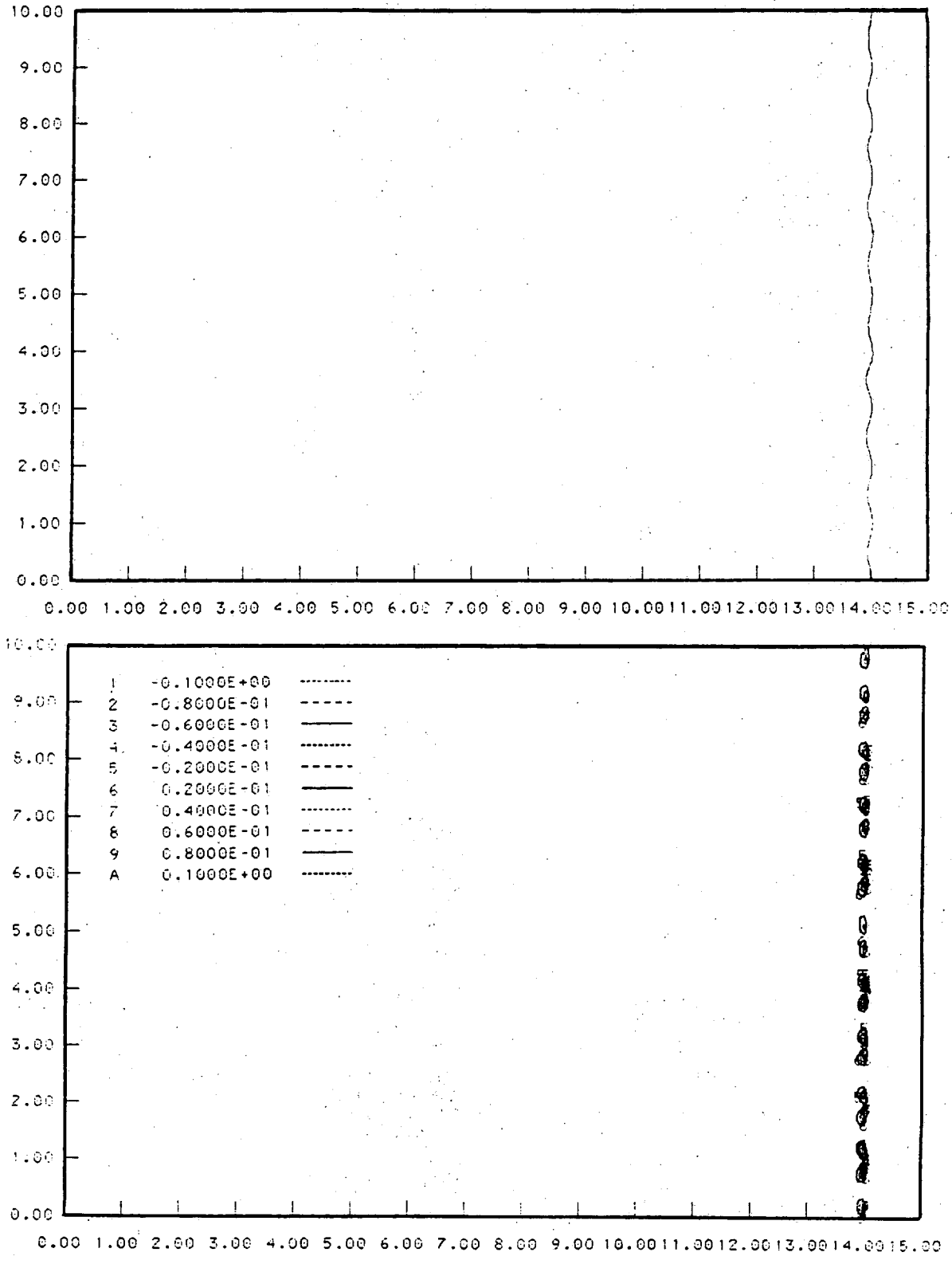

FOULNESS SHOCK TUBE CALCULATION

Interface plot and vorticity contours at t = 500 microseconds

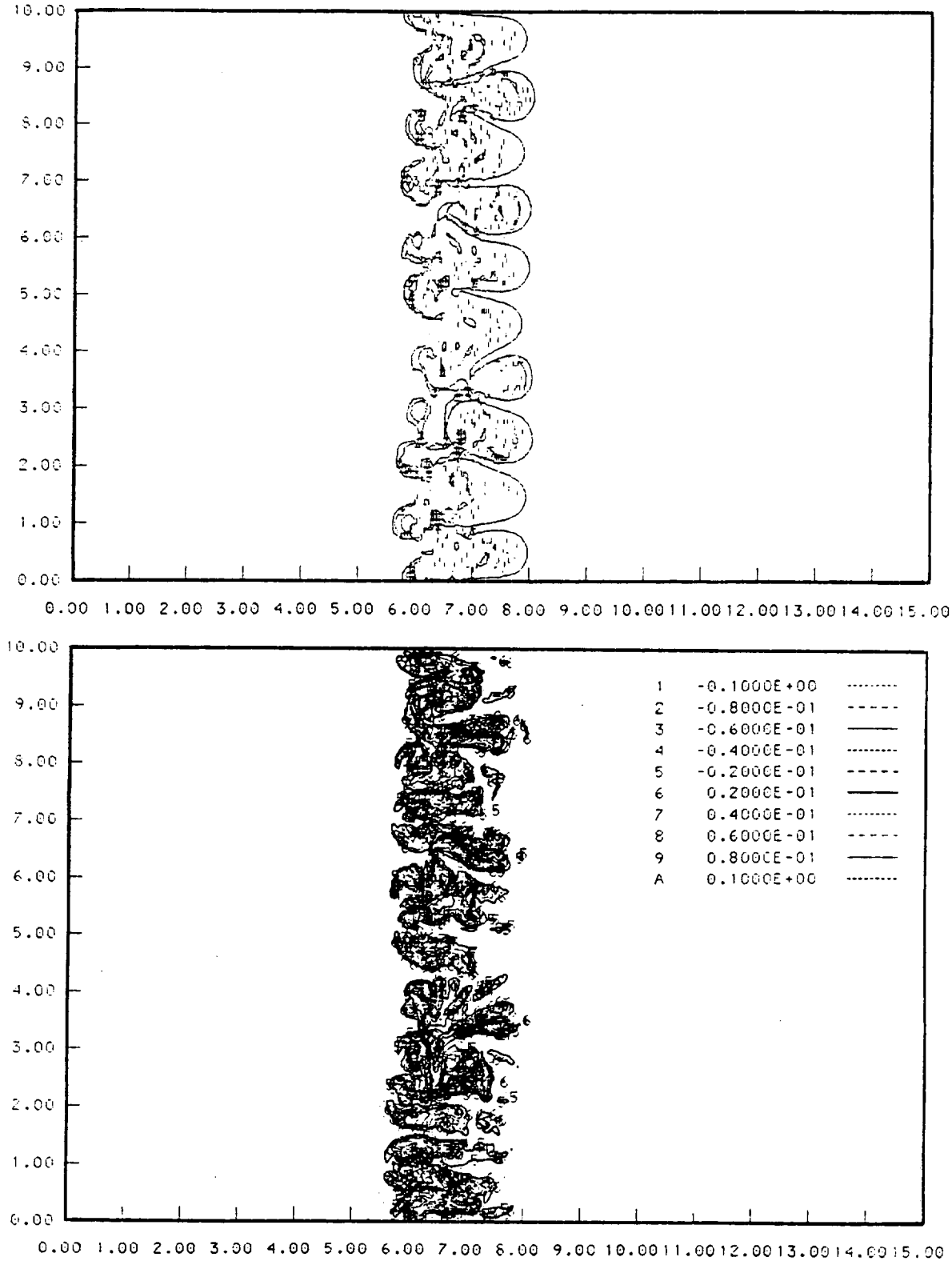

FOULNESS SHOCK TUBE CALCULATION

Interface plot and vorticity contours at t = 1000 microseconds

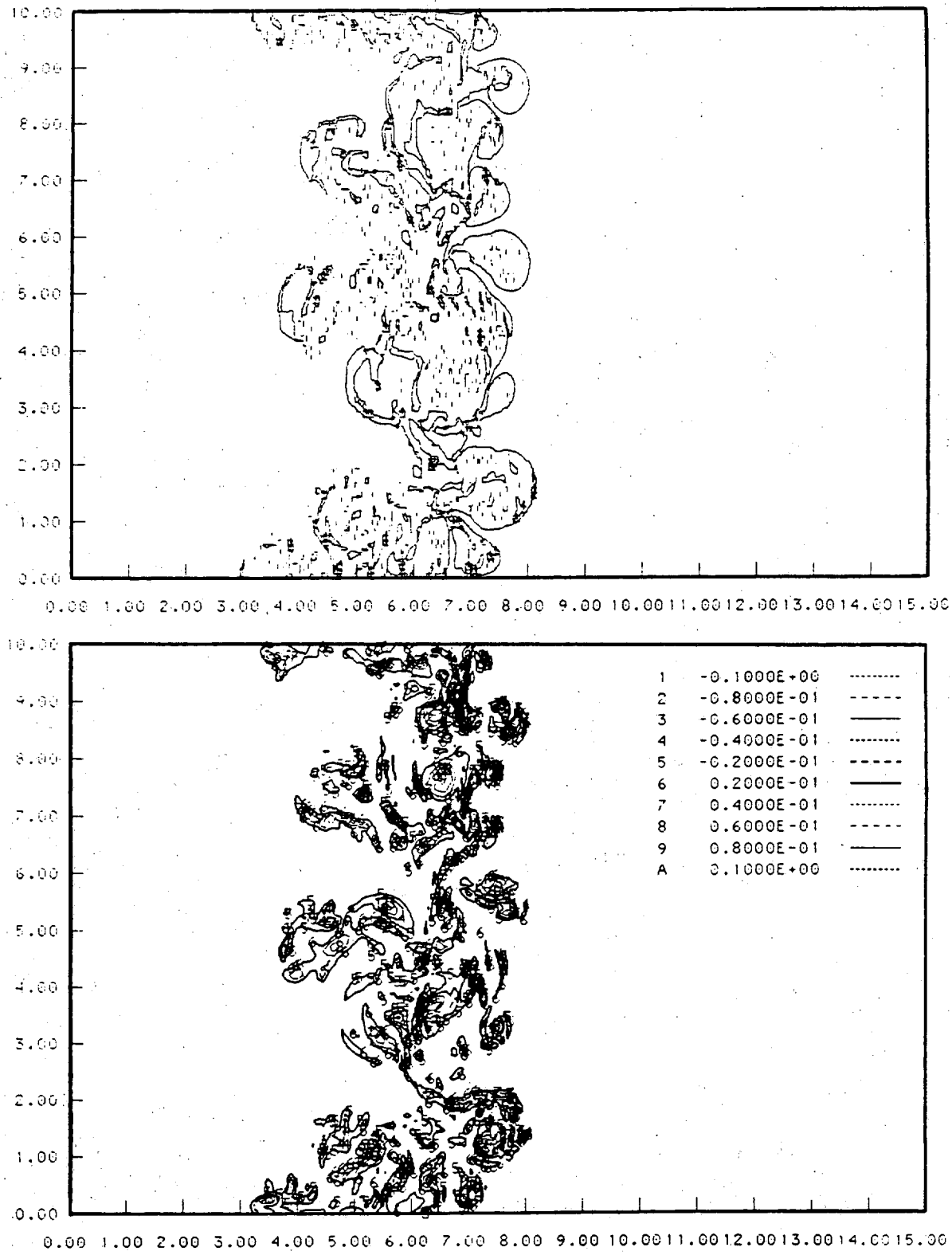

FOULNESS SHOCK TUBE CALCULATION

Density spectrum across the centre of the mix region

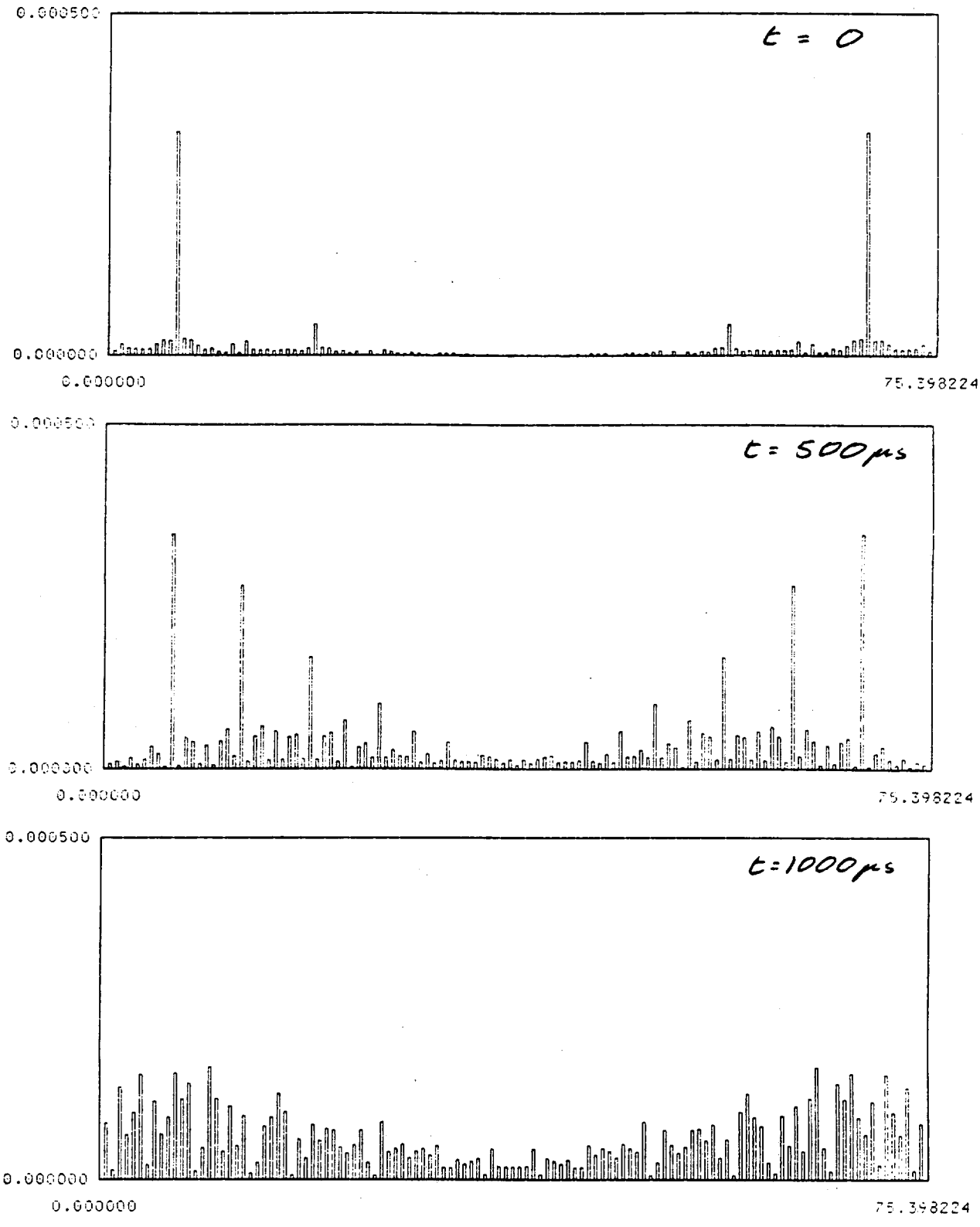

FOULNESS SHOCK TUBE CALCULATION

Comparison of volume fractions at t = 1000 microseconds

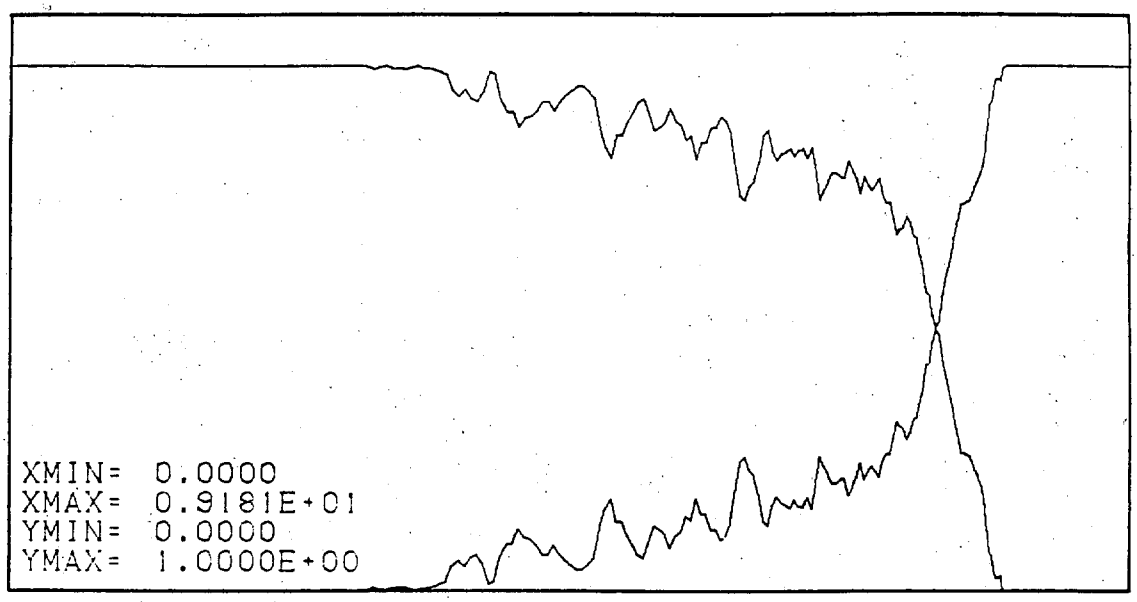

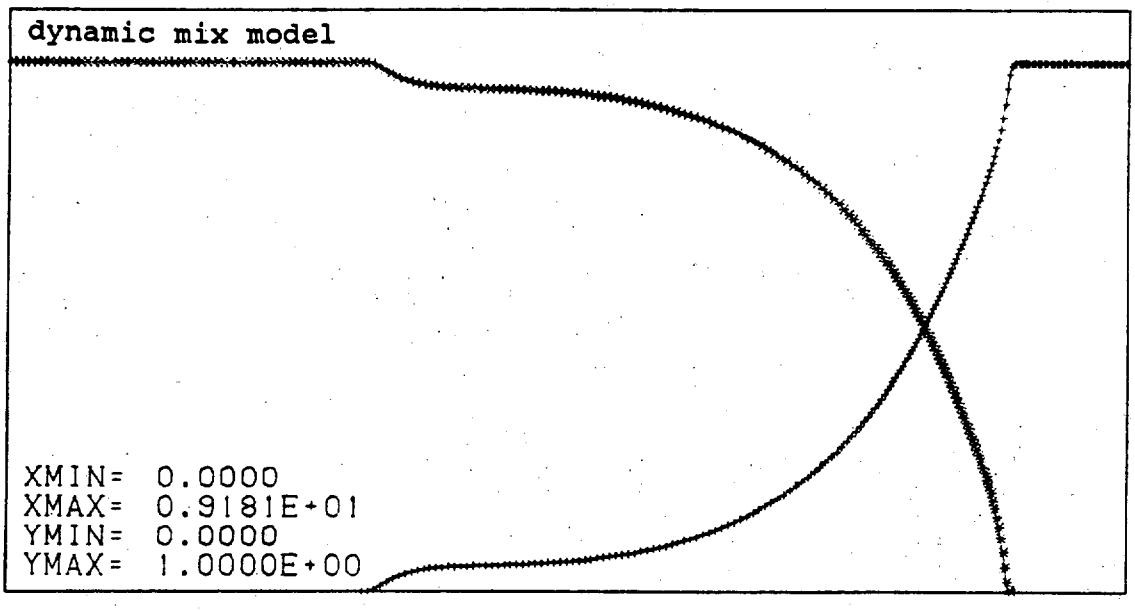

FOULNESS SHOCK TUBE CALCULATION

Comparison of calculated mix limits and experiment

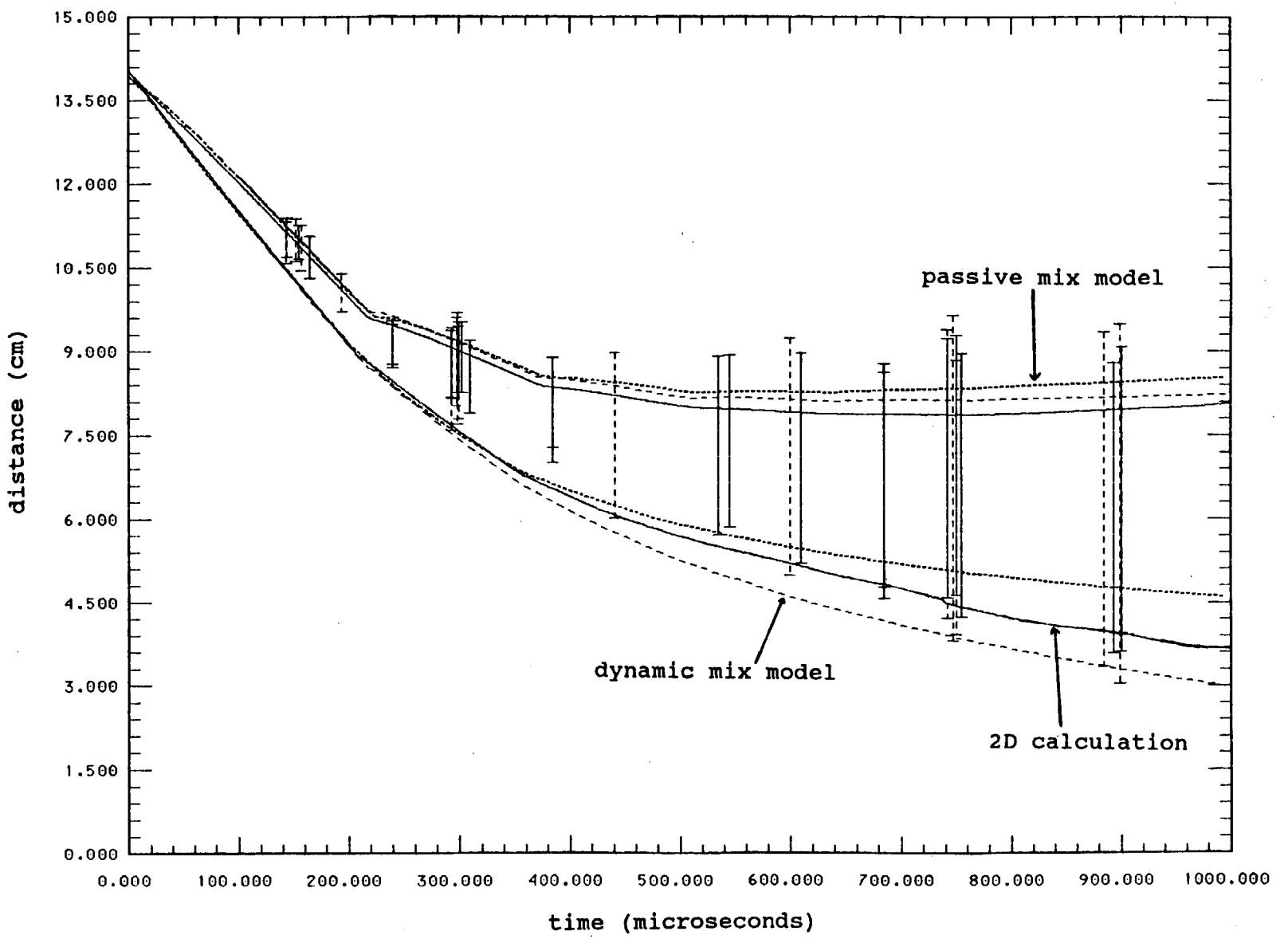

FOULNESS SHOCK TUBE CALCULATION

Comparison of calculated mix width and experiment

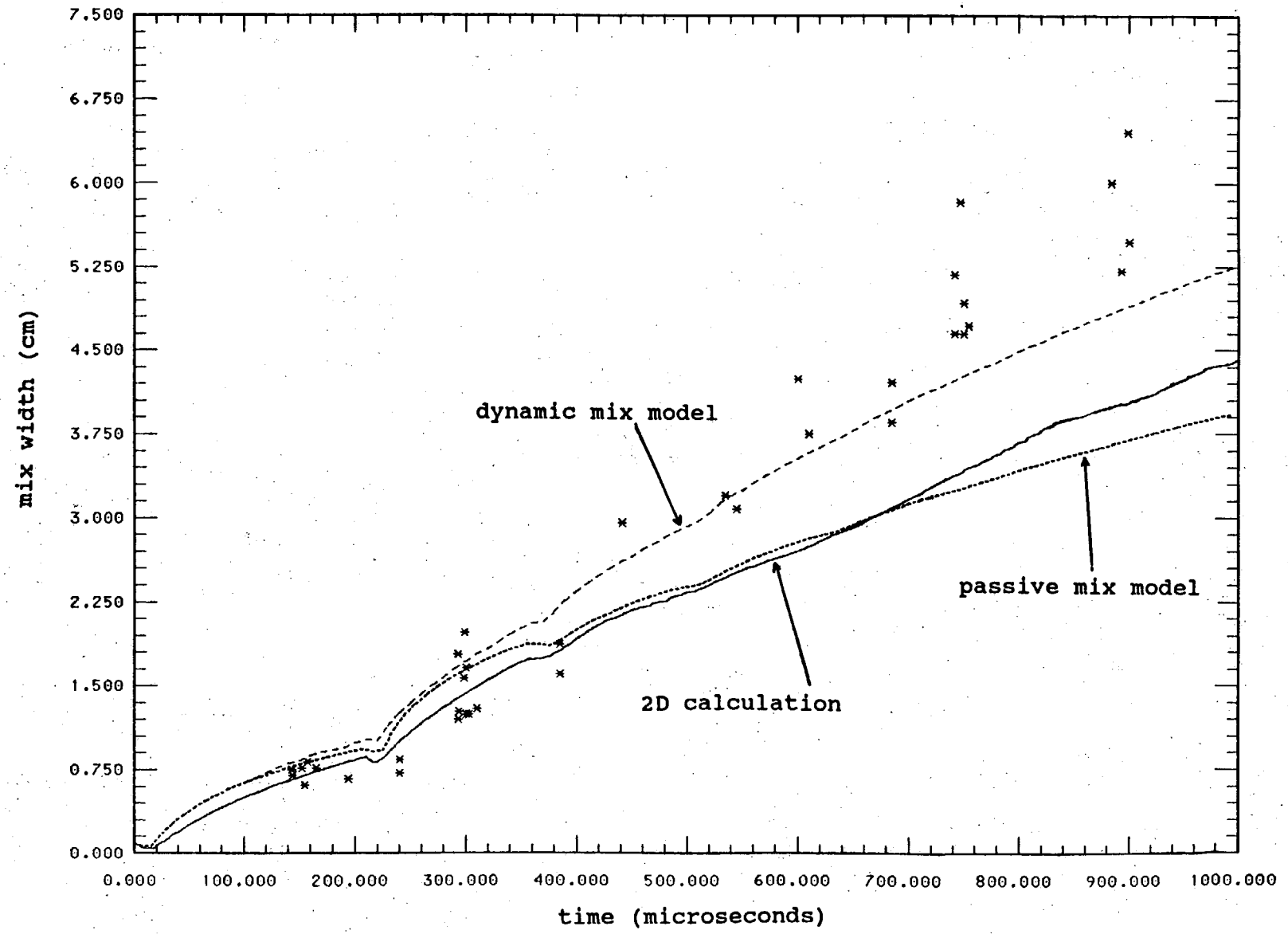

FOULNESS SHOCK TUBE CALCULATION

Comparison of mix velocities from three calculations

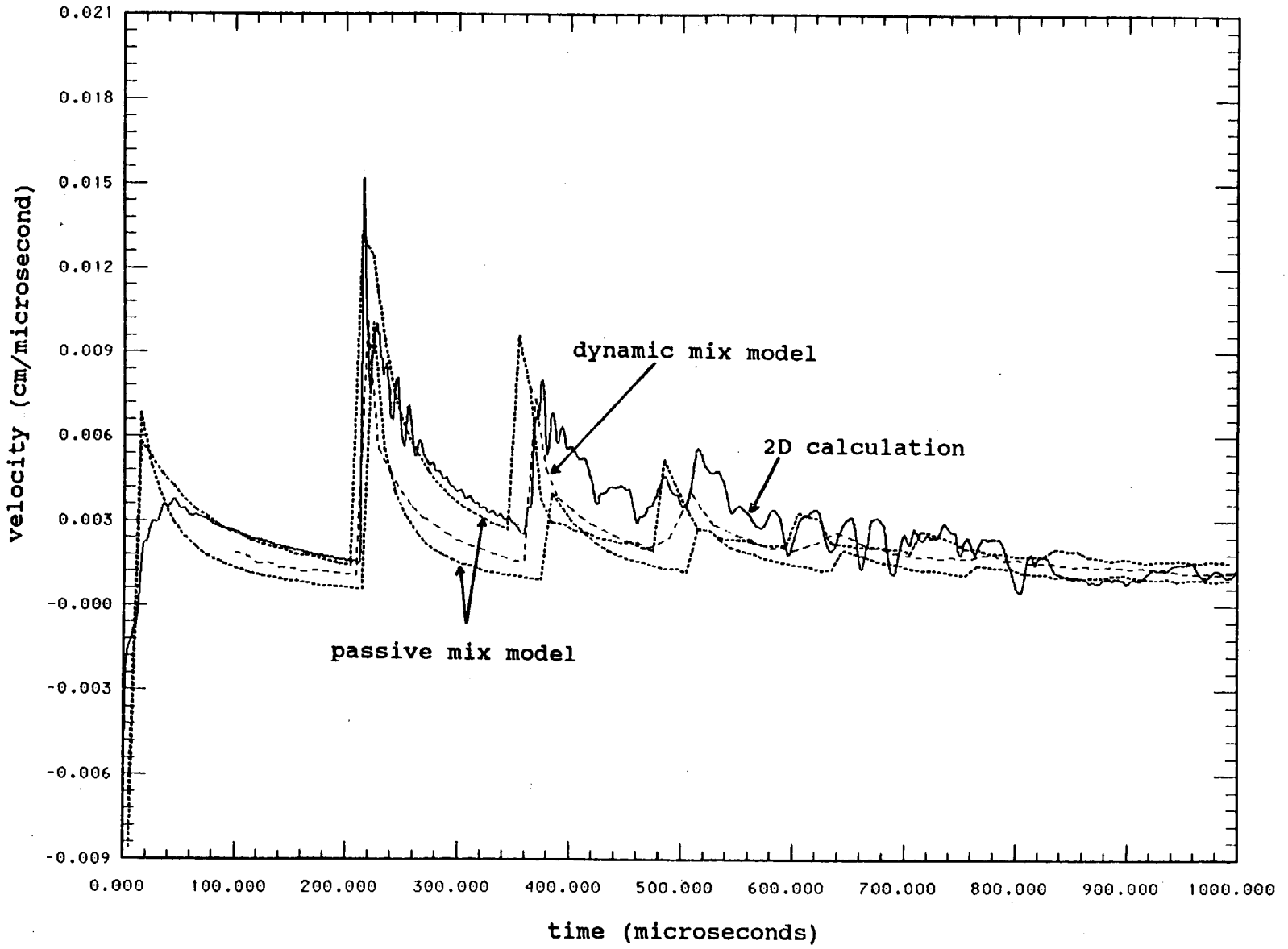

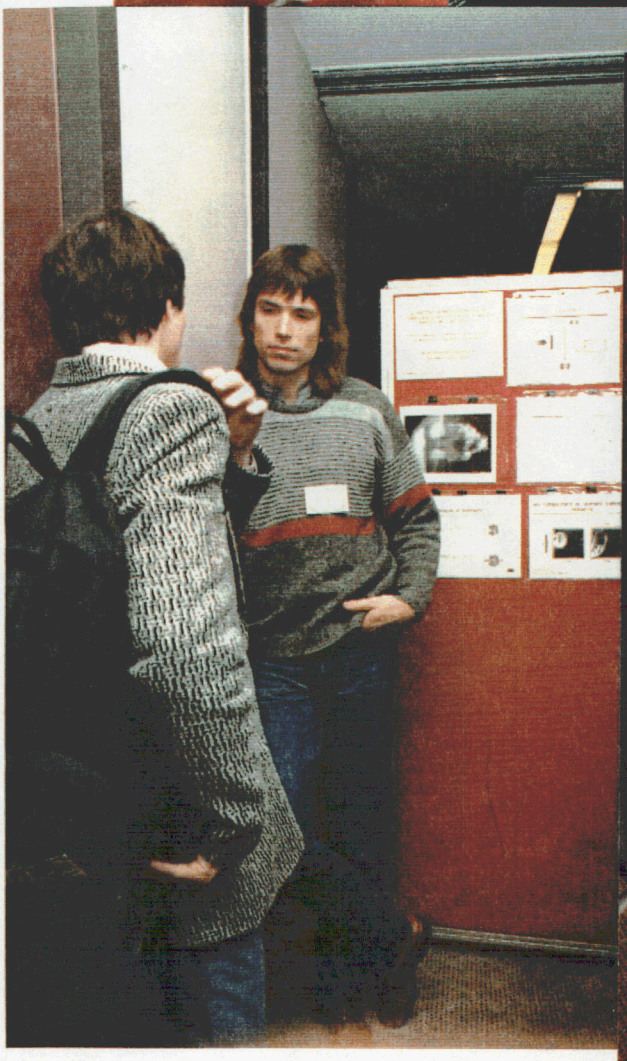

Pleasanton, USA *Edited by V. Rupert*

TWO-DIMENSIONAL SIMULATION OF CONTACT SURFACE INSTABILITIES IN SHOCK-TUBES

Didier Besnard and Jean-François Haas
Commisariat à l'Energie Atomique
Centre d'Etudes de Limeil-Valenton
94195 Villeneuve-St-Georges Cédex, France

ABSTRACT

Numerical simulations of the interaction of Mach 1.3 shock waves and gaseous interfaces between air and helium or SF6 were carried out using EAD, a 2D, second order non-viscous Eulerian code. The interface, described either by a single sinusoidal wave or a combination of sinusoidal waves of random amplitudes is subjected to Rayleigh-Taylor instability induced by the incident shock and successive waves reflected from the shock tube end wall. The evolution of the subsequent mixing zone thickness and the kinetic energy of the fluctuating velocity field associated with the mixing are extracted from the simulation and compared with theoretical estimates based on an quasi-incompressible analysis of the instability.

INTRODUCTION

We present some results of numerical simulations of the interaction of shock waves and random contact surfaces between two gases of different densities. The simulations are carried out using EAD [1], a 2D, second order, non-viscous Eulerian code and represent various shock-tube experiments where a planar shock-wave accelerates a contact surface and later brings it to rest because of its reflection(s) on the shock-tube end wall. Because of the acceleration, the nominally flat interface (usually a membrane thinner than 1μm) breaks in an incontrollable fashion, thus imposing on the gaseous interface some random scales which are then amplified due to the shock-induced Rayleigh-Taylor (Richtmyer-Meshkov) instability. As we do not attempt, for the moment, to simulate the details of this rupture, we treat instead the shock-induced deformation of a random contact surface defined by 31 modes of wavelength spaced between 0.1L and 0.4L (L is the tube width, here 2.5 cm) and of random amplitude chosen according to a Gaussian law such that the interface rms σ is on the order of 1 mm. Details on the simulations have been described earlier [2,3].

These finely meshed numerical experiments are done in order to obtain quantities such as the fluctuating kinetic energy (FKE) of the mixing process, which are difficult to get from laboratory experiments. We use strip averaging in a direction transverse to the mean flow to obtain one-dimensional profiles of pressure, density, concentration and components of the "turbulent stress tensor", which can be compared with the profiles calculated by turbulence transport models imbedded in 1D codes or used to initialize the fully developped turbulence models which cannot treat the initial linear and nonlinear phases of the instability[2]. More precisely, we concentrate on the local fluctuating kinetic energy defined as:

$$\overline{\rho}\,k = \left(\overline{\rho u_k u_k} - \overline{\rho}\,\hat{u}_k\hat{u}_k\right) \qquad \text{where } \overline{\rho}\,\hat{u}_k = \overline{\rho u_k} \qquad (1)$$

We then integrate $\overline{\rho}\,k$ along the mean flow direction, over the extent of the mixing zone, or over the total computational box, to obtain the kinetic energy (per unit area) of the fluctuating velocity field restricted to the mixing zone (ZFKE) or including also the energy due to the perturbed transmitted and reflected waves (TFKE). The time

evolution of FKE and the mixing zone thickness (MZT) can again be compared with predictions of the models or used to initialize them[2,3]. Such models have been presented elsewhere [4].

SINGLE MODE INTERFACE

Simulations describing the interaction of a Mach 1.3 shock with a single mode air/helium or SF6 interface have been carried as a benchmark for comparison with other codes. They are used here to check our evalution of the FKE involved in mixing against a theoretical estimate derived from the Richtmyer-Meshkov analysis. The physical quantities are based on recent Caltech shock tube experiments [5] with 10 cm of helium or SF6 between the interface and the end plate and a channel height of 11.3 cm. In this region, the grid is made with 200 X 200 computational cells, each of an approximately square size (0.05 cm X 0.0565 cm). The sinusoidal interface has an amplitude of 0.2 cm and a wavelength of 3.23 cm, thus the resolution in amplitude is average (4 cells). For each case, calculations with or without the end wall allow the observation of the interface deformation with or without the effect of the reflected waves.

The light to heavy case i.e. air (density $\rho_1 = 1.22\ 10^{-3}$ g/cm^3, specific heat ratio $\gamma_1 = 1.4$) upstream and SF6 ($\rho_2 = 6.1554\ 10^{-3}$ g/cm^3, $\gamma_2 = 1.06$) downstream is illustrated on figure 1 with (a) a section of the initial interface (0 μs) and (b) at 1500 μs after the reflected shock and the second wave which is a rarefaction (the interface is the line on the left). The trajectory of the mixing zone defined by a spanwise averaged mass concentration of either material between 0.005 and 0.995 appears on figure 2, showing at 0.1 ms the small compression by the incident shock and R-M induced growth of the mixing zone, then, starting at 0.8 ms, the large compression caused by the reflected shock which forces the disturbed interface to reverse its shape and finally a long period of sustained growth. Figure 3 gives the evolution of the fluctuating kinetic energy in the mixing zone and the total mesh with the jumps of FKE at shock passage.

In the heavy to light case with helium ($\gamma_2 = 1.667$, $\rho_2 = 1.68\ 10^{-4}$ g/cm^3) downstream, the interface shape at late time (750 μs) with the effect of the reflected shocks appears on figure 4. Figure 5 describes the trajectory of the mixing zone and shows that the interface reverses its shape, with MZT going to 0 at 0.1 ms before growing again, at a decaying rate in the absence of reflected shocks or at a sustained rate because of its excitation by 4 or 5 reflected shocks of decreasing strength. The successive enhancement of FKE by the shocks is clearly seen on figure 6.

The linear formula for the Richtmyer-Meshkov (R-M) instability giving the growth rate of the interpenetration reads:

$$\frac{dL}{dt} = \frac{4\ \pi\ a}{\lambda} A\ V \qquad (2)$$

where V is the mean interface velocity, $A = \frac{\rho_2 - \rho_1}{\rho_2 + \rho_1}$ (Atwood number) and a (amplitude) are calculated either at initial condition (subscript 0), after compression by the incident shock (subscript i) or the transmitted shock (subscript t).

C. Leith [6] has derived from the linear R-M analysis the kinetic energy of the fluctuating velocity field (FKE) per transversal cm^2 in the reference frame moving at the interface velocity V:

$$FKE = \frac{\pi a^2}{2\lambda} V^2 A (\rho_2 - \rho_1) \quad (3)$$

Here the densities and Atwood number are calculated after the interaction and the subscripts 0, i, t refer now to the initial amplitude a or compressed by the incident and transmitted shocks respectively. This estimate is based on a quasi incompressible hypothesis since one assumes that the perturbation velocity field has established itself instantaneously, i.e. the fluid everywhere has been compressed and impulsively set into motion with a mean translational velocity V at initial time.

The growth rate from the simulation (subscript s) measured at early time (from 0.1 to 0.3 ms for SF6 or 0.2 ms for helium) and the peak value of ZFKE and TFKE occuring when the incident shock passes over the interface have been chosen for the comparison below.

	air/SF6	air/helium		air/SF6	air/helium
$\frac{dL_0}{dt}$	52.3	127	FKE_0	6492	7192
$\frac{dL_i}{dt}$	36.9	84.4	FKE_i	3428	4037
$\frac{dL_t}{dt}$	27.0	104	FKE_t	1834	6175
$\frac{dL_s}{dt}$	37.7	92.8	ZFKE	6049	2528
			TFKE	19526	8617

The initial deformation rate for the air/SF6 case is close to the R-M formula with compression by the incident shock, while in the air/helium case it falls between the 2 compressed values. For air/SF6 the peak ZFKE is close to the incompressed R-M value but for air/helium it is too small as the fluctuating velocity field exists beyond the shrinking MZ. It appears that, in that case, TFKE fits better the theoretical value.

RANDOM MULTI-MODE AIR/HELIUM INTERFACE

We have ran a number of simulations of the interaction of Mach 1.3 shocks and random multimode air-helium interfaces of different rms but without reflected shocks. We discuss here first the results of a set of 3 simulations of the same system with 3 different grid sizes denoted F (fine, 0.01cm), M (medium, 0.0125 cm) and C (coarse, 0.02 cm) on figures 9 to 12. As for the single mode air/helium interface problem, the interaction of the Mach 1.3 shock with the random multi-mode interface described in the introduction (and similar to that on fig. 10a) leads to a R-M induced reversal but at a different rate for each mode. Therefore the mixing zone shrinks without vanishing completely (at 15 μs) and then expands (figure 7). At the same time FKE peaks and then decreases (figures 8 and 9). We have studied the dependence of this peak and decay rate on mesh size and found that the calculation have not converged. The MZT growth rate (measured from a log-log version of figure 7) was measured to be 0.7, 0.6 and 0.43 after a linear phase lasting up to 40 μs for the fine, medium and coarse meshes respectively, and the corresponding decay rates of FKE was -0.7, -0.87 and -1.05 (about the same rate for ZFKE and TFKE). The dimensionless ratio ZFKE/DKE, where DKE is the translational kinetic energy of the mixing zone decays as $t^{-1.4}$, independently of the mesh size.

The results for the fine mesh (MZT and FKE variation close to $t^{2/3}$ and $t^{-2/3}$ respectively) should be compared with two possible length scales for this impulsive

instability problem: either V t or $(E_0)^{1/3}\, t^{2/3}$ with $E_0 = FKE_0/\overline{\rho}$ where FKE_0 is the peak of fluctuating kinetic energy as defined in [6] and calculated above. Dimensional arguments indicate that the choice of V t leads to an unrealistic linearly increasing FKE. The other choice leads to a variation of k (analogous to ZFKE/DKE) as $(E_0)^{2/3}\, t^{-2/3}$ and constant FKE as stated in [5]. We conclude that the decay of FKE in the simulation is the effect of numerical dissipation i.e. the loss of the energy of the eddies at cell size.

Looking at the pressure and velocity field we have found[7] that form drag accounts for much of the velocity decrease of the large eddies. We also estimate that viscous effects are negligeable in this problem. Simulations of the decay of large ideal vorticies have shown that numerical dissipation enters for less than 15% in their FKE decrease[7]. We therefore believe that the large scales are well described.

A study of the dependence of peak FKE on σ has been made for Mach 1.3 shocks and air-helium interfaces. The results follow a theoretically derived linear relation [6] based on a statistical extrapolation of (3) and adapted to our 2D random interfaces:

$$FKE_0 = k\, \sigma\, V^2\, A\, (\rho_2 - \rho_1) \qquad (4)$$

and allow the evaluation of k: 0.1 for TFKE (a better choice for the air/helium case) and 0.04 for ZFKE. Another theoretical prediction [8]: ZFKE/DKE=0.09 A^2, could not be verified because, even at the end of the simulation, the initial interface conditions were not forgotten.

Complete simulations of shock tube experiments with the interaction of a Mach 1.2 incident shock and subsequent reflected waves with multimode interfaces (medium grid) have also been performed for comparison with turbulence models [2,3]. The initial interface appears on fig. 10 a and density field at 350 µs on fig. 10 b.TMZ and FKE evolutions are shown on figures 11 and 12 with comparison to the results of turbulent transport model results (Turgau, BHR).

CONCLUSION

Future calculations will be aimed at reaching a self-similar stage, by starting with a thin but highly corrugated contact surface and following its motion very late. We need also to study the interaction with higher shock Mach numbers. We thank M. Bonnefille, J. Gambart and H. Lelong for their help.

REFERENCES

1- C. Coste et al, in "Computing Methods in Applied Science and Engineering", Glowinski and Lions Eds., North Holland (1982).
2- D.C. Besnard, J.F. Haas, et R.M. Rauenzahn, "Advances in Fluid Turbulence", CNLS Conference, May 16-20, 1988, Physica D,(1989) in print.
3- D.C. Besnard, J.F. Haas, et R.M. Rauenzahn, "International Workshop on the Physics of Turbulent Compressible Mixing" Proceedings, October 24-27, 1988, Princeton, USA, Springer-Verlag, to be published.
4- D.C. Besnard et. al. in "Shock Waves and Shock Tubes", Proceedings of the 16th ISSWST, H. Grönig ed., VCH Verlagsgesellshaft, 1988.
5- M. Brouillette and B. Sturtevant, in "Advances in Fluid Turbulence", CNLS Conference, May 16-20, 1988, Physica D,(1989) in print.
6- C. E. Leith, Lawrence Livermore National Laboratory working paper (1985).
7- D.C. Besnard and J.F. Haas, proceedings of the ISCFD, Nagoya, August 28-31 1989.
8- K.O. Mikaelian, Lawrence Livermore National Laboratory UCRL-93977 (1986).

Figure 1a Single mode interface

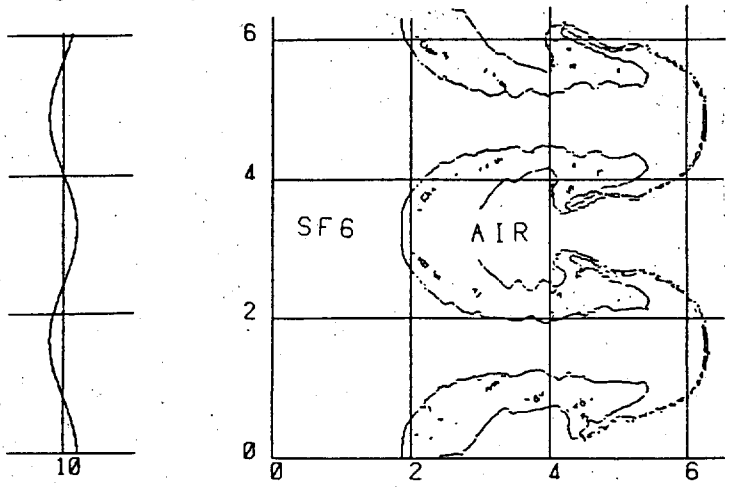

Figure 1b Air/SF6 interface at 1.5 ms

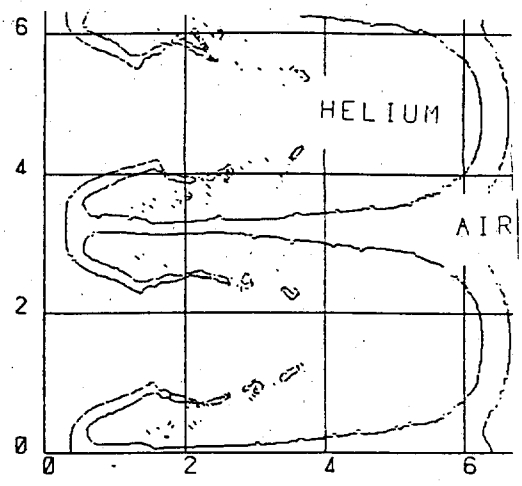

Figure 4 Air/helium interface at 0.75 ms

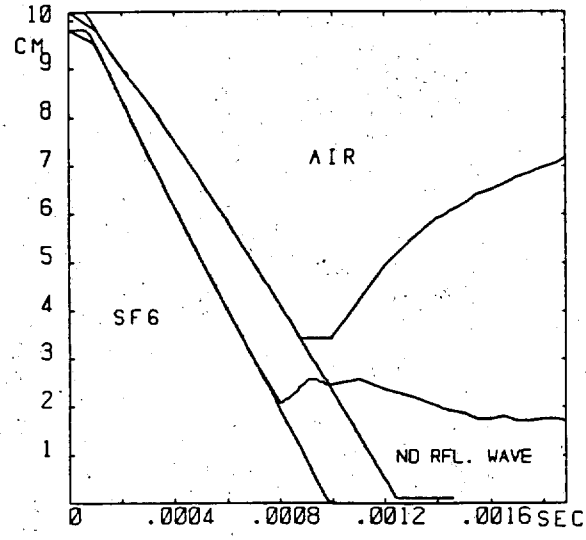

Figure 2 Trajectory of the air/SF6 mixing zone

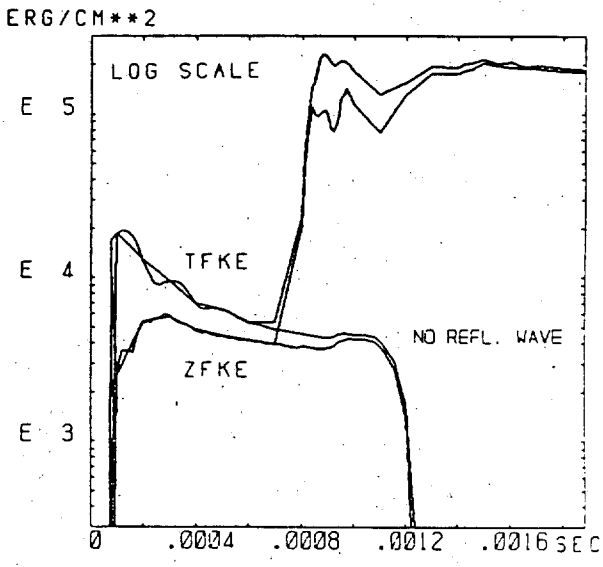

Figure 3 FKE in the air/SF6 case

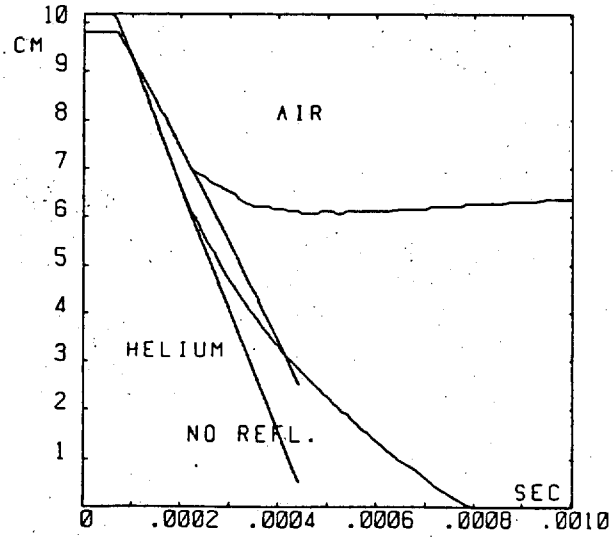

Figure 5 Trajectory of the air/helium zone

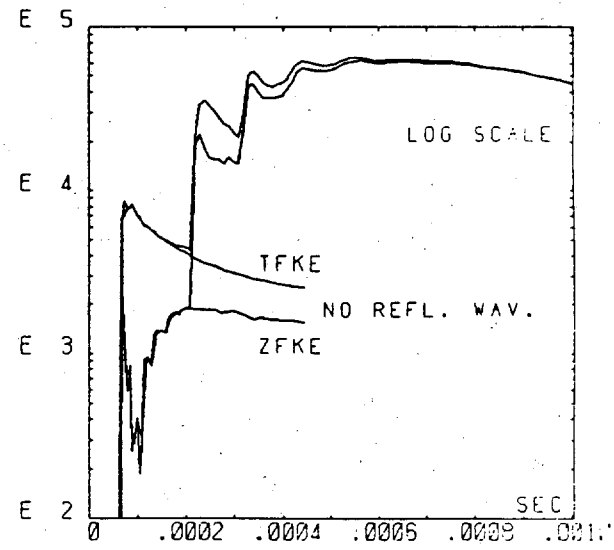

Figure 6 FKE in the air/helium case

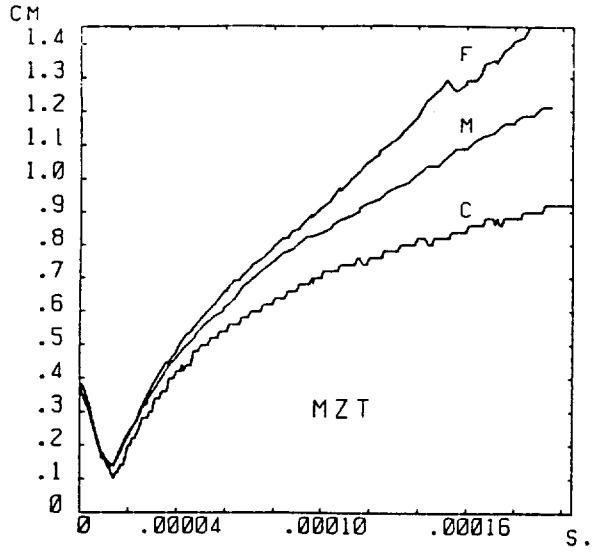

Figure 7 Thickness in the multimode case

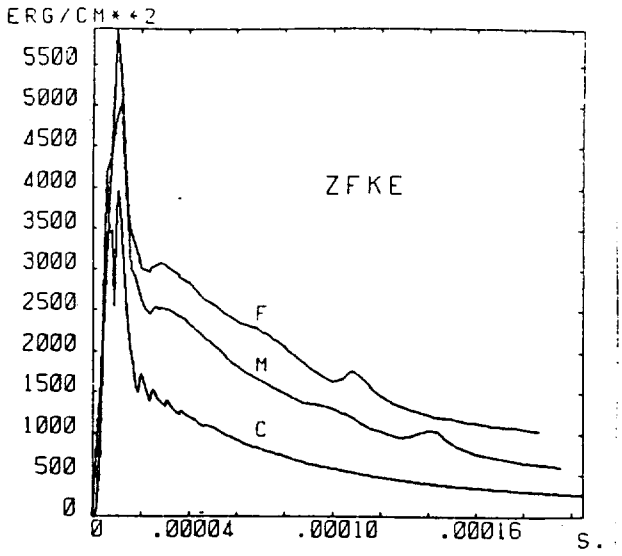

Figure 8 ZFKE in the multimode case

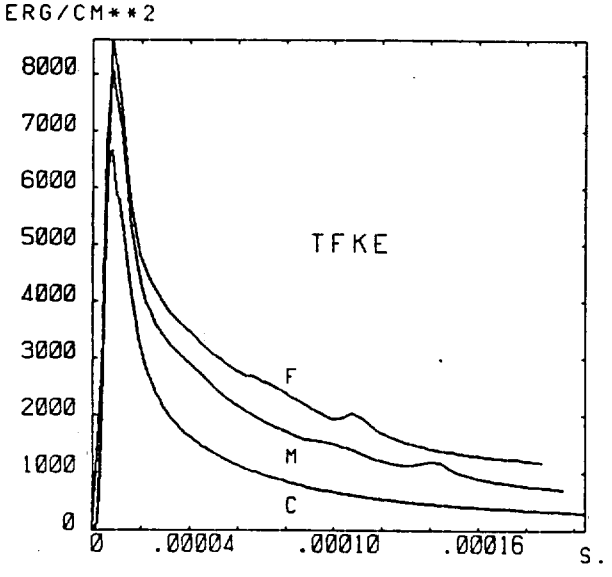

Figure 9 TFKE in the multimode case

Figure 10a Initial multimode interface

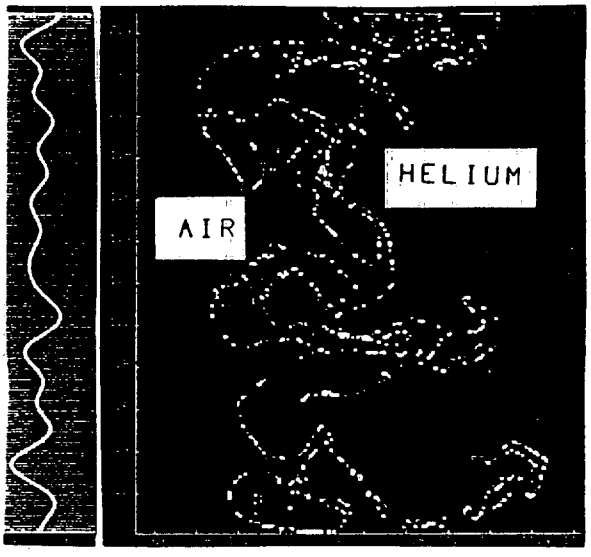

Figure 10b Density field at 0.35 ms

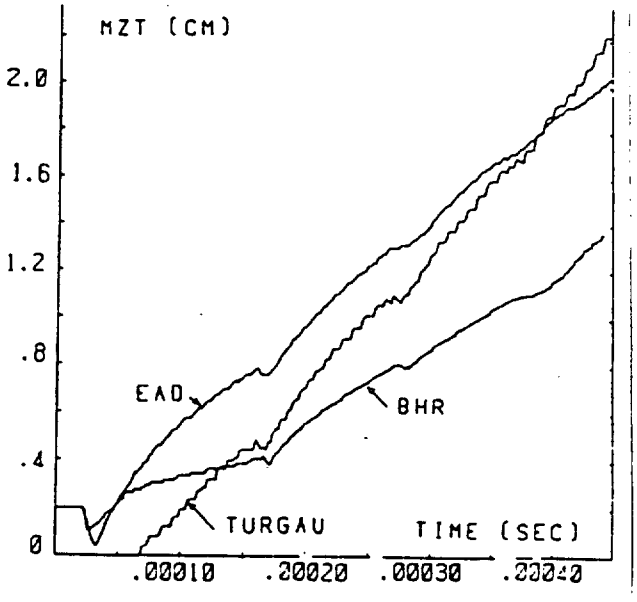

Figure 11 Thickness vs. time (multimode)

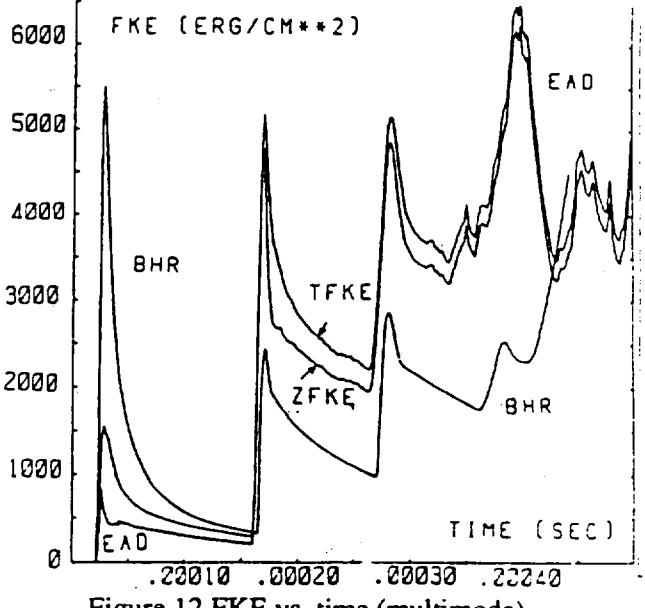

Figure 12 FKE vs. time (multimode)

2-DIMENSIONAL SIMULATION OF SHOCK-INTERFACE INTERACTION

D. Besnard, J. Gambart and J.F. Haas

Commissariat a l'Energie Atomique
Centre d'Etudes de Limeil-Valenton
94195 Villeneuve St Georges Cedex
France

Numerical experiments performed to date

Benchmark calculations:
Single mode and multiple (5) mode air-helium or air-SF6 interfaces: checks on the growth rate and the mixing energy of the Richtmyer-Meshkov instability in its linear phase.

Random multiple (31) modes air-helium interface.
Study of the dependance of the growth rate and mixing energy on interface variance and mesh size.

Study of the effect of the reflected shocks on the mixing energy

Study of the numerical dissipation with simulations of vorticies.

CURRENT DIAGNOSTICS

-2D MAPS:

pressure, density, $\nabla \cdot u$ (compression) and $\nabla \times u$ (vorticity); linear, log. and arsinh.

-1D PROFILES:

pressure, density, concentration, density variance, "Reynolds stress tensor" defined by:

$$\overline{\rho}\, k = (\overline{\rho u_k u_k} - \overline{\rho}\, \hat{u}_k \hat{u}_k) \qquad \overline{\rho}\, \hat{u}_k = \overline{\rho u_k}$$

-SPACE INTEGRATED VARIABLES

mixing zone thickness (MZT), kinetic energy of the velocity field associated to the interface deformation obtained by integrating ρk over the mixing zone (ZFKE) or the total computation box (TFKE).

RESULTS

FKE resides in and around the interpenetration zone with a minor part associated to the perturbed waves.

The peaks in the time evolution of FKE occur at shock passage with a much higher value for the reflected shocks.

The peak obtained at the first interaction can be compared with a theoretical estimation based on an instantaneous and incompressible analysis of the Richtmyer-Meshkov instability (Leith).

In the case of a random multimode interface, the peak of FKE is proportional to the interface variance.

Peak value and post shock decay rate of FKE as well as the growth rate of the interpenetration zone are dependent on mesh size: effects of numerical and physical dissipation (in which proportion?)

FUTURE CALCULATIONS

Higher shock Mach number (3-6) and different Atwood numbers (conditions of the University of Provence experiments).

Random multimode interfaces with small non-linear defects

More simulations of simple systems to understand better the physical and numerical dissipation.

Diagnostics: spectral analysis of the flow and decomposition of FKE into acoustical, entropy and vortical modes.

PLEASANTON HILTON

Poster Bernard. Haas

contents

3 pages of text

4 prints AIR-SF6 multimode

3 time evolutions "

6 profiles of KE "

4 prints Ar-He. multimode

4 time evolution "

6 profiles of KE "

2 prints Ar-helium nonmode # benchmark

4 time evolution Ar-helium single mode } benchmark

5 profiles of KE "

2 prints Ar-SF6 nonmode # benchmark

7050 Johnson Drive Pleasanton, California 94566 415/463-8000
Reservations 1-800/HILTONS

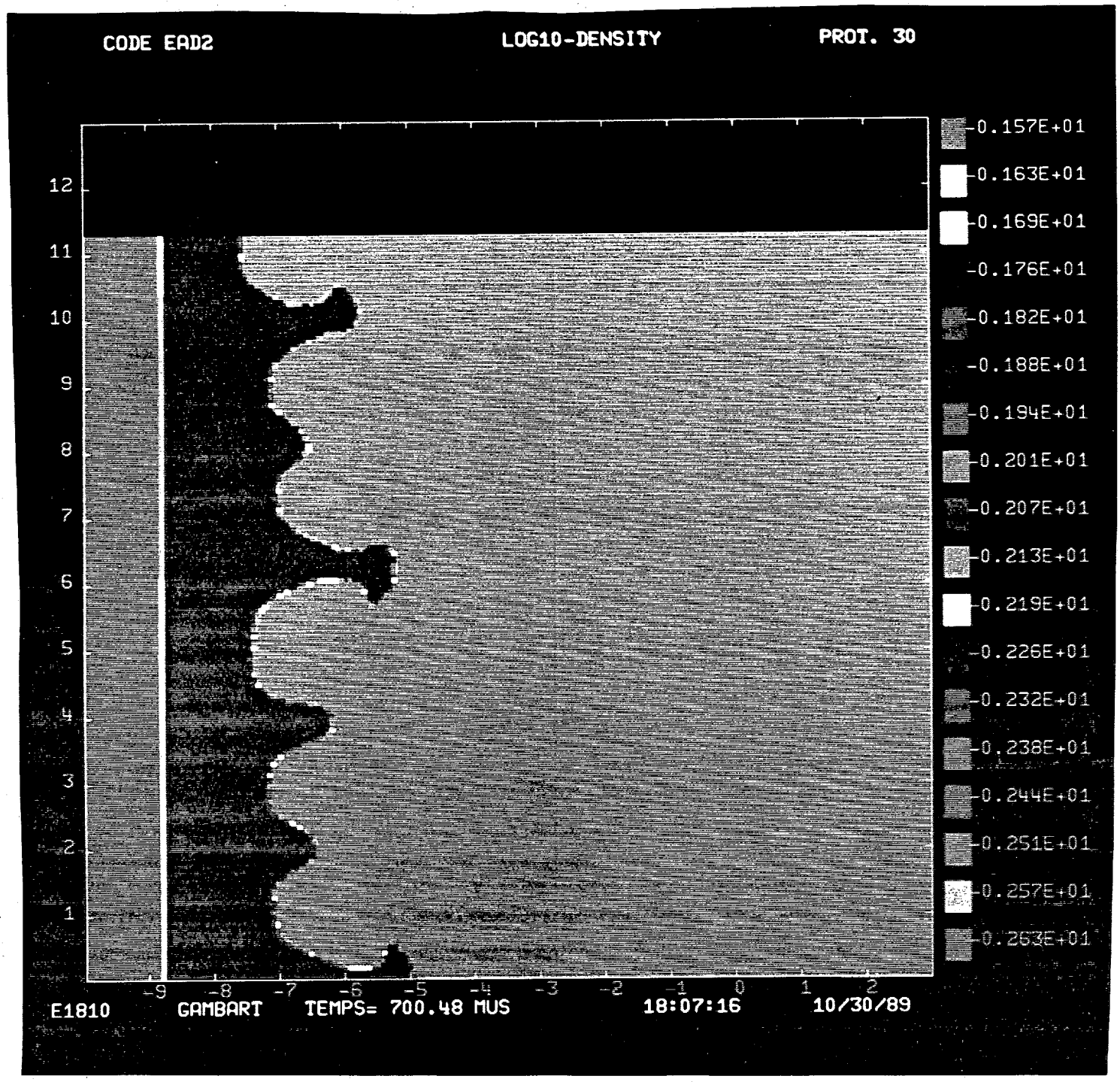
CODE EAD2
LOG10-DENSITY
PROT. 30
0.157E+01
0.163E+01
0.169E+01
0.176E+01
0.182E+01
0.188E+01
0.194E+01
0.201E+01
0.207E+01
0.213E+01
0.219E+01
0.226E+01
0.232E+01
0.238E+01
0.244E+01
0.251E+01
0.257E+01
0.263E+01
12
11
10
9
8
7
6
5
4
3
2
1
-9
-8
-7
-6
-5
-4
-3
-2
-1
0
1
2
E1810
GAMBART
TEMPS= 700.48 MUS
18:07:16
10/30/89

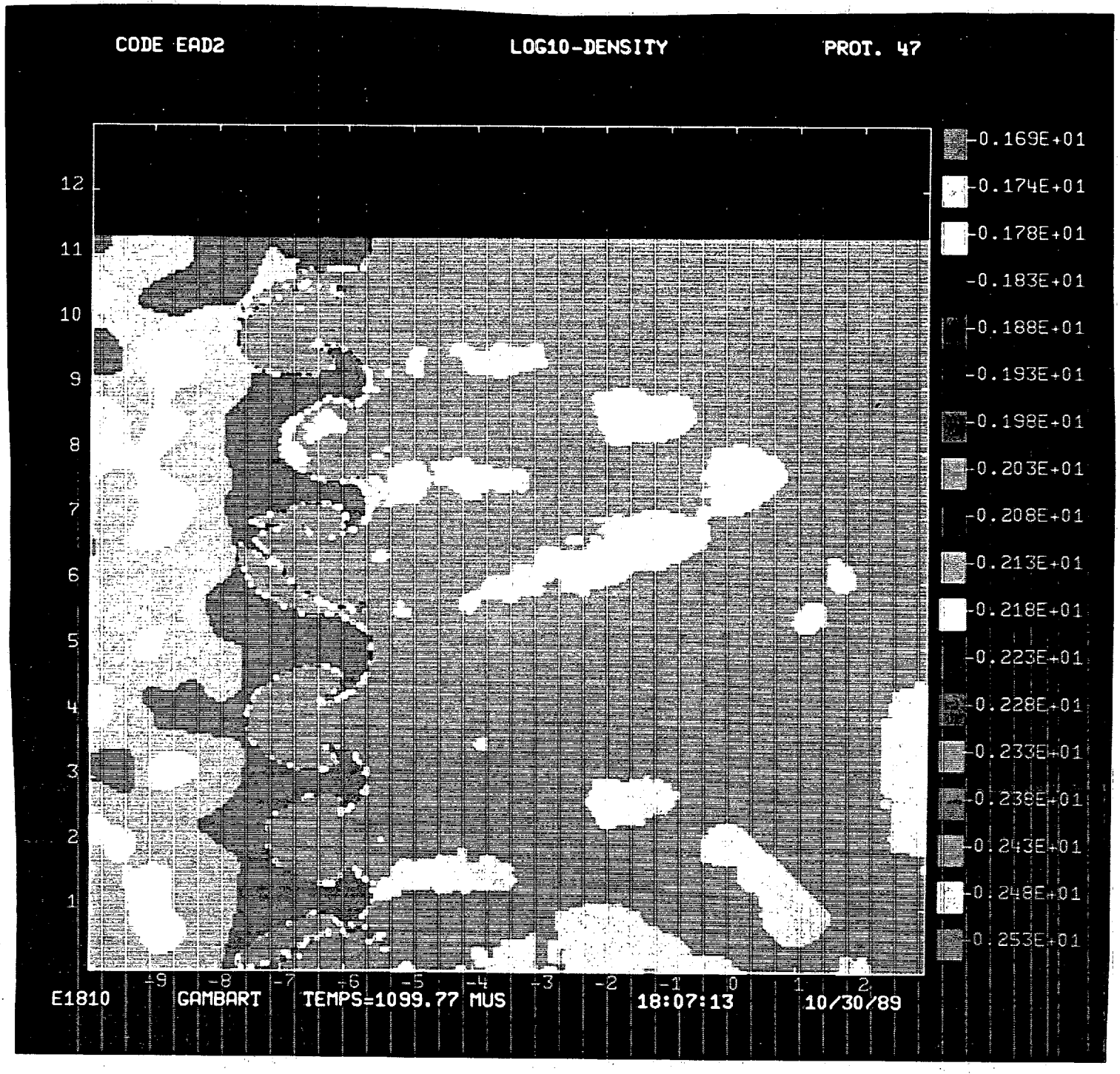
CODE EAD2
LOG10-DENSITY
PROT. 47
-0.169E+01
-0.174E+01
-0.178E+01
-0.183E+01
-0.188E+01
-0.193E+01
-0.198E+01
-0.203E+01
-0.208E+01
-0.213E+01
-0.218E+01
-0.223E+01
-0.228E+01
-0.233E+01
-0.238E+01
-0.243E+01
-0.248E+01
-0.253E+01
12
11
10
9
8
7
6
5
4
3
2
1
-9
-8
-7
-6
-5
-4
-3
-2
-1
0
1
2
E1810
GAMBART
TEMPS=1099.77 MUS
18:07:13
10/30/89

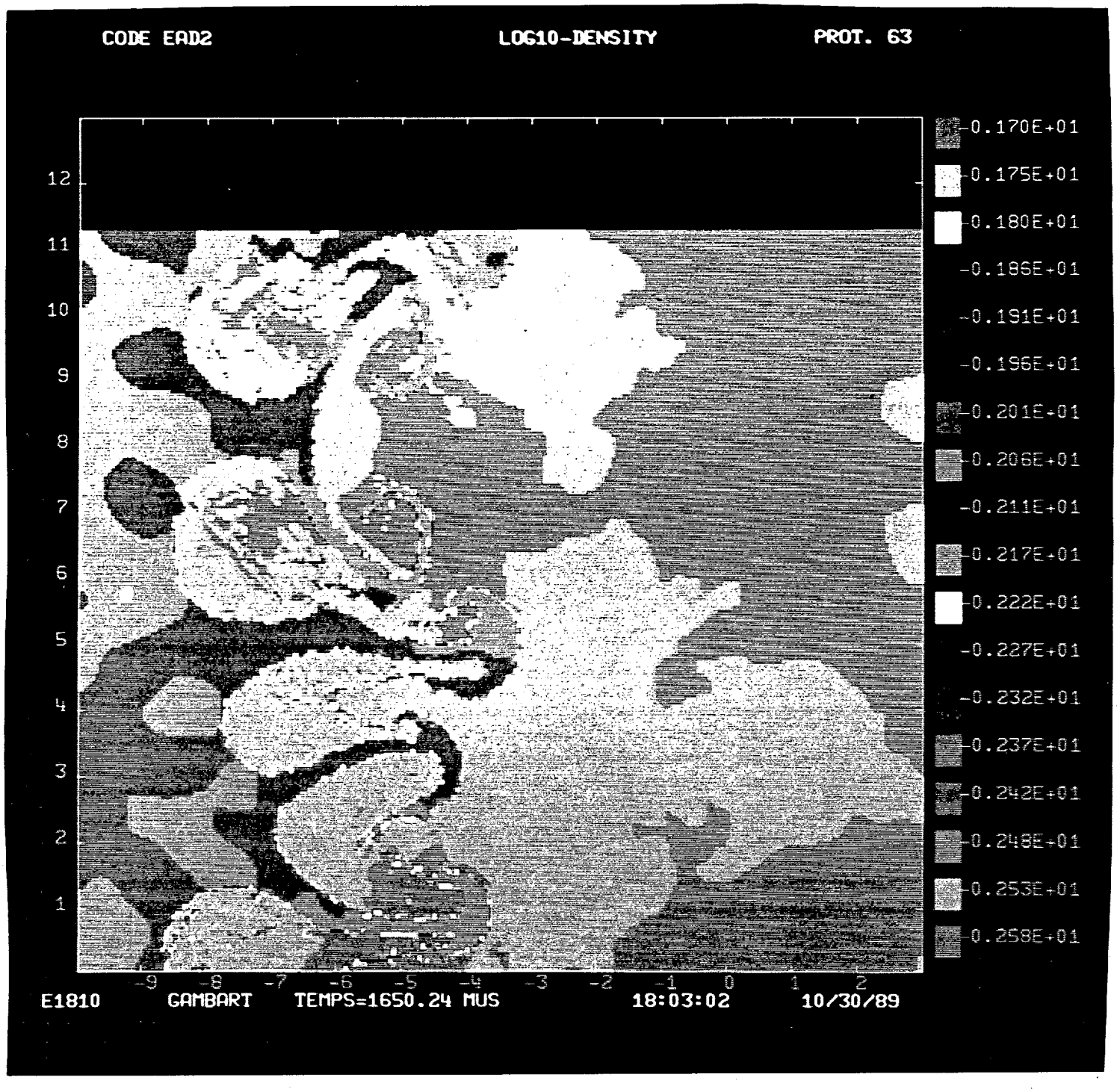
CODE EAD2
LOG10-DENSITY
PROT. 63
12
11
10
9
8
7
6
5
4
3
2
1
-0.170E+01
-0.175E+01
-0.180E+01
-0.186E+01
-0.191E+01
-0.196E+01
-0.201E+01
-0.206E+01
-0.211E+01
-0.217E+01
-0.222E+01
-0.227E+01
-0.232E+01
-0.237E+01
-0.242E+01
-0.248E+01
-0.253E+01
-0.258E+01
-9 -8 -7 -6 -5 -4 -3 -2 -1 0 1 2
E1810 GAMBART TEMPS=1650.24 MUS 18:03:02 10/30/89

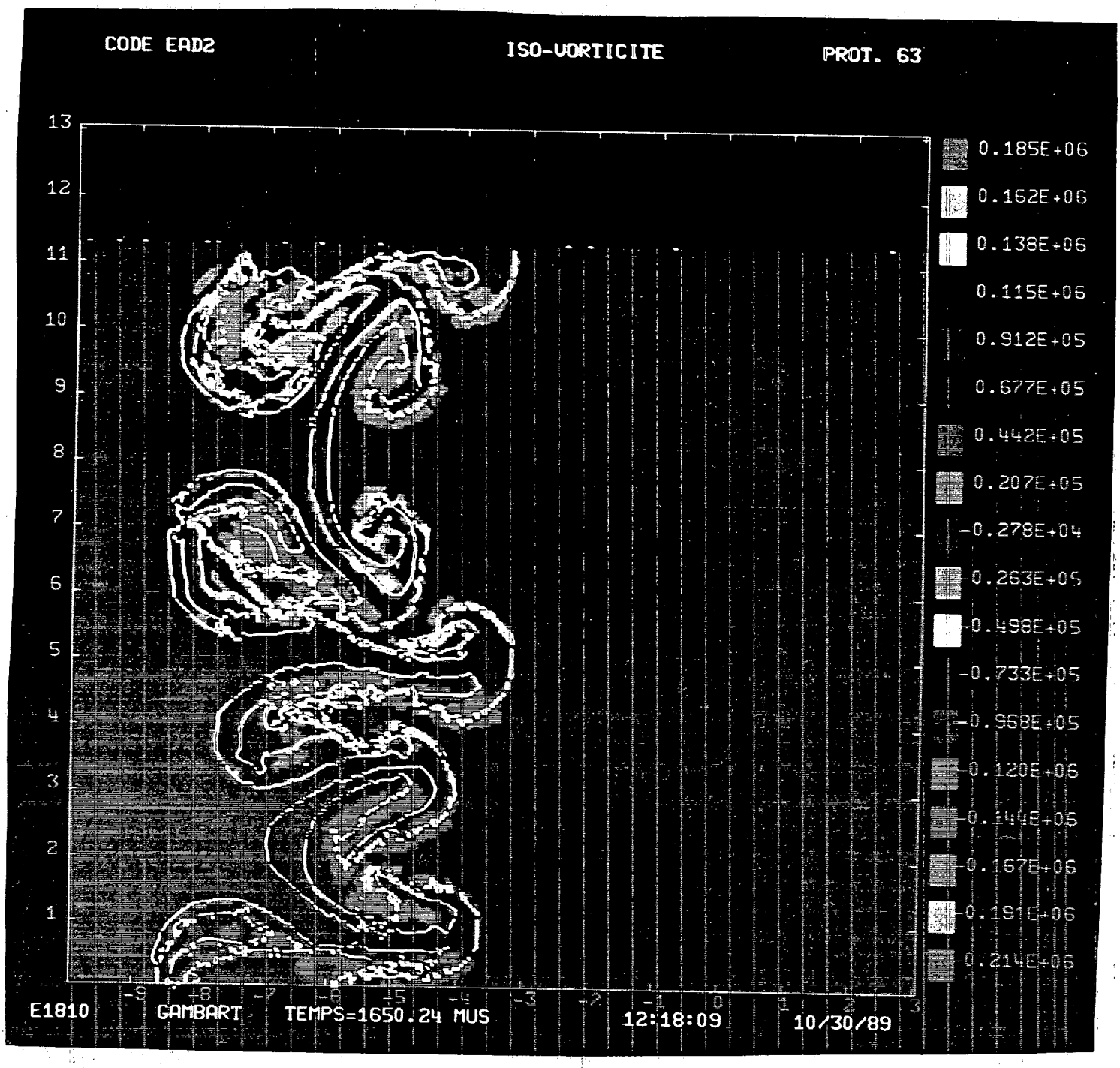
CODE EAD2
ISO-VORTICITE
PROT. 63
13
12
11
10
9
8
7
6
5
4
3
2
1
0.185E+06
0.162E+06
0.138E+06
0.115E+06
0.912E+05
0.677E+05
0.442E+05
0.207E+05
-0.278E+04
-0.263E+05
-0.498E+05
-0.733E+05
-0.968E+05
-0.120E+06
-0.144E+06
-0.167E+06
-0.191E+06
-0.214E+06
E1810
GAMBART
TEMPS=1650.24 MUS
12:18:09
10/30/89

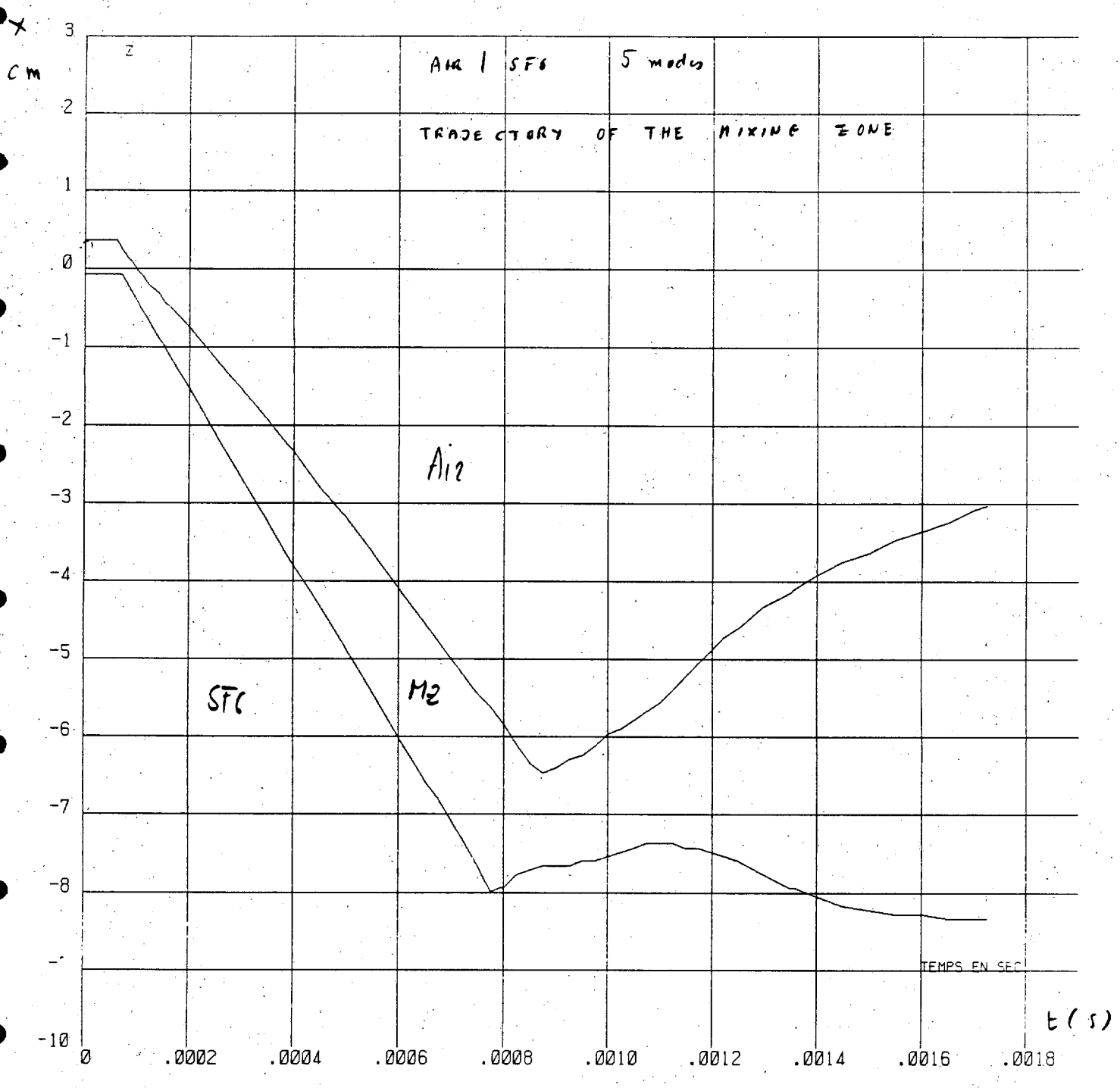
X
Cm
Z
AIR 1 SF6 5 mods
TRAJECTORY OF THE MIXING ZONE
AIR
SF6
M2
TEMPS EN SEC
t (s)
3
2
1
0
-1
-2
-3
-4
-5
-6
-7
-8
-10
0
.0002
.0004
.0006
.0008
.0010
.0012
.0014
.0016
.0018

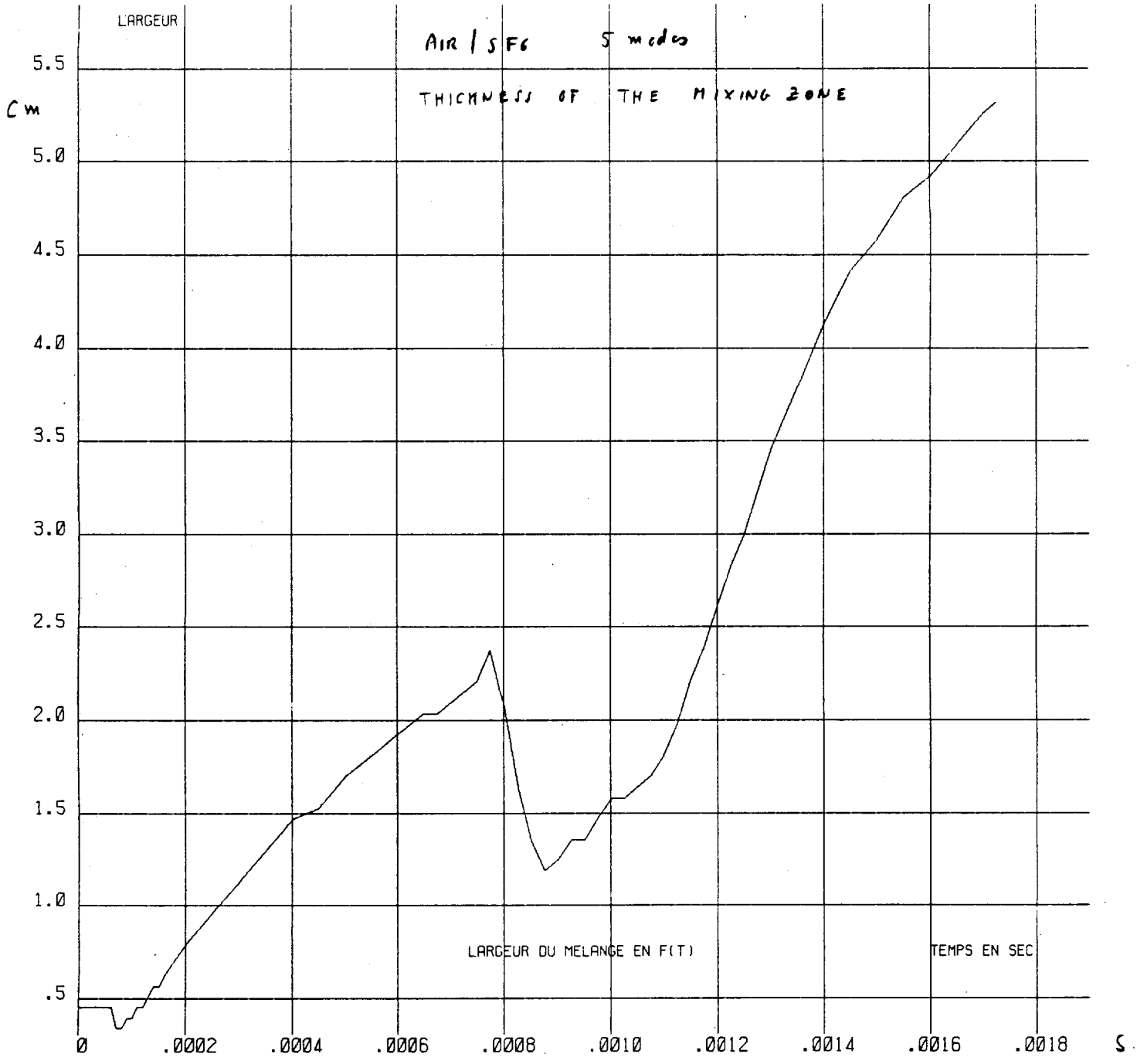
LARGEUR
AIR / SF6 5 modes
THICKNESS OF THE MIXING ZONE
Cm
5.5
5.0
4.5
4.0
3.5
3.0
2.5
2.0
1.5
1.0
.5
LARGEUR DU MELANGE EN F(T)
TEMPS EN SEC
0
.0002
.0004
.0006
.0008
.0010
.0012
.0014
.0016
.0018
S

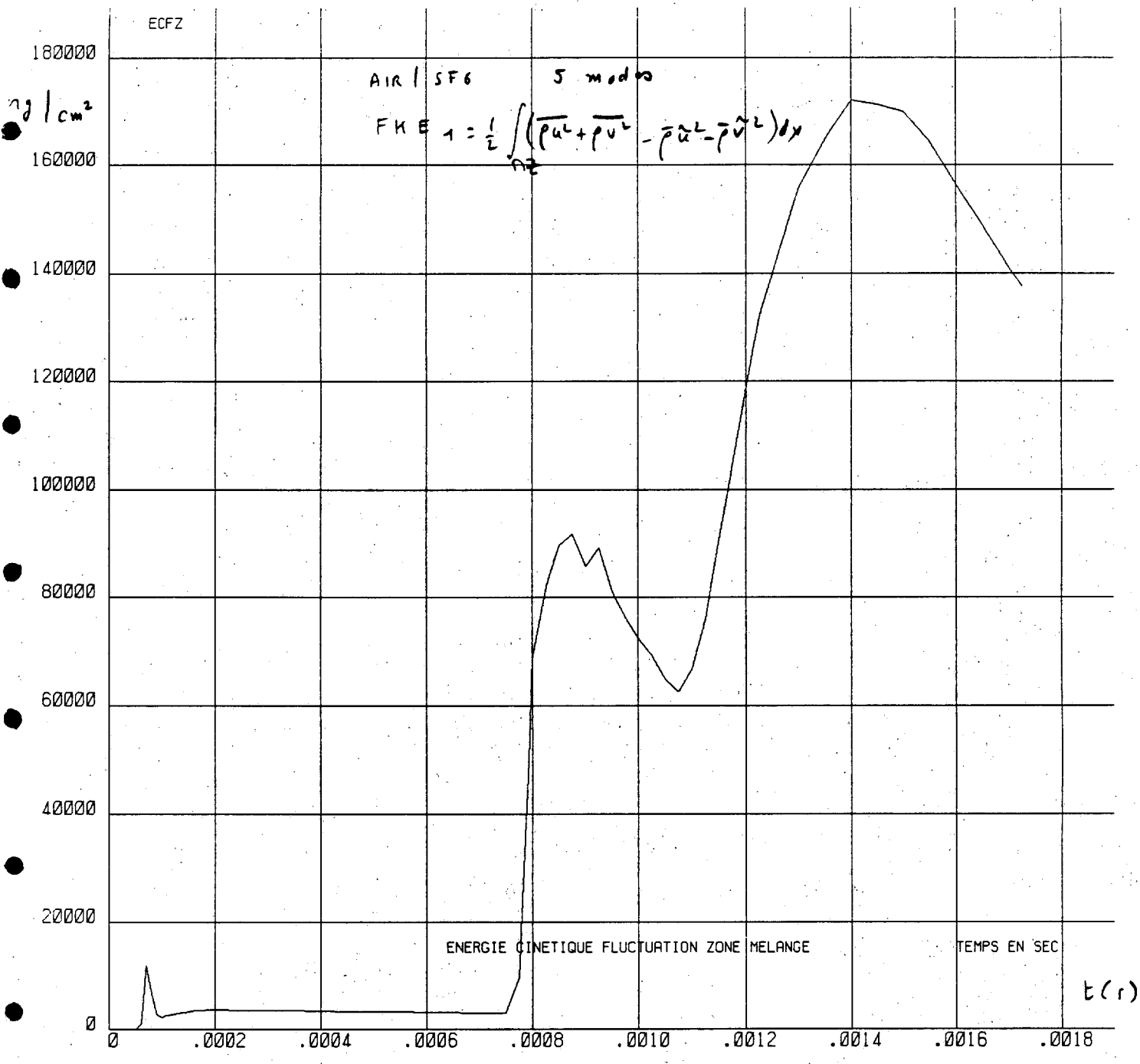
ECFZ
AIR / SF6
5 modes
$FKE_1 = \frac{1}{2}\int_{nz}(\overline{\rho u^2} + \overline{\rho v^2} - \bar{\rho}\tilde{u}^2 - \bar{\rho}\tilde{v}^2)dx$
mJ / cm²
180000
160000
140000
120000
100000
80000
60000
40000
20000
0
ENERGIE CINETIQUE FLUCTUATION ZONE MELANGE
TEMPS EN SEC
t(r)
0
.0002
.0004
.0006
.0008
.0010
.0012
.0014
.0016
.0018

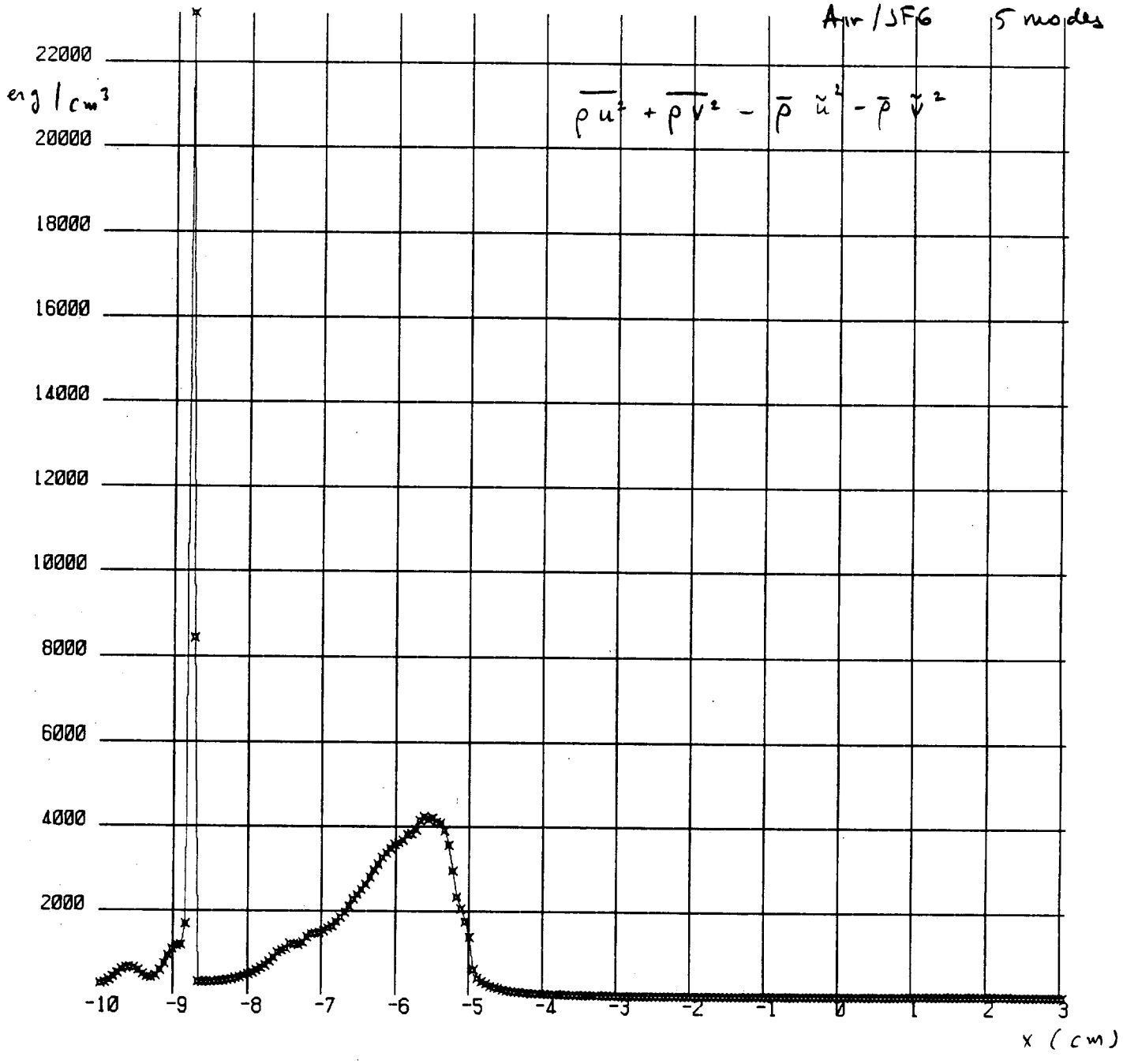
Air/SF6 5 modes
erg/cm³
$\overline{\rho u^2} + \overline{\rho v^2} - \bar{\rho}\,\breve{u}^2 - \bar{\rho}\,\breve{v}^2$
22000
20000
18000
16000
14000
12000
10000
8000
6000
4000
2000
-10 -9 -8 -7 -6 -5 -4 -3 -2 -1 0 1 2 3
x (cm)
GAMBART E1810 153713 11/03/89 T= 0.70048E-03 RUU+RVV R= 0.28250E-01 LIGNE 1

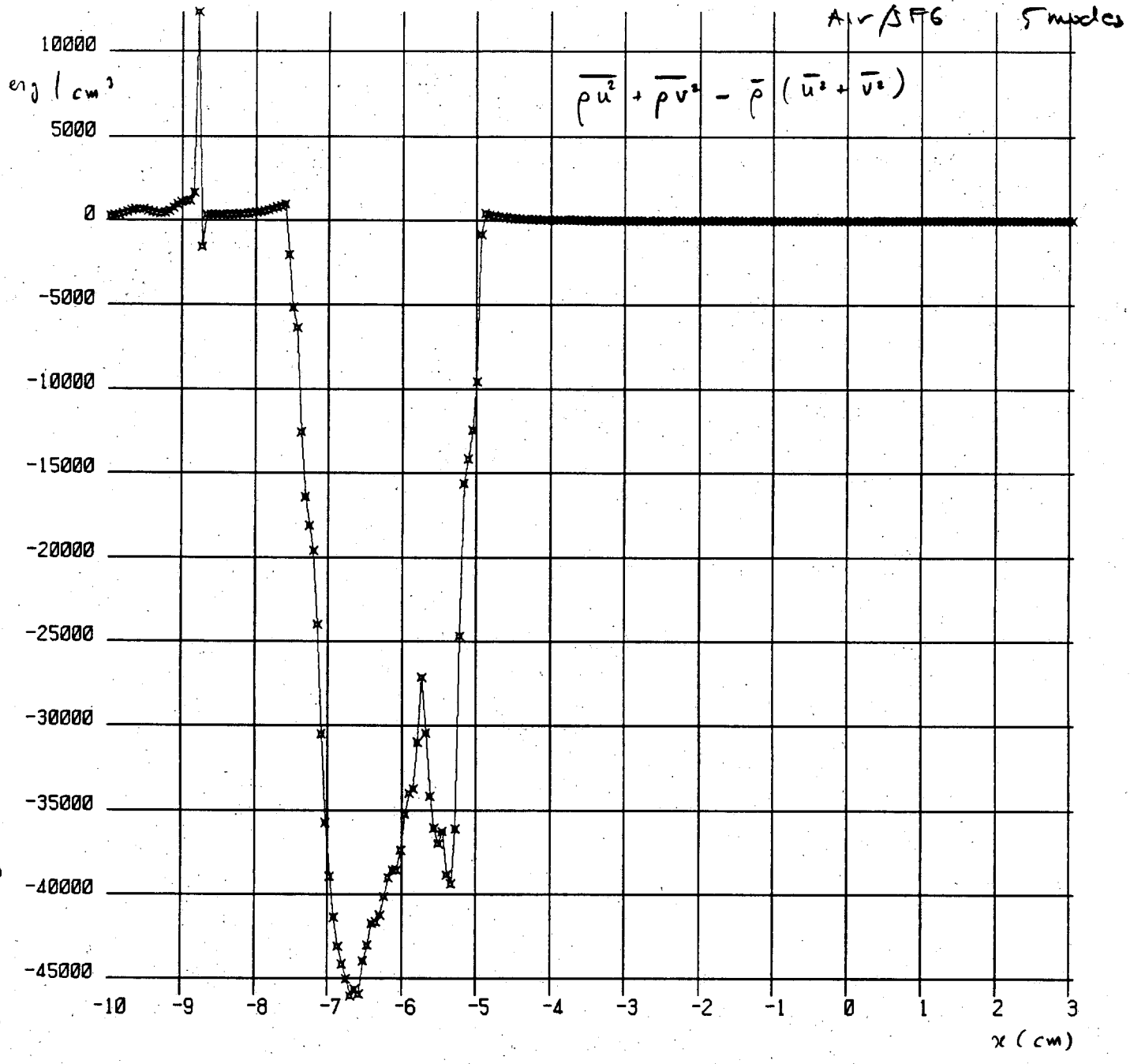

GAMBART E1810 153713 11/03/89 T= 0.70048E-03 TUU+TVV R= 0.28250E-01 LIGNE 1

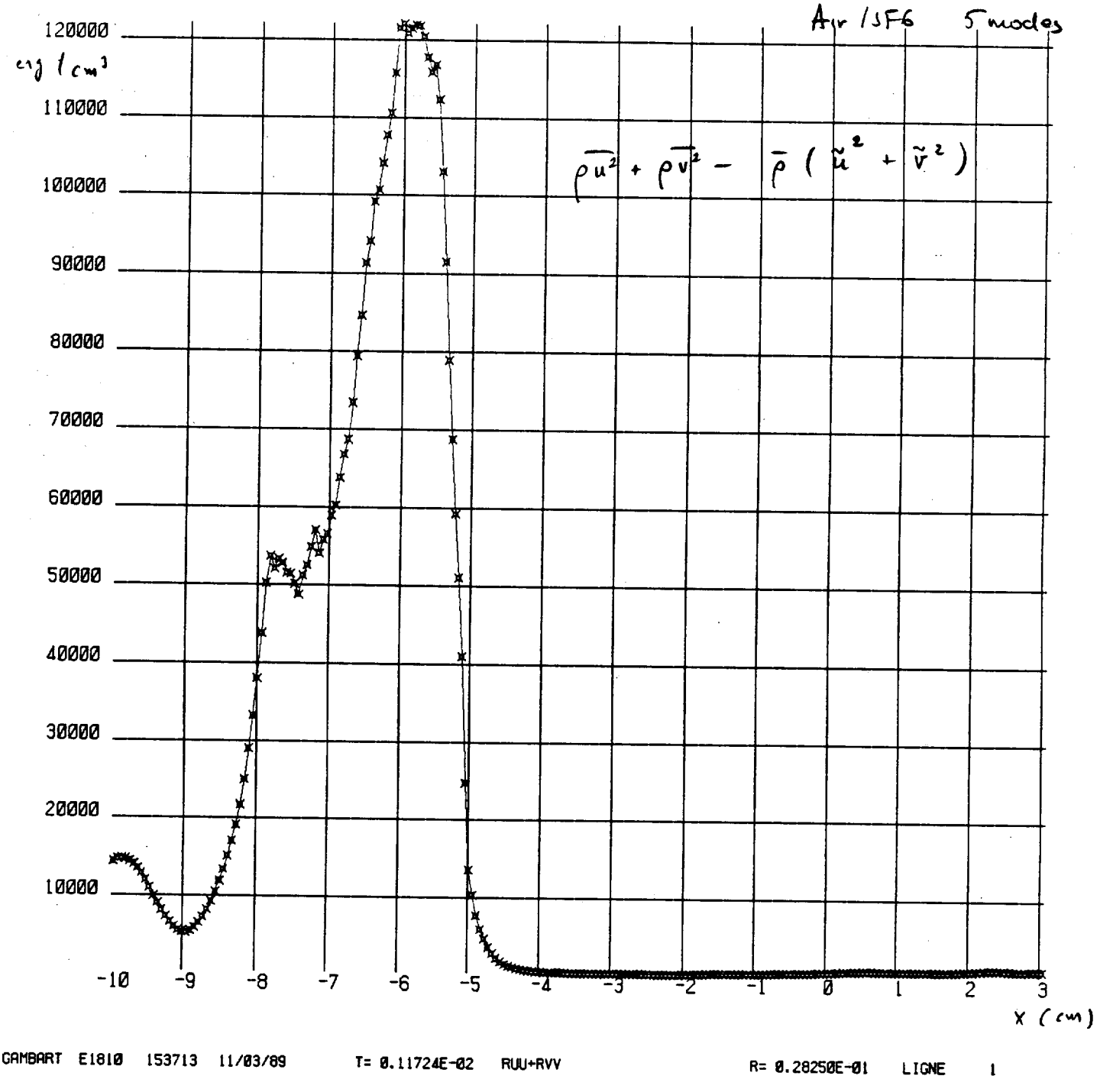
Air /SF6 5 modes
erg / cm³
120000
110000
100000
90000
80000
70000
60000
50000
40000
30000
20000
10000
$\overline{\rho u^2} + \overline{\rho v^2} - \bar{\rho}(\tilde{u}^2 + \tilde{v}^2)$
-10
-9
-8
-7
-6
-5
-4
-3
-2
-1
0
1
2
3
X (cm)
GAMBART E1810 153713 11/03/89
T= 0.11724E-02 RUU+RVV
R= 0.28250E-01 LIGNE 1

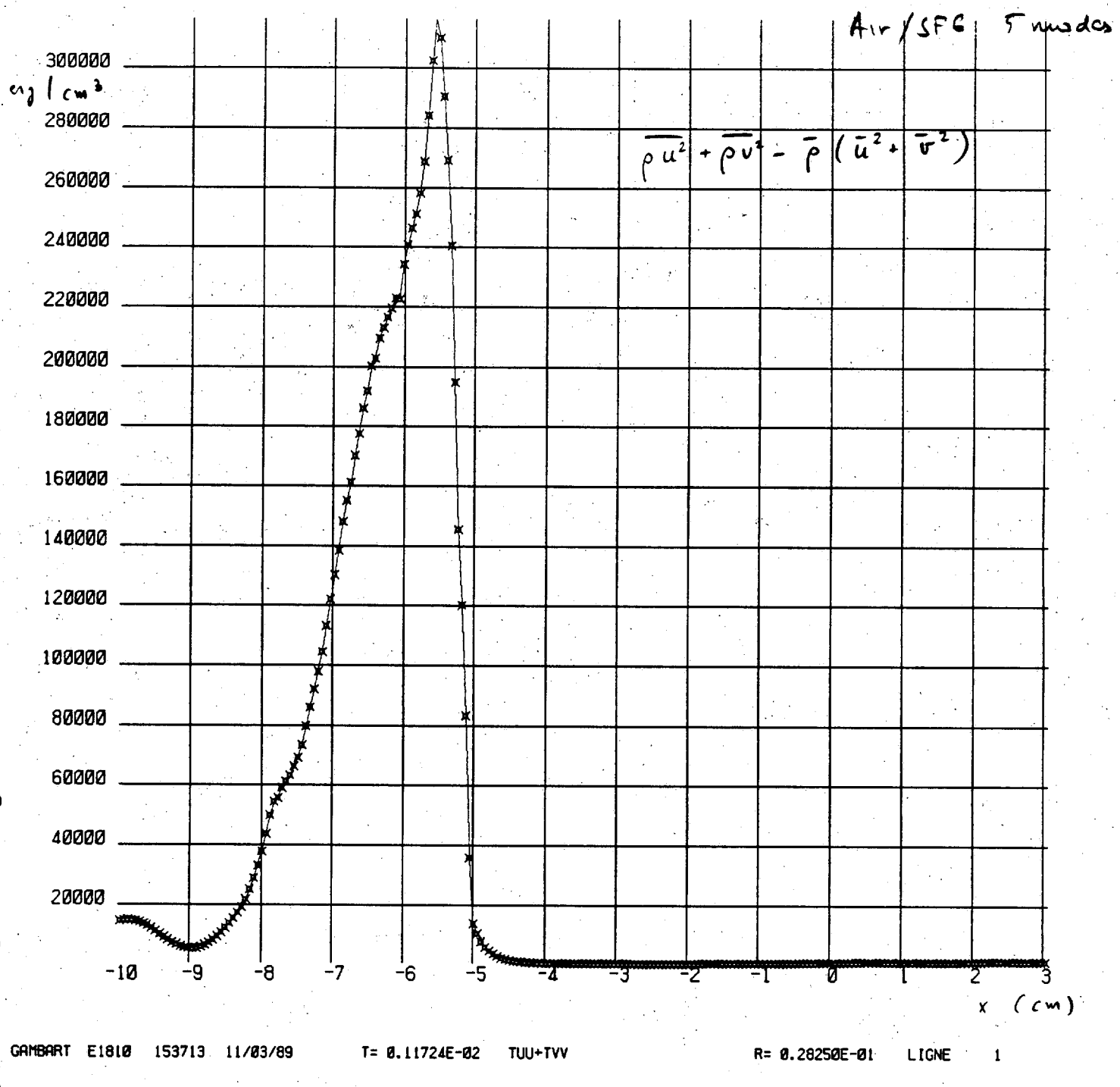

GAMBART E1810 153713 11/03/89 T= 0.11724E-02 TUU+TVV R= 0.28250E-01 LIGNE 1

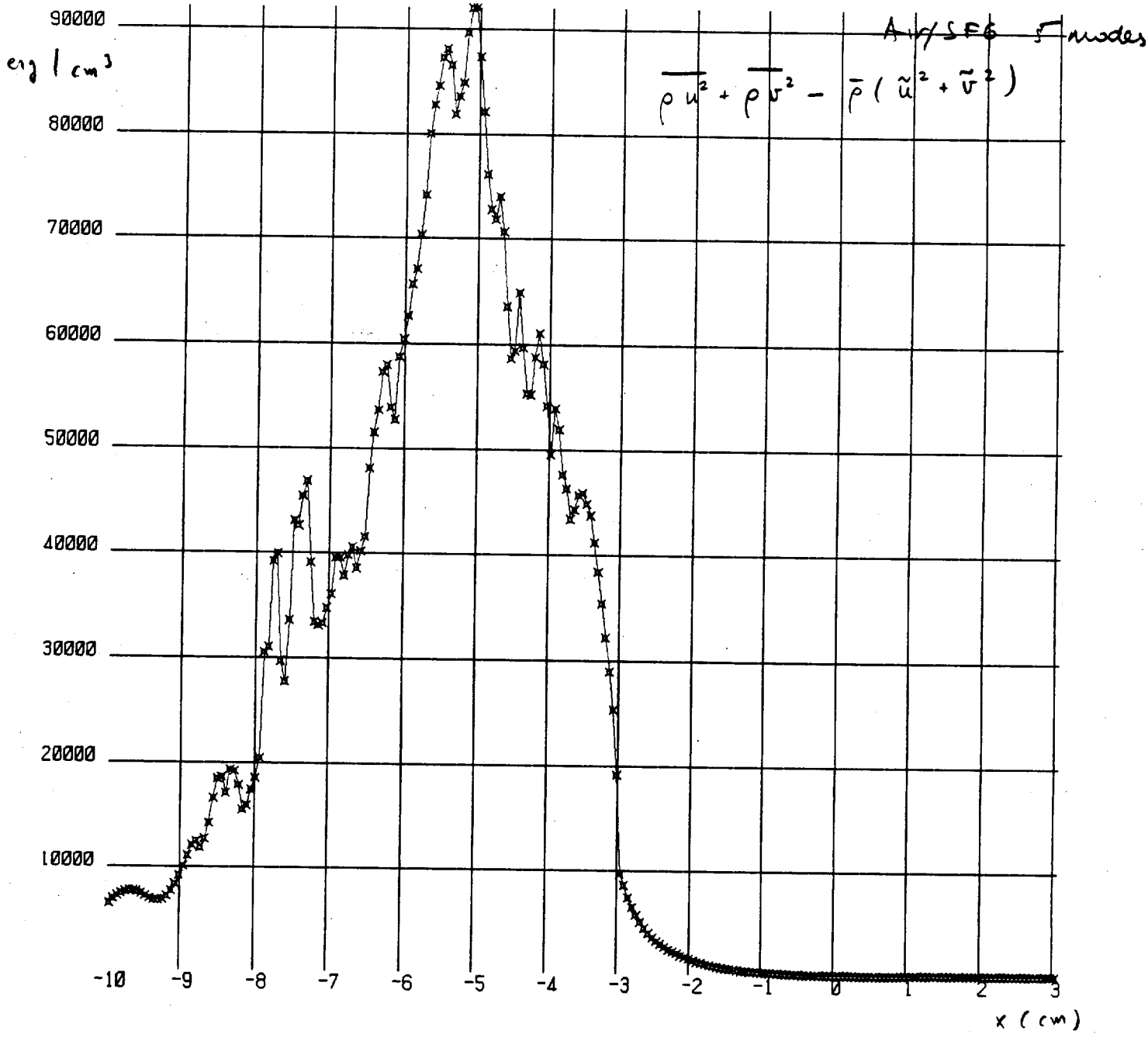
90000
80000
70000
60000
50000
40000
30000
20000
10000
erg / cm³
$\overline{\rho u^2} + \overline{\rho v^2} - \bar{\rho}(\tilde{u}^2 + \tilde{v}^2)$
-10
-9
-8
-7
-6
-5
-4
-3
-2
-1
0
1
2
3
x (cm)
GAMBART E1810 180104 11/03/89
T= 0.17253E-02 RUU+RVV
R= 0.28250E-01 LIGNE 1

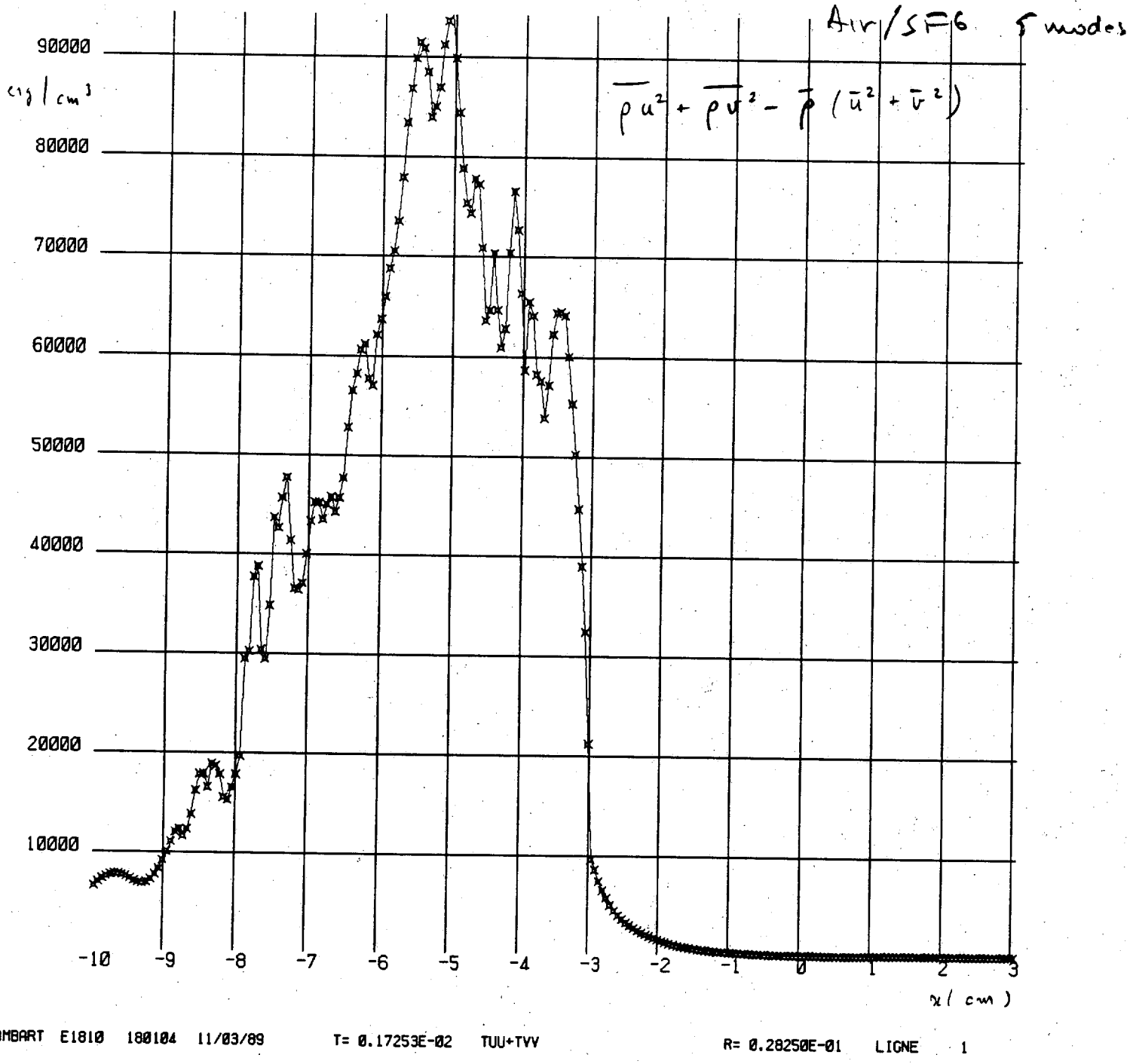
Air/SF6 5 modes
$\overline{\rho u^2} + \overline{\rho v^2} - \bar{\rho}(\bar{u}^2 + \bar{v}^2)$
erg / cm³
90000
80000
70000
60000
50000
40000
30000
20000
10000
-10 -9 -8 -7 -6 -5 -4 -3 -2 -1 0 1 2 3
x (cm)
GAMBART E1810 180104 11/03/89
T= 0.17253E-02 TUU+TVV
R= 0.28250E-01 LIGNE 1

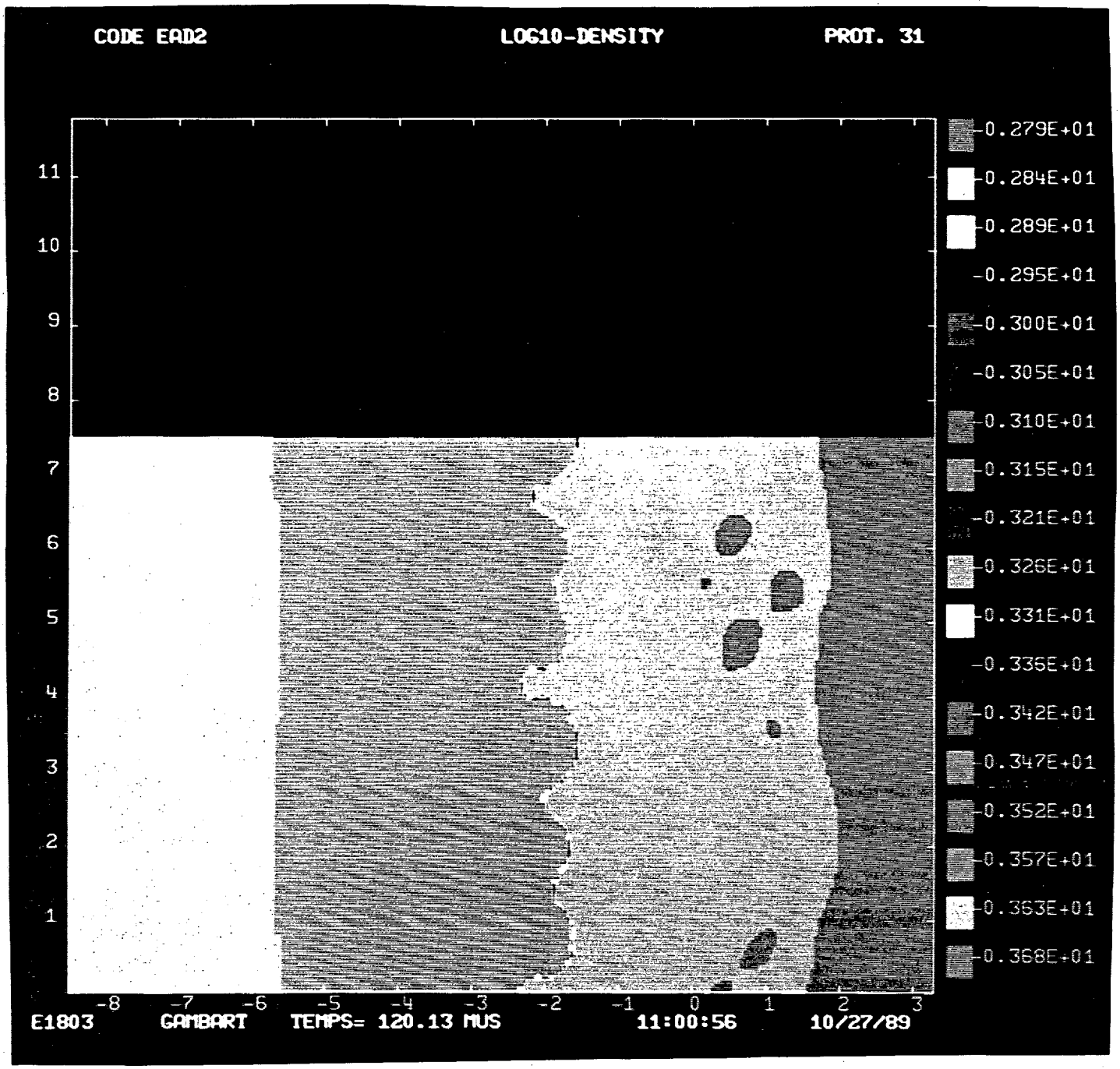
CODE EAD2
LOG10-DENSITY
PROT. 31
11
10
9
8
7
6
5
4
3
2
1
-8
-7
-6
-5
-4
-3
-2
-1
0
1
2
3
-0.279E+01
-0.284E+01
-0.289E+01
-0.295E+01
-0.300E+01
-0.305E+01
-0.310E+01
-0.315E+01
-0.321E+01
-0.326E+01
-0.331E+01
-0.336E+01
-0.342E+01
-0.347E+01
-0.352E+01
-0.357E+01
-0.363E+01
-0.368E+01
E1803
GAMBART
TEMPS= 120.13 MUS
11:00:56
10/27/89

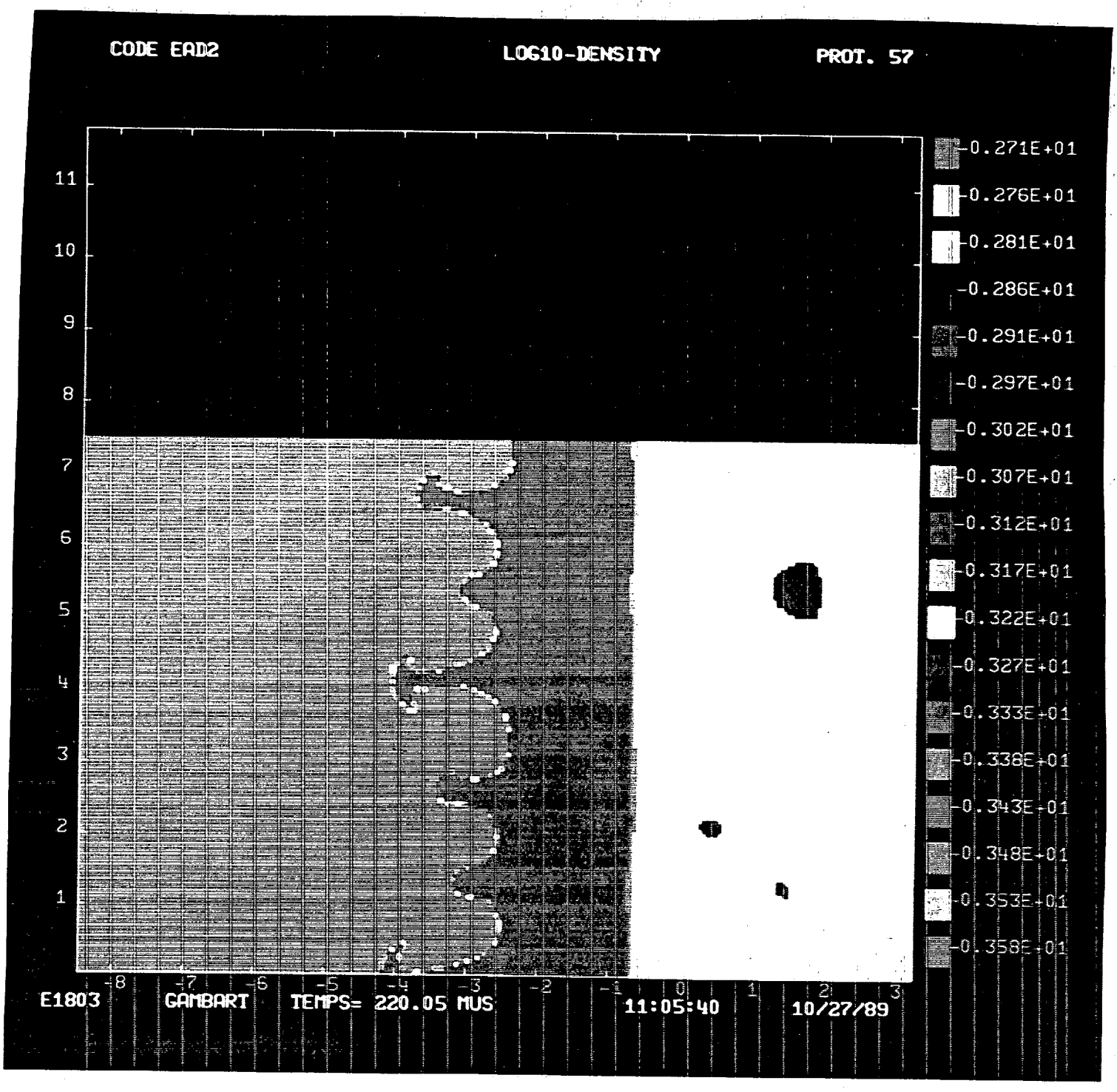
CODE EAD2
LOG10-DENSITY
PROT. 57
11
10
9
8
7
6
5
4
3
2
1
-0.271E+01
-0.276E+01
-0.281E+01
-0.286E+01
-0.291E+01
-0.297E+01
-0.302E+01
-0.307E+01
-0.312E+01
-0.317E+01
-0.322E+01
-0.327E+01
-0.333E+01
-0.338E+01
-0.343E+01
-0.348E+01
-0.353E+01
-0.358E+01
-8
-7
-6
-5
-4
-3
-2
-1
0
1
2
3
E1803
GAMBART
TEMPS= 220.05 MUS
11:05:40
10/27/89

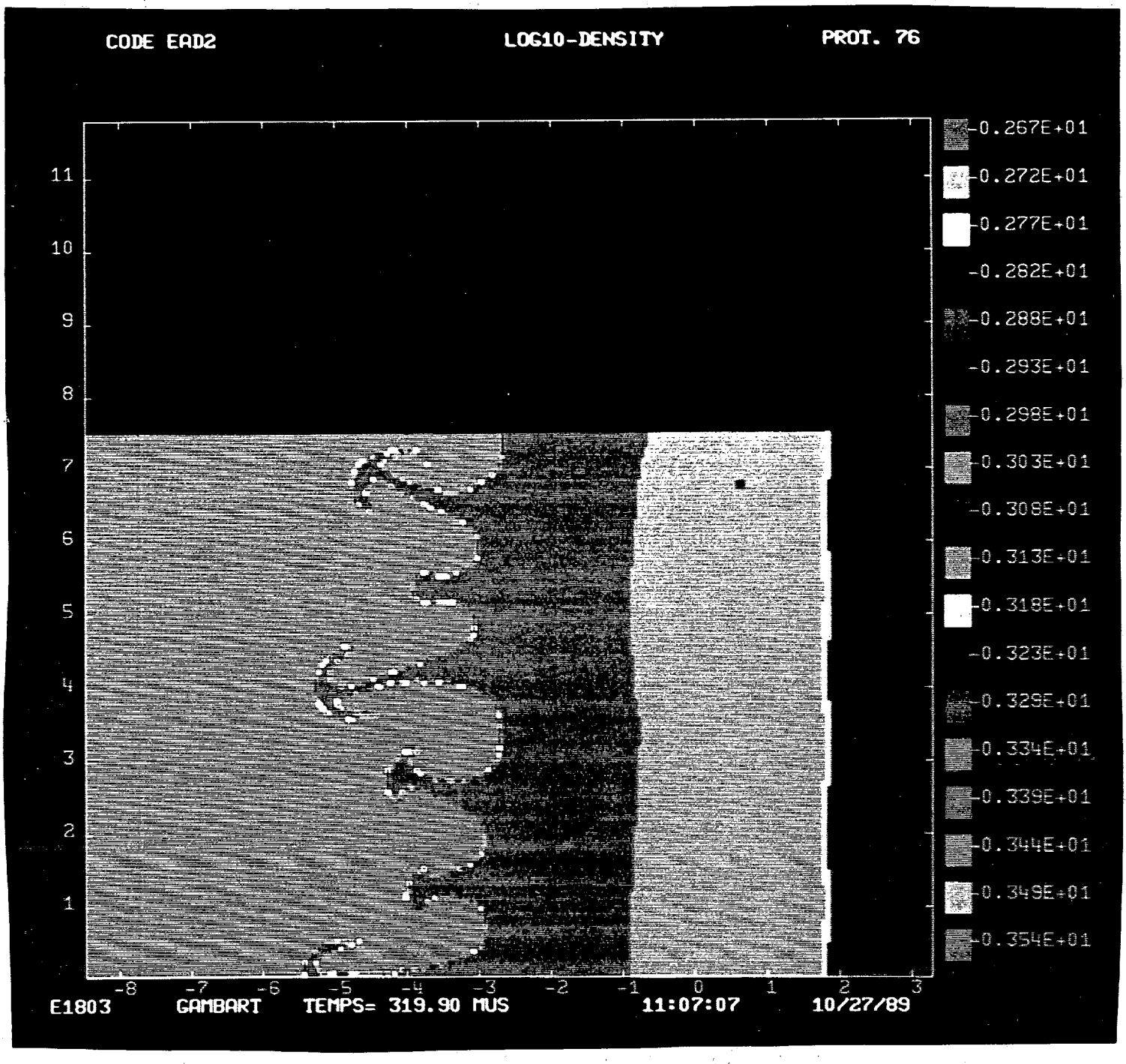
CODE EAD2
LOG10-DENSITY
PROT. 76
-0.267E+01
-0.272E+01
-0.277E+01
-0.282E+01
-0.288E+01
-0.293E+01
-0.298E+01
-0.303E+01
-0.308E+01
-0.313E+01
-0.318E+01
-0.323E+01
-0.329E+01
-0.334E+01
-0.339E+01
-0.344E+01
-0.349E+01
-0.354E+01
11
10
9
8
7
6
5
4
3
2
1
-8 -7 -6 -5 -4 -3 -2 -1 0 1 2 3
E1803 GAMBART TEMPS= 319.90 MUS 11:07:07 10/27/89

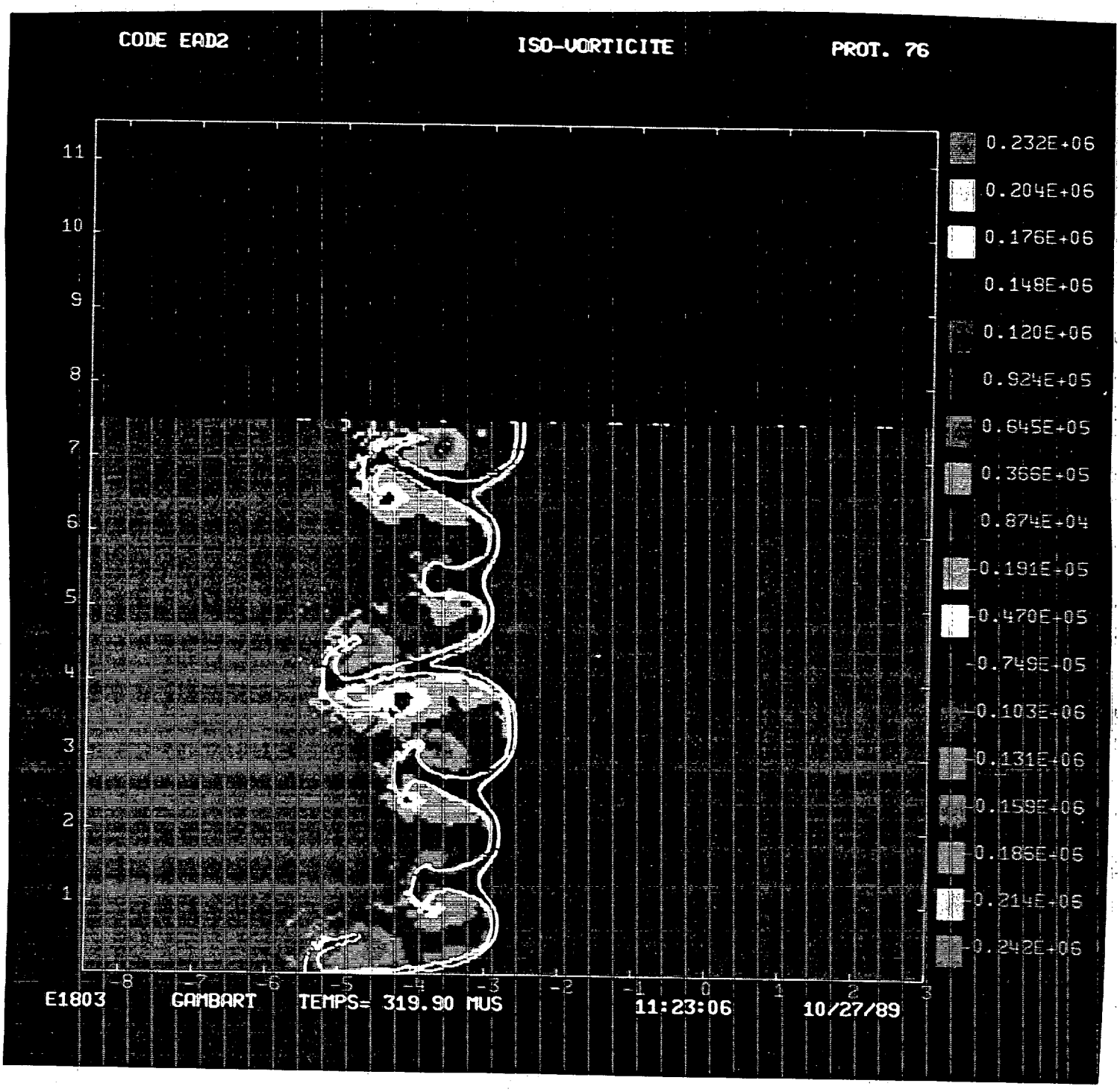
CODE EAD2
ISO-VORTICITE
PROT. 76
11
10
9
8
7
6
5
4
3
2
1
-8
-7
-6
-5
-4
-3
-2
-1
0
1
2
3
0.232E+06
0.204E+06
0.176E+06
0.148E+06
0.120E+06
0.924E+05
0.645E+05
0.366E+05
0.874E+04
-0.191E+05
-0.470E+05
-0.749E+05
-0.103E+06
-0.131E+06
-0.159E+06
-0.186E+06
-0.214E+06
-0.242E+06
E1803
GAMBART
TEMPS= 319.90 MUS
11:23:06
10/27/89

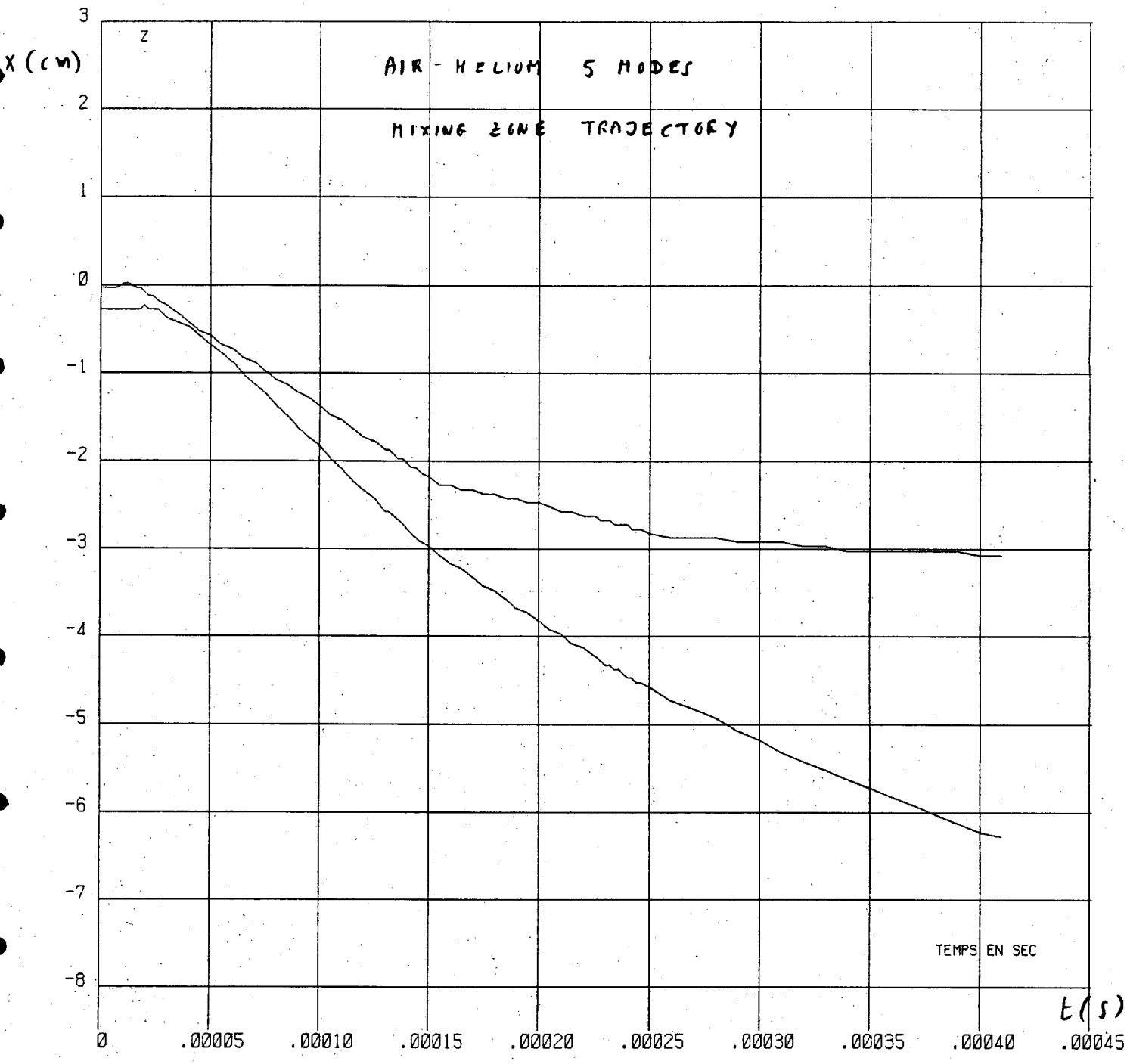
Z
X (cm)
AIR - HELIUM 5 MODES
MIXING ZONE TRAJECTORY
TEMPS EN SEC
t(s)
3
2
1
0
-1
-2
-3
-4
-5
-6
-7
-8
0
.00005
.00010
.00015
.00020
.00025
.00030
.00035
.00040
.00045

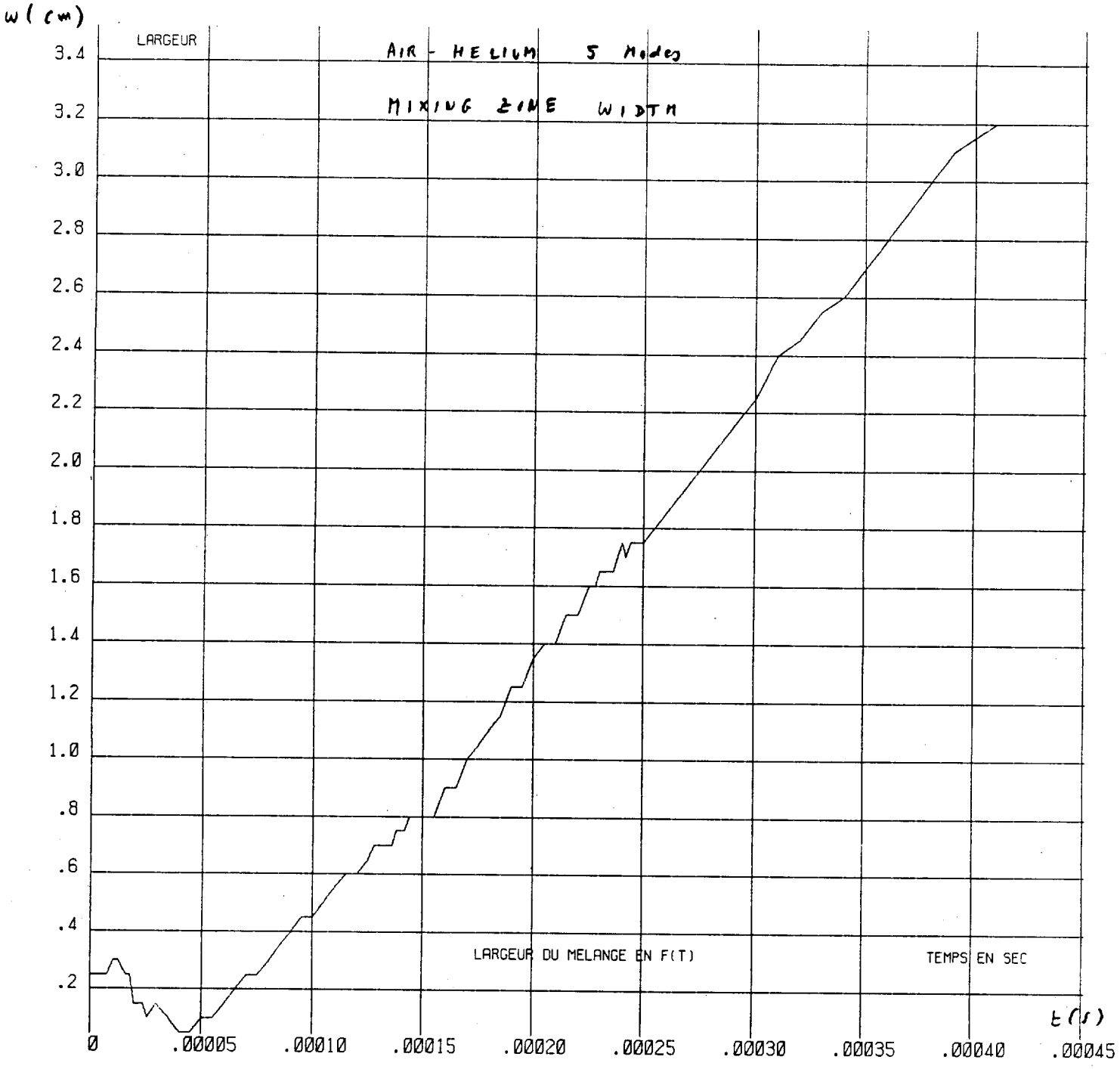
w (cm)
LARGEUR
AIR - HELIUM 5 Modes
MIXING ZONE WIDTH
3.4
3.2
3.0
2.8
2.6
2.4
2.2
2.0
1.8
1.6
1.4
1.2
1.0
.8
.6
.4
.2
LARGEUR DU MELANGE EN F(T)
TEMPS EN SEC
t (s)
0
.00005
.00010
.00015
.00020
.00025
.00030
.00035
.00040
.00045

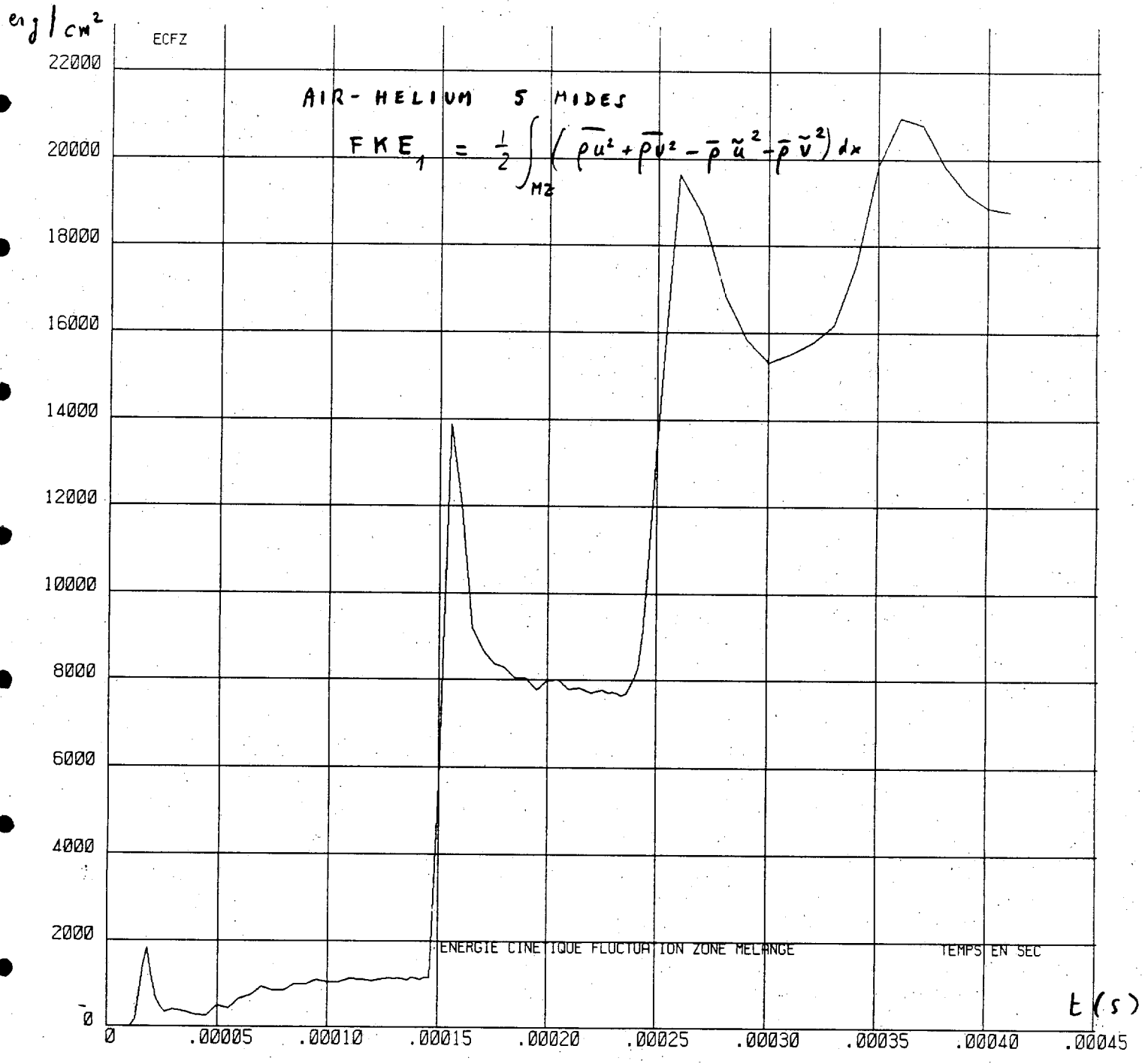
erg/cm²
ECFZ
AIR - HELIUM 5 MIDES
$FKE_1 = \frac{1}{2}\int_{MZ}\left(\overline{\rho u^2} + \overline{\rho v^2} - \bar{\rho}\tilde{u}^2 - \bar{\rho}\tilde{v}^2\right) dx$
22000
20000
18000
16000
14000
12000
10000
8000
6000
4000
2000
0
ENERGIE CINETIQUE FLUCTUATION ZONE MELANGE
TEMPS EN SEC
t(s)
0
.00005
.00010
.00015
.00020
.00025
.00030
.00035
.00040
.00045

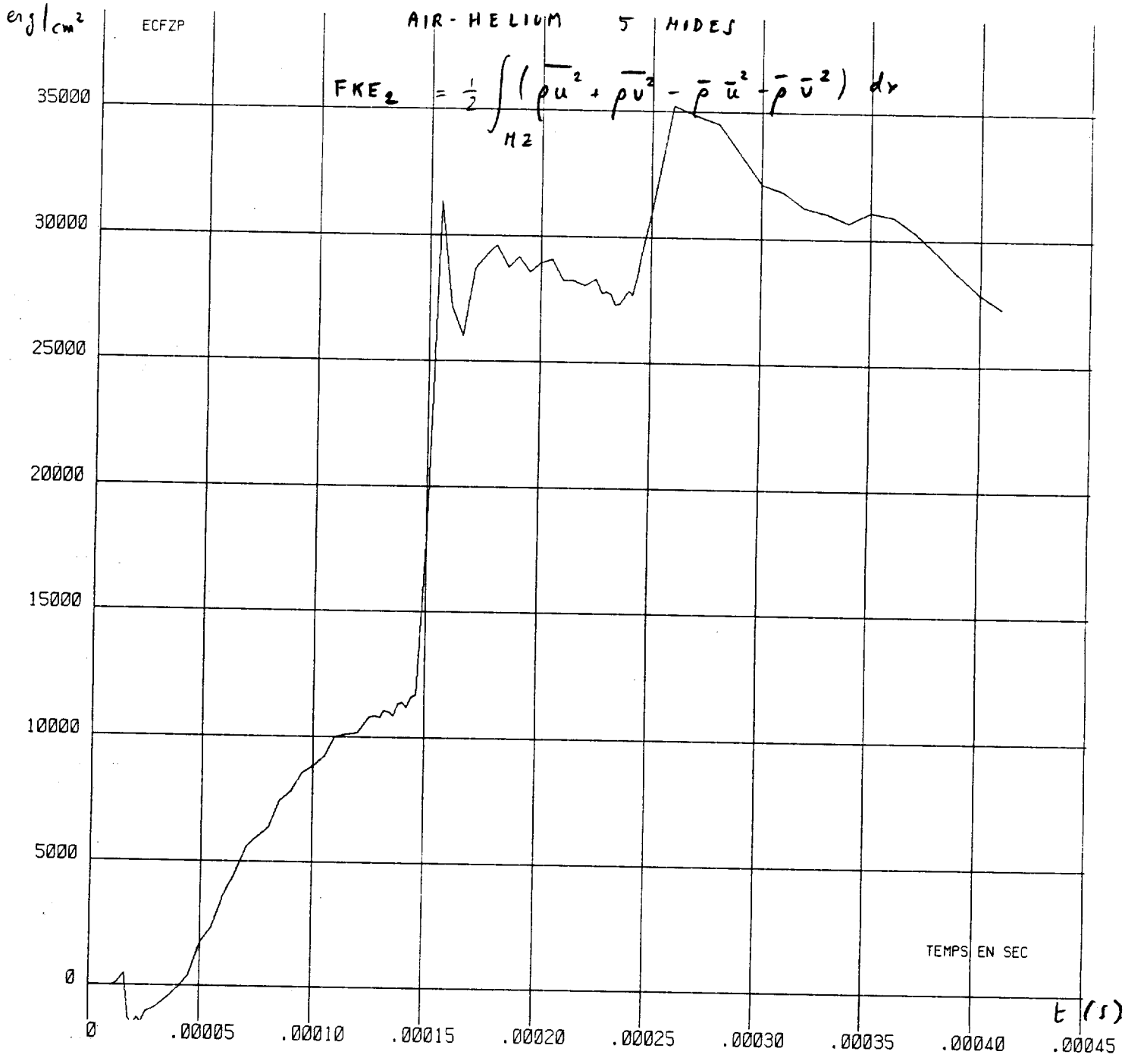
erg/cm²
ECFZP
AIR - HELIUM 5 MIDES
$FKE_2 = \frac{1}{2}\int_{M2}(\overline{\rho u^2} + \overline{\rho v^2} - \bar{\rho}\,\bar{u}^2 - \bar{\rho}\,\bar{v}^2)\,dx$
35000
30000
25000
20000
15000
10000
5000
0
TEMPS EN SEC
t (s)
0
.00005
.00010
.00015
.00020
.00025
.00030
.00035
.00040
.00045

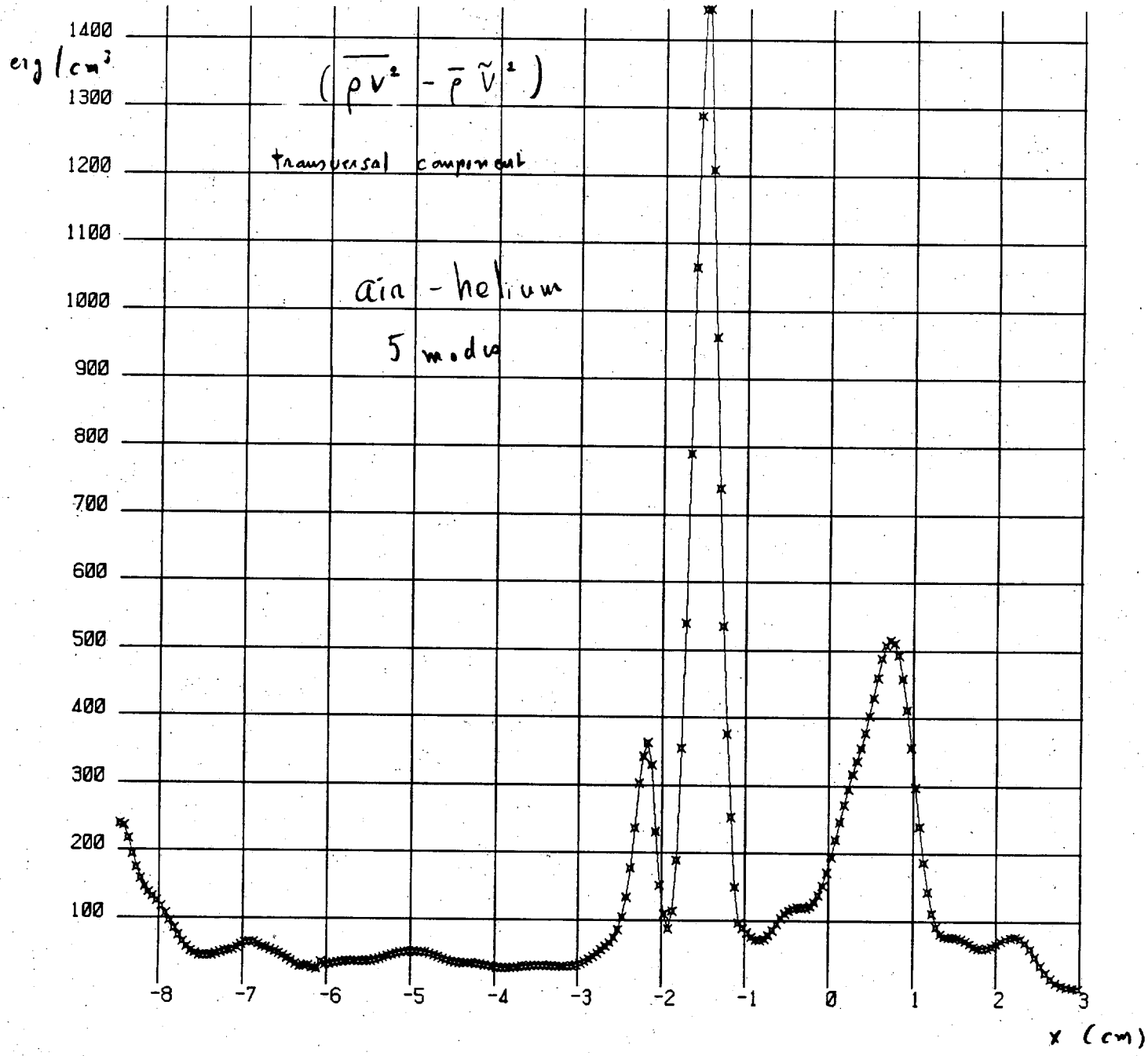
erg / cm³
$(\overline{\rho v^2} - \bar{\rho}\tilde{v}^2)$
transversal component
air - helium
5 mod
1400
1300
1200
1100
1000
900
800
700
600
500
400
300
200
100
-8
-7
-6
-5
-4
-3
-2
-1
0
1
2
3
x (cm)
GAMBART E1803 165644 10/25/89
T= 0.11515E-03 RUU TENS REYNOLDS
R= 0.25000E-01 LIGNE 1

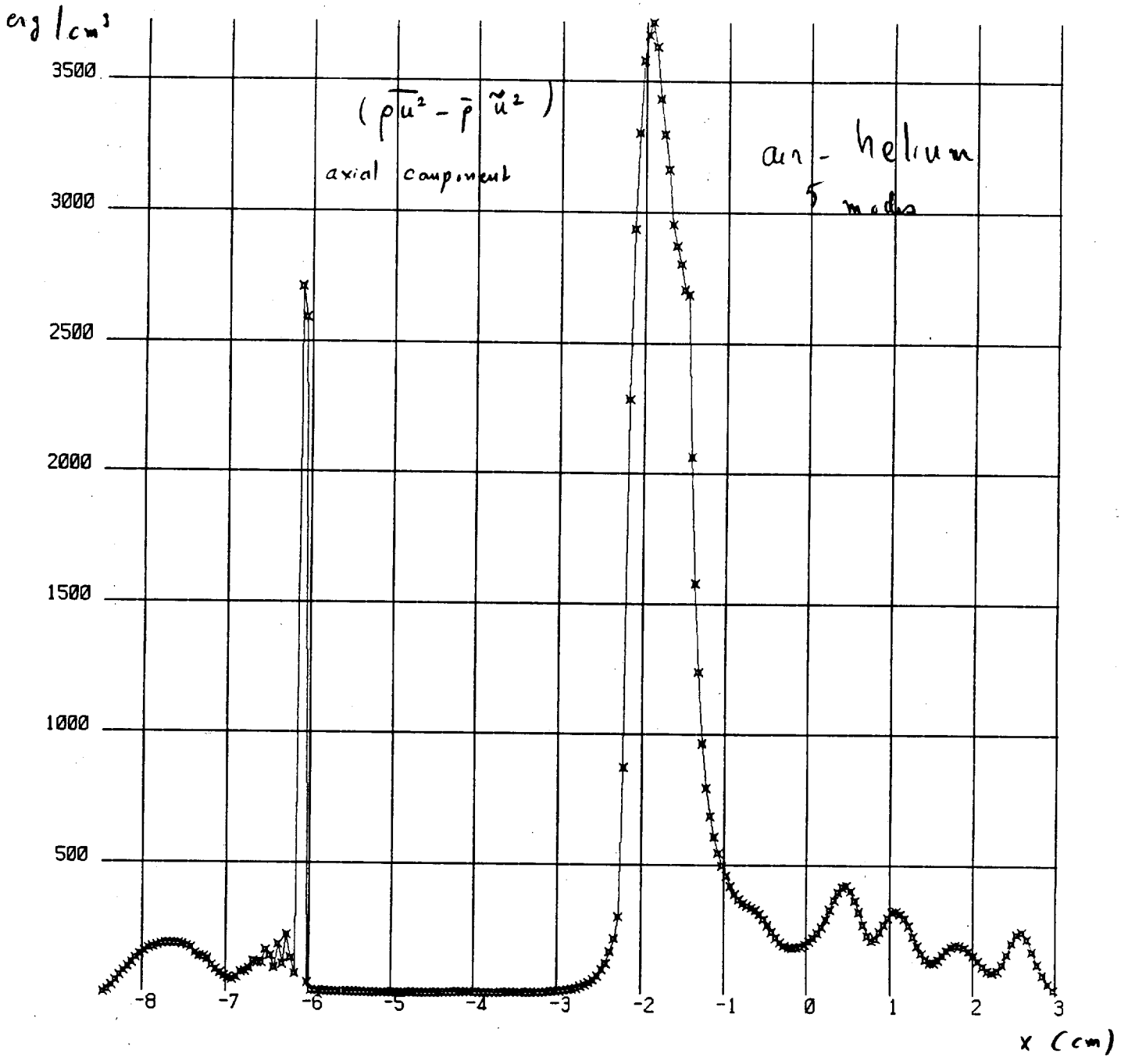

GAMBART E1803 165644 10/25/89 T= 0.11515E-03 RVV TENS REYNOLDS R= 0.25000E-01 LIGNE 1

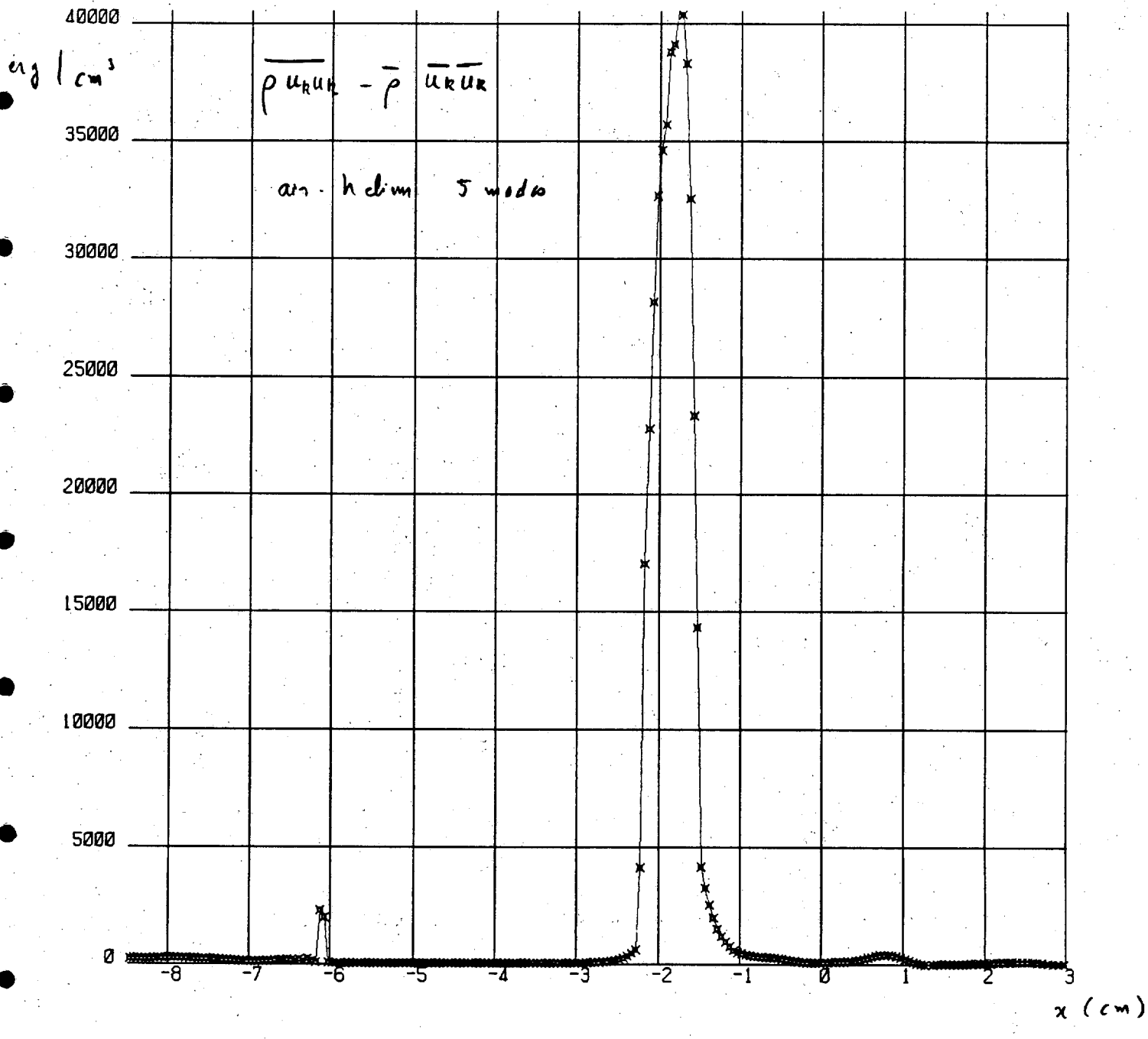
40000
35000
30000
25000
20000
15000
10000
5000
0
erg / cm³
$\overline{\rho u_k u_k} - \bar{\rho}\,\bar{u}_k \bar{u}_k$
air - helium 5 modes
-8
-7
-6
-5
-4
-3
-2
-1
0
1
2
3
x (cm)
GAMBART E1803 165644 10/25/89
T= 0.11515E-03 TUU+TVV
R= 0.25000E-01 LIGNE 1

$\bar{\rho} k = \left(\overline{\rho u_k u_k} - \bar{\rho} \hat{u}_k \hat{u}_k \right)$ Air/Helium 5 mole

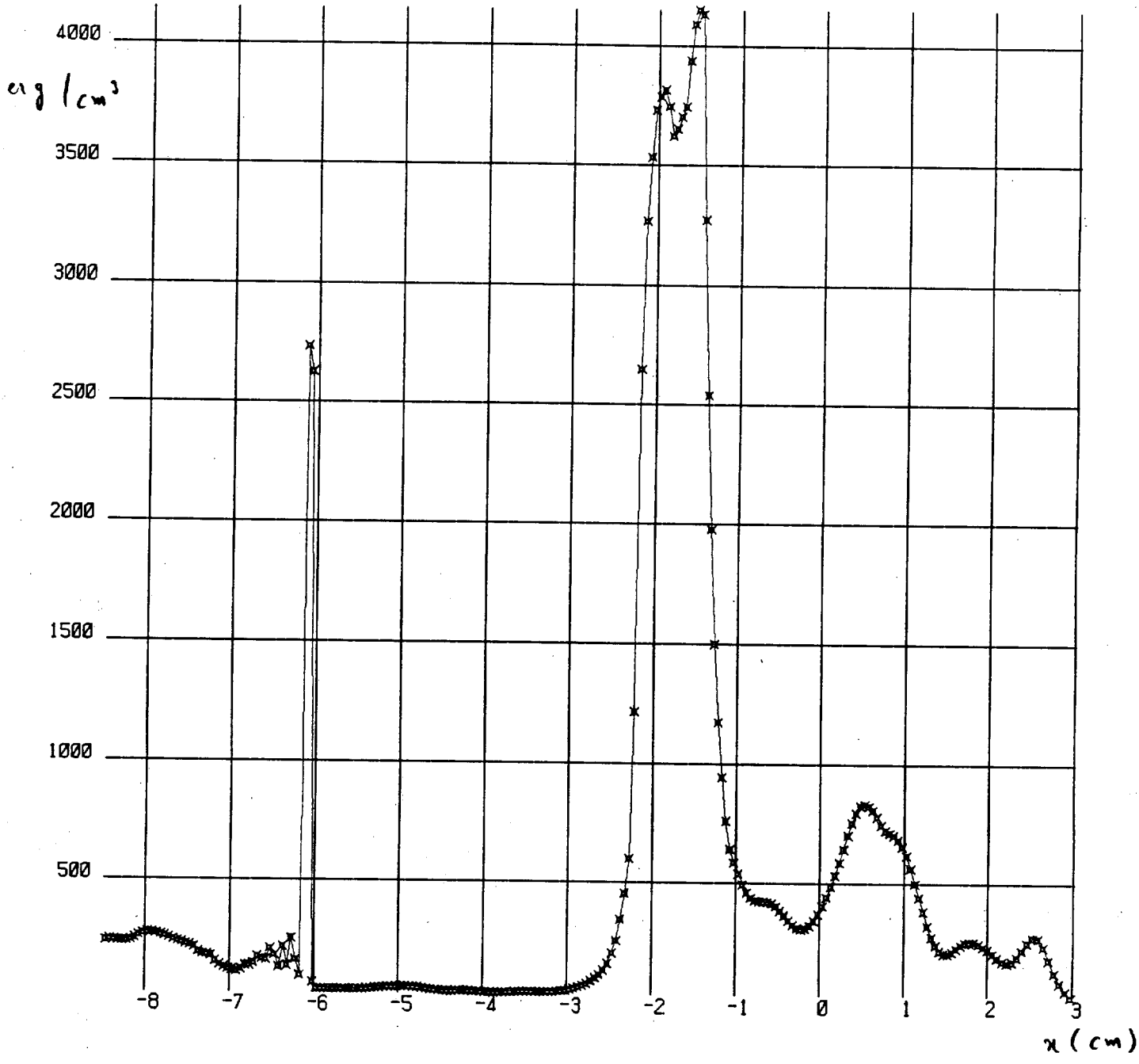

GAMBART E1803 165644 10/25/89 T= 0.11515E-03 RUU+RVV R= 0.25000E-01 LIGNE 1

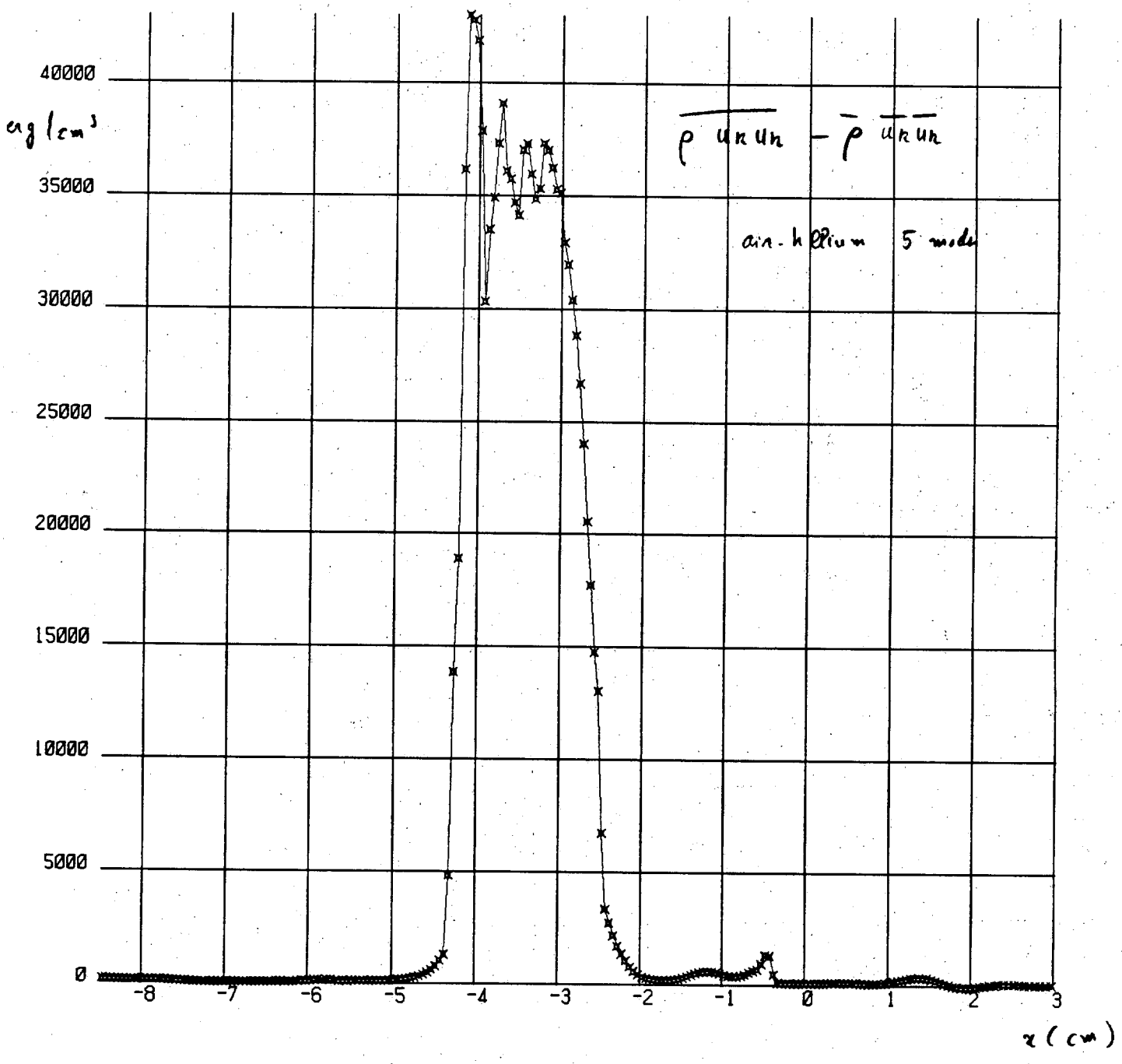
40000
35000
30000
25000
20000
15000
10000
5000
0
-8
-7
-6
-5
-4
-3
-2
-1
0
1
2
3
x (cm)
air-helium 5 mode
GAMBART E1803 165644 10/25/89
T= 0.22993E-03 TUU+TVV
R= 0.25000E-01 LIGNE 1

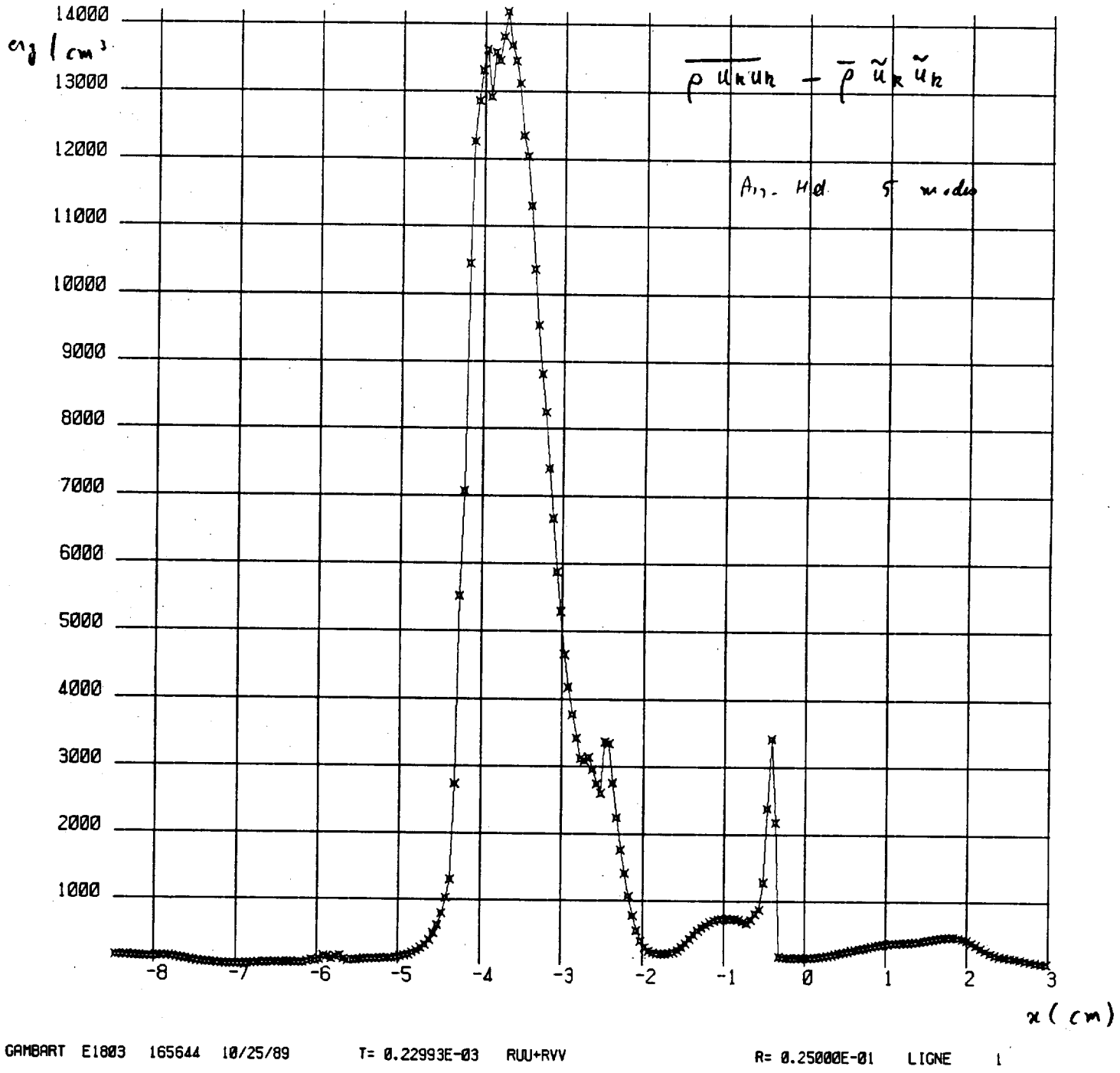
erg / cm³
14000
13000
12000
11000
10000
9000
8000
7000
6000
5000
4000
3000
2000
1000
$\overline{\rho u_k u_h} - \bar{\rho} \tilde{u}_k \tilde{u}_h$
Ajj. Hd 5f mode
-8
-7
-6
-5
-4
-3
-2
-1
0
1
2
3
x (cm)
GAMBART E1803 165644 10/25/89
T= 0.22993E-03 RUU+RVV
R= 0.25000E-01 LIGNE 1

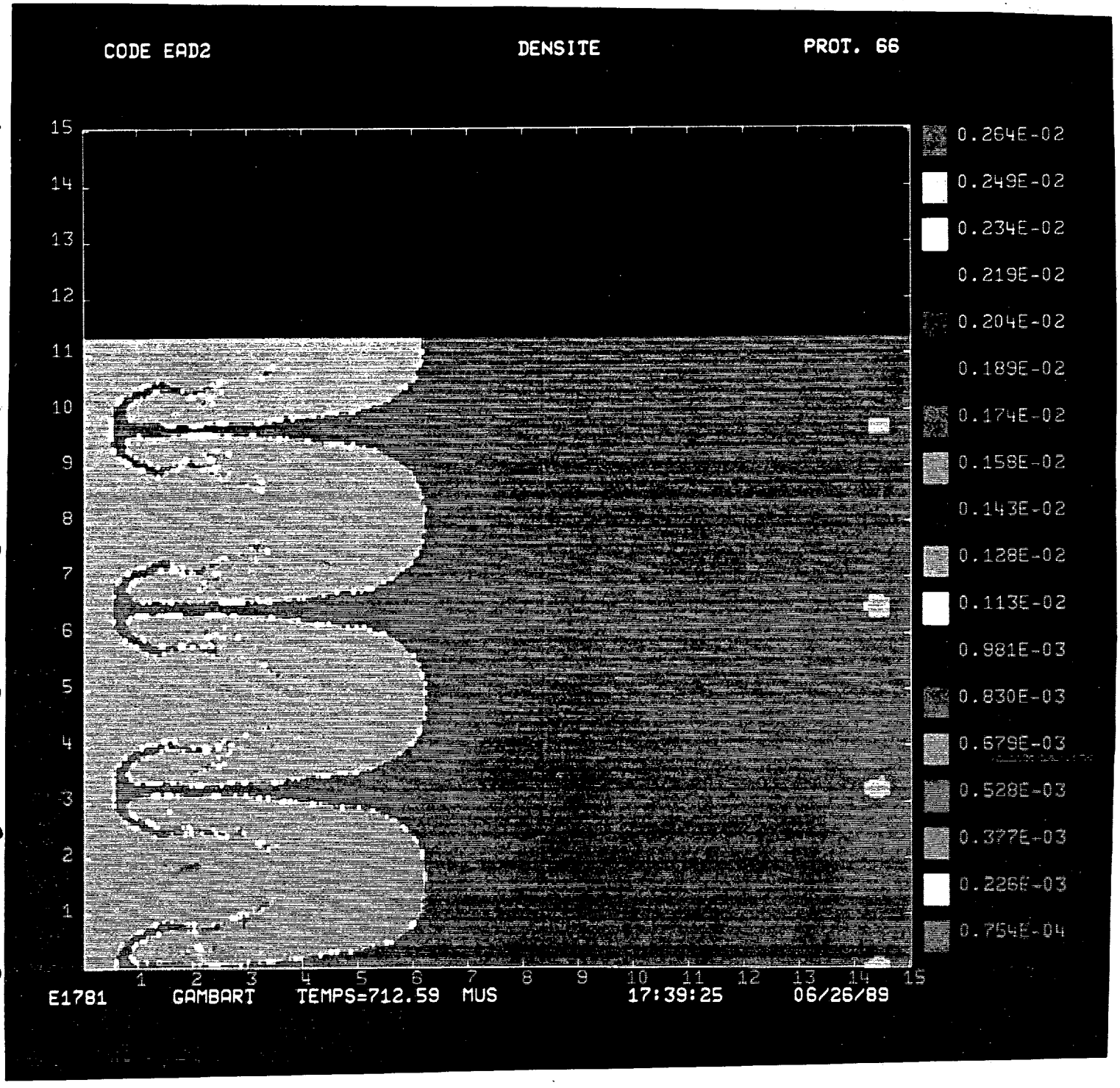
CODE EAD2
DENSITE
PROT. 66
0.264E-02
0.249E-02
0.234E-02
0.219E-02
0.204E-02
0.189E-02
0.174E-02
0.158E-02
0.143E-02
0.128E-02
0.113E-02
0.981E-03
0.830E-03
0.679E-03
0.528E-03
0.377E-03
0.226E-03
0.754E-04
E1781 GAMBART TEMPS=712.59 MUS 17:39:25 06/26/89

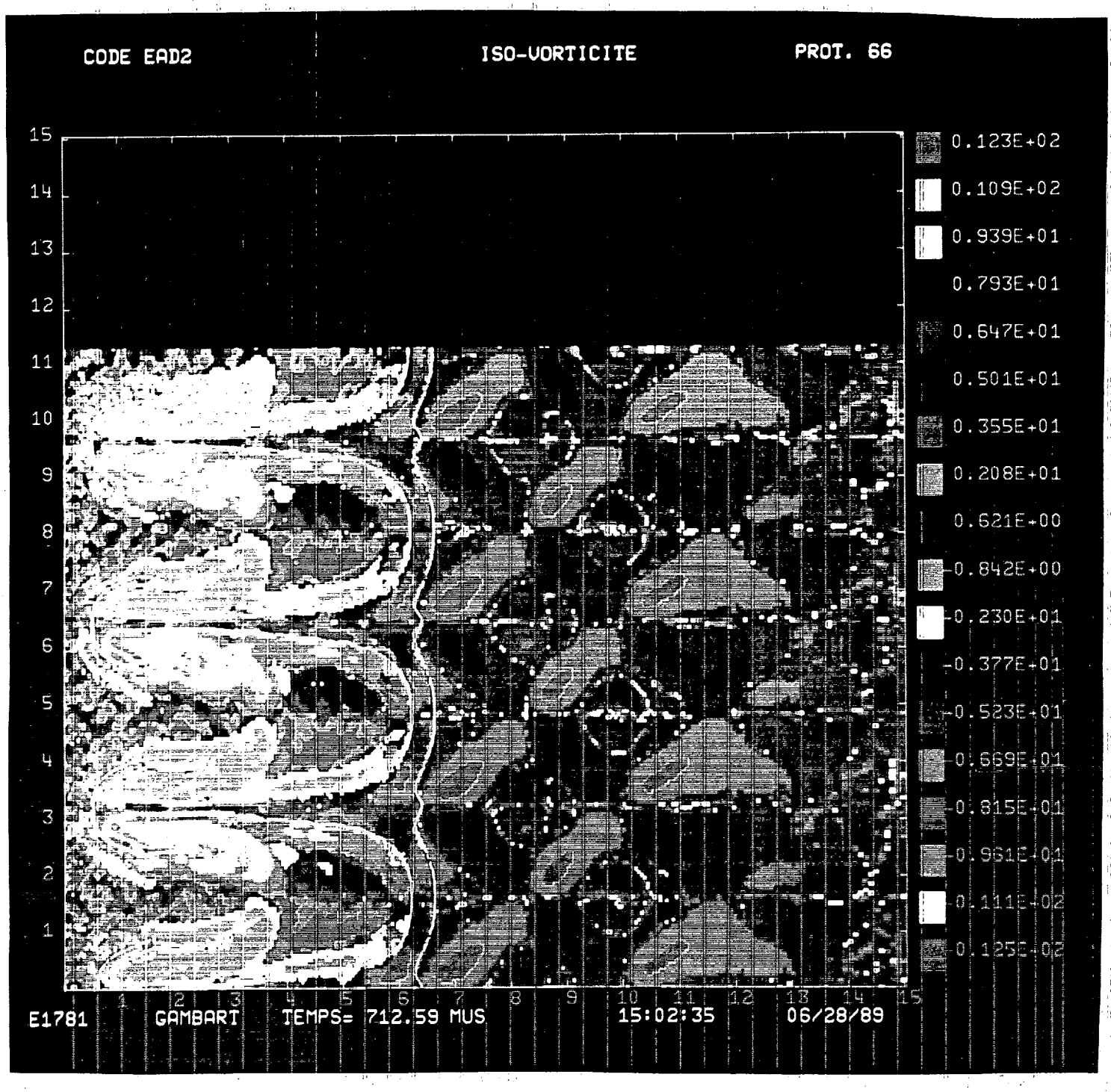
CODE EAD2
ISO-VORTICITE
PROT. 66
0.123E+02
0.109E+02
0.939E+01
0.793E+01
0.647E+01
0.501E+01
0.355E+01
0.208E+01
0.621E+00
-0.842E+00
-0.230E+01
-0.377E+01
-0.523E+01
-0.669E+01
-0.815E+01
-0.961E+01
-0.111E+02
-0.125E+02
E1781
GAMBART
TEMPS= 712.59 MUS
15:02:35
06/28/89

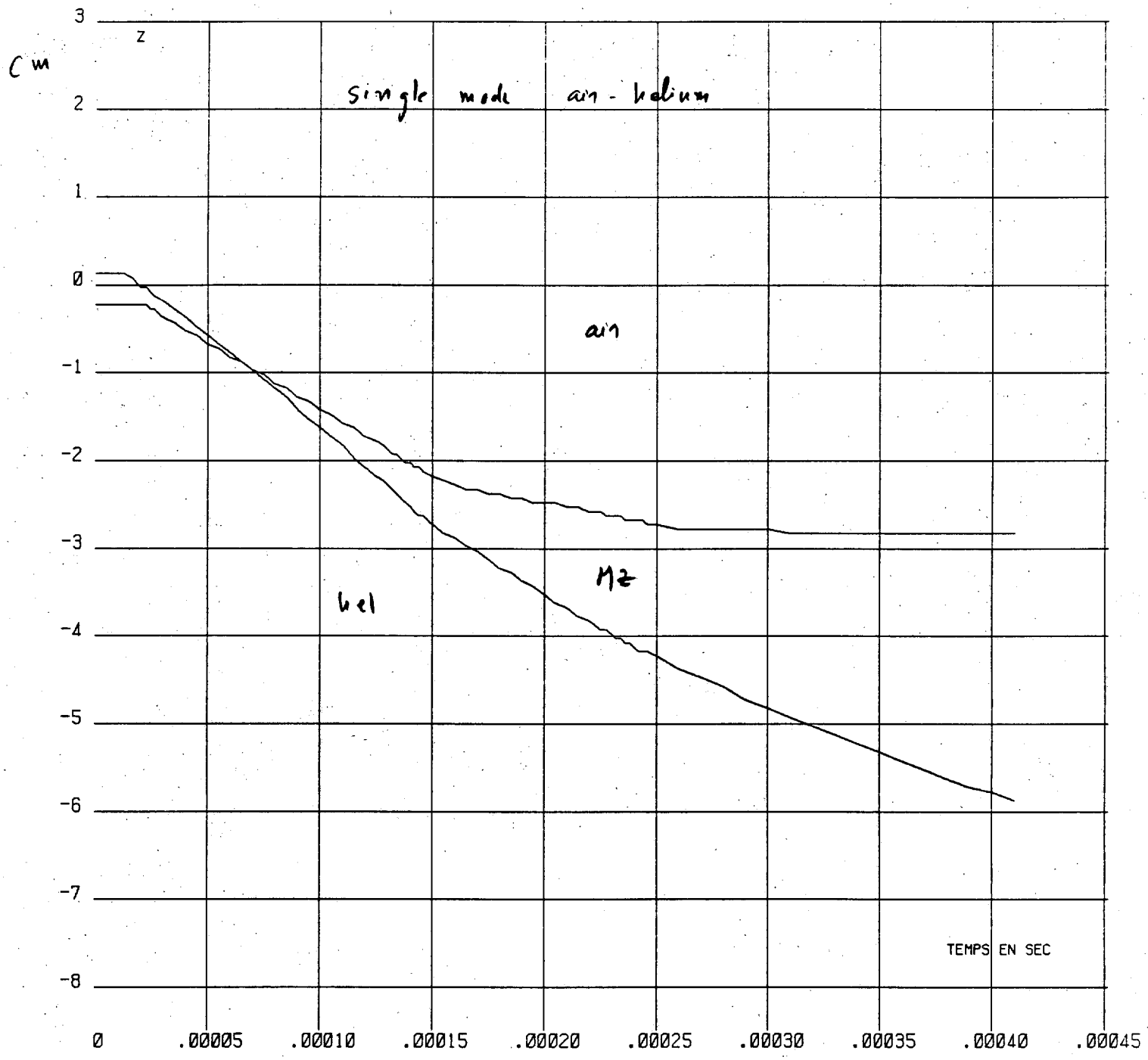
Z
Cm
single mode air - helium
air
hel
Mz
TEMPS EN SEC
3
2
1
0
-1
-2
-3
-4
-5
-6
-7
-8
0
.00005
.00010
.00015
.00020
.00025
.00030
.00035
.00040
.00045

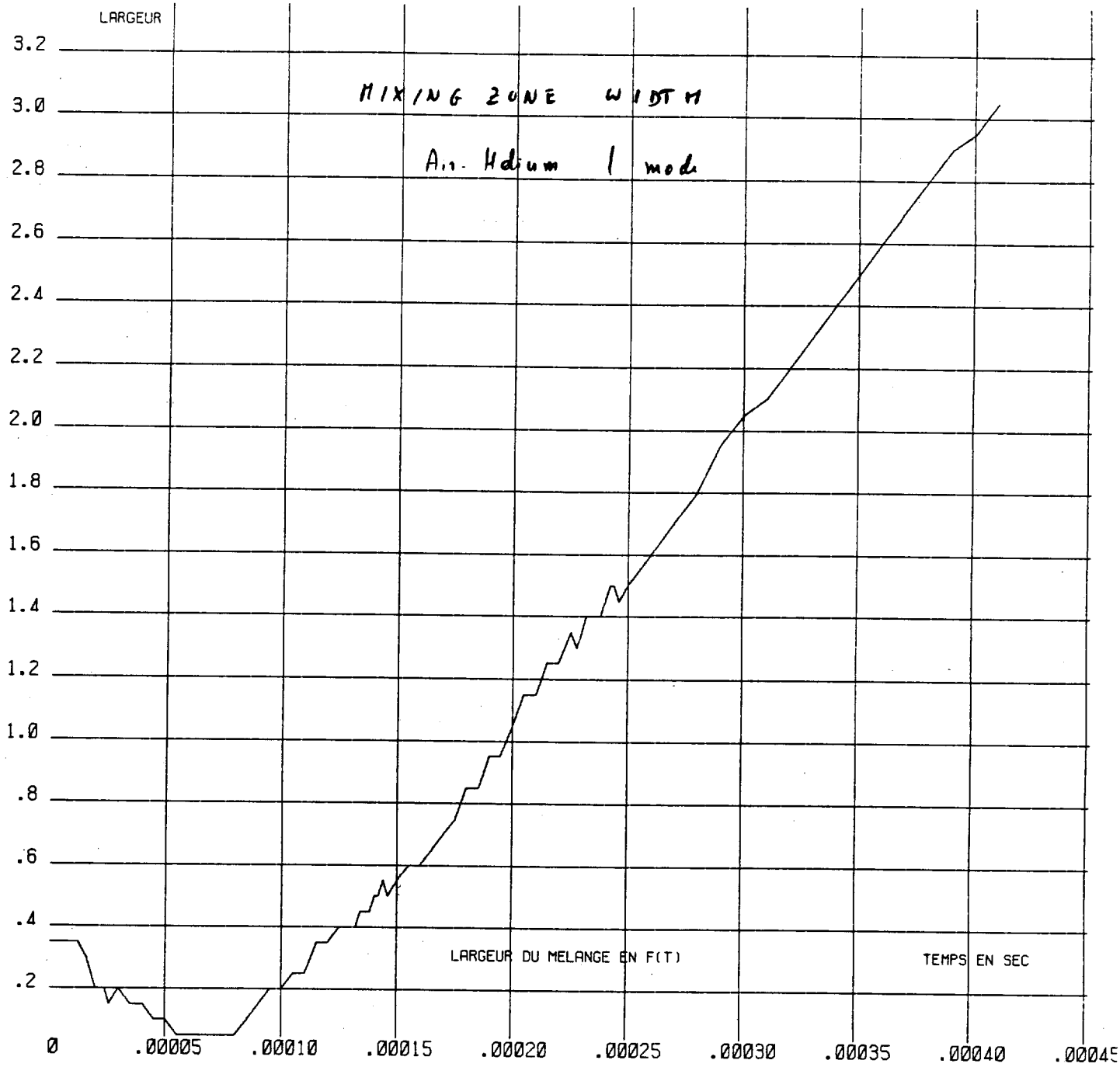
LARGEUR
3.2
3.0
2.8
2.6
2.4
2.2
2.0
1.8
1.6
1.4
1.2
1.0
.8
.6
.4
.2
MIXING ZONE WIDTH
Air Helium I mod
LARGEUR DU MELANGE EN F(T)
TEMPS EN SEC
0
.00005
.00010
.00015
.00020
.00025
.00030
.00035
.00040
.00045

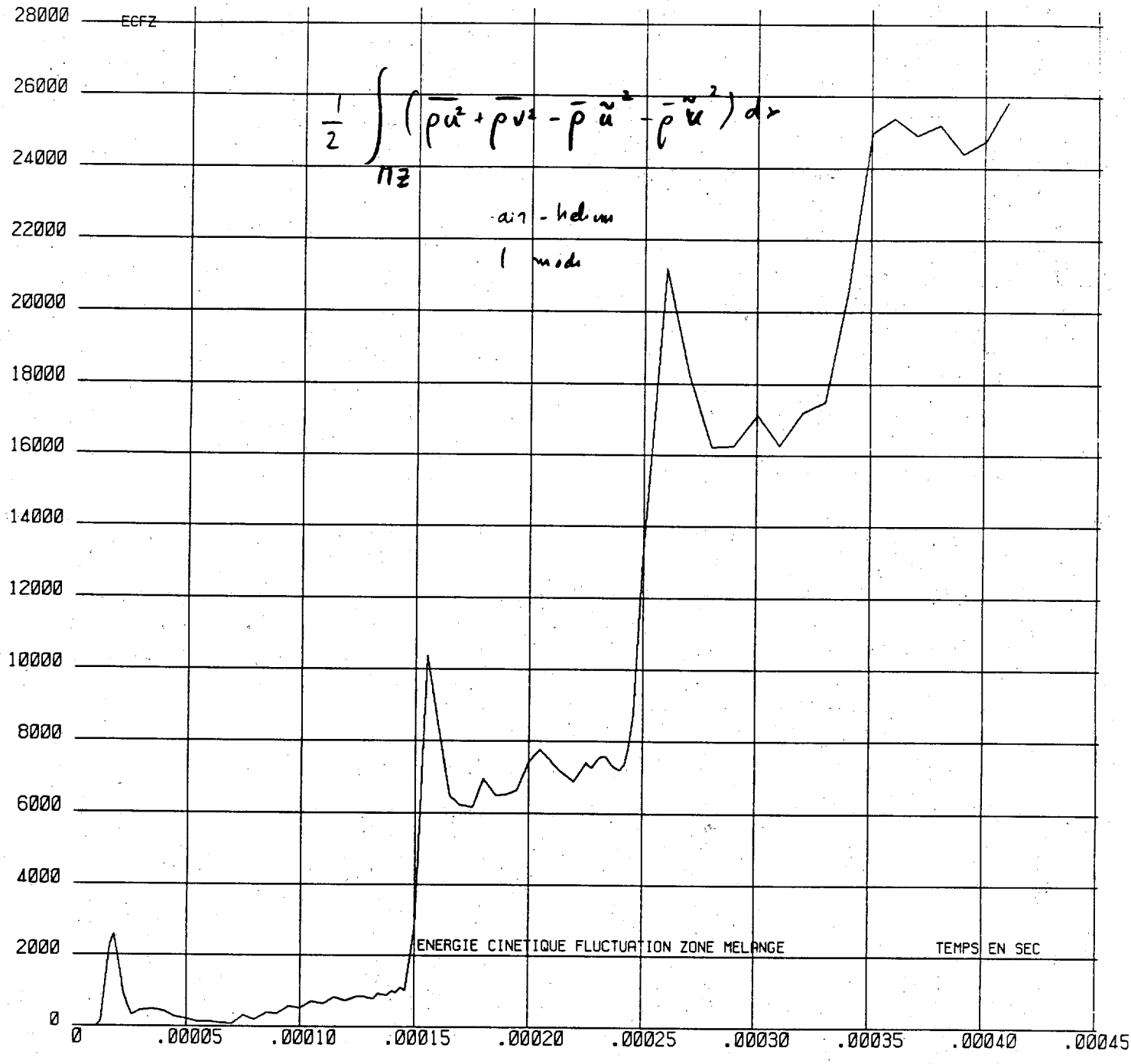
28000
26000
24000
22000
20000
18000
16000
14000
12000
10000
8000
6000
4000
2000
0
ECFZ
$\frac{1}{2}\int_{Hz}(\overline{\rho u^2}+\overline{\rho v^2}-\bar{\rho}\tilde{u}^2-\bar{\rho}\tilde{v}^2)\,dx$
air - helium
1 mode
ENERGIE CINETIQUE FLUCTUATION ZONE MELANGE
TEMPS EN SEC
0
.00005
.00010
.00015
.00020
.00025
.00030
.00035
.00040
.00045

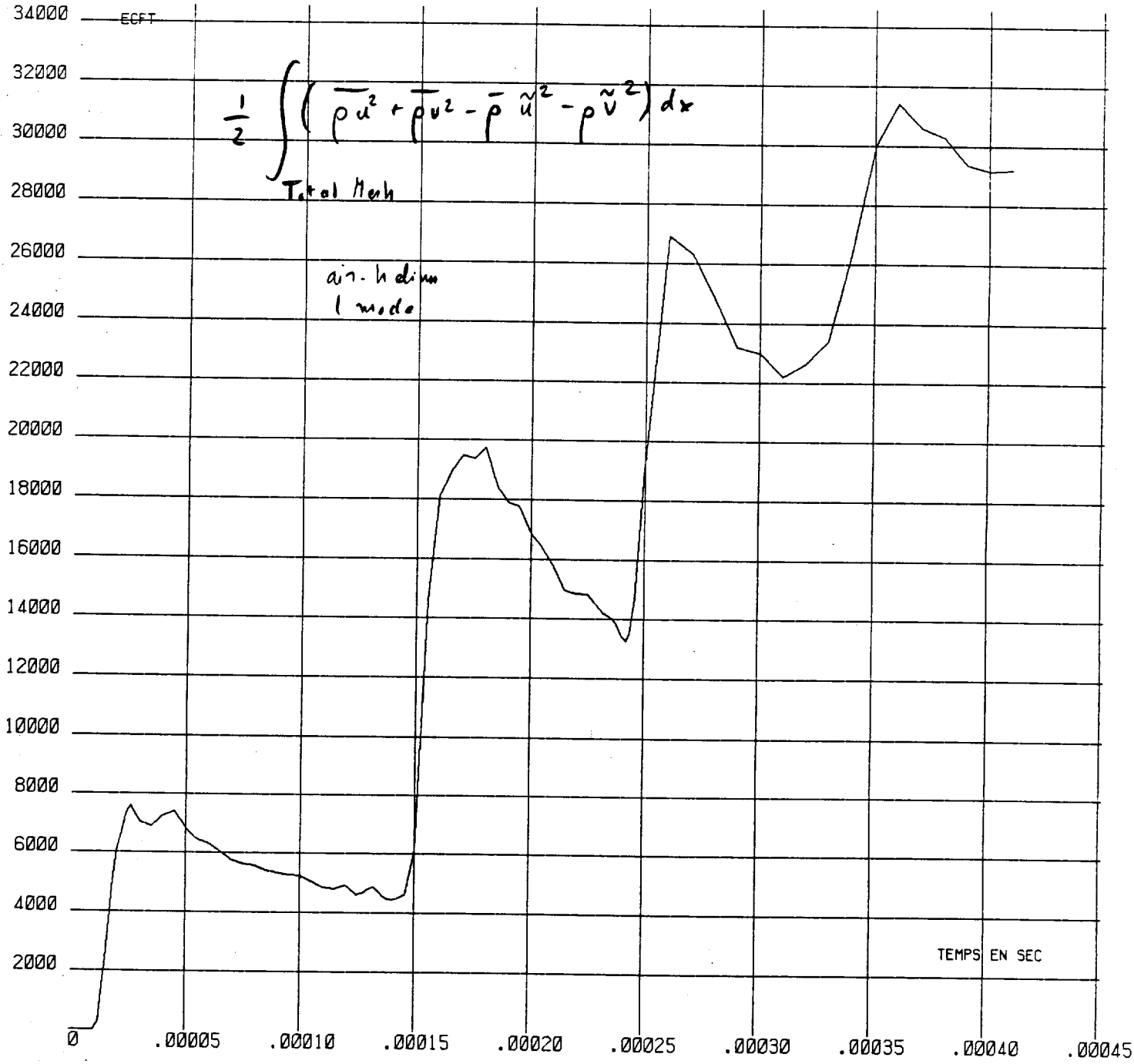
ECFT
$\frac{1}{2}\int\left(\overline{\rho}\overline{u^2}+\overline{\rho}\overline{v^2}-\bar{\rho}\tilde{u}^2-\rho\tilde{v}^2\right)dx$
Total Mesh
air-helium
1 mode
34000
32000
30000
28000
26000
24000
22000
20000
18000
16000
14000
12000
10000
8000
6000
4000
2000
0
.00005
.00010
.00015
.00020
.00025
.00030
.00035
.00040
.00045
TEMPS EN SEC

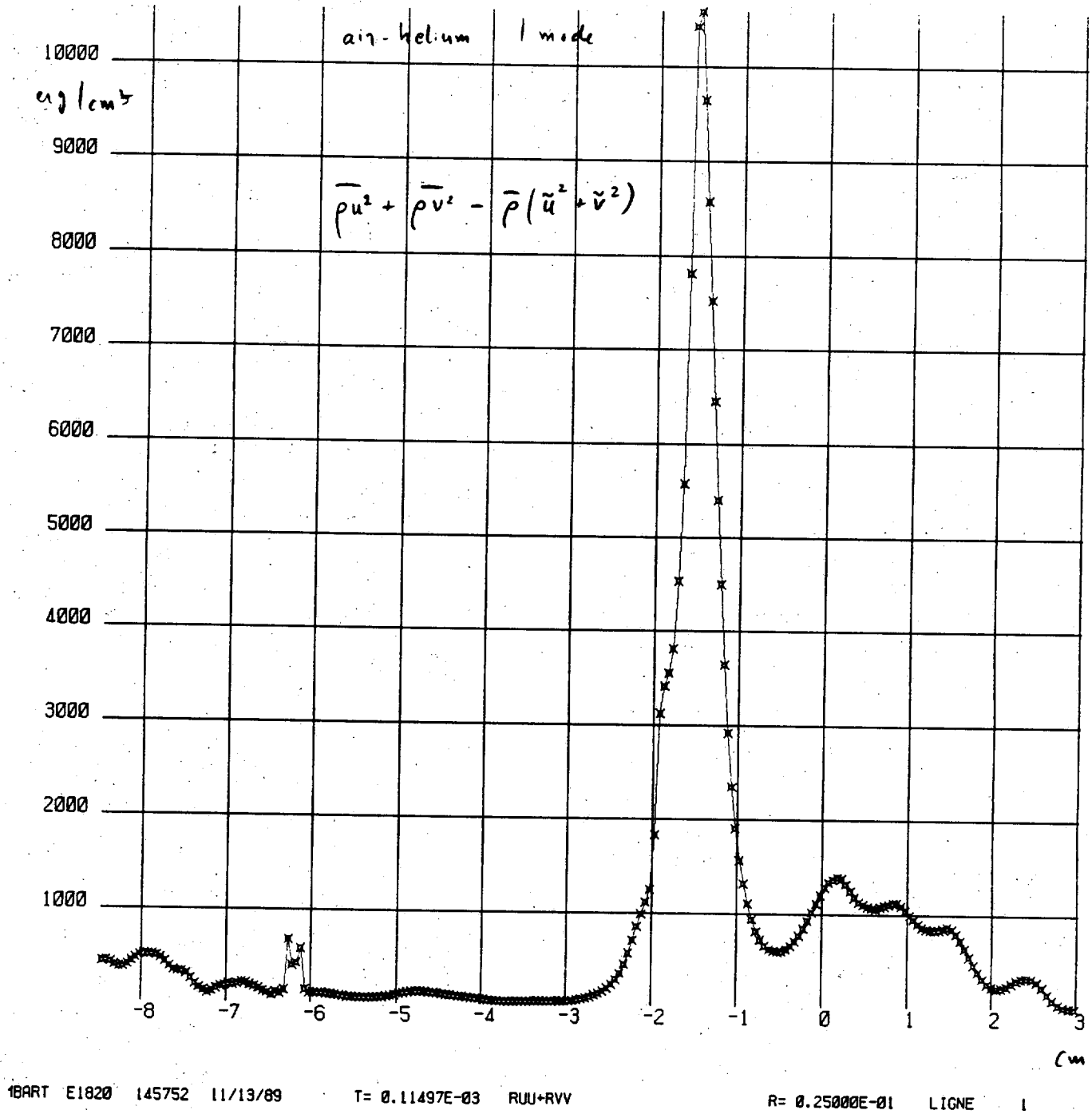
air - helium 1 mode
erg/cm³
$\overline{\rho u^2} + \overline{\rho v^2} - \bar{\rho}(\tilde{u}^2 + \tilde{v}^2)$
10000
9000
8000
7000
6000
5000
4000
3000
2000
1000
-8
-7
-6
-5
-4
-3
-2
-1
0
1
2
3
Cm
1BART E1820 145752 11/13/89
T= 0.11497E-03 RUU+RVV
R= 0.25000E-01 LIGNE 1

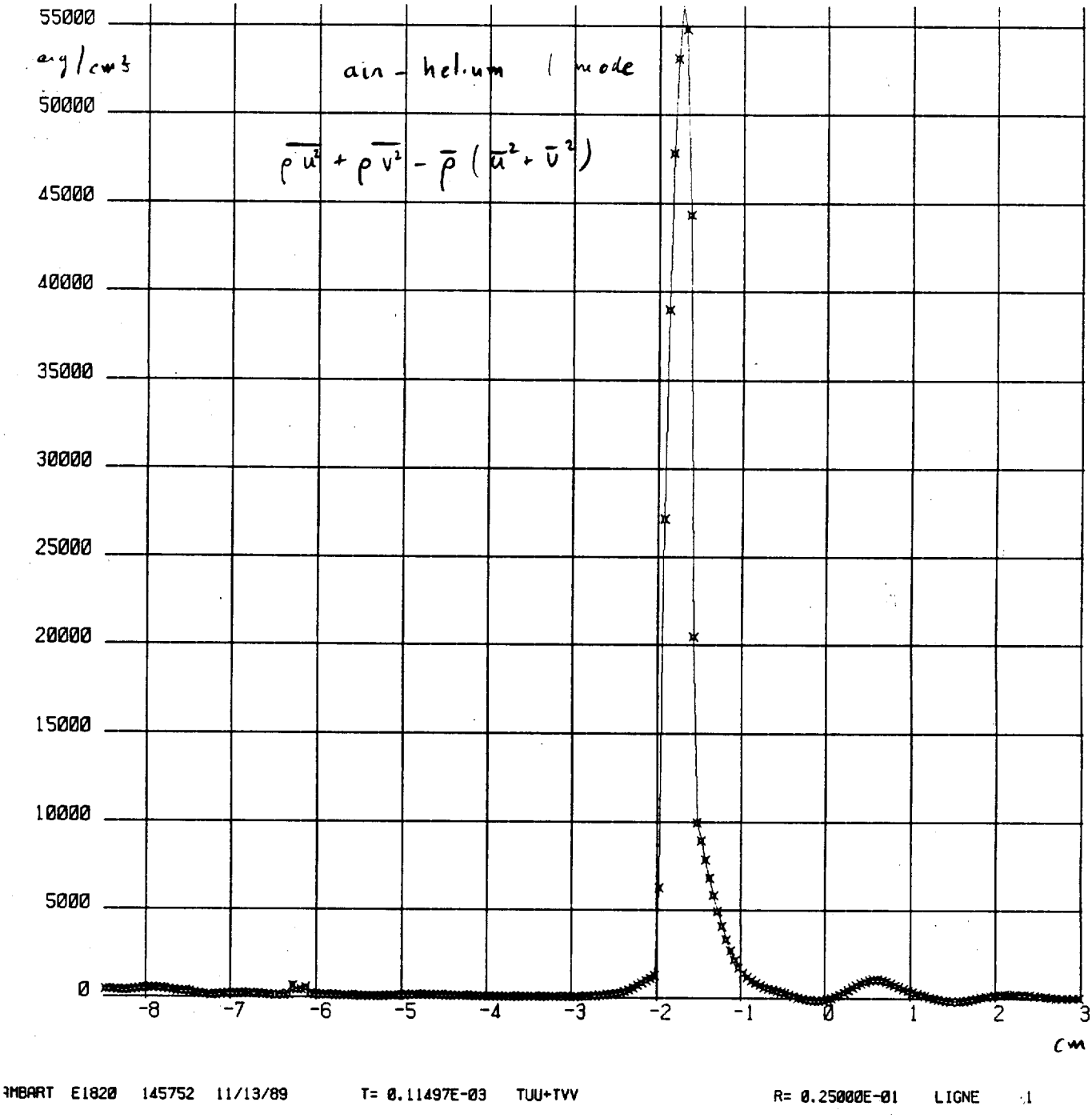
55000
erg/cm3
air - helium 1 mode
$\overline{\rho u^2} + \overline{\rho v^2} - \bar{\rho}(\tilde{u}^2 + \tilde{v}^2)$
50000
45000
40000
35000
30000
25000
20000
15000
10000
5000
0
-8
-7
-6
-5
-4
-3
-2
-1
0
1
2
3
cm
MBART E1820 145752 11/13/89
T= 0.11497E-03 TUU+TVV
R= 0.25000E-01 LIGNE 1

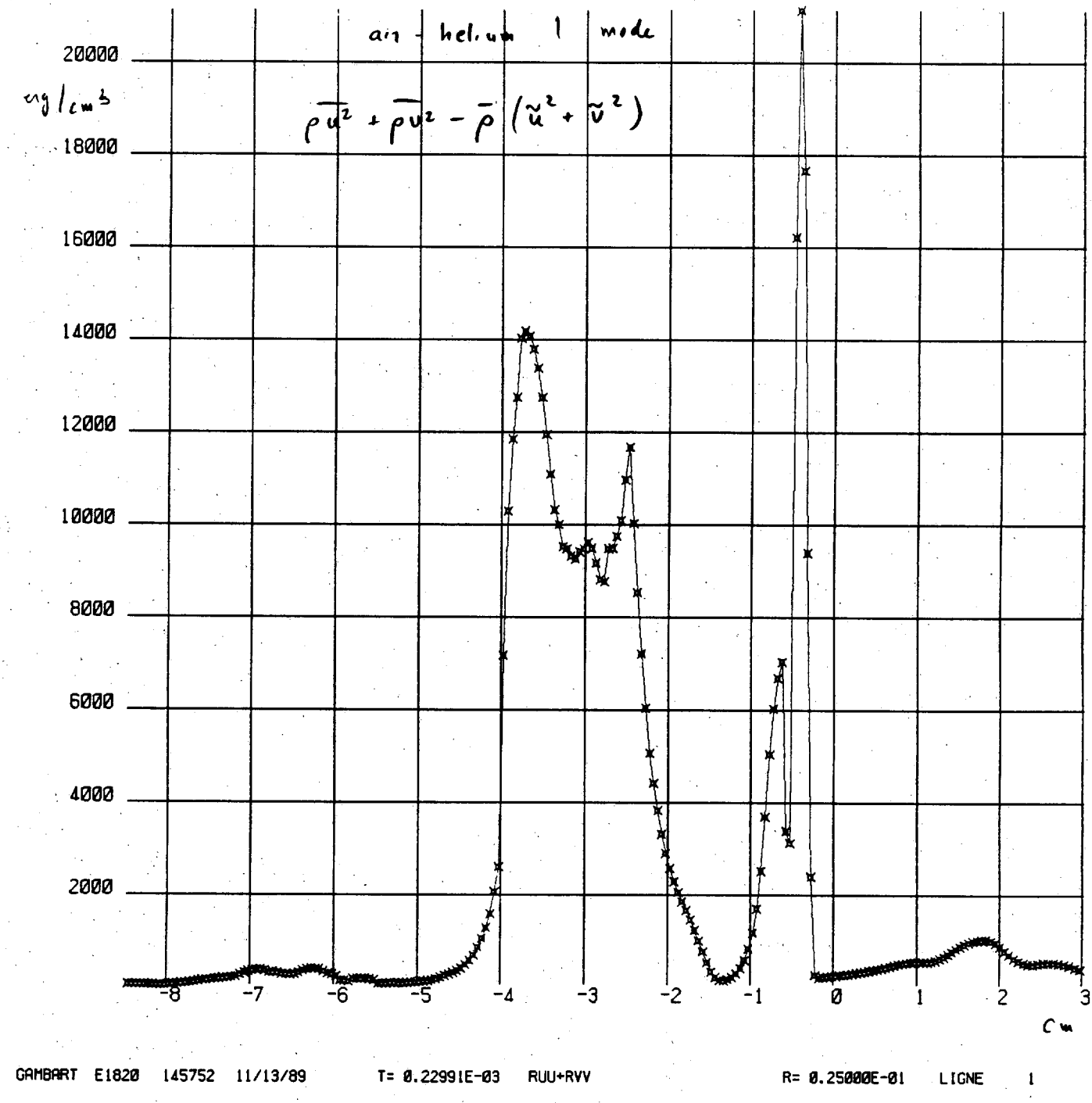
air - helium 1 mode
$\overline{\rho u^2} + \overline{\rho v^2} - \bar{\rho}(\tilde{u}^2 + \tilde{v}^2)$
erg/cm³
20000
18000
16000
14000
12000
10000
8000
6000
4000
2000
-8
-7
-6
-5
-4
-3
-2
-1
0
1
2
3
Cm
GAMBART E1820 145752 11/13/89
T= 0.22991E-03 RUU+RVV
R= 0.25000E-01 LIGNE 1

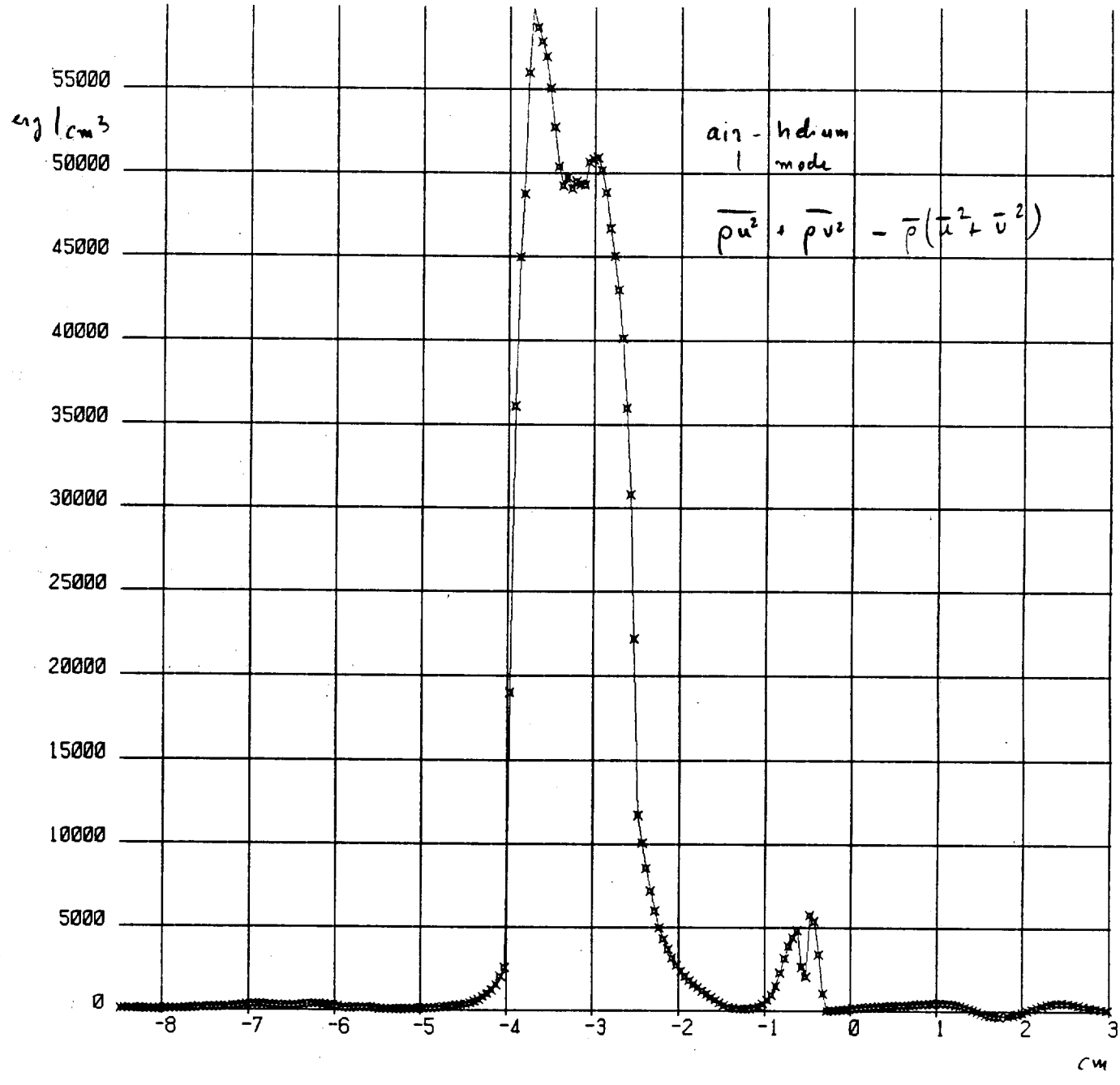
55000
erg / cm3
50000
45000
40000
35000
30000
25000
20000
15000
10000
5000
0
-8
-7
-6
-5
-4
-3
-2
-1
0
1
2
3
cm
air - helium
mode
$\overline{\rho u^2} + \overline{\rho v^2} - \bar{\rho}(\tilde{u}^2 + \tilde{v}^2)$
GAMBART E1820 145752 11/13/89
T= 0.22991E-03 TUU+TVV
R= 0.25000E-01 LIGNE 1

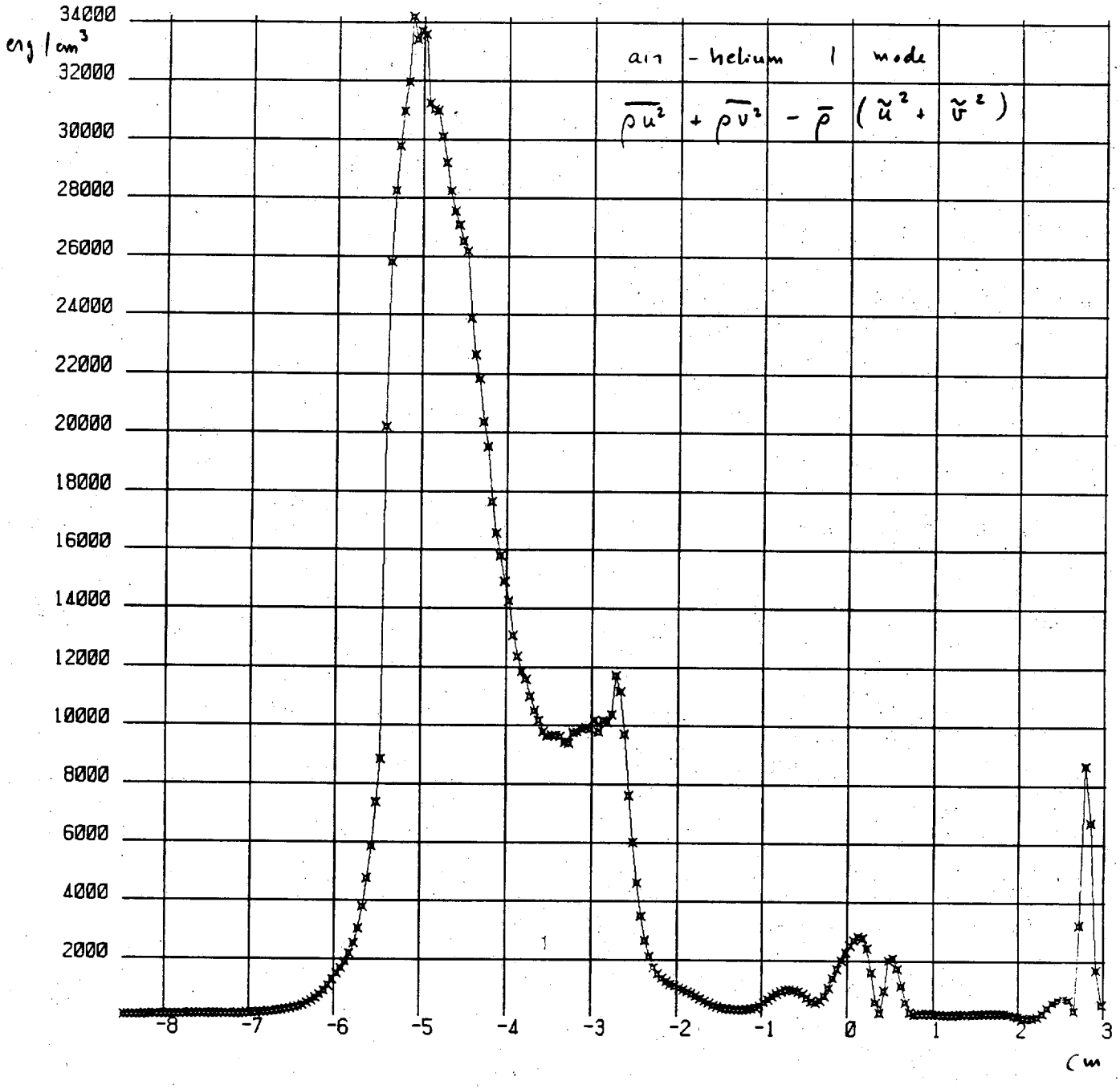
air - helium 1 mode
$\overline{\rho u^2} + \overline{\rho v^2} - \bar{\rho}(\tilde{u}^2 + \tilde{v}^2)$
erg / cm³
34000
32000
30000
28000
26000
24000
22000
20000
18000
16000
14000
12000
10000
8000
6000
4000
2000
-8 -7 -6 -5 -4 -3 -2 -1 0 1 2 3
Cm
GAMBART E1820 145752 11/13/89
T= 0.36009E-03 RUU+RVV
R= 0.25000E-01 LIGNE 1

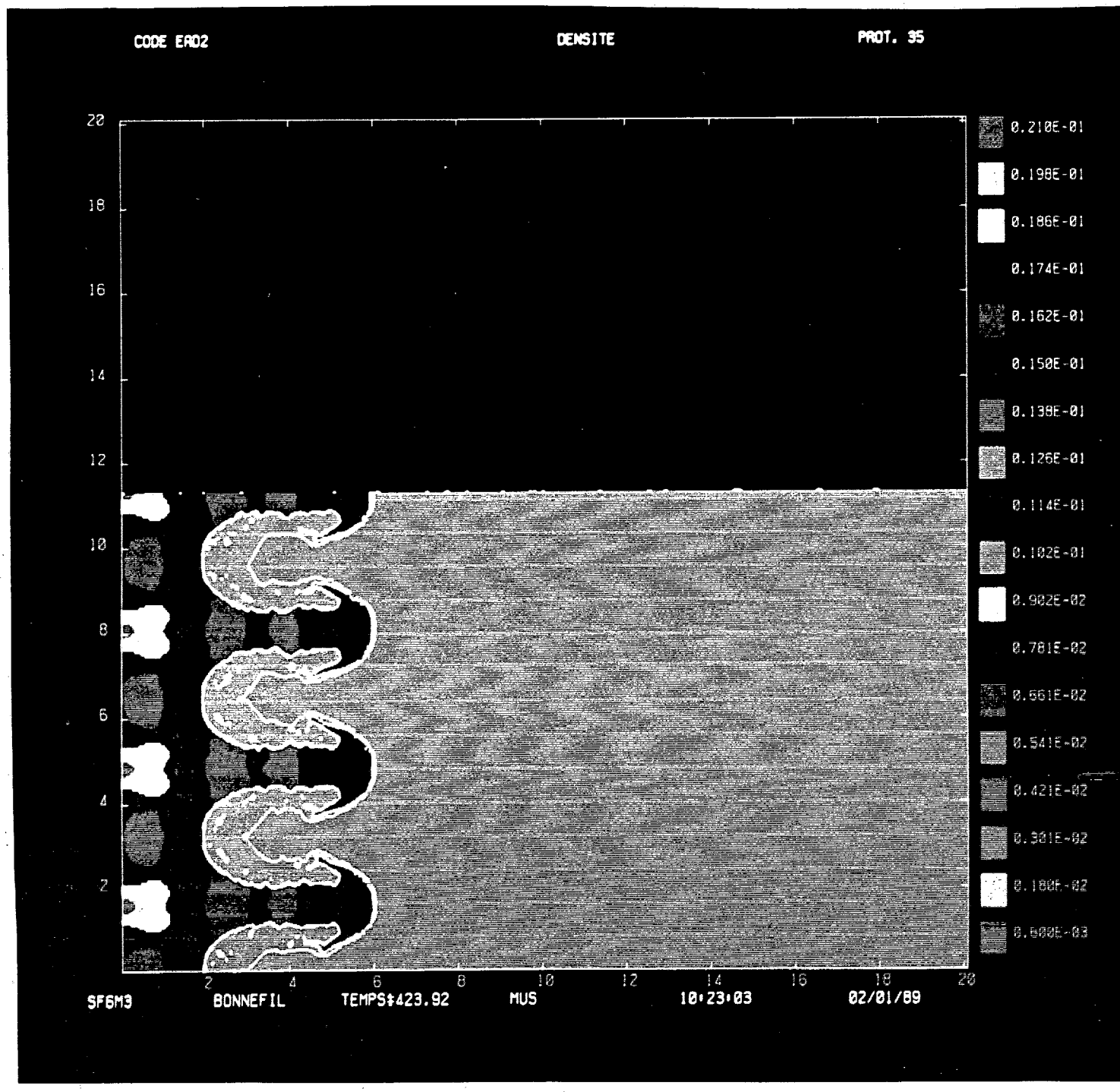
CODE ERD2
DENSITE
PROT. 35
20
18
16
14
12
10
8
6
4
2
2
4
6
8
10
12
14
16
18
20
0.210E-01
0.198E-01
0.186E-01
0.174E-01
0.162E-01
0.150E-01
0.138E-01
0.126E-01
0.114E-01
0.102E-01
0.902E-02
0.781E-02
0.661E-02
0.541E-02
0.421E-02
0.301E-02
0.180E-02
0.600E-03
SF6M3
BONNEFIL
TEMPS=423.92
MUS
10:23:03
02/01/89

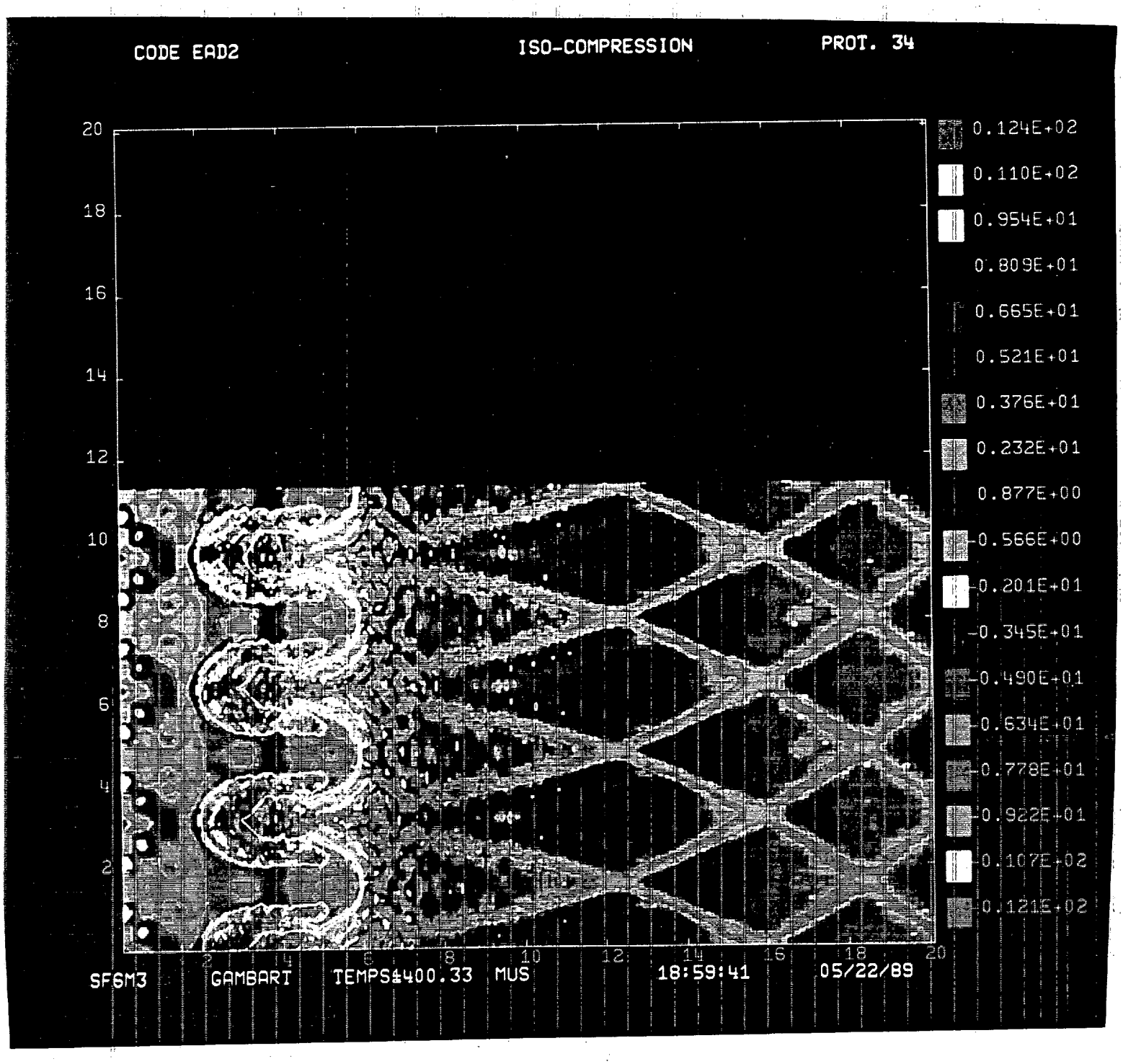
CODE EAD2
ISO-COMPRESSION
PROT. 34
0.124E+02
0.110E+02
0.954E+01
0.809E+01
0.665E+01
0.521E+01
0.376E+01
0.232E+01
0.877E+00
-0.566E+00
-0.201E+01
-0.345E+01
-0.490E+01
-0.634E+01
-0.778E+01
-0.922E+01
-0.107E+02
-0.121E+02
SF6M3 GAMBARI TEMPS±400.33 MUS 18:59:41 05/22/89

TEST PROBLEM CALCULATIONS

with

CAVEAT

A 2-D ALE Code with Mixed-cell Treatment

by

Rick Rauenzahn
T-3, LANL

TP6A - air-He - single wavelength pert.

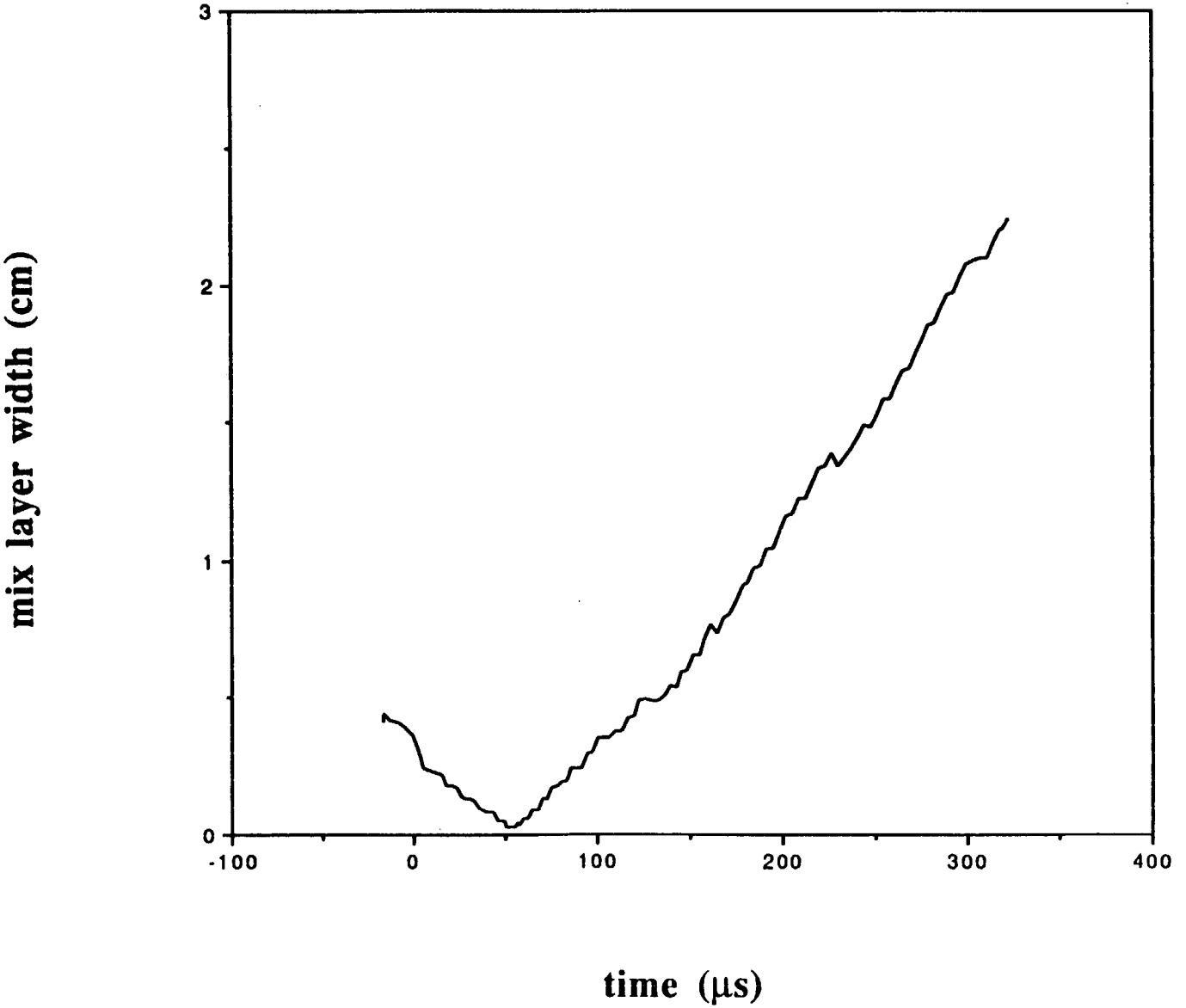

TP6A - air-He - single wavelength pert.

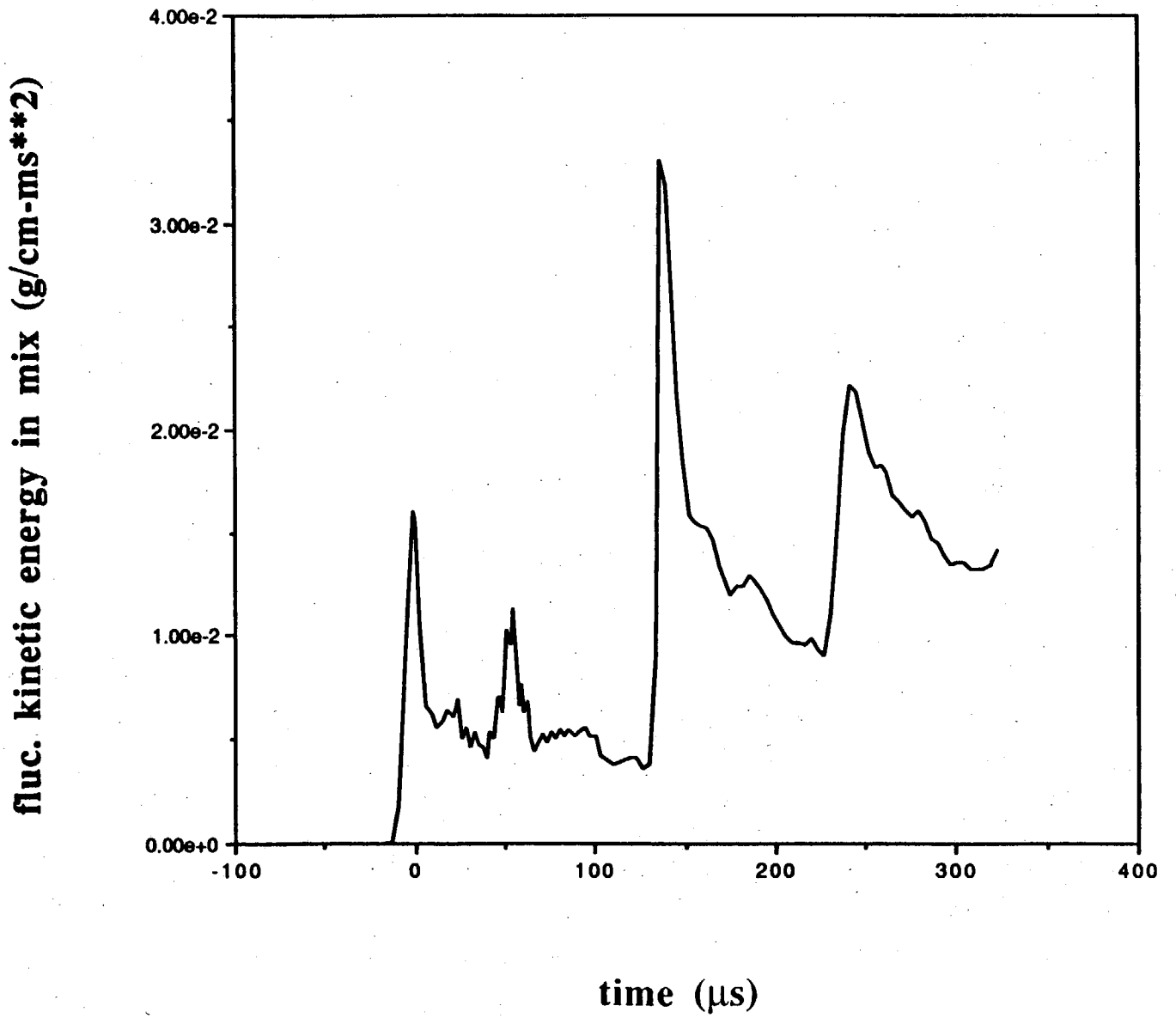

RANGE FOR VARIABLE θ IS:
1.2943E+00 TO 1.8153E+00

TEST PROBLEM 6A

Single λ

PRESSURE

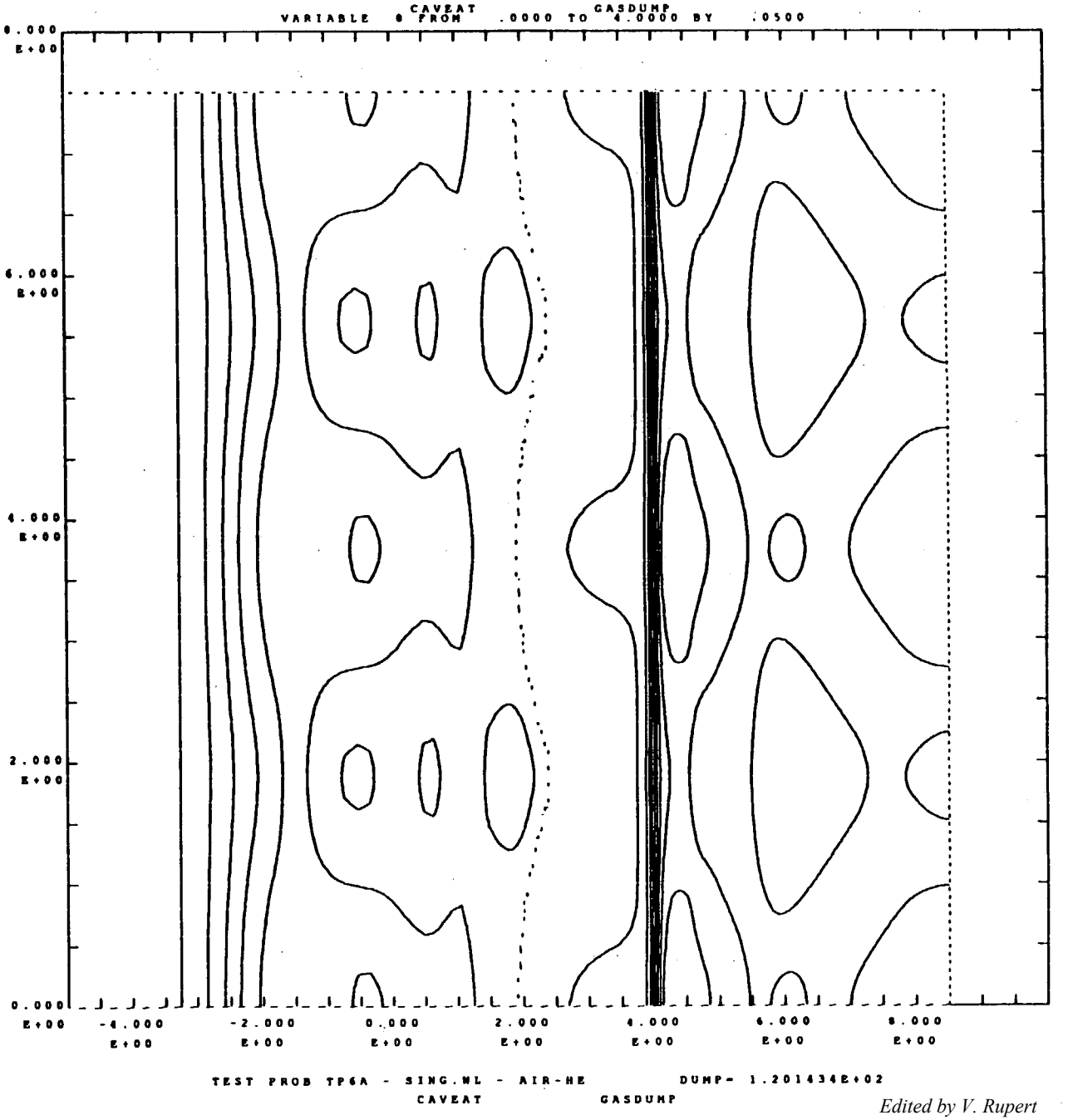

TEST PROB TP6A - SING.ML - AIR-HE
CAVEAT
DUMP- 3.201818E+02
GASDUMP
CAS VERSION 5/25/89
RANGE FOR VARIABLE 8 IS:
1.34622E+00 TO 2.44356E+00
VARIABLE 8 FROM .0000 TO 4.0000 BY .0500
CAVEAT
GASDUMP

RANGE FOR VARIABLE 5 IS:
-2.3775E-02 TO 2.3775E-02

TEST PROBLEM 6A

Single λ

VORTICITY

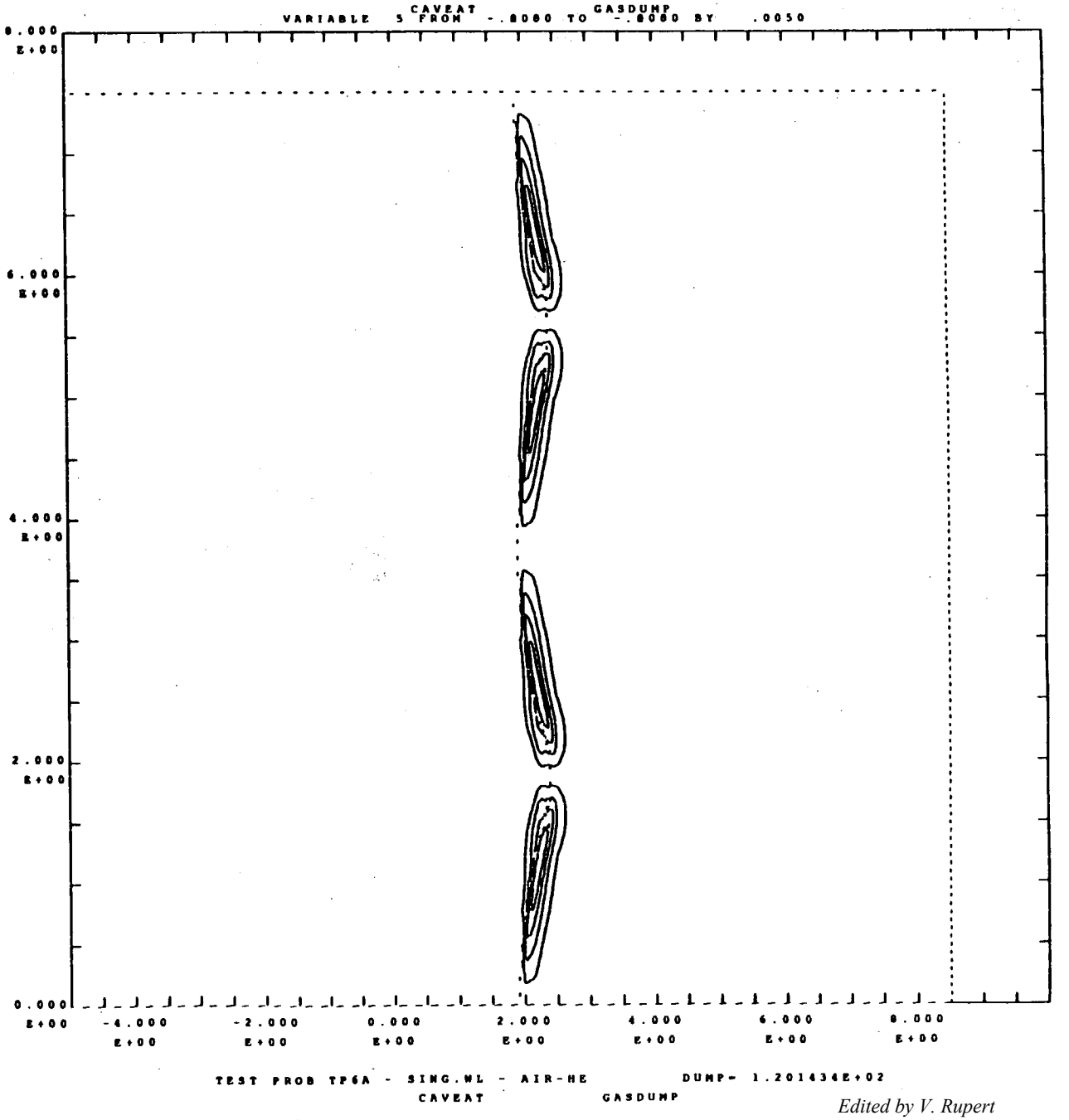

Pleasanton, USA

Edited by V. Rupert

RANGE FOR VARIABLE 5 IS:
-5.4291E-02 TO 5.4295E-02

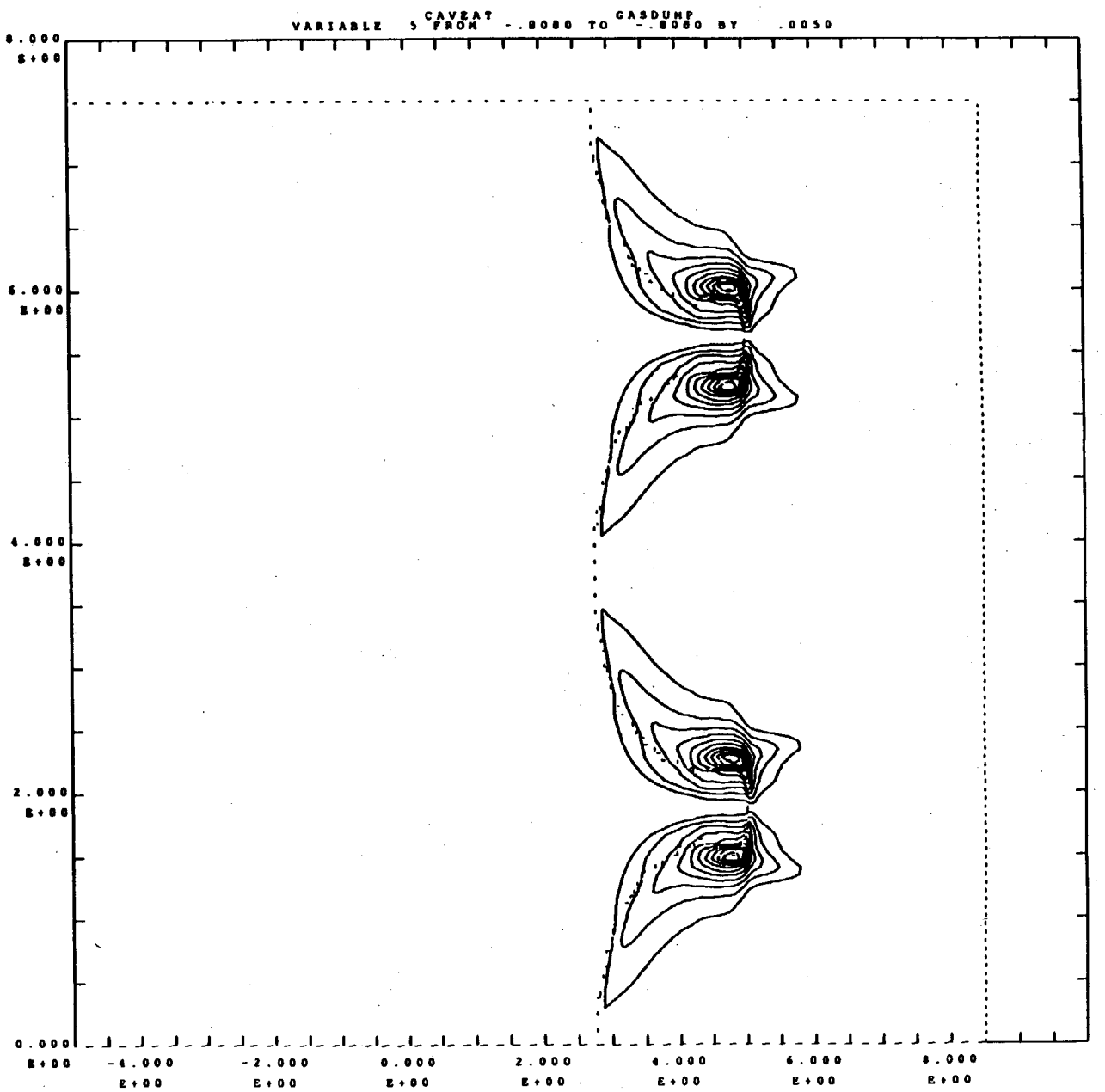

TEST PROBLEM 6A

Multiple λ

VOLUME FRACTION OF HE

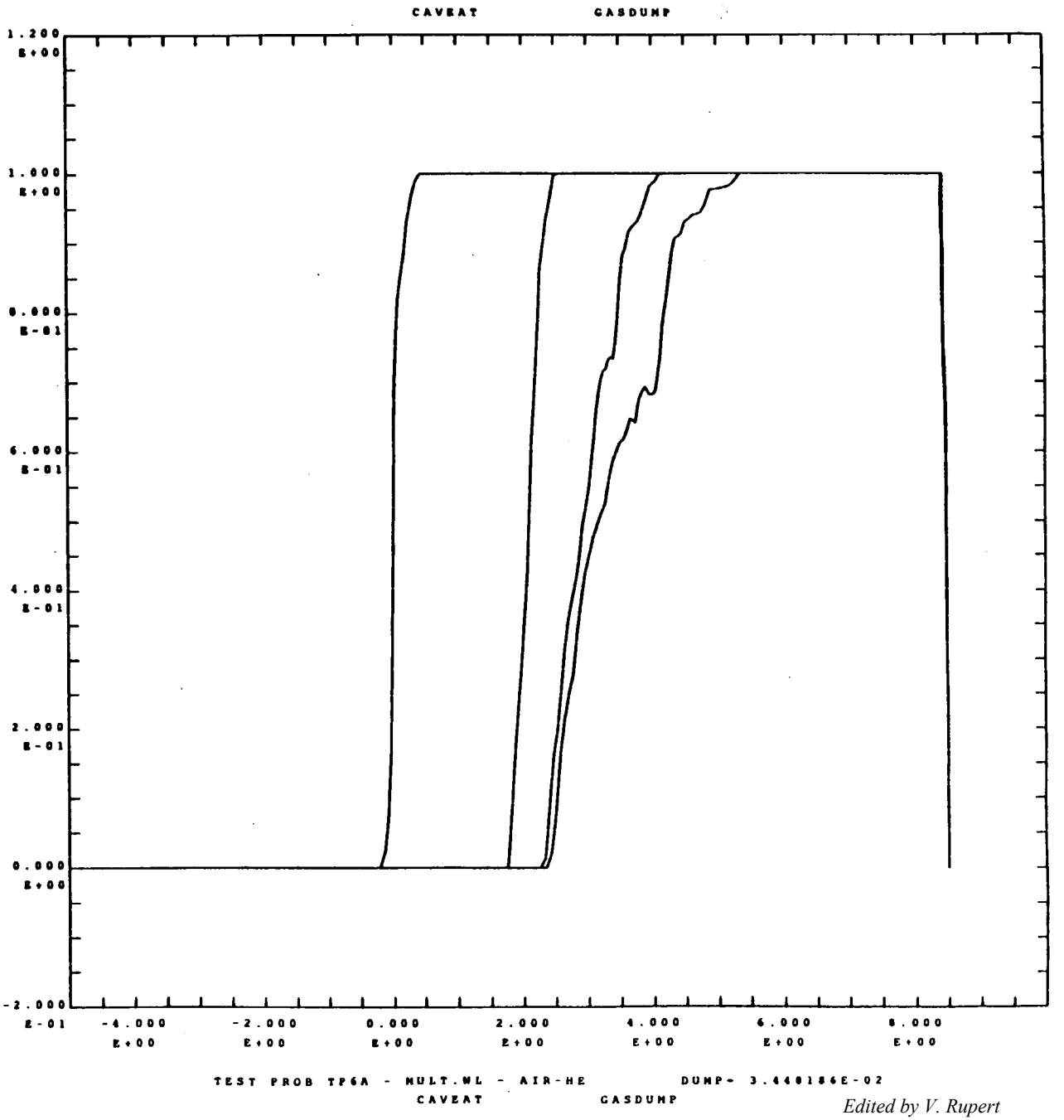

TEST PROBLEM 6A

Multiple λ

AVERAGED DENSITY

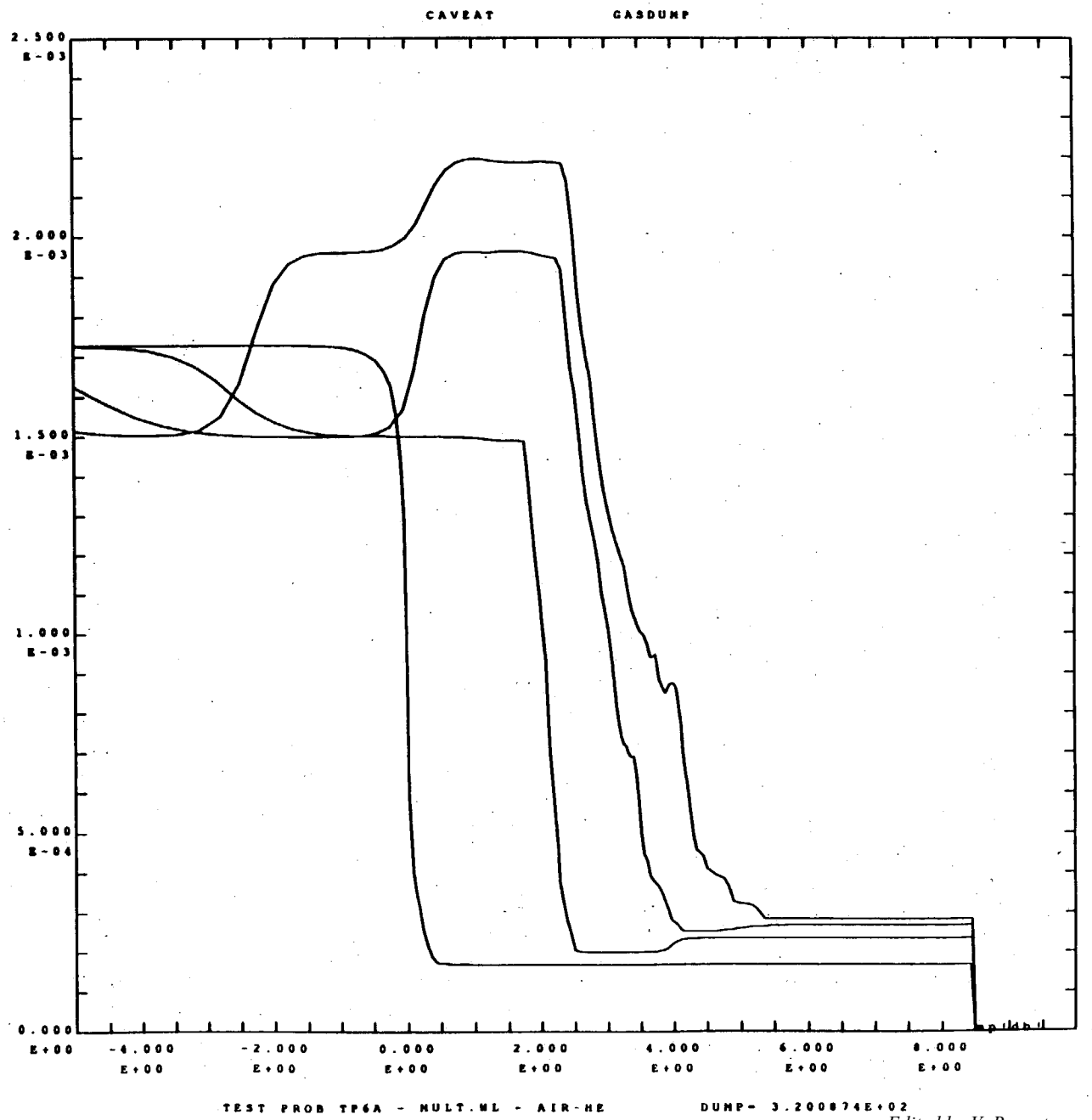

TEST PROBLEM 6A

Multiple λ

AVERAGED FLUC. KE

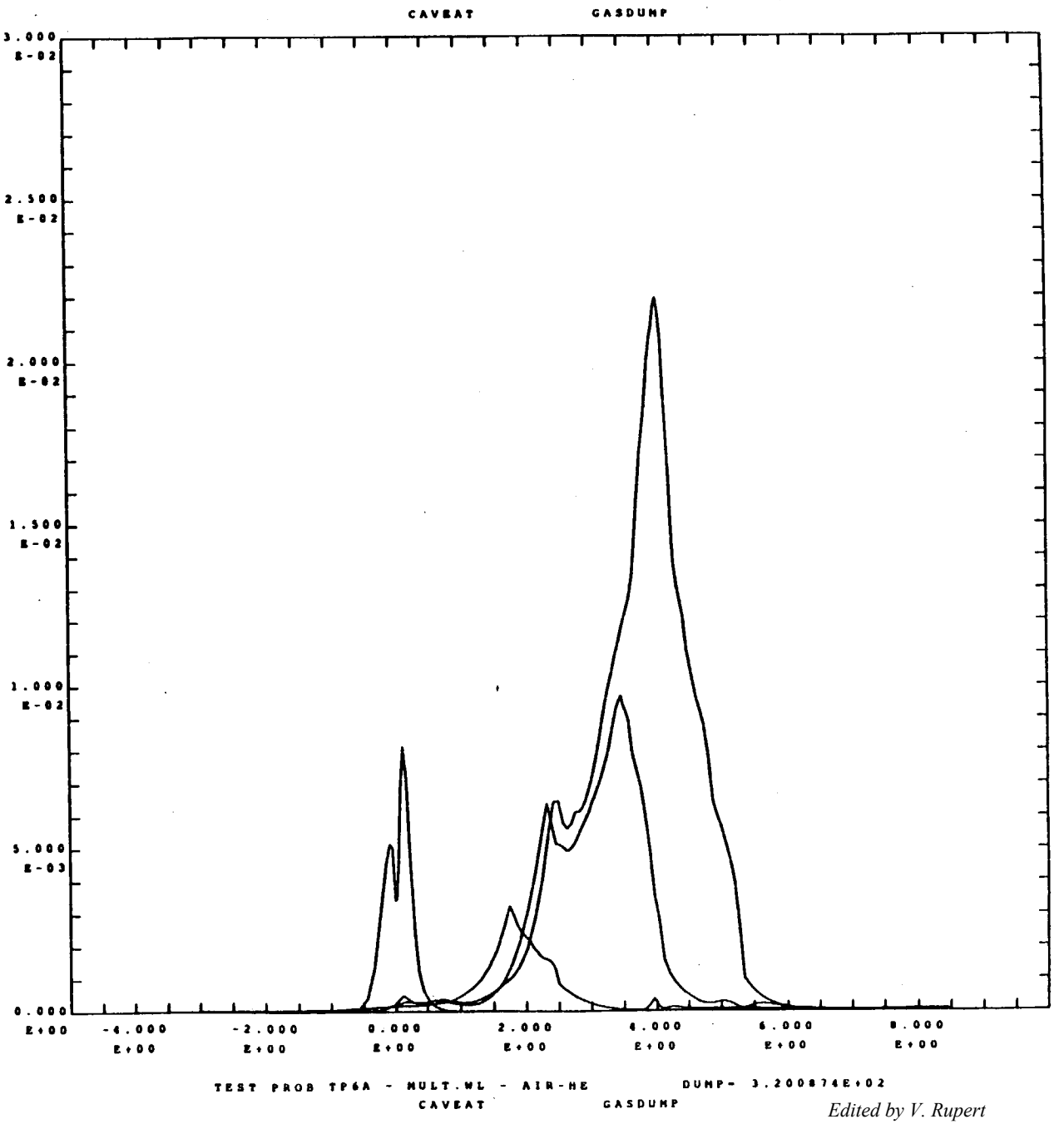

TP6A - air-He - mult. wavelength pert.

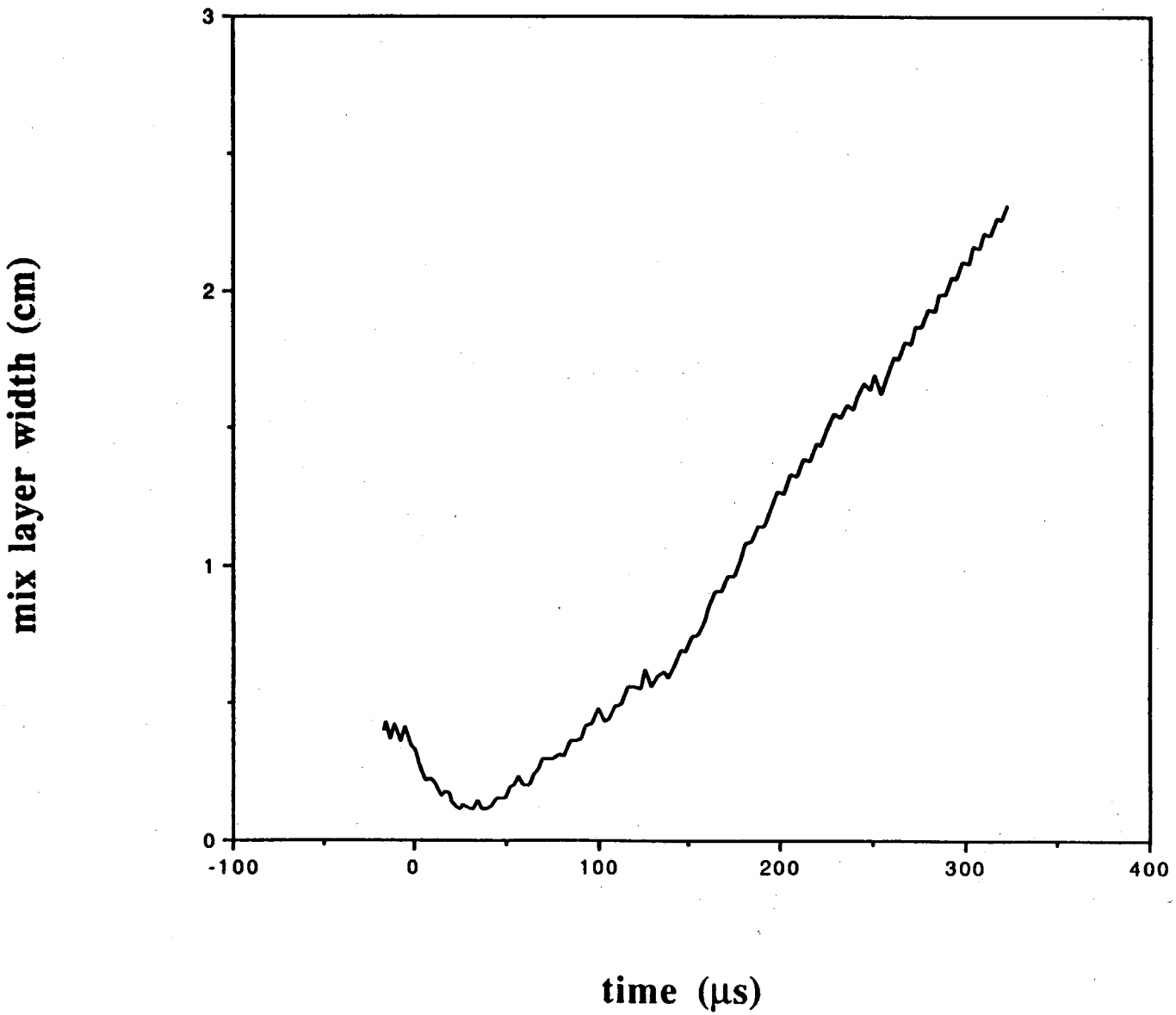

TP6A - air-He - mult. wavelength pert.

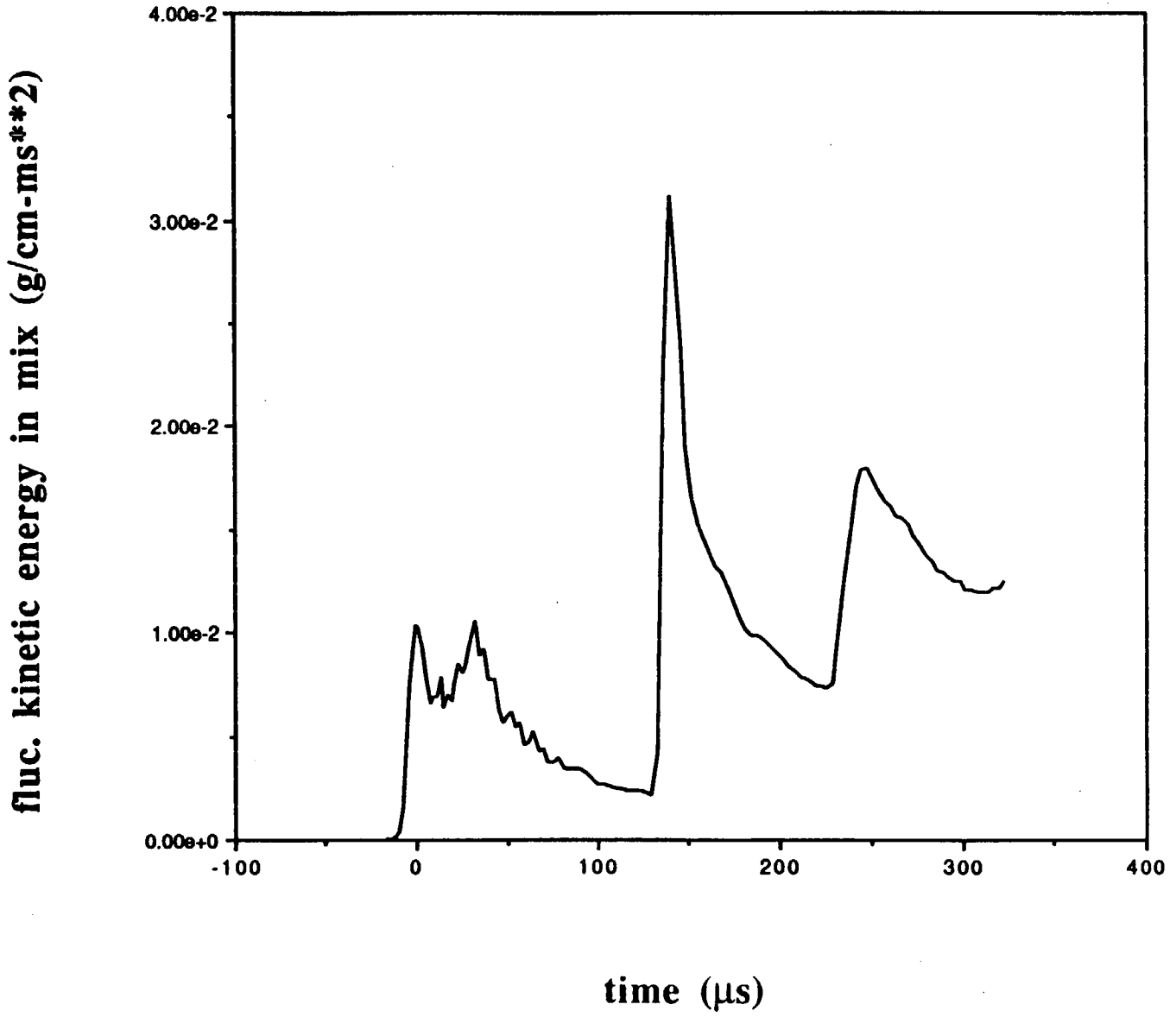

RANGE FOR VARIABLE θ IS:
1.3156E+00 TO 1.7960E+00

TEST PROBLEM 6A

Multiple λ

PRESSURE

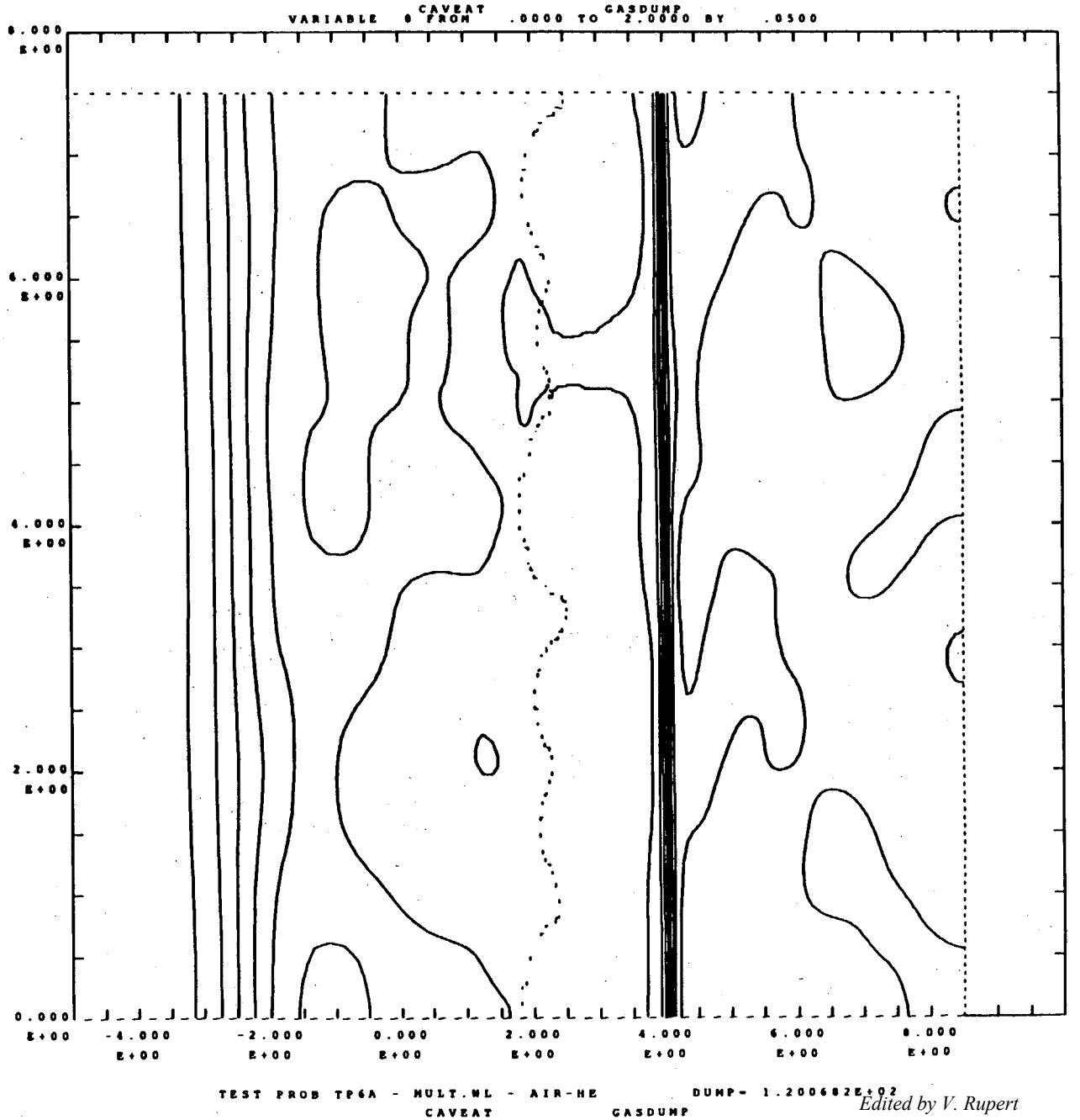

RANGE FOR VARIABLE 8 IS:
1.3401E+00 TO 2.4312E+00

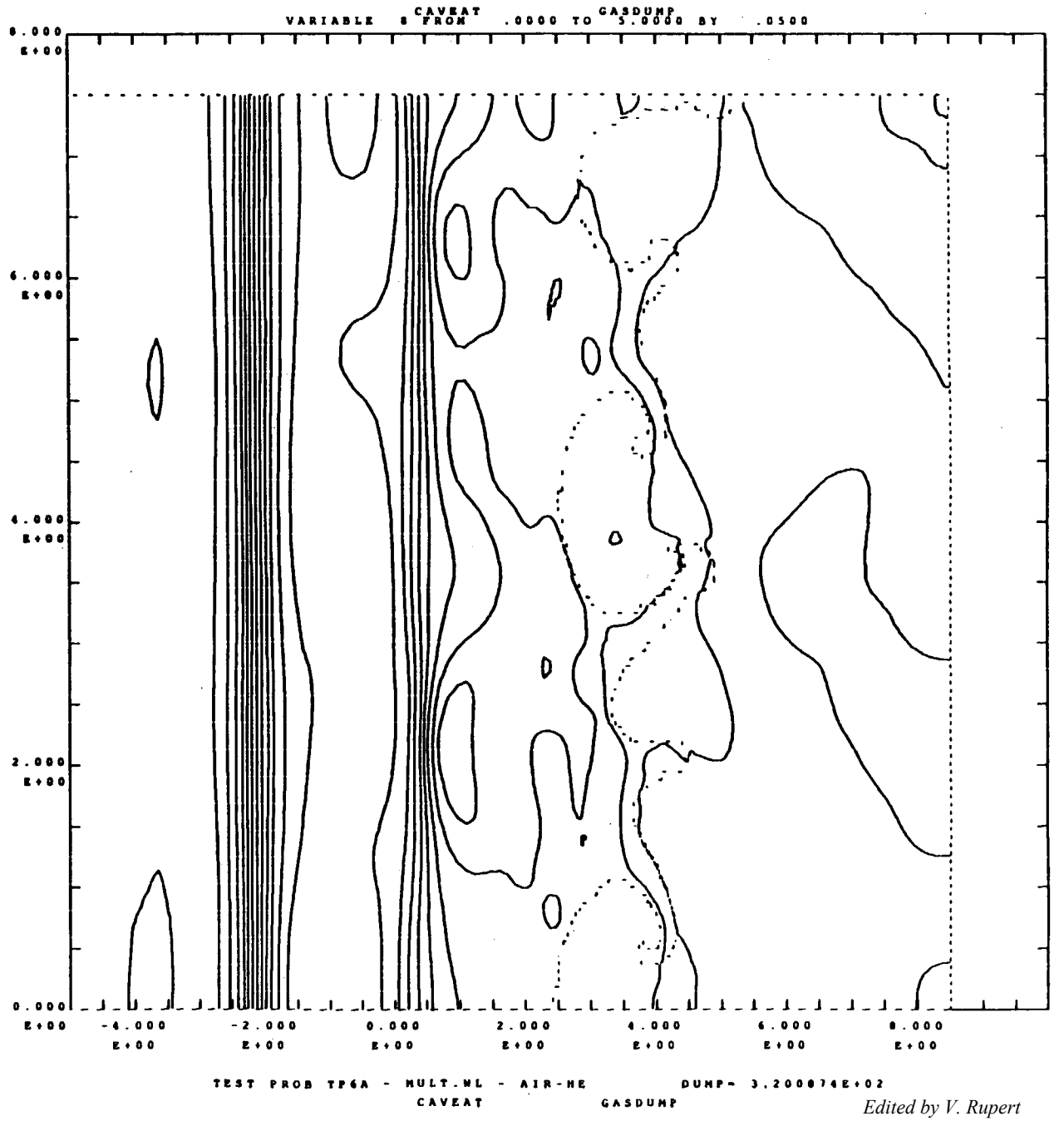

GAS VERSION 5/25/89

Pleasanton, USA

Edited by V. Rupert

TEST PROBLEM 6A

Multiple λ

VORTICITY

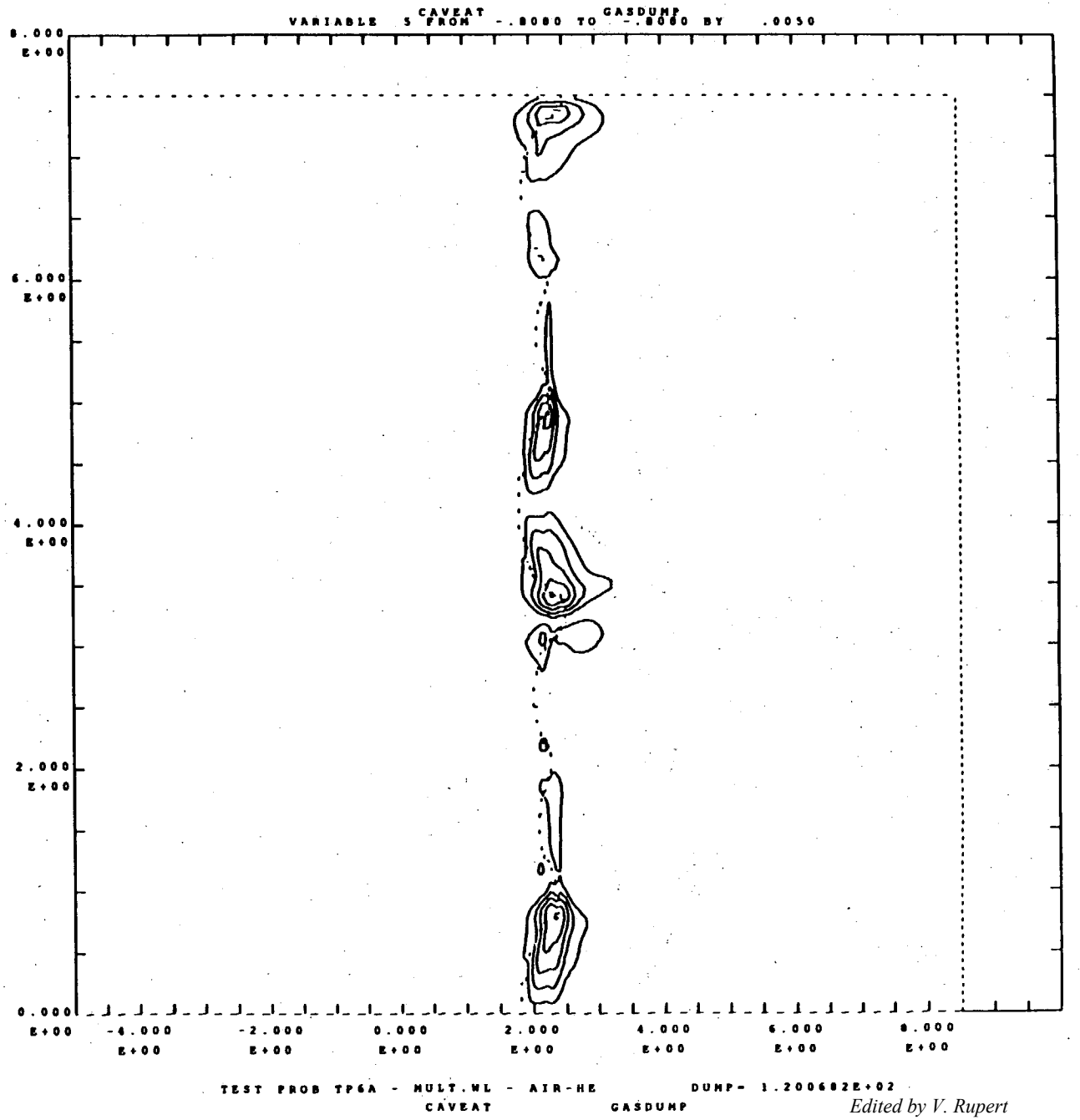

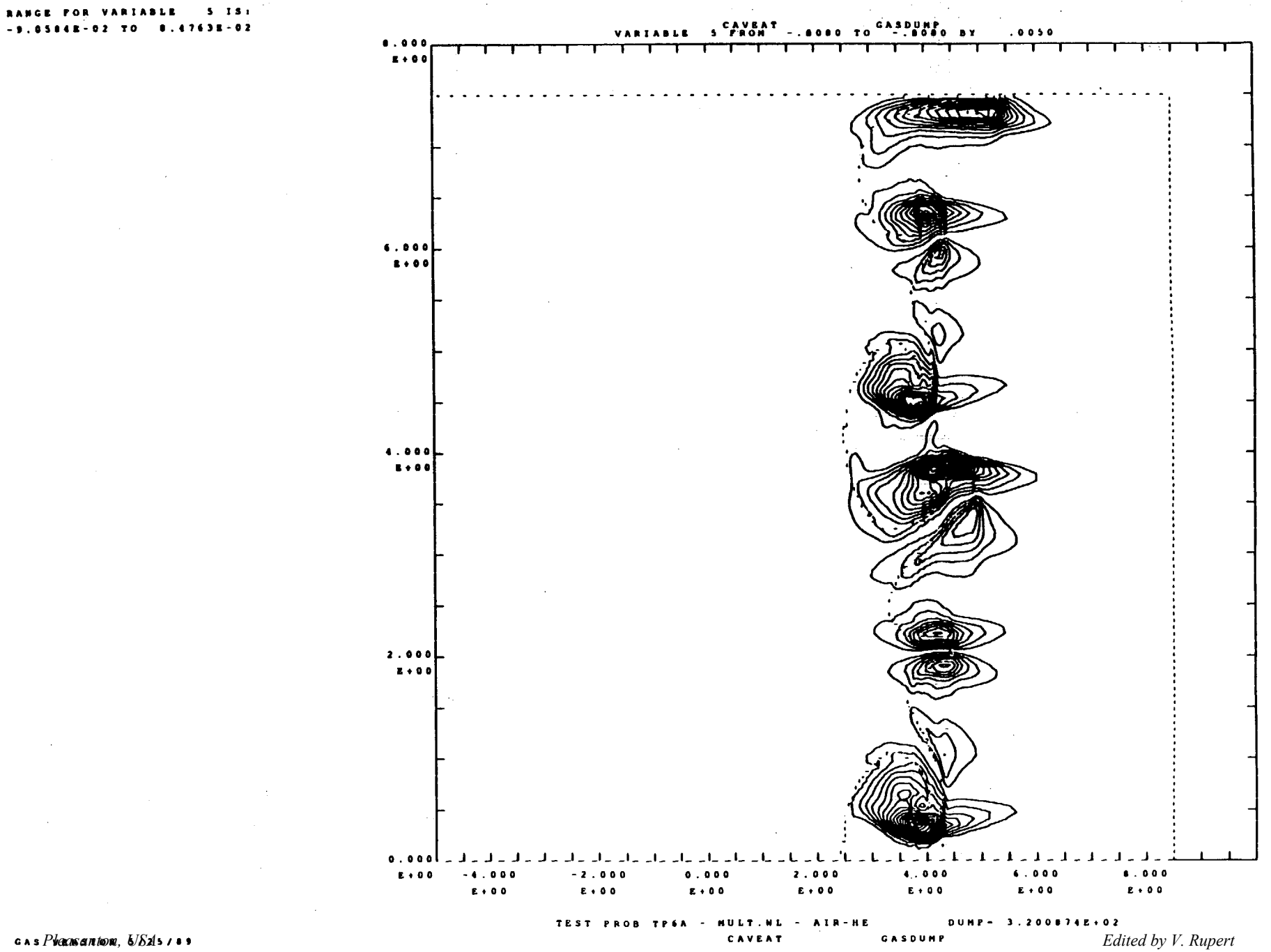
RANGE FOR VARIABLE 5 IS:
-9.0584E-02 TO 8.4763E-02
VARIABLE 5 FROM -.8080 TO -.8080 BY .0050
CAVEAT
GASDUMP
8.000 E+00
6.000 E+00
4.000 E+00
2.000 E+00
0.000 E+00
-4.000 E+00
-2.000 E+00
0.000 E+00
2.000 E+00
4.000 E+00
6.000 E+00
8.000 E+00
TEST PROB TP6A - MULT.NL - AIR-HE
DUMP= 3.200874E+02
CAVEAT
GASDUMP

TP6B - air-SF6 - single wavelength pert.

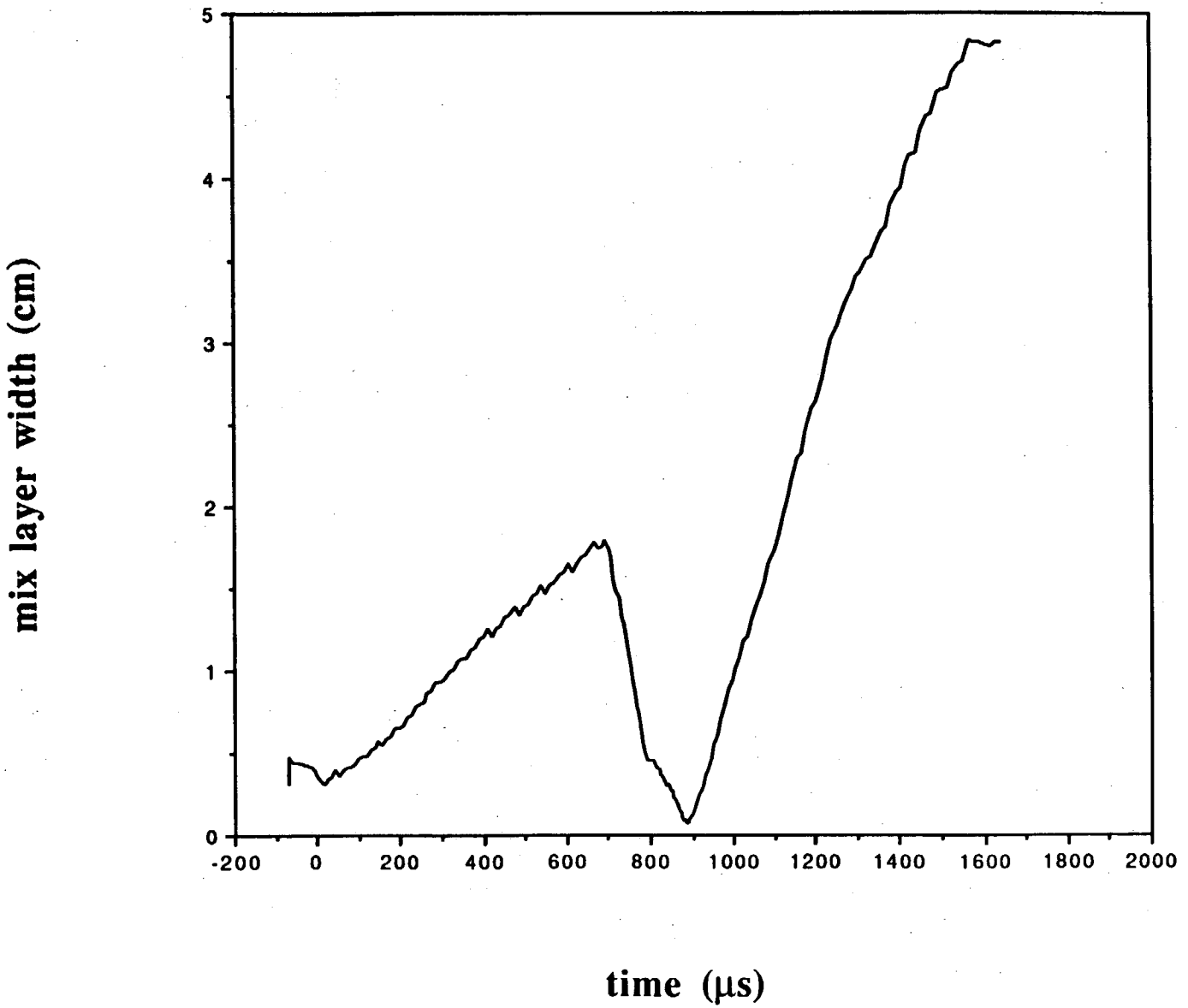

TP6B - air-SF6 - single wavelength pert.

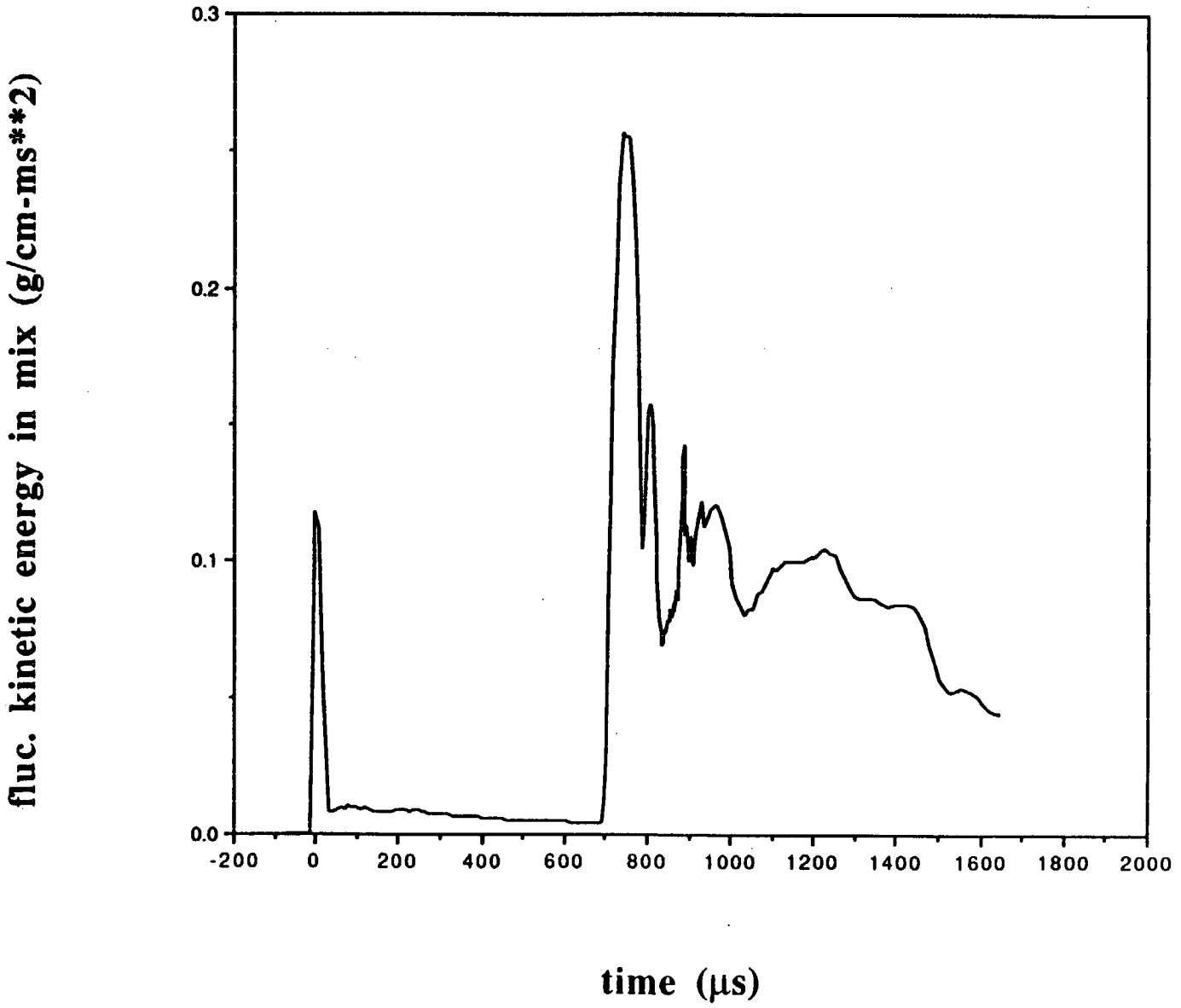

RANGE FOR VARIABLE 8 IS:
1.8984E+00 TO 5.2520E+00

TEST PROBLEM 6B

Single λ

PRESSURE

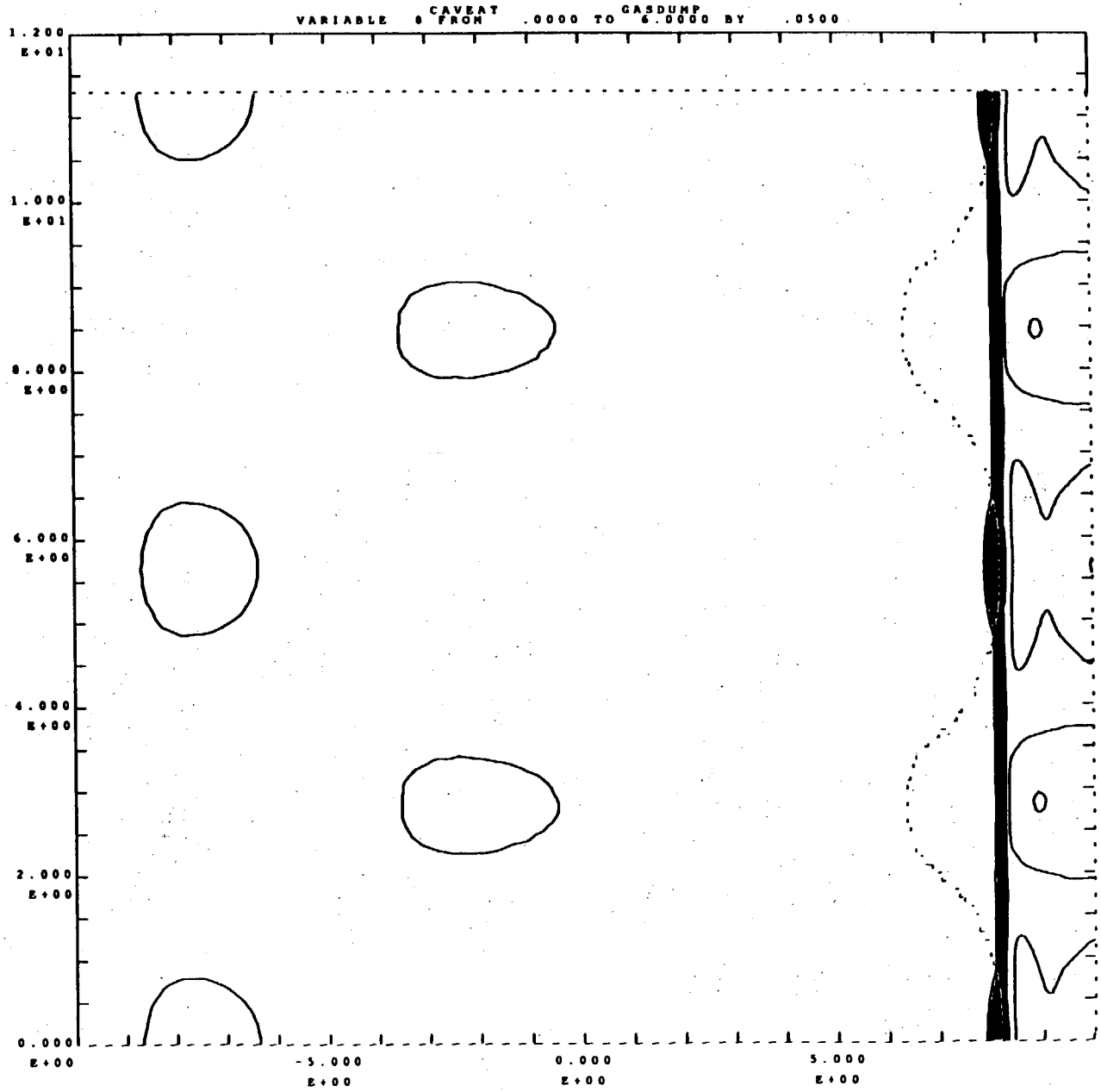

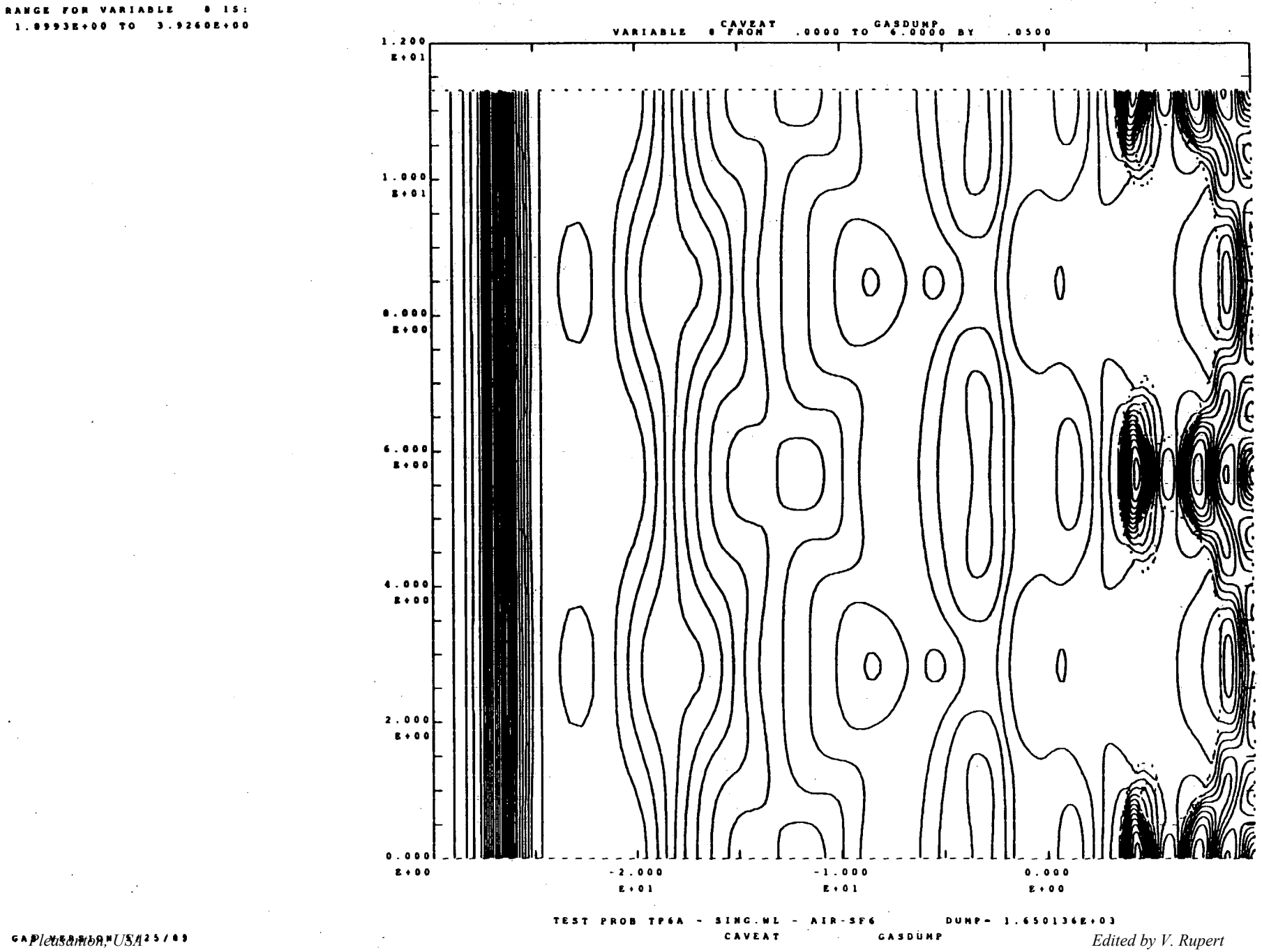

Pleasanton, USA *Edited by V. Rupert*

RANGE FOR VARIABLE 5 IS:
-5.2280E-02 TO 5.2280E-02

TEST PROBLEM 6B

Single λ

VORTICITY

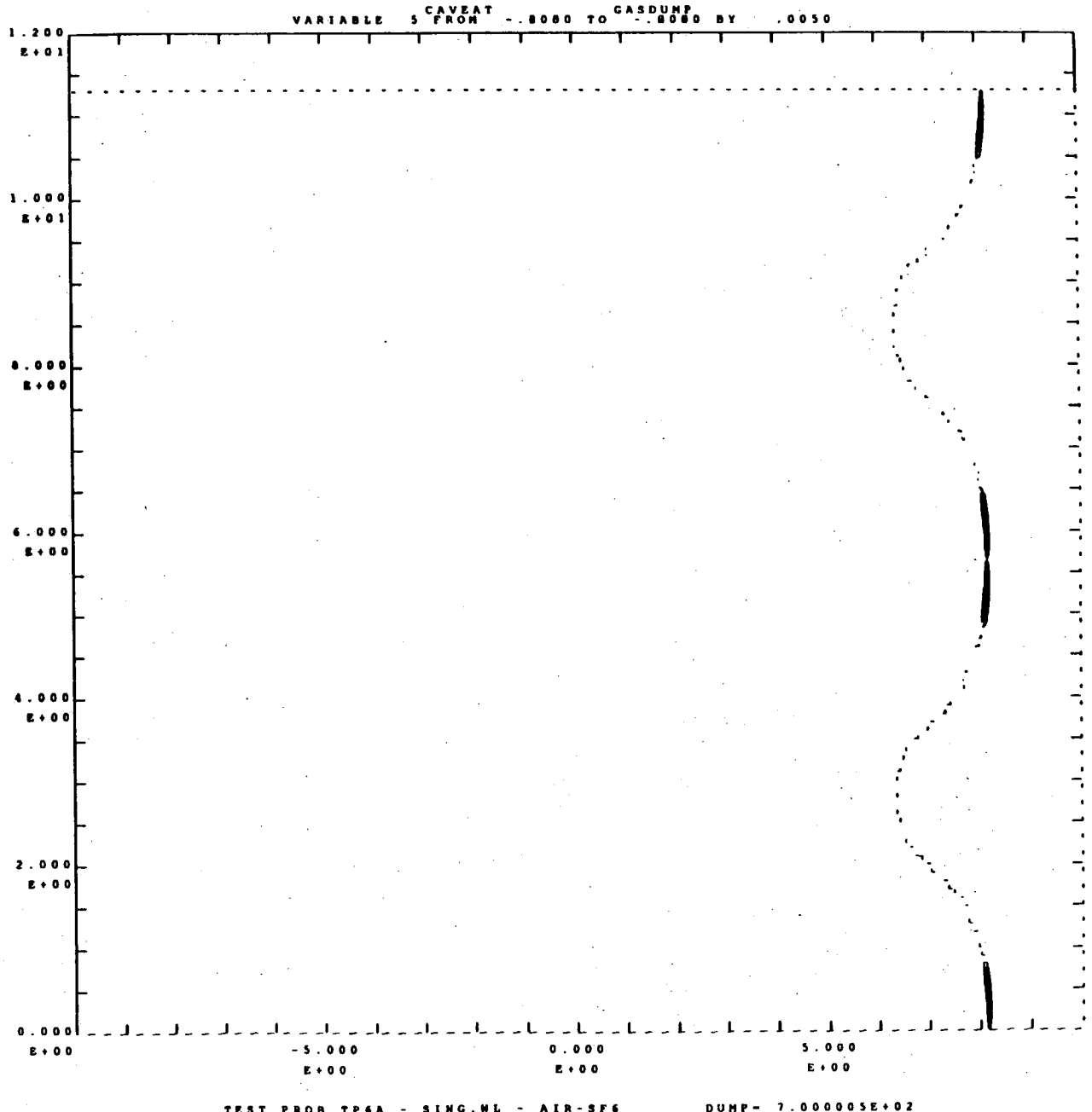

RANGE FOR VARIABLE 5 IS:
-2.0021E-02 TO 2.0021E-02

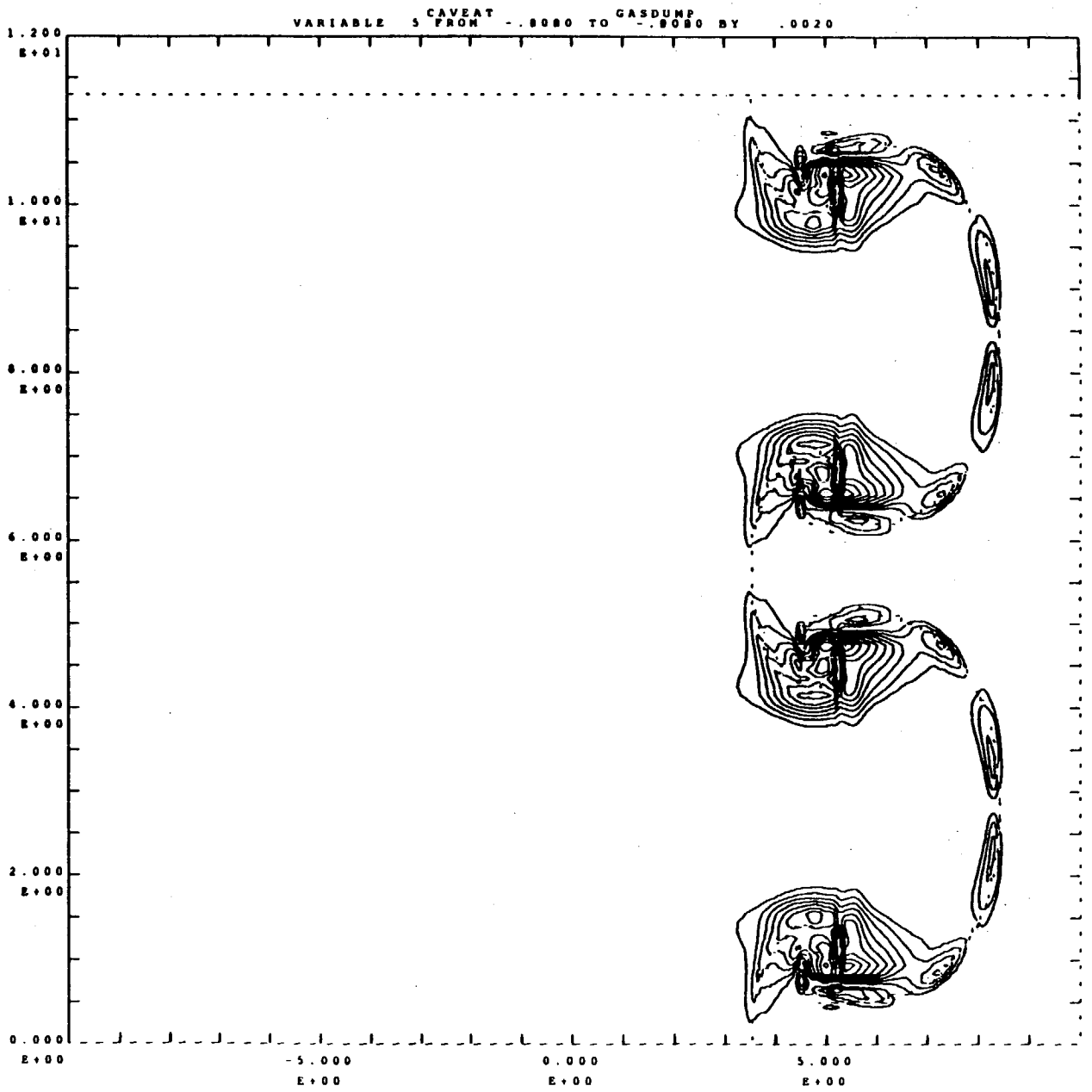

TEST PROBLEM 6B

Multiple λ

VOLUME FRACTION OF SF_6

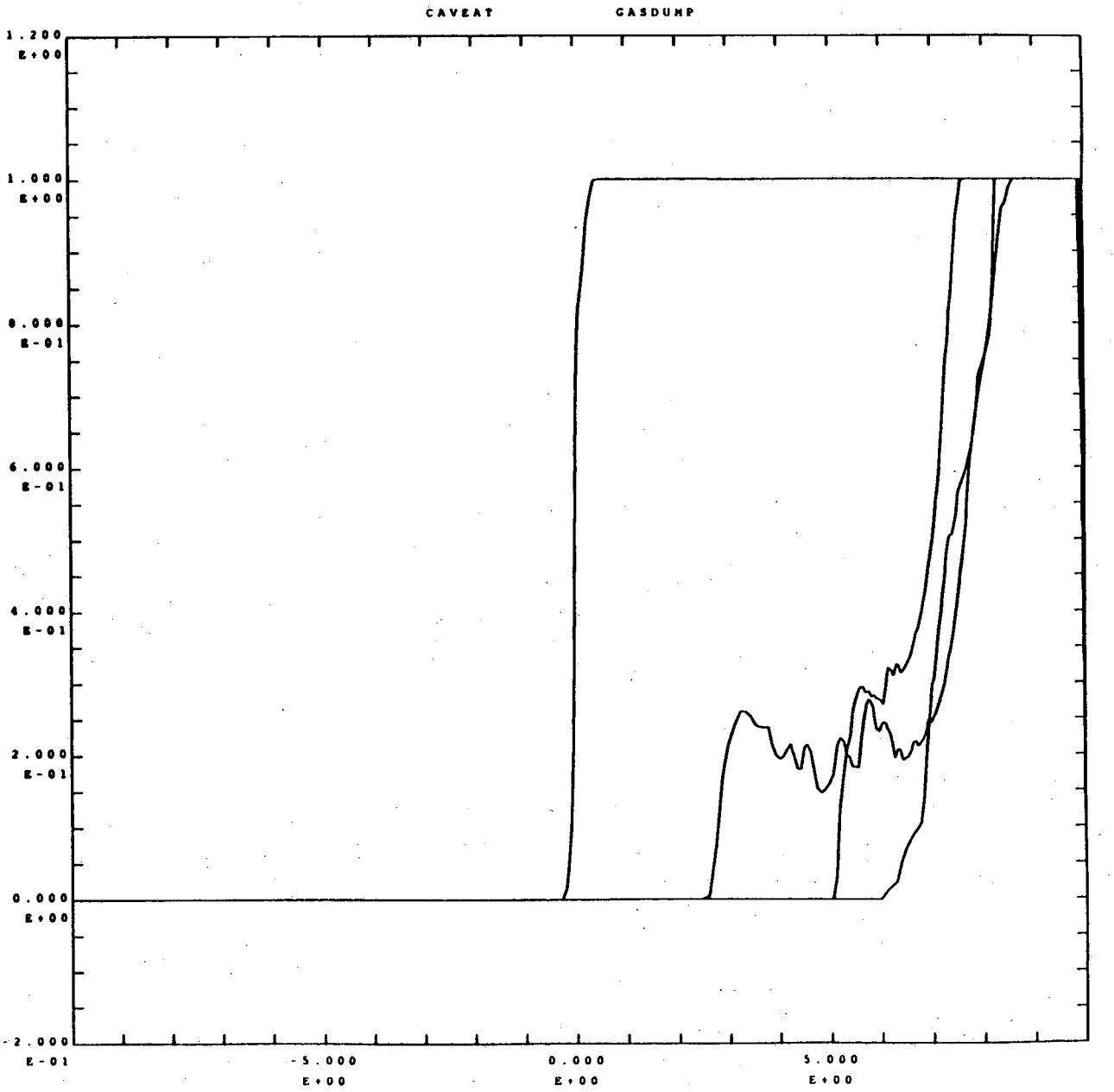

TEST PROBLEM 6B

Multiple λ

AVERAGED DENSITY

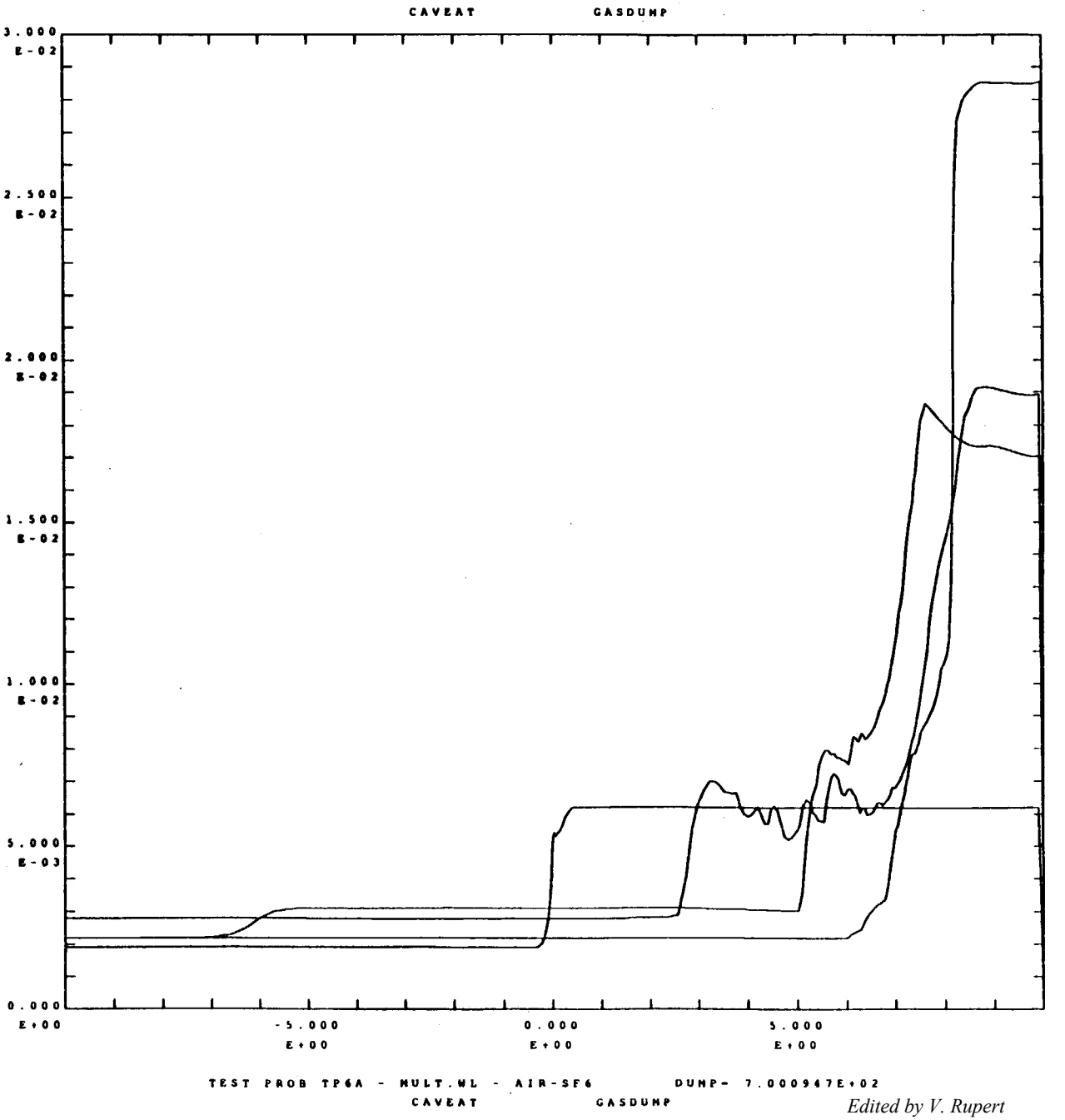

TEST PROBLEM 6B

Multiple λ

AVERAGED FLUC. KE

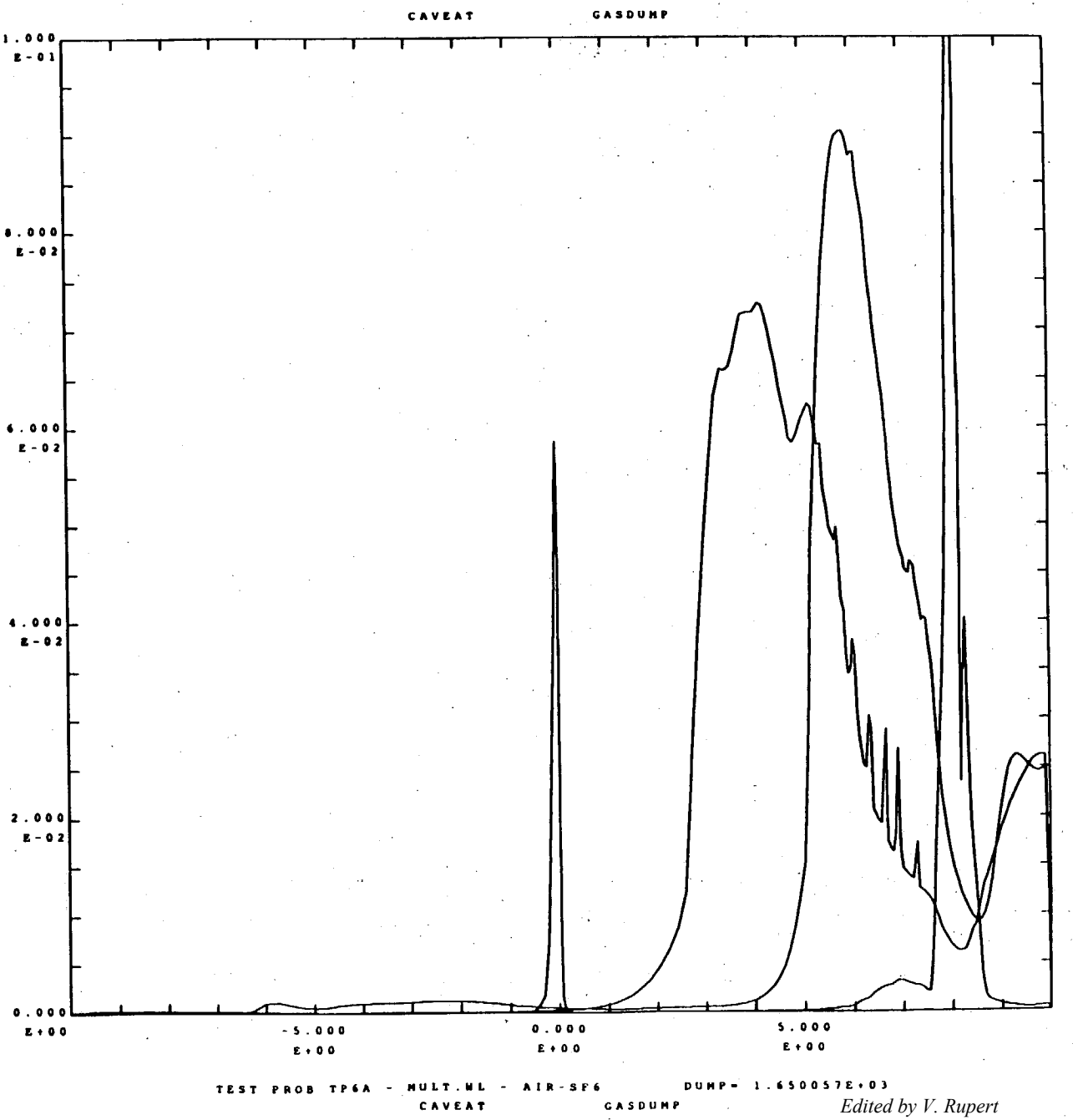

TP6B - air-SF6 - mult. wavelength pert.

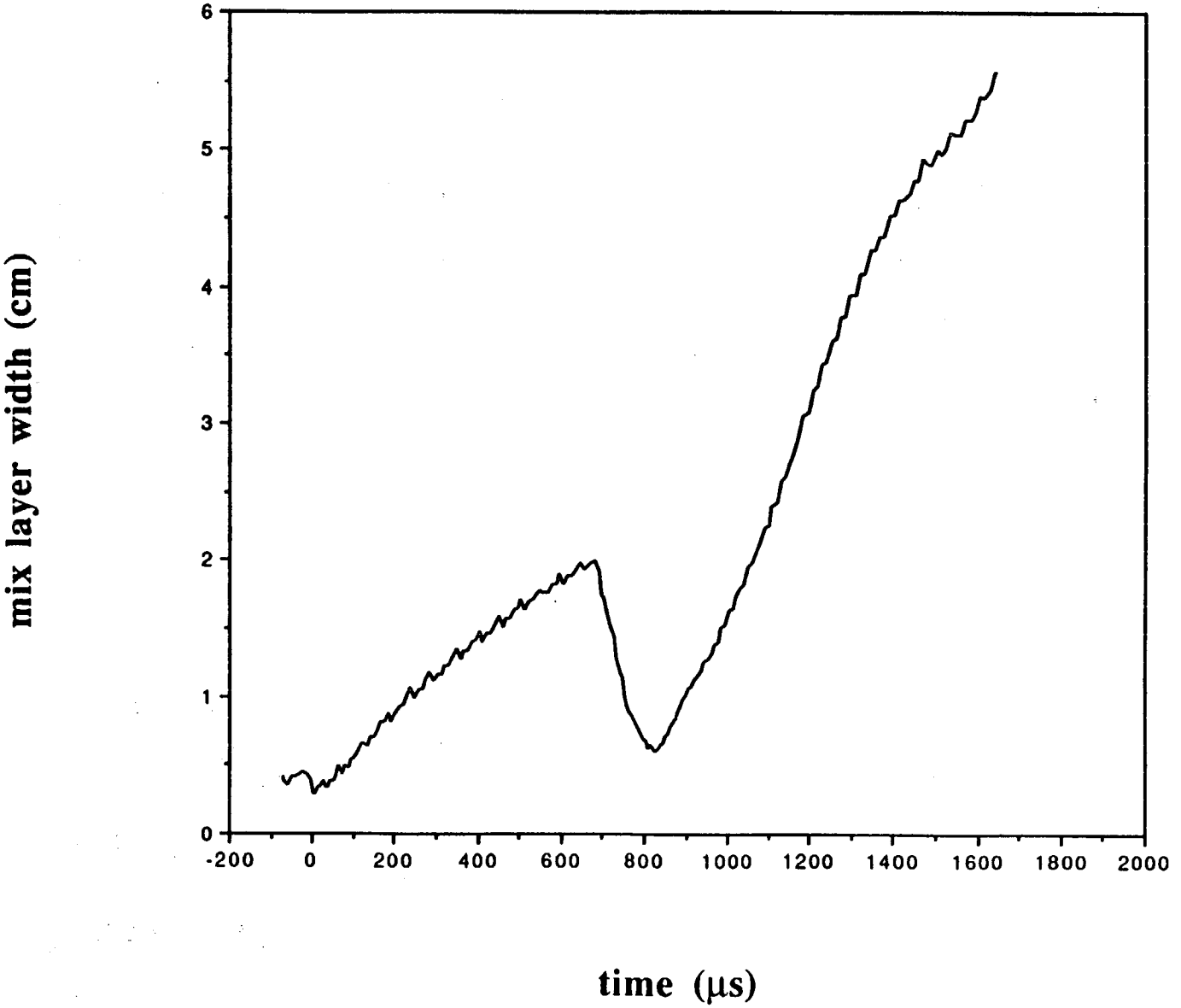

TP6B - air-SF6 - mult. wavelength pert.

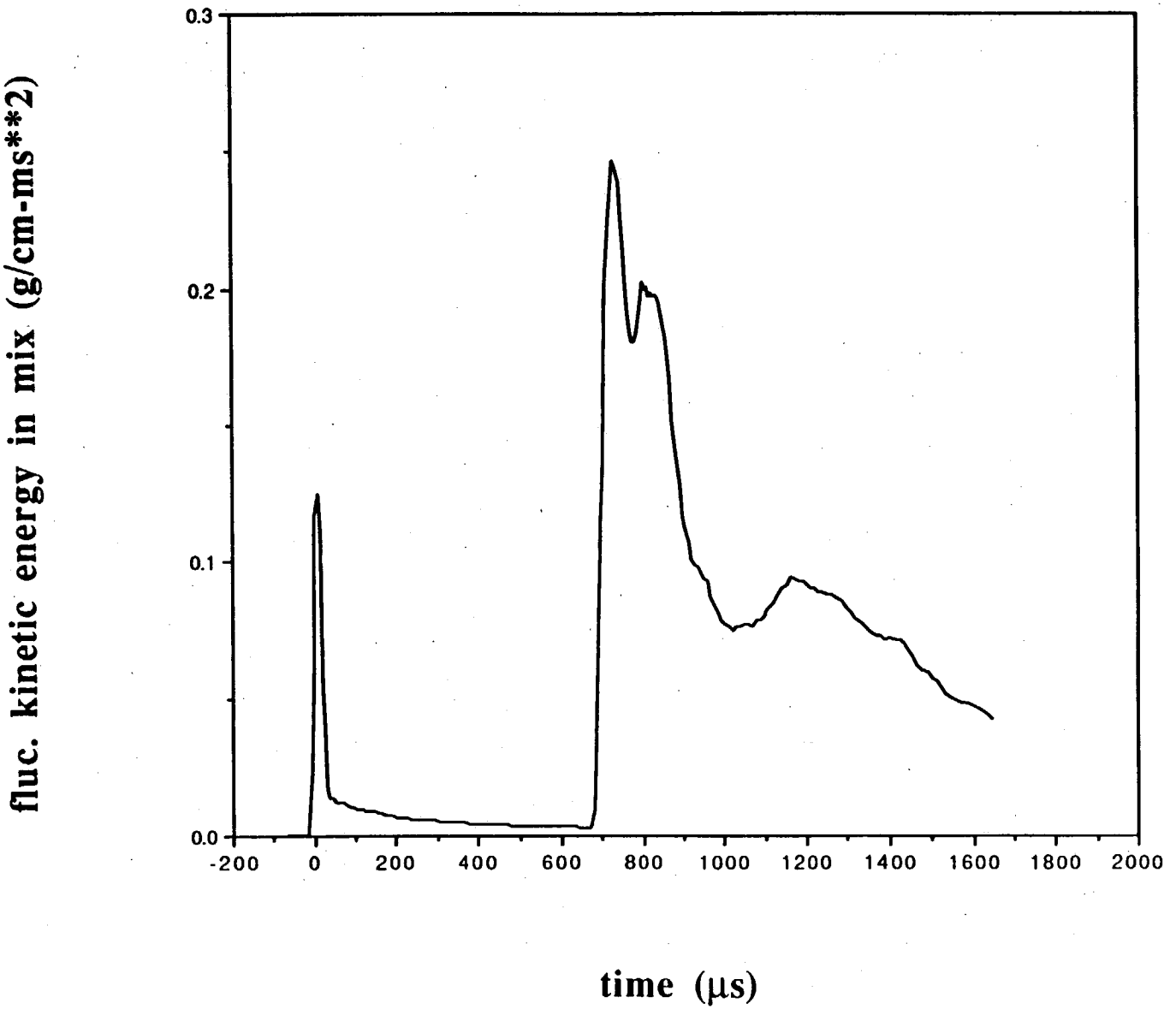

RANGE FOR VARIABLE 8 IS:
1.8983E+00 TO 5.2437E+00

TEST PROBLEM 6B

Multiple λ

PRESSURE

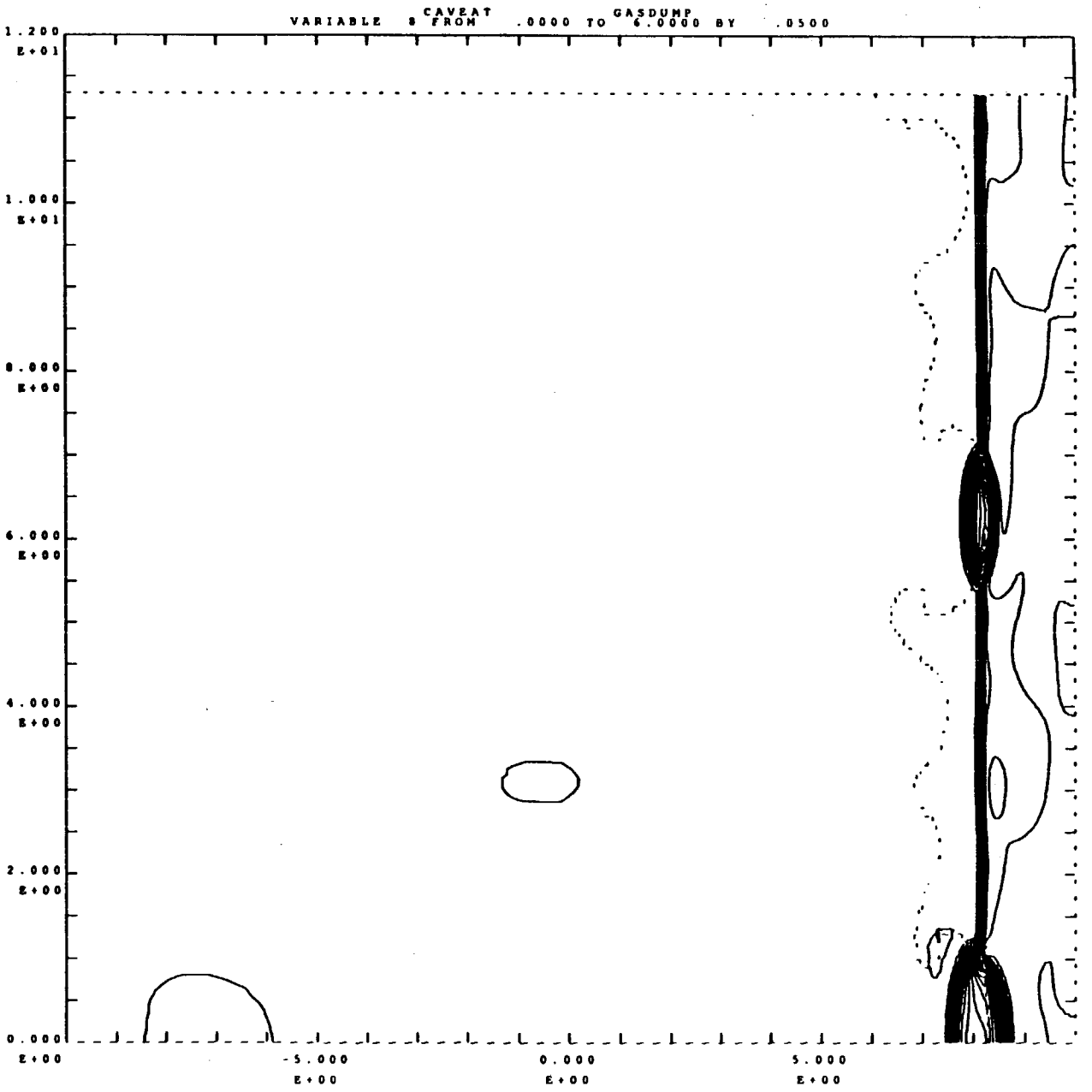

Pleasanton, USA

Edited by V. Rupert

RANGE FOR VARIABLE 0 IS:
1.0993E+00 TO 3.0123E+00

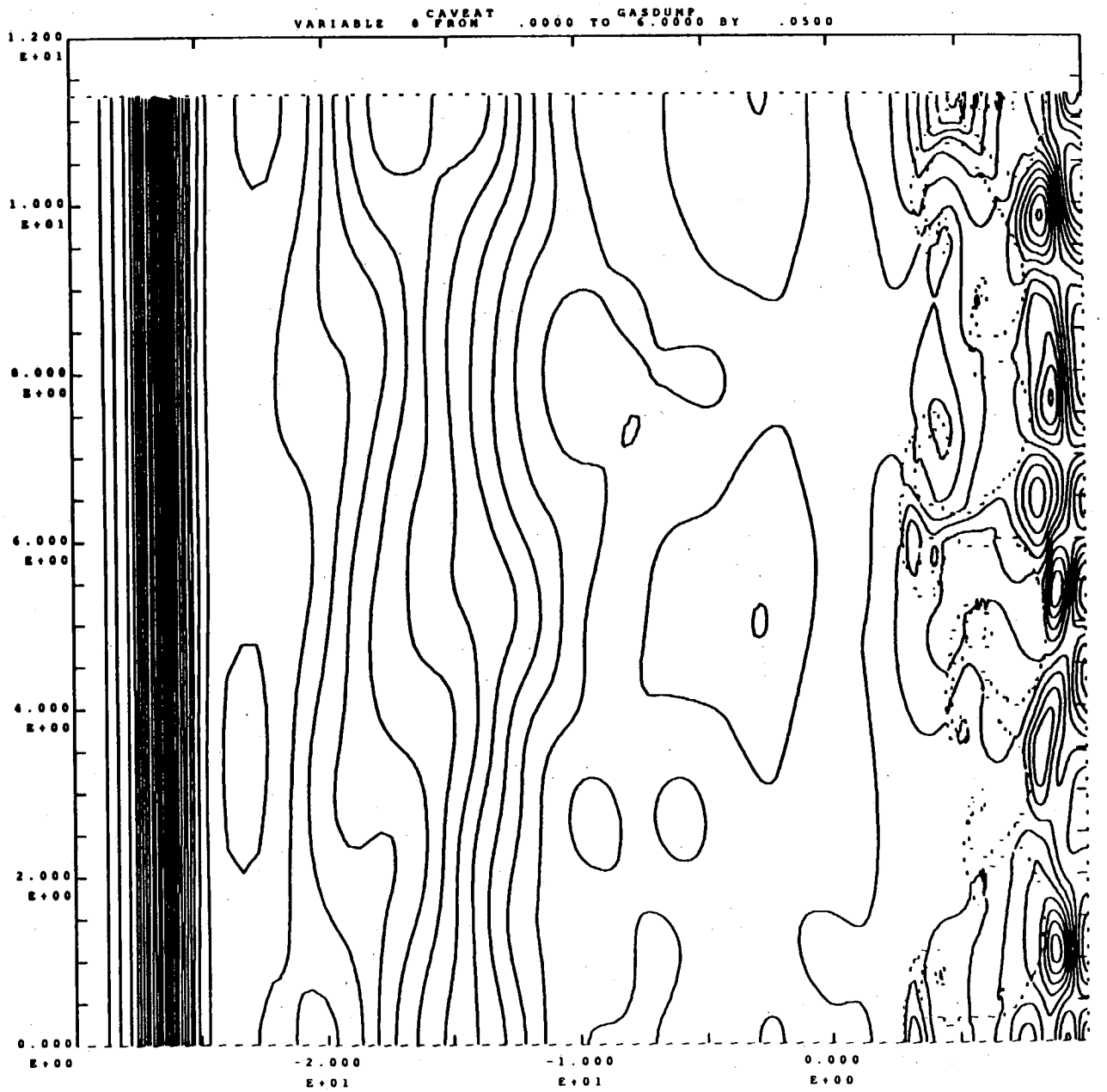

GAS VERSION 5.2.5-89

TEST PROBLEM 6B

Multiple λ

VORTICITY

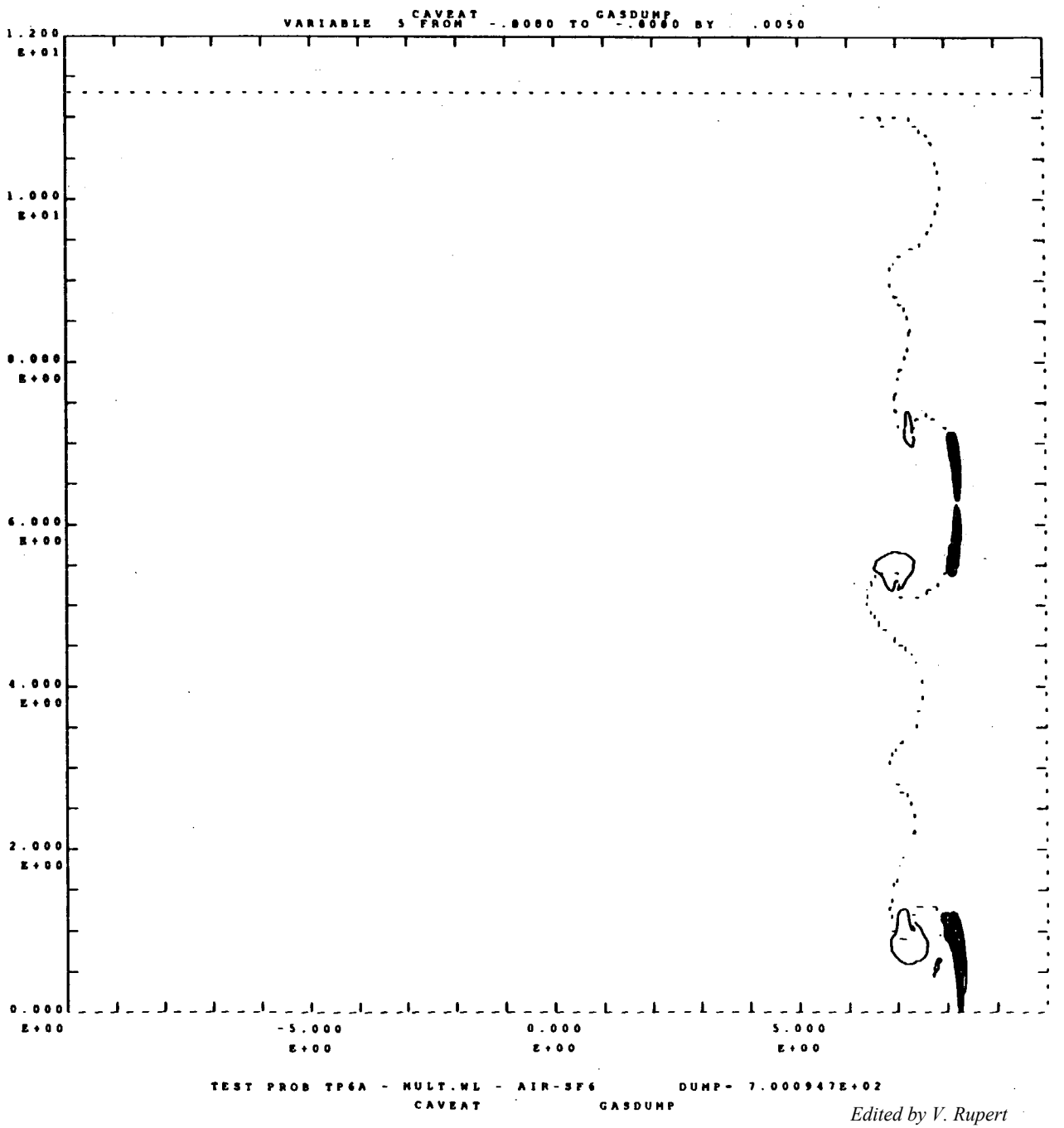

Pleasanton, USA

Edited by V. Rupert

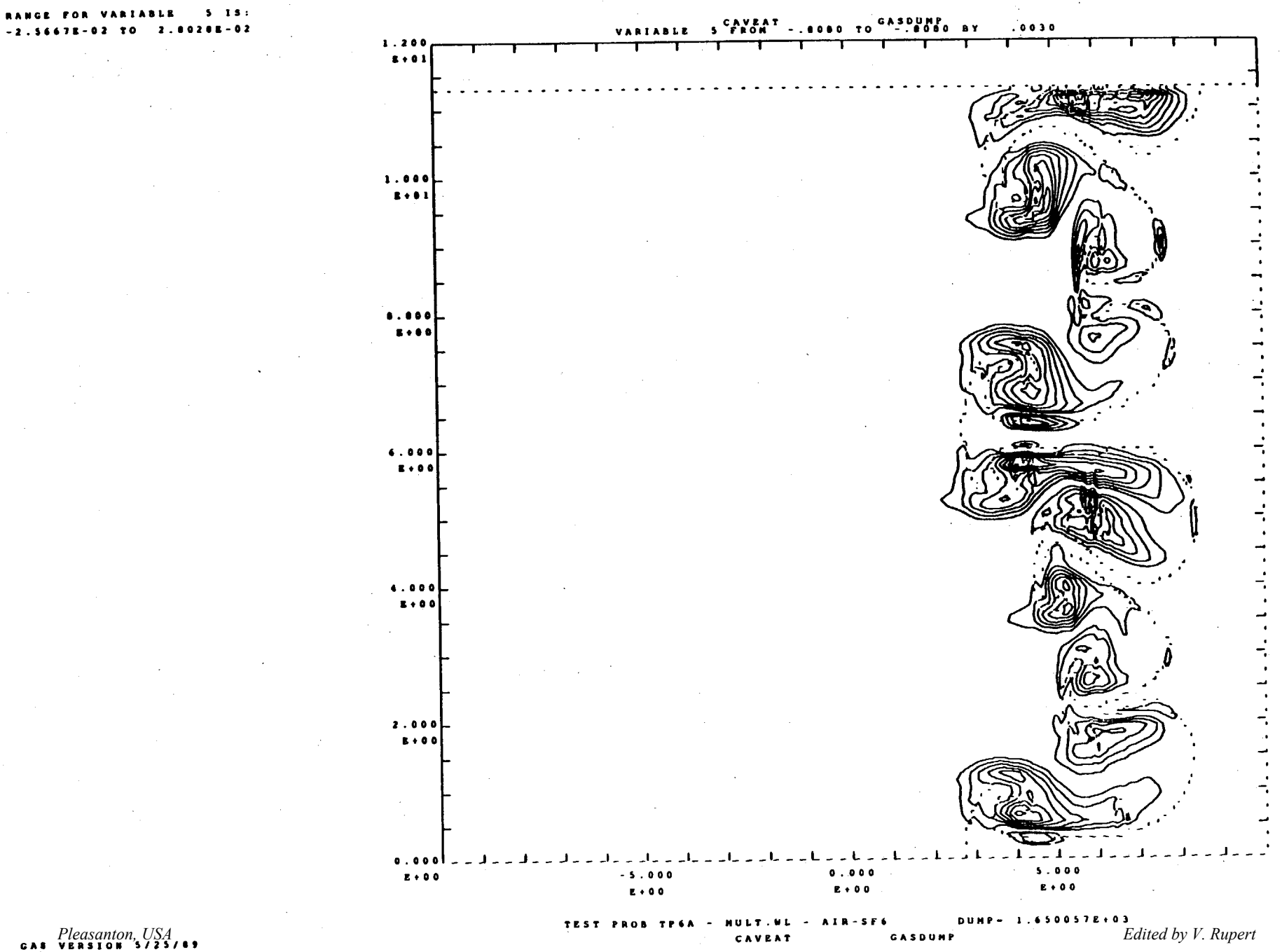
RANGE FOR VARIABLE 5 IS:
-2.5667E-02 TO 2.8028E-02
VARIABLE 5 FROM CAVEAT -.8080 TO GASDUMP -.8080 BY .0030
1.200 E+01
1.000 E+01
8.000 E+00
6.000 E+00
4.000 E+00
2.000 E+00
0.000 E+00
-5.000 E+00
0.000 E+00
5.000 E+00
TEST PROB TP6A - MULT.ML - AIR-SF6 DUMP= 1.650057E+03
CAVEAT GASDUMP

Pleasanton, USA *Edited by V. Rupert*

REFERENCE PROBLEMS

Viviane Rupert

International Workshop on RM and RT Mixing
Pleasanton November 1989

ACKNOWLEDGMENTS

AMR CODE

John Bell

Lila Chase

Phil Colella

Ted Feretta

Mike Welcome

CALE

Robert Tipton

DIFFERENT SCHEMES WERE USED

The AMR code uses an adaptive mesh algorithm. For these problems, the mesh could be refined by powers of four over three levels in critical areas, here in the perturbed part of the flow, around the interfaces.. The mesh remains rectangular throughout the problem

The basic mesh size was .625 cm for the air/He case, and .7065 for the air/SF6 case.

Hence,the finest grid dropped to 390 μm and 441μm respectively.

Cale is an Arbitrary Lagrangian Eulerian code.

This was the first application of this code to an RM instability problem and the calculations were not optimized.

The basic mesh size was 0.06x0.16cm. The air region had a weight of three relative to the He region , in the mesh redistribution scheme.

VCR 1 12/1/89 9:06 AM

SIMULATION OF AIR / SF6 EXPERIMENT

(i) No perturbations

(ii) Single wavelength

$x = 0.24 \cos(2\pi\ 2y/W)$ cm

(iii) Multiple wavelength

$x = \Sigma\ a_n \cos(2\pi\ ny/w)$

n	a_n
0.5	0.05 cm
1.5	0.10
2.0	0.07
3.5	0.11
5.5	0.09

VCR 8 12/1/89 9:06 AM

PROBLEM DEFINITION : AIR / SF6 , M=1.32

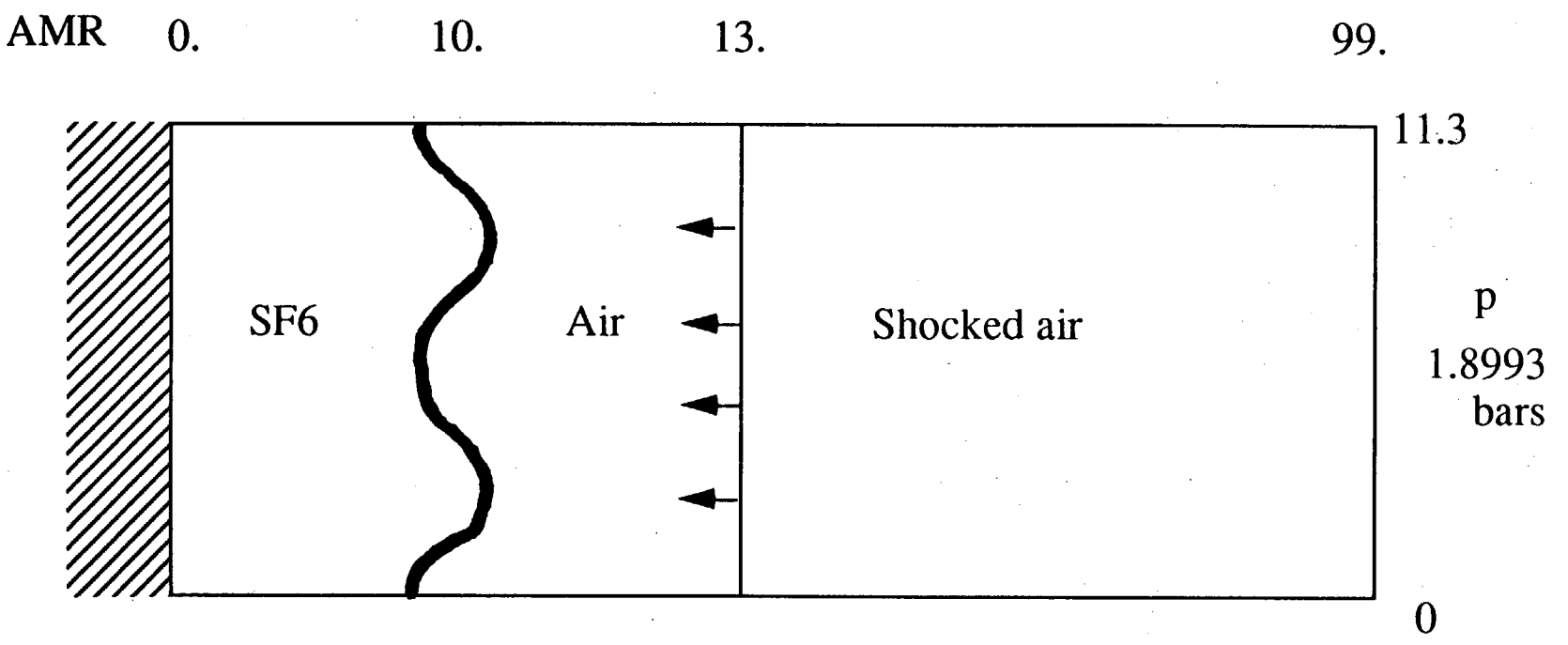

ρ mg/cm3	6.187	1.225	1.9
p bar	1.013	1.013	1.8993
γ	1.06	1.4	1.4

VCR 5 12/1/89 9:06 AM

Interface and mix boundaries

Air/SF6 - M = 1.32 - AMR calculation

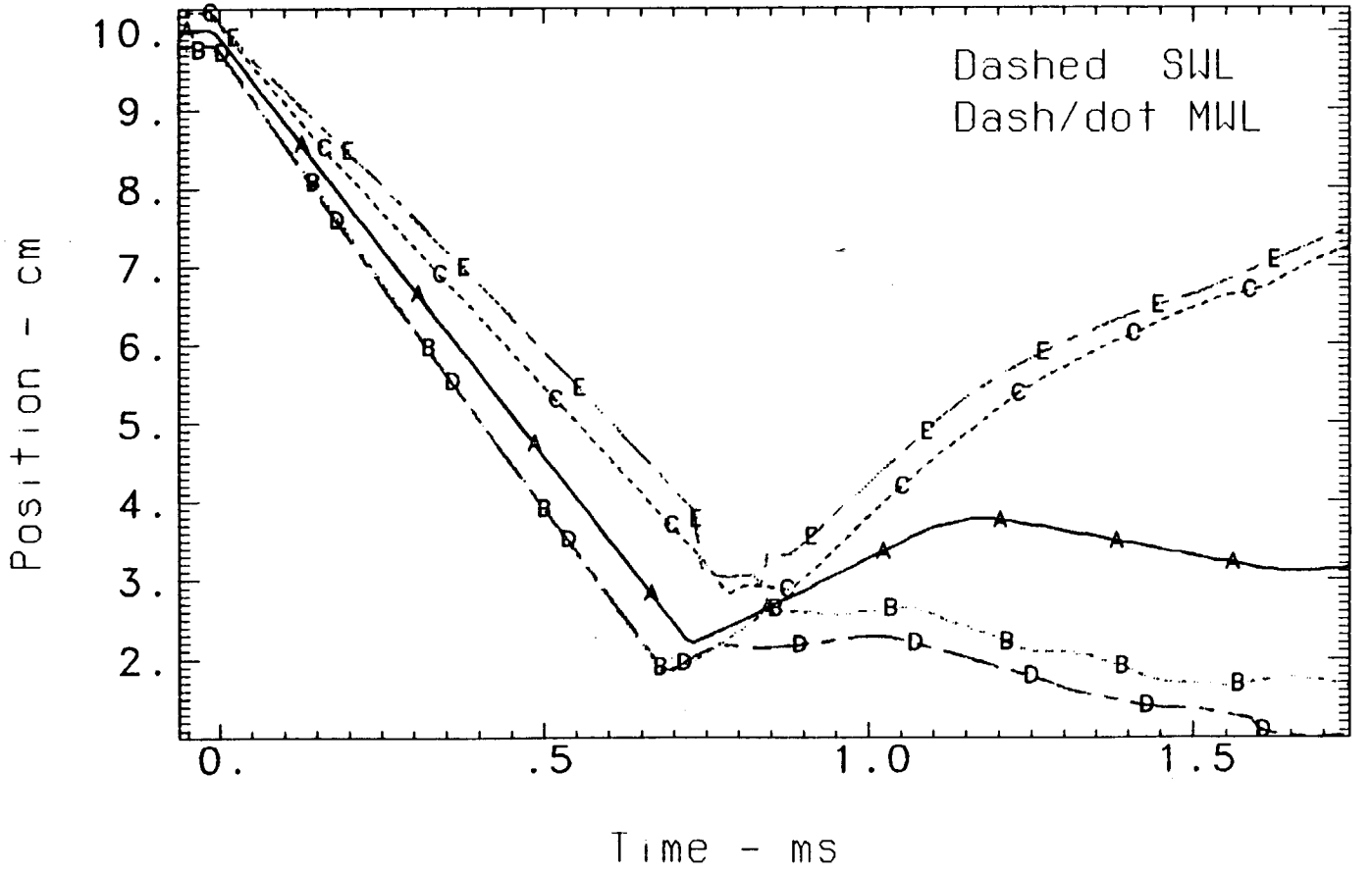

VCR 11/11/89-2

Mix widths for Air/SF6

M = 1.32 - AMR calculation

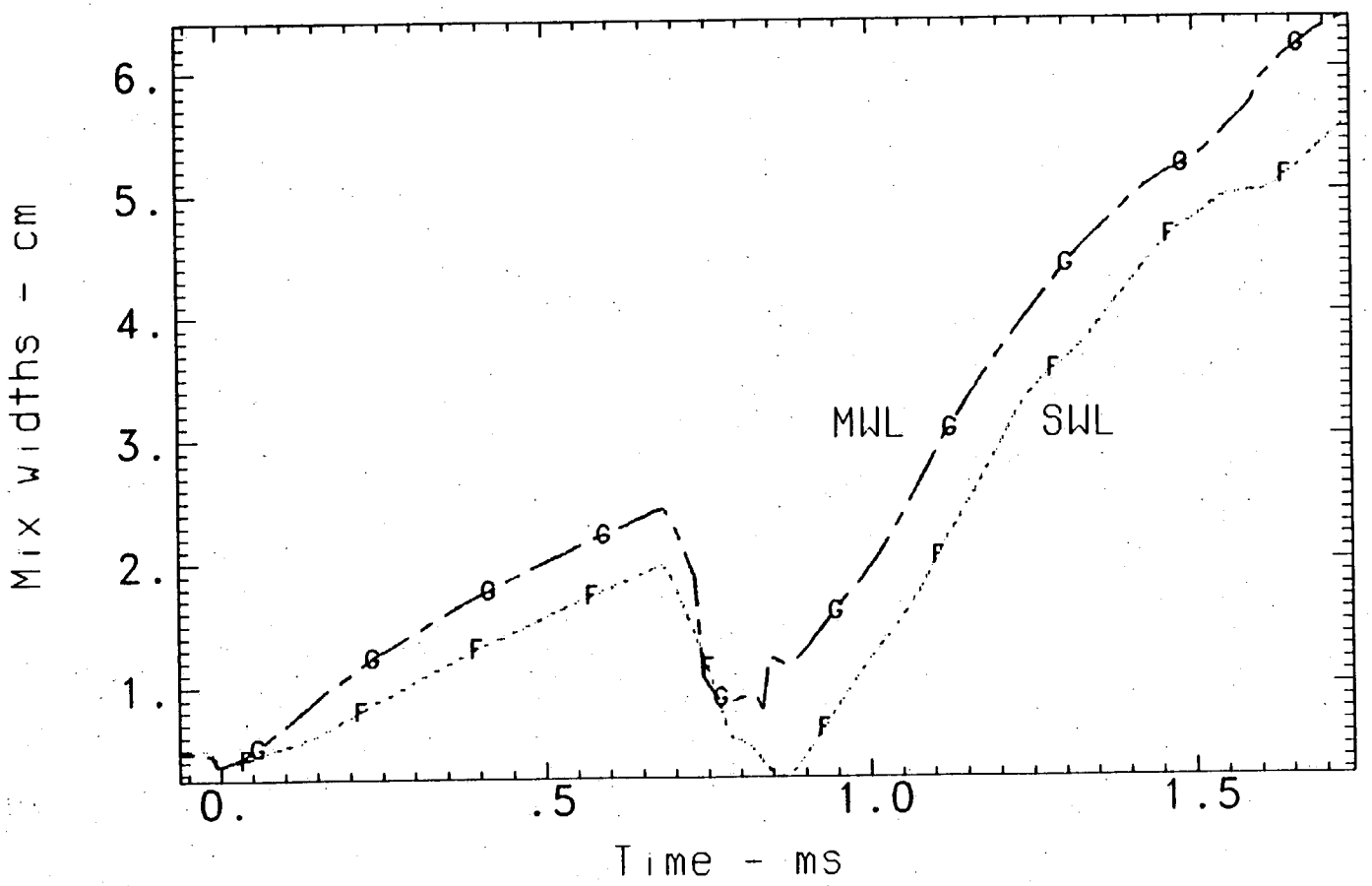

VCR 11/11/89-3

Fluctuating energy - Air/SF6

Curve A for SWL, curve B for MWL

Total FKE - bar

Time	SWL	MWL
0.70	.095	.063
1.1	.463	.488
1.65	.399	.291

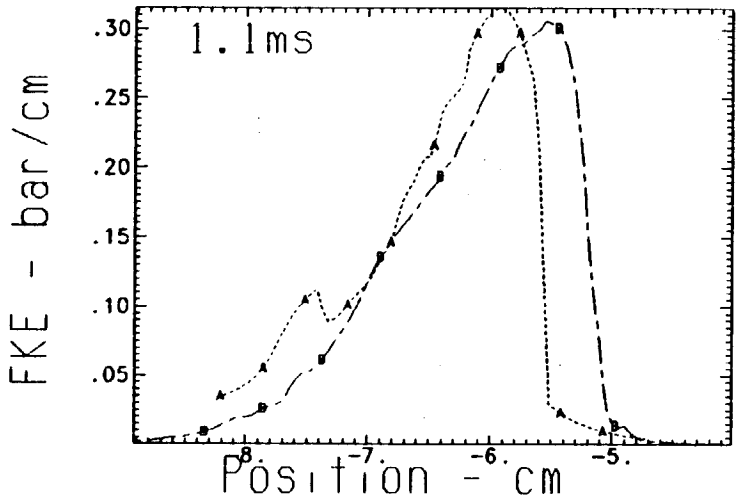

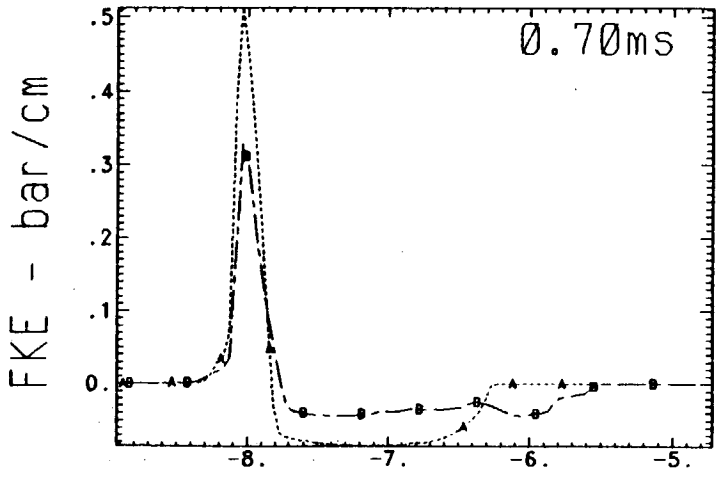

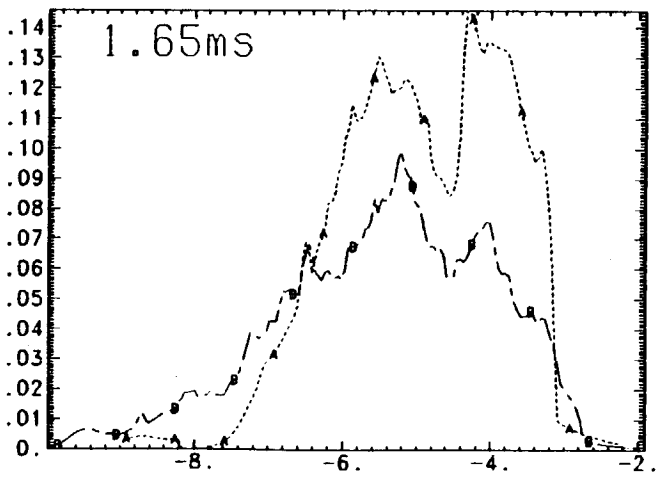

Position - cm

VCR 11/11/89-19:15

Air/SF6 - M = 1.32 - No perturbations

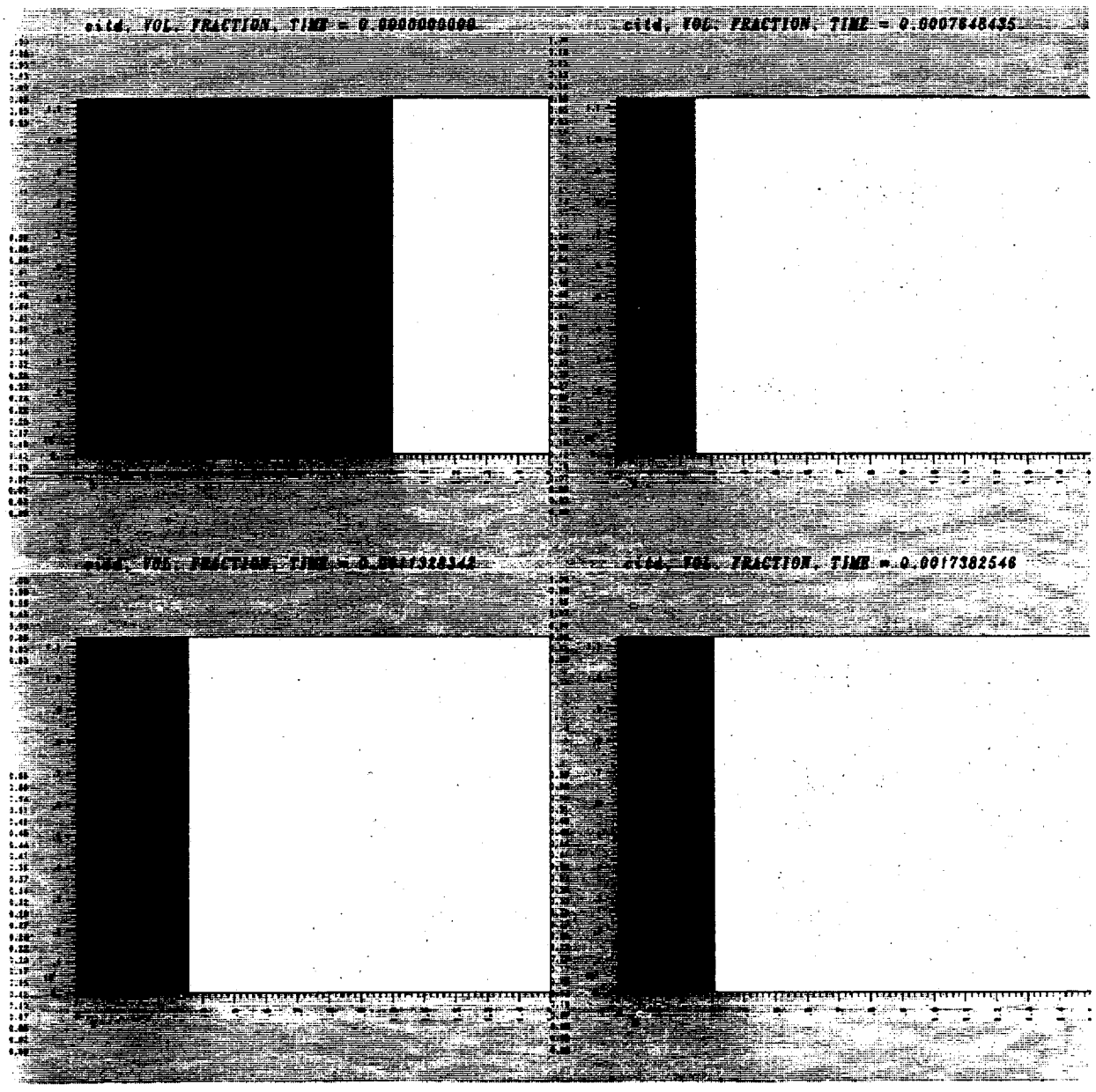

Air/SF6 - M = 1.32 - SWL - 0.70ms

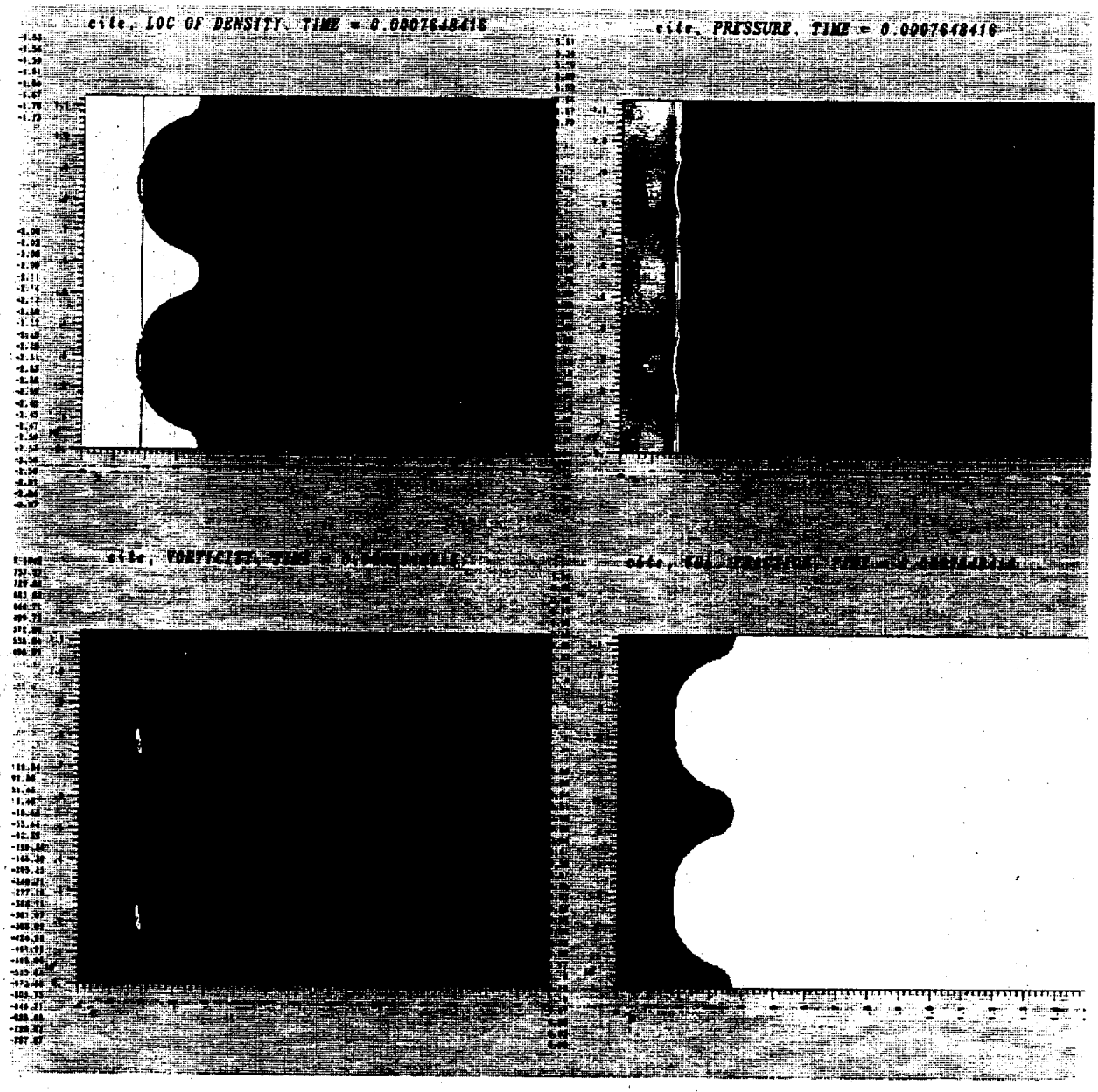

Air/SF6 - M = 1.32 - SWL - 1.08ms

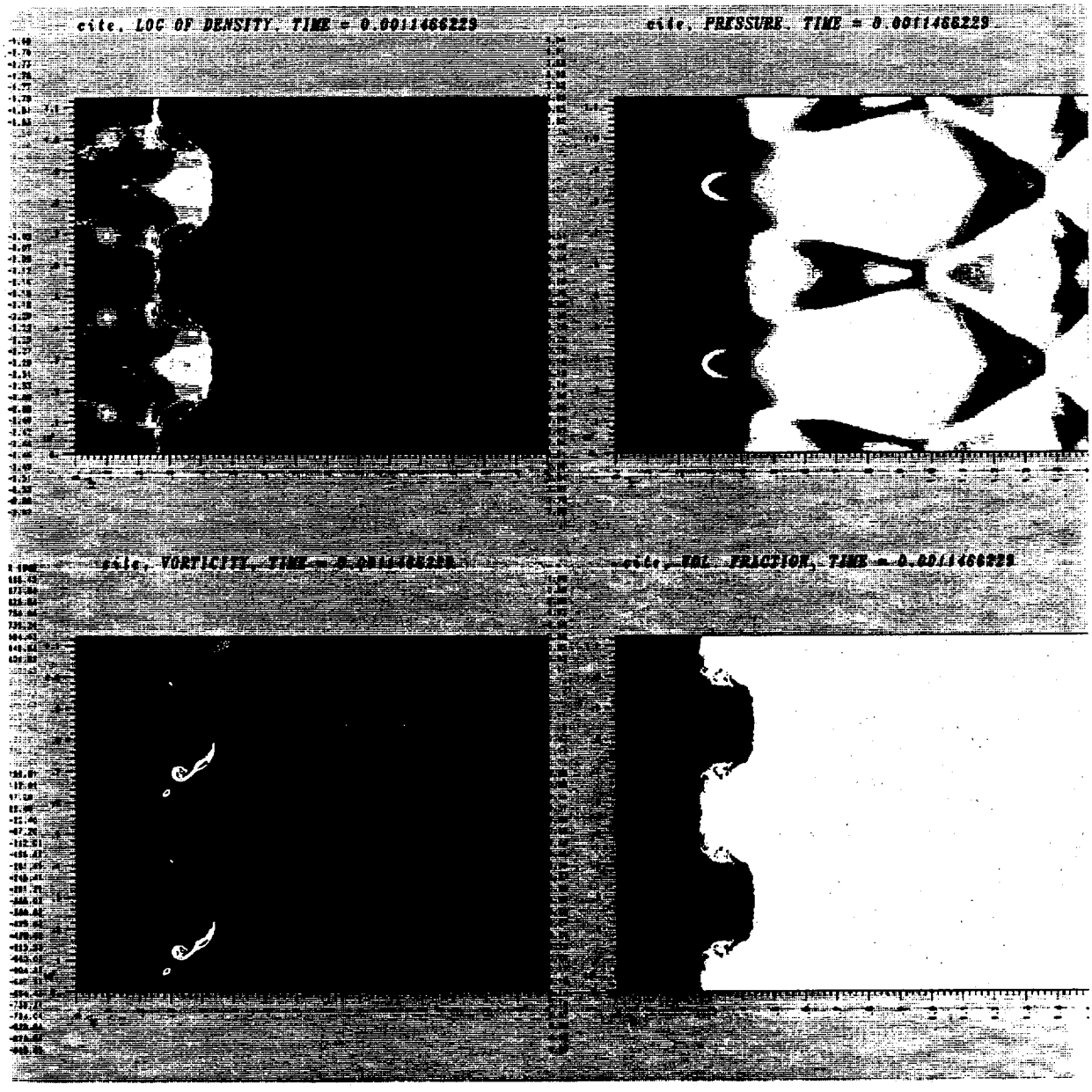

Air/SF6 - M = 1.32 - SWL - 1.65ms

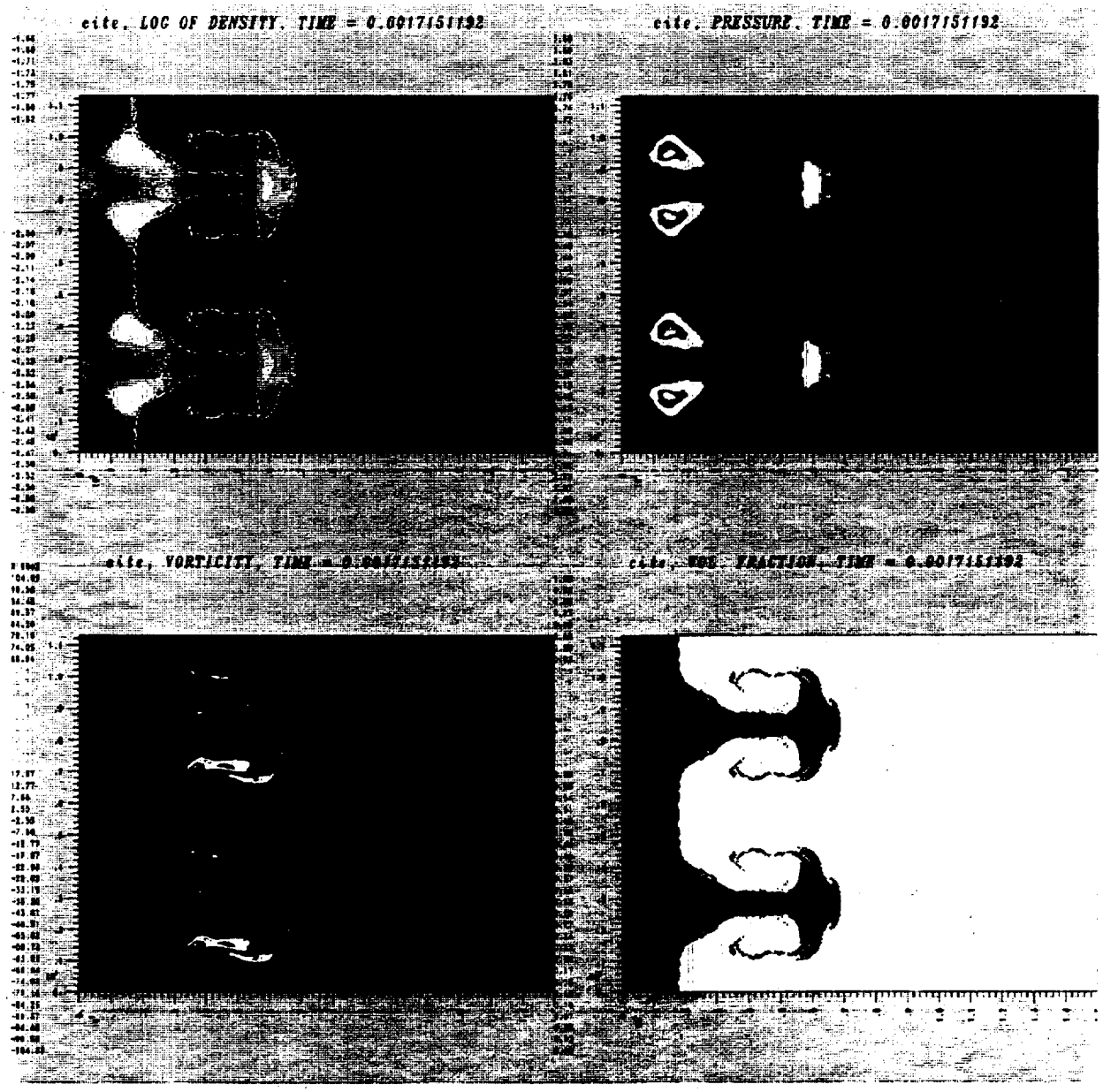

Air/SF6 - M = 1.32 - MWL - 0.70ms

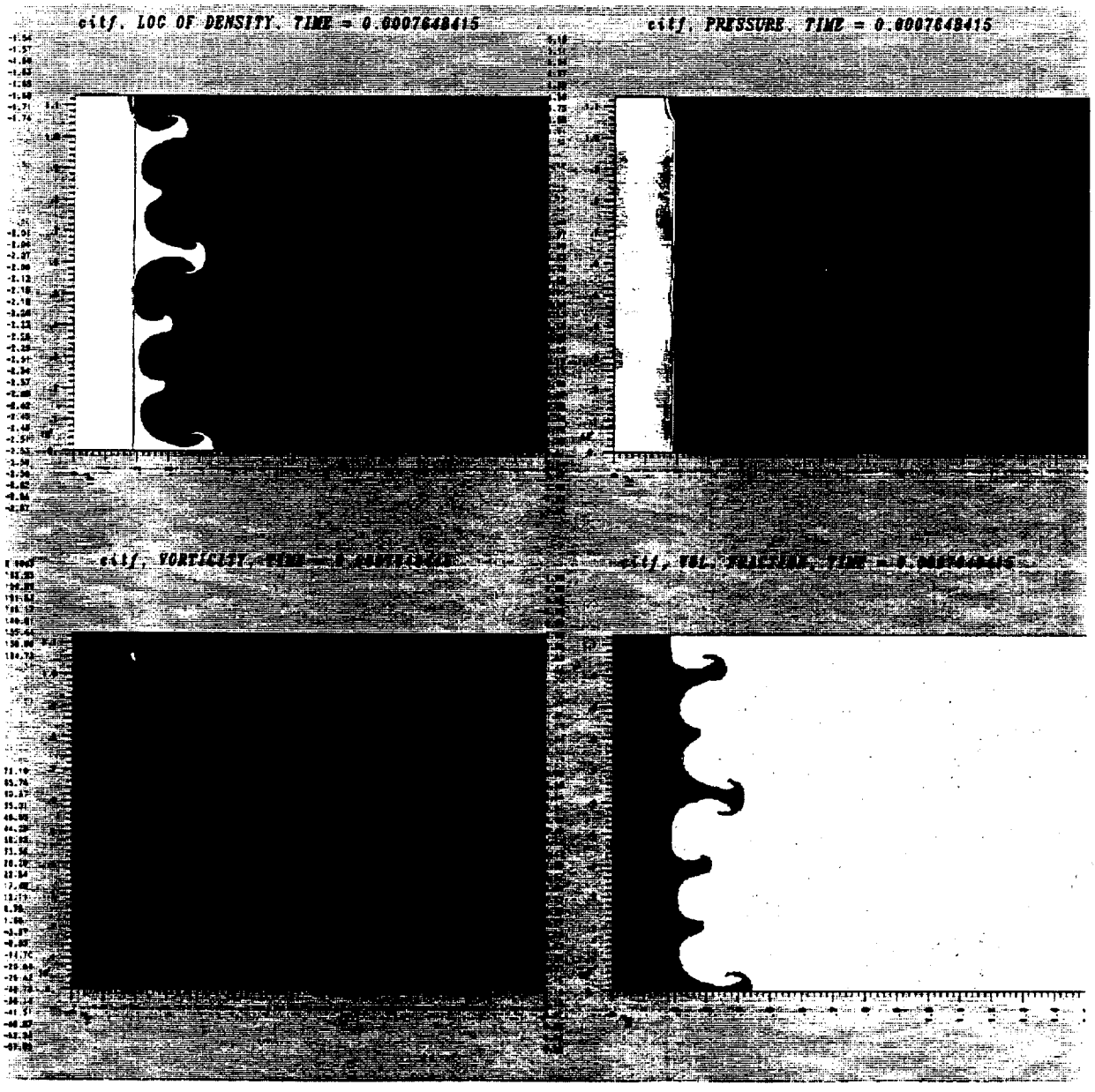

Air/SF6 - M = 1.32 - MWL - 1.07ms

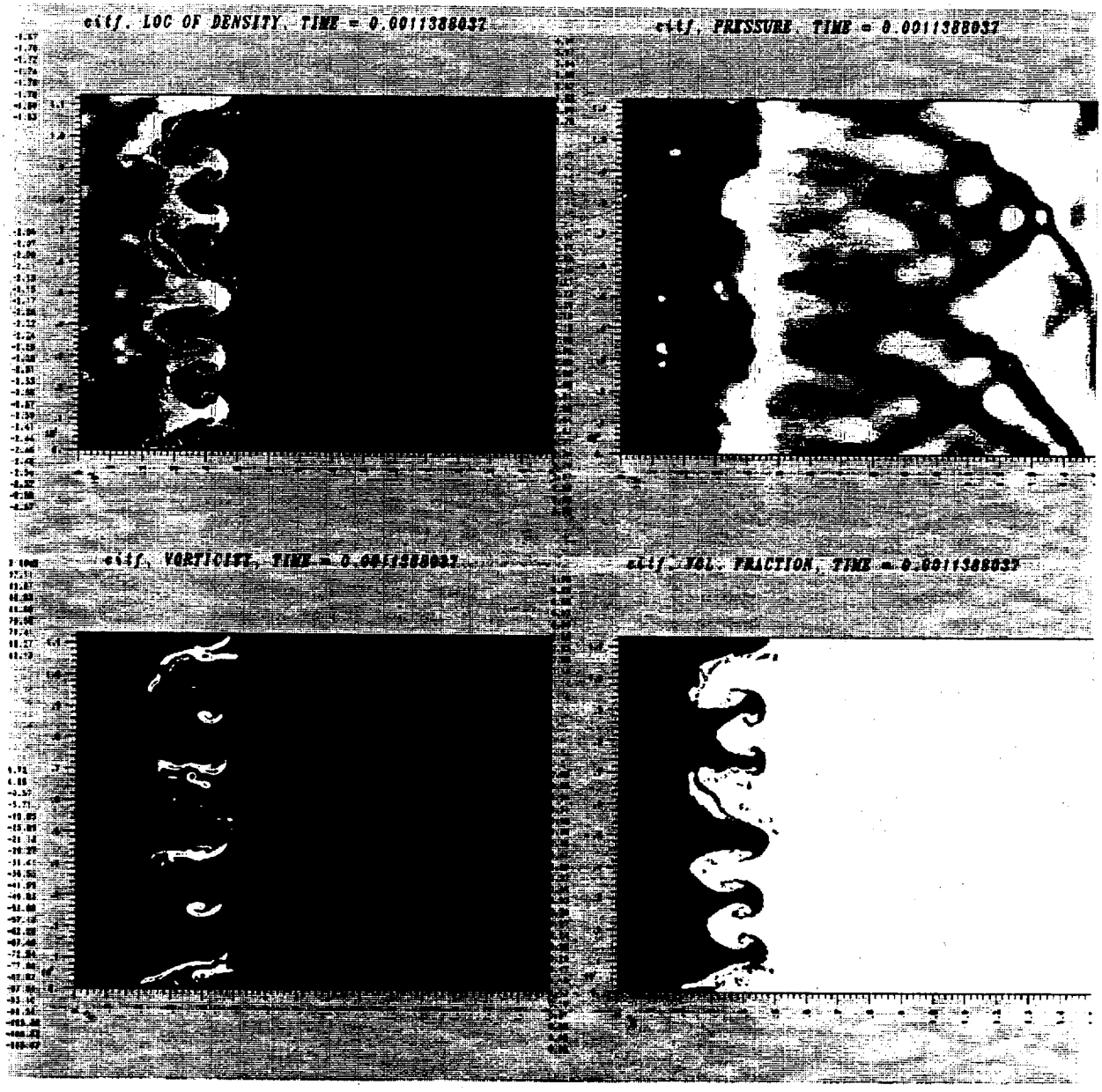

Air/SF6 - M = 1.32 - MWL - 1.69ms

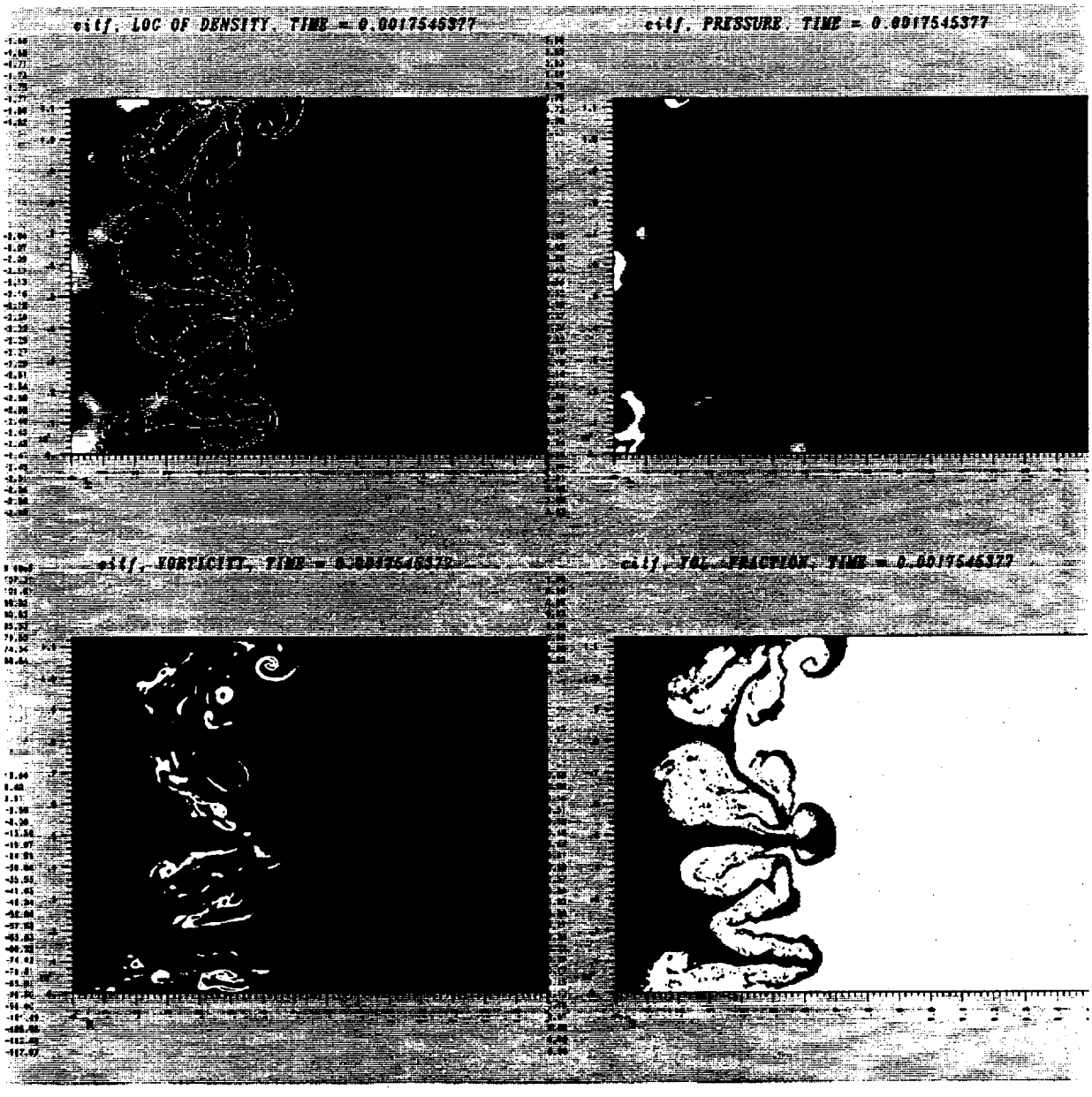

SIMULATION OF AIR / He EXPERIMENT

(i) No perturbations

(ii) Single wavelength

$x = 0.24 \cos(2\pi\ 2y/W)$ cm

(iii) Multiple wavelength

$x = \Sigma\ a_n \cos(2\pi\ ny/w)$

n	a_n
0.5	0.05 cm
1.5	0.10
2.0	0.07
3.5	0.11
5.5	0.09

VCR 7 12/1/89 9:06 AM

PROBLEM DEFINITION : AIR / He , M=1.24

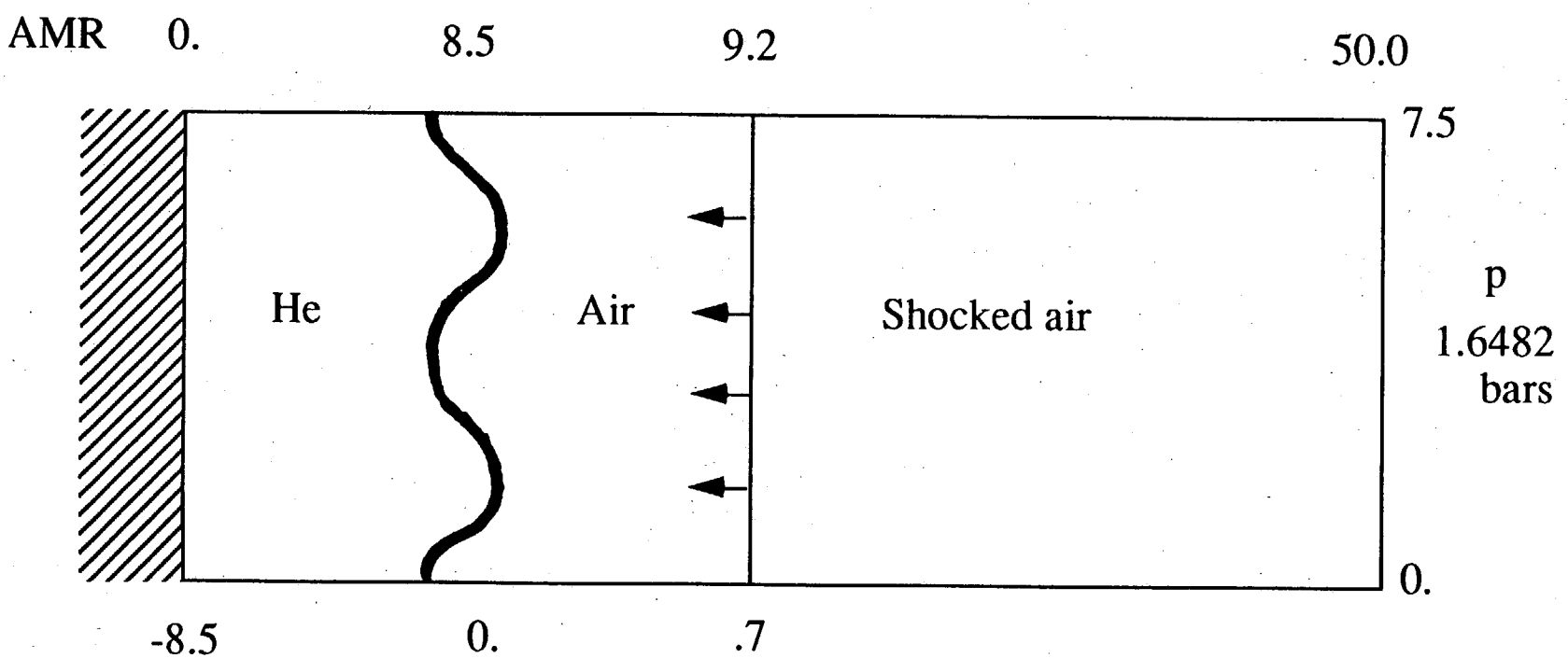

ρ mg/cm3	0.1694	1.225	1.7285
p bar	1.013	1.013	1.6482
γ	1.67	1.4	1.4

VCR 6 12/1/89 9:06 AM

Interface and mix boundaries

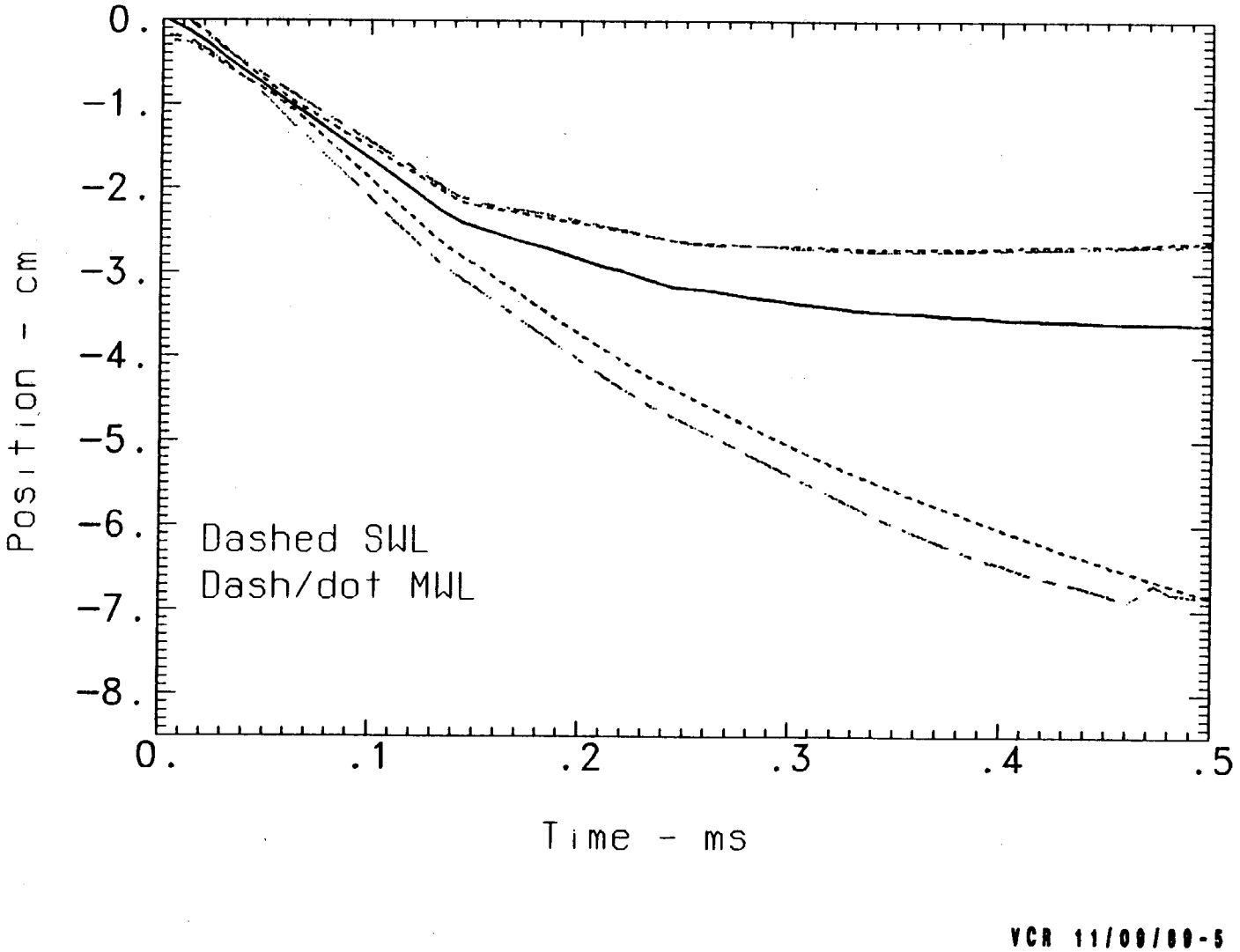

Mix widths for Air/He

M = 1.24 - AMR calculation

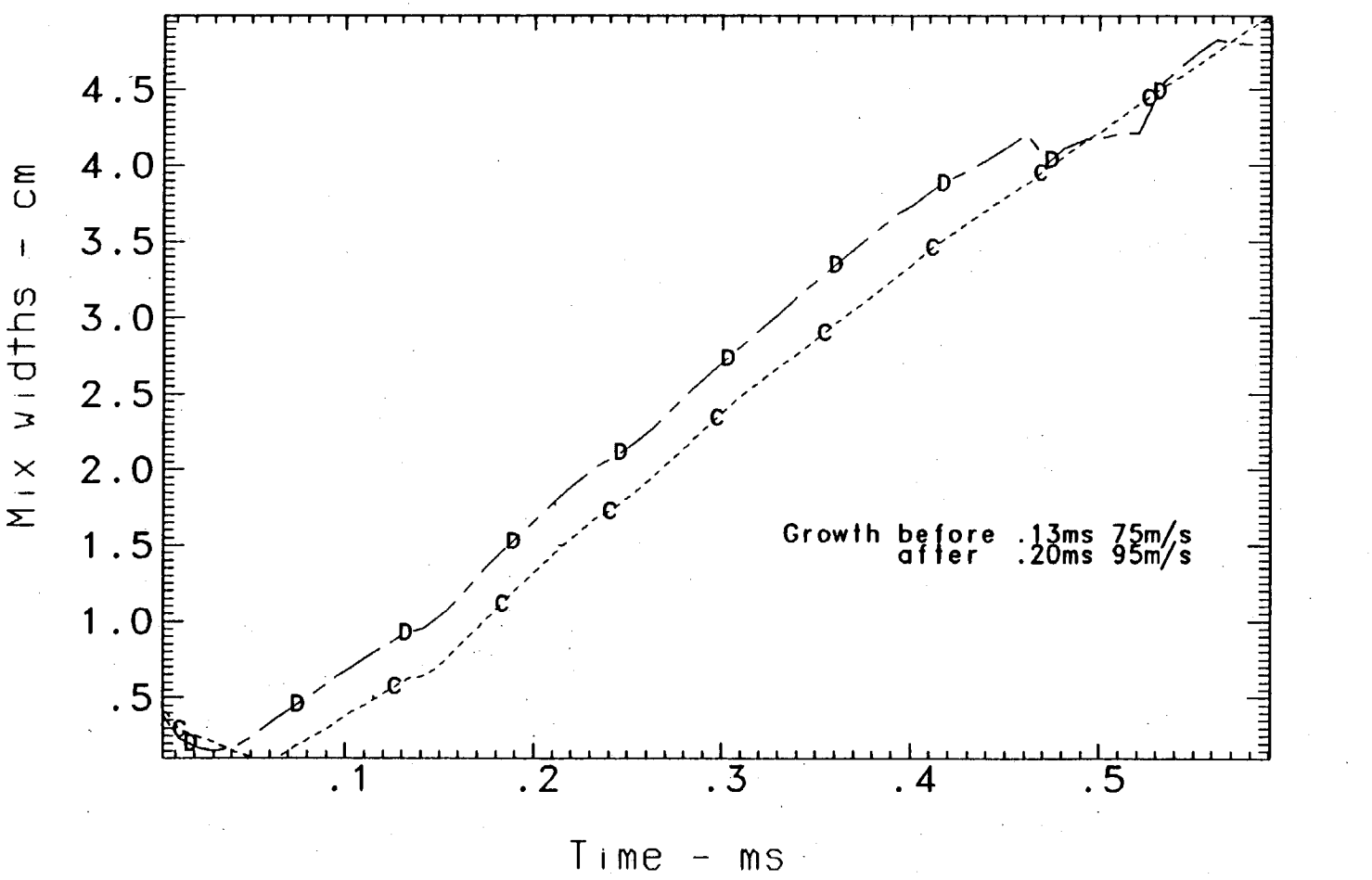

Fluctuating energy - Air/He

Curve A for SWL, curve B for MWL

Total FKE - bar

Time	SWL	MWL
0.12	.036	.036
0.22	.083	.068
0.33	.099	.067

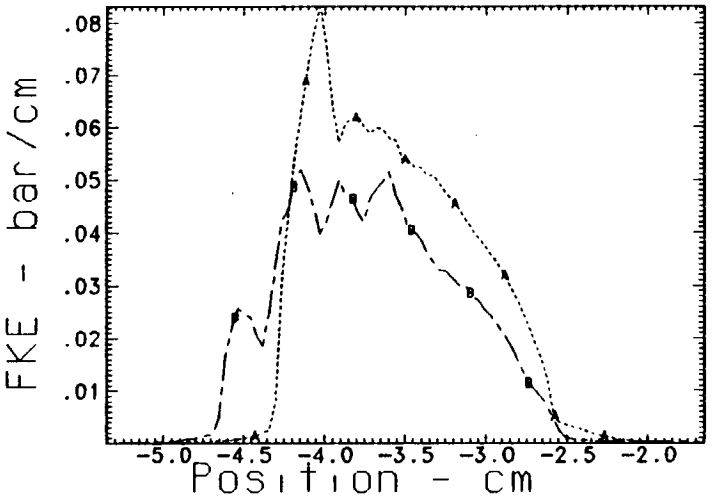

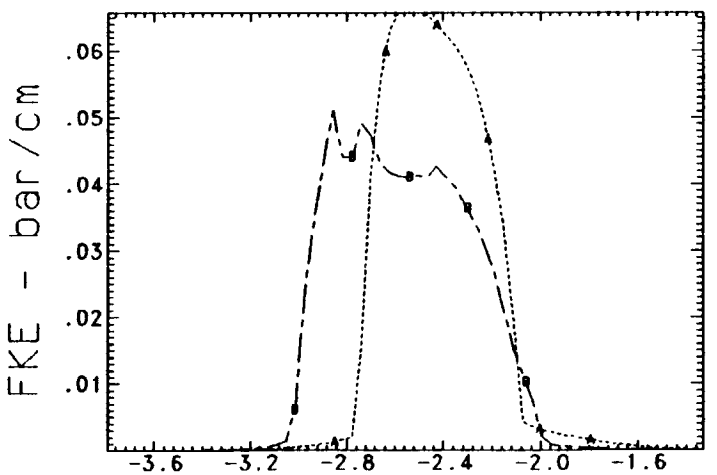

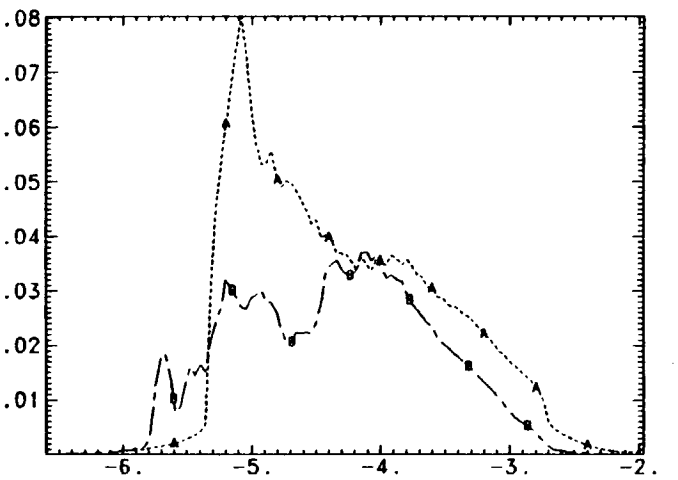

Position - cm

VCR 11/13/89-19:08

Air/He - M = 1.24 - SWL - 0.12ms

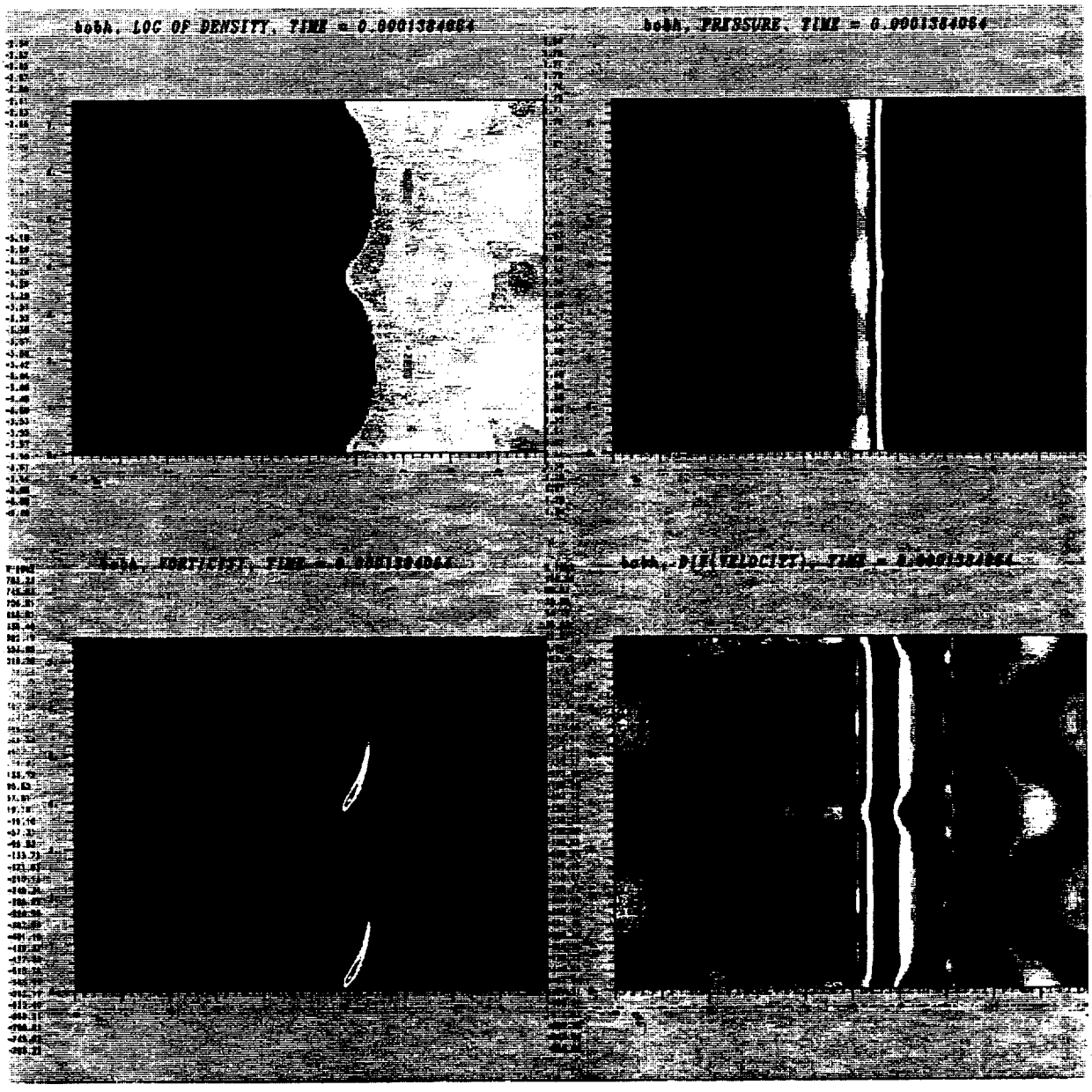

Air/He - M = 1.24 - SWL - 0.23ms

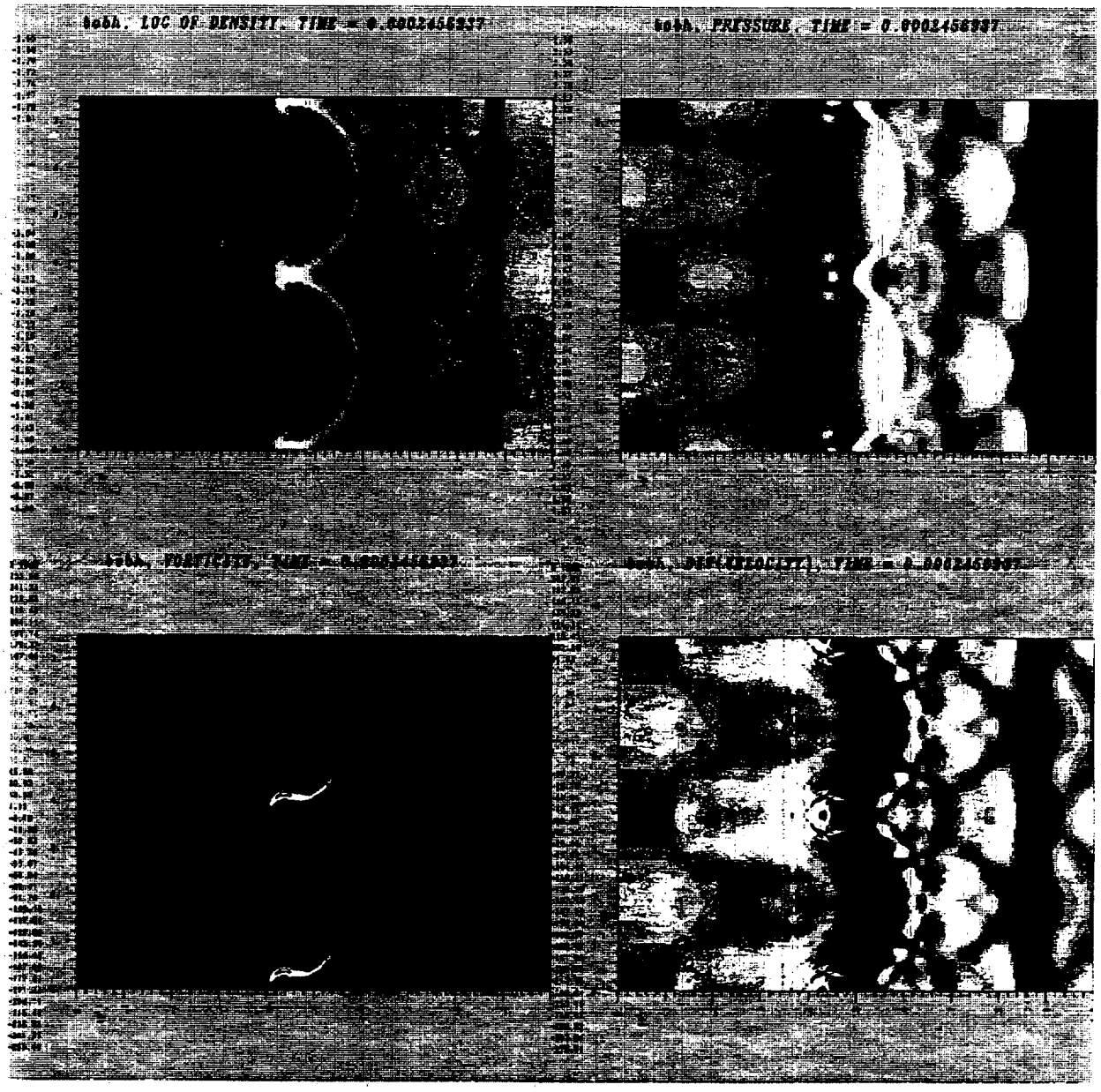

Air/He - M = 1.24 - SWL - 0.31ms

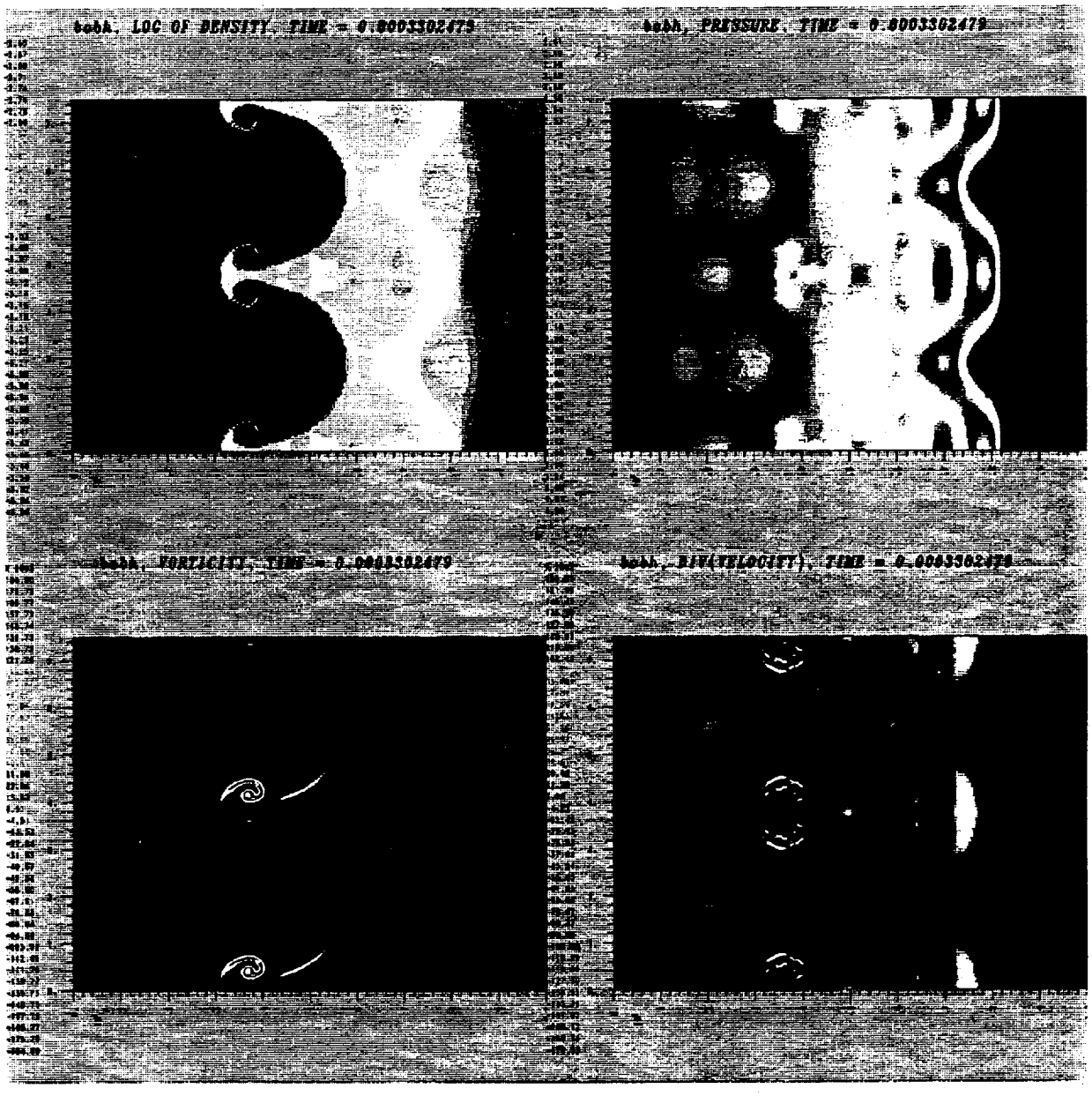

Air/He - M = 1.24 - MWL - 0.12ms

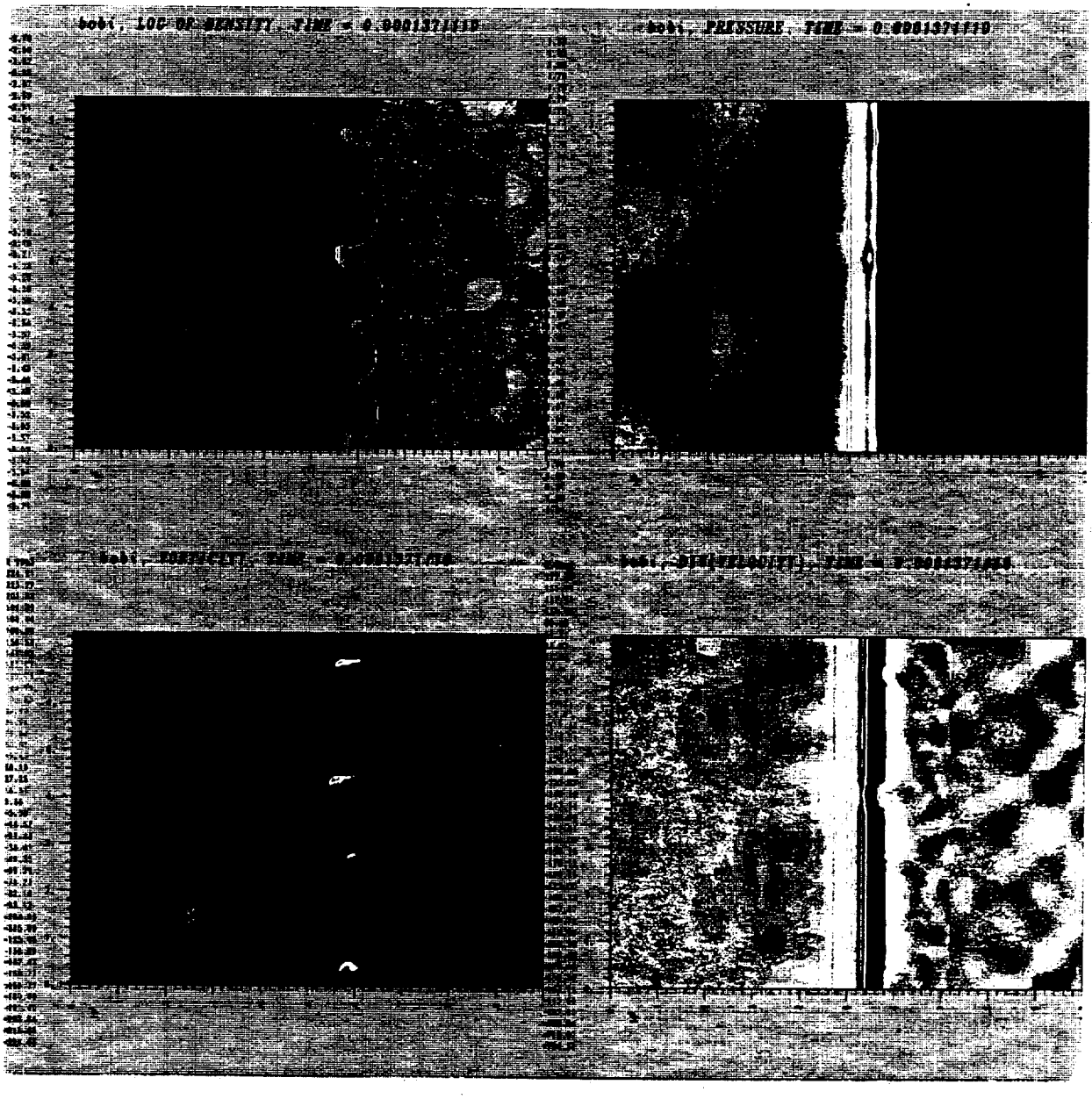

Air/He - M = 1.24 - MWL - 0.23ms

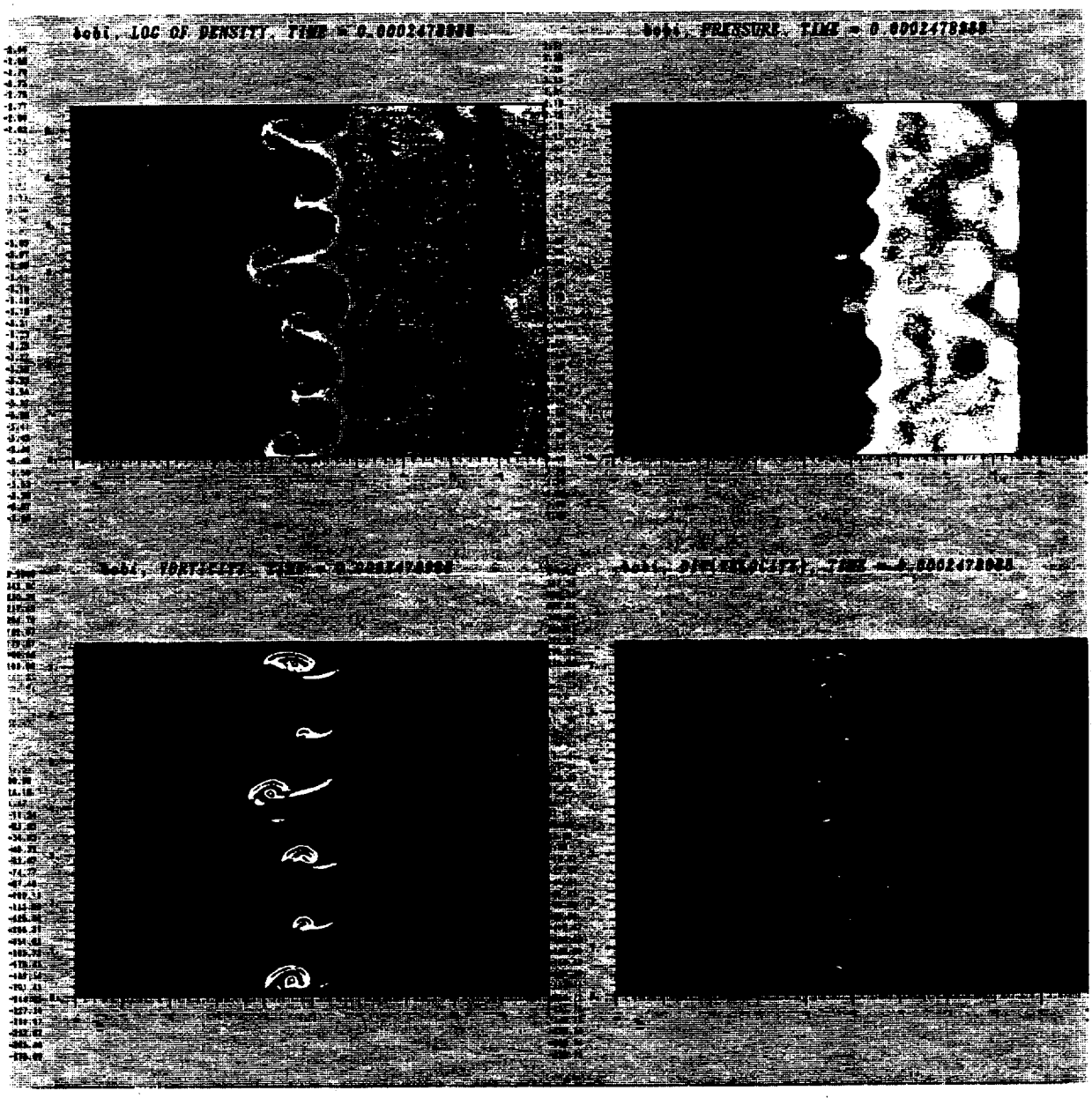

Air/He - M = 1.24 - MWL - 0.31ms

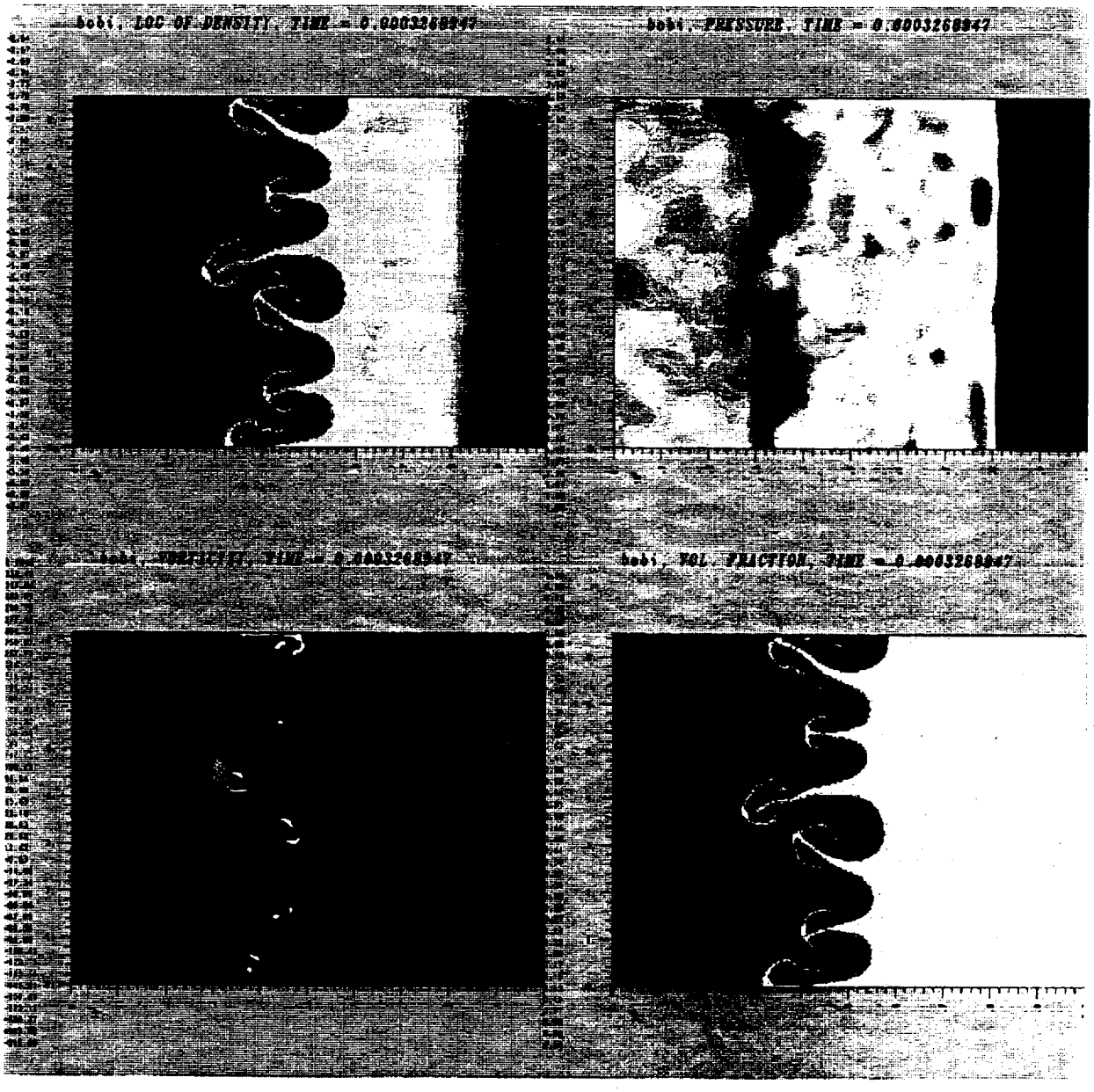

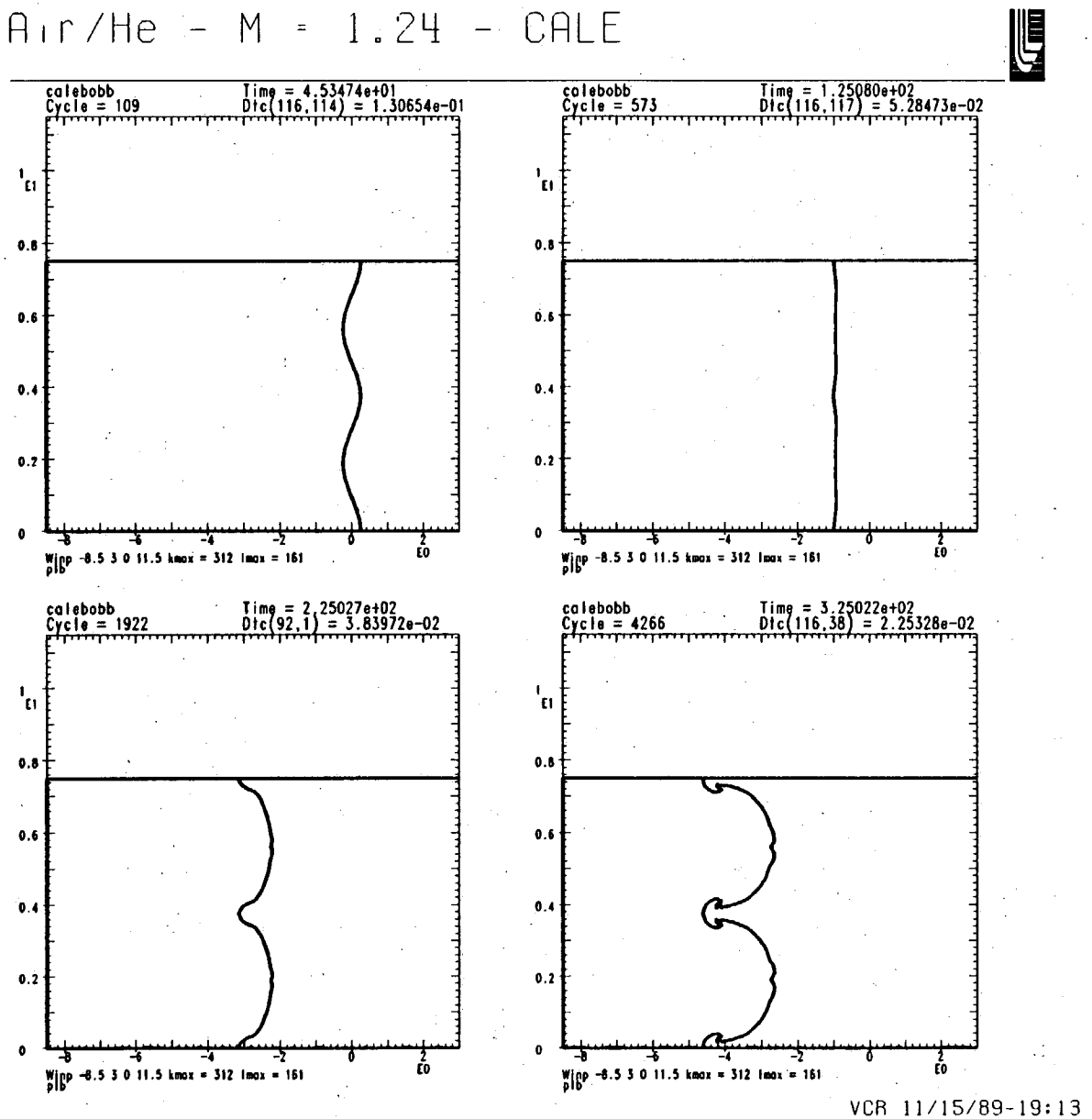
Air/He - M = 1.24 - CALE
calebobb
Cycle = 109
Time = 4.53474e+01
Dtc(116,114) = 1.30654e-01
calebobb
Cycle = 573
Time = 1.25080e+02
Dtc(116,117) = 5.28473e-02
calebobb
Cycle = 1922
Time = 2.25027e+02
Dtc(92,1) = 3.83972e-02
calebobb
Cycle = 4266
Time = 3.25022e+02
Dtc(116,38) = 2.25328e-02
Wipp -8.5 3 0 11.5 kmax = 312 lmax = 161
plb
VCR 11/15/89-19:13

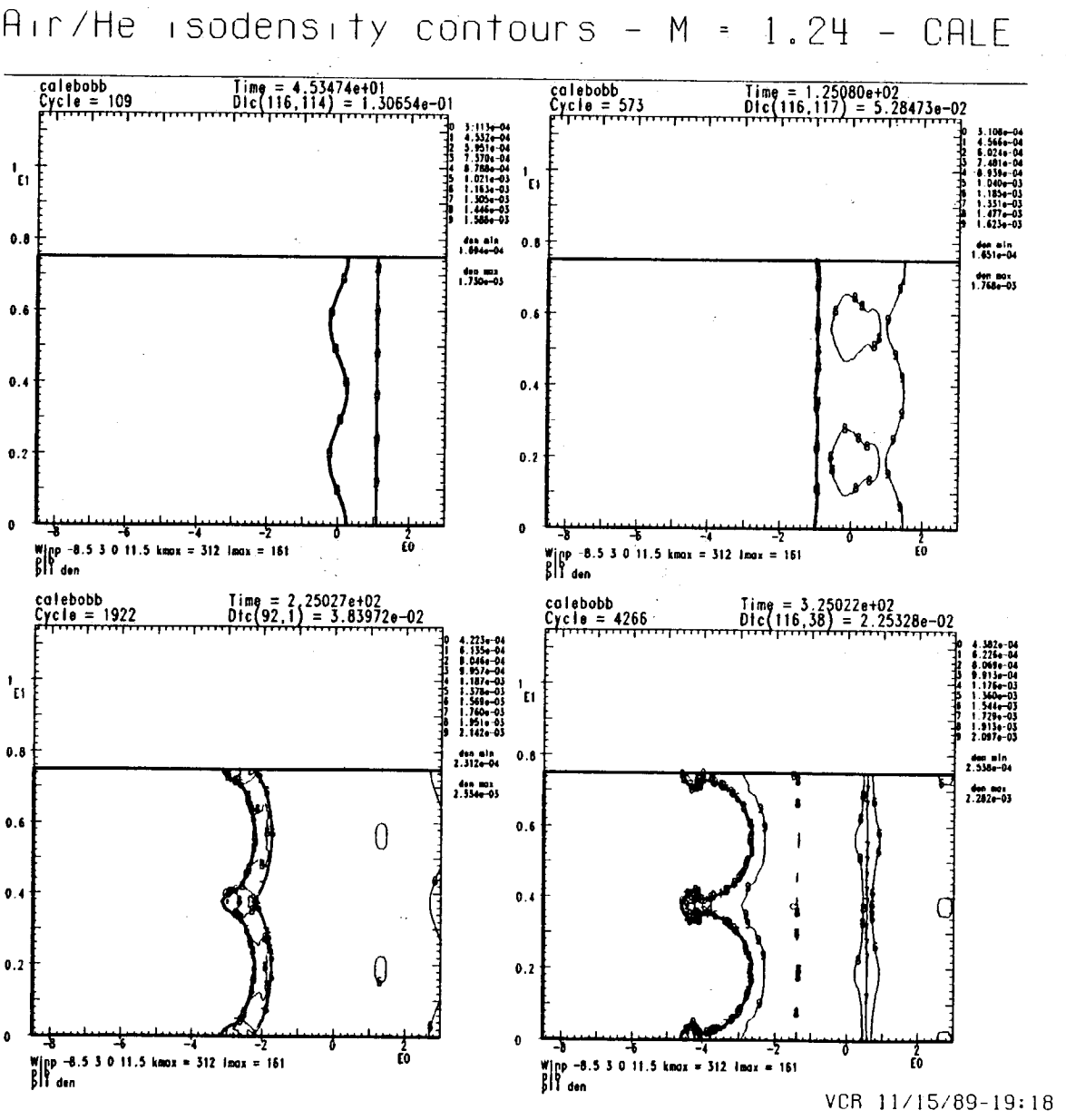
Air/He isodensity contours - M = 1.24 - CALE
calebobb
Cycle = 109
Time = 4.53474e+01
Dtc(116,114) = 1.30654e-01
calebobb
Cycle = 573
Time = 1.25080e+02
Dtc(116,117) = 5.28473e-02
calebobb
Cycle = 1922
Time = 2.25027e+02
Dtc(92,1) = 3.83972e-02
calebobb
Cycle = 4266
Time = 3.25022e+02
Dtc(116,38) = 2.25328e-02
Wipp -8.5 3 0 11.5 kmax = 312 lmax = 161
den
VCR 11/15/89-19:18

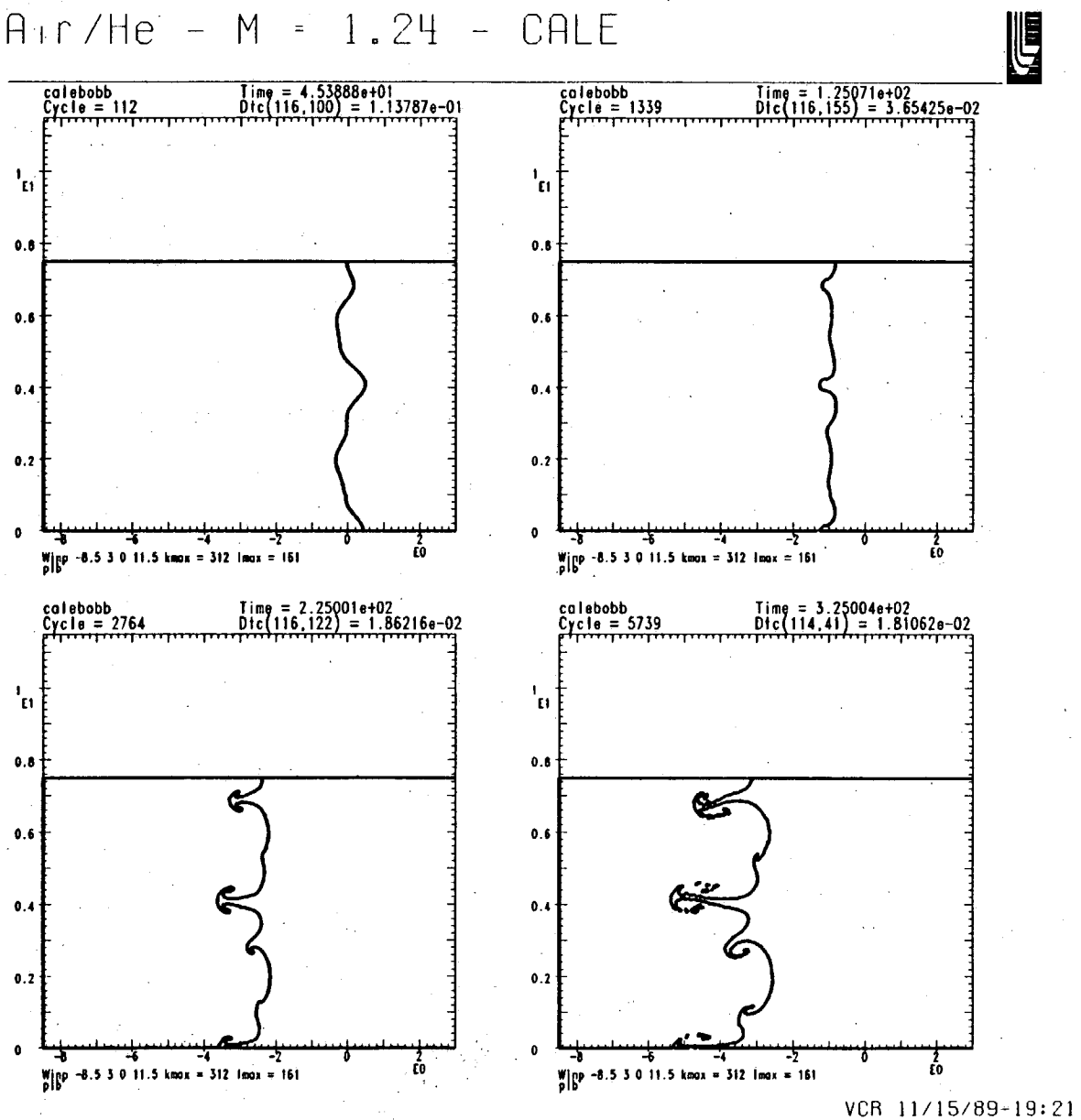
Air/He - M = 1.24 - CALE
calebobb
Cycle = 112
Time = 4.53888e+01
Dtc(116,100) = 1.13787e-01
calebobb
Cycle = 1339
Time = 1.25071e+02
Dtc(116,155) = 3.65425e-02
calebobb
Cycle = 2764
Time = 2.25001e+02
Dtc(116,122) = 1.86216e-02
calebobb
Cycle = 5739
Time = 3.25004e+02
Dtc(114,41) = 1.81062e-02
Wimp -8.5 3 0 11.5 kmax = 312 lmax = 161
plb
VCR 11/15/89-19:21

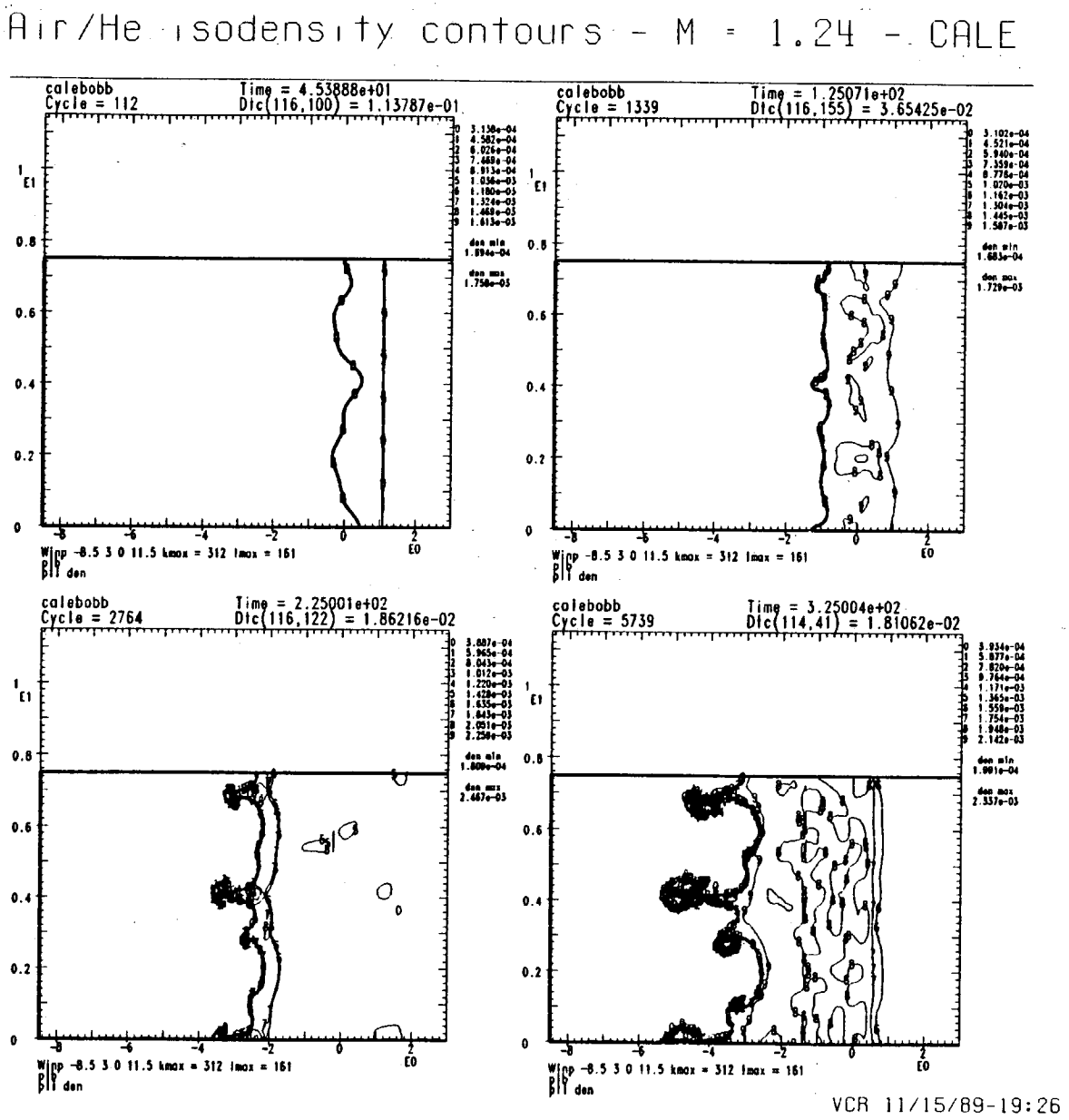
Air/He isodensity contours - M = 1.24 - CALE
calebobb
Cycle = 112
Time = 4.53888e+01
Dic(116,100) = 1.13787e-01
calebobb
Cycle = 1339
Time = 1.25071e+02
Dic(116,155) = 3.65425e-02
calebobb
Cycle = 2764
Time = 2.25001e+02
Dic(116,122) = 1.86216e-02
calebobb
Cycle = 5739
Time = 3.25004e+02
Dic(114,41) = 1.81062e-02
VCR 11/15/89-19:26

SUMMARY

These calculations need to be analyzed in detail, and compared with available experimental results, and other calculations. Note that they do not include the boundary layers or membranes. Hence some differences should be expected when comparing with experimental results.

For the air/He case, results show a faster growth rate than measured by Benjamin.

One of the current advantage of the AMR code, is to provide information on vorticity, and enable us to calculate the fluctuating kinetic energy.

The latter is an approximation of the turbulent kinetic energy in the problem, and should help us in normalizing ke type models.

Three dimensional calculations will soon be possible, so that comparisons with experiments will be more realistic.

The CALE code has not yet been exercised to it's full potential. The results presented here were obtained with a fairly coarse mesh compared with that ultimately used in the AMR calculations. A more refined mesh will be investigated, as the run time is quite short.

VCR 3 12/1/89 9:06 AM

Pure Eulerian Hydrodynamics Calculations of the Two Standard Test Problems

Michael Wehner
B-Division
Lawrence Livermore National Laboratory
Livermore, CA 94550
USA

Purely Eulerian hydrodynamics calculations of the two standard test problems discussed at this conference are presented. Spatial resolution is an important issue regarding the nature of the bubbles and spikes formed at the unstable interface. Calculations with square zones 1 mm on a side indicate that the light-to-heavy test problem (SF_6-air) is better resolved than the same zoning on the heavy-to-light problem (He-Air). This is due simply to the observation that the one problem is bigger across than the other. A refinement of the mesh to 1/2 mm square zones for the multiple wavelength perturbation indicates substantially better resolution of the interface features. The spikes are substantially narrower and regions of increased vorticity are much more evident. However, the length of the bubble and spike features are approximately the same, illustrating the relatively insensitive nature of the mixing length to the spatial mesh.

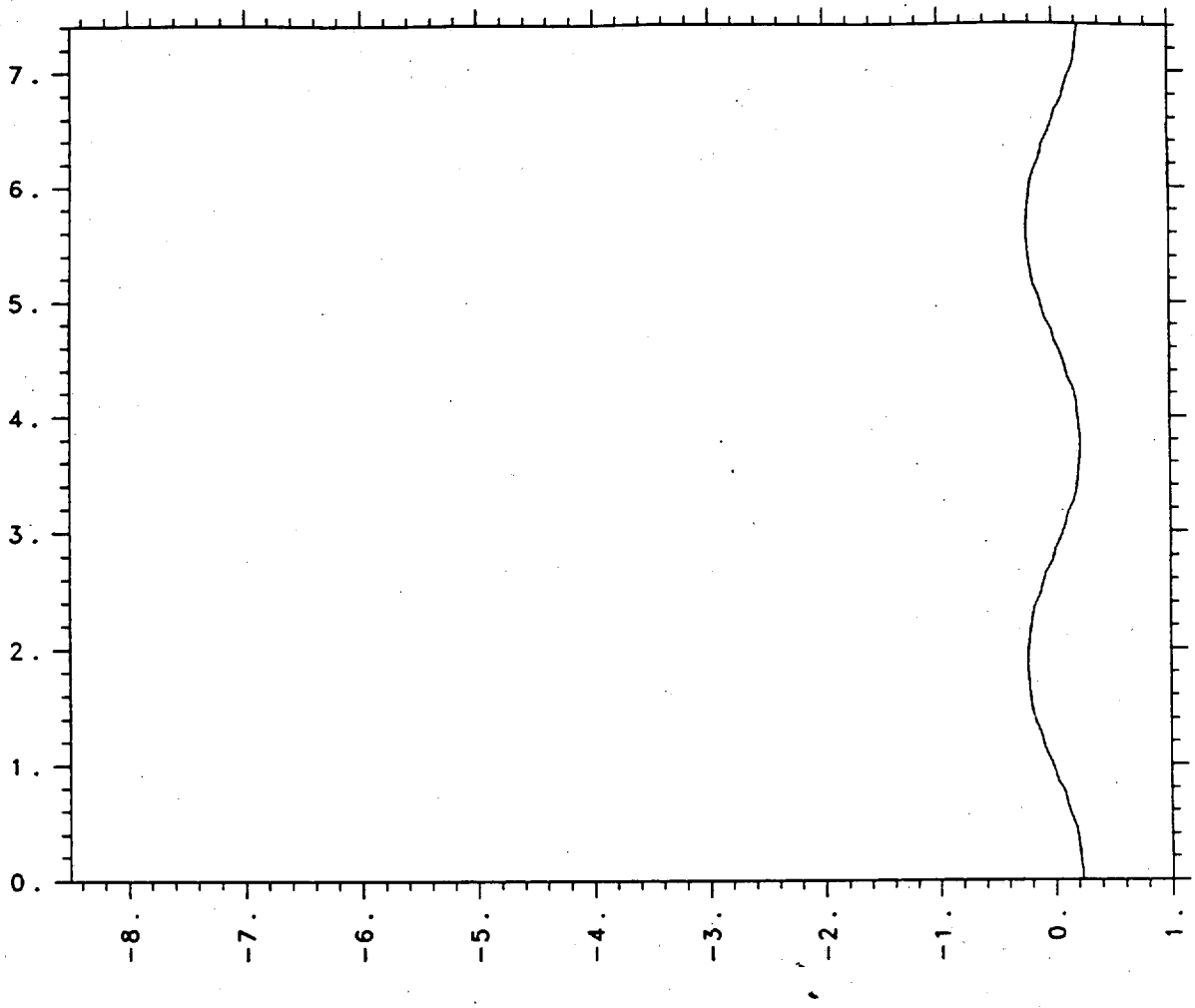

00000 bnd
0. BOX/ID: box c55 MTV wehner REGION: all 11:00:13 11/28/89 g

He-Air Test Problem
Single Wavelength Perturbation

T = 0.0

1 mm square zones

Axis label units are centimeters

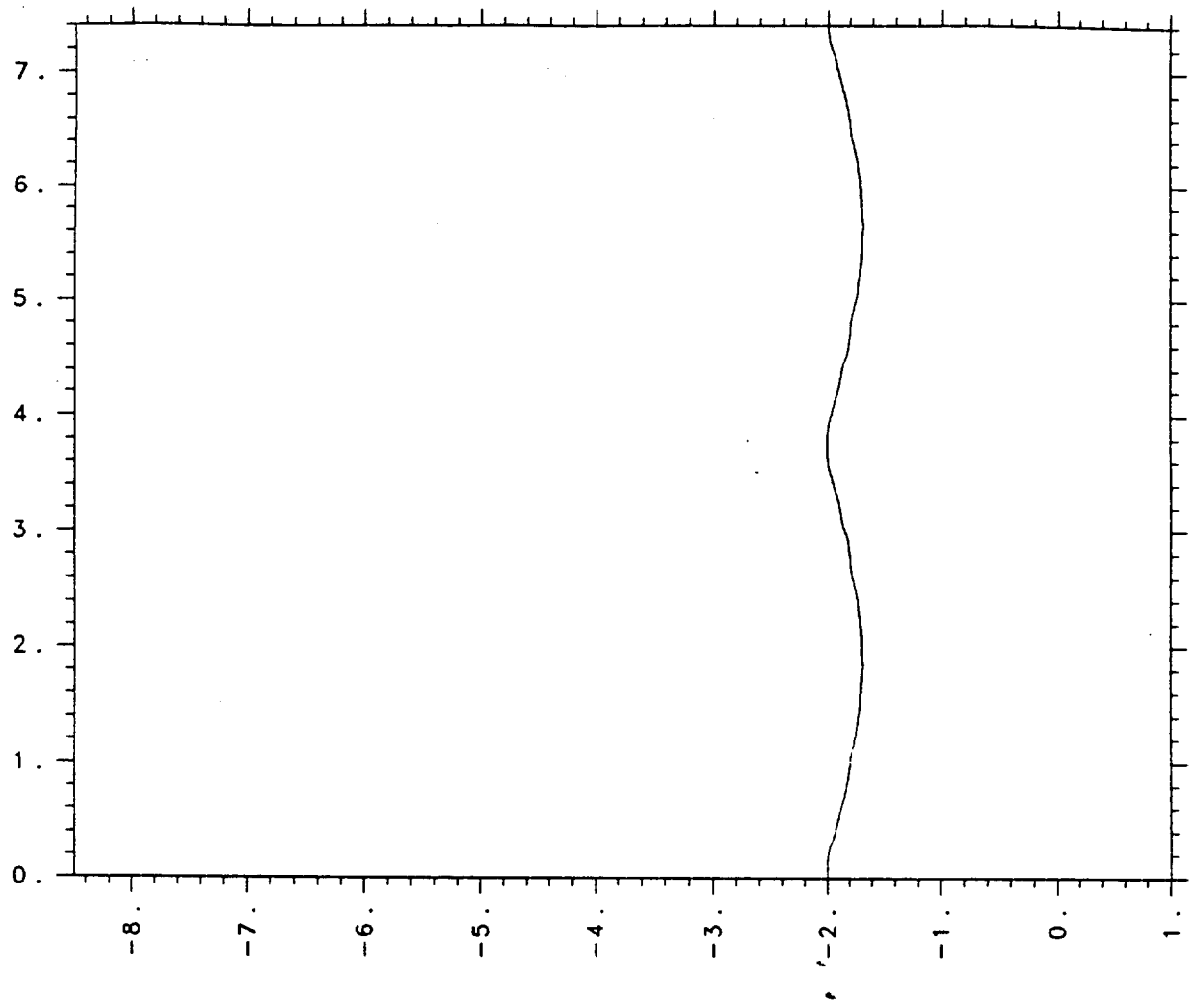

00352 bnd
1.2015e+02 BOX/ID: box c55 MTV wehner REGION: all 11:00:22 11/28/89 g

He-Air Test Problem
Single Wavelength Perturbation

T = 0.12 milliseconds

1 mm square zones

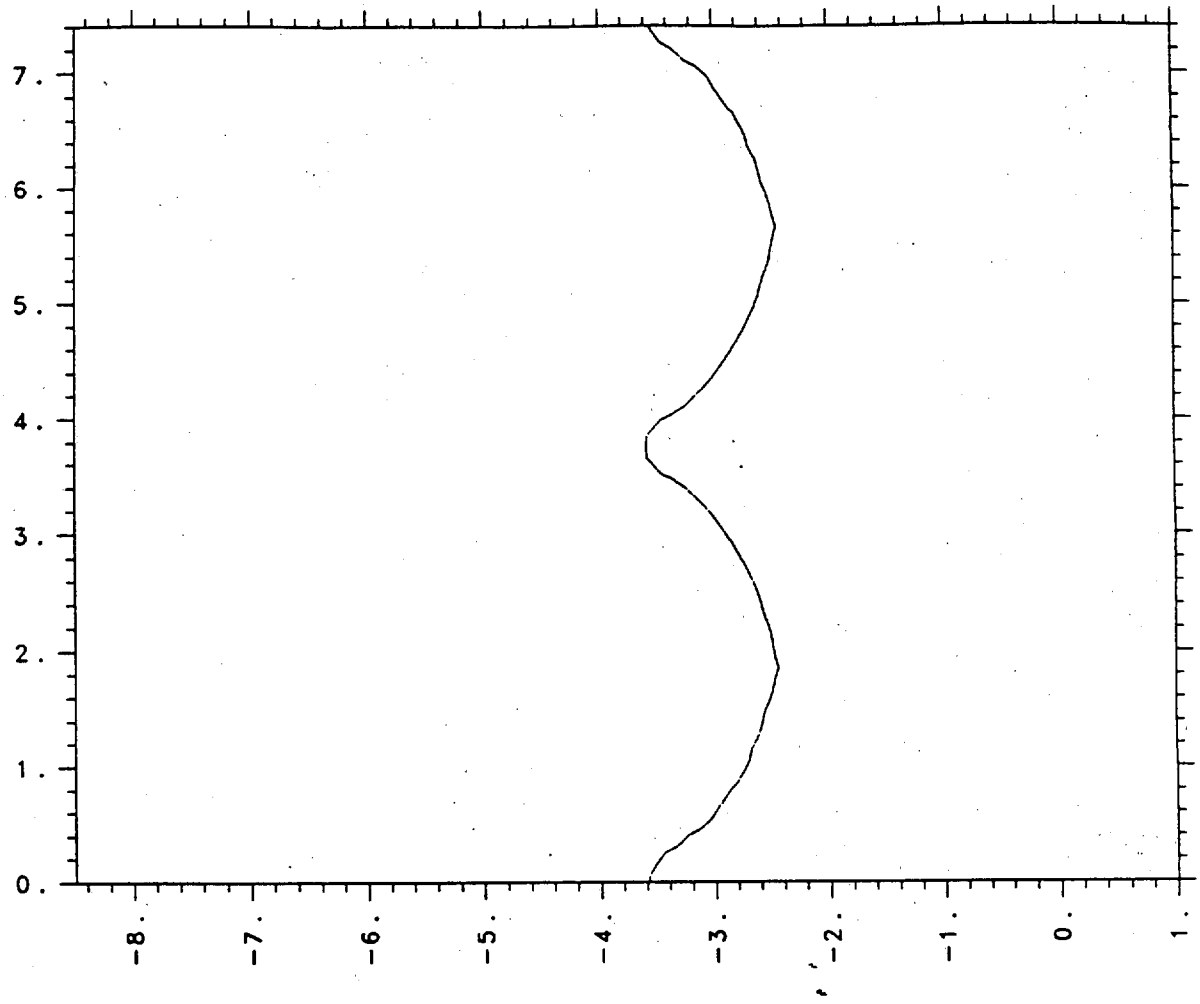

00620 bnd
2.2006e+02 BOX/ID: box c55 MTV wehner REGION: all 11:00:29 11/28/89 9

He-Air Test Problem
Single Wavelength Perturbation

T = 0.22 milliseconds

1 mm square zones

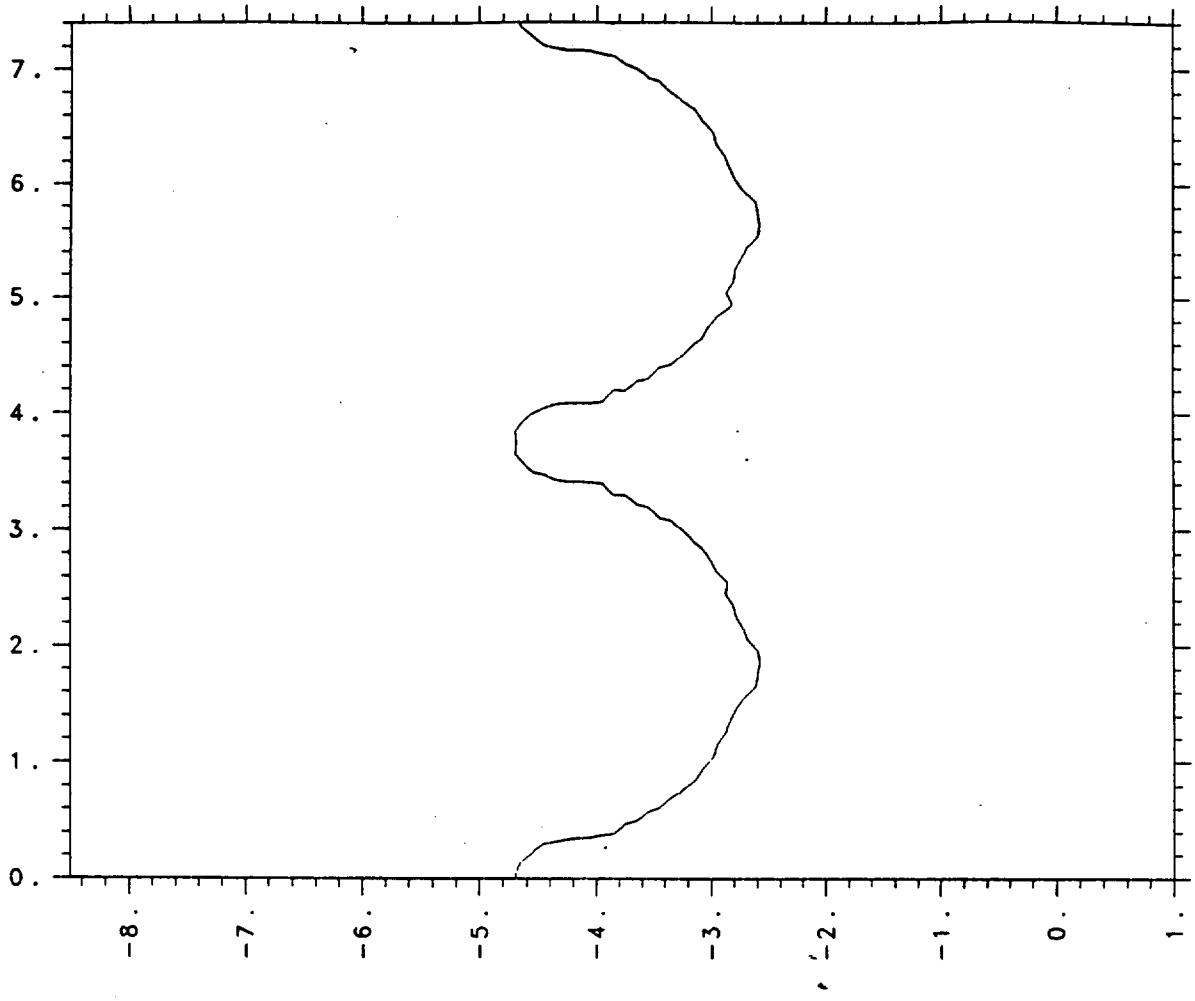

00892 bnd
3.2014e+02 BOX/ID: box c55 MTV wehner REGION: all 11:00:38 11/28/89 g

He-Air Test Problem
Single Wavelength Perturbation

T = 0.32 milliseconds

1 mm square zones

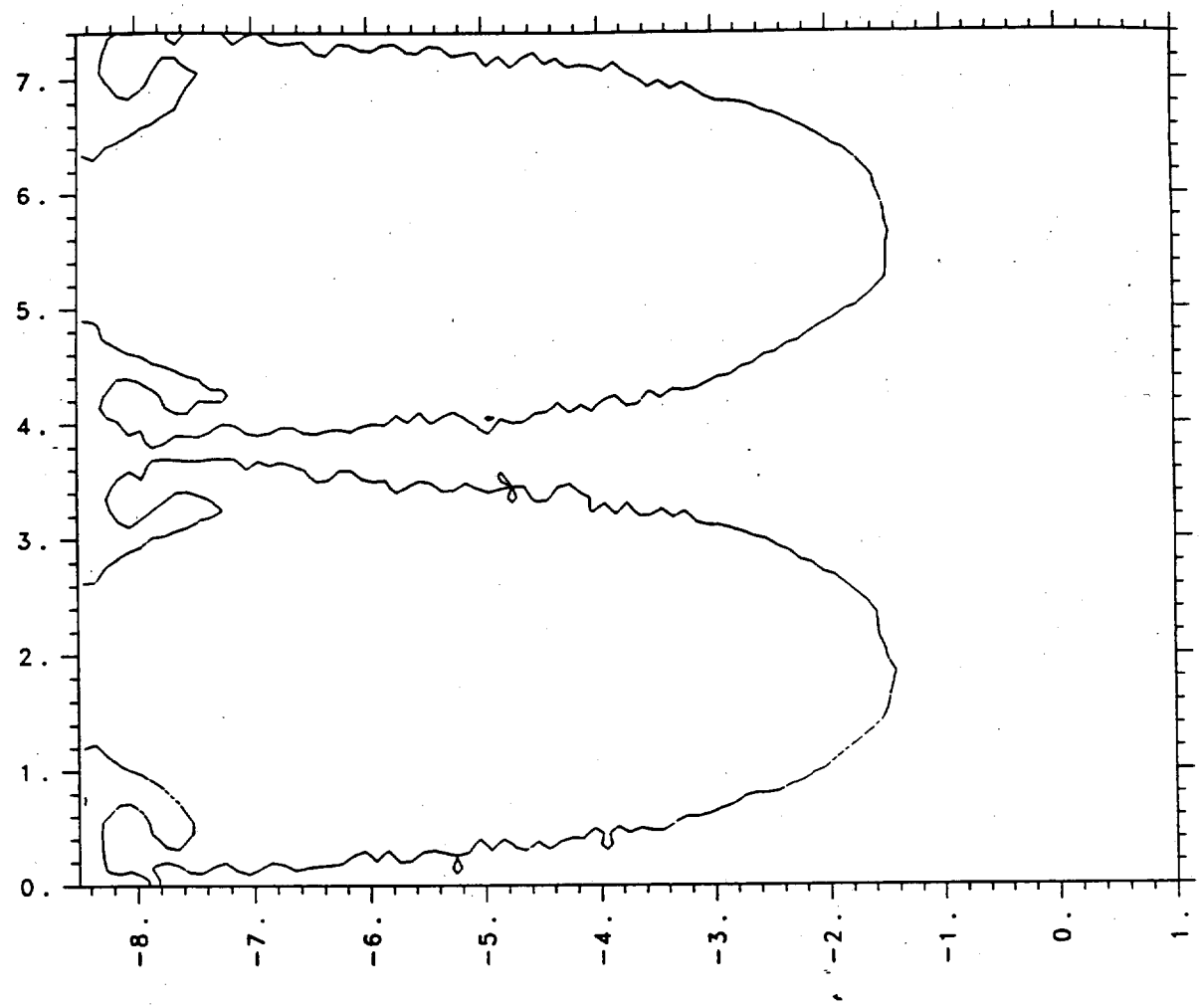

02814 bnd
1.0000e+03 BOX/ID: box c55 MTV wehner REGION: all 11:00:47 11/28/89 9

He-Air Test Problem
Single Wavelength Perturbation

T = 1.0 milliseconds

1 mm square zones

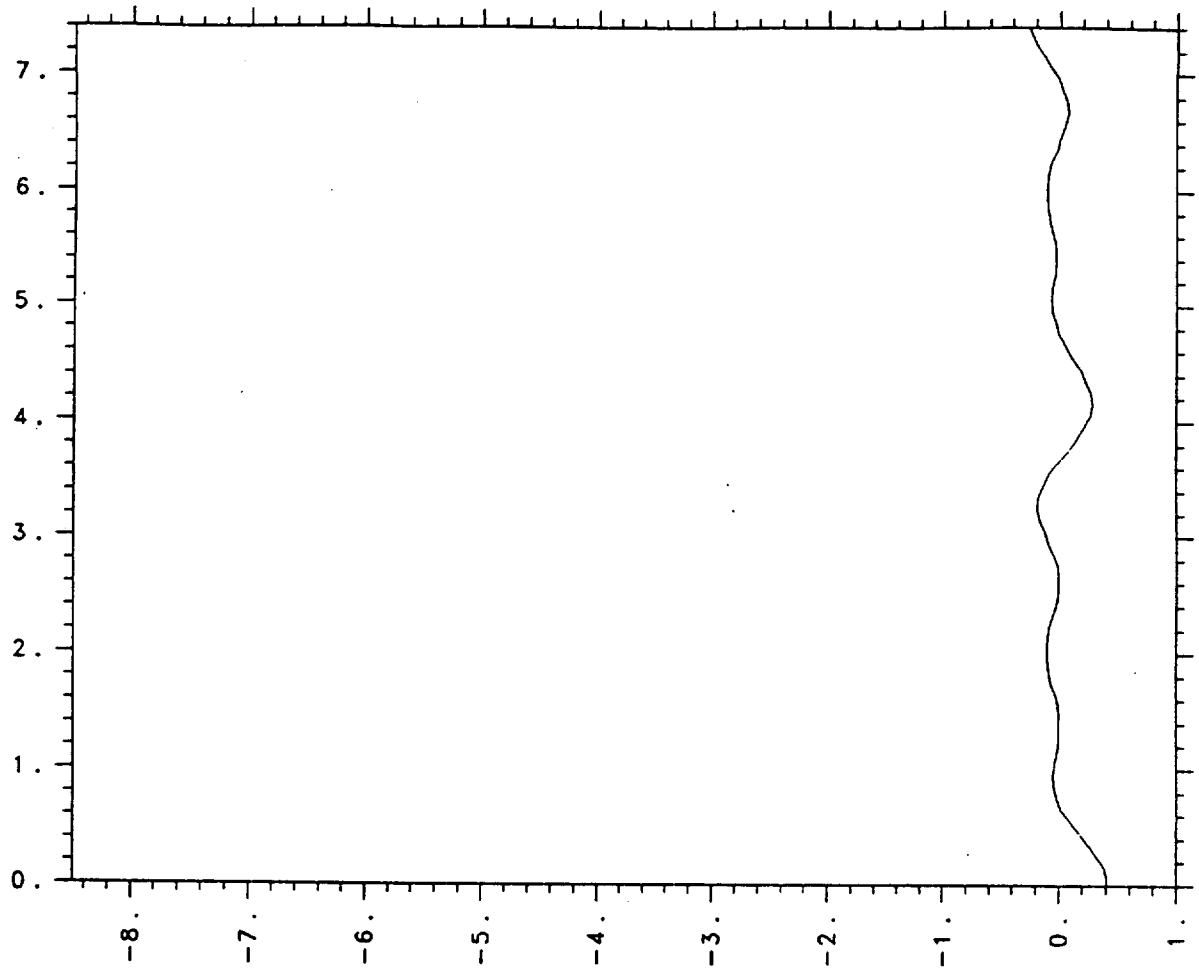

00000
0.

bnd

BOX/ID: box c55 MTV wehner REGION: all 10:55:17 11/28/89 g

He-Air Test Problem
Multiple Wavelength Perturbation

T = 0.0

1 mm square zones

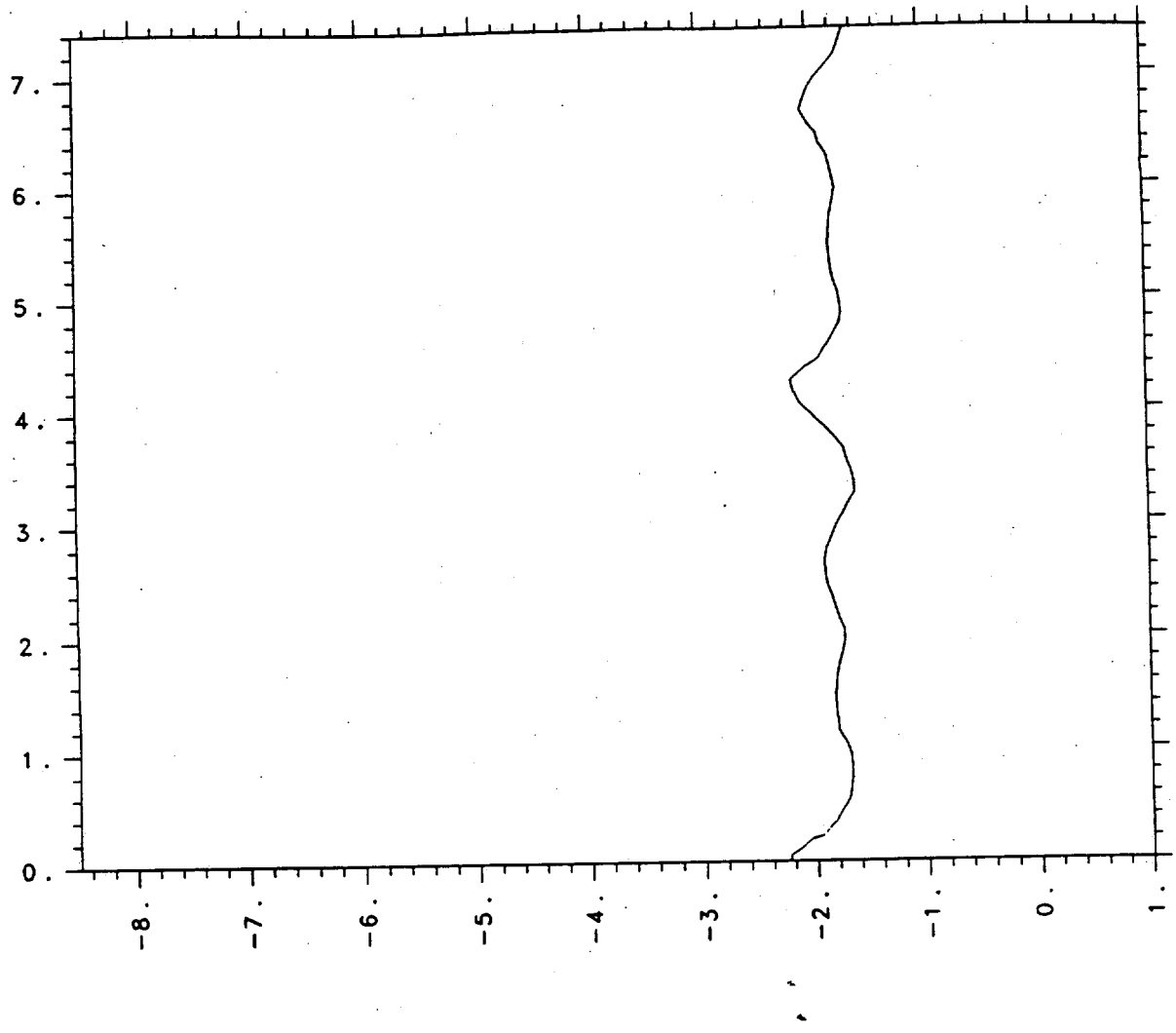

00352 bnd
1.2016e+02 BOX/ID: box c55 MTV wehner REGION: all 10:55:23 11/28/89 9

He-Air Test Problem
Multiple Wavelength Perturbation

T = 0.12 milliseconds

1 mm square zones

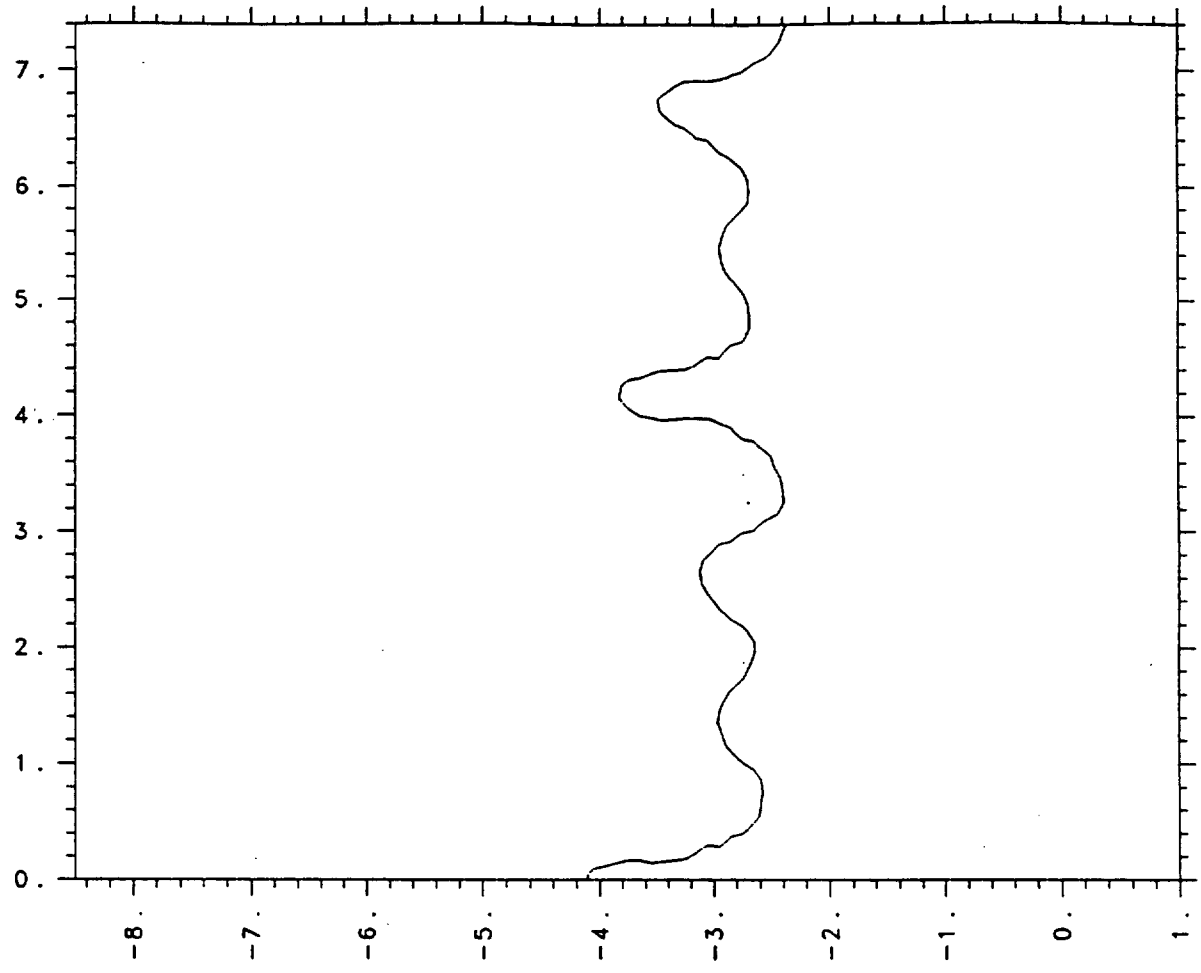

00620 bnd
2.2019e+02 BOX/ID: box c55 MTV wehner REGION: all 10:55:31 11/28/89 g

He-Air Test Problem
Multiple Wavelength Perturbation

T = 0.22 milliseconds

1 mm square zones

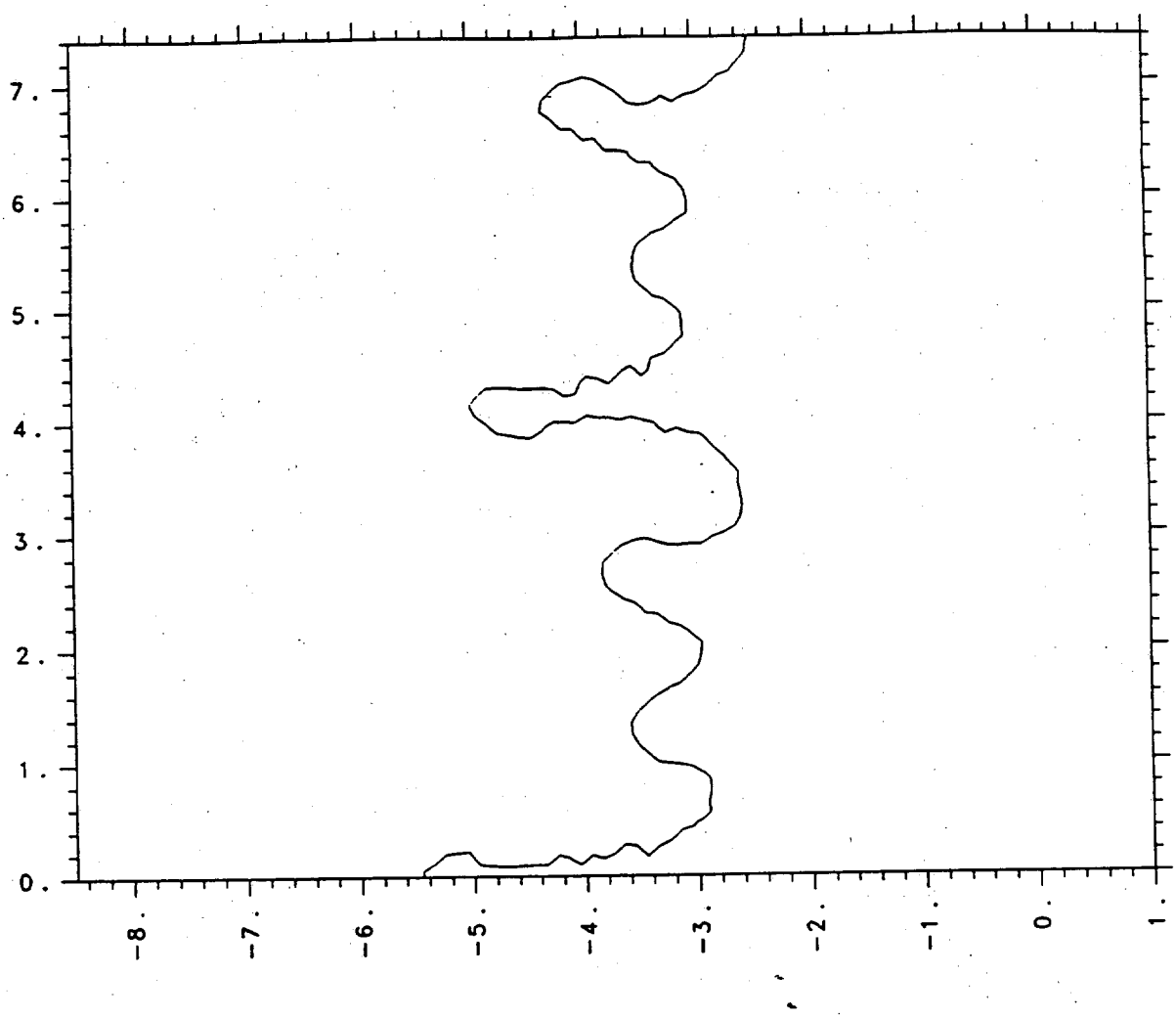

00893 bnd
3.2007e+02 BOX/ID: box c55 MTV wehner REGION: all 10:55:41 11/28/89 0

He-Air Test Problem
Multiple Wavelength Perturbation

T = 0.32 milliseconds

1 mm square zones

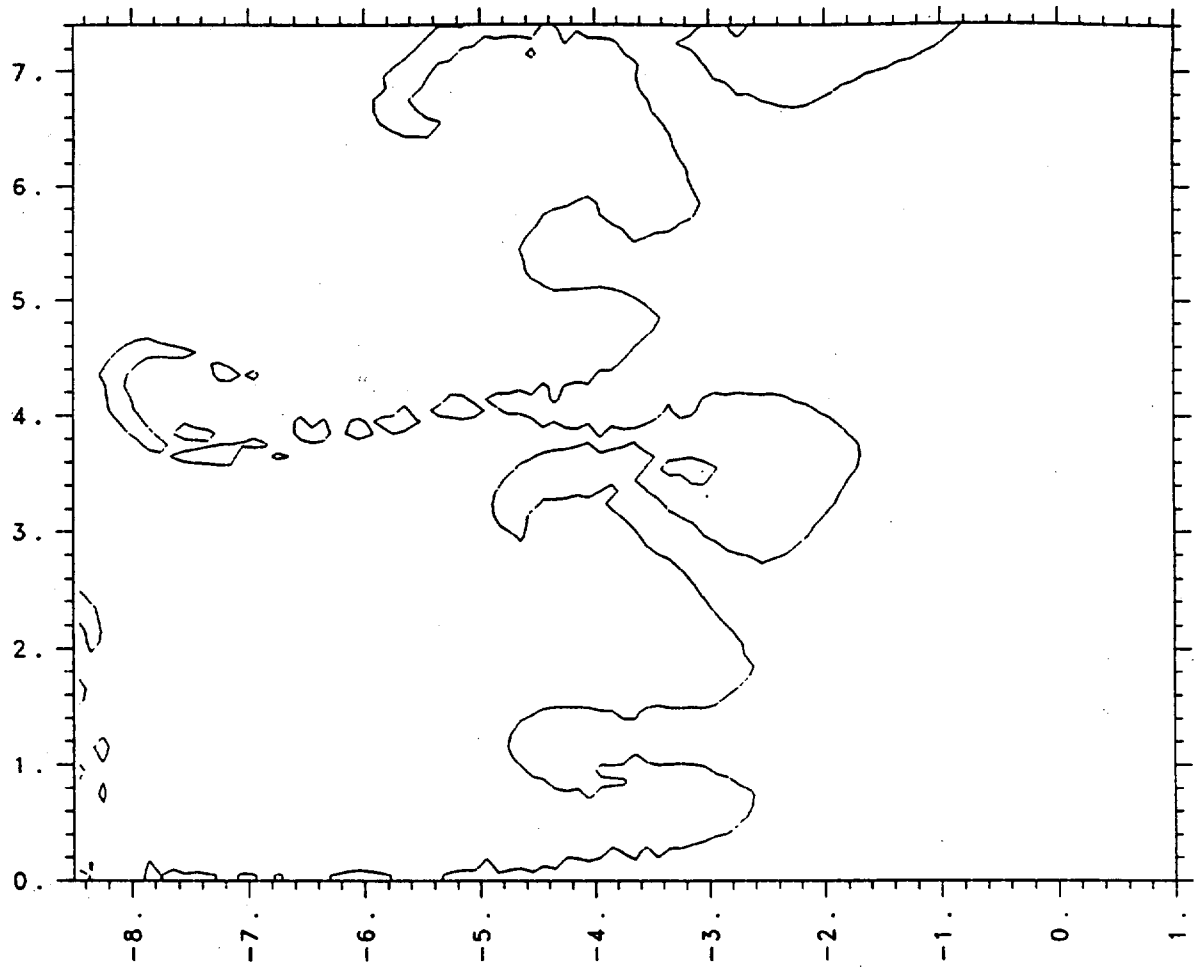

02649 bnd
9.3916e+02 BOX/ID: box c55 MTV wehner REGION: all 10:55:51 11/28/89 g

He-Air Test Problem
Multiple Wavelength Perturbation

T = 0.94 milliseconds

1 mm square zones

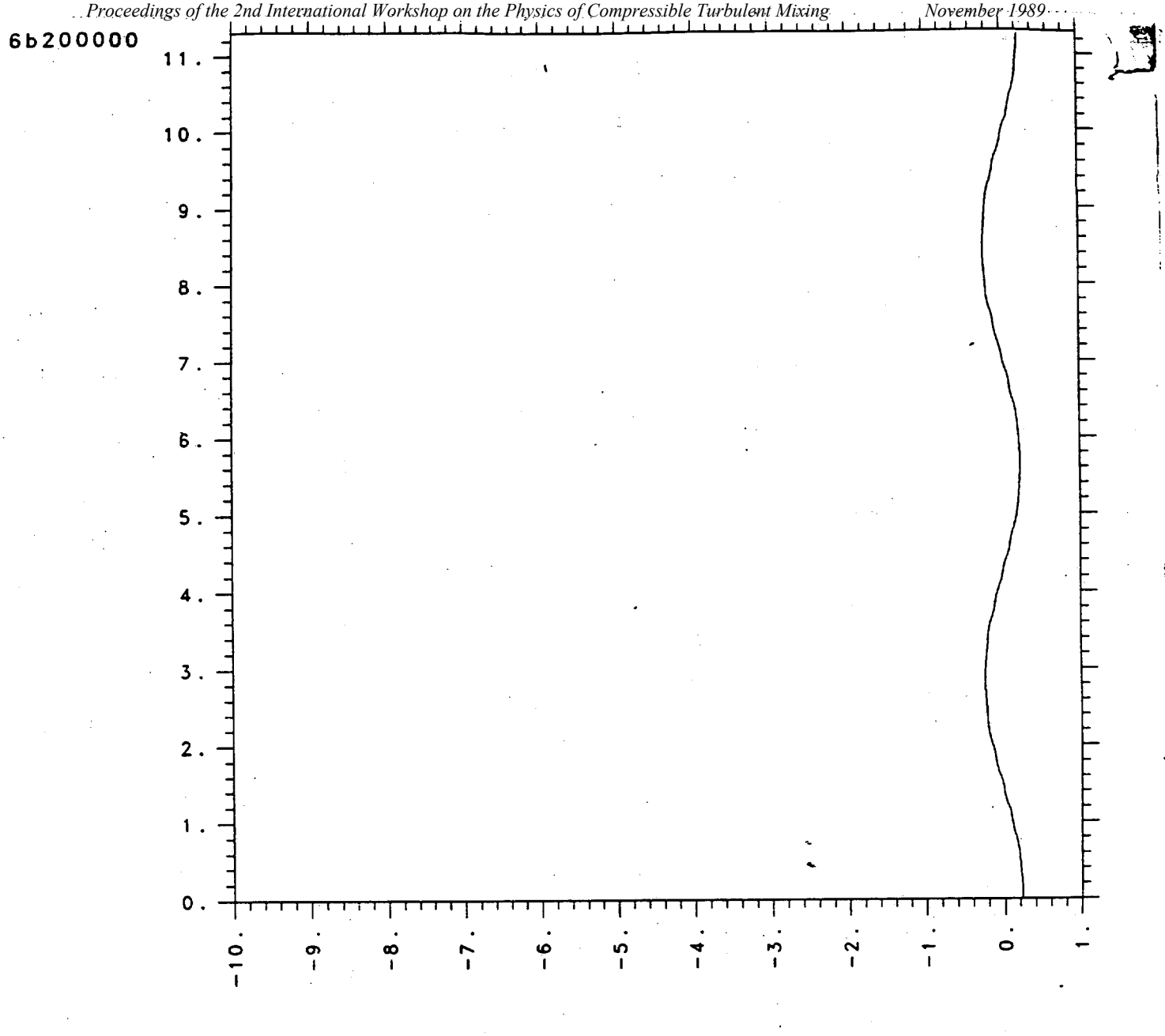

SF_6-Air Test Problem
Single Wavelength Perturbation

T = 0.0

1 mm square zones

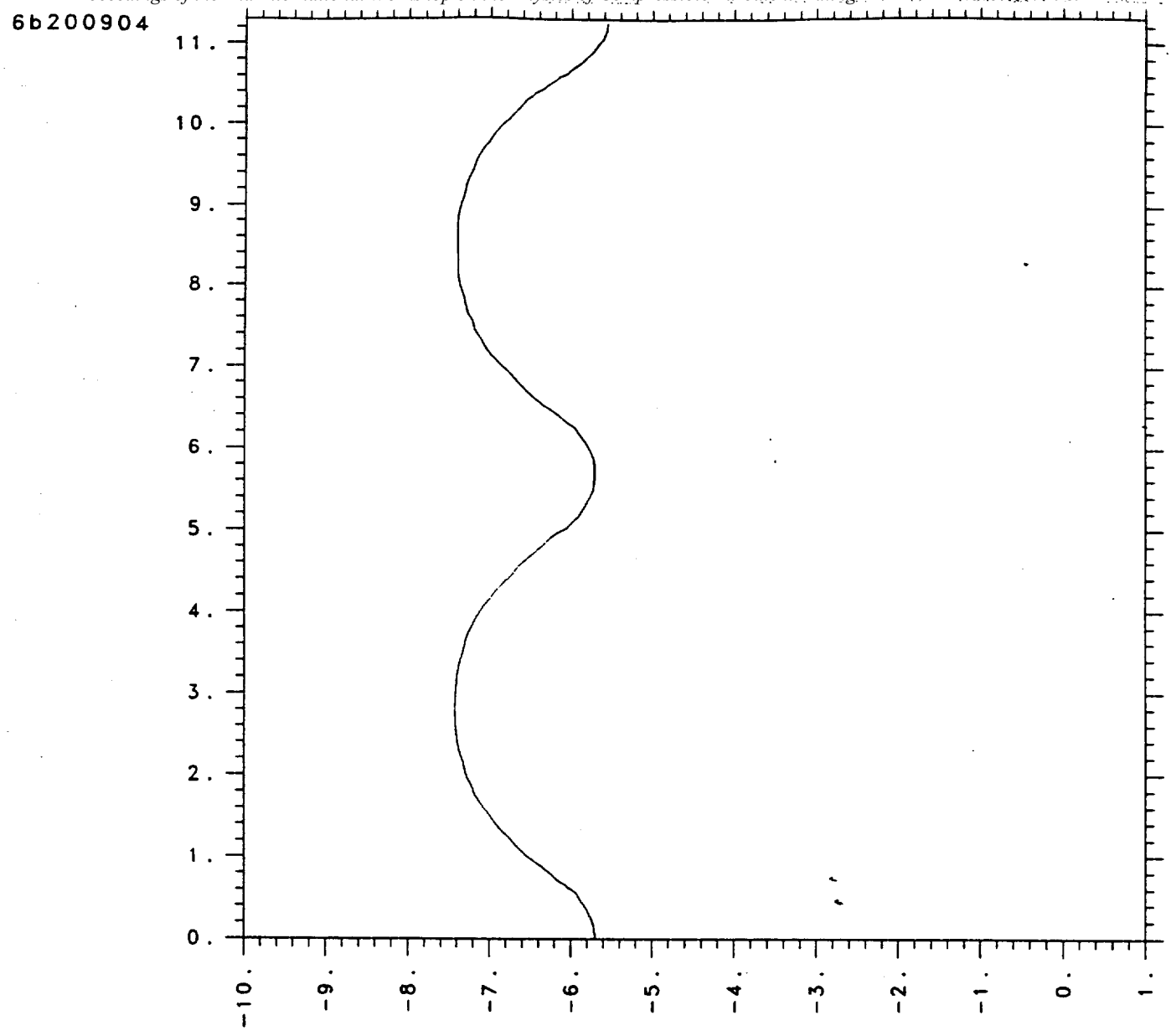

SF_6-Air Test Problem
Single Wavelength Perturbation

T = 0.7 milliseconds

1 mm square zones

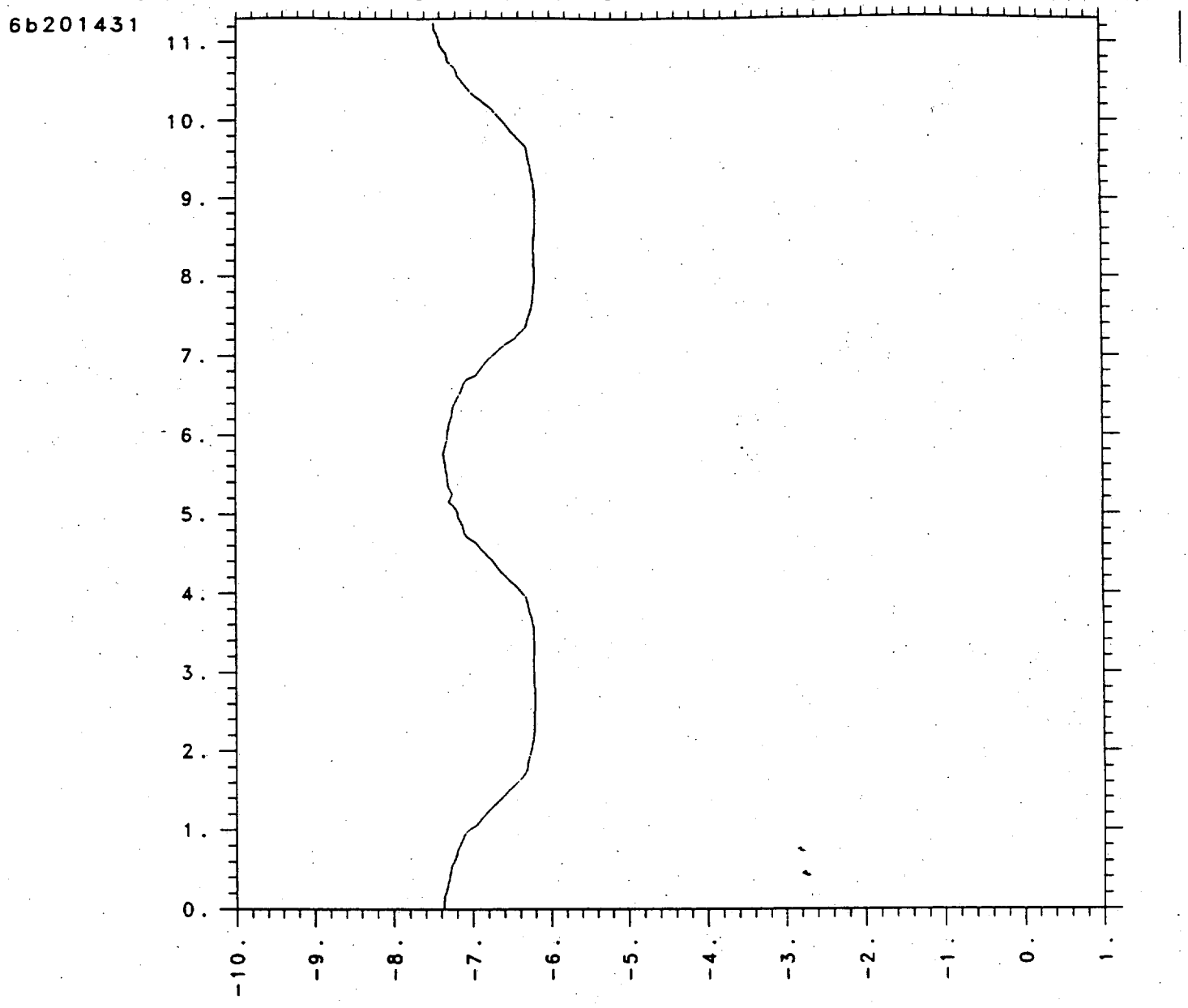

SF_6-Air Test Problem
Single Wavelength Perturbation

T = 1.1 milliseconds

1 mm square zones

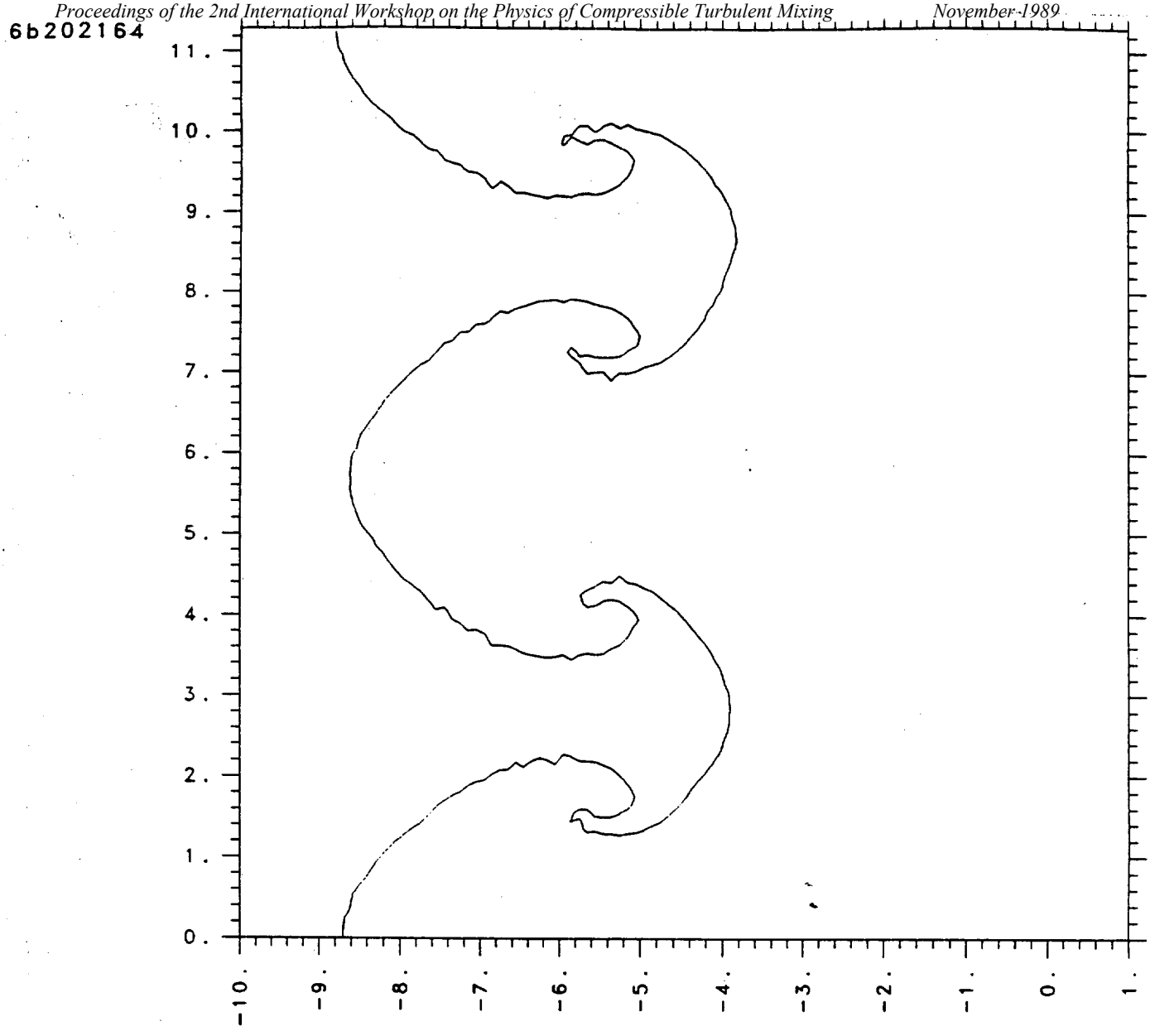

SF_6-Air Test Problem
Single Wavelength Perturbation

T = 1.65 milliseconds

1 mm square zones

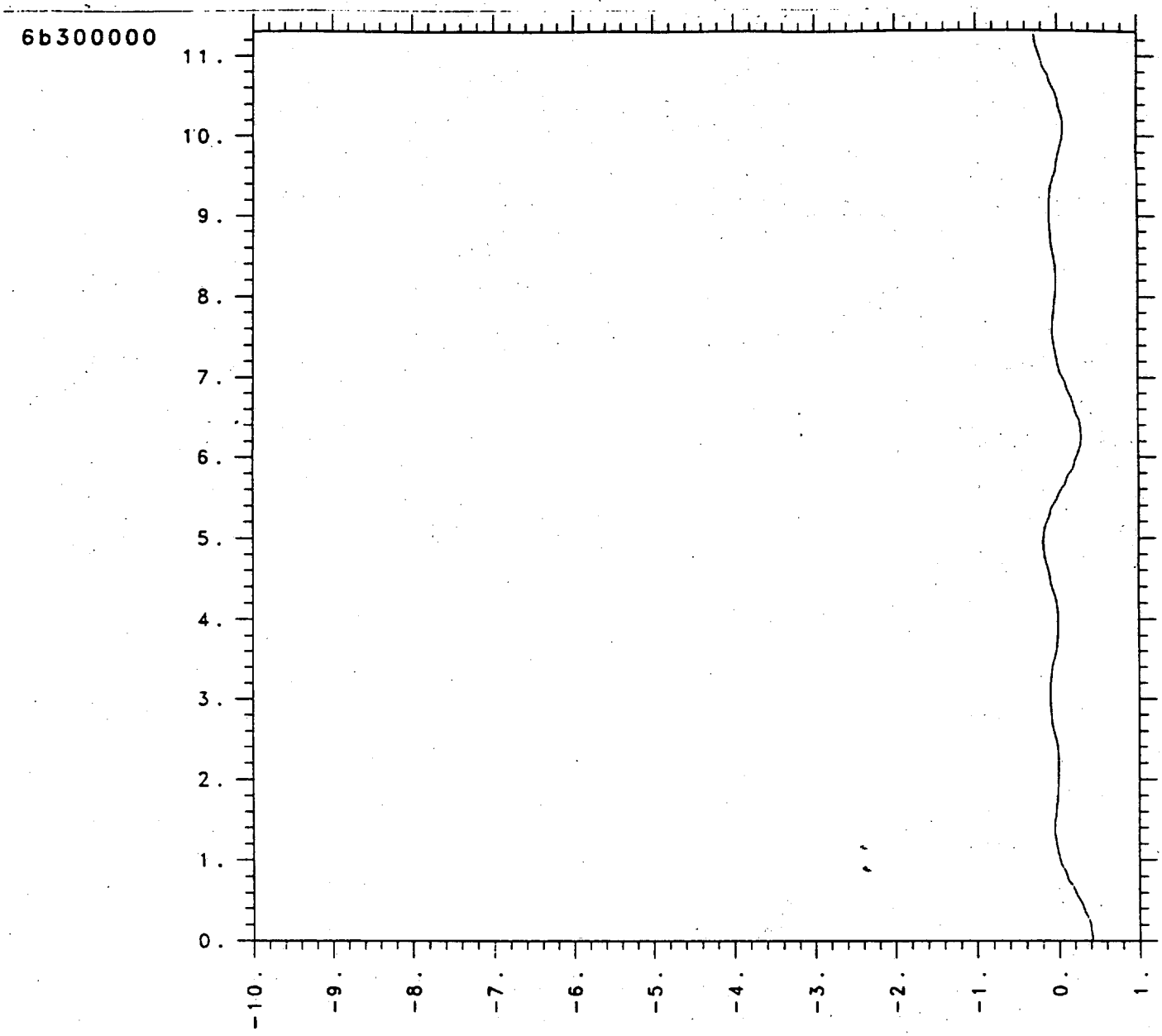

SF_6-Air Test Problem
Multiple Wavelength Perturbation

T = 0.0

1 mm square zones

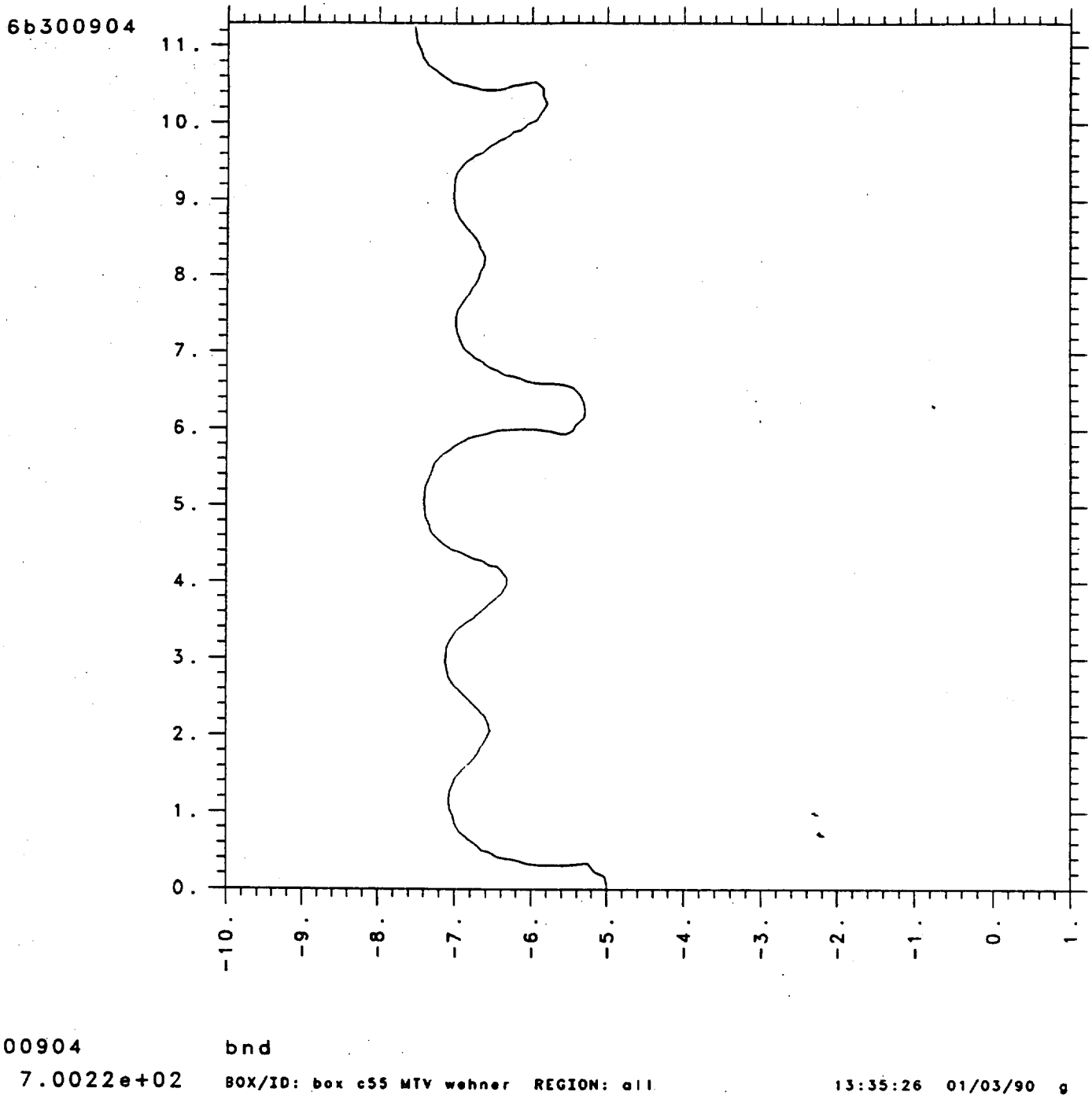

SF_6-Air Test Problem
Multiple Wavelength Perturbation

T = 0.70 milliseconds

1 mm square zones

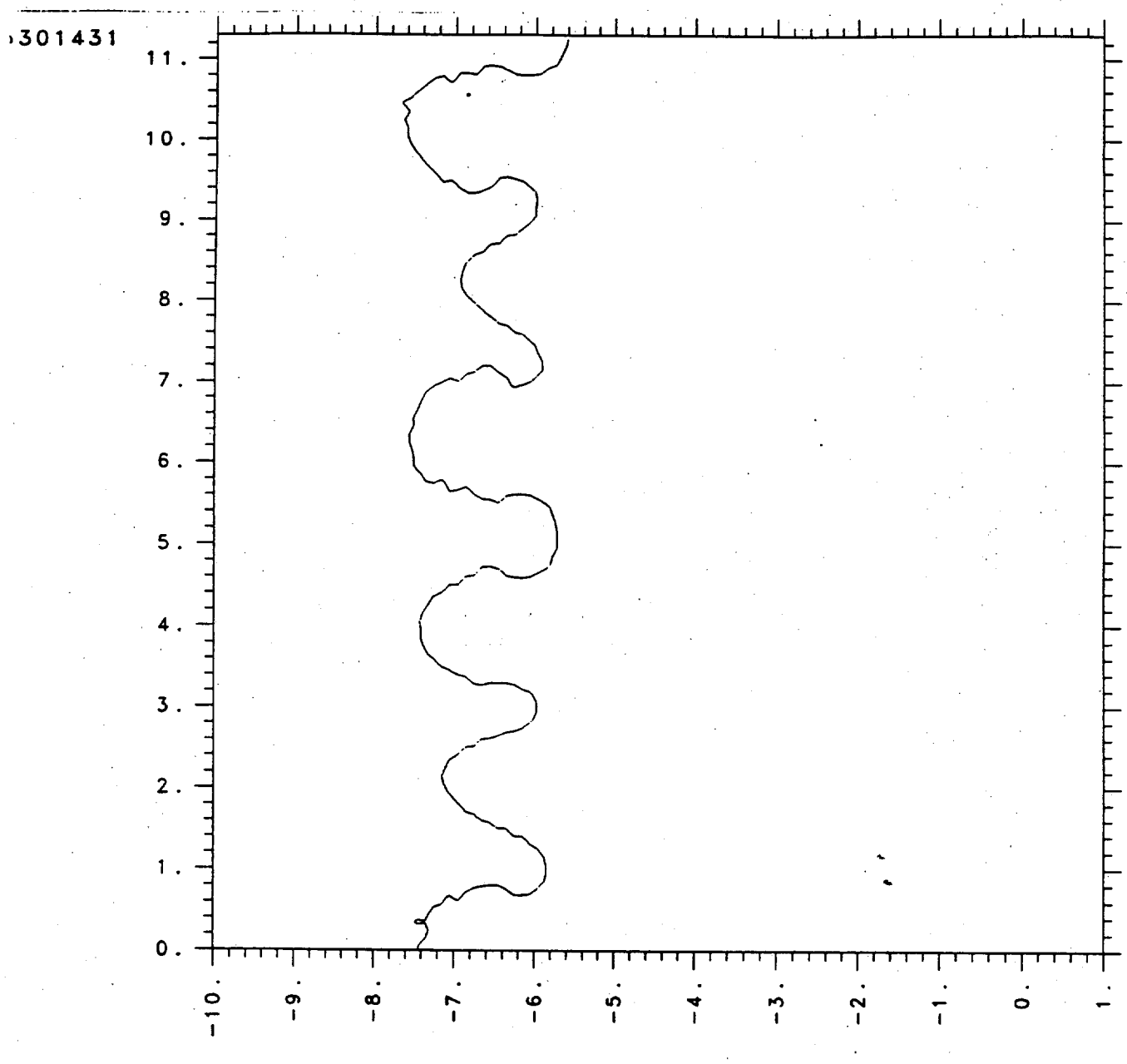

SF_6-Air Test Problem
Multiple Wavelength Perturbation

T = 1.10 milliseconds

1 mm square zones

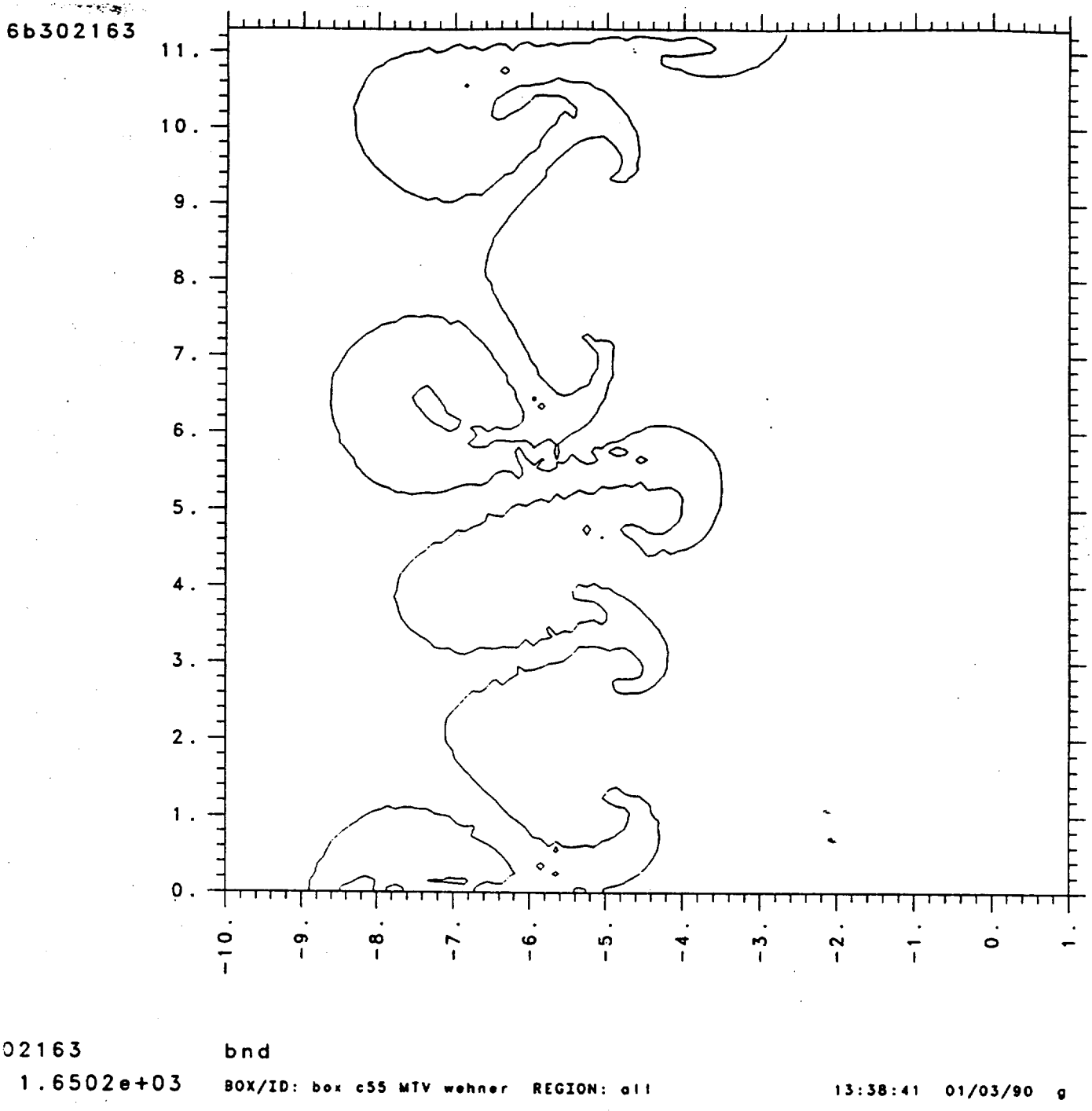

SF_6-Air Test Problem
Multiple Wavelength Perturbation

T = 1.65 milliseconds

1 mm square zones

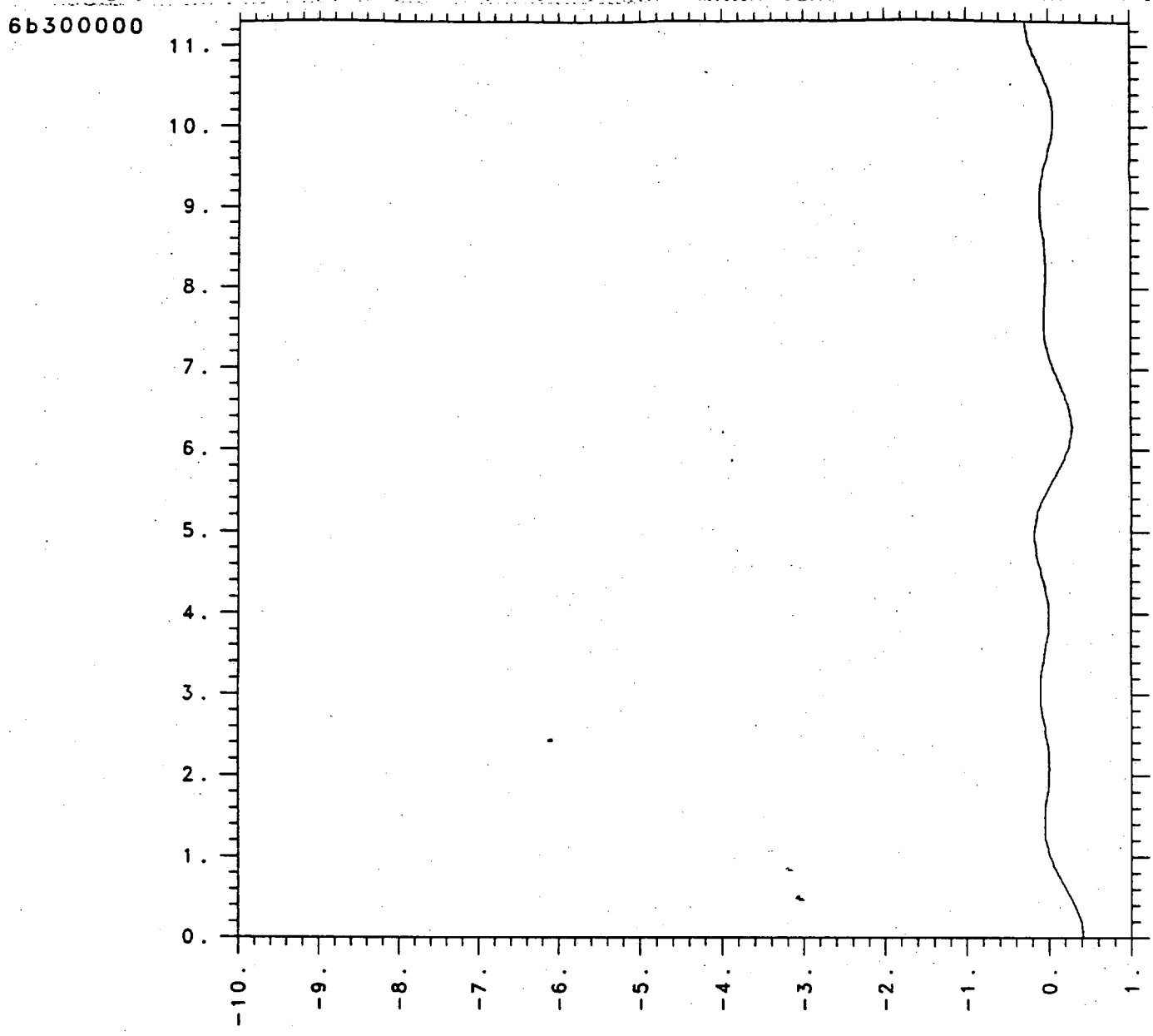

SF_6-Air Test Problem
Multiple Wavelength Perturbation

T = 0.0

1/2 mm square zones

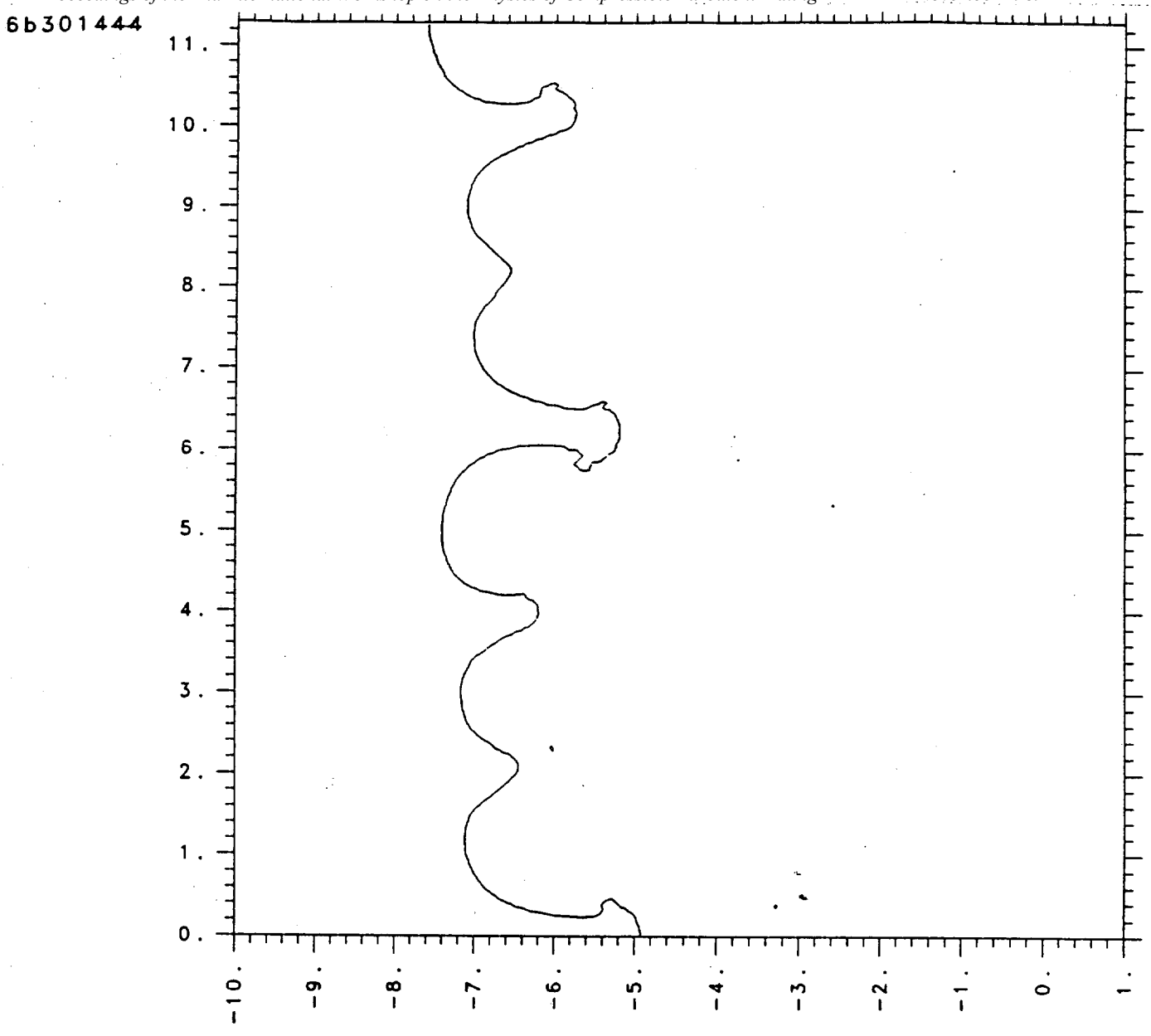

SF_6-Air Test Problem
Multiple Wavelength Perturbation

T = 0.70 milliseconds

1/2 mm zones

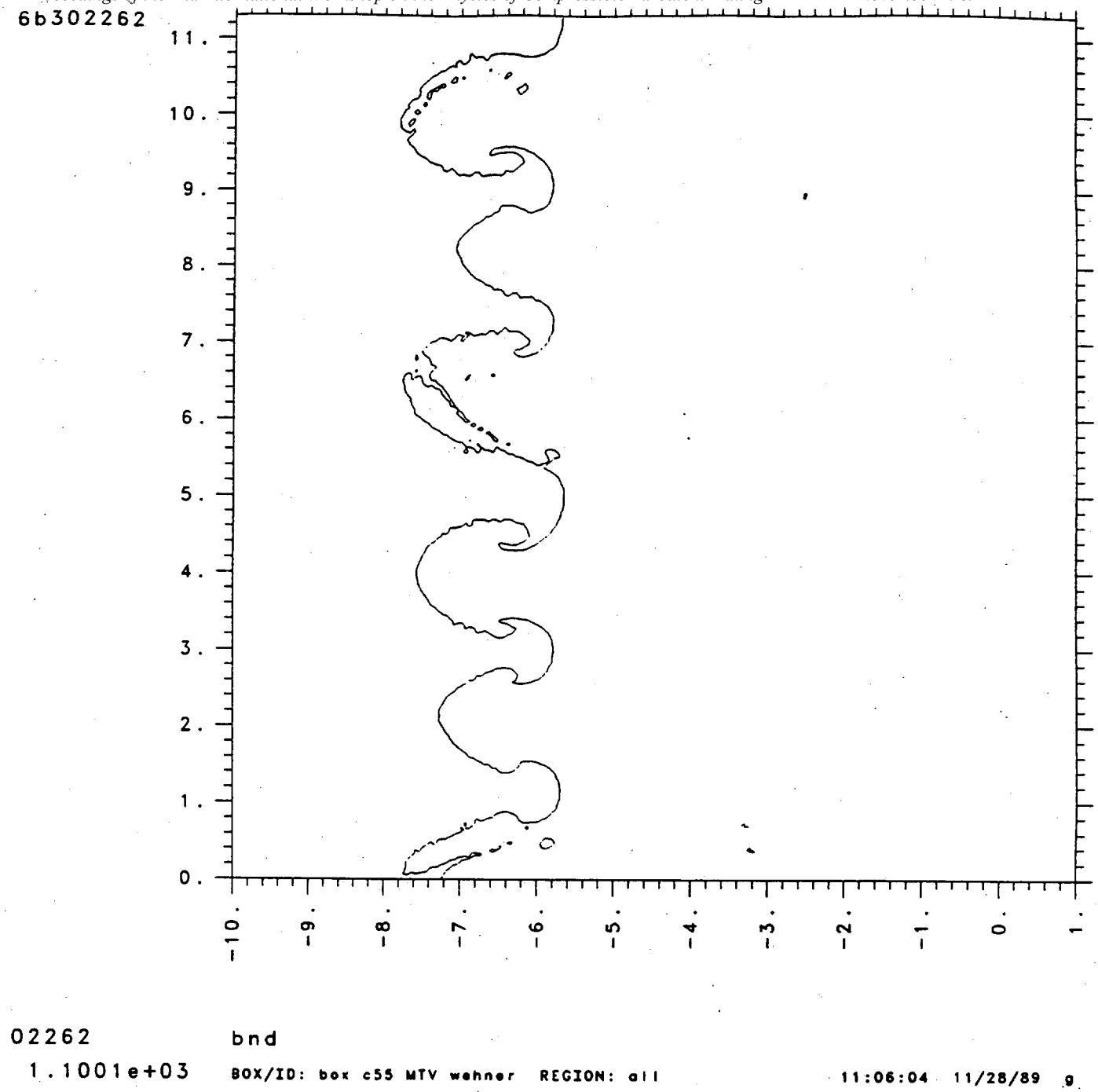

SF_6-Air Test Problem
Multiple Wavelength Perturbation

T = 1.10 milliseconds

1/2 mm square zones

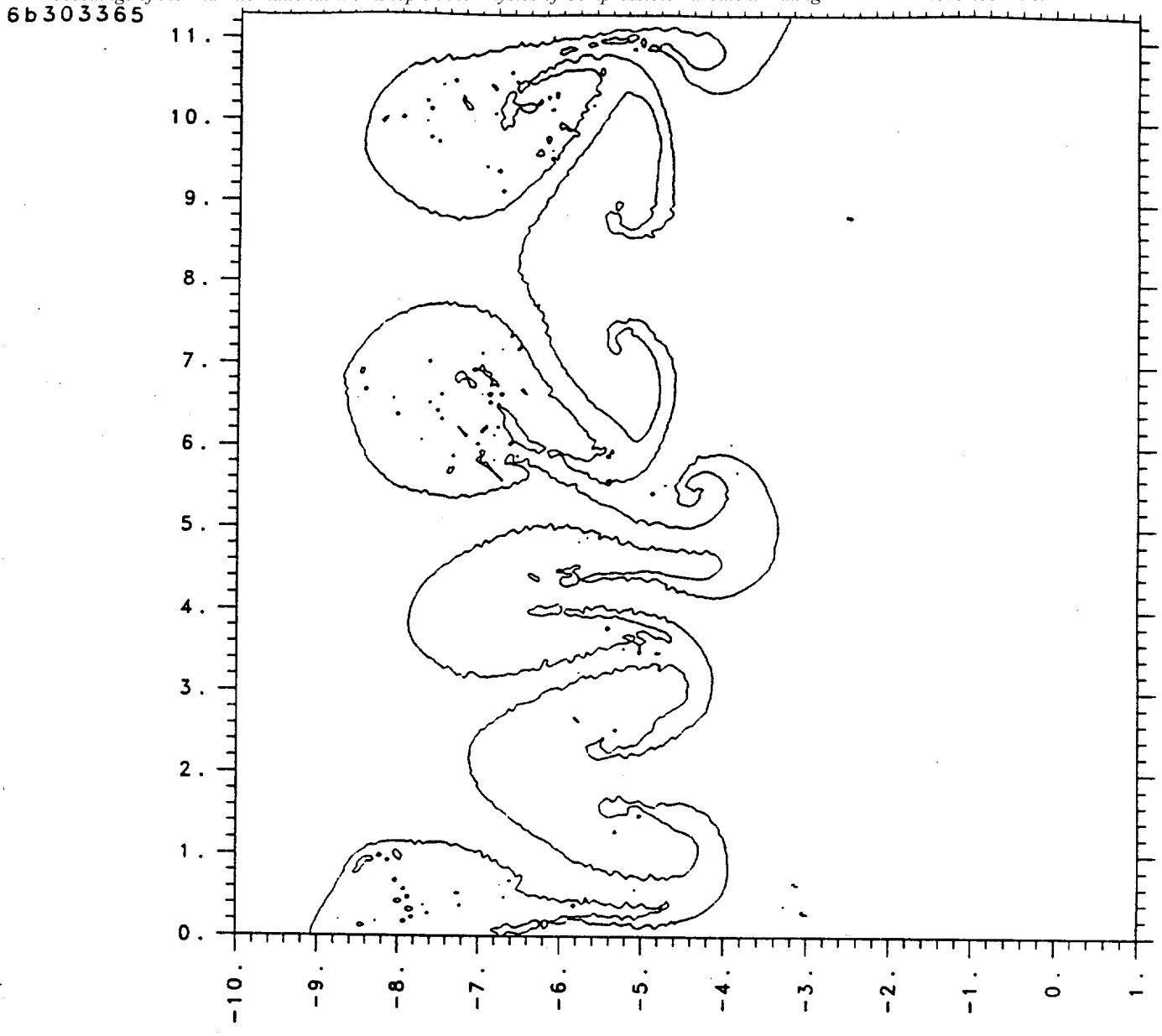

SF_6-Air Test Problem
Multiple Wavelength Perturbations

T = 1.65 milliseconds

1/2 mm square zoning

Notice that the improvement in resolution has produced much narrower spikes.

SHOCK INDUCED DIPOLAR VORTEX STRUCTURE AND COMPRESSIBLE TURBULENCE

by

Xiaolong Yang , Norman J. Zabusky

Rutgers, The State University of New Jersey
Department of Mechanical & Aerospace Engineering
New Brunswick, New Jersey

and

I - L Chern
Argonne National Laboratory and University of Chicago

I. Introduction

1. Single interface problem

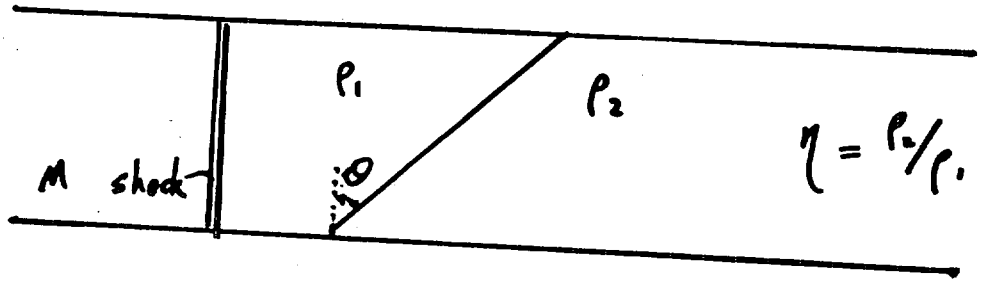

2. Double interfaces (or slab) problem

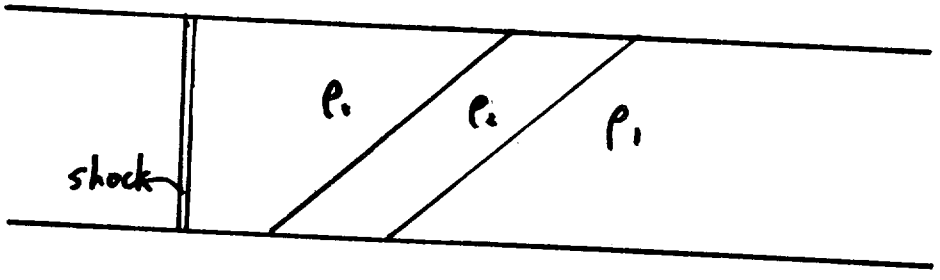

II. Experimental Work

Haas and Sturtevant (1984)

III Direct Numerical Simulation

1. The Numerical Model

2. Objectives:

- Juxtaposition of DNS and Shadowgraphes
- Vorticity deposition and evolution analysis
- Observation and Quantification

Overview

M	angle θ	interface(s)	expeiment	simulation
1.2	30°	air/R22	✓	
1.2	30°	air/He	✓	✓
1.2	60°	air/R22	✓	✓
1.2	60°	air/He	✓	✓
1.05	30°	air/R22/air	✓	✓
1.05	30°	air/He/air	✓	✓
1.2	30°	air/He/air		✓
1.5	30°	air/He/air		✓

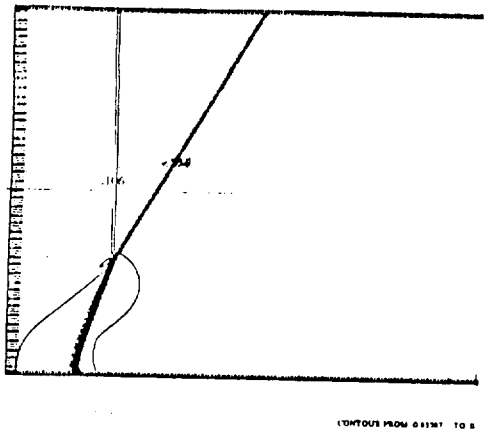

$M = 1.2$

Air / He

$\theta = 30°$

Density

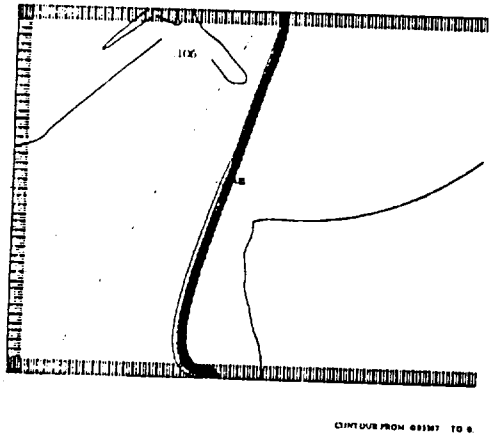

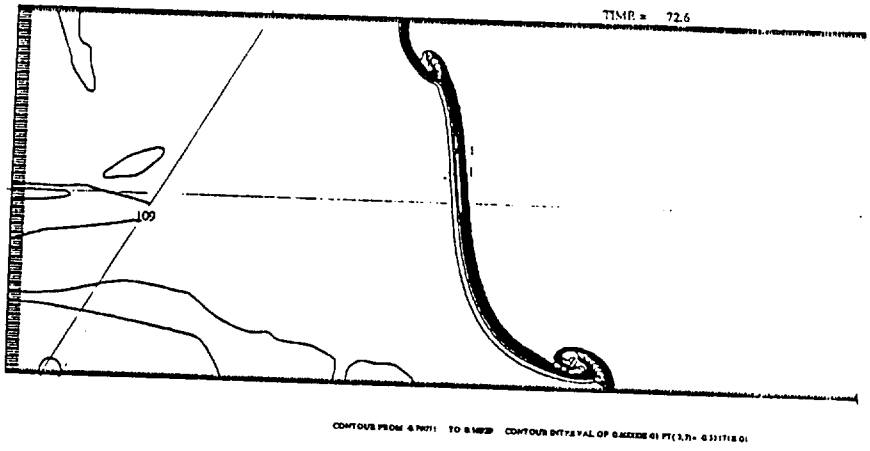

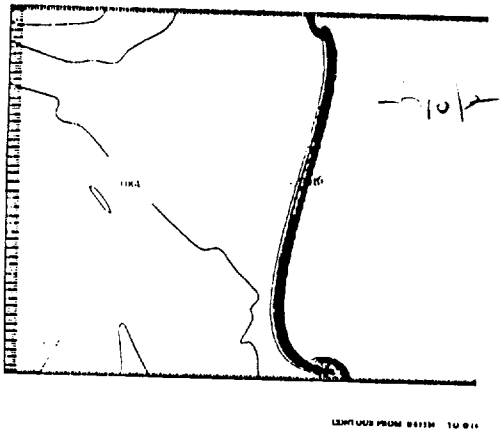

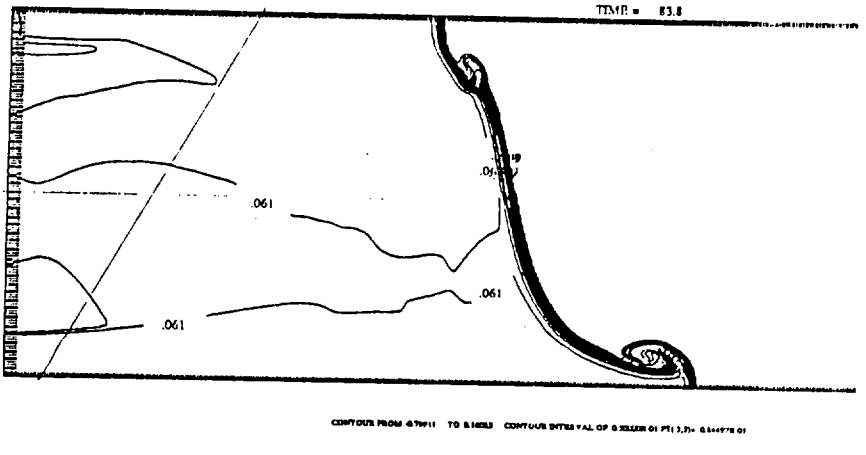

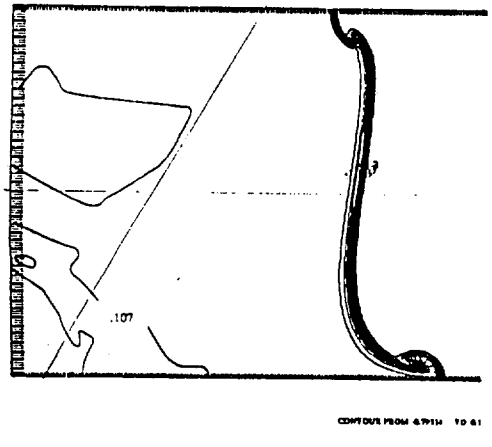

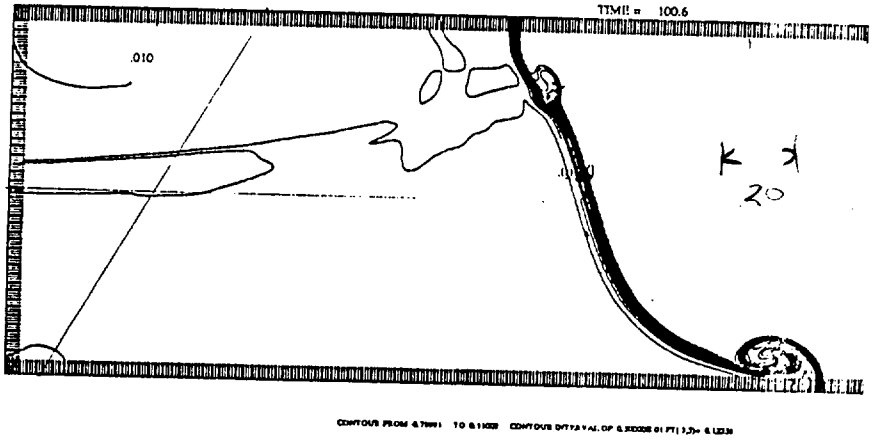

Air/R22 $M = 1.2$ $\theta = 60°$

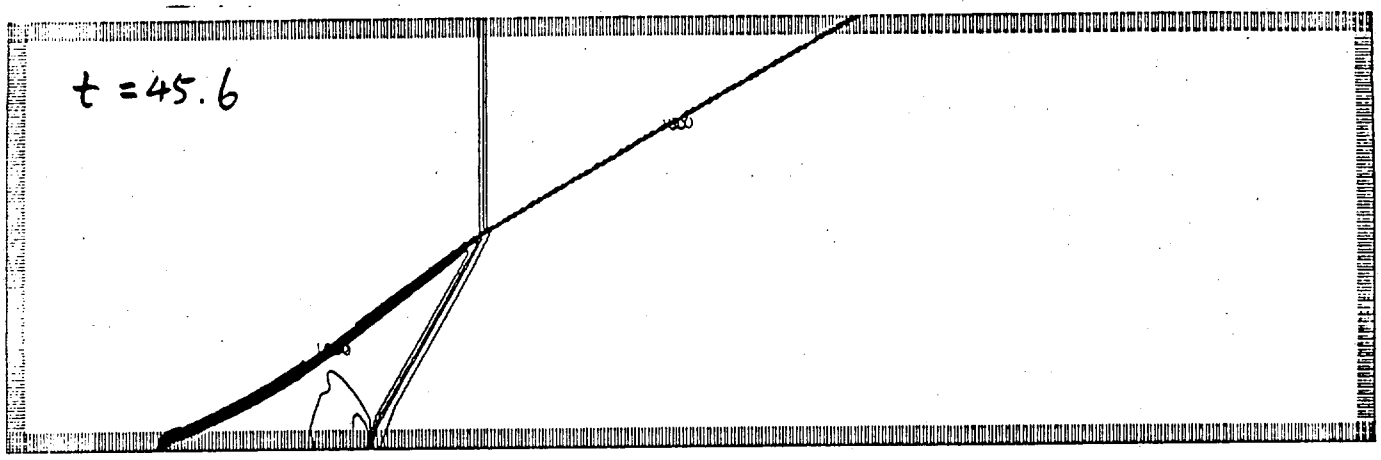

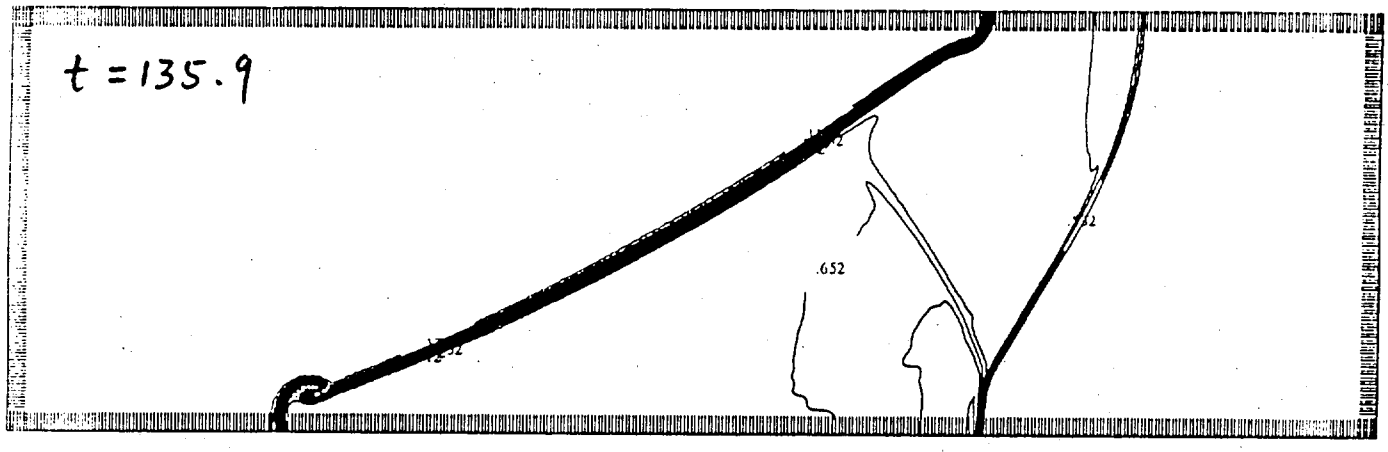

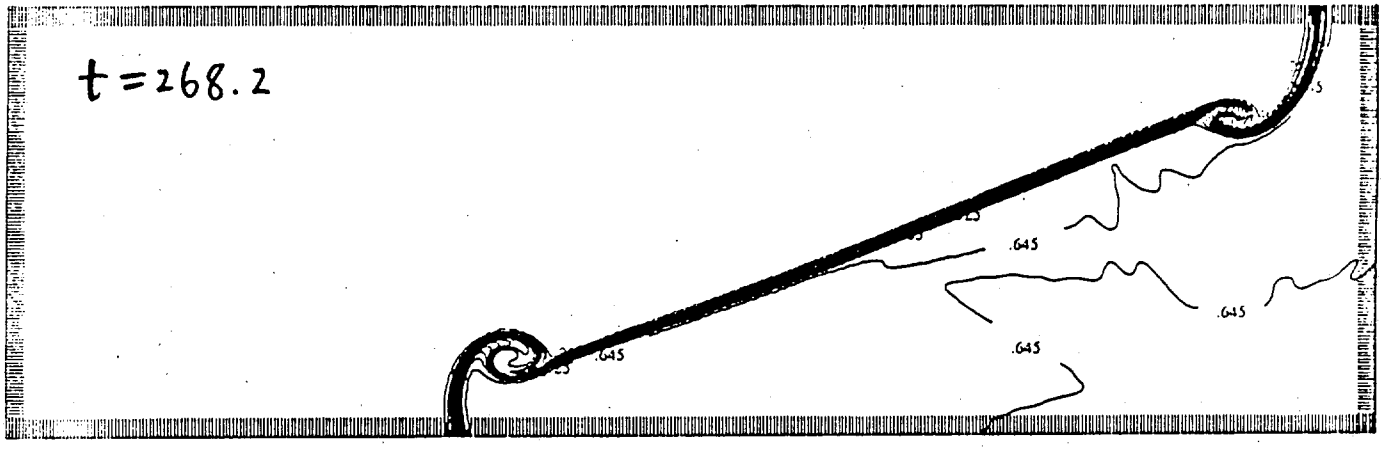

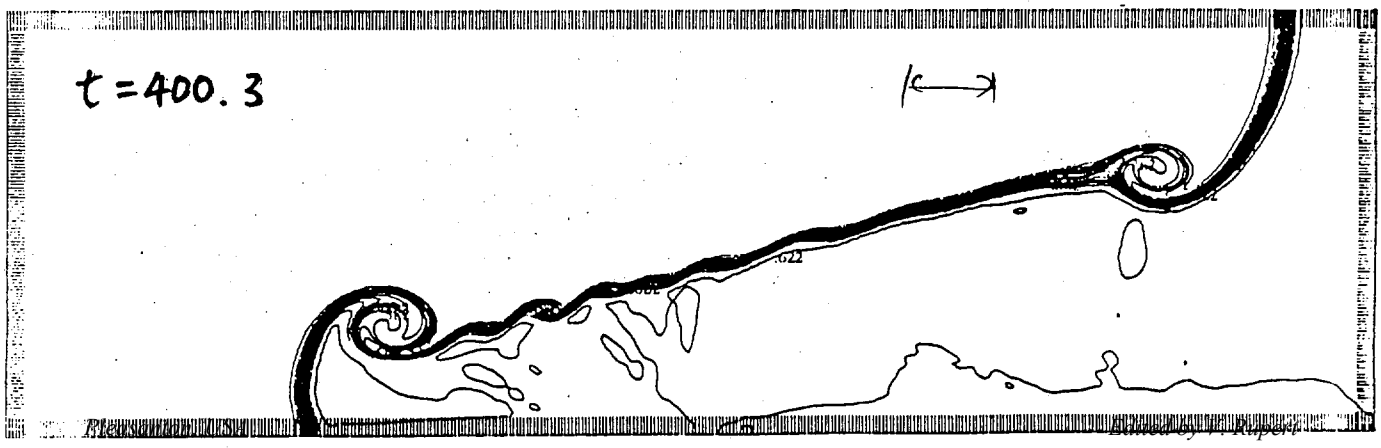

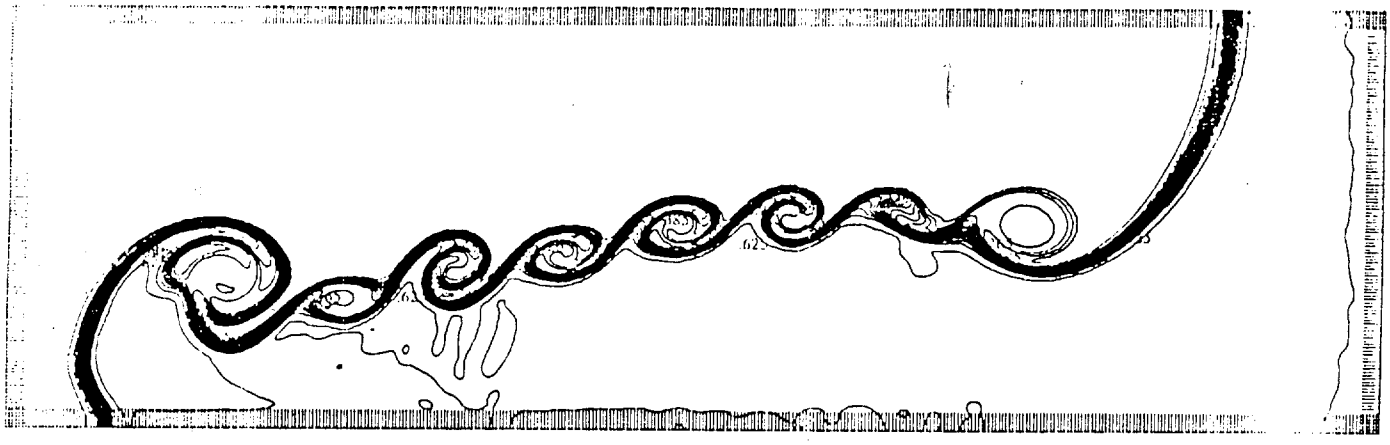

CONTOUR FROM 0.17476 TO 0.65476 CONTOUR INTERVAL OF 0.[illegible] OF PT(3,3) = 0.18122

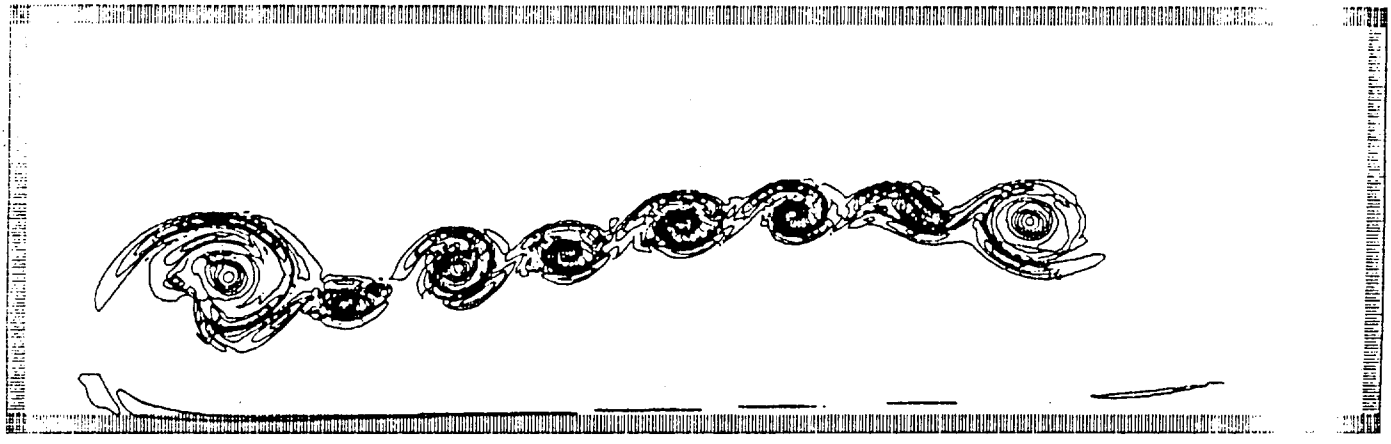

CONTOUR FROM 0.13376 TO 0.36224E-01 CONTOUR INTERVAL OF 0.10000E-01 PT(3,3) = 0.45166E-01 LABELS SCALED BY 10000

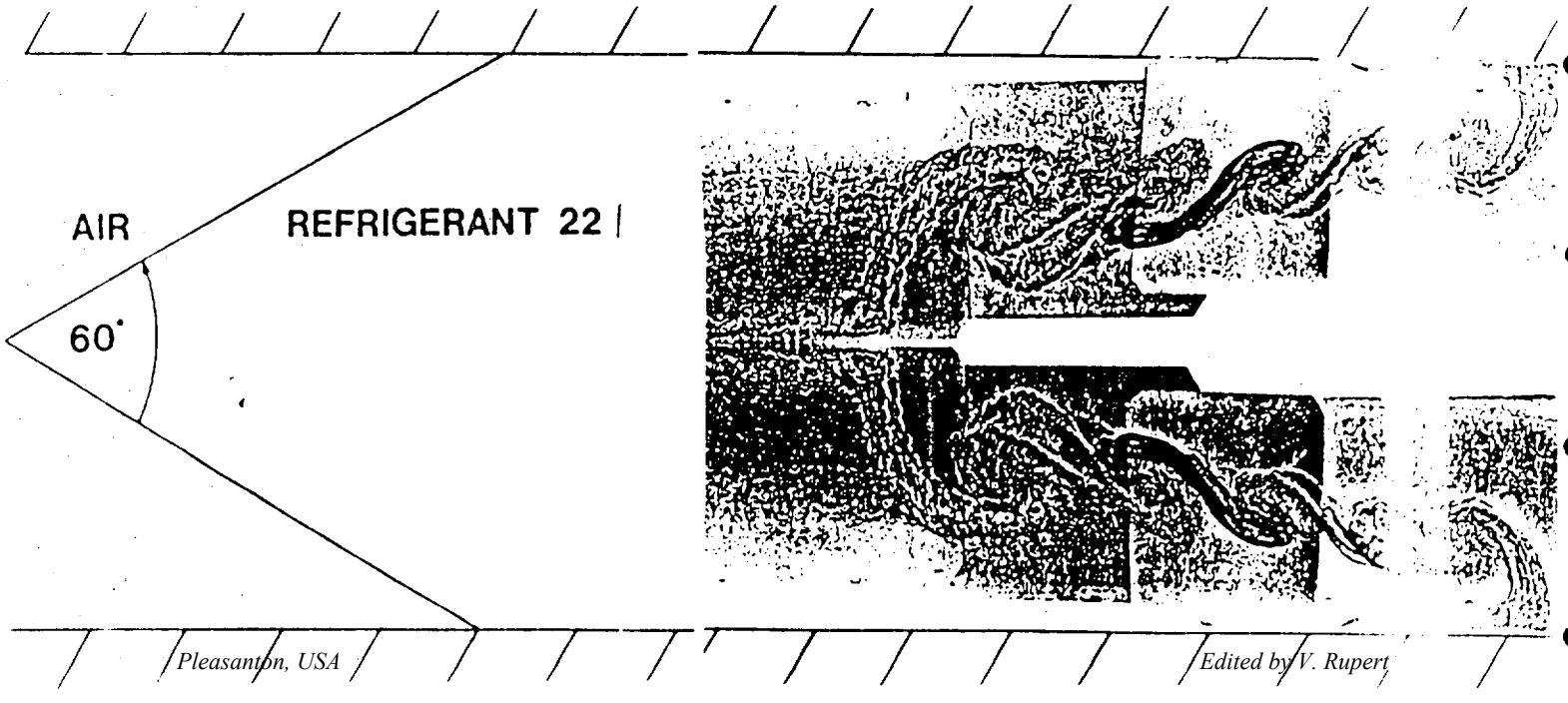

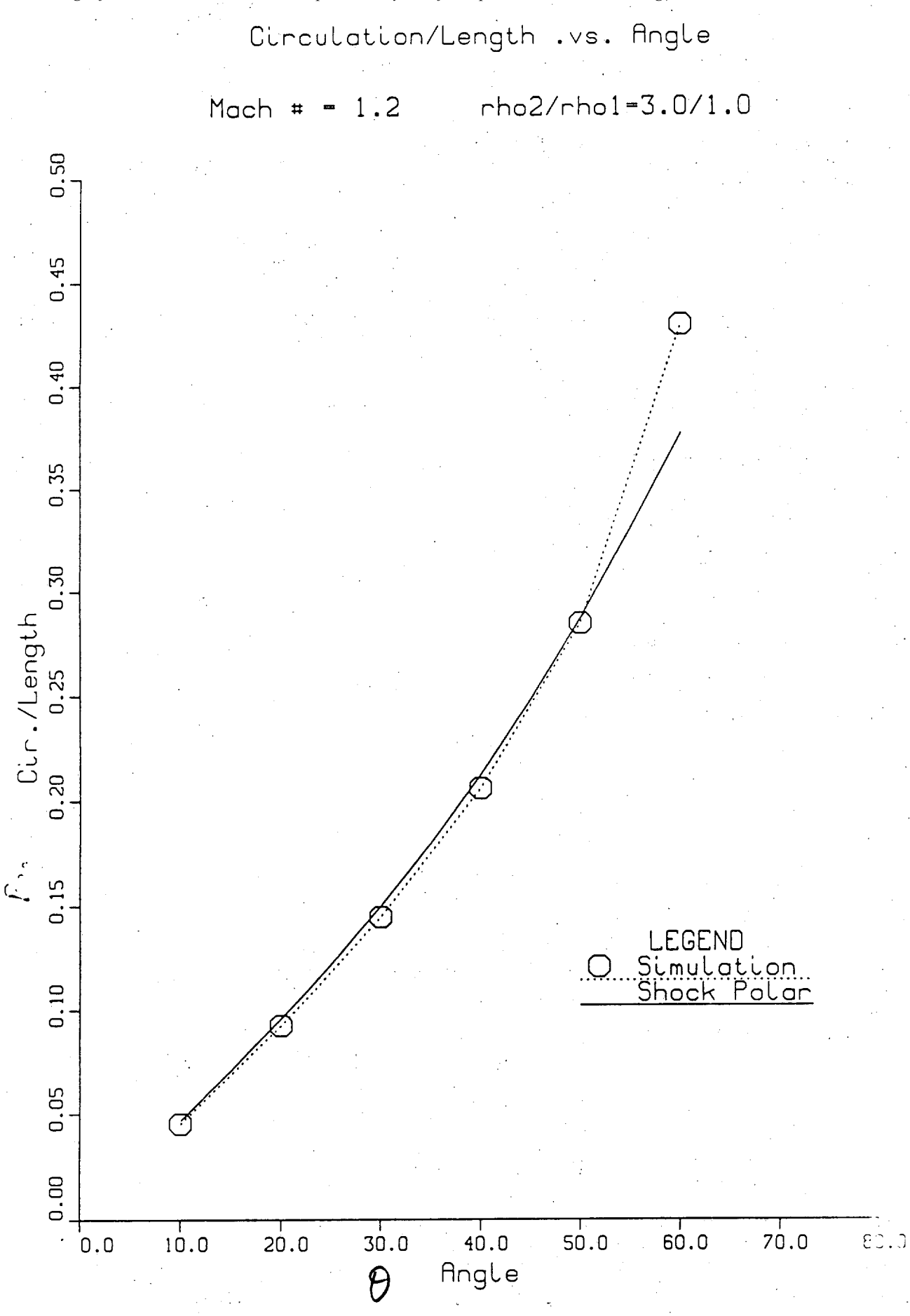
Circulation/Length .vs. Angle
Mach # = 1.2
rho2/rho1=3.0/1.0
Circ./Length
0.00
0.05
0.10
0.15
0.20
0.25
0.30
0.35
0.40
0.45
0.50
0.0
10.0
20.0
30.0
40.0
50.0
60.0
70.0
θ
Angle
LEGEND
Simulation
Shock Polar

M = 1.05 Air/R22/Air θ = 30°

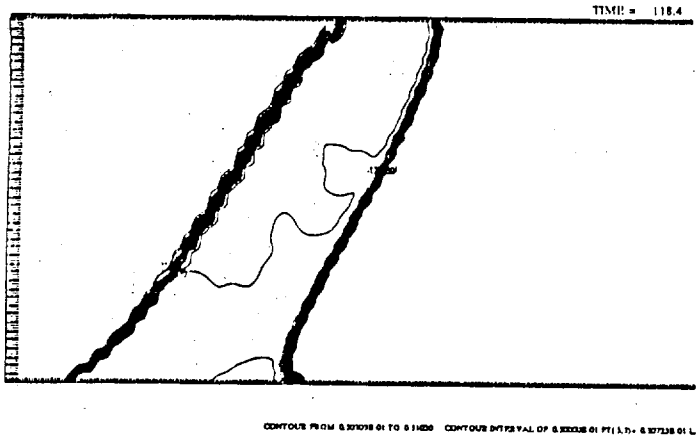

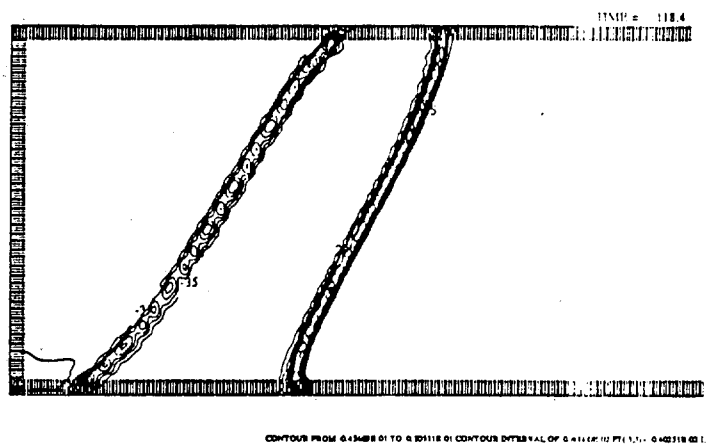

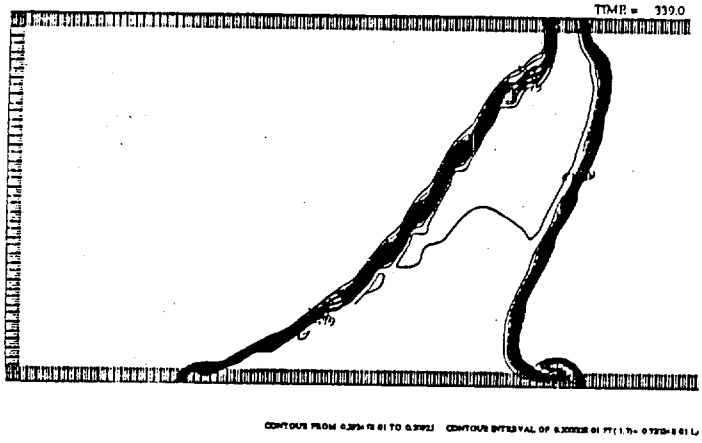

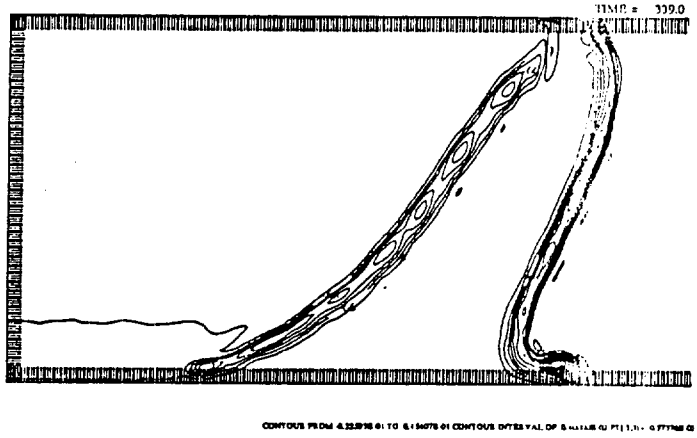

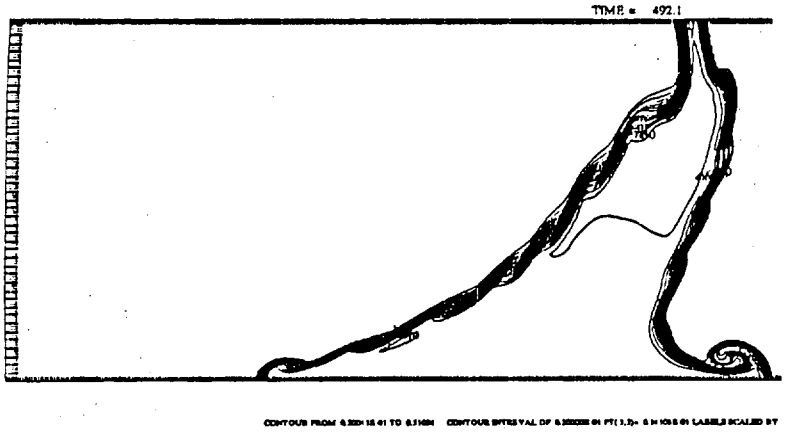

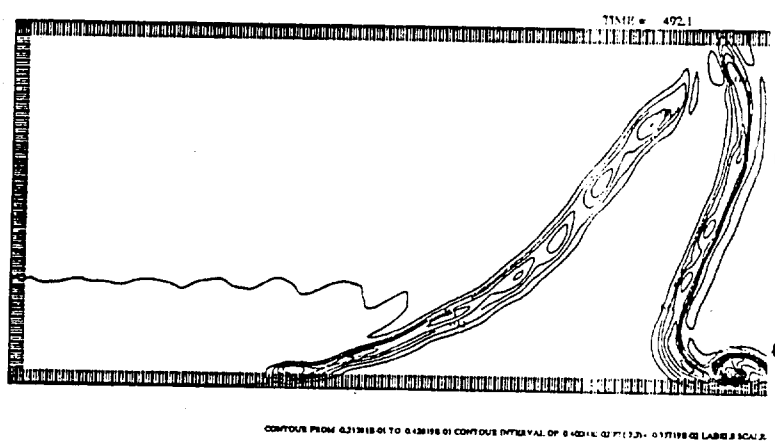

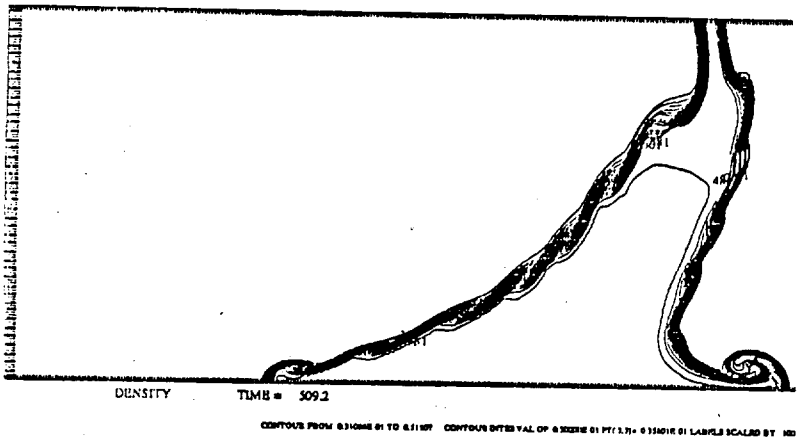

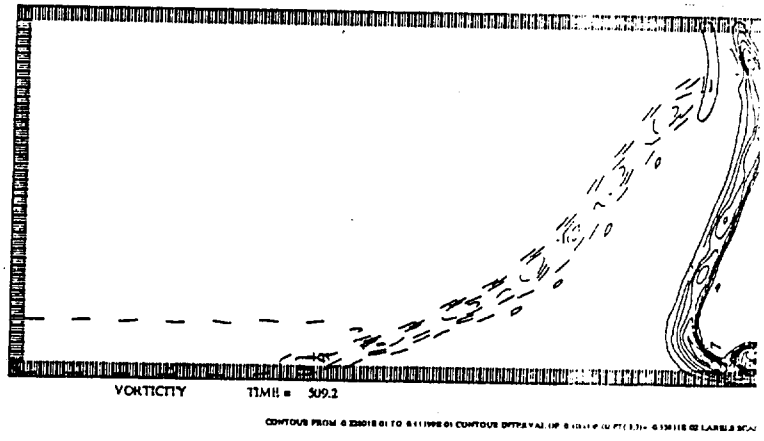

Air/He/Air $M = 1.05$ $\theta = 30°$

w

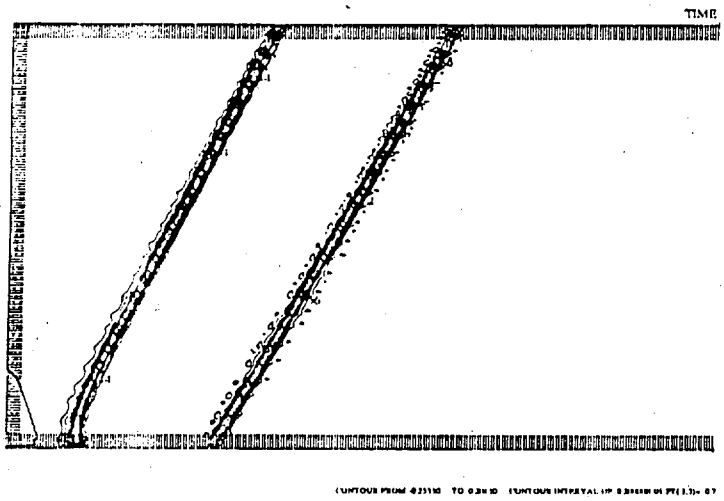

ρ

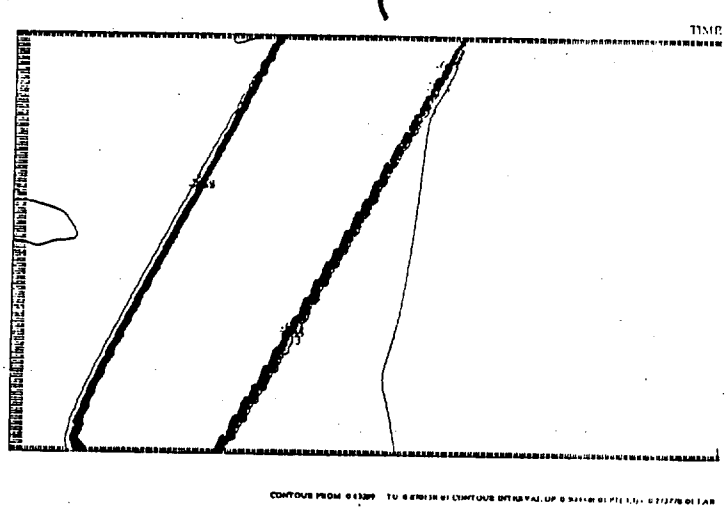

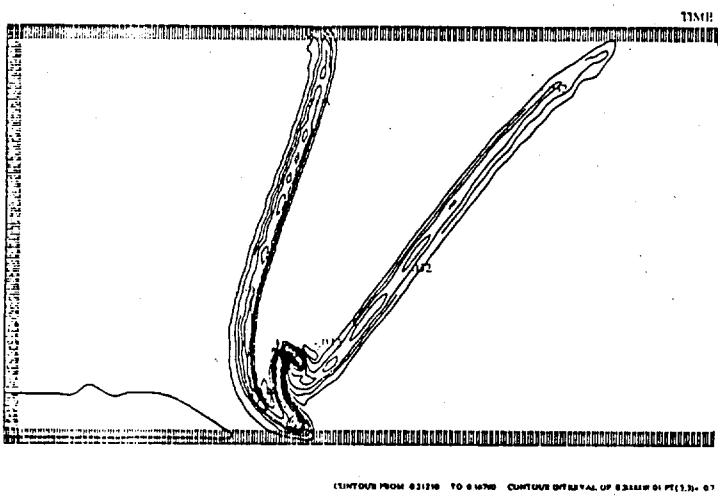

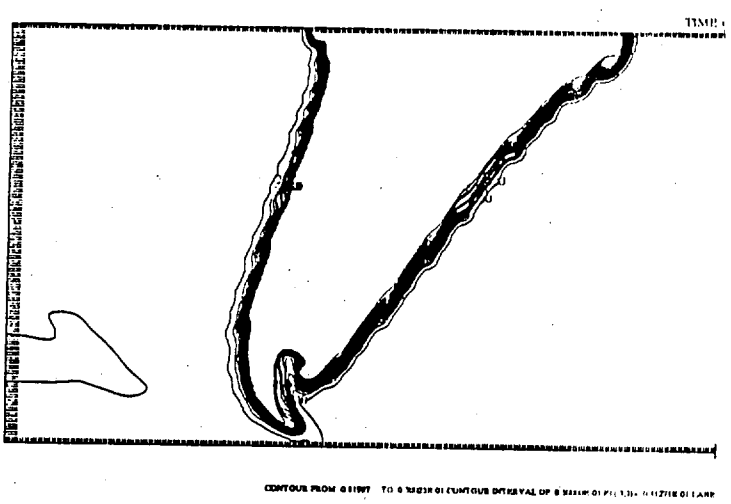

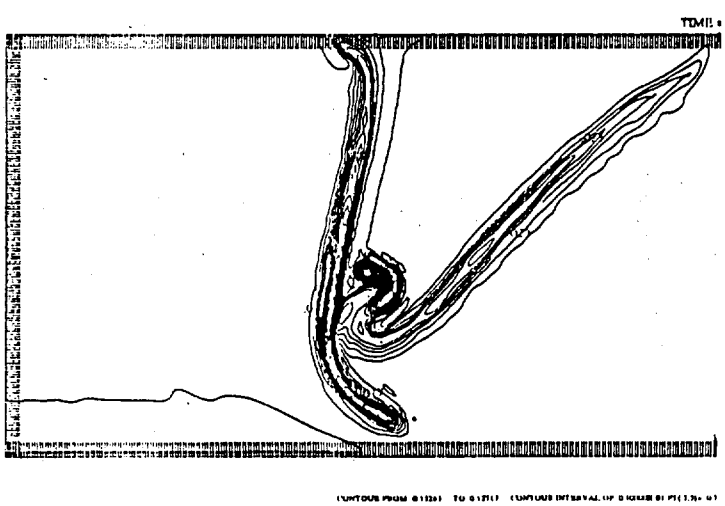

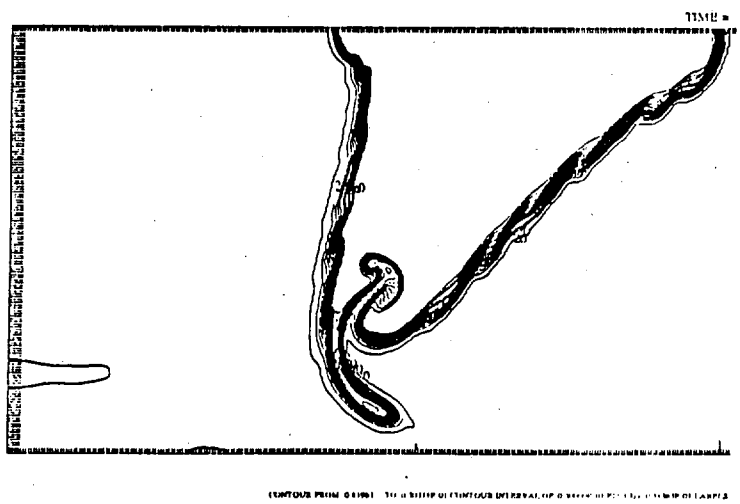

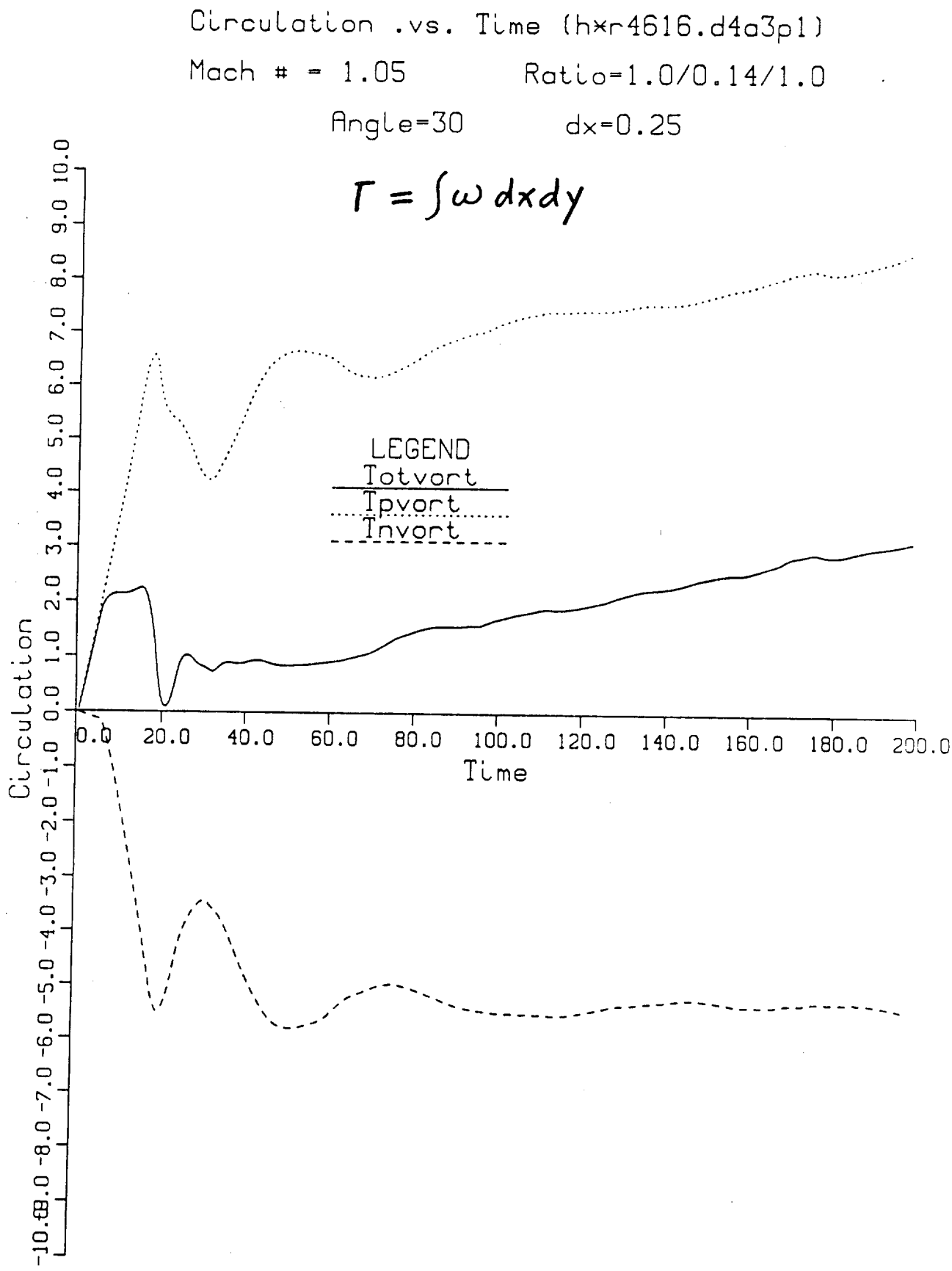
Circulation .vs. Time (h*r4616.d4a3p1)
Mach # = 1.05
Ratio=1.0/0.14/1.0
Angle=30
dx=0.25
$\Gamma = \int \omega \, dx dy$
LEGEND
Totvort
Tpvort
Tnvort
Circulation
Time
10.0
9.0
8.0
7.0
6.0
5.0
4.0
3.0
2.0
1.0
0.0
-1.0
-2.0
-3.0
-4.0
-5.0
-6.0
-7.0
-8.0
-10.0
0.0
20.0
40.0
60.0
80.0
100.0
120.0
140.0
160.0
180.0
200.0

Air/He/Air $M = 1.2$ $\theta = 30°$

P

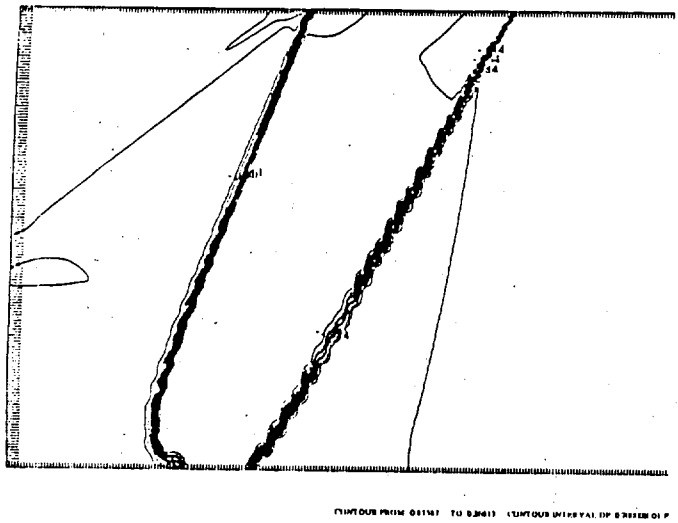

ω

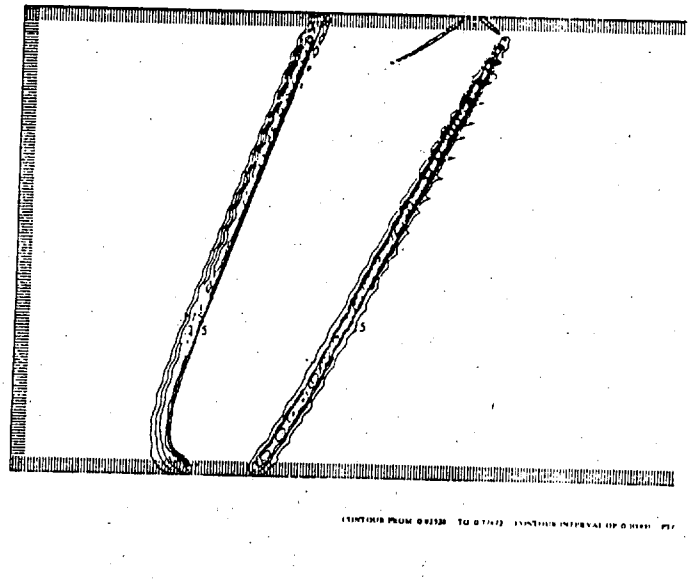

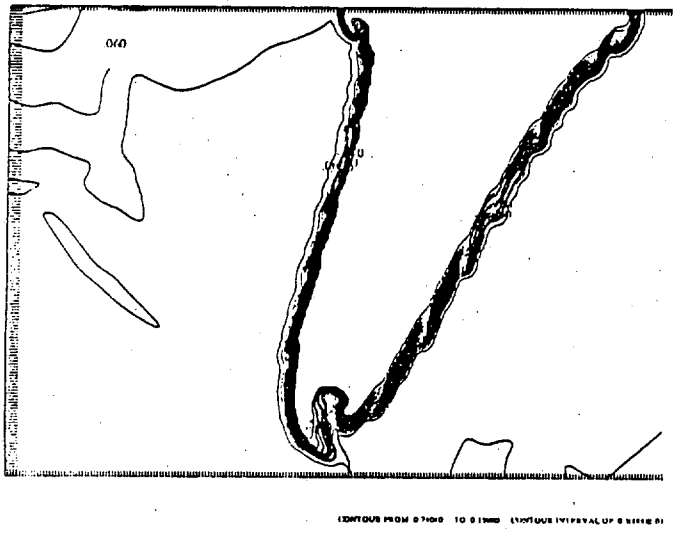

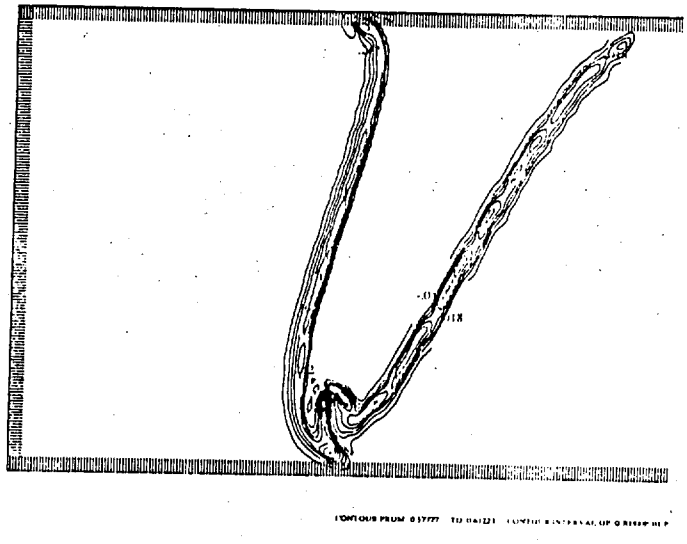

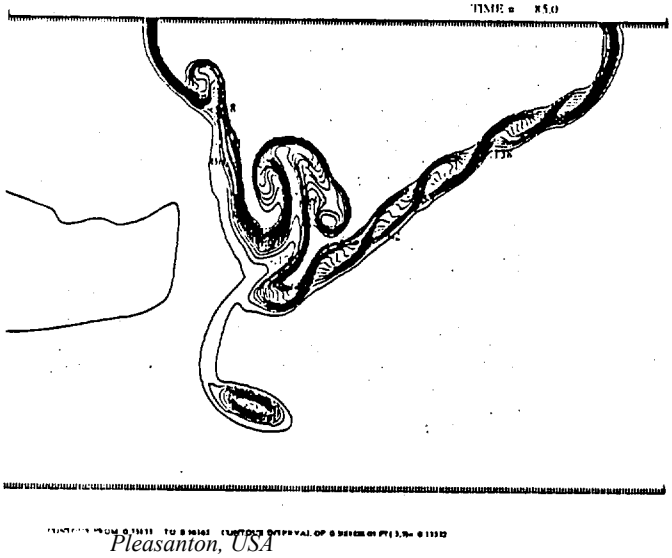

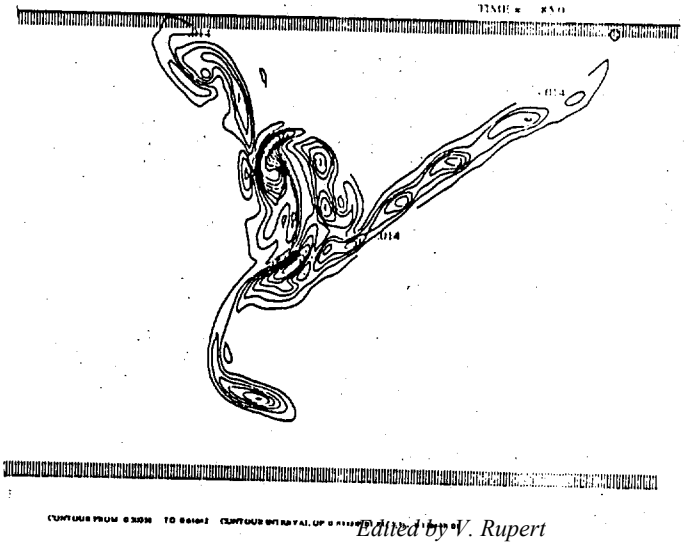

Air/He/Air $M = 1.5$, $\theta = 30°$

ρ

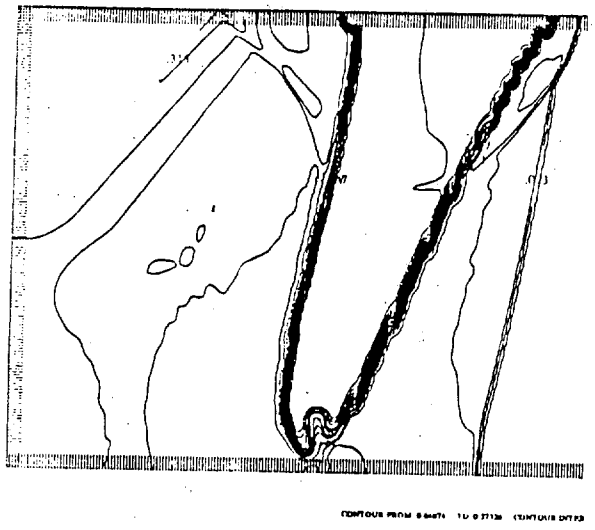

ω

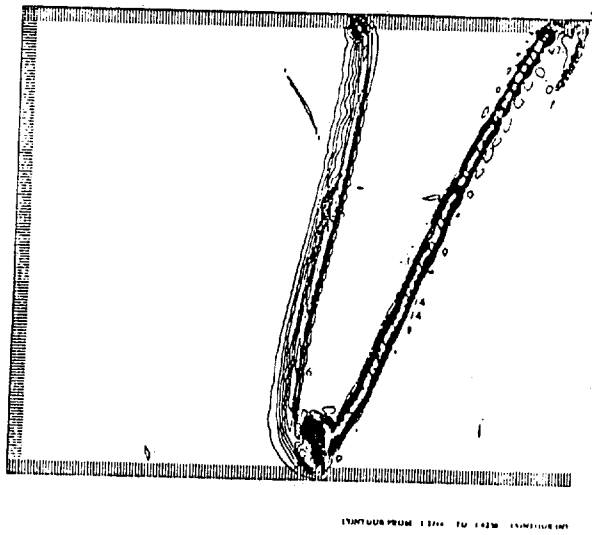

T

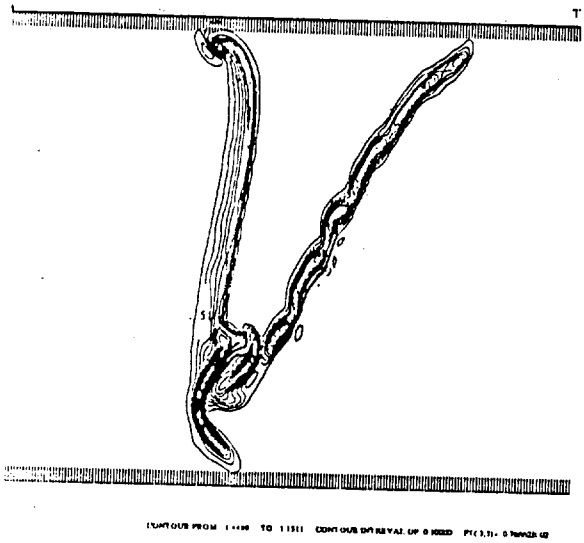

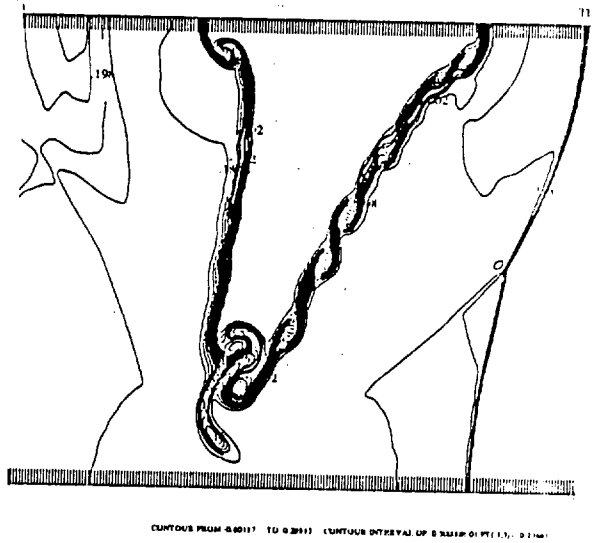

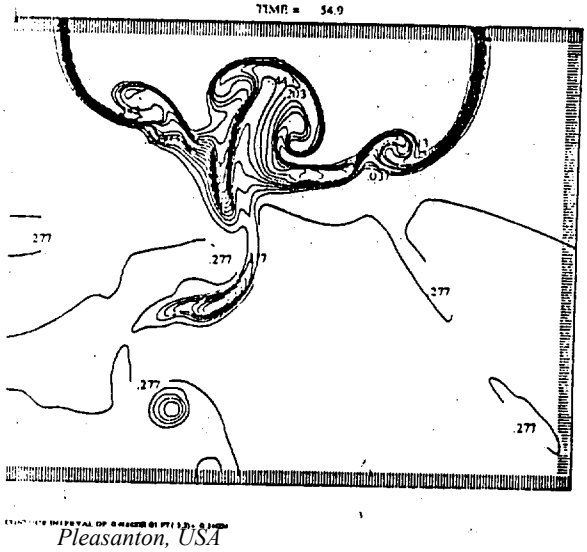

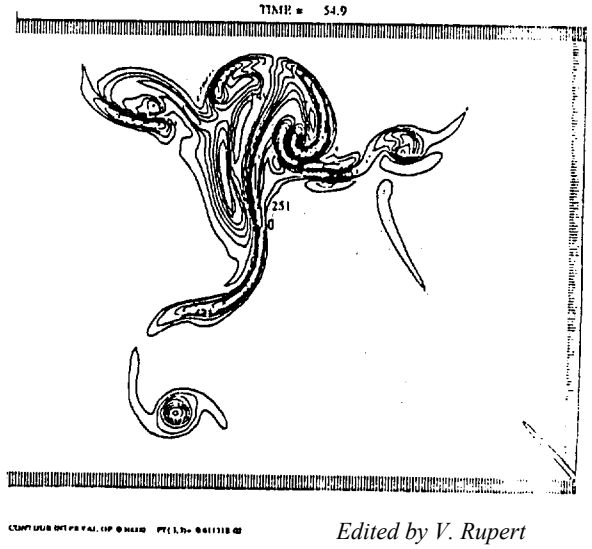

Breakthrough Time at Different Mach Number

Mach. #	Circulation	vorticity ~~Merger~~ binding	Breakthrough
1.5	(+) 45.5/(-) 45.0	$t = 14$	$t = 15$
1.2	(+) 22.3/(-) 19.9	$t = 28$	$t = 30$
1.05	(+) 6.55/(-) 5.55	$t = 85$	$t = 90$

Conclusion

1. Simulation of Flow Fields
   - Single interface
   - Double interfaces
2. Vorticity Deposition and Evolution
3. Breakthrough via dipolar vortex binding
4. Compressible Turbulence
   - Role of dipolar vortex
   - Baroclinic induction of opposite signed vorticity "layer".

CHELYABINSK STATE UNIVERSITY

COMPUTED SIMULATION OF MIXING INCDUCED BY RICHTMYER - MESHKOV INSTABILITY BY MEANS OF TWO - DIMENSIONAL PROGRAM COMPLEXES

N.N ANUCHINA, V.I. VOLKOV, A.E. GUSEVA

N.S. ESKOV, V.N. OGIBINA, A.V. POLYONOV

COMPUTED SIMULATION OF MIXING, INDUCED BY RICHTMYER-MESHKOV'S INSTABILITY, BY MEANS OF TWO-DIMENSIONAL PROGRAM COMPLEXES

by

N.N.Anuchina, V.I.Volkov, A.E.Guseva, N.S.Eskov,
V.N.Ogibina, A.V.Polyonov

ABSTRACT

Computations, simulating the development of turbulence, induced by Richtmyer-Meshkov's instability, in the system consistent with Meshkov's experiment /1/, were performed by using two different two-dimensional program complexes "MECH" and "MAH". In spite of the given difference in the initial state, the mixing growth rates, after passing the first reflected shock wave through the interface between gases, appear to be close in both computations and to be in satisfactory agreement with the experimental rate, measured by Meshkov /1/.

INTRODUCTION

In the given work we should like to illustrate some features of Richrmyer-Meshkov's mixing origination and development while using computations by the two-dimensional programs realizing the direct turbulence simulation. The situation was considered when the first shock wave crossed the interface between gases in the direction from the heavy gas to the light one. The distance from the interface to the right wall was in agreement with E.E.Meshkov's experiments /1/. On the left boundary, taken for reducing count time near the interface of gases, it was specified the simplified boundary condition conforming with the first shock wave with Mach number $M \simeq 1.3$:

$$\rho = 1.83 \text{ bar} \quad \text{or} \quad u = 15.2 \text{ cm/ms}$$

The aim of the performed work was to investigate the mixing development after passing through the interface between gases the shock wave, reflected from the right boundary. The mentioned above simplification, in the boun dary condition on the left boundary, did not effect upon the motion of the studied interface in time interval of our interest.

The problems were computed by two different program complexes MECH and MAH. The initial perturbations of the interface in the computations, perfomed by the different complexes, were differed. It gave the different zone width at the moment of passing through it the reflected shock wave and allowed to evaluate the rate of the zone development for the two different initial states.

The presented work is an initial step of the proposed work, in which it is suggested, besides the problems of scale deformations characterizing the density inhomogeneities and the turbulent energy anisotropy, to study such problems of the result convergency. Therefore, the above-mentioned results have, in general, an illustrative character.

1. Computations by the program complex MECH

In the plane system, consisting of two gases, having the parameters:

piston	region I	region II
P = 1.83	15 cm	31.9 cm
ρ_0	$1.2 \cdot 10^{-3}$	$0.1663 \cdot 10^{-3}$
p_0	1.01325	1.01325
γ	1.4	1.63

Fig.1

the motion of substances is considered as a result of acting the soft piston with P=1.83

The shock wave (SW), formed by the piston, is moving from left to right at first in the heavy gas, then in the light one. While passing through the contact boundary (CB) the unstable condition is arised /1/, leading to development of any perturbations, taking place in the flow in the vicinity of the contact boundary (CB).

Behaviour of CB, after passing SW through it, is investigated as well as the mixing zone development and interaction between the mixing zone and the waves, reflected from the right hard wall

It is suggested that this motion is described by the system of the instationary two-dimensional equations of gas dynamics. The investigation is performed by means of computations, carried out by the program complex "MECH", which realizes the irregular differential Euler's method. This method is the modification of the particles in cell-method, suggested in /2/ and developed in /3/.

It allows to describe the motion of multicomponent media in a complex geometry and large deformations of contact boundaries. Particles in the given modification are used only in the vicinity of CB. By means of these particles flows of substances are computed only from cells, including a number substances, or from cell with another substance.

In the rest of cases to compute mass, impulse and energy flows (continuous flows) it is used approximation of the continuity equation.

As the motion of SW up to approaching CB is one-dimensional, two-dimensional computation was begun from $t = 0.310282$ when SW was at the distance $Z = 13.85$. The boundary with applied pressure moved at the distance $Z = 4.5$. Geometry of layers in computations by the program complex "MECH" at $t = 0.310282$ had the form:

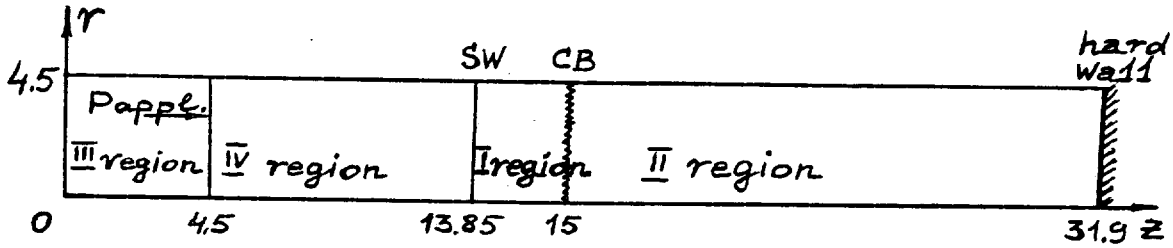

Fig.2

Regions I and II are the regions I,II in the Fig.1; region III is introduced for describing the interface motion with applied pressure; region IY is separated from the region I and the substance in it conforms to the substance state in the region I behind SW, i. e.

$\rho_o = 0.0018275$
$P_o = 1.83$
$\gamma = 1.4$
$U_o = 15.2$

Regions I and IY were joined into one region while computing.

As the perturbation development was treated after passing SW through CB, this CB was assumed to be randomly perturbated. It had a form of a broken line with 75 points of

breaks in a plane, this line crossed the surface Z = 15 about 34 times. The perturbation amplitude, being equal to the difference between the maximun value and the minimum one (Z) at CB, was determined to be equal to 0.4.

For describing CB we distributed in the near-boundary cells over 4 x 4 particles. Some results of conducted computations are given in Fig. X-T diagram of moving the boundaries and the shock wave is presented in Fig.3.

Velocity fields are given for the definite moments (two moments before arriving the reflected shock wave and two moments after its arrival) in Fig 4 -7. The constant density lines on the same moments are given in Fig 4a - 7a. The mixing zone width is plotted versus time in Fig.8.

2. Computations by the program MAH

Computations were carried out by the program, which realizes Lagrange-Euler numerical method for calculating axially symmetric gas-dynamic flows. This method is the modification of the method given in the work of Hert and Amsden /4/. Difference equations of this method were obtained by approximating of the integral laws of conservation of mass, pulse and total energy on the random rectangular mesh. Integrating is divided in the two stages. Lagrange equations are solved in the first stage, in the second stage accounting of convectional flows appearing in case of non-coincidence of the law of the difference mesh apexes motion with Lagrange law, takes place. The method allows both a regular description of contact boundaries when they are mesh coordinate lines, and irregular, when marker sets are used for the description of contact discontinuities. Markers are located directly on the lines separating substances and determine their positions. At the irregular description of the contact discontinuities boundaries can cross Euler mesh cells at random, in so doing cells containing several different substances are formed and the account of similar cells on the different calculation stages is carried out by this method. The plane system consisting of two layers of ideal gases (Fig.9) is computed by the given program. The system has parameters:

ρ_I = 0.001205
ρ_I = 1.01325
γ_I = 1.4

ρ_{II} = 0.0001663
ρ_{II} = 1.01325
γ_{II} = 1.63

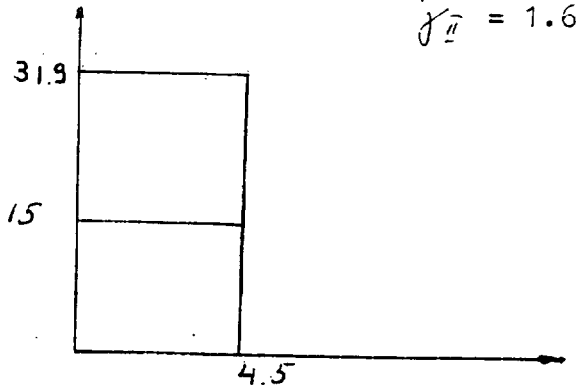

Fig.9

The condition "rigid wall" was specified on the left, right and upper boundaries of the system. Condition "normal velocity" u =const is on the bottom boundary. Small scale random perturbation with the mean amplitude of 0.15 cm and the mean period of 0.3 cm was specified on the contact boundary. A polygonal line having 31 points of inflection which crossed the straight line Z =15 thirty times was used for the perturbation description. In Fig.10 - 13 we see the form of the surface dividing gases in 4 time moments, which demonstrates perturbation development (2 moments before the shock wave arrival and 2 - after the arrival). Mixing zone width - time relation is given in Fig.8, in comparison with mentioned above results by MECH. Turbulent energy profiles are given in Fig 14.15 for 4 time moments. $K = \frac{1}{2}\left\{\overline{(V-\bar{V})^2} + \overline{U^2}\right\}$ Positins of mixing zone boundaries are also marked for the same moments. The field of chaotic velocities (velocities with substraction of the constant component) in some moment after passing of the first shock wave is given in Fig.16.

3. Discussion of the results

In the calculations the characteristic scale was not being determined, but it is seen by visual way from Fig 4-7, characterizing mixing states, that the process of the mixing development displays some simularity, that is scale enlarging at the width encreasing.

Turbulent energy profiles illustrate the main peculiarity of the process - that is generation of a pulsation energy in the moment of shock wave passing through a disturbed surface and then a small blurring and attenuation of it. This peculiarity is also given in Fig.16, where the presence of considerable vortical movements in the vicinity of the boundary after passing of the first wave is illustrated. Despite the difference in mixing zone width by the moment of the arrival of the reflected shock wave, realized in two simulations - 1.05 cm (MECH) - 0.53 mm (MAH) rates of the mixing zone development after reshock in the both calculations appeared to be close $\dot{l}$ =7.3 cm /ms (MECH); $\dot{L}$ = 7.7 cm/ms (MAH). These values satisfactorily agree with the experimental results of Meshkov E.E. /1/ - $\dot{L}_э$ 7.0 cm/ms.

LITERATURE

1. V.A.Andronov, S. M.Bakhrah, E.E.Meshkov, V.H.Mohov, V.V.Nikiforov, A.K.Pevnitski, A.J.Tolshmyakov
Turbulent Mixing on the Contact Surface Accelerated by Shock Waves.
Sov.J.Exp.& Theor. Physics,v.71, issue 2(8), p.806-811, 1976

2.F.H.Harlow
Numerical Method of Particles in Cells for Problems of Hydrodynamics.
In coll. "Computational Methods in Hydrodynamics", M.,MIR, 1967

3.N.N.Anuchina
On Computational Methods of Compressible Liquid Flows with Large Deformations. Numerical Methods of Continuum Mechanics.v.1,N 4, 1970

4.C.W.Hirt, A.A.Amsden, J.L.Cook
An Arbitrary Lagrangian-Eulerian Method for All Flow Speeds.
J.of Comput Physics,143,1974

z - t ДИАГРАММА ДВИЖЕНИЯ УДАРНЫХ ВОЛН (УВ), КОНТАКТНОЙ ГРАНИЦЫ (КГ) И ГРАНИЦЫ С ПРИЛОЖЕННЫМ ДАВЛЕНИЕМ.

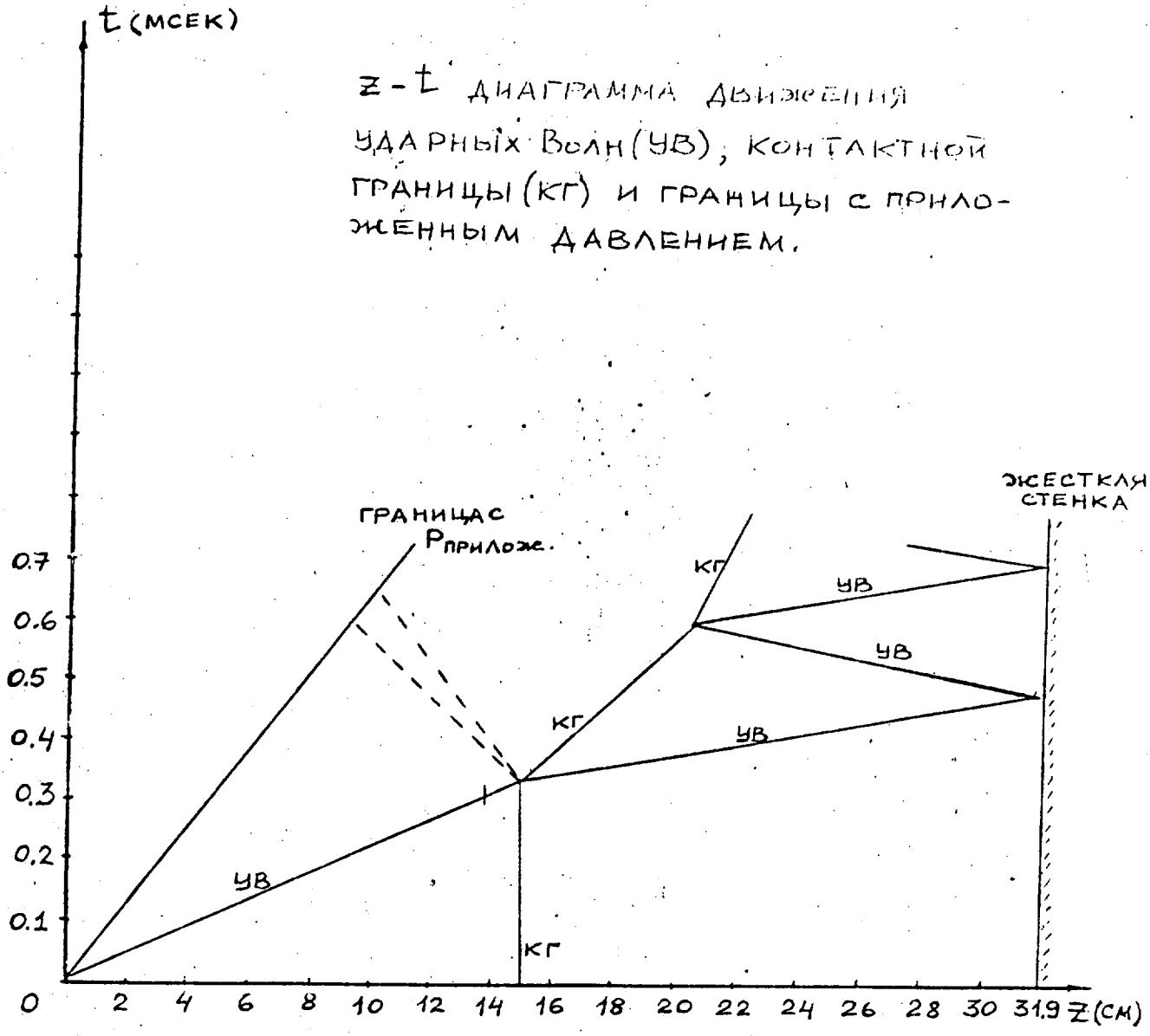

Рис. 3

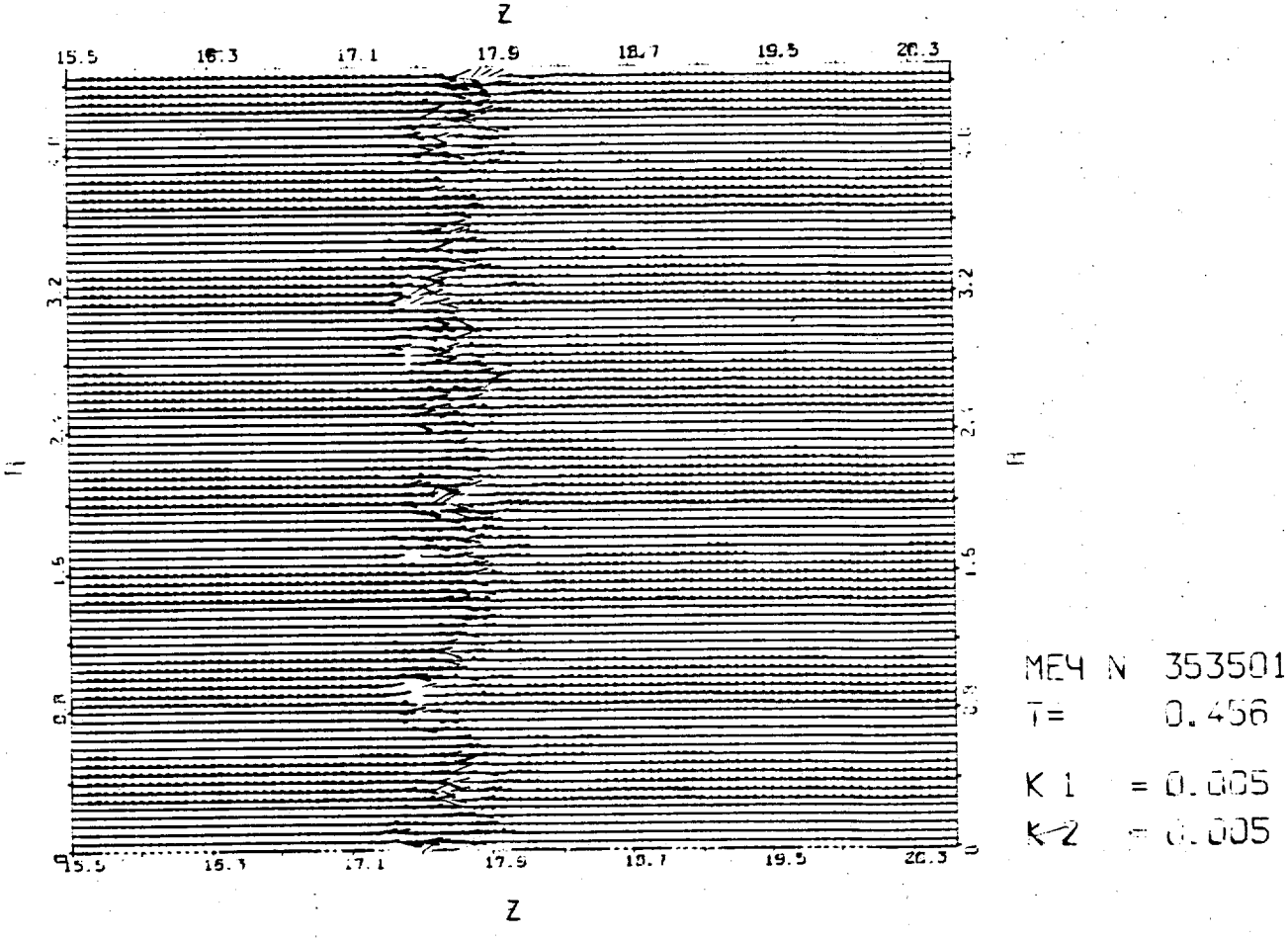
Z
15.5
16.3
17.1
17.9
18.7
19.5
20.3
3.2
1.5
0.8
0
R
MEM N 353501
T= 0.456
K 1 = 0.005
K 2 = 0.005

Fig.4.

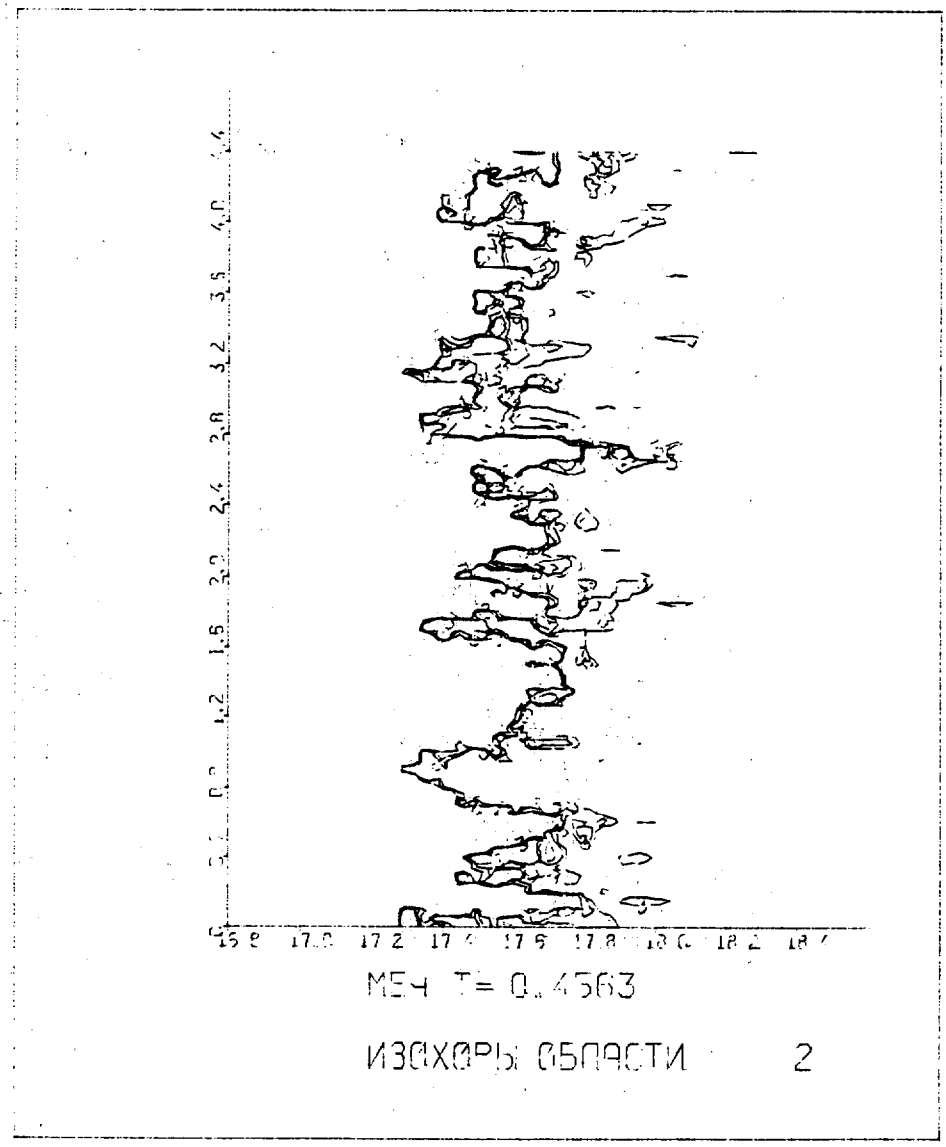

Fig. 4-a

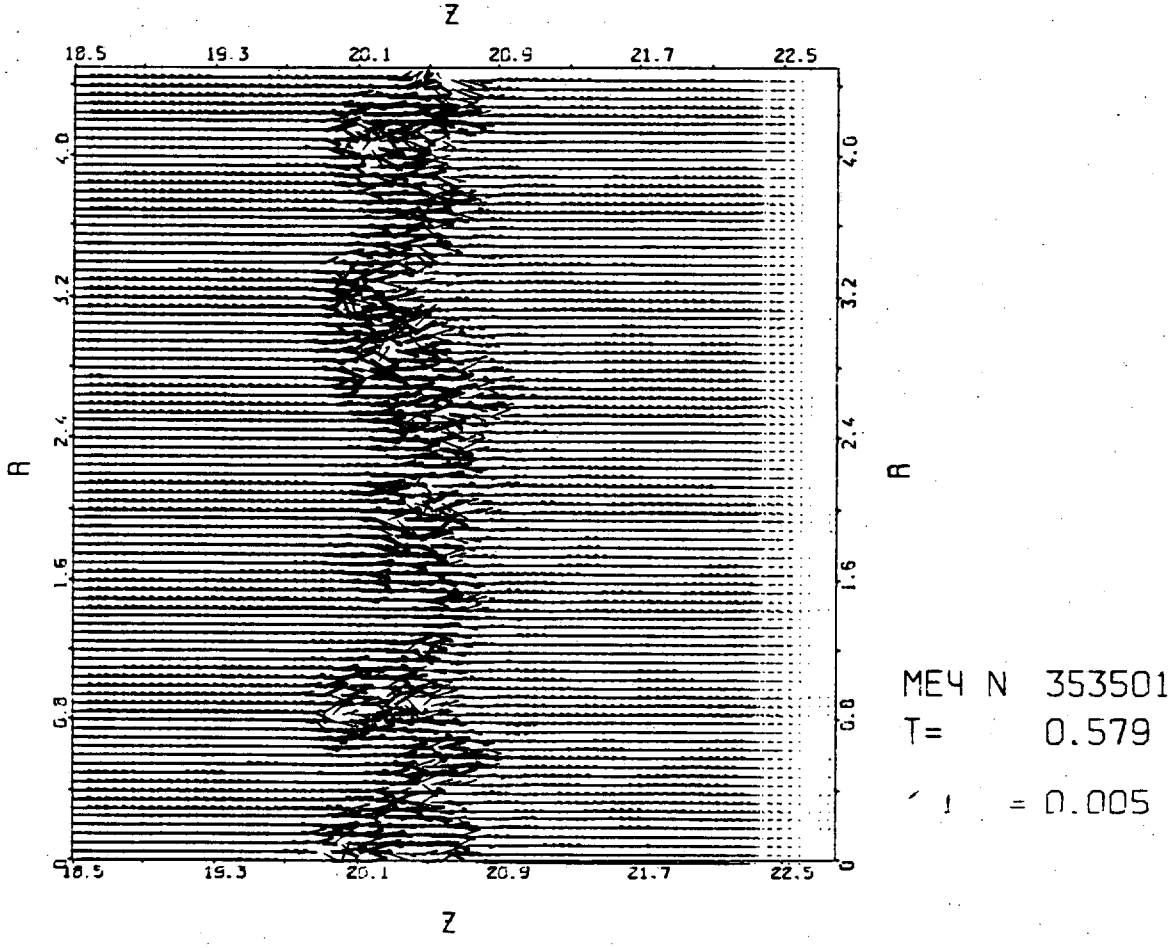

Fig. 5.

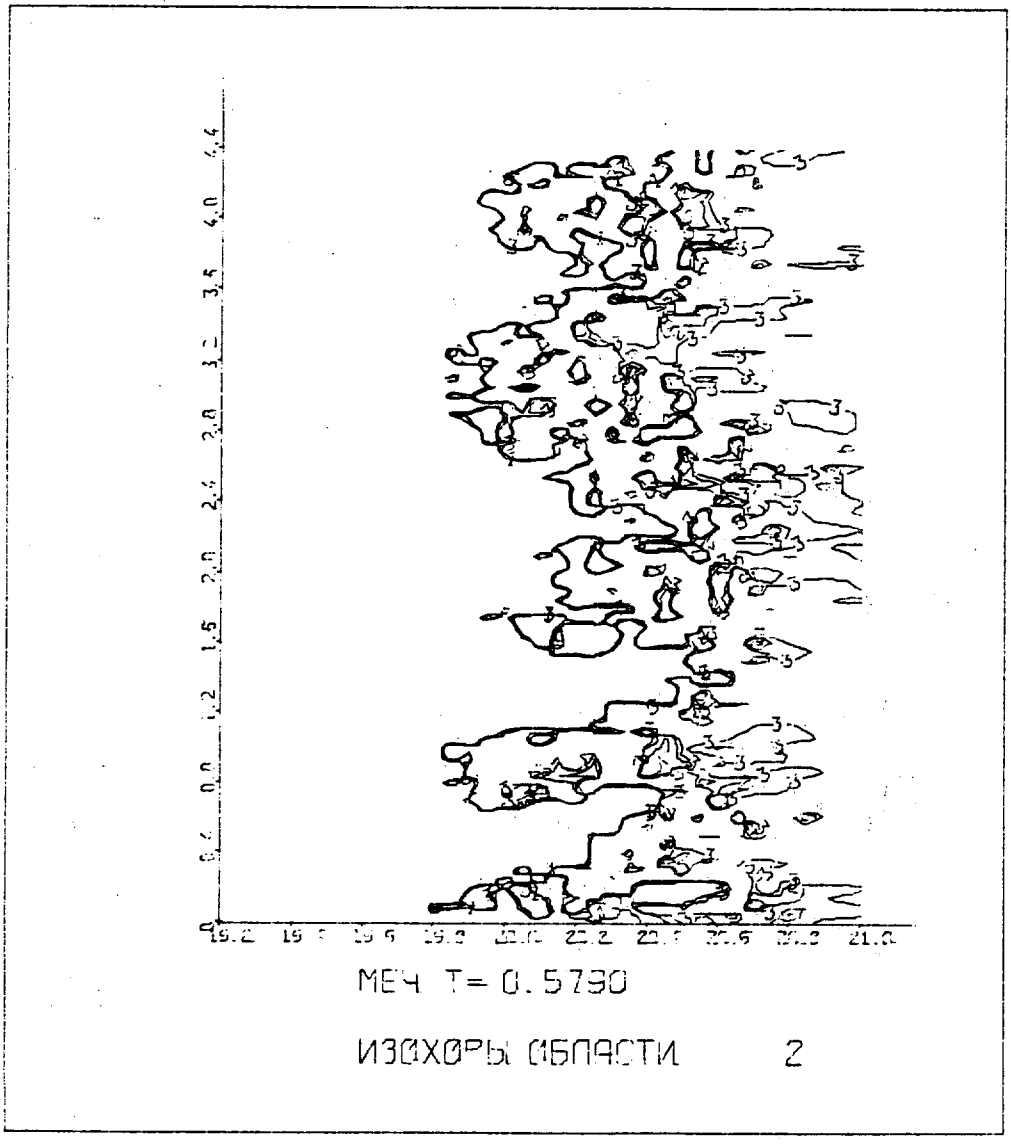
1 1.700-04
2 1.900-04
3 2.000-04
МЕЧ T= 0.5730
ИЗОХОРЫ ОБЛАСТИ 2
26.10.89, МЯШ 1

Fig. 5a

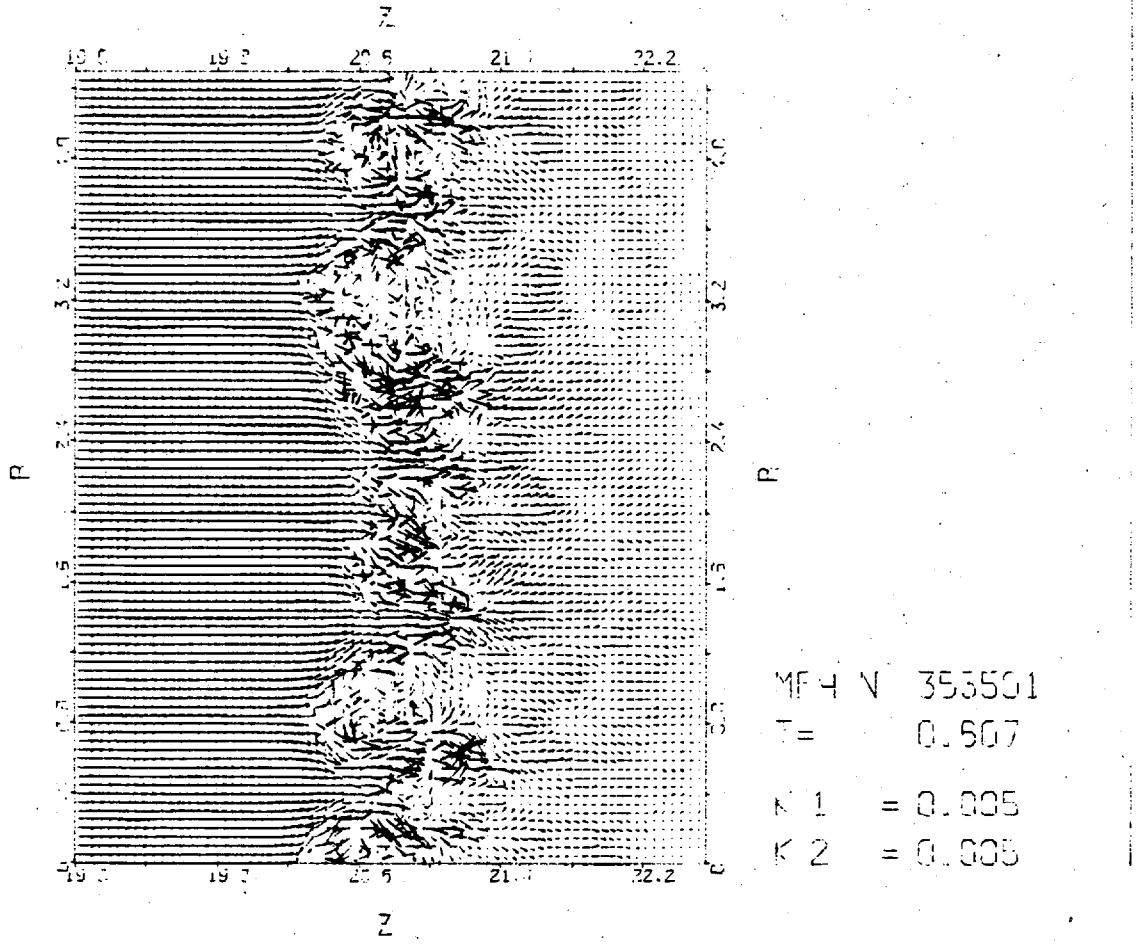

Fig. 6

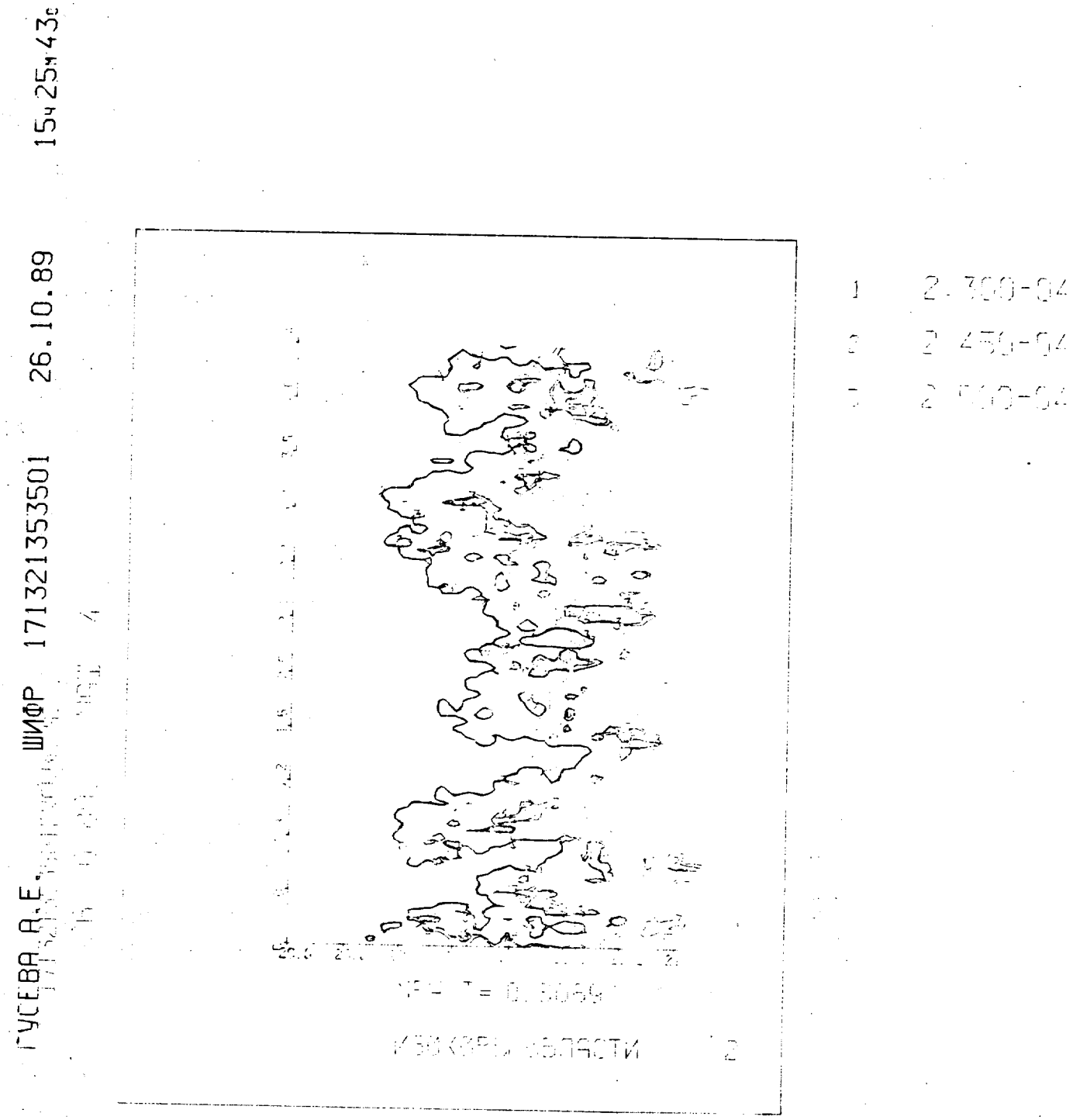
ГУСЕВА А.Е. ШИФР 1713213535O1 26.10.89 15ч 25м 43с
1 2.700-04
2 2.450-04
3 2.210-04

Fig. B9

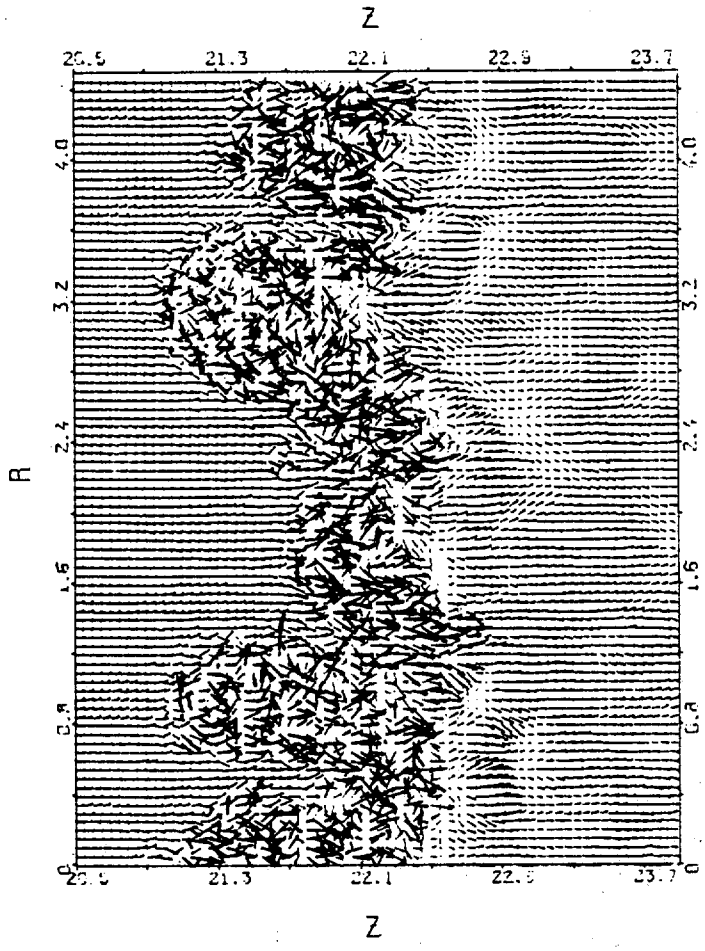

ШИФР 171301 25.10.89

БУСЕВА А.Е.

8.5 9

Fig. 4

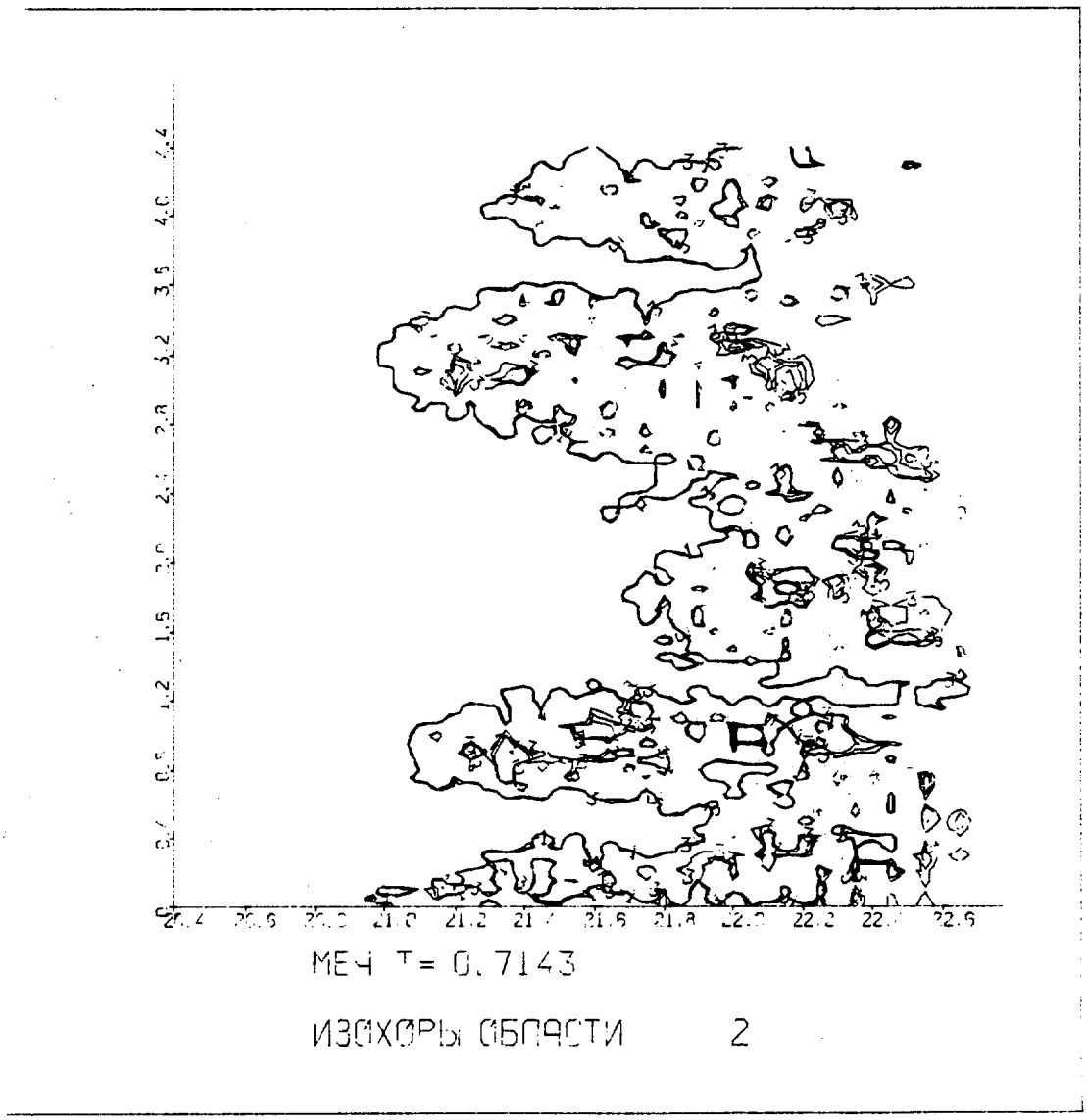

Fig. 7-a

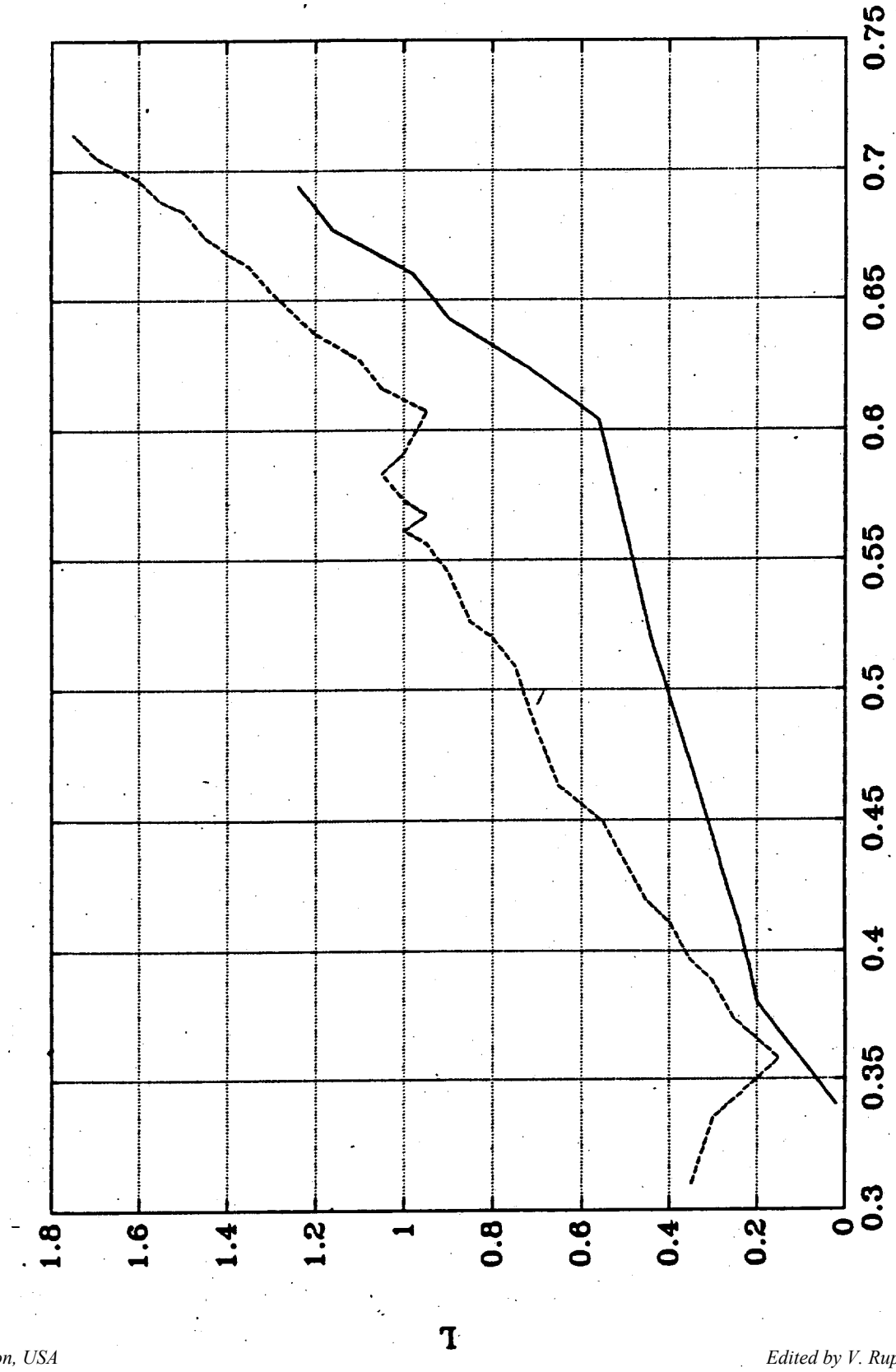

Fig. 8.

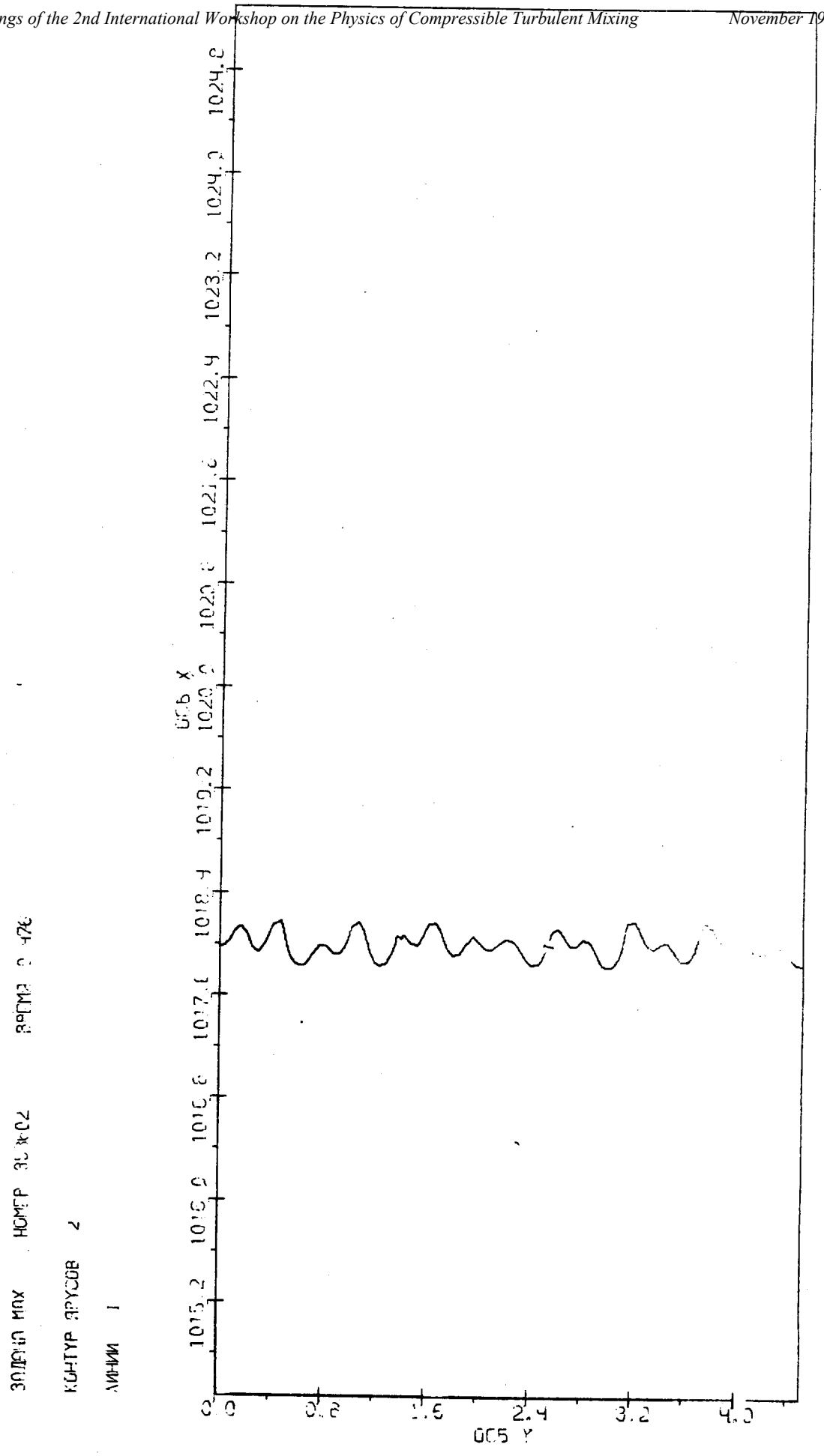
ЗОЛОТО ИЛХ
НОМЕР 3
ВРЕМЯ
КОНТУР ЗРУСОВ 2
ЛИНИИ 1
1015.2
1024.8
1024.0
1023.2
1022.4
1019.2
1018.4
0.0
0.8
1.6
2.4
3.2
4.0
ОСЬ Х
ОСЬ Y

Fig. 10.

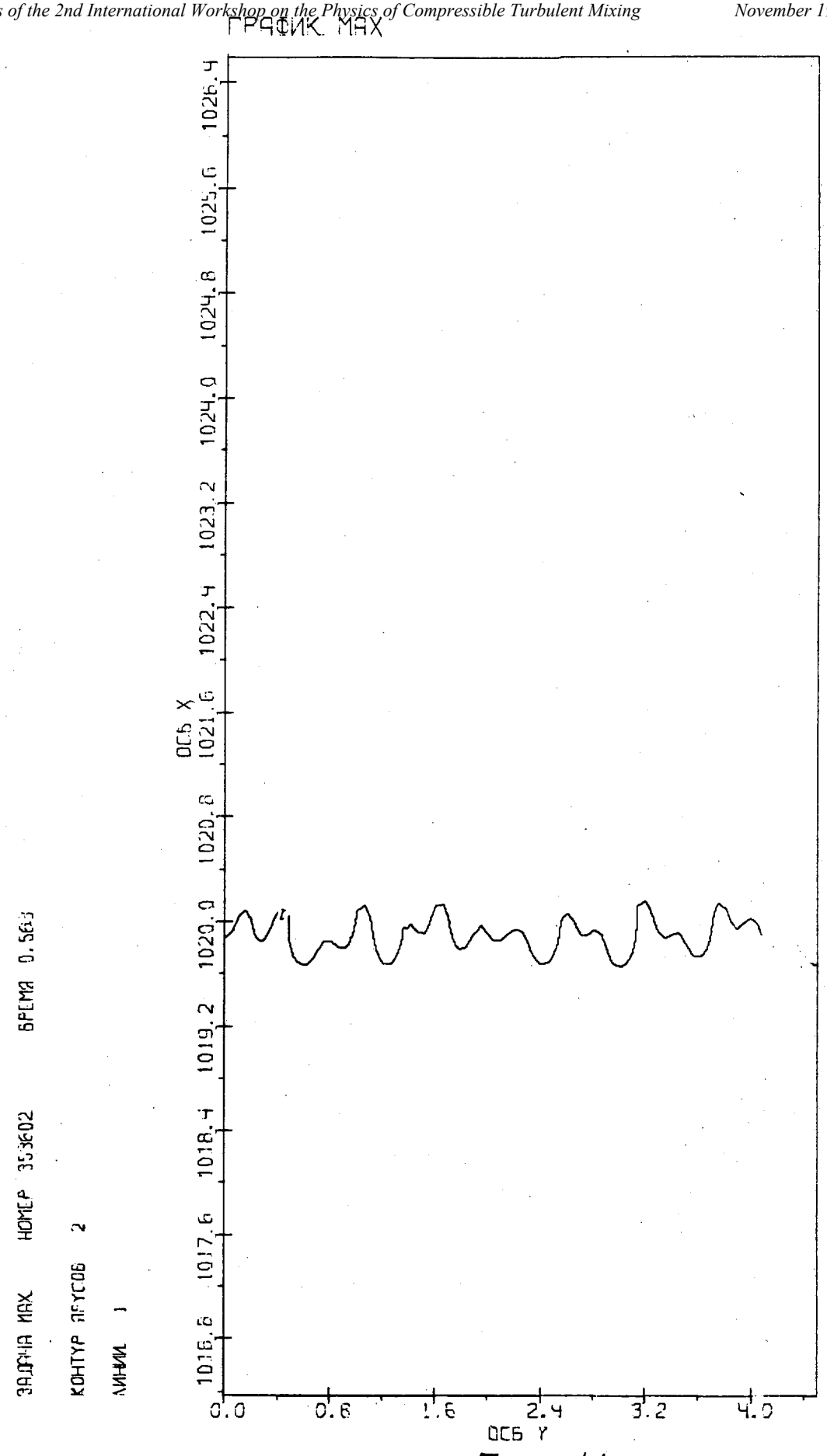
ГРАФИК МАХ
1026.4
1025.6
1024.8
1024.0
1023.2
1022.4
1021.6
1020.8
1020.0
1019.2
1018.4
1017.6
1016.8
ОСЬ X
0.0
0.8
1.6
2.4
3.2
4.0
ОСЬ Y
ЗАДАЧА МАХ НОМЕР 353602 ВРЕМЯ 0.563
КОНТУР ЛУЧОВ 2
ЛИНИЙ 1

Fig. 11.

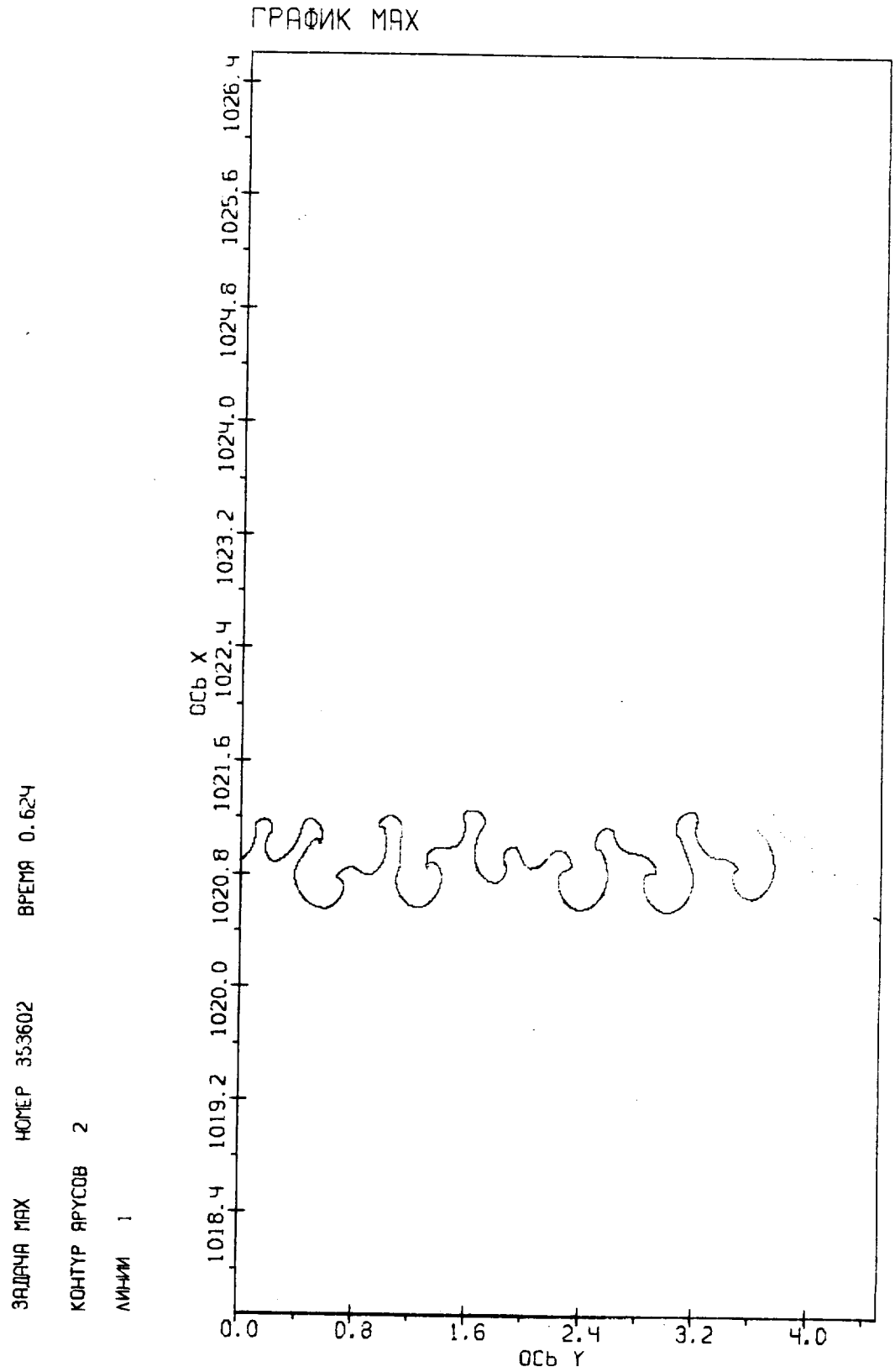
ГРАФИК МАХ
ЗАДАЧА МАХ НОМЕР 353602 ВРЕМЯ 0.624
КОНТУР ЯРУСОВ 2
ЛИНИИ 1
ОСЬ X
1018.4
1019.2
1020.0
1020.8
1021.6
1022.4
1023.2
1024.0
1024.8
1025.6
1026.4
0.0
0.8
1.6
2.4
3.2
4.0
ОСЬ Y

Fig. 12

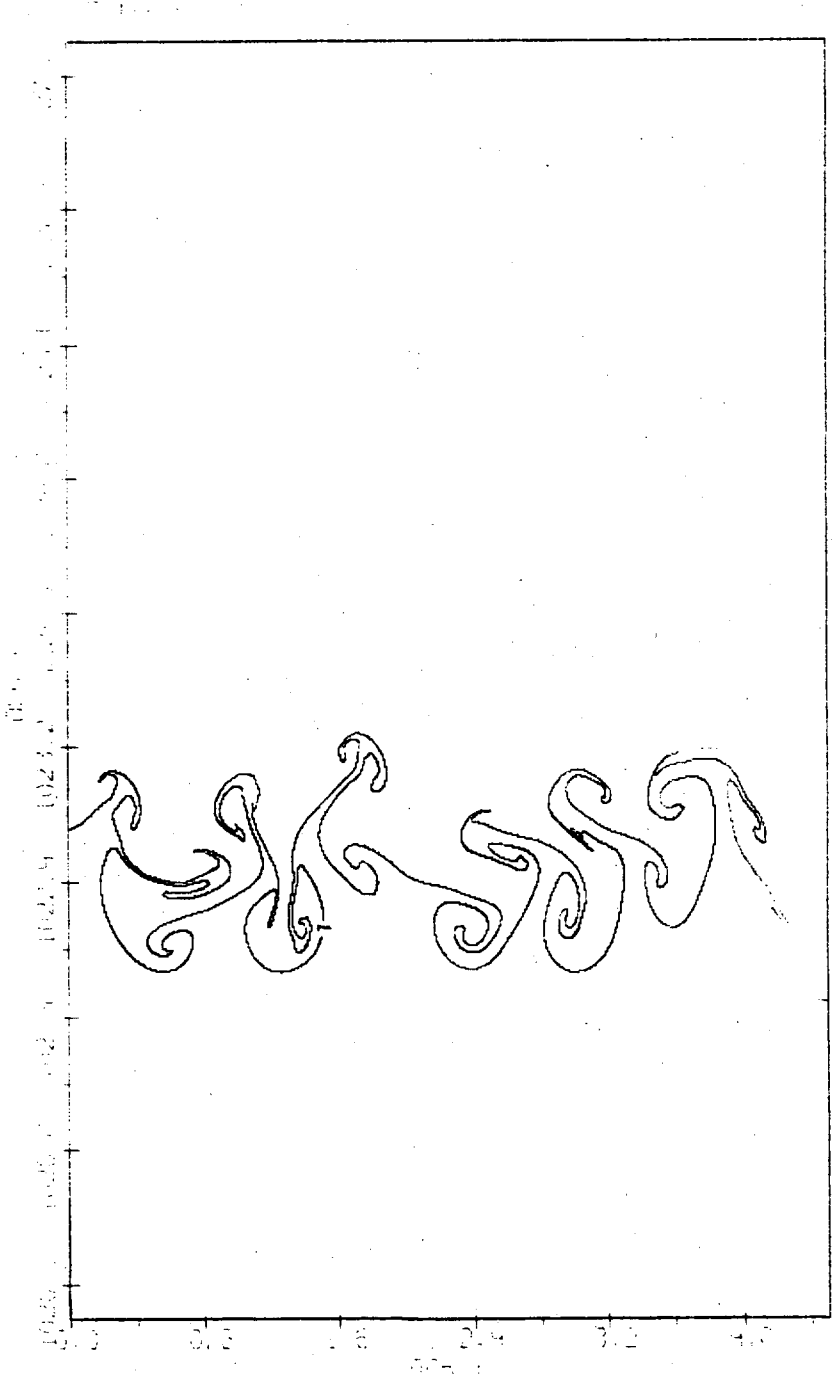

Fig. 13.

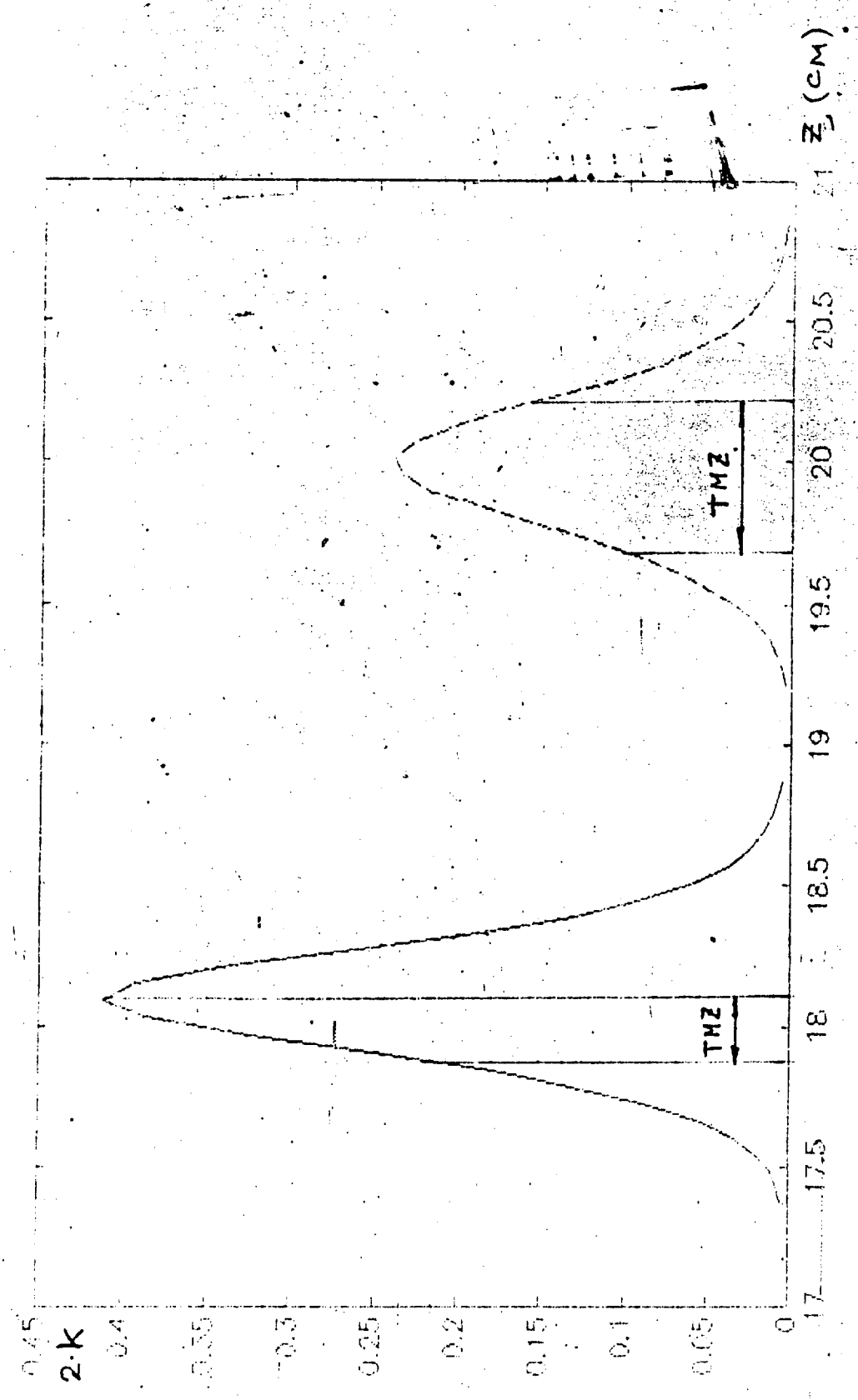
Z (cm)
17
17.5
18
18.5
19
19.5
20
20.5
21
THZ
THZ
2·K
0
0.05
0.1
0.15
0.2
0.25
0.3
0.35
0.4
0.45

Fig. 14.

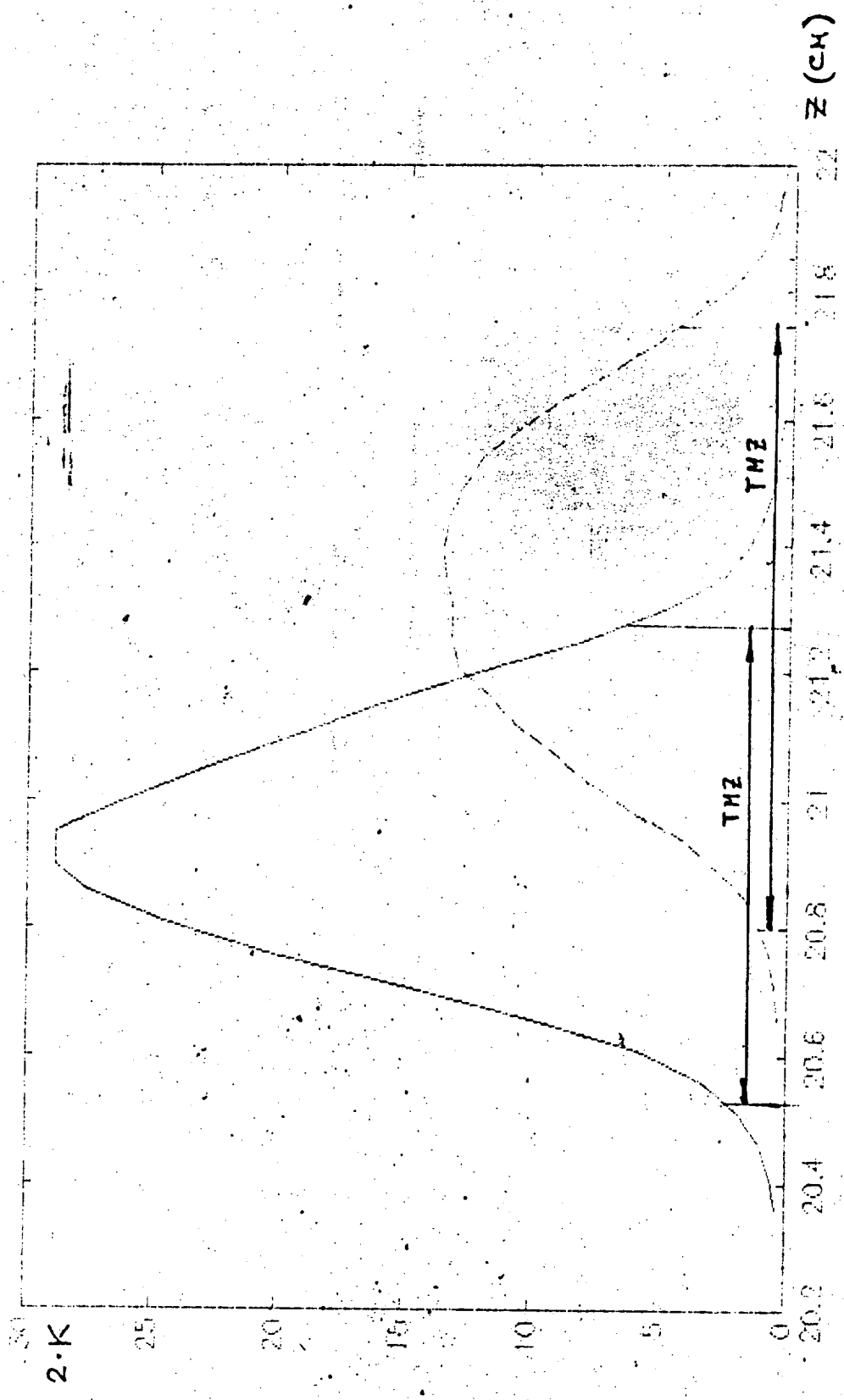
Z (CM)
22
21.8
21.6
21.4
21.2
21
20.8
20.6
20.4
20.2
TM2
TM2
2·K
30
25
20
15
10
5
0

Fig. 16.

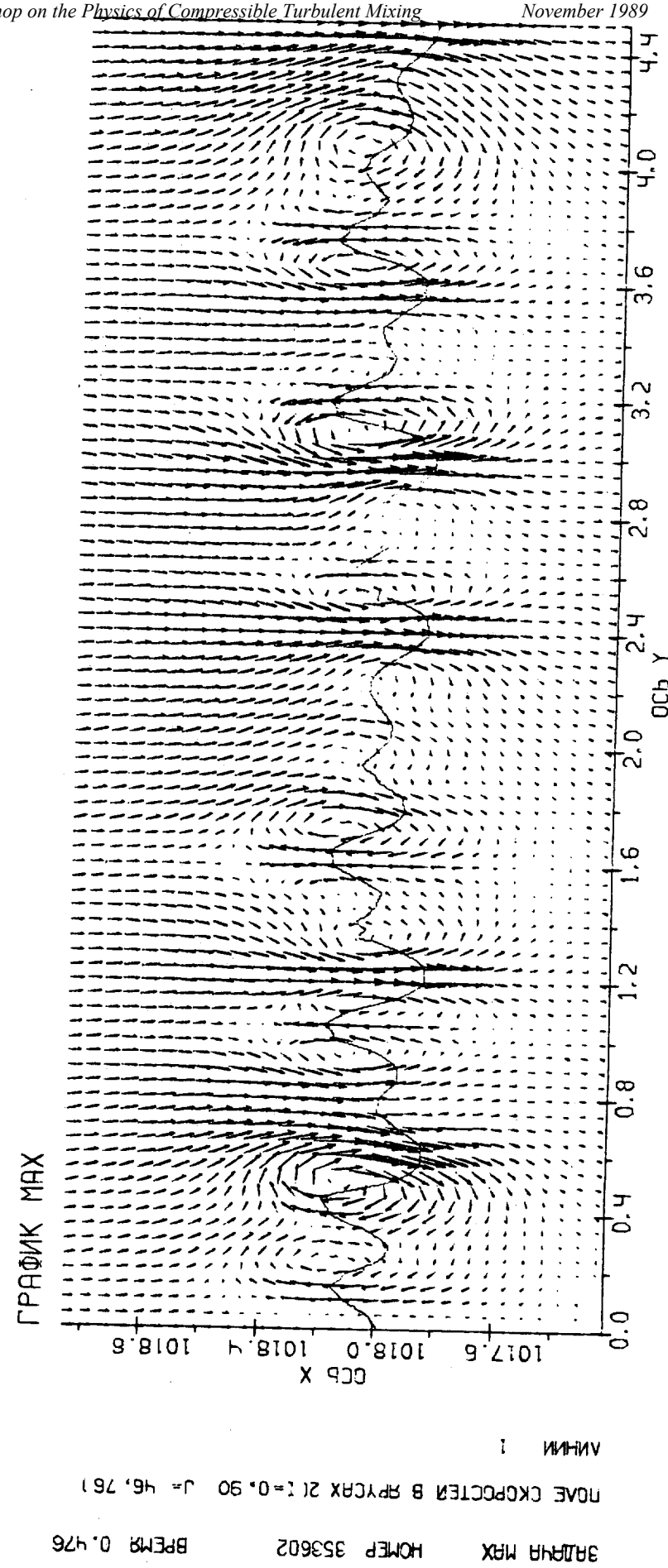
ГРАФИК МАХ
ОСЬ X
1017.6
1018.0
1018.4
1018.8
0.0
0.4
0.8
1.2
1.6
2.0
2.4
2.8
3.2
3.6
4.0
4.4
ОСЬ Y
ЛИНИИ 1
ПОЛЕ СКОРОСТЕЙ В ЗАРУСАХ Z(1=0.90 J= 46, 76)
ЗАДАЧА МАХ НОМЕР 353602 ВРЕМЯ 0.476

Fig. 16

NUMERICAL SIMULATIONS OF RICHTMYER-MESHKOV INSTABILITIES IN SHOCK TUBES

KARNIG O. MIKAELIAN

LAWRENCE LIVERMORE NATIONAL LABORATORY

LIVERMORE, CALIFORNIA

International Exchange on RM & RT Mixing

November 16 & 17, 1989

LLNL

Using an arbitrary lagrangian-eulerian ALE code we simulate the evolution of single-scale, double-scale, and multi-scale perturbations at the interfaces between various gases (air, helium, and SF_6) in shock-tube experiments. Perturbations grow after the passage of the first shock (Mach 1.2 in air) and following subsequent re-shockings of the air/helium and air/SF_6 interfaces.

These are extracts from a longer report, "**Simulation of the Richtmyer-Meshkov Instability and Turbulent Mixing in Shock-Tube Experiments**", UCID-21328, January 1988.

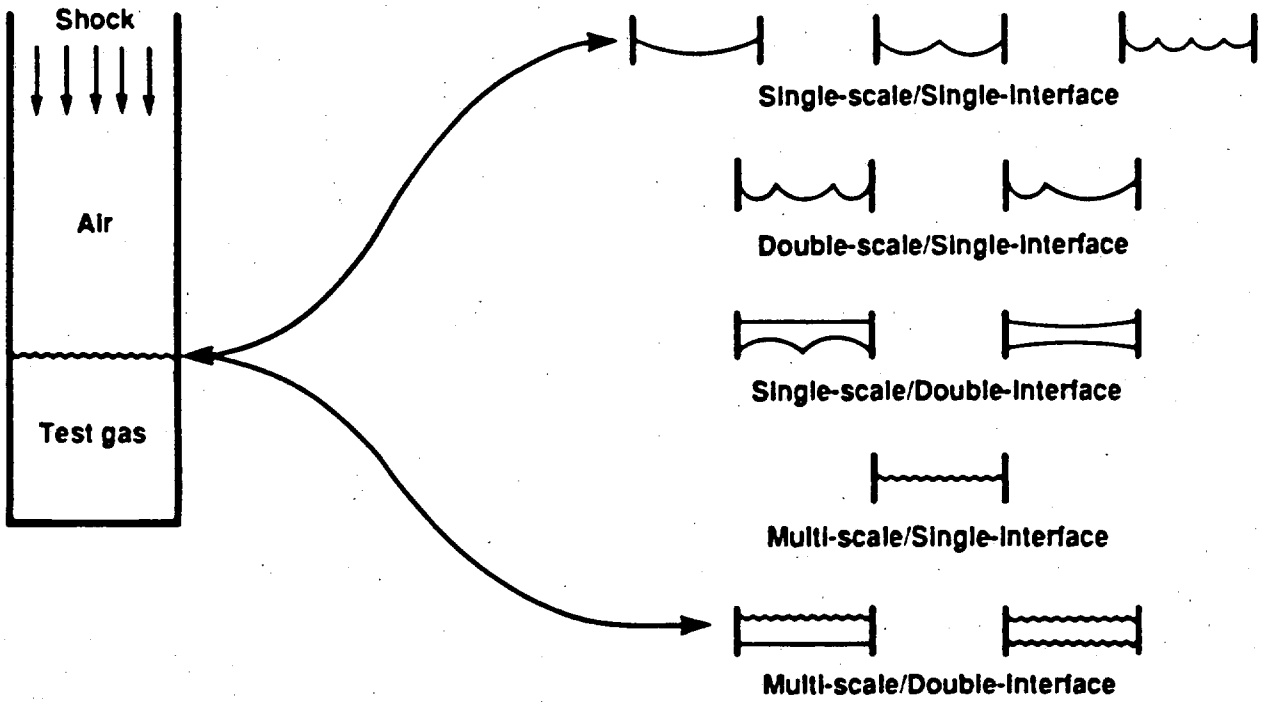
Shock
Air
Test gas
Single-scale/Single-interface
Double-scale/Single-interface
Single-scale/Double-interface
Multi-scale/Single-interface
Multi-scale/Double-interface

Fig. 1

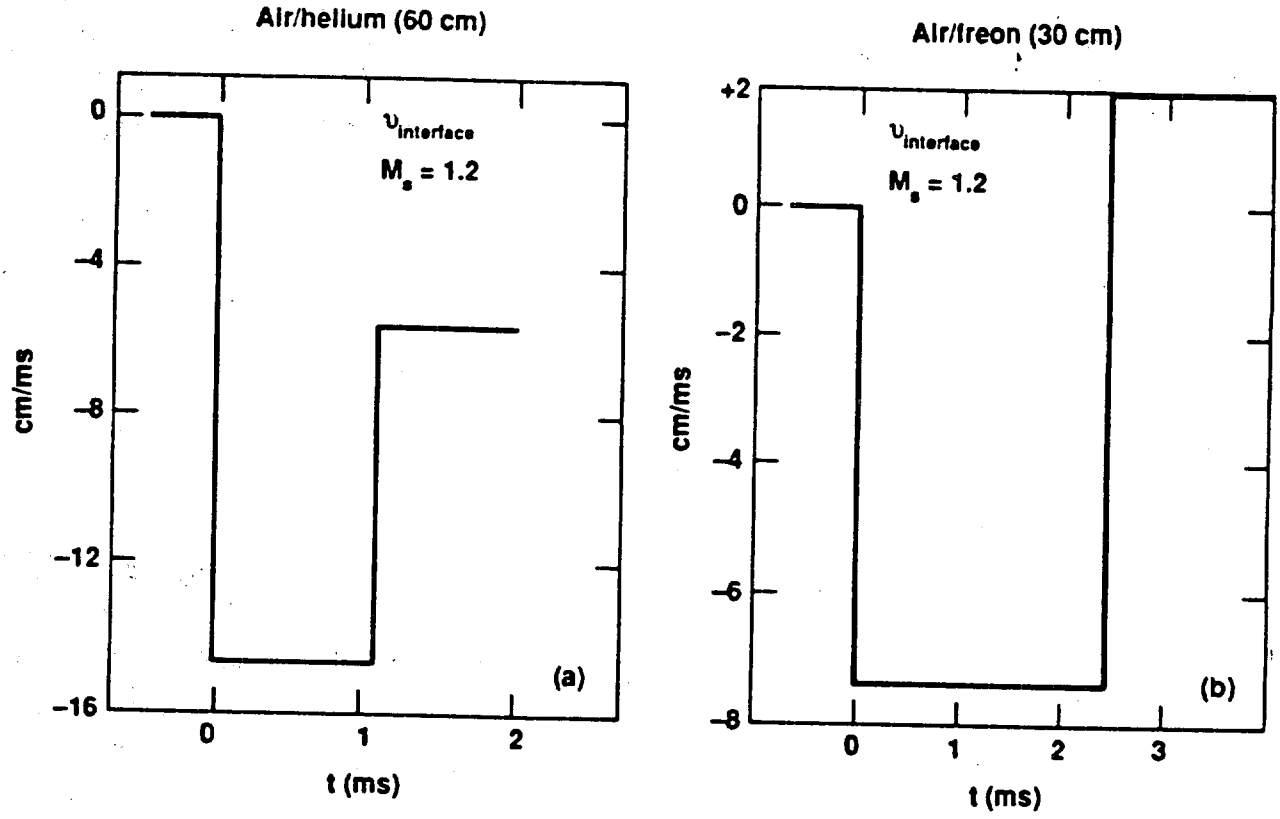
Air/helium (60 cm)
$v_{interface}$
M_s = 1.2
0
-4
-8
-12
-16
cm/ms
0
1
2
t (ms)
(a)
Air/freon (30 cm)
$v_{interface}$
M_s = 1.2
+2
0
-2
-4
-6
-8
cm/ms
0
1
2
3
t (ms)
(b)

Fig. 2

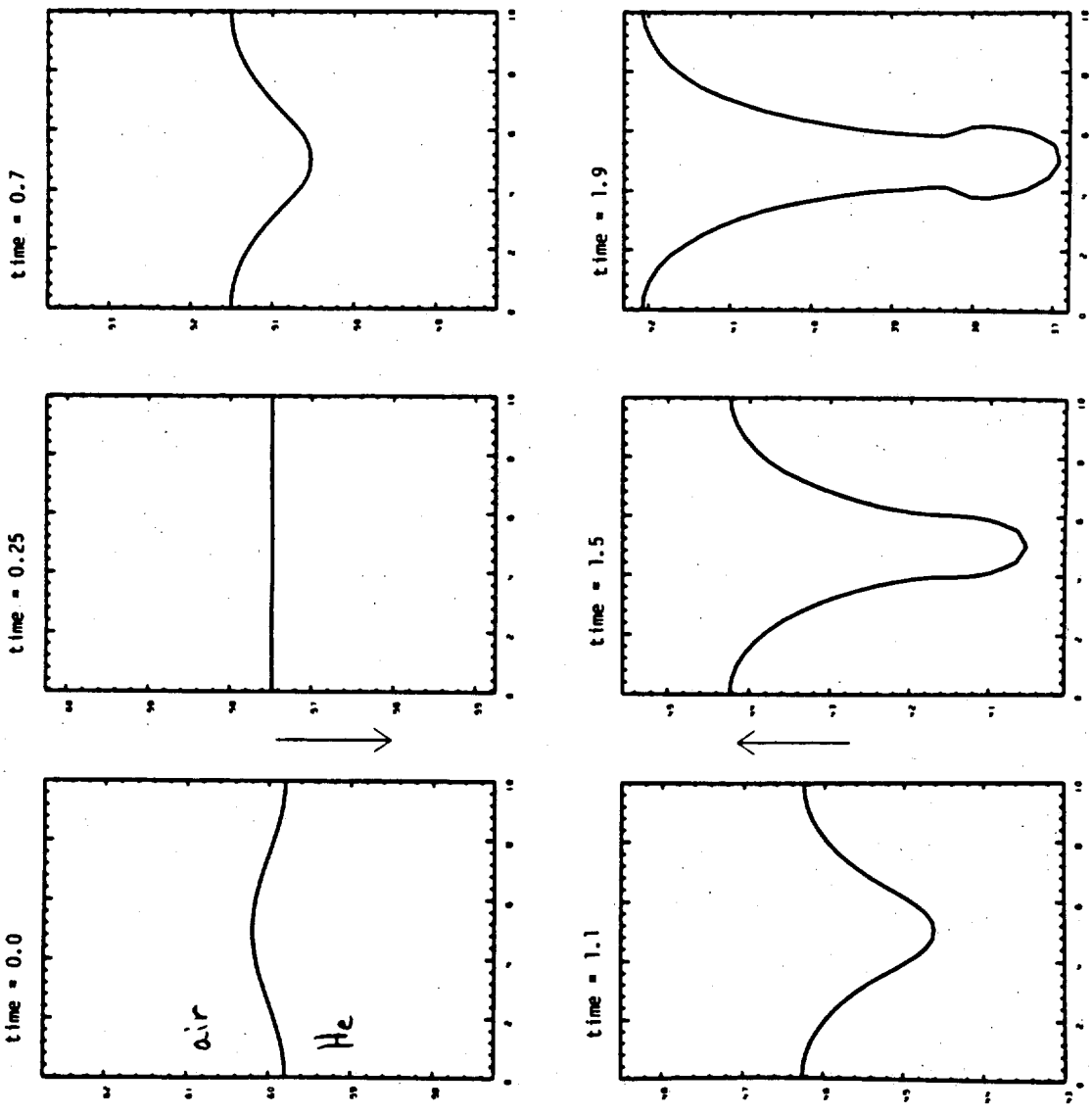

Fig. 3

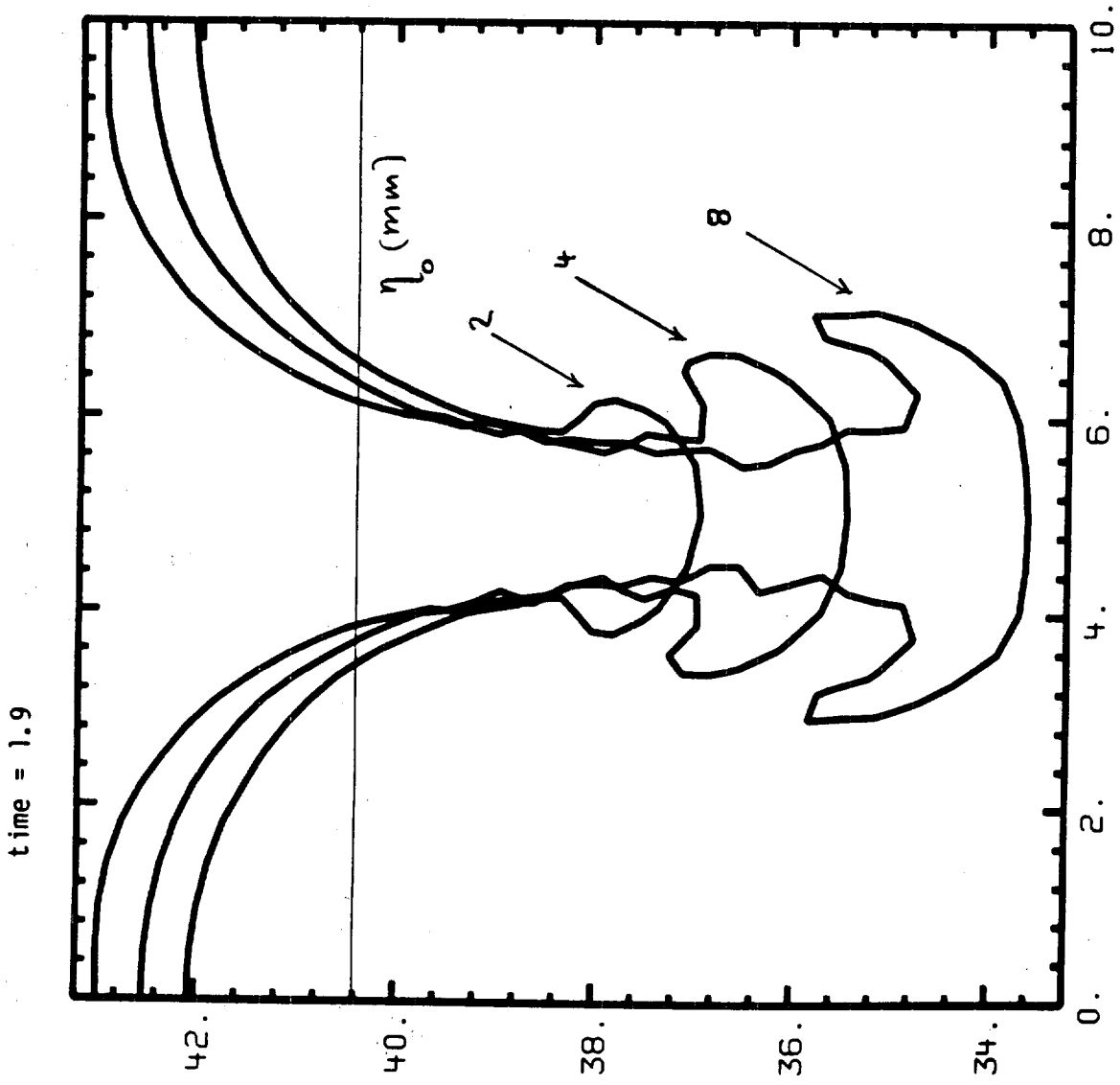

Fig. 5

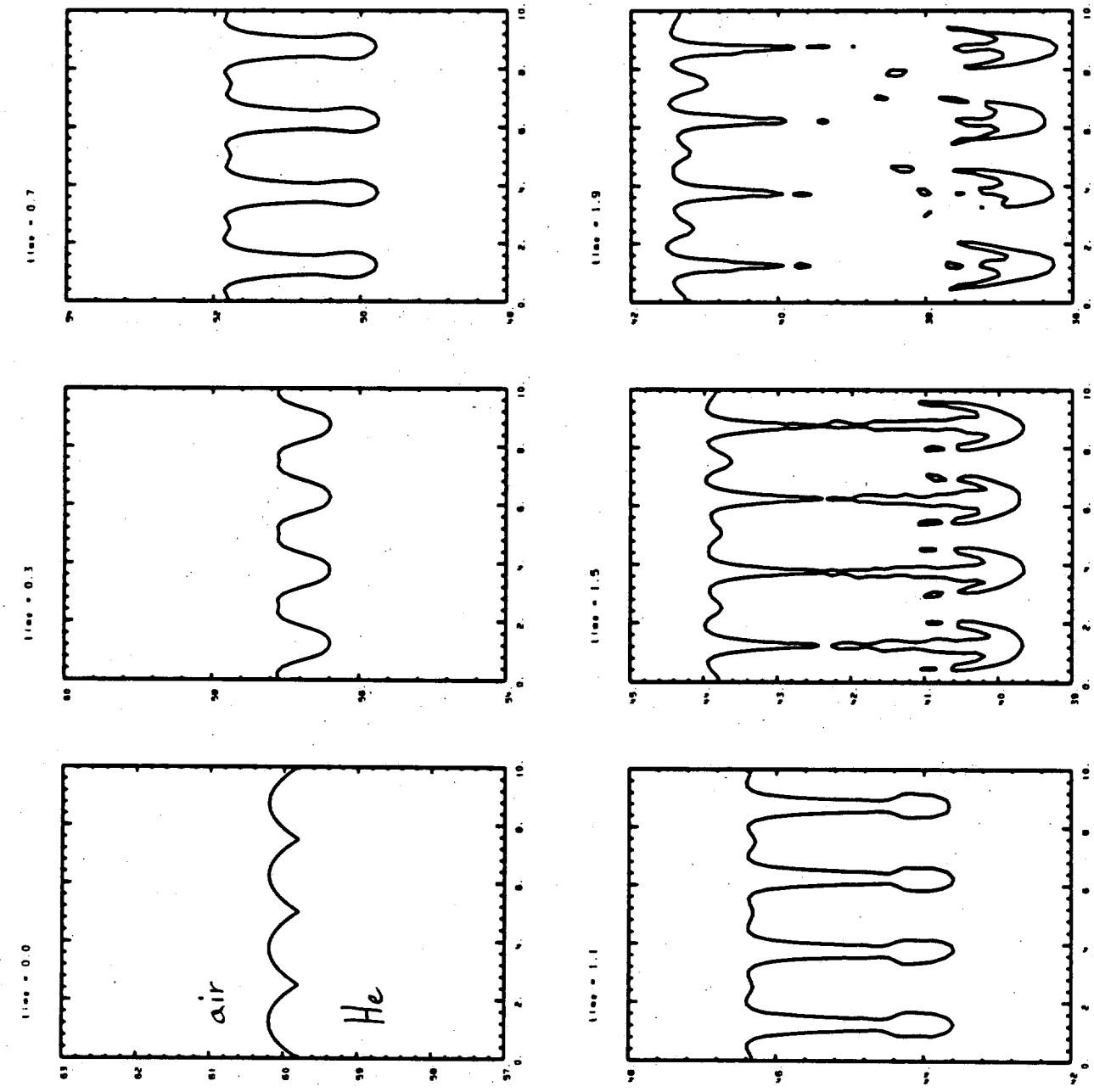

Fig. 9

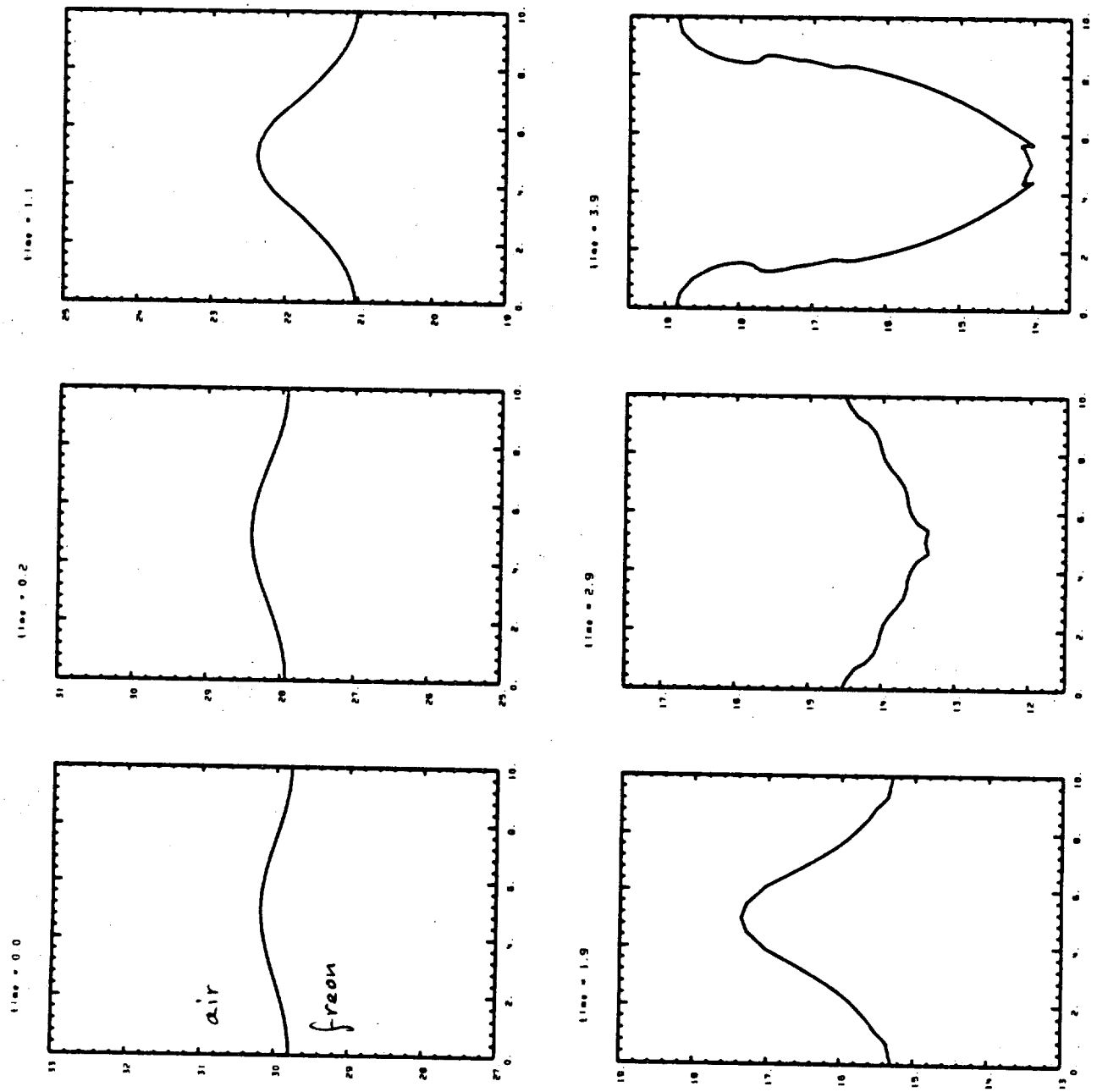

Fig. 12

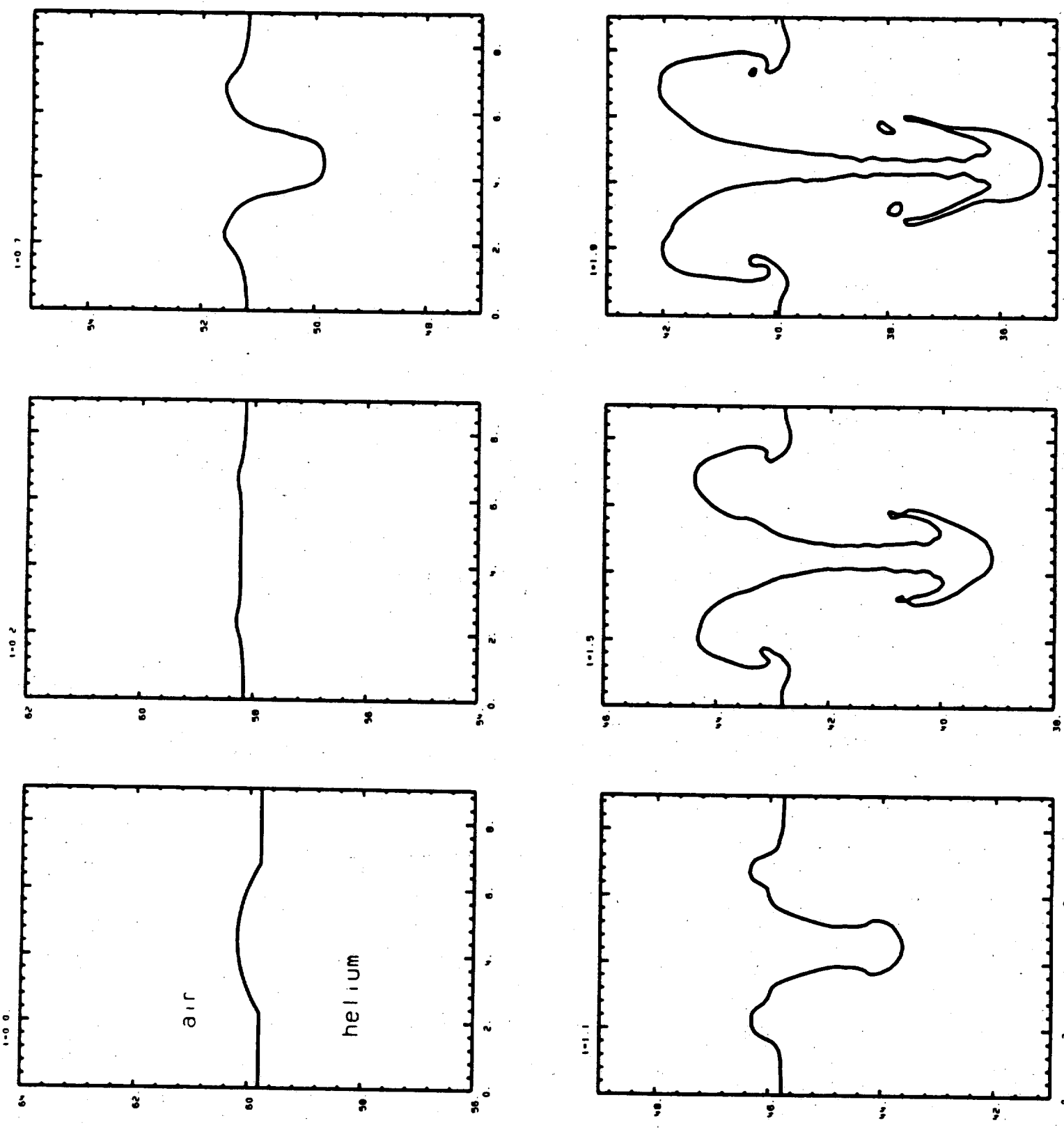

Fig. 22

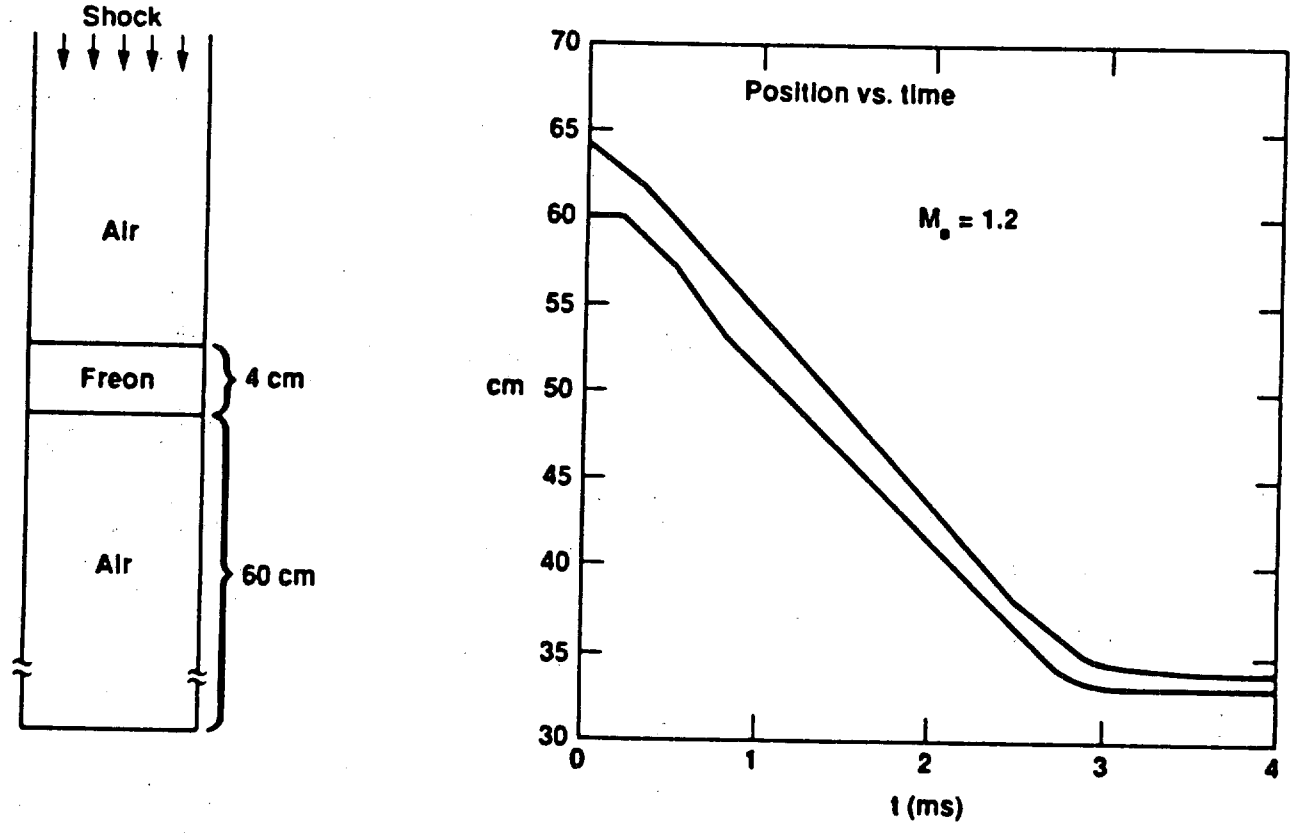
Shock
Air
Freon
4 cm
Air
60 cm
Position vs. time
M_s = 1.2
cm
70
65
60
55
50
45
40
35
30
0
1
2
3
4
t (ms)

Fig. 15

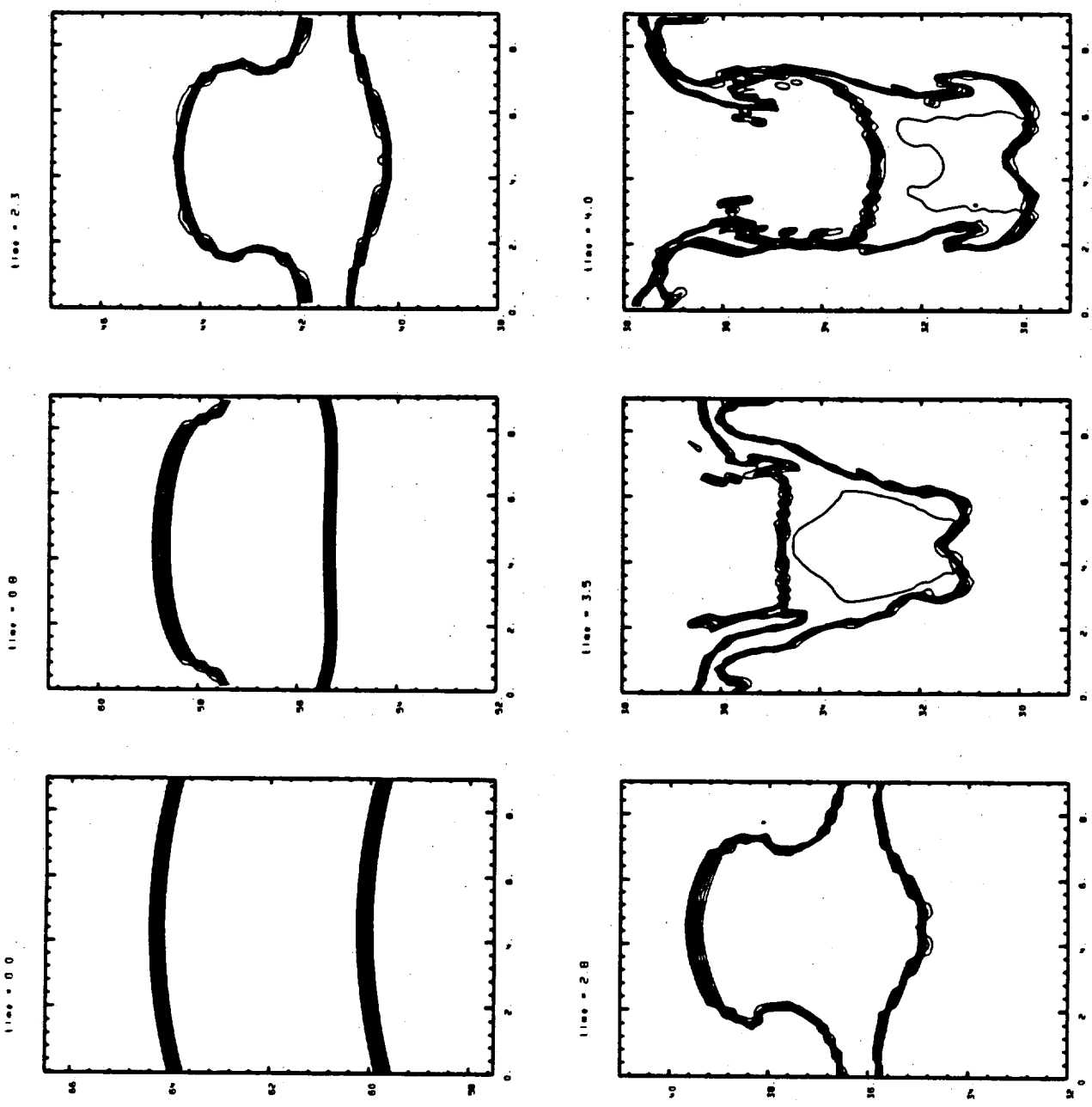

Fig. 17

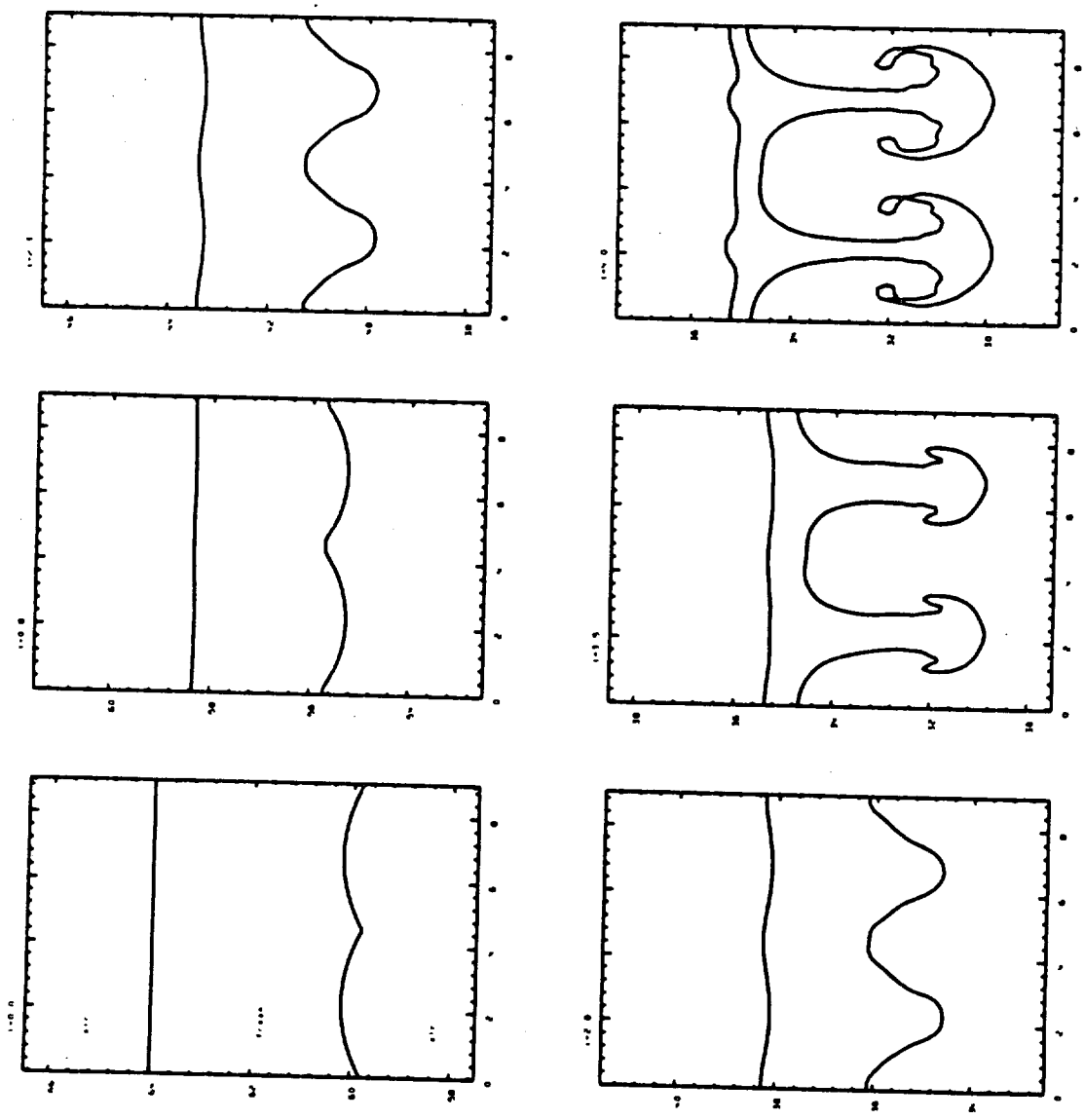

Fig. 19

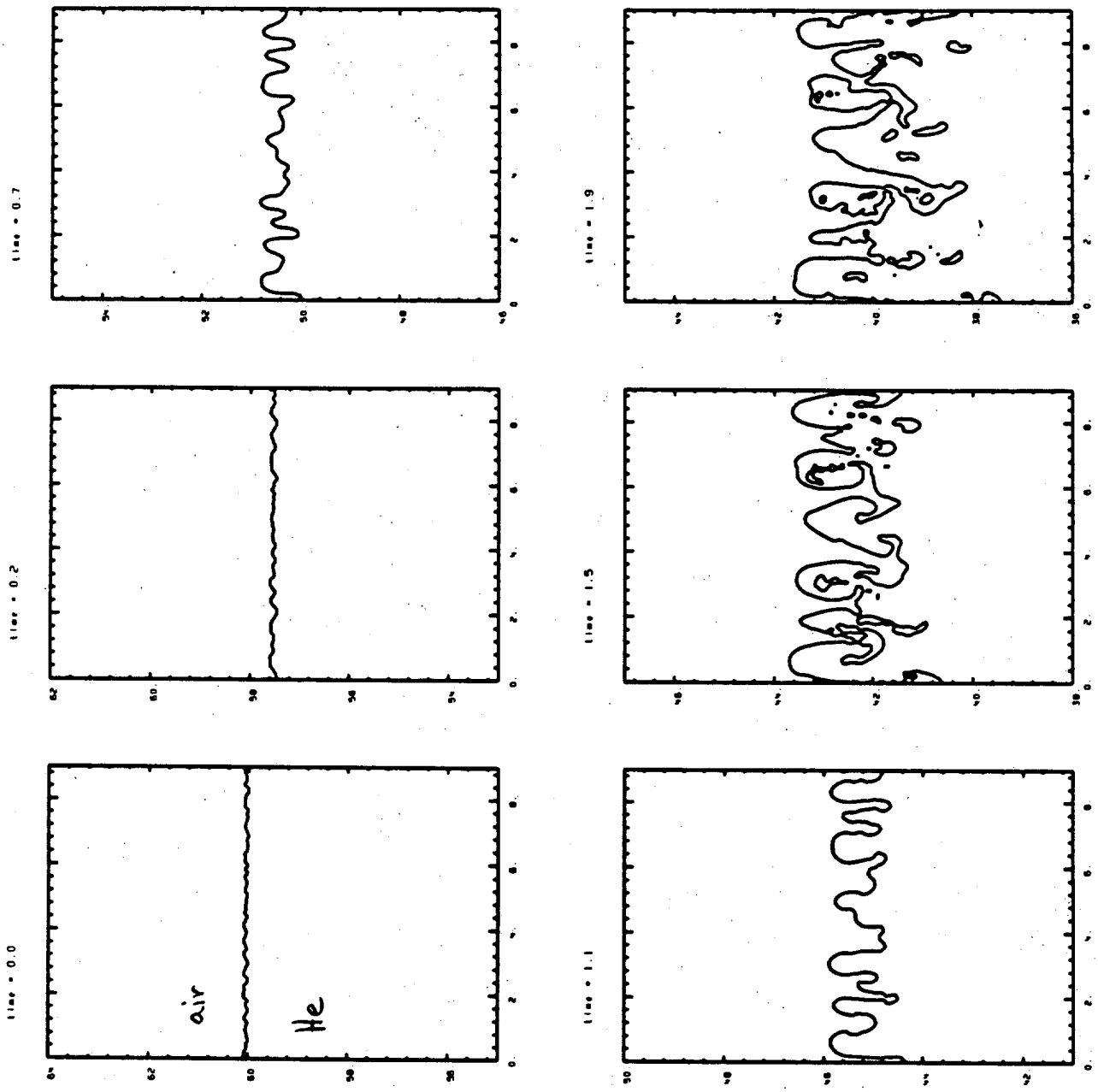

Fig. 27

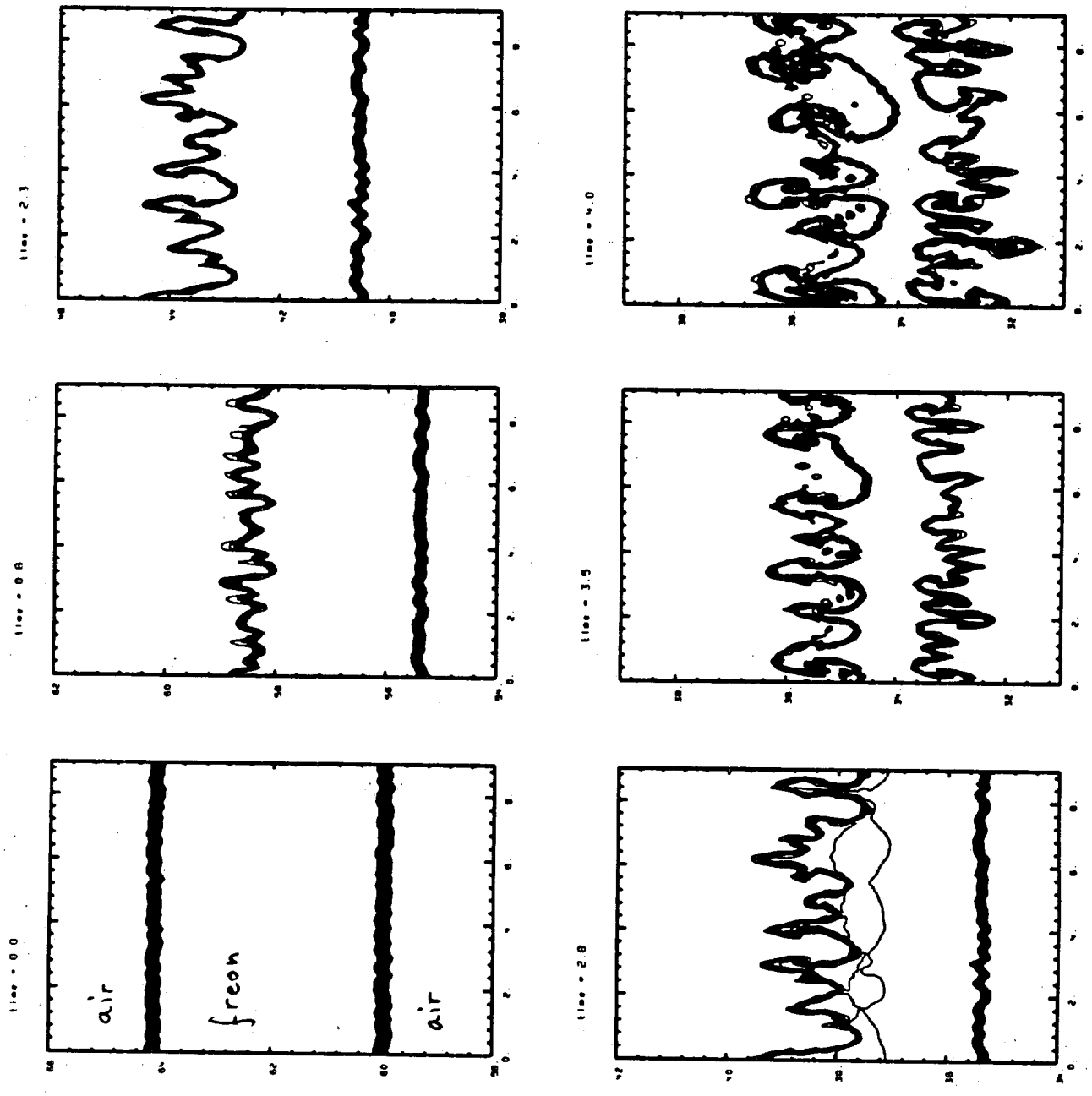

Fig. 40

TEST PROBLEMS: TP6A and TP6B*

These problems were run on a 1-D Lagrangean hydro calculation with a dynamic mix model implemented by W. P. Crowley. The model has amplitude growth equations based on a model by Layzer (1955) and suggested by D. Youngs' rocket sled experiments at AWE-Aldermaston in that the amplitudes grow as:

$$h = \alpha g t^2,$$

where α is the Atwood number and g is the acceleration.

Thus, the early initial time development of the amplitude is ignored and the model seeks to match the moderate time evolution of the perturbation with correct limits to the growth of the amplitude in the small and large limits. The presence of shocks is accommodated by monitoring the quantity, αg, and examining various cases.

The growth of the amplitude leads to concomitant mass and energy exchange across zones to simulate an evolving mix layer. Mass mixing is done in proportion to the growth of the spike and bubble amplitudes. However, the code does not currently allow for continued calculation of the spike/bubble amplitude beyond the thickness of a region.

Inasmuch, as the calculation was 1-D, no effort was made to seriously consider explicit initial single or multi-wave length or amplitude initial conditions. The unperturbed and the mix calculations are compared.

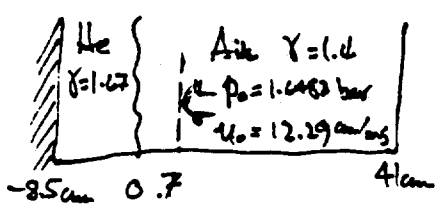

-tp6a-

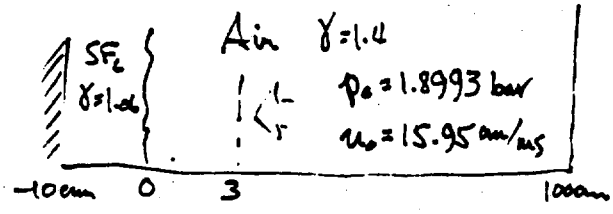

-tp6b-

Ned Dairiki

*This work was performed under the auspices of the U.S. Department of Energy by Lawrence Livermore National Laboratory under contract No. W-7405-Eng-48. MISC-4953.

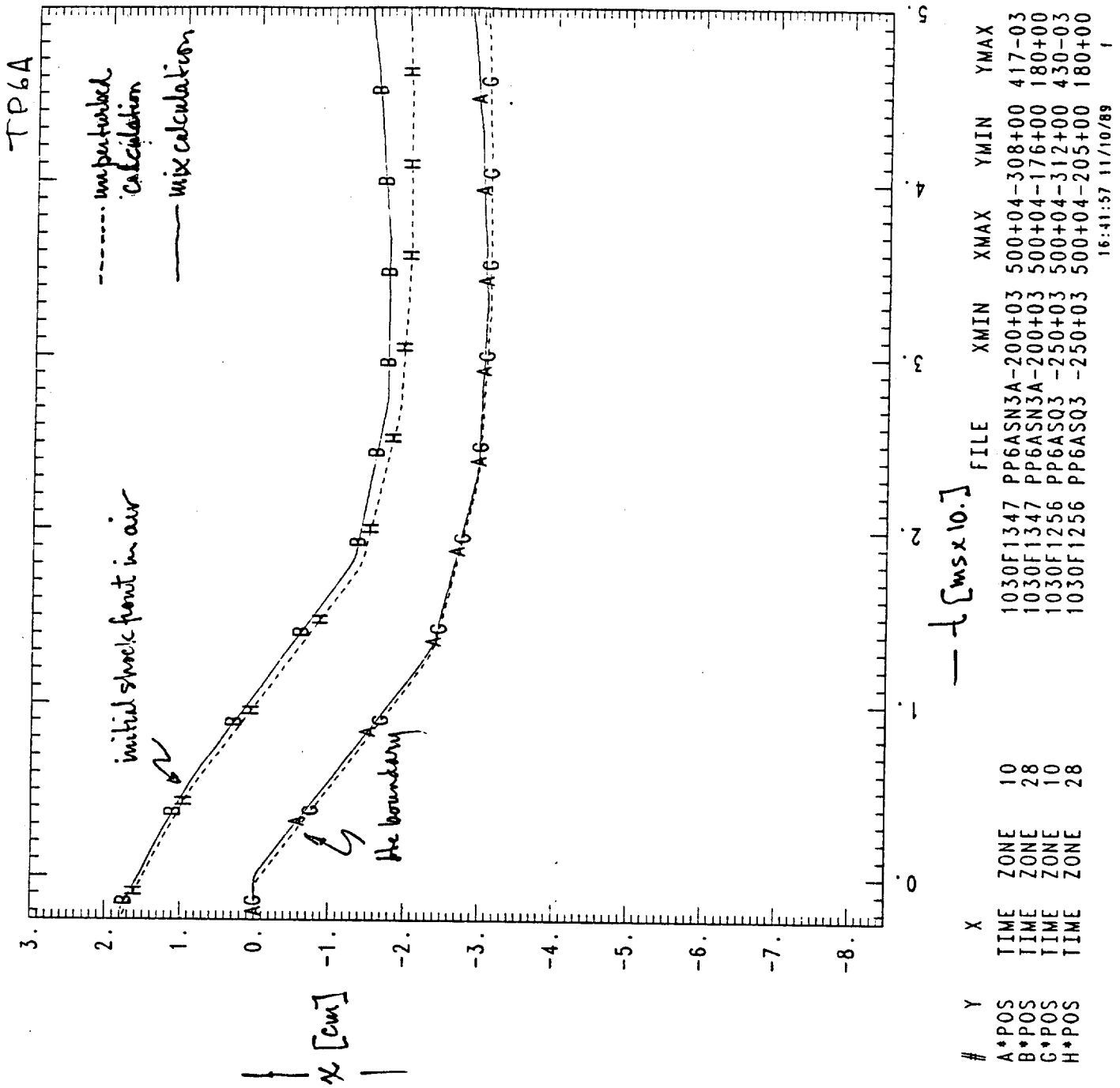
TP6A
unperturbed calculation
mix calculation
initial shock front in air
the boundary
x [cm]
t [ms x 10.]
Y X FILE XMIN XMAX YMIN YMAX
A*POS TIME ZONE 10 1030F1347 PP6ASN3A -200+03 500+04 -308+00 417-03
B*POS TIME ZONE 28 1030F1347 PP6ASN3A -200+03 500+04 -176+00 180+00
C*POS TIME ZONE 10 1030F1256 PP6ASQ3 -250+03 500+04 -312+00 430-03
H*POS TIME ZONE 28 1030F1256 PP6ASQ3 -250+03 500+04 -205+00 180+00
16:41:57 11/10/89 1

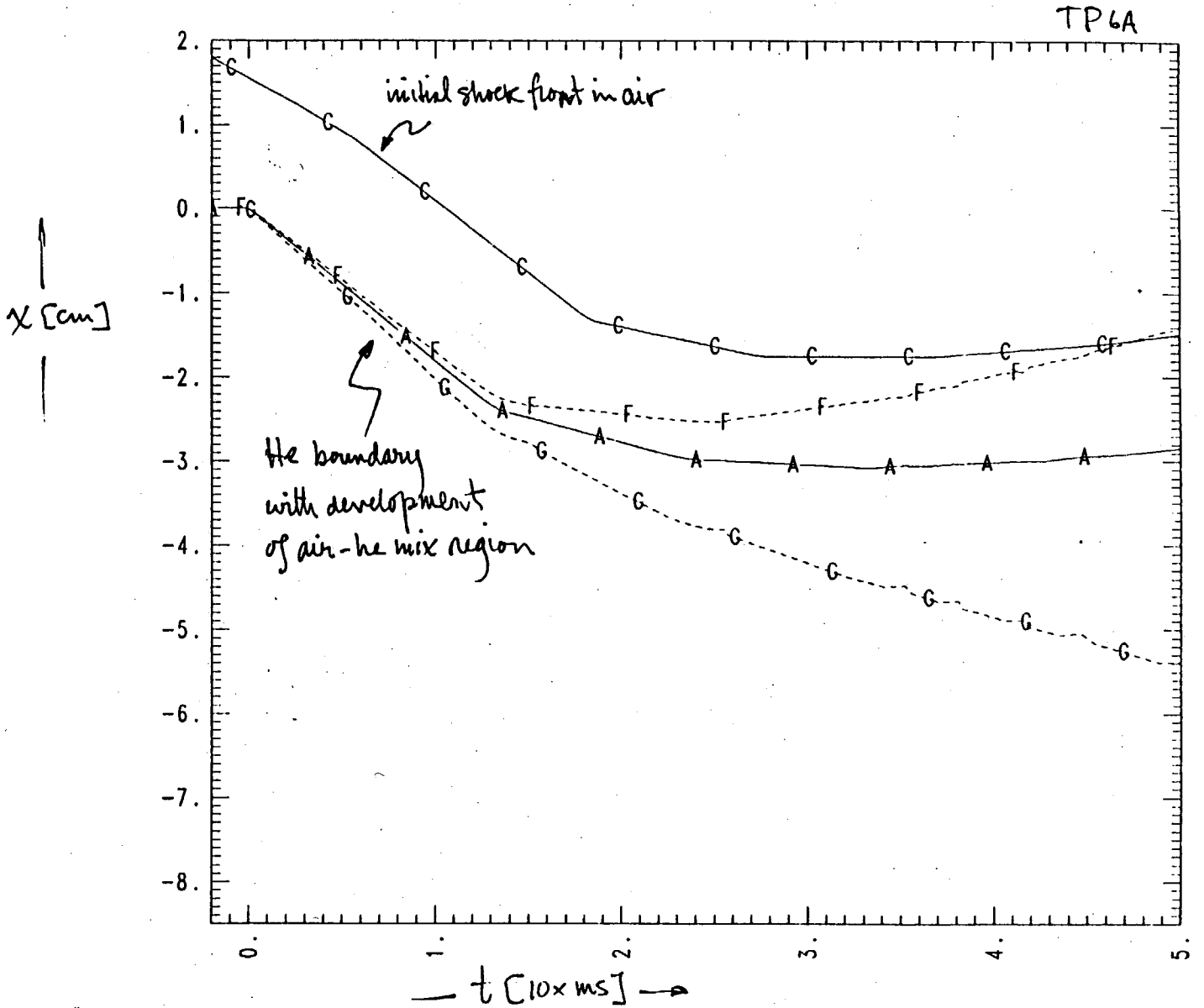

#	Y	X			FILE	XMIN	XMAX	YMIN	YMAX
A	*POS	TIME	ZONE	10	1030F1347	PP6ASN3A	-200+03	500+04	-308+00	417-03
B	*POS	TIME	ZONE	69	1030F1347	PP6ASN3A	-200+03	500+04	348+01	413+01
C	*POS	TIME	ZONE	28	1030F1347	PP6ASN3A	-200+03	500+04	-176+00	180+00
F	SUM	A	D				-200+03	500+04	-254+00	443-03
G	DIF	A	E				-200+03	500+04	-539+00	381-03

13:52:48 10/30/89 1

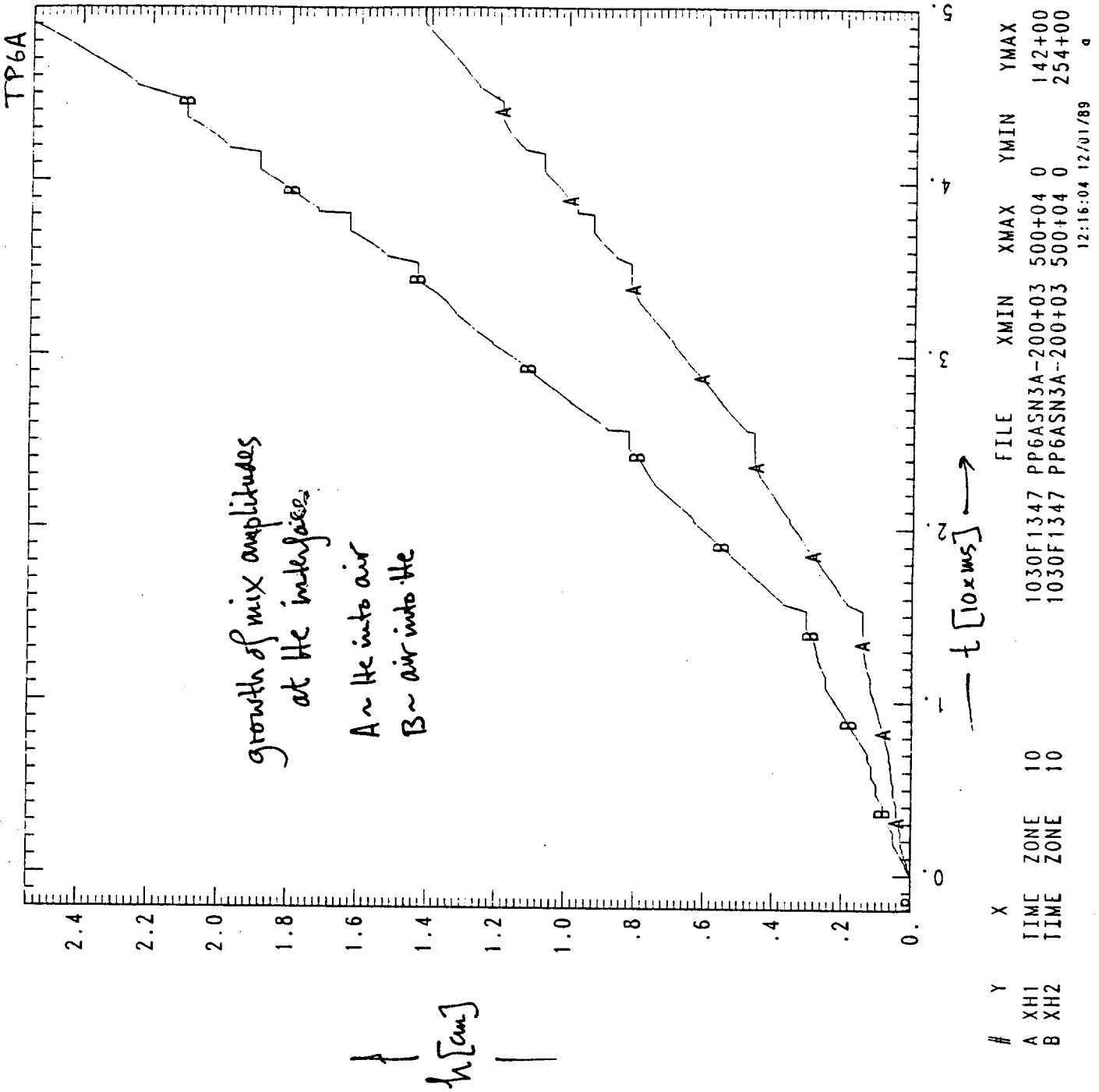
TP6A
growth of mix amplitudes
at the interfaces
A ~ He into air
B ~ air into He
h [cm]
t [10 x ms]
Y X FILE XMIN XMAX YMIN YMAX
A XH1 TIME ZONE 10 1030F1347 PP6ASN3A -200+03 500+04 0 142+00
B XH2 TIME ZONE 10 1030F1347 PP6ASN3A -200+03 500+04 0 254+00
12:16:04 12/01/89

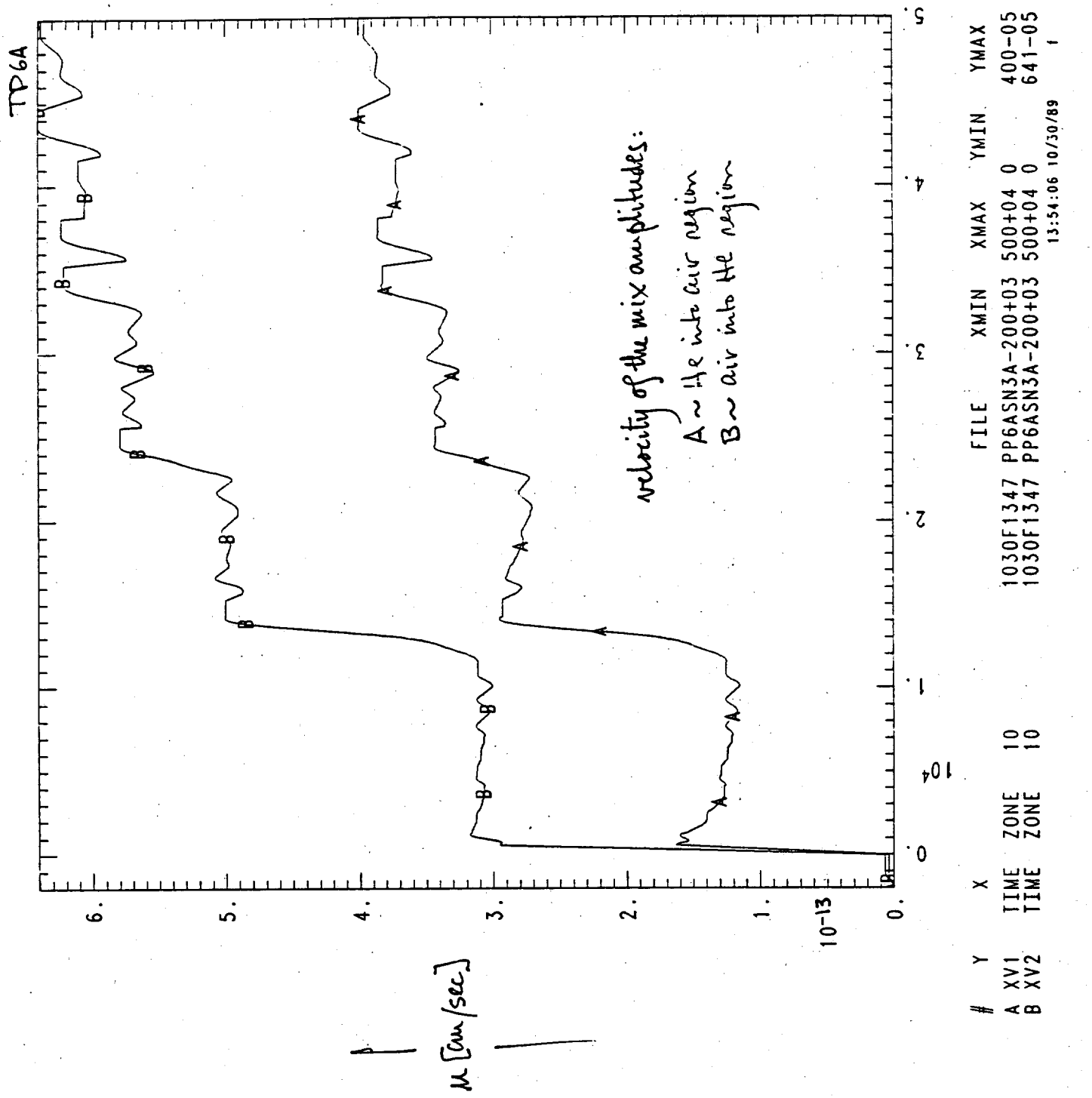
TP6A
velocity of the mix amplitudes:
A ~ He into air region
B ~ air into He region
u [cm/sec]
10⁻¹³
10⁴
FILE XMIN XMAX YMIN YMAX
1030F1347 PP6ASN3A-200+03 500+04 0 400-05
1030F1347 PP6ASN3A-200+03 500+04 0 641-05
13:54:06 10/30/89
Y X
A XV1 TIME ZONE 10
B XV2 TIME ZONE 10

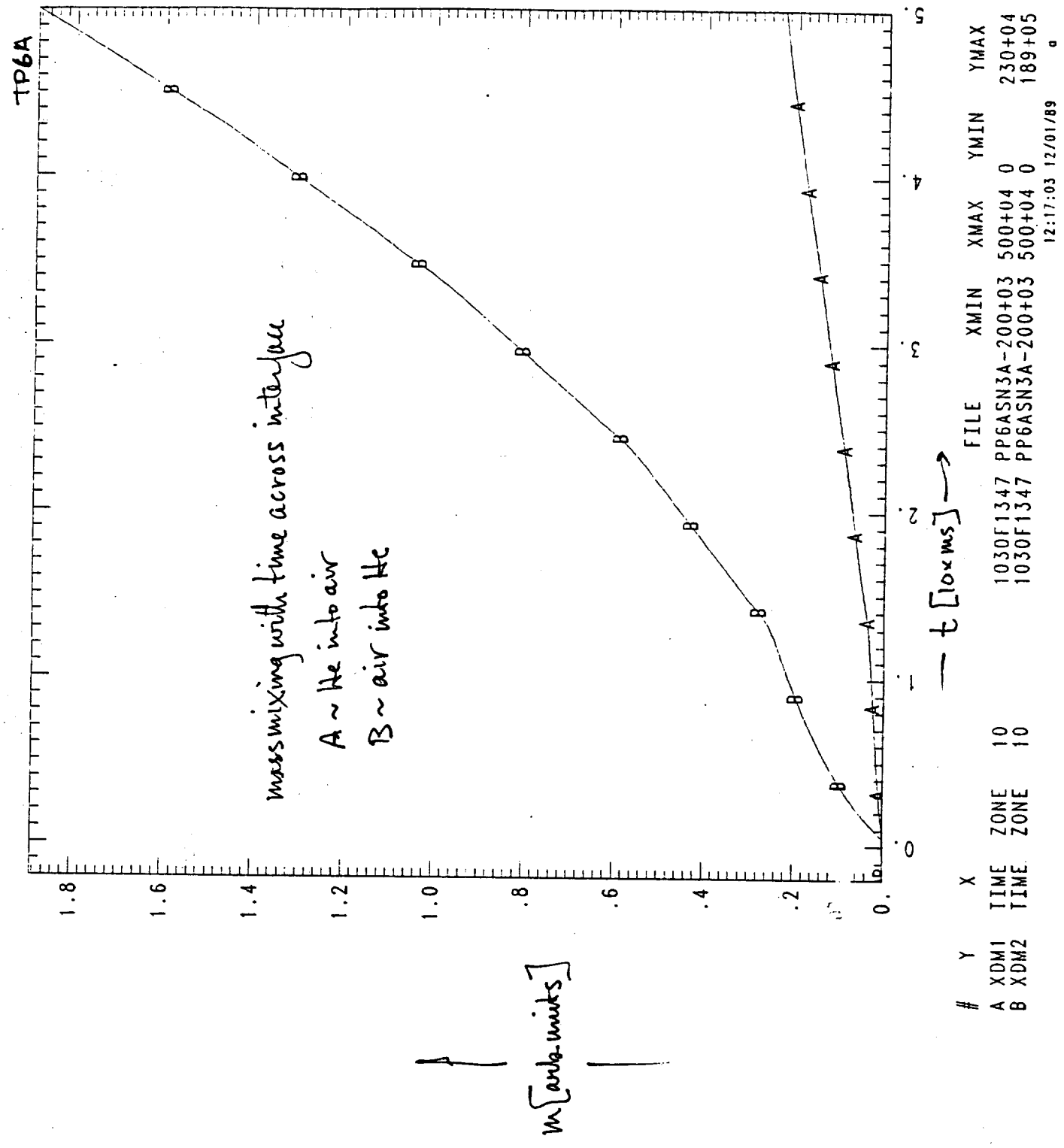
TP6A
mass mixing with time across interface
A ~ He into air
B ~ air into He
1 [arb. units]
t [10x ms]
Y X FILE XMIN XMAX YMIN YMAX
A XDM1 TIME ZONE 10 1030F1347 PP6ASN3A-200+03 500+04 0 230+04
B XDM2 TIME ZONE 10 1030F1347 PP6ASN3A-200+03 500+04 0 189+05
12:17:03 12/01/89

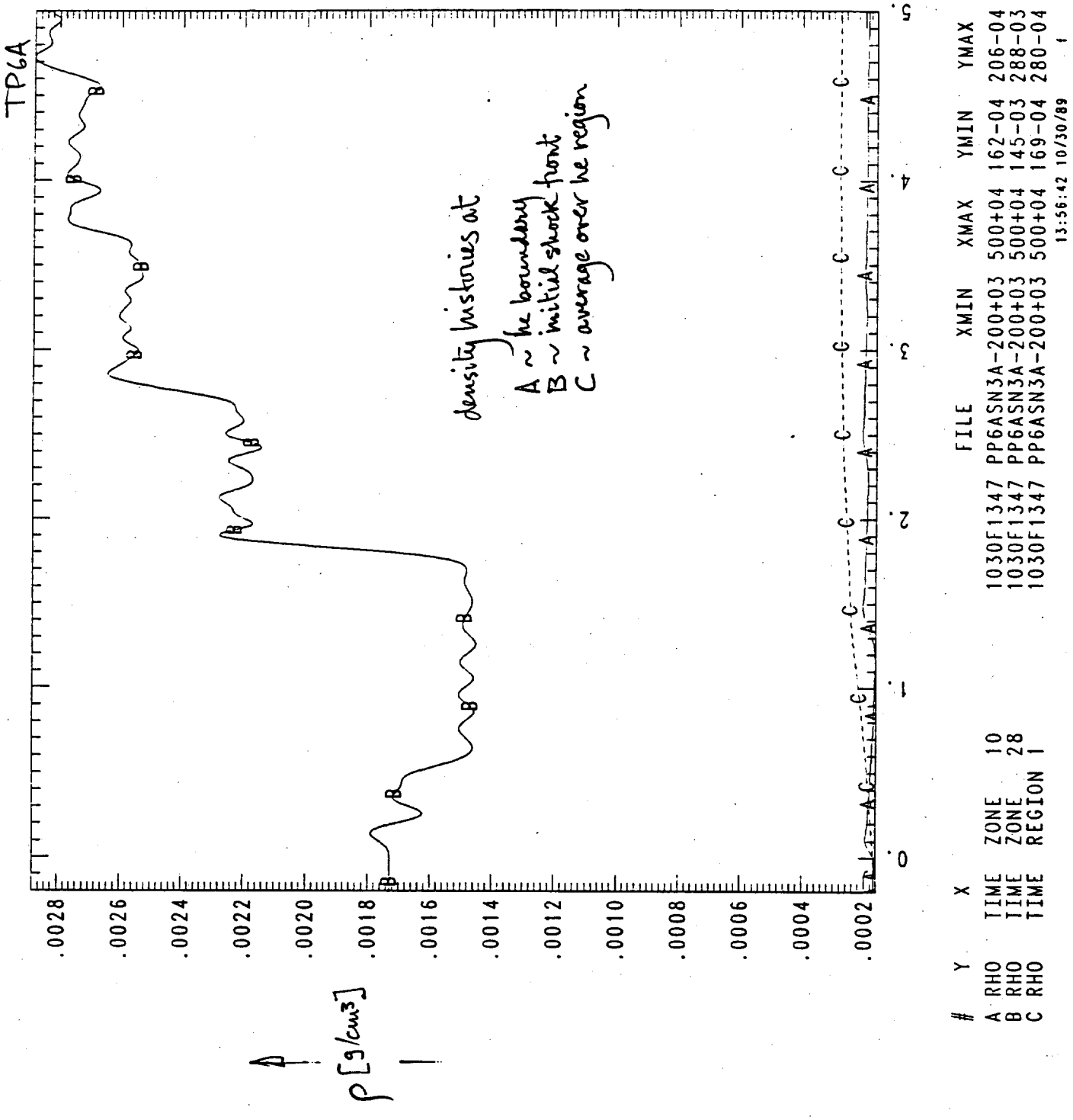
TP6A
density histories at
A ~ the boundary
B ~ initial shock front
C ~ average over he region
ρ [g/cm³]
.0028
.0026
.0024
.0022
.0020
.0018
.0016
.0014
.0012
.0010
.0008
.0006
.0004
.0002
0.
1.
2.
3.
4.
5.
Y X FILE XMIN XMAX YMIN YMAX
A RHO TIME ZONE 10 1030F1347 PP6ASN3A-200+03 500+04 162-04 206-04
B RHO TIME ZONE 28 1030F1347 PP6ASN3A-200+03 500+04 145-03 288-03
C RHO TIME REGION 1 1030F1347 PP6ASN3A-200+03 500+04 169-04 280-04
13:56:42 10/30/89 1

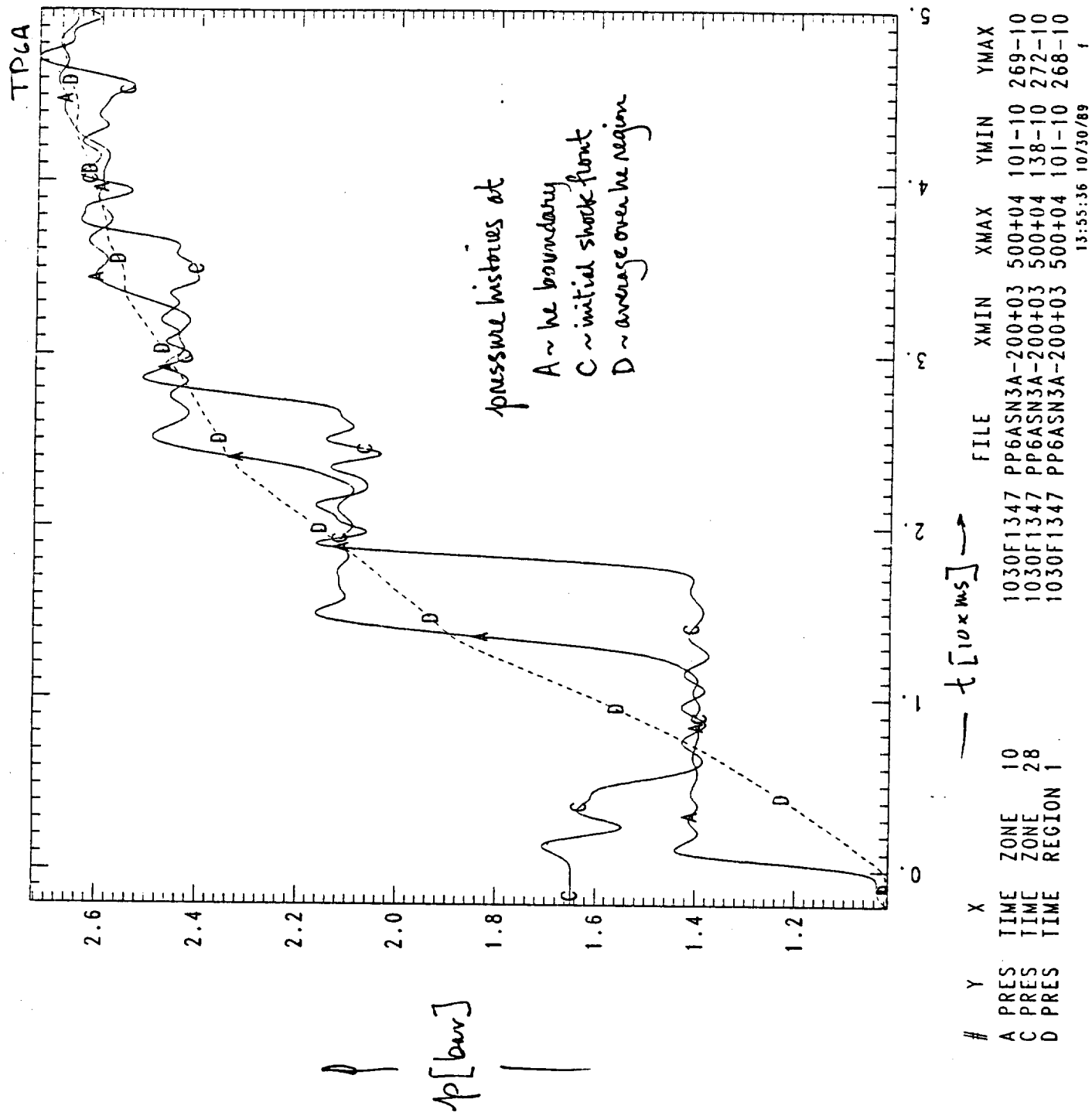
TP6A
pressure histories at
A ~ the boundary
C ~ initial shock front
D ~ average over the region
ρ [bar]
t [10 x ms]
Y X FILE XMIN XMAX YMIN YMAX
A PRES TIME ZONE 10 1030F1347 PP6ASN3A-200+03 500+04 101-10 269-10
C PRES TIME ZONE 28 1030F1347 PP6ASN3A-200+03 500+04 138-10 272-10
D PRES TIME REGION 1 1030F1347 PP6ASN3A-200+03 500+04 101-10 268-10
13:55:36 10/30/89 1

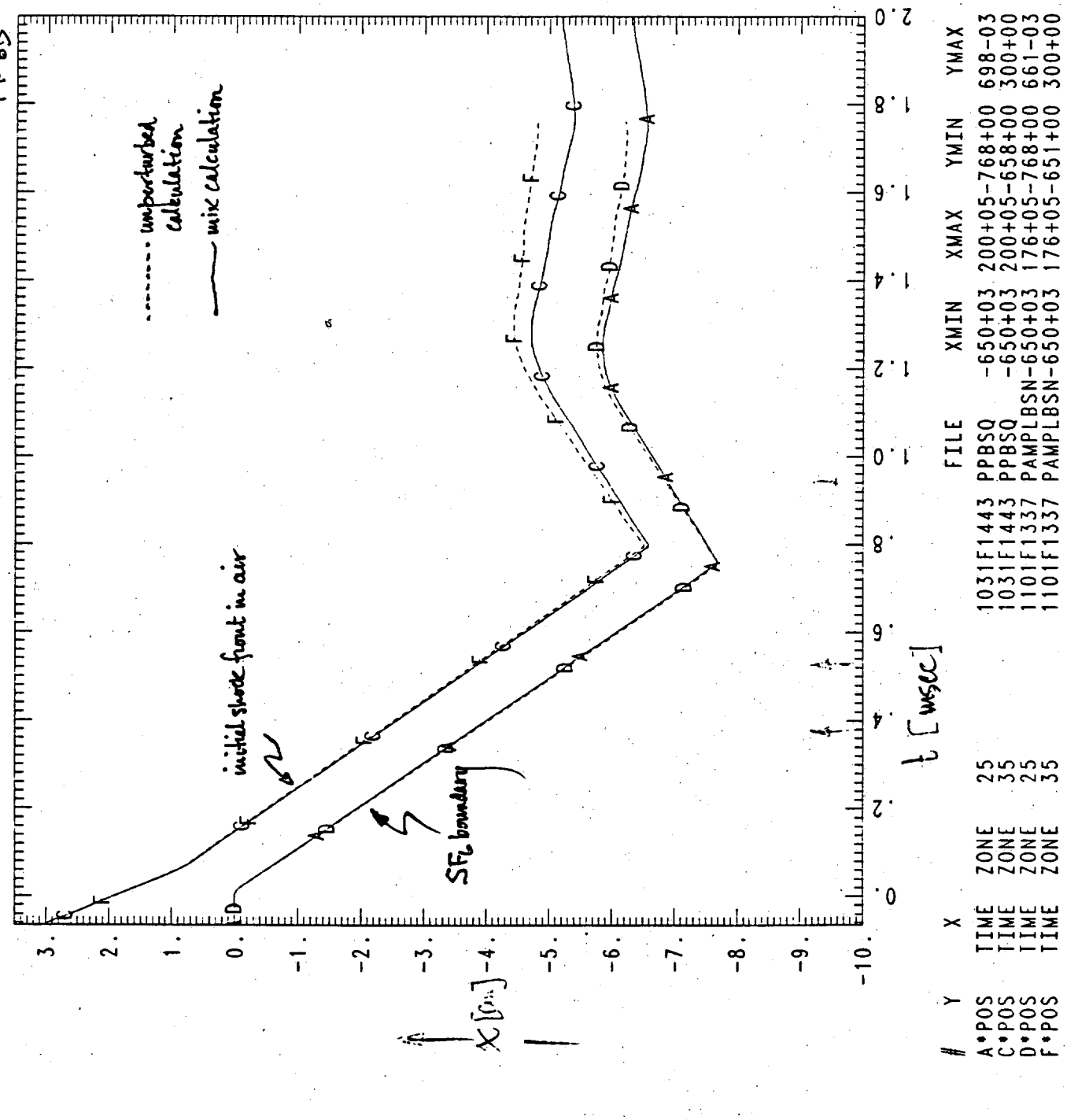
TP 68
unperturbed calculation
mix calculation
initial shock front in air
SF6 boundary
x [cm]
t [msec]
Y X FILE XMIN XMAX YMIN YMAX
A*POS TIME ZONE 25 1031F1443 PPBSQ -650+03 200+05-768+00 698-03
C*POS TIME ZONE 35 1031F1443 PPBSQ -650+03 200+05-658+00 300+00
D*POS TIME ZONE 25 1101F1337 PAMPLBSN-650+03 176+05-768+00 661-03
F*POS TIME ZONE 35 1101F1337 PAMPLBSN-650+03 176+05-651+00 300+00
15:25:02 11/01/89

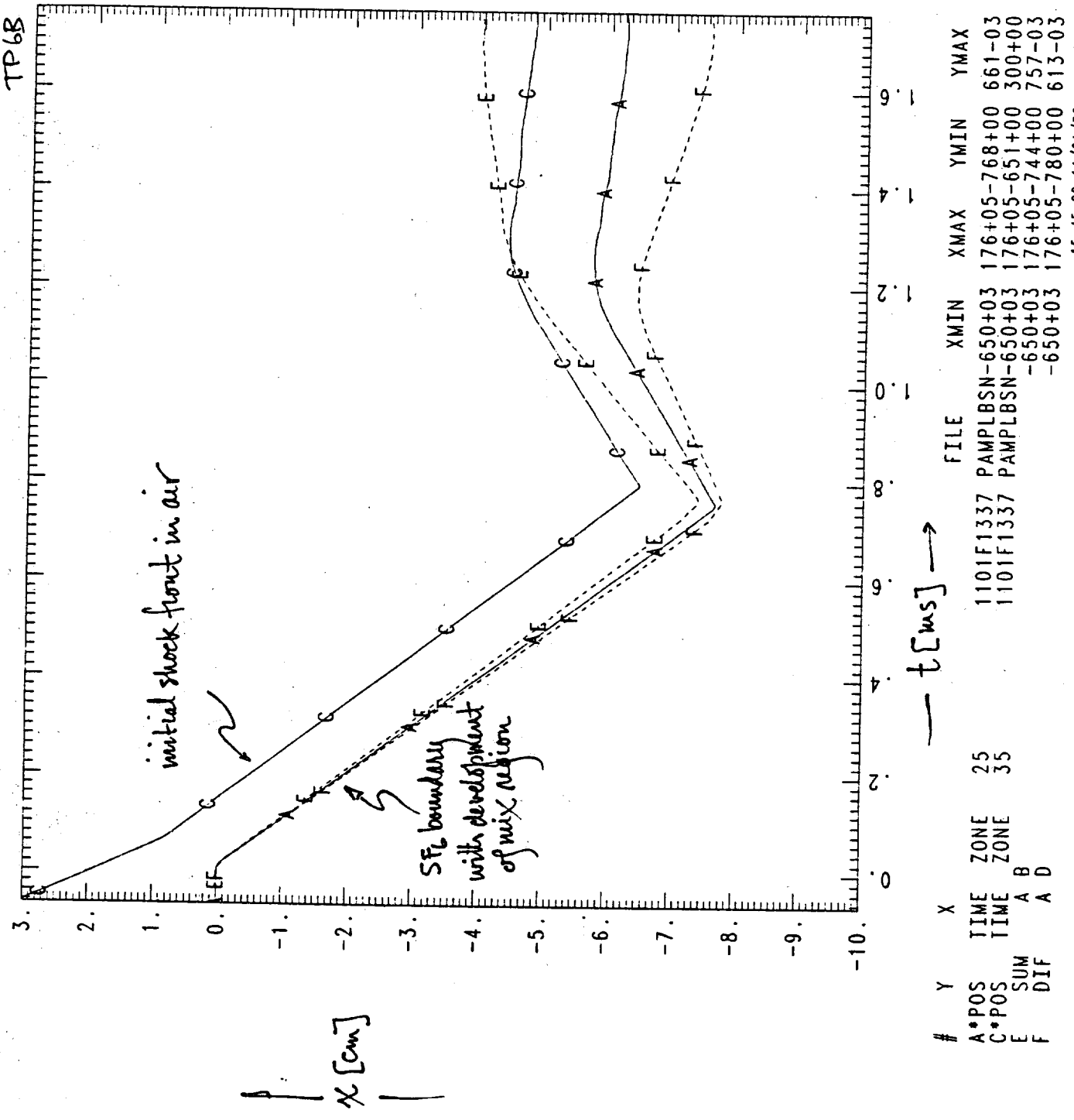
TP6B
initial shock front in air
SF6 boundary with development of mix region
x [cm]
t [ms]
Y X FILE XMIN XMAX YMIN YMAX
A*POS TIME ZONE 25 1101F1337 PAMPLBSN -650+03 176+05 -768+00 661-03
C*POS TIME ZONE 35 1101F1337 PAMPLBSN -650+03 176+05 -651+00 300+00
E SUM A B -650+03 176+05 -744+00 757-03
F DIF A D -650+03 176+05 -780+00 613-03
15:45:29 11/01/89

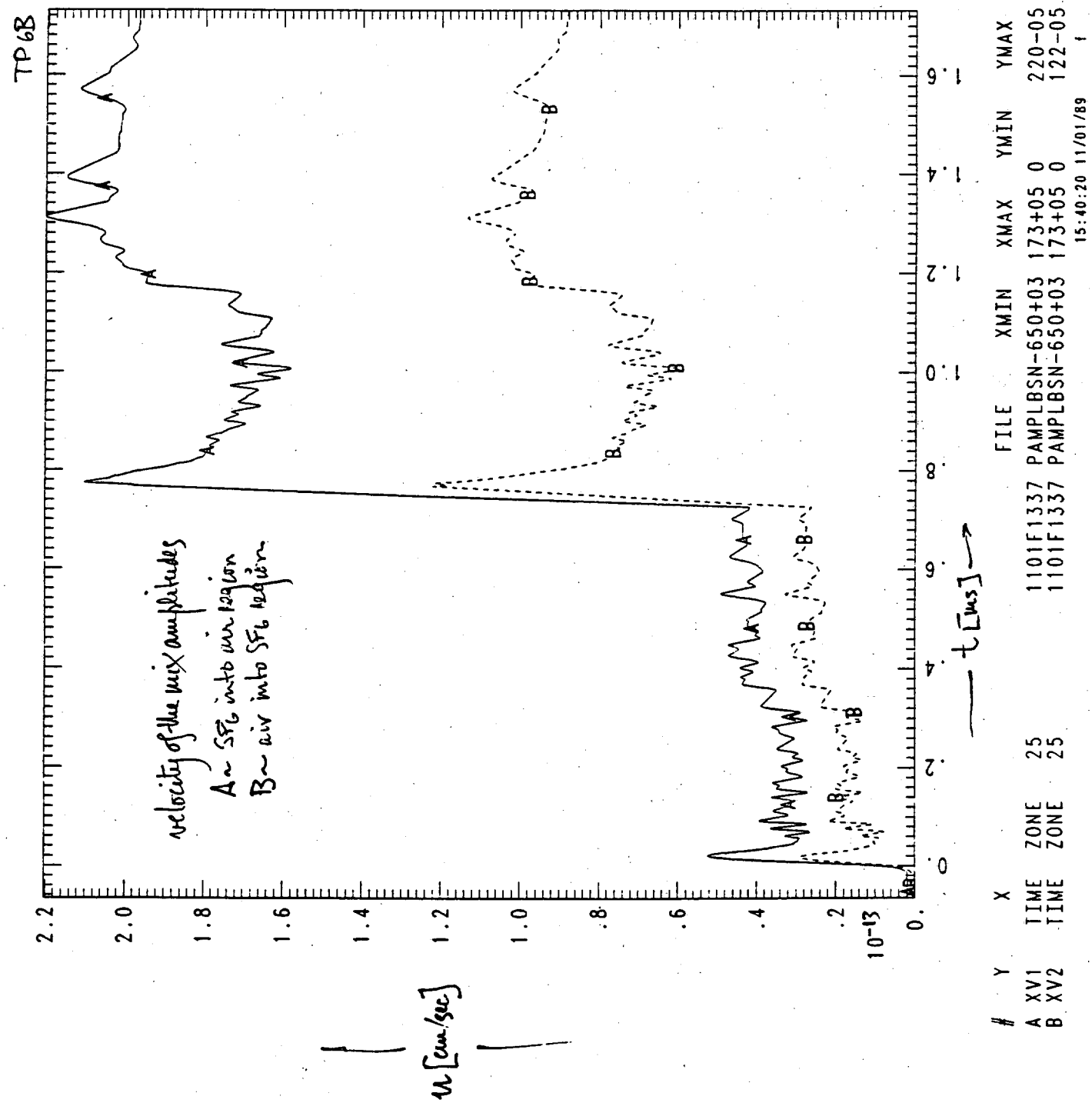
TP68
velocity of the mix/amplitudes
A ~ SF6 into air region
B ~ air into SF6 region
u [cm/sec]
t [ms]
FILE XMIN XMAX YMIN YMAX
1101F1337 PAMPLBSN-650+03 173+05 0 220-05
1101F1337 PAMPLBSN-650+03 173+05 0 122-05
15:40:20 11/01/89
Y X
A XV1 TIME ZONE 25
B XV2 TIME ZONE 25

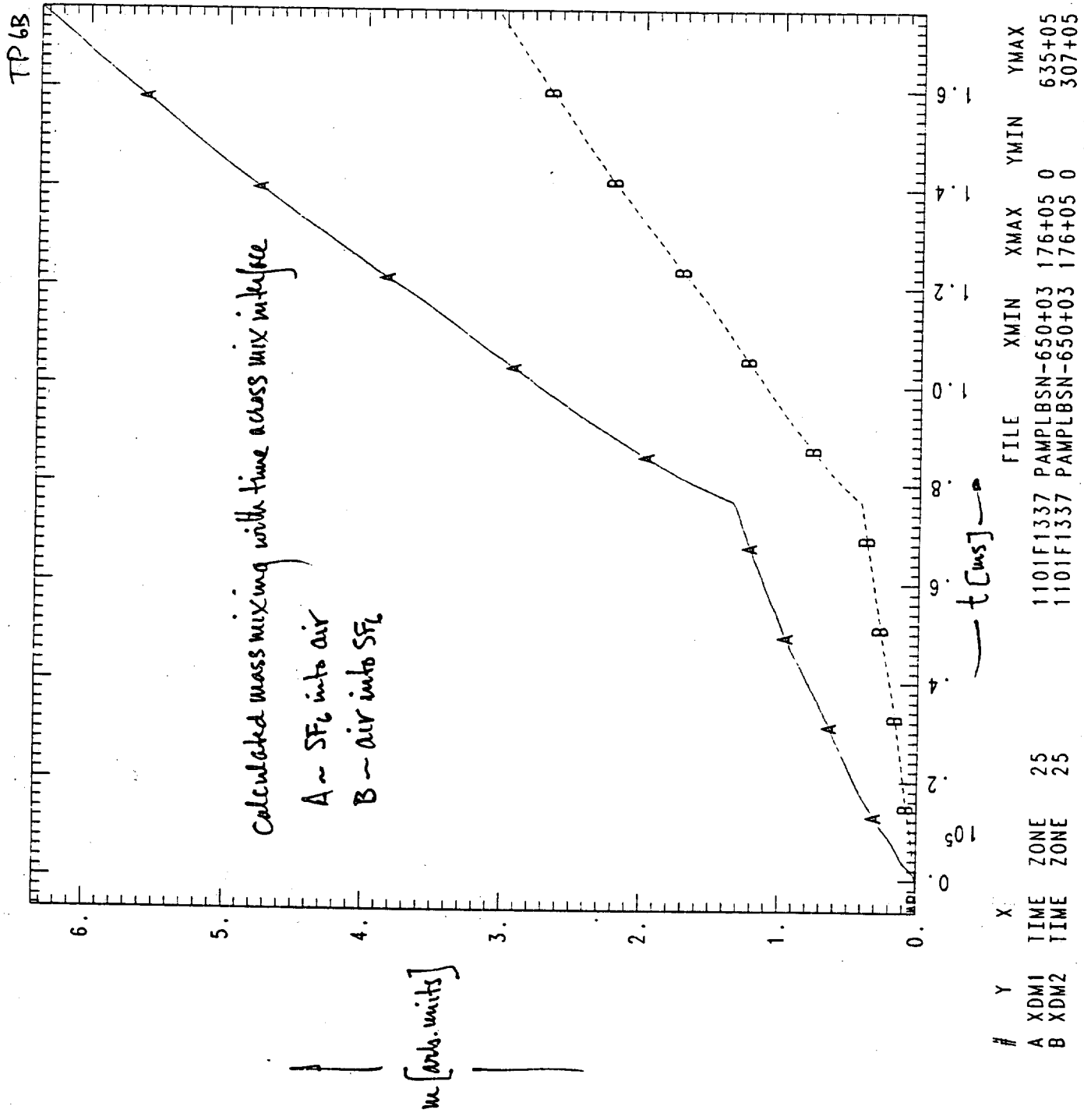
TP 6B
Calculated mass mixing with time across mix interface
A ~ SF6 into air
B ~ air into SF6
m [Arb. units]
t [ms]
0.
1.
2.
3.
4.
5.
6.
.2
.4
.6
.8
1.0
1.2
1.4
1.6
10^5
Y X FILE XMIN XMAX YMIN YMAX
A XDM1 TIME ZONE 25 1101F1337 PAMPLBSN-650+03 176+05 0 635+05
B XDM2 TIME ZONE 25 1101F1337 PAMPLBSN-650+03 176+05 0 307+05
15:42:35 11/01/89

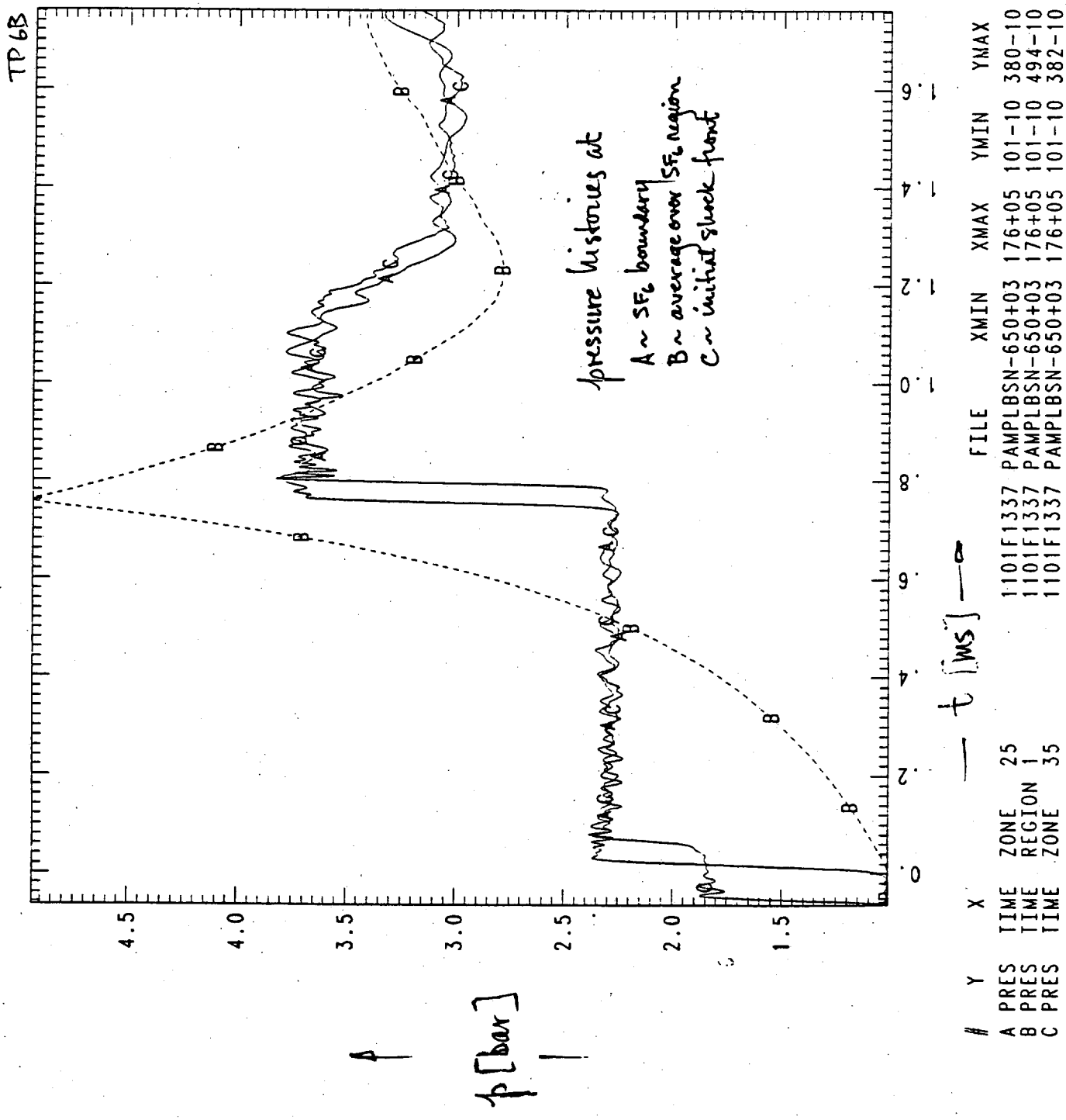
TP 68
pressure histories at
A ~ SF6 boundary
B ~ average over SF6 region
C ~ initial shock front
p [bar]
t [ms]
Y X FILE XMIN XMAX YMIN YMAX
A PRES TIME ZONE 25 1101F1337 PAMPLBSN-650+03 176+05 101-10 380-10
B PRES TIME REGION 1 1101F1337 PAMPLBSN-650+03 176+05 101-10 494-10
C PRES TIME ZONE 35 1101F1337 PAMPLBSN-650+03 176+05 101-10 382-10
15:32:55 11/01/89 1

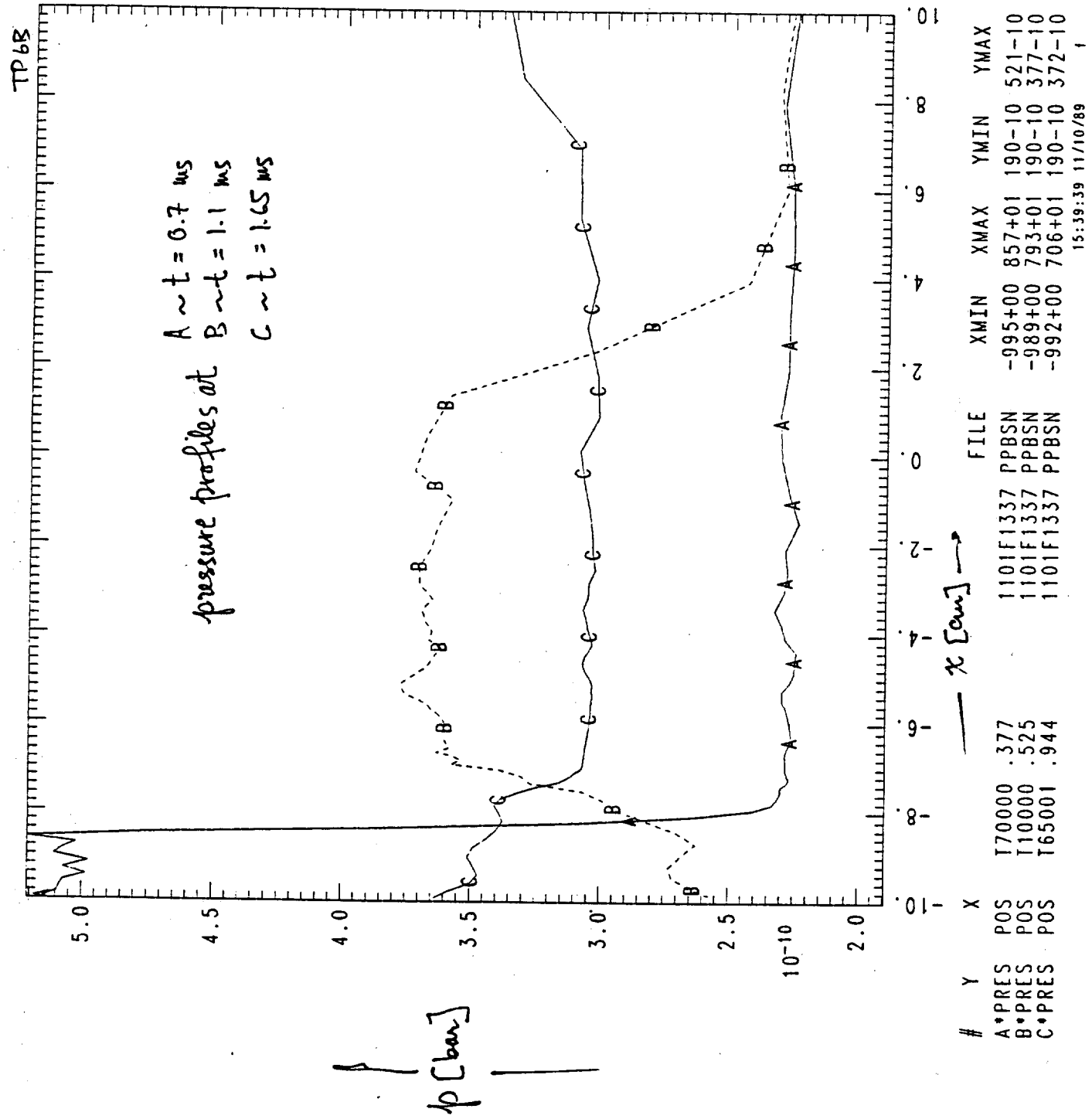
TP68
pressure profiles at A ~ t = 0.7 ms
B ~ t = 1.1 ms
C ~ t = 1.65 ms
p [bar]
x [cm]
Y X FILE XMIN XMAX YMIN YMAX
A*PRES POS T70000 .377 1101F1337 PPBSN -995+00 857+01 190-10 521-10
B*PRES POS T10000 .525 1101F1337 PPBSN -989+00 793+01 190-10 377-10
C*PRES POS T65001 .944 1101F1337 PPBSN -992+00 706+01 190-10 372-10
15:39:39 11/10/89

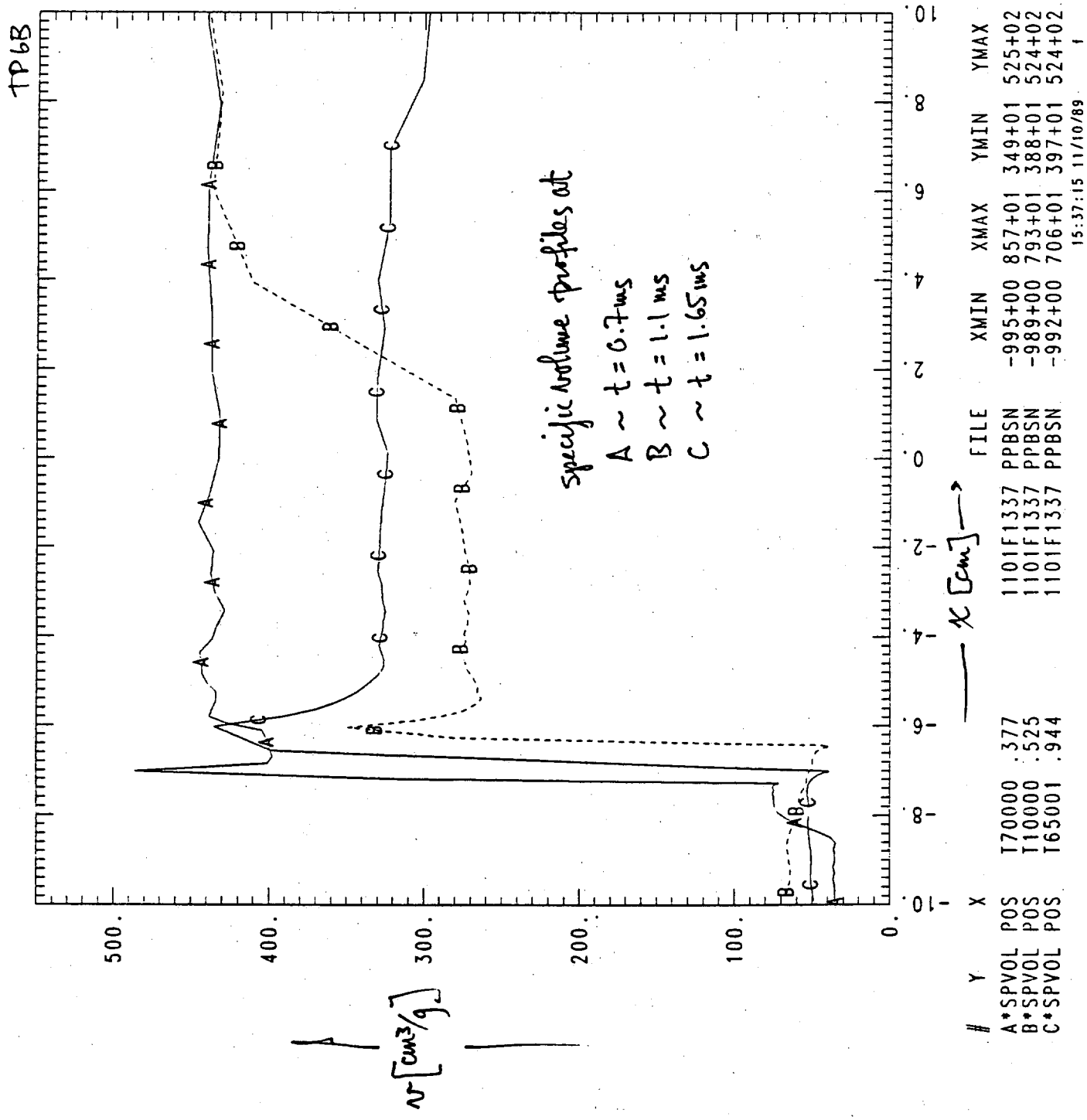
TP6B
specific volume profiles at
A ~ t = 0.7 ms
B ~ t = 1.1 ms
C ~ t = 1.65 ms
v [cm³/g]
x [cm]
Y X FILE XMIN XMAX YMIN YMAX
A*SPVOL POS T70000 .377 1101F1337 PPBSN -995+00 857+01 349+01 525+02
B*SPVOL POS T10000 .525 1101F1337 PPBSN -989+00 793+01 388+01 524+02
C*SPVOL POS T65001 .944 1101F1337 PPBSN -992+00 706+01 397+01 524+02
15:37:15 11/10/89 1

Proceedings of the 2nd International Workshop on the Physics of Compressible Turbulent Mixing
Pleasanton, USA
November 1989
Edited by V. Rupert

Asynchronous Free Lagrange Calculations FLIT2D

Peter G. Eltgroth
Lawrence Livermore National Laboratory
L-298
Livermore, CA 94550

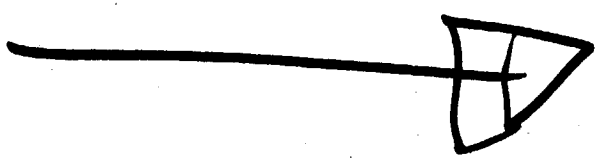

Brief Code Rationale

- The possibility of parallel processing provided some of the initial impetus for this research.
- Regions communicate across space and time using causality as an organizing principle.
- A coordinate system is used only to track the where and the when of events. The topology of communication is completely separate from coordinate choice.
- The code decides on neighbors (communicating regions) by determining the minimum necessary communication to accomplish an update.

Asynchronous Free Lagrange Calculations

- Not yet working satisfactorily for R-T applications.
- At least two problems are apparent.
  - Noise introduced by asynchronous update procedures appears to swamp information needed for accurate results.
  - The use of triangulation for the description of physics updates demands careful difference schemes.
- The asynchronous methods in place appear to handle stable shock problems adequately.
- The noise problem can be partially overcome by enforcing tighter time step controls. More efficient methods are being investigated.

FLIT2D Code Status TP6A

- With internodal spacing near x = 0 of 0.1 cm., and time advance limited by the requirement that nodal volumes change by no more than 10%, the code shows adequate average (1D) behavior, but no sign of R-T instability (2D).

- With internodal spacing near x = 0 of 0.1 cm., and time advance limited by the requirement that nodal volumes change by no more than 1%, R-T instability starts to be resolved - but just barely.

- Typical run time for 3000 node problem is 10^+ hours on a MIPS 120 computer.

TPCA "MESH"

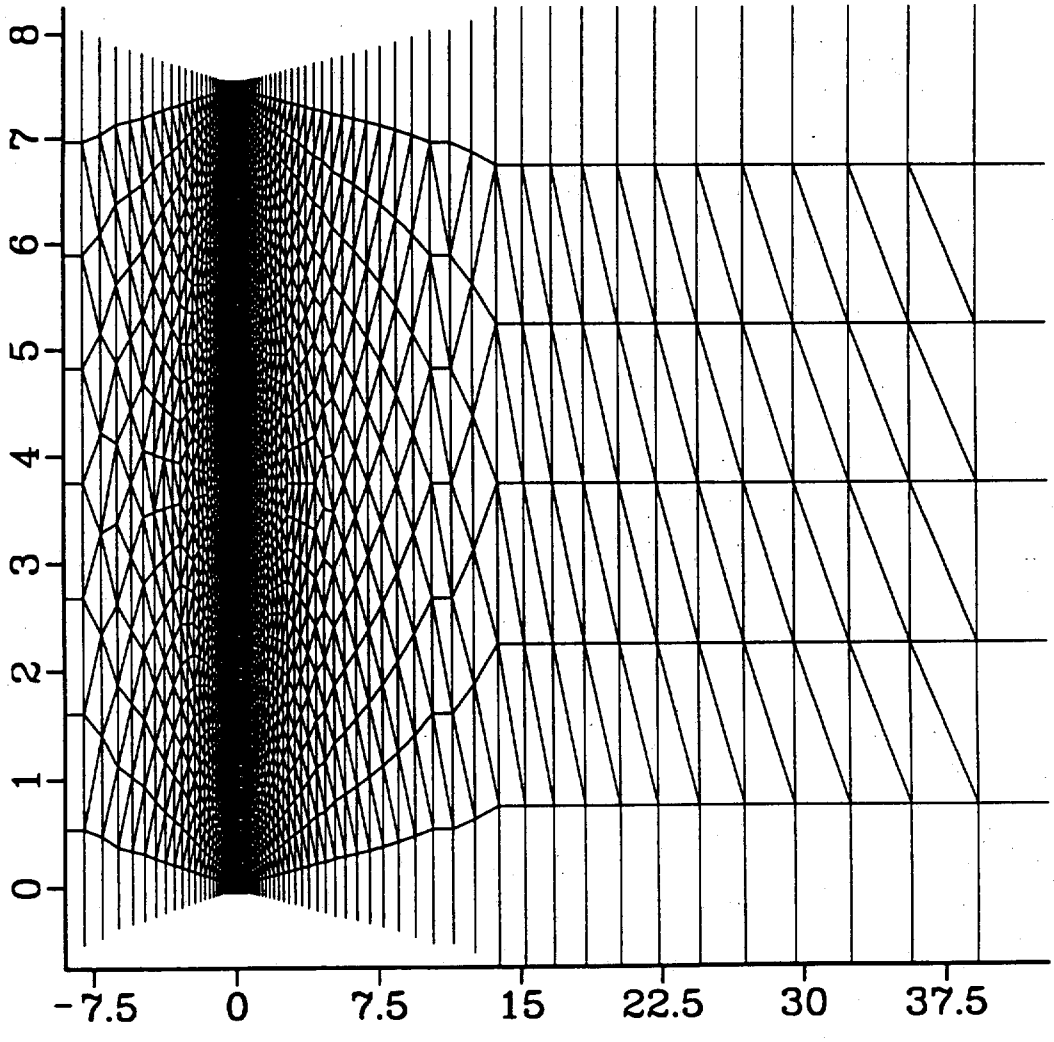

TPGA "CELLS"

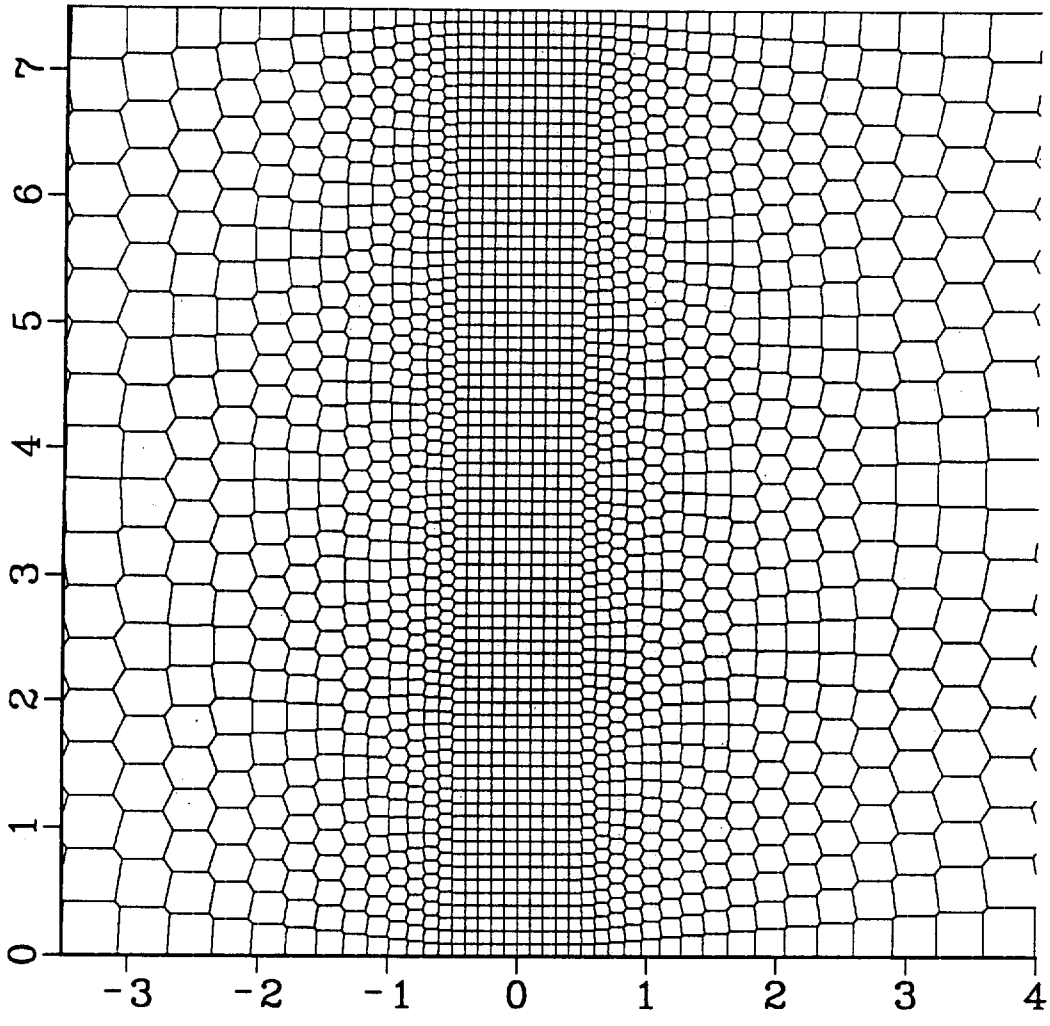

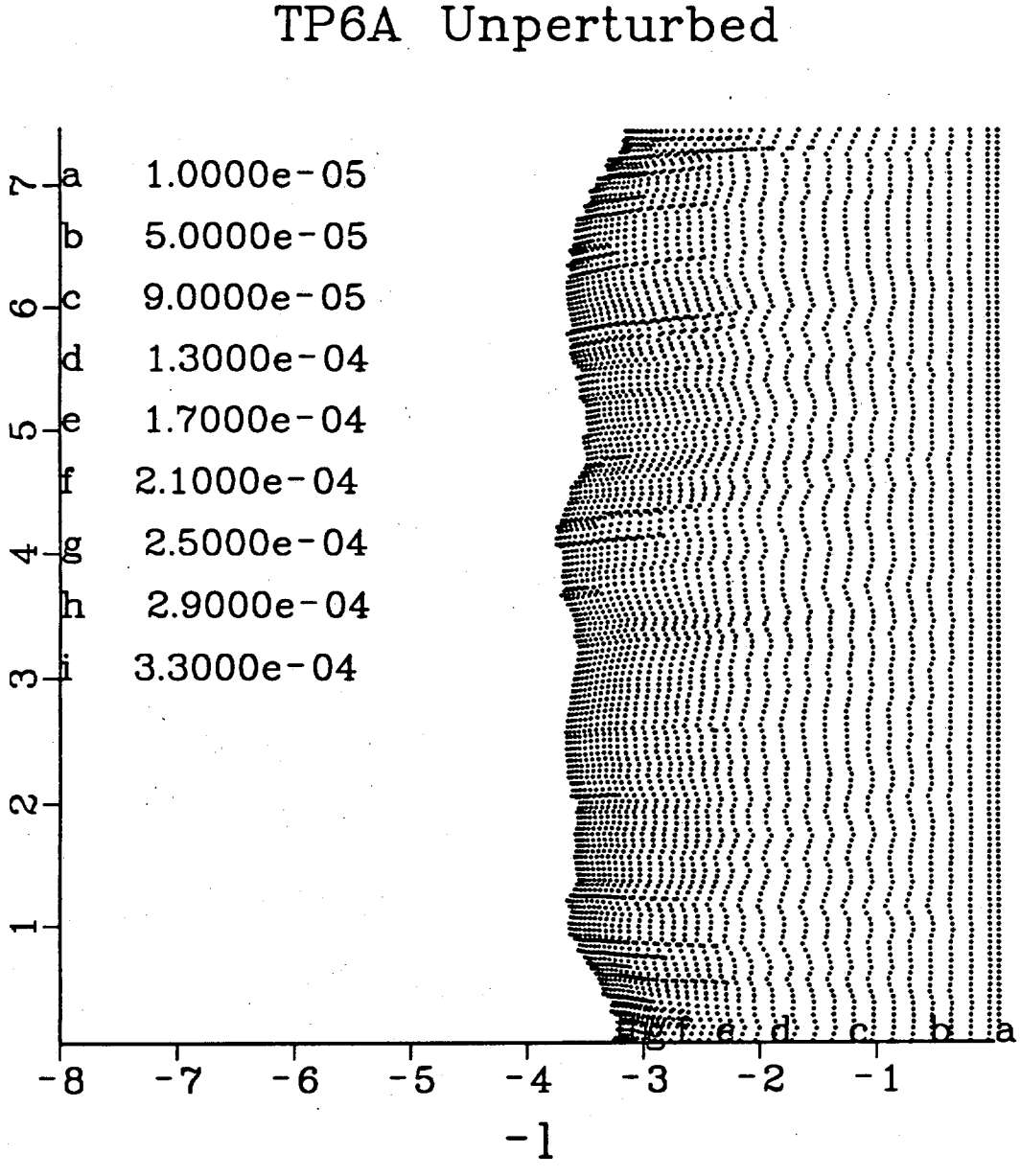
TP6A Unperturbed
a 1.0000e-05
b 5.0000e-05
c 9.0000e-05
d 1.3000e-04
e 1.7000e-04
f 2.1000e-04
g 2.5000e-04
h 2.9000e-04
i 3.3000e-04
1
2
3
4
5
6
7
-8
-7
-6
-5
-4
-3
-2
-1
-l

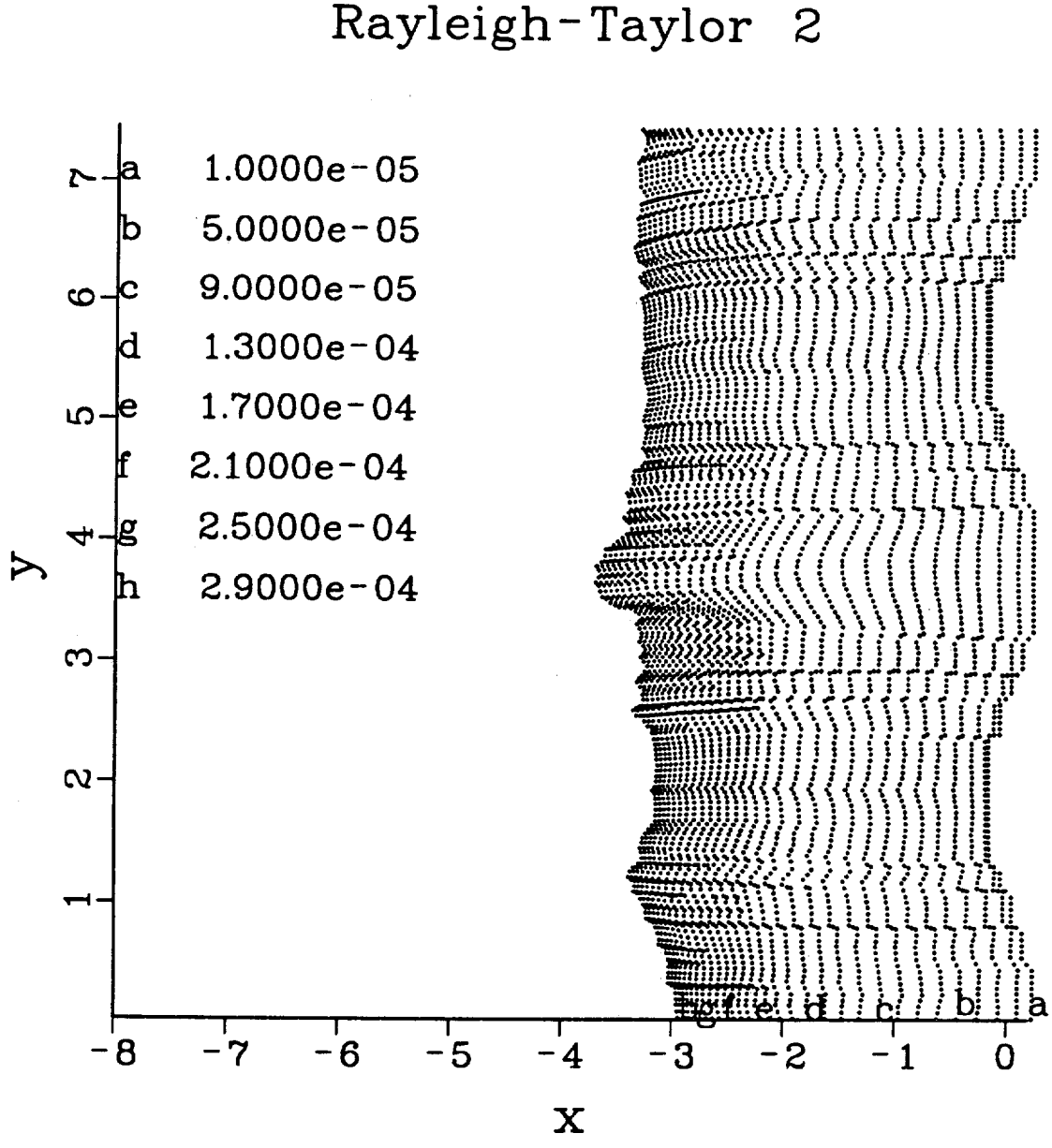
Rayleigh-Taylor 2
a 1.0000e-05
b 5.0000e-05
c 9.0000e-05
d 1.3000e-04
e 1.7000e-04
f 2.1000e-04
g 2.5000e-04
h 2.9000e-04
y
x
1
2
3
4
5
6
7
-8
-7
-6
-5
-4
-3
-2
-1
0

Numerical simulations with a 1D $\tilde{K}$-$\tilde{\varepsilon}$ mix model on Vivianne's shock tube test problems.

Michel BONNET, Serge Gauthier & Patrick SPITZ

Commissariat à l'Energie Atomique (C.E.A.)
Centre d'Etudes de Limeil-Valenton
Boite Postale 27
94195 Villeneuve-St-Georges, FRANCE.

REYNOLDS EQUATIONS.

- Mass :

$$\frac{D}{Dt}\bar{\rho} + \bar{\rho}\,\frac{\partial}{\partial x}\tilde{u} = 0$$

- Concentration :

$$\bar{\rho}\,\frac{D}{Dt}\tilde{c} + \frac{\partial}{\partial x}\overline{\rho c'u'} = 0$$

- Momentum :

$$\bar{\rho}\,\frac{D}{Dt}\tilde{u} + \frac{\partial}{\partial x}\bar{p} + \frac{\partial}{\partial x}\sigma_{11} = 0$$

- Specific internal energy :

$$\bar{\rho}\,\frac{D}{Dt}\tilde{e} + \bar{p}\,\frac{\partial}{\partial x}\tilde{u} + \frac{\partial}{\partial x}\overline{\rho h'u'} + \frac{1}{\bar{\rho}}\,\Omega_1\,\frac{\partial}{\partial x}\bar{p} - \bar{\rho}\,\tilde{\varepsilon} = 0$$

- Turbulent fluxes :

$$\overline{\rho c'u'} = -\,\bar{\rho}\,\frac{c_0}{\sigma_c}\,\frac{\tilde{k}^2}{\tilde{\varepsilon}}\,\frac{\partial}{\partial x}\tilde{c}$$

$$\sigma_{11} = -\,\frac{4}{3}\,\bar{\rho}\,c_0\,\frac{\tilde{k}^2}{\tilde{\varepsilon}}\,\frac{\partial}{\partial x}\tilde{u} + \frac{2}{3}\,\bar{\rho}\,\tilde{k}$$

$$\overline{\rho h'u'} = -\,\bar{\rho}\,\frac{c_0}{\sigma_h}\,\frac{\tilde{k}^2}{\tilde{\varepsilon}}\,\frac{\partial}{\partial x}\left(\tilde{e} + \frac{\bar{p}}{\bar{\rho}}\right)$$

$$\Omega_1 = -\,\frac{1}{\bar{\rho}}\,\overline{p'u'}$$

$\tilde{K}$ - $\tilde{\varepsilon}$ mix model.

- $$\bar{\rho} \cdot \frac{D}{Dt} \tilde{K} + \frac{\partial}{\partial x} \overline{\rho K'u'} - \frac{1}{\bar{\rho}} \Omega \frac{\partial}{\partial x} \bar{p} + \sigma_{11} \cdot \frac{\partial}{\partial x} \tilde{u} + \bar{\rho} \tilde{\varepsilon} = 0$$

- $$\bar{\rho} \cdot \frac{D}{Dt} \tilde{\varepsilon} + \frac{\partial}{\partial x} \overline{\rho \varepsilon' u'} - C_{\varepsilon 0} \frac{\tilde{\varepsilon}}{\tilde{K}} \frac{\Omega}{\bar{\rho}} \frac{\partial}{\partial x} \bar{p} + C_{\varepsilon 1} \frac{\tilde{\varepsilon}}{\tilde{K}} \sigma_{11} \cdot \frac{\partial}{\partial x} \tilde{u}$$
$$+ C_{\varepsilon 2} \bar{\rho} \frac{\tilde{\varepsilon}^2}{\tilde{K}} + C_{\varepsilon 3} \bar{\rho} \tilde{\varepsilon} \frac{\partial}{\partial x} \tilde{u} = 0$$

- Turbulent fluxes :

$$\overline{\rho K'u'} = - \bar{\rho} \frac{C_D}{\sigma_K} \cdot \frac{\tilde{K}^2}{\tilde{\varepsilon}} \frac{\partial}{\partial x} \tilde{K}$$

$$\overline{\rho \varepsilon' u'} = - \bar{\rho} \frac{C_D}{\sigma_\varepsilon} \cdot \frac{\tilde{K}^2}{\tilde{\varepsilon}} \frac{\partial}{\partial x} \tilde{\varepsilon}$$

$$\Omega = - \frac{C_D}{\sigma_\rho} \frac{\tilde{K}^2}{\tilde{\varepsilon}} \frac{\partial}{\partial x} \bar{p}$$

- Equation of state for perfect gases.

- Model constants :

C_D	σ_R	σ_c	σ_K	σ_ε	$C_{\varepsilon 0}$	$C_{\varepsilon 1}$	$C_{\varepsilon 2}$	$C_{\varepsilon 3}$
0.09	0.9	0.7	0.87	1.3	0.85	1.47	1.9	0.

σ_ρ : calibration parameter.

Initialization of turbulence.

* At $t \simeq t_{shock}$

$$L_0 (cm) = 2\left[1+\beta(At)\right] \alpha |At^*| |\Delta U| \Delta t \qquad \text{YOUNGS}$$

$$K_0 = 0.093\ At^{*2} \qquad \text{MIKAELIAN}$$

$\alpha = 0.07$ (YOUNGS et AL)

At^* . Atwood number after shock passage.

$|\Delta U|$ = velocity jump at the interface

Δt = " transition time from laminar to turbulent state ".

$\simeq 1\ \mu s$

β : function of At (see YOUNGS et AL)

* The $\tilde{K}-\tilde{\varepsilon}$ model is turned on at t_B with:

$$L_{INIT} = L_0 \cdot \left(\frac{t_B - t_{shock}}{\Delta t}\right)^{\frac{1}{3}}$$

$$K_{INIT} = K_0 \left(\frac{t_B - t_{shock}}{\Delta t}\right)^{-\frac{1}{3}}$$

$$\varepsilon_{INIT} = \frac{K_{INIT}^{\frac{3}{2}}}{L_{INIT}}$$

EXPERIMENT	HELIUM / AIR	SF6 / AIR
ΔX (cm)	0.02	0.17
Mesh size	1000	1000
L_{AIR} (cm)	11.5	160.
t_{shock} (μs)	271.	3580
t_B (μs)	300	3700
L_{INIT} (cm)	0.0175	0.0167
K_{INIT}	0.0176	0.0105

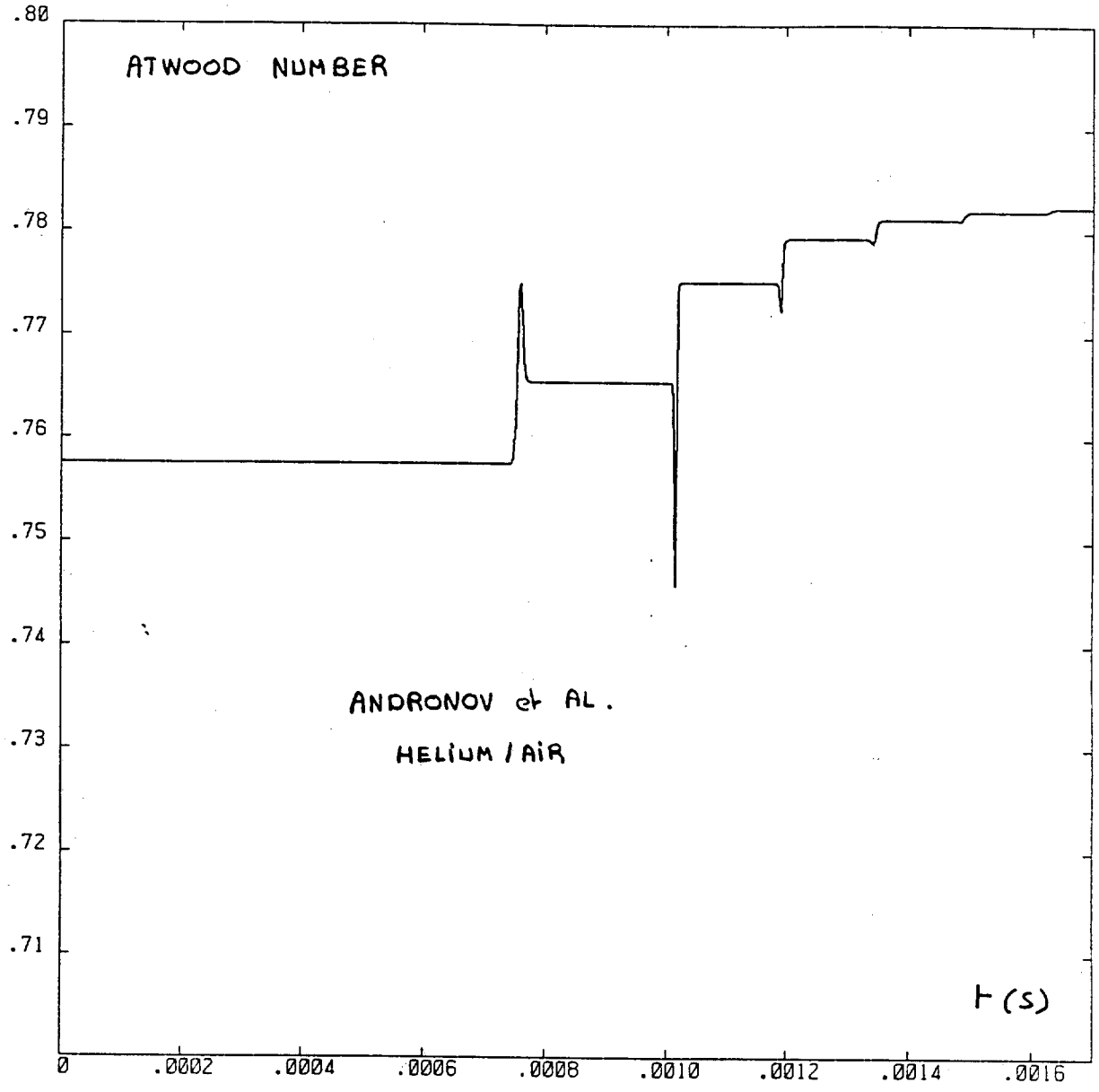
ATWOOD NUMBER
.80
.79
.78
.77
.76
.75
.74
.73
.72
.71
ANDRONOV et AL.
HELIUM / AIR
t (s)
0
.0002
.0004
.0006
.0008
.0010
.0012
.0014
.0016

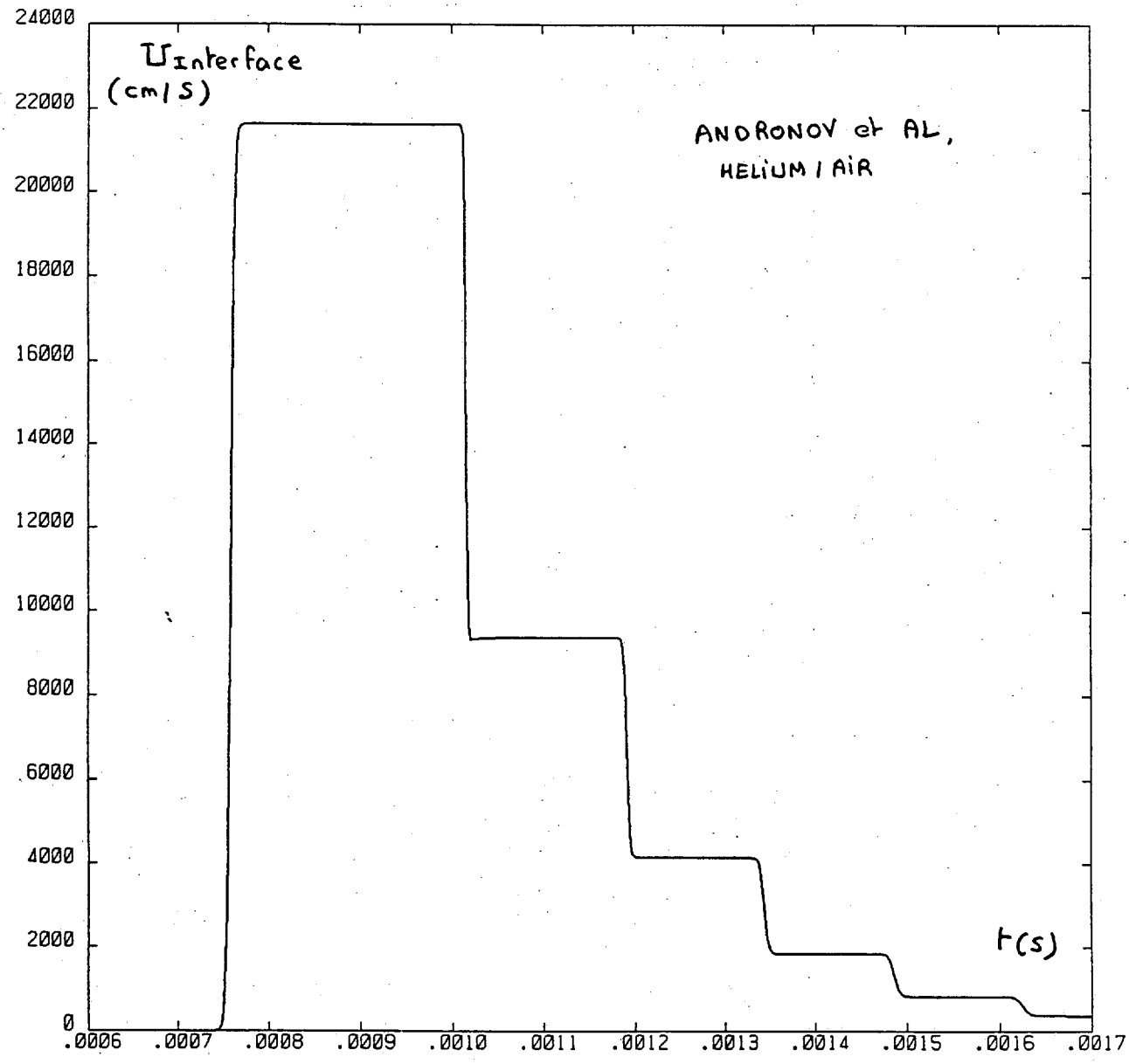
24000
22000
20000
18000
16000
14000
12000
10000
8000
6000
4000
2000
0
$U_{Interface}$ (cm/s)
ANDRONOV et AL,
HELIUM / AIR
t(s)
.0006
.0007
.0008
.0009
.0010
.0011
.0012
.0013
.0014
.0015
.0016
.0017

CALIBRATION OF σ_p.

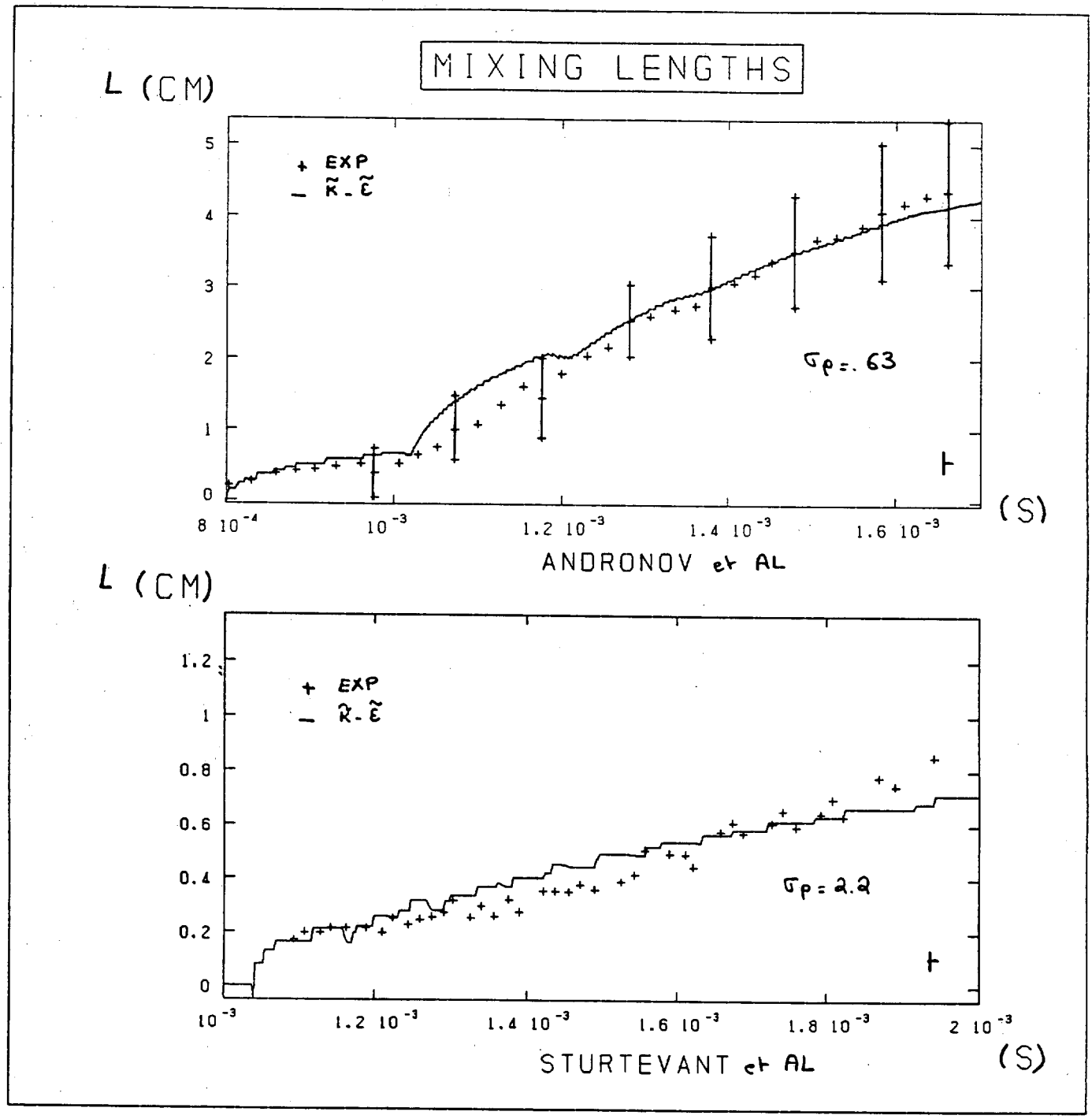

HELIUM / AIR

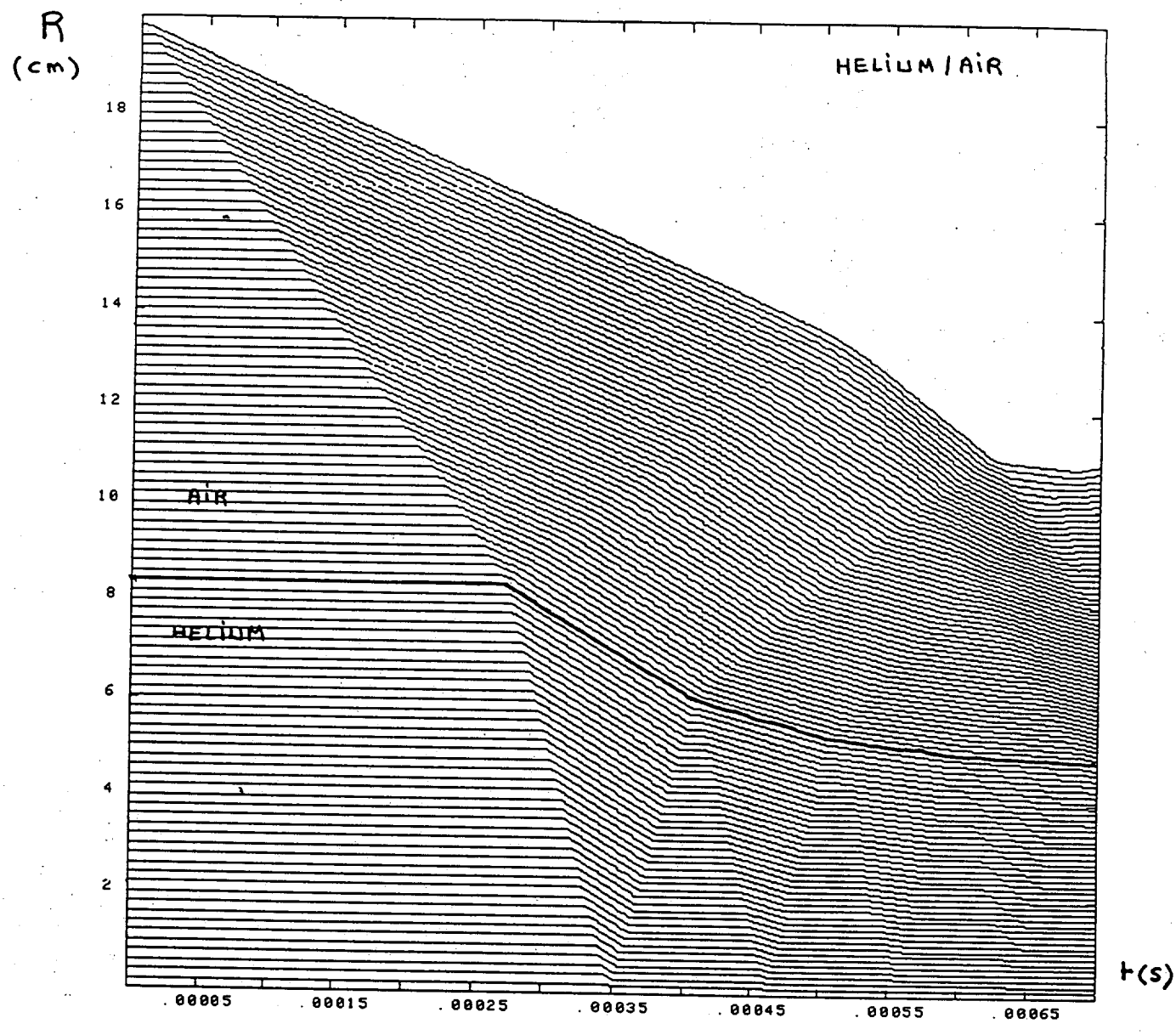
R
(cm)
HELIUM / AIR
18
16
14
12
10
8
6
4
2
AIR
HELIUM
.00005
.00015
.00025
.00035
.00045
.00055
.00065
t(s)

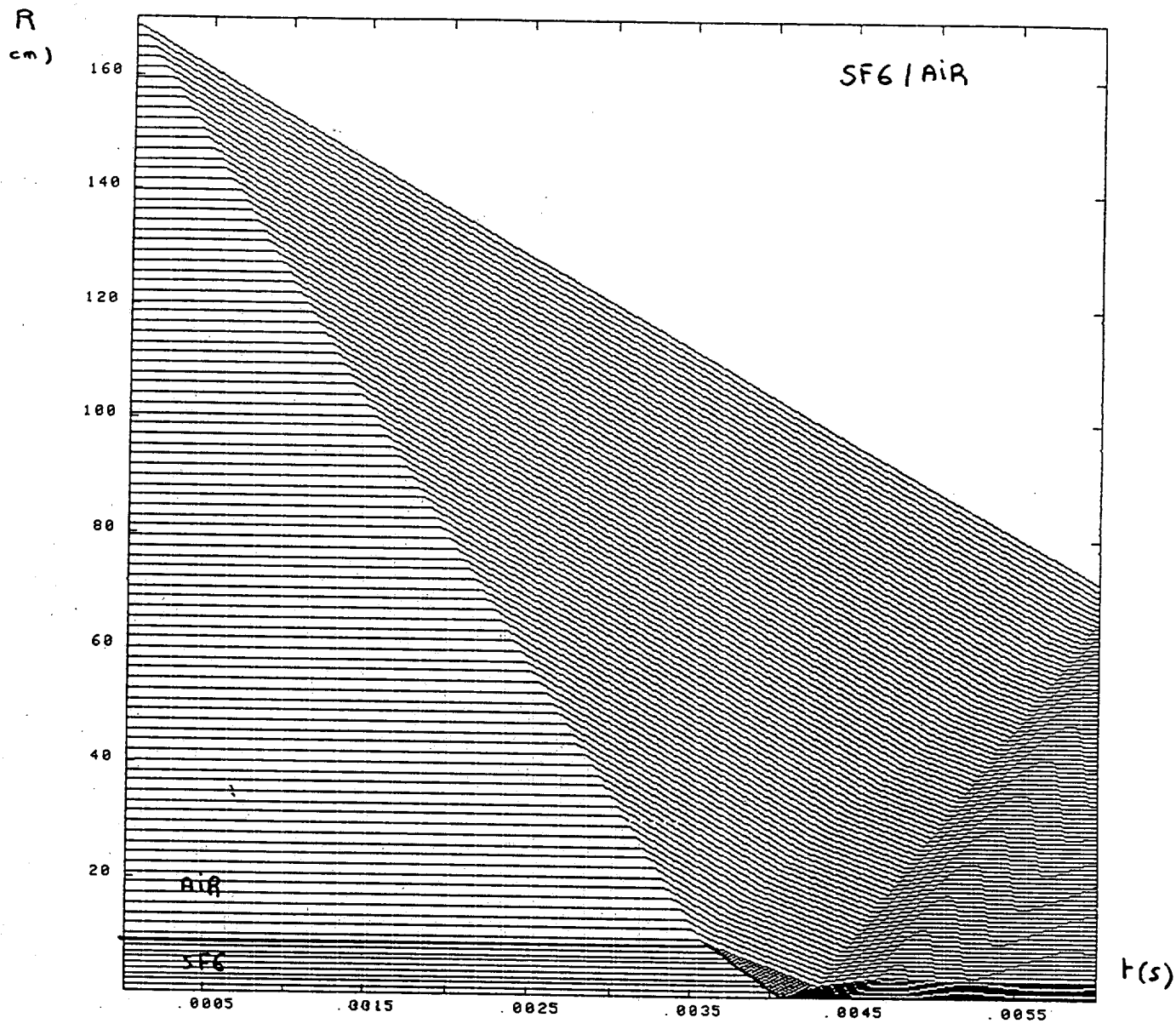
R
(cm)
160
140
120
100
80
60
40
20
SF6 / AIR
AIR
SF6
.0005
.0015
.0025
.0035
.0045
.0055
t(s)

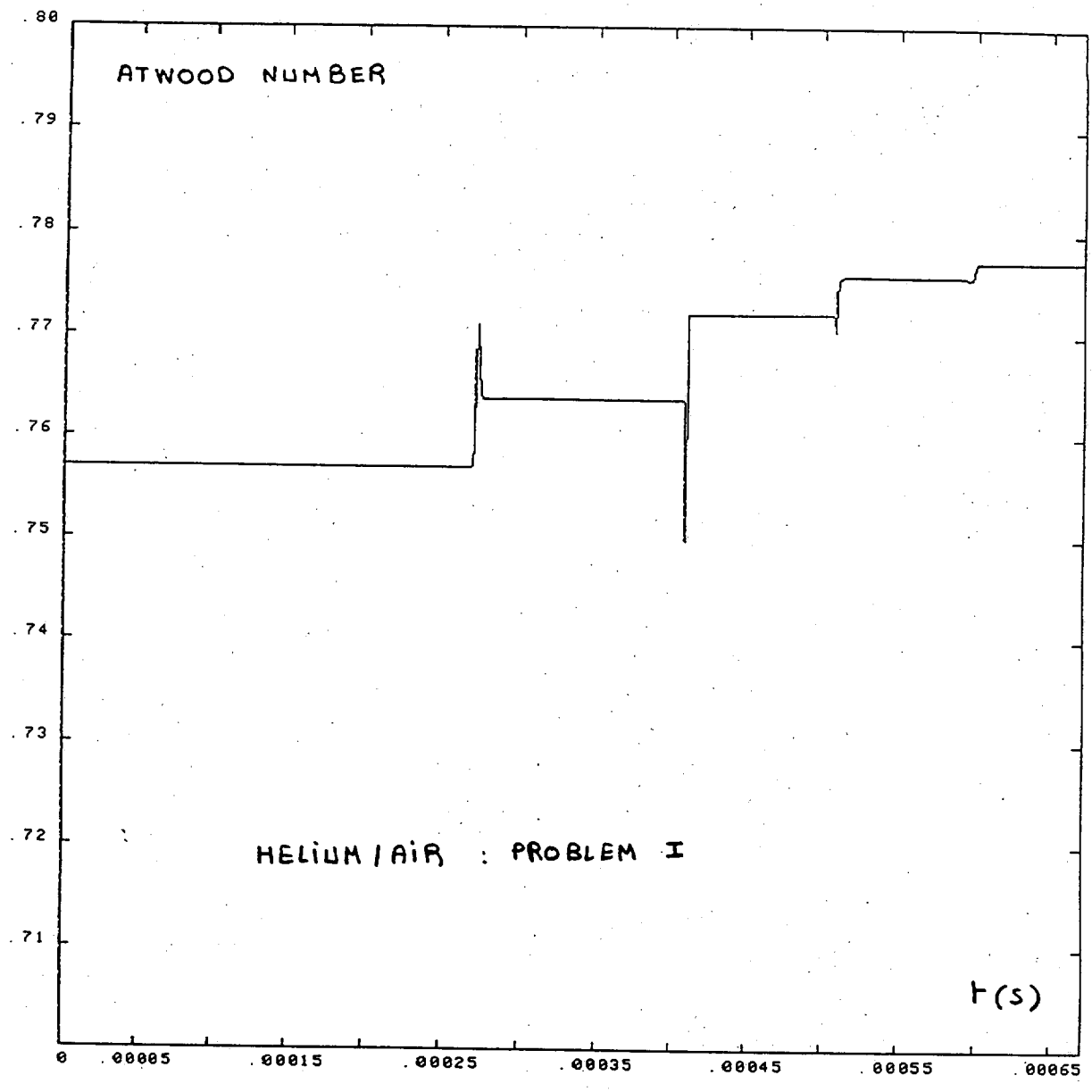
ATWOOD NUMBER
.80
.79
.78
.77
.76
.75
.74
.73
.72
.71
HELIUM / AIR : PROBLEM I
t(s)
0
.00005
.00015
.00025
.00035
.00045
.00055
.00065

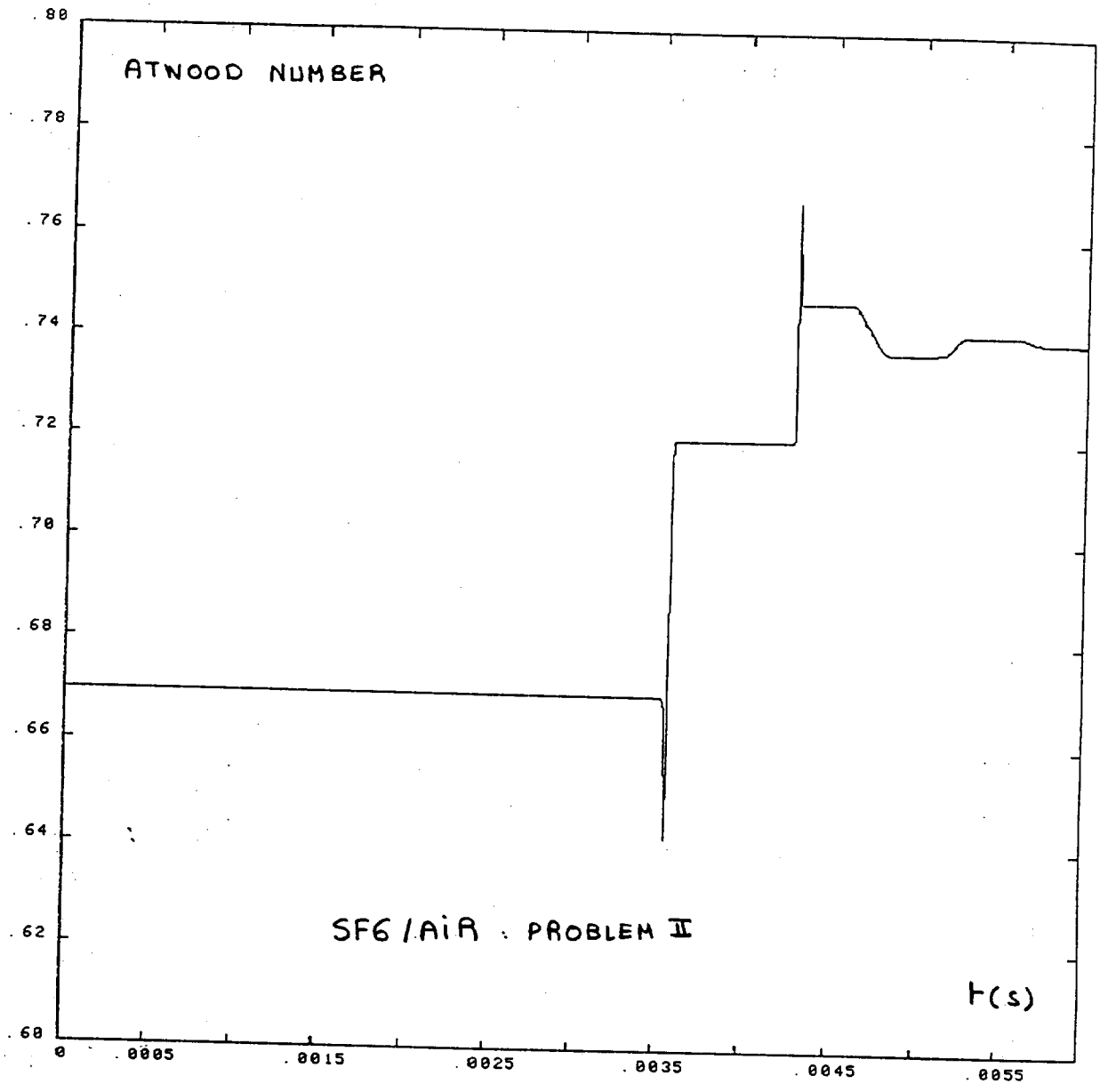
ATWOOD NUMBER
.80
.78
.76
.74
.72
.70
.68
.66
.64
.62
.60
0
.0005
.0015
.0025
.0035
.0045
.0055
SF6/AIR : PROBLEM II
t(s)

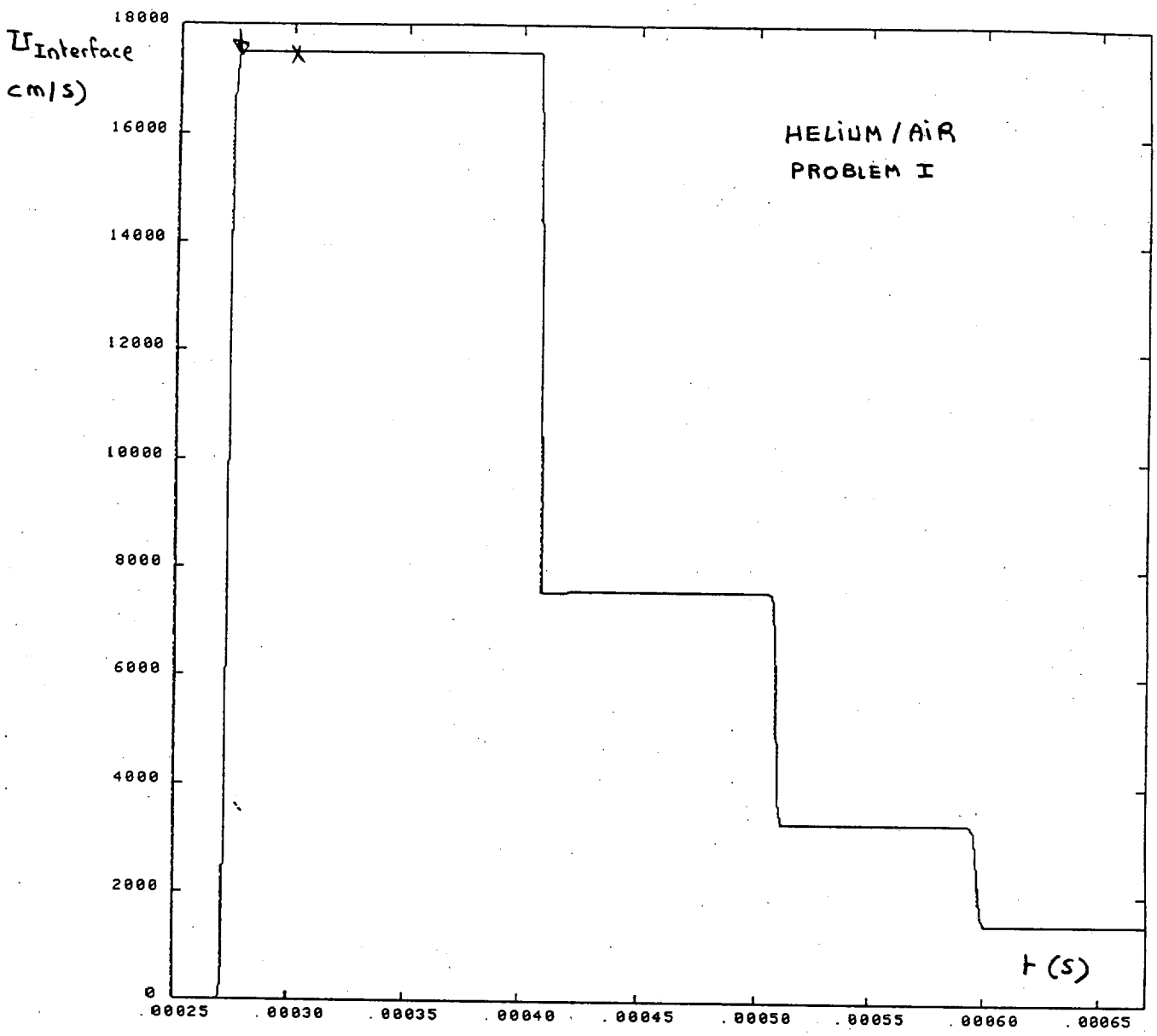
$U_{Interface}$ cm/s)
18000
16000
14000
12000
10000
8000
6000
4000
2000
0
.00025
.00030
.00035
.00040
.00045
.00050
.00055
.00060
.00065
HELIUM / AIR
PROBLEM I
t (s)

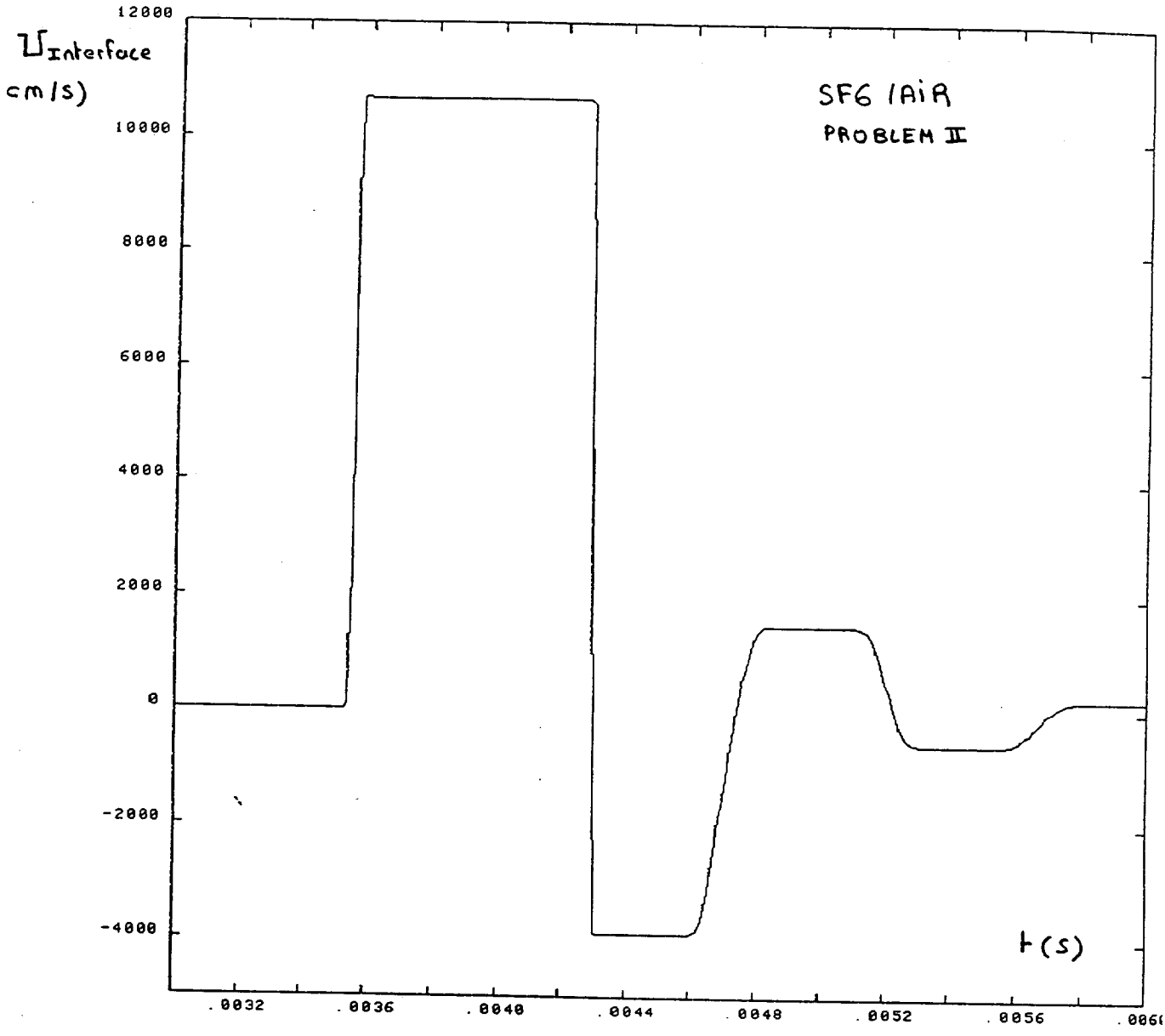
U Interface
cm/s)
12000
10000
8000
6000
4000
2000
0
-2000
-4000
SF6 /AIR
PROBLEM II
t(s)
.0032
.0036
.0040
.0044
.0048
.0052
.0056

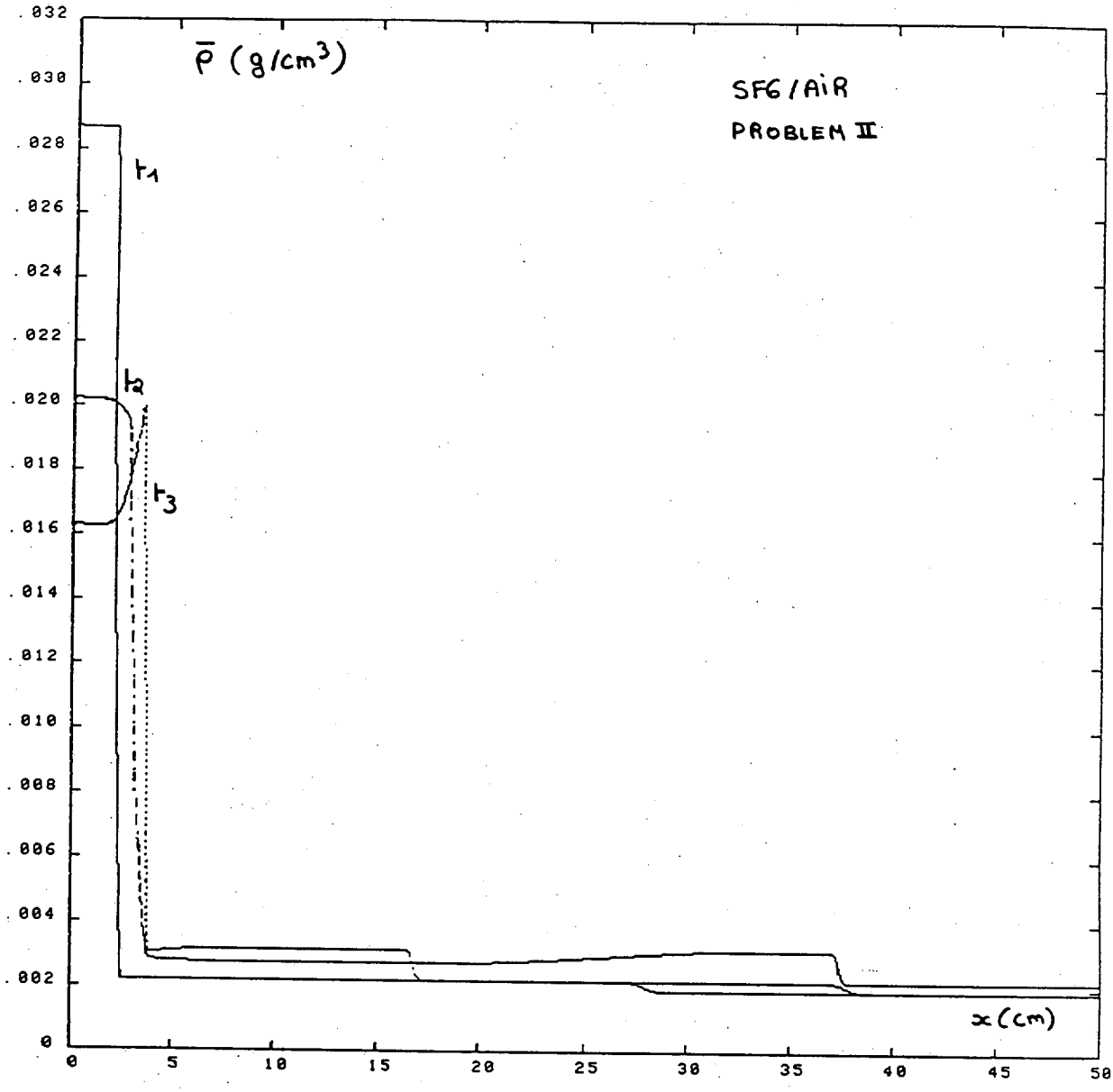
$\bar{\rho}$ (g/cm^3)
SF6/AIR
PROBLEM II
t_1
t_2
t_3
x (cm)
.032
.030
.028
.026
.024
.022
.020
.018
.016
.014
.012
.010
.008
.006
.004
.002
0
0
5
10
15
20
25
30
35
40
45
50

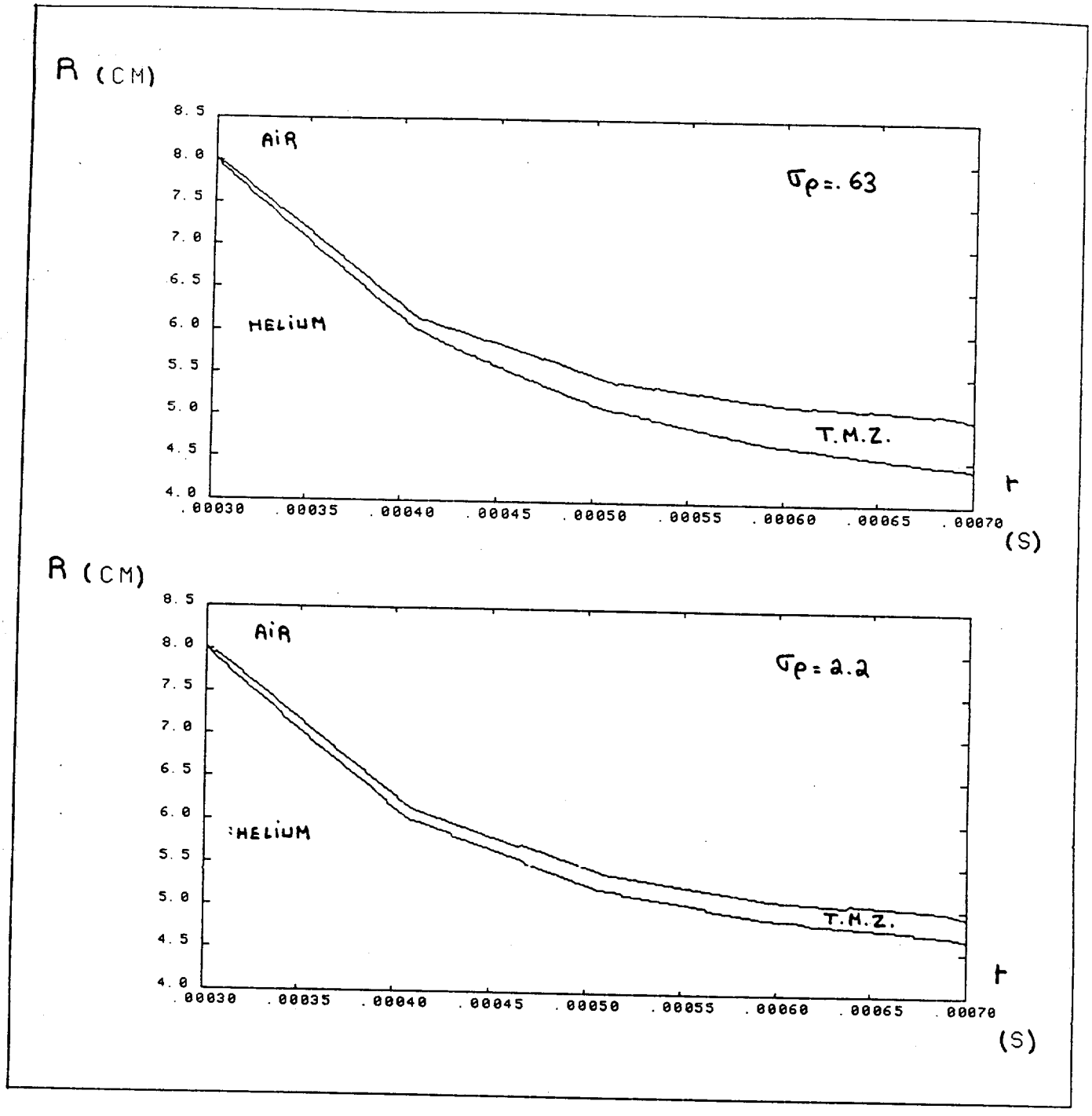

HELIUM / AIR - PROBLEM I.

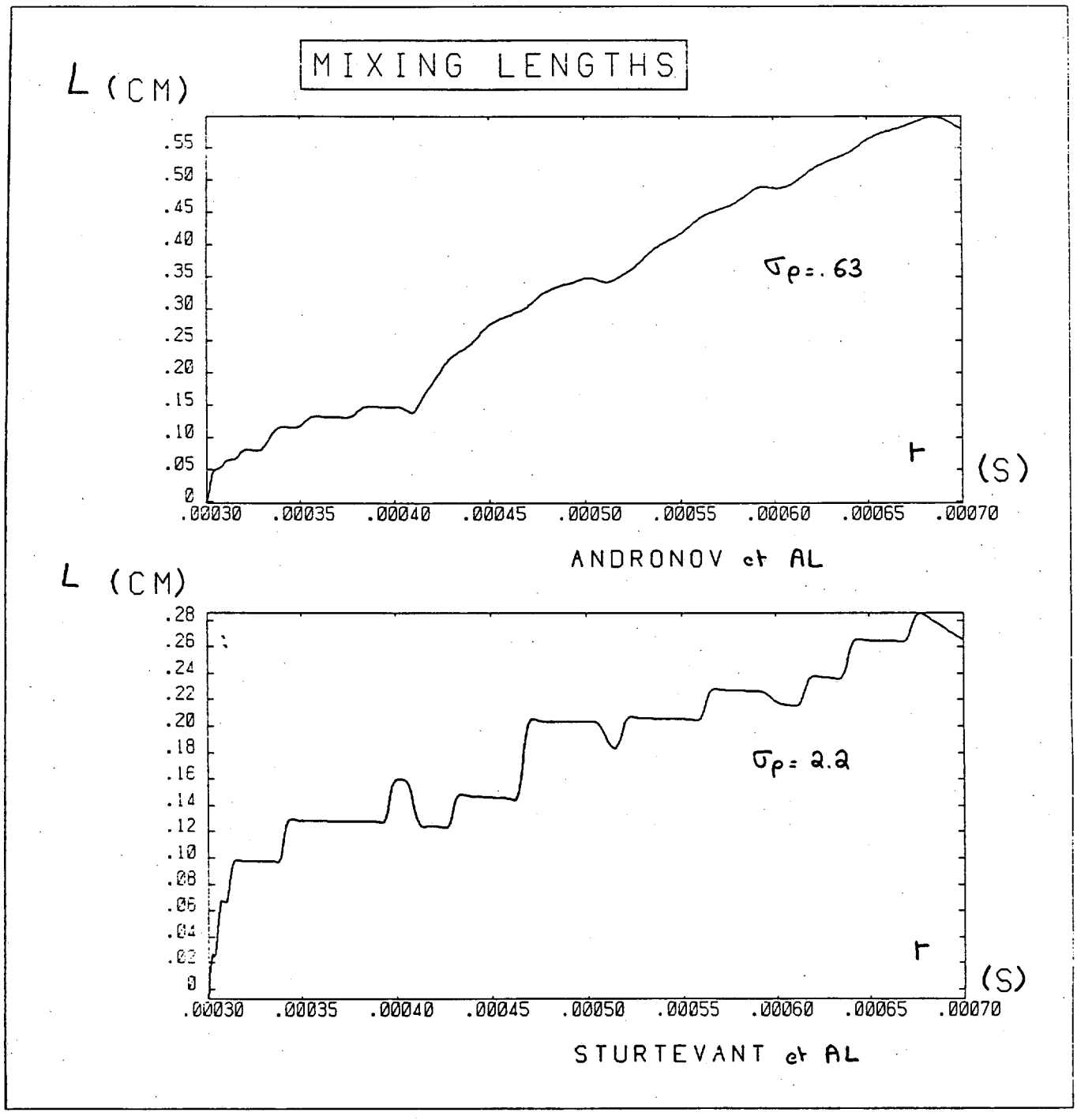

HELIUM / AIR : PROBLEM I

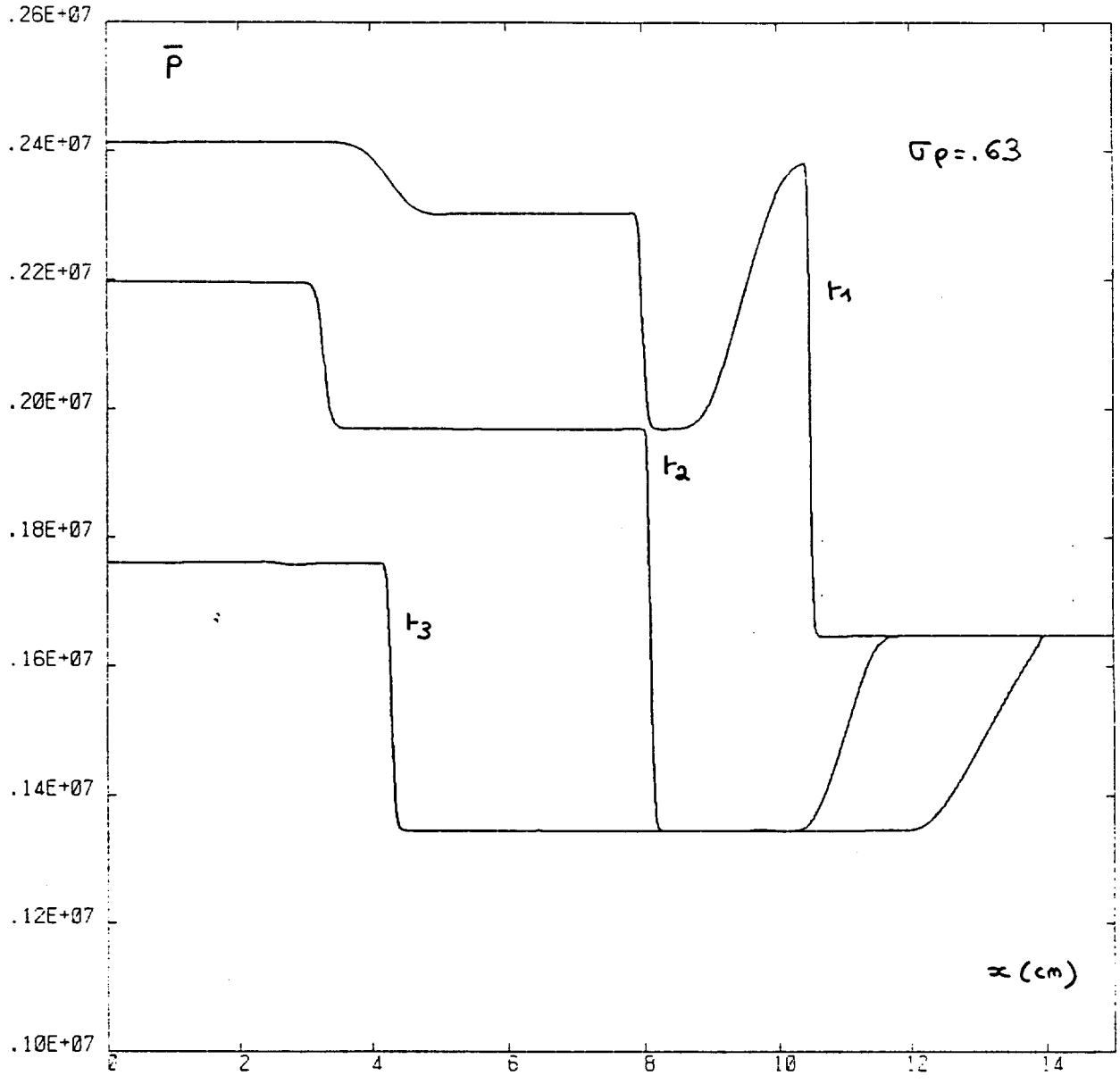

HELIUM / AIR : PROBLEM I

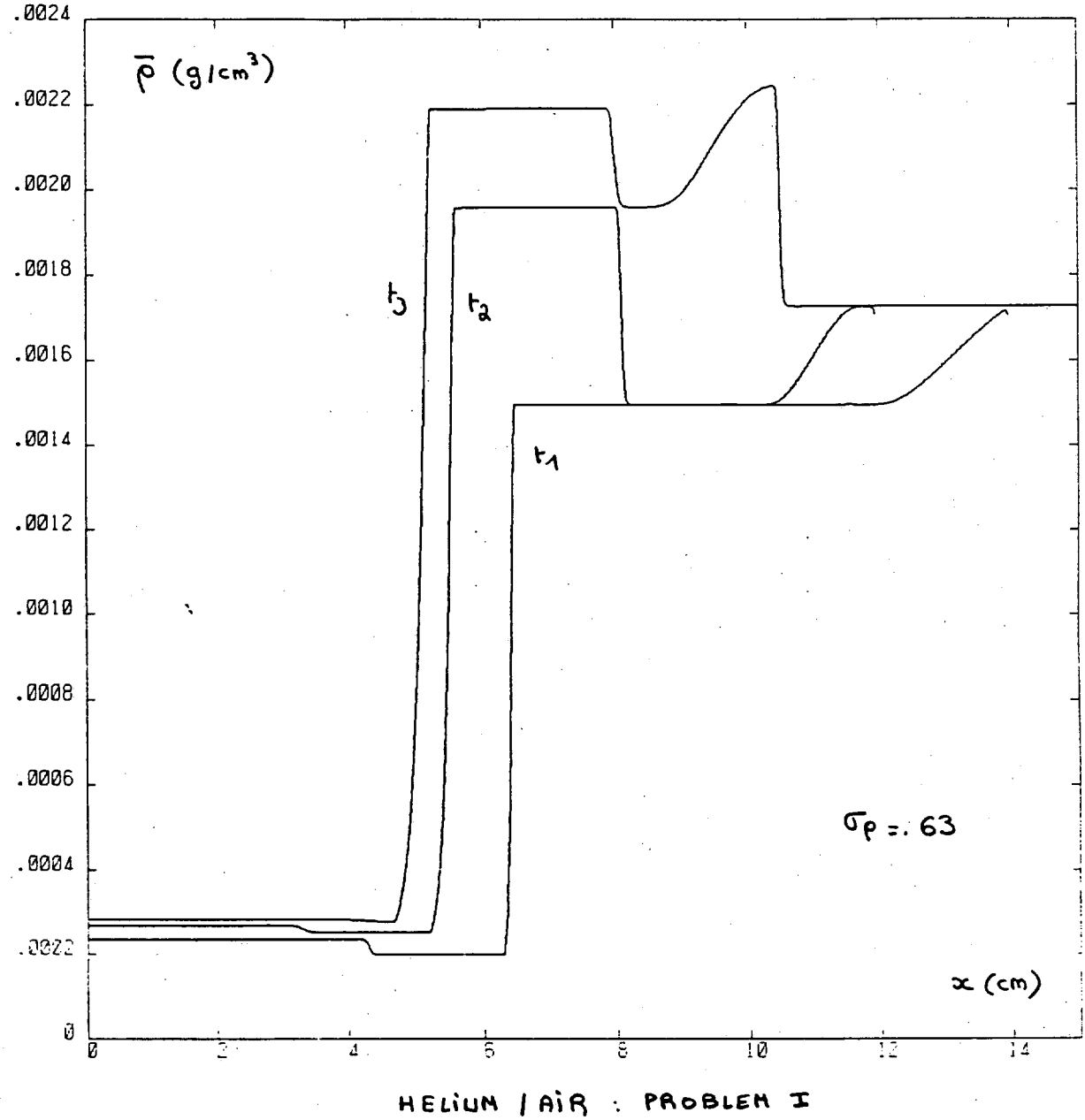

HELIUM / AIR : PROBLEM I

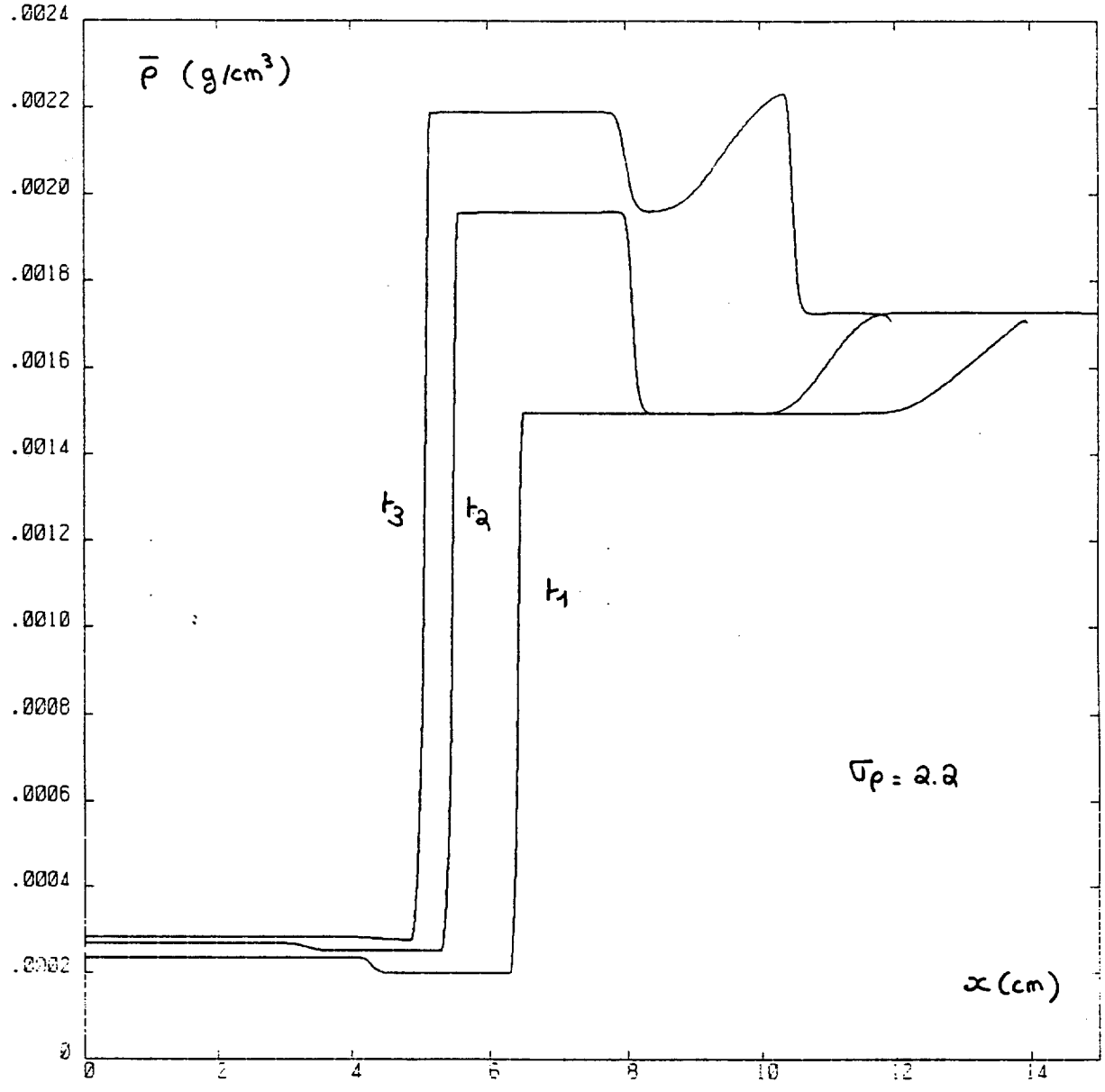

HELIUM / AIR : PROBLEM I.

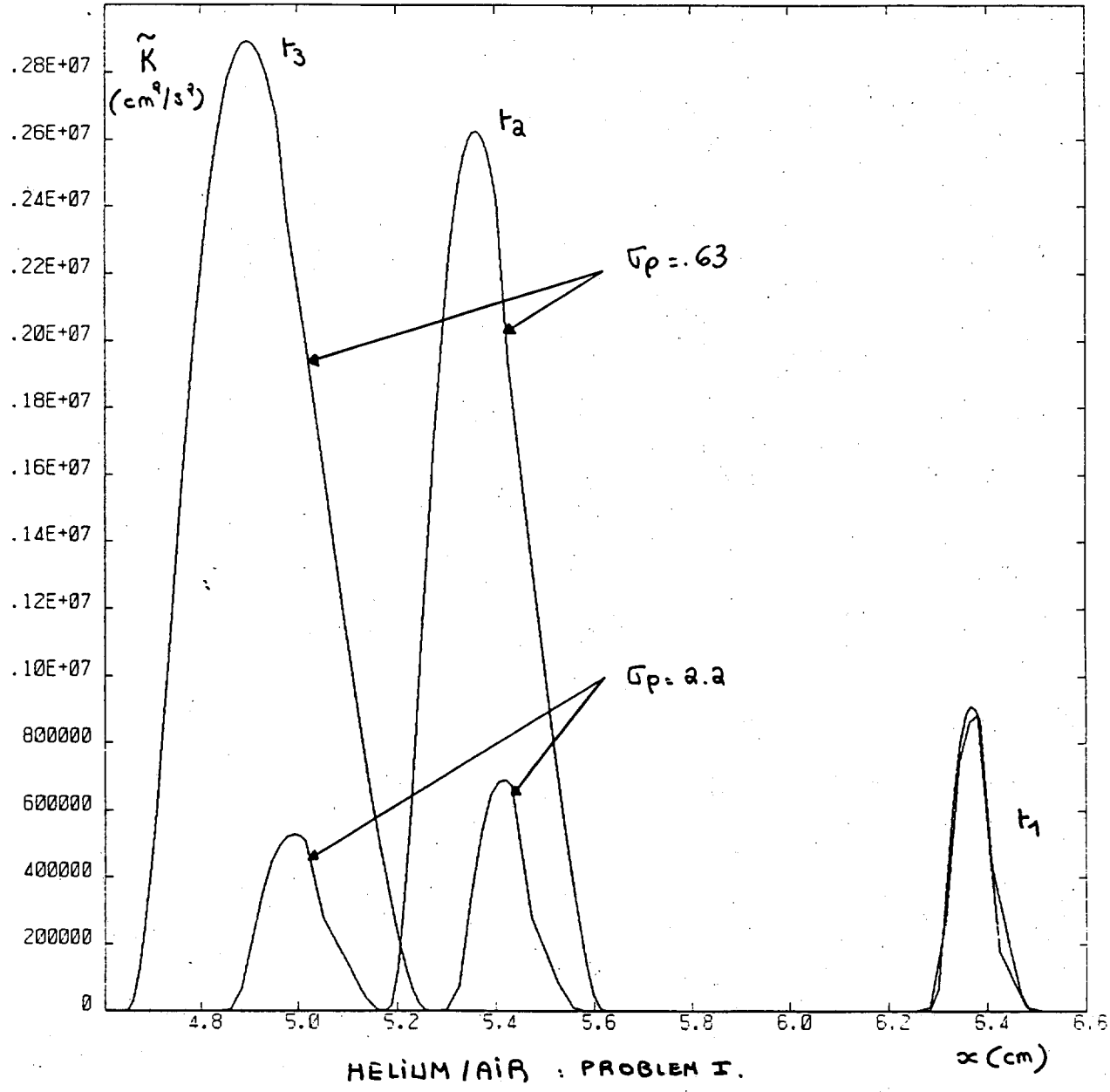
$\tilde{K}$ (cm²/s²)
.28E+07
.26E+07
.24E+07
.22E+07
.20E+07
.18E+07
.16E+07
.14E+07
.12E+07
.10E+07
800000
600000
400000
200000
0
4.8
5.0
5.2
5.4
5.6
5.8
6.0
6.2
6.4
6.6
x (cm)
t_3
t_2
t_1
$\sigma_\rho = .63$
$\sigma_\rho = 2.2$
HELIUM / AIR : PROBLEM I.

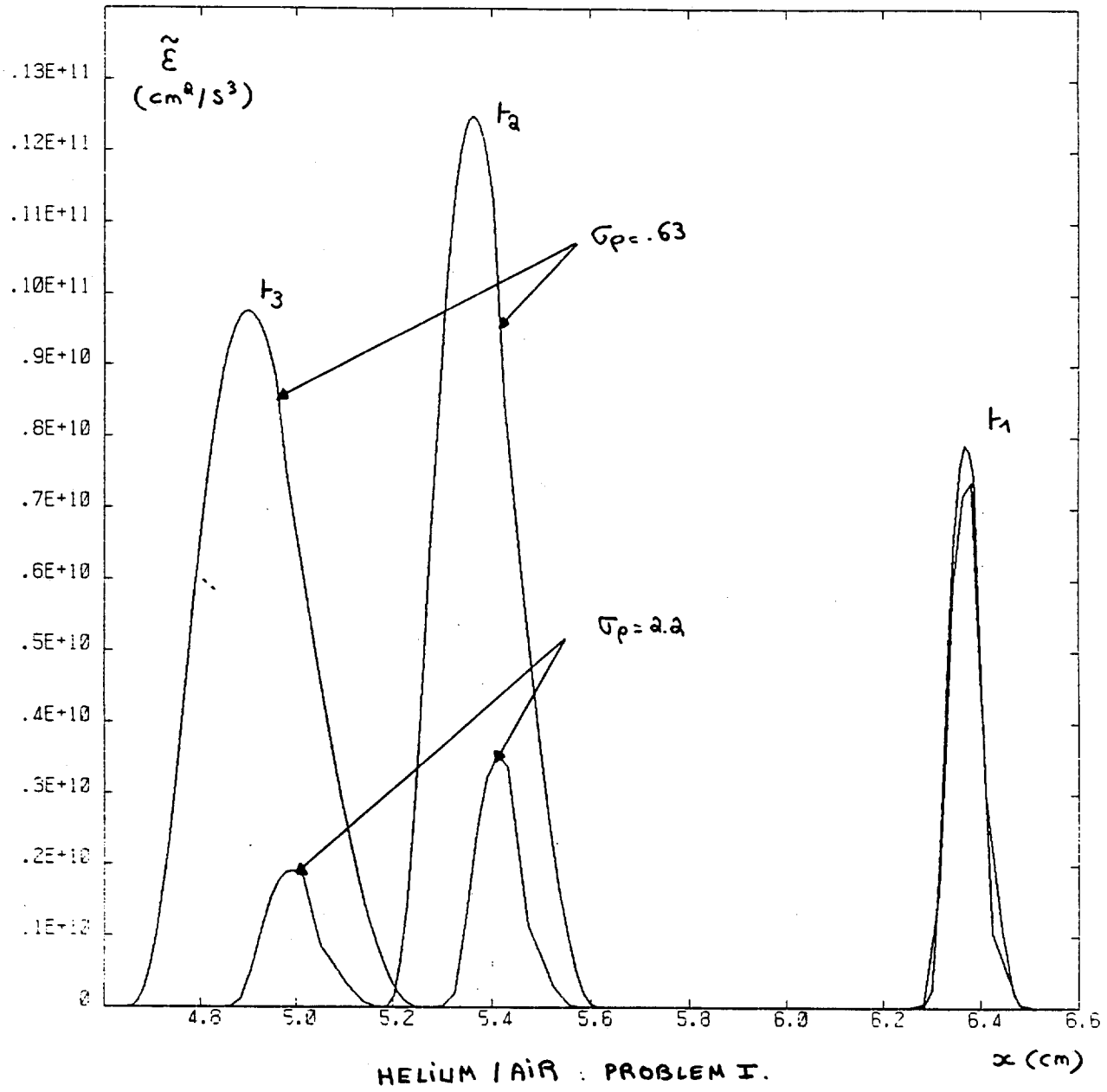
$\tilde{\varepsilon}$
(cm²/s³)
.13E+11
.12E+11
.11E+11
.10E+11
.9E+10
.8E+10
.7E+10
.6E+10
.5E+10
.4E+10
.3E+10
.2E+10
.1E+10
0
4.8
5.0
5.2
5.4
5.6
5.8
6.0
6.2
6.4
6.6
x (cm)
t_2
t_3
t_1
$\sigma_p = .63$
$\sigma_p = 2.2$
HELIUM / AIR . PROBLEM I.

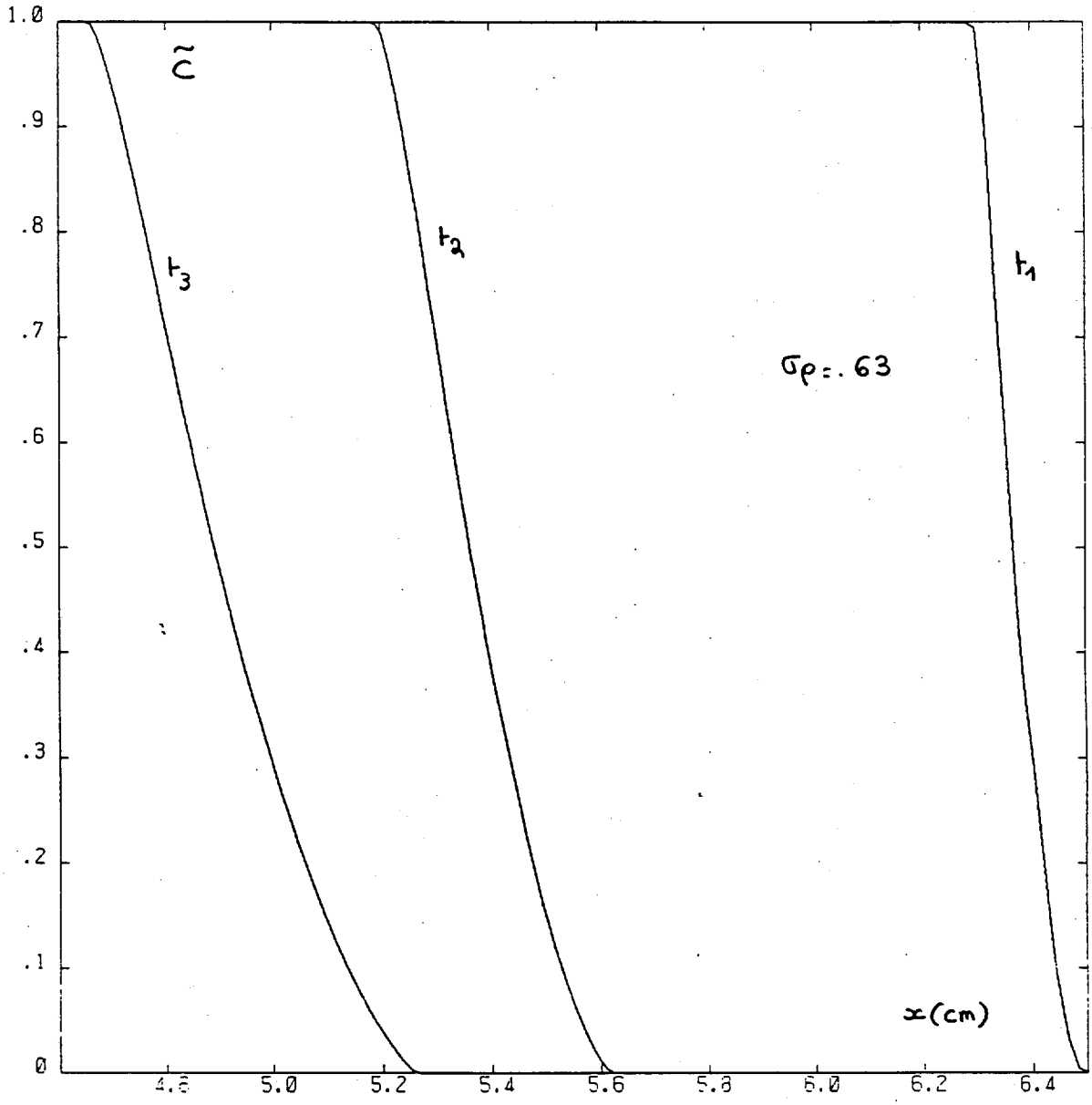

HELIUM / AIR : PROBLEM I.

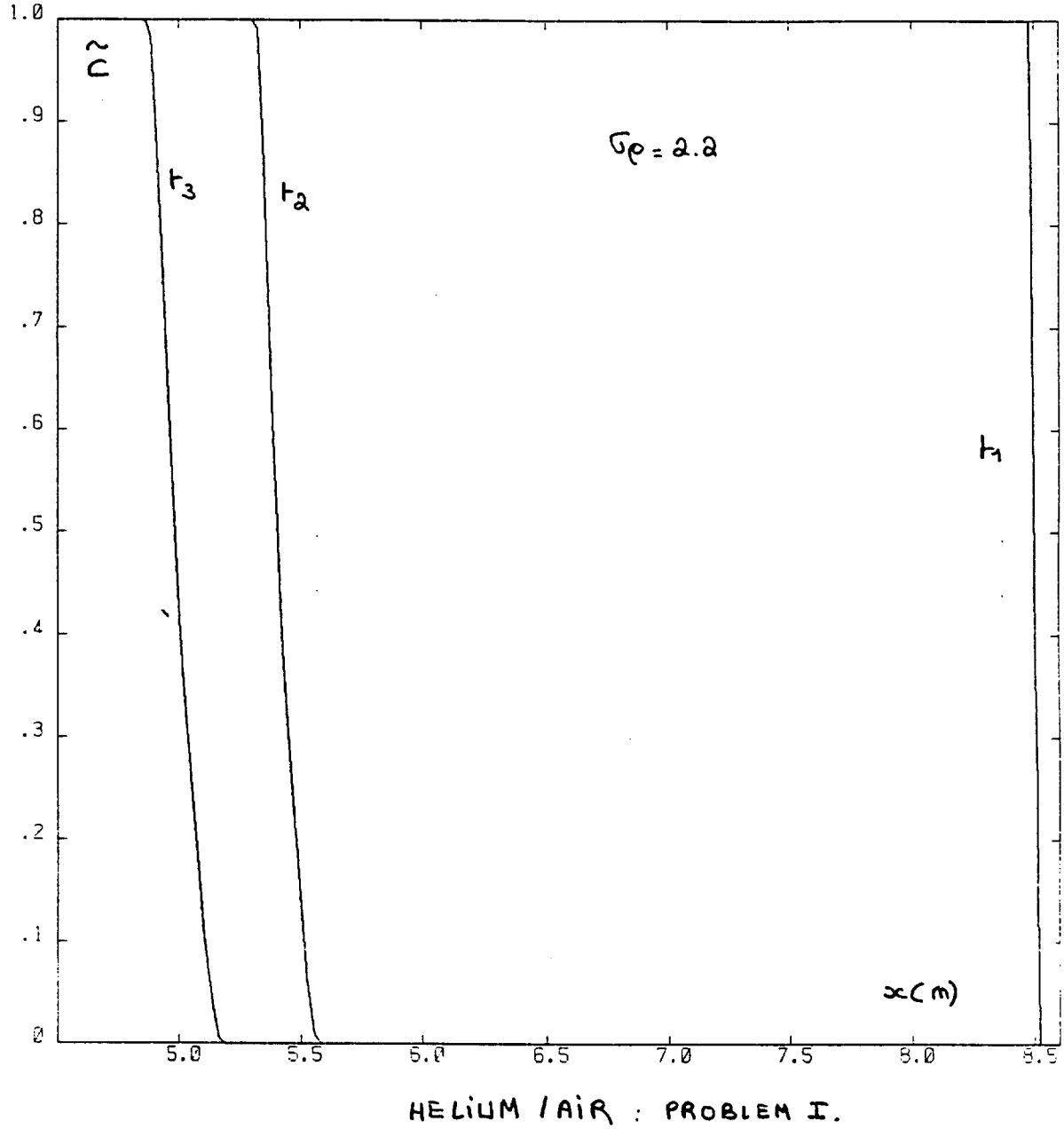

HELIUM / AIR : PROBLEM I.

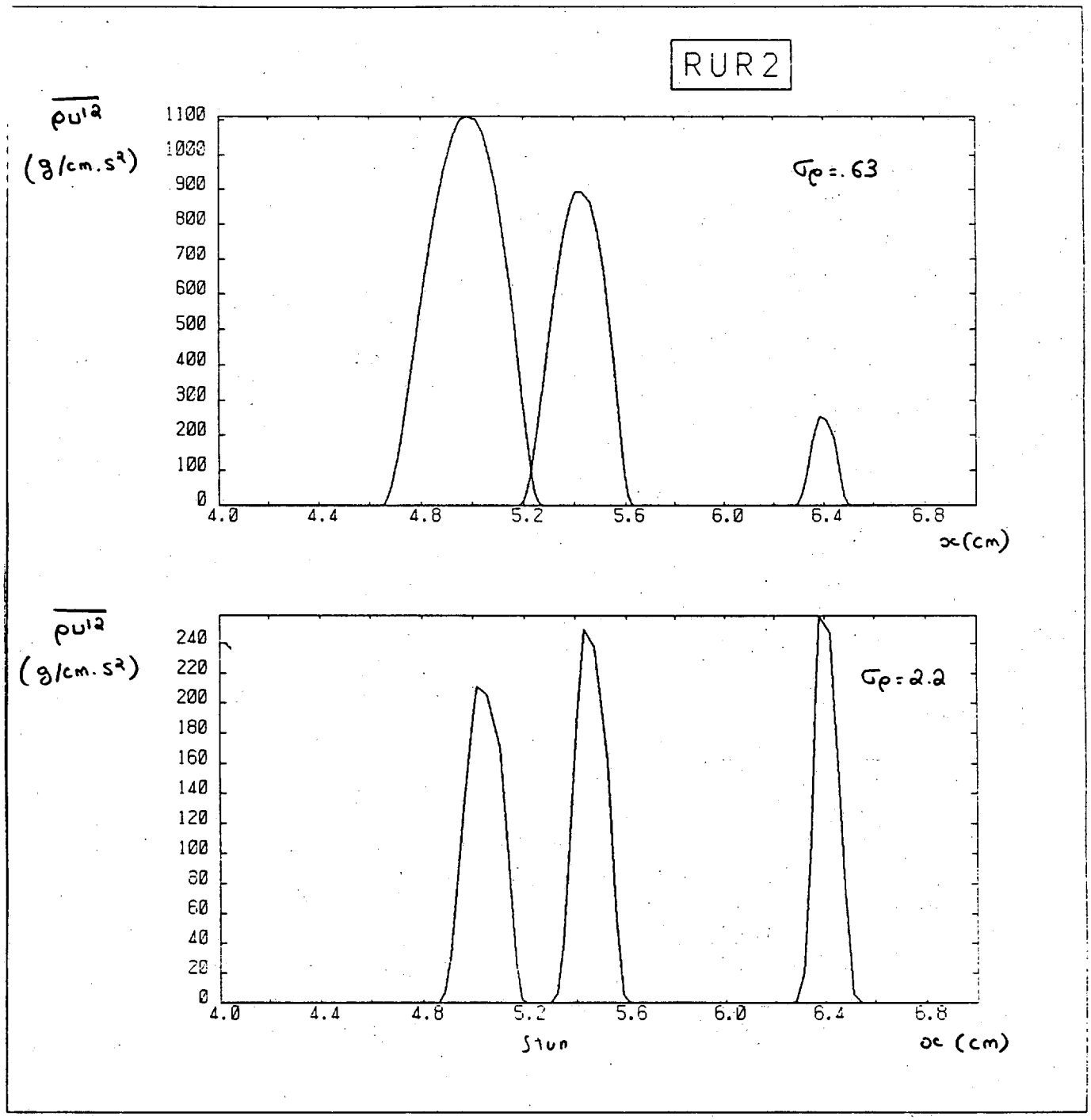

PROBLEM I . HELIUM / AIR

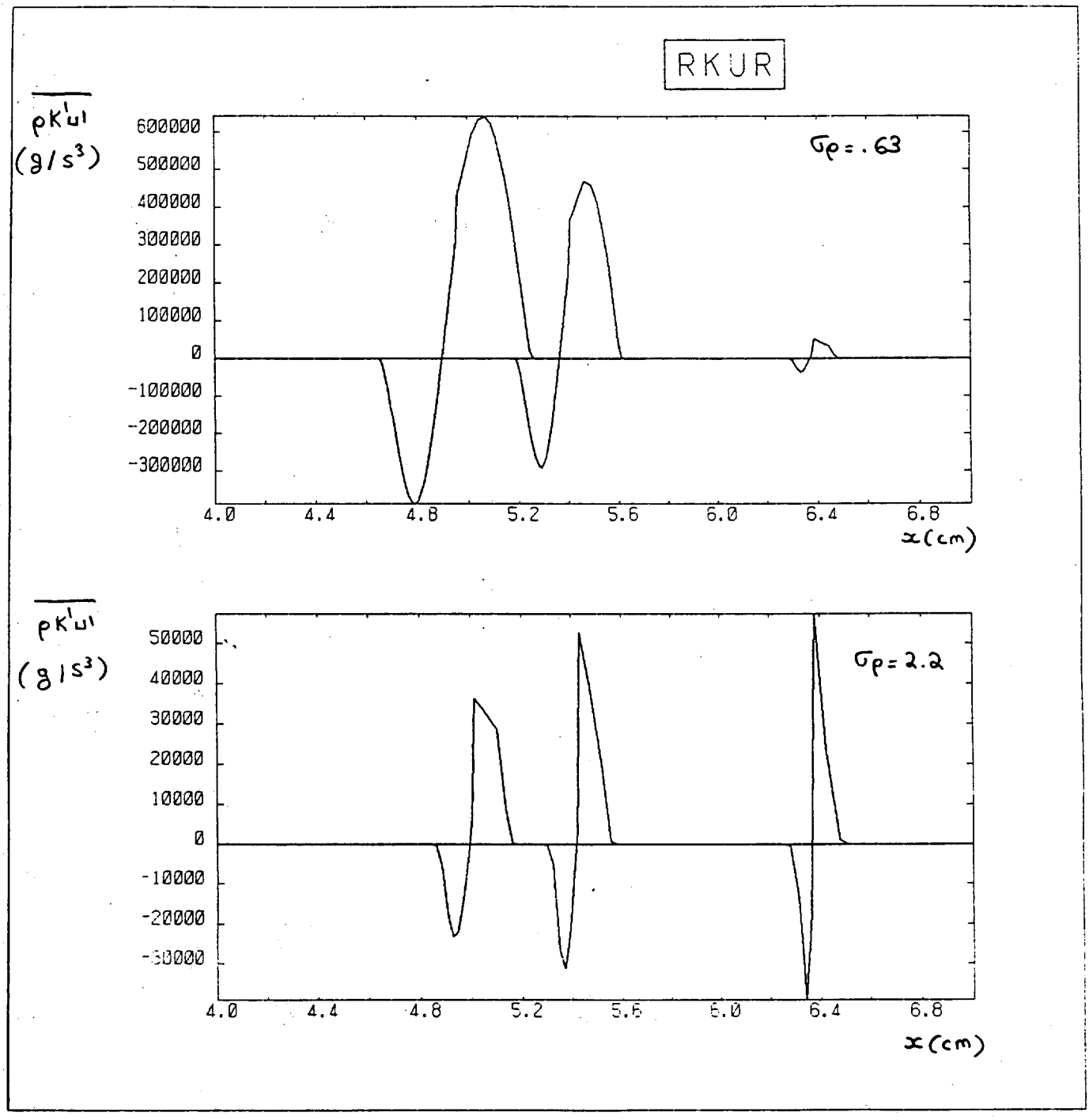

PROBLEM I - HELIUM / AIR

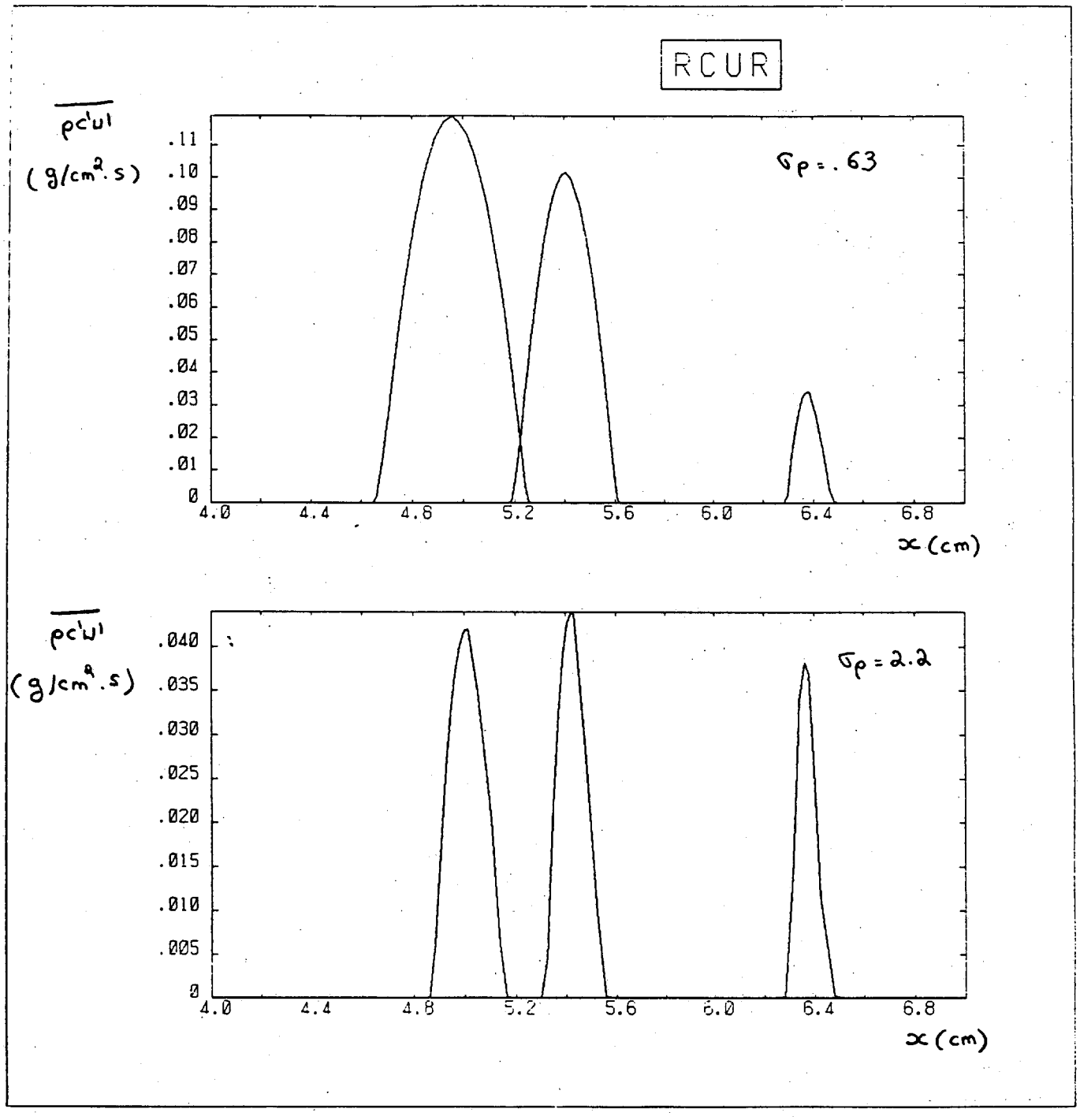

HELIUM/AIR : PROBLEM I

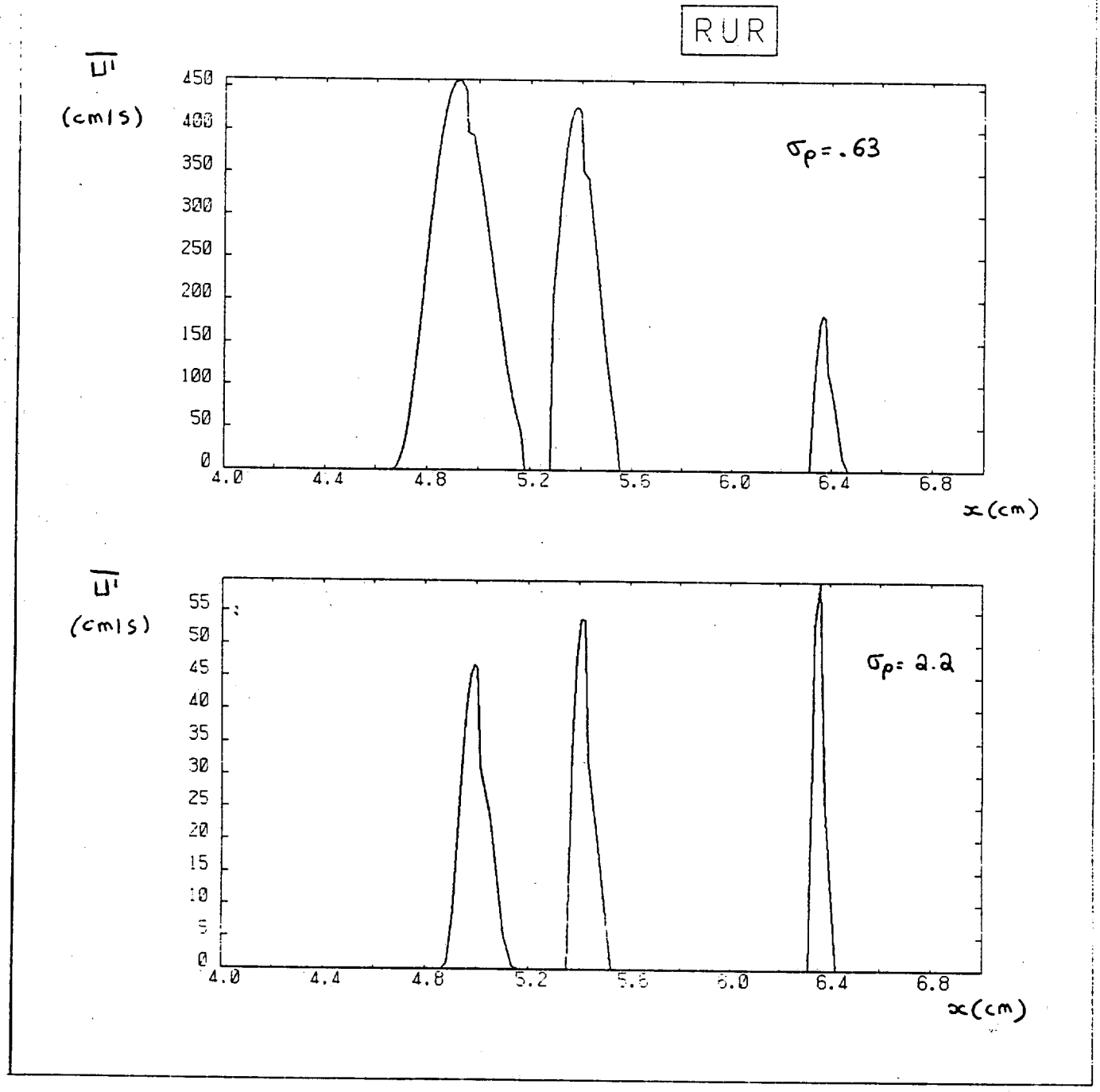

HELIUM / AIR : PROBLEM I.

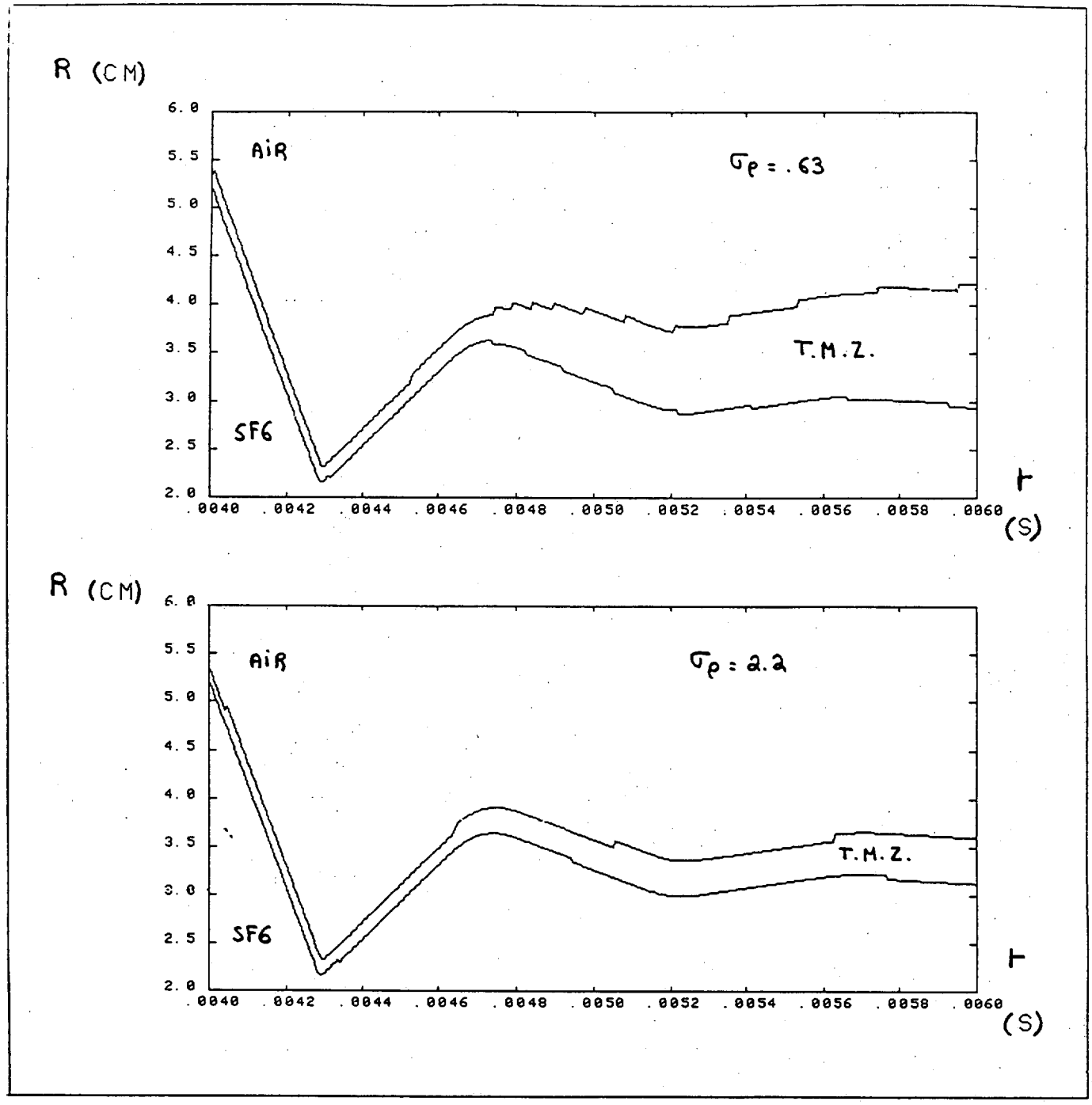

SF6 / AIR : PROBLEM II.

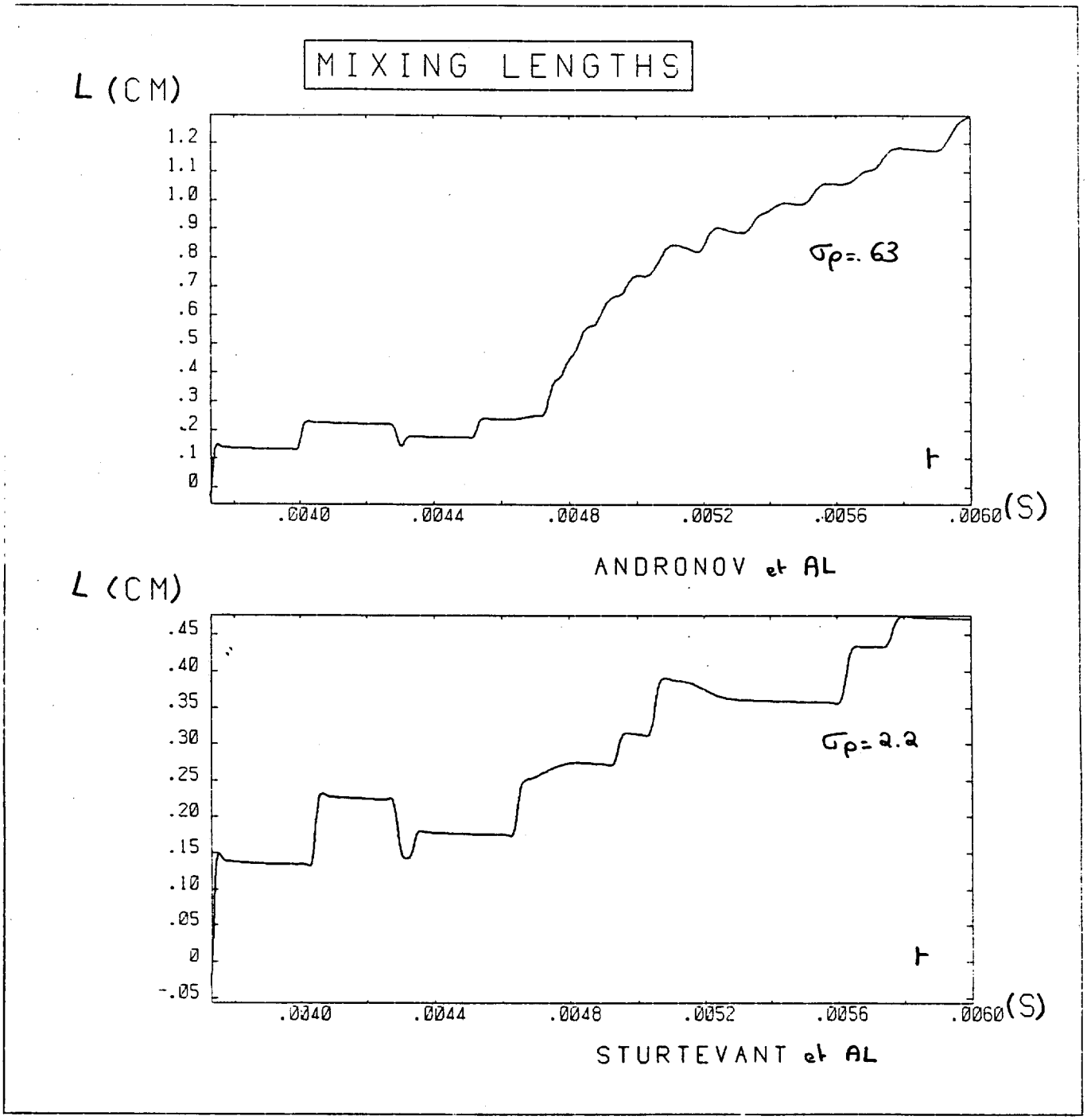

SF6 / AIR : PROBLEM II.

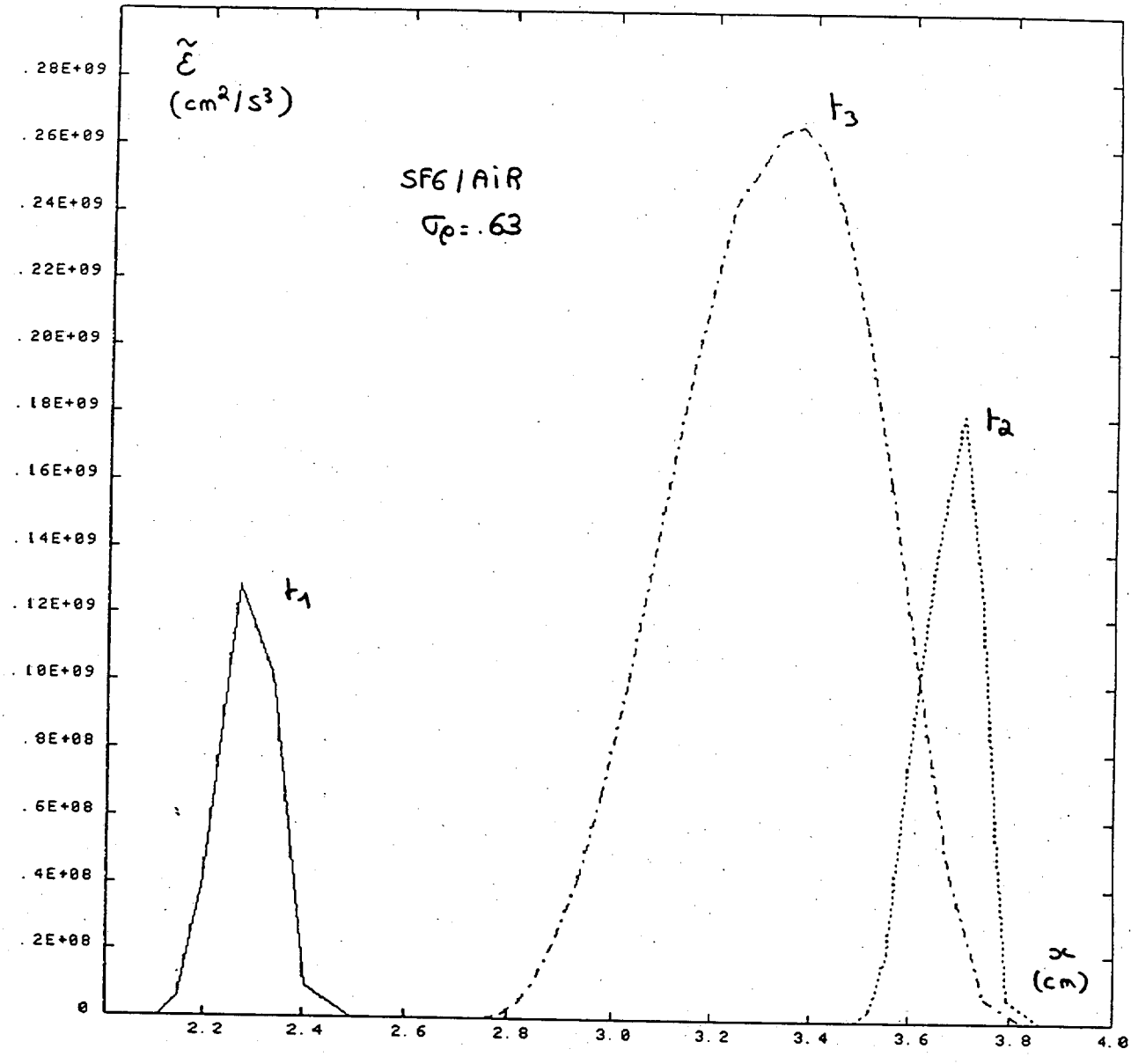
$\tilde{\varepsilon}$
(cm²/s³)
.28E+09
.26E+09
.24E+09
.22E+09
.20E+09
.18E+09
.16E+09
.14E+09
.12E+09
.10E+09
.8E+08
.6E+08
.4E+08
.2E+08
0
SF6/AIR
σ_ρ=.63
t_1
t_2
t_3
2.2
2.4
2.6
2.8
3.0
3.2
3.4
3.6
3.8
4.0
x
(cm)

PROBLEM II

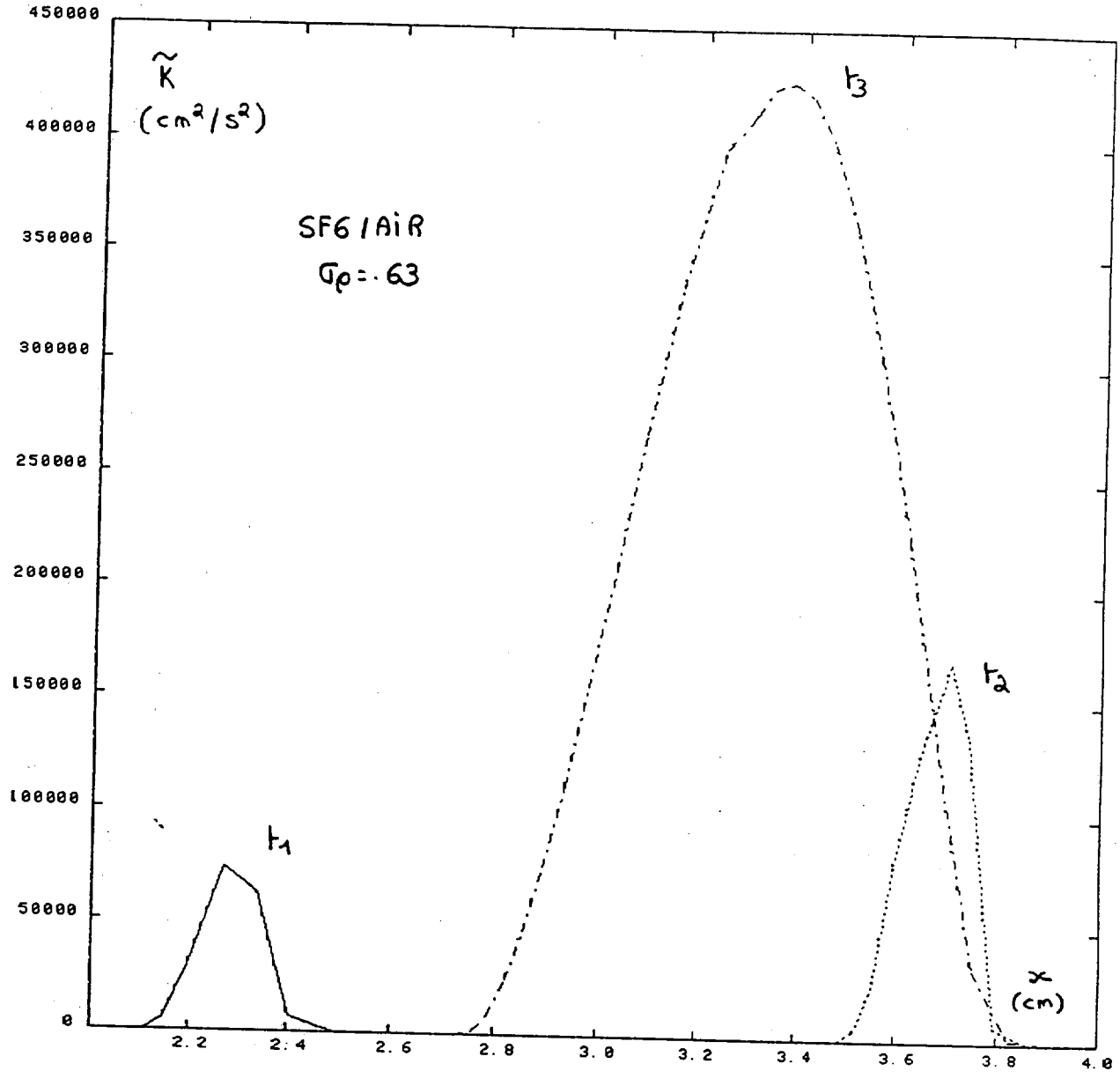
450000
400000
350000
300000
250000
200000
150000
100000
50000
0
$\tilde{K}$
(cm^2/s^2)
SF6/AiR
$\sigma_\rho = .63$
t_1
t_2
t_3
2.2
2.4
2.6
2.8
3.0
3.2
3.4
3.6
3.8
4.0
x
(cm)

PROBLEM II.

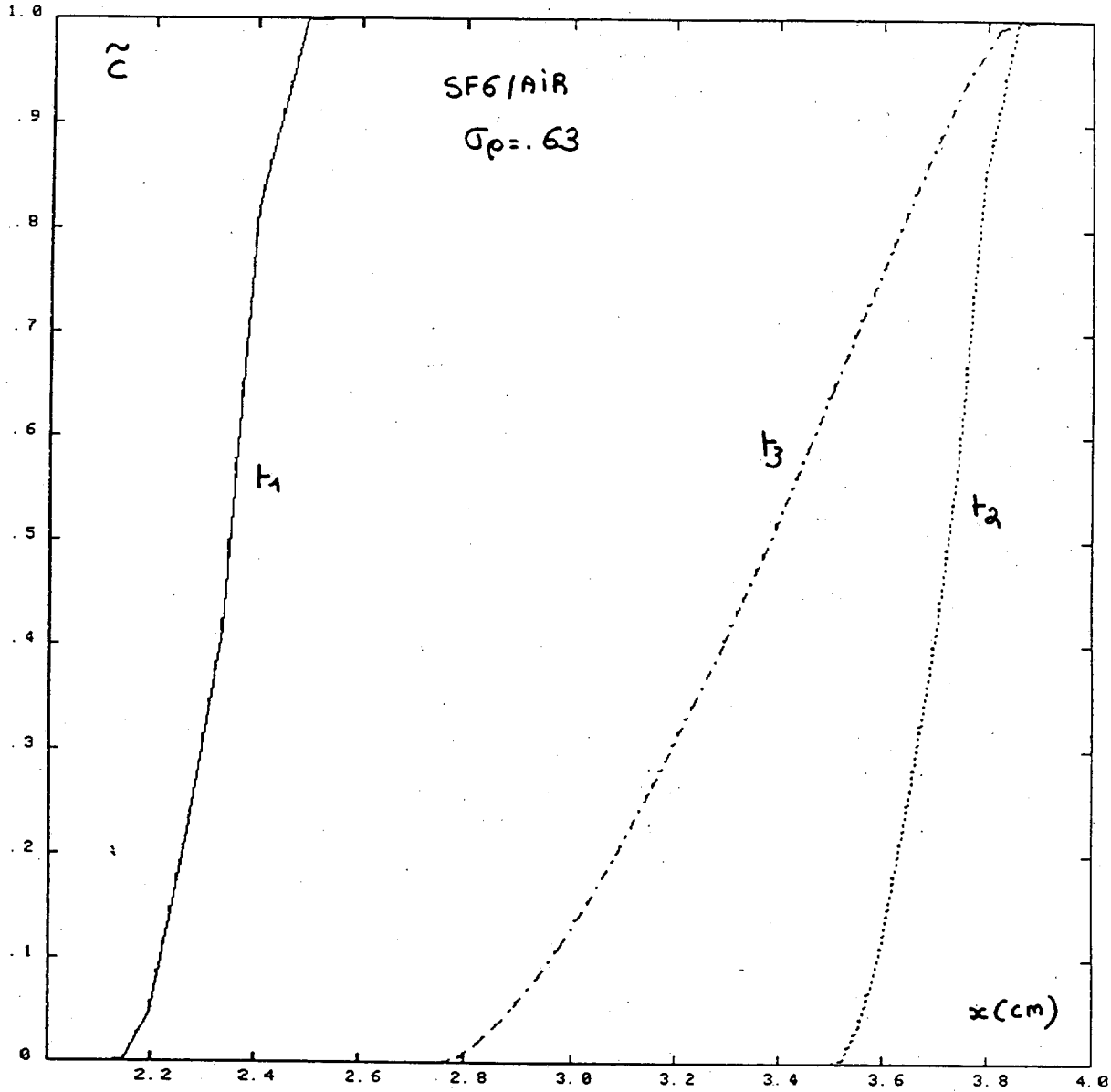
$\tilde{C}$
SF6/AIR
σ_ρ=.63
t_1
t_3
t_2
x(cm)
1.0
.9
.8
.7
.6
.5
.4
.3
.2
.1
0
2.2
2.4
2.6
2.8
3.0
3.2
3.4
3.6
3.8
4.0

PROBLEM II.

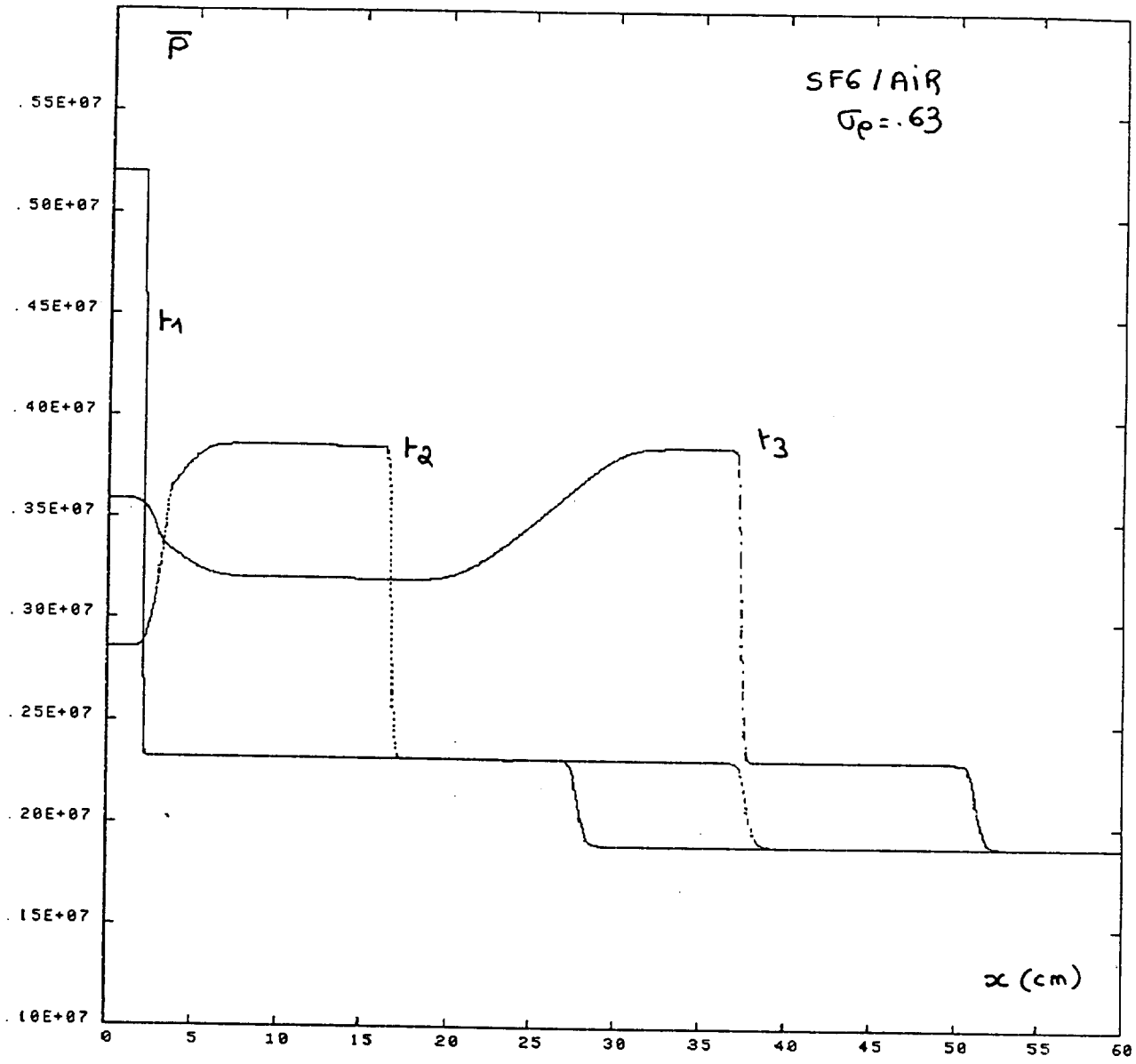
$\bar{P}$
SF6 / AiR
$\sigma_\rho = .63$
.55E+07
.50E+07
.45E+07
.40E+07
.35E+07
.30E+07
.25E+07
.20E+07
.15E+07
.10E+07
t_1
t_2
t_3
x (cm)
0
5
10
15
20
25
30
35
40
45
50
55
60

PROBLEM II.

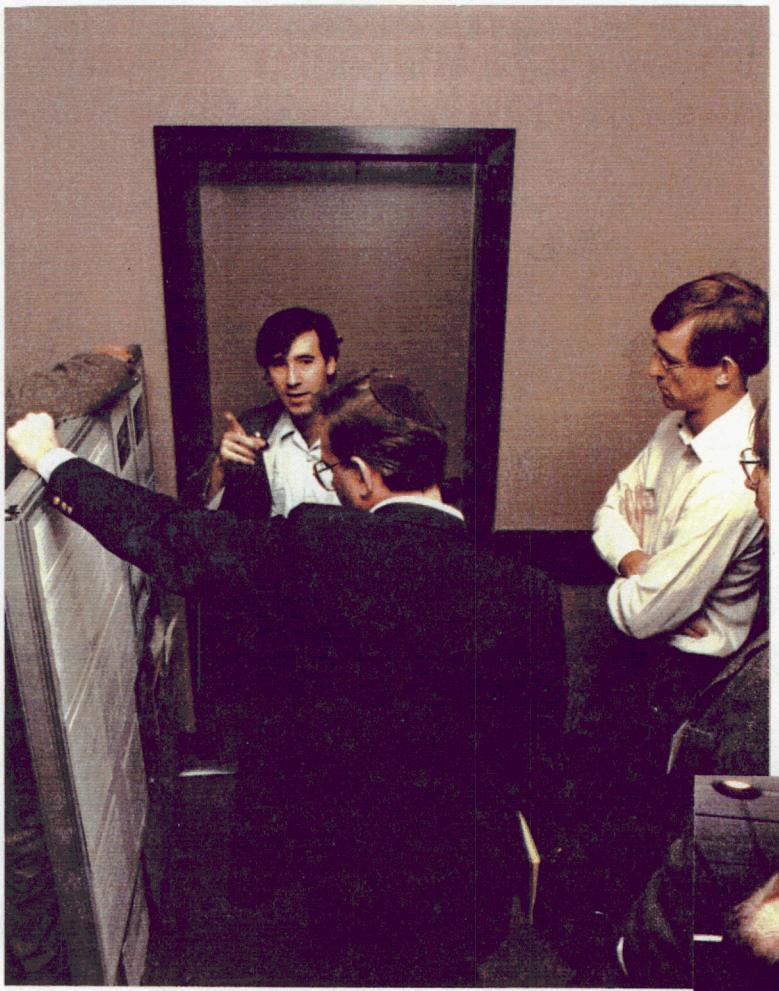

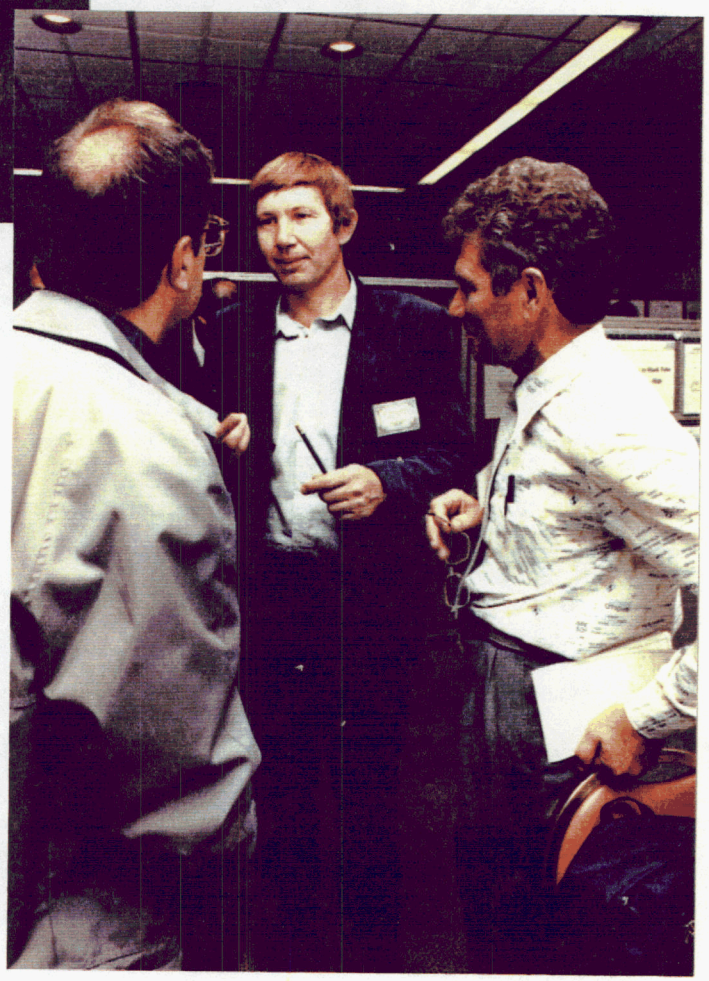

Bill Powers of Los Alamos National Laboratory (9)

Model Equations

1- Hydrodynamics in average center of mass (excluding viscosity)

momentum: $$\frac{\partial \bar{\rho}\tilde{\underline{u}}}{\partial t} + \nabla\cdot\bar{\rho}\tilde{\underline{u}}\tilde{\underline{u}} = -\underline{\nabla} P - \underline{\nabla}\cdot\underline{\underline{R}}$$

$$\overline{\rho\underline{u}} \equiv \bar{\rho}\,\tilde{\underline{u}} = \bar{\rho}\,\bar{\underline{u}} - \overline{\rho'\underline{u}'} \equiv \bar{\rho}(\bar{\underline{u}} - \underline{\omega})$$

$$\underline{\underline{R}} = \overline{\rho(\underline{u}-\tilde{\underline{u}})(\underline{u}-\tilde{\underline{u}})} \equiv \text{Reynold's Stress}$$

Here $(\overline{\cdots})$ indicates ensemble average
$\underline{\omega}$ is the turbulent velocity

mass: $$\frac{\partial \bar{\rho}}{\partial t} + \nabla\cdot\bar{\rho}\tilde{\underline{u}} = 0$$

Internal energy: $$\frac{\partial \bar{\rho}\tilde{I}}{\partial t} + \nabla\cdot\bar{\rho}\tilde{\underline{u}}\tilde{I} = -P\nabla\cdot(\tilde{\underline{u}}-\underline{\omega}) + \bar{\rho}\alpha\epsilon + \underline{\nabla}\cdot K\underline{\nabla}T$$

Here, T is temperature, ϵ is the rate turbulent energy decay.
α is a constant

2- Multifluid Equations

$$\frac{\partial \rho_i}{\partial t} + \underline{\nabla}\cdot\rho_i\underline{u}_i = 0$$

$$\bar{\rho}\left\{\frac{\partial}{\partial t} + \tilde{\underline{u}}\cdot\nabla\right\}\left\{\frac{\rho_i}{\bar{\rho}}(\underline{u}_i - \tilde{\underline{u}})\right\} = -\rho_i(\underline{u}_i - \tilde{\underline{u}})\cdot\nabla\tilde{\underline{u}} + \frac{\rho_i}{\rho}\nabla\cdot(\underline{\underline{R}} + P) - \nabla\cdot(\underline{\underline{R}}_i + P_i) + \sum_j \rho_i \nu_{ij}(\underline{u}_j - \underline{u}_i)$$

where i refers to the i-th species

$\underline{\underline{R}}_i = \rho_i(\underline{u}_i - \tilde{\underline{u}})^2$ is species Reynolds Stress

and collision frequency $\nu_{ij} = \frac{\rho_j}{\bar{\rho}}\frac{c_i}{\Lambda_{ij}}$

c_i is the sound speed of i-th species

Λ_{ij} is a mean free collision length

Λ_{ij}, the collision mean free path, has both a molecular and turbulent contribution

$$\Lambda_{ij} = \delta_{ij} + \alpha_{ij} c_i \frac{\bar{\rho}}{\rho} \nu_t$$

where ν_t is a turbulent viscosity.

$$\nu_t = \frac{k^2}{\epsilon} ,$$

where k is the turbulent kinetic energy ($R_{ii} = \frac{1}{2}\bar{\rho} k$)

α_{ij} are adjustable constants.

δ_{ij} are set close to the expected molecular collision path between species i and j.

---

3 - Turbulent equations

- ν_t determined from equations for

a- the turbulent kinetic energy

$$\frac{\partial \bar{\rho} k}{\partial t} + \nabla \cdot \bar{\rho} \tilde{\underline{u}} k = \underline{\omega} \cdot \nabla P - \underline{\underline{R}} \cdot \nabla \cdot \tilde{\underline{u}} + \nabla \cdot \bar{\rho} \nu_t \nabla k - \alpha \bar{\rho} \epsilon$$

$$\underline{\underline{R}} = \frac{2}{3} k \underline{\underline{\delta}} - \underline{\underline{\Gamma}}$$

b- $\underline{\underline{\Gamma}}$ determined from PDE's or Boussonesq-like approximation

$$\underline{\underline{\Gamma}} = -\bar{\rho} \nu_t \left\{ \nabla \circ u - \frac{2}{3} \underline{\underline{\delta}} \nabla \cdot u \right\}$$

where $\nabla \circ u$ is symmetric product

c- rate of decay of k

$$\frac{\partial \bar{\rho} \epsilon}{\partial t} + \nabla \cdot \bar{\rho} \tilde{\underline{u}} \epsilon = \nabla \cdot \left(\frac{\rho \nu_t}{\sigma_\epsilon} \nabla \epsilon \right) + C_{\epsilon 3} \bar{\rho} \epsilon \nabla \cdot u + \frac{\epsilon}{k} \left\{ C_{\epsilon 4} \underline{\omega} \cdot \nabla P - C_{\epsilon 1} \underline{\underline{R}} \cdot \nabla \cdot u - C_{\epsilon 2} \bar{\rho} \epsilon \right\}$$

d- A PDE equation $\underline{\omega}$ or a chunk mix approximation

$$\underline{\omega} = \sum_i \alpha_i (\tilde{\underline{u}} - \underline{u}_i)$$

Here, α_i are volume fractions. If we assume the chunks within a cell are in temperature and pressure equilibrium, α_i can be determined.

For ideal gases, $\alpha_i = c_i$, the number fractions.

Procedure

1- For shock-tube problems, the molecular mean free path remains virtually constant throughout problem.
   a- pick a molecular mean free path.

2- A finite mean free path δ_{ij} will initiate mix when shock first passes through.

3- Initial mix brings turbulent velocity $\underline{w}$ up off the floor.

4- When $\underline{w}$ comes up, the turbulent kinetic energy k also comes up.

5- An initial parameter s_0 also initializes $\epsilon = \frac{k^{3/2}}{s_0}$.

   s_0 is set to the default value of $10^{-12} * \{\text{problem size}\}$.

6- larger s_0 means a smaller $\epsilon \Rightarrow k$ comes up faster.

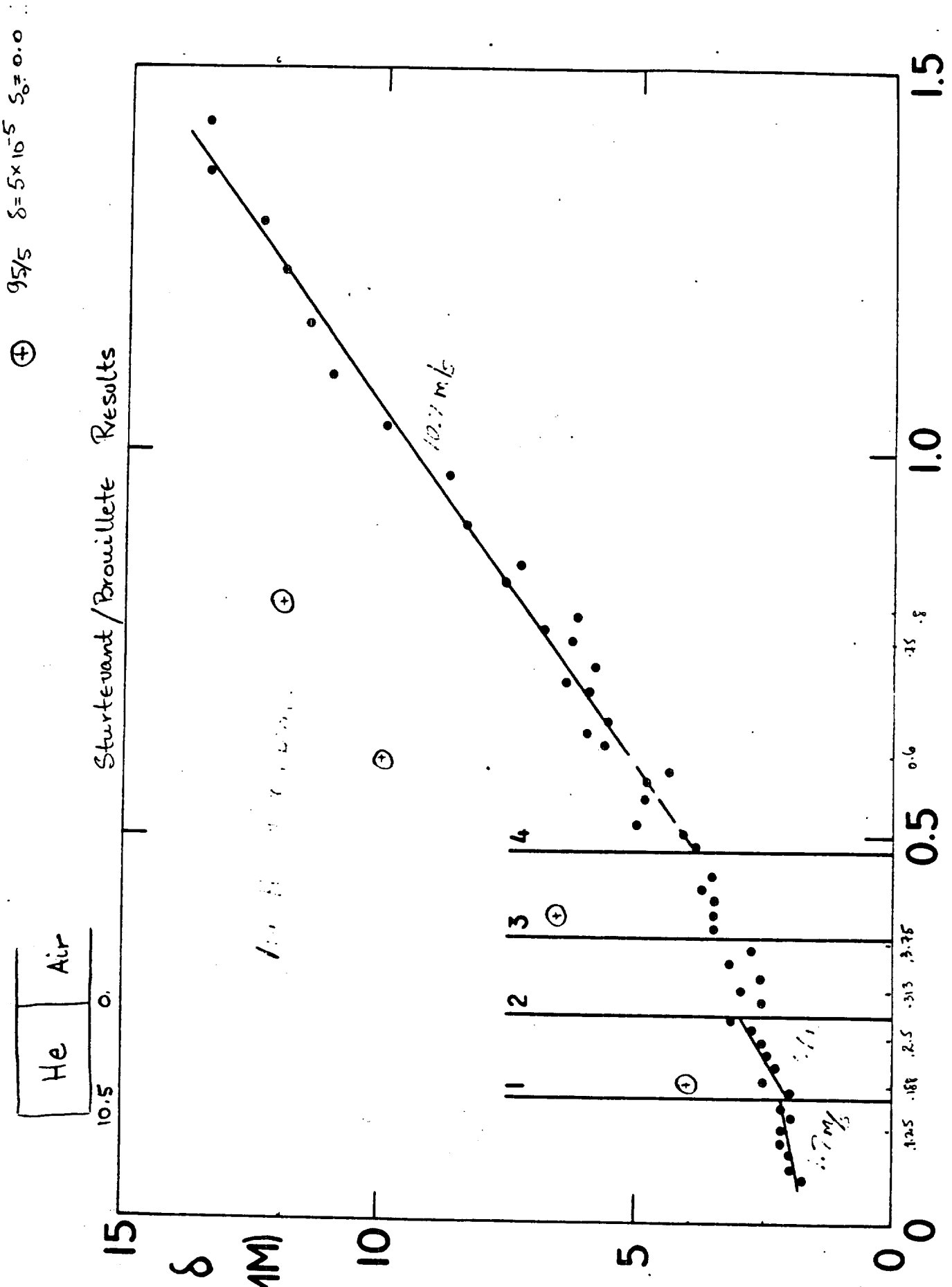
95/5 δ=5×10⁻⁵ S₀=0.0
Sturtevant/Brouillete Results
He
Air
10.5
0.
δ (MM)
T(MS)
15
10
5
0
0.5
1.0
1.5
1
2
3
4

FIGURE 10

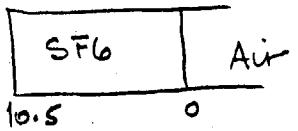

⊕ 95/5 $\delta = 1 \times 10^{-4}$ $S_0 = 1 \times 10^{-4}$

Sturtevant / Brouillette Results

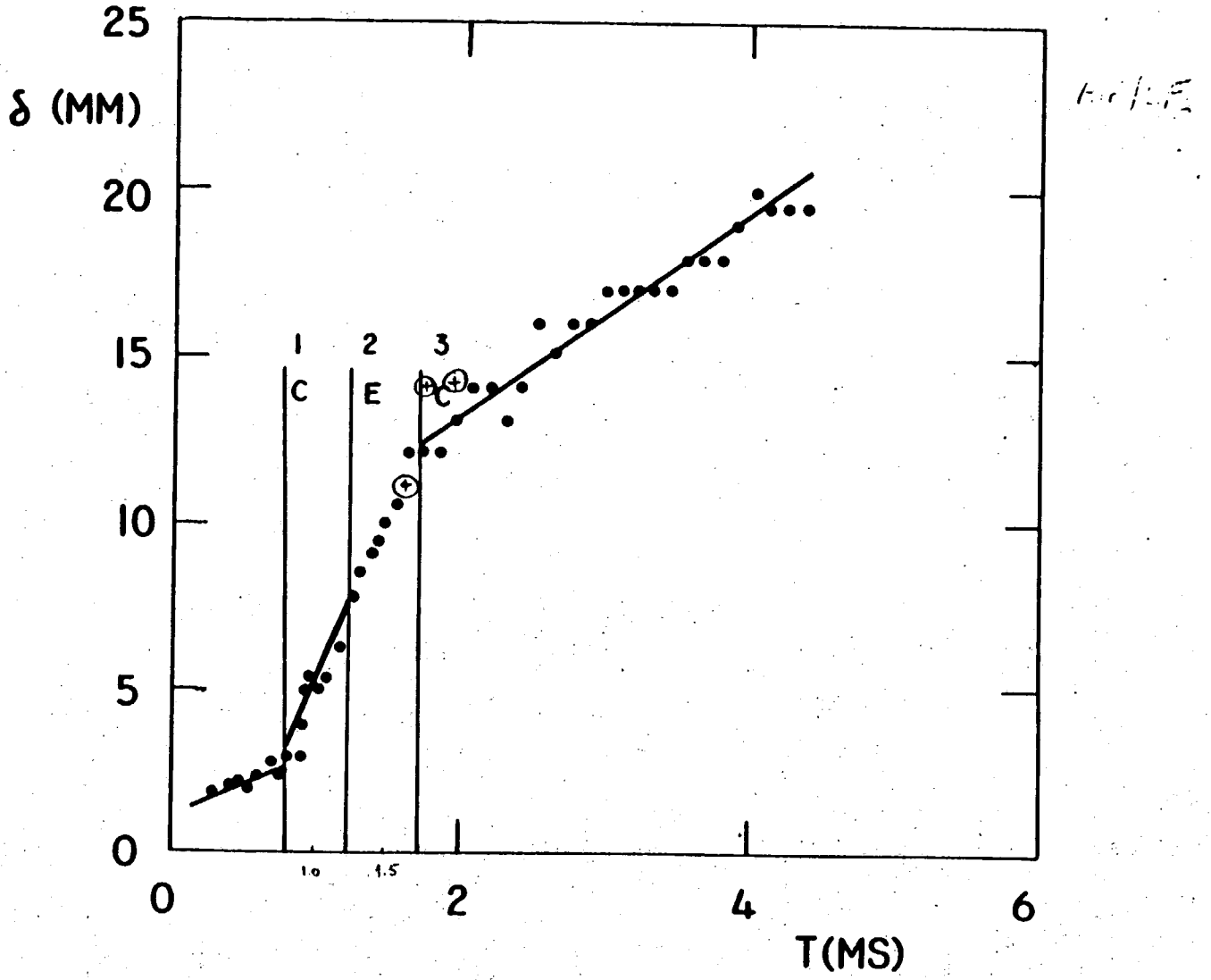

FIGURE 7

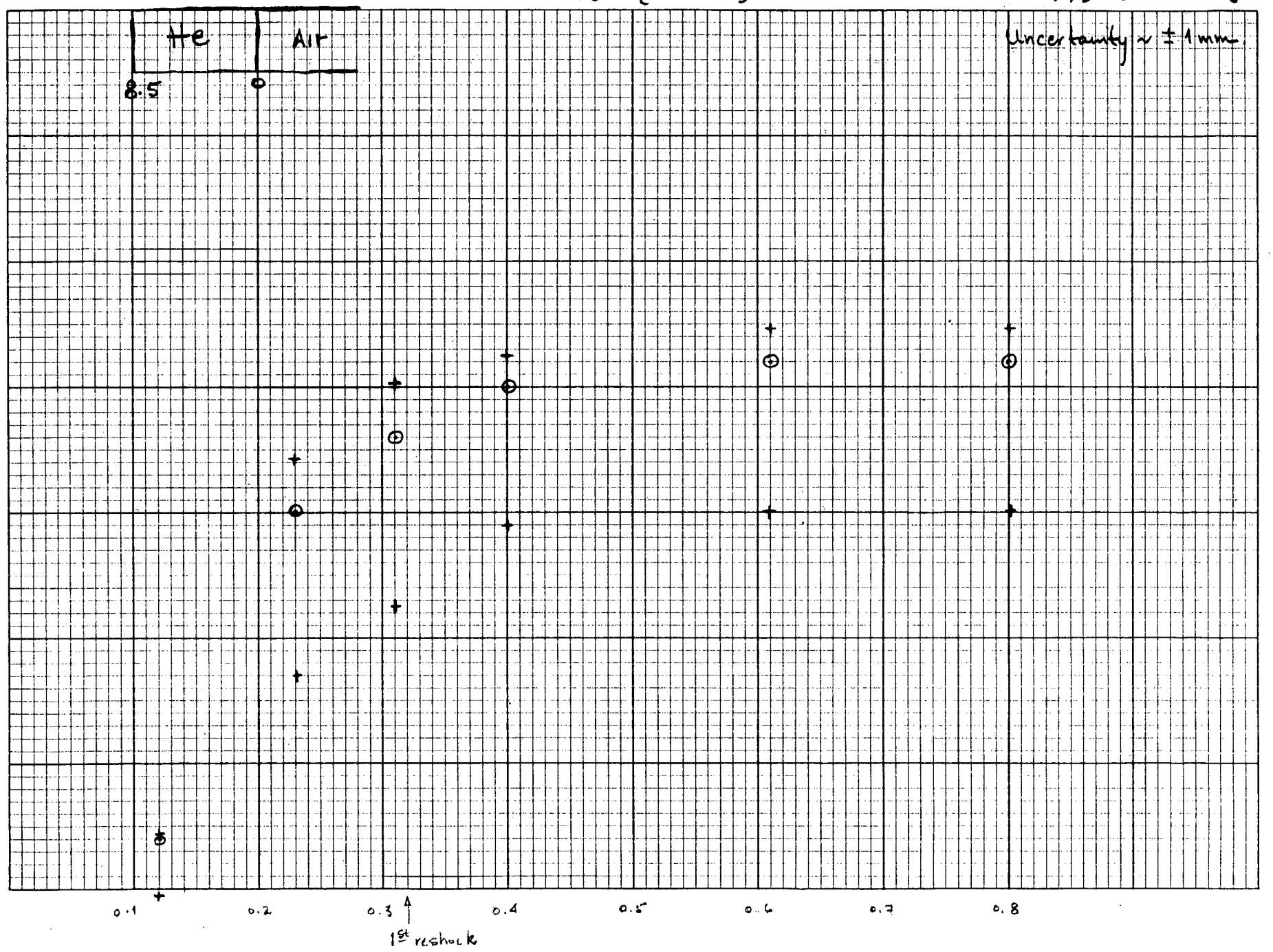

Air/He
$\delta = 1 \times 10^{-4}$
$S_0 = 0.0$

TP6A

```
* PROBLEM  3 PLOT  1
* PROBLEM NAME TP6A3
* K=    2   L1=    1   L2=   51
* X VAR:   L
* Y VAR:   FRAC01
* FILE         TP6A3DA
* TIME    0.0000000
* CYCLE       0
* PROBLEM  3 PLOT  2
* PROBLEM NAME TP6A3
* K=    2   L1=    1   L2=   51
* X VAR:   L
* Y VAR:   FRAC01
* FILE         TP6A3DA
* TIME     101333.8
* CYCLE      580
* PROBLEM  3 PLOT  3
* PROBLEM NAME TP6A3
* K=    2   L1=    1   L2=   51
* X VAR:   L
* Y VAR:   FRAC01
* FILE         TP6A3DA
* TIME     113249.0
* CYCLE      640
* PROBLEM  3 PLOT  4
* PROBLEM NAME TP6A3
* K=    2   L1=    1   L2=   51
* X VAR:   L
* Y VAR:   FRAC01
* FILE         TP6A3DA
* TIME     123063.6
* CYCLE      700
* PROBLEM  3 PLOT  5
* PROBLEM NAME TP6A3
* K=    2   L1=    1   L2=   51
* X VAR:   L
* Y VAR:   FRAC01
* FILE         TP6A3DA
* TIME     131326.4
* CYCLE      760
* PROBLEM  3 PLOT  6
* PROBLEM NAME TP6A3
* K=    2   L1=    1   L2=   51
* X VAR:   L
* Y VAR:   FRAC01
* FILE         TP6A3DA
* TIME     150403.6
* CYCLE      900
* SCALE OPTION   USE
* X-AXIS:  5.000     :  20.00
* SCALE OPTION   USE
* Y-AXIS: 0.0000     :  1.000
?
```

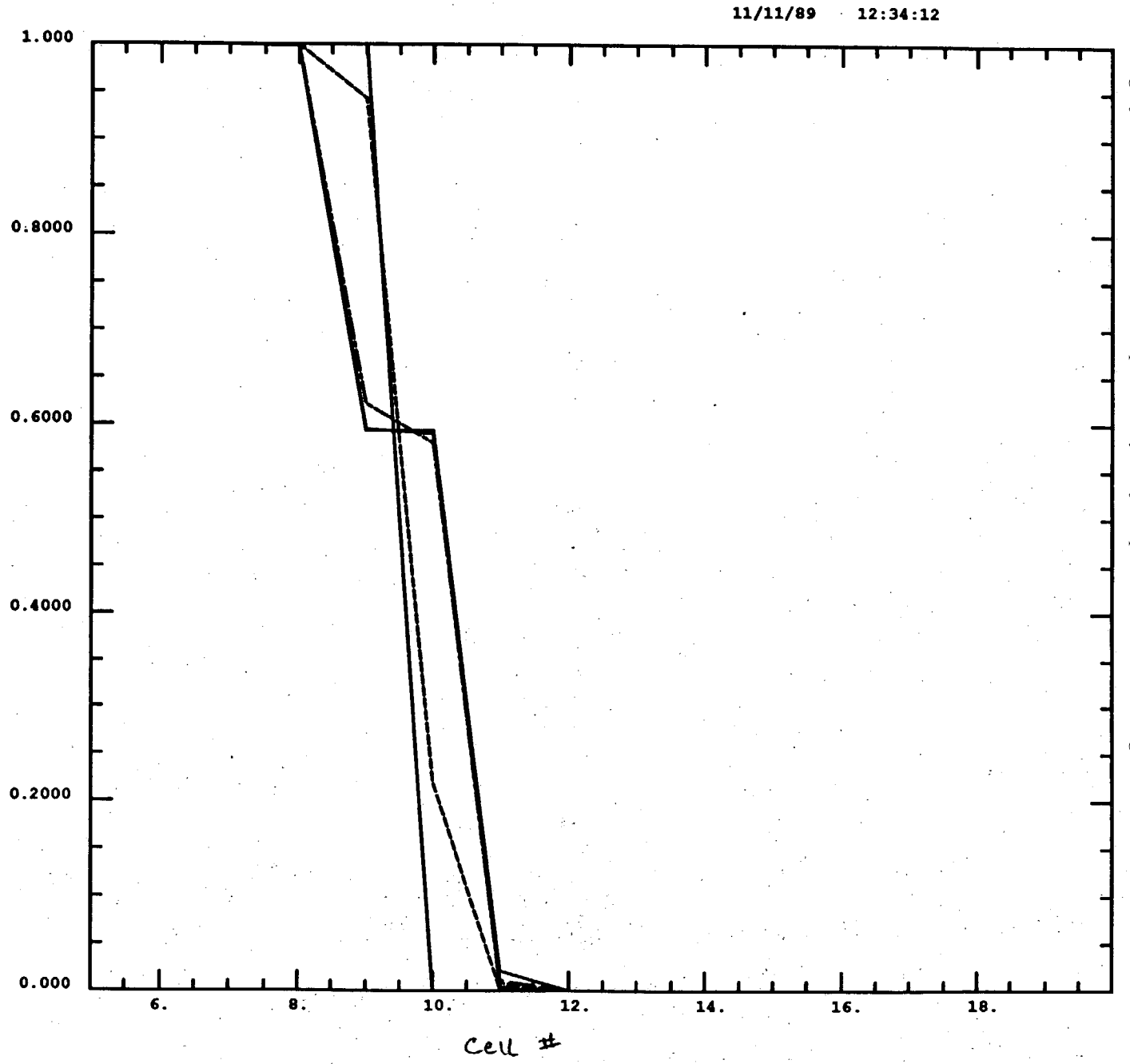

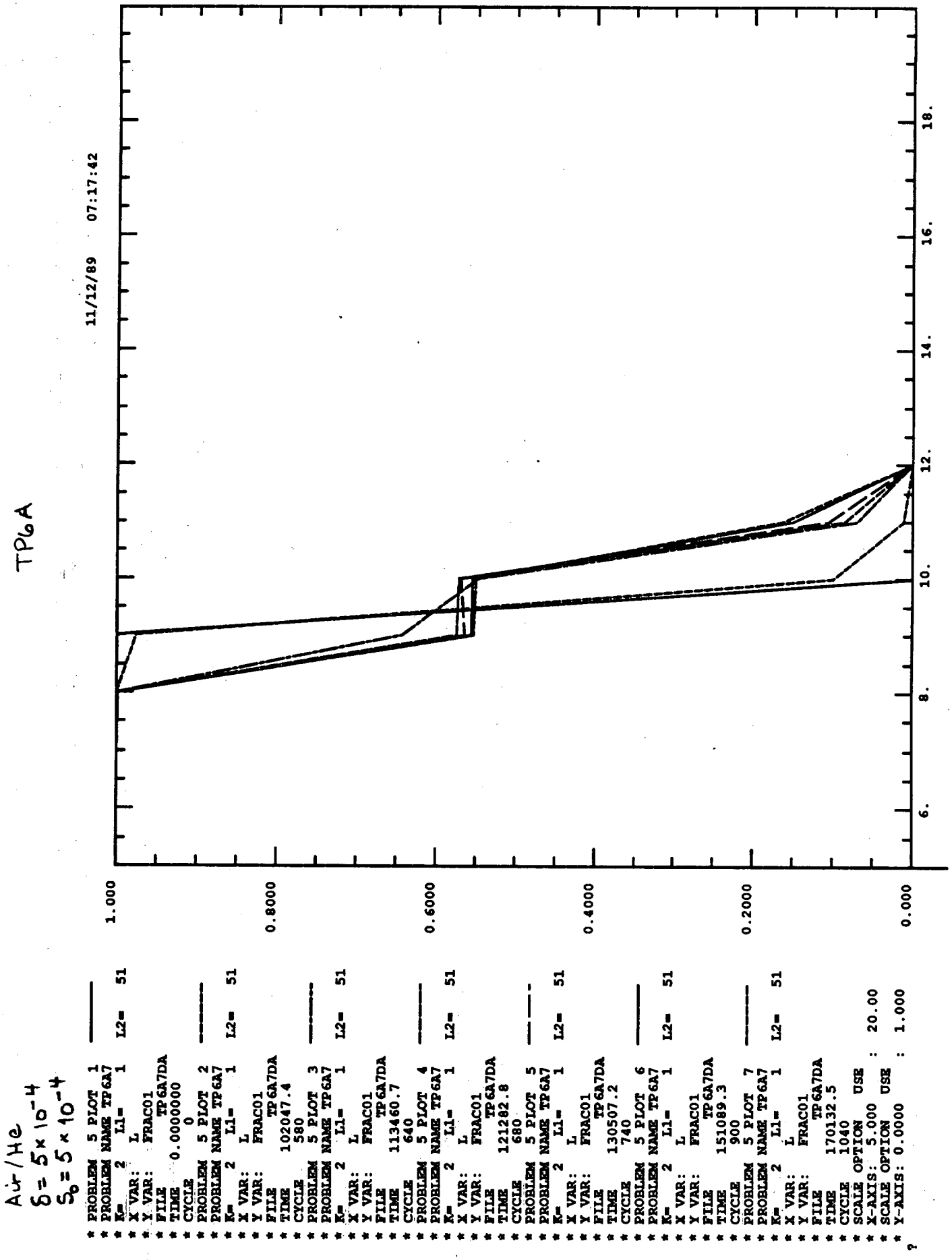
TP6A
Air/He
δ = 5 × 10⁻⁴
S₀ = 5 × 10⁻⁴
11/12/89 07:17:42
1.000
0.8000
0.6000
0.4000
0.2000
0.000
6.
8.
10.
12.
14.
16.
18.
* PROBLEM 5 PLOT 1
* PROBLEM NAME TP6A7
* K= 2 L1= 1 L2= 51
* X VAR: L
* Y VAR: FRAC01
* FILE TP6A7DA
* TIME 0.0000000
* CYCLE 0
* PROBLEM 5 PLOT 2
* PROBLEM NAME TP6A7
* K= 2 L1= 1 L2= 51
* X VAR: L
* Y VAR: FRAC01
* FILE TP6A7DA
* TIME 102047.4
* CYCLE 580
* PROBLEM 5 PLOT 3
* PROBLEM NAME TP6A7
* K= 2 L1= 1 L2= 51
* X VAR: L
* Y VAR: FRAC01
* FILE TP6A7DA
* TIME 113460.7
* CYCLE 640
* PROBLEM 5 PLOT 4
* PROBLEM NAME TP6A7
* K= 2 L1= 1 L2= 51
* X VAR: L
* Y VAR: FRAC01
* FILE TP6A7DA
* TIME 121282.8
* CYCLE 680
* PROBLEM 5 PLOT 5
* PROBLEM NAME TP6A7
* K= 2 L1= 1 L2= 51
* X VAR: L
* Y VAR: FRAC01
* FILE TP6A7DA
* TIME 130507.2
* CYCLE 740
* PROBLEM 5 PLOT 6
* PROBLEM NAME TP6A7
* K= 2 L1= 1 L2= 51
* X VAR: L
* Y VAR: FRAC01
* FILE TP6A7DA
* TIME 151089.3
* CYCLE 900
* PROBLEM 5 PLOT 7
* PROBLEM NAME TP6A7
* K= 2 L1= 1 L2= 51
* X VAR: L
* Y VAR: FRAC01
* FILE TP6A7DA
* TIME 170132.5
* CYCLE 1040
* SCALE OPTION USE
* X-AXIS: 5.000 : 20.00
* SCALE OPTION USE
* Y-AXIS: 0.0000 : 1.000
?

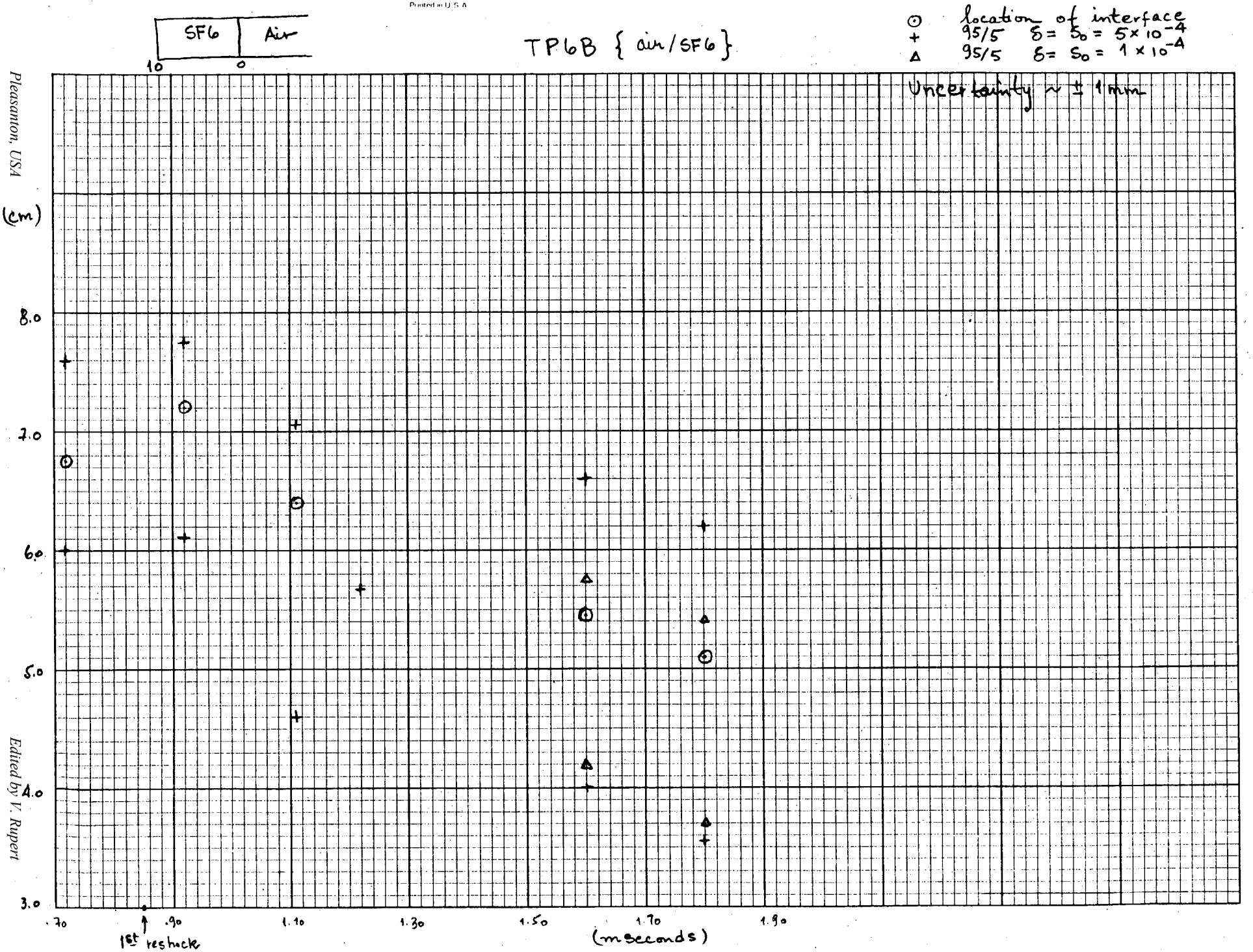

Edited by V. Rupert

Air/SF6

$\delta = 1 \times 10^{-4}$

$S_0 = 1 \times 10^{-4}$

```
* PROBLEM  5 PLOT  1  ————
* PROBLEM NAME TP6B4
* K=    2   L1=    1   L2=   53
* X VAR:   L
* Y VAR:   FRAC01
* FILE         TP6B4DA
* TIME   0.0000000
* CYCLE      0
* PROBLEM  5 PLOT  2  - - - -
* PROBLEM NAME TP6B4
* K=    2   L1=    1   L2=   53
* X VAR:   L
* Y VAR:   FRAC01
* FILE         TP6B4DA
* TIME    161567.3
* CYCLE     880
* PROBLEM  5 PLOT  3  - - - -
* PROBLEM NAME TP6B4
* K=    2   L1=    1   L2=   53
* X VAR:   L
* Y VAR:   FRAC01
* FILE         TP6B4DA
* TIME    181567.3
* CYCLE     980
* PROBLEM  5 PLOT  4  - - - -
* PROBLEM NAME TP6B4
* K=    2   L1=    1   L2=   53
* X VAR:   L
* Y VAR:   FRAC01
* FILE         TP6B4DA
* TIME    201567.3
* CYCLE    1080
* PROBLEM  5 PLOT  5  — — . -
* PROBLEM NAME TP6B4
* K=    2   L1=    1   L2=   53
* X VAR:   L
* Y VAR:   FRAC01
* FILE         TP6B4DA
* TIME    249567.3
* CYCLE    1320
* PROBLEM  5 PLOT  6  ————
* ALTERED CURVE   6
* PROBLEM NAME TP6B4
* X VAR:   L
* Y VAR:   FRAC01
* FILE         TP6B4DA
* TIME    269567.3
* CYCLE    1420
* PROBLEM  5 PLOT  7  - - - -
* ALTERED CURVE   7
* PROBLEM NAME TP6B4
* X VAR:   L
* Y VAR:   FRAC01
* FILE         TP6B4DA
* TIME    289567.3
* CYCLE    1520
* SCALE OPTION   USE
* X-AXIS:  5.000     :  20.00
* SCALE OPTION   USE
* Y-AXIS: 0.0000     :  1.000
?
```

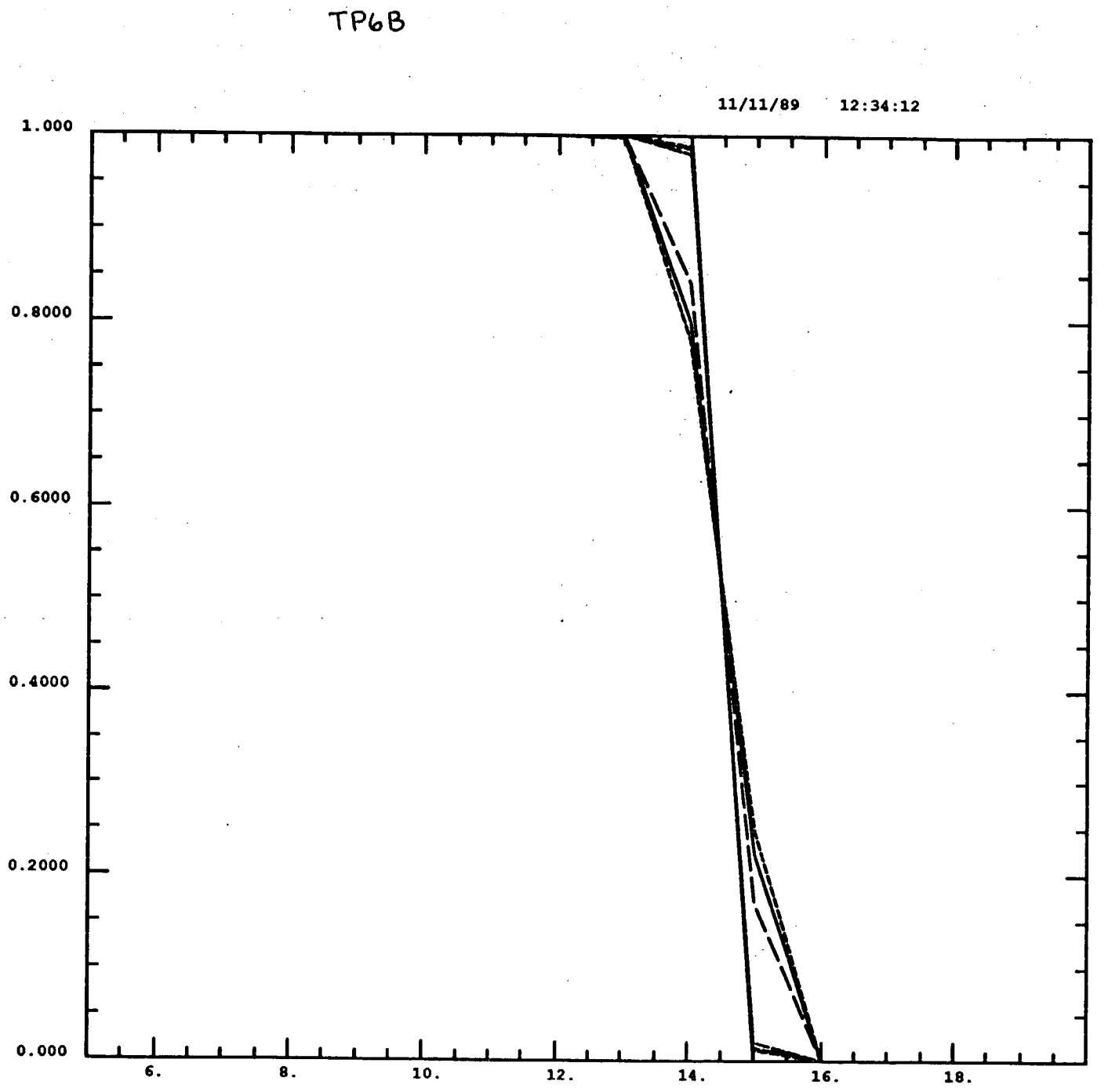

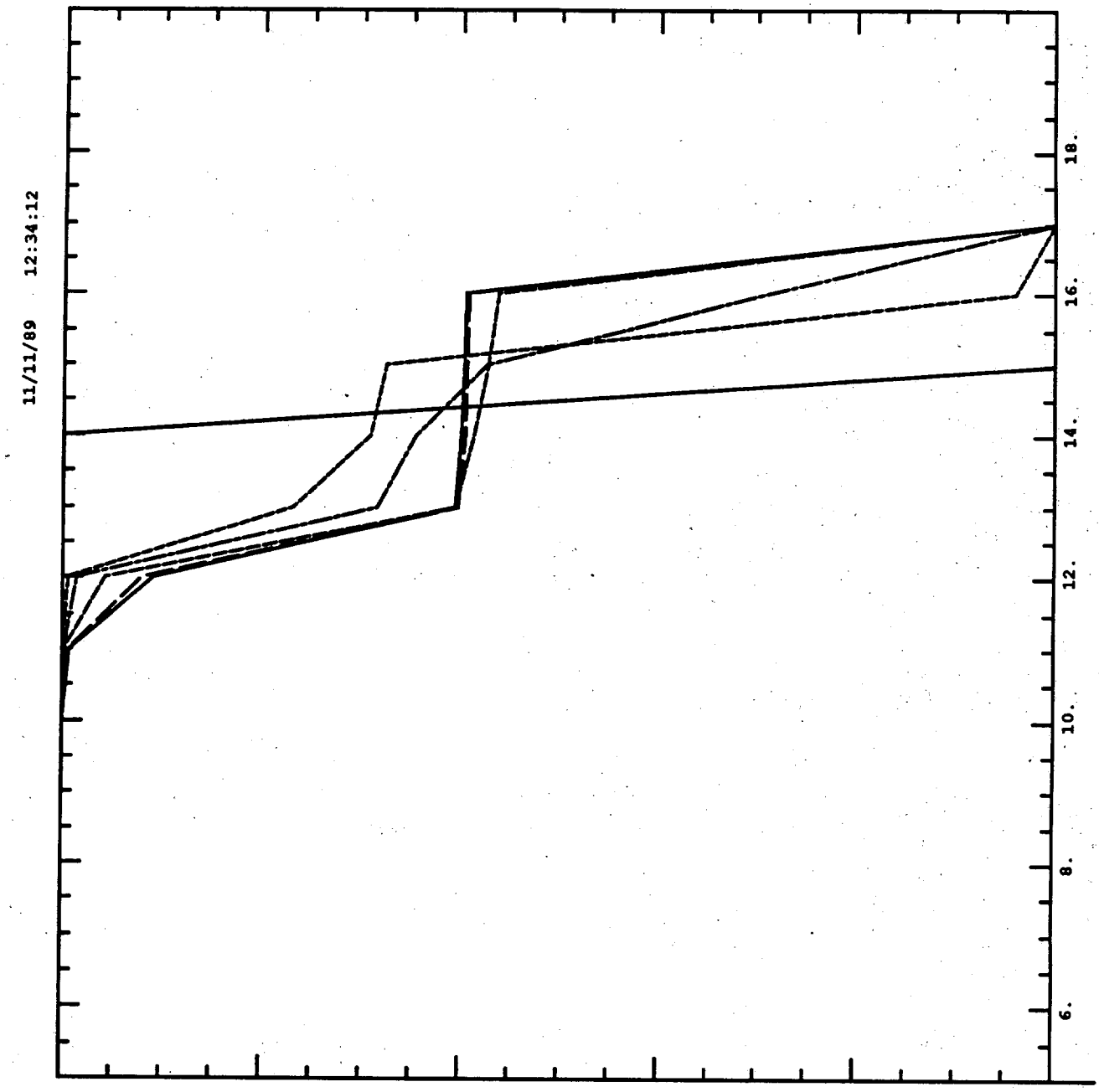

TP6B

Air/SF6
$\delta = 5 \times 10^{-4}$
$\delta_0 = 5 \times 10^{-4}$

```
* PROBLEM  3 PLOT  1
* PROBLEM NAME TP6B7
* K=   2   L1=   1   L2=  53
* X VAR:        L
* Y VAR:     FRAC01
* FILE        TP6B7DA
* TIME    0.0000000
* CYCLE           0
* PROBLEM  3 PLOT  2
* PROBLEM NAME TP6B7
* K=   2   L1=   1   L2=  53
* X VAR:        L
* Y VAR:     FRAC01
* FILE        TP6B7DA
* TIME       161567.3
* CYCLE         880
* PROBLEM  3 PLOT  3
* PROBLEM NAME TP6B7
* K=   2   L1=   1   L2=  53
* X VAR:        L
* Y VAR:     FRAC01
* FILE        TP6B7DA
* TIME       181567.3
* CYCLE         980
* PROBLEM  3 PLOT  4
* PROBLEM NAME TP6B7
* K=   2   L1=   1   L2=  53
* X VAR:        L
* Y VAR:     FRAC01
* FILE        TP6B7DA
* TIME       201567.3
* CYCLE        1080
* PROBLEM  3 PLOT  5
* PROBLEM NAME TP6B7
* K=   2   L1=   1   L2=  53
* X VAR:        L
* Y VAR:     FRAC01
* FILE        TP6B7DA
* TIME       249567.3
* CYCLE        1320
* PROBLEM  3 PLOT  6
* ALTERED CURVE  6
* PROBLEM NAME TP6B7
* X VAR:        L
* Y VAR:     FRAC01
* FILE        TP6B7DA
* TIME       269567.3
* CYCLE        1420
* SCALE OPTION   USE      :  20.00
* X-AXIS:  5.000
* SCALE OPTION   USE      :  1.000
* Y-AXIS:  0.0000
?
```

Solution of Rayleigh-Taylor Test Problem

J. Glimm
SUNY Stony Brook

X. L. Li
NJIT

in collaboration with

R. Menikoff
LANL

D. Sharp
LANL

Q. Zhang
NYU

Main Results - RT problem

(1) Highly resolved complex interface

(2) Agreement with experiment

$\alpha = .06$ 2D

$h(t)$ = mixing layer height = $\alpha A g t^2$

up to ~ $1\frac{1}{2}$ generation bubble merger

(3) Late time $\alpha \simeq .04$

Due to <u>exact</u> 2D aspect of computation: multi-phase disconnection of flow

(4) Validation by comparison to analytic results, mesh refinement, other computations

(5) Theoretical Model, Renormalization Group Fixed Point. Proof of $h = \alpha A g t^2$ behavior.

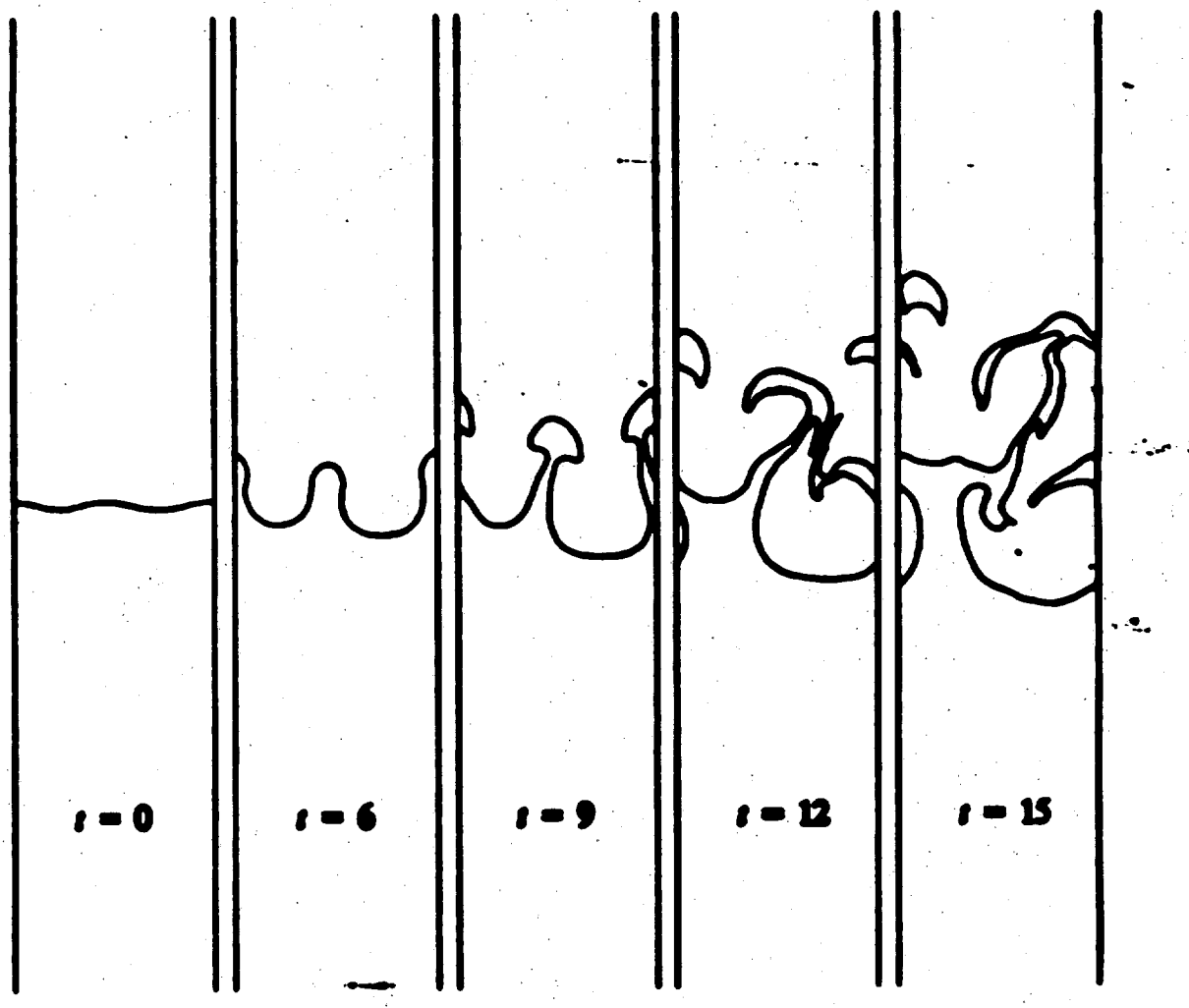

Figure 3.2.1. Successive times in a two bubble merger process. The compressibility and density ratio for this case are $M^2 = 0.1$ and $D = 5$ respectively. It can be seen that the large bubble overtakes the smaller one at $t = 12$. The velocity of the large bubble is accelerated during the merger while the velocity of the small bubble is reversed, see Figure 3.2.2.

(8)

Mode-Mode Interaction

(a) Bubble Vel ≠ Vel of single mode theory

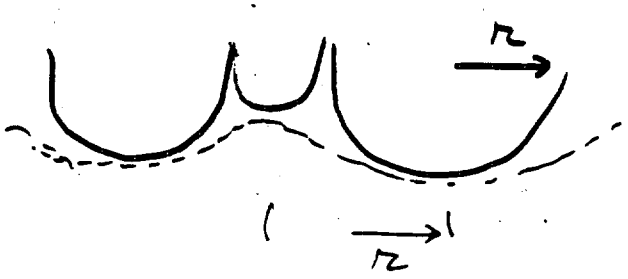

$v_{bubble} \simeq v_{single\ mode} + v_{envelope}$

both specified from Single mode theory

(b) Bubble merger – dynamic change of length scales

Superposition Theory

$$v_{chaotic} = v_{bubble} + v_{envelope}$$

Test against experiment:

5 - 20 % agreement

Test against computations:

Distinct Regimes

agreement
disagreement
└ causes understood

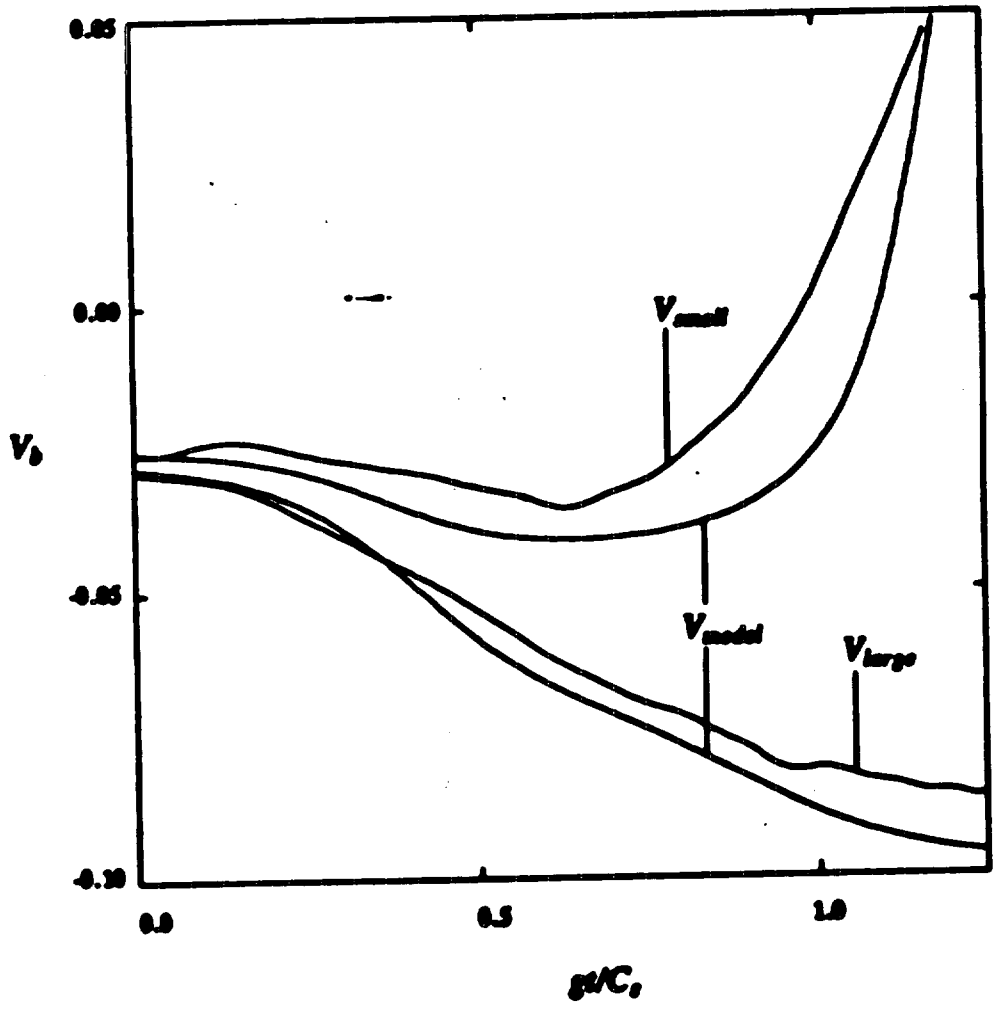

Figure 3.2.2. The plots of bubble velocities vs. time for the two bubble merger simulation. The result shows that the small bubble is accelerated at the beginning and is then decelerated after about $t = 5$. The small bubble is washed out downstream after its velocity is reversed. The large bubble is under constant acceleration. The smooth curves represent the bubble motion as predicted by the superposition hypothesis.

Test Problem Parameters:

Grid: 100 x 200

Domain: 1 x 2

Interface: Multi mode
about 25 initial bubbles
Sum of Fourier frequencies
24-34 wavelengths / domain
Amplitudes from Gaussian distribution

Boundary Conditions:
Periodic on sides
Reflecting Top + Bottom

EOS = γ-law gas $\gamma = 1.4$

$$A = \frac{\rho_2 - \rho_1}{\rho_2 + \rho_1} \qquad D = \frac{\rho_2}{\rho_1}$$

$$M^2 = \frac{\lambda g}{c_h} \qquad c_h = \text{sound speed heavy fluid}$$

Note: Value of M^2 is approximate due to:

variable bubble size in space, especially in time

Case I: $M^2 = .1$, $D = 2$ $(A = .33)$

Case II: $M^2 = .1$, $D = 5$ $(A = .667)$

Case III: $M^2 = .01$, $D = 5$ $(A = .667)$

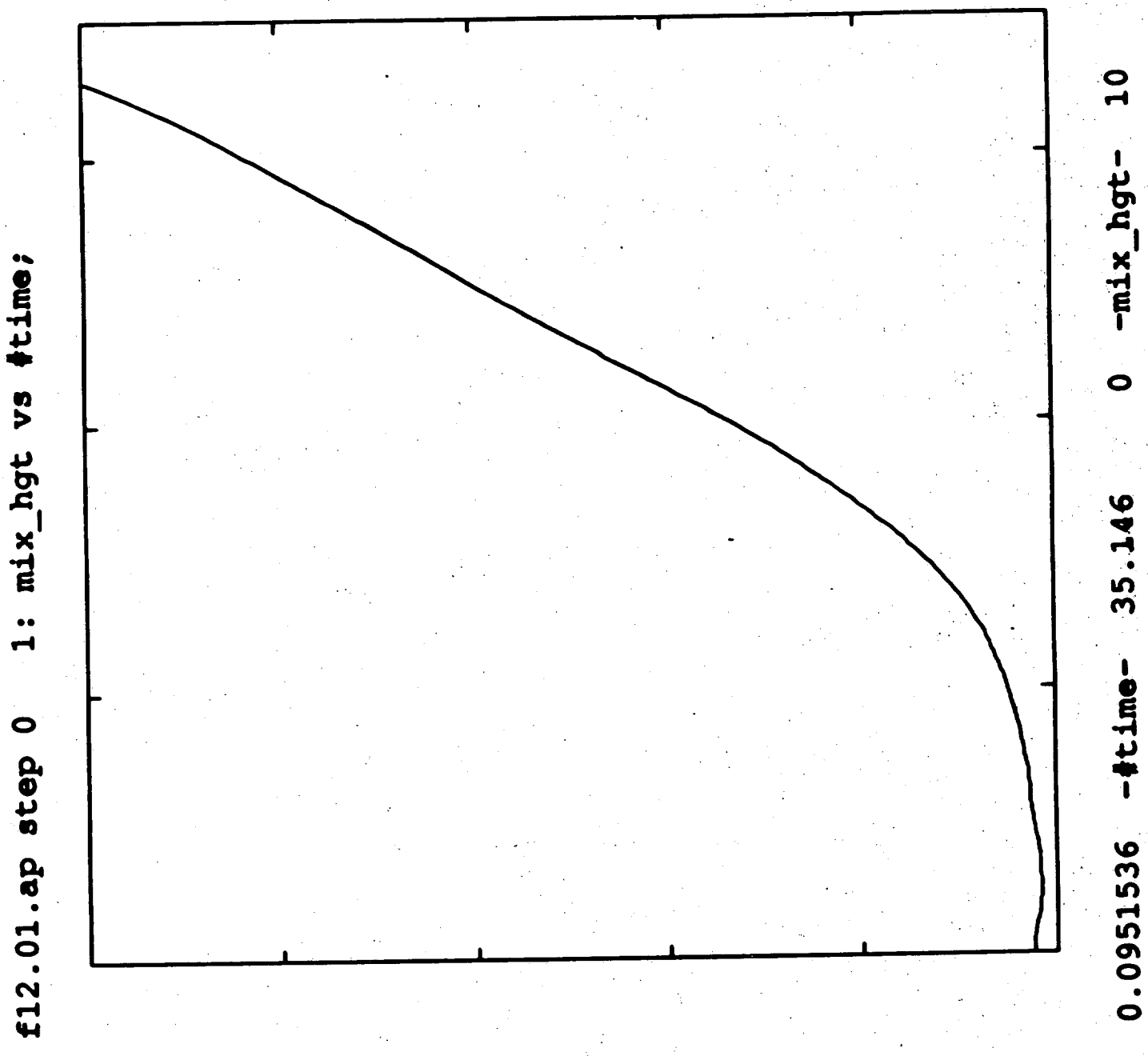
f12.01.ap step 0 1: mix_hgt vs #time;
0.0951536 -#time- 35.146 0 -mix_hgt- 10

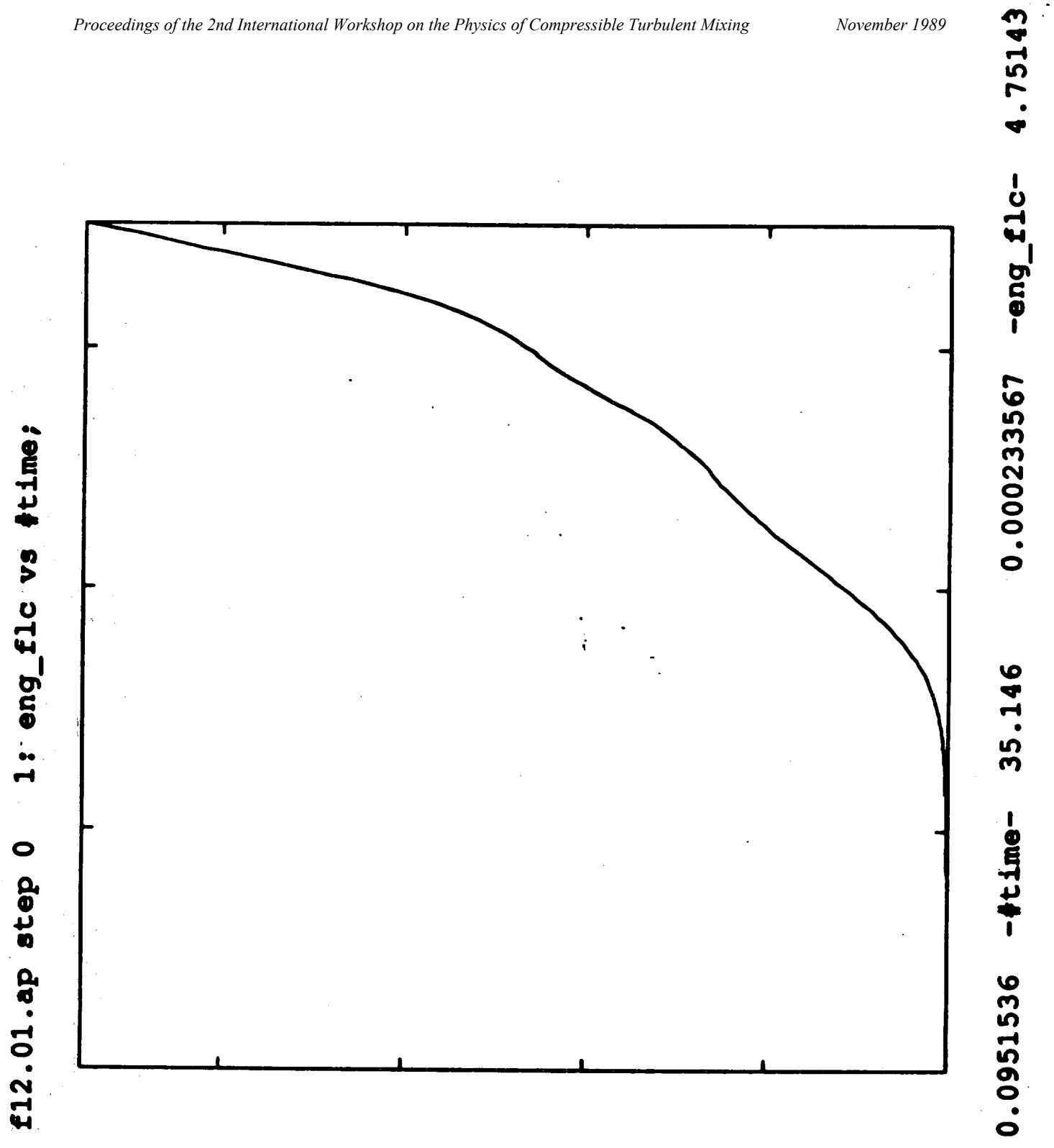
f12.01.ap step 0 1: eng_flc vs #time;
0.0951536 -#time- 35.146
0.000233567 -eng_flc- 4.75143

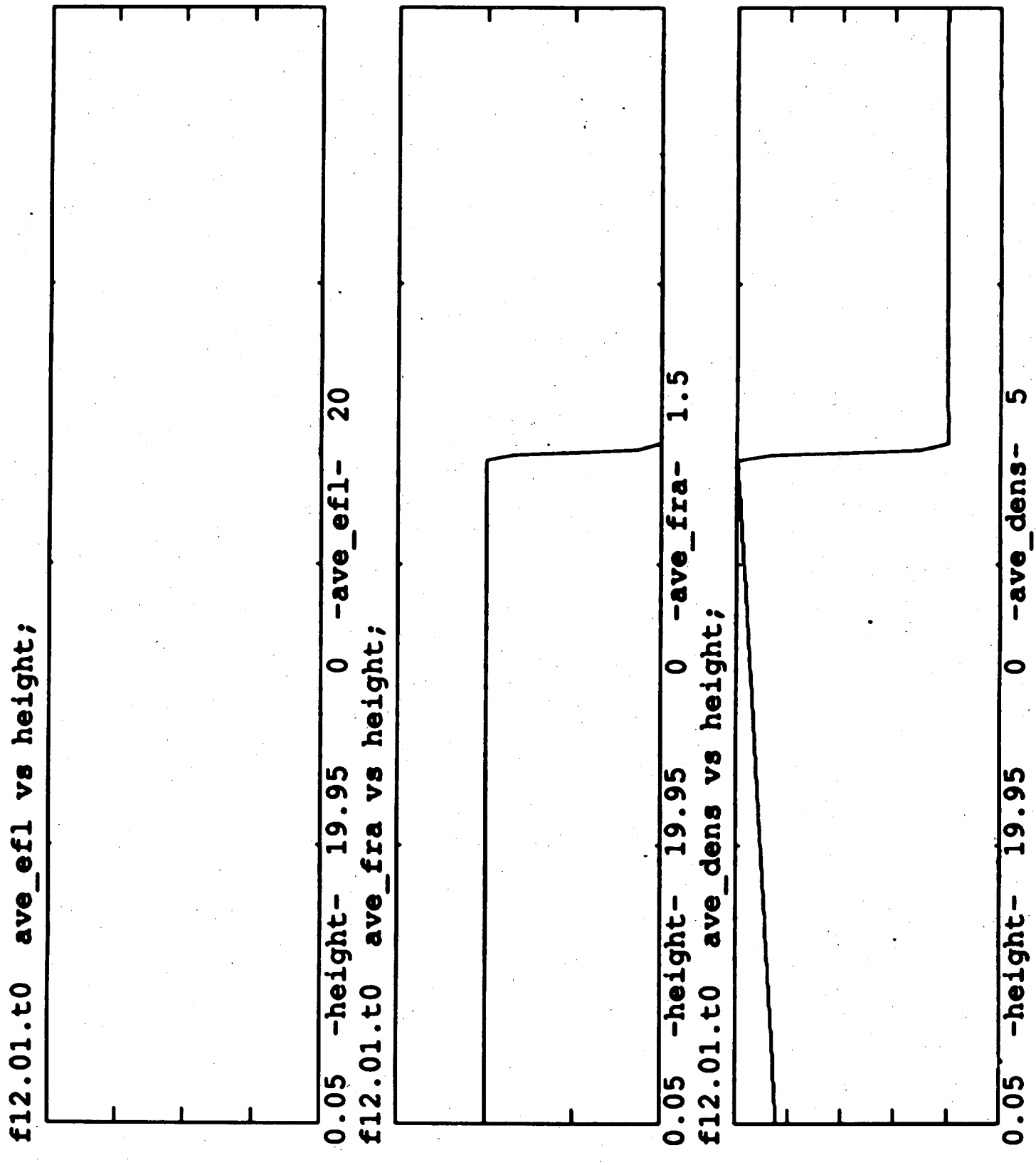
f12.01.t0 ave_efl vs height;
0.05 -height- 19.95 0 -ave_efl- 20
f12.01.t0 ave_fra vs height;
0.05 -height- 19.95 0 -ave_fra- 1.5
f12.01.t0 ave_dens vs height;
0.05 -height- 19.95 0 -ave_dens- 5

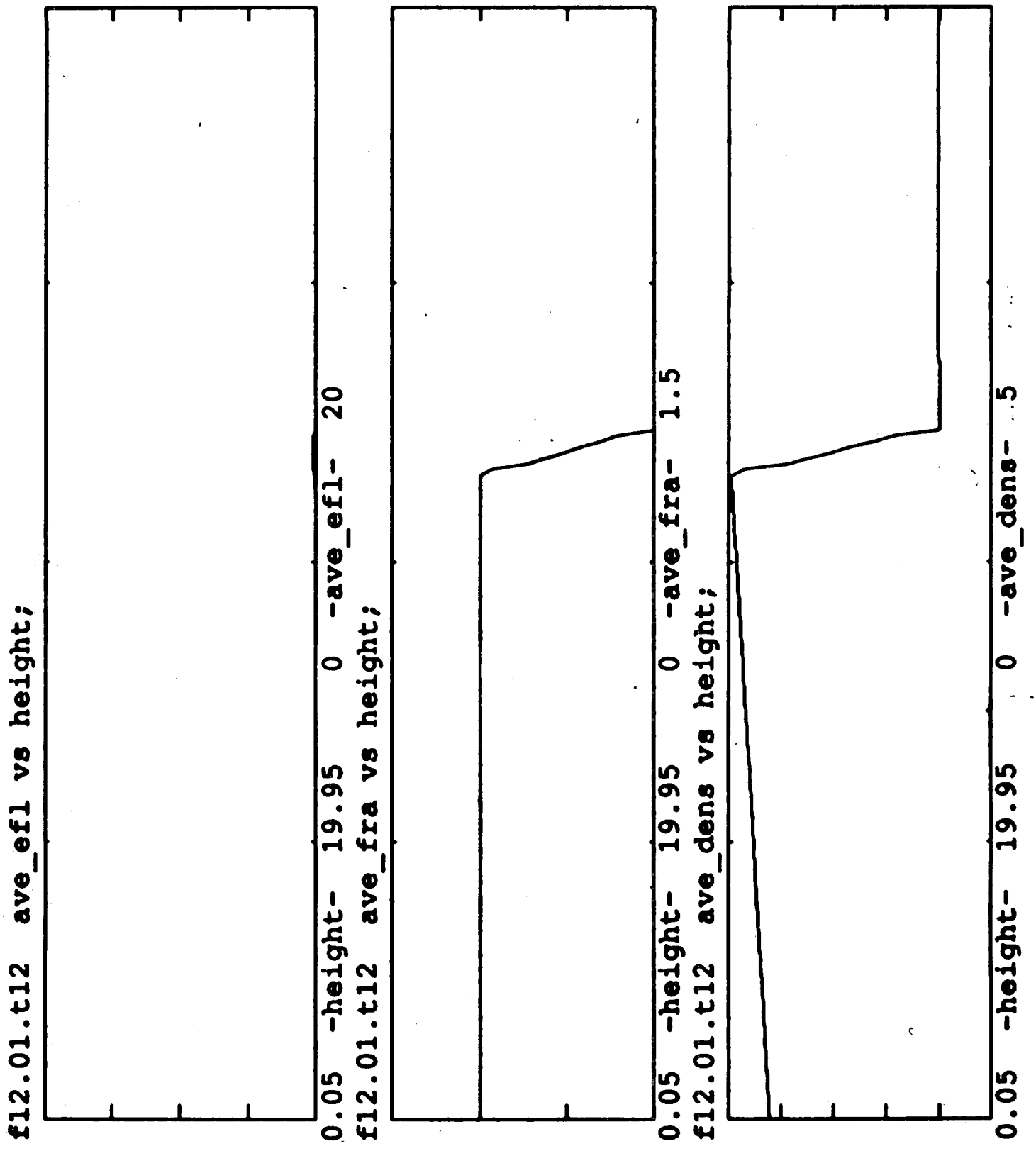
f12.01.t12 ave_efl vs height;
0.05 -height- 19.95 0 -ave_efl- 20
f12.01.t12 ave_fra vs height;
0.05 -height- 19.95 0 -ave_fra- 1.5
f12.01.t12 ave_dens vs height;
0.05 -height- 19.95 0 -ave_dens- 5

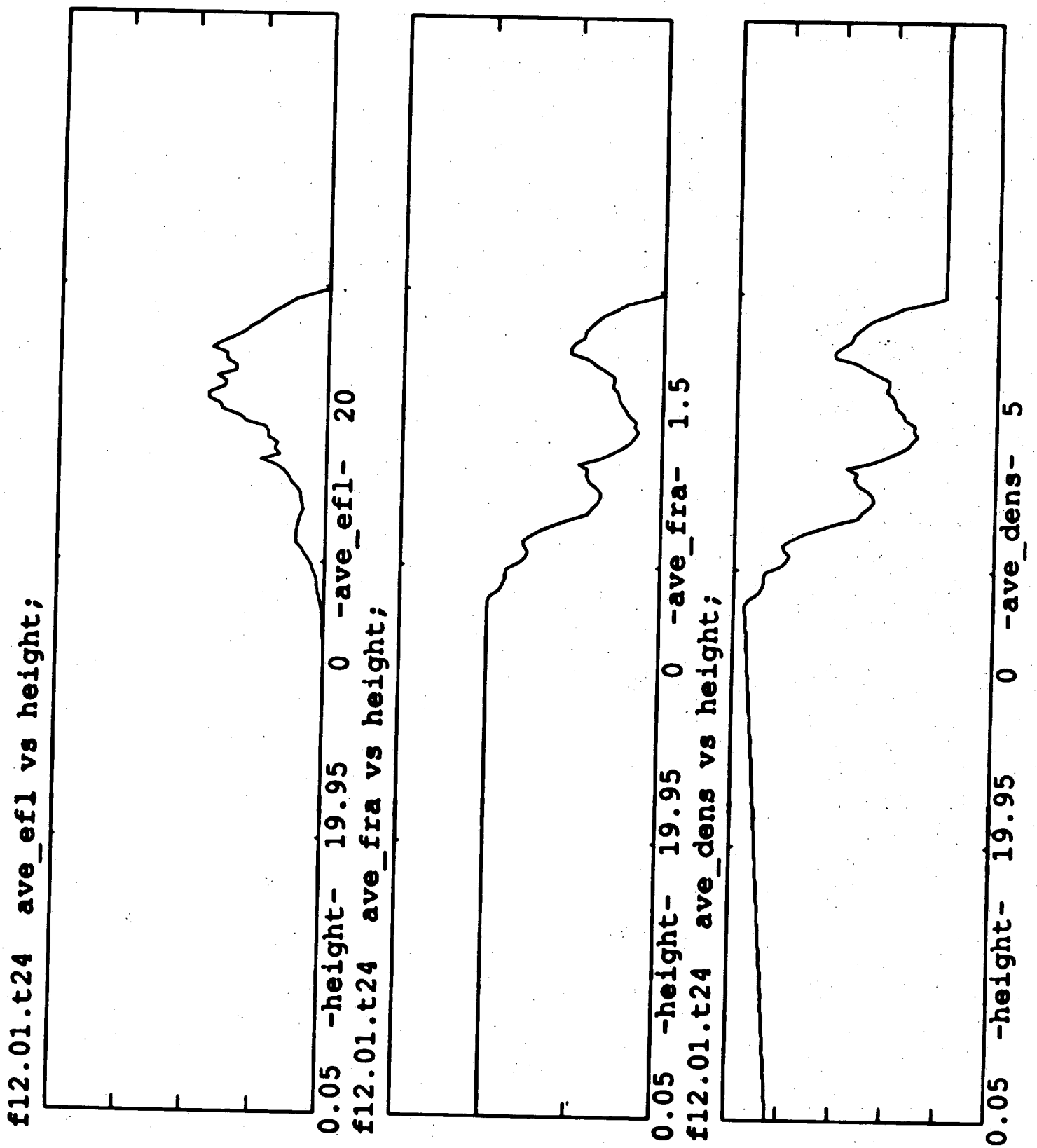
f12.01.t24 ave_efl vs height;
0.05 -height- 19.95 0 -ave_efl- 20
f12.01.t24 ave_fra vs height;
0.05 -height- 19.95 0 -ave_fra- 1.5
f12.01.t24 ave_dens vs height;
0.05 -height- 19.95 0 -ave_dens- 5

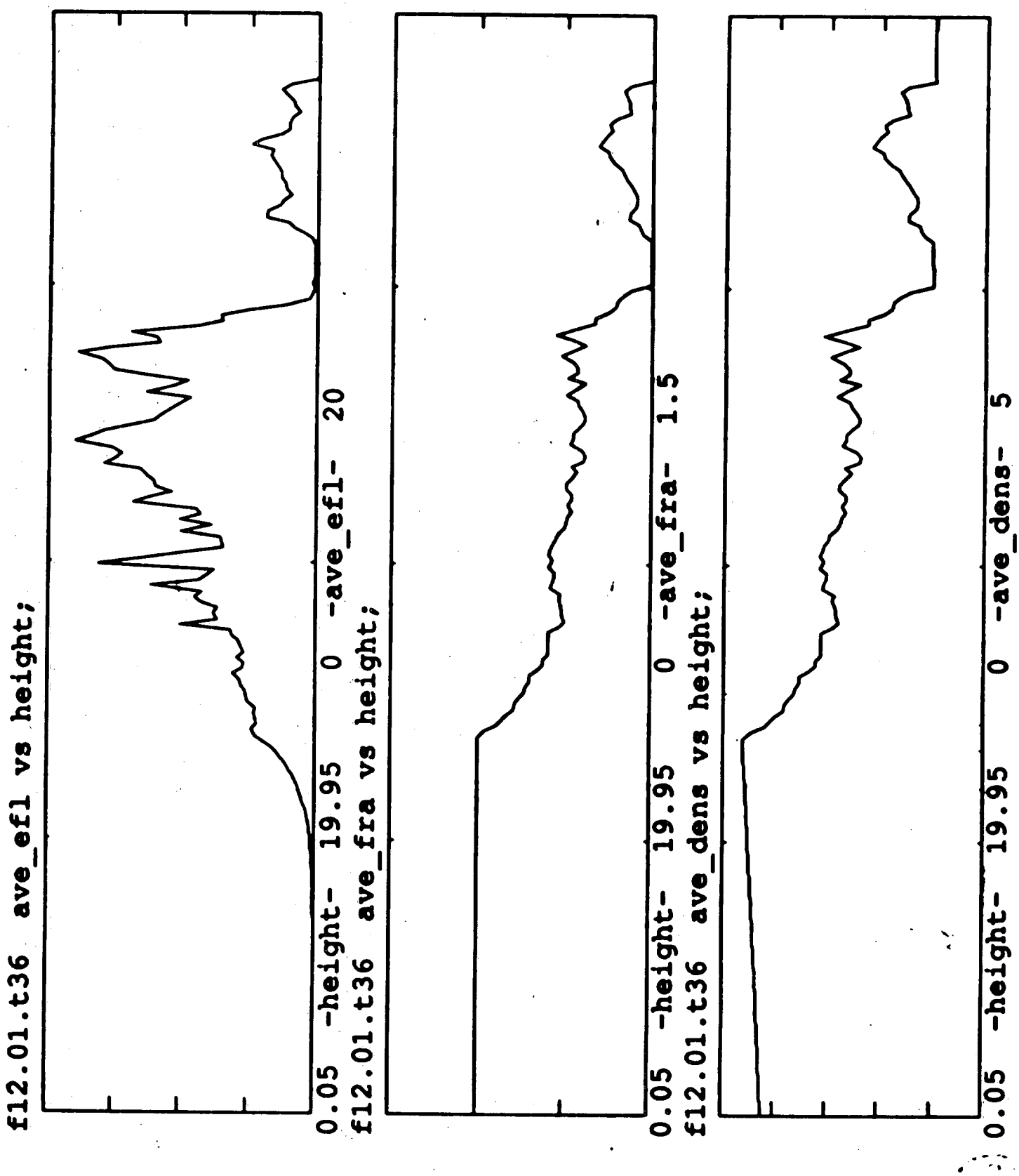
f12.01.t36 ave_efl vs height;
0.05 -height- 19.95 0 -ave_efl- 20
f12.01.t36 ave_fra vs height;
0.05 -height- 19.95 0 -ave_fra- 1.5
f12.01.t36 ave_dens vs height;
0.05 -height- 19.95 0 -ave_dens- 5

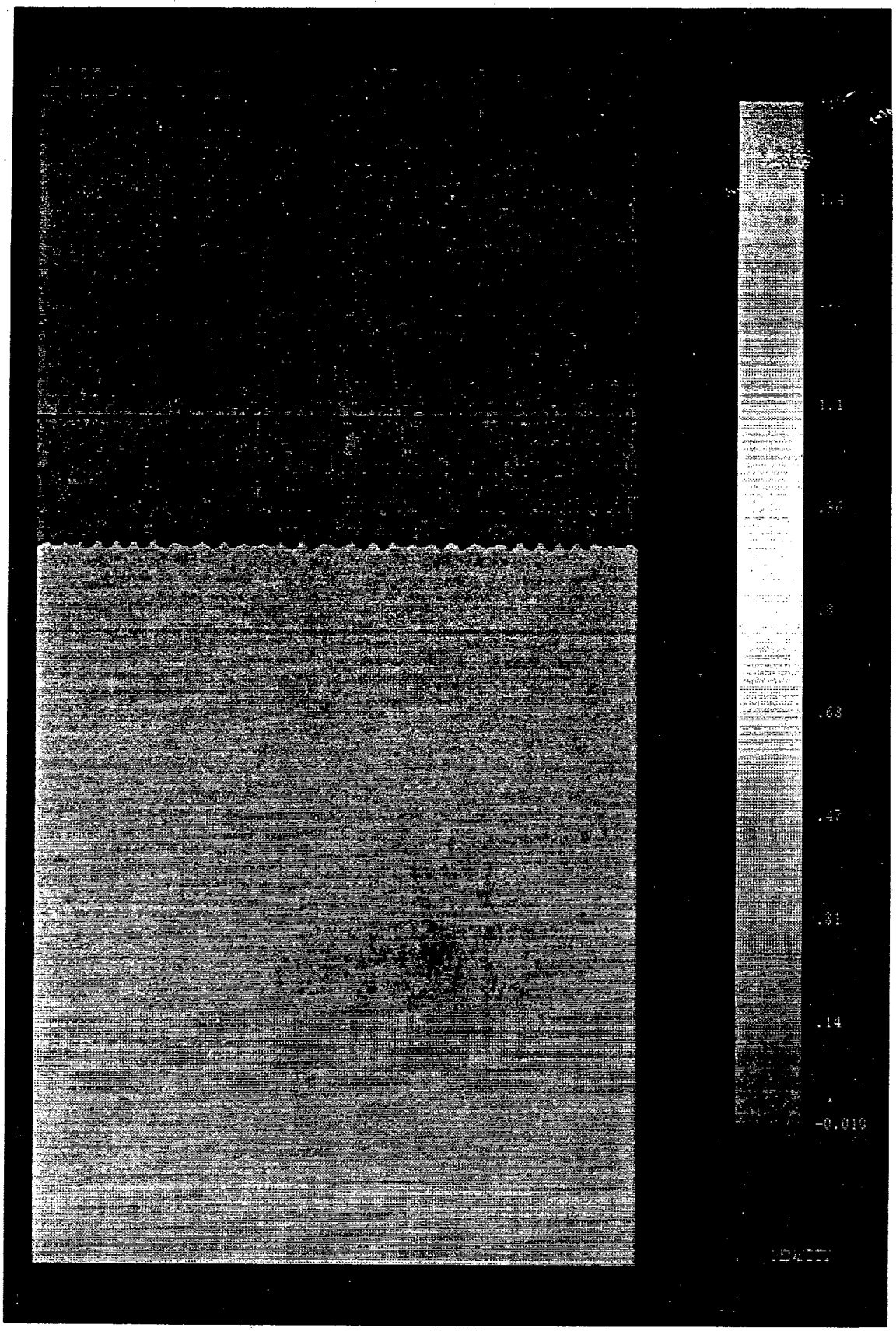
1.1
.66
.63
.47
.31
.14
-0.016

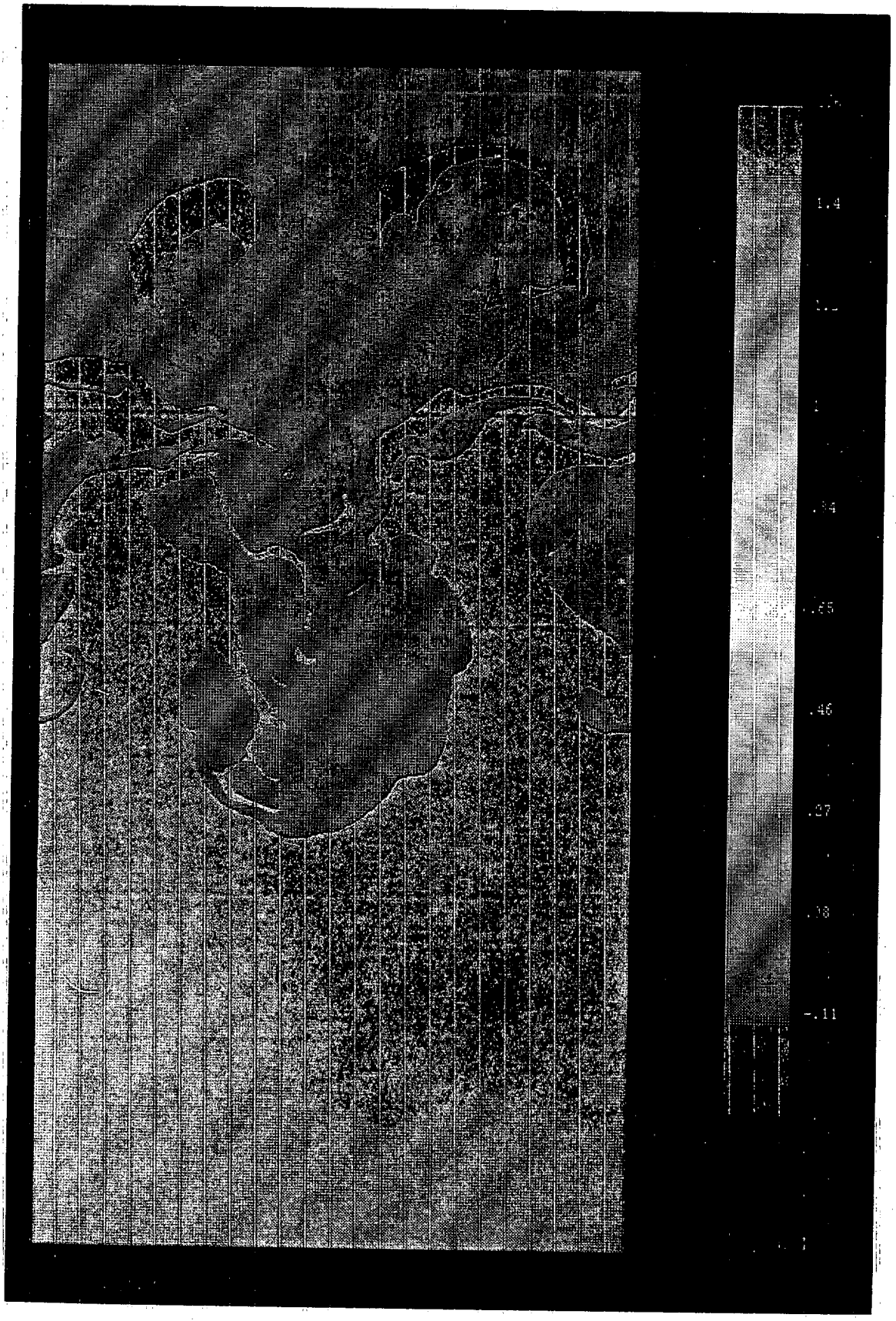
1.4
.84
.65
.46
.27
.08
-.11

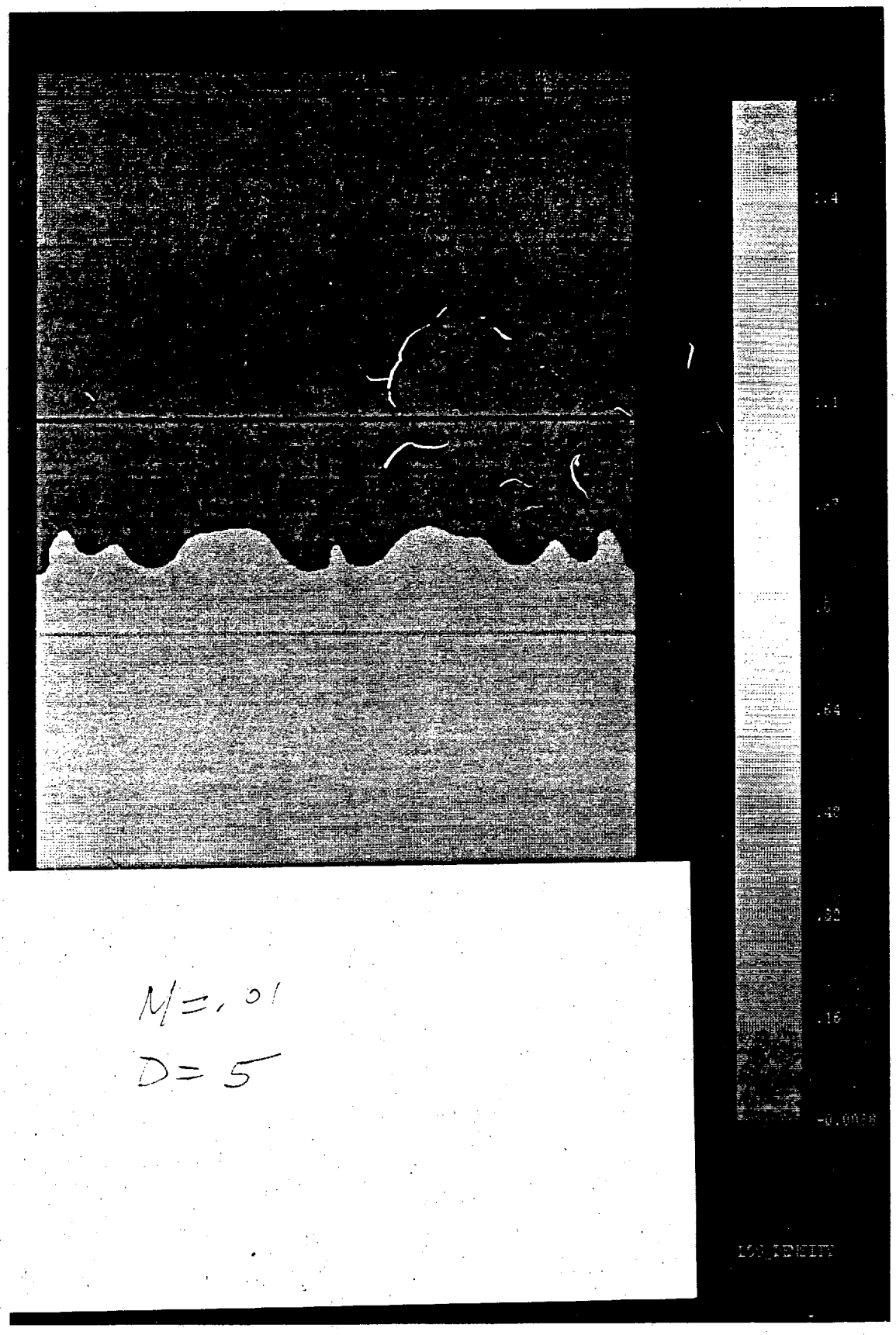
1.4
1.1
.64
.16
M=.01
D=5

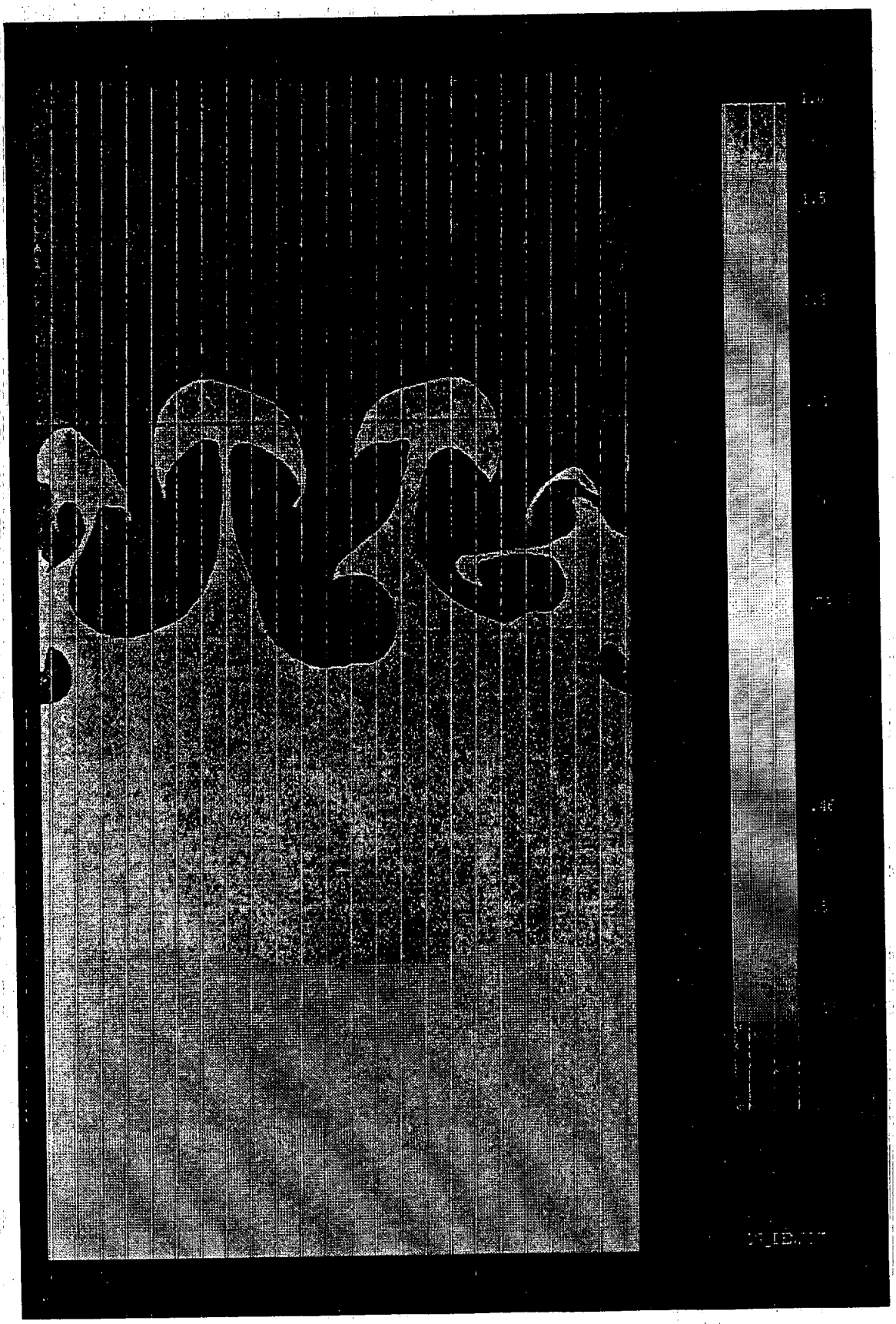

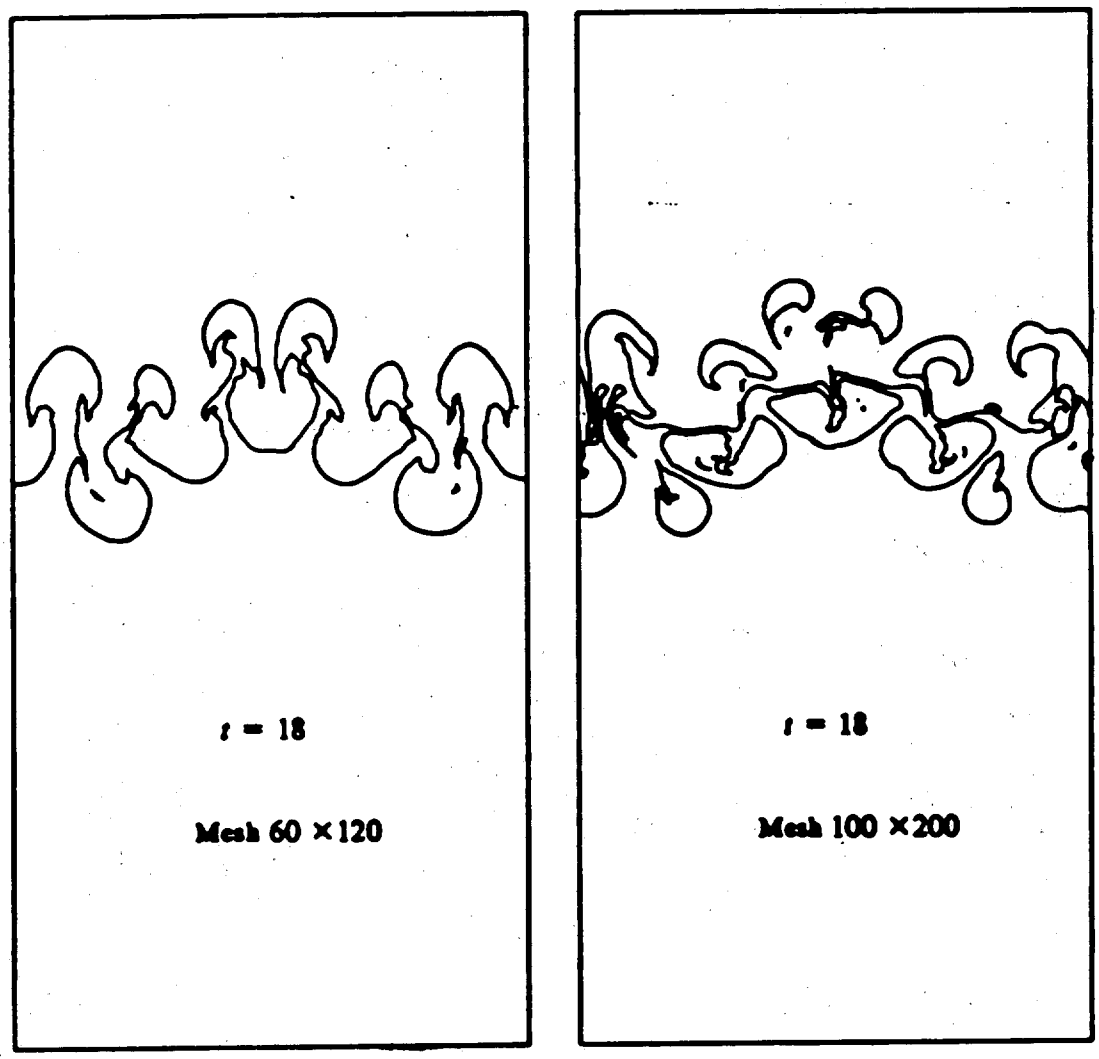

Figure 4.1. Plots of interfaces for Rayleigh-Taylor instability at different mesh refinement. The left plot has a mesh 60 × 120 and the right plot has a mesh 100 × 200. The results show that the interface becomes complicated as the mesh becomes finer. However, the large scale structure of the fluid interface is unchanged after certain mesh refinement.

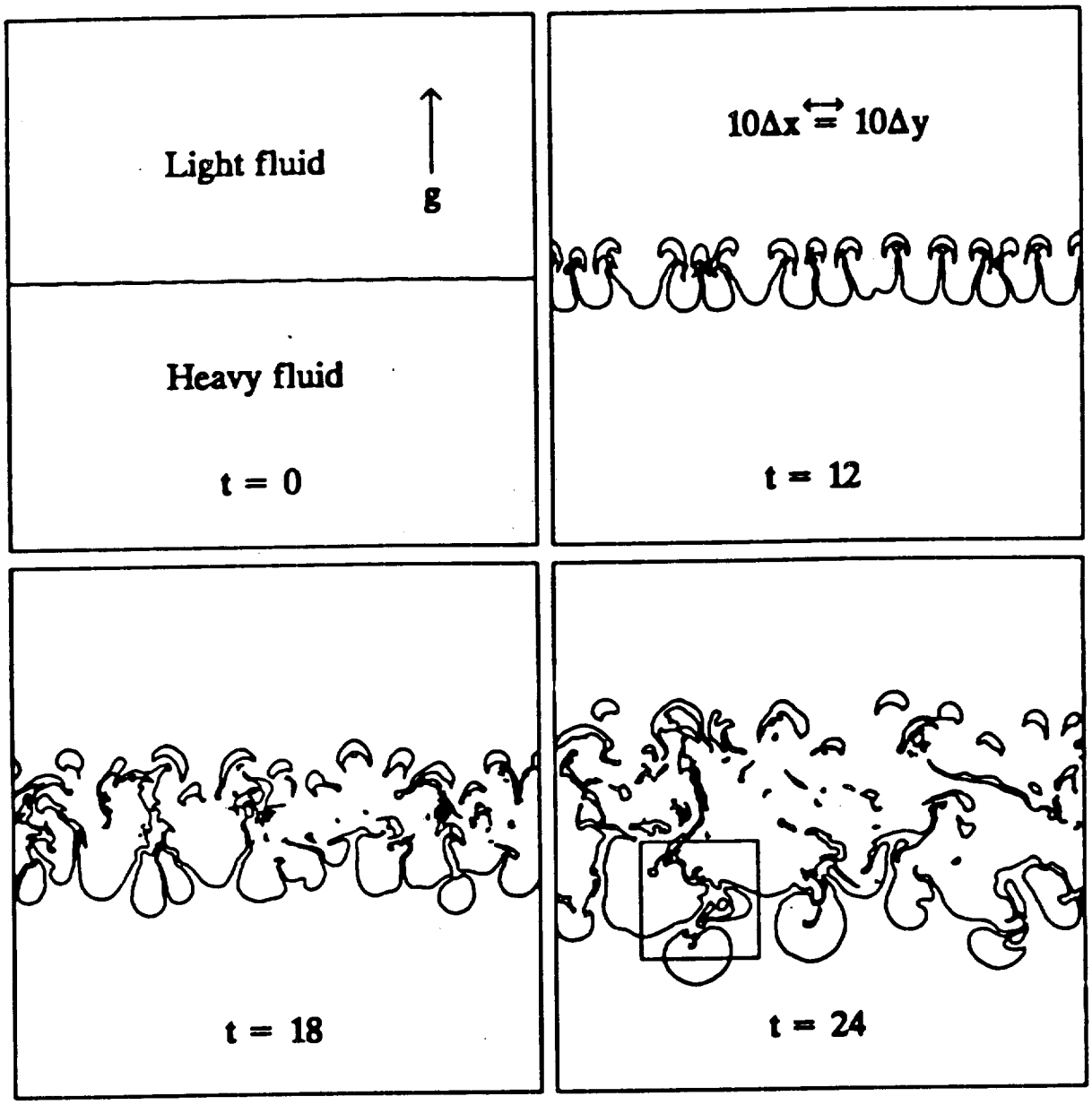

Fig. 3 Plots of material interface for successive time steps with 14 bubbles initially. The interface separates the materials with different density. (The density ratio is 10.) The heavy material lies above and the light material lies below. The interface is unstable under the influence of the gravity, which points upwards. Only the middle half of the computation is shown in the figure, since nothing of interest occurs in the rest part of the computation domain. There are 140 by 140 grid cells for the portion of the computation domain shown here. An enlarged plot for region inside the solid box of last time frame is given in Fig. 4.

Fig. 4 The enlarged plot of the segment inside the solid box of last time frame of Fig. 3. There are 30.8 by 30.8 grids inside the region shown here.

INTERNATIONAL EXCHANGE ON RM AND RT MIXING

PLEASANTON, CA, NOVEMBER 16 and 17, 1989

DIRECT 3D NUMERICAL SIMULATION OF RAYLEIGH-TAYLOR MIXING

D L Youngs

AWE Aldermaston, UK

A. The 3D code TURMOIL3D

B. 3D Simulation of Rayleigh-Taylor Mixing

Comparison with the experiments of Linden and Redondo

C 3D Simulation of Richtmyer-Meshkov single shock experiments

A. TURMOIL 3D

TURMOIL 3D is a simple 3D compressible Eulerian code written for the specific purpose of calculating RT and RM in 3D.

The numerical method is based on that used in PETRA.

Interface tracking is not used:

(a) simplifies calculation

(b) in reality the fluids mix at a molecular level.

Treat initial interface as discontinuity in density or mass fraction.

Explicit compressible technique

For each time step : Lagrangian phase
Advection phase

Can use several Lagrangian steps per advection step - greatly speeds up low Mach No. calculations.

Advection phase : XYZ advection and
ZYX advection for alternate steps.

Monotonic advection method of Van Leer used.

Perfect gas equations of state.

Lagrangian phase $\rho^{n}_{i+\frac{1}{2},j+\frac{1}{2},k+\frac{1}{2}} \longrightarrow \tilde{\rho}^{n}_{i+\frac{1}{2},j+\frac{1}{2},k+\frac{1}{2}}$

$u^{n}_{ijk} \longrightarrow \tilde{u}^{n}_{ijk}$

etc

Advection phase $\tilde{\rho}^{n}_{i+\frac{1}{2},j+\frac{1}{2},k+\frac{1}{2}} \longrightarrow \rho^{n+1}_{i+\frac{1}{2},j+\frac{1}{2},k+\frac{1}{2}}$

$\tilde{u}^{n}_{ijk} \longrightarrow u^{n+1}_{ijk}$

etc

Monotonic advection method ensures

$\rho^{n+1}_{i+\frac{1}{2},j+\frac{1}{2},k+\frac{1}{2}}$ lies within range of values of $\tilde{\rho}^{n}$ for neighbouring points

u^{n+1}_{ijk} lies within range of values of $\tilde{u}^{n}$ for neighbouring points

Spurious numerical oscillations eliminated
- robust method

Long wavelength modes - negligible numerical damping

Short wavelength (a few x Δx) - numerical viscosity and diffusion introduced

Non-linear dissipation inherent in numerical scheme
$\therefore$ no need to add subgrid eddy viscosity.

Facilities added for turbulent mixing problems:

- **Periodic boundary conditions**
- **Fourier analysis (2D analysis applied to a plane section)**
- **Moving mesh option (for shock tube problems)**

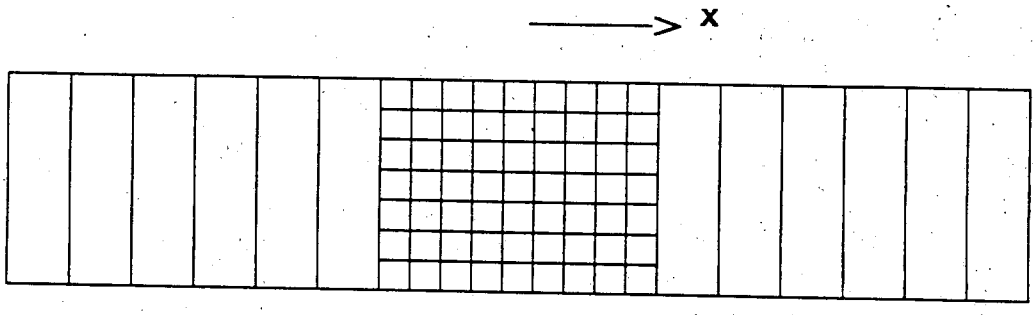

1D Lagrangian region **3D region (x-direction mesh moves with plane averaged x-velocity)** **1D Lagrangian region**

B. RAYLEIGH-TAYLOR MIXING

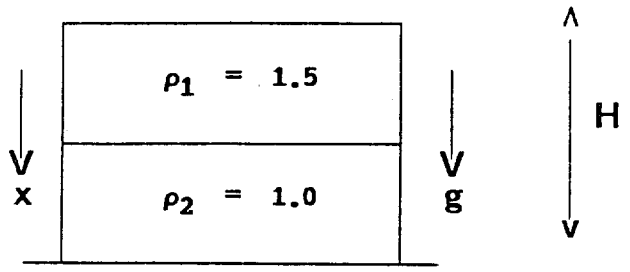

Size of box : 1 x 1 x 1

Boundary conditions : x-direction, rigid wall
y,z direction, periodic.

Main objective : to calculate the degree of molecular mixing

Compare with experimental results of Linden and Redondo.

Initial hydrostatic pressure high enough to ensure low Mach. No. flow.

~ 10 Lagrangian steps per advection step.

Density difference exaggerated to ensure density changes due to compressibility are small compared to $\rho_1 - \rho_2$

Small density differences - Boussinesq approximation valid.

Results independent of density ratio and tank height H if plotted against scaled time

$$\tau = \left\{ \frac{\rho_1 - \rho_2}{\rho_1 + \rho_2} \frac{g}{H} \right\}^{1/2} t$$

Width of mixed region (from rocket rig experiments)

$$\delta = 0.12 \frac{\rho_1 - \rho_2}{\rho_1 + \rho_2} gt^2$$

$\therefore$ mixed region fills tank when

$$\delta = H$$

ie $$H = 0.12 \frac{\rho_1 - \rho_2}{\rho_1 + \rho_2} gt^2$$

ie $$\tau = 1/\sqrt{(0.12)} = 2.9$$

Calculations run to $\tau = 10$

Initial perturbation

$$\zeta(y,z) = S \sum_{m=0}^{M} \sum_{n=0}^{N} \left\{ a_{mn} \cos \frac{2\pi my}{Y} \cos \frac{2\pi nz}{Z} + b_{mn} \cos \frac{2\pi my}{Y} \sin \frac{2\pi nz}{Z} + c_{mn} \sin \frac{2\pi my}{Y} \cos \frac{2\pi nz}{Z} + d_{mn} \sin \frac{2\pi my}{Y} \sin \frac{2\pi nz}{Z} \right\}$$

$M = [N_y/4]$

$N = [N_z/4]$

at least 4 zones per wavelength

$a, b, c, d = 0$ for $(m, n) = (0,0), (0,1), (1,0), (1,1)$

otherwise chosen from a Gaussian distribution.

S = scaling factor chosen to give

$$\langle \zeta^2 \rangle^{1/2} = 0.08\, \Delta x = 0.02\, \lambda_{min}$$

Mesh sizes used

On CRAY XMP2-2 at AWE, Aldermaston	32 x 32 x 32 44 x 44 x 44 44 x 44 x 1 80 x 80 x 1
On CRAY XMP4-16 at RARDE, Fort Halstead	80 x 80 x 80

4 calculations in each set.

Dissipation of density and velocity functions.

Assume Kolmogorov/Oboukhov picture applies:

Inertial transfer from low wavenumbers to high wavenumbers + dissipation (diffusion or viscosity) at high wavenumbers.

Decay of fluctuations determined by rate of inertial transfer, insensitive to dissipation mechanisms - the possibility of using 3D simulation, which cannot resolve the small scales at which diffusion and viscosity act in real situations, depends on this.

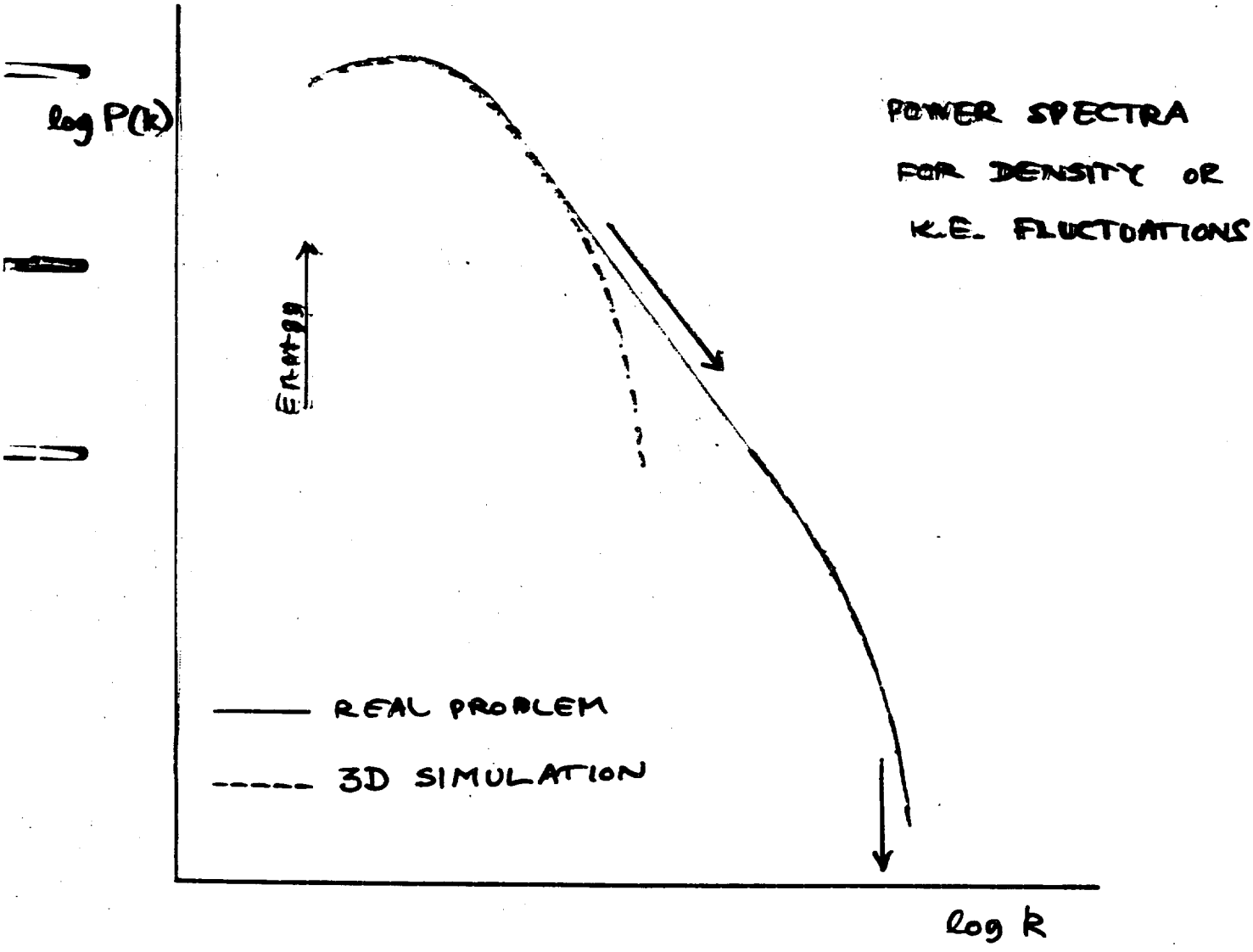

$$\langle u_i' u_i' \rangle \text{ or } \langle (\rho - \bar{\rho})^2 \rangle = \int P(k)\, dk$$

- high Re : $\langle (\rho - \bar{\rho})^2 \rangle$ independent of values of viscosity and diffusion coefficients
- RT problem, gt^2 similarity solution
  $\langle (\rho - \bar{\rho})^2 \rangle = F\left(\frac{x}{\delta}\right) (\rho_1 - \rho_2)^2$
- 3D simulation : should get $\langle (\rho - \bar{\rho})^2 \rangle$ approximately correct in 3D calculations

VOLUME FRACTION CONTOURS FOR
80 x 80 x 80 MESH CALCULATION

Vertical plane section

VOLUME FRACTION CONTOURS FOR
80 x 80 x 80 MESH CALCULATION

Horizontal plane section, x = 0.5 through initial interface

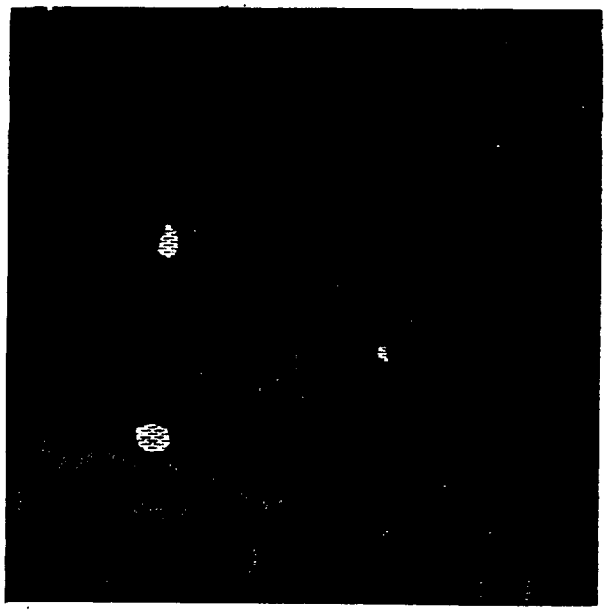

$\tau = 2.0$

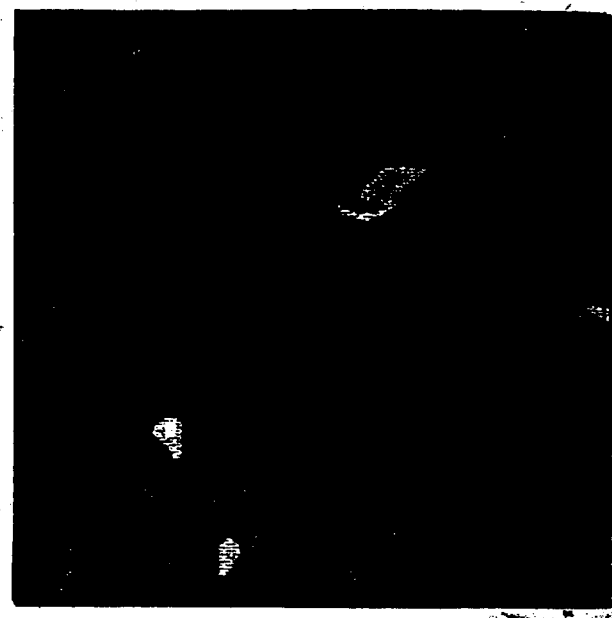

$\tau = 2.5$

$\tau = 3.0$

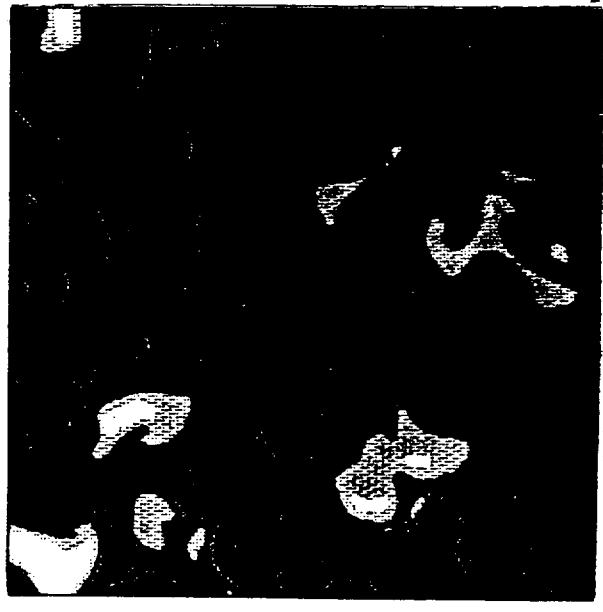

$\tau = 4.0$

80 x 80 x 80 zones calculation

Volume fraction contours for horizontal plane section ($x = \frac{1}{4}$)

above initial interface

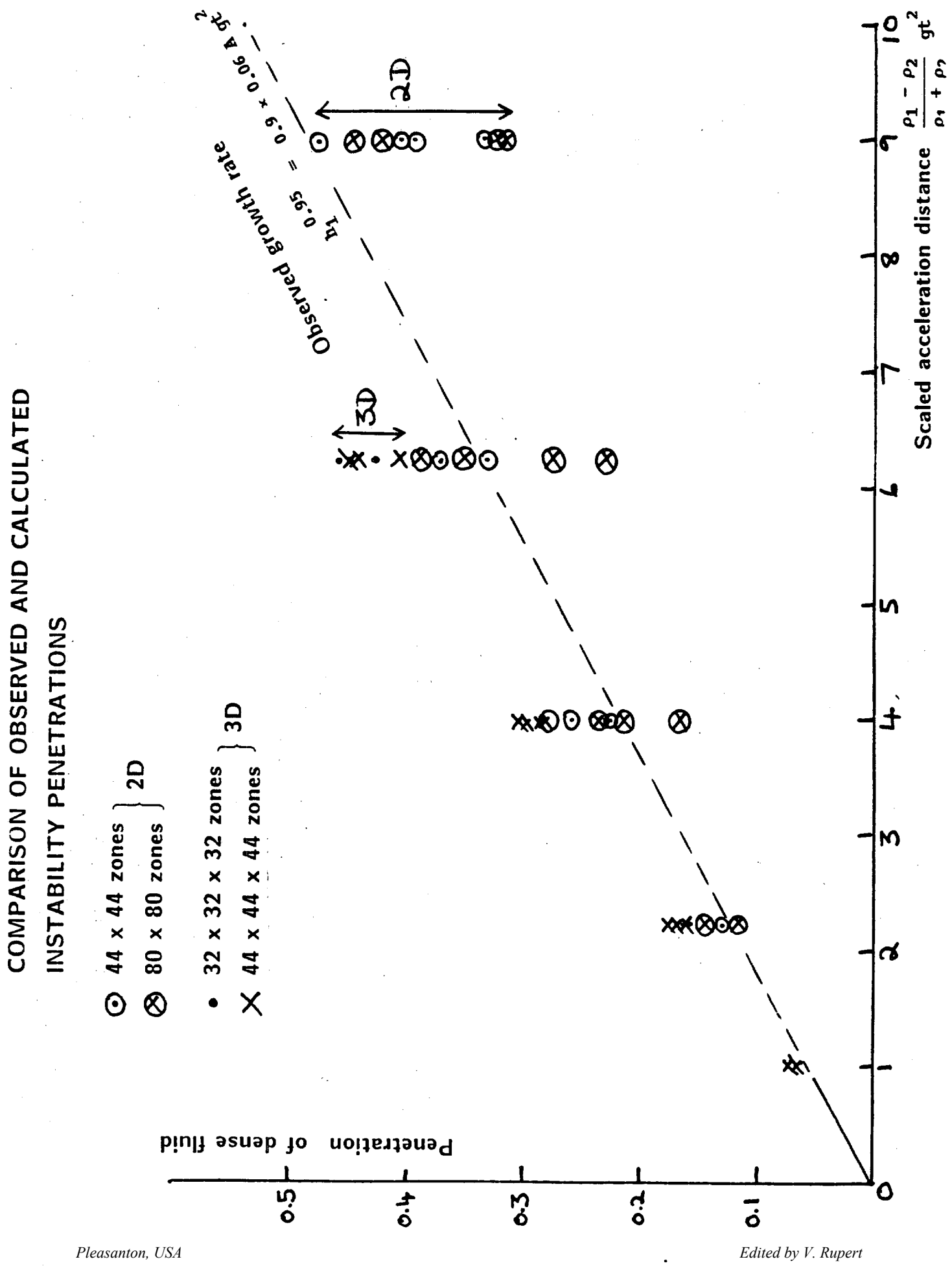
COMPARISON OF OBSERVED AND CALCULATED
INSTABILITY PENETRATIONS
44 x 44 zones
80 x 80 zones
2D
32 x 32 x 32 zones
44 x 44 x 44 zones
3D
Observed growth rate
$h_1 = 0.95 = 0.9 \times 0.06\ A g t^2$
2D
3D
Penetration of dense fluid
0.5
0.4
0.3
0.2
0.1
0
1
2
3
4
5
6
7
8
9
10
Scaled acceleration distance $\frac{\rho_1 - \rho_2}{\rho_1 + \rho_2} gt^2$

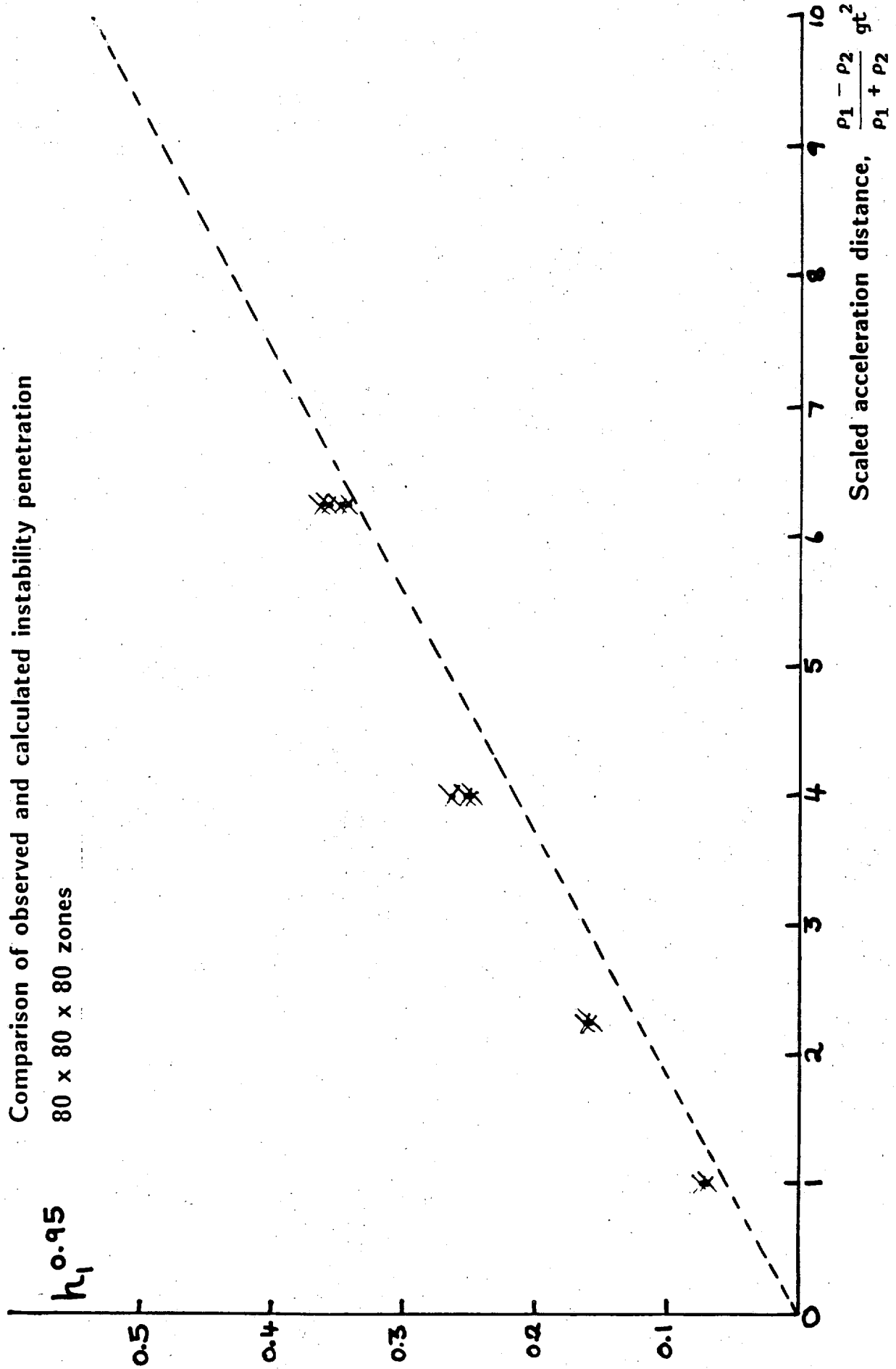
Comparison of observed and calculated instability penetration
80 x 80 x 80 zones
$h_1^{0.95}$
0.5
0.4
0.3
0.2
0.1
0
1
2
3
4
5
6
7
8
9
10
Scaled acceleration distance, $\frac{\rho_1 - \rho_2}{\rho_1 + \rho_2} gt^2$

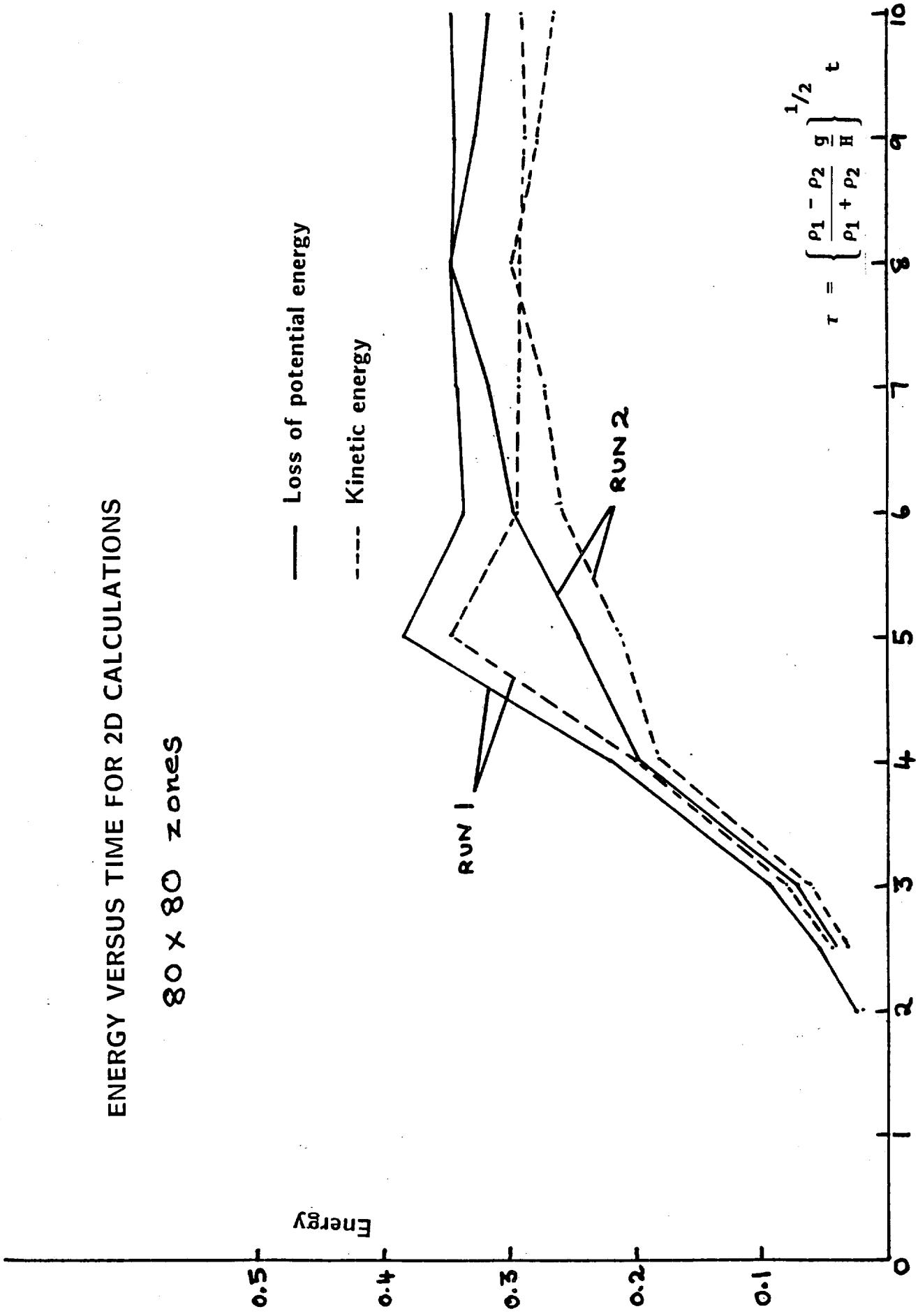
ENERGY VERSUS TIME FOR 2D CALCULATIONS
80 X 80 zones
Loss of potential energy
Kinetic energy
RUN 1
RUN 2
Energy
0.5
0.4
0.3
0.2
0.1
0
1
2
3
4
5
6
7
8
9
10
$\tau = \left\{\frac{\rho_1 - \rho_2}{\rho_1 + \rho_2}\frac{g}{H}\right\}^{1/2} t$

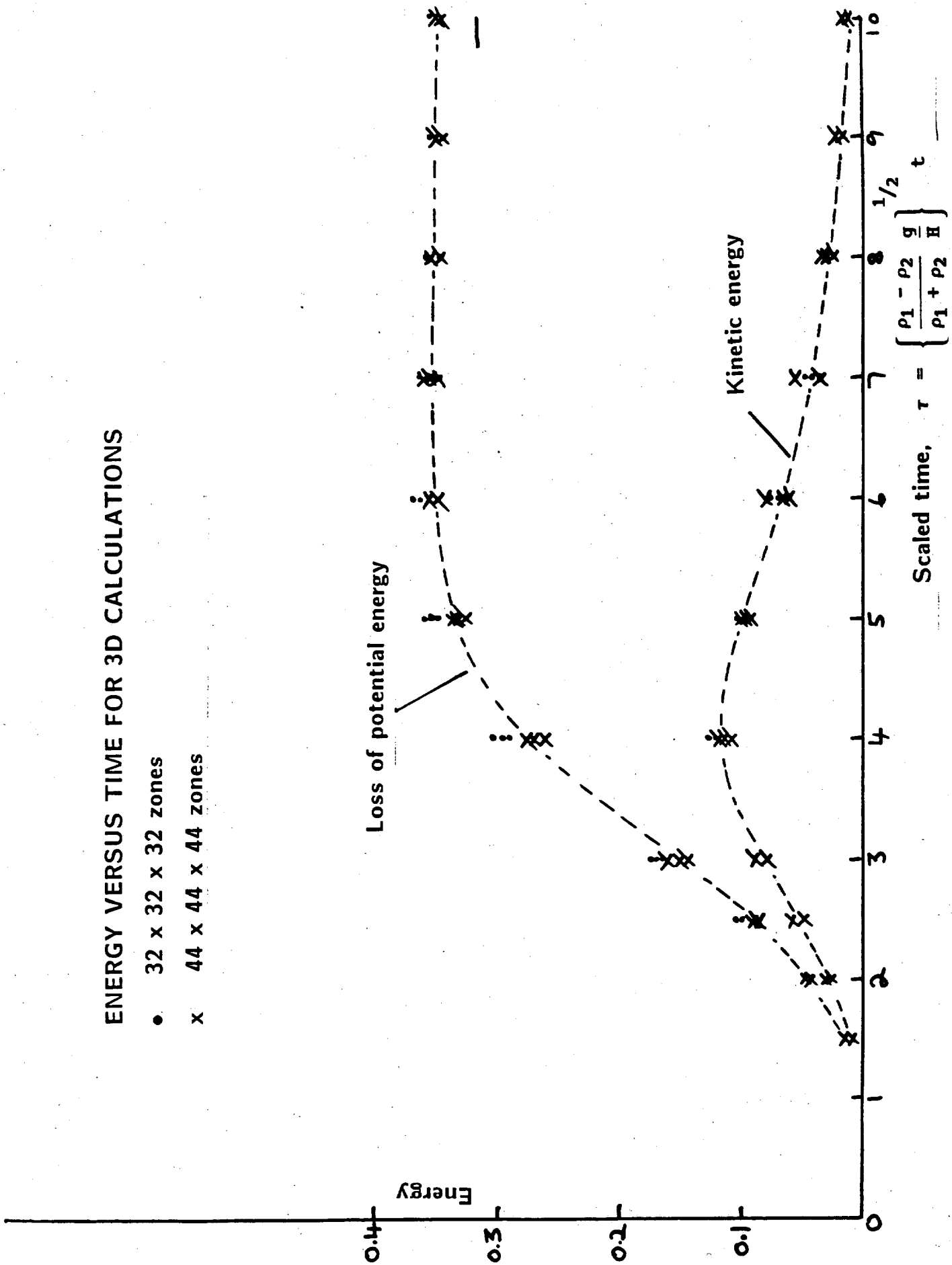
ENERGY VERSUS TIME FOR 3D CALCULATIONS
• 32 x 32 x 32 zones
x 44 x 44 x 44 zones
Loss of potential energy
Kinetic energy
Energy
0.4
0.3
0.2
0.1
0
1
2
3
4
5
6
7
8
9
10
Scaled time, $\tau = \left[\frac{\rho_1 - \rho_2}{\rho_1 + \rho_2} \frac{g}{H}\right]^{1/2} t$

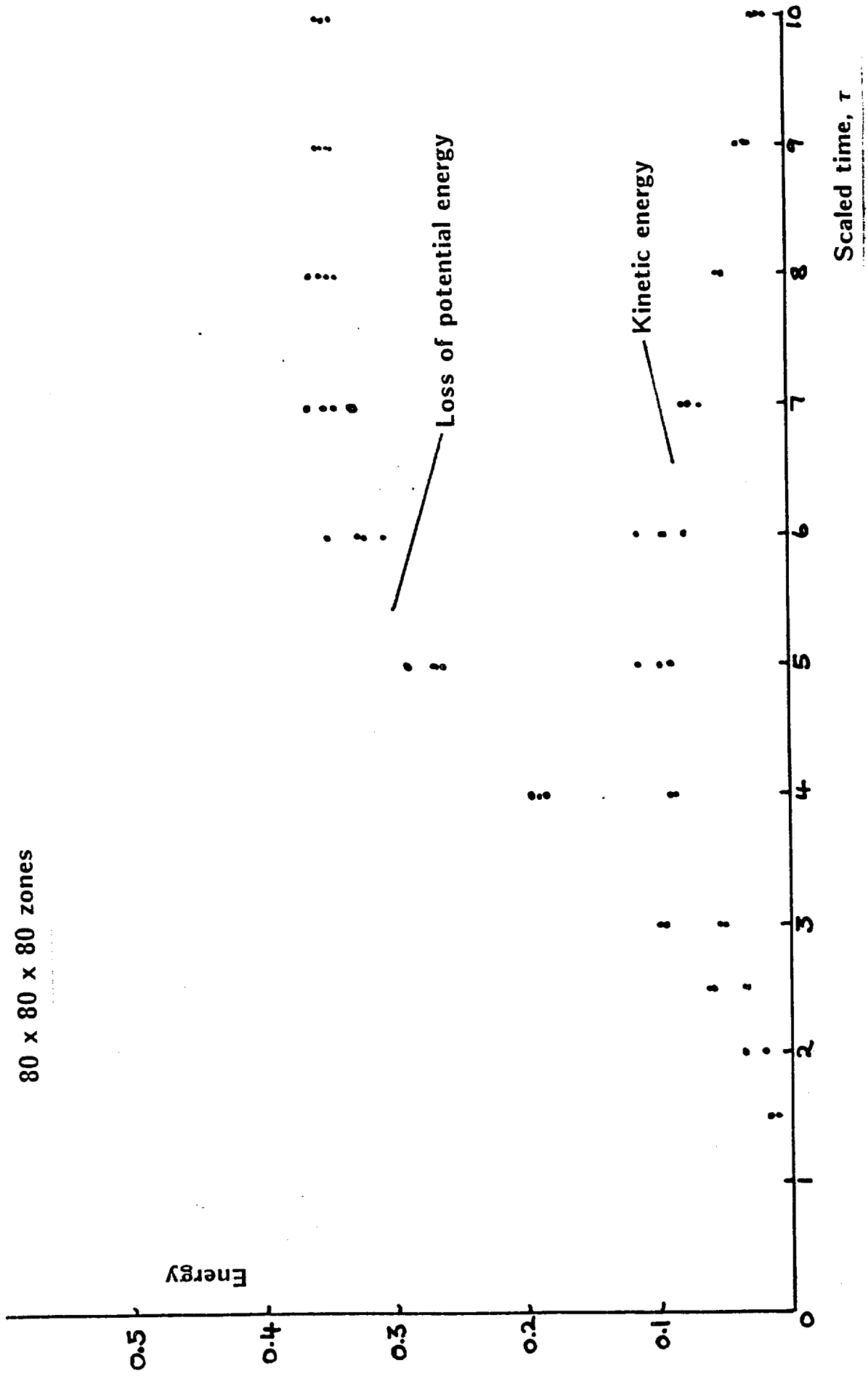
80 x 80 x 80 zones
Energy
0.5
0.4
0.3
0.2
0.1
0
1
2
3
4
5
6
7
8
9
10
Scaled time, τ
Loss of potential energy
Kinetic energy

2D Calculations : little K.E. dissipation
⇒ from numerical diffusion

3D Calculations : high K.E. dissipation
insensitive to mesh size
⇒ inertial transfer to high wavenumber
+ dissipation at high wavenumber is being calculated

Kinetic Energy Dissipation for the 3D Calculations

Run No.	Change in PE - KE / Change in PE					
	44^3 mesh			80^3 mesh		
	$\tau = 2$	$\tau = 2.5$	$\tau = 3.0$	$\tau = 2$	$\tau = 2.5$	$\tau = 3.0$
1	0.34	0.41	0.45	0.44	0.47	0.49
2	0.35	0.41	0.46	0.44	0.46	0.48
3	0.37	0.42	0.46	0.43	0.46	0.48
4	0.36	0.42	0.45	0.43	0.45	0.47
Mean	0.36	0.42	0.46	0.44	0.46	0.48

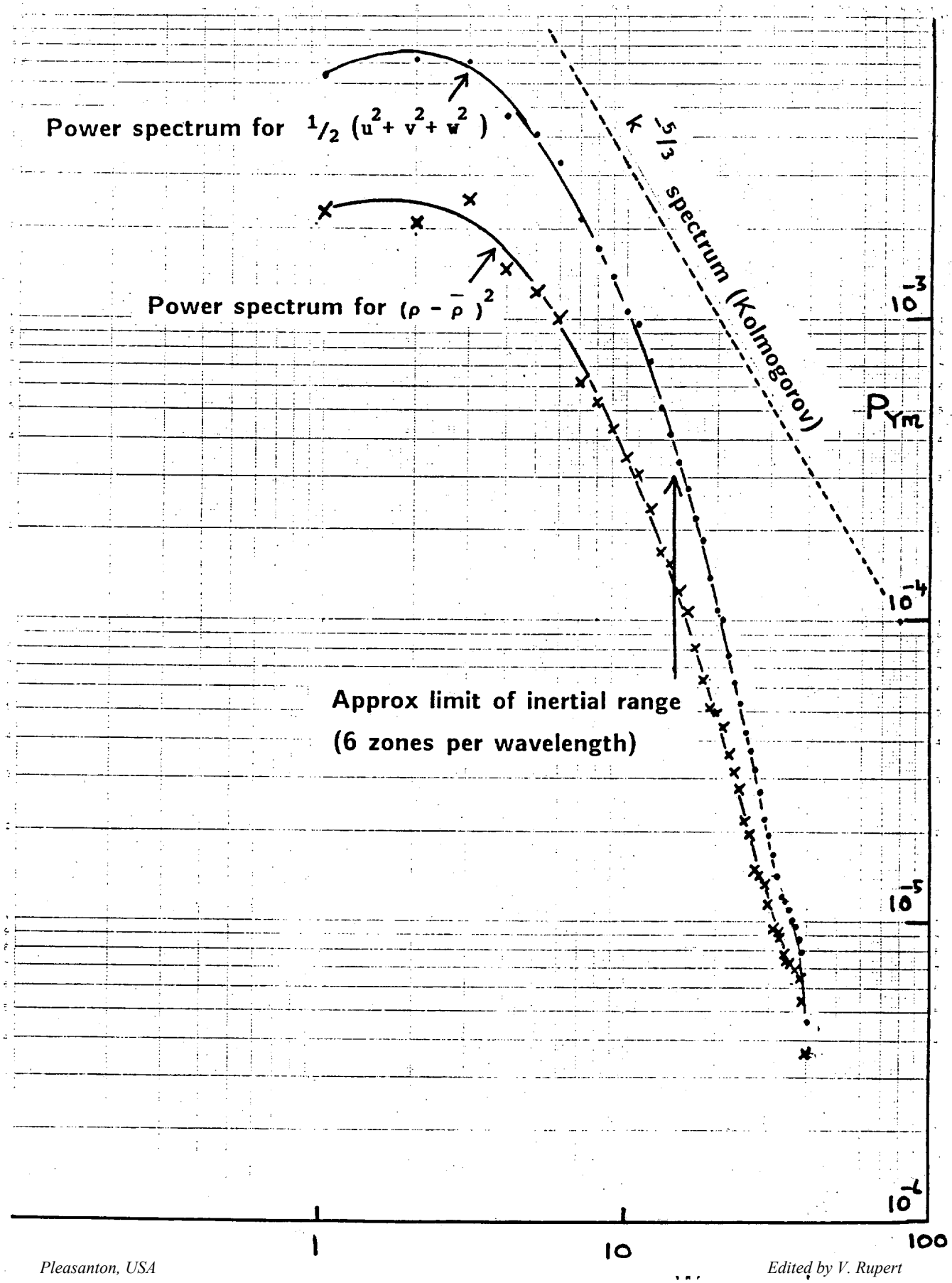
One dimensional power spectra for plane x = 0.5
80 x 80 x 80 zones calculations at τ = 2.5
Power spectrum for 1/2 (u² + v² + w²)
Power spectrum for (ρ − ρ̄)²
k^-5/3 spectrum (Kolmogorov)
Approx limit of inertial range
(6 zones per wavelength)
P_YM
10^-3
10^-4
10^-5
10^-6
1
10
100

Fall off of power with k is more rapid than

$k^{-5/3}$ (Kolmogorov) but

Mesh resolution inadequate to represent the inertial range.

Non-equilibrium situation:-

k (in middle of region) $\sim t^2$

Dominant length scale $\sim t^2$

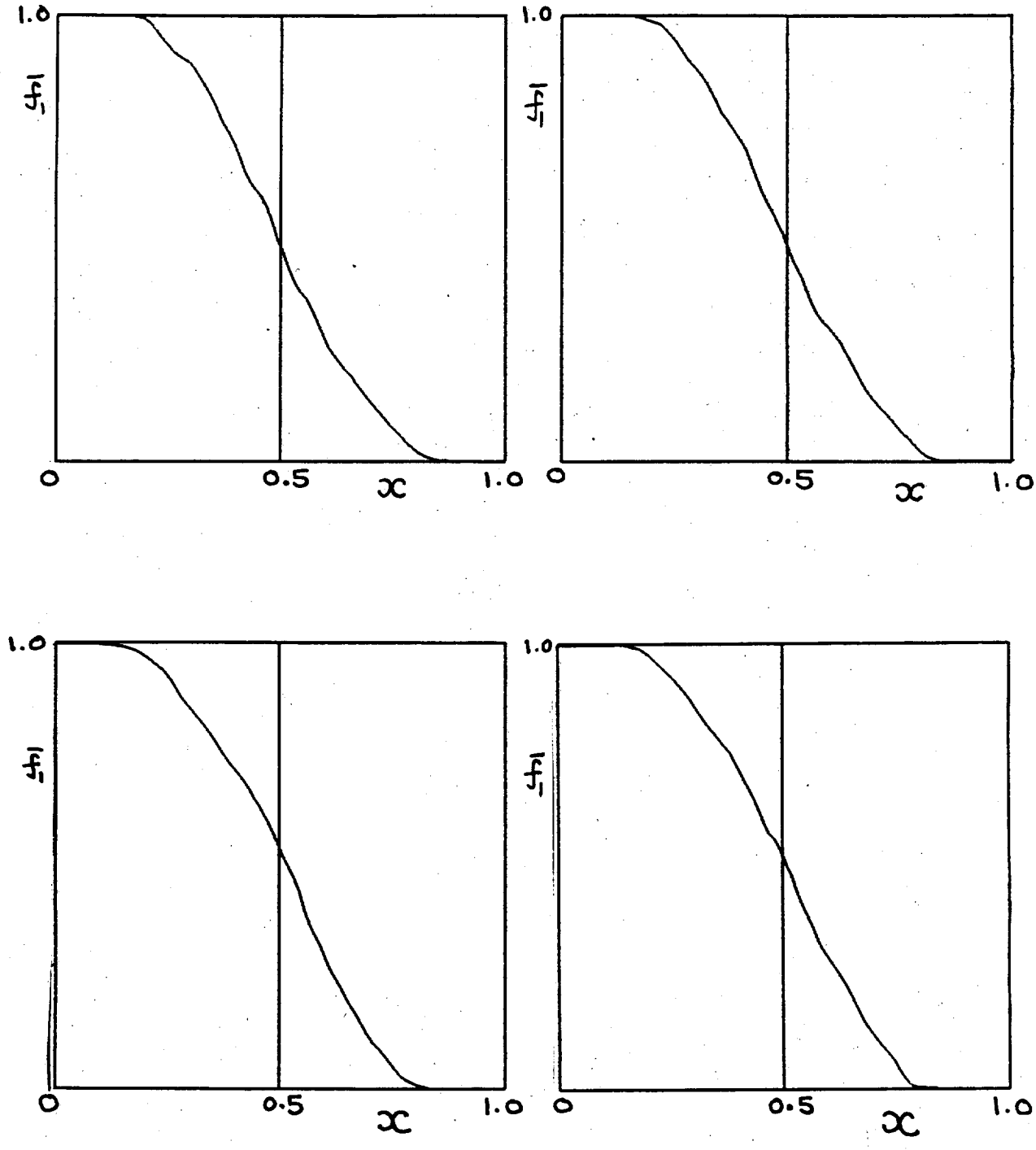

Volume fraction distribution at τ = 2

80 x 80 x 80 zones

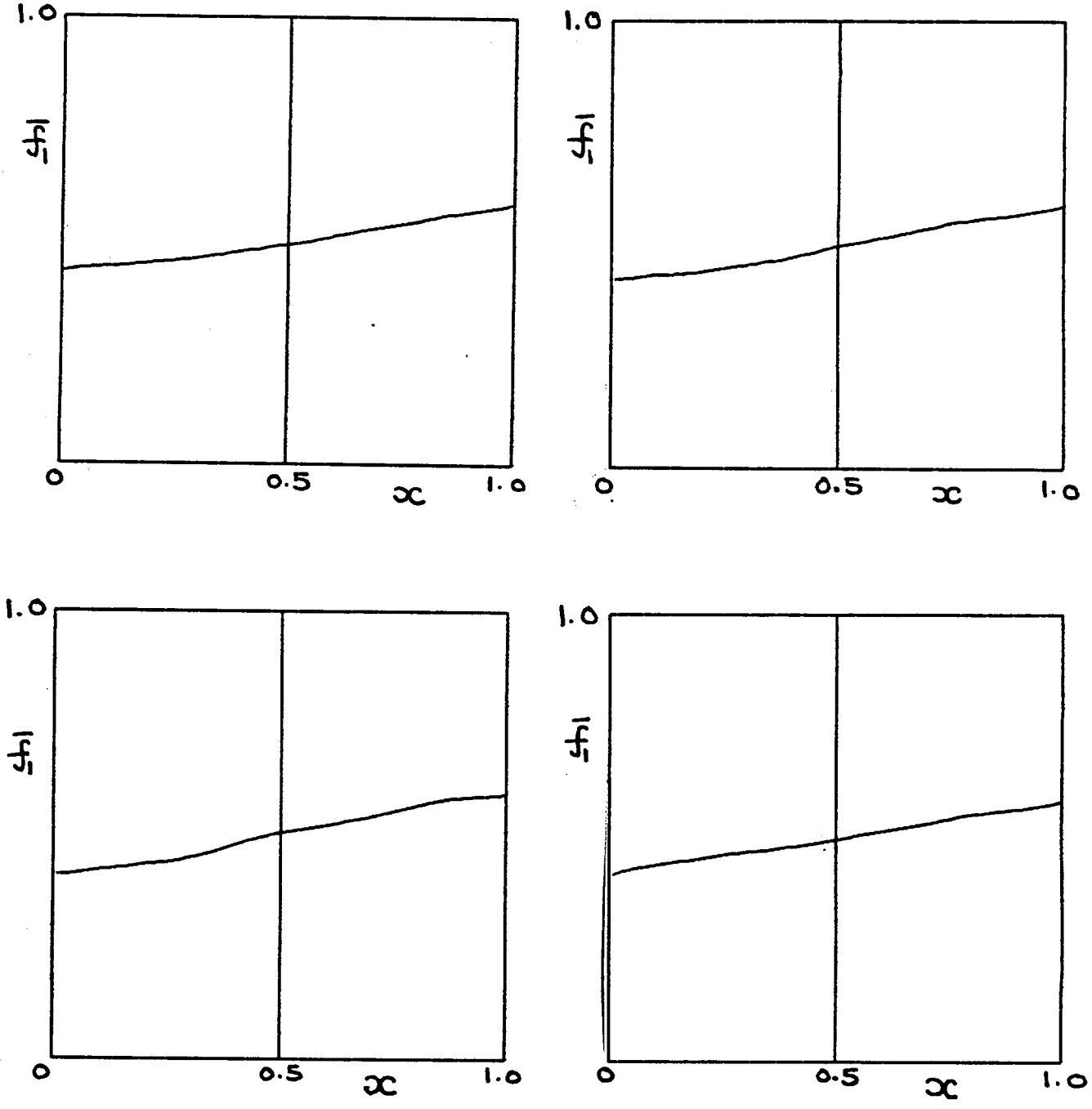

Volume fraction distribution at end of calculation, τ = 10

80 x 80 x 80 zones

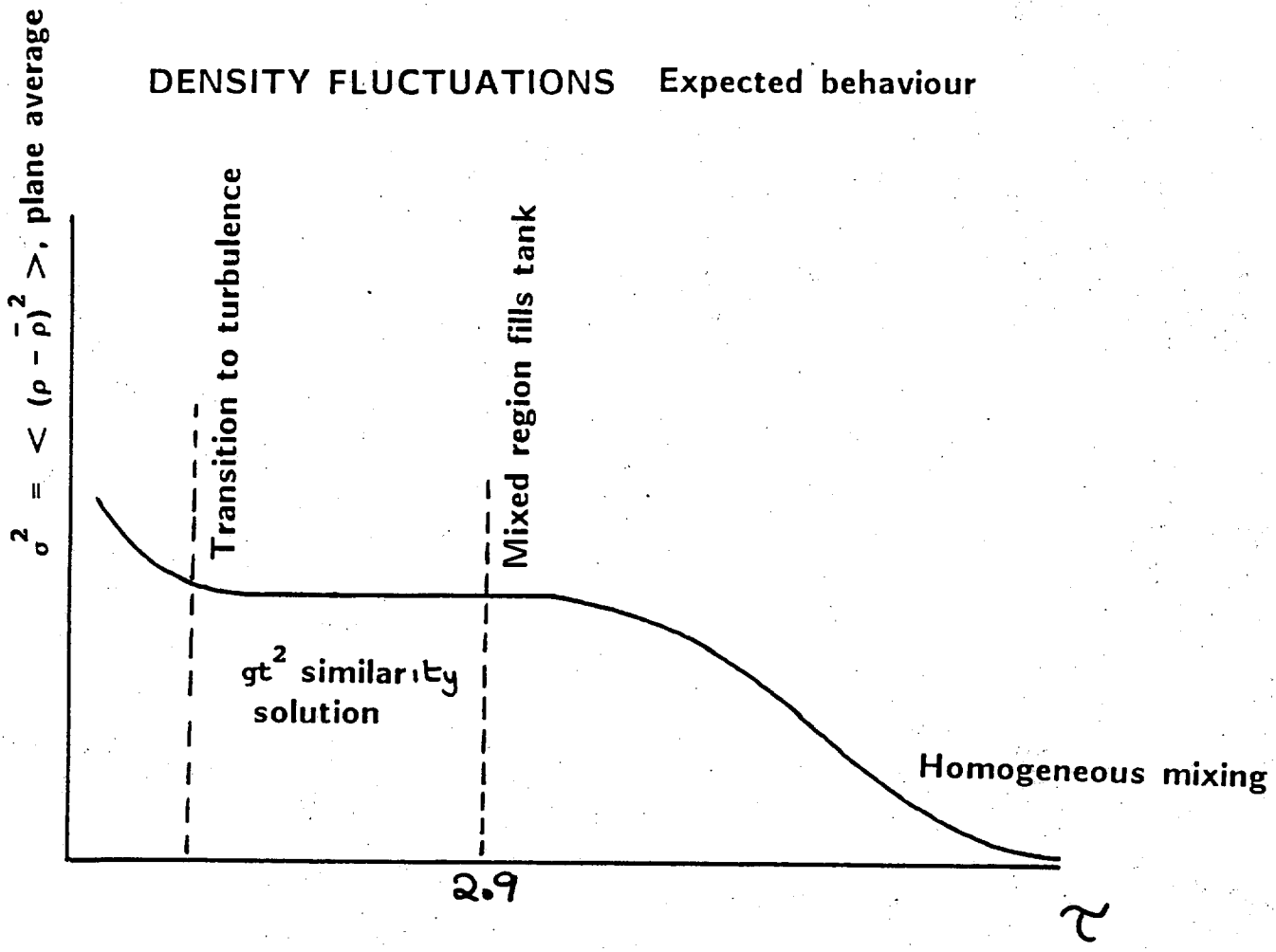
DENSITY FLUCTUATIONS Expected behaviour
$\sigma^2 = \langle (\rho - \bar{\rho})^2 \rangle$, plane average
Transition to turbulence
Mixed region fills tank
gt^2 similarity solution
Homogeneous mixing
2.9
τ

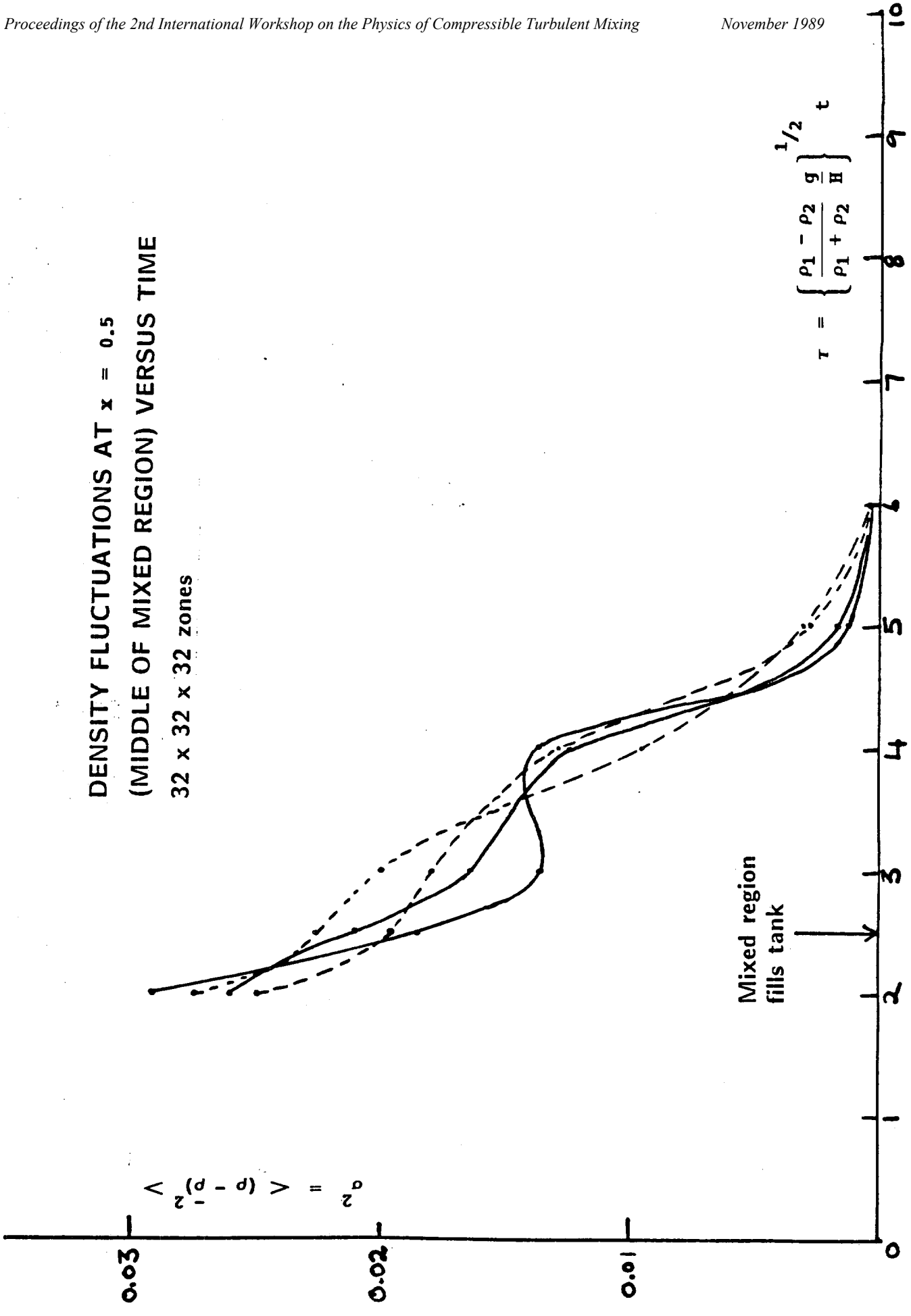
DENSITY FLUCTUATIONS AT x = 0.5
(MIDDLE OF MIXED REGION) VERSUS TIME
32 x 32 x 32 zones
$\sigma^2 = \langle (\rho - \rho_1)^2 \rangle$
0.03
0.02
0.01
0
1
2
3
4
5
6
7
8
9
10
Mixed region fills tank
$\tau = \left\{ \frac{\rho_1 - \rho_2}{\rho_1 + \rho_2} \frac{g}{H} \right\}^{1/2} t$

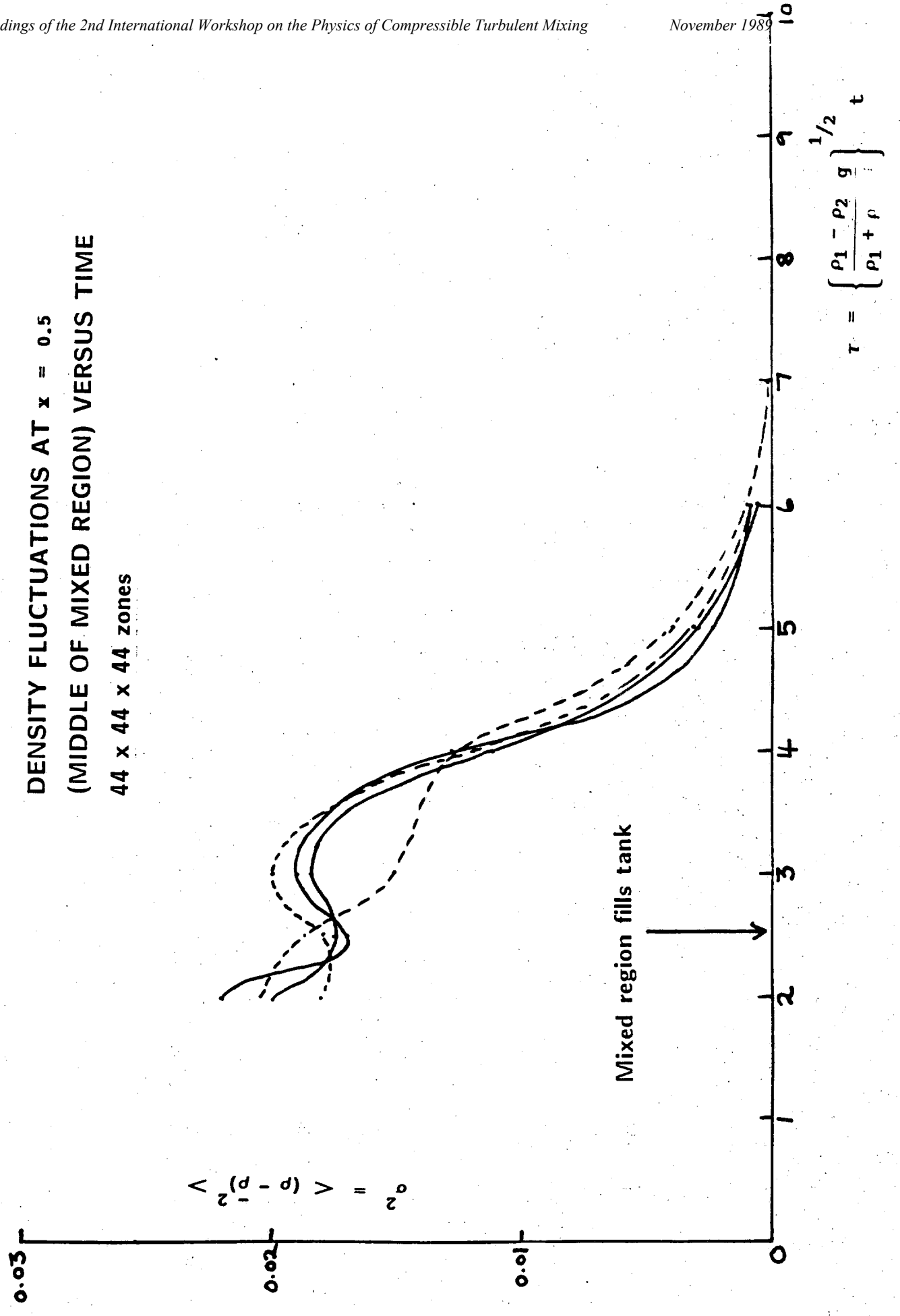
DENSITY FLUCTUATIONS AT x = 0.5
(MIDDLE OF MIXED REGION) VERSUS TIME
44 x 44 x 44 zones
$\sigma^2 = \langle (\rho - \bar{\rho})^2 \rangle$
0.03
0.02
0.01
0
1
2
3
4
5
6
7
8
9
10
Mixed region fills tank
$\tau = \left\{ \frac{\rho_1 - \rho_2}{\rho_1 + \rho} \frac{g}{} \right\}^{1/2} t$

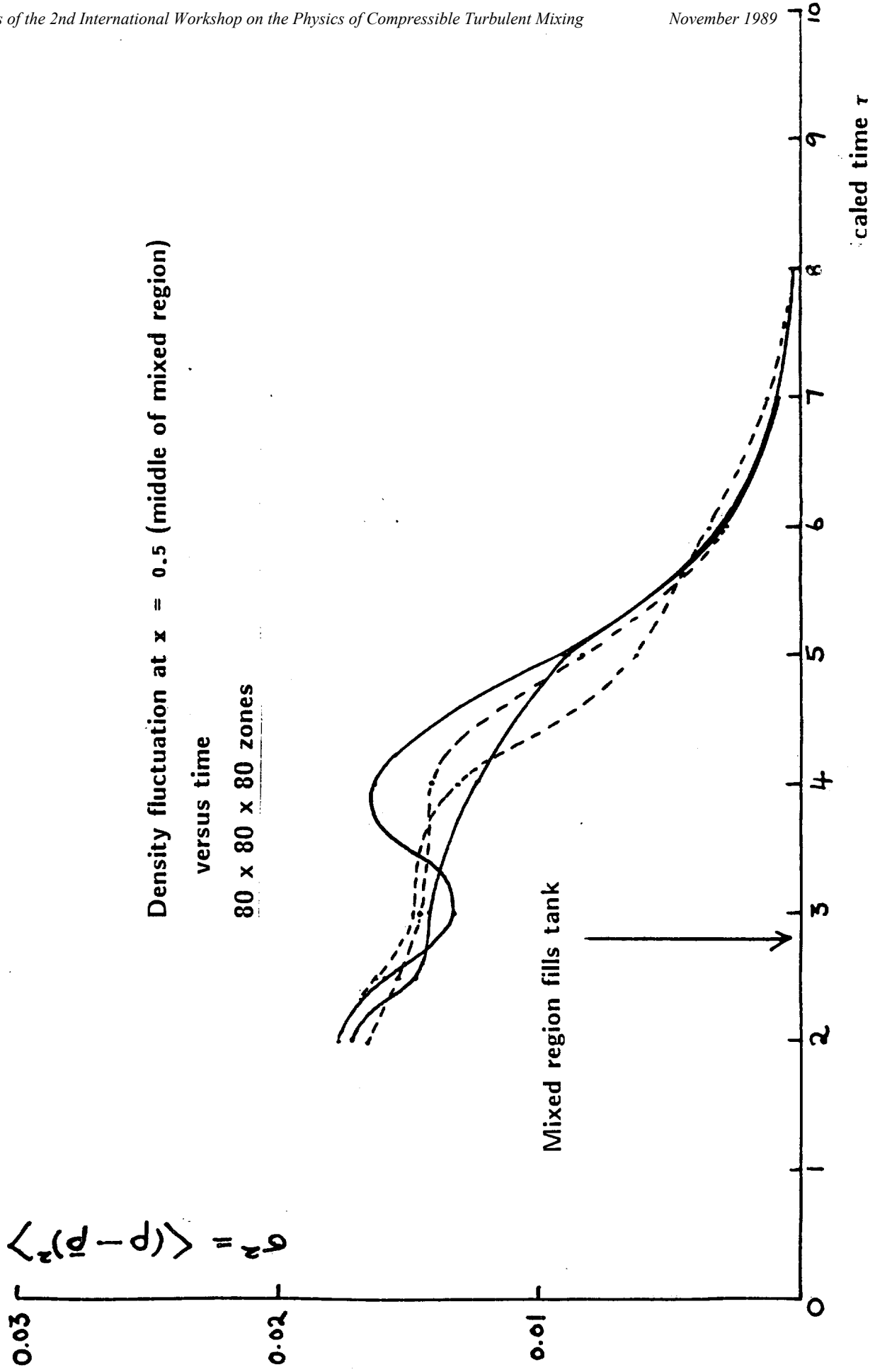
Density fluctuation at x = 0.5 (middle of mixed region)
versus time
80 x 80 x 80 zones
Mixed region fills tank
$\sigma^2 = \langle (\rho - \bar{\rho})^2 \rangle$
0.03
0.02
0.01
0
1
2
3
4
5
6
7
8
9
10
caled time τ

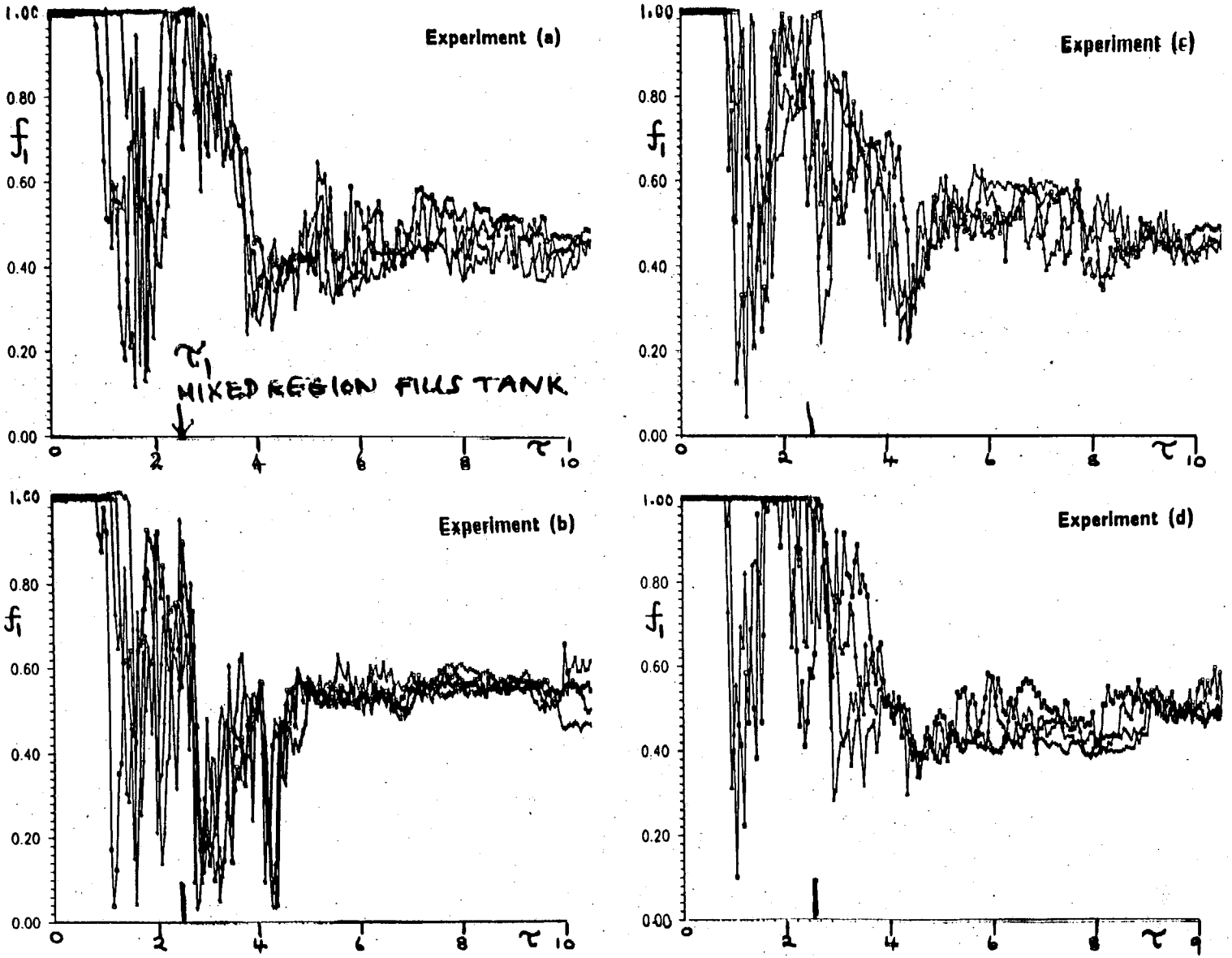

FLUID 1 VOLUME FRACTION VERSUS SCALED TIME (Experiments of Linden and Redondo)

Conductivity probe heights: 4, $6\frac{1}{2}$, 9, $11\frac{1}{2}$, 14 cm above initial interface.

time for density fluctuation to decay ~ $2\tau_1$

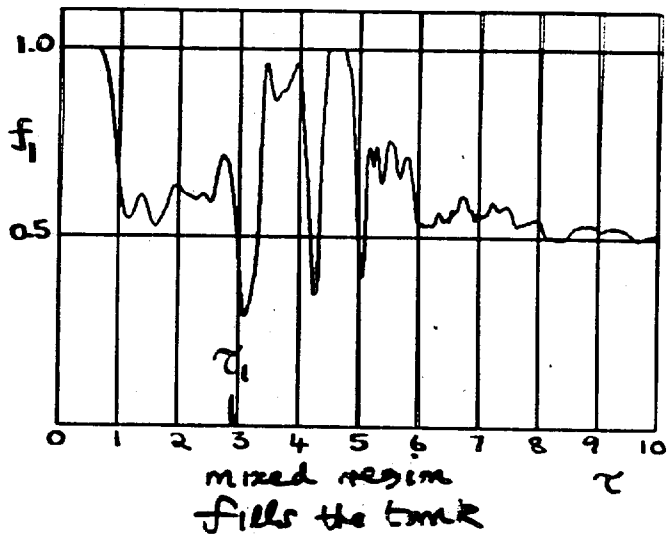

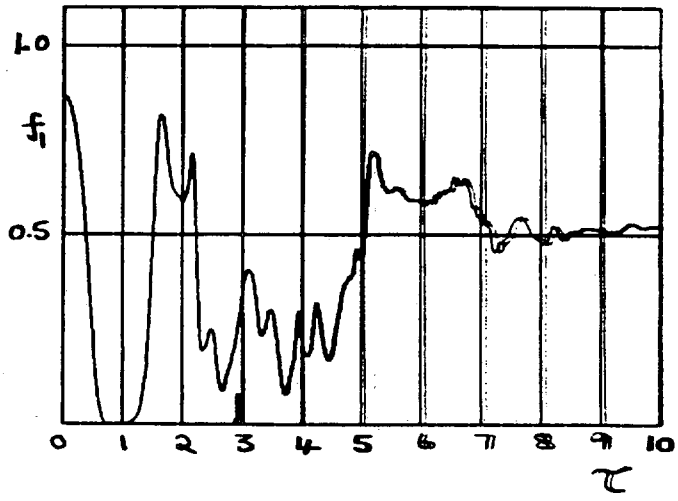

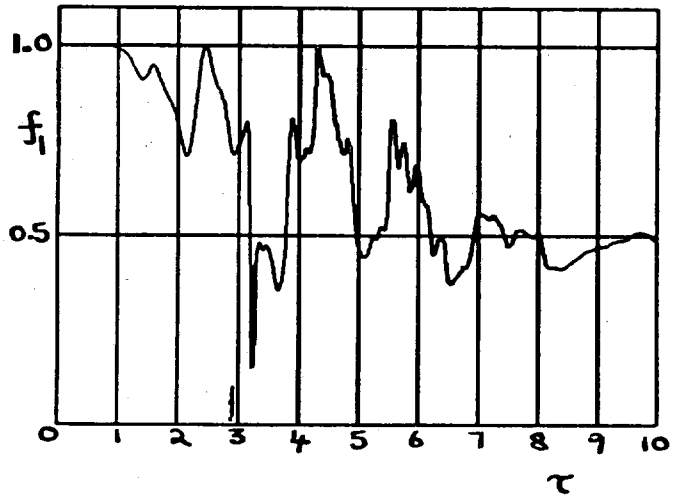

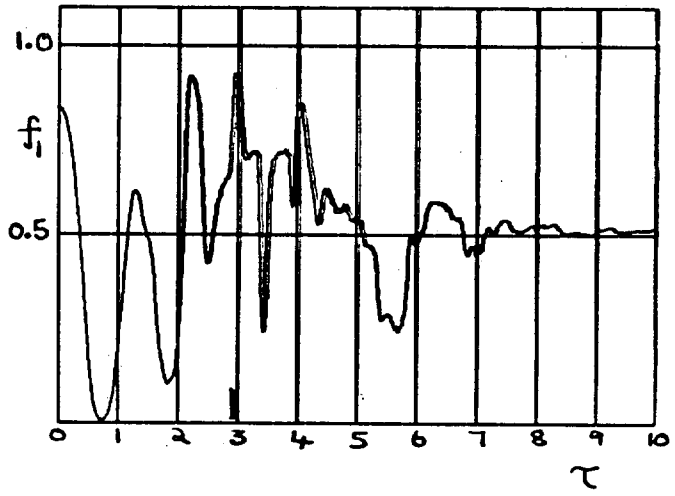

VOLUME FRACTION VERSUS SCALED TIME

FOR 4 POINTS IN THE PLANE $x = 1/2$ (Centre of Mixed Region)

80 x 80 x 80 CALCULATIONS

Time for density fluctuations to decay away $\sim 2\tau_1$

Molecular mixing fraction

Volume fraction for fluid 1

$$f_1 = \frac{\rho - \rho_2}{\rho_1 - \rho_2}$$

$$f_2 = 1 - f_1$$

$\bar{f}_1$, $\bar{f}_2$ plane averages of f_1 and f_2

Reaction rate between fluid 1 and fluid 2 $\propto f_1 f_2$

Define molecular mixing fraction

$$\theta = \frac{\int \overline{f_1 f_2}\, dx}{\int \bar{f}_1 \cdot \bar{f}_2\, dx}$$

$$= \frac{\text{total reaction rate}}{\text{total reaction rate if no fluctuations in any horizontal plane section}}$$

$$\theta = 1 - \frac{\int \sigma^2\, dx}{\int \bar{f}_1\, \bar{f}_2\, dx}, \quad \sigma^2 = \langle (f_1 - \bar{f}_1)^2 \rangle$$

$0 \leq \theta \leq 1$

The Molecular Mixing Fraction for the 2D Calculations

Run No.	θ = Molecular Mixing Fraction			
	τ = 2.5		τ = 3.0	
	44^2 zones	80^2 zones	44^2 zones	80^2 zones
1	0.72	0.63	0.77	0.62
2	0.69	0.68	0.62	0.62
3	0.67	0.59	0.64	0.52
4	0.64	0.73	0.69	0.67
Mean	0.68	0.66	0.68	0.61

The Molecular Mixing Fraction for the 3D Calculations

Run No.	θ = Molecular Mixing Fraction					
	τ = 2.0			τ = 2.5		
	32^3 zones	44^3 zones	80^3 zones	32^3 zones	44^3 zones	80^3 zones
1	0.58	0.65	0.75	0.68	0.70	0.77
2	0.57	0.65	0.74	0.67	0.71	0.76
3	0.56	0.66	0.74	0.67	0.71	0.76
4	0.57	0.66	0.74	0.67	0.72	0.75
Mean	0.57	0.66	0.74	0.67	0.71	0.76

USAGE OF COMPUTER TIME

CRAY-XMP, one processor

Mesh	Mean CPU Time (min)	CPU time/(mesh-step) (μs)
44 x 44 x 1	$1^1/_2$	46
80 x 80 x 1	$8^1/_2$	42
32 x 32 x 32	15	46
44 x 44 x 44	$46^1/_2$	39
80 x 80 x 80	525 (9 hr)	40

Each time step consists of 8 to 10 Lagrangian steps

+ 1 advection step

C. RICHTMYER-MESHKOV MIXING (Single shock)

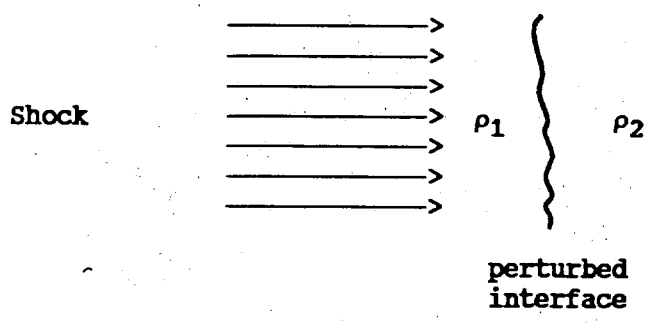

Single wavelength : $u = \frac{2\pi a_o}{\lambda} \Delta U \frac{\rho_1 - \rho_2}{\rho_1 + \rho_2}$

ΔU = change in interface velocity due to shock

Initial KE imparted by shock obtained by summing over Fourier modes (Leith formula).

As a rule $u \ll$ sound speed behind shock

$\therefore$ almost incompressible flow after shock has passed.

Then $\frac{dK}{dt} = -\epsilon$

where K = total turbulence KE

ϵ = turbulence dissipation

Linear regime : $K \sim \bar{\rho}\, \lambda\, u^2$

$$\epsilon = 0$$

$$\therefore \quad u = \text{a constant}$$

and width of mixed region, $\delta \propto t$

Non-linear regime:

Suppose that the mixed region is described by a similarity solution with length scale δ

Then $$K = {}^1/_2\,(1+\alpha)\,\bar{\rho}\delta\,.\,u^2$$

$$\epsilon = -\,c_1\,.\,\bar{\rho}\delta\,.\,\frac{u^3}{\delta}$$

$$\dot{\delta} = c_2\, u$$

α (added mass), c_1, c_2 constants

Solution $\delta \sim t^p$, see also Sturtevant (and reference to Barenblatt) Physica D37.

Substitution in above equation gives

$$p = \frac{2}{3+\beta}\,, \qquad \beta = \frac{2c_1}{(1+\alpha)c_2}$$

$$p = \frac{2}{3 + \beta}$$

$$\beta = -\frac{\dot{K}}{K} \Big/ \frac{\dot{\varepsilon}}{\varepsilon}$$, exact result if similarity hypothesis valid

$$= \frac{\text{Growth time scale}}{\text{Dissipation time scale}}$$

Dimensional analysis then indicates

$$\varepsilon \sim L_o^{1-p} \left[\frac{\rho_1 - \rho_2}{\rho_1 + \rho_2} \Delta U \cdot t \right]^p$$

L_o = a length scale associated with the initial conditions

Time variation of ε, dependence on initial conditions are 3D problems.

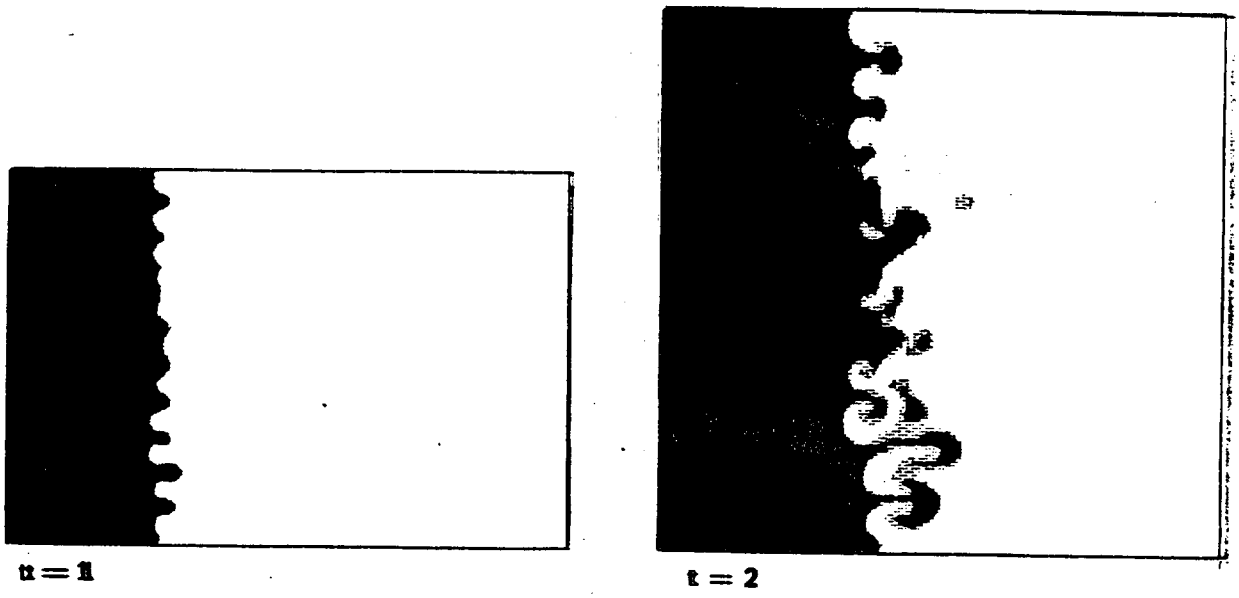

RICHTMYER-MESHKOV PROBLEM
80 x 80 x 80 zones

Density contours for XY plane section

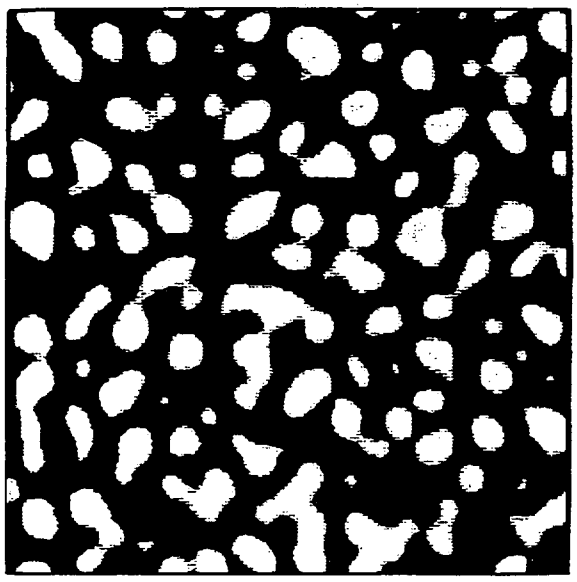

t = 1

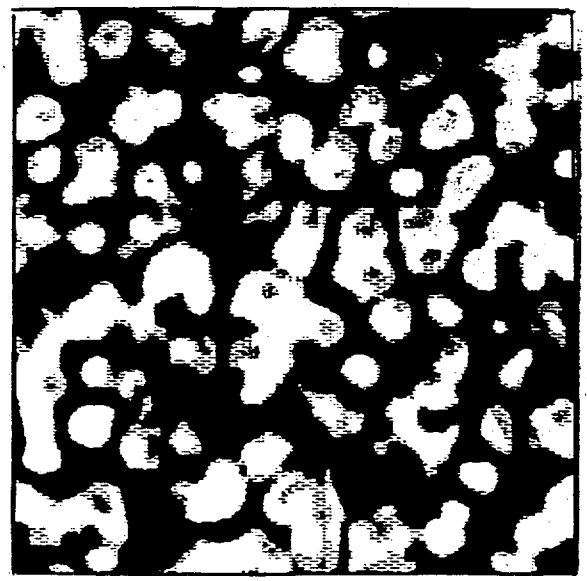

t = 2

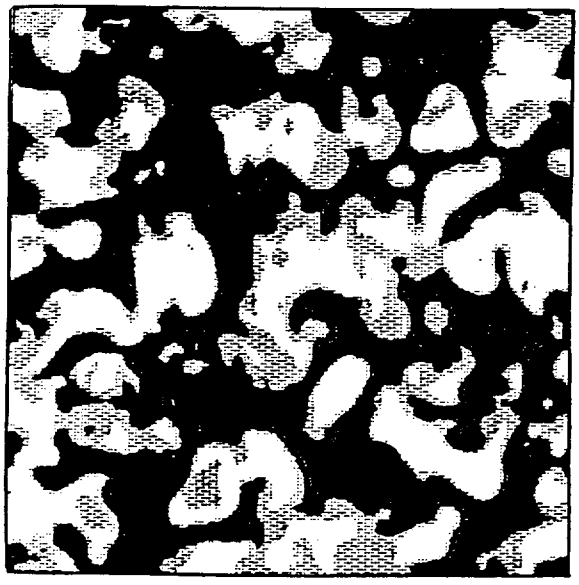

t = 4

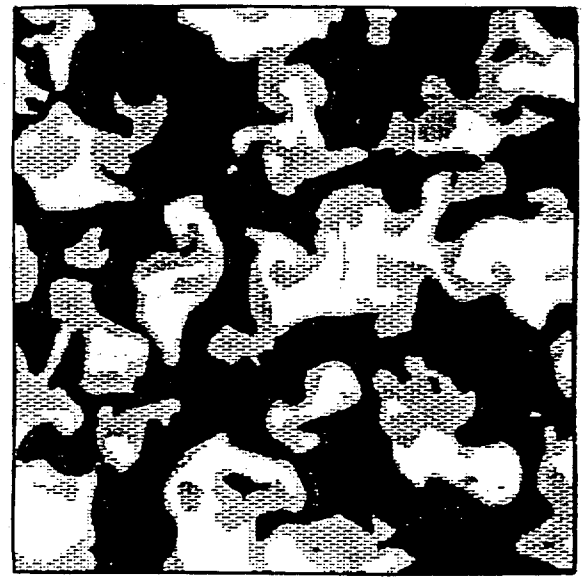

t = 8

RICHTMYER-MESHKOV PROBLEM
80 x 80 x 80 zones

Density contours for YZ plane, section through middle of mixed region

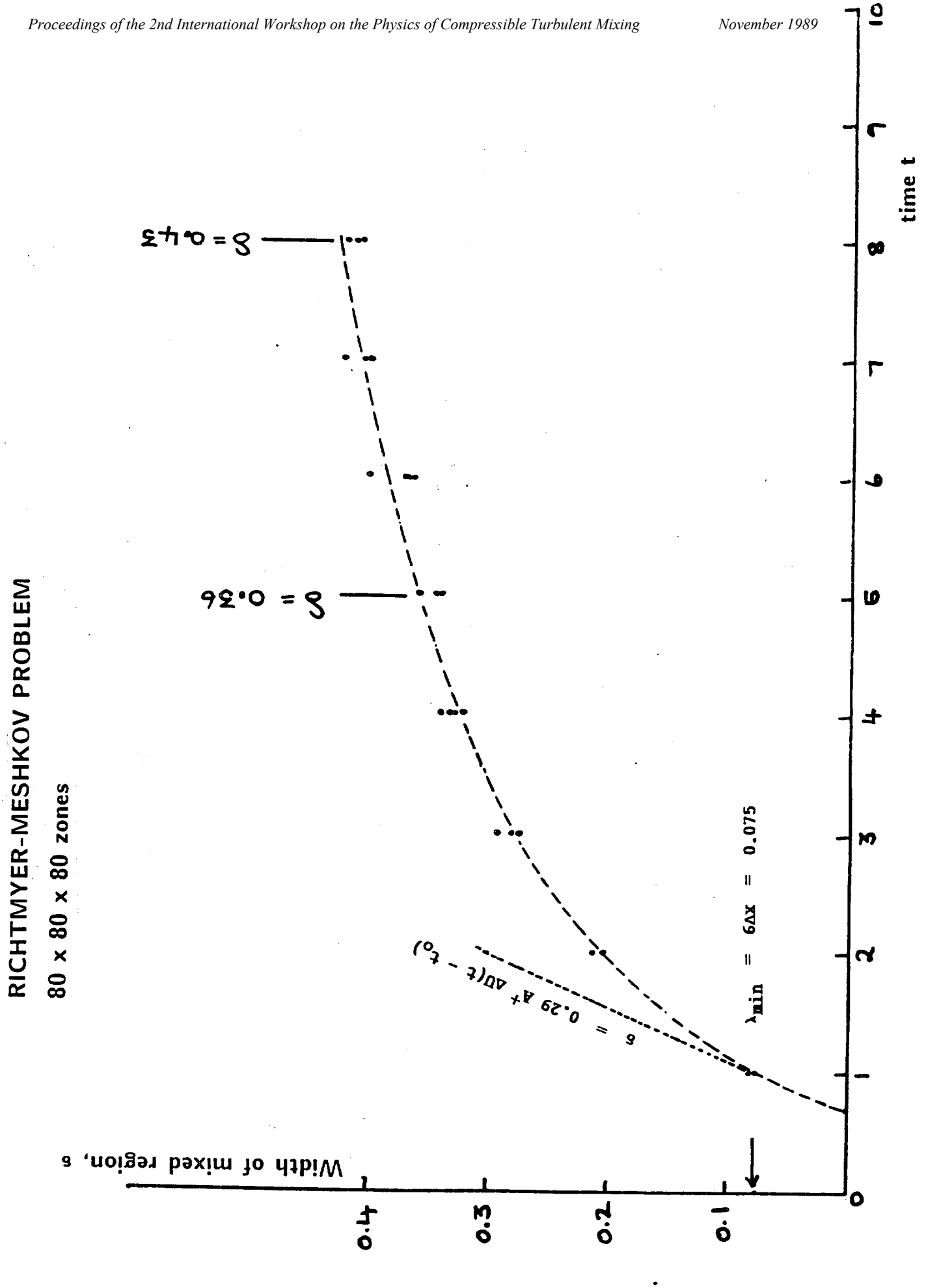
RICHTMYER-MESHKOV PROBLEM
80 x 80 x 80 zones
Width of mixed region, δ
time t
δ = 0.43
δ = 0.36
δ = 0.29 A+ ΔU(t - t0)
λmin = 6Δx = 0.075

$$\beta = \frac{K_1 - K_2}{K_1 + K_2} \times \frac{\sigma_1 + \sigma_2}{\sigma_1 - \sigma_2} = \frac{7.6 - 5.6}{7.6 + 5.6} \times \frac{0.43 + 0.36}{0.43 - 0.36} \sim 1.7$$

$$\Rightarrow \sigma \sim t^p \text{ where } p = \frac{2}{3 + \beta} = 0.43$$

need finer mesh calculation to obtain reliable value.

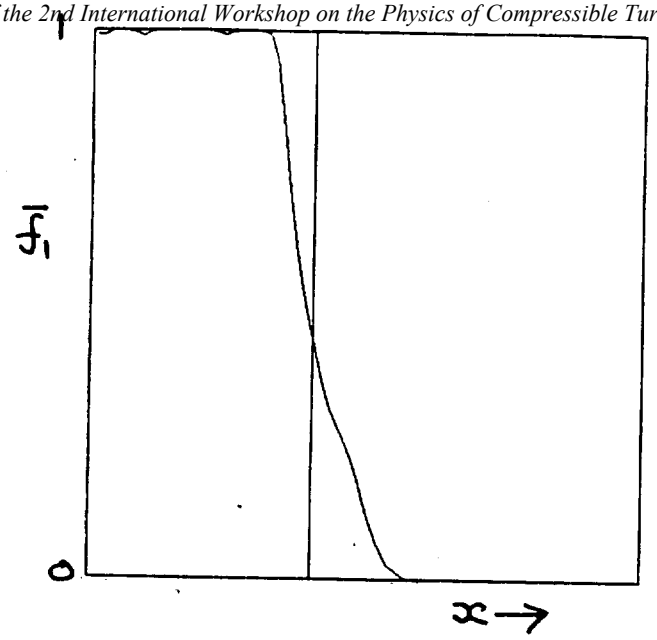

Run 1 **80 x 80 x 80 zones**

$t = 2$

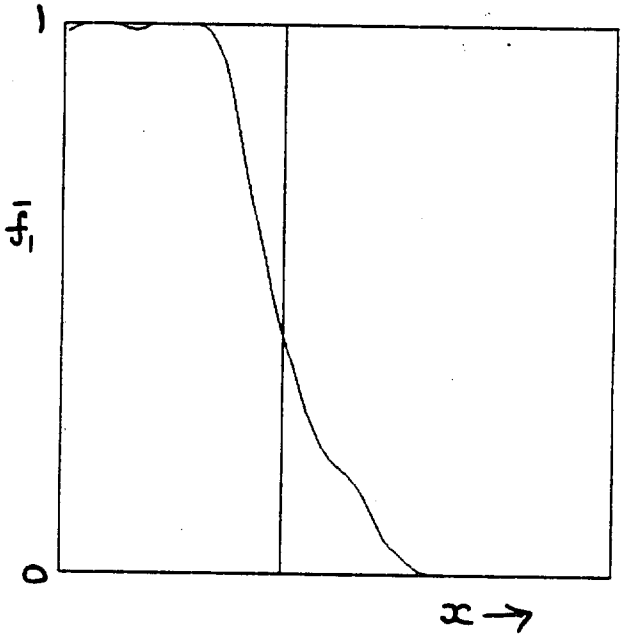

$t = 4$

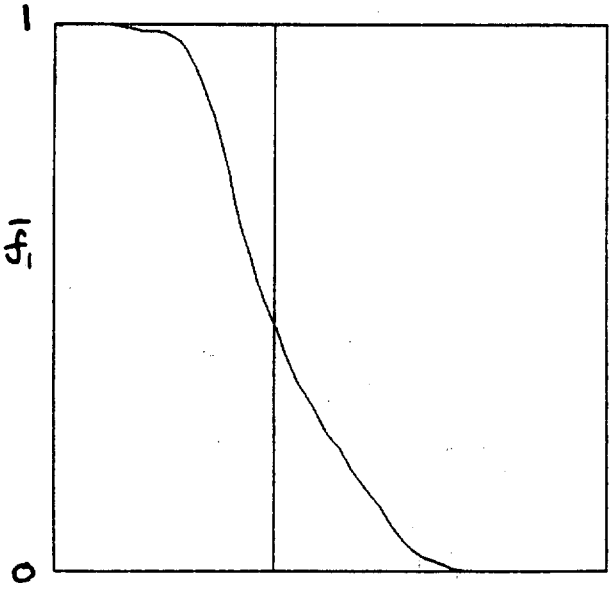

$t = 8, \quad \theta = 0.73$

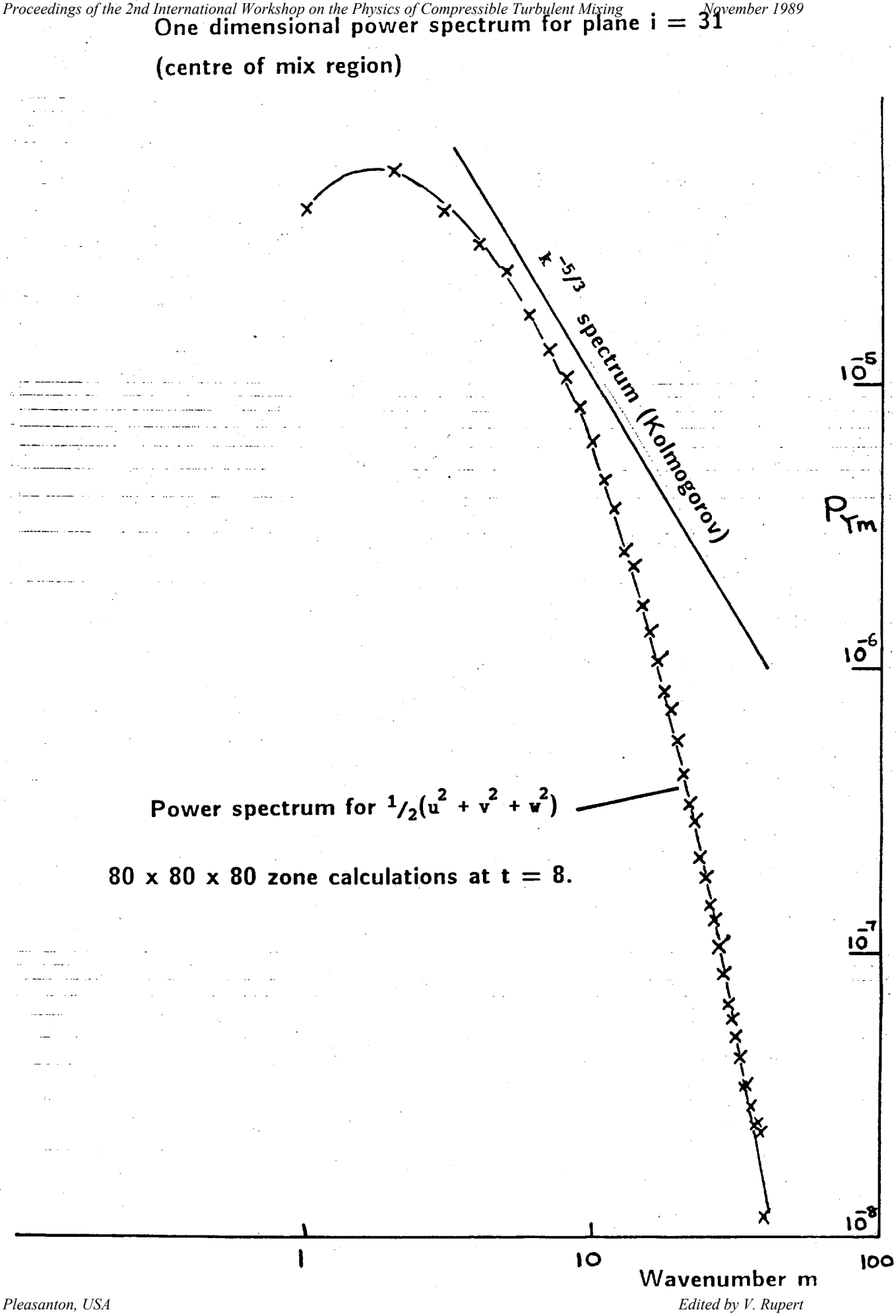
One dimensional power spectrum for plane i = 31
(centre of mix region)
k -5/3 spectrum (Kolmogorov)
Power spectrum for ½(u² + v² + w²)
80 x 80 x 80 zone calculations at t = 8.
P_Tm
10⁻⁵
10⁻⁶
10⁻⁷
10⁻⁸
1
10
100
Wavenumber m

The similarity solution assumes that there is a region of turbulence associated with the mixed region.

However, the forward moving shock and rarefaction travelling back from the interface, perturb the fluid far away from the mixed region.

The early stage in the calculations was examined more closely to see if these perturbations were likely to affect the mixing zone and to look at the behaviour of the 3D/1D boundaries.

t = 1.2

turbulence kinetic energy

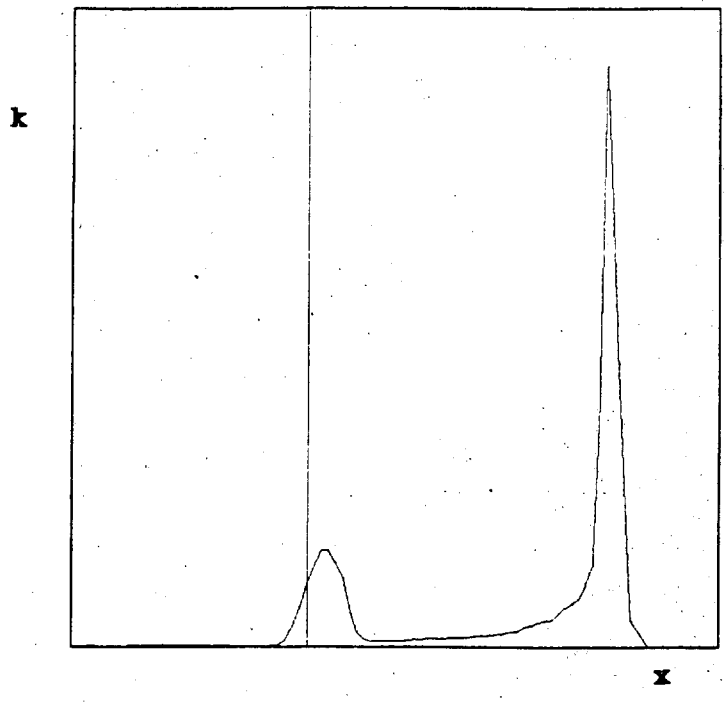

vorticity

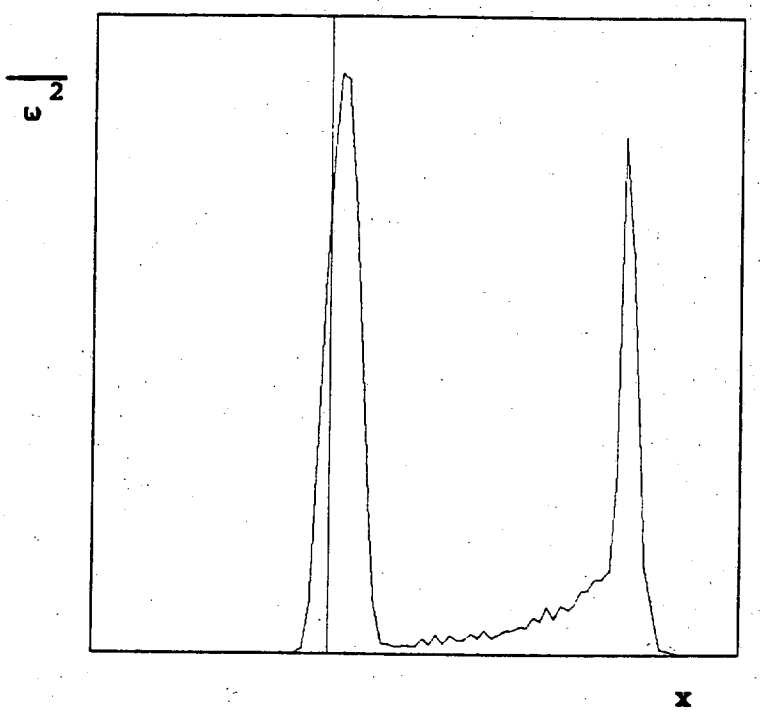

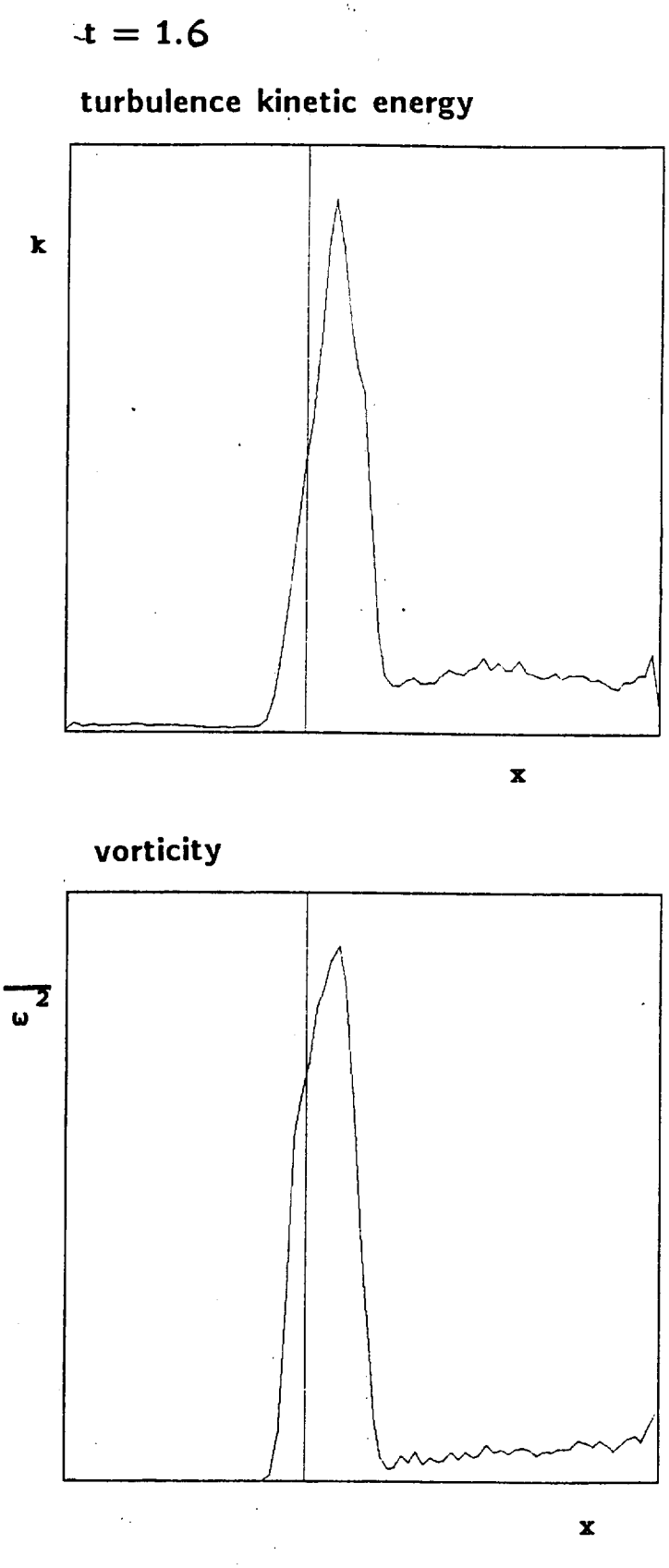
t = 1.6
turbulence kinetic energy
k
x
vorticity
ω²
x

Proceedings of the 2nd International Workshop on the Physics of Compressible Turbulent Mixing November 1989

STRUCTURE OF RT FLOWS

J. M. REDONDO
&
P. F. LINDEN

UNIVERSITY OF CAMBRIDGE
Department of Applied Mathematics and Theoretical Physics
Silver Street, Cambridge, England CB3 9EW

Telephone: Cambridge (0223) 337900. Direct Line: (0223) 337911
Telex: 81240 CAMSPL G. FAX 33 7918

INTRODUCTION

Since the work of Richardson [1], it has been considered that turbulence can be modelled in terms of a hierarchy of eddies, or scales . In the inertial subrange the energy cascade provides a recurrent dynamical mechanism that makes different scales visually similar. This "self similar" description of turbulent flows suggests that the theory of fractals developed by Mandelbrot [2,3,4] , may be applicable to turbulence [5,6]. As the Euclidean dimension, E, of ordinary objects , a characteristic dimension called the fractal dimension , D , is defined, which gives a measure of the fragmentation or roughness.

The definition a fractional geometrical dimension can be made, by recognizing that the dimension of an object may be used as an exponent in measuring its size [2] . The general formula is:

$$N = \left(\frac{1}{\sigma}\right)^D \quad ; \quad D = \frac{\log N}{\log\left(\frac{1}{\sigma}\right)} \qquad \sigma = \text{scale},\ N = \text{no. ssp.}$$

see references [2-6] for further details.

This paper presents measurements of the fractal dimension of a density interface

Fractal analysis is a convenient method for investigating the structure of Rayleigh-Taylor Instability.

DISCUSSION

In Laboratory three dimensional flows there is a sufficiently large range of scales , Ranging from the size of the box L (50 cm) to the kolmogorov length scale η (0.1-1 mm small scale eddies) It is possible geometrically to extract usefull information which can be related to turbulent parameters. Statistical analisis of turbulent flows is usually done in terms of a mean (corrected for non steadines) and small scale fluctuations : $u = U + u'$. Here U = 0. Fractal analysis of density interfaces, in a similar way as the spectrum of velocity

Rayleigh-Taylor (RT) instability is the name given to the motion that develops when light fluid is accelerated into a heavy fluid. This can occur, for example, as a result of local density inversions of a stratified fluid. Linear stability theory dates back to Taylor [19] and Chandrasekhar [20] recent reviews of the development to finite amplitude can be found in [21-24]. The characteristic of the instabilities observed at high density ratios is the production of 'bubbles' and 'spikes'. Secondary phenomena include the development of

Kelvin-Helmholtz instability on the side of the 'spikes', amalgamation of bubbles and the production of small turbulent scales. The motion is essentially three-dimensional in character, with the interface having a fractal quality as the instability develops. Here we report measurements on the visual description of the interface, including fractal analisis as described below.

The experiments

The experiments were carried out in a perspex tank 50 cm deep, 40 cm long and 20 cm wide. The tank had a removable aluminium sheet 1.5 mm in thickness which separated a layer of brine from a layer of fresh water below. The two layers of fluid were initially at rest and the experiment was initiated by sliding the aluminium sheet horizontally through a slit in one end wall of the tank. Flow visualization was either by shadowgraph or by adding dye to one of the layers. LIF was also used, with illumination provided by a thin (2mm) sheet of light from a 200mW argon laser. Records of the flow were made using video and still photography. The video images were digitised to obtain quantitative information.

All the experiments were conducted with two layers of equal depth, with a range of initial density differences $\frac{\Delta\rho}{\rho}$ from 0.0005 to 0.098 . Only the experiments with $\frac{\Delta\rho}{\rho}$ between 0.005 and 0.065 are considered fully representative of the RT instability since for lower values of the density difference the initial disturbance caused by the plate removal caused considerable

uncertainties and at high values the growth rate of the instability was comparable with the velocity of the plate. See reference [21] for further information.

Experimental results

Qualitative results

The front grows symmetrically about the original interface position, and that motion develops over a range of lengthscales. There is some variation in the thickness of the mixing region during the early stages which results from removing the plate through one end of the tank and there are strong flows generated in the immediate vicinity of the end walls of the tank. In the central region of the tank the mixing region is of approximately uniform thickness. The lengthscales which appear initially are those produced by vortices shed from the trailing edge of the plate. These are typically 5-10 cm in length. Superimposed on these vortices are small scale instabilities, associated with RT instability. At later times the lengthscales of the dominant motions increase by vortex pairing. Eventually the whole system overturns on the scale of the tank.

Quantitative results, Growth of the mixing region

The thickness δ of the mixing region was determined from flow visualization. If we assume that the rate of advance of

the mixing front depends only on

$$g' = g\frac{\Delta\rho}{\rho} \tag{10}$$

and the instantaneous thickness, dimensional analysis gives

$$\frac{d\delta}{dt} = 2(cg'\delta)^{1/2} \tag{11}$$

Integration and application of the boundary condition $\delta = \delta_0$ at $t = 0$ shows

$$\delta^{1/2} = (\delta_0)^{1/2} + (cg')^{1/2}\ t \tag{12}$$

Thus δ_0 represents a 'virtual origin' corresponding to the initial displacement produced by withdrawal of the plate. At large times, when $\delta \gg \delta_0$,the above formula is equivalent to the result given by [24,26].

$$\delta = cg't^2 \tag{13}$$

The data is consistent with a constant value of $c = 0.035 \pm 0.005$. This value is in agreement with those obtained at large density differences $(\Delta\rho/\rho)$ [22,24,26].

Lengthscales

A range of lengthscales occurred during the RT process ranging from 5mm to the scale of the tank. The behaviour was similar for all of the densities analysed. Initially small

disturbances could be seen which corresponded with the most unstable lengthscale λ_m between 3mm and 1.5mm. Superimposed on this scale 4 to 6 wavelengths of the order of 50 to 100 mm developed due to the removal of the barrier. As the RT instability front advanced new small scales could be seen developing,see figure . Some could be identified as KH billows and some as small vortex pairs. The large disturbances merged as the RT front advanced leaving one or two larger protuberances by the time the RT front reached the bottom of the tank.

The experiments show that RT instability involves a number of interacting scales and processes. Small scale instabilities (consistent in scale and growth rate to those predicted by linear theory) occur and are superimposed on a larger scale instability of the interface. This larger instability leads to the formation of blobs of fluid which penetrate into the layers on either side. Secondary instabilities in the form of Kelvin-Helmholtz billows form on the sides of the blobs. There appears to be little mixing across the leading edge of the blob, but fluid is entrained around the sides in a manner reminiscent of a falling plume or thermal, described in [25,26].

Fractal structure of the Rayleigh Taylor turbulent front

The fractal dimension was calculated on LIF video tapes of the evolution of the RT front in a similar way as indicated in 2.1.2. Both sides and elevation views were analysed. Fig-

ure 7 shows a typical plot of N vs. σ^{-1} It indicates roughly a self-similar behaviour, but there is a predominance of two scales (indicated by arrows) that correspond to the bubble size and the dominant KH instability on the side of the blob. If different regions of the front are averaged, figure 8. the linear fit takes into account the statistical nature of the mixing process. This plot shows that the front defines a statistical fractal set. The development of full fractal structure takes 1-2 seconds for the range of densities used. An example of the time development of the fractal dimension is shown in figure . The slight decrease in fractal dimension after three seconds might be due to the influence of the box walls on the flow and is not considered significative. The large error bars are a reflection of the different cascading mechanisms observed in the flow visualization.

Models of stratification and rotation effects on the inertial subrange must take into account the modified cascade of vorticity and the observation that an inverse cascade (Energy been extracted by the large scales from the small turbulent scales). This can only be done introducing non-linear transfer terms in the vorticity equations. The restoring force of the interface can be modelled by reducing the perpendicular extension of the vortex. the same is true for rotation effects in wich coriolis forces modify the isotropy of inertial cascades.

(LASER induced fluorescence,LIF). The thickness of the beam of light was less than 0.5 cm. (0.2 cm for a laser sheet) which is greater than the Kolmogorov scale ,η , given by:

$$\eta = \left(\frac{\nu^3}{\epsilon}\right)^{\frac{1}{4}}$$

Values of ϵ can be calculated using the estimate for the viscous dissipation $\epsilon \propto \frac{u'^3}{\ell}$, and substituting the experimental values for u' and ℓ given above, we obtain a range of Kolmogorov scales for all the experiments of $0.02 \leq \eta \leq 0.1cm.$, indicating that small scale fractal structure was constrained by the thickness of the light beam rather than by viscous dissipation.

Data analysis.

The method used to find the relation between the fractal dimension of the stratified turbulence and the local Richardson number is as follows . After setting the distance from the grid to the density interface , the grid oscillations were started. Once the turbulence reached a steady state , 3 to 5 photographs were taken of the interface. These photographs were projected and the position of the interface was marked on a square grid for analysis. Some of the experiments were video-taped and the image was processed directly.

The curves marking the interface position were covered by grids of squares of decreasing size, and the number of squares which were intersected by the interface for each size were counted. This process was repeated 5 times over different

photographs or different sections of the same photograph for each grid size, thus obtaining $N(\sigma)$. The interval between the smallest and the largest number of squares counted was plotted in a log - log plot of N versus σ , and the linear fit that could cover most of the data was considered to represent the average homogenous fractal dimension for the experiment. Some of the images of the interface were digitized using a B.B.C. master microcomputer or a IBM AT Compatible microcomputer ,a video camera and a digitizer . A program followed the procedure mentioned above , finding $N(\sigma)$ for each box size until the limit of resolution of the computer screen. In addition , the maximum displacement of the interface ,λ ,was measured on all the photographs for each Richardson number and non dimensionalized with the integral lengthscale of the turbulence, ℓ,

Results

Qualitative features.

The visualization of the turbulent density interface by means of slit lighting with fluorescein in the lower layer shows ,as indicated in figure 1 ,that as the Richardson number of the experiment increases, the convolutions of the interface are reduced in their vertical scales . Photographs of the interface show that there are different perturbation scales between the maximum vertical scale ,λ , and the minimum resolvable scale ,δ . The range of different vertical scales observed on the interface decreases as the Richardson number increases .

fluctuations can give information on the distribution of energy between different eddy sizes.

fractals in a turbulent(vortical) fluid

The underlining characteristic of a fractal set is the self-similarity of scales in the sense that there are smaller and smaller scales which mantain some relation between them. This relationship can vary in the following ways:

a) For an Exact Fractal set ,such as the Koch curve, the interface looks exactly the same when looked under different magnifications.

b) In an Statistical Fractal set, (sometimes called Fat Fractal) the interface only looks statistically similar when the scale is reduced. For different parts of the interface, the fractal dimension changes slightly, but we can define a mean or average fractal dimension.

c) A Self-Affine Fractal set is by nature anisotropic and there are different scaling laws for the different coordinates.

The vorticity or concentration isolines are not exactly self-similar, as small scale visual structure is not, in general, identical to the larger convolutions, and there is a random component in the distribution of the various eddy sizes. The interfaces, in fact, are self-affine in an statistical sense(subjected to contractions, rotations, inversions, etc.). They can be interpreted in terms of mean fractal dimensions, and also as multiple, varying fractal dimensions, which depend on the scale, σ,

or on the scalar threshold. In order to have a consistent quantitative information about a density or a vorticity contour it is necesary to identify the initial step of the fractal calculation (box-counting algorithm) as in turbulent flows the large scale coherent structures can modify the local structure of the flow and therefore the fractal dimension.

Relation between the spectrum of turbulence and the fractal dimension

This review section is based on work by Mandelbrot and Turcotte [2-5], Both the spectrum of turbulent velocity and of a scalar field (such as dye concentration) are used in order to relate the geometrical self-similarity to the dynamical one.

Let us consider that we have a signal (assume it is the density concentration, a temperature, velocity of Kinetic energy density). In principle, such a signal can be described by a power law if there are no dominant scales as: " The power-law distribution is the only one that does not include a characteristic scale in the problem ".

If the description of the signal is temporal, we assume that the frequency spectrum has the shape:

$$S(f) = f^{-\beta} \tag{14}$$

where f is the frequency and β a constant that determines the relative importance of large and small fluctuations.

If the distribution of the signal is spatial, we can use a wave-number definition, such as in turbulence, and write

$$S(k) = k^{-\beta} \tag{15}$$

If the constant β is zero, then the signal is produced by random noise, if β is two, then Brownian motion is the process underlying. Turbulence is characterized by $\beta = 5/3$ in the inertial subrange, but a wide range of the exponent $\beta \approx 1$ can be considered as turbulent, it is also called fractional Brownian motion. In figure 10 examples of signals with varying spectral exponents can be seen.

The probability, P, that for a fractal set we intersect the set at a step σ is

$$P = N\sigma^E = \sigma^{E-D} \tag{16}$$

where we have used the definition of fractal dimension,(1,2) D,

$$N = \sigma^{-D} \tag{17}$$

and E is the euclidean dimension where the fractal set is imbeded and N is the number of steps.

We can consider σ indistinctly as a temporal ,T, or a spatial, R, step.

For a temporal step in an E-dimensional space { t,x,y,z,ρ,etc..}.

$$\frac{P}{T^{E-D}} = \text{constant} . \tag{18}$$

For Fractional Brownian motion the probability that two points have close values is a function of the distance (in time or space).

Let the fractal function be $\rho(t)$, then the probability of

$$P\left(\frac{\rho(t+T)-\rho(t)}{T^H} \leq \rho_o\right) = F(\rho_o) \tag{19}$$

where $F(\rho)$ is a gaussian function, and H is called the Hausdorff dimension.

by comparing the above expressions, we define

$$H = E - D \tag{20}$$

which states that the Hausdorff Dimension plus the Fractal dimension must equal the Euclidean dimension.

As the variance of a signal is defined as

$$V(T) = < (\rho(t+T)-\rho(t))^2 > \tag{21}$$

we can relate

$$V(T) \approx T^{2H} \approx T^{2E-2D} \tag{22}$$

Using $T = 1/f$,and the description of the spectral density function, $S(f)$, we have

$$S(f) \approx T^{\beta} \tag{23}$$

and as

$$S \propto T \int_0^T \rho^2(t) e^{-ift}\, dt \approx TV \tag{24}$$

we can relate

$$S(f) \approx TV \approx T^{2H-1} \approx T^{2E+1-2D} \tag{25}$$

so a relationship between the exponent of the spectral density function and the fractal dimension can be found as:

$$\beta = 2E + 1 - 2D \tag{26}$$

and

$$D = E + \frac{1-\beta}{2} \tag{27}$$

In the case that E = 3 ,then $D = 3.5 - \beta/2$, so, for turbulence ($\beta = 5/3$) we have D = 2.66. This is consistent, but overestimates experimental results on laboratory turbulence and vertical cloud fractal dimensions [6,16,29] which in some sense we can assume that follow (for a short time) the vorticity isolines (as due to the structure of the vorticity equation, it is easily seen that vorticity diffuses in a similar way as concentration).

Turbulence models introducing Intermittency and body forces

Since Kolmogorov derived through dimensional arguments his spectral relations

$$E(k) = c\epsilon^{2/3}k^{-\frac{5}{3}} \tag{28}$$

For Fractional Brownian motion the probability that two points have close values is a function of the distance (in time or space).

Let the fractal function be $\rho(t)$, then the probability of

$$P\left(\frac{\rho(t+T)-\rho(t)}{T^H} \leq \rho_o\right) = F(\rho_o) \tag{19}$$

where $F(\rho)$ is a gaussian function, and H is called the Hausdorff dimension.

by comparing the above expressions, we define

$$H = E - D \tag{20}$$

which states that the Hausdorff Dimension plus the Fractal dimension must equal the Euclidean dimension.

As the variance of a signal is defined as

$$V(T) = < (\rho(t+T)-\rho(t))^2 > \tag{21}$$

we can relate

$$V(T) \approx T^{2H} \approx T^{2E-2D} \tag{22}$$

Using $T = 1/f$,and the description of the spectral density function, $S(f)$, we have

$$S(f) \approx T^{\beta} \tag{23}$$

and as

$$S \propto T \int_0^T \rho^2(t) e^{-ift}\, dt \approx TV \tag{24}$$

where ϵ is the dissipation that can be estimated from turbulent parameters as

$$\epsilon \propto \frac{u'^3}{\ell} \tag{29}$$

Some researchers found that agreement was not as good as the earlier succesess of the teory and Obukov and Kolmogorov [32,34] introduced a correction by taking into account the intermittency of the distribution, by adding a factor. $(\ell k)^N$ where N is called the intermittency, and represents the average number of vortices which are formed when a larger vortice decays.

$$E(k) = c\epsilon^{2/3}k^{-\beta}\left(\ell k\right)^N \tag{30}$$

Let us assume that each vortex has its linear size divided in two. Using the β model [35]. if at each step of the intermittent cascade, n, the energy spectrum is discontinous, the only energetic wave numbers will be

$$k_n = \frac{1}{\ell_n} = \frac{2^n}{\ell} \tag{31}$$

and the velocity is v_n with turnover time

$$t_n = \ell_n / v_n \quad . \tag{32}$$

Considering that eddies of size l_{n+1} only occupy a fraction of the total volume, β , then

$$\beta^n = (N/2^3)^n \tag{33}$$

where N is the average number of eddies formed from a larger one.

As the fractal dimension also gives an estimate of the volume occupied by the next generation of eddies in the Kolmogorov cascade sense then using (1) and (2).

$$\beta^n = (2^D/2^3) = (\ell_n/\ell)^{3-D} \tag{34}$$

As the Kinetic energy, E_n is only defined in term of the active regions:

$$E_n \propto \beta^n v_n^2 \tag{35}$$

we can use (29) and write

$$\epsilon \propto E_n/t_n \propto \beta^n \frac{v_n^3}{\ell_n} \tag{36}$$

and we get

$$E(k) \propto (\epsilon \ell_n)^{2/3}\ k^{-5/3}\ (\ell k)^{D/3-1} \tag{37}$$

which is a modified intermittent cascade.

The stratification can be accounted for in two ways, first by introducing an intermittent factor dependent on the Richardson number, and secondly by reducing only the vertical scales .

In a stratified fluid the vertical scales of motion are suppressed if the vertical lengthscale is greater than the Ozmidov scale.

$$Lo = (\epsilon/N^3)^{1/2}\ , \tag{38}$$

The boundary can be thought of as a strong density interface . Their results show how the vertical turbulent velocity fluctuations decrease as the wall is approached . The interesting relationship with the observed decrease of the fractal dimension near a density interface is that there is a change in slope of the velocity spectrum $\phi_{ii}(k)$,depending on the proximity of the wall (or strength of stratification) in the range $\ell > k > \eta$, being η the Kolmogorov length scale as defined above. The simulation of a density interface by a rigid surface is supported by McDougall's [10] experiments ,and so we expect a similar change in the velocity spectrum near an interface [14,15].

Consider two intermediate vertical length scales λ and δ , which correspond to the maximum deflections of density interfaces and to the minimum resolvable scale,respectively, from a given photograph . These scales correspond to two Richardson numbers such that $Ri_\lambda < Ri_\delta$. and : $\ell > \lambda > \delta >> \eta$. as shown in Figure . As the Richardson number increases ,the length scale interval between λ and δ decreases, and it is more difficult to define a fractal dimension ,because for a totally flat interface $D \rightarrow 1$. The effect of increasing the Richardson number can be seen in this figure where Ri_δ is larger than Ri_λ , so the corresponding vertical velocity spectrum is reduced, thus reducing also the maximum vertical scales. It is not yet conclusively known what the relation is between the slope of the velocity spectrum and the fractal dimension in an inhomogeneous fluid. The shape of the vertical velocity spec-

1.40 in the unstratified limit (Ri $\rightarrow$ 0) to 1 for strongly stratified flows (Ri $\rightarrow \infty$) . This leads support to the claim that homogeneous turbulence has a fractal dimension of 1.37 to 1.43 [19] and it also agrees with the results of Lovejoy [6] that clouds , as seen by satellite and not affected by stratification , exibit a fractal structure of dimension 1.34 .

The theoretical relation (27), overestimetes the experimental fractal dimensions if we assume $D_3 = D_2 + 1$, and $\beta = 5/3$ .Further work is needed in order to determine both β and D and take into account the influence of perpendicular dimensions on the analysis.

The exhibition of the fractal structure of a density interface requires that the interface be in statistical equilibrium .The experiments described above produce equilibrium conditions over long time-scales as the Richardson number only changes as a result of migration of the interface which is a slow process for $Ri \geq 10$. The hierarchy of scales of interface distortion requires a self-similar turbulent energy spectrum in the layer stirred by the grid. Evidence for such a spectrum in homogeneous and non-homogeneous fluids is provided by other studies of mixing boxes [10,11,14].

The effect of increasing stratification on the fractal dimension can be discussed by referring to the results of Hunt and Graham [27] for the spectrum of turbulence advected near a boundary moving at the same speed as the flow. The parameter $Y = z/\ell$ measures the distance from the plane surface .

Most of the assumptions made when deriving the relationships between the fractal dimension and turbulence parameters suppose homogeneous isotropic turbulence. It is not clear if all of these can be used in stratified flows. Further work, both experimental and theoretical will be necessary to resolve some of the open problems [33,35]. For the RT unstable flow, the emerging picture of the growth of the turbulent layer can be interpreted in the following way, as the density interface starts to accelerate, small scale perturbations of lengthscale given by linear theory appear [19,20]. As the bubbles grow up to 10 cm. secondary instabilities like Kelvin-Helmholtz or vortex pairing appear, increasing the range and the value of the fractal dimension up to a value of $D_2 = 1.3$. The influence of the side walls on the unstable flow can avoid reaching a fully turbulent flow, which would give a maximum fractal dimension of $D_2 = 1.4$.

The present laboratory experiments have been done for zero-mean turbulence influenced by a sharp density interface, due to their simplicity, other types of flows should be examined in a similar way.

ACKNOWLEDGEMENTS

The authors would like to thank the H.S.E. and the M.O.D. for their support. We would also like to thank S. Dalziel and R. Perkings for their help in the use of the digitizer and C. Vassilicos for many helpful discusions.

Proceedings of the 2nd International Workshop on the Physics of Compressible Turbulent Mixing
Pleasanton, USA
November 1989
Edited by V. Rupert

SECOND ORDER MODE COUPLING ANALYSIS SHOWS HOW MOST RAYLEIGH-TAYLOR SYSTEMS FORGET INITIAL CONDITIONS

International Exchange on RM & RT Mixing
Pleasanton, CA

November 16–17, 1989

Steven W. Haan

LAWRENCE LIVERMORE NATIONAL LABORATORY

*This work was performed under the auspices of the U.S. Department of Energy by the Lawrence Livermore National Laboratory under Contract No. W-7405-ENG-48.

Several people have helped me with this work

- Hans-Jörg Kull — unpublished work on coupling of parallel modes, helped me get started
- Dave Munro — helped me understand basic math of incompressible RT
- Jill Dahlburg, Steve Weber, John Lindl, Max Tabak — useful conversations
- Jill Dahlburg, John Gardner, Garry Doolen, and Karnig Mikaelian — shared simulation results

Pleasanton, USA
Edited by V. Rupert
November 1989

We want to understand nonlinear Rayleigh-Taylor growth

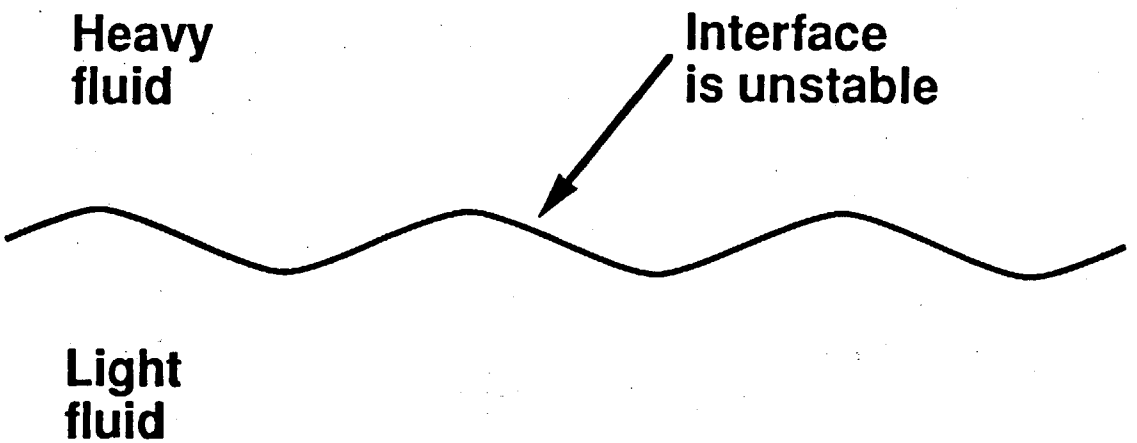

Some background:

1. Single modes grow until amp $\approx \lambda \times 0.1$ before nonlinear evolution begins. Analytic solutions to third order in ka (Ingraham 1954, various others through Jacobs and Catton 1988), evolution to spikes and bubbles.

2. With multiple modes, nonlinear short wavelengths "feed" long wavelengths (Youngs 1984).

Pleasanton, USA
Edited by V. Rupert
Proceedings of the 2nd International Workshop on the Physics of Compressible Turbulent Mixing
November 1989

We have tried to exploit an analytic mode-coupling approach

Heavy fluid

$$\vec{u} = -\vec{\nabla}\,\varphi_H,\ \nabla^2\,\varphi_H = 0$$

$$\rho = \rho_H$$

$$P = \rho_H\left[\frac{\partial\varphi_H}{\partial t} - \frac{1}{2}u^2 - gz\right]$$

Interface is unstable

Tension T on surface z(x,y)

Light fluid

$$\vec{u} = -\vec{\nabla}\,\varphi_L,\ \nabla^2\,\varphi_L = 0$$

$$\rho = \rho_L$$

$$P = \rho_L\left[\frac{\partial\varphi_L}{\partial t} - \frac{1}{2}u^2 - gz\right]$$

Use standard (exact) formulation for R-T interface between inviscid, incompressible fluids.

Boundary conditions on φ_H and φ_L at z(x,y).

Fourier transform to

$$z(\vec{k}) = \frac{1}{L^2}\int dxdy\, e^{-i\vec{k}\cdot\vec{x}}\, z(\vec{x})$$

Expand system of equations to second order, get

$$\ddot{z}(\vec{k}) = \gamma(k)^2\, z(\vec{k}) + \alpha k \sum_{k_2}\left[\dot{z}(\vec{k}_2)\,\dot{z}(\vec{k}-\vec{k}_2)\,G_1(\hat{k},\hat{k}_2) + z(\vec{k}_2)\,\ddot{z}(\vec{k}-\vec{k}_2)\,G_2(\hat{k},\hat{k}_2)\right]$$

where G_1 and G_2 are algebraic functions of angles $\hat{k}\cdot\hat{k}_2$, $\hat{k}_2\cdot(\vec{k}-\vec{k}_2)\Big/\left|\vec{k}-\vec{k}_2\right|$

SH-01-U-11-/89-D24

This set of equations can be sensibly solved at intermediate times when nonlinearity is weak

(1) Diff. eq. $\ddot{Z}_k = \gamma(k)^2 Z_k + \alpha k \sum_{k_2} \left[\dot{Z}_{k_2} \dot{Z}_{k-k_2} G_1(\vec{k}, \vec{k}_2) + Z_{k_2} \ddot{Z}_{k-k_2} G_2(\vec{k}, \vec{k}_2) \right]$

Approximate linear solution $Z_k(t) = Z_k^{lin}(t) = Z_k(0) \cosh \gamma(k)t$

Substitute into sum in (1), solve to get

(2) $$Z_k(t) = Z_k^{lin}(t) + \alpha k \sum_{k_2} Z_{k_2}^{lin}(t) Z_{k-k_2}^{lin}(t) W(\vec{k}, \vec{k}_2, t)$$

where W is algebraic function of $\gamma(k)$ etc. Dimensionless, order unity. Weak t dependence (cosh $\leftrightarrow$ exp).

Solution procedure justified iff sums in (1) and (2) are dominated by terms which themselves are still close to linear.

We also have to consider the phases of the modes

$$(2)\quad Z_k(t) = Z_k^{lin}(t) + \sum_{k_2} Z_{k_2}^{lin}(t)\, Z_{k-k_2}^{lin}(t)\, W(\vec{k}, \vec{k}_2, t)$$

This is a sum of complex numbers of various phases. Typically $\langle Z_{k_1} Z_{k_2} \rangle = \delta(k_1 + k_2)$ for translation invariant systems, so "average value" of summand is zero.

How can we handle this?

1. Numerical simulations have known phase, we can compare directly with Eq. (2). Note simulations must also make realistic choice of phases!

2. Quadrature sum probably reasonable for "typical" surfaces

3. Also working on a bump model where

$$Z(\vec{x}, t=0) = \sum_{j=1}^{N} b(\vec{x} - \vec{x}_j) \quad \text{(average over } x_j = \text{position of bump j)}$$

XDIV-11-U-5/89-SH-D15

Proceedings of the 2nd International Workshop on the Physics of Compressible Turbulent Mixing
Pleasanton, USA
November 1989
Edited by V. Rupert

The second order theory is appropriate only for very limited purposes

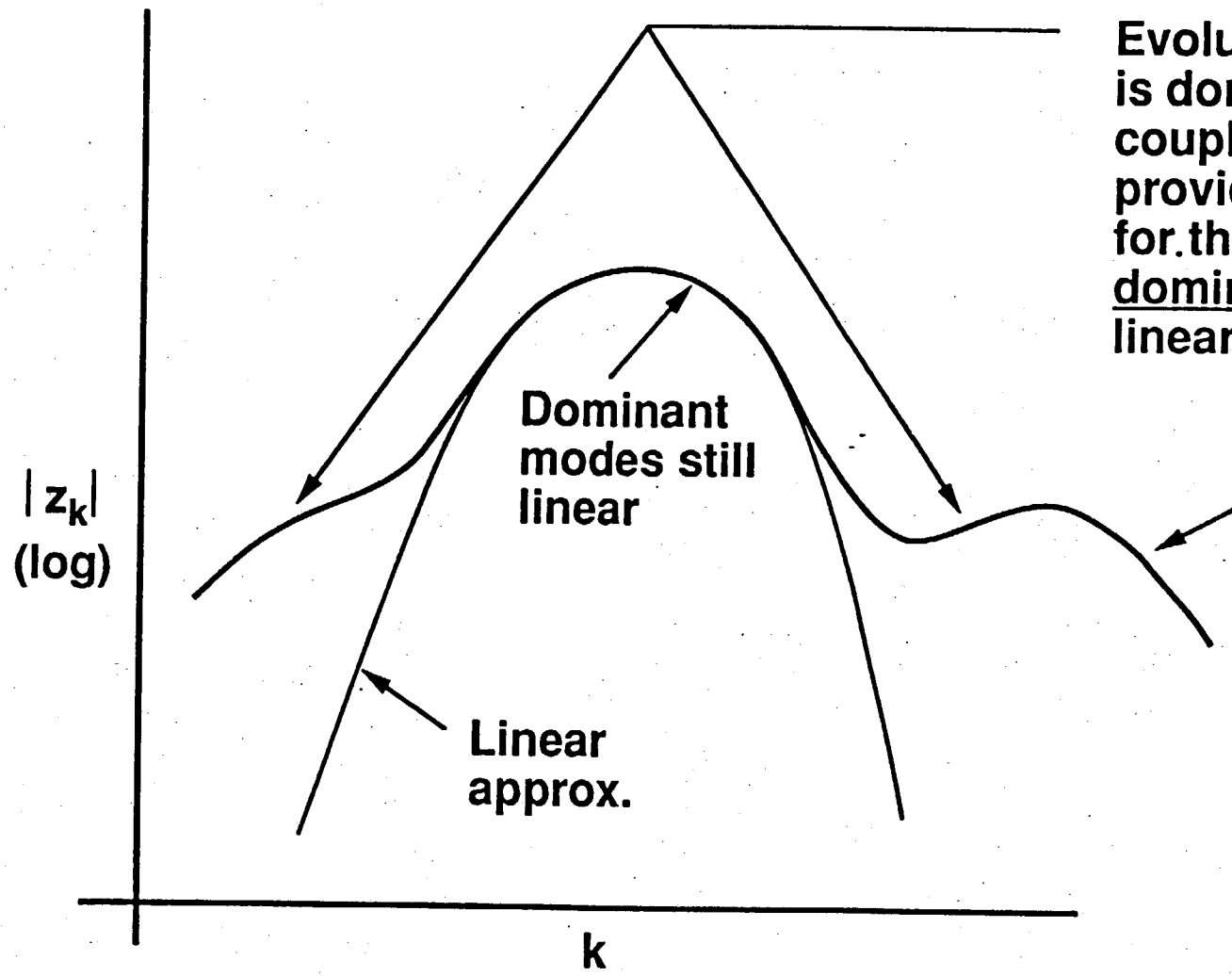

Evolution of some modes is dominated by mode coupling. Our theory provides reliable estimate for these modes iff dominant modes are still linear

The physical process is the same as single mode spike/bubble formation

For single modes, second harmonic represents spike/bubble formation:

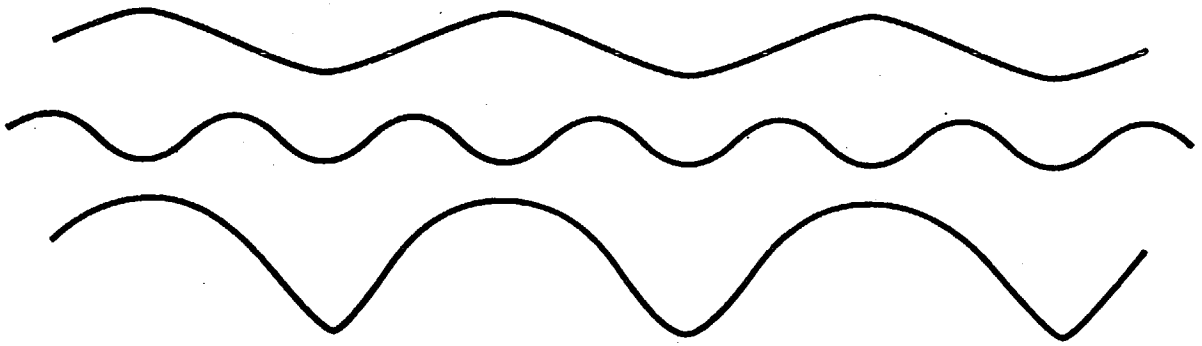

Sine wave

+ 2nd harmonic

= Spikes/bubbles

Multiple modes have same phenomenon <u>locally:</u>

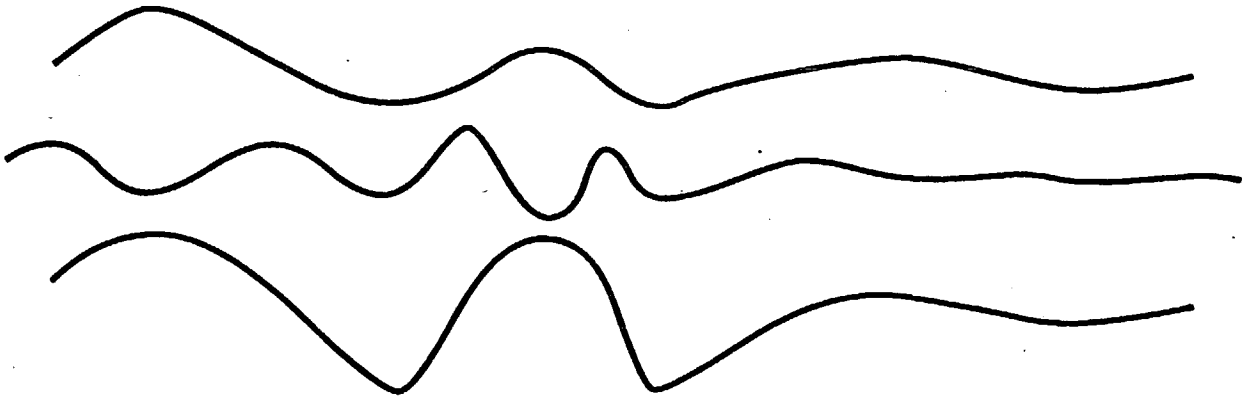

Linear sum of lots of modes

+ harmonics as appropriate

= Local Spikes/bubbles

XDIV-2-U-5/89-SH-D14

Mode coupling theory agrees very well with LASNEX simulations by Mikaelian

"Incompressible" fluid, ρ_H/ρ_L = 10/1 at g=100 μm/ns^2

2D: all modes parallel.

Initial amplitude 10^{-9} cm in modes 2,3,4,5,6,7,8 $\times$ $k_o = 2\pi/(100\mu m)$, cosine modes with phases +,-,+,-, ...

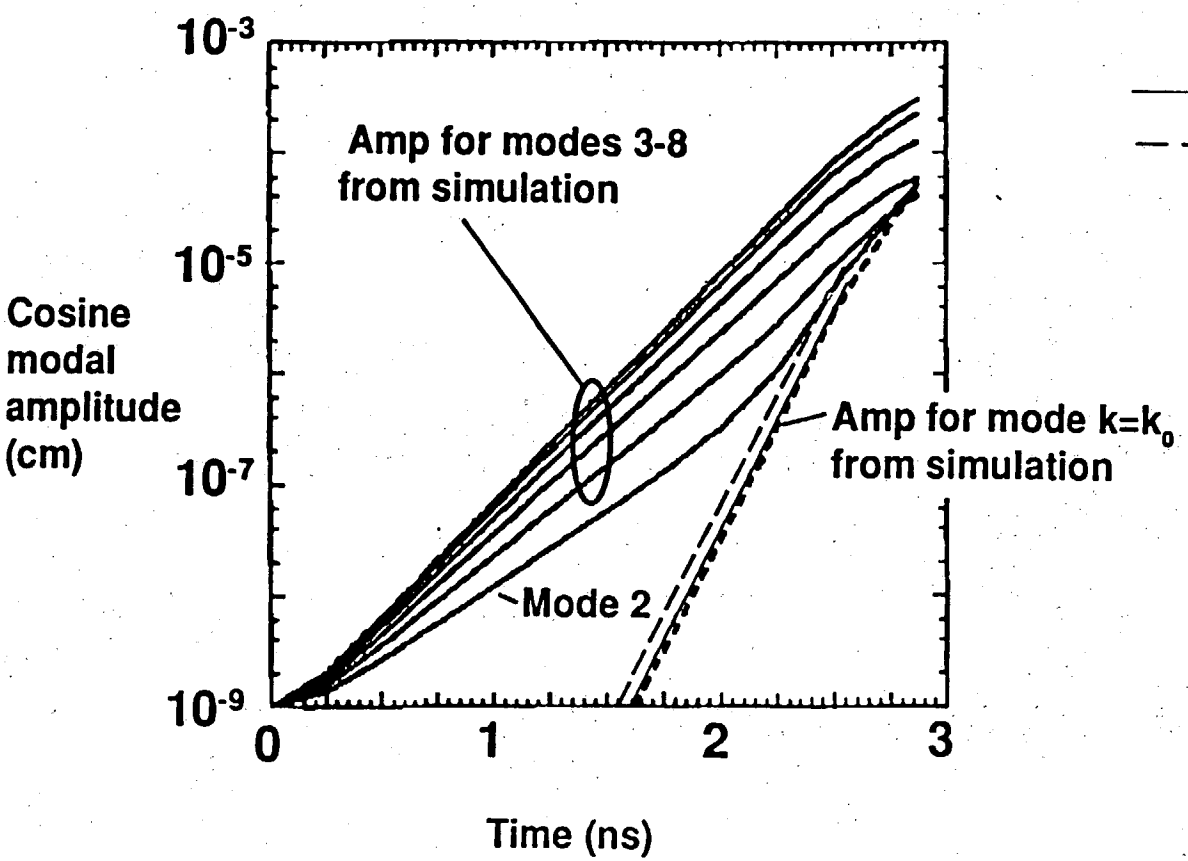

Agreement equally good with calculation where $k=k_o$ had initial amp 10^{-9} cm, and another with initial phases ++...+ (sign change in that case for $k=k_o$!)

XDIV-12-U-5/89-SH-D15

Proceedings of the 2nd International Workshop on the Physics of Compressible Turbulent Mixing

Theory can also be applied to continuous spectra of modes

- Have to specify phase. These results assume random phase. Parameters appropriate for Read and Youngs' experiment, including surface tension. Initial amp thermal excitations. Three times shown: 32, 36, 40 ms. Mode coupling theory invalid at $t \geq 40$ ms.

Note that initial amp has become irrelevant for both long and short λ. Nonlinear effects dominate.

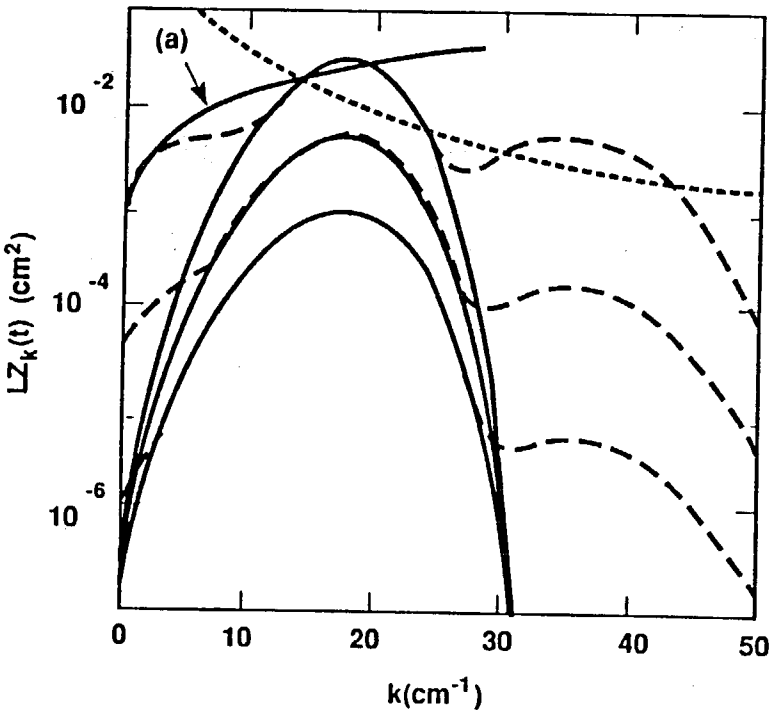

Linear theory

With mode coupling

$4/k^2$ (see below*)

(a) Simple hand formula to estimate coupling to long wavelengths, given linear theory

Have similar-looking results for a wide variety of circumstances

*When LZ_k gets to ~$4/k^2$, rms ~ typical λ and system is in nonlinear regime.

Mode coupling theory shows harmonic generation to long and short λ, as does 3D multimode simulation by Dahlburg and Gardner

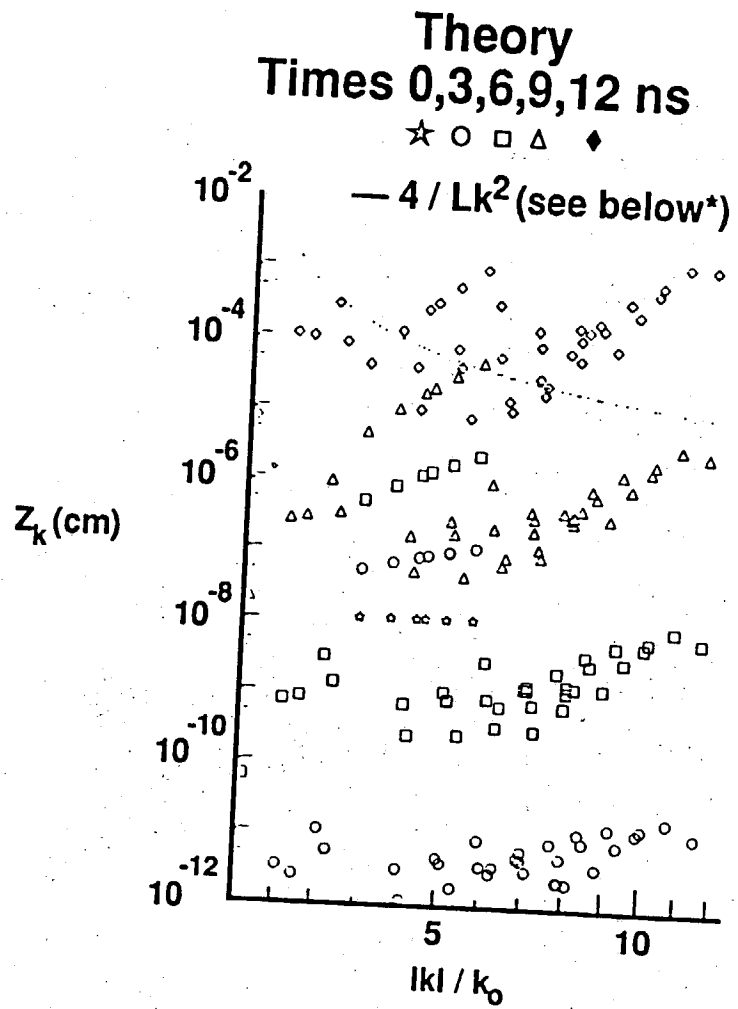

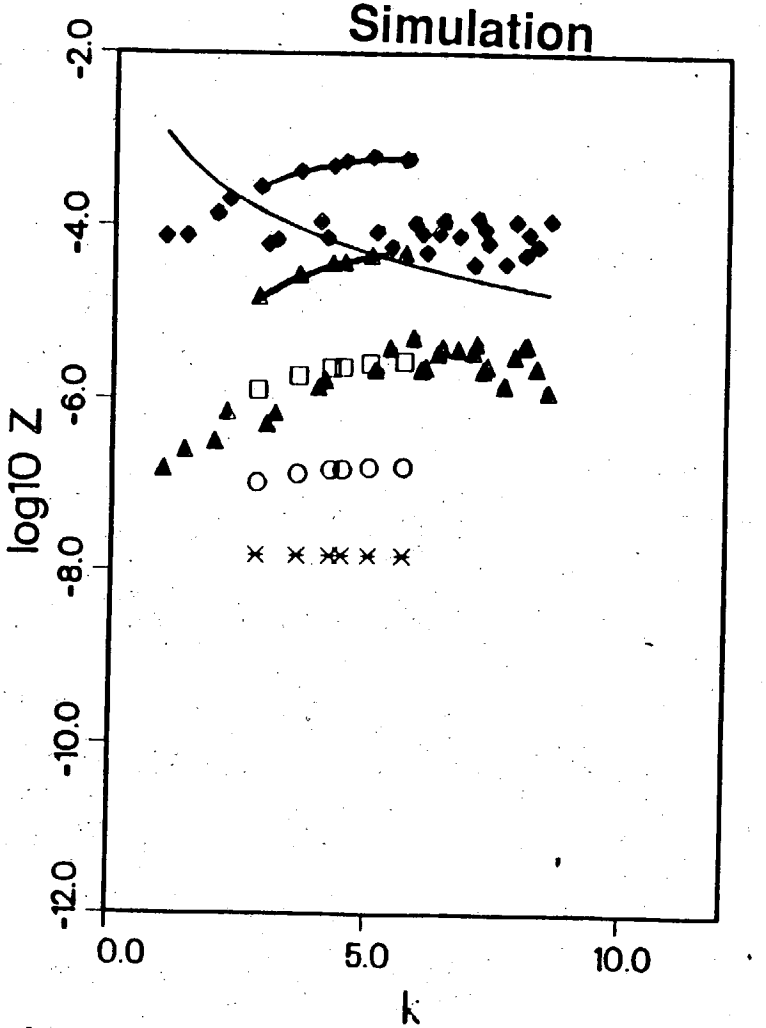

*$4/Lk^2$ is onset of nonlinear saturation assumed in our predictive mix model

We can also compare to Dahlburg and Gardner's 3D multimode simulation

They ran a spectrum of 18 modes. Growth on an ablating interface — peak linear growth (per Takabe and Morse) at $k = 40\ k_o$; $k = 6\ k_o$ has γ reduced by ablation by about 20% ($k_o = 2\pi/120\ \mu m$)

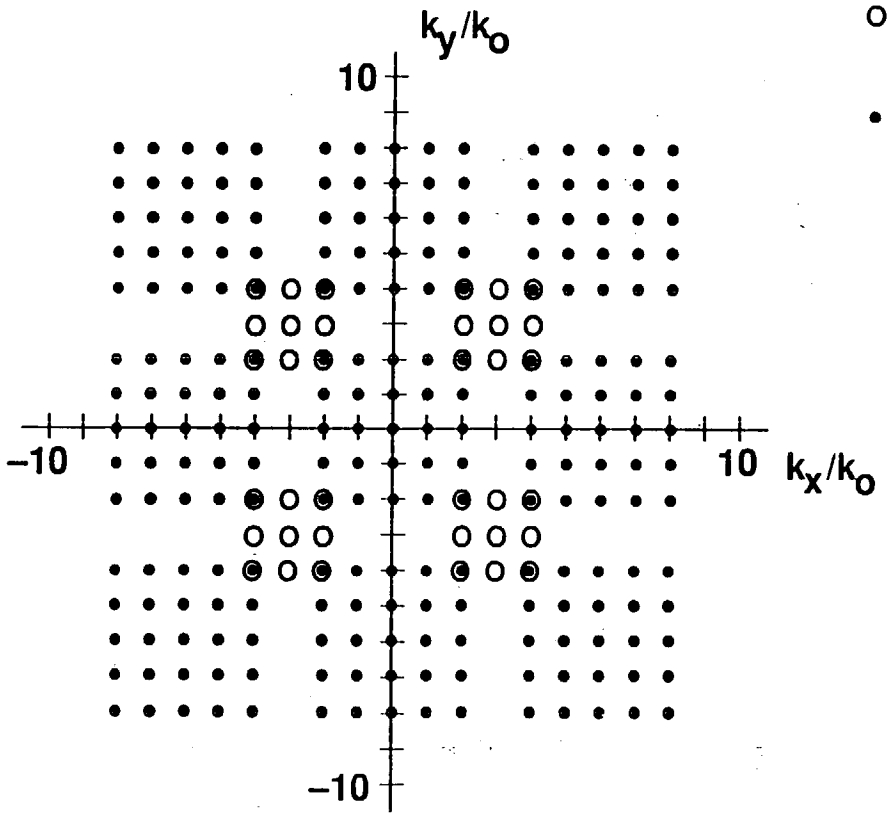

o = modes initially nonzero

• = modes driven by second order coupling

XDIV-13-U-5/89-SH-D16

Conclusion: Second order mode coupling has proven valuable in several ways

- Corroborates numerical simulations, both 2D and 3D
- Corroborates onset of saturation at ~$1/Lk^2$, as assumed in our (hopefully) predictive mix model. May depend on phase correlations; mode coupling theory can help us find out.
- Explicitly shows when and how long wavelength modes are generated from short wavelength nonlinearities
  - Will help us understand when models neglecting this physics are inappropriate
  - We hope to incorporate this understanding into better predictive models

Pleasanton, USA
Edited by V. Rupert
November 1989

CHELYABINSK STATE UNIVERSITY

THE HETEROGENEOUS kε MODEL OF GRAVITATIONAL MIXING

A.V. POLYONOV

The Heterogeneous kε Model of Gravitational Mixing

A.V. POLYONOV

Chelyabinsk State University

ABSTRACT

It has been obtained the equations for semiemperical turbulent kε - model considering the mix heterogeneity. The equations contain the true thermodynamic parameters of each mix component. The members including ∇p have been added to the diffusion flow and to the generation member of the k - equation. The form of the ε - equation provides the opportunity of the consideration of a scale grinding and allows to avoid the unlimited scale lenth growth in the bounded system.

INTRODUCTION

The effects connected with the mixture component compressibility, are displayed in the gravitational mixing process under one of the following conditions: the presence of substantial pressure gradient in the mixing zone, the change of pressure as time proceed the components dencity change due to heatexchange.

The known semiempirical models - Belyenkii - Fradkin model [1], its modified version [2], and more complex model described in paper [3] - consider some effects, connected with compressibility, but this consideration is far from complete. The models consider the mixture as a homogeneous one, while direct numerical simulation [4], [5] and experiments indicate the heterogeneous character of mixing; that is the mixture consists of separate parts and pieces, which display individual thermodynamic parameters of each component.

The distinction of individual dencities determines the difference of the buoyancy of the each component. This difference at a standart situation, when ∇p and $\nabla \rho$ have different signs, furthers the turbulent diffusion and, when ∇p and $\nabla \rho$ have the same marks, it causes the separation.

The difference of individual component densities varies as a result of a heatexchange between the components, as well as of

various compressibility at changeable pressure, and this changes the difference of the buoyancy and in this way influences on the intensity of the mixing development.

The proposed suggestions to consider turbulent mixing in a heterogeneous model-work [4], for example, assume using of different laminar velocities for each component; these velocities are determined by the pulse transfer equation and include the interaction force between components. However, defining this force for turbulent motion causes sufficient difficulties. The second principal shortcoming, such an approach suffers from, is caused by disregarding the turbulent generation on account of the convective instability.

The present paper displays the model, describing the iterpenetration at turbulent diffusion approaching. The consideration of the effects, mentioned above, is supposed to be conducted by adding the item which is proportional to the difference of pushing-out forces to a diffusion mass flow.

The equations of the model in point such as the equations for determining individual thermodynamic characteristics describing the turbulent diffusion of internal energy for each mixture component, with considering heatexchange,and the equation for the turbulent pulsation energy, are derived by averaging the corresponding hydrodynamic transfer equations, with considering heterogeneity, while presenting a number of correlations in a gradient form. An additional term in the

diffusion flow leads to appearing an item in the generation member of the pulsation energy equation; this item is proportional to the difference in true component densities and it contains an empirical constant β.

One-dimentional case is treated all averaged characteristics of motion to depend only on one coordinate in the direction, in which the average velocity component is not a zero one. In the purpose of greater evidences and simplicity the consideration is conducted for two-component system.

I. MASS AND PULSE TRANSFER EQUATIONS

We shall proceed from the equation of multicomponent medium motion. The composition of each component is characterized by two its parameters - true density $\overset{\circ}{\rho}_i$ and temperature T_i - by which it is possible to calculate the rest component thermodynamic characteristics, such as a pressure $p\,(\overset{\circ}{\rho}_i, T_i)$, which we assume the same for all components and an enternal energy $E_i(\overset{\circ}{\rho}_i, T_i)$. Partial component densities are connected with the true component density and averaged one by the following relation:

$$\rho_i = \alpha_i \overset{\circ}{\rho}_i = c_{i_0} \rho,$$

where α_i - volume concentration,

c_{i_0} - mass concentration.

By averaging we determine c_i and $\overset{\circ}{\rho}_i$ by means of the following equalities:

(1-1) $$\overline{\alpha}_i \overset{\circ}{\rho}_i = \overline{\alpha_i \rho_{i_0}}; \quad c_i \overline{\rho}_i = \overline{c_{i_0} \rho_i}$$

The continuity equation for each component in the treated one-dimentional case has the form [6]:

(1-2) $$\frac{\partial \rho_i}{\partial t} + \frac{\partial \rho_i u_i^{\alpha}}{\partial x_{\alpha}} = 0$$

Averaging the equation (1-2) and introducing, similiar to [7], "flow" velocity v_i, which has only one component in our case,

(1-3) $$v_i = \frac{\rho_i u_i}{\bar{\rho}_i} = \bar{u}_i + \frac{\rho_i' u_i'}{\bar{\rho}} .$$

we obtain:

(1-4) $$\frac{\partial \bar{\rho}_i}{\partial t} + \frac{\partial \bar{\rho}_i v_i}{\partial x} = 0 .$$

Summing the equations (1-4) over all the components we obtain:

(1-5) $$\frac{\partial \bar{\rho}}{\partial t} + \frac{\partial \bar{\rho} v}{\partial x} = 0 .$$

where

(1-6) $$\bar{\rho} = \sum_i \bar{\rho}_i$$

(1-7) $$v = \frac{1}{\bar{\rho}} \sum \bar{\rho}_i v_i = \frac{\sum \overline{\rho_i' u_i'}}{\bar{\rho}} .$$

By using (1-5) the equation (1-2) can be written in the following form:

(1-8) $$\frac{d\bar{\rho}_i}{dt} + \frac{\partial}{\partial x}\bar{\rho}_i (v_i - v) + \bar{\rho}_i \frac{\partial v}{\partial x} = 0$$

$$\frac{d}{dt} = \frac{\partial}{\partial t} + v \frac{\partial}{\partial x} .$$

Denoting the mass turbulent flow of the "i"th-component by I_i:

(1-9) $$I_i = \bar{\rho} (v_i - v) ,$$

rewrite (1-8) in the form:

(1-10) $$\frac{d\bar{\rho}_i}{dt} + \frac{\partial I_i}{\partial x} + \bar{\rho}_i \frac{\partial v}{\partial x} = 0 .$$

By using (1-5) we obtain from (1-10):

(1-11) $$\bar{\rho} \frac{dc_i}{dt} + \frac{\partial I_i}{\partial x} = 0 .$$

We write the flow in accordance with [8] in the form:

$$I = -L\left[\left(\frac{1}{\beta_1} - \frac{1}{\beta_2}\right)\nabla p + \frac{\rho D}{L}\nabla c\right] = \rho D\left[\frac{L}{\rho D}\left(\frac{1}{\beta_1} - \frac{1}{\beta_2}\right)\nabla p - \nabla c\right] .$$

Here $\frac{1}{\beta_1}$, $\frac{1}{\beta_2}$ are specific volumes of mixture components (we assume $\beta_1 > \beta_2$).

L - kinetic coefficient,

ρ - mixture dencity,

p - pressure,

c - first gas concentration.

The coefficient at ∇p - P = $\frac{L(\frac{1}{\beta_2} - \frac{1}{\beta_1})}{\rho D}$, for ideal gases is equal to:

$$P = \left[\frac{1}{\beta_2} - \frac{1}{\beta_1}\right] \frac{c_1 c_2 M_1 M_2 (\frac{c_1}{M_1} + \frac{c_2}{M_2})}{R\,T} ,$$

where c_1 , c_2 - mass gas concentrations,

M_1 , M_2 -molecular weights.

The thermal energy of one-gramm mixture is equal to $R \cdot T \cdot (\frac{c_1}{M_1} + \frac{c_2}{M_2})$. It must be replace by turbulent motion energy "k" and it is necassary to introduce the true density ratio instead of the molecular weight ratio using the relation $\frac{M_1}{M_2} = \frac{\rho_1}{\rho_2}$. Then we obtain for the coefficient P :

$$P = \frac{\beta_1 - \beta_2}{\bar{\rho}^2} \cdot \frac{c(1-c)}{k}$$

and the expression for the flow can be written in the following form:

(1-12) $$I = \bar{\rho} D \left[\beta \frac{\rho_1^0 - \rho_2^0}{\bar{\rho}^2} \cdot \frac{c(1-c)}{k} \nabla \bar{p} - \nabla c\right] ,$$

where β -the empirical coefficient.

The member, which comprises $\nabla \bar{p}$, depends on the mixture heterogeneity ; while aligning heterogeneities by heat conduction, for example, the effect of this member is decreased and its contribution vanishes at $\beta_1 = \beta_2$.

The turbulent diffusion coefficient, entering the expression (1-12), is defined by the standard way, by applying the energy of turbulent pulsations "k" and their scale "l_T": $D \approx l_T \cdot k$. In the standard situations at the gravitational instability the signs of $\nabla\bar{p}$ and ∇c are different, the two members act in the same direction and it is impossible to discriminate their contributions (we remind you, that "c" is the concentration of the heavy component and $\rho_1 > \rho_2$). It would be possible to hope for determing the value of coefficient β by experiments, which realize the separation in the mixture by changing the acceleration sign. However, as it is obvious from the computations, the turbulent scale is strongly ground while changing the acceleration sign, and, in fact, the separation is absent.

Therefore, in the propose of calibration, it is necessary to look for the such situation which realizes the same signs for $\nabla\bar{p}$ and $\nabla\bar{\rho}$ without displaying nonautomodel effects. These conditions are satisfied by the experiment, which realizes the separation while the gravity immersing a heavy layer of limited thickness into a light fluid.

Such experiment has not been perfomed yet, horwever, the estimate were obtained as result of two-dementional computation, which realized the direct simulation of the gravitational mixing. The computation was conducted by the programm complex "MECH" [11], which realized the irregular Euler differential

solution of unsteady two-dimentional gasodynamic flows for multicomponent media with complex geometries and large contact boundary deformations. This method is a modification of the method of particles in a cell, which was proposed in [9] and developed in [10]. Particles are used in this method only in the vicinity of contact boundaries. By means of these particles there are computed flows only from cells, contaning different substances, or from the cell with a substance into the cell with another substance. In the rest cases for determining the flows of pulse, mass and energy the approximation of the continuity equation as well as the pulse and energy transfer equations (continuous flows) are used. Some applications of this method for investigating the gravitational instability, collision process, etc. are described in [11], [5].

It was computed the development of turbulence, arising as a result of random initial perturbations on the unsteady boundary, separating the light and heavy layers. The heavy layer has a limited thickness.

In the process of turbulence development, when it goes out on the upper boundary, an area arises in a part of turbulent zone, where the signs of $\nabla\bar{p}$ and $\nabla\bar{\rho}$ are the same, and the separation takes place. The estimated value of the discussed additional term was obtained under the following suggestion: the separation is not progressing at any moment, that is, the turbulent flow in the zone, where the signs of ∇p and $\nabla\rho$

coincide, is a zero one. Then

$$\beta(n-1)\left[\frac{c}{n}+1-c\right]\frac{c(1-c)}{k}\cdot g \simeq \nabla c ,$$

where $n=\frac{\beta_1}{\beta_2}$. The value of β was found to be $\beta=0.2\div0.3$. At this value of β in the usual mixing zone, where the signs of $\nabla\bar{p}$ and $\nabla\bar{\rho}$ are different the additional term is comparable with the traditional one, though it is less by a factor of 1.5÷2.

We consider the pulse transfer without dividing the mixture into components. We average the Navier-Stokes equation

$$\frac{\partial \rho u_\alpha}{\partial t}+\frac{\partial \rho u_\alpha u_\beta}{\partial x_\beta}=-\frac{\partial p}{\partial x_\alpha}+\frac{\partial \sigma'_{\alpha\beta}}{\partial x_\beta} .$$

Hereby we pass on to the "flow" velocities $v_\alpha=\frac{\overline{\rho u'_\alpha}}{\rho}$ and neglect by the third correlation and the products of the second ones, as well as the viscosity influence on the averaged flow. In the treated one-dimentional case we obtain:

$$\text{(1-13)} \qquad \frac{\partial \bar{\rho} v}{\partial t}+\frac{\partial \bar{\rho} v^2}{\partial x}+\frac{\partial \bar{p}}{\partial x}=-\frac{\partial \overline{\rho u'^2_x}}{\partial x} ,$$

and introducing the kinetic energy of turbulent pulsations "k"-

$$\text{(1-14)} \qquad \bar{\rho} k=\frac{1}{2}\overline{\rho(u'^2_x+u'^2_y+u'^2_z)}=\frac{2+\chi}{2\chi}\overline{\rho u'^2_x} ,$$

where χ - parameter, which characterizes asymmetry

$$\text{(1-15)} \qquad \chi=\frac{\overline{\rho u'^2_x}}{\overline{\rho u'^2_y}} ,$$

we obtain instead of (1-13):

$$\text{(1-16)} \qquad \frac{\partial \bar{\rho} v}{\partial t}+\frac{\partial \bar{\rho} v^2}{\partial x}+\frac{\partial \bar{p}}{\partial x}=-\frac{2\chi}{2+\chi}\cdot\frac{\partial(\bar{\rho} k)}{\partial x} .$$

Thus, four equations for a two-component mixure - two equations for the pulse transfer and two continuity equations -

are substituted by the following equations:

-the equation (1-16) for the pulse transfer of the averaged motion,

-the continuity equation (1-5) for the averaged motion,

-the equations (1-12) and (1-11) describing the component interpenetration.

The equation (1-12), with considering (1-9), (1-7), defines the velocity difference v_1-v_2:

$$(1\text{-}17) \qquad v_1-v_2=\frac{I}{\bar{\rho}c(1-c)} = \beta D\frac{\overset{\circ}{\rho}_1-\overset{\circ}{\rho}_2}{\bar{p}^2 k}\cdot\nabla\bar{p} - \frac{D\nabla c}{c(1-c)} .$$

II. EQUATIONS FOR INTERNAL ENERGIES TRANSFER

The equation, defining the internal energy change of i-th-mixture component, related to the mass unit, with respect to time, is the following:

$$\frac{d_i E_i}{dt} = T_i \frac{d_i S_i}{dt} + \frac{p}{\rho_{i0}^2} \cdot \frac{d_i \rho_{i0}}{dt} .$$

where $\frac{d_i}{dt} = \frac{\partial}{\partial t} + u_i \frac{\partial}{\partial x}$ .We consider that the heat generation is composed of the set energy generation and the thermal flow, that is $\rho_{i0} T_i \frac{d_i S_i}{dt} = \mathrm{div}\xi\nabla T + \rho_{i0} \dot{\varepsilon}_{i0}$,where $\dot{\varepsilon}_{i0}$ is the set intensity of energy generation on the mass unity of i-th-component. We introduce the volume concentration $\alpha_i = \frac{\rho_i}{\rho_{i0}}$ and use the continuity equation (1-2). We obtain:

$$(2\text{-}1) \quad \rho_i \frac{d_i E_i}{dt} = \alpha_i \mathrm{div}\xi\nabla T + \rho_i \dot{\varepsilon}_{i0} - p\left[\frac{\partial \alpha_i}{\partial t} + \nabla(\alpha_i u_i)\right] .$$

By using the continuity equation (1-2) we write $\rho_i \frac{d_i E_i}{dt}$ in the form:

$$\rho_i \frac{d_i E_i}{dt} = \rho_i \frac{\partial E_i}{\partial t} + \rho_i u_i \frac{\partial E_i}{\partial x} = \frac{\partial \rho_i E_i}{\partial t} + \frac{\partial \rho_i u_i E_i}{\partial x} .$$

Averaging the equation (2-1), defining $\bar{\rho}_i \epsilon_i = \overline{\rho_i E_i}$, ignoring the third correlations and the product of the second correlations and using (1-9) we obtain:

$$(2\text{-}2) \quad \frac{\partial \bar{\rho}\epsilon_i}{\partial t} + \frac{\partial}{\partial x}\left[I_i \epsilon_i + \bar{\rho}\epsilon_i v_i + \overline{\rho' u' E_i'}\right] = \overline{\alpha_i \mathrm{div}\xi\nabla T} + \bar{\rho}\dot{\varepsilon}_{i0} - p\left[\frac{\partial \alpha_i}{\partial t} + \nabla(\alpha_i u_i)\right] .$$

The pressure pulsations are of the same order as the energy pulsations, which we ignore in the internal energy balance.

The member, comrpising the velocity pulsations, can be

presented in a gradient form using Prandtl's approach. By analogy with [7] we suppose, that the scalar characteristic transfer of the system is realized by jets, having the pulsation velocity "u'" in the direction of OX axis, passing through the way "l'" in that direction and then losing the pulsation velocity. Only those jets will reach the level "x", which arise at the level "x-l'", and they give rise to the pulsation of the transfer value θ, which is equal to

$$(2\text{-}3)\quad \theta'=\bar{\theta}(x-l')-\bar{\theta}(x)+\frac{\partial\theta}{\partial S}\Big|_p\delta S+\frac{\partial\theta}{\partial p}\Big|_S\delta p=-\frac{\partial\bar{\theta}}{\partial x}l'+\frac{\partial\theta}{\partial S}\Big|_p\delta S+\frac{\partial\theta}{\partial p}\Big|_S\delta p\ ,$$

where δS and δp represent the jets thermodynamic characteristic changing in the case of transfer to the level "x" from the level "x-l'". We consider, that $\delta p=l'\nabla\bar{p}$, $\delta S=0$ (It is possible to take account of heat conductivity while transfering in manner used Nikiforov in paper [3]). Then the correlation $\overline{u'\theta'}$ will be equal to:

$$(2\text{-}4)\quad \overline{u_x'\theta'}=-\overline{u_x'l'}\cdot\frac{\partial\bar{\theta}}{\partial x}+\overline{u_x'l'}\cdot\frac{\partial\theta}{\partial p}\Big|_S\nabla p=-D\left[\frac{\partial\bar{\theta}}{\partial x}-\frac{\partial\theta}{\partial p}\Big|_S\nabla\bar{p}\right]\ ,$$

where

$$(2\text{-}5)\quad D=\overline{u_x'l'}=l_T\cdot(2k^{\frac{1}{2}})\ ;\ l_T\sim\left[\frac{\chi}{2+\chi}\right]^{\frac{1}{2}}\ .$$

Here χ is the parameter, characterizing the simmetry, it is defined by the equality (1-16), and l_T is the characteristic scale of the turbulent motion, the determination of which is produced by one of the accepted semiempirical ways, for example, in the program "TURINB" [2] it is considered to be proportional

to the mixing zone width. It is assumed in this paper to find the scale value from the equation defining the intensity of the turbulent energy dissipation $\mathcal{E}_t$ which is suggested to be connected with scale by Kolmogorov's automodelic relation: $\mathcal{E}_t=\frac{k^{3/2}}{l_T}$. In our considering there are two diffusion coefficients: $D_1=\overline{u'_1 l'_1}$ and $D_2=\overline{u'_2 l'_2}$, which we assume to be the same and equal to the common diffusion coefficient, defined by the average energy of the pulsation motion for mixture and the characteristic pulsation scale (l_T).

Thus, we write $\overline{u'_i E'_i}$, using (2-4)

$$\overline{u'_i E'_i}=-D\left(\nabla\varepsilon_i-\frac{\partial\varepsilon_i}{\partial p}\Big|_S\nabla\bar{p}\right) . \tag{2-6}$$

The member, taking into account the heat conduction can be written as the sum of two members corresponding to the transfer along the axis OX, which coincide with the averaged motion direction, and to the transfer in the perpendicular direction.

We assume $\frac{\partial\bar{T}}{\partial y}\propto\frac{\bar{T}_2-\bar{T}_1}{a}$, where $\bar{T}_1$, $\bar{T}_2$ are the component temperatures, "a" is a transversal scale of heterogeneities - $a\cong a_1+a_2$, where a_1, a_2 are the transversal scales of heterogeneous generations. Then

$$\alpha_1\frac{\partial}{\partial y}\xi\frac{\partial\bar{T}}{\partial y}\cong\frac{\alpha_1\bar{\xi}}{a_1}\frac{\bar{T}_2-\bar{T}_1}{a}\cong\frac{\bar{\xi}}{a^2}(\bar{T}_2-\bar{T}_1)=\lambda\frac{\bar{\xi}}{l_T^2}(\bar{T}_2-\bar{T}_1) ,$$

and the considered member is written in the form:

$$\alpha_1\operatorname{div}\xi\nabla T\cong\alpha_1\frac{\partial}{\partial x}\bar{\xi}_1\frac{\partial T_1}{\partial x}+\lambda\frac{\bar{\xi}}{l_T^2}\cdot(\bar{T}_2-\bar{T}_1) . \tag{2-7}$$

where λ is the constant, which requires the selection while solving model poblems, $\bar{\xi}_i$, $\bar{\xi}$ are the first component heat conductivity coefficient, and average one for the mixture.

Let us consider the correlation $\overline{\alpha_i u_i}$,which enter (2-2). In accordance with (1-3) and with the determination of $\overset{\circ}{\rho}_i$ while ignoring the third correlations and the product of the second correlations we have:

$$\bar{\rho}_i v_i = \overline{\rho_i u_i} = \overline{\overset{\circ}{\rho}_{i\circ} \alpha_i u_i} \cong \overset{\circ}{\rho}_i \overline{\alpha_i u_i} + \bar{\alpha}_i \overline{\overset{\circ}{\rho}_{i\circ} u_i'}$$

The correlation of $\overline{\overset{\circ}{\rho}_{i\circ} u_i'}$ is presented in the gradient form:

$$\overline{\overset{\circ}{\rho}_{i\circ} u_i'} = -D\left(\nabla\rho - \frac{\partial \overset{\circ}{\rho}_i}{\partial p}\Big|_S \nabla\bar{p}\right)$$

Expressing the velocity v_i by the flow I_i in accordance to (1-9):

$$v_i = \frac{I_i}{\bar{\rho}_i} + v \ ,$$

we find:

$$\overline{\alpha_i u_i} = \bar{\alpha}_i \frac{I_i}{\bar{\rho}_i} + \bar{\alpha}_i v + \frac{D\bar{\alpha}_i}{\overset{\circ}{\rho}_i}\left(\nabla \overset{\circ}{\rho}_i - \frac{\partial \overset{\circ}{\rho}_i}{\partial p}\Big|_S \nabla\bar{p}\right) .$$

Subtituting (2-6), (2-7), (2-8) into (2-2) we find the transfer equations for the component internal energy:

$$\frac{\partial \bar{\alpha}_1 \overset{\circ}{\rho}_1 \epsilon_1}{\partial t} + \frac{\partial}{\partial x}\left[I\epsilon_1 + \bar{\alpha}_1 \overset{\circ}{\rho}_1 \epsilon_1 v - \bar{\alpha}_1 \overset{\circ}{\rho}_1 D\left(\nabla\epsilon_1 - \frac{\partial \epsilon_1}{\partial p}\Big|_S \nabla\bar{p}\right)\right] = \bar{\alpha}_1 \frac{\partial}{\partial x}\bar{\xi}_1 \frac{\partial \bar{T}_1}{\partial x} +$$

$$+ \lambda \frac{\bar{\xi}}{l_r}_2 (\bar{T}_2 - \bar{T}_1) + \bar{q}\overset{\circ}{\rho}_1 \dot{\epsilon}_{1\circ} - \bar{p}\left[\frac{\partial \bar{\alpha}_1}{\partial t} + \frac{\partial}{\partial x}\left[\bar{\alpha}_1 v + \frac{I}{\bar{\rho}_1} + \frac{D\bar{\alpha}_1}{\bar{\rho}_1}\left(\nabla \overset{\circ}{\rho}_1 - \frac{\partial \overset{\circ}{\rho}_1}{\partial p}\Big|_S \nabla\bar{p}\right)\right]\right] ;$$

(2-9)

$$\frac{\partial \bar{\alpha}_2 \overset{\circ}{\rho}_2 \epsilon_2}{\partial t} + \frac{\partial}{\partial x}\left[-I\epsilon_2 + \bar{\alpha}_2 \overset{\circ}{\rho}_2 \epsilon_2 v - \bar{\alpha}_2 \overset{\circ}{\rho}_2 D\left(\nabla\epsilon_2 - \frac{\partial \epsilon_2}{\partial p}\Big|_S \nabla\bar{p}\right)\right] = \bar{\alpha}_2 \frac{\partial}{\partial x}\bar{\xi}_2 \frac{\partial \bar{T}_2}{\partial x} -$$

$$- \lambda \frac{\bar{\xi}}{l_r}_2 (\bar{T}_2 - \bar{T}_1) + \bar{\alpha}_2 \overset{\circ}{\rho}_2 \dot{\epsilon}_{2\circ} - \bar{p}\left[\frac{\partial \bar{\alpha}_2}{\partial t} + \frac{\partial}{\partial x}\left[\bar{\alpha}_2 v - \frac{I}{\bar{\rho}_2} + \frac{D\bar{\alpha}_2}{\rho_2}\left(\nabla \overset{\circ}{\rho}_2 - \frac{\partial \overset{\circ}{\rho}_2}{\partial p}\Big|_S \nabla\bar{p}\right)\right]\right] :$$

where I is determined by the expression (1-12).

Assuming $\bar{T}_1=\bar{T}_2$, summing up equations (2-9), determining the internal energy, related to the mass unit of the mixture $\epsilon=c\epsilon_1+(1-c)\epsilon_2$, and assuming (1-12) with $\overset{\circ}{\rho}_1=\overset{\circ}{\rho}_2$ we obtain the energy transfer equation with suppositions accepted in TURINB:

$$\frac{\partial\bar{\rho}\epsilon}{\partial t}+\frac{\partial}{\partial x}\left[\bar{\rho}\epsilon v-\bar{\rho}D\left(\nabla\epsilon-\frac{\partial\epsilon}{\partial p}\Big|_S\nabla\bar{p}\right)\right]= \tag{2-10}$$

$$=\frac{\partial}{\partial x}\lambda\frac{\partial\bar{T}}{\partial x}+\bar{\rho}\dot{\epsilon}_o-\bar{p}\nabla v-\bar{p}\frac{\partial}{\partial x}\left[\frac{D}{\bar{\rho}}\left(\nabla\bar{\rho}-\frac{\partial\bar{\rho}}{\partial p}\Big|_S\nabla\bar{p}\right)\right] .$$

This equation is more precise, than the equation, which is accepted in TURINB, because in deriving TURINB's equation [2] there were simplifications on the assumption of a small value of $\nabla p/p$ compared to $\nabla\rho/\rho$ and to $\nabla\epsilon/\epsilon$.Under these assumptions both equations - (2-10) and TURINB's equation - agree.

III. THE EQUATION FOR THE TURBULENT PULSATIONS ENERGY

The equation for the kinetic enery density of turbulent pulsations can be obtained by averaging the pulse transfer equations and the continuity equation,and it has form [7]:

$$\frac{\partial E_T}{\partial t}+\frac{\partial}{\partial x_\alpha}\left[E_T\bar{u}_\alpha+\frac{1}{2}\overline{\rho u_\beta'^2 u_\alpha'}+\overline{p'u_\alpha'}-\overline{u_\beta'\sigma'_{\alpha\beta}}\right]= \tag{3-1}$$

$$=\overline{p'\frac{\partial u_\alpha'}{\partial x_\alpha}}-\bar{\rho}\varepsilon_t-\overline{\rho u_\alpha' u_\beta'}\frac{\partial \bar{u}_\beta}{\partial x_\alpha}+\overline{\rho u_\alpha'}\frac{d\bar{u}_\alpha}{dt} \quad .$$

Here $\frac{d}{dt}=\frac{\partial}{\partial t}+\bar{u}_\beta\frac{\partial}{\partial x_\beta}$:

$$E_T=\frac{1}{2}\overline{\rho u_\alpha'^2} \quad . \tag{3-2}$$

$$\sigma'_{\alpha\beta}=\mu\left(\frac{\partial u_\alpha'}{\partial x_\beta}+\frac{\partial u_\beta'}{\partial x_\alpha}-\frac{2}{3}\frac{\partial u_i'}{\partial x_i}\delta_{\alpha\beta}\right)+\zeta\frac{\partial u_i'}{\partial x_i}\delta_{\alpha\beta} \quad . \tag{3-3}$$

$\mu=\nu\rho$, and ζ -are viscous coefficiens.

$$\bar{\rho}\varepsilon_t=\bar{\sigma}_{\alpha\beta}\frac{\partial \bar{u}_\beta}{\partial x_\alpha} \quad . \tag{3-4}$$

$\bar{\sigma}_{\alpha\beta}$ differ from $\sigma'_{\alpha\beta}$ only by substitution of pulsation values $u'=u-\bar{u}$ by averaged ones.

The turbulent pulsation energy, related to a mass unit, is denoted by "k" and it is defined as follows:

$$k=\frac{\bar{E}}{\bar{\rho}}_T=\frac{\frac{1}{2}\overline{\rho u_\alpha'^2}}{\bar{\rho}} \quad . \tag{3-5}$$

By using (3-5), the continuity equation (1-5) and introducing the "flow" velocity - $v=\bar{u}+\frac{\overline{\rho u'}}{\bar{\rho}}$,we have the following for the treated one-dimensional case from the equation (3-1):

$$\frac{\partial\bar{\rho}k}{\partial t}+\frac{\partial}{\partial x}\left[\bar{\rho}kv-k\overline{\rho u}+\frac{1}{2}\overline{\rho u_\beta^2 u_\alpha}+\overline{p u_\alpha}-\overline{u_\beta \sigma_{\alpha\beta}}\right]=$$

(3-6)

$$=-\overline{\rho u_\alpha}\frac{dv}{dt}-\bar{\rho}\varepsilon-\overline{\rho u_\alpha^2}\frac{\partial v}{\partial x}+\overline{p\frac{\partial u_\alpha}{\partial x_\alpha}} .$$

While obtaining (3-6) we ignored the product of the second correlations as well as the third correlations. Using this approximation for calculating the correlations in the left-hand side of (3-6) $\overline{\rho u}=\overline{\rho u_\alpha}$ and $\overline{\rho u_\beta^2 u_\alpha}$, it is enough to content by Prandtl's presantation to one member:

(3-7) $$\overline{\rho u_\alpha}=-D\frac{\partial\bar{\rho}}{\partial x} \; ; \quad \frac{1}{2}\overline{\rho u_\beta^2 u_\alpha}=-D\frac{\partial\bar{\rho}k}{\partial x} .$$

The two members, going into the equation (3-6) and comprising pressur pulsations, can be combined into one member, which is equal to $u_\alpha\frac{\partial p}{\partial x_\alpha}=u_\alpha\frac{\partial p}{\partial x}+u_\beta\frac{\partial p}{\partial y}+u_\varepsilon\frac{\partial p}{\partial z}$. In this sum the first member characterizes decreasing the turbulent pulsations energy in OX direction because of acting the resistance forces $-\frac{\partial p}{\partial x}$ - on jets, moving with the velocity u' (on the average $\frac{\partial p}{\partial x}>0$ for $u'>0$ and vice versa). The second member and the third one define the pulsation generation in two directions, which are perpendicular to OX as a result of OX-jets slowing down (on the average $\frac{\partial p}{\partial y}>0$ for $u_\gamma<0$ and vice versa). Pulsation energy transforming from one direction to another in the balance equation (3-6) can be disregarded, and reducing the pulsation energy, given by the first member $(\overline{u_\alpha\frac{\partial p}{\partial x}})$, we shall consider as if it was included in the member $\bar{\rho}\varepsilon$. This member is

supposed to be independent of the viscosity in accodance with Kolmogorov's hypothesis and, as usual, we present it in a automodel form:

$$\bar{\rho}\varepsilon_t=\bar{\rho}\,\frac{k^{3/2}}{l_T}. \tag{3-8}$$

The member $\overline{u'_\beta\sigma'_{\alpha\beta}}$, which is equal of the order of the magnitude to the value $\overline{u'_\beta\sigma'_{\alpha\beta}}\sim\nu\rho\overline{u'_\beta\frac{\partial u'_\beta}{\partial x}}\sim\nu\bar{\rho}\frac{\partial k}{\partial x}$ and it is ignored as usual by the comparison with the member, obtained in (3-7) $D\bar{\rho}\frac{\partial k}{\partial x}$, as $D\gg\nu$ for the treated flows.

The member $\overline{\rho u'^2_x\frac{\partial v}{\partial x}}$ is transformed by using expression (1-14), (1-15):

$$\overline{\rho u'^2_x\frac{\partial v}{\partial x}}=\frac{2\chi}{2+\chi}\bar{\rho}k\frac{\partial v}{\partial x}=-\frac{2\chi}{2+\chi}k\frac{d\bar{\rho}}{dt} \tag{3-9}$$

We find the correlation $\overline{\rho u}'$, entering the generation member of the right-hand side of (3-6):

$$\overline{\rho u}'=\overline{\alpha_1\mathring{\rho}_{1o}(u_1-\bar{u})}+\overline{\alpha_2\mathring{\rho}_{2o}(u_2-\bar{u})},$$

where $\bar{u}=\overline{\alpha_1u_1}+\overline{\alpha_2u_2}$.

Using (2-8) and presenting correlations $\overline{\rho_{io}u'_i}$ in a gradient form, we obtain:

$$\overline{\rho u}'=\bar{\alpha}_1\bar{\alpha}_2(\mathring{\rho}_1-\mathring{\rho}_2)(v_1-v_2)-\frac{D\bar{\alpha}_1^2\bar{\rho}}{\bar{\rho}_1}\left(\frac{\partial\bar{\rho}_1}{\partial x}-\frac{\partial\bar{\rho}_1}{\partial p}\Big|_S\nabla\bar{p}\right)-\frac{D\bar{\alpha}_2^2\bar{\rho}}{\bar{\rho}_2}\left(\frac{\partial\bar{\rho}_2}{\partial x}-\frac{\partial\bar{\rho}_2}{\partial p}\Big|_S\nabla\bar{p}\right).$$

Expressing v_1-v_2 through the flow in accordance with (1-17) we find:

$$\overline{\rho u}'=D\beta\frac{c(1-c)}{k}\cdot\frac{(\mathring{\rho}_1-\mathring{\rho}_2)^2}{\bar{\rho}_1\bar{\rho}_2}\nabla\bar{p}-D\left[\nabla\bar{\rho}-\frac{\partial\bar{\rho}}{\partial p}\Big|_S\nabla\bar{p}\right]. \tag{3-10}$$

where the expression (1-12) was used.

Using the received presentations (3-7), (3-8), (3-9) we obtain from (3-6):

$$(3\text{-}11)\quad \overline{\rho}\frac{dk}{dt} - \frac{\partial}{\partial x}\overline{\rho}D\frac{\partial k}{\partial x} + \overline{\rho}\frac{k^{3/2}}{l_r} = \frac{dv}{dt}(-\overline{\rho u}') + \frac{2\chi}{2+\chi}k\frac{d\overline{\rho}}{dt},$$

where $\overline{\rho u}'$ is defined by the expression (3-10). We notice, that for incompressible fluids the relation of two members, consisting the generation member, - an additional one, which comprises $\nabla\overline{p}$, and the traditional one, which is proportional to $\nabla\rho$, - is the same as the relation of the corresponding members consisting the mass turbulent flow. Consequently, the member with $\nabla\overline{p}$ in 3-10 is comparable with the traditional one (consisting 0.5÷0.7 from it) for the previously estimated value of β=0.2÷0.3.

Thus, the true densities difference of the components, constituting the mixture, has a notable influence on the interpenetration velocity (on the mass turbulent flow) as well as on the intensity of turbulence development.

IV. $\mathcal{E}_t$- EQUATION

While obtaining $\mathcal{E}_t$-equation we shall proceed from turbulent motion common featuers according to which changing in time of any scalar value transferd by the flow can be written in following form:

(4-1) $$\frac{d\mathcal{E}}{dt}t = (\text{gener.}) - (\text{dissip.}) + (\text{diff.})$$

The diffusion member form is known:

(4-2) $$(\text{diff.}) = C_{\mathcal{E}_1}\frac{\partial}{\partial x}\bar{\rho}D\frac{\partial \mathcal{E}}{\partial x}t$$

While finding the first two members we assume for $\mathcal{E}_t$ the Kolmogorov's automodel form:

(4-3) $$\mathcal{E}_t = \frac{k^{3/2}}{l_T}$$

Generation and dissipation for k is taken from equation (3-11), thus the problem is reduced to defining generation and dissipation of the scale. The equation for the scale is to be written in the form:

(4-4) $$\frac{dl}{dt}T = C_1 \cdot \Sigma|\overline{\alpha_i u_i'}| - C_2 \cdot k^{1/2} .$$

Here α_i - volume concentration of the i-th component, u_i' - its turbulent velocity, C_1, C_2 - some constants.

Such recording assumes that the scale generation is solely realized due to interpenetration of volumes and that it is proportional to the volume flow. That is we suppose that the scale generation is obviously independent of mass flows ($\overline{\rho u'}$) as

well as of changing the potential energy ($\overline{\rho u}'g$) (it depends on these factors through dependencies of u_i' and k on them).

The form of the second member assumes that the time of the scale dissipation is proportional to the time of characteristic votex revolution.

It is appropriate to remember that the form of $\mathcal{E}_{t-}$-equation adopted in TURINB produces the scale generation by means of two members [12]:

$$\frac{dl_{TURINB}}{dt} = C_1 \cdot \overline{\rho u}' \cdot g \frac{l}{\overline{\rho} k} \tau + C_2 \cdot k^{1/2} .$$

Such form is inconsistent with the physical picture obtained while performing simulationns by code MECH:

1.The form adopted in TURINB supposes explicit dependence of scale generation on acceleration. Results obtained by the code MECH give the the relation $l_\tau = d \cdot L$, where L - zone width and d - constant which do not change when g is vanihing.

2.The form adopted in TURINB excludes grinding the scale and connects its enlarging with k. Results obtained by the code MECH eghibit that grinding of the scale take place while decreasing the interpenetration intensity: the assummption of the connection of the scale generation with turbulent energy is wrong.(The assumption was taken from the work of Launder B.E. et.al., treated in [13].)

The member $\overline{a_i u_i'}$, entering the suggested expression for the scale (4-4) was obtainod above (s.2):

$$(4\text{-}5)\qquad \overline{\alpha_i u_i'} = \bar{\alpha}_i \frac{I_i}{\bar{\rho}_i} + \bar{\alpha}_i v + \frac{D\bar{\alpha}_i}{\mathring{\rho}_i}\cdot\left(\nabla\mathring{\rho}_i - \frac{\partial\mathring{\rho}_i}{\partial p}\Big|_S \nabla\bar{p}\right) .$$

Conidering (4-1).(4-2).(4-3).(4-4). and also proposing $D=l_T\cdot k^{1/2}=c_\mu\frac{k^2}{\varepsilon_t}$ we obtain the ε_t-equation:

$$(4\text{-}6)\quad \bar{\rho}\frac{d\varepsilon_t}{dt}+\left[\frac{3}{2}-C_2\right]\bar{\rho}\frac{\varepsilon_t^2}{k} = \frac{3}{2k}\varepsilon_t\frac{dv}{dt}(-\overline{\rho u}')-c_1\frac{\varepsilon^2}{k^{3/2}}\rho\Sigma|\overline{\alpha_i u_i'}|$$

where $\overline{\alpha_i u_i'}$ is given by the expression (4-5), $\overline{\rho u}'$ - by (3-10). As $c_2>0$ then $c_{6_2}=\frac{3}{2}-c_2<1.5$ while Launder et.al. and following them TURINB take $c_{6_2}=1.92$. The turbulent development computation with $c_{6_2}=1.92$ shows the unlimited scale lenth growth in the bounded system.

The similar approach is also appropriate in the usual homogeneous kε-model, having no true density parameters and volume concentration.Hence the following simplifications are assumed:

1) Each component diffusion caused by its true density gradient is neglected.

2) The member containing Vp is not considered in the diffusion flow.

3)It is assumed true densities relation to be considered in time and spase. Then considering $\bar{\rho}_i=\alpha_i\mathring{\rho}_i=c_i\bar{\rho}$ and $\frac{1}{\bar{\rho}}=\Sigma\frac{c_i}{\mathring{\rho}_i}$ we obtain the expression for the volume concentration, which involves only true densities ratio:

$$\alpha_i = \frac{c_i}{\mathring{\rho}_i\Sigma\frac{c_k}{\mathring{\rho}_k}} .$$

Substituting the expression obtained above into the equation (4-5) and considering $I_i = -\bar{\rho}D\nabla c_i$ and $v = \frac{\overline{\rho u}'}{\bar{\rho}} = -D\frac{\nabla\bar{\rho}}{\bar{\rho}}$ we obtain:

$$|\alpha_i u_i'| = \frac{c_i D}{\rho_i^\circ \sum \frac{c_k}{\rho_k^\circ}} \left| \frac{\nabla c_i}{c_i} + \frac{\nabla\bar{\rho}}{\bar{\rho}} \right| . \tag{4-6}$$

The expression (4-6) can be obtained by using Prandtl's approach:

$$\overline{\alpha_i u_i'} = -D\frac{\partial \alpha_i}{\partial x} ,$$

where $\alpha_i = \frac{\bar{\rho} c_i}{\rho_i^\circ}$. Whence $\nabla\alpha_i = \frac{\alpha_i}{c_i}\nabla c_i + \frac{\alpha_i}{\bar{\rho}}\nabla\bar{\rho}$

Uncompress.:

$$\bar{\rho}\frac{d\varepsilon_t}{dt} + \left[\frac{3}{2} - C_2\right]\bar{\rho}\frac{\varepsilon_t^2}{k} = \frac{3\varepsilon_t}{2k}\frac{dV}{dt}\left(-\overline{\rho u'}\right) - C_\mu \cdot C_1 \rho k^{1/2}\varepsilon \frac{2\nabla\rho}{\rho_1^\circ - \rho_2^\circ}$$

CONCLUSION

1.The following equations, describing the one-dimentional motion of the two-component medium with considering the turbulent mixing, were obtain:

-the equation (3-11), determining the pulsation kinetic energy - "k";

-the equation (4-6), determing the intensity of the turbulent energy dissipation - $\mathcal{E}_t$

-the equation (1-11), determining the component diffusion transfer;

-the continuity equation (1-5);

-the pulse transfer equation (1-16);

-the two internal energy tranfer equations (2-9).

The seven equations define any seven parameters of mixture, for example, $\overset{o}{\rho}_1, \overset{o}{\rho}_2, c, k, v, \bar{p}$.

By means of the set equations of state-

$$\epsilon_1=\epsilon_1(\overset{o}{\rho}_1, \bar{T}_1),\ p_1=p_1(\overset{o}{\rho}_1, \bar{T}_1);$$

$$\epsilon_2=\epsilon_2(\overset{o}{\rho}_2, \bar{T}_2),\ p_2=p_2(\overset{o}{\rho}_2, \bar{T}_2);$$

it is possible to define the rest thermodynamic component parameters - $\bar{T}_1, \bar{T}_2, \epsilon_1, \epsilon_2$.

2.The turbulent flow of mass and the generation member, defining the intensity of increasing the energy of the turbulent motion in the derived equations contain members which are

proportional to the true density difference of the components, which constitute the mixture.

3.The separation, observed in the gravity immersion process of heavy fluid layer into a light fluid in two-dimentional calculation by simulating the turbulence allows to estimate that the mentioned additional members are comparable with the traditional ones. This means that processes changing the true component densities in the mixure have a noticable influence on the interpenetration intensity and on the turbulent energy increasing.

4.The form of $\mathcal{E}_t$-equation provides the opportunity of the consideration of a scale-grinding which is absent in the usual $k\mathcal{E}_t$-code as well it allows to avoid the unlimited scale lenth growth in the bounded systems.

REFERENCES

1.Belenkii S.Z.,Fradkin E.S. The Theory of Turbulent Mixing.Papers of Phys. Ins. of SA USSR, 1965, v.29.

2.Neuvadzaev V.E.,Yakovlev V.G. ASTQ, 1984,2(16),p.17-25.

3.Andronov V.N. et.al. Papers of SA USSR, 1982,v.264,1,p.76-82.

4.D.L.Yongs. Numerical Simulation of Turbulent Mixing by Rayleigh-Taylor Instability.Physica 12D(1984)32-34, North-Holland. Amsierdam.

5.Anuchina N.N.,Ogibina V.N. Phys. Mech. of Non-Gom. Mediums, S.D. of S.A. USSR, Novosibirsk, 1984, p.173-184.

6.Nigmatulin R.I. The Foundation of Heterogeneous Mediums Mechanics. M.,Science,1978.

7.Monin A.S., Yaglom N.I. Statistical Hydromechanics, M.,Science, 1964.

8.S.R. de Groot. Thermodynamics of Irreversable Processes. M. 1956.

9.Harlow F.N. The Numerical Method of Particles in Sells for the Tasks of Hydrodynamics. M. MIR. 1967.

10.Anuchina N.N. Numerical Methods of Mechanics, Novosybirsk, v.1, 4, 1970.

11.Anuchina N.N., Gadgieva V.V., Elsukov V.P., et. al. I.S.M. of M.V.Keldish. Preprint 177, 1985, Moskow.

12.V.E.Neuvazhaev, V.G.Yakovlev

Gravitational Mixing Computation by kε-Model. Sov.J.VANT,Ser. Theor. and Appl. Phys.,1988,1,p.28-36.

Handbook of Turbulence. Volume 1. Fundamentals and Applications. Mir. Moscow. 1980.

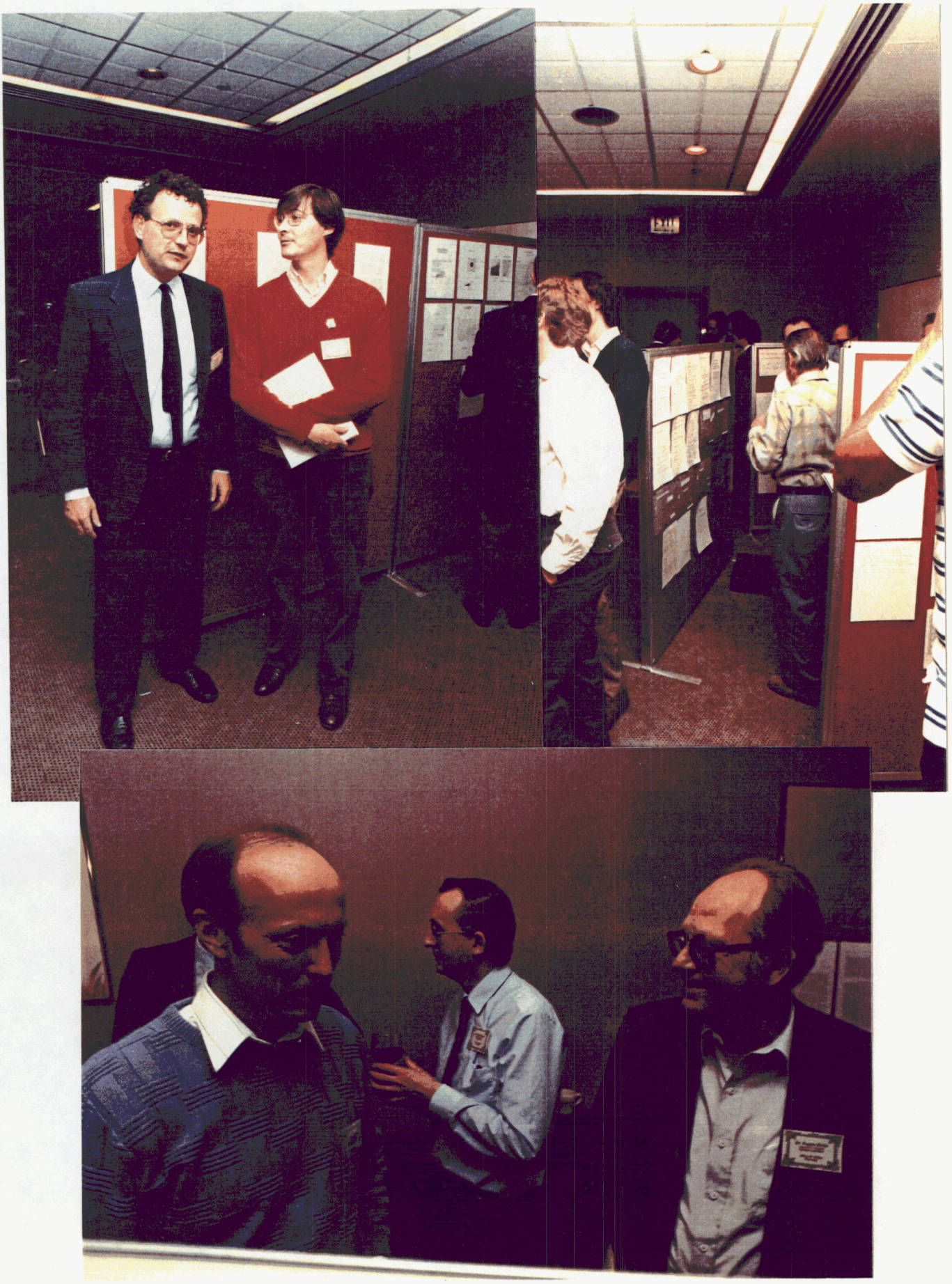

NUMERICAL CALCULATION OF INTERFACES TURBULENT MIXING BY RAYLEIGH-TAYLOR INSTABILITY ON THE BASIS OF SEMIEMPIRICAL MODELS

V.E.Neuvazhayev, V.G. Yakovlev

State University, Chelyabinsk

Semiempirical models of gravitational turbulent mixing with one (k-model) and two (kε-model) eqilibrium equations are considered. Propeties of models solved self-similarly for incompressible liquid are investigated. Mixing effective width dependence upon Atwood number is determined. Finitely difference method of equation solution for general case of nonself-semilarity is observed. k- and kε- models are compared.

INTRODUCTION

It is well known that the interface of gases or fluids with different densities is unstable to infinitesimal pertubations if the acceleration is directed from the light substance to the heavy one. This phenomenon is also simulated by the heavy fluid laid over the light one in the gravitational field characterized by the acceleration g. Such an instability is called the Rayleigh-Taylor instability.

Viscosity and surface tension as well as initial perturbations are of importance while beginning and developing of turbulent mixing zone. If viscosity and surface tension are negligible and initial perturbations are chaotic, the instability leads to interface destruction and turbulent mixing.

Turbulence being the result of shear instability, when one layer is sliding over the other, has been considered by many authors. There is a number of semiempirical models being able to describe sufficiently wide classes of applied problems.

Turbulent mixing in the gravitational field has a number of peculiarities related first of all to the fact that a main portion of turbulence energy is conserved not in vortices but in the chaotic jets of a heavy substance penetrating light one. That's why gravitational turbulence deserves a special consideration.

S.Z.Belyenkiy and E.S Fradkin [5] began theoretical studing of that phenomenon. They devised a diffusion type semiempirical model with one parameter. This model was suitable for describing a mixing under isothermic conditions. Its simpliest version came to the determination of a turbulent diffusion coefficient by means of desired solution gradients.

These authors [9] generalized the model to nonisothermic motion and created a numeric method for solving the problem.

Investigations of model properties under various conditions are given in [6-12]. The model of such a type was devised in [2]. [1] deals with a more complicated model with equations for second order correlations. It takes into account turbulence anisotropy and density pulsation.

Experimental and theoretical studying of turbulent mixing are considered in [1,2,4,13,15].

The present paper concerns determination of equations describing a kε-model. It has an advantage over a k-model in describing a mixing of an arbitrary number of substances and in generalization to multidimensional equations. The models are compared and some peculiarities of numerical calculation and influence of turbulance initial period are discussed.

1. kε-MODEL WITH FIVE PARAMETRES

A disadvantage of a semiempirical model with equilibrium equation for turbulence kinetic energy, where the turbulence scale l is connected with mixing width L, is that the mixing width changes abruptly at the moment of mixing areas interaction. It does not agree with reality.

There are models with equations for the turbulence scale l or for the coefficient of diffusion D for shear flows with free boundaries. In this case the turbulence is discribed by two additional equations: the one for turbulence kinetic energy k and, for example, for the turbulence scale l. These two equations are added to gas-dynamic equations which are obtained after averaging and which contain coefficients of turbulence viscosity and thermal conductivity. As the second additional equation one often uses a transfer equation for the dissipation velocity of turbulence kinetic energy denoted by ε_t. In contrast to k-model with one equation such models are called kε-models.

Initial equations were inspired by P.Harsha's overview [14]. In the present paper generation terms and additional terms accounting for compressibility are different. These terms are underlined in the following equations :

$$(1.1)\quad \rho\frac{dk}{dt} + \rho\varepsilon_t = \underline{\rho D\omega^2} + \alpha_8\rho\frac{\partial}{\partial m}r^{2s}\rho^2 D\frac{\partial k}{\partial m} + \underline{\frac{2}{3}k\frac{d\rho}{dt}},$$

$$(1.2)\quad \rho\frac{d\varepsilon_t}{dt} + c_{2\varepsilon}\rho\frac{\varepsilon_t^2}{k} = \underline{c_\mu c_{1\varepsilon}\rho k\omega^2} + \alpha_{8\varepsilon}\rho\frac{\partial}{\partial m}r^{2s}\rho^2 D\frac{\partial\varepsilon_t}{\partial m} + \underline{\frac{4}{3}\varepsilon_t\cdot\frac{d\rho}{dt}},$$

where $\frac{d}{dt} = \frac{\partial}{\partial t} + u\frac{\partial}{\partial r}$, $D=c_\mu k^2/\varepsilon_t$ - diffusion coefficient entering in turbulent heat flux and in turbulent fluxes of mixture components in initial equations:

$$(1.3)\quad \frac{d\epsilon}{dt} + P\frac{d(1/\rho)}{dt} + \frac{\partial}{\partial m}(Q+q) = \epsilon_0(t).$$

$$(1.4)\quad \frac{dc_i}{dt} + \frac{\partial j_i}{\partial m} = 0, \quad i = 1,2,\ldots,N,$$

$$(1.5)\quad q=-r^{2s}\rho^2 D\left[\frac{\partial \epsilon}{\partial m} + P\frac{\partial(1/\rho)}{\partial m}\right].$$

$$(1.6)\quad j_i=-r^{2s}\rho^2 D\frac{\partial c_i}{\partial m},$$

$$(1.7)\quad \frac{du}{dt} + r^s\cdot\frac{\partial P}{\partial m} = 0,$$

$$(1.8)\quad \frac{d(1/\rho)}{dt} - \frac{\partial}{\partial m}(r^s u) = 0,$$

$$(1.9)\quad \omega^2=\frac{du}{dt}\left[r^s\cdot\frac{\partial \rho}{\partial m} + \frac{g}{a^2}\right],$$

$$(1.10)\quad \partial m=\rho r^s \partial r, \quad s=0,1,2.$$

p and a are the pressure and the sound velocity of the mixture, ρ is the mixture density, c_i are mass concentration of the i-th component.

kϵ-model constants are c_μ, $c_{1\epsilon}$, $c_{2\epsilon}$, α_8, $\alpha_{8\epsilon}$.

Equation (1.2) for k-model is substituted by the following expression:

$$(1.11)\quad \epsilon_t=\nu k^{3/2}/l, \quad l=\alpha L_{э\phi}.$$

k-model constants are $\nu=1.25$, $\alpha=0.338$, $\alpha_8=0.3$.

2. SELF-SIMILAR SOLUTIONS FOR INCOMPRESSIBLE FLUIDS. ASYMPTOTIC PROPETIES OF MODELS

Important properties of turbulent mixing models can be derived if we restrict ourselves to the case of mixing of two incompressible fluids under constant acceleration. In this case an equations number is reduced substantially and the problem reduces to a boundar-value problem for ordinary differential equations.

Self-similar solutions for k-model under different types of Atwood numbers

$$(2.1)\quad A = \frac{\rho_1-\rho_2}{\rho_1+\rho_2}$$

are constructed in [10,12]. It's also shown there that if the effective width $L_{э\phi}$ of mixing area is described as a distance between points which nondimensional density δ

(2.2) $$\delta = \frac{\rho - \rho_1}{\rho_1 - \rho_2}$$

is taken values 0.1 and 0.9, then with a sufficient accuracy a connection of $L_{э\phi}$ with movement $S=g_0 t^2/2$ is described by linear dependence:

(2.3) $$L_{э\phi} = 0.787\alpha^2 A \cdot 2S.$$

A comparison with the experimental data of the paper [4] makes it possible to choose α и α_g constants, besides, with the help of α_g it's possible to achieve a sufficient agreement with nondimensional profile of density δ.

Analysis of specific solutions shows, that k- and ε- functions are bellshaped. That's why it seems natural to consider an approximate model assuming $\frac{\partial k}{\partial r} = \frac{\partial \varepsilon_t}{\partial r} = 0$. In this case the solution is represented in an analitical form and the acceleration g can be an arbitrary function of time. In particular if the acceleration is considered as constant up to the some moment t_0 and then as being equal to zero, the solution for the effective width will be as follows:

(2.4) $$L_{э\phi} = \frac{0.1 c_\mu (c_{2\varepsilon} - c_{1\varepsilon})^2}{[c_{2\varepsilon}(0.5-P_0)-0.25+P_2][c_{1\varepsilon}(0.5-P_0)-0.25+P_2]} A g_0 t^2, \quad t \le t_0.$$

(2.5) $$L_{э\phi} = L_{э\phi}(t_0)\left[\frac{t}{t_0}\right]^{\frac{1.5-c_{2\varepsilon}}{(1-c_{2\varepsilon})(1-P_0)+P_0-P_2}}, \quad t > t_0.$$

$$P_0 = -0.5 - \frac{2}{3\pi} A^2, \qquad P_2 = -0.5 - \frac{4}{3\pi} A^2 .$$

From this it follows: 1) attenuation degree of turbulent mixing is determined by a single constant $c_{2\varepsilon}$; 2) analytical dependence of attenuation degree and mixing intensity $L_{э\phi}/S$ upon Atwood number is established; 3) solution of (2.5) is an asymptotics for the problem on mixing a layer with a width L_0 and nonzero values of k and ε_t when sources giving rise to turbulence are turned off.

3. SOME PECULIARITIES CONCERNING NUMERICAL REALIZATION. THE INFLUENCE OF INITIAL TURBULENCE LEVEL

Equations (1.1) -(1.9) are approximated by the following noniterative difference scheme: (here ε_t is used without t):

(3.1) $$\frac{k_i^{n+1} - k_i^n}{\tau} + \varepsilon_i^n = D_i^n \omega^2{}_i^{n+1} + \alpha_g \left[\left[r^{2s} \rho^2 \right]_{i+\frac{1}{2}}^{n+1} D_{i+\frac{1}{2}}^n \frac{k_{i+1}^{n+1} - k_i^{n+1}}{m_{i+\frac{1}{2}}} - \right.$$

$$-\left[r^{2s}\rho^2\right]^{n+1}_{i-\frac{1}{2}} D^n_{i-\frac{1}{2}} \left[k_i^{n+1} \cdot \frac{k_i^{n+1} - k_{i-1}^{n+1}}{m_{i-\frac{1}{2}}} + \frac{2}{3} k_i^n \cdot \frac{\ln(\rho_i^{n+1}/\rho_i^n)}{\tau} \right].$$

$$(3.2)\quad \frac{\epsilon_i^{n+1} - \epsilon_i^n}{\tau} + \left[\frac{\epsilon}{k}\right]_i^n c_{2\epsilon} \epsilon_i^n = \left[\frac{\epsilon}{k}\right]_i^n c_{1\epsilon} D_i^n \omega^2{}_i^{n+1} + \alpha_{8\epsilon} \left[\left[r^{2s}\rho^2\right]^{n+1}_{i+\frac{1}{2}} D^n_{i+\frac{1}{2}} \times \right.$$

$$\left. \times \frac{\epsilon_{i+1}^{n+1} - \epsilon_i^{n+1}}{m_{i+\frac{1}{2}}} - \left[r^{2s}\rho^2\right]^{n+1}_{i-\frac{1}{2}} D^n_{i-\frac{1}{2}} \frac{\epsilon_i^{n+1} - \epsilon_{i-1}^{n+1}}{m_{i-\frac{1}{2}}} + \frac{4}{3} \epsilon_i^n \cdot \frac{\ln(\rho_i^{n+1}/\rho_i^n)}{\tau} \right].$$

Difference equations system approximating equations (1.1)-(1.9) is solved with a method of separate "progonka" [9]. The following values are calculated sequentially: $u_i, \rho_{i+\frac{1}{2}}, r_i, k_i, \epsilon_i, c_{i+\frac{1}{2}}, T_{i+\frac{1}{2}}$ (temperature). Some infinitesimal values determinating an initial level of turbulence (background) are taken as initial values for k_0, ϵ_0. Approximation of $\partial\rho/\partial m$ derivative being infinite at the interface at the initial moment of instability developing on the finite interval leads to essential loss of accuracy. Therefore for calculating k_i, ϵ_i at the points laying near the interface when mixing begins to develop the self-semilarity solution (2.5) is used. This method corresponds to the infinitesimal initial level of turbulence.

4. THE CHOICE OF CONSTANTS. COMPARISION OF MODELS ON TEST PROBLEMS

The constant $c_{1\epsilon}=1.43$ is takeh from the work [14]. The constant $c_{2\epsilon}=1.85$ is chosen in such a way that the exponent in (2.5) is equal to 2/7. The constant $c_\mu=3.5$ is chosen while comparing a calculated intensity with experimental one [4]. The constants $\alpha_8=0.5$ and $\alpha_{8\epsilon}=0.85$ are chosen while comparing a calculated density profile with an experimental one for $\rho_1/\rho_2=3$.

A comparison of nondimensional density profiles for kε- and k-models is shown in fig.1. Mixing intensity dependence upon the Atwood number is shown in fig.2.

It was determined theoratically that mixing of a layer having a width X_0 assimptotically followed a linear relationship to time:

$$L = Brt,$$

where $r=\sqrt{(n-1)/ng}\cdot X_0 t$ for a light layer placed into a heavy one [5] and $r=\sqrt{(n-1)g}\cdot X_0 t$ for a heavy layer placed into a light one [7]. While calculating ρ_1/ρ_2 the distance between points, where $0.01 < \delta < 0.99$, was taken as a width L. It was determined that B is equal to 0.367 according to k-model and B is equal to 0.621

according to kε-model. The differences between these two values make it necessary to carry out an appropriate experiment.

Mixing zones interaction is shown in fig 3. It can be stated, that there is a qualitative agreement and a slight quantitative disagreement.

Numerical calculation of the model was carried out by means of TURINB code [3].

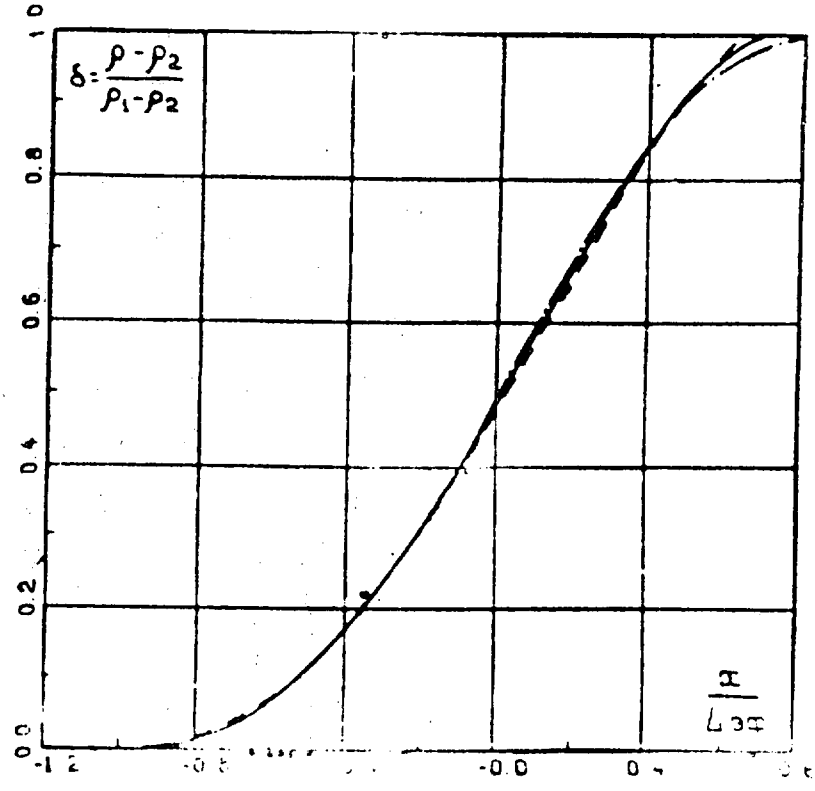

Fig.1 Density profiles for $\rho_1/\rho_2=3$
---- experiment, —— kε-model, —·— k-model

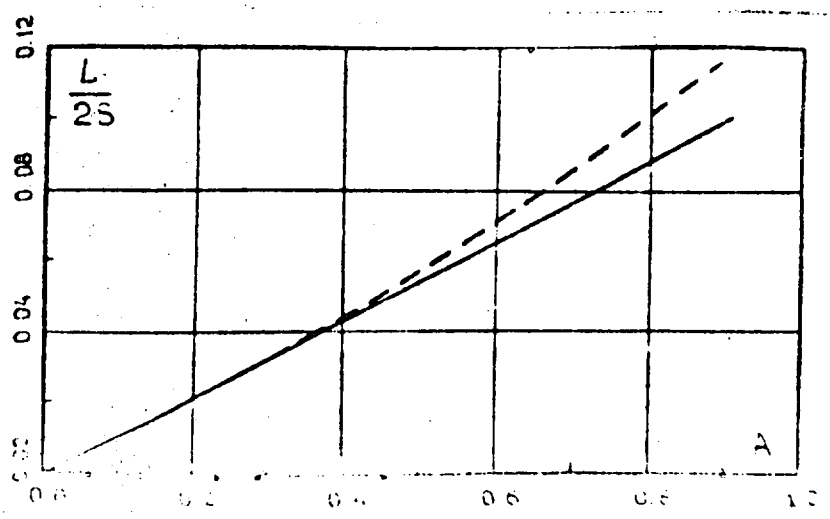

Fig.2 Mixing intensity dependence upon the Atwood number
---- kε-model, —— k-model

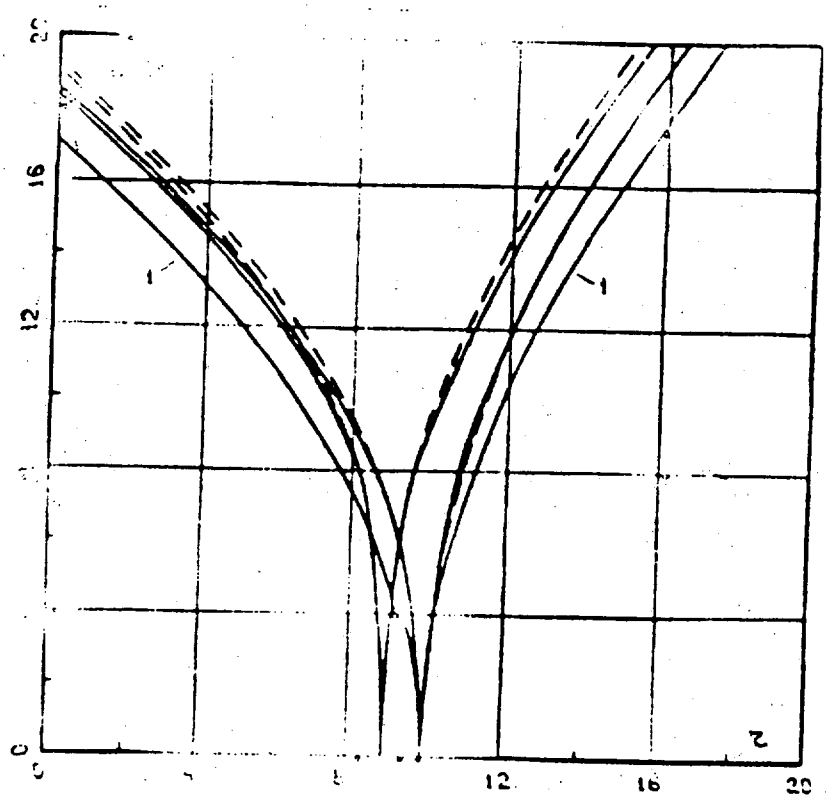

Fig.3 (r,t) diagram for $\rho_1/\rho_2/\rho_3$=1/1.5/3
1-calculation without intermediate according to k-model;
—— kε-model, —·— k-model

REFERENCES

1. Андронов В.А., Бахрах С.М., Мешков Е.Е. и др. Докл. АН СССР, 264, 1, 76 (1982).
2. Андронов В.А., Бахрах С.М., Мешков Е.Е. и др. ЖЭТФ,71,2(8),806 (1976).
3. Андрюшенко Н.В., Банных В.И., Легонькова Г.С. Сб. Численные методы мех. спл. среды, 8,3,16 (1977).
4. Анучина Н.Н., Кучеренко Ю.А., Неуважаев В.Е. и др. Механика жидкости и газа, 6, 157 (1978).
5. Беленький С.З., Фрадкин Е.С. Труды Физ. института АН СССР, 29, 207 (1965).
6. Неуважаев В.Е. Докл. АН СССР, 222, 5, 1053 (1975).
7. Неуважаев В.Е. ПМТФ, 6, 82 (1976).
8. Неуважаев В.Е. ПМТФ, 2, 46 (1988).
9. Неуважаев В.Е., Яковлев В.Г. ЖВМ и МФ, 2, 440 (1976).
10. Неуважаев В.Е., Яковлев В.Г. ПМТФ, 4, 74 (1976).
11. Неуважаев В.Е., Яковлев В.Г. ПМТФ, 2, 85 (1981).
12. Неуважаев В.Е., Яковлев В.Г. Сб. Вопросы атомной науки и техники, серия: Методики и программы численного решения задач матем. физики, 2(16), 17 (1984).
13. Read K.J. Physica, 12D, 45 (1984).
14. Харша П. Турбулентность. Принципы и применения, 207,М., Мир, (1980).
15. Youngs D.L. Physica, 12D, 32 (1984).

The Statistical Model of the Turbulent Mixing Zone and Its Applying to the Experiments Analysis

V.I. ANISIMOV & A.V. POLYONOV

Chelyabinsk State University

ABSTRACT

Comparative analysis of exprerimental results obtained while investigating the gravitational turbulent mixing in the experiments with the electromagnetic shock tube and on the Rocket - Rig apparatus in AWE was carried out on the basis of the suggested statistical model of the turbulent mixing zone. Difference in coefficients for the automodel slope is considered as failing to achieve the automodel state in the experiments with the shock tube.

CHELYABINSK STATE UNIVERSITY

THE STATISTICAL MODEL OF THE TURBULENT MIXING ZONE AND ITS APPLYING TO THE EXPERIMENTS ANALYSIS

V.I. ANISIMOV, A.V. POLYONOV

ABSTRACT

Comparative analysis of exprerimental results obtained while investigating the gravitational turbulent mixing in the experiments with the electromagnetic shock tube and on the Rocket - Rig apparatus in AWE was carried out on the basis of the suggested statistical model of the turbulent mixing zone. Difference in coefficients for the automodel slope is considered as failing to achieve the automodel state in the experiments with the shock tube.

INTRODUCTION

Statistical turbulence nature always suggests carrying out the averaging to obtain some parameters which characterize its state. The parameter of great interest for studying gravitational turbulence is the mixing zone width for some moment. Averaging over a very large number of realizations of the state under investigation is required. For the most frequently occuring plane case this is equivalent to averaging over a very large surface which considerably exceeds the zone width. In practice, both in specific applications and in the experiments, we deal with finite systems.

Neglecting the statistical nature while treating experimental data, that is quite usual nowdays, leads to a noticeable error as a result. Very often a mistake is made when the growth rate of the turbulent mixing zone is being determined. In the experiment this growth takes place at the constant value of the mixed zone area, i. e., in the process of the turbulent mixing development the relative reduce of the observation turbulent mixing zone area occurs, that is not taken into account during treatment and leads to underestimating of the growth of the turbulent mixing zone. Results, obtained in the experiment, are usually used for the calibratican of semiempirical codes which operate with averaged values. Then the problem arises to

establish the conformity between the width of the turbulent mixing zone in a particular finite system and some width in calculations. For this purpose we suggest to use the statistical model which parameters are selected rather approximately as yet because of the lack of the experimental data.

I. THE STATISTICAL MODEL OF THE TURBULENT MIXING ZONE

A concentration profile, obtained as a result of the calculations according to this or that model, appeares to have the form of the smooth curve that assumes the averaging over the infinite large number of experiments or for the one - dimentional case - the averaging over the infinite surface. In practice, we deal with a system of finite sizes. It is considered that mixing is carried out by spikes of different forms. A very convenient method for defining the mixing zone width in the experiment consists in determinating the position of the most advanced spike [1], [2], [3]. Mixing can be presented as interpenetration of the components volumes in the form of spikes having a length which at each time moment is equal on the average to ls (characteristic of the turbulent scale). We shall obtain the formula for the volume fraction of one of the substance depending upon the spike length. Various spike forms are assumed towards heavy and light substance, since in this case a better conformity with experiments is available.

In case of penetration of the light substance into the heavy one, spikes are assumed to have the form of the rotation paraboloid which can be obtaned by rotating the parabola $y = y_0 - kx^2$, located in the plane XOY, around the axis OY. In so doing, the mean value of the volume fraction on the plane XOZ is

equal to the ratio of the area, outlined by the statistical average paraboloid on this plane to the mean value of the area per one paraboloid - square of the side c (see Fig. 1). Below it will be seen that such an assumption is realized for the cases of practical interest.

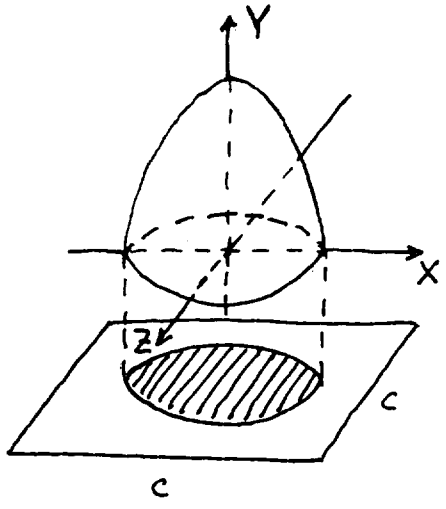

Fig. 1.

Spike lengths of the light substance y_0 are regarded to be random values, distributed by the normal law with mean value ls and some quadratic deviation σ. Then the probability of obtaining the spike with the length in the range from y_0 to $y_0 + dy_0$ will be:

$$\omega(y_0)dy_0 = \frac{1}{\sigma\sqrt{2\pi}} e^{-\frac{(y_0-ls)^2}{2\sigma^2}} dy_0 .$$

The volume fraction of the light substance at height y with a given value y_0 is

$$a(y,y_0) = \frac{\pi x^2}{c^2} = \frac{\pi(y_0-y)}{kc^2} .$$

Let us choose the coordinate system in such a way that the value y = 0 should correspond to the volumetric concentration which is equal to $a(0,y_0) = 0.5$. Then at $y = 0$, $y_0 = ls$:

$$kc^2 = 2\pi ls \quad \text{and} \quad a(y,y_0) = \frac{y_0-y}{2ls} .$$

Finally we obtain the profile of the averaged volume fraction of the light substance in the heavy one:

$$a(y) = \frac{1}{2\sigma l_s\sqrt{2\pi}} \int_{y<y_0}^{\infty} (y_0-y)\, e^{-\frac{(y_0-l_s)^2}{2\sigma^2}}\, dy_0 .$$

Note that

$$a\left\{\frac{y}{l_s}\right\} = \frac{l_s}{2\sigma\sqrt{2\pi}} \int_{y<y_0}^{\infty} \frac{(y_0-y)}{l_s} e^{-\frac{(y_0-l_s)^2}{2\sigma^2}}\, d\,\frac{y_0}{l_s} .$$

depends only on the ratio $\frac{l_s}{\sigma}$ but not on l_s and σ separately (see Fig. 2). The condition $a(0) = 0.5$ is fulfilled with good accuracy at $\frac{l_s}{\sigma} \geq 2$ (see Fig. 3).

For the case of penetration of the heavy substance into the light one, the penetration is assumed to be carried out as spikes, having the form of a rotation cone $(y_0-y)^2 = kx^2$. Repeating the given above considerations we shall obtain the expression for the profile of the averaged volumetric concentration of the heavy substance in the light one:

$$a(y) = \frac{1}{2\sigma l_s^2\sqrt{2\pi}} \int_{y<y_0}^{\infty} (y_0-y)^2\, e^{-\frac{(y_0-l_s)^2}{2\sigma^2}}\, dy_0 .$$

Note that

$$a\left\{\frac{y}{l_s}\right\} = \frac{l_s}{2\sigma\sqrt{2\pi}} \int_{y<y_0}^{\infty} \frac{(y_0-y)^2}{l_s^2} e^{-\frac{(y_0-l_s)^2}{2\sigma^2}}\, d\,\frac{y_0}{l_s}$$

also depends only upon the ratio $\frac{l_s}{\sigma}$, but not upon l_s and σ separately (see Fig. 4). The condition $a(0) = 0.5$ is fulfilled with good accuracy at $\frac{l_s}{\sigma} \geq 12$ (see Fig. 5).

The ratios $\frac{l_s}{\sigma}$ for both cases are selected on the basis of the comparison of the obtained concentration profile with the experimental one, given in [2]. These profiles are in good agreement at values $\frac{l_s}{\sigma} = 6$ for the case of penetration of the light substance into the heavy one, and $\frac{l_s}{\sigma} = 22$ for the case of penetration of the heavy substance into the light one. In Fig. 6 dimentionless concentration profiles are given as a function of nondimentional coordinate: o - experimental data from the paper [2], —— our model, --- code TURINB [4], where the improved semiempirical model of Belenki - Fradkin is realized. (The semiempirical model, used in TURINB have been calibrated with experimental data [3]).

Now we determine the mean value of the height of the most advanced spike depending upon the number of spikes on the area using the offered statistical model. The probability that the most advanced spike among N spikes on some area has the length in the range from l upto l + dl and the other spikes have the smaller length, is:

$$P(l)dl = N\omega(l)dl \left[\int_{-\infty}^{l} \omega(y)dy \right]^{N-1}$$

where $\omega(l)$ - the function of the spikes lengths distribution

$$\omega(l) = \frac{1}{\sigma\sqrt{2\pi}} e^{-\frac{(l-l_s)^2}{2\sigma^2}}.$$

Then the half of the mixing zone width is determined as a mean value of the most advanced spike width:

$$L = \int_0^\infty l P(l)dl = \frac{N}{\sigma\sqrt{2\pi}} \int_0^\infty e^{-\frac{(l-ls)^2}{2\sigma^2}} \, l \left[\frac{1}{\sigma\sqrt{2\pi}} \int_{-\infty}^{l} e^{-\frac{(y-ls)^2}{2\sigma^2}} dy \right]^{N-1} dl.$$

Note that

$$\frac{L}{ls} = \frac{N\sigma}{ls\sqrt{2\pi}} \int_0^\infty e^{-\frac{(l-ls)^2}{2\sigma^2}} \, \frac{l}{\sigma} \left[\frac{1}{\sigma\sqrt{2\pi}} \int_{-\infty}^{l} e^{-\frac{(y-ls)^2}{2\sigma^2}} dy \right]^{N-1} d\frac{l}{\sigma}$$

also depends only upon the ratio $\frac{ls}{\sigma}$.

The dependence of $\frac{L}{ls}$ upon the number of observed spikes N on some area is shown in Fig. 7, Fig. 8 - for the case of penetration of the light substance into the heavy one with $\frac{ls}{\sigma} = 6$, and for the case of penetration of the heavy substance into the light one with $\frac{ls}{\sigma} = 22$.

Measuring mixing zone width in experiments by the most advanced spike we should have obtained the true value of the mixing zone and the automodel slope, provided we carried out observations on the infinite area. In the real experiment we mesure turbulent mixing zone width at some fixed area S. In the course of mixing development the reduction of the relative observation area (area related to the square of the turbulent mixing zone width) takes place. As a result, the number of spikes on the area also decreases, that is why the probability to reqister a far spike appeares to be reduced that is the turbulent mixing zone width in the experiment grows not so intensive as in the automodel case, which suggests increasing of the observation area proportionally to the square of zone width.

To check up our model let as consider the case when the relative observation area reduces, for example, by a factor of 4. We shall use photographs of the turbulent mixing zone from the paper [2] (see Fig 9). According to our model we have the relation:

$$\frac{L}{L'} = \frac{f(N)}{f(N/4)} \qquad *)$$

where L' is the turbulent mixing zone width measured over one fouth part of the frame. Using Fig. 9 and dependences obtaned above (see Fig. 7,8) it is easy to find that the relation mentioned above *) is fulfilled at assumed $\frac{ls}{\sigma}$ towards the light fluid side and the heavy fluid side.

Thus the coinsidence of our consentration profile with the eperimental one and the check up given above prove the legitimacy of the suggested approach to the structure of turbulent mixing zone.

On this basis we can find the automodel slope value using some definite number of spikes on the observation area, that corresponds to some number of spikes of the component volume fraction. If we know the turbulent mixing zone width at some moment and the number of spikes on the observation area, then for any time moment using the dependence $L \sim f(N)$ we can find the turbulent mixing zone width corresponding to the accepted spikes number, that is to the assumed concentration, and by this concentration we can obtain the automodel slope value. (It should be noted that the value of the automodel slope depends on the

accepted volume fraction).

Thus we can compare the results obtained on different experimental facilitics by introducing corresponding corrections.

II. ANALYSIS OF THE STATIC EXPERIMENTS

We apply the suggested statistical model of the turbulent mixing zone to analysis of the experiments of the number 35 and 99, performed in AWE, in which the mixing of two different density layers is explored at the static gravity field, created by the rocket motors [1], [2].

Howerver, at first we shall make remarks concerning the treated method of the experimental results processing.

One of main characteristics of the gravitational turbulence is the growth rate of the turbulent mixing zone in the automodel case. This mixing occurs when two semiinfinite layers are mixing as result of the infinitesimal initial perturbations and at the negligible influence of viscosity, surface tension and other dimensional factors. The only parameter of lenth dimension is in this case the combination gt^2. Thus the dependence of the TMZ width on time can be written by

$$L = \alpha(A)\,\frac{gt^2}{2}$$

where α is the coefficient, defined only by the density ratio expressed by Atwood number $A = \frac{\rho_1-\rho_2}{\rho_1+\rho_2}$. The main purpose of considered experiments is to obtain the value of α.

One of the main troubles while finding α is the effect of the conditions of turbulence forming, leading to the deviation

from the automodel dependence $L \sim t^2$. This dependence approaches to linear as usual only asymptotically at large time values, attaining of which in the particular experiment may to present a problem. That is why, it is desirable to use such experimental data processing method which would allow to determine the value of the automodel slope as early as possible. Evaluating of α is possible only under the condition of reaching the automodel state, i. e. such state when any characteristics of this state are determined only by parameters characterizing the state, as it is, and are independent of the history. Such parameters appears to be the mixing zone width L and acceleration ρ. Then, we have the following from considerations of dimensionality:

$$\frac{dL}{dt} = \beta g^{1/2} L^{1/2}$$

whence, for slight dependence of acceleration on time we obtain:

$$L^{1/2} = \frac{\beta}{2} \int g^{1/2} dt + \text{const.}$$

The conducted analysis indicates the way of evaluating of α. It is necessary to plot $L^{1/2}$ versus $\int g^{1/2} dt$ on the basis of experimental data, then, beginning from the moment when the derivative $\frac{dL^{1/2}}{dg^{1/2}}$ stops to change, it is possible to consider that the automodel state of the system is reached, in this case the value of the derivative itself, determines the automodel slope:

$$\beta = \sqrt{2\alpha} = \frac{2}{g^{1/2}} \frac{dL^{1/2}}{dt}.$$

Note that the discribed way is not a new one. It is readily to undestand that while plotting the given dependence in other coordinates, for example $L \sim \left[\int g^{1/2} dt \right]^2$, as in the works [1], [2], this dependence even at automodel motion, may differ from the rectilinear one, and it will depend on the way of transition to the given automodel motion. This may be visually illustrated by the case when the motion is presented in the automodel way, but we have no points of time reading and we have to adopt some moment $t \neq 0$ as an initial reading.

That is why, in the given work, for the case of a slight dependence of acceleration on time, it is used processing in coordinates $L^{1/2}$ versus $\int g^{1/2} dt$.

In works [1], [2] results of turbulent mixing at the interface between different densities media are given, the mixing is induced by Rayleigh - Taylor's instability development, obtained by the method which allows to reach almost constant acceleration in case of large transit distances. Using our model, we process results of the experiment № 99 from the work [2], at density ratio equal to $\frac{\rho_1}{\rho_2} = 13.5$. The plot, presented in this work, demonstrates the dependence of penetration depth of the light fluid into the more dense one h_1 on value $X = \frac{\rho_1 - \rho_2}{\rho_2 + \rho_1} \left[\int_0^t g^{1/2} dt \right]^2$. We obtain the coefficient of the automodel slope using the given above processing and refering all

points of the plot to the one volume fraction a = 0.04. It is appropriate to remember the early derived relationship, connecting the depth of penetration with the member of spikes at the observed area $h_1 = ls\, f(N)$. The number of spikes in the area ls^2 is denoted by $\aleph$ and is determined as follows:

$$\aleph = \frac{ls^2 N}{S},$$

whence

$$ls = \sqrt{\frac{\aleph S}{N}} \quad \text{and} \quad h_1 = \sqrt{\frac{\aleph S}{N}}\, f(N)$$

By means of photographs, given in the work (Fig. 9, 10, 11), the number of spikes is determined visually in some time moments while taking the depth of penetration of the light fluid into the heavy one from the plot and using the observation area value S, we determine the value of $\aleph$ for each picture and select the average value of $\aleph$. As we do not know the angle, at which the turbulent mixing zone is seen, the distance from the camera to tank and a number of other parameters, we shall consider that we see spikes existing in the nearer row in the photographs. Whence, we obtain $\aleph \approx 3$ for spikes penetrating into the heavy substance. For more accurate determination of $\aleph$ it is necessary to conduct the additional investigation. Assuming this value of $\aleph$, we determine the number of spikes as well as the volume fraction for all values of h_1 - i. e. for all points of the plot. Then, each point of h_1 - the penetration depth - is reduced to the same volume fraction a = 0.04 and the coefficient α, corresponding to

this concentration, is evaluated.

In the expression

$$h_1^{1/2} = \alpha^{1/2} \frac{\int g^{1/2} dt}{\sqrt{2}} \qquad \alpha = 0.084$$

Assuming $\frac{h_2}{h_1} = 1.75$, as given in the treated work, and considering that the number of spikes in one or another side is approximately the same for each time moment likewise we obtain the coefficient α of penetration of the light fluid into the heavy one for the same concentration of 4% : $\alpha = 0.095$. The total rate of growing turbulent zone mixing $\alpha = 0.179$. Computations while using the code TURINB give the following values of α: $\alpha = 0.108$ - for penetrating the light substance into the heavy one, $\alpha = 0.119$ - for penetrating the heavy substance into the light one and $\alpha = 0.227$ - for the total width of the zone at the same concentration equal to 4%.

Carrying out analogous processing the results of the experiment № 35 from the work [1] with the density ratio $\frac{\rho_1}{\rho_2} = 3$, we obtain the following values of the automodel slope coefficient: $\alpha = 0.063$; $\alpha = 0.053$; $\alpha = 0.116$ for penetration of the light substance into the heavy one, the heavy substance into the light one and for the total width of zone, respectively. (For the same volume fraction equal to 4%). Computations by TYRINB give the following results in this case: $\alpha = 0.0575$; $\alpha = 0.0572$; $\alpha = 0.115$, respectively.

Refinements, introduced by us into the experimental data

processing (using the suggested model and processing by roots), reduce the experimental data spread in evaluating the automodel coefficient. In Fig. 12 it is given the plot of the penetration depth of the light substance into the heavy one versus the value of $X = \frac{\rho_1-\rho_2}{\rho_2+\rho_1}\left[\int_0^t g^{1/2}dt\right]^2$. In Fig. 13 it is presented the plot, obtained by us while using the suggested refinements. It is seen that the function in Fig. 13 deviates by a smaller value than in Fig. 12 (correlation coefficients are equal to 0.998 and 0.996, respectively).

III. ANALYSIS OF EXPERIMENTS PERFORMED IN THE ELECTROMAGNET SHOCK TUBE (EMST)

Now we shall analyse the experiments, performed in EMST by Vasilenko A.M. and coworkers. The experimental procedure is in detail described in the work [5] and consists in generating the pulse shock wave and the rerefaction wave, following by the shock wave. While effecting of such mode the interface between two gases at first undergoes the impulsive acceleration and then this interface is smoothly decelerated, in this case, at the appropriate selection of gas densities, there arises the Rayleigh - Taylor's instability on it. In Fig. 14 it is given R - T diagram for $\frac{\rho_1}{\rho_2} = 13.5$, taken from computation which is in good agreement with the experiment. Acceleration in the process of the studied motion is changed by a factor of two, that is why, it is interesting to determine if such experiment can give the value of the constant, characterizing the automodel slope. Processing of the computation data shows that plotting $L^{1/2}$ versus $\int g^{1/2} dt$ leads to the value of the slope $\alpha = 0.271$ (for the volume fraction equal to 4%), whereas in the automodel case we obtain the value $\alpha = 0.227$. Here it is appropriate to note that processing with using $\int g^{1/2} dt$ offers such disadvantage that it does not take into consideration inertia of eddies and leads to

the sufficient overestimate of the slope while its evaluating under the conditions of sharp descreasing the acceleration. For example, turning - off the acceleration at some moment while processing with using $L^{1/2}$ versus $\int g^{1/2}dt$, it is possible to obtain $\alpha \to \infty$. The alternative method of processing is the method, used in [5], in wich the zone width is $L^{1/2}$ proportional to $S^{1/2} = \left[\int dt \int g dt \right]^{1/2}$. Processing of the computation data by this method gives the coefficient $\alpha = 0.237$ which is in good agreement with the automodel value.

Thus the conducted above analysis reveals that while processing the experimental results, obtained in EMST, with using the the dependence of $L^{1/2} \sim S^{1/2}$, we should have obtained the value of the automodel slope rather exactly if there were no other sources of errors.

Now, we estimate its value while using the data, kindly offered by the authors of the previously mentioned work. Photographs of the turbulent mixing zone in the stated time moments are given in Fig. 15, 16. The automodel slope, determined by this photographs, appears to be equal to $\alpha = 0.62$ that is in a poor agreement with the computed value. While comparing Fig. 15, 16 with Fig. 9, 10, 11 it is possible to note that 1) although we have the same relative zone width in Fig. 9, 16 a number of spikes is markedly smaller in Fig. 16 than in Fig 9; 2) while

increasing the mixing zone (Fig. 15, 16) the number of spikes in it is not decreasing proportionally to square of the mixing zone width, as it must be in the automodel case and as it is observed in the previous series of experiments, but practically it remains constant; 3) computation by the code TURINB gives for the time moments presented in photographs the mixing zone value which is far smaller than the experimental value. If we accept in one computation the initial roughness at which the mixing zone width will be the same both in computations and in experiment for the presented time moments, then the coefficient of the automodel slope, obtained by computation, appears to be by 35% smaller than the coefficient, obtained experimentally. (Note that in the experimental procedure it is reqistered only the total mixing zone width, that is why, it is difficult to give its value in some other concentration. However, due to the fact that the spike number fails to decrease in the presented photographs, the mixing zones for both time moments are already corresponding to the identical concentration equal to 0.0002% for the case of penetrating the heavy substance into the light one and to 0.02% for the case of penetrating the light substance into the heavy one. The estimated value of the coefficient of the automodel slope, for the concentration equal to 4% in both sides is equal to $\alpha = 0.41$).

All this provides good grounds to believe that in experiments while using EMST and such experimental procedure the automodel state have not been reached yet.

CONCLUSION

In the given work

I. The statistical model of the turbulent mixing zone is suggested; it treates the mixed zone as totality of spikes having lengths which are distributed according to the normal law. This model allows:

1) to relate the zone width, measured in the particular experiment in the system of finite sizes, to the specific concentration in system of infinite sizes,

2) to make the necessary corrections to the experimentally measured mixing zone width for adjusting its value in different time moments to the identical concentrations.

II. On the basis of the suggested model there have been processed the results of statistic experiments, described in works [1], [2] for the two density ratios of the volume fractions of 4% and there have been performed the comparison with the computed data, obtaned by the code TURINB.

These results are presented in a tabular form:

ρ_1/ρ_2		works [1], [2]	TURINB
3	h_1	0.063	0.0575
	h_2	0.053	0.0572
	h_1+h_2	0.116	0.1147
13.5	h_1	0.084	0.1081
	h_2	0.095	0.1191
	h_1+h_2	0.179	0.227

III. The analysis have been carried out, and the results of experiments, performed in the electromagnet shock tube [5], were processed. It has been noted the nonautomodel features revealing that, apparently, had been caused by effects of the large scale perturbations in the given experimental procedure. The excess of the rate of developing the turbulent mixing over the automodel one was estimated to be equal to 35%.

REFERENCES

1. Read. K. I.

Experimental investigation of turbulent mixing by Raylei-Taylor instability. Physica 12D (1984) 45-58.

2. Youngs D. L.

Experimental Investigation of Turbulent Mixing by Rayleigh - Taylor Instability. Report at the Workshop in Princeton (USA). Physics of Compressible Turbulent Mixing. October 24-27, 1988.

3. Kucherenko Y.A., Tomashev G.G. et al

Experimental Investigation of Gravitational Turbulent Mixing in Automodel Mode. Sov. J. VANT, 1988, 1.

4. Neuvazhaev V.E. Yakovlev V.G

Model and Method for Numerical Computation of Turbulent Mixing of Interface moving with acceleration. Sov. J. VANT, 1984, 2(16).

5. Vasilenko A. M.

Experimental investigation of Gravitational Instability and Turbulization at Noble Gas Interface. Report at the Workshop in Princeton (USA). Physics of Compressible Turbulent Mixing. October 24-27, 1988.

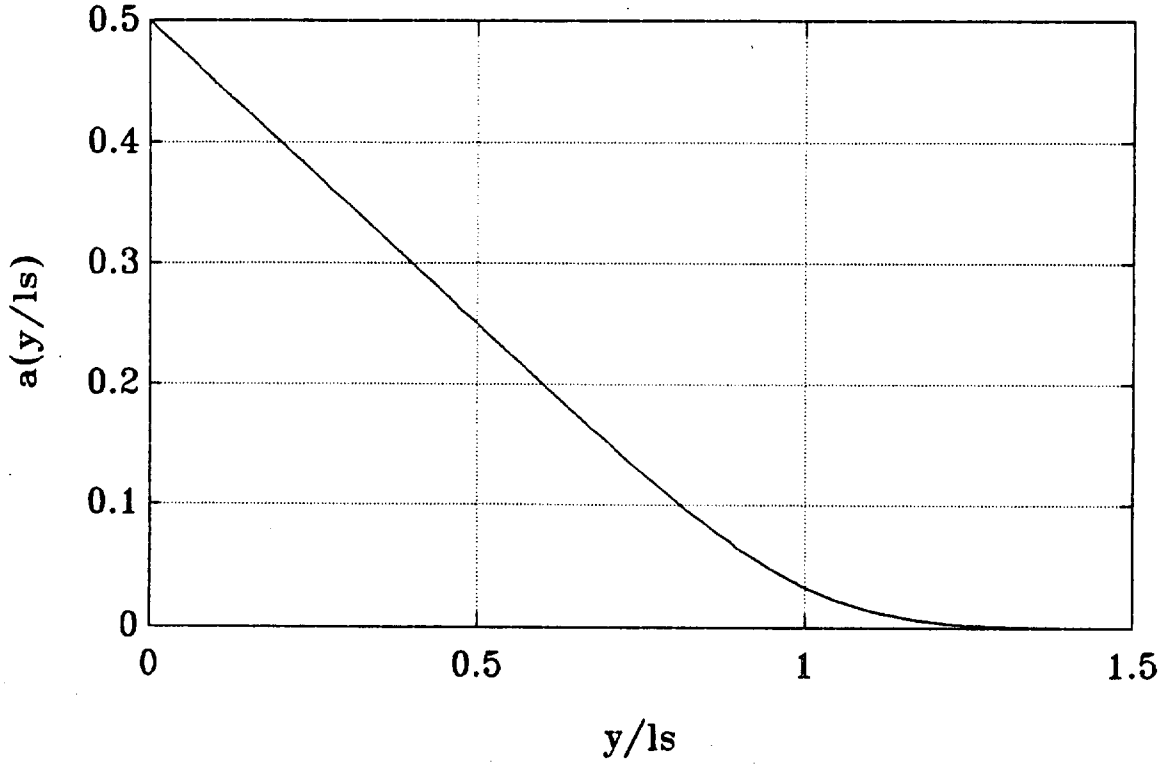
0.5
0.4
0.3
0.2
0.1
0
a(y/ls)
0
0.5
1
1.5
y/ls

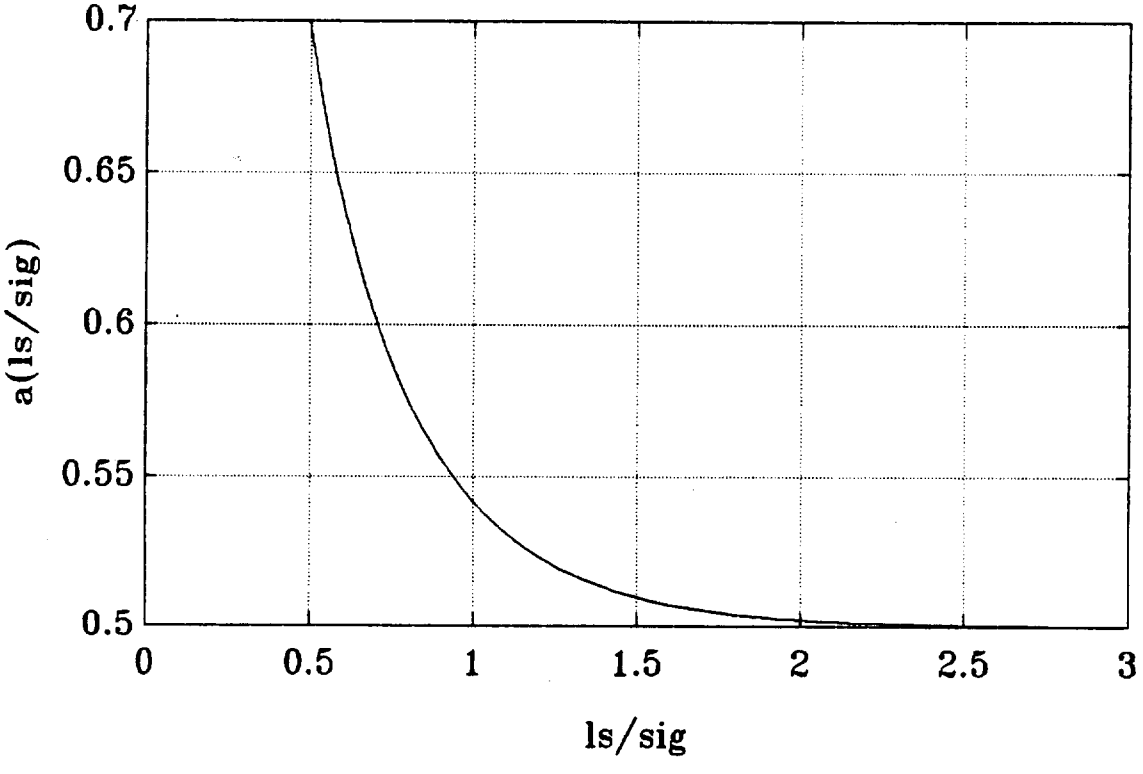
0.7
0.65
0.6
0.55
0.5
a(ls/sig)
0
0.5
1
1.5
2
2.5
3
ls/sig

Fig. 2, 3.

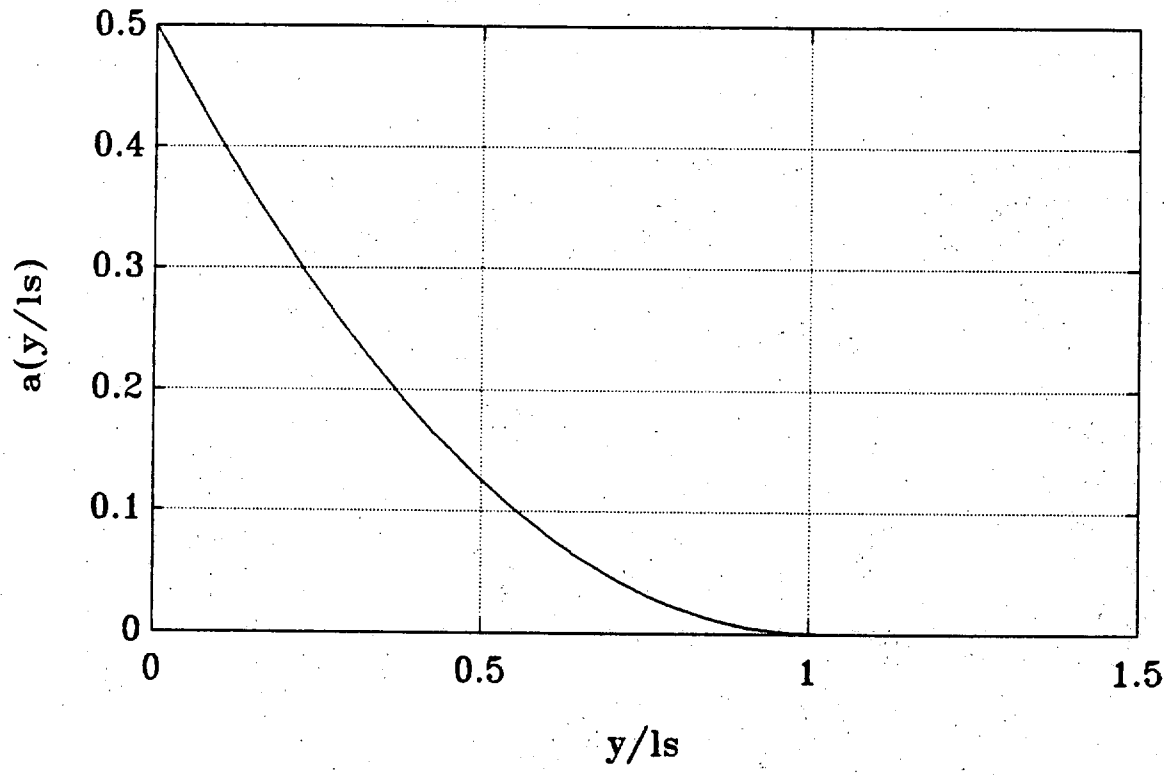
0.5
0.4
0.3
0.2
0.1
0
a(y/ls)
0
0.5
1
1.5
y/ls

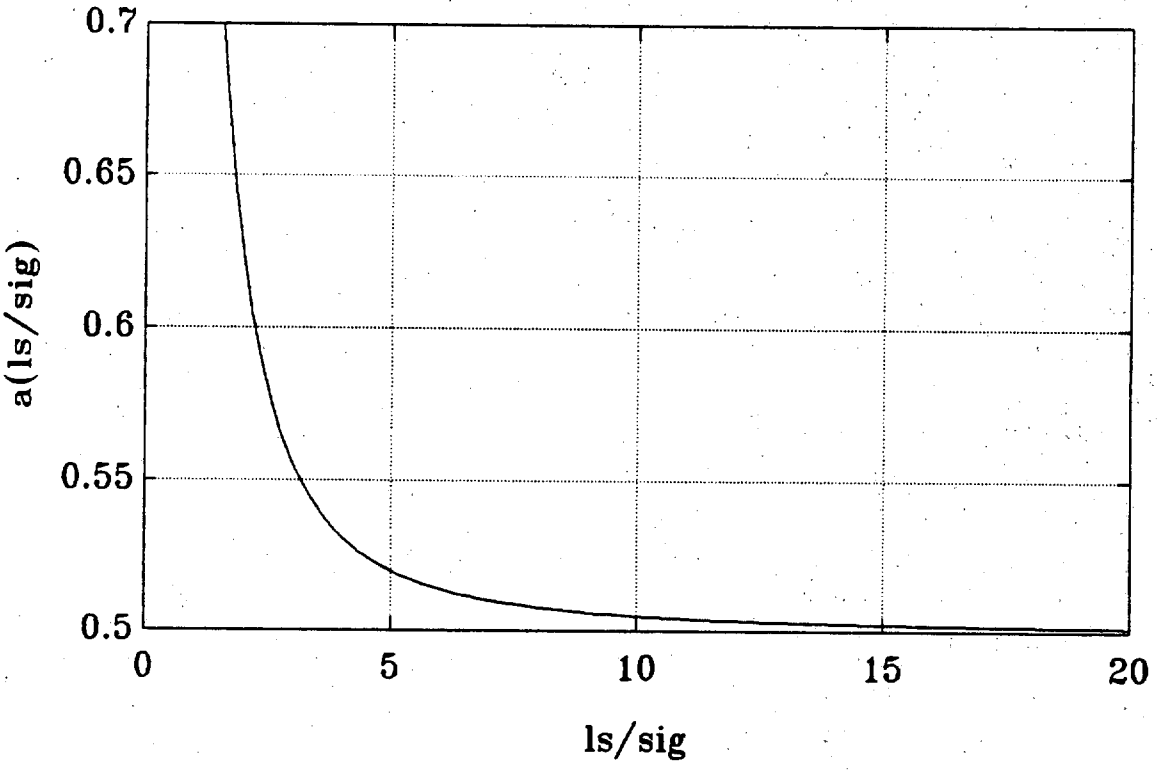
0.7
0.65
0.6
0.55
0.5
a(ls/sig)
0
5
10
15
20
ls/sig

Fig. 4, 5.

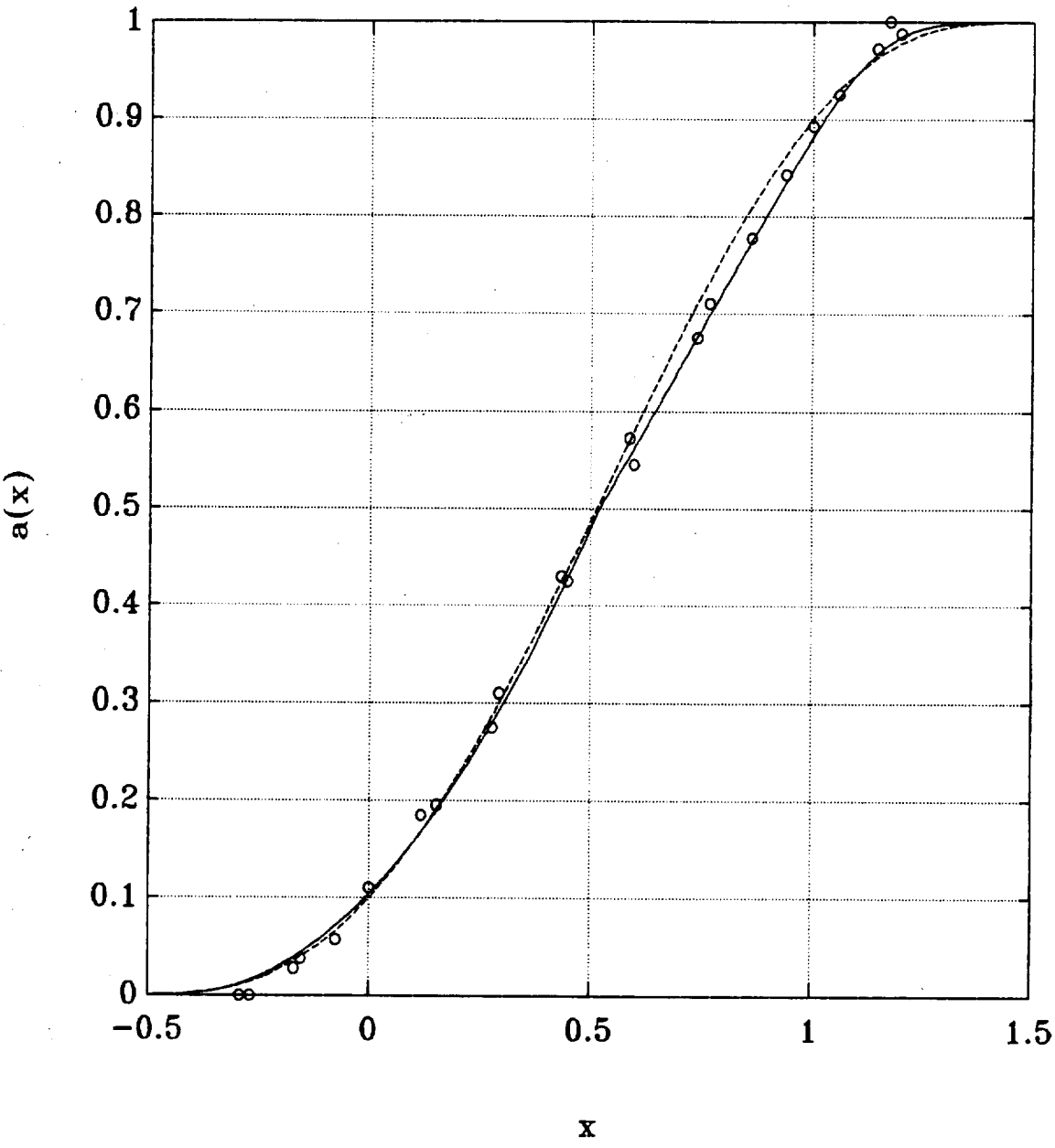

Fig. 6.

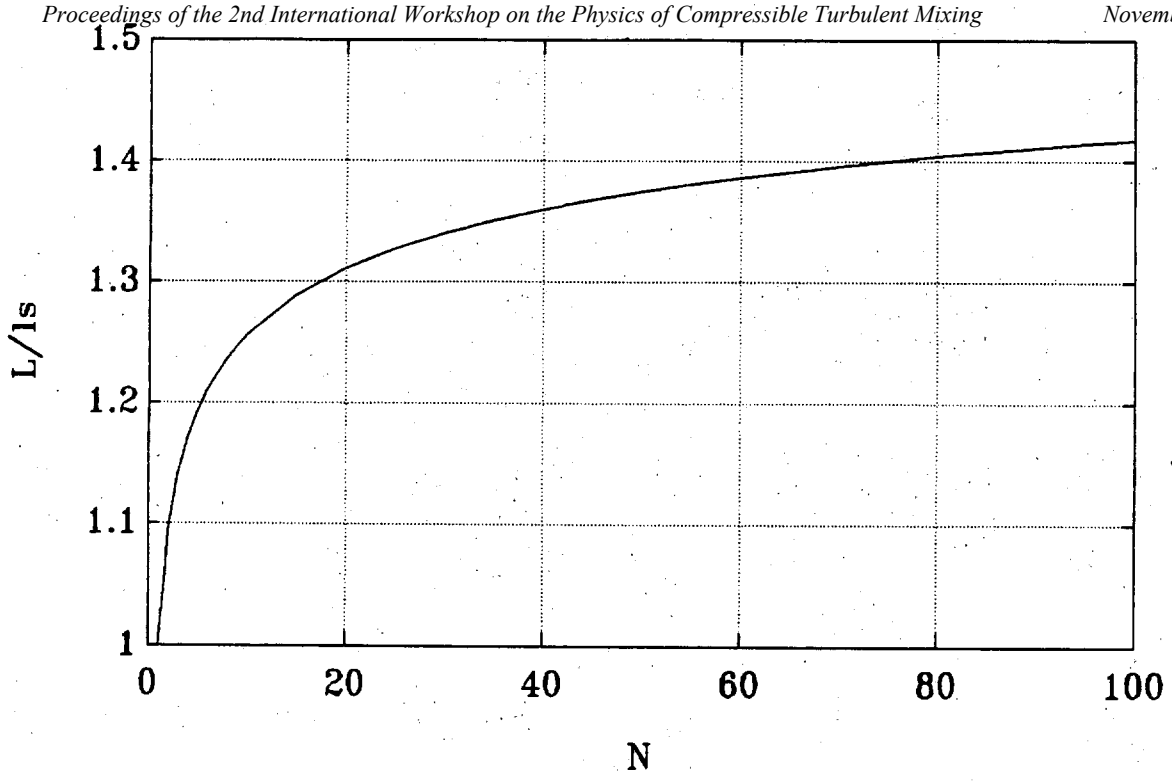
1.5
1.4
1.3
1.2
1.1
1
L/ls
0
20
40
60
80
100
N

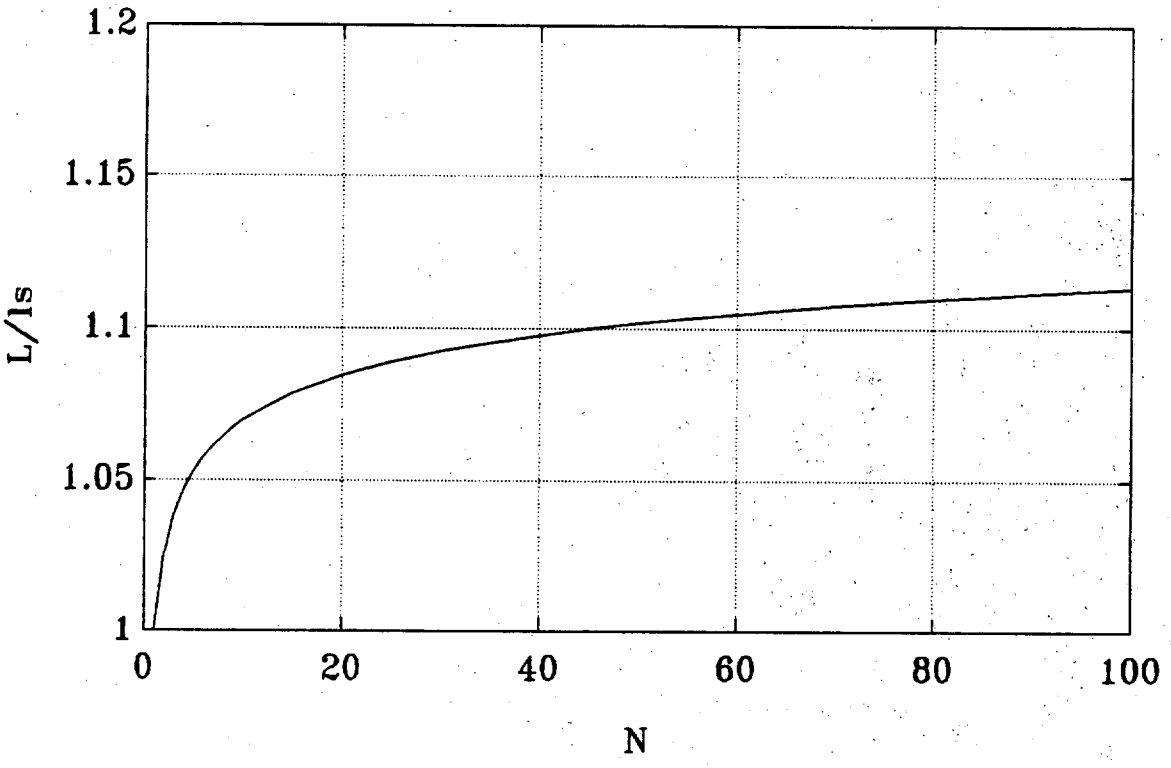
1.2
1.15
1.1
1.05
1
L/ls
0
20
40
60
80
100
N

Fig. 7, 8.

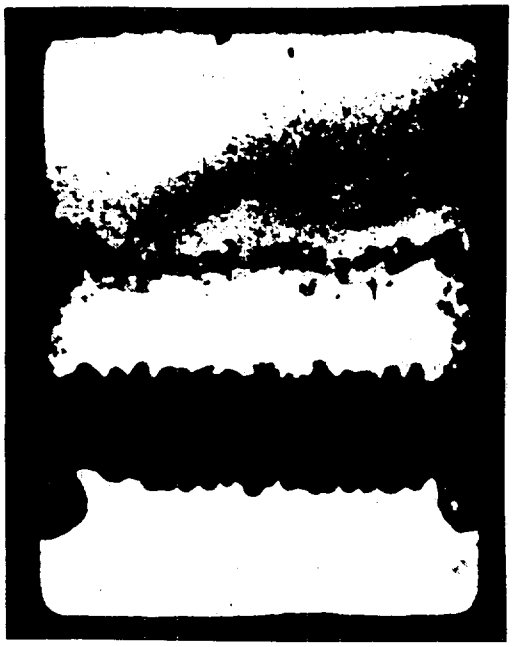

Fig. 9.

Fig. 10.

Fig. 11.

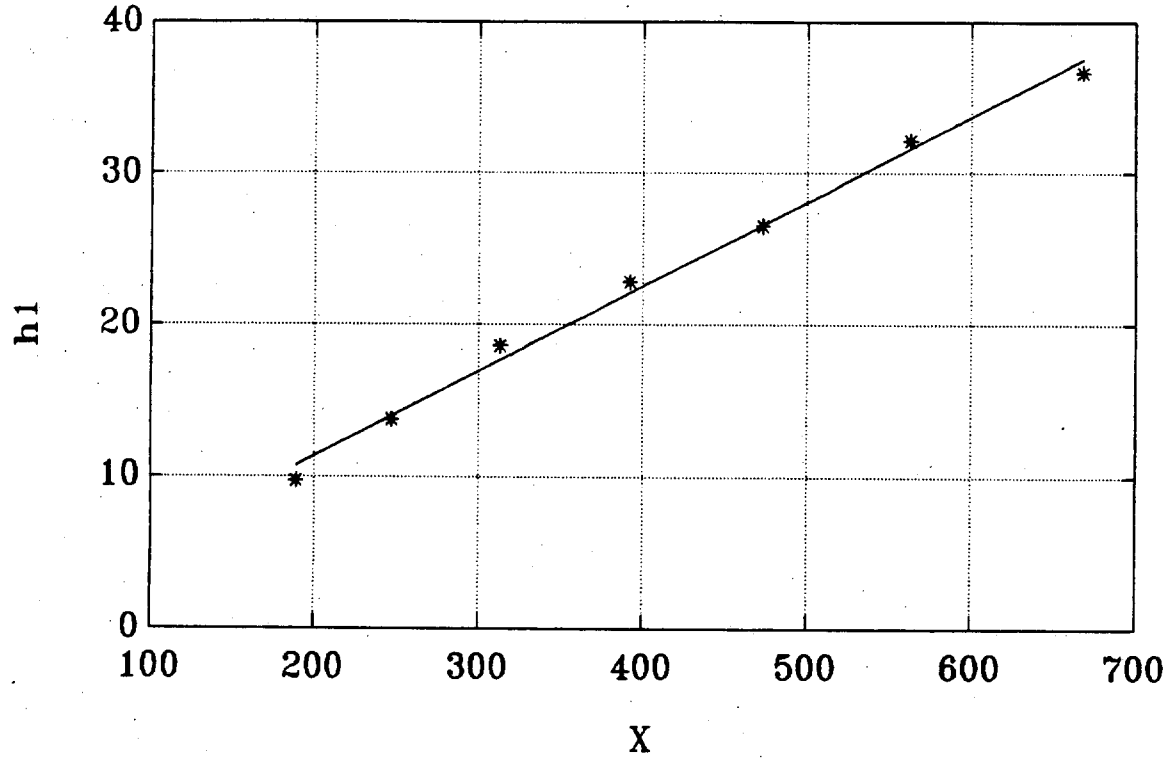
40
30
20
10
0
h1
100
200
300
400
500
600
700
X

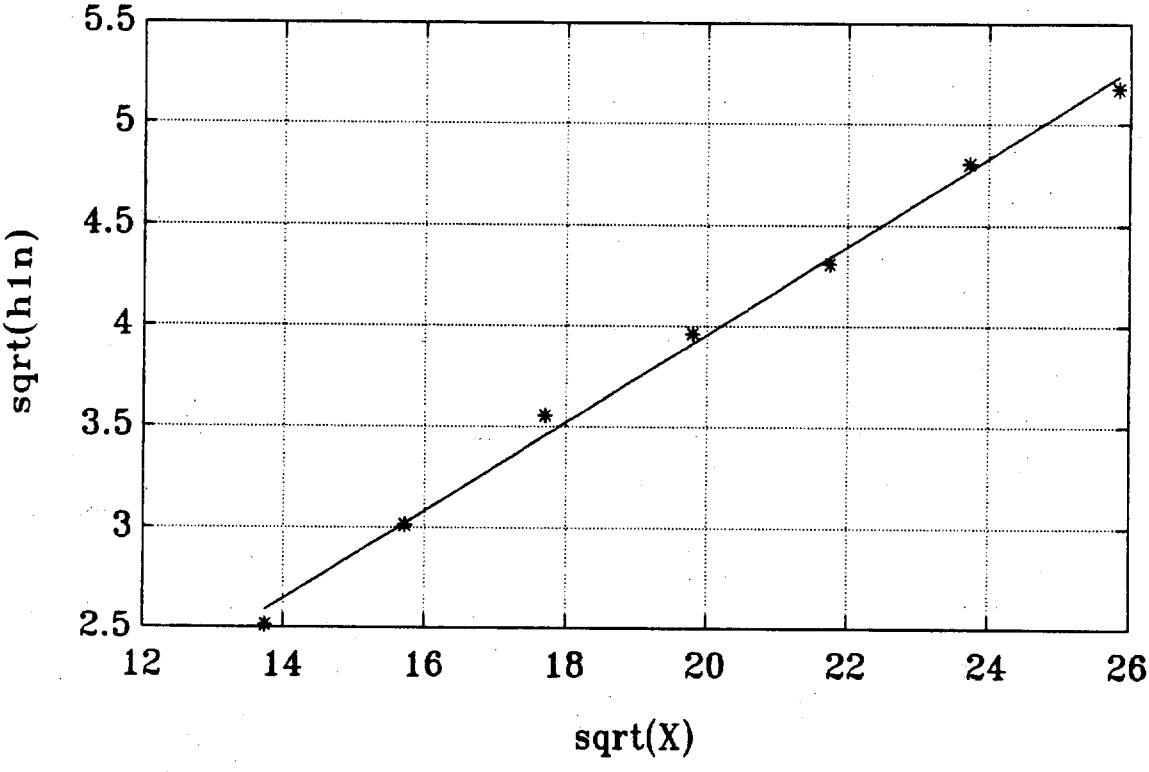
5.5
5
4.5
4
3.5
3
2.5
sqrt(h1n)
12
14
16
18
20
22
24
26
sqrt(X)

Fig. 12, 13.

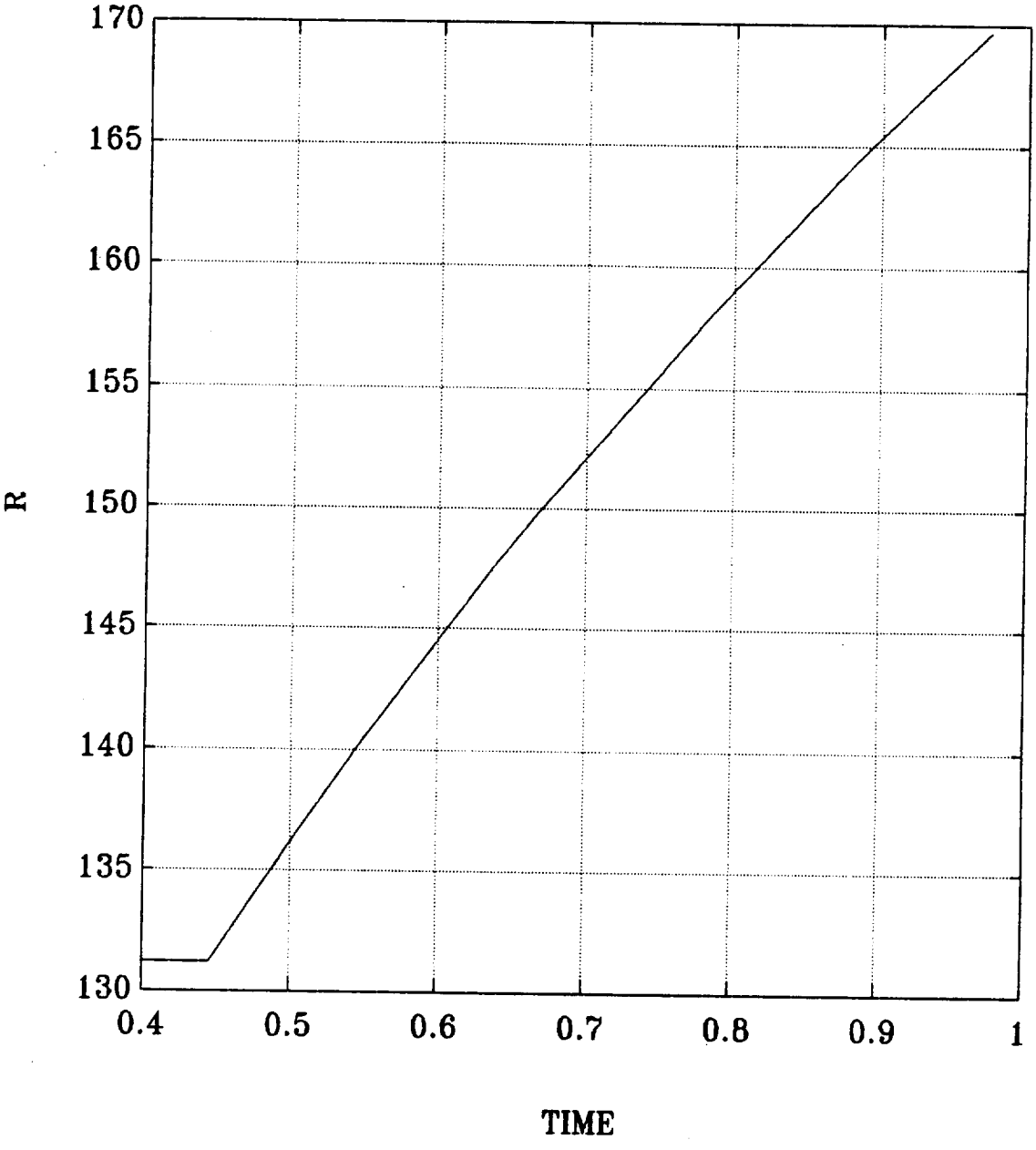

Fig. 14.

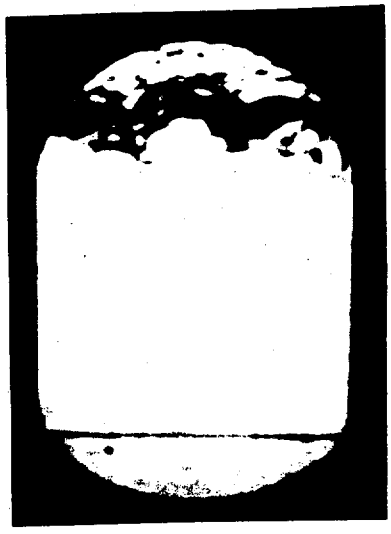

Fig. 15.

Fig. 16.

CHELYABINSK STATE UNIVERSITY

TO THE PROBLEM OF AUTOMODEL STATE IN RICHTMYER - MESHKOV'S MIXING

A.V. POLYONOV

TO THE PROBLEM OF AUTOMODEL STATE IN RICHTMYER - MESHKOV'S MIXING

A.V.Polyonov

It is pointed out that $K\varepsilon$ -model is inapplicable for describing Richtmyer-Meshkov's mixing without using the conditions for increment of the turbulent energy in the shock-wave front. Dependence of this condition on the existing turbulence anisotropy is illustrated. Considering the similarity of the initial perturbations with the same amplitude-wave length ratio,it is substantiated the existence of the asymptotic state, consisting in that the mixing development velocity in the initial portion is independent on the perturbation amplitude, however, this state lasts for the infinitesimal time while the initial amplitude of perturbations tends to zero.

Richtmyer-Meshkov's instability arises on the rough interface between media having different densities, while passing through this interface the shock wave, normally incident on the surface and generating the impulsive acceleration at the interface. The most essential difference between this form of instability and Rayleigh - Taylor's instability, which takes place while prolonged accelerating the interface, consist in that the turbulent energy source in one case (Rayleigh - Taylor's) is the potential energy of the gravitational field, but in the other case - turbulent energy is pulsed generated during the short time interval close to the moment of passing the shock wave through the rough interface.

There are many works, devoted to theoretical investigation as well as to experimental observations of phenomena arising at the development of Richtmyer-Meshkov's instability (see, for example, /1/ - /4/). It is indicated /1/ that increasing the perturbation amplitude at the interface is satisfactory described by the following relation :

$$\dot{a} = 2\pi \frac{a_0}{\lambda} A \cdot \Delta v \qquad (1)$$

where a_0 and λ are initial amplitude and perturbation length, respectively, A is Atwood's number $A = \frac{\rho_1 - \rho_2}{\rho_1 + \rho_2}$, Δv is interface velocity changing as a result of passing the shock wave through it. (Values of a_0, ρ_1, ρ_2 are taken directly after the shock - wave passing). Applicability of the equation (1) means that the only characteristic parameter with the dimensional representation of velocity is Δv.

The arising pulsation velocity after the shock-wave passing is proportional to the growth rate of perturbation amplitude. Then, the pulsation motion energy per mass unit is equal to $K \sim \frac{a_0^2}{\lambda^2}$. Perturbations behind the shock wave and the rarefaction wave cover the region, being away from the interface at a distance equal to the wave length. This determines the size of the region with the nonzero pulsation velocity. That is why, the total turbulent energy, generated by the shock wave, is directly proportional to

the square of the characteristic amplitude and inversely proportional to the average length of the perturbation wave. This conclusion is in agreement with the given in /4/ result of Leith's estimation. This conclusion also points to dependence of arising turbulence on some values, characterizing the initial perturbation on the surface, and that is why, the supposition of existing the stage independing on initial perturbations, mentioned in /4/, is not indisputable.

The quoted above evaluation of the turbulent energy may be generilized to the case of passing the shock wave through the mixing zone:

$$K \sim \frac{\ell_{\parallel}^2}{\ell_{\perp}^2}(\Delta v)^2 \quad ; \quad E_{tot} \sim \frac{\ell_{\parallel}^2}{\ell_{\perp}^2} \cdot \ell_{\perp} \cdot (\Delta v)^2$$

where $\ell_{\parallel}$, $\ell_{\perp}$ are characteristic scales of turbulence in the direction of propagating the shock wave and in the perpendicular direction, respectively: Relation $\frac{\ell_{\parallel}}{\ell_{\perp}}$, connected with the anisotropy of turbulence $\chi = \frac{K_{\parallel}}{K_{\perp}}$, may be considered to be constant for the wide range of cases.

Some rather general conclusions can be deduced from considerations of similarity. Let us consider two systems differing by the amplitude of initial perturbations (a_0 and a) which are similar to each other. At large Reynolds number, i.e., in cases of great interest for the practical applications, it is possible to neglect the effect of viscosity and that is why, the gas dynamics similarity takes place.

Let us assume that we have the distribution in time and space of some dimensionless physical value, for example, the average volume concentration of one of the components in the mixing zone $\alpha_0(x,t)$ in the system characterizing by the amplitude a_0. Then, the distribution of the average volume concentration, for the case of developing the perturbations with the amplitude a, will be equal to

$$\alpha(x,t) = \alpha_0\left(\frac{x a_0}{a}, \frac{t a_0}{a}\right)$$

For the mixing layer thickness which can be determined as the value, being proportional to $\int_{-\infty}^{\infty} \alpha(x,t)\left[1-\alpha(x,t)\right] dx$ it is possible to obtain the equation:

$$\frac{L(t)}{a} = \frac{L_0\left(\frac{a_0 t}{a}\right)}{a_0} \quad \text{or} \quad L(t) = a \cdot f\left(\frac{t}{a}\right) \qquad (2)$$

As it was noticed above, the only characteristic parameter with the dimensional representation of velocity, needed for making the variable in (2) dimensionless is Δv - changing the velocity of boundary while passing the shock wave through it. Then the equation (2) may be written in the form:

$$L = a \cdot \varphi(\xi) \qquad \text{where} \quad \xi = \frac{t \cdot \Delta v}{a}$$

The rate of the zone width development in the initial moment turns out to be independent on the initial perturbations

$$L' = \Delta v \cdot \varphi'(\xi)$$

The experiment demonstrates that during the substantial time interval the function appears to be linear: $L = 2a + \beta t$

i.e. $\varphi(\xi) = 2 + \gamma \cdot \xi$

where γ - empirical constant ($\beta = \gamma \cdot \Delta v$). Then, while the amplitude tends to zero we shall have the asymptotic state for which

$$L_{\text{asympt.}} = \gamma \cdot \Delta v \cdot t$$

i.e. the growth rate of turbulent zone in this condition coincides with that for the particular initial perturbation.

However, this state remains at $a \to 0$ during the time interval $\tau \to 0$ that follows from (2), where we suppose $\varphi(\xi)$ to be limited at $\xi \to \infty$. (Upon consideration of similarity it is possible to state that conserving the growth rate of turbulent mixing may take place till K = constant).

In the turbulent diffusion approximation we have: $L^2 = D_t \cdot t$, whence, considering $D_t \sim \ell_{\parallel} \cdot K^{1/2}$, we obtain:

$$L' \sim \Delta v \, \frac{\ell_{\parallel}}{\ell_{\perp}} \, \frac{\ell_{\parallel}}{L}$$

It should be remembered that we supposed perturbations to be similar, i.e. identity of the relation $\frac{a}{\lambda}$, that usually takes place in cases of practical applications; however, possibility of extending the mixing zone development rate, obtained from the experiments with the shock tube, to the far case of developing in some particular application requires an additional substantiation.

Performing two-dimensional computations may help to form our representations, realizing the direct simulation of instability development and Richtmyer-Meshkov's mixing. These representations are necessery for creating semiempirical models, suitable for describing this form of turbulence. They help us to obtain the condition in the shock-wave front for $K\varepsilon$ -model or to define more exactly the used ones (see, for example, /5/). Computations of this mixing form, while applying $K\varepsilon$ -model, but without using the condition in the shock-wave front, are not representative. Let us discuss this problem in more detail. The equation for turbulent energy generation is written in the form (/6/), (we retain only principal members):

$$\frac{dK}{dt} = \frac{1}{\rho} g \mathcal{D}_t \left(\nabla \rho - \frac{\partial \rho}{\partial p}\Big|_S \nabla p \right) + \dots$$

For simplicity, we consider the gas in which the abrupt change in density is reached by the abrupt change in the internal energy. The equation may be rewritten in the form:

$$\frac{dK}{dt} = \frac{1}{\rho} g \mathcal{D}_t \nabla S$$

where S - specific entropy. ($\mathcal{D}_t$ - turbulent diffusion coefficient). If we integrate this equation for obtaining the turbulent energy increment in the shock-wave front, we obtain:

$$\Delta K = \frac{1}{\rho_\varphi} (\Delta v)_\varphi \cdot (\nabla S)_\varphi \cdot \mathcal{D}_{t.\varphi}$$

All values in the right side of the latter equation are taken in the shock-wave front, and they are discontinuous, however, the main difficulty is that $(\nabla S)_\varphi \to \infty$.

LITERATURE

1.R.D.Richtmyer
Comm.Pur.Appl.Math. 8(1960)297

2.E.E.Meshkov
Izvestiya Ac.Sci. USSR,Mech. of Fl.&Gas,1969, N 5,p.151

3.E.E.Meshkov
Some Experimental Results Investigation of Gravitational Instability of Interfaces between Media with Different Densities. Preprint. Inst.Appl.Math.by name of M.V.Keldish. Ac.Sci.USSR,1981

4.M.Brouillette, B.Sturtevant
Growth Induced by Multiple Shock Waves Normally Incident on Plane Gaseous Interfaces. Proceeding of CNLS Annual Conference, May 16,1988, Elsevier, 1989

5.V.V.Nikiforov
Turbulent Mixing at Interface between Media with Different Densities.
Sov.J.VANT,Ser.Theor.& Appl.Physics, 1985, Issue 1,p.3-8

6.V.E.Neuvazhaev, V.G.Yakovlev
Gravitational Mixing Computation by $K\varepsilon$-Model.
Sov.J.VANT,Ser.Theor.& Appl.Physics, 1988, Issue 1, p.28-36

CHELYABINSK STATE UNIVERSITY

TO THE PROBLEM OF AUTOMODEL SLOPE DETERMINATION AT GRAVITATIONAL MIXING DEVELOPMENT

A.V. POLYONOV

TO THE PROBLEM OF AUTOMODEL SLOPE DETERMINATION AT GRAVITATIONAL MIXING DEVELOPMENT

by

A.V.Polyonov

ABSTRACT

In the report relative to determining the auromodel coefficient characterizing the velocity of mixing development, it is substantiated, on the basis of common self-similarity properties, the experimental result processing method, coming to plotting $L^{1/2}$ versus $\int g^{1/2} dt$ (L is the mixing zone width, g - acceleration).

Gravitational turbulent mixing development is usually described by the semiempirical model, equations of which include a number of coefficients, selected in according to some calibration experiments (see, for example, /1/,/2/.

One of main characteristics of the gravitational turbulence is the velocity of turbulent mixing development in the automodel case, which is realized in the system, consisting of two semi-infinite layers of incompressible fluid in a gravitation field while initiating the turbulent mixing by negligible perturbations and under negligible influence of viscosity, surface tension and other factors. The only parameter with the dimensional representation of length in this case is the combination of gt^2, that is why, the mixing zone width versus time may be written in the form

$$L = \alpha(A)\frac{g t^2}{2} \qquad (1)$$

where α - coefficient, depending only on the densities relation, characterized by Atwood's number $A = \frac{\rho_2 - \rho_1}{\rho_2 + \rho_1}$

Many experimental works are devoted to obtaining α (see, for example, /3/, /4/, /5/). One of the principal difficulties in evaluating α is the effects of the initial conditions of turbulence forming, that leads to deviation from automodel dependence of L on t^2 at the initial stage. This dependence is becoming linear, as usual, only asymptotically at large time values, reaching of which is difficult in each particular case. That is why, it is desirable to select such experimental data processing method, which allows to determine the value of automodel slope as early as possible.

Evaluating of α is possible, but only after setting the automodel state in the system, i.e. such system, any characteristics of which are determined only by parameters, characterising the state, as it is, and are independent of the history. Such parameters are the value of the mixing zone width L and acceleration g. Then, we have from consideration of dimensionality:

$$\frac{dL}{dt} = \beta g^{1/2} L^{1/2} \qquad (2)$$

whence we obtain

$$L^{1/2} = \frac{\beta}{2} g^{1/2} t + C \qquad (3)$$

where C - constant, connected with conditions of automodel state achievement.

If such state arises at the initial moment, when the mixing zone width is infinitesimal, then, from the expression (3) we have:

$$L = \frac{\beta^2}{2} \frac{g t^2}{2}$$

that coincides with the expression (1) ($\alpha = \frac{\beta^2}{2}$).

From the expression (2) it is possible to obtain generalization in case of the slight dependence of acceleration upon time. We have:

$$L^{1/2} = \frac{\beta}{2} \int g^{1/2} dt + C$$

This expression is available only for the sufficient small value of $\dot{g}$. The acceptable rate of changing g is larger than the period of the main scale vortexes:

$$\tau_g \ll \tau_\ell = \frac{\ell}{(2K)^{1/2}}$$

Treating $\ell = 0.25L$, evaluating K from the potential energy change $K \approx \frac{1}{12} A g L$

we obtain the condition for $\dot{g}$:

$$\dot{g} \ll \frac{2 A^{1/2} g^{3/2}}{L^{1/2}}$$

When this condition is not satisfied, the automodel state is not reached and, that is why, there are no basis to speak about the automodel slope.

The conducted treatment shows the way to evaluate α. It is necessary to plot $L^{1/2}$ versus $\int g^{1/2} dt$; beginning from the moment, when the derivative $\frac{dL^{1/2}}{g^{1/2} dt}$ stops to change, it is possible to consider that the automodel state of the system is reached, whence the value of the derivative $\frac{dL^{1/2}}{g^{1/2} dt}$ determines the automodel slope: $\beta = \sqrt{2\alpha} = \frac{2}{g^{1/2}} \frac{dL^{1/2}}{dt}$

The described way is not a new one. It is known that Kikoin with collaborators /6/ processed likewise the results of his experiments. V.E.Neuvazhaev and V.G.Yakovlev have studied the features of solving the equations for the semiempirical model TURINB as well as have recommended the above described method of the experimental data processing /7/. Such method is also used in the work /8/. However, as there is no Kikoin's substantiation of the chosen method for the data processing, and results, obtained by V.E.Neuvazhaev and V.G.Yakovlev, may be referred not to a common feature of the automodel motion but to the feature of the specific model, and also, possibly, due to lack of information, a large number of experimental works keep on using the method of the automodel slope determination by means of plotting L versus, so-called, transit distance, which is proportional to t^2, but not $\sqrt{L}$ versus $\int g^{1/2} dt$ (see, for example, /4/,/5/). Whence, according to the equation (3)

$$L = \left(\frac{\beta g^{1/2} t}{2} + \frac{C}{2} \right)^2$$

i.e., the slope is not a constant one at the moment when the automodel state is realized. The automodel slope in plotting L versus t^2 is reached only asymptotically, when $t \to \infty$, and its determination by such method is not so accurately.

As an example, we consider the automodel mixing developing in which, for simplicity, we shall consider that the automodel state setting takes place immediately. Let us consider the following two cases of mixing development:

a) corresponding to some initial roughness, charactering by the value of L_0 ;

b) subjected to some delay t_0.

For the case a) we have the following, with using (3):

$$2L^{1/2} = \beta g^{1/2} t + 2L_0^{1/2} ;$$

$$L = L_0 + \frac{\beta^2}{2} \frac{g t^2}{2} + \beta g^{1/2} L_0^{1/2} t ;$$

whence

$$\frac{dL}{dS} = \frac{dL}{d\left(g\frac{t^2}{2}\right)} = \alpha \left(1 + \sqrt{\frac{L_0}{\alpha S}} \right),$$

where

$$S = \frac{g t^2}{2}$$

In the treated example of dependence of $\sqrt{L}$ on t the value of $\alpha = \beta^2/2$ is directly determined and exactly, but the value of α is overestimated by 10% (for $\alpha \simeq 0.2$) by using the dependence of L on t^2 even at the transit distance being equal to $S = 500\, L_0$.

b)Using (3) we have:

$$2L^{1/2} = \beta g^{1/2}(t - t_0)$$

$$L = \frac{\beta^2}{2}\frac{gt^2}{2} + \frac{\beta^2}{2}\frac{gt_0^2}{2} - \frac{\beta^2}{2} g t t_0$$

$$\frac{dL}{dS} = \frac{\beta^2}{2}\left(1 - \frac{t_0}{t}\right)$$

The latter example demonstrates that for reaching more higher accuracy than 10% in evaluating α, it is necessary to plot L versus t^2 for $t > 10\, t_0$, whereas the value of α may be determined at once by means of plotting $\sqrt{L}$ versus t, i.e. at $t \gtrsim t_0$.

LITERATURE

1. V.E.Neuvazhaev, V.G.Yakovlev
Model and Method of Numerical Computation of Turbulent Mixing Interface, Moving with Acceleration.
Sov.J.VANT, 1984, 2(16),p.17-25

2. V.A.Andronov, S.M.Bahrah, E.E.Meshkov,V.V.Nikiforov et al.
Experimental and Numerical Simulation of Turbulent Mixing in One-Dimensional Flows.
Rep. of Ac.Sci. USSR, 1982,v.264, N 1, pp.76-82

3. A.M.Vasilenko, O.M.Buryakov, V.F.Kuropatenko, V.I.Olhovskaya, V.P.Ratnikov,V.G.Yakovlev
Experimental Investigating the Gravitational Instability and Turbulization of Flow at Interface between Noble Gases.
Report at the Workshop on Physics of Compressible Turbulent Mixing, Princeton,USA,October 24-27,1988

4. Y.A.Kucherenko, G.G.Tomashev et al.
Experimental Investigation of Gravitational Turbulent Mixing in Automodel Mode.
Sov.J. VANT,1988, 1, p.13

5. David L.Youngs
Experimental Investigation of Turbulent Mixing by Rayleigh--Taylor Instability.
Report at the Workshop on Physics of Compressible Turbulent Mixing, Princeton, USA, October 24-27,1988

6. I.K.Kikoin,D.I.Voskoboinik, V.A.Dmitrievskii, V.I.Stefanov
Experimental Investigation of Turbulent Mixing of Fluids in the Field of Acceleration.
Report LIP Ac.Sci.USSR, Moscow,1953

7. V.E.Neuvazhaev, V.G.Yakovlev
Moving into the Automodel Mode in the Problem of Turbulent Mixing of two Liquid Layers in the Constant Gravity Field. Numerical Methods of Continuum Mechanics.
Ac.Sci.USSR, Siberian Department, v.2, N 3,p.127

8.P.F.Linden, J.M.Renado, C.P.Caulfield
Molecular Mixing in Rayleigh-Taylor Instability.
Report at the Workshop on Physics of Compressible Turbulent Mixing, Princeton, USA, October 24-27, 1988

Structure of Lagrangian Turbulence

J. A. Viecelli
Lawrence Livermore National Laboratory
Livermore, California
November 16, 1989

Topics

Geometrical scaling relationships deduced from theory

The Lagrangian structure function

Derivation of structure function exponent

Comparison of the theory with,
- **2D hydrodynamic computations**
- **Optical scattering results**
- **Meteorological data**
- **Dissipation fluctuation data**

The Lagrangian structure function yields scaling exponents for the mixing geometry

2D Slab average area fraction	**d=7/3**
3D Volume fraction	**d=23/6**
2D Slab average perimeter length	**d=4/3**
3D Surface area	**d=17/6**
3D Plane section perimeter length	**d=11/6**
2D Chord lengths	**d=1/3**
3D Chord lengths	**d=5/6**
3D Intermittency exponent	$\mu = H = 1/6$
2D Intermittency exponent	$\mu = H = 2/3$

A Lagrangian structure function can be defined from the number density N of Lagrange particles

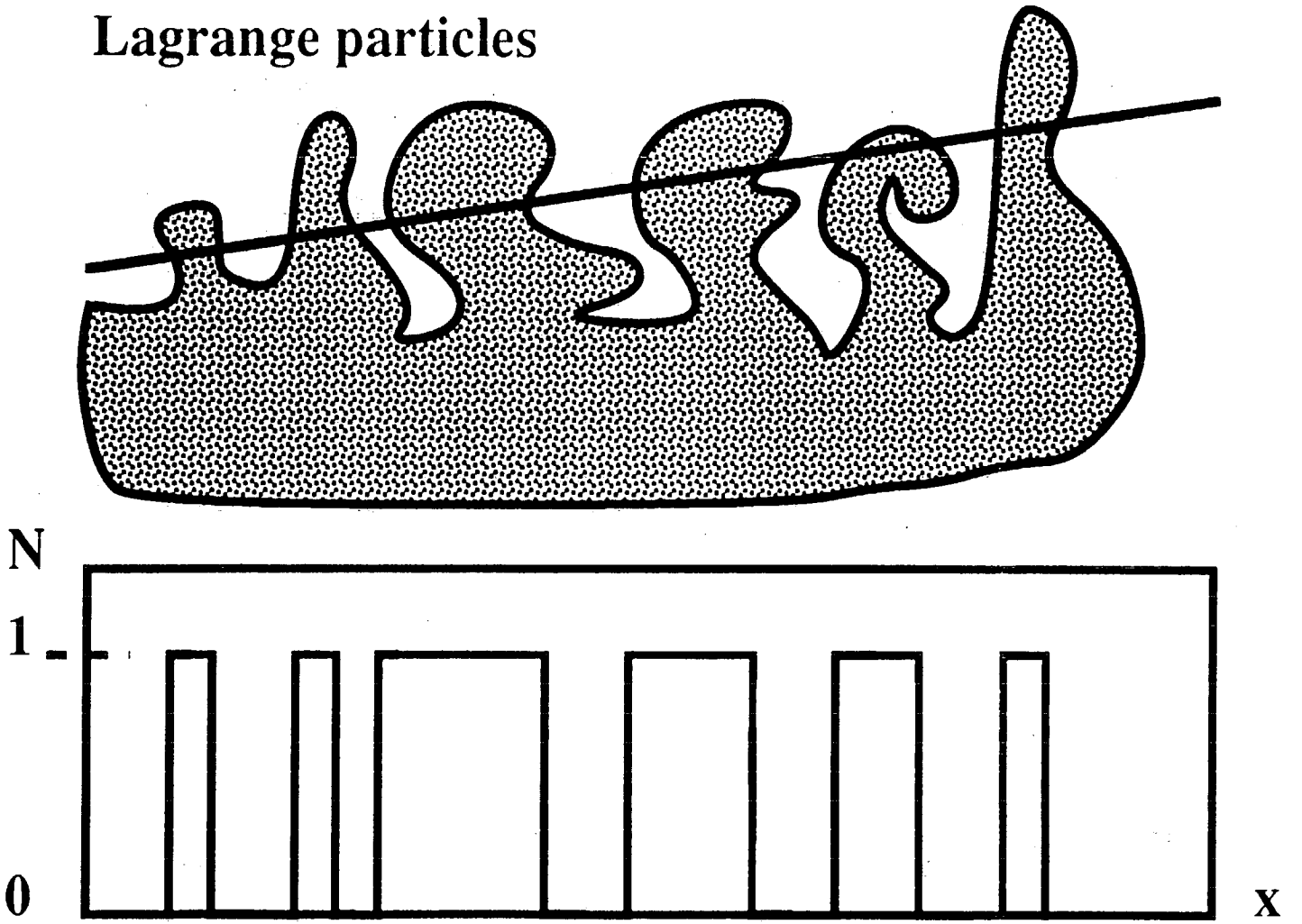

N is neither continuous nor differentiable

The Lagrangian structure function exponent depends on the Euclidean dimension

Two dimensions

$$D_L(r) \equiv \left\langle [N(r_o + r) - N(r_o)]^2 \right\rangle = C_L^2 \, r^{4/3}$$

Hurst exponent=2/3

Three dimensions

$$D_L(r) \equiv \left\langle [N(r_o + r) - N(r_o)]^2 \right\rangle = C_L^2 \, r^{1/3}$$

Hurst exponent=1/6

The Lagrange structure function exponent can be deduced from Richardson's diffusion law I

Small cloud of particles at t=0

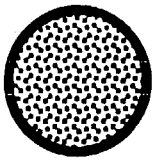

Late time mixing stage

$N_f \equiv$ **rms fraction of particles at radius r**

Richardson's Law

$$\langle r^2 \rangle = r^{4/3}\, t$$

$$N_f \cong \sqrt{\langle r^2 \rangle} \cong \sqrt{r^{4/3}} \cong r^{2/3}$$

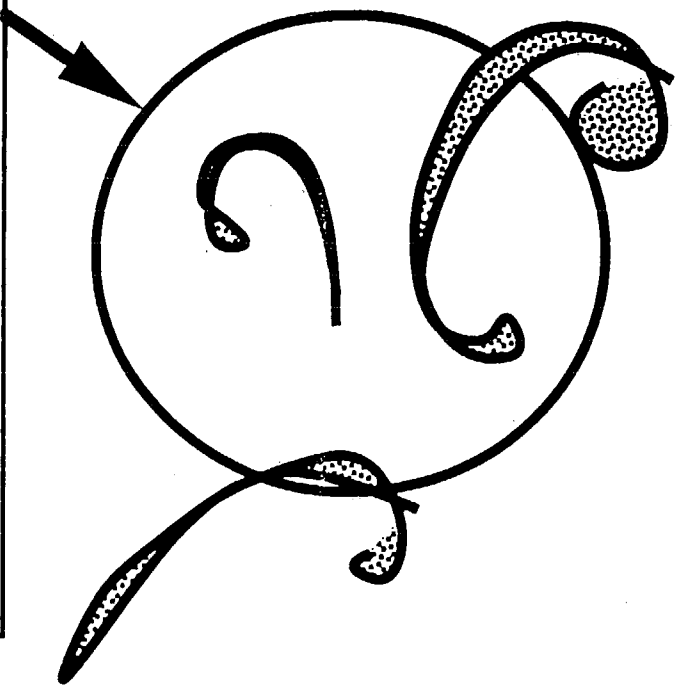

The Lagrange structure function exponent can be deduced from Richardson's diffusion law II

Number density of particles

$$N(r) \cong \frac{N_f}{r} \cong \frac{1}{r^{1/3}} \qquad \text{2D}$$

$$N(r) \cong \frac{N_f}{r^2} \cong \frac{1}{r^{4/3}} \qquad \text{3D}$$

Particle count

$$\Gamma(r) = \int_0^r 2\pi r N(r)\,dr \cong r^{5/3} \qquad \text{2D}$$

$$\Gamma(r) = \int_0^r 4\pi r^2 N(r)\,dr \cong r^{5/3} \qquad \text{3D}$$

The Lagrangian structure function is obtained from the integrated particle count

$\Gamma(r) \equiv$ average number of particles inside disk or sphere of radius r

Two dimensions

$$D_L(r) = \frac{1}{2\pi r}\frac{\partial \Gamma^2}{\partial r} = \frac{\Gamma}{\pi r}\frac{\partial \Gamma}{\partial r}$$

Three dimensions

$$D_L(r) = \frac{1}{4\pi r^2}\frac{\partial \Gamma^2}{\partial r} = \frac{\Gamma}{2\pi r^2}\frac{\partial \Gamma}{\partial r}$$

Sample Lagrangian geometry produced by 2D Rayleigh-Taylor instability of a plane layer

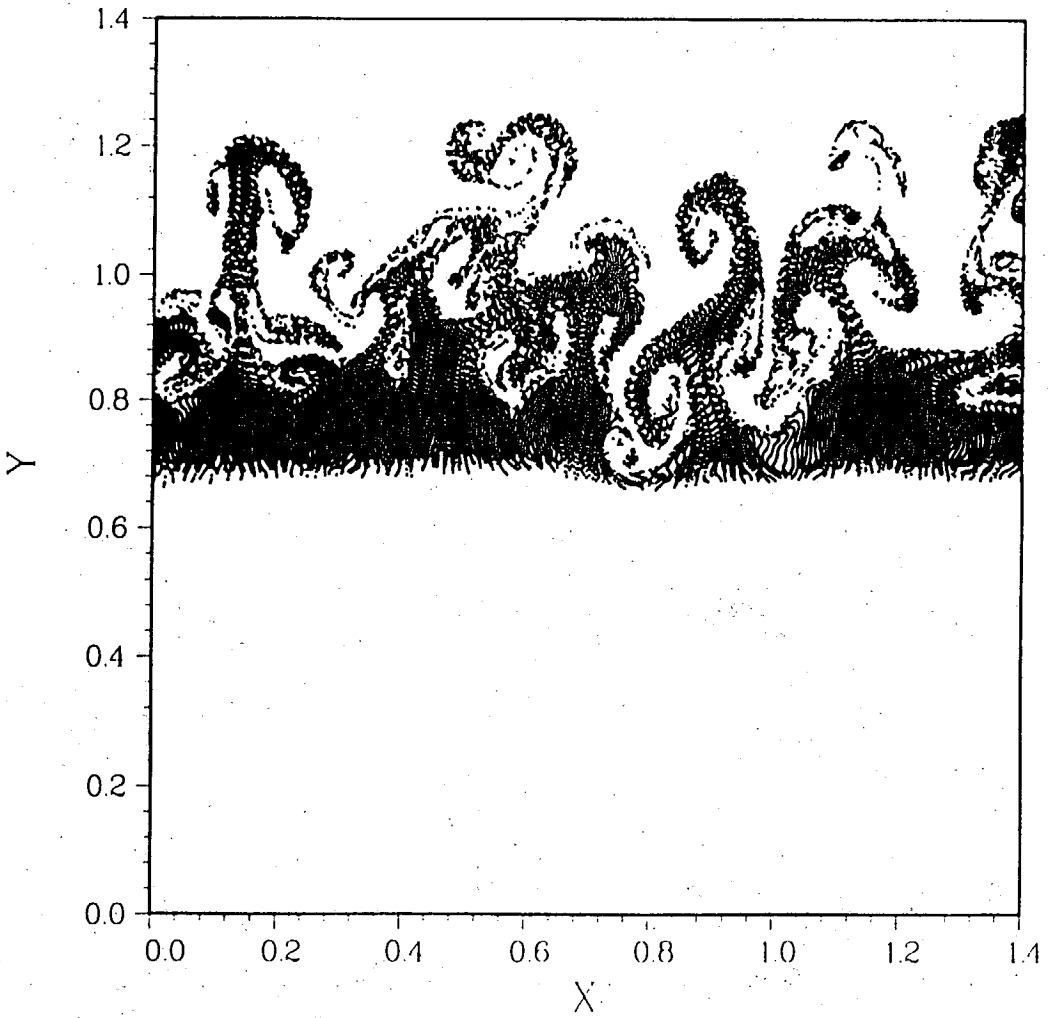

Integrated Lagrange particle counts obtained from the Rayleigh-Taylor problem

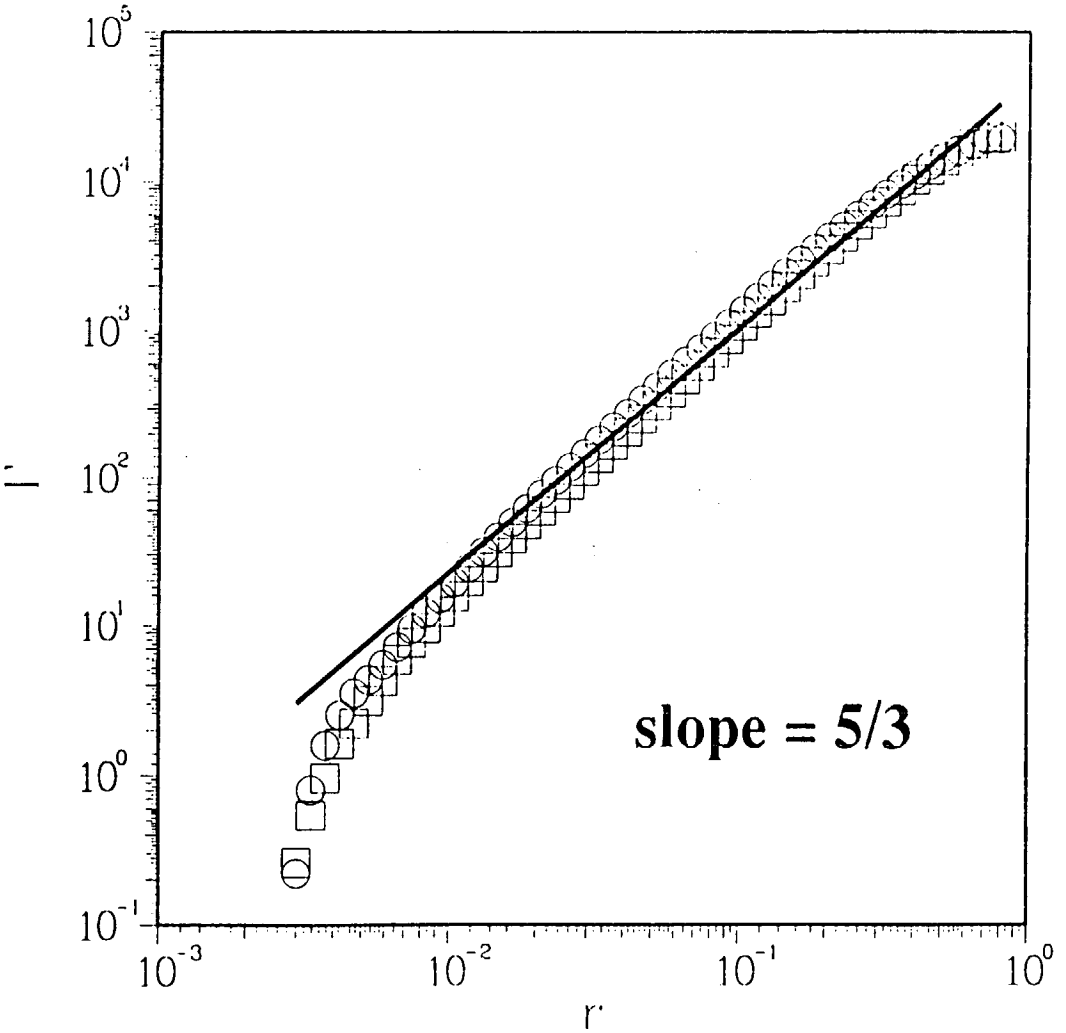

Chord length probability density obtained from the Rayleigh-Taylor problem

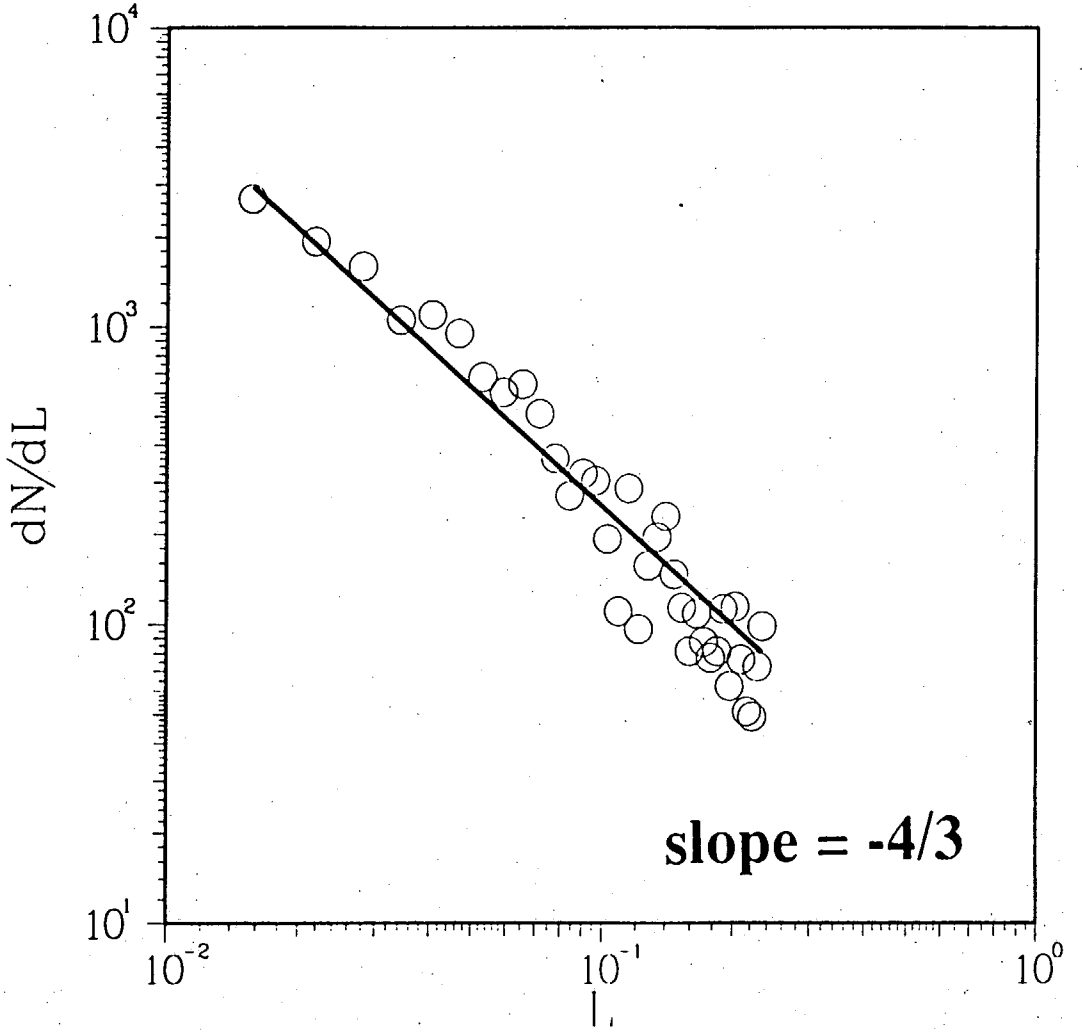

Integrated vortex filament count obtained from 2D shear flow instability

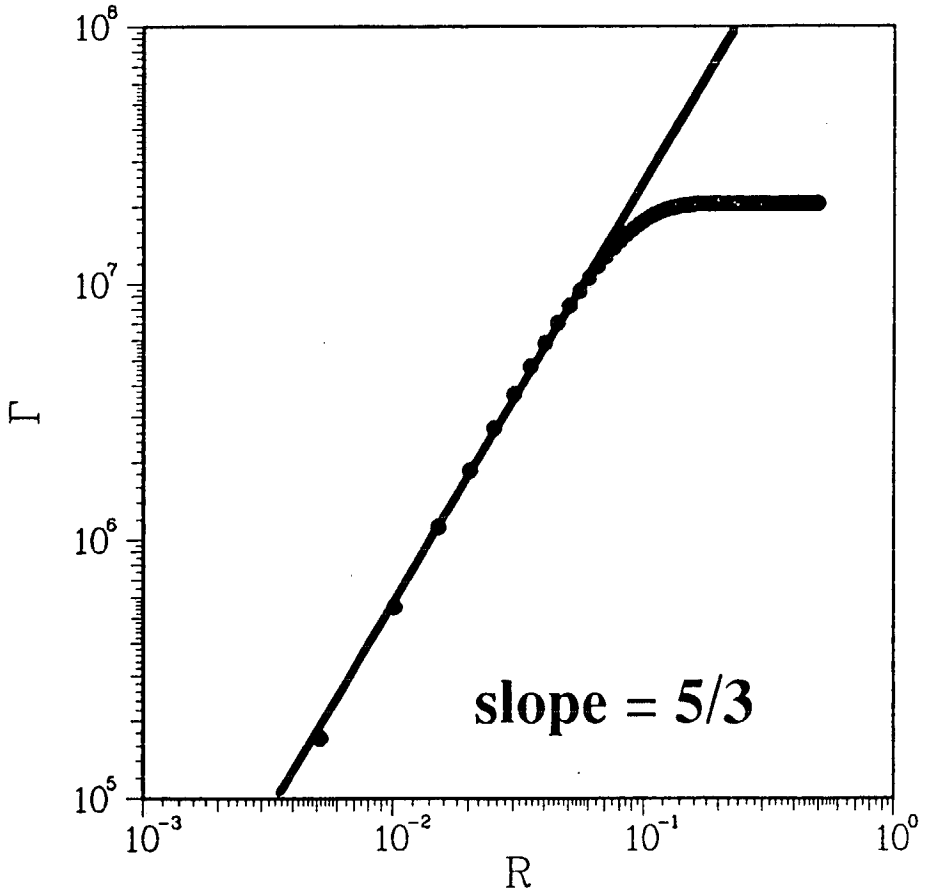

3D plane section perimeter scaling exponent is consistent with optical scattering results I

The optical phase shift depends on the length of temperature contours in plane section

$$\langle \varphi^2 \rangle \propto \langle \delta n(\lambda)^2 \rangle \times f\left(\frac{L}{\lambda}\right)$$

ray paths **Temperature contours**

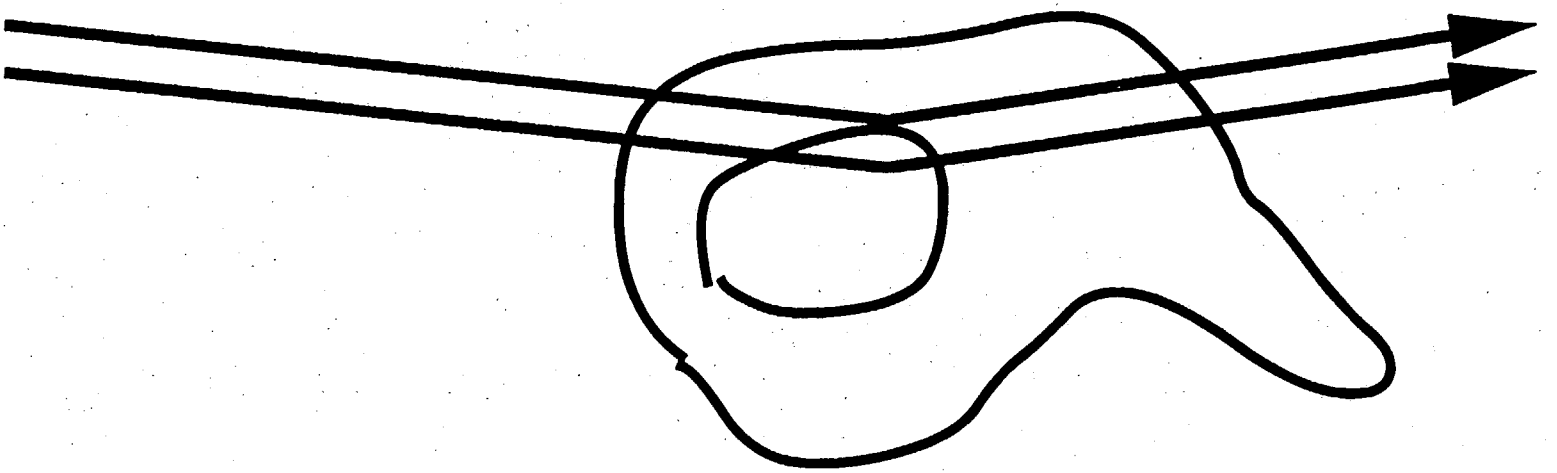

3D plane section perimeter scaling exponent is consistent with optical scattering results II

Path length dependence

$$\sigma_I^2 \cong 0.657\, C_n^2 \left(\frac{2\pi}{\lambda}\right)^{7/6} L^{11/6}$$

$$\langle \varphi^2 \rangle \cong \sigma_I^2$$

Rearranging

$$< \varphi^2 > \cong \text{const} \times [\, C_n^2 \lambda^{2/3} \,] \times \left[\frac{L}{\lambda}\right]^{11/6}$$

$$\langle \varphi^2 \rangle \propto \langle \delta n(\lambda)^2 \rangle \times f\left(\frac{L}{\lambda}\right)$$

Scaling result for slab average perimeter length is consistent with cloud and rainfall patterns

Area-perimeter relationship for 2D fractal object

$$\text{Log}\, P = \frac{d}{2} \text{Log}\, A$$

Lovejoy, Science 218, 9 (1982)

Measured area-perimeter relationship from radar and satellite data over scale range from 10km to 10,000 km. Found

$$\text{Log}\, P \approx 0.675\ \text{Log}\, A$$

$$d \approx 1.35$$

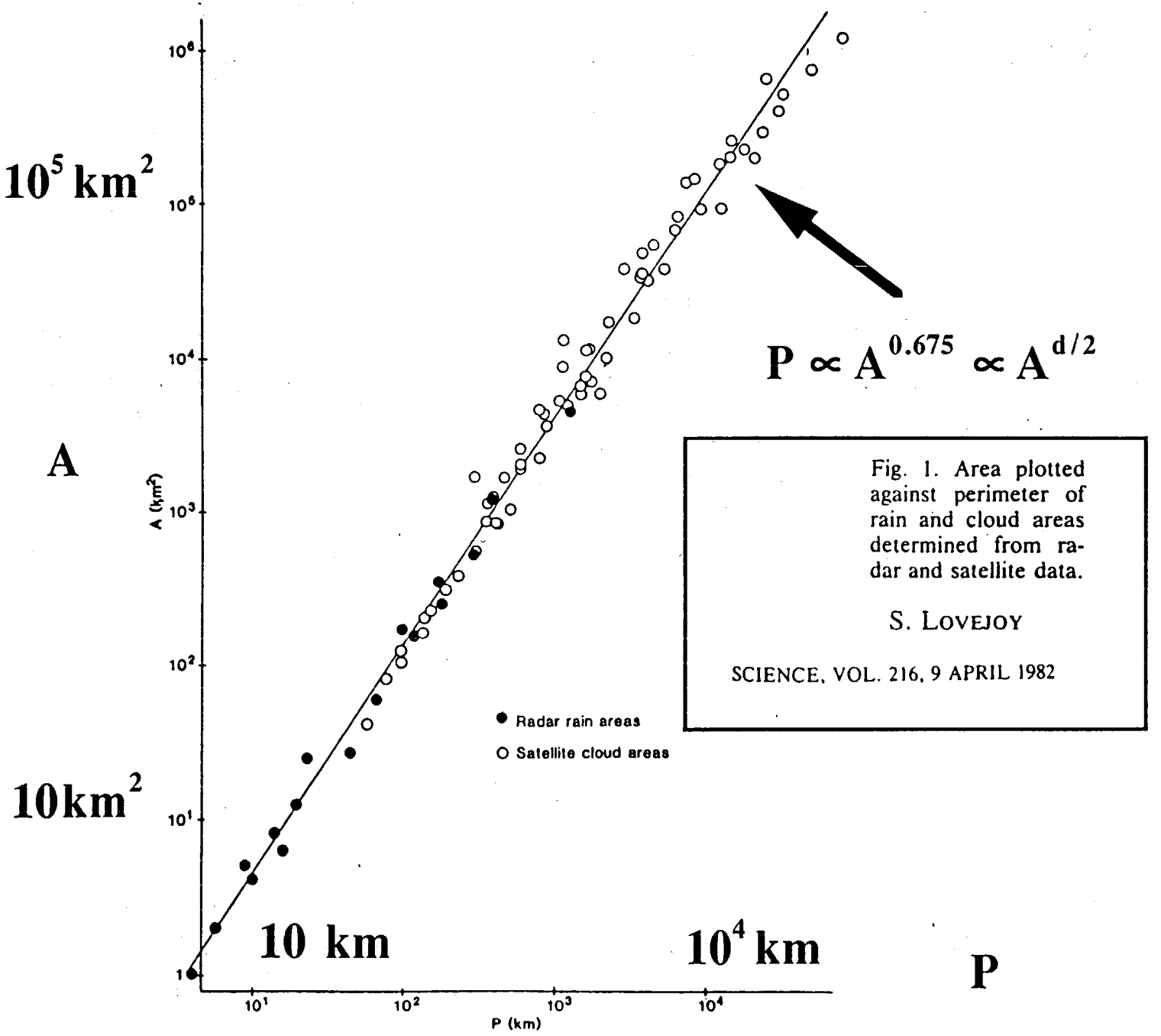

Fig. 1. Area plotted against perimeter of rain and cloud areas determined from radar and satellite data.

S. LOVEJOY

SCIENCE, VOL. 216, 9 APRIL 1982

Hurst's measurements of H for natural phenomena related to the large scale features of the weather indirectly yield an estimate of the intermittency exponent for 2D turbulence

	measured H
Rainfall	0.70 ± 0.09
Temperatures	0.68 ± 0.09
Pressures	0.63 ± 0.07
River & lake levels	0.71 ± 0.08

Hurst referred to the method he invented for analyzing hydrological statistics as "rescaled range analysis" or R/S analysis. His exponent K is the Hurst exponent.

data from Hurst et al. 1965 (Feder 1988)

3D Hurst exponent is consistent with recent measurements of dissipation fluctuation statistics

$$\langle \varepsilon(x+r)\varepsilon(x) \rangle \propto r^{-\mu_\varepsilon}$$

There is a long history of measurement, but Antonia and Anselmet et al. showed that previous results based on power spectra need to be corrected for subtraction of the mean square of the dissipation fluctuations

Current estimates	$\mu_\varepsilon \cong \mu \equiv H$
Antonia et al. (1981)	**0.2**
Anselmet et al. (1984)	0.2 ± 0.05

Shocks and Turbulence

Doug Rotman

Lawrence Livermore National Laboratory

Pleasanton, USA *Edited by V. Rupert*

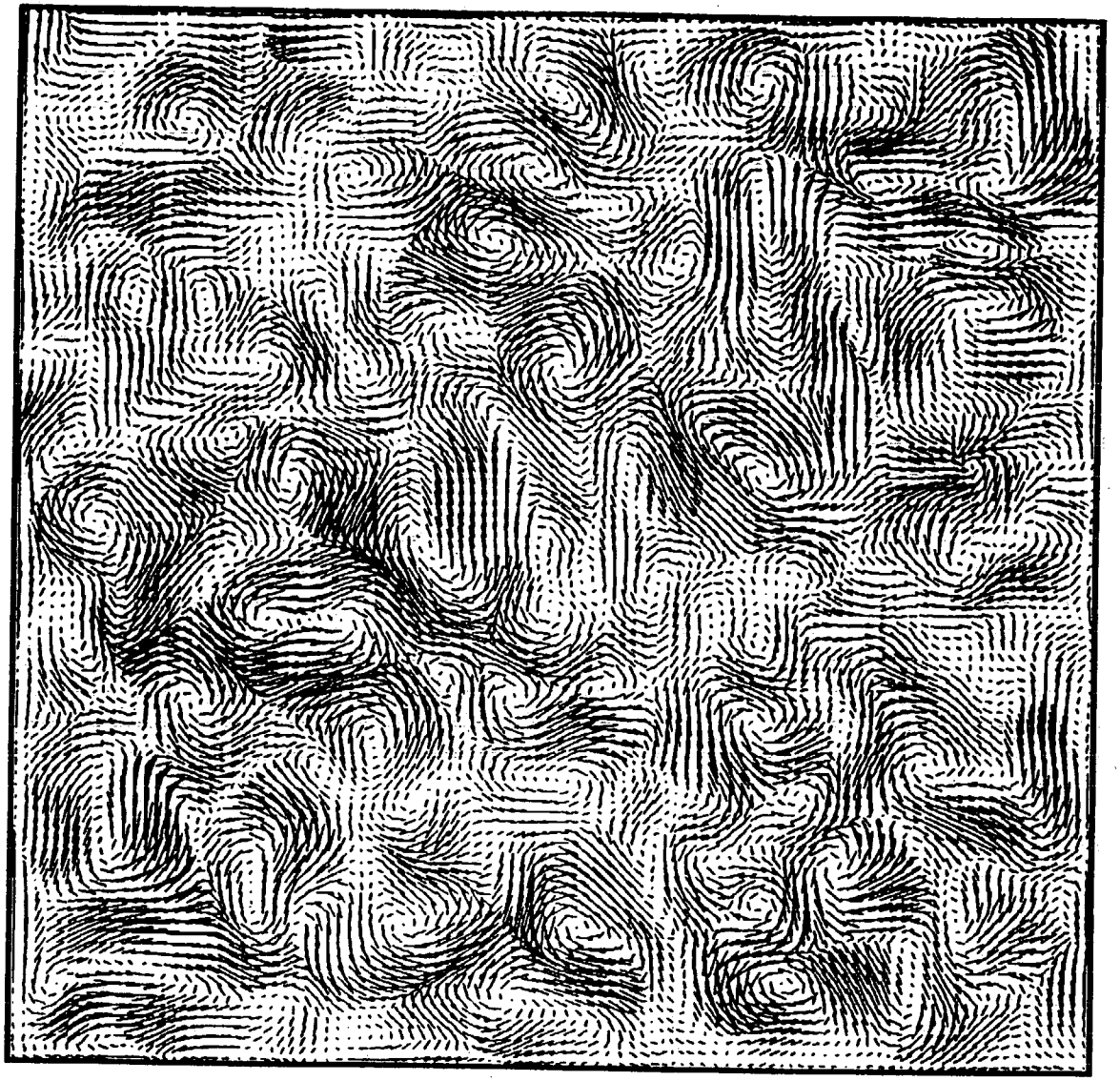

Initial Turbulent Velocity Field

Pleasanton, USA *Edited by V. Rupert*

Spectrum of Initial Turbulent Field

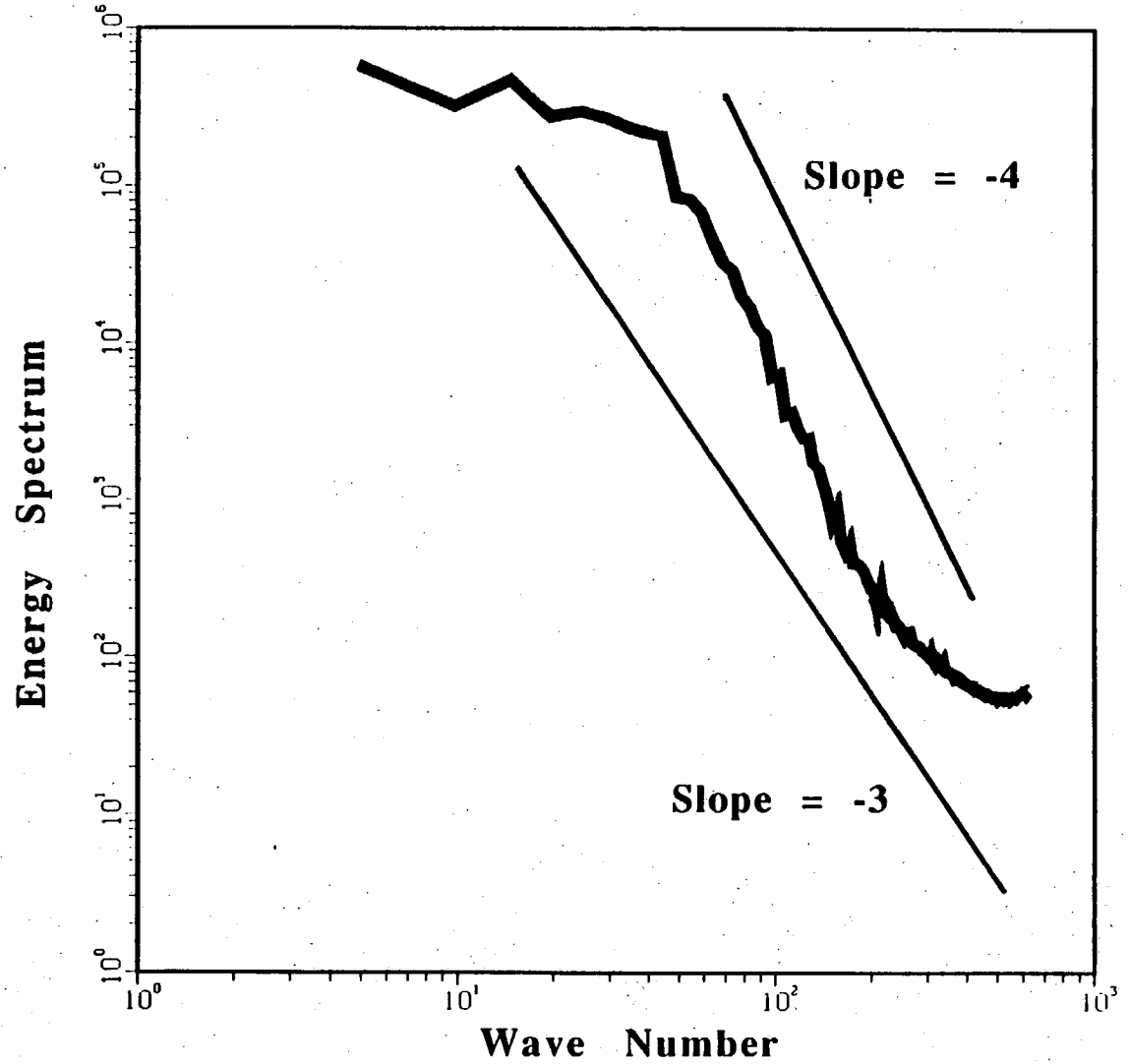

Turbulence Level = 0.04%

Density Ratio = 2.78

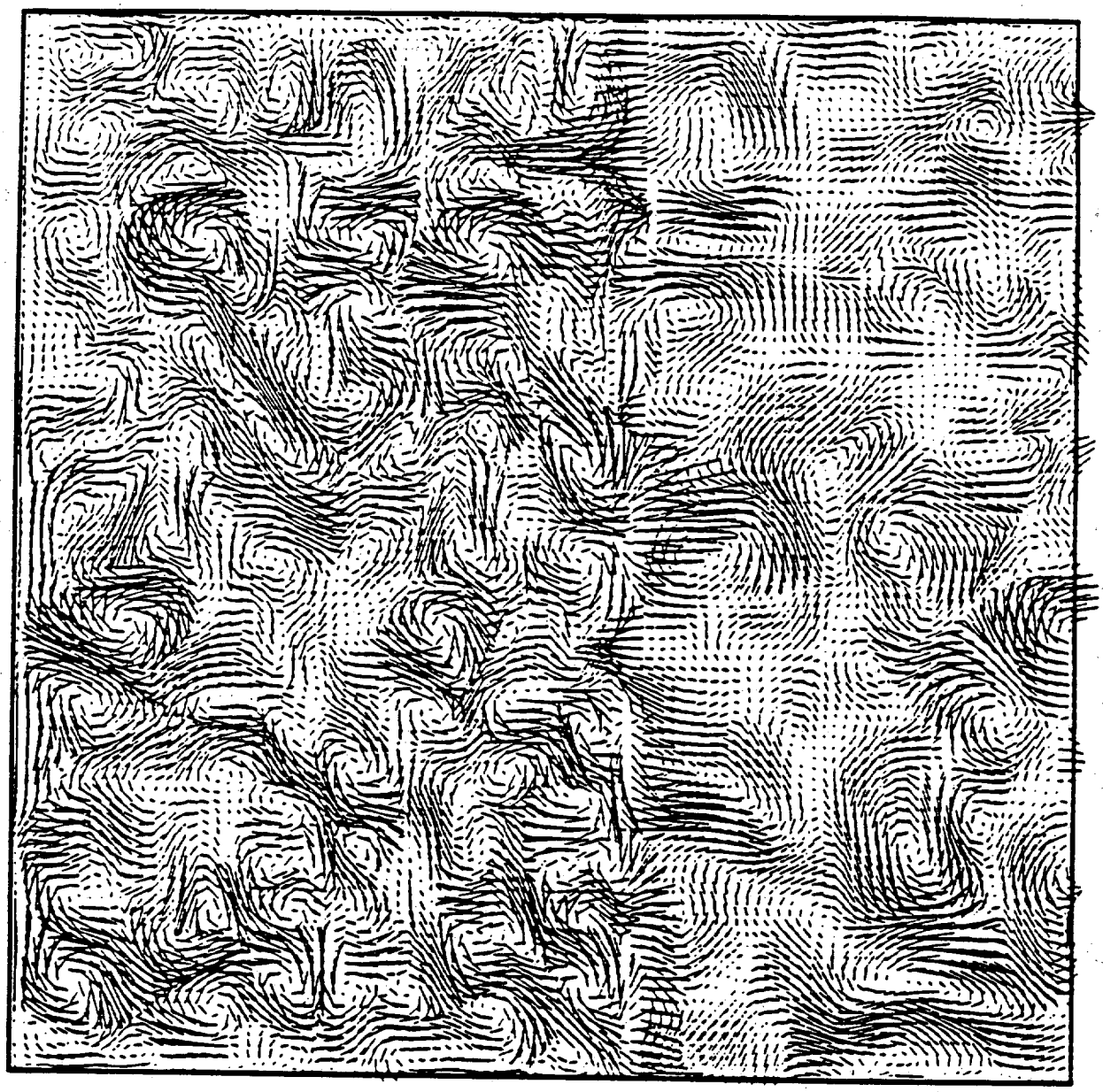

Velocity Field

Pleasanton, USA *Edited by V. Rupert*

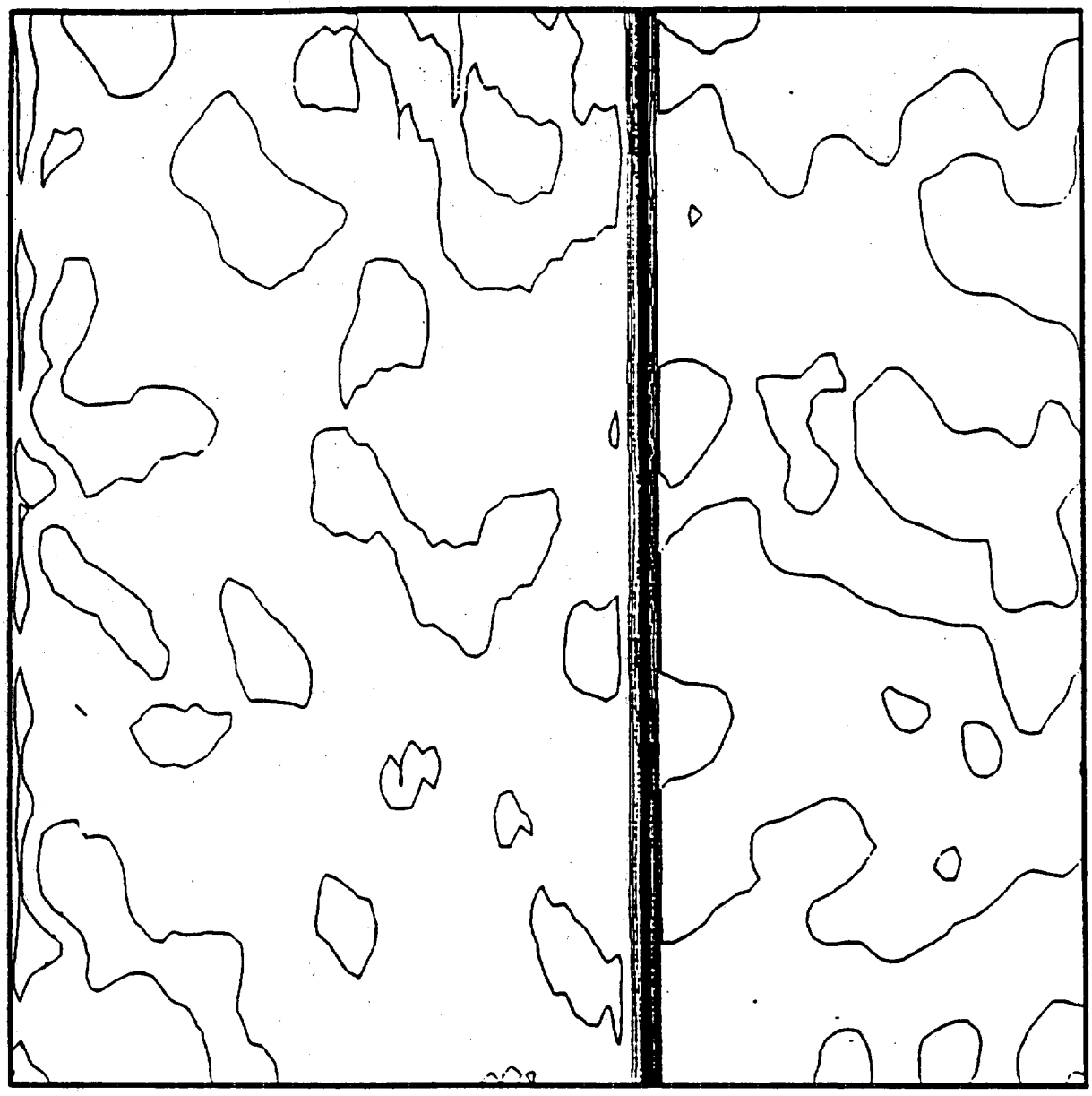

Density Contour

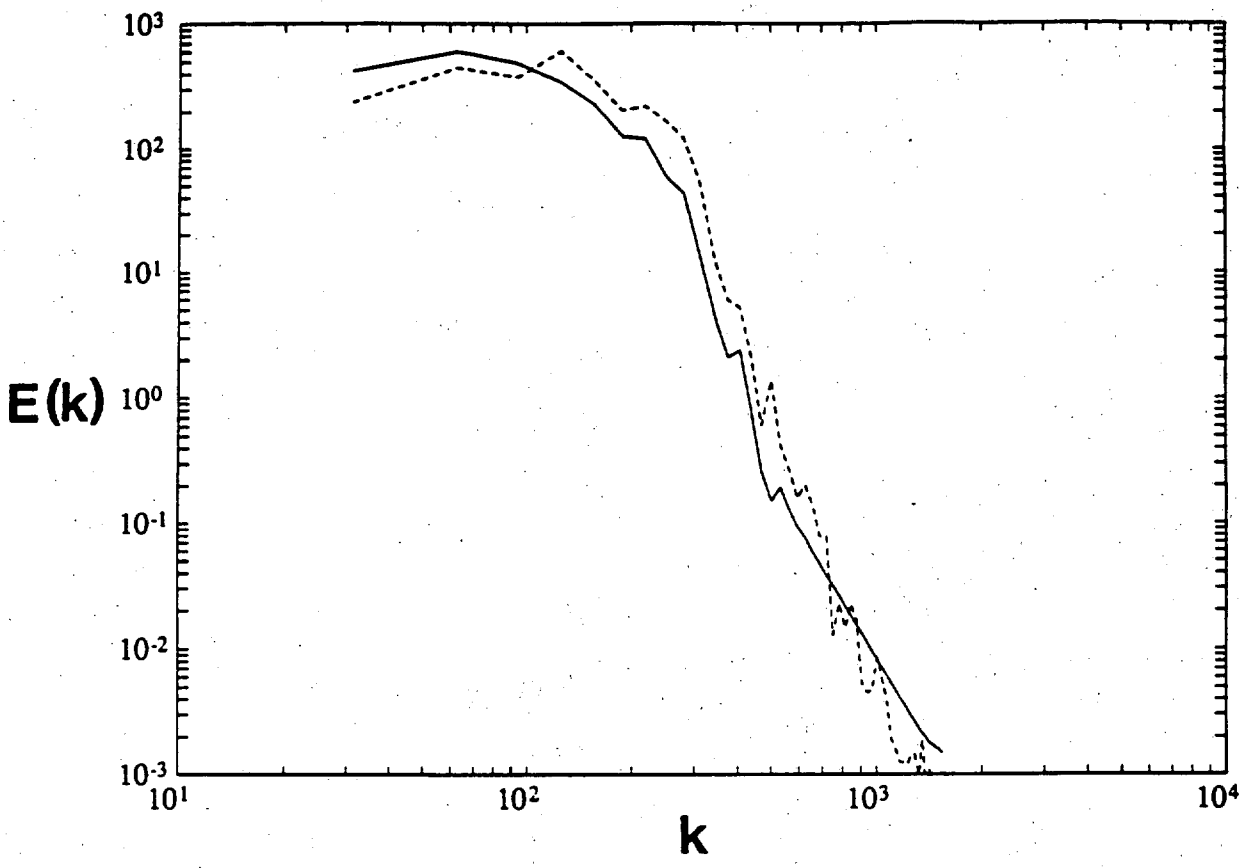

$$\tilde{k} = \frac{\int k\, E(k)\, dk}{\int E(k)\, dk}$$

$$\frac{\tilde{k}_{after}}{\tilde{k}_{before}} = 1.4$$

Turbulence Level = 25.%

Density Ratio = 2.78

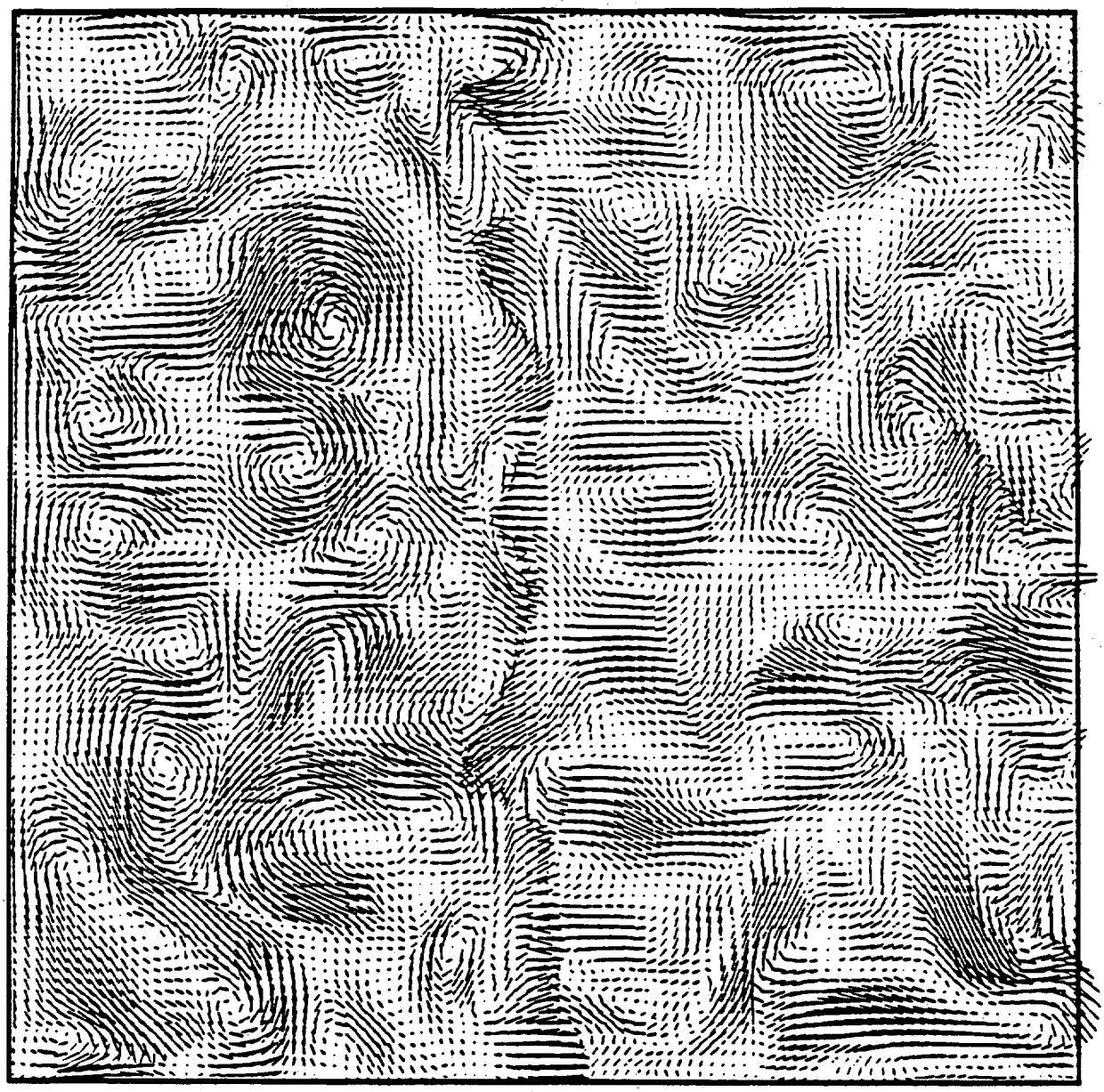

Velocity Field

Pleasanton, USA *Edited by V. Rupert*

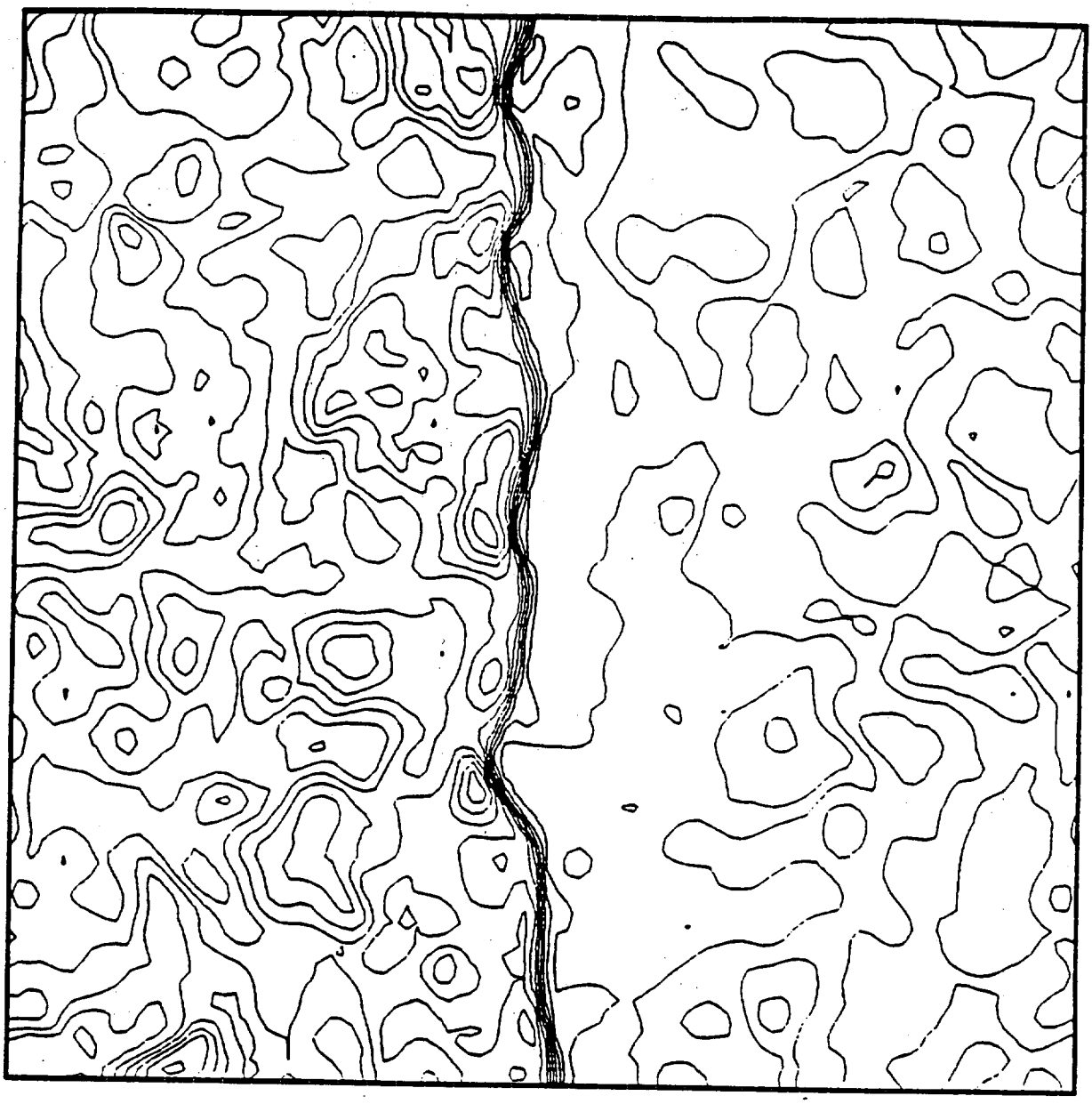

Density Contour

Pleasanton, USA *Edited by V. Rupert*

Turbulence Amplification vs. Initial Turbulent Kinetic Energy

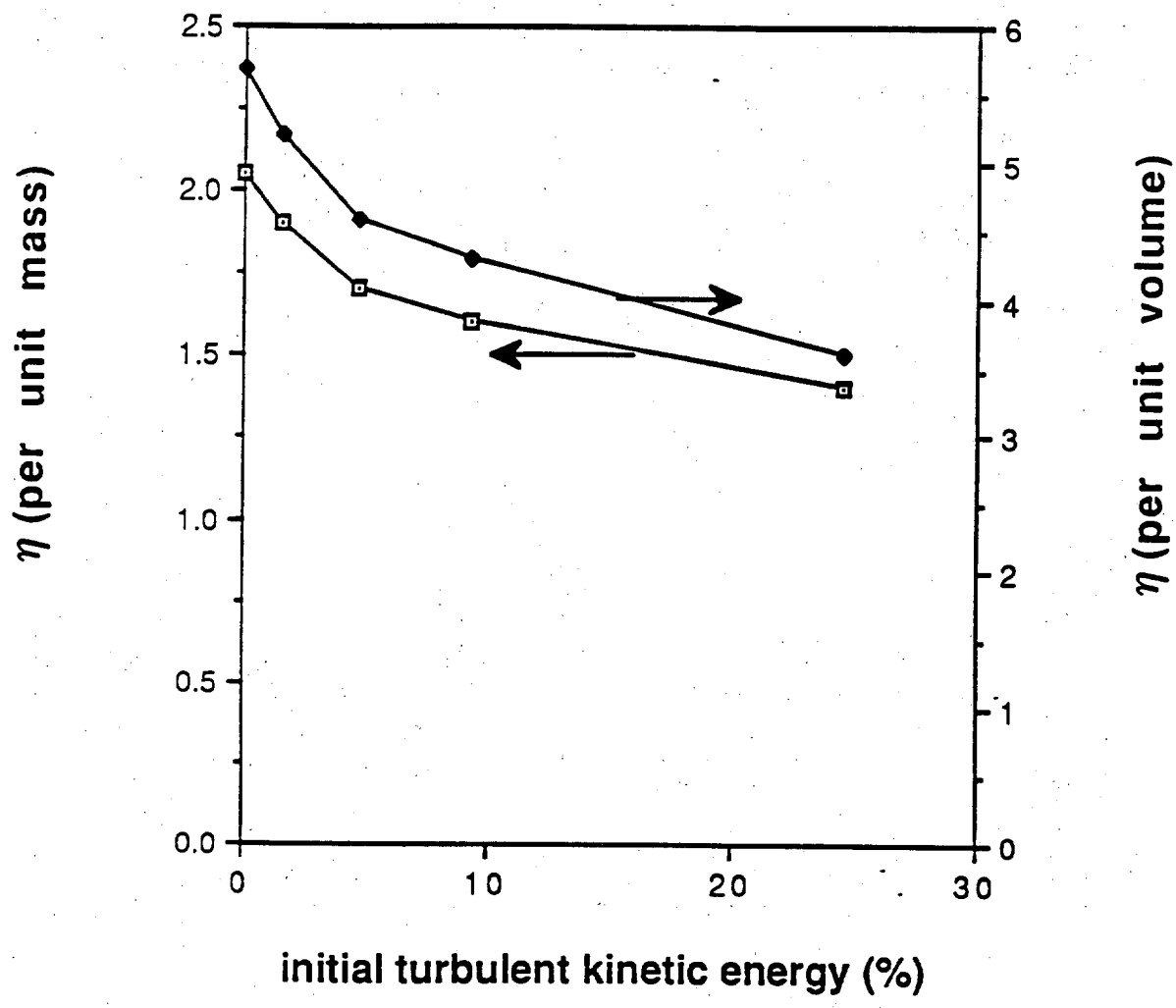

$$\eta = \frac{\left(\frac{1}{2}\left(u'^2 + v'^2\right)\right)_{\text{post shock wave}}}{\left(\frac{1}{2}\left(u'^2 + v'^2\right)\right)_{\text{pre shock wave}}}$$

Turbulence Amplification vs. Mach Number

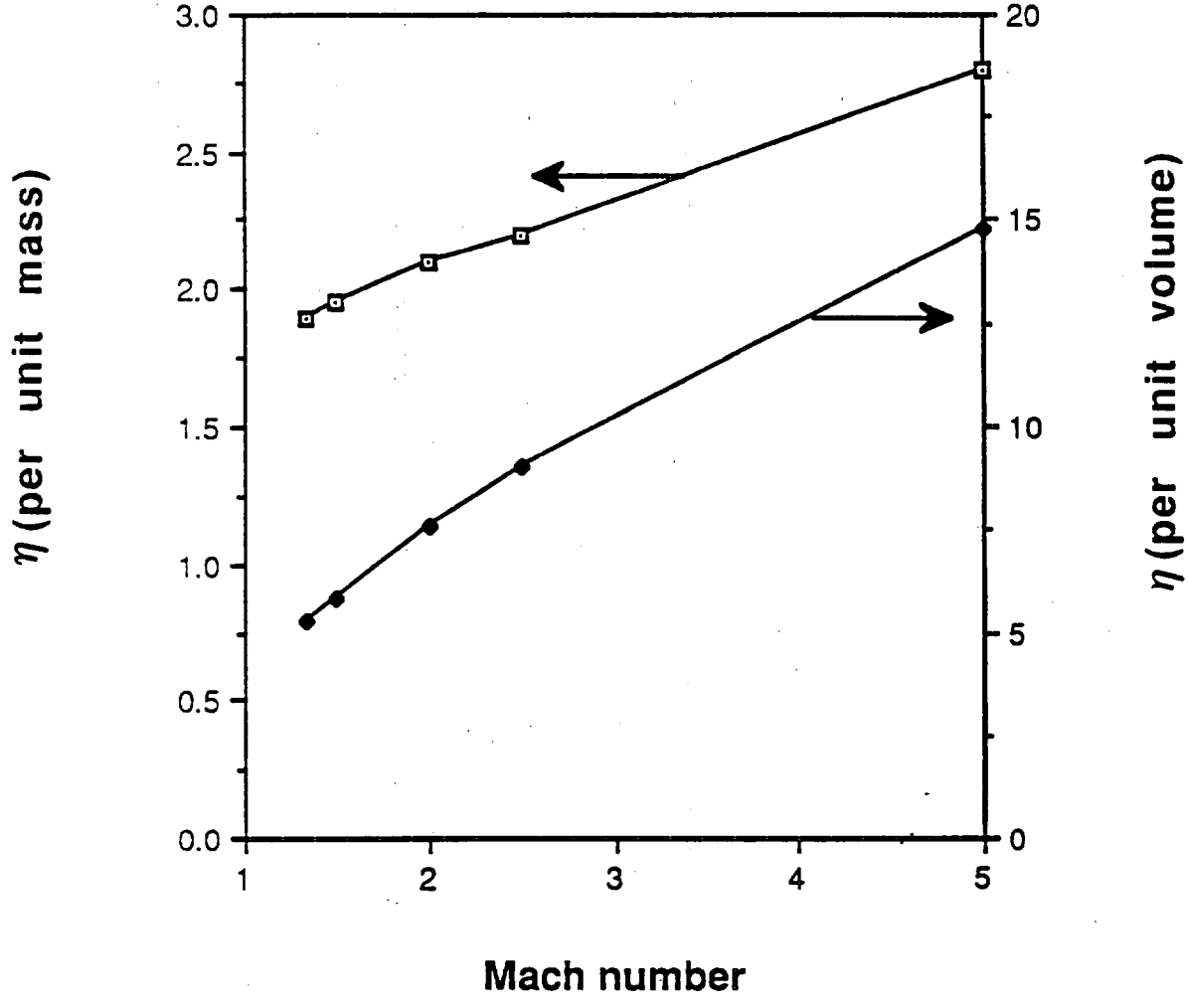

$$\eta = \frac{\left(\frac{1}{2}\left(u'^2 + v'^2\right)\right)_{\text{post shock wave}}}{\left(\frac{1}{2}\left(u'^2 + v'^2\right)\right)_{\text{pre shock wave}}}$$

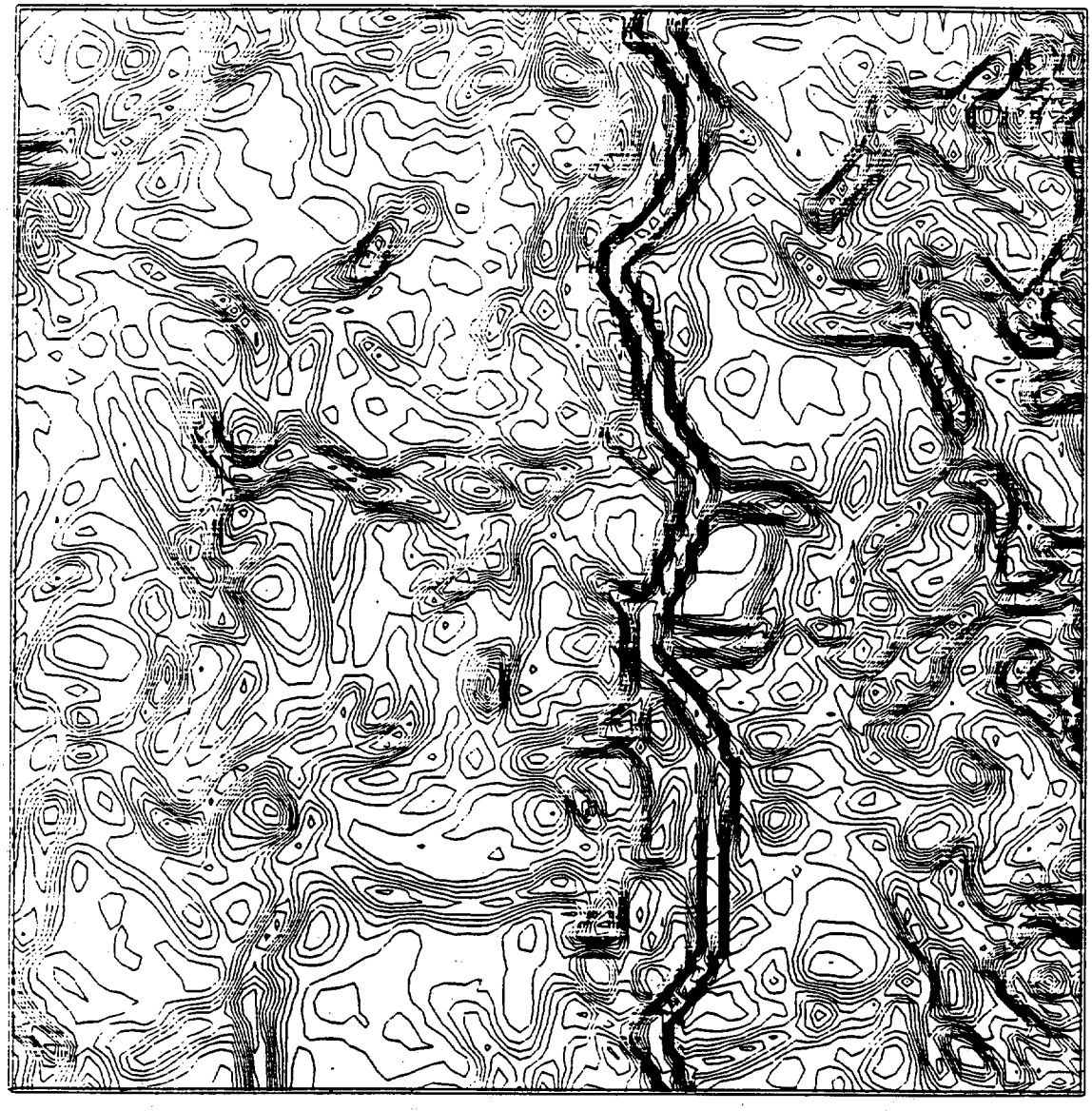

Divergence of velocity for case of very strong initial turbulence

Pleasanton, USA *Edited by V. Rupert*

CONCLUSIONS

Shock waves can amplify the turbulent kinetic energy of a flow by as much as 5 times

Increasing the initial turbulent kinetic energy tends to decrease the amplification

Shock waves will decrease the turbulent eddy size resulting in turbulence of smaller scales

Increasing the turbulent kinetic energy can cause a straight shock to become distorted and curved

STOCHASTIC BACKSCATTER IN A SUBGRID-SCALE MODEL: PLANE SHEAR MIXING LAYER

C. E. Leith

Center for Compressible Turbulence
Lawrence Livermore National Laboratory
Livermore, CA 94550

The traditional Smagorinsky subgrid-scale viscosity $(C_S\lambda)^2 S$ has been supplemented by the addition of stochastic backscatter. The random acceleration is derived from a vector potential $C_b|S\delta t|^{3/2}\lambda^2(\delta t)^{-2}g$. Here S is the local strain rate, λ is the grid resolution length scale, δt is the time step, and g is a unit random gaussian. It is found that values $C_S = 0.2$ for the Smagorinsky constant and $C_b = 0.4$ for the backscatter constant give a robust calculation of the two-dimensional shear mixing layer with the observed growth rate and with realistic emergence of random coherent eddy structures.

SUBMITTED AS A LETTER TO PHYSICS OF FLUIDS A, AUGUST, 1989

is the length scale of dominant eddies and C_1 is a dimensionless constant. For the Smagorinsky model, λ is the resolution length scale of the grid, and the subgrid-scale turbulent energy K is determined by a local balance between its shear production and its dissipation. By simple dimensional scaling analysis the dissipation rate of turbulence is estimated as $\varepsilon = C_2K^{3/2}/\lambda$ where C_2 is another dimensionless constant. Local shear production depends on the deviatoric strain rate tensor

$$S_{ik} = \partial u_i/\partial x_k + \partial u_k/\partial x_i - (2/3)(\partial u_j/\partial x_j)\,\delta_{ik} \qquad (1)$$

for the resolved velocity u_i in cartesian coordinates x_i. The associated eddy viscous stress tensor is $\nu_T S_{ik}$, and the local production rate of subgrid-scale turbulence is given by the eddy stress work $\nu_T S_{ik}(\partial u_i/\partial x_k) = \nu_T S^2$. Here the mean local strain rate is defined as $S = [S_{ik}\partial u_i/\partial x_k]^{1/2}$. The local balance condition becomes then the algebraic relation $\varepsilon = \nu_T S^2$ which determines the Smagorinsky viscosity coefficient, $\nu_T = (C_S\lambda)^2 S$, directly in terms of the strain rate S. Here C_S is the traditional Smagorinsky constant.

Stochastic backscatter, for isotropic homogeneous turbulence in three dimensions, has[2] a k^4 spectrum to lowest order in wavenumber k. This is achieved in a three-dimensional fluid dynamics code by introducing on the calculational grid an isotropic space- and time-white random acceleration vector potential from which are derived nondivergent random accelerations. The mean of the random acceleration potential is zero. Its variance is determined by the following dimensional scaling argument. The space derivative of a vector potential $\phi[L^2T^{-2}]$ is an acceleration $a[LT^{-2}]$

acceleration components are finally given by $a_i = \varepsilon_{ijk}\partial\phi_j/\partial x_k$ where ε_{ijk} is the standard alternating tensor.

The state of a compressible fluid is given by its density, ρ, velocity components, u_k, and specific energy, E, as functions of cartesian coordinates, x_k, and time, t. The evolution equations, modified for the subgrid-scale model, are

$$\partial\rho/\partial t + \partial(\rho u_k)/\partial x_k = 0 \tag{5}$$

$$\partial(\rho u_i)/\partial t + \partial(\rho u_i u_k)/\partial x_k = -\partial P/\partial x_i + \partial(\rho \nu_T S_{ik})/\partial x_k + \rho a_i \tag{6}$$

$$\partial(\rho E)/\partial t + \partial(\rho E u_k)/\partial x_k = \partial[(\rho \nu_T/\sigma)\partial E/\partial x_k]/\partial x_k + \rho \nu_T S_{ik}\,\partial u_i/\partial x_k - P\partial u_k/\partial x_k - \rho a_i u_i \tag{7}$$

Although these equations have the usual appearance of the equations of compressible fluid flow, there are some subtle differences in interpretation. The dependent variables are mass-weighted averages[4] over the subgrid-scale turbulence. Thus in Eq. (5) eddy transport of mass is implicitly included by the use of mass-averaged velocity components. In the momentum equation (6), the gas pressure is given by, say, a γ-law equation of state, $P = (\gamma - 1)\rho E$. Turbulence behaves thermodynamically like a $\gamma = 5/3$ gas and induces a turbulent pressure given by $p_T = (2/3)\rho K$, but we include p_T in P just as we include the turbulent kinetic energy K in E. We ignore the equation of state discrepancy which, in any case, vanishes if the gas also has $\gamma = 5/3$. The constant σ that appears in the eddy

The choice $U = 1$ characterizes the shear and establishes the time scale. The gas temperature is such that the sound speed is 4. At this convective Mach number, 1/4 , compressibility effects are known[8] to be negligible. The time step $\delta t = 0.05$ is well below any limit imposed by stability conditions. The model constants are chosen as $C_S = 0.2$, $C_b = 0.4$, and the eddy Prandtl number as $\sigma = 0.7$. The simulations are for 1000 time steps to $t = 50$, and each takes about 2 minutes of CRAY 1 time. They differ only in the initial seed used in the random number generator, and therefore they represent independent realizations of the evolving turbulent flow.

Figure 1 shows the integral width Θ as a function of time for the five realizations as distinguished by symbols. The unadorned straight line in the figure shows the experimentally determined slope, $d\Theta/dt = 0.032$. The rough agreement between the model runs and the experimental result is not accidental but was achieved by the choice of C_b to which the early time slope was found to be roughly proportional.

Figure 2 displays contour maps of the flow at time $t = 25$ in the realization shown in Fig. 1 with open squares. Fig. 2(a) shows the spanwise vorticity with contour values 0.2, 0.4, 0.6, 0.8, and 1.0. Most qualitative information about such flows has been obtained from shadowgraphs[9] that display the gradient of the mixing ratio of the original two fluids. In order to simulate such an image, the upper and lower fluids were distinguished by the values 0.0 and 1.0 of a passive scalar marker which was embedded in the flow and diffused with an eddy Schmidt number of 0.7. Its concentration is shown in Fig. 2(b) with contour values 0.1, 0.3, 0.5, 0.7, and 0.9. Closely spaced contours correspond to a relatively high gradient and a

REFERENCES

1 J. Smagorinsky, Mon. Weather Rev. **91**, 99 (1963).

2 D. C. Leslie and G. L. Quarini, J. Fluid Mech. **91**, 65 (1979); R. H. Kraichnan, J. Atmos. Sci. **33**, 1521 (1976).

3 H. Rose, J. Fluid Mech. **81**, 719 (1977).

4 A. Favre, Phys. Fluids **26**, 2851 (1983).

5 C. W. Hirt, A. A. Amsden, and J. L. Cook, J. Comp. Phys. **14**, 227 (1974).

6 L. D. Cloutman, J. Comp. Phys. **73**, 349 (1987).

7 F. K. Browand and B. O. Latigo, Phys. Fluids **22**, 1011 (1979).

8 D. W. Bogdanoff, AIAA J. **21**, 926 (1983); D. Papamoschou and A. Roshko, J. Fluid Mech. **197**, 453 (1988).

9 G. L. Brown and A. Roshko, J. Fluid Mech. **64**, 775 (1974); L. P. Bernal, Phys. Fluids **31**, 2533 (1988).

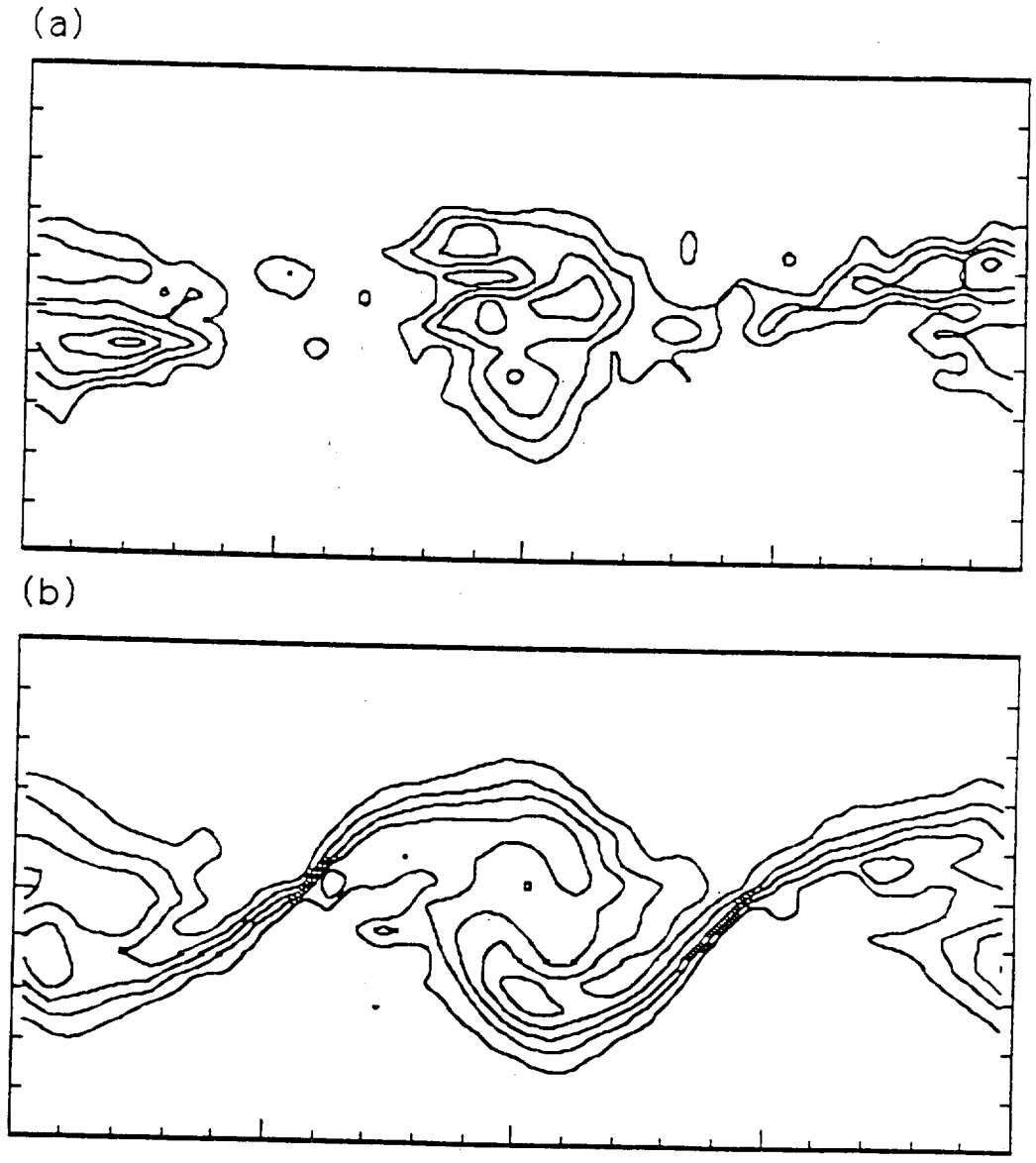

Fig. 2: Contour maps of (a) vorticity and (b) a scalar fluid marker for one realization at time t = 25.

NUMERICAL SIMULATION OF THE DECAY OF TURBULENT SWIRLING FLOW

LAWRENCE D. CLOUTMAN

L-035
Lawrence Livermore National Laboratory
Livermore, California 94550

I. Introduction

Experimental measurements of the cold swirling flow in a constant volume combustion bomb were simulated with two different computational fluid dynamics programs. This problem is of interest for three reasons. First, it provides a relatively straightforward test problem for the fluid dynamics algorithms and turbulence models. Second, the relatively complete set of published experimental conditions and results makes possible a meaningful comparison with numerical simulations. Third, it helps us understand the physics of swirling flows by predicting more details of the flow than can be measured easily.

The calculations presented here were performed with the KIVA [1,2] and COYOTE [3] hydrodynamics programs. KIVA was written primarily to produce numerical solutions of the full nonlinear, transient, compressible-flow, Navier-Stokes equations in two and three dimensions for the conditions found in internal combustion engines, although it is not restricted to those applications. The program includes moving boundaries, chemical reactions, and turbulence models. The numerical algorithm is based on the arbitrary Lagrangian-Eulerian (ALE) technique.

The COYOTE program is an improved and extended version of the SOLA-ICE Eulerian fluid dynamics program [4]. The difference equations have been modified to improve the accuracy and to allow a nonuniform mesh, the swirl equation was added, and the KIVA physics packages were added. The resulting program can therefore run the same two-dimensional problems as KIVA provided the mesh contains only fixed rectangular cells.

The experiment was performed in a constant volume combustion bomb [5] shown schematically in Fig. 1. The chamber is a right circular cylinder with a metal cylindrical wall and flat glass windows on the ends for optical access. A shrouded valve in the cylindrical wall is used to establish a swirling flow. The decay of swirl was measured with laser Doppler velocimetry (LDV), and temperatures were measured with a thermocouple. Measurements were taken along one radius on the midplane of the bomb and along one line parallel to the symmetry axis at half the radius. These lines are indicated by dashed lines in Fig. 1.

II. Governing Equations

Both programs are based on the Navier-Stokes equations for a mixture of compressible gases. We use the mass weighted, single velocity representation.

Mass conservation is expressed by the continuity equation for each species k:

$$\frac{\partial \rho_k}{\partial t} + \nabla \cdot (\rho_k \vec{u}) = -\nabla \cdot \vec{J}_k + R_k, \tag{1}$$

where ρ_k is the density of species k, t is time, $\vec{u}$ is the velocity, and R_k is the rate at which species k is created by chemical reactions. The diffusional mass flux is given by Fick's law,

$$\vec{J}_k = -\rho D \nabla(\rho_k/\rho), \tag{2}$$

where ρ is the total density, and D is the species diffusivity. Since we are interested primarily in turbulent flows, we assume D is independent of species. Eq. (1) may be summed over species to obtain the total continuity equation

$$\frac{\partial \rho}{\partial t} + \nabla \cdot (\rho \vec{u}) = 0. \tag{3}$$

The momentum equation is

$$\frac{\partial (\rho \vec{u})}{\partial t} + \nabla \cdot (\rho \vec{u}\vec{u}) = \rho \vec{g} - \nabla P - \nabla \cdot \mathcal{T}, \tag{4}$$

where $\vec{g}$ is the gravitational acceleration, P is the pressure, and $\mathcal{T}$ is the stress tensor

$$\mathcal{T} = -\mu[\nabla \vec{u} + (\nabla \vec{u})^T] - \mu_1 \nabla \cdot \vec{u}\, \mathcal{I}. \tag{5}$$

Here $\mathcal{I}$ is the unit tensor, and μ is the coefficient of viscosity, and μ_1 is the second coefficient of viscosity, which we normally set equal to $-2\mu/3$.

We choose to express energy conservation in terms of the specific thermal internal energy I:

$$\frac{\partial (\rho I)}{\partial t} + \nabla \cdot (\rho I \vec{u}) = -P \nabla \cdot \vec{u} - \mathcal{T} : \nabla \vec{u} - \nabla \cdot \vec{q} + \sum_k H_k R_k, \tag{6}$$

where $\vec{q}$ is the diffusional heat flux, and H_k is the heat of formation of species k. The heat flux is the sum of Fourier's law and enthalpy diffusion:

$$\vec{q} = -K \nabla T + \sum_k h_k \vec{J}_k, \tag{7}$$

where K is the conductivity, h_k is the specific enthalpy of species k, and T is the temperature.

The equation of state is the sum of partial pressures for each species treated as an ideal gas:

$$P = \sum_k R \rho_k T / m_k, \tag{8}$$

where R is the universal gas constant, and m_k is the molecular weight of species k. The internal energy is given by

$$\rho I = \sum_k \rho_k I_k(T), \tag{9}$$

where the species thermal internal energies I_k are functions of temperature derived from published tables of enthalpies [6, 7].

The COYOTE and KIVA hydrodynamics programs have the option of using a SGS turbulence model. The SGS approach is based on the concept of calculating all details of the flow down to a limit imposed by grid resolution, and modeling only the smaller flow features. Reynolds [8] describes one approach for implementing SGS by using a filter function to separate the SGS mean flow from the small-scale features. The filter function incorporates an arbitrary length scale that is usually related to the computational cell size in practice. Rogallo and Moin [9] provide a more detailed discussion that emphasizes the practical difficulties encountered in accurately carrying out SGS calculations. Our model may be derived by using a filter function to derive the three-dimensional mean flow equations, then modeling the turbulent correlations with flux gradient approximations to give mean flow equations of the same form as the original Navier-Stokes equations with enhanced diffusivities. The resulting three-dimensional equations may be specialized to two-dimensional Cartesian or (axisymmetric) cylindrical coordinates as required. We use a mass-weighted average, whose use in turbulence modeling goes back at least to Cowling [10]. The final governing equations are just Eqs. (1) - (9) where the dependent variables are taken to be the mass-weighted mean flow variables, and the diffusivities are the sum of molecular and eddy diffusivities. This model not only has great simplicity, it also preserves the Galilean and tensor invariance of the original equations. The eddy viscosity may be modeled by an algebraic expression [11] or by introducing a transport equation for the SGS turbulence kinetic energy density (for example, Refs. [1, 12]).

The algebraic eddy viscosity is

$$\mu_t = \rho c^2 \Delta^2 \mid [\nabla \vec{u} + (\nabla \vec{u})^T] : \nabla \vec{u} \mid^{1/2}, \tag{10}$$

where c is a constant of order 0.1 - 0.2 and Δ is the computational cell size. Deardorff takes Δ equal to the geometric mean of the cell width in the three coordinate directions. Ramshaw [13] argues that this eddy viscosity expands the turbulence microscale up to the computational cell size, analogous to the expansion of the shock wave thickness from a few molecular mean free paths up to a few computational cell widths by the usual artificial viscous pressure. Since the size of the smallest eddies we can resolve is a few times the length of the longest side of a cell, we prefer to choose Δ as the maximum of the three cell widths. SGS seems to work best for cubical cells, so we also try to avoid large aspect ratios where this distinction becomes significant. Eddy diffusivities of heat and species are calculated from Eq. (10) by introducing a turbulent Prandtl number and a turbulent Schmidt number in the usual fashion.

The turbulence transport model consists of one transport equation for the turbulence kinetic energy density K:

$$\frac{\partial \rho K}{\partial t} + \nabla \cdot (\rho K \vec{u}) = \nabla \cdot [(\mu + \mu_t) \nabla K)] - \frac{2}{3} \rho K \nabla \cdot \vec{u} - \mathcal{T} : \nabla \vec{u} - \frac{D_t \rho K^{3/2}}{\Delta}, \tag{11}$$

and

$$\mu_t = A_t \rho \Delta K^{1/2}, \tag{12}$$

where A_t and D_t are constants. This K is not the same as the k in the standard $k-\epsilon$ model, although the transport equations are similar. We do not need an analog of the ϵ equation because we have legislated the SGS turbulence length scale.

Because turbulence is intrinsically three-dimensional, the usefulness of SGS models in two-dimensional numerical simulations has been questioned and needs examination. There is no question that three-dimensional calculations are required if one wants to correctly simulate all flow features with length scales down to the limit of grid resolution for an arbitrary turbulent flow. For our present application, the requirements are much less severe. Since we are interested only in simulating the largest scale flow features with modest accuracy (say, 5 or 10% relative errors), and these large-scale features are strongly two-dimensional, plausibility arguments can be given supporting the present use of SGS [14]. The ultimate test, however, is how well the calculations reproduce the experimental data.

III. THE NUMERICAL SOLUTIONS

The calculations with COYOTE and KIVA presented here use the same set of physical and numerical parameters to the extent possible. Both programs use the same enthalpy tables for nitrogen and oxygen, which are used to model air. The initial values of oxygen density and nitrogen density are 3.1096×10^{-4} and 1.0809×10^{-3} g/cm^3, respectively. The wall temperature is held fixed at 300 K, and the boundary layer model is a wall function based on the logarithmic law-of-the-wall approximation and the Reynolds analogy [1].

We now show the comparison between the experimental data and the best COYOTE calculation out to 300 ms. The turbulence model is the one-equation transport model with $A_t = 0.117$, $D_t = 1.4$, turbulent Prandtl number Pr = 0.7, length scale 0.3 cm, and initial turbulence kinetic energy density of 25 cm^2/s^2. The initial condition in the calculation was taken as Dyer's measurements at 100 ms. The swirl velocity was assumed to be independent of axial position, and the velocity in the plane of the mesh was assumed to be zero. The temperature field had to be extrapolated from the values along the two lines on which measurements were taken. The axial distribution was assumed to be self-similar in the radial direction with the scaling factor chosen to force agreement between the initial temperature field and the experimental measurements on the radial line. The density field was adjusted to provide a uniform initial pressure field of 8.61×10^6 dynes/cm^2. We used a 52 by 20 mesh made mostly of square cells 0.8 mm on a side, with a slight refinement next to the walls. This mesh represents half of the bomb, assuming symmetry about the midplane.

Figure 2 shows the radial distribution of temperature at the midplane of the bomb. Experimental data points are indicated by the circles. The dotted lines represent piecewise-linear fits to the experimental points, and the solid lines represent our calculated results. The computational initial condition at 100 ms is slightly different from the dotted line: the curves drawn by Dyer to connect his widely separated experimental points seemed more reasonable than a strictly linear fit, so some of these curvature effects were included in our initial condition. Except for the point at the very center of the bomb, the calculation

agrees with the measurements to within the 10 K experimental uncertainty. Considering the incomplete knowledge of the initial temperature distribution and other complications discussed later, the agreement shown here is satisfactory.

Figure 3 shows the axial temperature distribution at the half radius point. The initial temperature appears 7 K higher than the measurements because the top data point at $z = 0$, which should be the same as the top data point at $r = 2$ cm in Fig. 3, is lower by that amount. Apparently this situation is due to two independent sets of measurements at that point in space and is consistent with the 10 K uncertainty in the temperature measurements. Again, the agreement is good considering the uncertainties.

The calculated rate of heat loss at the center of the bomb is too slow at late times relative to the rate during the first 50 ms. I conjecture that this is due to suppression of turbulence generation by the artificial rigid boundaries imposed at the axis of symmetry and bomb midplane in the present calculations. A full three-dimensional KIVA simulation of the entire chamber would be required to unambiguously test this hypothesis.

Figure 4 shows the radial swirl distribution at the midplane of the bomb. The solid lines represent the numerical solution. Again, the agreement is quite good, especially in the outer half of the bomb. The peaks of the calculated curves shift very slightly inward, although not quite as much as in the experimental curves. The visual impression of the experimental points is that the swirl consists of a rigid body vortex in the inner 1-2 cm of the bomb plus a $1/r$ vortex in the outer parts. The transition between them extends from about $r = 1.5$ to 2.5 cm at 100 ms. The transition gradually moves inwards and gets thinner at later times. None of the numerical solutions seems to have this qualitative behavior to a significant extent.

Figure 5 shows the axial distribution of swirl at the half radius point. At this radial location, the experimental and calculated swirl decay rates are in excellent agreement. We predict no significant axial variation of swirl, in agreement with the experiment and the other two numerical solutions. No rapid drop of swirl to zero indicating resolution of boundary layers is seen in either the calculations or the experiments. Simple estimates of the boundary layer thickness on the cylindrical walls and the windows suggest our cell size would have to be reduced to approximately 0.1 mm before we would begin to see a dramatic velocity drop at the boundary.

We consider the agreement between the calculation and the experiment to be quite good considering the difficulties and uncertainties involved. First, we are simulating a turbulent flow with incompletely characterized initial and boundary conditions. Measurements along two lines had to be extrapolated to fill the mesh with initial values. Second, the turbulence model has not been adequately tested. Indeed, this problem represents the first in a series of validation calculations sufficiently complete and physically based to be used for determining SGS parameter values. Third, precession of the instantaneous axis of swirl and other possible three-dimensional effects cannot be included in our two-dimensional simulation. In particular, the symmetry axis and bomb midplane in the calculation may inhibit physically realized motions in the mean flow. Fourth, the assumption of symmetry about the midplane of the bomb may inhibit production of turbulence kinetic energy in the middle of the bomb. Finally, we are comparing one realization of an ensemble to an ensemble average, and we can only hope that this particular realization is similar to the average.

The boundary layer on the window drives a recirculating flow that is most pronounced in the outer 40% of the bomb. Flow is inward along the window, as shown in Fig. 6. This pattern stays the same at later times, but the maximum speed drops to 230 cm/s at 200 ms and to 152 cm/s at 300 ms. Peak speed in the initial transient was 450 cm/s. Using Fig. 4 to estimate the swirl velocity along the window, we see that the flow pattern on the window should be an inward spiral with a 10:1 pitch, as is seen in shadowgraphs of this experiment [5].

The calculated turbulence kinetic energy density is in serious disagreement with the measurements of turbulence intensity, but this is not surprising. First, the measurements are an ensemble average, which should be systematically larger than a SGS value by an amount that depends on the computational resolution. Second, the experimental turbulence intensity measurements include three-dimensional effects such as precession of the fluid's instantaneous axis of rotation. Such motions are suppressed in the axisymmetric calculations. Third, only one component of what may be significantly anisotropic turbulence was measured. The transport model for K assumes isotropic turbulence. Therefore, a meaningful quantitative comparison is not possible. However, an examination of some of the qualitative features of the turbulence is interesting. The maximum value occurs near the window, and the minimum value occurs near the bomb's center. The value on the cylindrical wall is always a little over half of the maximum value. The experimental data show much larger turbulence levels in the interior of the bomb than near the outer wall, possibly for the reasons just enumerated. It probably will be necessary to perform a three-dimensional simulation of the entire volume of the bomb to sort out the questions about the turbulence intensities.

Figures 7-10 are the same as Figs. 2-5 except that the solution was produced by the KIVA program with Deardorff's algebraic SGS model [11]. The parameters used are $c = 0.2$, length scale $\Delta = 0.3$ cm, and turbulent Prandtl number $\mathrm{Pr} = 0.7$. The run of temperature with radius is shown in Fig. 7, and the results are very close to those shown in Fig. 2. The chief difference is a slight improvement in the temperature at $r = 0$ in the KIVA solution. The run of temperature with axial position is shown in Fig. 8, and the agreement with Fig. 3 is also quite good. Comparison of the radial swirl distributions in Figs. 4 and 9 shows that KIVA dissipates angular momentum slightly too slowly with these SGS parameters, but the agreement is still quite good. The same comment applies to the axial swirl distributions shown in Figs. 5 and 10.

The COYOTE program was also run with the same algebraic turbulence model as used in KIVA. The solution is virtually identical to that produced by the transport model, and what slight differences there are tend to be in the direction of the differences between the KIVA and COYOTE solutions discussed in the previous paragraph. We conclude that although the solutions are quite sensitive to the parameter values used in the turbulence models, a unique parameter set for each model could be found that gives good agreement with the experiments. We also conclude, given the vast differences in the finite-difference methods used in the two programs, that we probably are using adequate resolution in our calculations. Calculations using a uniform mesh of 0.8 mm squares were quite similar to those just described, and the heat transfer to the walls was only approximately 6% less on the uniform mesh. A run was made in which the number of zones in each direction was

increased by 50 percent. The same SGS parameters, including the length scale, were used as for the coarse mesh solutions. There was no noticable difference between the finely and coarsely resolved solutions.

Several additional solutions have been run with KIVA. A developmental version of KIVA in which the subcycling algorithm was replaced by an ICE pressure iteration based on the conjugate residual method [15] rather than SOR produced results very similar to those just presented. A three-dimensional 60° sector calculation with the same r-z zoning as the two-dimensional runs but with 18 zones in the θ direction was terminated 2.42 ms into the problem because of the long run times, but the agreement with the two-dimensional solutions was excellent. In comparing the standard KIVA solution, the fine mesh solution, and the three-dimensional sector solution, we find all three produce temperature and swirl velocity contours that are indistinguishable.

IV. SUMMARY AND CONCLUSIONS

The COYOTE and KIVA programs were able to model the swirl decay and heat transfer in the combustion bomb within the experimental uncertainty. Predicted turbulence intensity did not agree as well with the measurements, but the difference may not be significant for reasons given in the previous section. These solutions are discussed in detail in Ref. [14].

The following observations on the computational model are suggested by the simulations presented here. First, the ICE method based on the conjugate residual solver for the pressures is more robust and efficient at the very low Mach numbers typical of combustion devices, and its use is recommended in place of SOR iterations or acoustic subcycling. Second, The use of SGS for two-dimensional simulations for engineering purposes appears to be feasible even though its theoretical justification is weak and caution must be exercised in its application. However, there are many unanswered questions as to the generality of this approach and about the optimum values of the SGS parameters and their universality. In particular, it was necessary to modify the SGS parameters (especially the length scale) from those given by Deardorff [11] to get good results. It is interesting that similar changes were required in both programs, which use quite different finite difference methods. Given the practical difficulties of the SGS model in general [9] and the simplified nature of our present model, more development is needed before SGS modeling can be considered a reliable off-the-shelf engineering tool in spite of its successful application to other problems [16]. Third, this problem would make an excellent test problem for other turbulence models, such as $k-\epsilon$. A comparison of performance between the two turbulence models would be interesting. Finally, it would be desirable to make a three-dimensional solution of the entire chamber.

ACKNOWLEDGEMENTS

This work was supported by the Energy Conversion and Utilization Technologies program of the U. S. Department of Energy and was performed at Los Alamos National Laboratory and Lawrence Livermore National Laboratory under contract number W-7405-ENG-48.

REFERENCES

1. A. A. Amsden, J. D. Ramshaw, P. J. O'Rourke, and J. K. Dukowicz, KIVA: A computer program for two- and three-dimensional fluid flows with chemical reactions and fuel sprays. Los Alamos National Laboratory report LA-10245-MS (1985).

2. A. A. Amsden, J. D. Ramshaw, L. D. Cloutman, and P. J. O'Rourke, Improvements and extensions to the KIVA computer program. Los Alamos National Laboratory report LA-10534-MS (1985).

3. L. D. Cloutman, COYOTE: A computer program for 2D reactive flow simulations. Lawrence Livermore National Laboratory report, in preparation.

4. L. D. Cloutman, C. W. Hirt, and N. C. Romero, SOLA:ICE: A numerical solution algorithm for transient compressible fluid flows. Los Alamos National Laboratory report LA-6236 (1976).

5. T. M. Dyer, Characterization of one- and two-dimensional homogeneous combustion phenomena in a constant volume bomb. SAE paper 790353, 88, 1196 (1979).

6. D. R. Stull and H. Prophet, *JANAF Thermochemical Tables*, 2nd ed. (U. S. Department of Commerce/National Bureau of Standards, NSRDS-NBS 37, June 1971).

7. M. W. Chase, J. L. Curnutt, A. T. Hu, H. Prophet, A. N. Syverud, and L. C. Walker, JANAF thermochemical table, 1974 supplement. *J. Phys. Chem. Ref. Data* 3, 311 (1974).

8. W. C. Reynolds, Modeling of fluid motions in engines–an introductory overview. In: *Combustion modeling in reciprocating engines* (Edited by J. N. Mattavi and C. A. Amann) Plenum Press, New York, 41 (1980).

9. R. S. Rogallo and P. Moin, Numerical simulation of turbulent flows. *Ann. Rev. Fluid Mech.*, 16, 99 (1984).

10. T. G. Cowling, The stability of gaseous stars. *Mon. Not. Royal Ast. Soc.* 96, 42 (1935).

11. J. W. Deardorff, On the magnitude of the subgrid scale eddy coefficient. *J. Comput. Phys.* 7, 120 (1971).

12. J. W. Deardorff, The use of subgrid transport equations in a three-dimensional model of atmospheric turbulence. *J. Fluids Eng.* 95, 429 (1973).

13. J. D. Ramshaw, Alternate interpretation of the subgrid scale eddy viscosity. Los Alamos Scientific Laboratory report LA-7955-MS (1979).

14. L. D. Cloutman, Numerical simulation of the decay of turbulent swirling flow in a constant volume combustion bomb. *Comp. & Fluids* 17, 437 (1989).

15. P. J. O'Rourke and A. A. Amsden, Implementation of a conjugate residual iteration in the KIVA computer program. Los Alamos National Laboratory report LA-10849-MS (1986).

16. L. D. Cloutman, Numerical simulation of turbulent premixed combustion and decay of turbulent swirling flow. In: *Extended abstracts of the joint conference of the Western States and Japanese sections*, The Combustion Institute, Pittsburgh, 154 (1987).

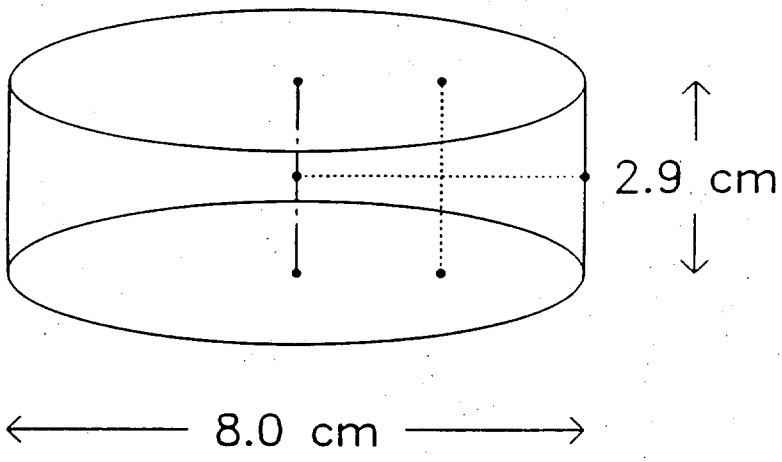

Figure 1. Schematic of the combustion bomb. The experimental measurements were made along the two dashed lines.

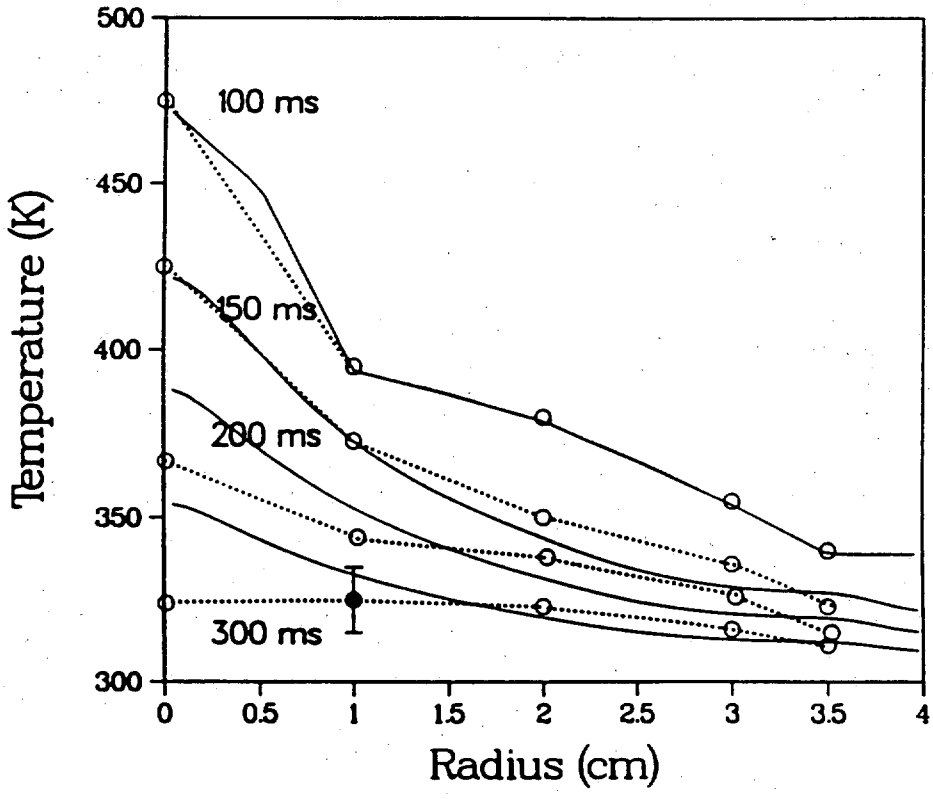

Figure 2. Temperature as a function of radius along the midplane of the bomb for the COYOTE solution using the SGS transport model. The experimental error of ± 10 K is illustrated by the error bar shown on the 300 ms curve.

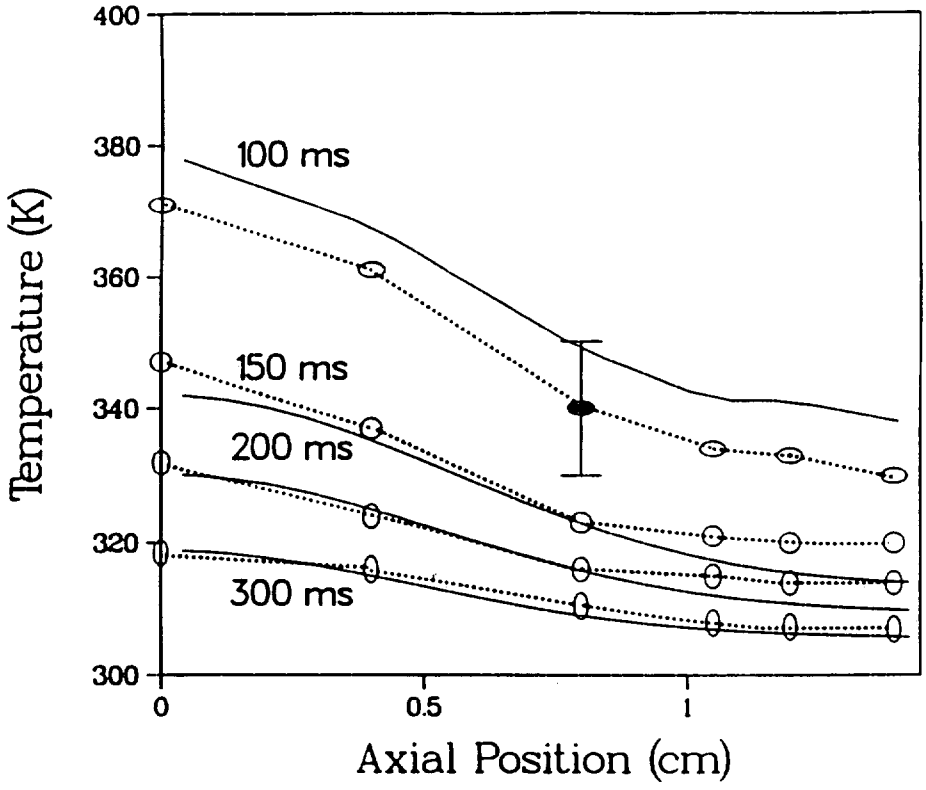

Figure 3. Temperature as a function of axial position on the half-radius line.

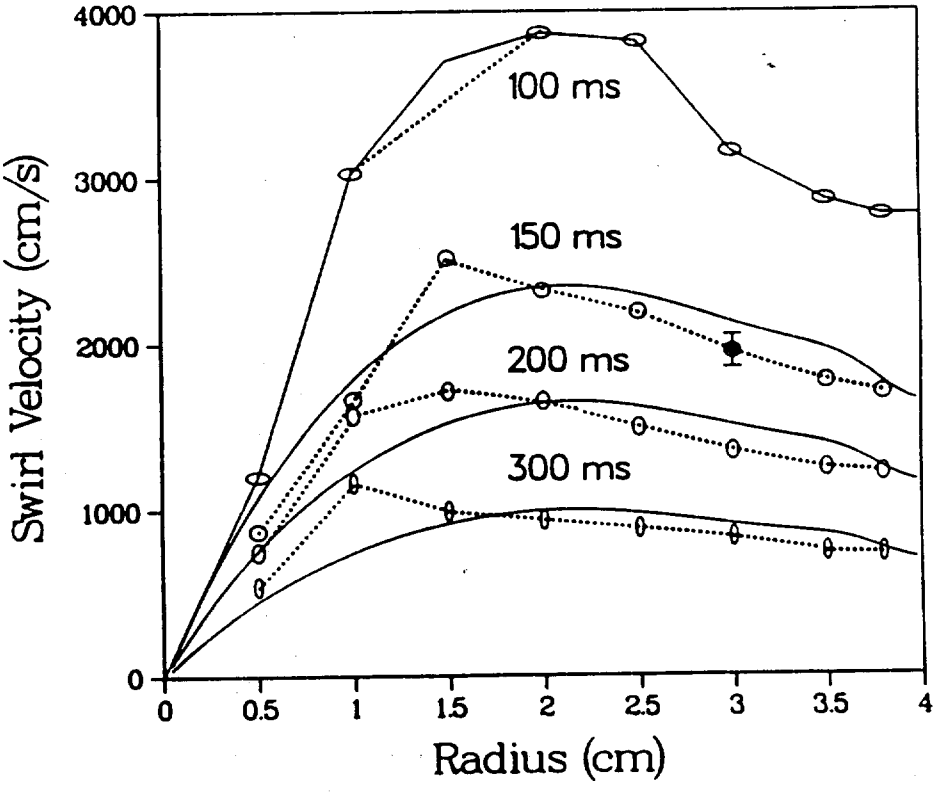

Figure 4. Swirl velocity as a function of radius along the midplane of the bomb. The error bar indicates the 1 m/s repeatability of the averaged measurements.

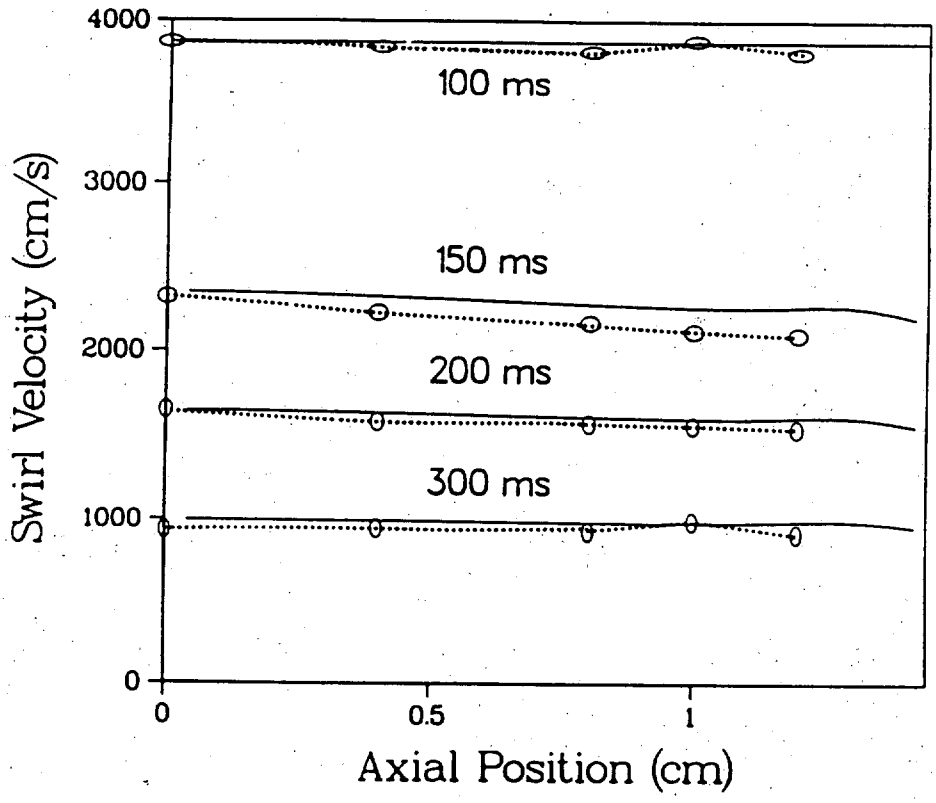

Figure 5. Swirl velocity as a function of axial position on the half-radius line.

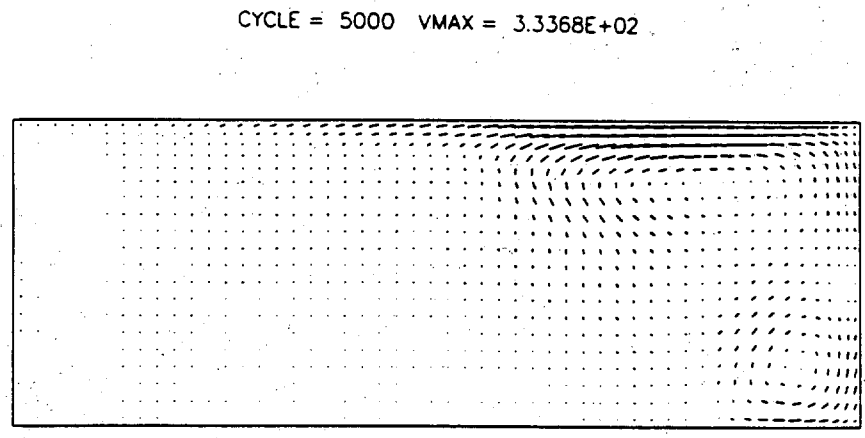

Figure 6. [illegible], velocity vectors, [illegible] at 150 ms form the COYOTE solution.

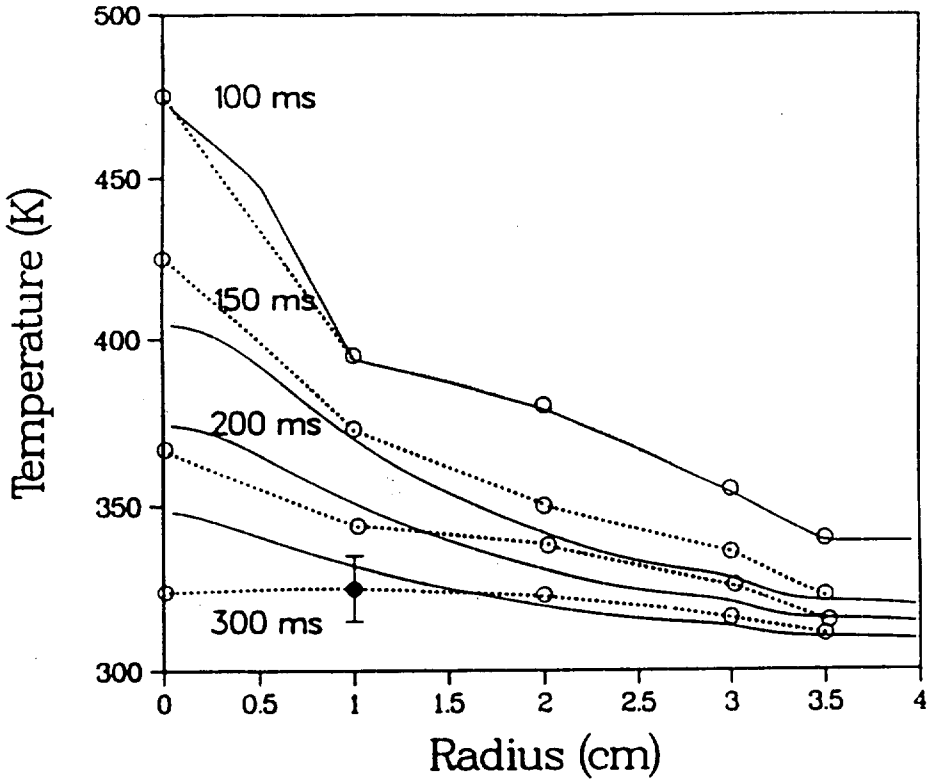

Figure 7. Temperaure as a function of radius along the midplane of the bomb for the KIVA solution using the algebraic SGS model.

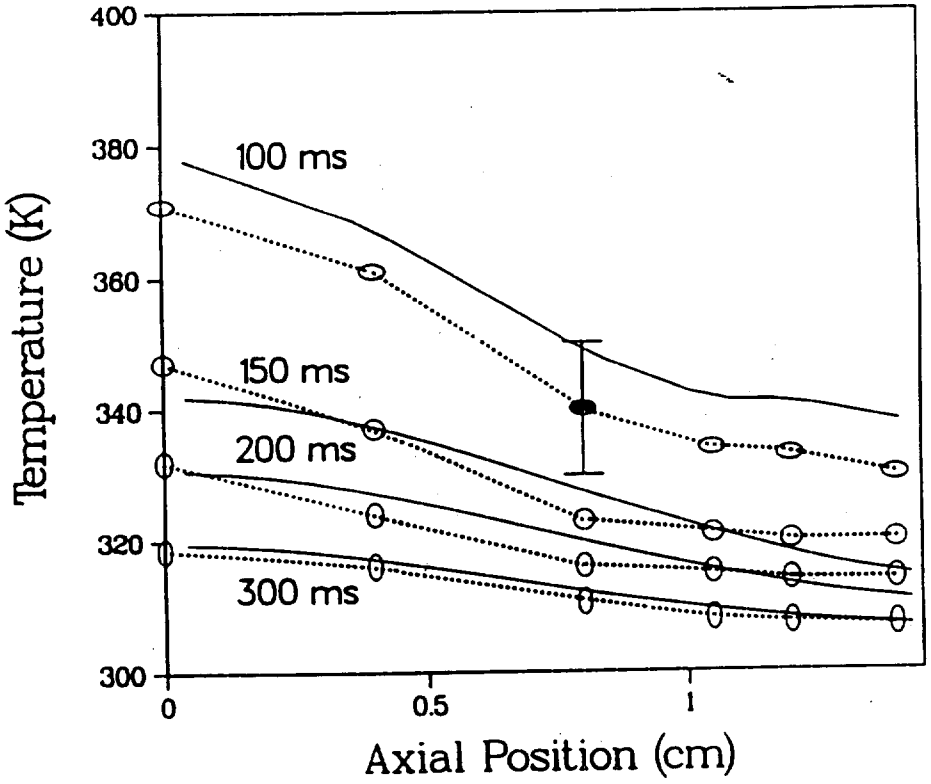

Figure 8. Temperature as a function of axial position on the half-radius line.

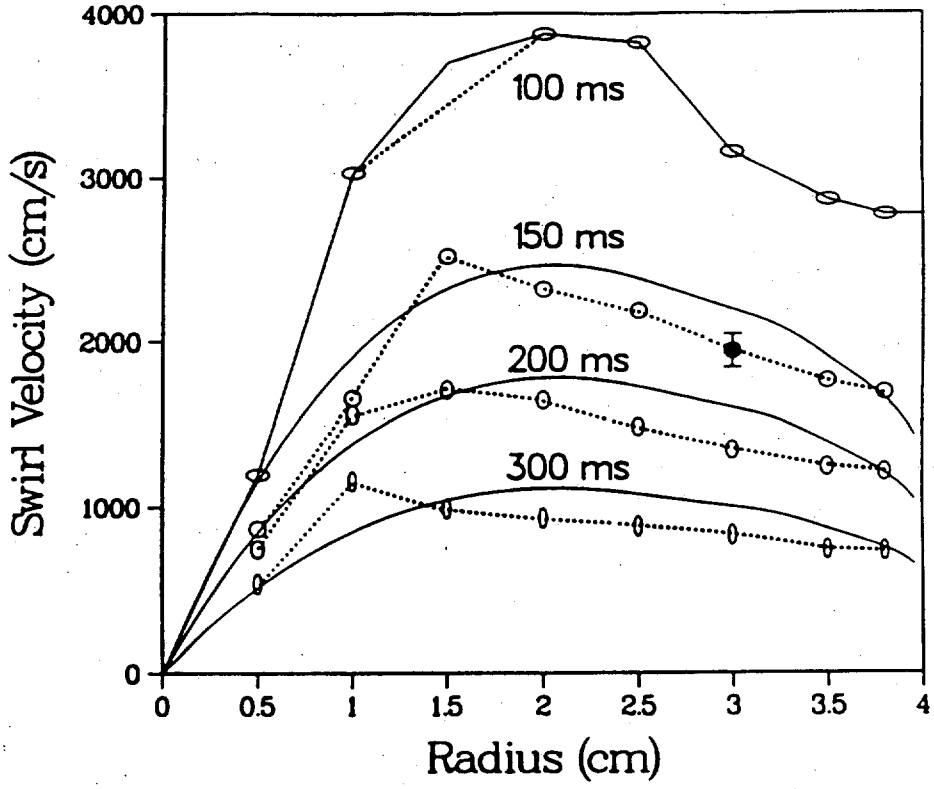

Figure 9. Swirl velocity as a function of radius along the midplane of the bomb.

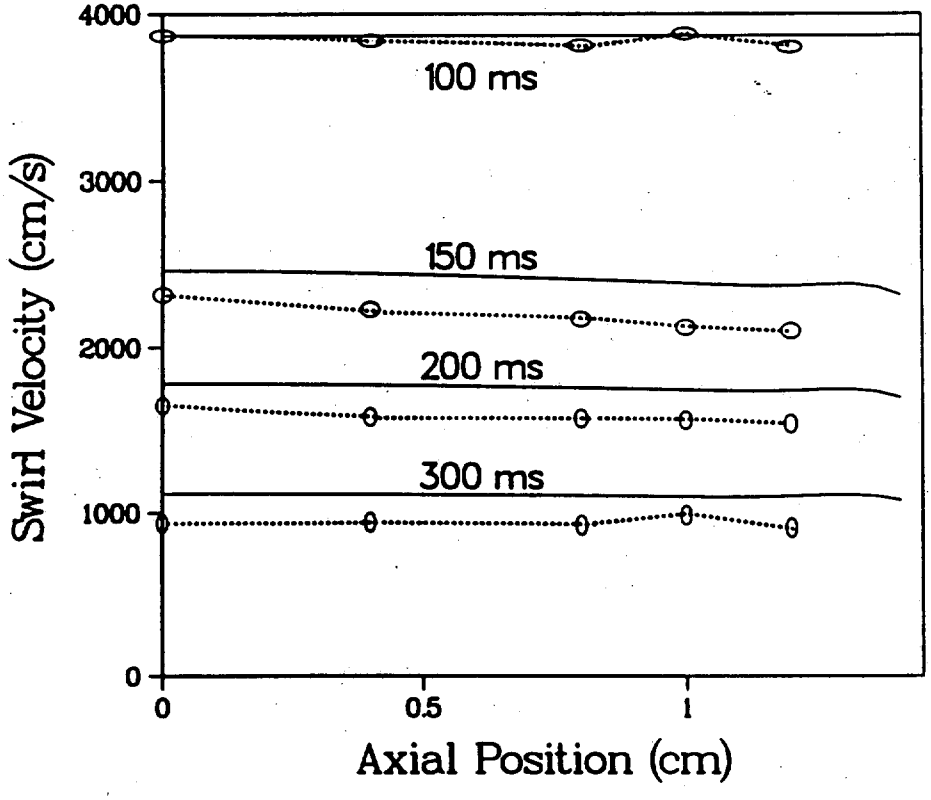

Figure 10. Swirl velocity as a function of axial position on the half-radius line.

Numerical Studies of Incompressible Richtmyer-Meshkov Instability in a Stratified Fluid

Thu Pham
Philip G. Saffman
Daniel I. Meiron
Applied Mathematics 217-50
Caltech
Pasadena, CA. 91125

1. Use of impulsive pressure distributions to compute kinetic energy of a continuously stratified fluid accelerated impulsively by a shock. Fluid is assumed incompressible.

2. Calculation of initial conditions for numerical simulation

3. Preliminary numerical simulations

Richtmyer-Meshkov Instability

- Acceleration is impulsive - acts for zero time
- Imparts finite momentum
- Shocks propagating normal to a density interface will roughly have this effect
- R-M instability occurs independently of the direction of the acceleration
- grown of perturbations is linear in time.

R-M Instability in Continuously Stratified Fluids

- Experiments undertaken by Sturtevant, Brouillette, Bonazza
- Novel feature - continuous density stratification
- Interest in dependence on initial density distribution of the width of turbulent mixing layer in late stage
- R-T instability in continuous stratification first undertaken by Rayleigh for exponential density stratification
- Later work by Chandrasekhar; Mikaelian obtained approximate growth rates by treating fluid layers with constant density.

Fluid Acceleration by Impulsive Pressure Distributions

- Goal: to calculate dependence of the initial kinetic energy of the disturbance on the density profile and fluctuations

- Determines initial conditions for non-linear numerical simulation

- Initial energy densities are found for turbulence model calculations of the development of the mixing layer.

- Assume fluids are incompressible - reasonable approximation when shocks are weak
- Consider a longitudinally infinite medium set in motion by passage of shock
- After transmitted and reflected shocks have travelled a large distance relative to width of layer, there is a uniform velocity far from mixing region - V
- In experiments the shocks are reflected back to mixed region for repeated impulse - we don't consider this additional perturbation

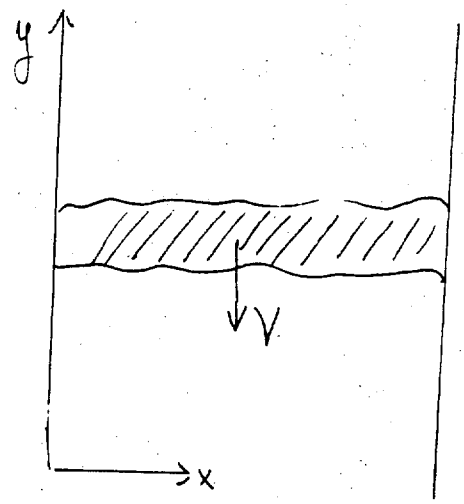

$$t = 0^-; \quad \rho_0(x,y) = \overline{\rho}(y) + \epsilon\rho'(x,y)$$

$$\overline{\rho}(y) \to \rho_{1,2} \quad \text{as } y \to \pm\infty$$

$$\rho'(x,y) \to 0 \quad \text{as } y \to \pm\infty$$

$$\int\int \rho'(x,y)dxdy = 0$$

- Initial velocity field $t = 0^+$, $(u, v) \rightarrow (0, -V)$ as $y \rightarrow \pm\infty$
- Pressure is impulsive: $P = \overline{P}(x, y)\delta(t)$
- Initial motion is a balance between acceleration and pressure gradient:

$$
\begin{aligned}
u_t &= -\frac{1}{\rho_0} P_x \\
v_t &= -\frac{1}{\rho_0} P_y \\
u_0(x, y) &= -\frac{1}{\rho_0} \overline{P}_x H(t) \\
v_0(x, y) &= -\frac{1}{\rho_0} \overline{P}_y H(t) \\
u_x + v_y &= 0
\end{aligned}
$$

- Poisson equation for pressure:

$$\frac{\partial}{\partial x}\left(\frac{1}{\rho_0}\frac{\partial \overline{P}}{\partial x}\right)+\frac{\partial}{\partial y}\left(\frac{1}{\rho_0}\frac{\partial \overline{P}}{\partial y}\right)=0$$

- Boundary conditions:

$$\overline{P}_y \rightarrow \rho_{1,2} V \quad y \rightarrow \pm\infty$$

- Solution consists of mean flow plus perturbations

$$\overline{P}=V\int_0^y \overline{\rho} dy+\epsilon p'(x,y)$$

- Poisson equation:

$$\epsilon\left[\frac{\partial}{\partial x}\left(\frac{1}{\rho_0}\frac{\partial p'}{\partial x}\right)+\frac{\partial}{\partial y}\left(\frac{1}{\rho_0}\frac{\partial p'}{\partial y}\right)\right]=-V\frac{\partial}{\partial y}\left(\frac{\overline{\rho}}{\rho_0}\right)$$

- Note: Right hand side is $O(\epsilon)$
- Solve subject to $p'_y \to 0$ as $y \to \pm\infty$
- Kinetic Energy:

$$K=\frac{1}{2}\int\int \rho_0[(v+V)^2+u^2]dxdy$$

- Kinetic energy is relative to frame moving with velocity $-V$.

- Consider next small disturbances:

$$\rho' = (1/L)g(y/L)\cos kx$$

- L - characteristic length for $\overline{\rho}$
- Normalize ϵ:

$$\int g(\xi)d\xi = 1, \quad \xi = y/L$$

- Solve for $p' = Vf(y/L)\cos kx$
- Poisson equation becomes (originally due to Rayleigh)

$$\frac{d}{d\xi}\left(\frac{1}{\overline{\rho}}\frac{df}{d\xi}\right) - \frac{k^2L^2}{\overline{\rho}}f(\xi) = \frac{d}{d\xi}\left(\frac{g}{\overline{\rho}}\right)$$

- Boundary conditions: $f_\xi \to 0$ as $\xi \to \pm\infty$.

1. Given density fluctuation amplitudes $g(\xi)$
2. Compute $f(\xi)$
3. Compute P, u, v

- In general must solve this numerically
- In certain limiting cases uniform approximations can be derived
- Thick layer: $kL \to \infty$.

$$f(\xi) \sim -\frac{\overline{\rho}}{k^2 L^2}\frac{d}{d\xi}\left(\frac{g}{\overline{\rho}}\right)$$

$$K = \frac{\epsilon^2 V^2}{4L}\int_{-\infty}^{\infty}\frac{g^2}{\overline{\rho}}d\xi$$

- Thin layer: $kL \to 0$, boundary layer approximation outer solution

$$p' = \frac{\rho_1 V}{\rho_1+\rho_2}\cos kx \exp(-ky) \qquad y > 0$$

$$p' = -\frac{\rho_2 V}{\rho_1+\rho_2}\cos kx \exp(ky) \qquad y < 0$$

$$K = \frac{\epsilon^2 V^2 k}{4(\rho_1+\rho_2)}$$

- In general conclude that less kinetic energy is generated when layer is thick.

Application to a particular profile

$$\overline{\rho} = 1 + A \tanh(y/L) \quad A \; - \; \text{Atwoodratio}$$

$$g = \frac{1}{2} \frac{1}{\cosh^2(y/L)}$$

$$\rho_0 = \overline{\rho} + \frac{\epsilon}{2L} \frac{1}{\cosh^2(y/L)} \cos kx$$

$$K = \frac{\epsilon^2 k V^2}{2(\rho_1 + \rho_2)} E(\lambda, A), \quad \lambda = kL$$

$$E(\lambda, A) \sim 1/2 + \lambda \left(\frac{A^2 - 1}{4A} \right) \log \left(\frac{1+A}{1-A} \right) \qquad \lambda \to 0$$

$$E(\lambda, A) \sim \frac{1}{3\lambda} \qquad \lambda \to \infty$$

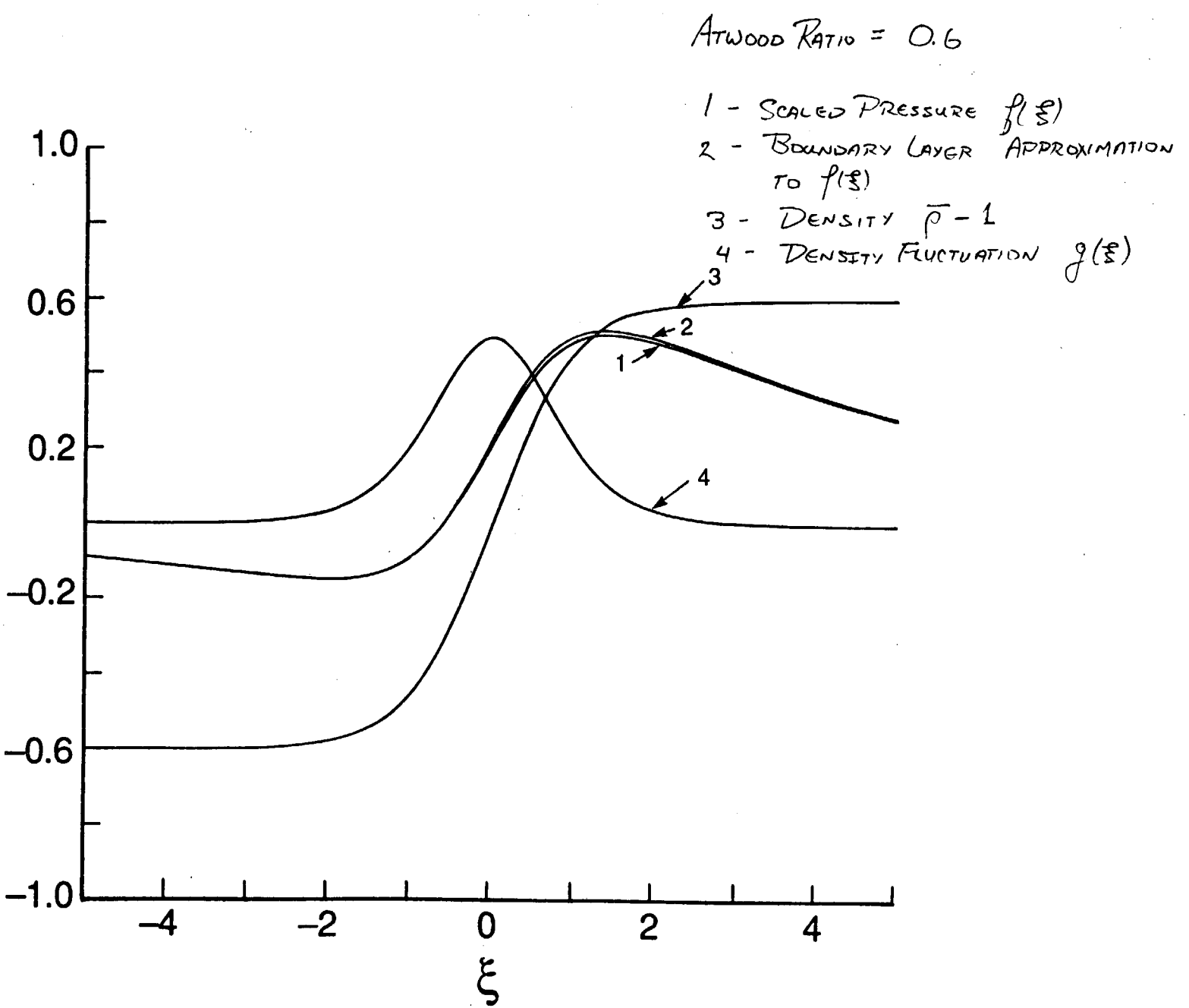
ATWOOD RATIO = 0.6
1 - SCALED PRESSURE f(ξ)
2 - BOUNDARY LAYER APPROXIMATION TO f(ξ)
3 - DENSITY ρ̄ - 1
4 - DENSITY FLUCTUATION g(ξ)
1.0
0.6
0.2
-0.2
-0.6
-1.0
-4
-2
0
2
4
ξ
1
2
3
4

Effects of Incompressible and Compressible Vortex Reconnection

ROBERT M. KERR[1], DAVINDER VIRK[1,2], FAZLE HUSSAIN[2]

[1]Geophysical Turbulence Program, National Center for Atmospheric Research, P.O. Box 3000, Boulder, CO 80307-3000
[2]Department of Mechanical Engineering, University of Houston, Houston, TX 77004

ABSTRACT

The reconnection of two anti-parallel viscous vortices is studied by both incompressible and compressible simulations in a periodic domain. Using symmetries along with increased resolution in the direction normal to the dividing plane allows Reynolds numbers (Re) based on circulation divided by viscosity range up to 3200 for the incompressible case. As Re is increased there is a significant increase in the peak vorticity that is consistent with a singularity of the three-dimensional, incompressible Euler equations in a finite time. However, a significant increase in the volume integral of enstrophy is not observed. After reconnection the energy spectrum obeys k^{-2}, consistent with vortex sheet formation in the reconnection region. In the compressible calculations weak shocks are formed. The vortex-shock interaction causes the vortices to be flattened. The peak vorticity in the symmetry planes is much lower for the high Mach number (M=2) case than that in the low M and incompressible calculations.

1 INTRODUCTION

Despite evidence that flow structures are dynamically significant at both the large and small scales of turbulent motion, it is still not understood what role these structures play in turbulent cascade, transport and noise production. Some experimental examples of structures in shear flows are horseshoe vortices in boundary layers and ribs that form the three-dimensional structure of a mixing layer (For reviews of experimental and numerical studies of coherent structures in turbulent shear flows see Metcalfe et al. (1985) and Hussain (1986).) Attempts to understand these structures using idealized vortex elements are limited by our ability to represent the Euler and Navier-Stokes equations with these methods. Attempts to understand their structure with viscous calculations of homogeneous turbulence are limited by resolution. For example, visualization of vorticity in viscous calculations suggests that vortex filaments are the dominant structures (Rogers & Moin, 1987). But analysis of strain rates in simulations of isotropic, forced turbulence

and the homogeneous shear calculation of Rogers & Moin (1987) suggest that the smallest resolved structures are sheets (Ashurst et al., 1987).

A related question is whether there is a singularity of the three-dimensional, incompressible Euler equations. A numerical study of vortex interactions by Kerr & Hussain (1989) (to be referred to as KH), where symmetries allow sufficient resolution to clearly identify vortex sheets, suggests that there is at least a singularity of the peak vorticity. KH reached their conclusions by using direct simulation of the Navier-Stokes equations with small viscosities to study vortex reconnection, or cut-and-connect. After reviewing those results and discussing their limitations, the role vortex reconnection might play in the turbulent cascade will be discussed and some new calculations exploring reconnection in compressible flows will be discussed.

2 INCOMPRESSIBLE RECONNECTION

All of the vortex reconnection calculations to be discussed are to some degree inspired by the vortex filament calculation of Siggia (1984). He emphasized two dynamic processes, first that vortex filaments tend to be anti-parallel at the point of closest approach and second that through self-induction this anti-parallel pair collapses in a finite time. Unfortunately Siggia's study fails as a model for the Euler equations because it does not address core deformation as the vortex filaments collapse and cannot determine the importance of viscosity, which is crucial to the reconnection process. The most extensive test of the validity of the late stages of Siggia's calculation are the three-dimensional viscous calculations of KH using spectral methods. In those calculations symmetries are assumed at planes between the vortices and along the vortices, to be called the dividing and symmetry planes respectively, and are used along with a fine mesh perpendicular to the dividing plane to provide enough resolution to simulate Reynolds numbers based on circulation divided by viscosity (Γ/ν) up to 3200.

In agreement with the calculation of Pumir & Kerr (1987) KH find that the reconnection region is dominated by vortex sheets. Figure 1 shows contours of local vorticity in the symmetry plane of the two original vortex tubes of KH for Re = 3200. Note how at a late time (figure 1c) the original vortex breaks into a head and what Melander & Hussain (1989) describe as threads. The second conclusion of KH is that while the vortex sheets inhibit singularity formation, figure 2 shows that the peak vorticity appears to increase rapidly (up to a factor of 8) as the viscosity approaches zero. They also find that the enstrophy increases slowly without any indication of singular behavior, suggesting that if there is a singularity in the peak vorticity that it occurs on a set of measure zero. At roughly the time of peak vorticity KH show that the drop in circulation in the plane shown in figure 1 becomes steeper as Re increases and the vorticity in the dividing plane between the two vortices increases significantly. Additional results not reported by KH are that the enstrophy production rate increases rapidly up to this time, then decreases rapidly, and that the peak rate-of-strain in the symmetry plane, defined by the enstrophy production divided by the enstrophy, increases at a slightly faster rate than the peak vorticity (that is greater than a factor of 8) and does not show any signs of saturation.

The suggestion by KH that there is only a singularity in the peak vorticity, if it is generalizable to all fluid turbulence, is not consistent with accepted dogma, which states that the volume integral of enstrophy has a singularity. This belief stems primarily from spectral closure analysis starting with Proudman & Reid (1954), but it is supported by the experimental observation that the velocity derivative skewness, which is related to the normalized enstrophy production, is independent of Re. In analogy with the two-dimensional magneto-hydrodynamic equations where a spectral closure (Pouquet, 1978) predicts a singularity, in a direct calculation (Frisch et al., 1983) current sheets inhibit the formation of a singularity. For the reconnection problem KH shows that vortex sheets inhibit singularity formation in a similar manner, but the analogy cannot necessarily be extended to turbulence in general unless the Re independence of the experimentally observed skewness can be accounted for. Another piece that must fit into this puzzle is the observation by Kerr (1987) that strain statistics support the appearance of sheet-like structures at small scales and that the dominant orientation of the strain is related to the skewness. Some aspects of this orientation are reported experimentally by Tsinober in these proceedings.

Energy spectra near the time of peak vorticity have been analyzed by fitting a $k^{-\gamma}\exp(-\delta k)$ form to the energy spectrum. Ideally, δ should be small enough that the simpler form $k^{-\gamma}$ could be fit by hand over some range, but in practice it was found that there was always a significant exponential component to the spectrum and that simply fitting $k^{-\gamma}$ overestimated γ. For the $\mathrm{Re}=3200$ calculation of KH $k^{-\gamma}\exp(-\delta k)$ was fit between wavenumbers 10 and 160 in order to capture both inertial subrange effects and dissipation range effects. Figure 3 shows that for $\mathrm{Re}=3200$ γ decreases up to the time of the peak vorticity, then appears to settle at a value of -2, which is consistent with vortex sheets. This result suggests that some of the structures observed in more viscous calculations of reconnection by Melander & Hussain (1989) are dominated by vortex sheets at higher Re. The length scale δ also decreases up to the time of the peak vorticity then is relatively constant. Because reconnection is a self-induction mechanism for producing small-scale structures, it had been hoped that it might provide a means for energy to be transferred to small scales and producing the experimental $k^{-5/3}$ spectrum without invoking classical cascade arguments. Clearly this goal was not reached since most of the energy stays in the large scales after the time of peak vorticity and the spectrum is not $k^{-5/3}$. Since a k^{-2} energy spectrum would indicate a logarithmic divergence in the integral enstrophy, determining how the energy spectrum reaches k^{-2} might shed some light on the singularity issues discussed above.

Before the time of peak vorticity vortex sheets can be identified only in the plane of symmetry, as in figure 1a. As shown in figure 7c after that time the flow can be divided into two regions. Following Melander & Hussain (1988) there is a region where vortex sheets form a dipole that grows normal to the symmetry plane. We expect that a viscous timescale is required to fully diffuse these sheets. Second, there is a region of reconnected vortices crossing the dividing plane between the two original vortices. In the vortex sheet region there is a self-induced velocity in the direction of the original vortices that pulls the reconnected vortices outward. This flow is very similar to the predictions for X-type magnetic field line reconnection by Parker (1957), although whether the MHD equations

have singular behavior has not been shown. A singularity of the inviscid MHD equations might explain nanoflares in the solar corona (Parker, private communication).

3 RELATION TO TURBULENT CASCADE

The inconsistency between the k^{-2} energy spectrum for reconnection and the observation of a $k^{-5/3}$ is similar to an inconsistency in two-dimensional turbulence that was recently resolved. It was suggested by Saffman (1971) that in analogy with the one-dimensional Burger's equation, where shocks yield a k^{-2} energy spectrum, that vorticity jumps in two dimensions should yield a k^{-4} energy spectrum. This was inconsistent with thermodynamic arguments by Batchelor (1969) and Kraichnan (1967) and atmospheric observations of large-scale quasi-two dimensional motion that suggested a k^{-3} energy spectrum. Recent calculations by Brachet et al. (1986) and analysis by Gilbert (1988) (and a mid-1970s calculation by Rogallo, private communication) find that initially there is a k^{-4} energy spectrum as vorticity jumps form from random initial conditions, then as these jumps are piled up and wrap around vortex cores a k^{-3} spectrum can form. Could an analogous process happen in three dimensions, converting vortex sheets with a k^{-2} spectrum into a $k^{-5/3}$ spectrum?

A process like this has been suggested in two theoretical papers by Parker (1969) and Lundgren (1982). With certain assumptions each paper shows how by piling up vortex sheets a $k^{-5/3}$ spectrum can be obtained. But several secondary predictions from these studies are not consistent. Parker makes a closure type of assumption and as a result predicts a singularity in the enstrophy. The closure assumption used assumes local wavenumber interactions, which is inconsistent with a calculation of low Re turbulence by Domaradzski (1988). Lundgren assumes a large-scale strain that converts a two-dimensional analysis similar to Gilbert (1988) into a three-dimensional spectrum and finds only an exponential increase in the enstrophy, which might be consistent with KH. The major drawbacks to Lundgren's analysis are that he does not provide a mechanism for producing the vortex sheets and his analysis assumes a single sheet wrapped around a core, whereas the calculation of Siggia (1984) shows that anti-parallel structures dominate.

What type of vortex structures appear in a calculation without the symmetries imposed by KH, but remaining more faithful to the Euler equations than the calculation of Siggia (1984)? The most relevant calculations of this type are by Melander & Zabusky (1986) and Chua & Leonard (1987), where vortices seem to pair, form sheets, then loop around the original filaments. Could this looping process produce the vortex piling we suspect is necessary to obtain the $k^{-5/3}$ spectrum? If so, how can we model this complex process? Could helicity constrain or enhance this process?

4 COMPRESSIBILITY

While reconnection has not answered all our questions about the cascade process, it still provides a unique mechanism for producing small-scale motion and the effects of this need to be investigated. Introducing compressibility effects provides more mechanisms to alter enstrophy and vorticity, e.g. non-barotropic production, viscous production. Also, shocks can form and interact with the vortices in the compressible simulations. To investigate the

influence of these mechanisms on vortex reconnection we have simulated a case with the same symmetries as the incompressible case of KH. However, due to higher computational requirements, for the compressible case Re is lower and equal to 700. We used divergence-free initial velocity fields with the Mach number (M) of 0.5 and 2.0 and a Prandtl number of 0.67.

Figures 4a-d show the circulation and the peak vorticities in the symmetry planes and dividing planes for both the $M=0.5$ and $M=2.0$ calculations. The $M=0.5$ calculation shows behavior that is very similar to the incompressible calculations, even though density plots show the formation of weak shocks on both sides of the vortices. In figure 4a the sum of the circulations in the symmetry and dividing planes is nearly constant, with the curves crossing near the time of peak vorticity in the symmetry plane in figure 4b. The peak vorticity in the symmetry plane in figure 4b drops a small amount initially, then increases by a factor 1.4, which is consistent with an incompressible calculation at $Re=800$. Vorticity plots show the same three regimes in time noted by Melander & Hussain: approach and deformation, bridging, and finally threading and dissipation. However, for $M=2.0$ the compressibility effects significantly change the scenario. While figure 4c shows that the sum of the circulations is still constant, the time at which the curves in figure 4c cross has changed and the behavior of the peak vorticity in the symmetry plane is significantly different. First there is a sharp drop in the peak vorticity, then a series of peaks due to the combined effects of periodicity, shocks, and non-barotropic vorticity production.

These effects can be partially explained by referring to contour plots. Figures 5a-e and 6a-e show the vorticity and density for a series of times from the $M=2$ calculation. In figure 5a at $t=1.8$ the initial Gaussian vortex has begun to flatten in a manner reminiscent of the incompressible cases, but in figure 5b note that the flattened vortex has not moved as close to the dividing plane as it did for the incompressible case in figure 1. This might be due to negative non-barotropic production of vorticity that is observed to be the same magnitude as vorticity production due to vortex stretching. Only in figure 5e at $t=36.5$, by which time dissipation has made the flow relatively incompressible, are the vorticity profiles similar to the incompressible case with a characteristic head and following tail.

The strong non-barotropic production is associated with shock formation. The initial density in these calculations was uniform, but by $t=1.8$ in figure 6a the density in the vortex core is half that in the surrounding fluid. Figure 6a also shows two shocks forming in front of and behind the vortex core. In figure 6b these shocks have moved away from the vortex core, with the trailing shock beginning to cross the periodic boundary on the left. By $t=14.8$ the shocks have crossed one another and the trailing shock is interacting with the leading edge of the vortex core in the center of the figure. The numerous minor maxima of the peak vorticity in figure 4d are associated with positive non-barotropic production as the shocks cross the periodic boundaries and interact with the original vortices.

Despite the distinctly different behavior of the peak vorticity and circulation for the $M=2.0$ calculation the overall aspects of the enstrophy are very similar to the incompressible calculations. The plot of enstrophy at $t=45.7$ (figure 7b), slightly before the crossover of the circulation, shows bridges perpendicular to the original vortex tubes

similar to an incompressible calculation at Re = 1600 (figure 7c). Note that only one-fourth of the two filaments is shown because of the symmetries highlighted in figure 7a.

The plots of ω_z in the xy dividing plane, for the M = 2.0 and M = 0.5 calculations are shown in figures 8a and 8b at the times when the circulation in xz symmetry plane has decayed to 20% of initial value. Note that the bridges are more flattened in the M = 2 calculation. This might be due to the shock interaction discussed. A density plot for M = 2 at t = 76.2 is shown in figure 9.

A comparison of the enstrophy production terms shows that the stretching production $\omega_i e_{ij} \omega_j$ (b) is dominant in the M = 0.5 simulation at all times, thus the results are similar to the incompressible case. However, in the M = 2.0 case the non-barotropic term $(\omega.(\nabla P \times \nabla(1/\rho))$ (c), and the divergence term $(\omega.\omega(\nabla.\vec{u}))$ (d) (even when $(\nabla.\vec{u})$ is zero initially) are of the same order of magnitude. The viscous dissipation term $\mu\omega.(\nabla(1/\rho) \times (\nabla \times \omega))$ (e) is an order of magnitude smaller. Three-dimensional iso-surface plots of these terms show that they are most significant in the bridges shown in figure 7b and near the symmetry plane. The contour plots of these terms in a plane passing through the bridges, for the M = 2.0 calculation, are shown in figure 10(a-e). In the enstrophy equation, the terms b and c are added while d and e are subtracted. The enstrophy in figure 10a can be divided into two regions. The cylindrical region of maximum enstrophy represents the threads; the remaining part of the original vortex. The region near the left boundary represents the bridging across the dividing plane. In figures 10b-d the contribution to the enstrophy production in the threads by each of the three terms is roughly equivalent. In the bridging region the only significant production term is the divergence production in figure 10d, whose magnitude is roughly twice the production by any of the terms in the threads. The viscous term in figure 10e is an order of magnitude less than the production terms in figures 10b-d and causes dissipation in both the bridges and the threads.

A comparison of the spectra of the solenoidal and compressible parts of the velocity field in the M = 0.5 and M = 2.0 cases was also done. We find that the energy is higher in the solenoidal part for the M = 0.5 case at all times, consistent with the predominantly incompressible behavior of this simulation. In the M = 2.0 case, however, at later times the energy is higher in the solenoidal part for low wavenumbers, but at higher wavenumbers the compressible part of the velocity has higher energy. This implies that the M = 2.0 calculation does have significant compressibility. This behavior of the energy is consistent with the simulations of isotropic turbulence by Passot & Pouquet (1987). Figures 11a,b show the solenoidal and compressible parts of the velocity field for M = 2.0 at t = 42.7, which is the time of maximum peak vorticity, to demonstrate this. The peak in the compressible part near k = 10 was not seen by Passot & Pouquet (1987) and might be related to acoustic noise generation.

In summary, it is increasingly becoming apparent that understanding turbulent structures will be an important part of any theory of turbulence. KH has shown how vortex sheets form and could be related to singularity formation. After the time of peak vorticity they observe vortex bridging across a plane of symmetry. These are only some of the structures that have been observed in direct simulations of turbulence. But great care must be

taken even in calculations where bridging similar to that described by KH and Melander & Hussain (1989) does appear. For example, in calculations by Kida & Takaoka (1987) and Melander & Zabusky (1986) another type of bridging forms parallel to the vortex sheets, but is not observed by KH and might be a viscous structure that is unrelated to the underlying inviscid phenomena. More comparisons with observed structures in incompressible flows, such as horseshoe vortices in boundary layers and ribs in mixing layers, need to be done to determine how important reconnection and vortex sheet formation are in observed turbulent flows. The compressible calculations demonstrate that some of the incompressible conclusions might not apply to the interaction of supersonic vortices. In particular, the evidence suggests that in the inviscid limit the peak vorticity is not singular. This could be because shock formation, which in the inviscid limit is singular, occurs first and introduces dissipative effects at an early time.

ACKNOWLEDGEMENTS

RMK acknowledges support of ARO MIPR No. 103-89 at the National Center for Atmospheric Research. DV acknowledges support of the Advanced Study Program at NCAR. NCAR is funded by the National Science Foundation. FH acknowledges support of DOE Grant No. DE-FG05-88ER13839.

REFERENCES

Ashurst, W. T., Kerstein, A. R., Kerr, R. M. & Gibson, C. H. 1987 *Phys. Fluids*, **30**, 2343.

Batchelor, G.K. 1969 *Phys. Fluids Suppl. II*, 233.

Brachet, M.E., Meneguzzi, M. & Sulem, P.-L. 1986 *Phys. Rev. Lett.* **57**, 683.

Chua, K. & Leonard, A. 1987 *Bull. Amer. Phys. Soc.* **32**, 2098.

Domaradzki, J. A., 1988 *Phys. Fluids*, **31**, 2747.

Frisch, U., Pouquet, A., Sulem, P.-L. & Meneguzzi, M. 1983 *J. Mécanique Théor. Appliquée* **2D**, 191.

Gilbert, A.D. 1988 *J. Fluid Mech.* **193**, 475.

Herring, J. R. & Kerr, R. M. 1982 *J. Fluid Mech.* **118**, 205.

Hussain, F. 1986 *J. Fluid Mech.* **173**, 303.

Kerr, R. M. 1987 *Phys. Rev. Lett.* **59**, 783.

Kerr, R. M. & Hussain, F. 1989 *Physica D.*

Kida, S. & Takaoka, M. 1987 *Phys. Fluids* **30**, 2911.

Kraichnan, R.H. 1967 *Phys. Fluids* **10**, 1417.

Lesieur, M. & Rogallo R. 1989 *Phys. Fluids A1*, 718–722.

Lundgren, T.S. 1982 *Phys. Fluids* **25**, 2193.

Melander, M. & Hussain, F. 1989 *Phys. Fluids A1*, 633.

Melander, M. & Zabusky, N. 1986 *IUTAM symposium on fundamental aspects of vortex motion*, Tokyo 116.

Metcalfe, R., Hussain, F. & Menon, S. 1985 *Turb. Shear Flows* V Cornell U., 4.13.

Parker, E. 1957 *J. Geophys. Res.* **62**, 509.
Parker, E. 1969 *Phys. Fluids* **12**, 1592.
Passot, T. & Pouquet, A. 1987 *J. Fluid Mech.* **181**, 441.
Pouquet, A. 1978 *J. Fluid Mech.* **88**, 1.
Proudman, I. & Reid, W. H. 1954 *Phil. Trans. Roy. Soc. (London)* **247**, 163.
Pumir, A. & Kerr, R. M. 1987 *Phys. Fluids* **58**, 1636.
Pumir, A. & Siggia, E. D. 1987 *Phys. Fluids* **30**, 1606.
Saffman, P.G. 1971 *Stud. Appl. Maths* **50**,377.
Rogers, M. M., & P. Moin, 1987 *J. Fluid Mech.*, **176**, 33.
Siggia, E. D. 1984 *Phys. Fluids* **28**, 794.

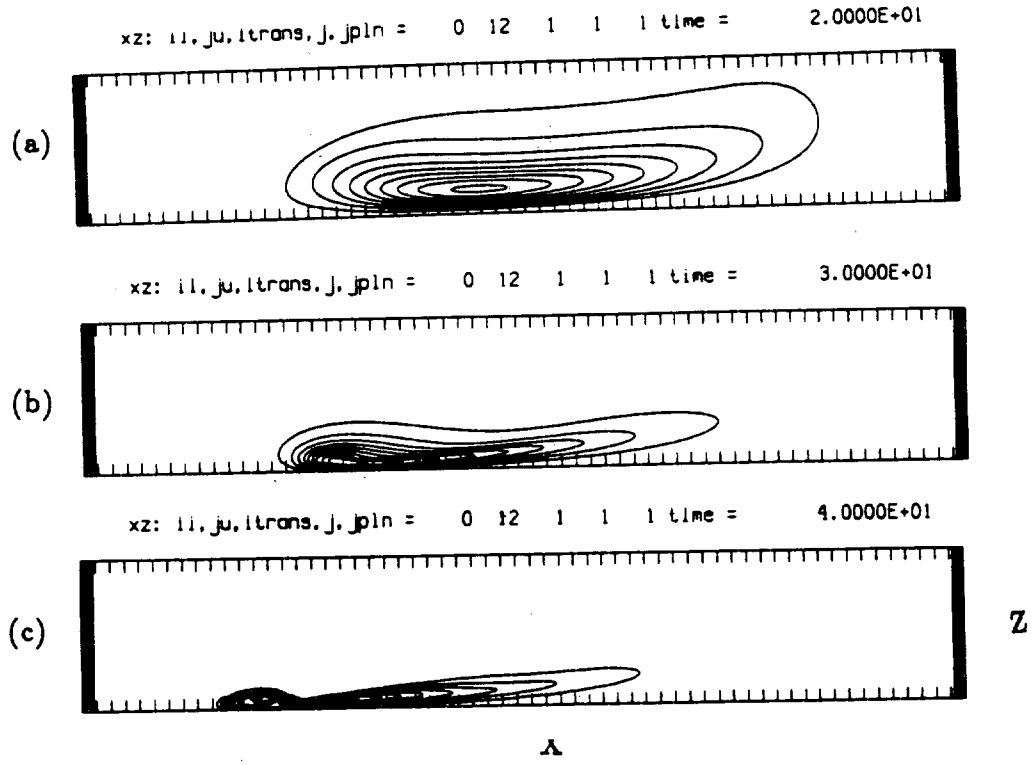

Figure 1. Contours of ω_y in xz symmetry plane at three times for Re = 3200, a: t = 20, b: t = 30, and c: t = 40.

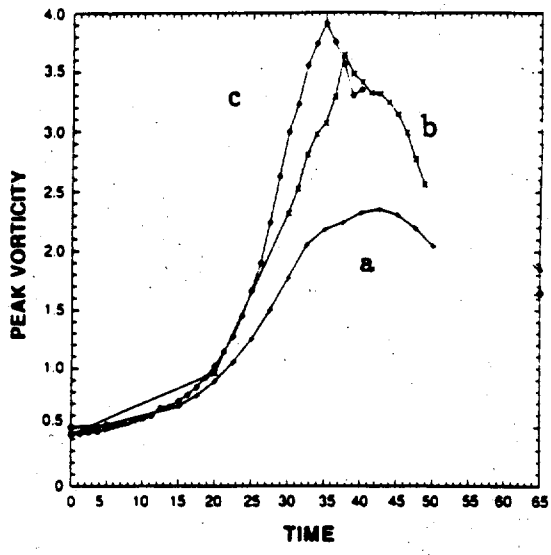

Figure 2. Peak vorticity as a function of time for three calculations. a: Re = 1600, b: Re = 2300, and c: Re = 3200.

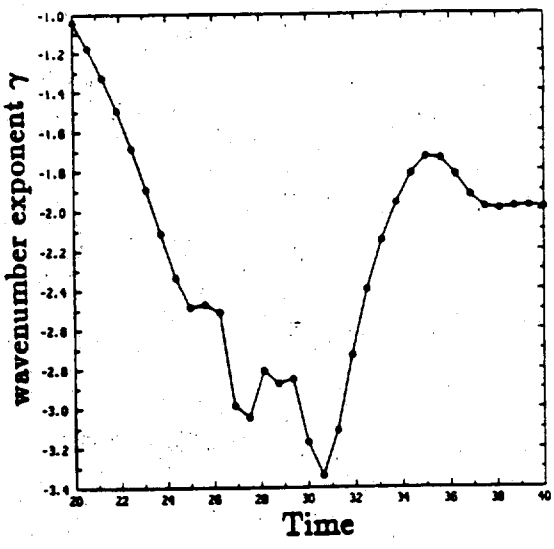

Figure 3. Wavenumber exponent γ as a function of time for Re = 3200.

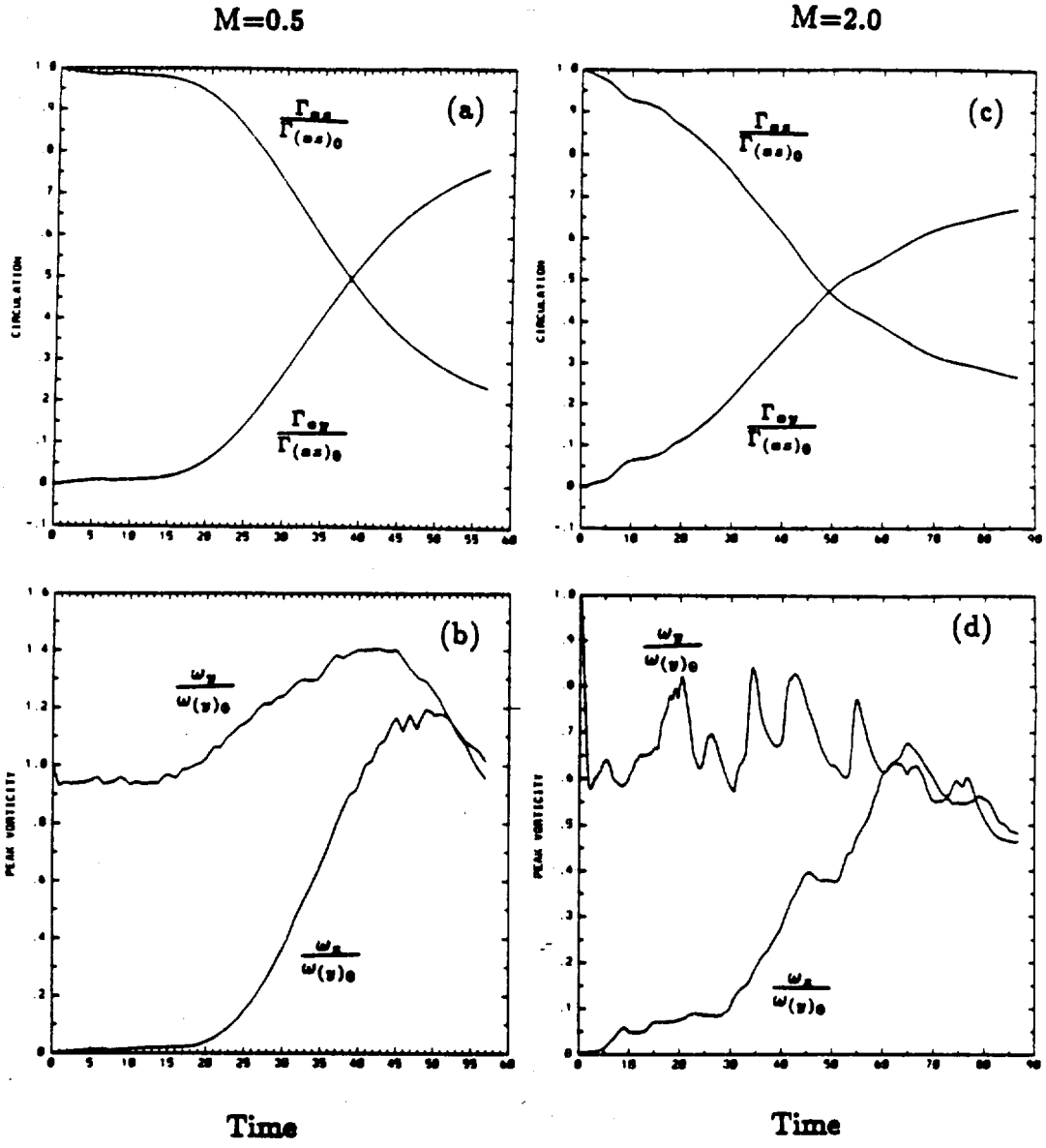

Figure 4. Circulation and peak vorticity in xz symmetry plane (Γ_{xz}, ω_y) and xy dividing plane (Γ_{xy}, ω_z), normalized by initial circulation ($\Gamma_{(xz)_0}$) and peak vorticity ($\omega_{(y)_0}$) in the xz symmetry plane.

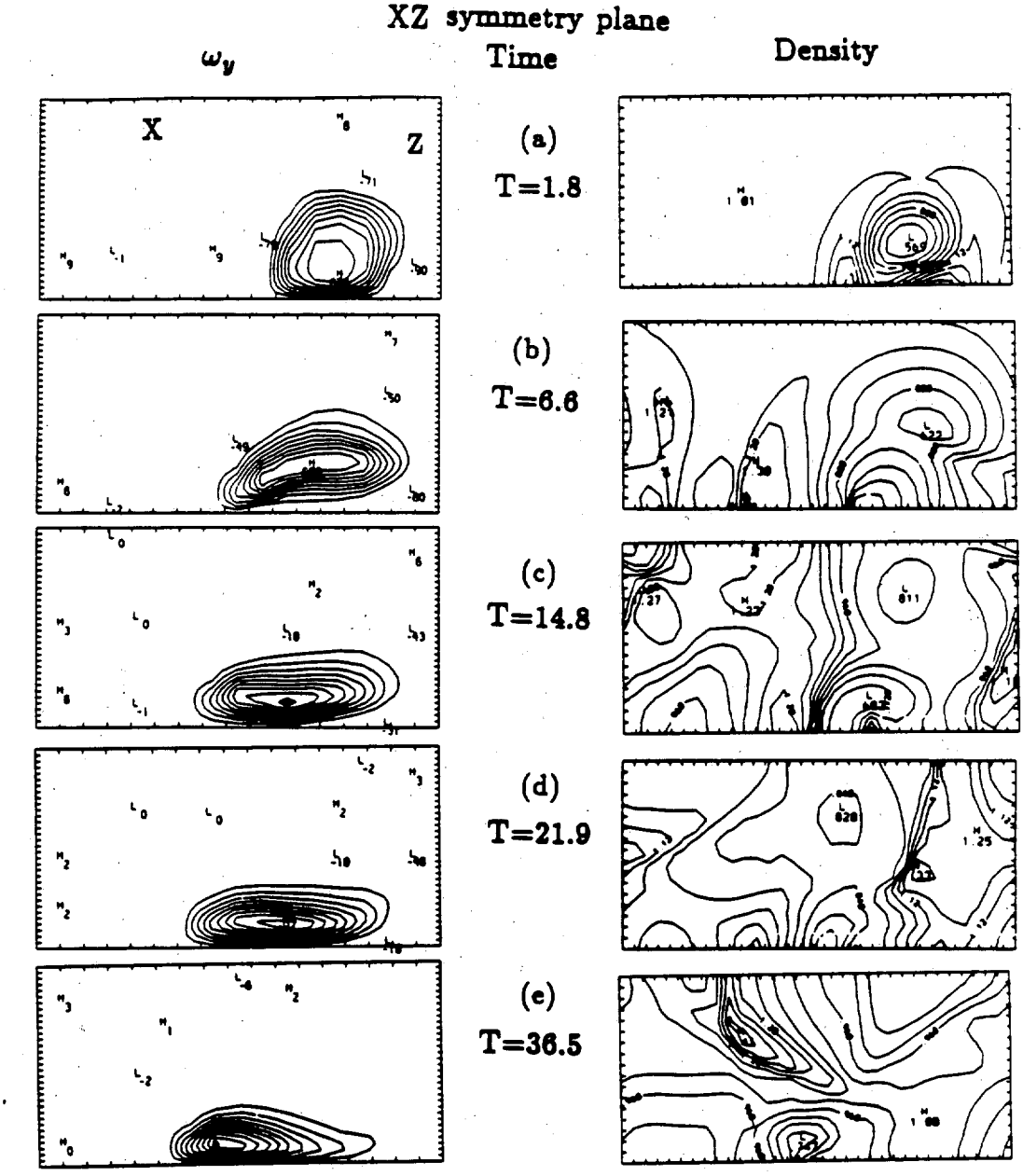

Figure 5. ω_y in xz symmetry plane at t = 8.6, for compressible case with M = 2.0.

Figure 6. ρ in xz symmetry plane at t = 8.6, for compressible case with M = 2.0.

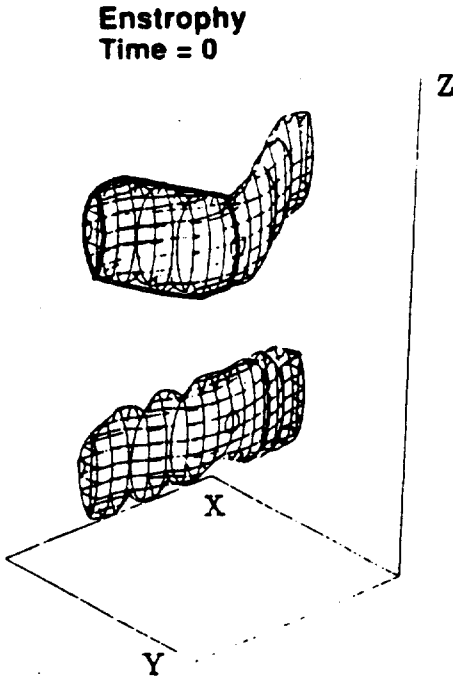

Figure 7a. Coordinate system and initial enstrophy field in a fully periodic domain. The quadrant that is actually calculated is highlighted.

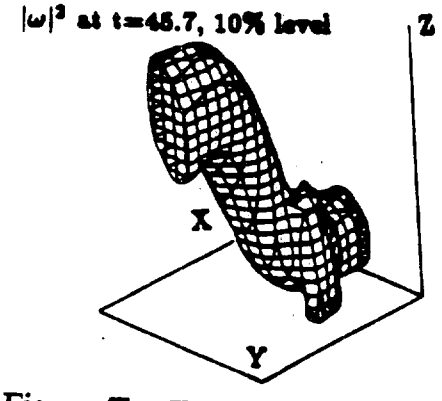

Figure 7b. Enstrophy at $t = 45.7$ for the compressible case with M = 2.0.

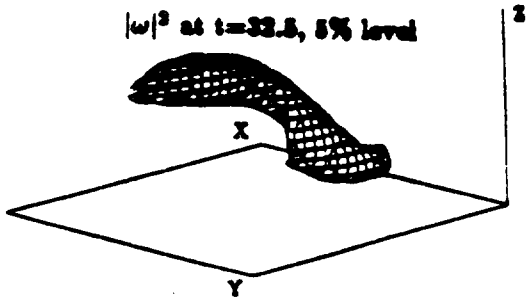

Figure 7c. Enstrophy at $t = 32.5$ (time of peak vorticity) from an incompressible calculation at $Re = 1600$.

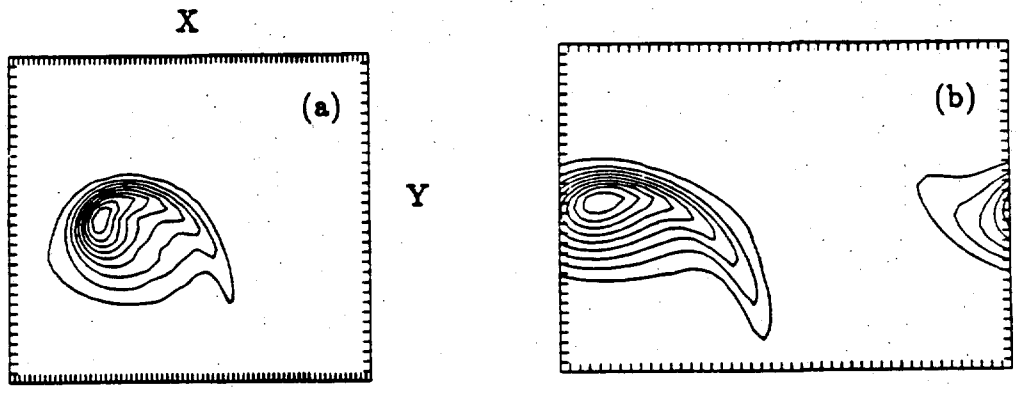

Figure 8. ω_z **in xy dividing plane for compressible simulations. (a) M = 0.5, t = 56.8, right-hand domain is not shown. (b) M = 2.0, t = 76.2, central domain in x is not shown.**

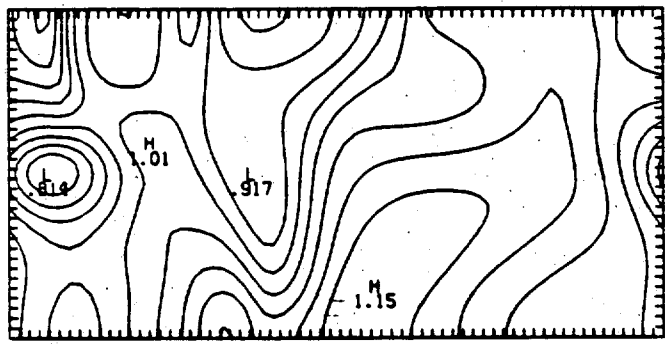

Figure 9. ρ **in xy dividing plane for M = 2.0 compressible case at t = 76.2.**

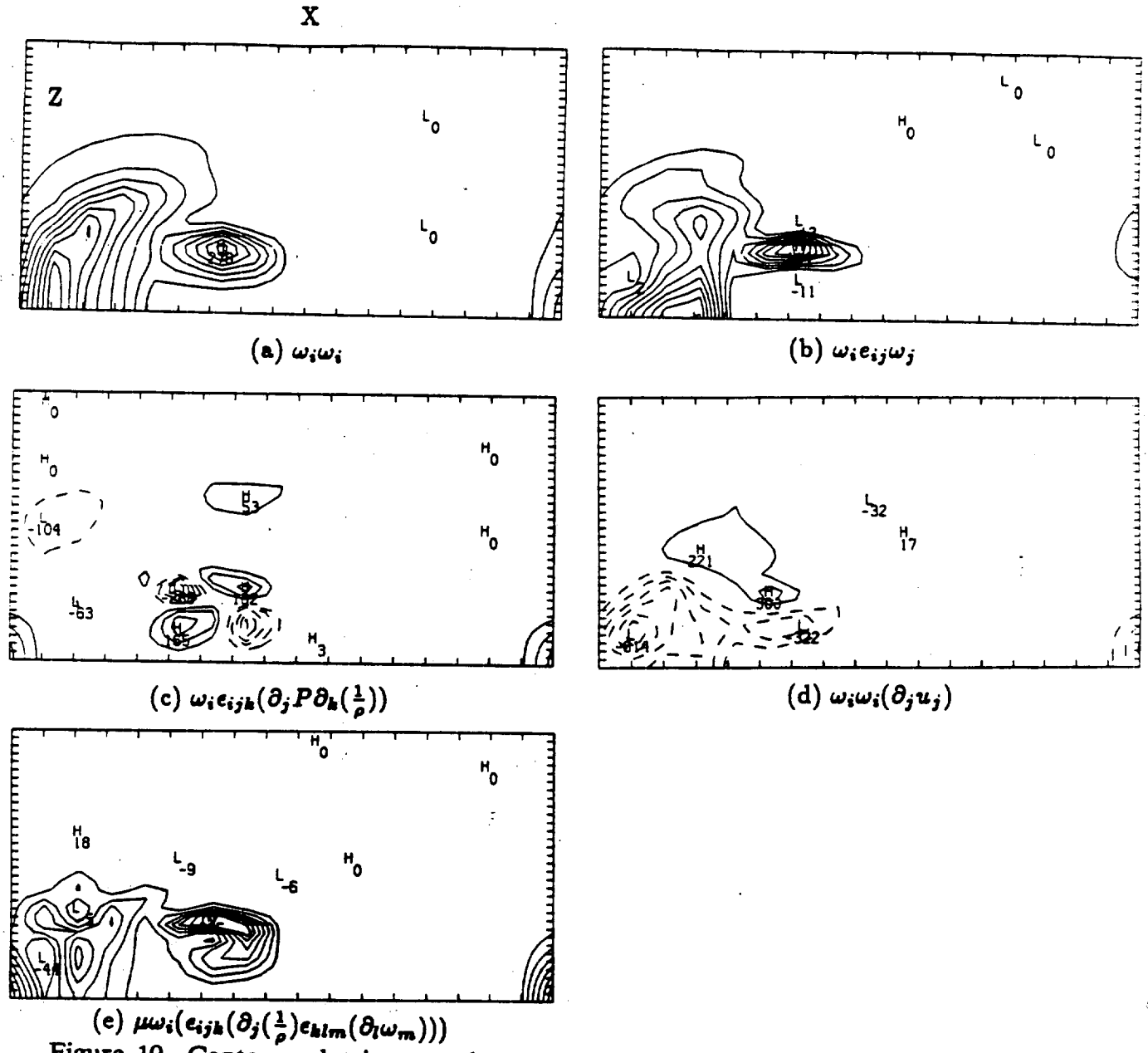

Figure 10. Contours plot in a xz plane passing through the bridges at t = 76.2, for compressible case with M = 2.0.

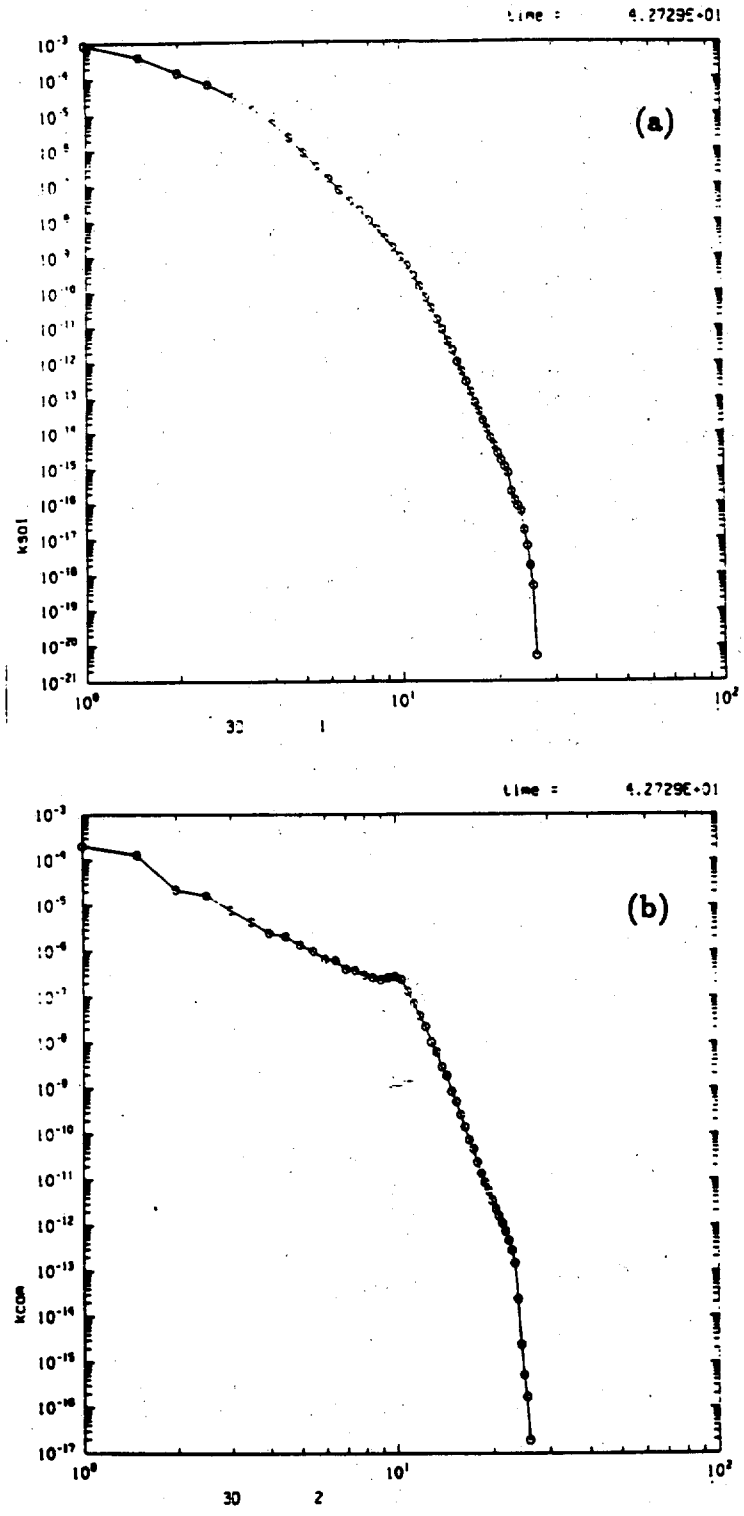

Figure 11. Three-dimensional kinetic-energy spectra for M=2.0 at t=42.7. (a): solenoidal part; (b): compressible part.

In a calculation of inviscid, three-dimensional incompressible vortex reconnection it is found that the peak vorticity roughly obeys (t*-t)**-1.28 and the rate-of-strain along the peak vorticity obeys (t*-t)**-1, with t*=30.2. This is consistent with Caffarelle et. al. (1982) who state that if there is a singularity of the Euler equations that sup(\omega) >= ((t^*)-t)**-1 and the simple conclusion from the vorticity equation that if the sup(\omega) obeys a power law that sup(strain along vorticity) goes as ((t^*)-t)**-1.

The last fully resolved calculation used 64 nodes along the vortex (y), 256 in the direction of propagation(x), and 512 perpendicular to the vortex (z). The initial condition was essentially a perturbation of wavelength pi on two anti-parallel vorticies centered pi/2 from the dividing plane between them with a Gaussian profile of exp(-r**2/0.5**2).

The box was of dimensions 4pi x 8pi x 4pi. Using symmetries the actual domain was 4pi x 4pi x 2pi.

The peak vorticity is located in the cusp between the head and tail and the alignment of rates-of-strain in the three cartesian directions at the location of the peak vorticity is roughly, 2:1:-3, coincidentally similiar to that found by Ashurst, Kerstein, Kerr and Gibson (1987).

Figure 1 show the peak vorticity as a function of time for the inviscid case, the 10 times the strain along the peak vorticity, and the peak vorticity from several viscous calculations. Figure 2 shows the vorticity contours in the xz symmetry plane at t = 22, 25 and 27 with the direction expanded 16 times. Figure 3 shows the cartesian components of the strain in the xz symmetry plane and in the xy plane through the peak vorticity at t=27.3. Note how the xy contour of the strain along the vorticity (e22) shows focussing where the vorticity is greatest.

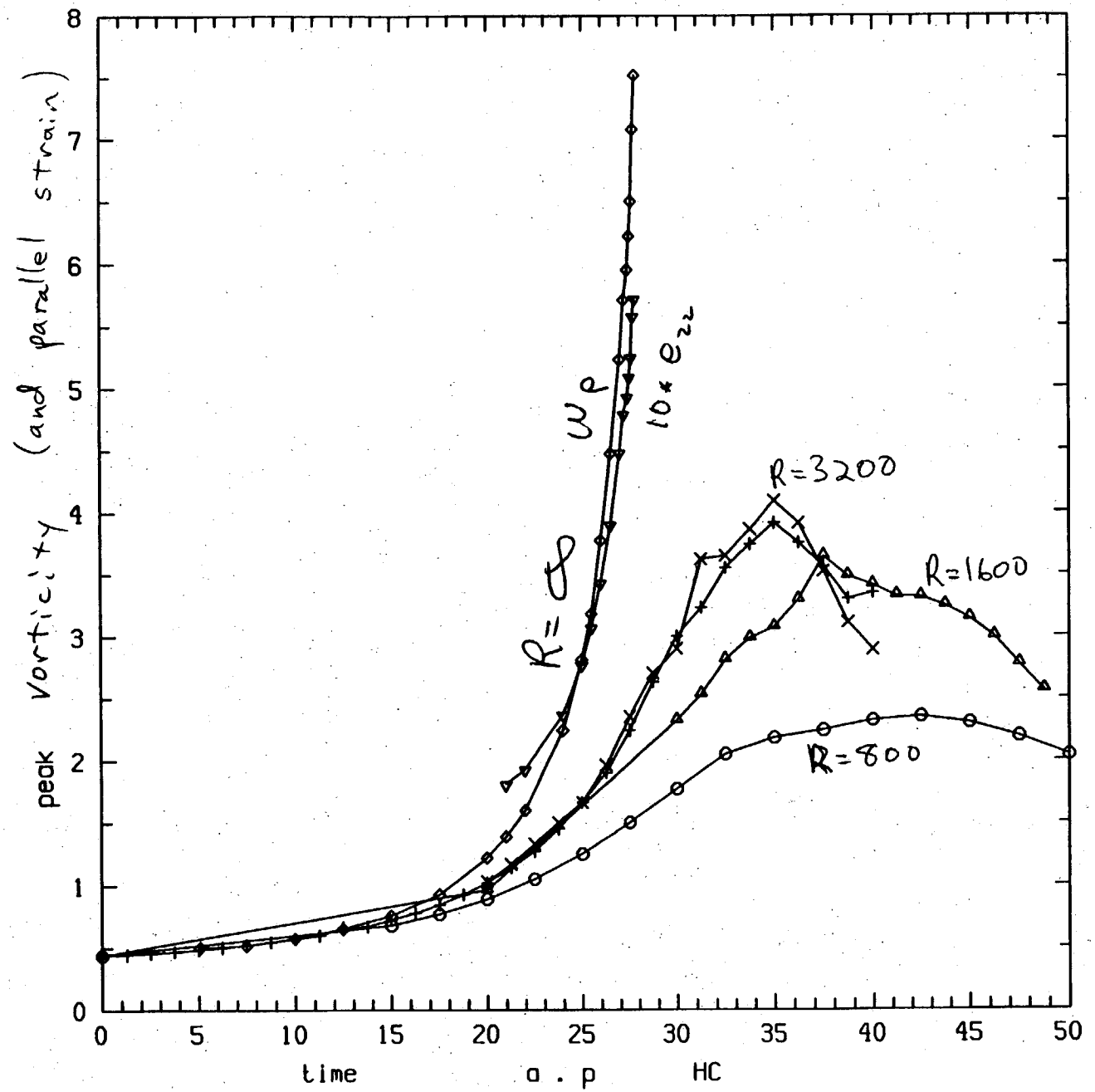
peak Vorticity (and parallel strain)
time
a . p
HC
R=∞ ωp
10* e22
R=3200
R=1600
R=800
0
1
2
3
4
5
6
7
8
0
5
10
15
20
25
30
35
40
45
50

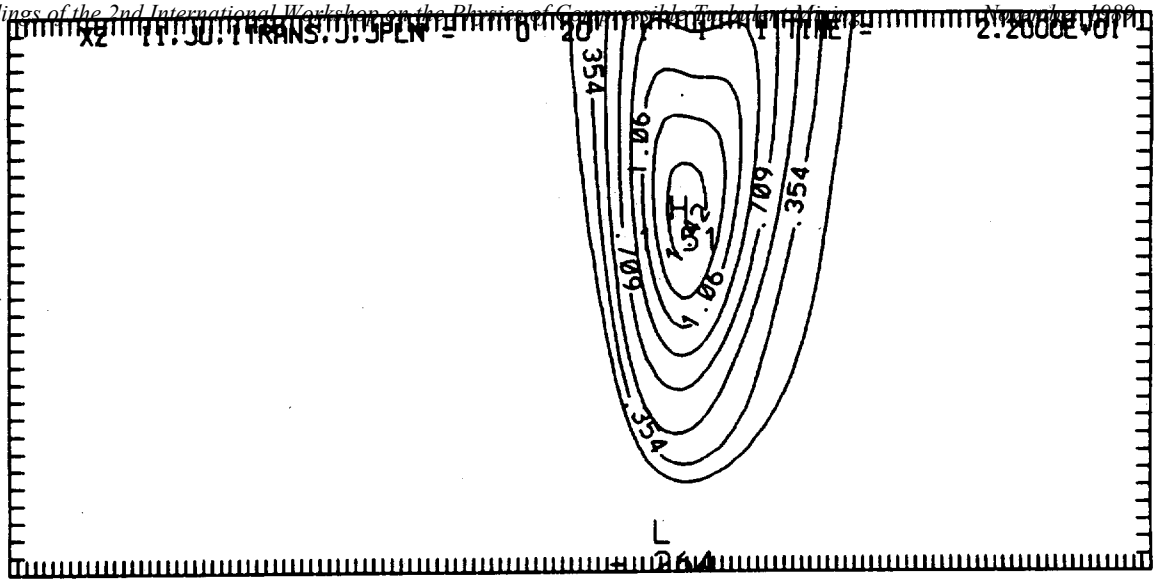
XZ
TIME =
2.2000E+01
.354
1.06
.709
1.42
.709
1.06
.354
L
H

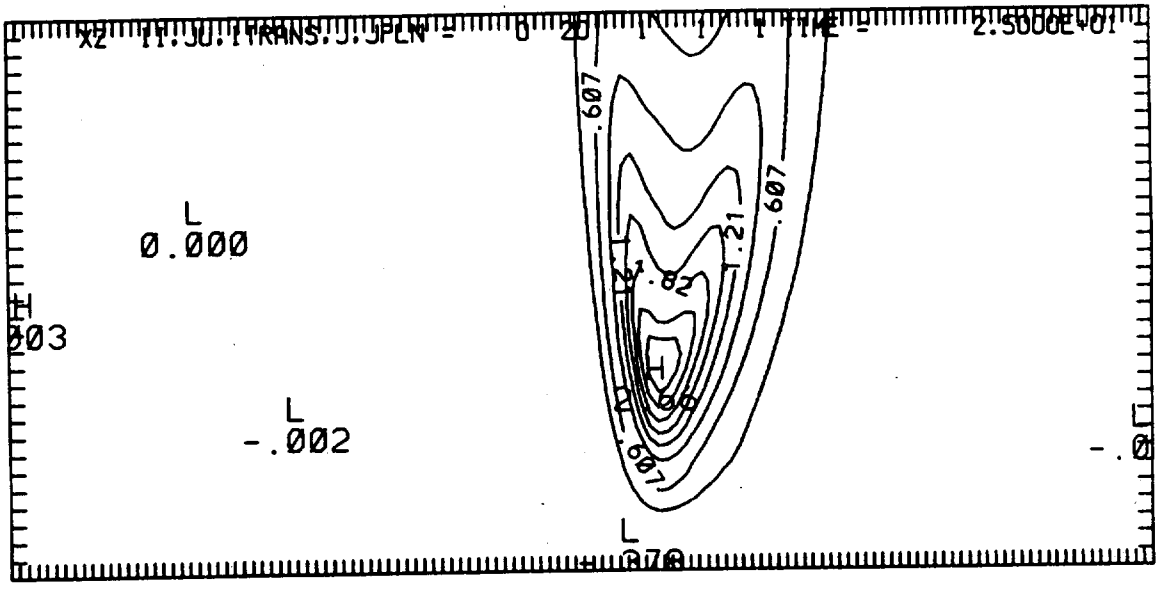
XZ
TIME =
2.5000E+01
.607
1.21
1.82
1.21
.607
L
0.000
H
.003
L
-.002
L
H

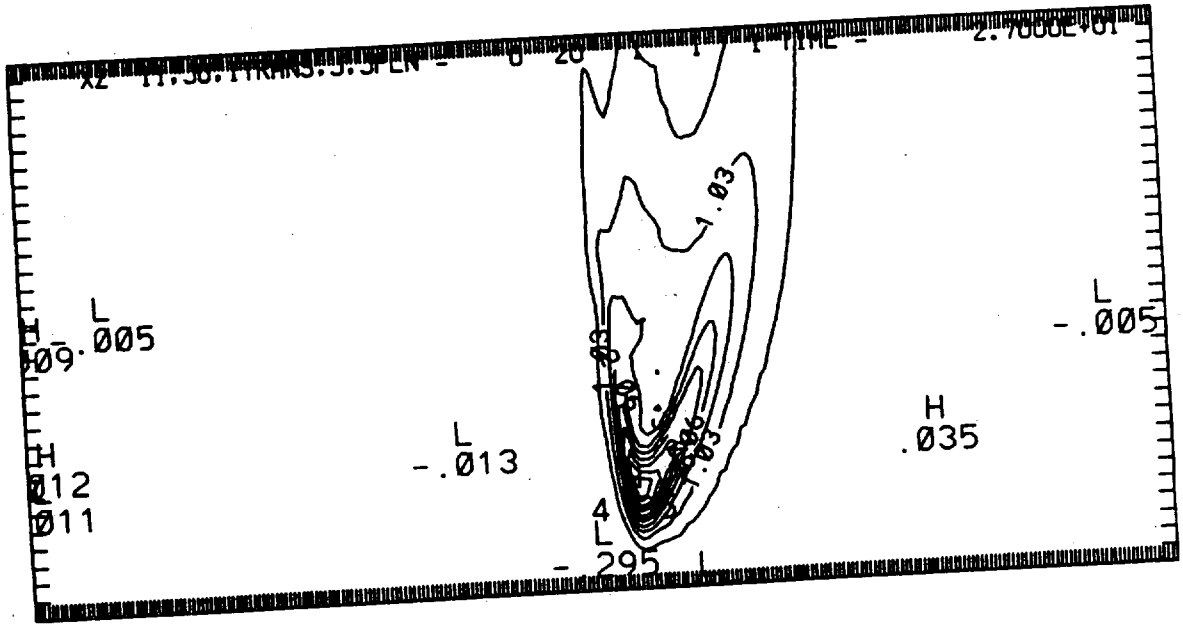
XZ
TIME =
2.7000E+01
1.03
L
-.005
H
.009
L
-.013
H
.035
H
.012
.011
4
L
-.295

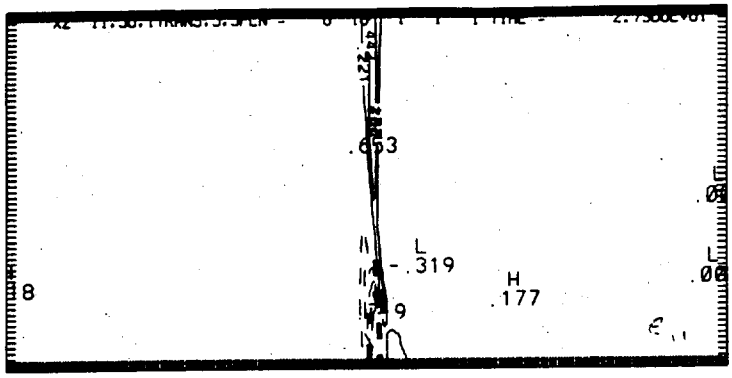

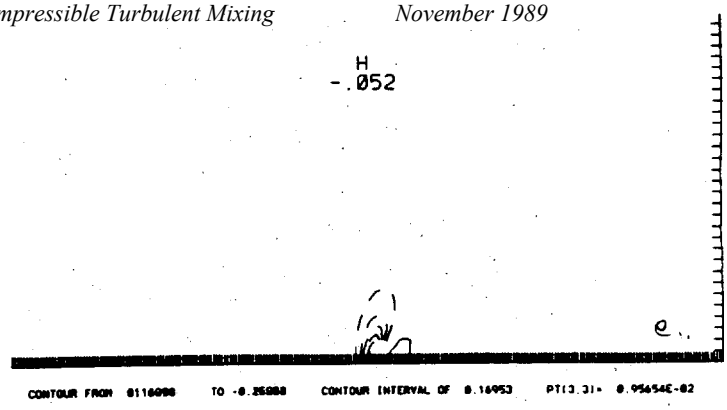

e_{11}

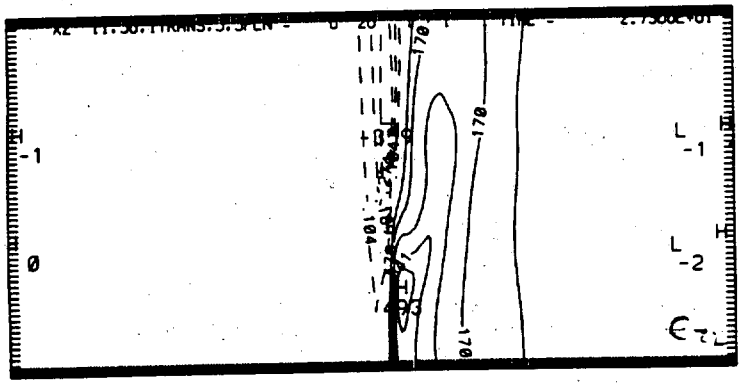

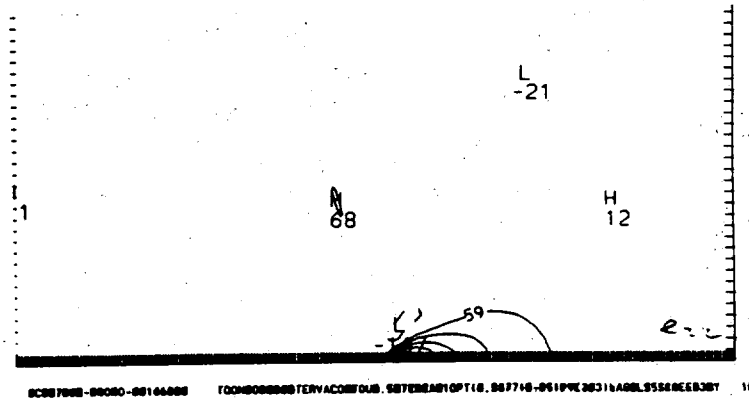

e_{22}

XZ - symmetry plane

XY, k = 7

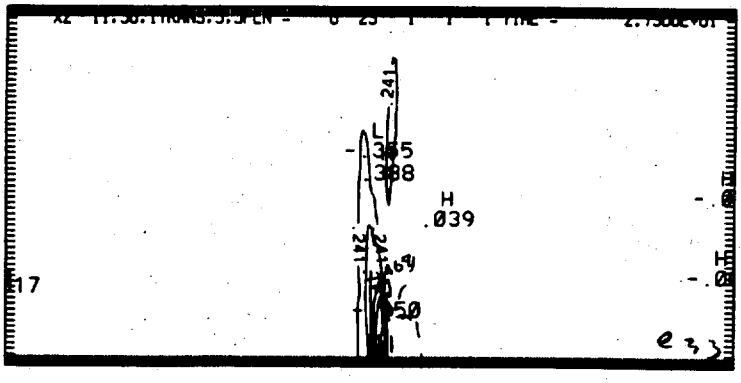

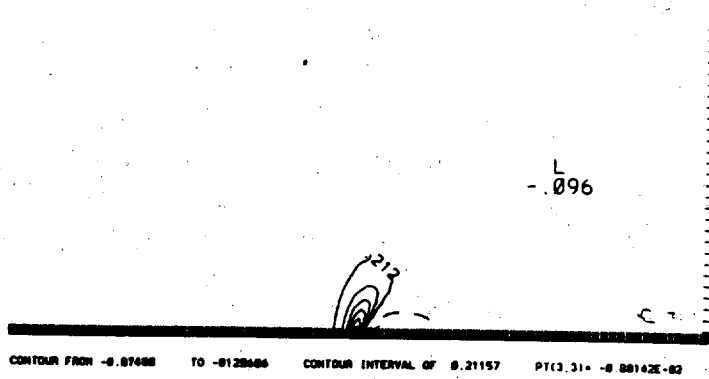

e_{33}

Philip Saffman 2-16-89

VORTEX RECONNECTION

(FUNDAMENTAL PROCESS IN TURBULENCE MECHANICS ?)

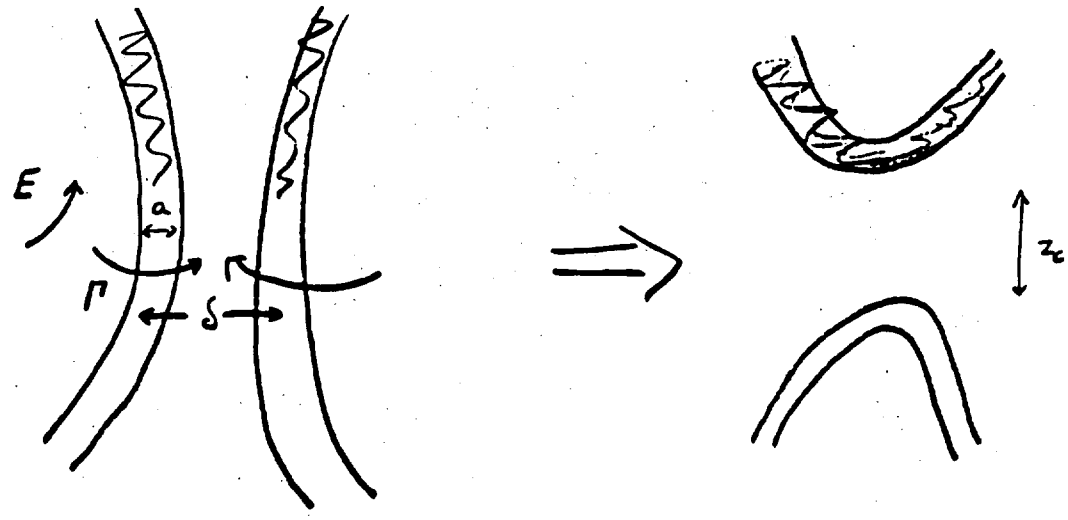

MECHANISM (i) VORTICITY CANCELLATION BY VISCOUS DIFFUSION

$\Longrightarrow$ (ii) PRESSURE RISE IN CORE

$\Longrightarrow$ (iii) AXIAL ACCELERATION

$\Longrightarrow$ (iv) VORTICITY CONVECTION

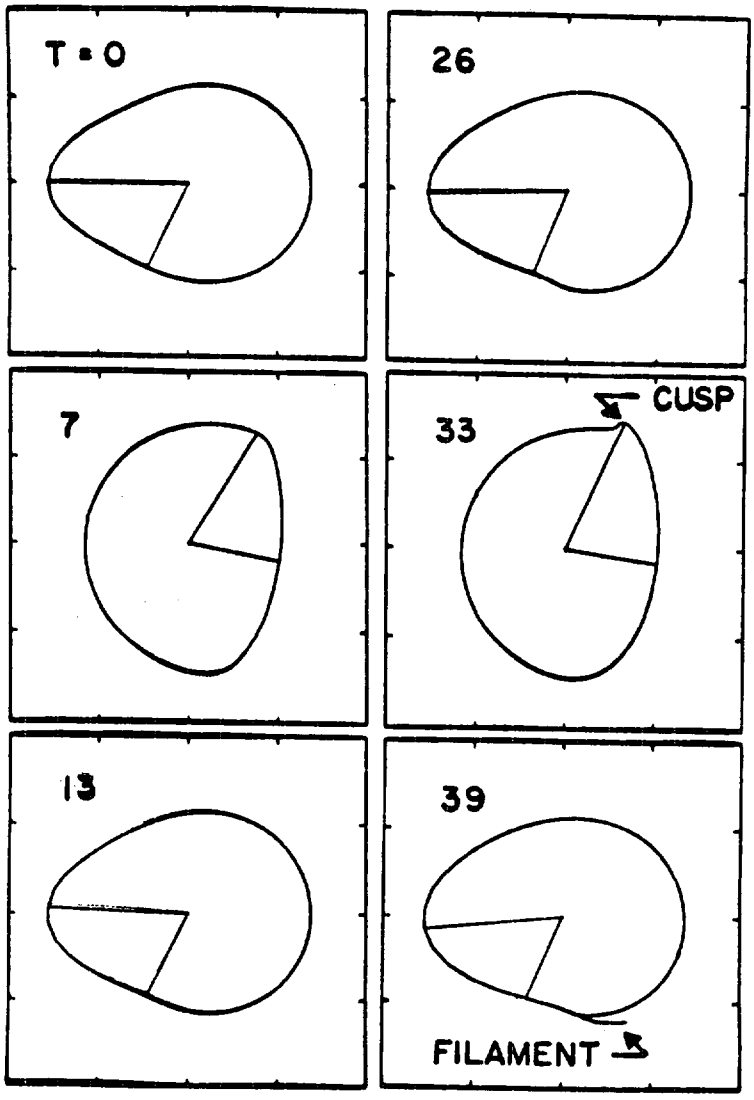

Fig. 4. Recurrence and breaking of a perturbed circular vortex $R(\alpha,0)=R_0\{1+\varepsilon\ \mathrm{sech}^2[(\pi-\alpha)/\Delta\alpha]\}$ where $\Delta\alpha=\pi/6$, $\varepsilon=0.6$. The profile of $R(\alpha,t)$ is shown at times t=0, 7, 13, 26, 33, and 39.

DEEM & ZABUSKY 1978

DRITSCHEL

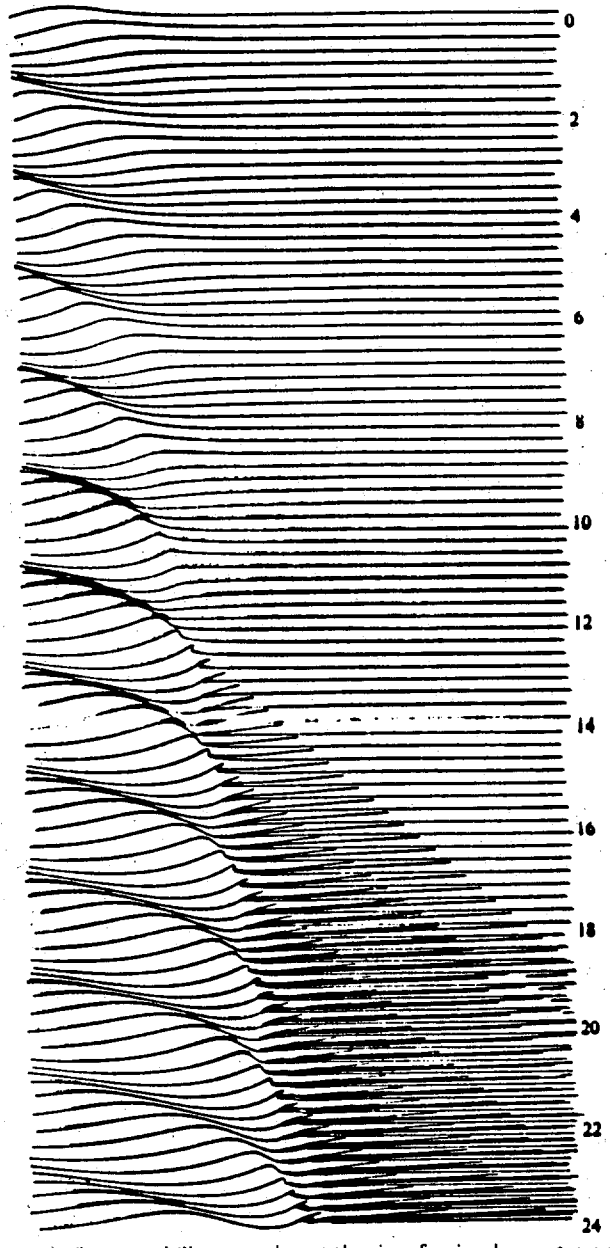

FIGURE 2. Simulations of repeated filamentation at the rim of a circular vortex patch by Dritschel*. Each line corresponds to a small part of the vortex boundary (across which the vorticity jumps discontinuously) drawn in polar coordinates. Evolution proceeds from top to bottom. Snapshots are spaced apart in time by one-eighth of the period of the undular motion of the interface. The nearly linear, periodic behaviour of the imposed disturbance observed early in the calculation eventually gives way to filamentation. The boundary then rapidly grows in complexity, not only from the nearly periodic generation of filaments, but also because filaments subsequently induce new filaments.

3

PULLIN

Nonlinear behaviour of a constant vorticity layer

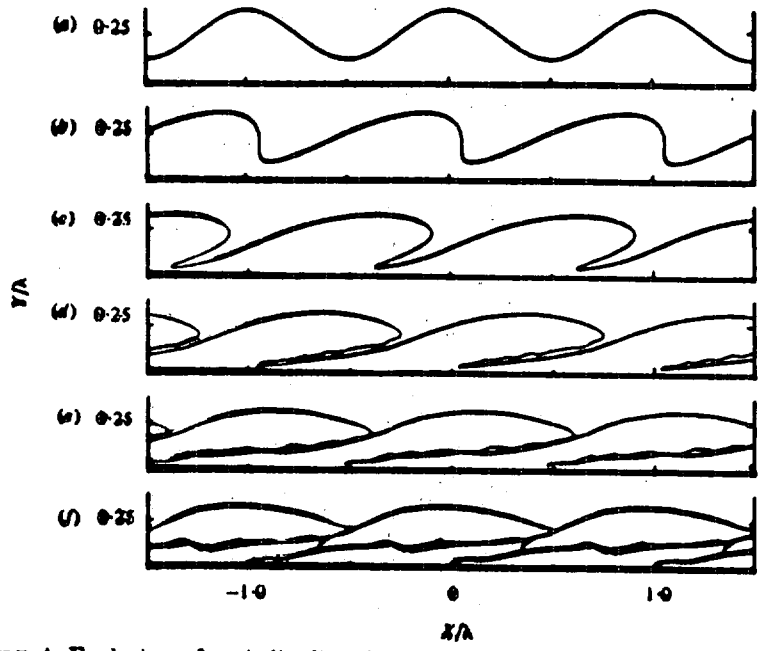

FIGURE 4. Evolution of periodic disturbance on vortical interface, $\delta/\lambda = 0{\cdot}25$, $\epsilon/\lambda = 0{\cdot}125$, $T = 13{\cdot}1339$. (a) $\tau = 0$, (b) $\tau = 2{\cdot}6995$, (c) $\tau = 5{\cdot}2844$, (d) $\tau = 7{\cdot}9140$, (e) $\tau = 10{\cdot}5144$, (f) $\tau = 13{\cdot}5649$.

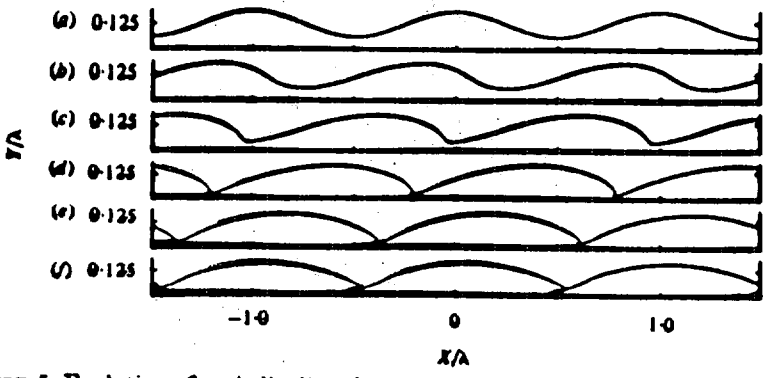

FIGURE 5. Evolution of periodic disturbance on vortical interface, $\delta/\lambda = 0{\cdot}125$, $\epsilon/\lambda = 0{\cdot}0625$, $T = 15{\cdot}8642$. (a) $\tau = 0$, (b) $\tau = 3{\cdot}1997$, (c) $\tau = 6{\cdot}5248$, (d) $\tau = 9{\cdot}5633$, (e) $\tau = 12{\cdot}7107$, (f) $\tau = 14{\cdot}3514$.

with s_j given by (21*b*). Equation (23) corresponds to a disturbance of amplitude $\epsilon/\lambda = 0{\cdot}125$ made up of fractions Δ and $1-\Delta$ respectively of two cosinusoidal modes with wavelengths 4δ and 2δ respectively. Values of $\Delta = 0{\cdot}25$, $0{\cdot}5$ and $0{\cdot}75$ were used. The results in figure 7 for $\Delta = 0{\cdot}5$ show the development of the two modes with the shorter wave mode evolving nonlinearly while being carried on the back of the rotational lobe corresponding to the longer wavelength. For $\Delta = 0{\cdot}25$, $0{\cdot}75$ the shorter

FILAMENTATION

STABLE (?) VORTICES

PRODUCE LONG THREADS.

CIRCULAR VORTEX PATCH

LINEARLY STABLE

L^1 NON LINEAR STABLE

BY SCHWARZ

$$\int \omega_t \, dS \leq \sqrt{\int \omega_t^2 \, dS \int \omega \, dS} = \text{CONSTANT}$$

$\int \omega_t^2 \, dS$: AM

$\int \omega \, dS$: STRENGTH

THEORY (?) OF FILAMENTATION

3 MECHANISMS

(i) LINEAR INSTABILITY $(a/b > 3)$
[POLVANI, FLIERL, ZABUSKY 1982]

(ii) NON-LINEAR INSTABILITY

[PULLIN, JACOBS, GRIMSHAW, SAFFMAN 1990]

(iii) WAVE BREAKING

[DRITSCHEL, 1988]

NO GROWTH IN AMPLITUDE

(ii) THEORY OF FILAMENTATION

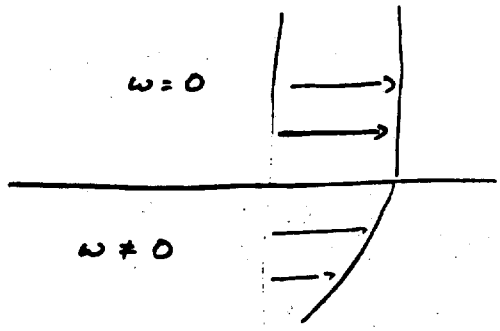

FILAMENTATION DUE TO NON-LINEAR INSTABILITY.

WAVES OF FINITE AMPLITUDE EXIST ON INTERFACE

INSTABILITY OF THESE WAVES PRODUCES FILAMENTATION BY GENERATION OF HYPERBOLIC STAGNATION POINTS IN FRAME OF REFERENCE MOVING WITH DISTURBANCE EXTREMA.

[redacted]

[redacted] TOO SMALL

7) 7/21/89

UNSTABLE

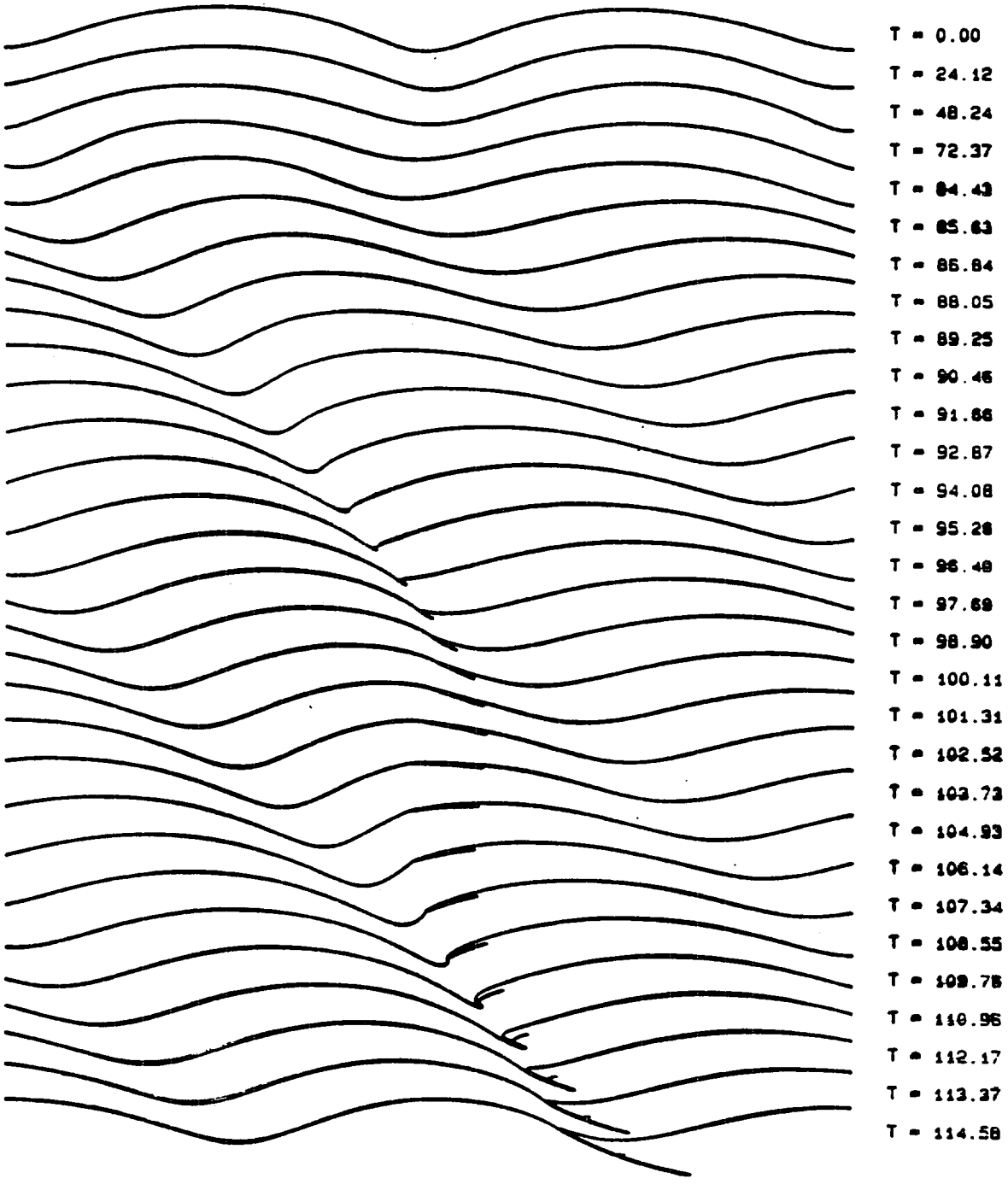

Figure 12.

8

STABLE

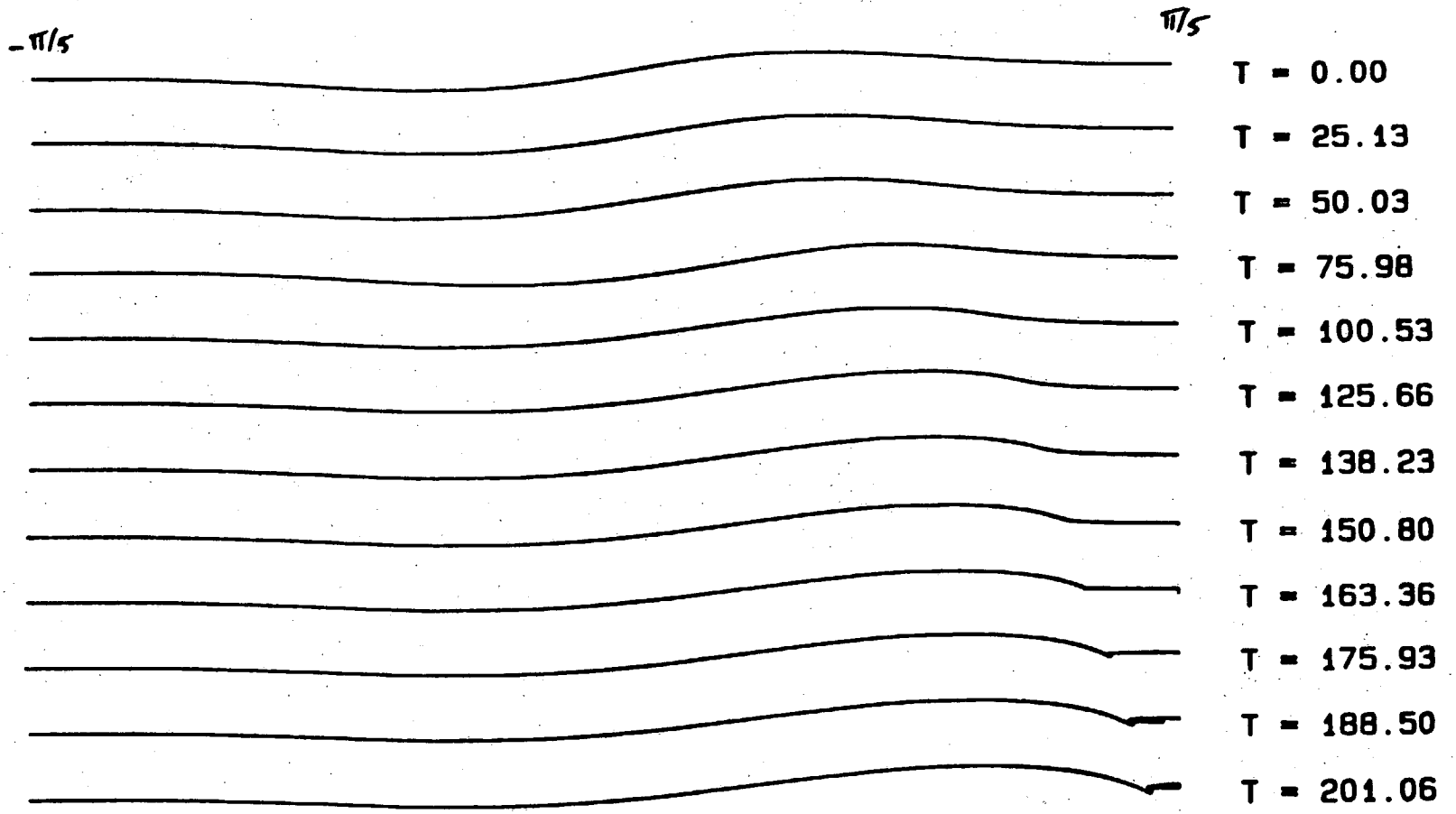

FIGURE 16

7/21/89

(iii) THEORY OF FILAMENTATION

WAVE BREAKING

CORNER FORMATION

NO AMPLITUDE CUT-OFF

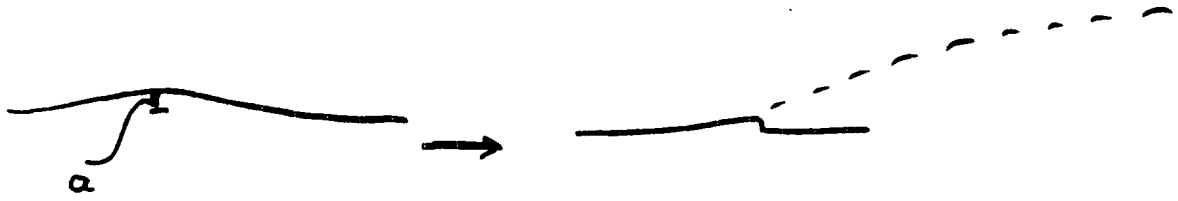

CAN SMOOTH PATCHES DEVELOP CORNERS ?

MWR WAVE EQUATION

NEAR CIRCULAR PATCHES

$$\phi = \frac{1}{2}(r^2 - r_0^2)$$

$$\phi_t + \frac{1}{2}\omega_0\left(\phi_\theta + \mathcal{H}\phi\right) - \frac{\omega_2}{r_0^2}\phi\phi_\theta = 0$$

$$\mathcal{H}\phi = \text{HILBERT TRANSFORM} = \frac{1}{2\pi}\int_0^{2\pi} \phi(\theta')\cot\frac{\theta-\theta'}{2}\,d\theta'$$

TIME TO BREAKING $\propto \frac{1}{a^2}$

[DRITSCHEL]

TIME TO BREAKING

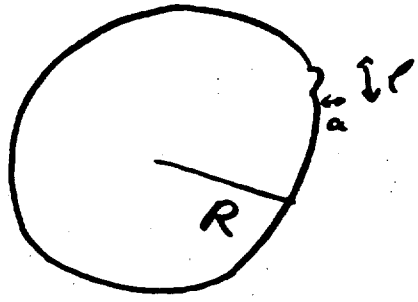

DRITSCHEL

$$t_B = \frac{l^2}{\omega a^2} f\left(\frac{l}{R}\right) \qquad f = ?$$

MINIMUM l ?

t_B (PURE MODE) ? > t_B (BUMP)

SYMPLECTIC INTEGRATION ?

A NEW VERTICAL SHOCK TUBE FOR RAYLEIGH-TAYLOR INSTABILITY MEASUREMENTS

C. Cavailler, P. Mercier and G. Rodriguez,
CEA, Centre d'Etudes de Vaujours-Moronvilliers, BP 7, 77370 Courtry, France

J.F. Haas
CEA, Centre d'Etudes de Limeil-Valenton, 94195 Villeneuve St Georges Cedex, France

ABSTRACT

A vertical shock tube built for the study of Rayleigh-Taylor instability induced turbulent mixing is described. The first results obtained by schlieren visualization concern the interaction between a Mach 1.55 shock wave and subsequent reflected waves and a 1.7 cm wide diffusive SF6-air mixing zone. The mixing zone behavior is compared to the evolutions obtained in other analogous experiments with the help of a turbulence model in a one-dimensional code.

INTRODUCTION

Turbulence models imbedded in hydro-codes are being developped in order to study the mixing of materials arising from Rayleigh-Taylor instabilities in compressible nonstationnary flows. For instance κ–ε models [1] have a transport equation for κ, the turbulent kinetic energy and its dissipation ε. These equations contain diffusion, dissipation and production terms usually modelled using first gradient laws. Coefficients for most of these terms are evaluated using experimental data which are mostly in the domain of incompressible single phase shear flows but the coefficients for the production terms dealing with Rayleigh-Taylor induced turbulence can be obtained from the measurement of interface instability and subsequent mixing in shock-tubes flows.

We have been using the results of a Soviet shock-tube experiment [2] where a Mach 1.3 shock-wave in air, normally incident on a air-helium contact surface, accelerates it before the shocks reflected from the end wall bring it back to rest by steps. A large growth rate (50 m/s) of the mixing zone thickness was reported, after the first reflected shock interacts with the thin mixing zone (2 mm) created by the incident shock. In this horizontal shock-tube experiment, the gases are initially separated by thin (0.5 μm) plastic membranes and it is assumed that most of the mixing observed after passage of the incident shock occurs because the perturbations due to membrane break-up.

Very recently, an extensive program of experiments were carried out at Caltech [3, 4] in both horizontal and vertical shock-tubes in order to visualize the details of shock-induced Rayleigh-Taylor instabilities, also called Richtmyer-Meshkov instabilities. Vertical shock-tubes allow the use of continuous interfaces obtained after retraction of a diaphragm as well as discontinuous contact surfaces (i.e. with membrane). The Caltech experiments made in the conditions of ref. 2 revealed that the apparently thick mixing zone then reported might in fact also controlled by three-dimensional structures due the reflected shock(s) interaction with the boundary layers and that the thickening rate of the mixing zone is about 5 times smaller [4]. The boundary layer effects have also been recognized in high Mach number experiments [5],

6. In view of this discrepancy between the Caltech and Soviet experiments, which reflects the dependence on the shock tube cross section and the adjustement of the schlieren system, an informal international agreement has been made to duplicate on different experimental facilities the same test conditions and to compare the results. The present paper is the beginning of our contribution to this endeavor.

DESIGN CRITERIA

This shock tube was designed for low Mach number operations ($M<1.6$) since we were interested in the conditions of the Andronov and Caltech experiments. The maximum internal pressure is therefore 10 bars which reduces construction costs and delays. It should be vertical because we wanted to create continuous diffusive interfaces as well as discontinuous contact surfaces. Diffusive interfaces are easier to simulate in the calculations because the thin plastic membrane used for the discontinuous contact surface introduces a second phase in the problem and the details of its rupture are not well known. The shock tube should fire upwards since the incident shock should interact with a stably stratified heavy-light molecular diffusion zone. Finally its cross section should be wide enough so that boundary layer effects do not dominate the flow and its length above the interface should be long in order to provide ample time between the reflected shocks.

DESCRIPTION

The vertical shock-tube at CEA Vaujours has been designed and constructed a year ago. The authors are pleased to acknowlege the advice of Prof. Sturtevant regarding shock-tube technology. Its main features and dimensions are given on figure 1, its cross section is a 8 cm square. In the present configuration, the driver gas (air) is separated from the test gas, sulphur hexafluoride (SF6) by the main diaphragm (below) and a diffusion zone between SF6 and the gas (air) in the upper experiment section is obtained after retraction of a sliding plate (above).

A photograph of the main diaphragm set-up appears on figure 2. It shows the driver and driven section flanges, 2 of the 3 pneumatic jacks used to join them and the diaphragm set on the lower flange. This diaphragm is made of a kapton sheet with conducting strips connected to 2 wires crossing at the center. To create a shock, the driver is first pressurized, then, at a preset time after the retraction of the sliding diaphragm, a strong DC current in the strips heats up and weakens the center of the sheet.

The experiment section is equipped with 2 glass windows 60 cm long. A diaphragm, made of 2 thin metal plates separated by a sheet of rubber and located at 54.4 cm from the end plate, can be retracted in a fraction of a second by a pneumatic jack, thus allowing the formation of a smooth molecular diffusion zone. A movable plug at the end of the experiment section is used to decrease the distance between the sliding plate and the reflecting end wall for the measurement of the influence on the mixing zone of the reverberation time between the reflected shocks. A photograph of the experiment section is shown on figure 3. One distinguishes through the long windows, the movable plug 13.2 cm above the sliding plate with its retracting mechanism on the left side of the tube.

We use the SF6-air combination because their diffusion coefficient (0.0885 cm^2/s) is about 10 times smaller than the one for the air-helium pair. With the main diaphragm in position and the sliding plate retracted, air is removed from the driven and experiment sections by pumping, then SF6 is introduced. After sliding the plate in position, SF6 in the experiment section is removed by flushing air at atmospheric

pressure. In order to reduce the effects of unavoidable leakage around the sliding diaphragm, SF6 and air are continuously being flushed up to a short time (4 s) before retracting the plate and firing the shock.

The shock pressure jumps at various locations along the test and experiment sections are recorded with polarized ferroelectric pressure transducers. They are used to measure the incident and transmitted shock speeds in the gases below and above the mixing zone, from which the gas composition can be deduced. In the runs shown here, it appears that there is approximatively 15% (in mass concentration) of SF6 in the "air" above the mixing zone. Flow visualization of the shocks and the mixing zone in the experiment section is performed with a schlieren system using a 0.4 μs (FWHM) spark-gap light source similar in design to the ones used at Caltech. Images are recorded on 400 ASA 4 by 5 inches film.

A sequence of photographs showing the diffusion zone at various times after the sliding plate has been fully retracted is presented on figure 4. The diffusion zone appears as a black layer with a white line on the center due to the vacuum grease left by the plate and perturbations on the edges which are waves due to the retraction process. The boundaries are well defined up to 1 second (prints 4a and 4b) and the layer thickens after that time (prints 4c, 4d and 4f). Thus the sequence of operations for the actual shock tube runs was defined. With air at 3.5 bar in the driver, and SF6 and air at 1bar in the driven and experiment sections respectively, we obtain a Mach 1.44 - 1.46 shock. We control the time for the rupture of the main diaphragm so that the shock reaches the diffusion layer 900 ms after retraction of the plate. The diffusion layer is then 1.7 cm wide.

RESULTS

Figure 5 shows a sequence of schlieren photographs of the interaction between a Mach 1.44-1.46 incident shock with the diffusion layer with reflected shocks obtained with the plug installed (13.2 cm between plate and plug). Print 5a (time 0) shows the already perturbed incident shock in the lower part of the diffusion layer. After 0.095 ms (print 5b), the transmitted shock (top) and the shocked layer (above the white line marking the initial plate position) and cylindrical reflected waves due a 0.5 mm groove on the left wall where the plate retracted can be seen. The same waves appear on print 5c (0.55 ms) with, at the top, the first reflected shock propagating trough the mixing zone, which still seems smooth. The layer is shown after interaction on print 5d (0.815 ms). The following print 5e (1.05 ms) displays weak compression waves above the layer and the second reflected shock below it propagating in a region of fine scale turbulence which we attribute to the once shocked boundary layers. We begin to see wave like features on the top of the layer which develop into large scale mushrooms and vorticies on the subsequent prints 5e to 5h (1.295, 1.845, 2.125 and 2.33 ms). As these structures totally disrupt the mixing layer, the measurement of an average thickness for comparison with 1D hydrocodes becomes problematic at late time.

COMPARISON WITH THE CALCULATION AND CONCLUSION

A numerical study of the dynamics of this interaction has been carried out using a κ–ϵ turbulence model imbedded in a 1D Lagrangian hydrodynamics code [1]. SF6 was represented as a perfect gas of specific heat ratio $\gamma = 1.09$, density $\rho = 5.98$ 10-3 g/cm^3 at 1 bar subjected to 2.15 bar upstream pressure boundary condition at 110 cm (175 computational cells) from the interface. The upper gas, air contaminated by SF6,

is described by $\gamma = 1.363$, $\rho = 1.333$ 10-3 g/cm^3 over a length of 13.2 cm (53 cells) or 54.4 cm (100 cells) to simulate the 2 cases investigated in the experiment. The initial cell size at the interface, 0.05 cm for SF6 and 0.25 cm for "air" insures the continuity of cell mass, which improves the mixing calculation.

Some seed turbulence was injected in the cells surrounding the interface at the beginning of the calculation in such a way that, at the time the incident shock reaches it, 5.6 ms later, a 1.7 cm wide diffusion zone was obtained. The coefficient of the Rayleigh-Taylor source term in the κ equation of the model is chosen by matching the evolution of the mixing zone thickness of the Soviet experiment [2] (as described in ref. 1) or the Caltech experiment [4] (a factor 5 decrease).

Figure 6 is the representation of the evolution of the mixing zone in a x-t diagram. The heavy bars indicate the measured position of the mixing zone. Circles and triangles represent the measured position of the shocks using flow visualization and the gauges respectively. The continuous lines are the calculated trajectory of the shocks and of the edges of the mixing zone using a set of constants compatible with the Caltech experiment. The dotted line was calculated using the model constants fitted to the Soviet experiment. Figure 7 is a comparison of the 2 calculations of the mixing zone thickness (MZT) and the experimental data. According to figures 6 and 7, this mixing zone evolution can be predicted using the code fitted on the Caltech results. Figure 8 is the evolution of the turbulent kinetic energy (TKE) showing before interaction a residual turbulent kinetic energy of 2 ergs/cm^2, 3 orders of magnitude below the energy after the interaction with the reflected shocks.

The comparison carried out using a κ–ε model indicates that the present experimental results are in accordance with the Caltech air/helium results and do not approach the trends reported in the Soviet experiment. Measurements on the mixing zone obtained with a discontinuous air-helium interface will be carried out using a second experiment section in order to confirm this conclusion.

REFERENCES

1 M. Bonnet, S. Gauthier and P. Spitz, "Numerical simulations with a κ–ε mixing model in the presence of shock waves", *proceedings of the international conference on the physics of compressible turbulent mixing*, Princeton 24-27 Oct. 1988 (Springer Verlag, to appear in 1989)

2 Andronov, V.A., Bakhrakh, S.M., Meshkov, E.E., Mokhov, V.N., Nikiforov, V.V., Pevnitskii, A.V. and Tolshmyakov, A.I. 1976 Turbulent Mixing at Contact Surface Accelerated by Shock Waves, *Sov. Phys. JETP*, **44**, 424.

3 B. Sturtevant, Rayleigh-Taylor Instability in Compressible Fluids, p. 89 in Shock-Waves and Tubes, *Proceedings of the 16 th ISSWT*, Aachen, 1987, edited by H. Grönig, VCH Verlagsgesellshaft, 1988.

4 M. Brouillette and B. Sturtevant, "Growth Induced by Multiple Shock Waves Normally Incident on Plane Gaseous Interfaces", in "Advances in Fluid Turbulence", *Proceedings of the CNLS Annual Conference*, May 16-20, 1988, Elsevier, 1989.

5 L. Houas, A. Fahrat, A. Ramdani, J. Fortès and R. Brun, "Concentration and temperature profiles in a shocked gaseous interface", in "Shock waves and shock tubes", *Proceedings of the 16th ISSWST*, H. Grönig ed. VCH Physik Verlag (1988).

6 D. Besnard, M. Bonnet, S. Gauthier, J.F. Haas and P. Spitz, "Numerical Simulation of Rayleigh-Taylor Instability Induced Turbulent Mixing in Shock Tube Flows", p. 709 in Shock-Waves and Tubes, *Proceedings of the 16 th ISSWT*, Aachen, 1987, edited by H. Grönig, VCH Verlagsgesellshaft, 1988.

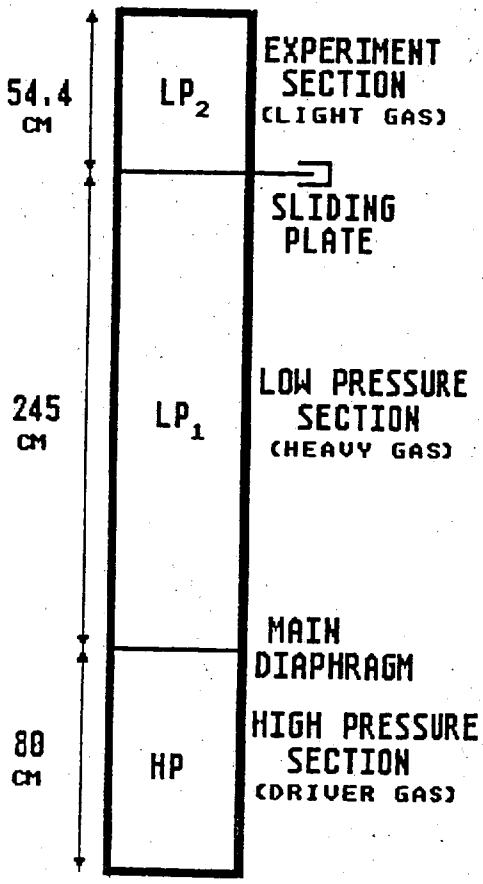

Fig. 1 : CEV-M SHOCK TUBE

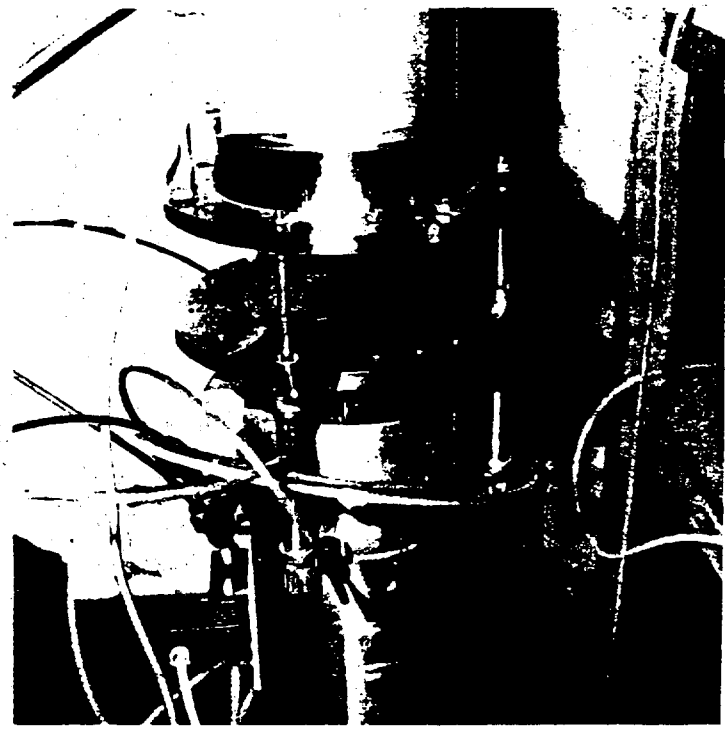

Fig. 2 : MAIN DIAPHRAGM

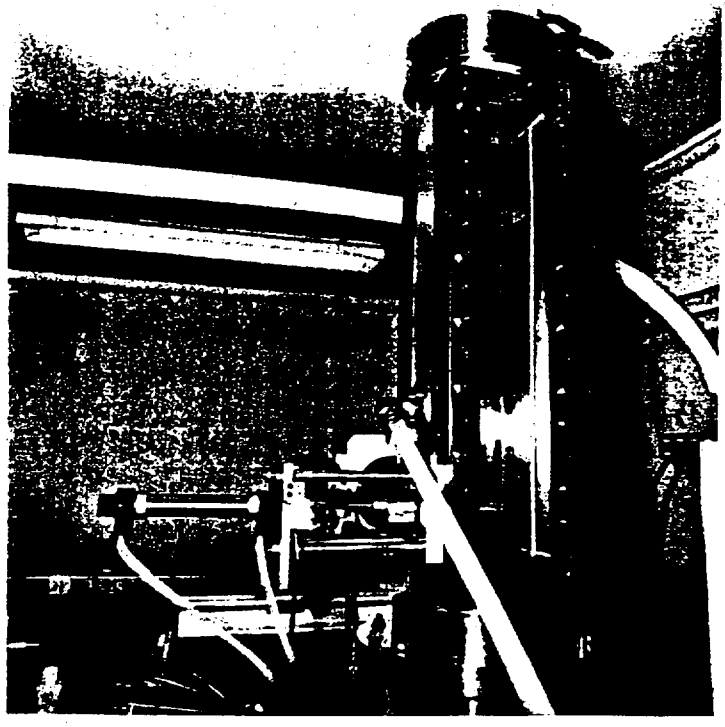

Fig. 3 : SLIDING PLATE

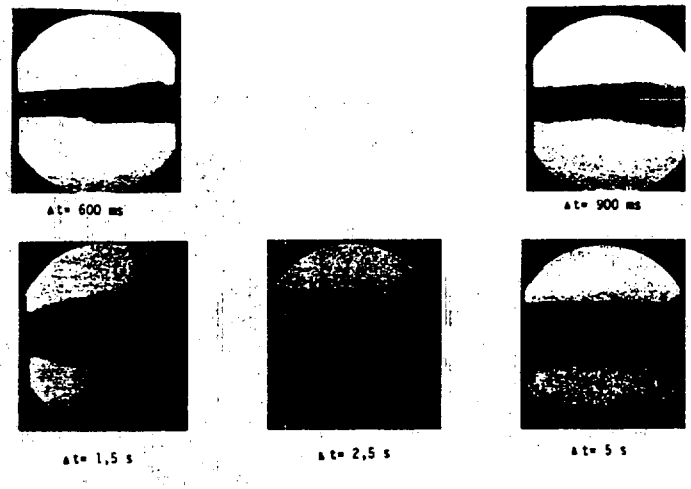

Fig. 4 : STATIC INTERFACE

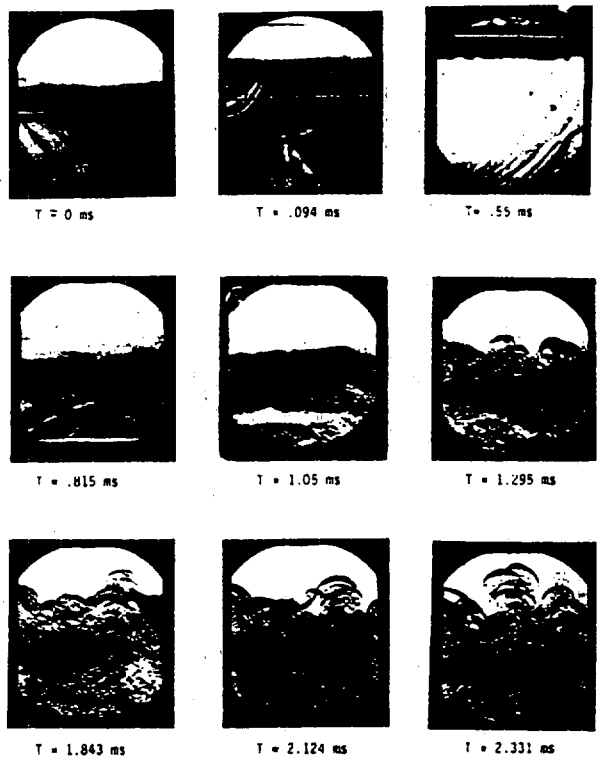

Fig. 5 : DYNAMIC INTERFACE

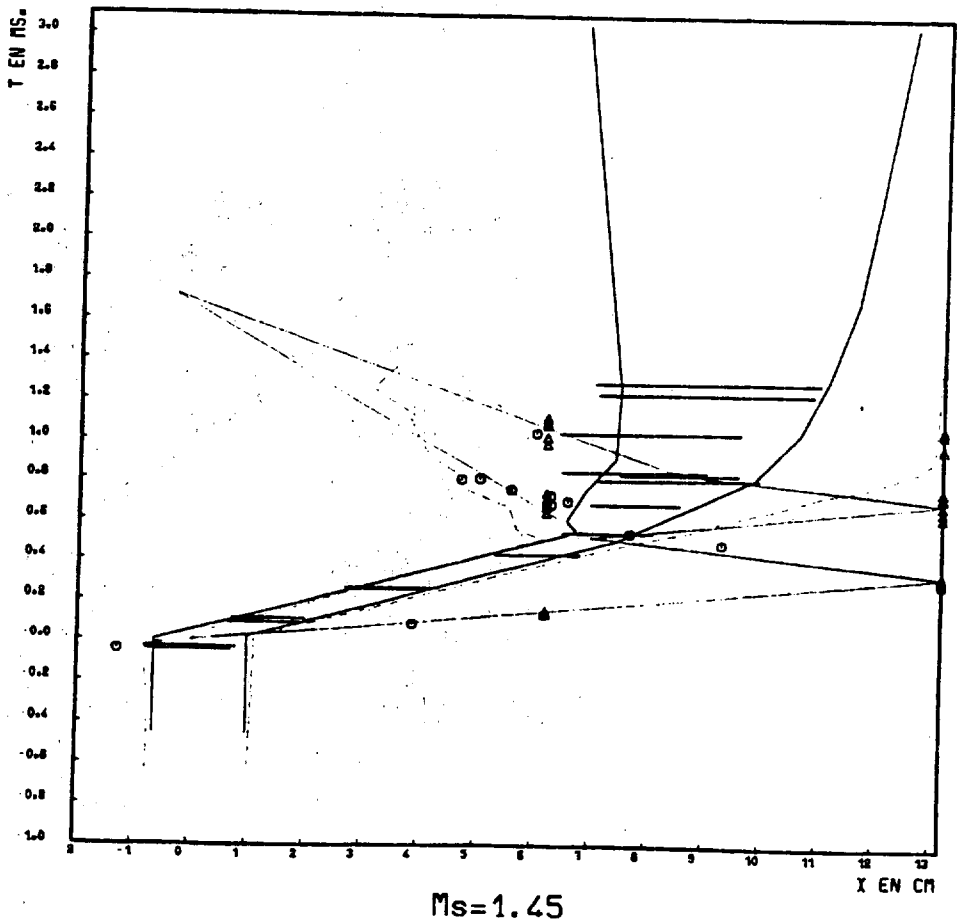

Fig. 6 : X-T DIAGRAM

SHOCK PHYSICS

AWE FOULNESS

Application of Holography to Shock Tube Experiments

N STEARMAN AWE
J EDWARDS CRANFIELD INSTITUTE OF TECHNOLOGY

Pleasanton, USA *Edited by V. Rupert*

SHOCK PHYSICS

AWE
FOULNESS

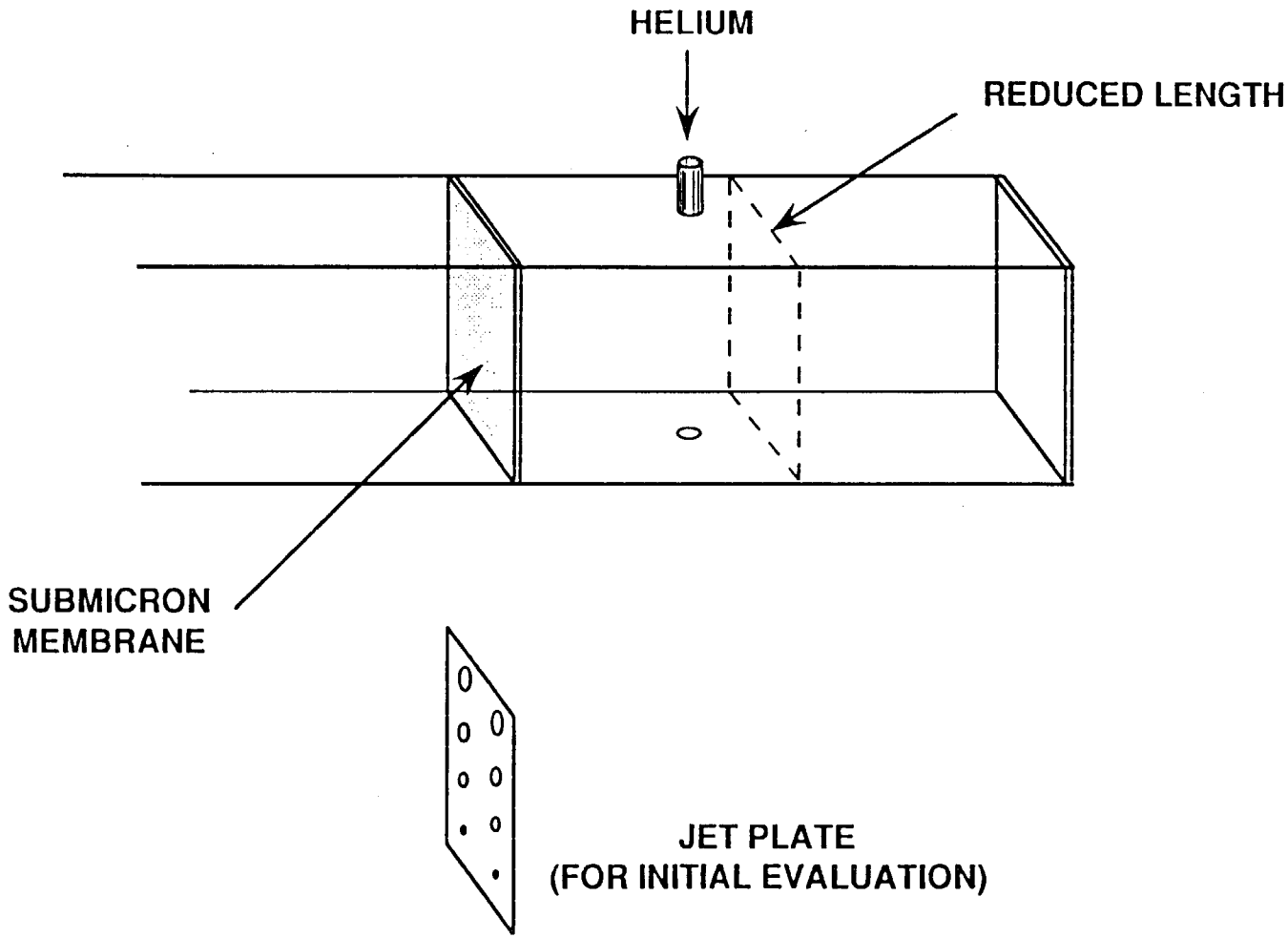

TEST SECTION

SHOCK PHYSICS

AWE FOULNESS

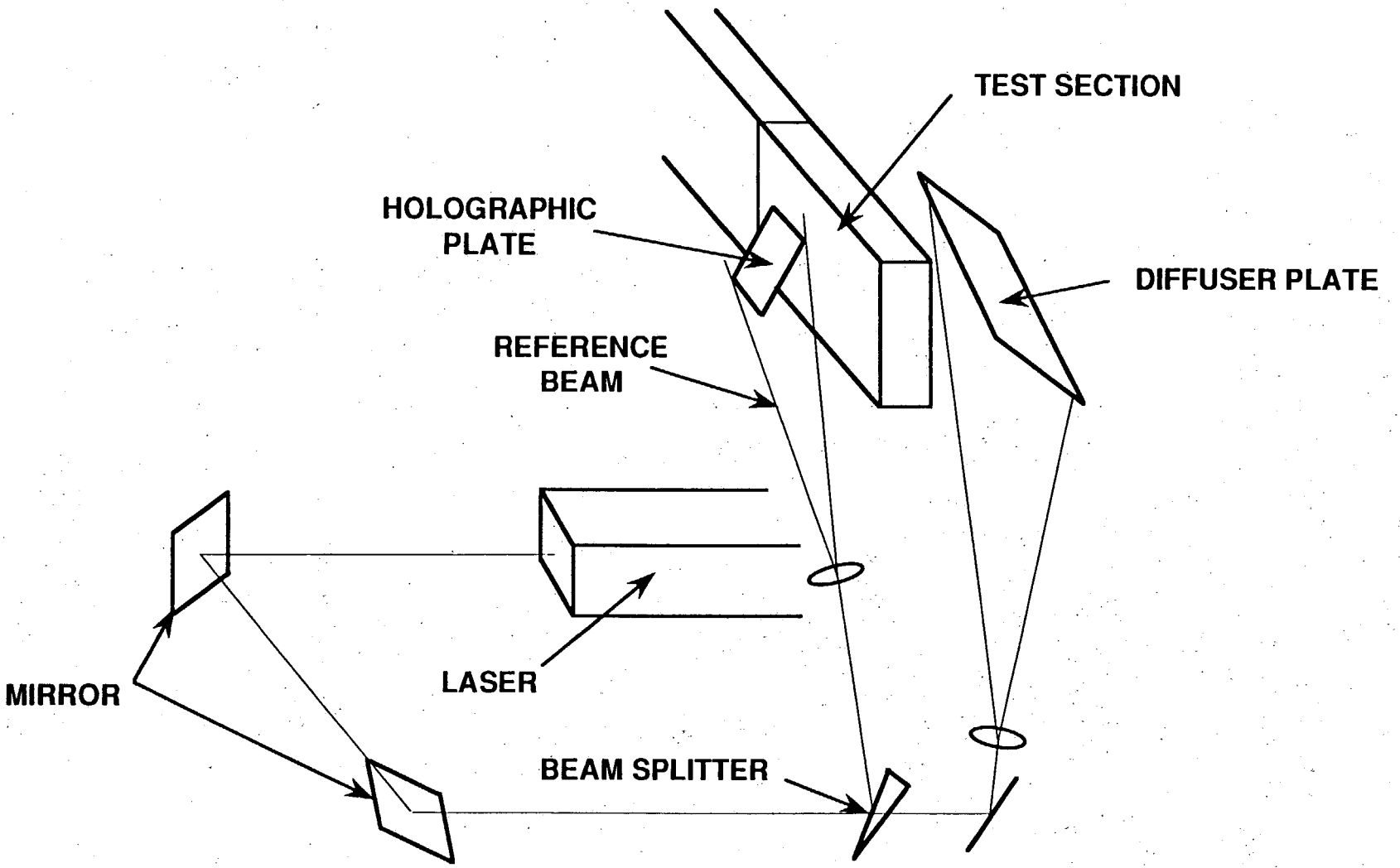

OPTICAL ARRANGEMENT

LASER CHARACTERISTICS

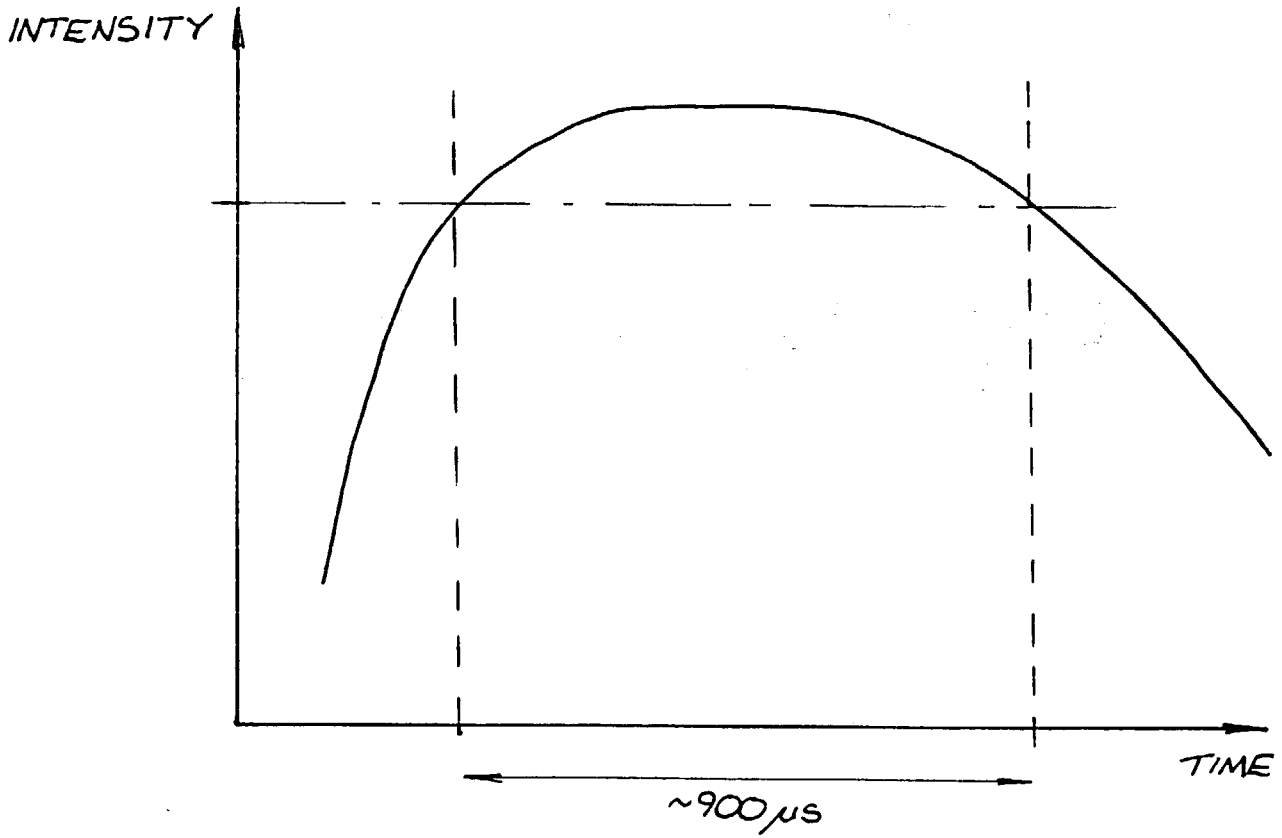

SHOCK PHYSICS

AWE
FOULNESS

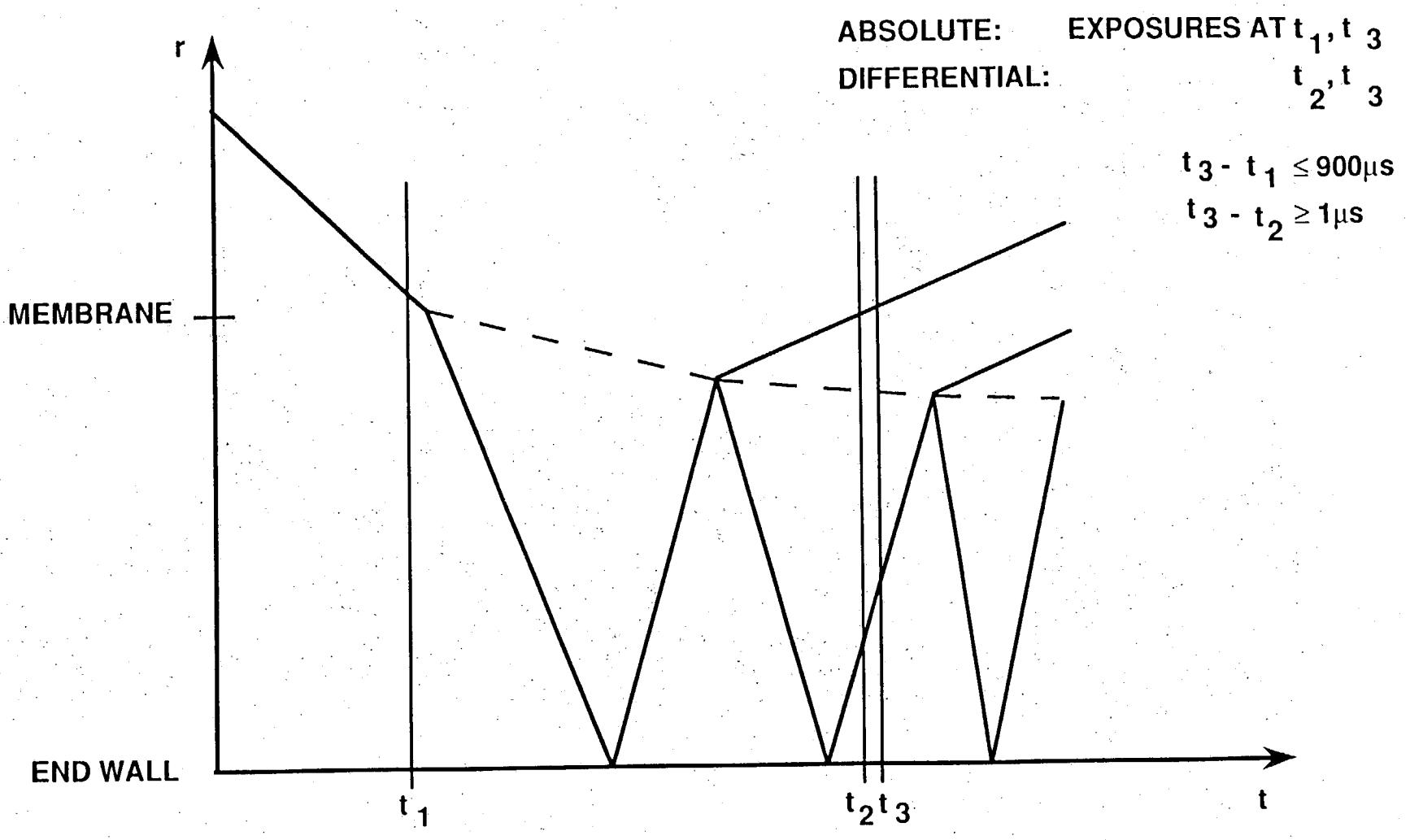

EXPOSURE TIMES

20 μs

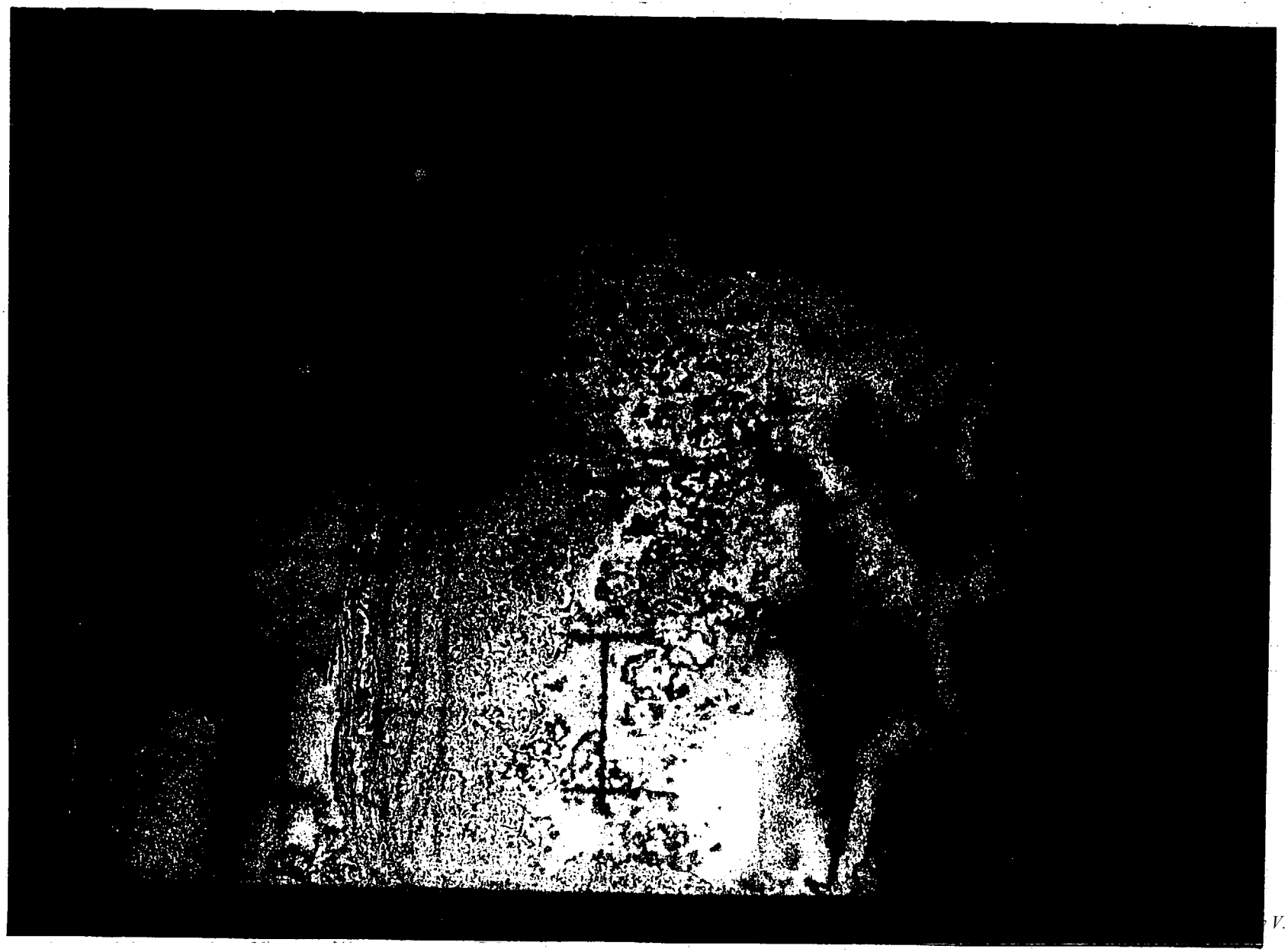

V. Rupert

5 μs

V. Rupert

1 μs

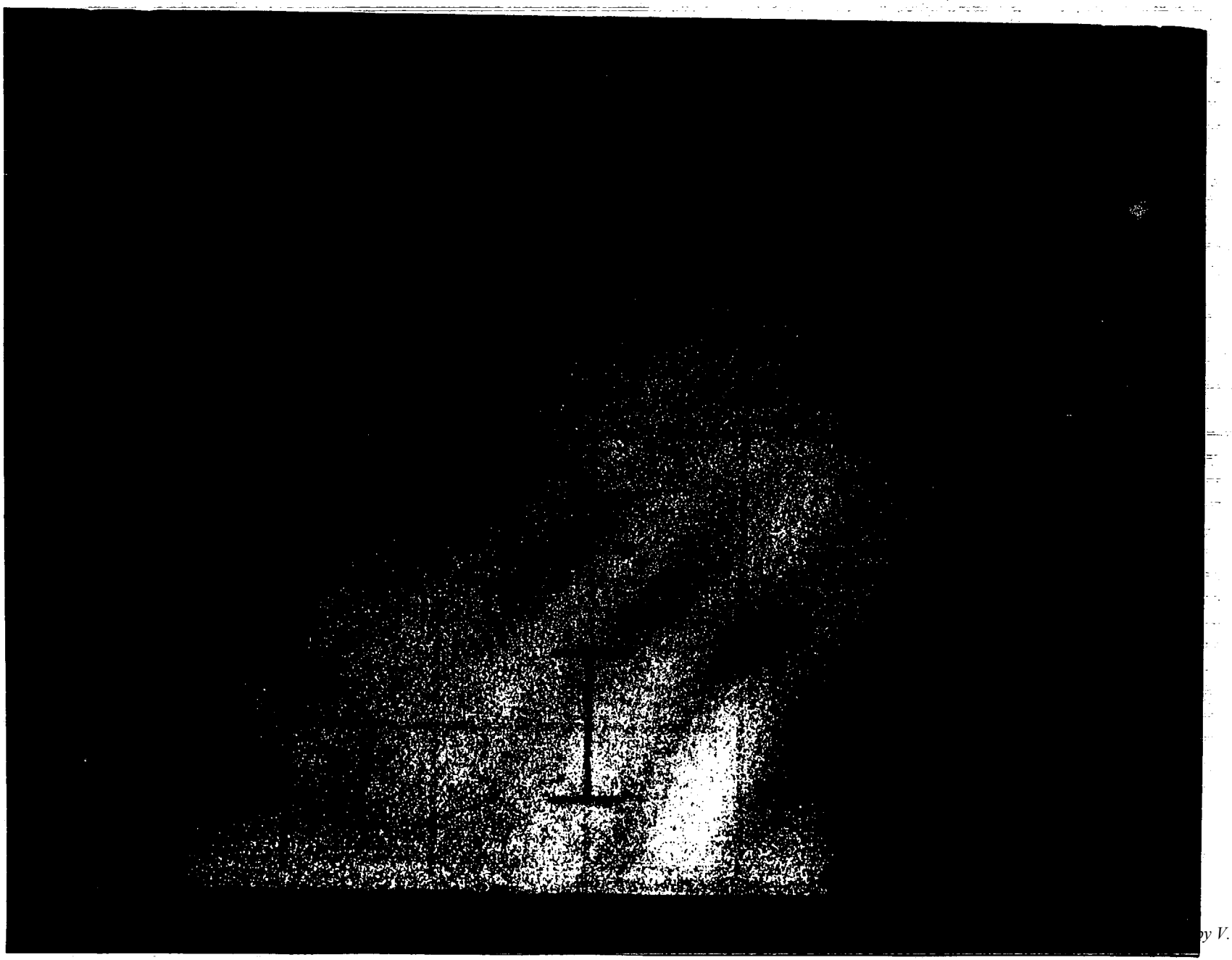

...y V. Rupert

$n - 1 = k\rho$ Gladstone - Dale

Helium : $k = 0.195 \times 10^{-3}$

Air : $k = 0.226 \times 10^{-3}$

$n_o = 1 + 3.198 \times 10^{-5}$ = Refractive index of Helium at s.t.p.

Fringe index, $N = \frac{(n - n_o)L}{\lambda}$

$L = 51 \times 10^{-3}$ m
$\lambda = 694 \times 10^{-9}$ m

The number of fringes counted from a baseline of Helium at 300K and 1 bar is as follows.

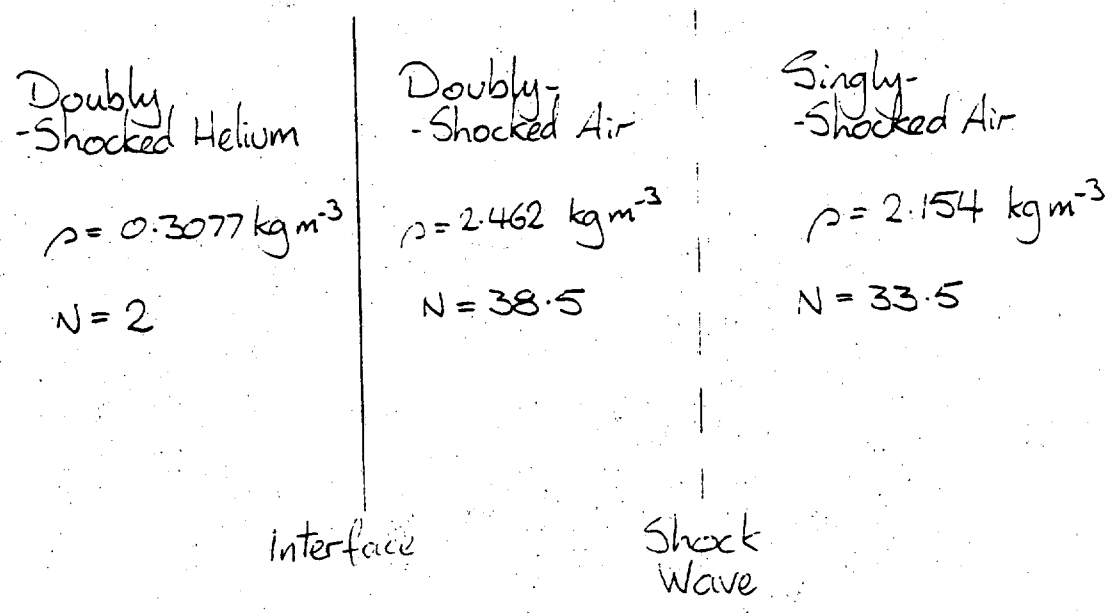

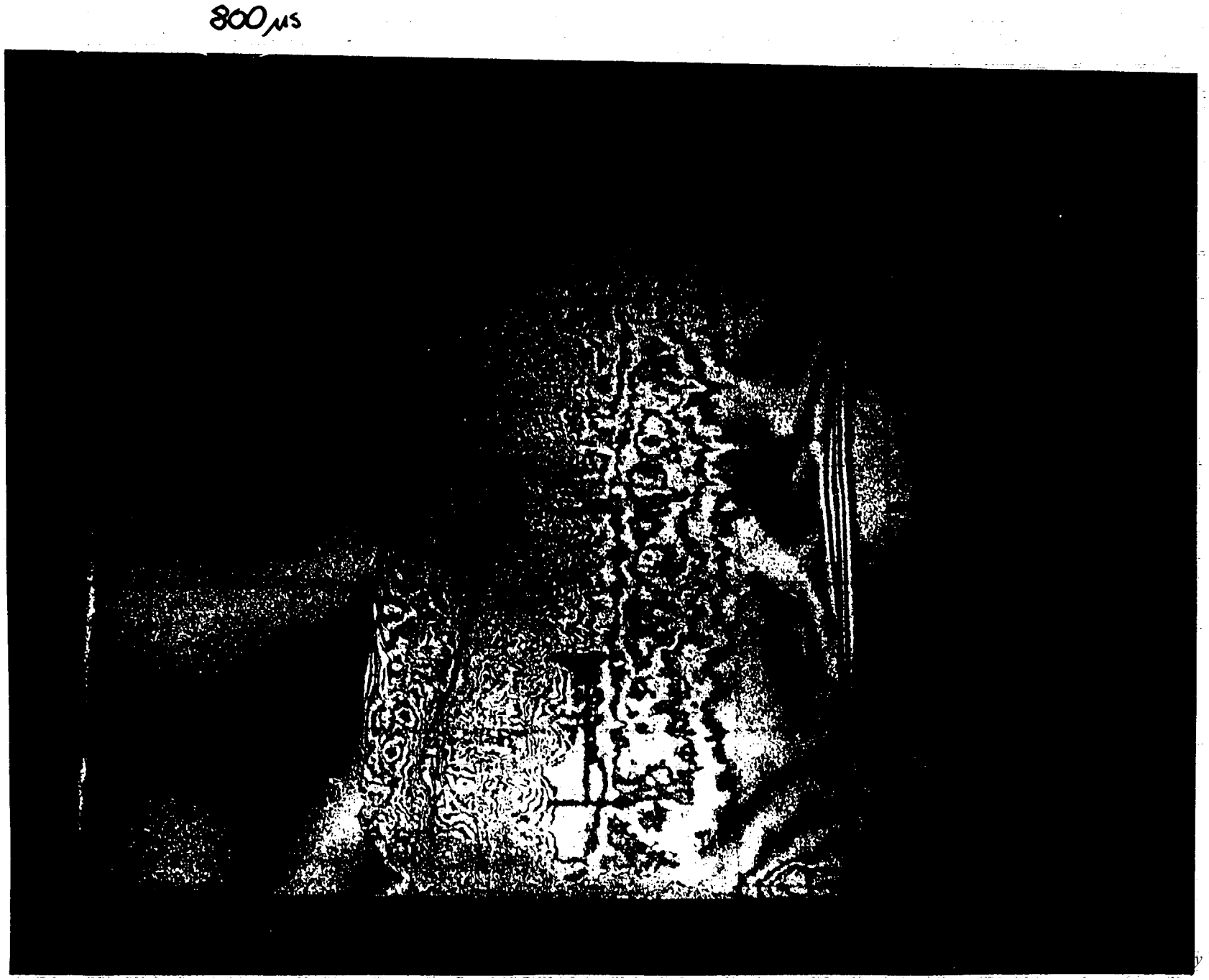

y V. Rupert

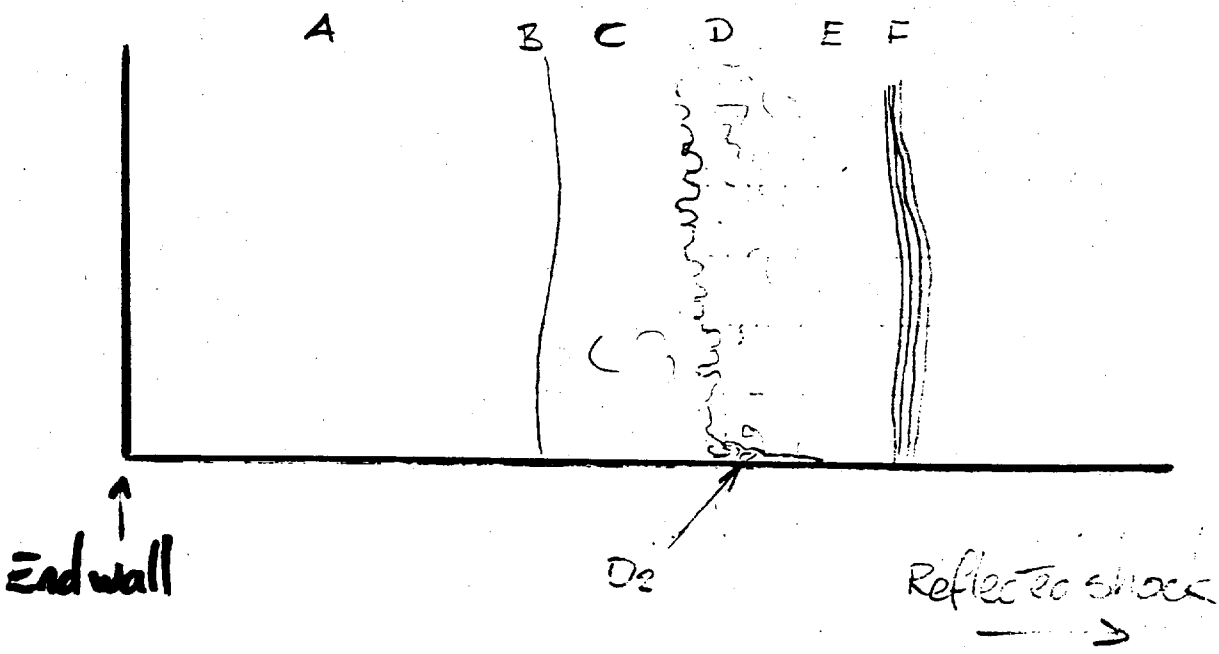

A = Double shocked region
B = continuous (intact) membrane
C = Highly turbulent mixing region
D = Boundary layer - effects
D_2 = Boundary layer visible on floor of tube
E = Region of perturbed air behind irregular shock
F = Reflected shock, distorted as a result of passage through mix region.

All holograms shown were taken ~800 μs after the shock first passed through the membrane.

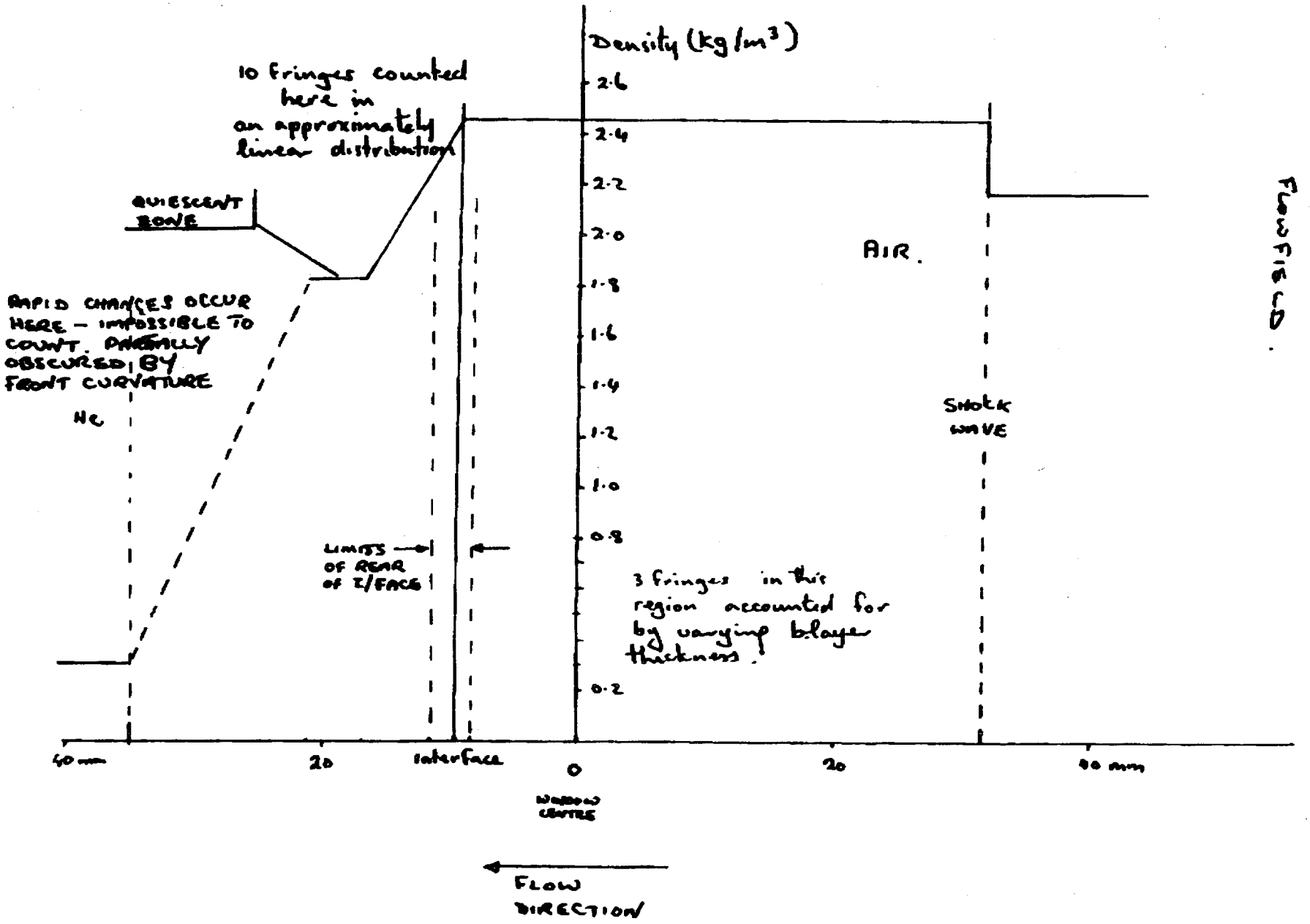
Density (kg/m³)
2·6
2·4
2·2
2·0
1·8
1·6
1·4
1·2
1·0
0·8
0·2
10 fringes counted here in an approximately linear distribution
QUIESCENT ZONE
RAPID CHANGES OCCUR HERE – IMPOSSIBLE TO COUNT. PARTIALLY OBSCURED BY FRONT CURVATURE
He
LIMITS OF REAR OF I/FACE
3 fringes in this region accounted for by varying bdaye thickness.
AIR.
SHOCK WAVE
DENSITY DISTRIBUTION THROUGH THE FLOWFIELD.
40 mm
20
Interface
0
WINDOW CENTRE
20
40 mm
FLOW DIRECTION

CONCLUSIONS

The studies to date have shown the benefit of interferograms as a means of differentiating between wall and bulk effects.

Absolute interferograms may be used to deduce volume fractions quantitatively, given that the pressure (density) and volume fraction of a single point in the field is known. (*In theory at least*)

Differential interferograms pick out the mix region alone since it is only these that optical path lengths are changing rapidly enough.

The further advantages of holography are at present in qualitative visualisation of the effects. In theory, however, tomographic techniques and fringe tracing could be used to build up a 3D volume fraction map.

Los Alamos Report LA-UR 89-3832 (revised 12-14-89)

Experimental results corresponding to standard problem 1

by Robert F. Benjamin
Los Alamos National Laboratory

Abstract

Experimental measurements of Richtmyer-Meshkov instability growth at air/SF_6 and air/helium interfaces are reported and compared with previous data, and with Richtmyer's equation based on linear perturbation analysis.

New diagnostics for shock tube experiments: Imaged Light Scattering

by Robert F. Benjamin
Los Alamos National Laboratory

Abstract

We are evaluating the feasibility of using imaged light scattering (ILS) to measure the unstable flow and mixing in a 2D section of a 3D (air/SF_6) Richtmyer-Meshkov flow instability. Using aerosol as a tracer in SF_6 gas, we find that the interpenetration of gases during reshocking is better defined in ILS photographs than observed in optical shadowgraphs, and there appears to be less small-scale mixing in ILS data. The "fuzziness" of the interfacial profile seen in shadowgraphs is not seen in the scattering data, which suggests that the boundary-layer flow causes an optical problem in the shadowgraphs.

Experimental results corresponding to standard problem 1

by Robert F. Benjamin

Los Alamos National Laboratory

This presentation was given Thursday morning, 16 November 1989 by Robert Benjamin. This manuscript contains annotated viewgraphs of the presentation and the companion poster talk.

Summary

Experimental measurements of Richtmyer-Meshkov instability growth at air/SF_6 and air/helium interfaces are reported and compared with previous data and with Richtmyer's equation based on linear perturbation analysis.

Viewgraph 1-1

Experimental results corresponding to standard problem 1

by Robert F. Benjamin

Los Alamos National Laboratory

International Exchange on R-M and R-T Mixing

16 November 1989

Viewgraph 1-2 is a schematic diagram showing the amplitude growth of the shock-induced interfacial instability known as the "Richtmyer-Meshkov Instability." The case of the shock moving from low-density gas into high-density gas (e.g., air/SF_6) shows amplitude growth without phase inversion, by comparison with the high-to-low density case (e.g., air/helium) having amplitude growth following phase inversion. This diagram illustrates the flow as being two-dimensional, which is believed to be a good approximation because experiments indicate that lateral effects are small. The interface in Los Alamos experiments is formed by a thin, cellulose nitrate membrane.

Viewgraph 1-3 is a qualitative comparison of air/air, air/SF_6 and air/helium interfaces subjected to single shock. We observe that the air/SF_6 interface amplitude grows without inversion and the air/helium interface grows after phase inversion.

Viewgraph 1-4 is a schematic diagram of a shock tube used to study this problem experimentally.

Viewgraph 1-5

Richtmyer's eq. for amplitude growth

for $k\eta_0 << 1$,

$d\eta / dt = k \eta_0 \Delta U [(\rho_2 - \rho_1) / (\rho_2 + \rho_1)]$

η = amplitude (= 1/2 peak-to-peak)

$k = 2\pi / \lambda$

ΔU = shock-induced change in particle speed

$(\rho_2 - \rho_1) / (\rho_2 + \rho_1)$ = Atwood number

But use "shock-compressed" values for η_0 and Atwood number

Richtmyer calculated the case of low-to-high density fluids, but experiments showed that the interface is unstable from either direction.

Viewgraph 1-6

Shock-tube experiment at Los Alamos

Cross-section: 75 x 75 mm

Wavelength of ripple: $\lambda = 37.5$ mm

Initial amplitude: $\eta_0 = 2.4$ mm

Initially, $k\eta_0 = 0.40$

Incident shock: Mach 1.24 in air

Results for single-λ, single-shock growth rate $d\eta/dt$:

air/SF_6: $d\eta / dt = 7.9$ m/s $\Delta U = 81$ m/s

air/He: $d\eta / dt = 18.9$ m/s $\Delta U = 185$ m/s

Viewgraphs 1-7 and 1-8 are plots of amplitude growth vs time for air/SF_6 and air/He. The measured growth rate is the slope of the fitted straight line through each dataset. Each dataset corresponds to a single experiment, from which amplitudes are measured from data acquired with a multi-frame electronic camera.

Viewgraph 1-9

Comparisons with Meshkov's experiments and Richtmyer's formula

LANL data higher than Meshkov (1969) measurements, but within experimental errors.

air/SF_6: $(d\eta / dt)_{LANL} / (d\eta / dt)_{RICHTMYER} = 0.58$

air/He: $(d\eta / dt)_{LANL} / (d\eta / dt)_{RICHTMYER} = 0.42$

Viewgraph 1-10

Problems

Corrections for shock compression of η_0 and Atwood number?

Use simulations to determine best method.

Why are experimental value of dh/dt lower than Richtmyer's formula?

Compressibility correction to Richtmyer's formula?

Measure growth rate of reshocked interface, but boundary layer and mix obscure the interface profile.

The problem of obscuration by the boundary layers is being addressed at various laboratories with light scattering methods and x-radiography.

RICHTMYER - MESHKOV INSTABILITY

LOW-TO-HIGH DENSITY (e.g., air/SF_6)

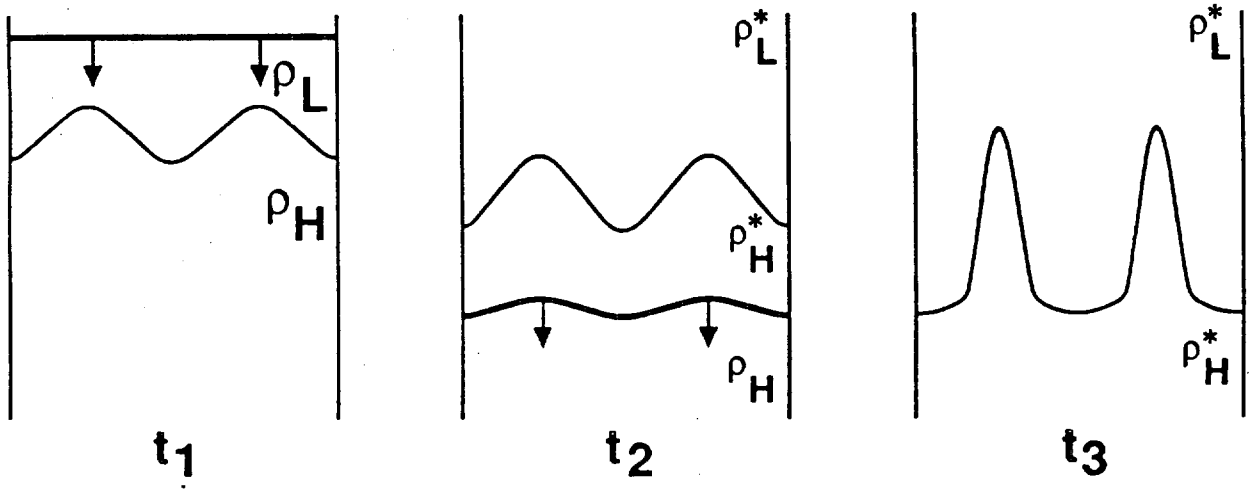

HIGH-TO-LOW DENSITY (e.g., air/helium)

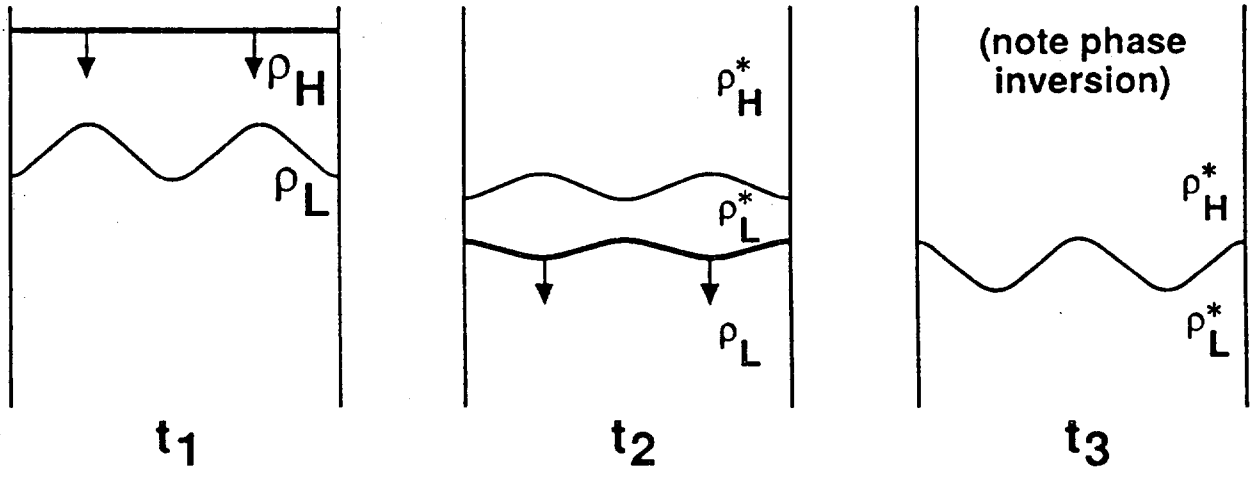

Viewgraph 1-2

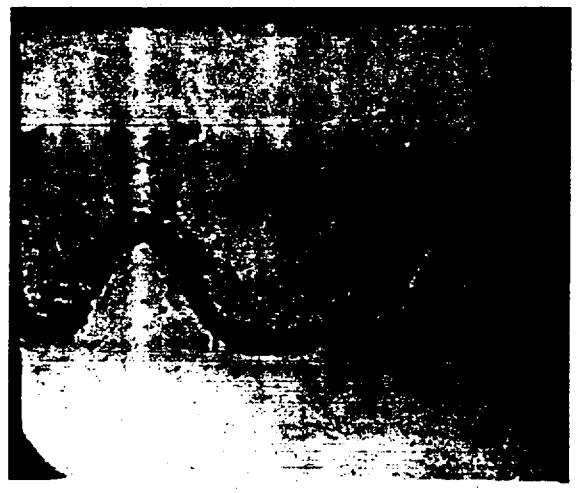

Viewgraph 1-3

VERSATILE SHOCK TUBE ENABLES SHADOWGRAPH OR SCHLIEREN OBSERVATION OF INTERFACIAL INSTABILITY

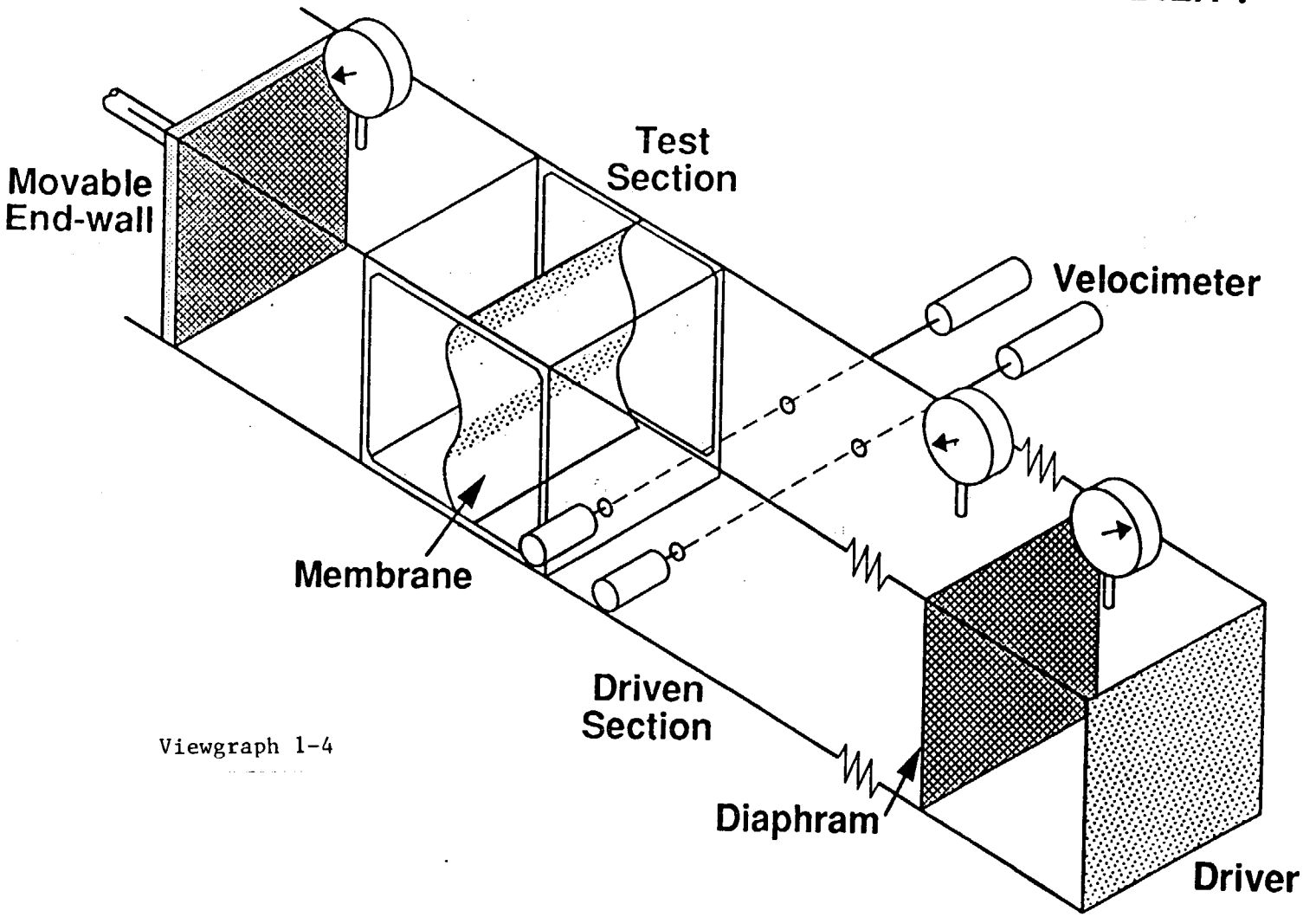

Viewgraph 1-4

Amplitude of perturbed interface vs time
Air/SF6 data

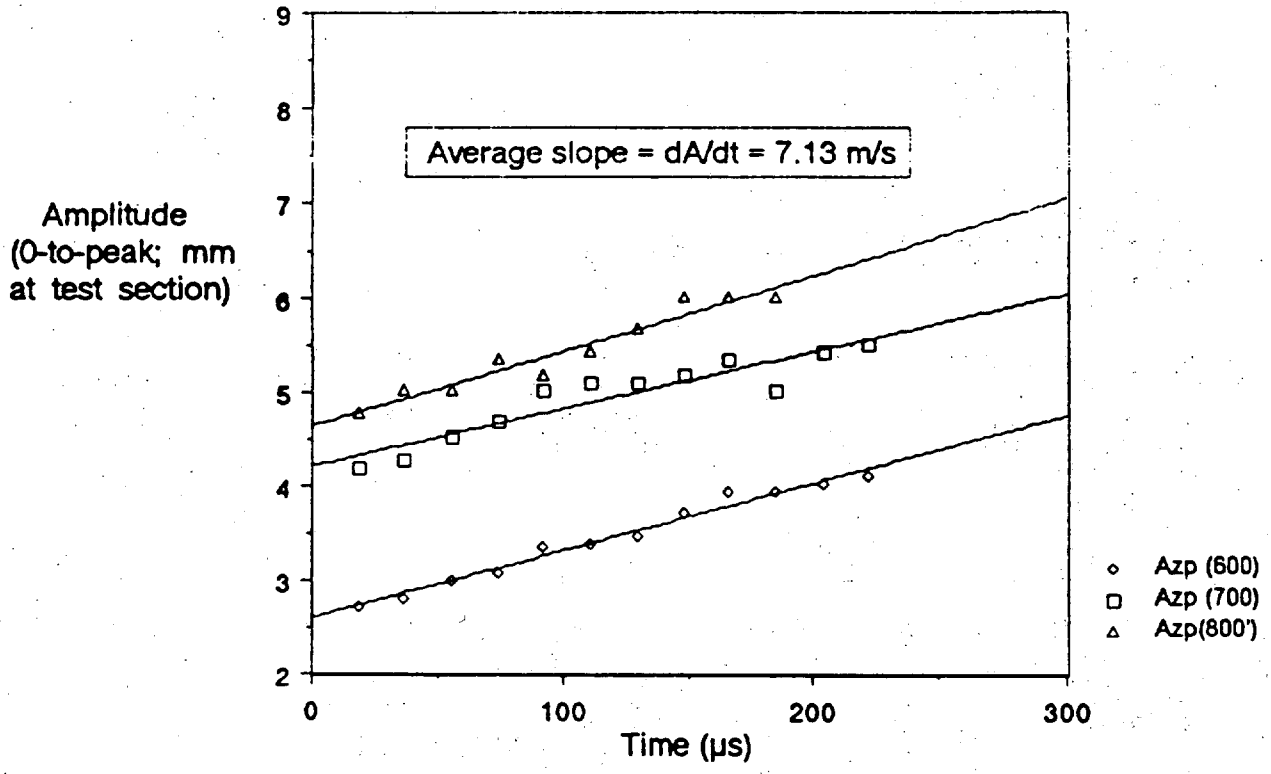

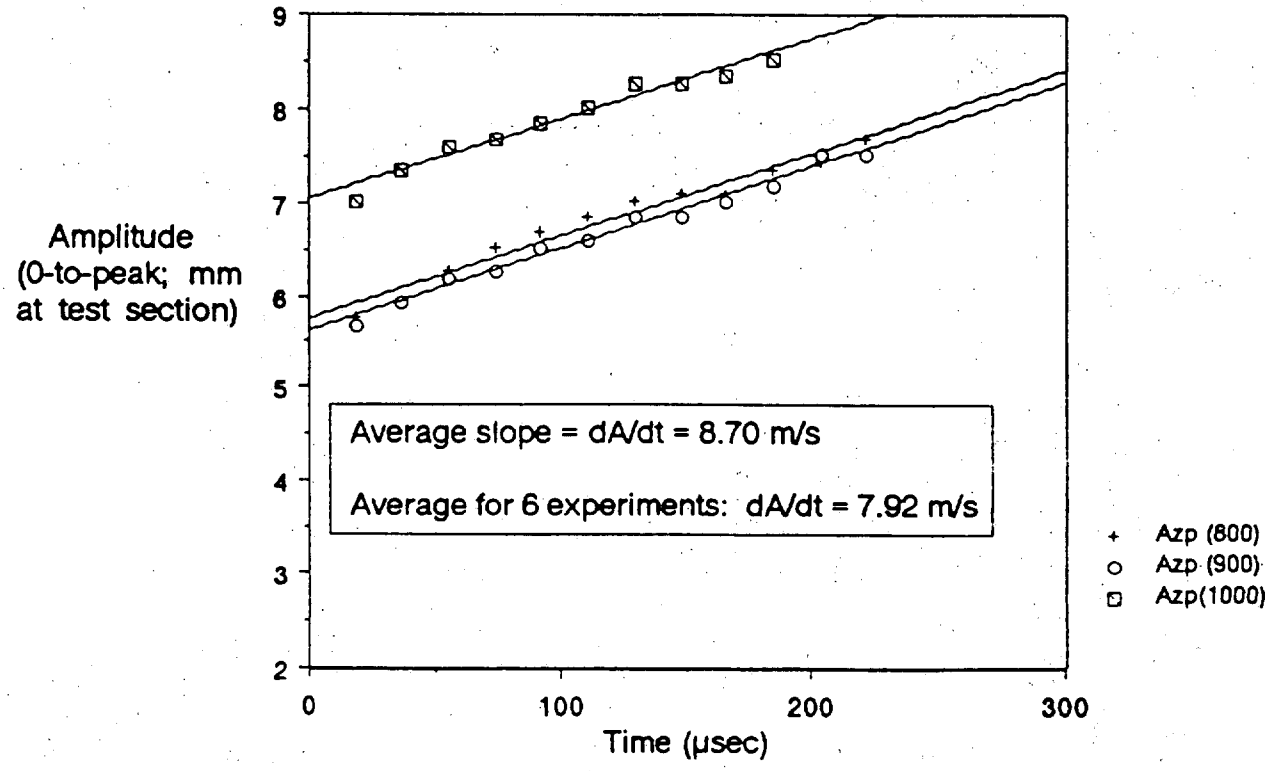

Viewgraph 1-7

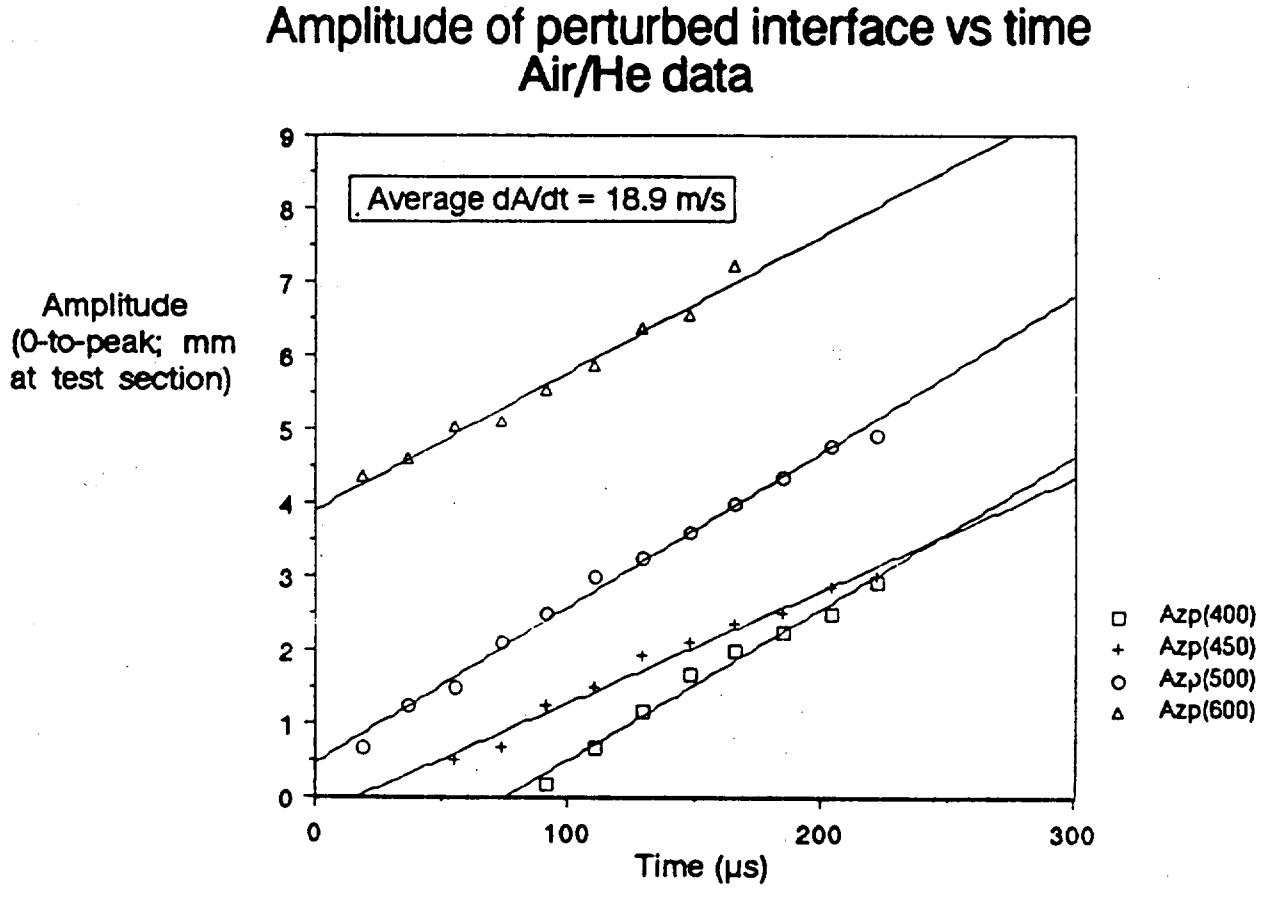

Viewgraph 1-8

New diagnostics for shock tube experiments:

Imaged Light Scattering

by Robert F. Benjamin

Los Alamos National Laboratory

This presentation was given Friday morning, 17 November 1989 by Robert Benjamin. This manuscript contains annotated viewgraphs of the presentation and the companion poster talk.

SUMMARY

We are evaluating the feasibility of using imaged light scattering (ILS) to measure the unstable flow and mixing in a 2D section of a 3D (air/SF_6) Richtmyer-Meshkov flow instability. Using aerosol as a tracer in SF_6 gas, we find that the interpenetration of gases during reshocking is better defined in ILS photographs than observed in optical shadowgraphs, and there appears to be less small-scale mixing in ILS data. The "fuzziness" present in shadowgraphs is not seen in the scattering data, which suggests that boundary-layer flow obscures the shadowgraph.

Viewgraph 2-1

New diagnostics for shock tube experiments: Imaged Light Scattering

by Robert F. Benjamin

Los Alamos National Laboratory

International Exchange on R-M and R-T Mixing, 16-17 November 1989

Viewgraph 2-2

Reasons for developing a scattering method

Shadowgraphs integrate the optical effects of boundary layer and bulk fluid;

the boundary layer seems to obscure instability and mixing in the bulk fluids.

Distinguish between (single-mode or few-mode) interpenetration and (multimode) mixing

---

Shadowgraphs and schlieren photos integrate refractive index changes along the optical axis. Although the boundary layer may be quite thin, its optical effect may dominate the image. In our shadowgraphs the optical signature of the boundary layer appears as a "fluffy," fuzzy material along the interfacial profile. In the Caltech work, the boundary layer is interpreted as a translucent region, by contrast to the mix region that is opaque. Comparison of the Caltech results with Soviet results suggests that the region that the Soviet researchers have labelled "turbulent mixing zone" may actually be the combination of bulk effects and boundary- layer effects.

Viewgraph 2-3 is a shadowgraph of an event in which an air/SF_6 interface experiences RM growth following impulsive acceleration by a single shock.

Viewgraph 2-4 is a shadowgraph of an air/ SF_6 interface being reshocked.

The fuzziness of the interface profile seen in single-mode growth is also present for nominally flat interfaces, or for a continuous interface, as measured by Sturtevant. To measure the instability growth and mixing of the *bulk* fluids, we cannot use shadowgraphy in which the optical axis passes through one or more boundary layers.

Note the **structure on the rarefaction** wave reflected into the SF_6. Perhaps this structure is a measure of the turbulence scale size at the interface.

Viewgraphs 2-5 shows a schematic diagram of the shock tube with the light scattering diagnostic. See also viewgraph 1-4 of the "Test problem 1" presentation for more details.

Viewgraph 2-6

Feasibility tests use DOS aerosol as tracer in heavy gas

SF_6, Freon

$\tau \approx 2$ μs for 0.3 μm particle to attain mean flow velocity (Mach 1.2 shock)

shock accln. of ptcl ≈ 0.2 m/s, but mean flow ≈ 100 m/s (0.1 mm/μs)

Interframe time = 20 μs

=> good tracer particles

But $\tau >$ interframe time for helium

These estimates show that these aerosol particles are useful tracer particles in a heavy gas like SF_6 or Freon, but not suitable for use in helium.

Viewgraph 2-7 is an image of the air/ SF_6 interface after reshocking. The image is produced by light scattering from the aerosol particles entrained in the SF_6 gas flow, and by scattering from membrane fragments.

Viewgraph 2-8

Diagnostics to measure scale-size

Scattering

Structure on rarefaction

- Measurable
- Correlated with structure on interface?

The structure on the rarefaction is definitely measurable, as seen in the shadowgraph of the reshock, viewgraph 2-4.

Viewgraph 2-9

Conclusion

Feasibility tests of imaged light scattering using tracer in heavy gas show different images than seen with shadowgraphs. It appears that imaged scattering enables measurement of a 2D section of instability and mix in bulk fluids.

GROWTH OF SINGLY-SHOCKED (M = 1.24) AIR / SF_6 INTERFACE

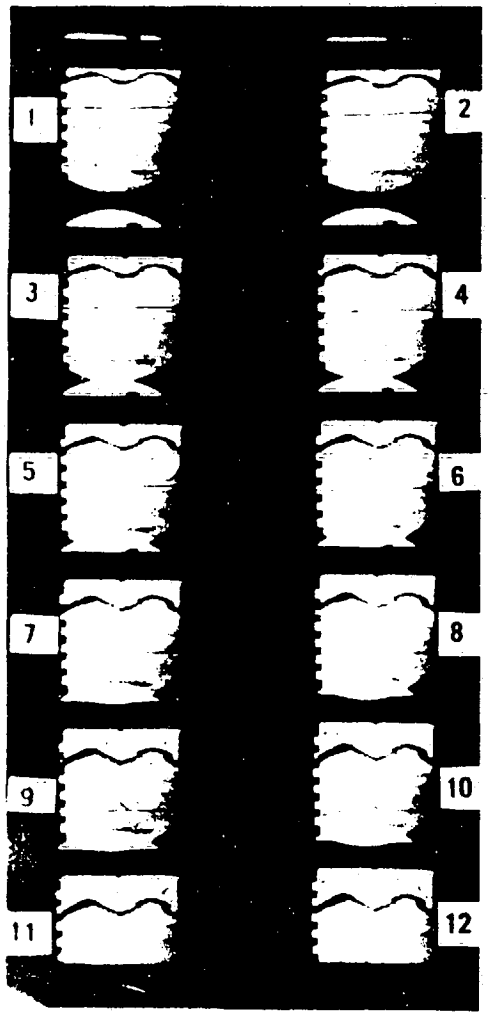

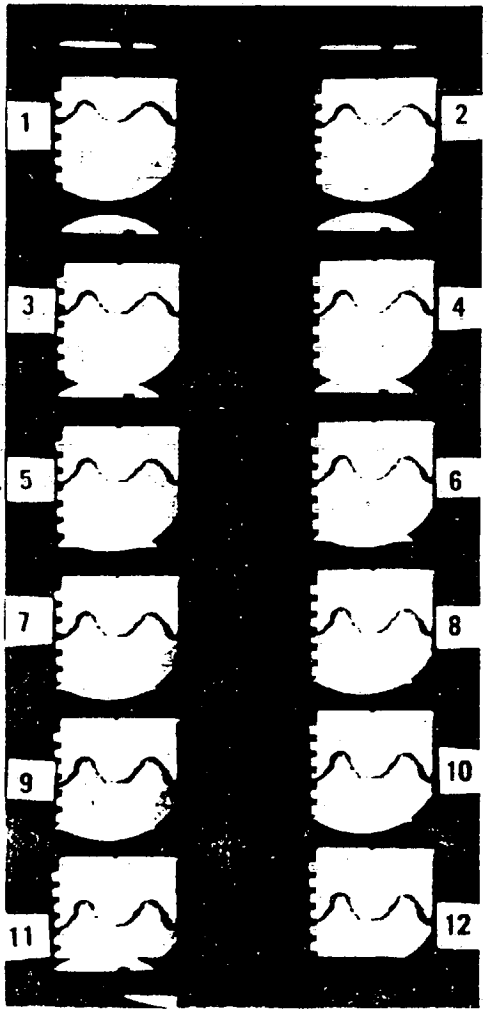

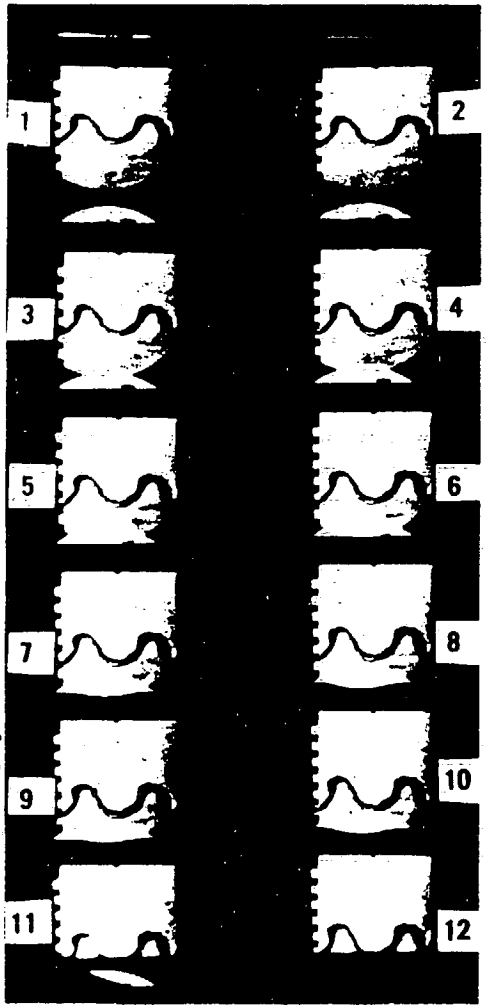

Viewgraph 2-3

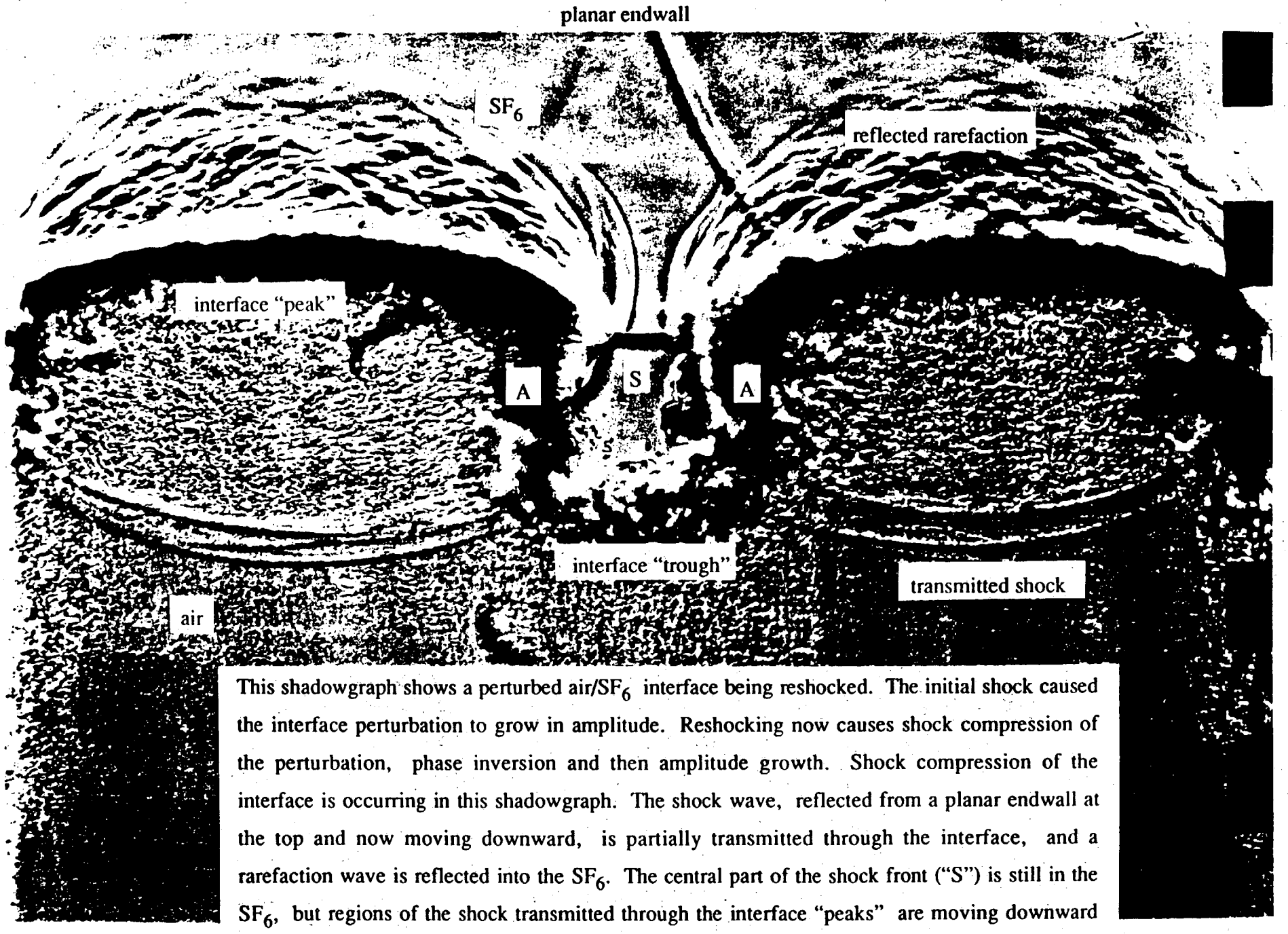

This shadowgraph shows a perturbed air/SF_6 interface being reshocked. The initial shock caused the interface perturbation to grow in amplitude. Reshocking now causes shock compression of the perturbation, phase inversion and then amplitude growth. Shock compression of the interface is occurring in this shadowgraph. The shock wave, reflected from a planar endwall at the top and now moving downward, is partially transmitted through the interface, and a rarefaction wave is reflected into the SF_6. The central part of the shock front ("S") is still in the SF_6, but regions of the shock transmitted through the interface "peaks" are moving downward in the air. Vorticity production is greatest at regions labeled "A."

LIGHT SCATTERING TECHNIQUE SAMPLES
BULK FLOW-FIELD (not boundary layer)

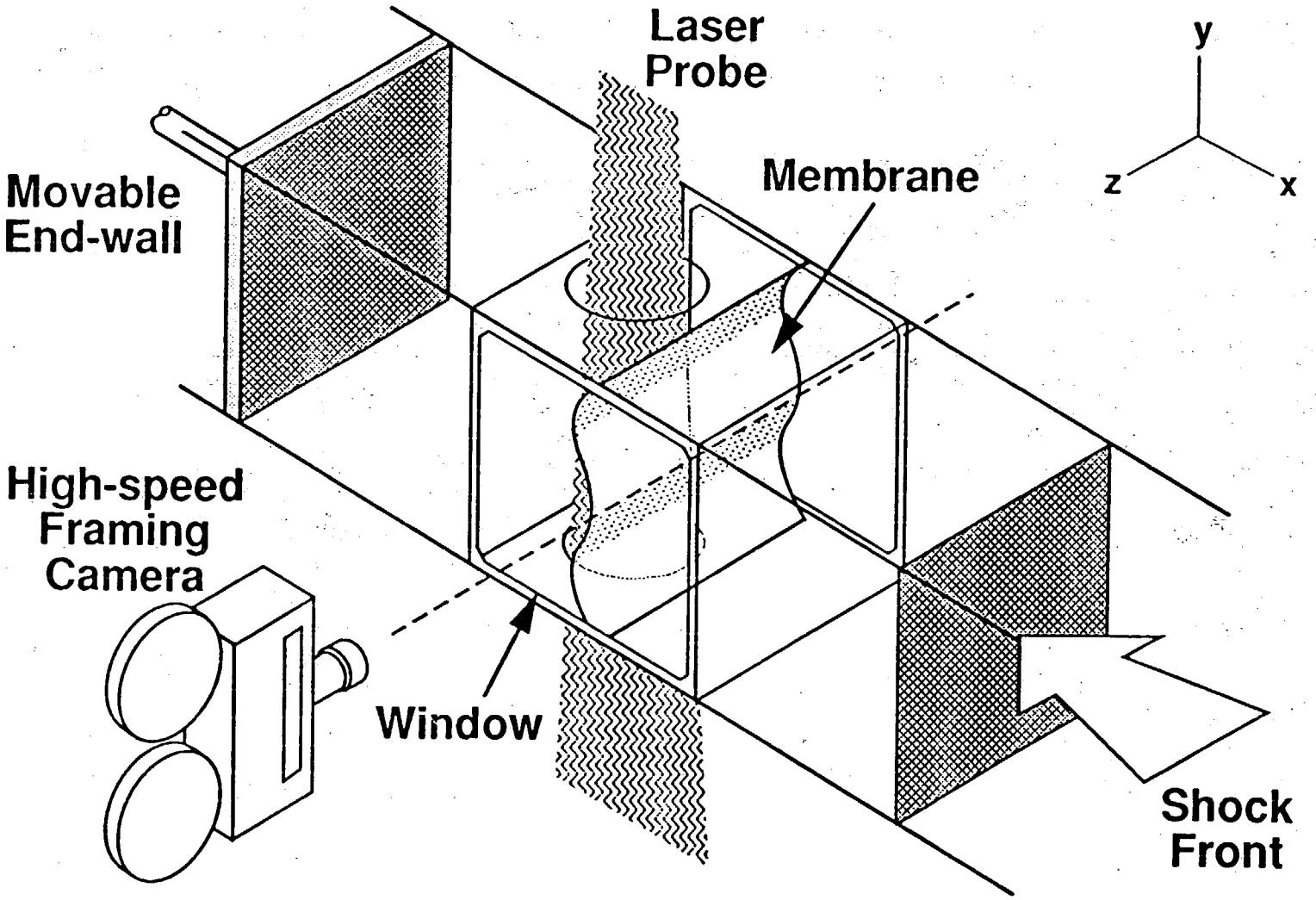

Viewgraph 2-5

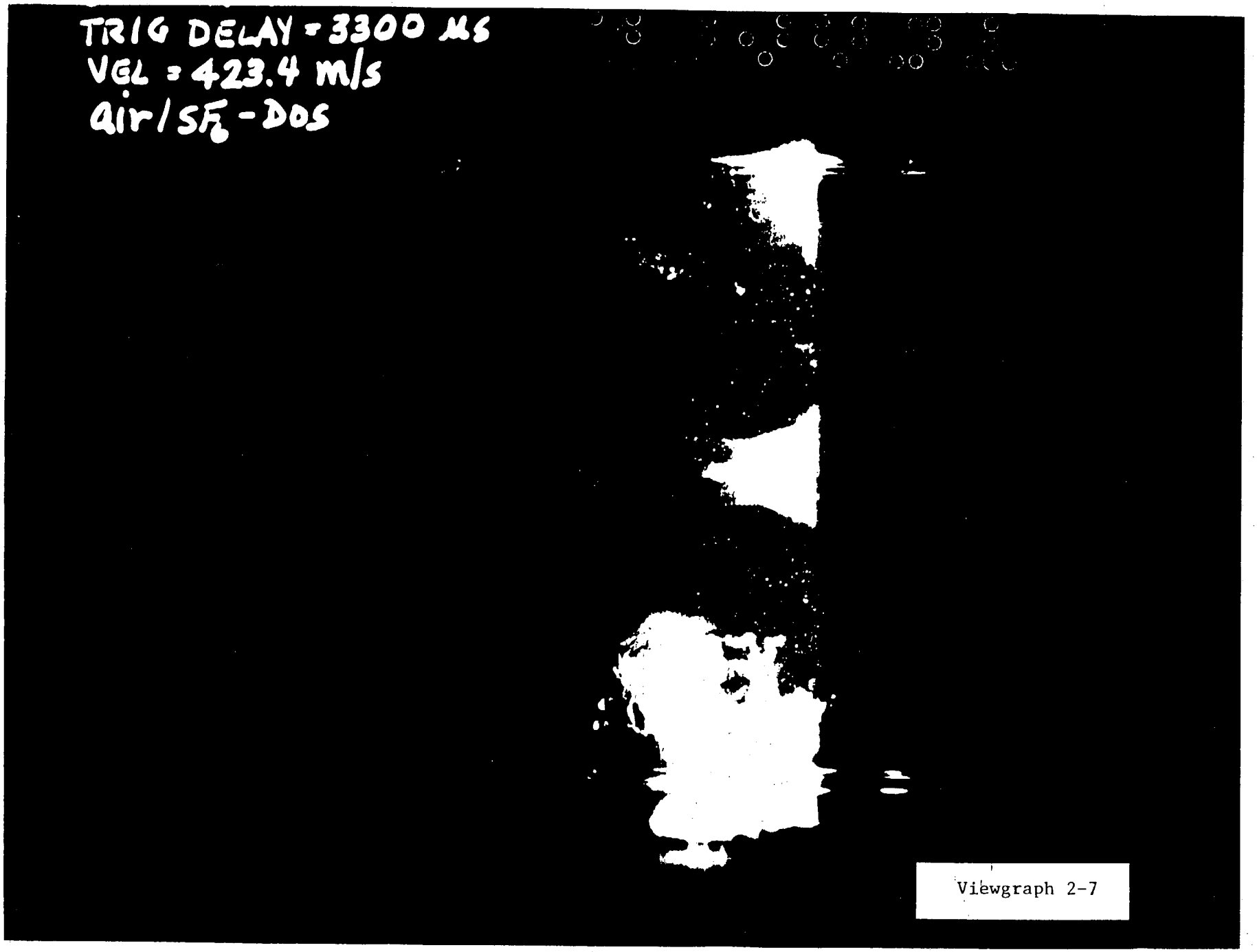
TRIG DELAY = 3300 MS
VGL = 423.4 m/s
Air/SF6 - DOS
Viewgraph 2-7

EXPERIMENTAL INVESTIGATIONS ON RICHTMYER-MESHKOV MIXING INDUCED BY HIGH MACH NUMBER SHOCK WAVES

L. Houas and J. Fortes

U.R.A. CNRS 1168, SETT, Milieux Hors d'Equilibre,
Université de Provence, Saint Jérome, 13397 Marseille cedex 13, FRANCE

The study of shock-accelerated interfaces between two fluids of different densities is known as the study of shock-excited Rayleigh-Taylor or Richtmyer-Meshkov instability. However, high Mach number shock-interface interaction experiments lead to turbulent three-dimensional flows which are difficult to describe in the framework of the simple Rayleigh-Taylor instabilities. In the present experiments, two gases are initially separated by a thin plastic membrane materializing the interface. Two measurement techniques have been used to observe the created turbulent mixing zone : CO_2 infrared absorption wich provides average temperature and density profiles in the mixing zone, CO_2 infrared emission wich gives the evolution of the mixing zone thickness. Another measurement of the mixing zone thickness is obtained by Schlieren photographs and compared to both emission thickness measurement and similar experiments at high Mach number conditions. Furthermore, qualitative informations on the turbulent mixing before and after interaction with the reflected shock are observed on the photographs.

1. INTRODUCTION

In the context of the inertial confinement fusion (ICF) an experimental work is undertaken to analyse the impulsive Rayleigh-Taylor instability. This instability is one of the causes of the generation and development of a turbulent mixing zone, between the shell material and thermonuclear combustible of an ICF pellet, which contributes to reduce the efficiency of nuclear reaction by an early break-up of the shell and a cooling of the combustible. While the phase of the linear growth of small perturbations on interface separating different fluids is relatively well understood, the phase of the non linear growth and the subsequent turbulent phase present some difficulties in their comprehension. Thus, the aim of the present work is to study in the simpler shock tube environment the evolution of the mixing zone created by the interaction of a high Mach number shock wave and a gaseous interface initially at rest.

Experiments are carried out in a double diaphragm shock tube. It has a square cross section (8.5 x 8.5 cm) and its total length is about 9 m. The test section is about 1.5 m long downstream the second diaphragm. The gases, carbon dioxyde upstream and helium or argon downstream, are initially separated by a thin plastic film (1.5 µm) which constitutes the second diaphragm. When a shock wave accelerates the interface, this one is subjected to the impulsive Rayleigh-Taylor instability also called Richtmyer-Meshkov instability. When the membrane is initially planar, that is the case in all the experiments presented in this paper, only the random small spatial scales created by the membrane break-up are excited and the turbulent mixing occurs soon.

The created mixing zone is later decelerated by the reflected shock wave from the end wall of the shock tube. The use of two gas pairs, CO_2/He and CO_2/Ar, allows to analyse the influence of the Atwood number ($|A_t|_{CO2/He} \approx 0.8$ and $|A_t|_{CO2/Ar} \approx 0.3$) on the instability and the subsequent turbulent mixing zone.

The CO_2 is used for its spectroscopic properties and He and Ar because they present no infrared emission or absorption in the domain of our experiments, also because their densities are respectively very different and close to that of the CO_2 and finally because of the regular reflection obtained for the incident shock wave.

Measurements are based on infrared emission or absorption of shock heated CO_2 (fig. 1.a)and enable us to obtain the trajectory and the thickness of the mixing zone as well as average temperature and CO_2 density profiles within. Schlieren vizualisations of the turbulent flow (fig. 1.b) provide another measurement of the mixing zone thickness and qualitative informations on the three-dimensional nature of the transmitted shock through the interface and the turbulent mixing after interaction.

The infrared techniques require strong shocks (Mach 3 - 4.5 in CO_2 and Ar, 2 - 2.5 in He) and therefore the velocities behind the shock (1000-2000 m/s) are well into the compressible range. Thus it is expected that mixing should be different from that obtained in the experiment of ref. 1 where a Mach number 1.3 shock interacts with an air/He interface, and perhaps more similar to recent experiments of ref. 2 where, for example, a Mach number 3 shock interacts, with He/Ar or Ar/He interfaces.

However, high Mach number shocks and low initial pressures lead to thicker boundary layers on the shock tube side walls and thus viscosity effects are always combined with the development of the instability.

2. WAVE DIAGRAMS AND MIXING ZONE THICKNESS

Measurements of the infrared emission (centered at 4.3 µm) of shock heated CO_2 provide the time evolution of the quantity $\rho(CO_2)\, Ev_3(T)$ where $Ev_3(T)$ is the average specific energy corresponding to the third mode of vibration of the CO_2 molecule and $\rho(CO_2)$ the density of CO_2. The optical set up is such that the infrared detector records the emission of a small volume of fluid at the center of the shock tube[3]. Platinum heat transfer gauges mounted flush at the walls are used to record the propagation of the shock waves. Using several gauges and infrared detectors (two or three) per shock tube run and combining the measurements from several runs at the same conditions enable us to build (x, t) diagrams of the shock waves and mixing zone

trajectories such as the ones shown in figures 2.a, 3.a and 4.a. The rise time of the signals from the infrared detectors provides the thickness history of the mixing zone. Figures 2.b, 3.b and 4.b show the evolution of the mixing zone thickness L for the 2 pairs of gases and different initial pressures, i.e. for different incident shock Mach numbers. The error on the thickness, for emission measurements, have been estimated to ± 2 mm. We also present in figure 2.b the evolution of the mixing zone thickness obtained by Schlieren photographs with and without taking into account three-dimensional (wall boundary layer) effects. The (x, t) diagrams show the transmitted shock in the rare gas, the reflected shock from the end wall and the waves resulting from its interaction with the mixing zone with x = 0 and t = 0 corresponding respectively to the initial position of the thin plastic membrane and the instant when the incident shock wave breaks it. The mixing zone trajectory is plotted from a distance of 20 cm from the initial position of the separating membrane (here 1.5 µm Mylar). Notice that the lines connect only data points from different runs and do not represent corresponding variations of velocity during the same test.

- experiments at 2000 Pa initial pressure :

Beyond 30-50 cm, the mixing zone velocity is fairly constant and higher than predicted by the Rankine-Hugoniot relations based on the measured shock velocity. This is a well known boundary layer effect in high Mach number shock tube experiments and we found it a little more pronounced for the CO_2/He case. Furthermore, the mixing zone seems to accelerate again after the interaction, which is contrary to the behavior observed for low Mach number experiments and non viscous numerical simulations. Figure 1.b shows that the CO2/Ar mixing zone is thin and thickens very slowly after 400 µs (i.e. beyond 40 cm from the initial position), but the unmeasured initial thickening rate must have been larger. The reflected shock causes first a compression and after a very rapid thickening. The CO2/He mixing zone (figure 3.b) thickens at an important rate up to the compression by the reflected wave and thickens again very quickly afterwards.

- experiments at 5000 Pa initial pressure (from flow vizualization) :

In this case, for both lower Atwood number (- 0.23) and flow velocities (470 m/s), figure 4.b shows that the CO2/Ar mixing zone is thicker than expected. This may be due to the more important Reynolds number.

Schlieren flow pictures are presented on figures 5, 6 and 7. Due to the optics of the compact Zeiss Schlieren apparatus the field of view is oval-shaped with 7 and 6 cm for the vertical and horizontal axis respectively. Some pictures (indicated by X) are centered on the shock tube axis, and others (indicated by X*) are closer to the upper wall of the shock tube in order to observe the wall boundary layer effects.

In the early time, we can observe the film wich is still present ahead of the mixing zone and only destroyed by the reflected shock. The boundary layer created by the incident shock causes the reflected shock to become rapidly three-dimensional as it crosses the mixing zone. Furthermore, we observe the different structure of the mixing zone before and after its deceleration by the reflected shock (figures 5 and 7). On picture 3 of figure 5, we observe the fibrous structure of the decelerated mixing zone with vertical layers which might indicate the anisotropy of the shocked turbulent field. That means that the turbulent mixing zone keeps well the memory of the shock passage through it. Later, starting at 50 µs, this structure disappears to be replaced by a more isotropic pattern similar to that of the turbulent boundary layer. Thus, the turbulent mixing zone begins to loose the memory of the shock passage. For a higher initial pressure and lower Mach number (figure 7), the vertical fibrous structure was never observed. At last, one can remark the particular aspect of the reflected shock after crossing the CO2/He turbulent mixing zone comparatively to the more classical one for the CO2/Ar case (figure 6).

3. COMPARISON WITH ZAITSEV EXPERIMENTS

Zaitsev's experiments were made with similar incident shock Mach numbers (3 vs 4 in our experiments) and shock tube cross section (7 vs 8.5 cm). Their separating membrane : 2 µm Lavsan or Dacron might have mechanical properties close to those of our 1.5 µm Mylar film. We have found that thicker (and stronger) membranes lead to thicker mixing zones and we expect that our membranes have a larger influence on the mixing zone compared to the experiments of Andronov et al.[1] and of Sturtevant[4] where weaker nitrocellulose films were used. Another important difference between Zaitsev's experiments and ours is the length of the test section : 37 vs 127 and 152 cm in our case.

Zaitsev's results are summarized in two formulas for the thickening rate (dL / dt) of the mixing zone before and after the reflected shock as a function of the velocity jump and the Atwood number A_t (calculated after shock compression).

- before reflected shock :

$$\frac{dL_1}{dt} = \left(0.02 + 0.07 \left| A_{t_1} \right| \right) U_1$$

for $At_1 < 0$ and where U_I is the measured mixing zone velocity.

- after reflected shock :

$$\frac{dL_2}{dt} = \left(0.05 + 0.85 \left| A_{t_2} \right| \right) \Delta U_R$$

for $At_2 > 0$ and where ΔU_R is the calculated velocity jump due to the reflected wave.

Figure 8 shows the evolution of the average thickening rates in our experiments and in Zaitsev's experiments for the accelerated (figure 8.a) and decelerated (figure 8.b) phases. The comparison shows that the thickening rate is in relatively good agreement with that predicted by Zaitsev in the short initial phase of

the mixing zone growth but our measured growth later is quite less than predicted. There is also some difference in the decelerated phase.

4. AVERAGE TEMPERATURE AND CO2 DENSITY PROFILES IN THE MIXING ZONE

4. 1 Principle

We present results obtained with a CO_2 laser absorption technique which has already been presented in ref. 3 in its first approach. Now, a more rigourous absorption coefficient model has been developed.
The study of the absorption coefficient of an optical active medium by an electromagnetic wave allows to know the thermodynamic state of this medium. In the context of our work, we had to study the thermodynamic state of a CO_2/He or CO_2/Ar supersonic gaseous mixing zones created by high Mach numbers shock wave / interface interaction.
For that, we need to know the absorption coefficient of the CO_2 molecule, in the gaseous mixings CO_2/He or CO_2/Ar for the transition Σ (00°1 - 10°0) when these media are traversed by a low continuous CO_2 laser beam, 7 watt power, 10.4 mm centered wave lenght and 425 ± 25 MHz widness in the standard operating conditions.
We use the semi-classical theory of the wave-matter interaction. The absorption coefficient is the result of the contributions of the laser induced absorption and emission as well as the spontaneous emission. We have taken into account the spectral width of the laser line and the spectral width of the CO_2 absorption line in the test section. This CO_2 absorption line is a function of the Doppler width due to the thermal molecular motion, a collisionnal width dependant on the gas pressure and temperature in the considered medium and its composition : that is a CO_2 Voigt profile. We also have taken into account the hot bands of the Σ (00°1 - 100°) transition wich can give a non negligible contribution to the absorption coefficient.
Thus, we have realised a theoretical model of the absorption coefficient of the CO_2 molecule in gaseous mixing media, CO_2/Ar or CO_2/He, which take into account of all the contributions precedently described.

4- 2 - The absorption coefficient

Let us, consider an absorbant medium with an elementary thickness dl, and crossed by a low intensity radiation I_0 with a frequency ν.
The intensity of this radiation changes of a quantity dI which is proportional to the incident intensity as predicted by the Bourguer-Lambert law :

$$dI = -\alpha I dl \qquad (1)$$

where α is a coefficient of proportionality called absorption coefficient and I the intensity after absorption. The integration of eq. (1) along the distance L gives the expression of the absorption coefficient α :

$$\alpha = \frac{1}{L} \mathrm{Log}\left(\frac{I_0}{I}\right) \qquad (2)$$

Let us now consider a system of particules submitted to a radiation I_0 with the frequency ν. Let N_l the number of molecules in the fundamental quantic state, N_u the number of molecules in the quantic excited state. Than, $\rho_{\nu lu}$, the density of the energy of the incident radiation is :

$$\rho_{\nu lu} = \frac{8\pi h \nu_{lu}^3}{c^3} \frac{1}{e^{\frac{h\nu_{lu}}{KT}} - 1} \qquad (3)$$

Assuming the thermodynamical equilibrium, there is equality between induced absorption, spontaneous emission and isotropic induced emission :

$$N_u B_{u\text{-}l} \rho_{\nu lu} + N_u A_{u\text{-}l} = N_l B_{l\text{-}u} \rho_{\nu lu} \qquad (4)$$

with the classical hypothesis of a Boltzmann distribution function for the population of the transition levels

$$\frac{N_l}{N_u} = g_l e^{-\frac{h\nu_{lu}}{KT}} \qquad (5)$$

and

$$g_l B_{l\text{-}u} = g_u B_{u\text{-}l} \qquad (6)$$

we obtain :

$$A_{u\text{-}l} = \frac{8\pi h \nu_{lu}^3}{c^3} B_{u\text{-}l} \qquad (7)$$

in relations (5) (6) and (7), N and g correspond respectively to the population and the statistic weigth of each considered level, A and B are Einstein coefficients, h is the Planck constant and c the light velocity. If we

suppose that the intensity variation dI of the incidend variation is due to induced emission and absorption, than we obtain :

$$dI = \frac{h\nu}{c}\left(N_u B_{u-l} - N_l B_{l-u}\right) I dl \qquad (8)$$

and combining relations (2), (6), (7) and (8) :

$$\alpha = \frac{h\nu}{c} g_l B_{l-u}\left(\frac{N_l}{g_l} - \frac{N_u}{g_u}\right) \qquad (9)$$

In the framework of the semi-classical theory of the interaction of radiation with matter , B_{u-l} is given by

$$B_{u-l} = \frac{8\pi^3}{3h^2} |R_{12}|^2 |R_{jj'}|^2 H f(\nu-\nu_0) \qquad (10)$$

where R_{12} is the matrix element term of the dipolar electrical moment depending on the change of the vibrational level and $R_{jj'}$ the matrix element term of the dipolar electrical moment depending on the change of the rotational level given by

$$|R_{jj'}| = \frac{S_{j'l'}}{g_j} \qquad S_{j'l'} = \frac{m^2-l^2}{m} \qquad (11)$$

and $H = 1 - C_1 m - C_2 m^2$ is the term which take into account the rotation-vibration interaction (~1 for CO_2), m = j or j + 1, C_2 ~10^{-3} and C_2 ~$(6 \pm 1)\ 10^{-5}$ are two constants and $f(\nu - \nu_0)$ the spectral profile of the absorption line of the incident radiation.

Thus, relation (9) becomes :

$$\alpha = \frac{8\pi^3 \nu}{3hc} g_l |R_{jj}|^2 |R_{12}|^2 H f(\nu - \nu_0)\left(\frac{N_l}{g_l} - \frac{N_u}{g_u}\right) \qquad (12)$$

The spectral profile $f(\nu - \nu_0)$ of the incident radiation is a Voigt profile. In the case of the CO_2/Ar or CO_2/He, combination of gaseous mixings, it is given by :

$$f_{Voigt}(\nu) = \frac{a}{\pi \Delta\nu_D}\sqrt{\frac{\ln 2}{\pi}} \int_{-\infty}^{+\infty} \frac{e^{-y^2}}{a^2 + (x-y)^2}\, dy \qquad (13)$$

with

$$x = \sqrt{(\ln 2)}\,\frac{(\nu-\nu_0)}{\Delta\nu_D} \qquad a = \ln 2\,\frac{\Delta\nu_c}{\Delta\nu_D}$$

and where $\Delta\nu_c$ is the collisional profile depending on the pressure and temperature of the gaseous mixing and $\Delta\nu_D$ the Doppler profile which is caracteristic of the thermal motion in the medium and where $\Delta\nu_c$ and $\Delta\nu_D$ are given by :

$$\Delta\nu_c = C P \gamma^{(j)}_{CO_2 - CO_2}\left[\Psi_{CO_2}\left(\frac{300}{T}\right)^{n_{CO_2 - CO_2}} + \sum_i \Psi_X \left(\frac{300}{T}\right)^{n_{CO_2 - X}} \left(\frac{\gamma^{(j)}_{CO_2 - X}}{\gamma^{(j)}_{CO_2 - CO_2}}\right)\right] \qquad (14)$$

with $C = 1.65\ 10^{-4}\ m^2\ k^{1/2}\ kg^{-1/2}$
and

$$\Delta\nu_D = 2\nu_0\sqrt{\frac{2\ln(2) KT}{Mc^2}} \qquad (15)$$

where Ψ_{CO2} is the mass concentration of CO_2 in the mixing CO_2 / X , Ψ_X is the mass concentration of argon or helium in the mixing CO2 / X (X = Ar, He) and

$$M = \frac{M_{CO_2} M_x}{M_{CO_2} + M_x}$$

4- 3 - General expression of the CO_2 absorption coefficient taking into account the hot bands

For a given line of the CO_2 infrared spectrum, one can find adjacent lines in near resonance with it and which contribute to the absorption of the CO_2 in this band in a non negligible quantity (~ 40 %). These bands are called hot bands. Thus, we have determined the bands contributing to the total absorption of the CO_2 for the transition Σ (00°1 - 100°) and calculated the percentage of the population of the transition low levels centered on a frequency near 961 cm^{-1} (10.4 μm). Transitions of which low levels have a population which can be considered as low are neglected, and the others are what we call hot bands.
Figure 9 shematizes the configurations that we have used for the study of the absorption coefficient of the CO_2 taking into account the hot bands contribution.
Thus, the total absorption coefficient correponds to the sum of the contribution of the principal band and the contribution of the hot bands :

$$\alpha = \alpha_0 + \sum_{i=1}^{n} \alpha_i \qquad (16)$$

where α_o is the absorption coefficient of the principal band and α_i the absorption coefficient of the i^{th} hot band.

- Absorption coefficient of the principal band

With the hypothesis of a Voigt profile (relation 13) the resonant absorption coefficient of the centered line is :

$$\alpha_0 = \frac{1}{\Delta\nu_0} \int_{\nu_0 - \frac{\Delta\nu_0}{2}}^{\nu_0 + \frac{\Delta\nu_0}{2}} \overset{0}{\alpha_0}(\nu)\, f_0(\nu)\, d\nu \qquad (17)$$

where α^o_o is given by relation 12
Considering $\Delta\nu_0/\nu_0$ as a small quantity, and whith :

$$\mathrm{erf}(x) = \frac{2}{\sqrt{\pi}} \int_0^x e^{-z^2} dz \qquad (18)$$

relation (17) becomes :

$$\alpha_0(\nu) = \overset{0}{\alpha_0}(\nu) \sqrt{\frac{\ln 2}{\pi}} \exp(a^2)(1 - \mathrm{erf}(a)) \qquad (19)$$

- Absorption coefficient of the hot bands

As previously said, when taking into account the non adjustement of the laser line and the i^{th} hot band we define a new profile :
$g_i(\nu) = f_{Voigt,i}(\nu) \cdot f_L(\nu_0 + k_i + \nu_i)$
where $f_{Voigt,i}$ is the Voigt profile for the hot band i and $f_l(\nu_o + k_i + \nu_i)$ is the value of the laser line profile (assumed to be Lorentzian) on the point $\nu = \nu_o + k_i + \nu_i)$, ν_o being the laser line frequency, ν_i the i^{th} hot band frequency and k_i the distance between them.

Then, the absorption coefficient of the i^{th} hot band is :

$$\alpha_i = \frac{1}{\Delta\nu_i} \int_{\nu_i - \frac{\Delta\nu_i}{2}}^{\nu_i + \frac{\Delta\nu_i}{2}} \overset{0}{\alpha_i}(\nu)\, f_i(\nu)\, d\nu \qquad (20)$$

where α_i is defined by relation (13).
The calculation of this integral gives :

$$\alpha_i(\nu) = \overset{0}{\alpha_i}(\nu)\frac{\Delta\nu_i}{\Delta\nu_D}\frac{1}{\left(1+4\left(\frac{k_i}{\Delta\nu_c}\right)^2\right)}\sqrt{\frac{\ln 2}{\pi}}\exp(a^2)(1-\mathrm{erf}(a))$$

Finally, the general expression of the absorption coefficient is :

$$\alpha_\omega(\rho,T) = \frac{8\pi_i\nu_0^3}{3KT}\sqrt{\frac{\ln 2}{\pi}}\left|R_{12}\right|^2\left|R_{jj}\right|^2\rho_{CO2}Q_v^{-1}\exp(a^2)\left(\frac{\sqrt{\pi/2}}{a+\left[(\pi-2)a/2\right]^q+p^2/4}^{1/q}\right)\sum_i\alpha(j_i,T)$$

with

$$\alpha(j_i,T) = \left(b_1 e^{\frac{-b_1 j_i(j_i+1)hc}{KT}} - b_2 e^{\frac{-b_2(j_i+j')(j_i+j'+1)hc}{KT}}\right)\left(1+\frac{1}{\left(1+4\left(\frac{k_i}{\Delta\nu_c}\right)^2\right)}\frac{\left|R'^2_{i,12}\right|}{\left|R^2_{12}\right|}\right)$$

where j_i is the rotational number of the i^{th} hot band, $j' = 0$ for a R line, $j' = -1$ for a P line, $R'_{i,12}$ is the intensity of the i^{th} hot band of the considered transition and $p \sim 1.902$, $i = 0$ corresponds to the principal band in the case where $k_i = 0$.

Absorption by the test gas CO_2 in the mixing zone of two continuous CO_2 laser lines, corresponding to transition beween the vibrational levels 00°1 --> 10°0 (about 10.4 µm wavelenght) yields average profiles of density, temperature and CO_2 mass concentration in the mixing zone. Average temperature and CO_2 density profiles have been obtained for two abscissa, respectively : 940 mm from the initial position of the interface, before interaction, for both CO_2/Ar and CO_2/He mixing zones, and 1180 mm, after interaction, only for the CO_2/Ar mixing zone (figures 10, 11 and 12). Initial conditions are those indicated in Table 1, columns 3 and 4. Error bars have been estimated to be ± 8% near pure CO_2 and larger near pure argon or helium.
In the accelerated phase, experimental values, at the edges of the mixing zone, are in fairly good agreement with calculations obtained with a Rankine-Hugoniot one dimensional model. In this phase, the shape of the curves, a sharp decrease between 0 and 10 µs followed by a residual slope up to 40 µs for helium, and a more regular evolution for argon, might tell something about the topology of the two mixing zones. One expects the penetration of CO_2 into helium to be in a form of long narrow jets because of the high Atwood number but a more symetrical interpenetration of CO_2 into argon. Figures 10.b and 11.b show the evolutions of average temperature and CO_2 density in the mixing zone just after the interaction with the reflected shock in the CO_2/Ar case. As the profiles indicate a wide region of constant temperature and density, it seems that the mixing zone has been already strongly homogenized by the first reflected shock.

5. CONCLUSION

High Mach number shock-interface interaction experiments in shock tubes lead to turbulent three-dimensional flows which are difficult to describe in the framework of the simple Rayleigh-Taylor or Richtmyer-Meshkov instabilities[5]. The results do not agree with simulations using hydrodynamic codes which do not take the boundary layers into account. However, even if the measurement methods are different, the obtained thicknesses are in rough agreement with previous high Mach number experiments in which boundary layer effects may also be important.
The 1.5 µm thick film has been founded to much thick and strong. We may use, in our future experiments, a more thin 0.5 µm thick nitrocellulose film. Bidimensional measurements of the mixing zone thickness are actualy in progres by emission technique in various hights in the shock tube, but, whith high Mach number shock experiments, wall effects make it difficult to observe more than two consecutive shock decelerations of the mixing zone. Finally, Shlieren thickness measurements whith both low Mach numbers - 1.5 - and higher pressure - 0.5 to 1 At - are also planed for comparison whith other experiments.

ACKNOWLEDGMENTS
This work is supported by the Centre d'Etudes de Limeil-Valenton (Commissariat à l'Energie Atomique).The authors want to thanks Pr. Jean Pourcin for many helpful discussions.

REFERENCES

1.V.A. ANDRONOV, S.M. BAKHRAKH, E.E. MESHKOV, V.V. MOKHOV, V.V. NIKOFOROV, A.V. PEVNITSHII and A.I. TOLSHMYAKOV, "Turbulent Mixing at Contact Surface Accelerated by Shock Waves", Sov. Phys. JETP, 44, 424 (1976).

2.S.G. ZAITSEV, E.V. LAZAREVA, V.V. CHERNOUKHA and V.M. BELYAEV, "Intensification of Mixing at the Interface Between Media of Different Densities Upon the Passage of Shock Wave Through It", Sov. Phys. Dokl., 30, 576 (1985).

3.L. HOUAS, A. FARHAT, A. RAMDANI, J. FORTES and R. BRUN, "Concentration and Temperature Profiles in a Shocked Gaseous Interface", Proceedings of the 16th International Symposium on Shock Waves and Shock Tubes, ed, H. Grönig, RWTH, Aachen, VCH Physik Verlag,p. 831 (1987).

4.B. STURTEVANT, "Rayleigh-Taylor Instability in Compressible Fluids", Shock Waves and Shock Tubes", Proceedings of the 16th International Symposium on Shock Waves and Shock Tubes, ed, H. Grönig, RWTH, Aachen, VCH Physik Verlag, p.89 (1987).

5.L. HOUAS, A. FARHAT and R. BRUN, "Shock Induced Rayleigh-Taylor Instability in the Presence of a Boundary Layer", The Physics of Fluids, Vol. 31, N°4, (1988).

Conditions	C.1	C.2	C.3	C.4	C.5
Couple of gases	CO_2/Ar	CO_2/He	CO_2/Ar	CO_2/He	CO_2/Ar
Test section lenth (cm)	152	152	127	127	127
Initial pressure (Pa)	1500/1500	1500/1500	2000/2000	2000/2000	5000/5000
Thickness measurements	E	E	E and P	E	P
M_I	4.2	4.2	3.7	3.7	3
M_T	4	2.4	3.5	2	2.8
U_I measured(m/s)	1030	1700	970	1240	676
U calculated (m/s)	817	1236	632	914	470
ΔU_R calculated (m/s)	840	840	675	555	390
At_1	- 0.48	-0.86	- 0.42	- 0.80	- 0.23
At_2	0 .67	0 .92	0.59	0.86	0.23

Table 1 : Experimental conditions

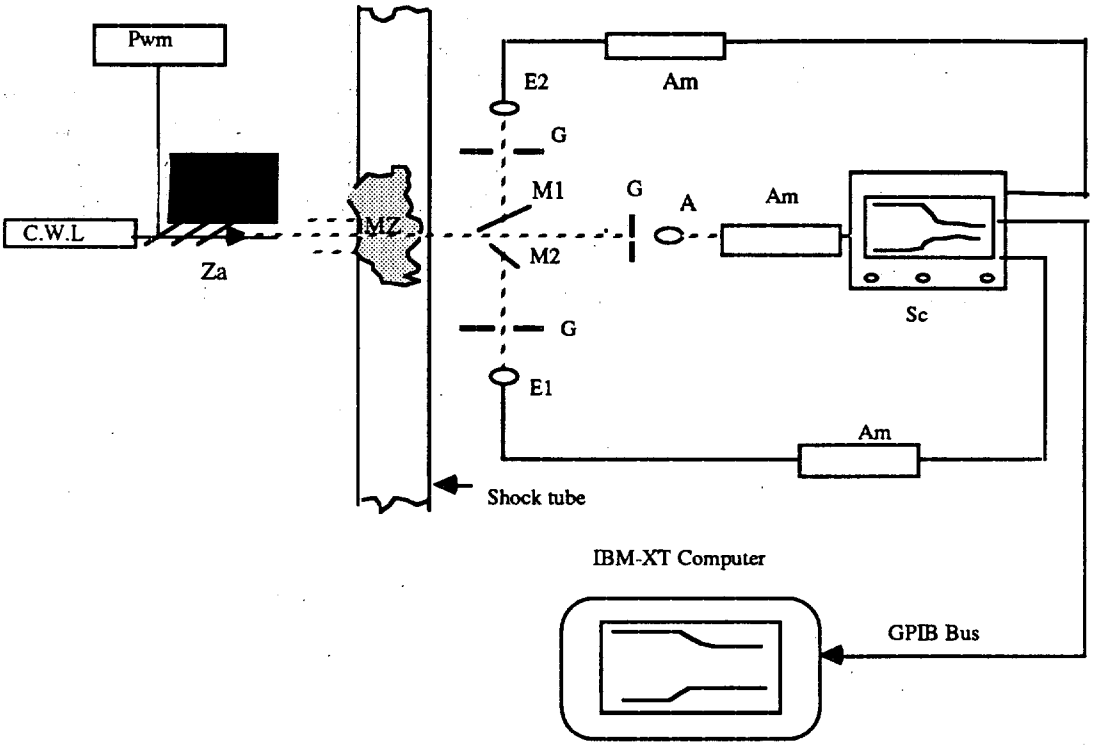

E2 , E1 , E3 - infrared colector
G - Narrow slit
M1 M2 - concave mirror
Pwm - Powermeter and spectral analyser
Sc -Numerical oscilloscope
Za - ZnSe and germanium attenuators
Am - amplifier
C - absorber coal
CWL - C.W.CO2 Laser

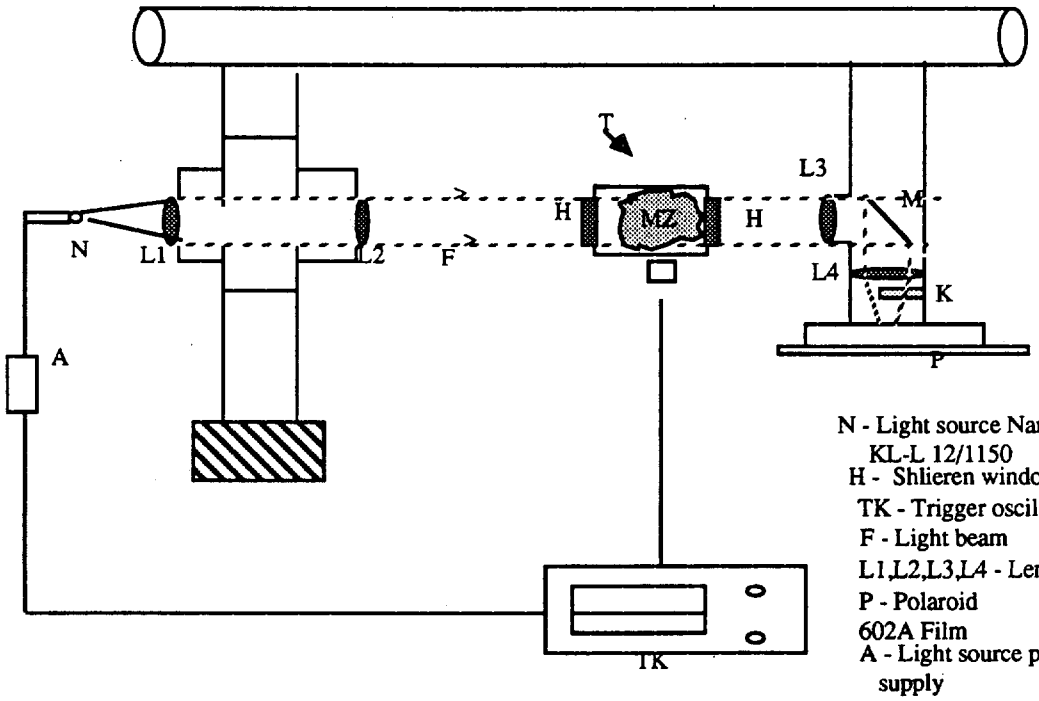

N - Light source Nanolite KL-L 12/1150
H - Shlieren window
TK - Trigger oscilloscope
F - Light beam
L1,L2,L3,L4 - Lenses
P - Polaroid 602A Film
A - Light source power supply
T - shock tube section

Figure 1 : Absorption - Emission and Shlieren optical setup

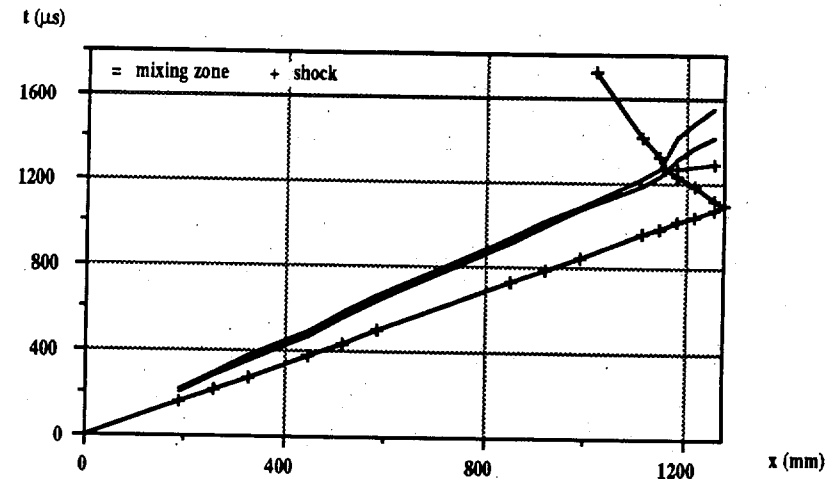

- a

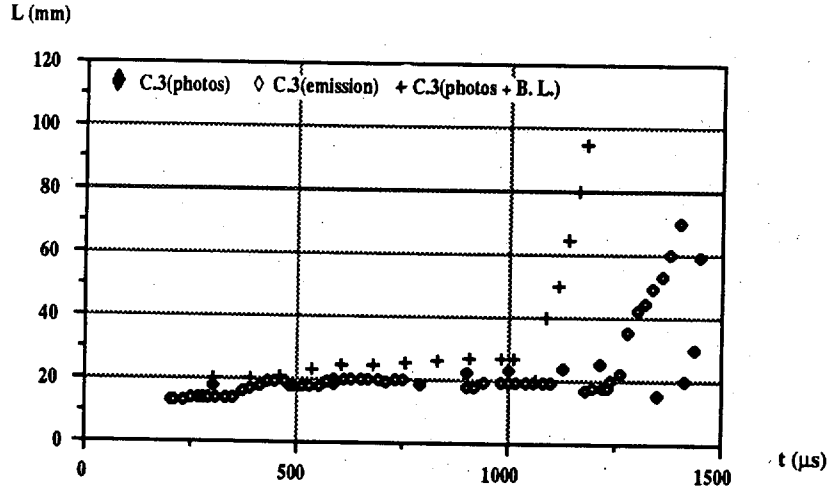

- b

Figure 2 : CO_2/Ar (x,t) diagram and mixing zone thickness (by emission measurements)

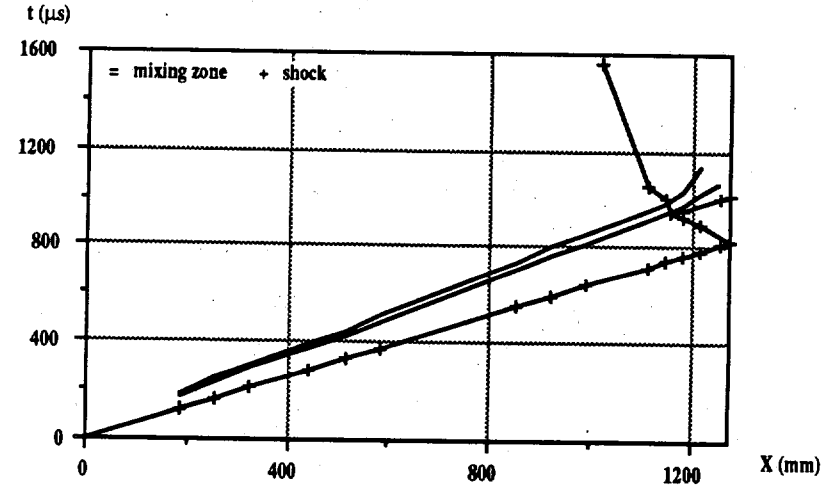

- a

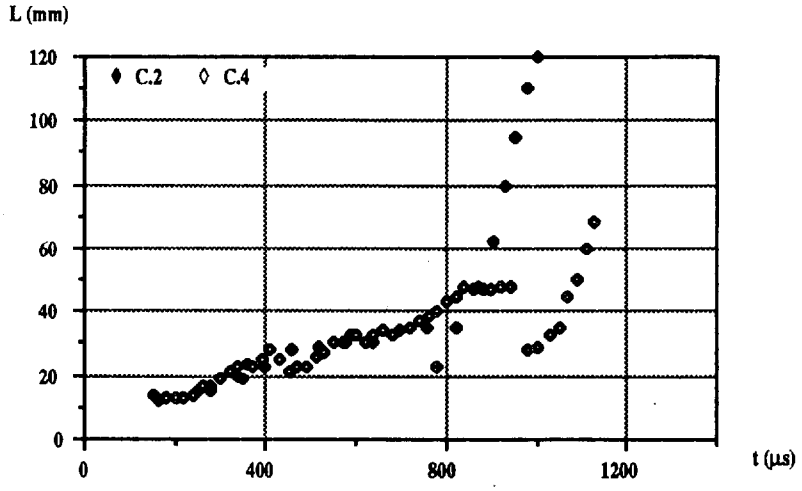

- b

Figure 3 : CO_2/He (x,t) diagram and mixing zone thickness (by emission measurements)

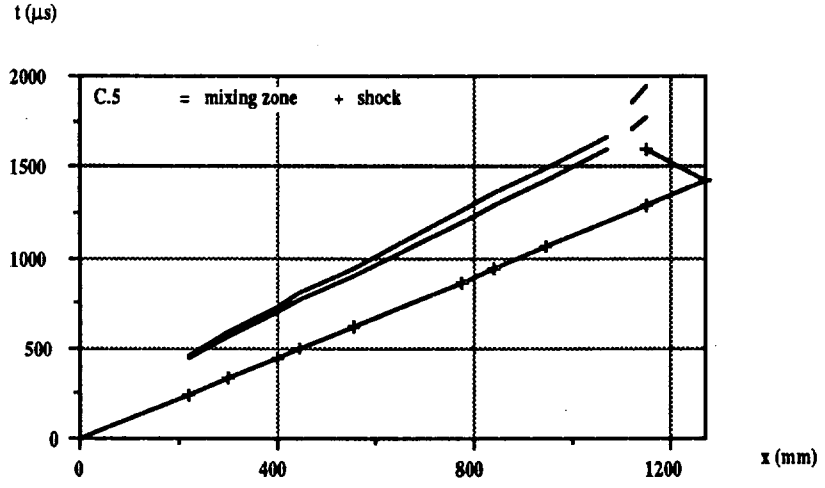

- a

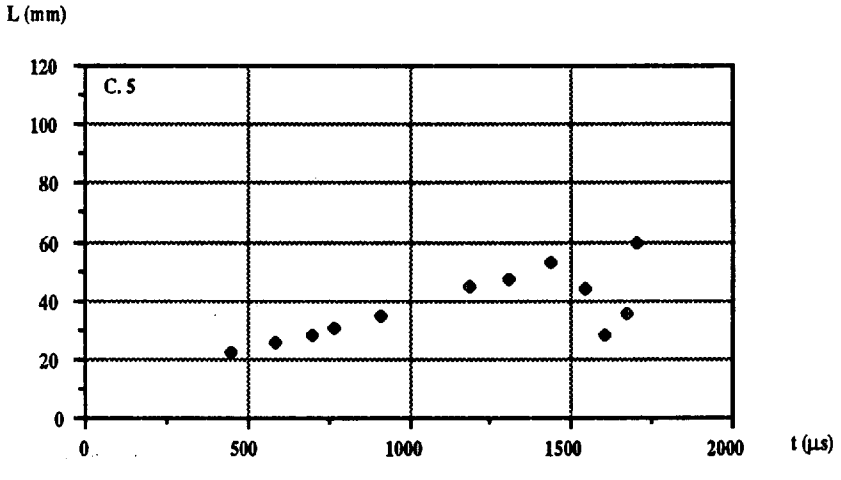

- b

Figure 4 : CO_2/Ar (x,t) diagram and mixing zone thickness (by Shlieren photograph measurements)

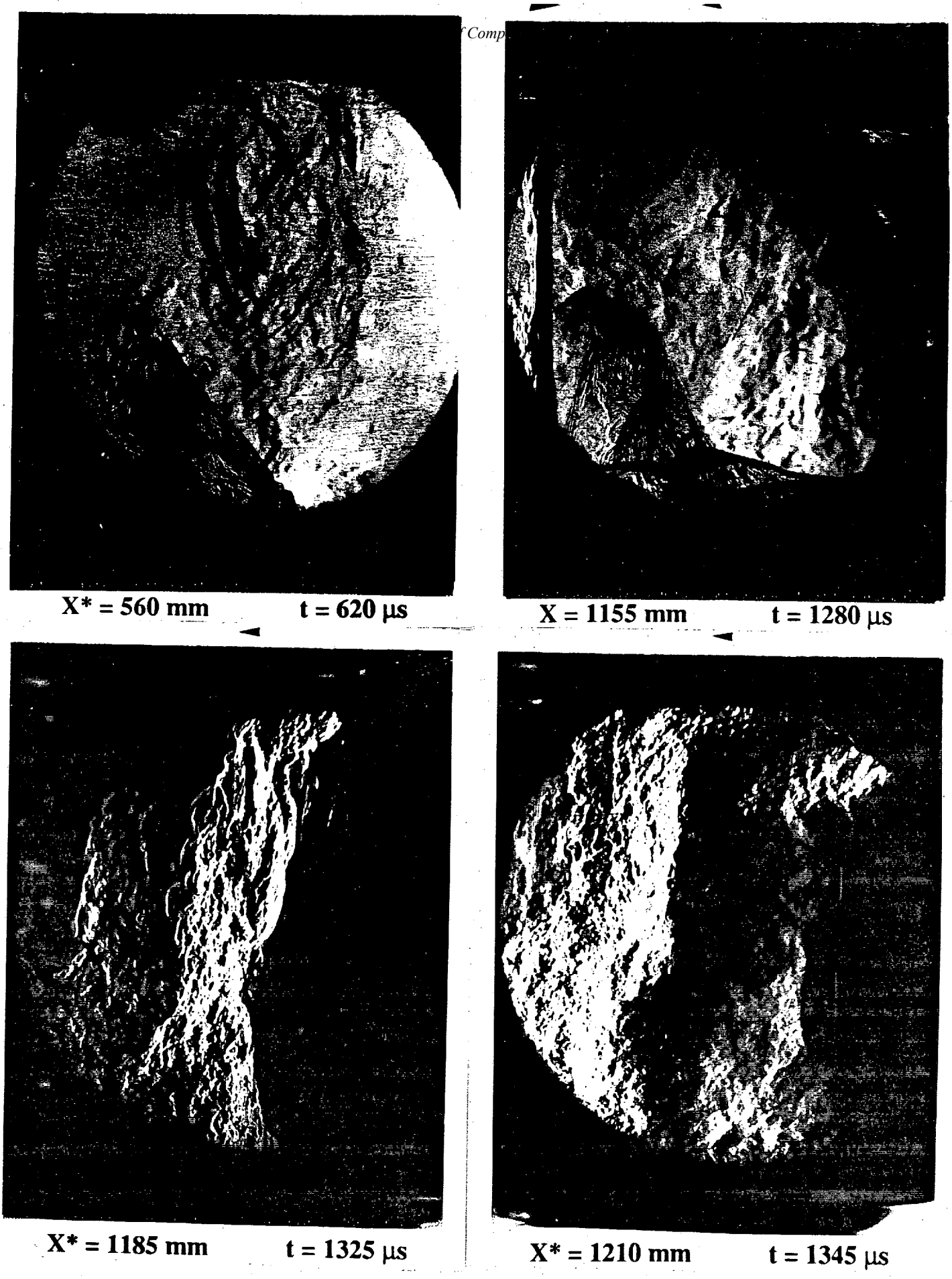

Figure 5 : The reflected shock - CO_2/Ar mixing zone interaction phase

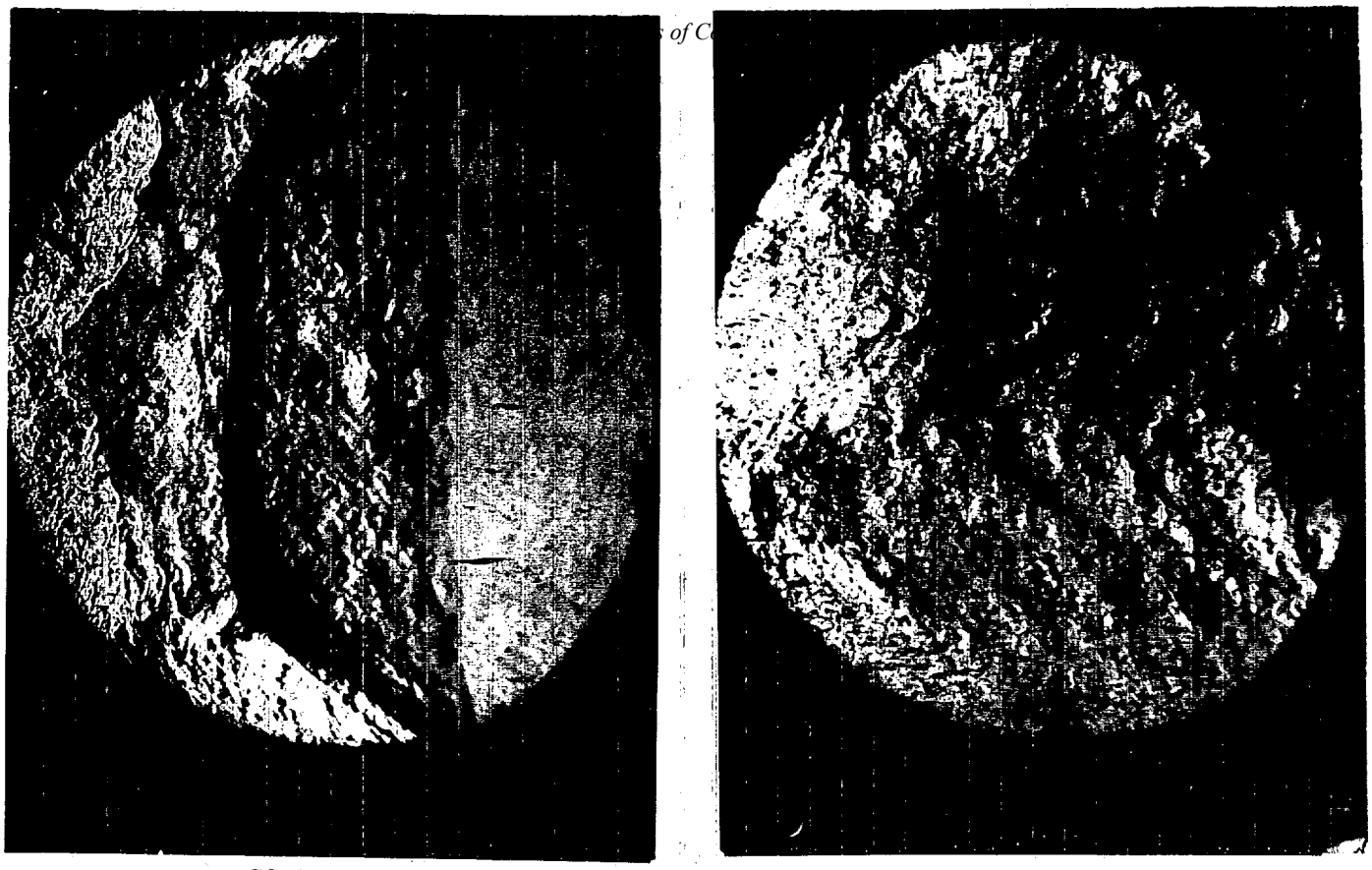

CO_2/Ar case CO_2/He case

Figure 6 : Deformation of the shock during its passage through the mixing zone

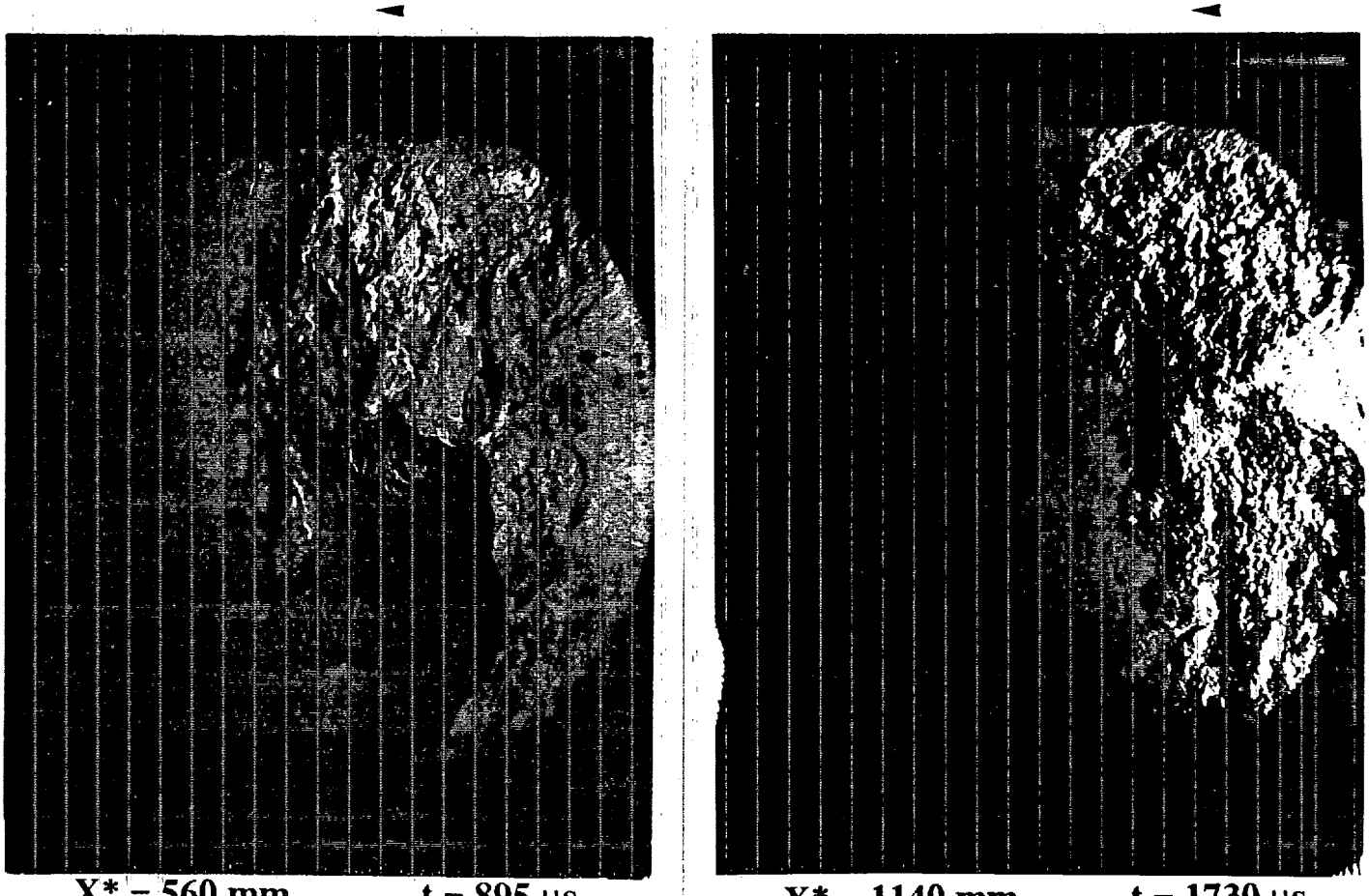

accelerated phase decelerated phase

Figure 7 : CO_2/Ar mixing zone before and after interaction with the reflected shock

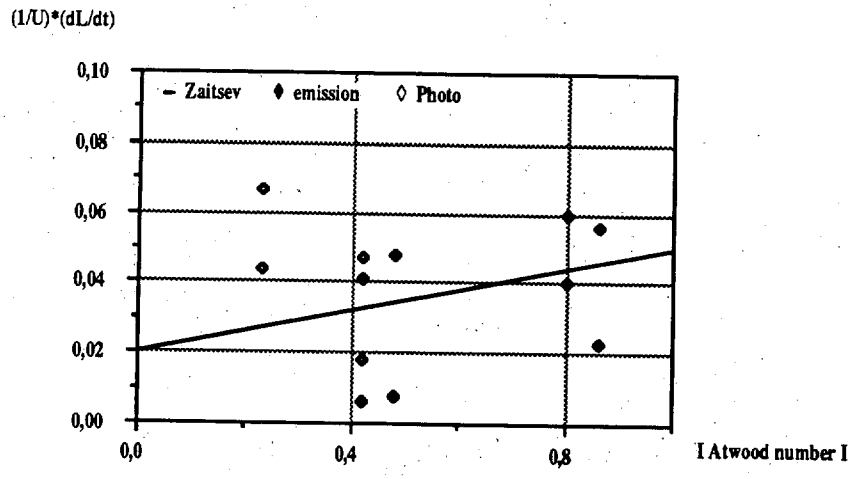

- a

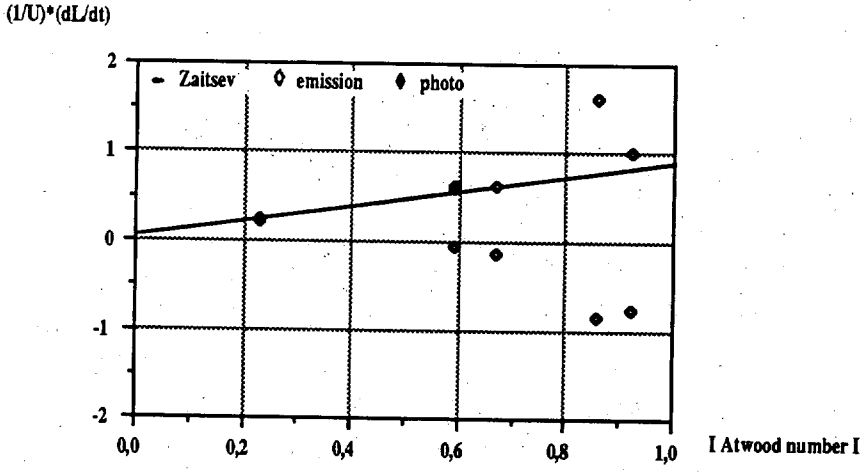

- b

Figure 8 : Evolution of the non dimensional mixing zone growth rate and comparison with Zaitsev's experiments

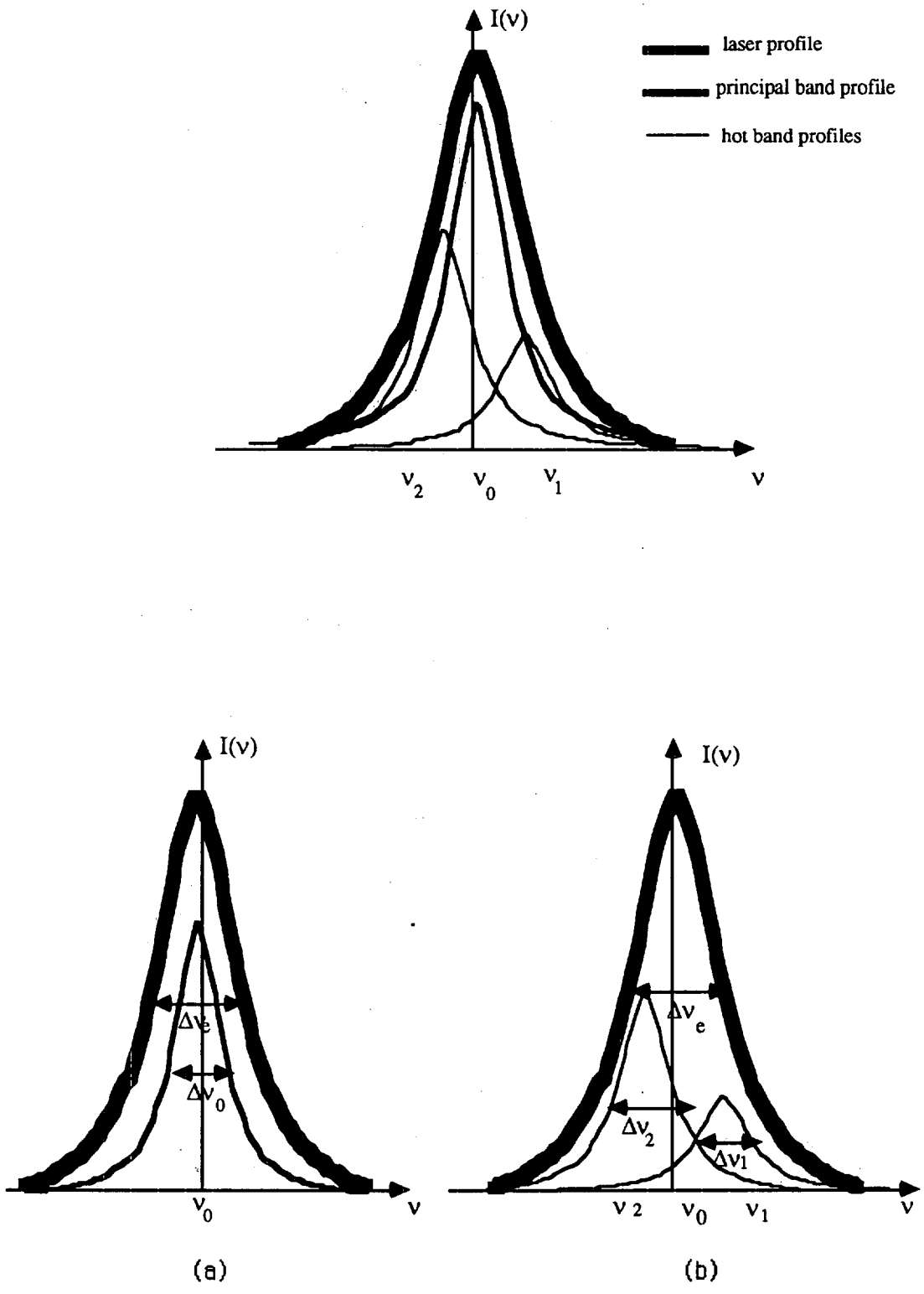

Figure 9 : Configurations of the profiles used : the laser line, the CO_2 principal line and the hot bands

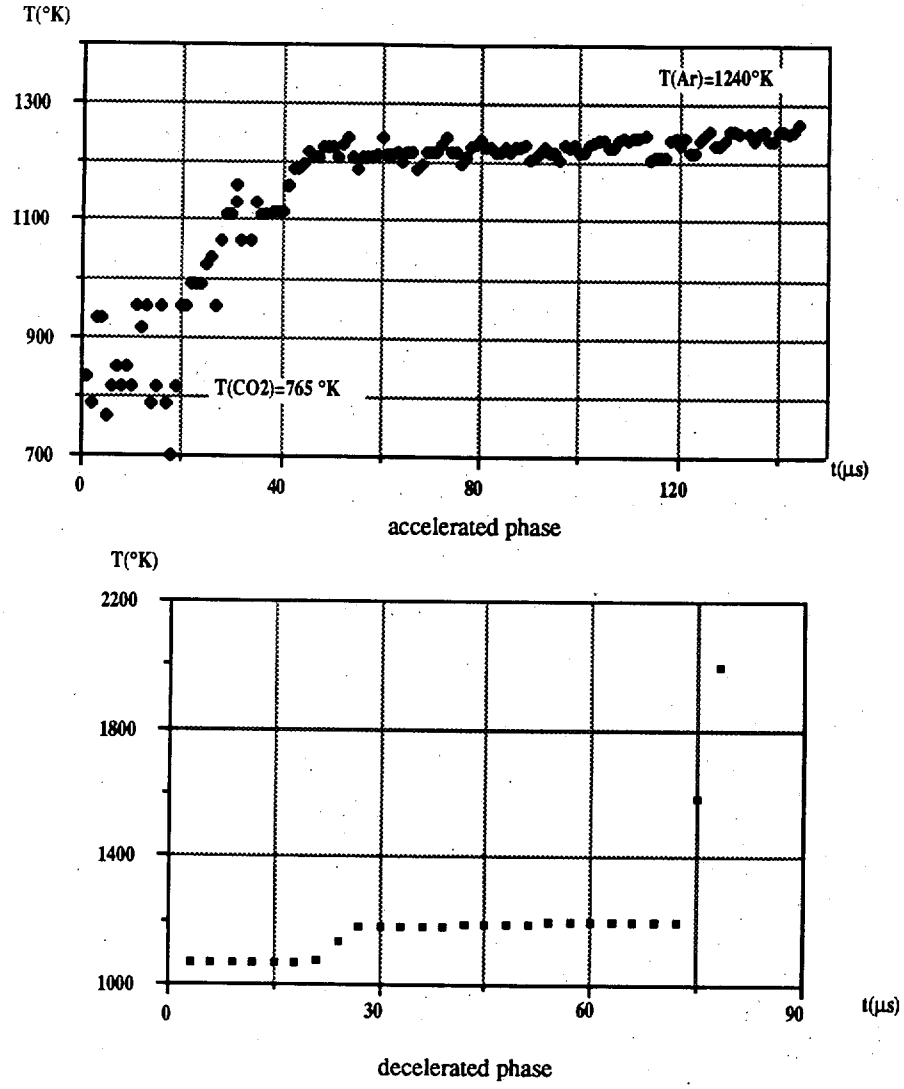

Figure 10 : Average temperature profile in the CO_2/Ar mixing zone in the accelerated and decelerated phases

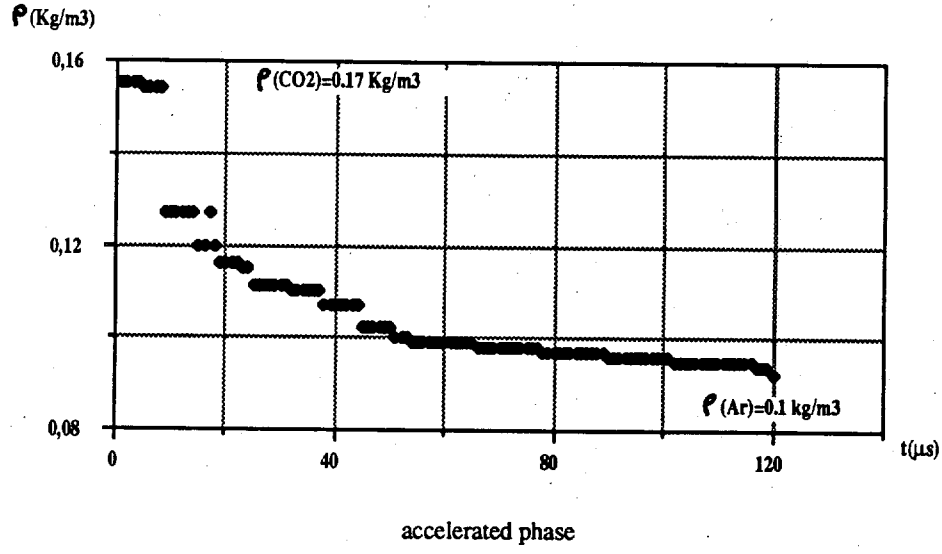

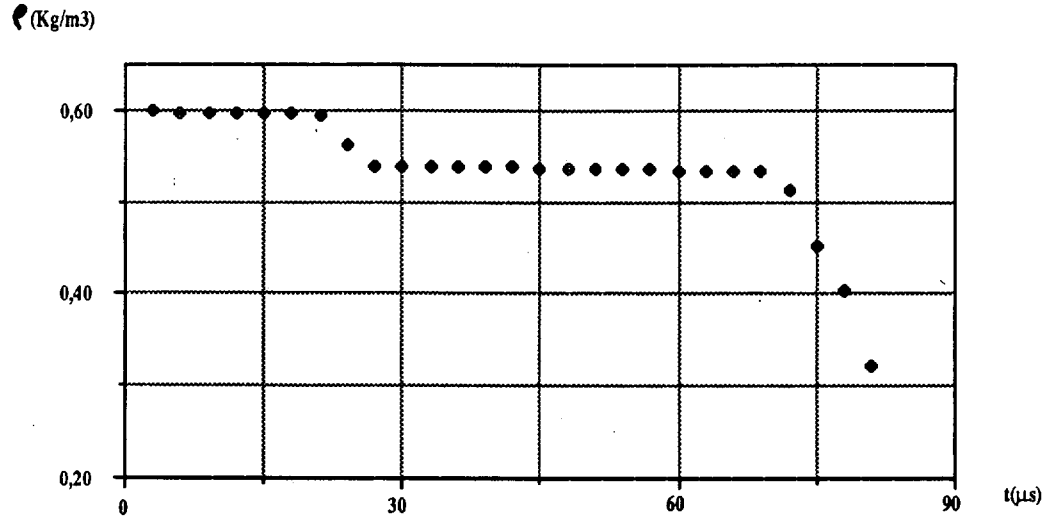

decelerated phase

Figure 11 : Average CO_2 density profile in the CO_2/Ar mixing zone in the accelerated and decelerated phases

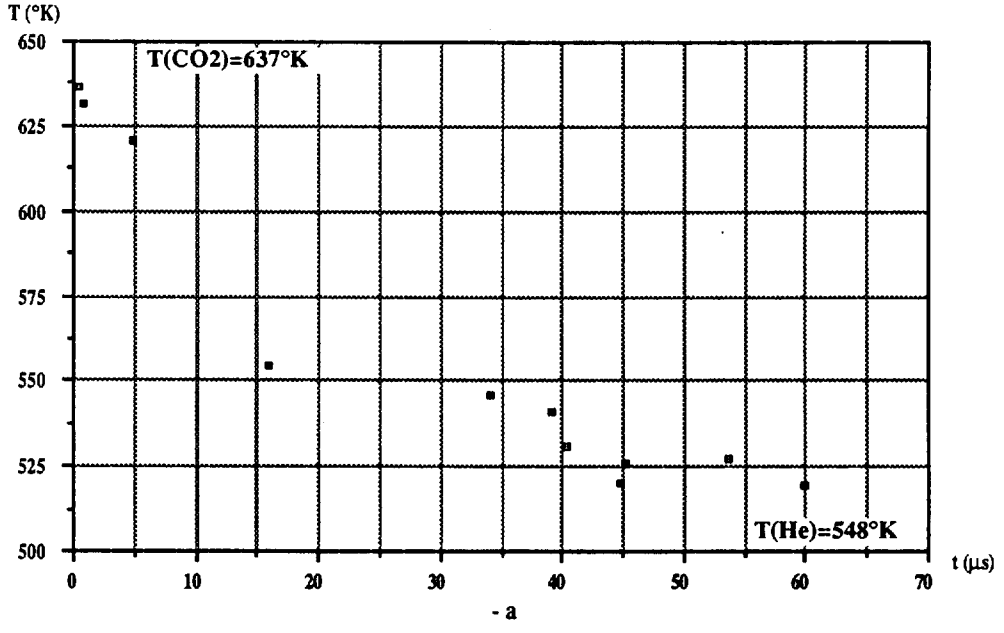

- a

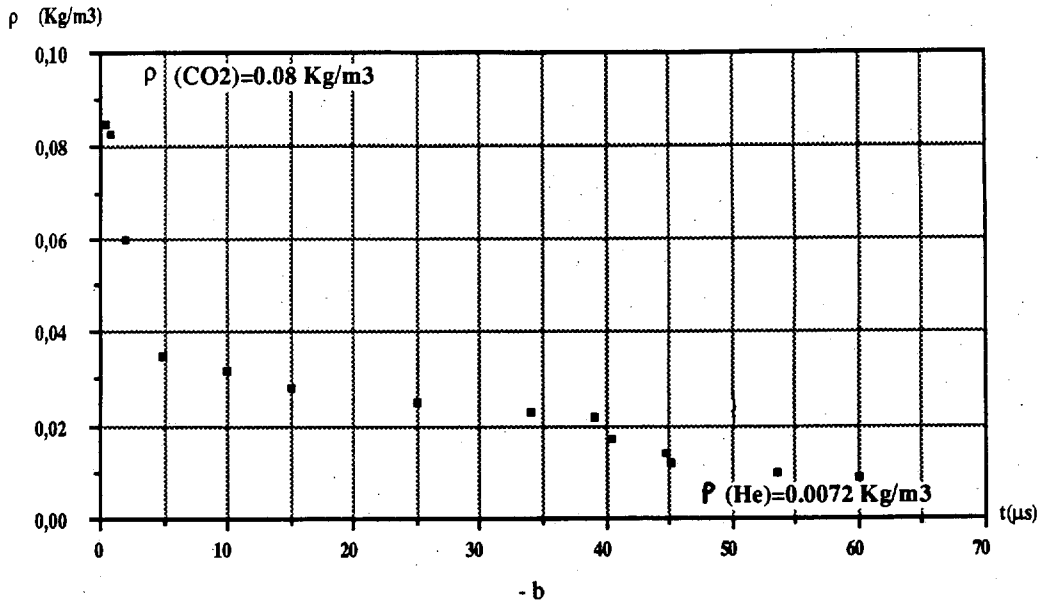

- b

Figure 12 : Average temperature and CO_2 density profiles in the CO_2/He mixing zone in the accelerated phase

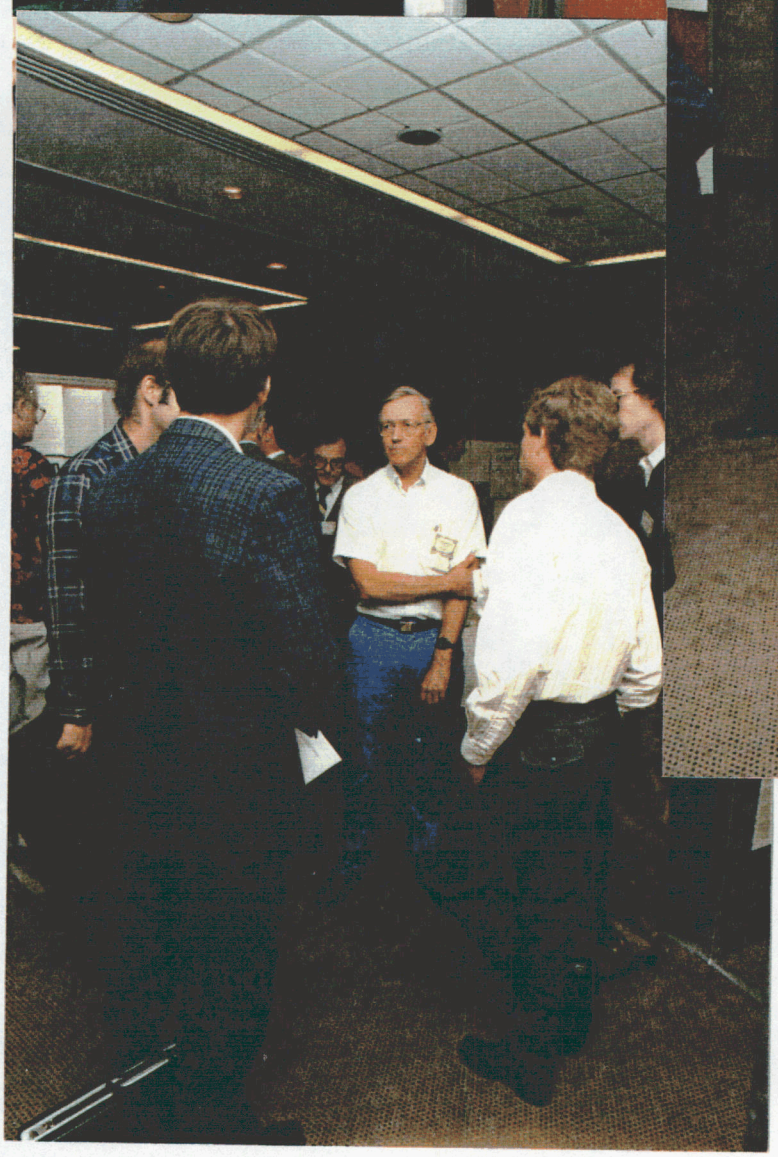

Richtmyer-Meshkov Instability at a continuous Interface

B. Sturtevant, R. Bonazza, M. Brouillette

$M_s = 1.1, 1.3, 1.5, 1.65$

I Multi-scale (Flat Interface) PhysicaD

1. Membrane (Thin)
   Incident & Reshock
   a. Air - He
   b. - Air
   c. - CO_2
   d. - R22
   e. - SF_6

2. Plate (Thick)
   Reshock
   a. Air - CO_2
   b. - R22
   c. - SF_6

II "Single Scale" ST Symp., Lehigh

1. Plate (Thick)
   1 Reshock, 2 Reshock
   a. Air - R22
   b. - SF_6

Close End Wall Configuration

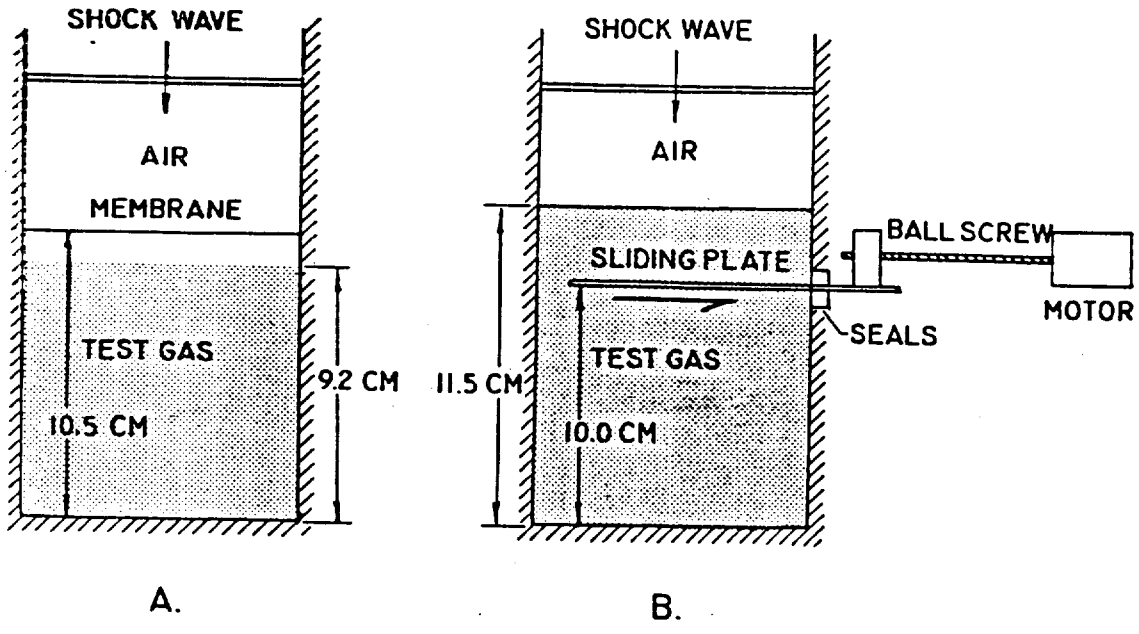

Figure 2.8 Location of interface for close end wall experiments.
The shaded area indicates the field of view of the flow visualization system.

12 / Long Time Configuration

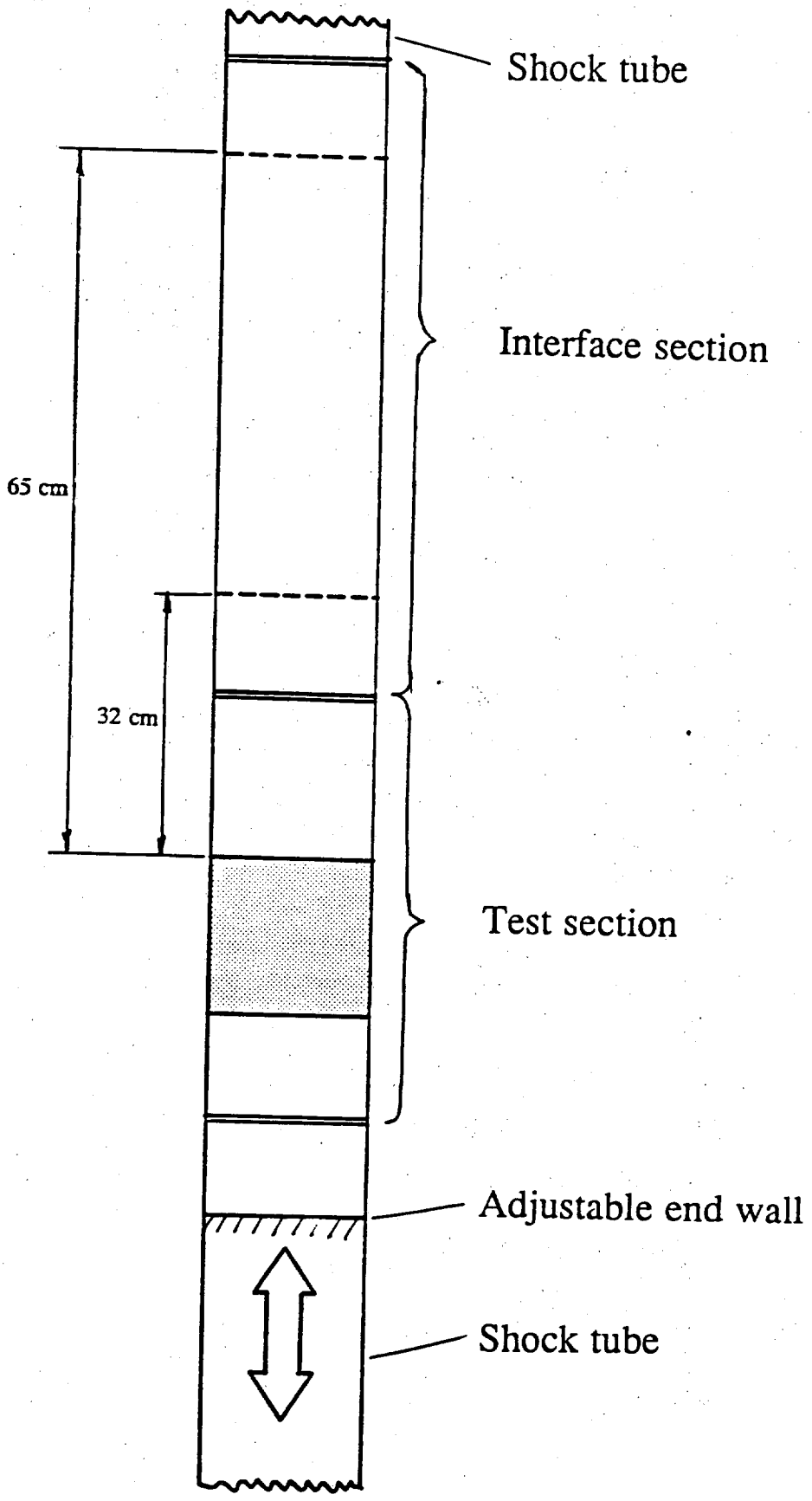

Shock-excited instability of single-scale perturbations on thick interfaces

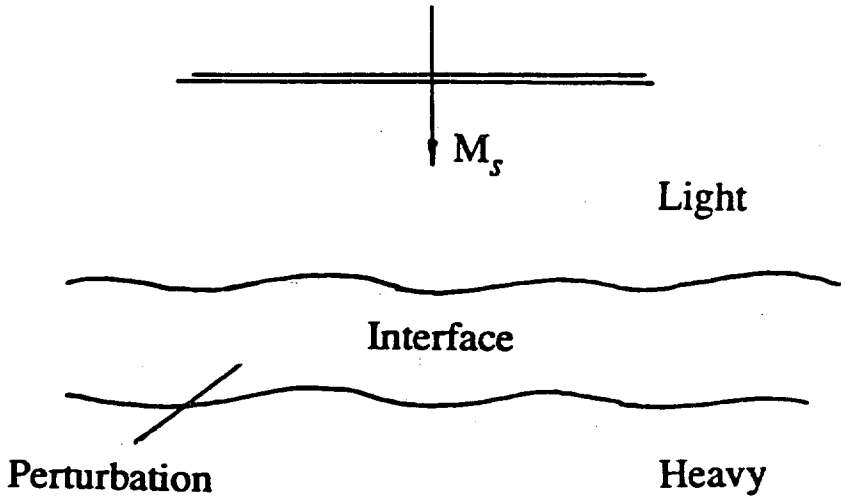

- one wave
- two waves
- many waves

Air/ R-22, SF_6

M_s = 1.12, 1.32, 1.48 and 1.66

Air/SF6 Ms=1.32 (LT)

t = 4.39 ms

t = 5.19 ms

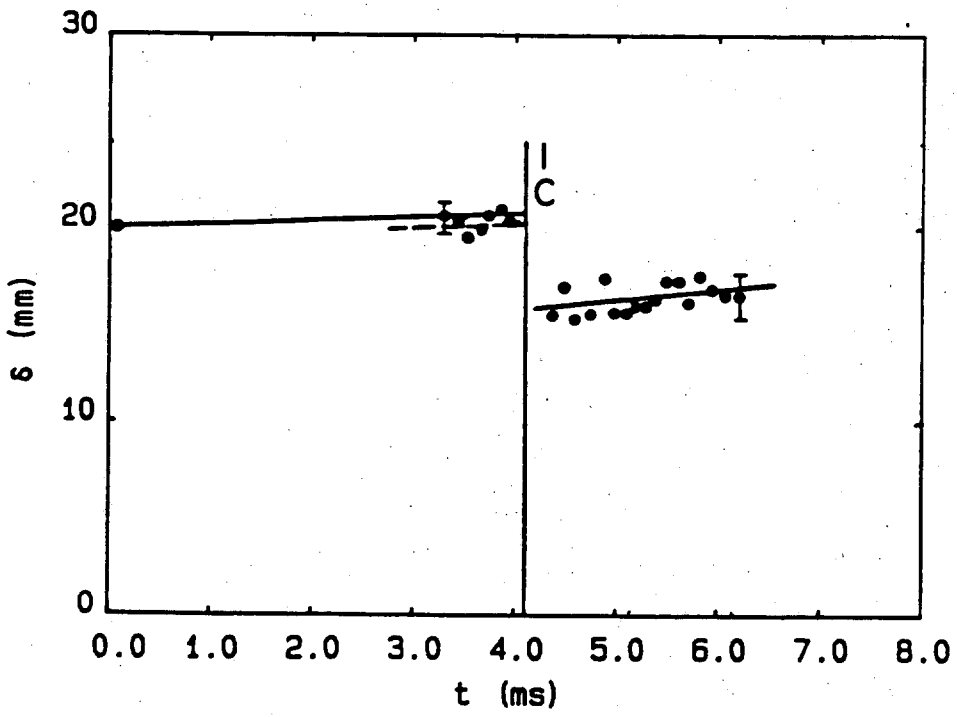

Time evolution of the thickness of the plane continuous interface between air and SF_6. M_s = 1.32, long time configuration.

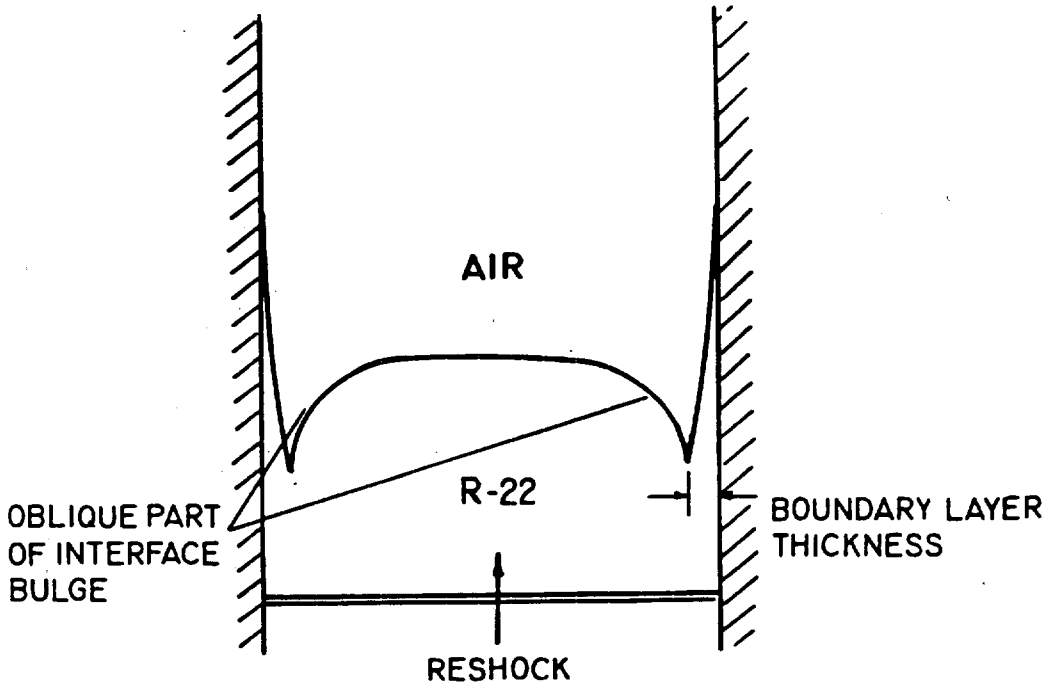

a. Perturbation obtained by a slight upward bulge on a light-heavy interface.

b. Formation of reverse wall vortex.
Air/R-22, M_s = 1.32, long time configuration.

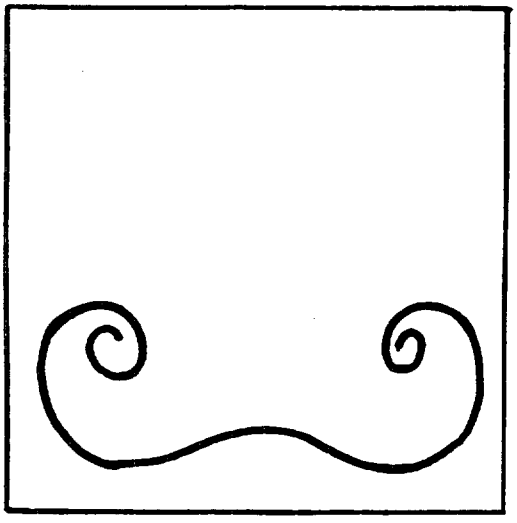

c. Schematic of reverse wall vortex

Figure 6.8 Reverse wall vortex.

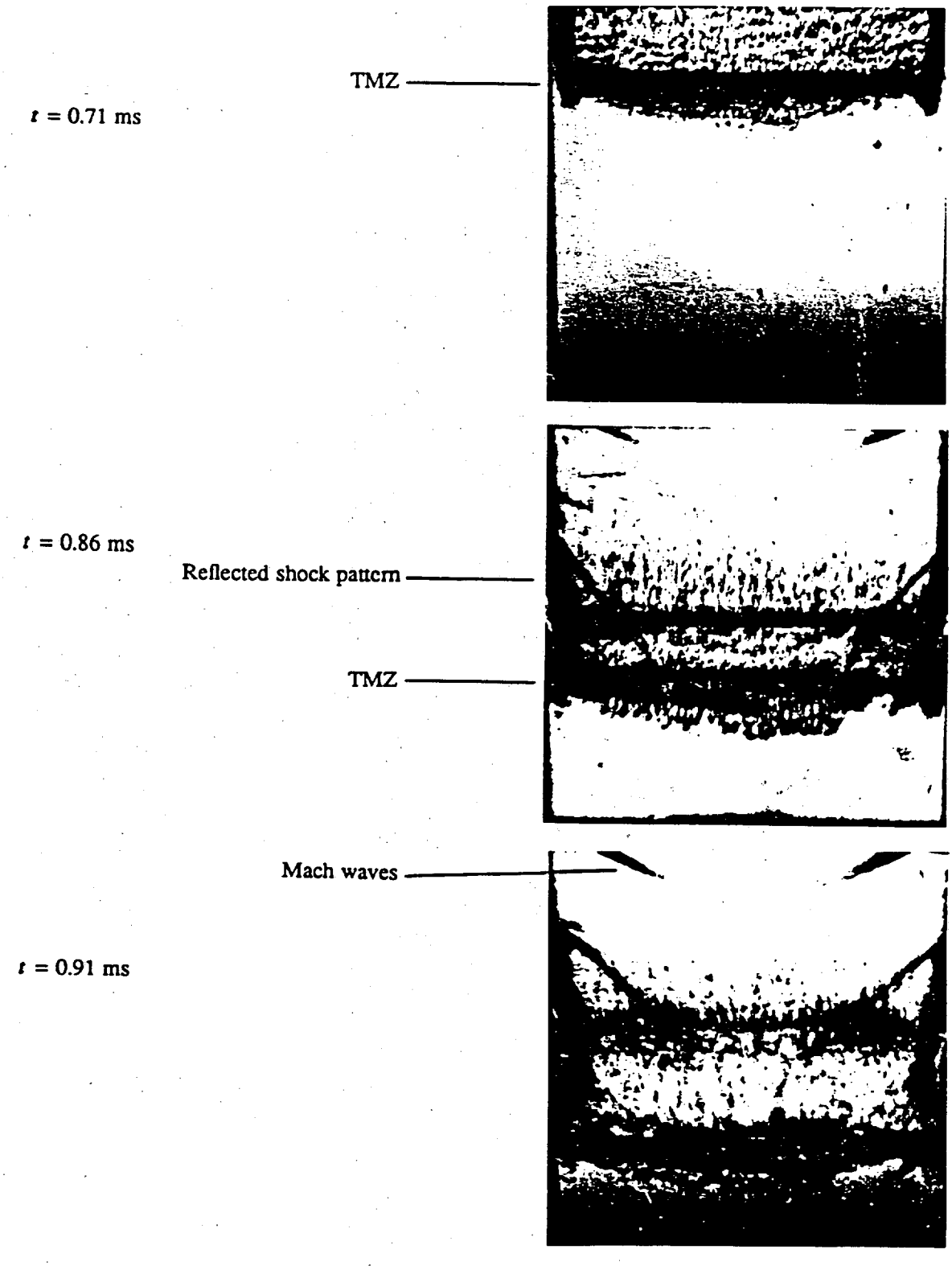

Figure 5.15b Richtmyer-Meshkov instability of a plane discontinuous interface between air and helium. M_s = 1.66, long time configuration.

X-Ray Densitometry, Singly-compressed Interface.
Contour Plot

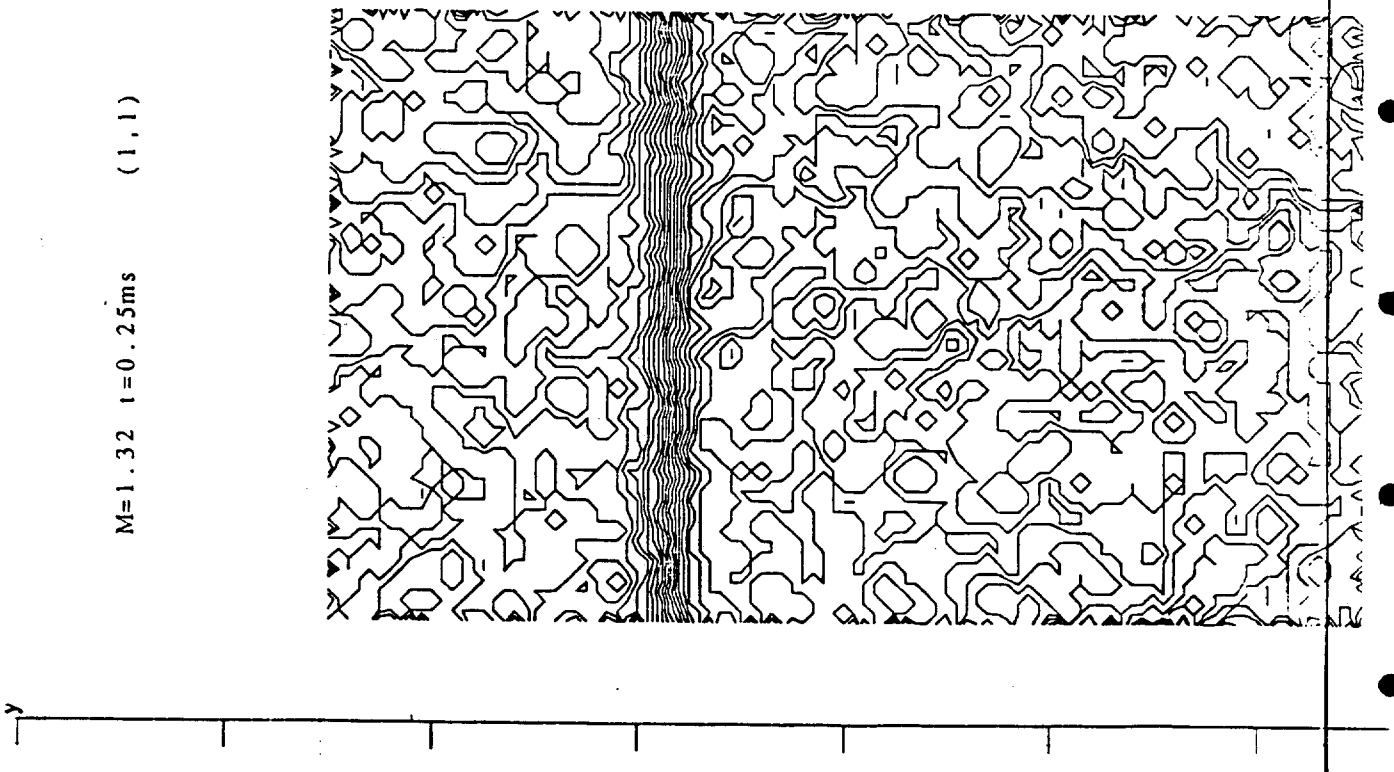

Small growth after incident shock.

t = 0.7 ms

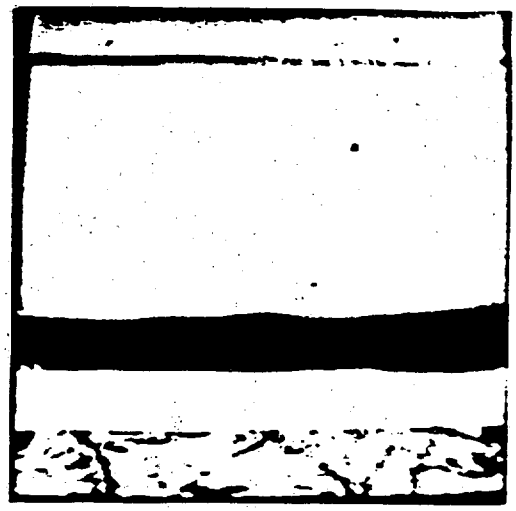

t = 3.3 ms

t = 4.0 ms

Single-scale Richtmyer-Meshkov instability at a continuous interface.
Air/SF_6 M_s = 1.32

More growth after reshock.

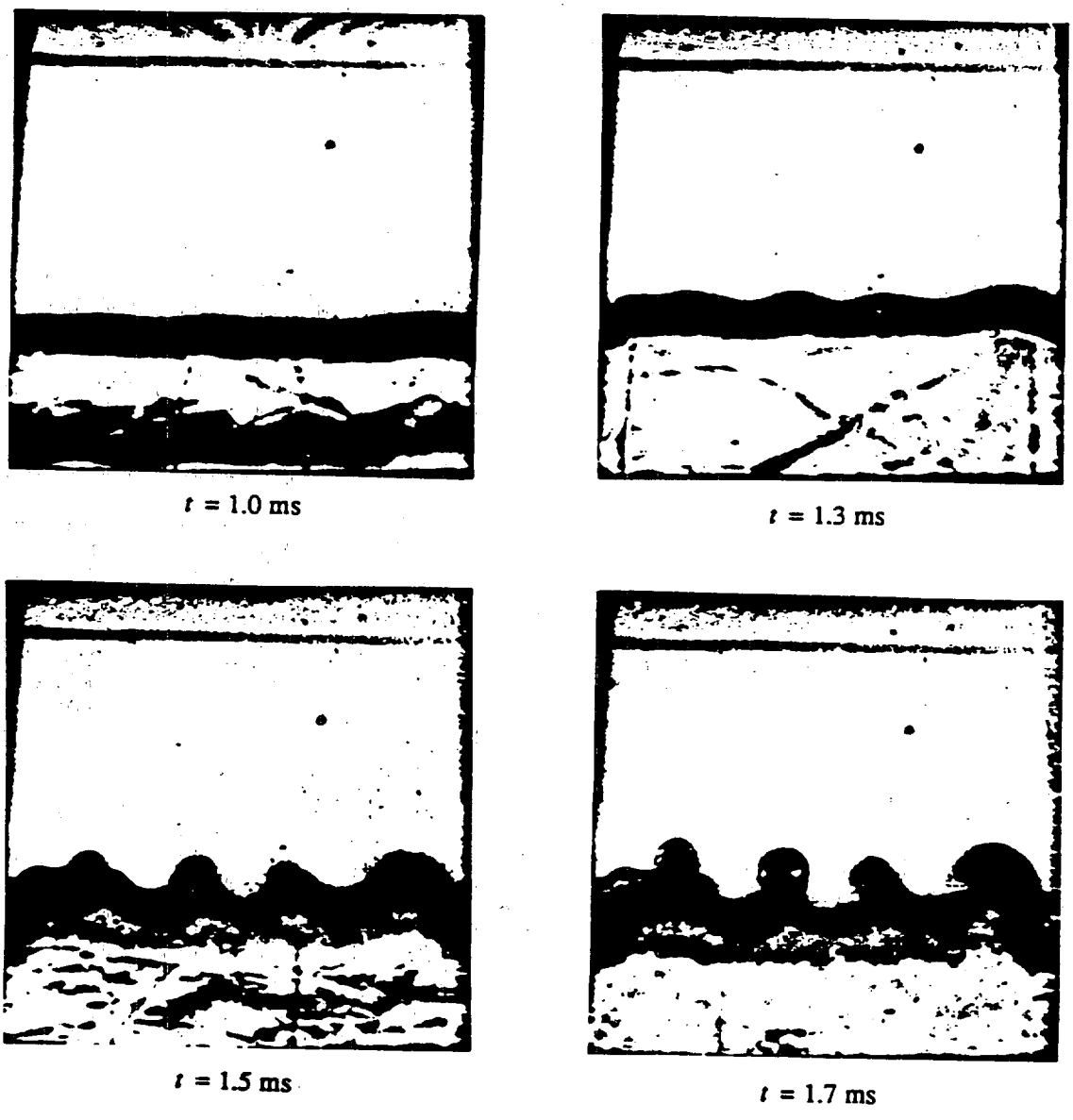

Single-scale Richtmyer-Meshkov instability at a continuous interface.
Air/SF_6 M_s = 1.32, close end wall configuration.

X-Ray Densitometry, Singly-compressed Interface.
Carpet Plot

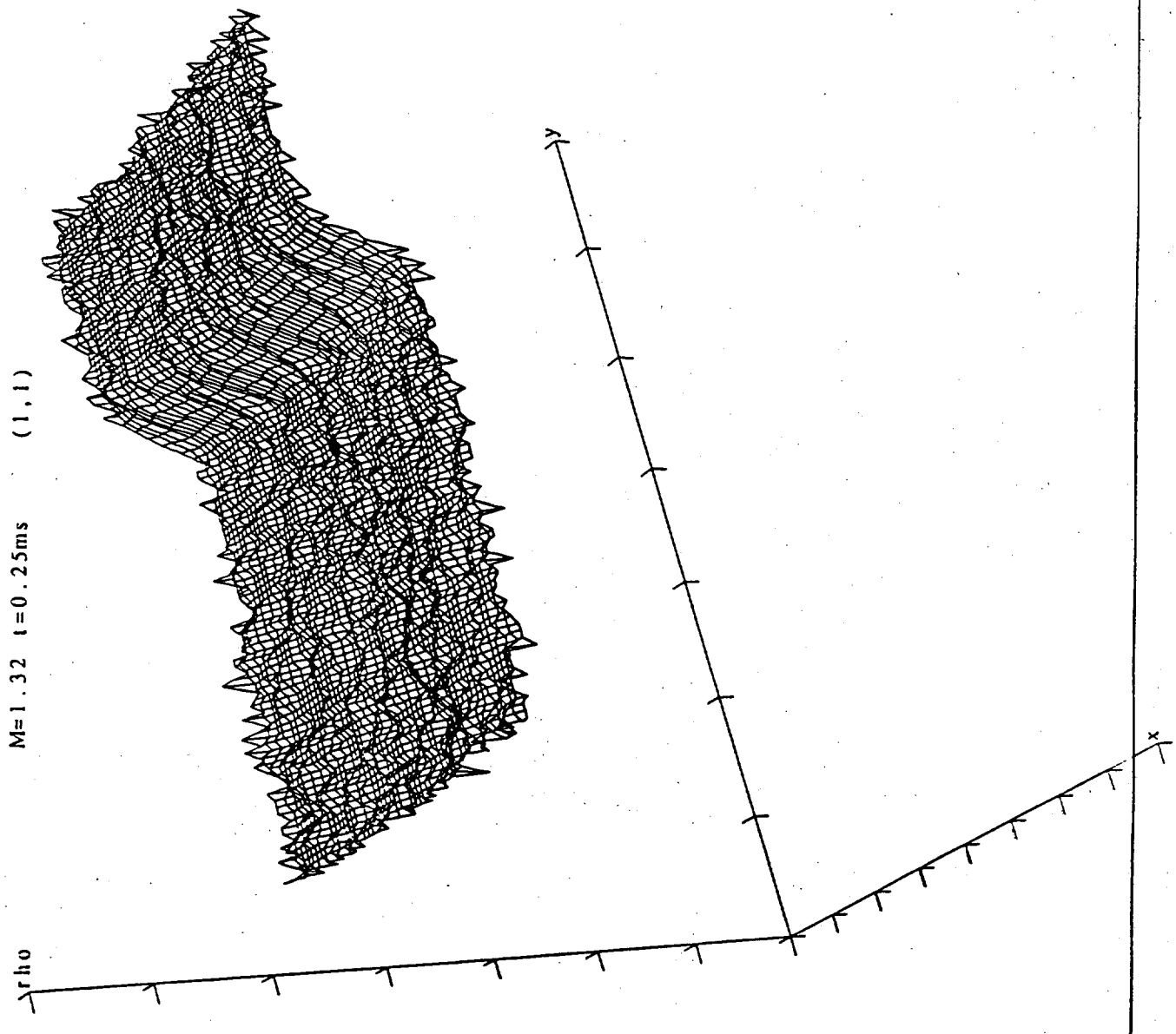

X-Ray Densitometry, Single Scale.
Contour Plot

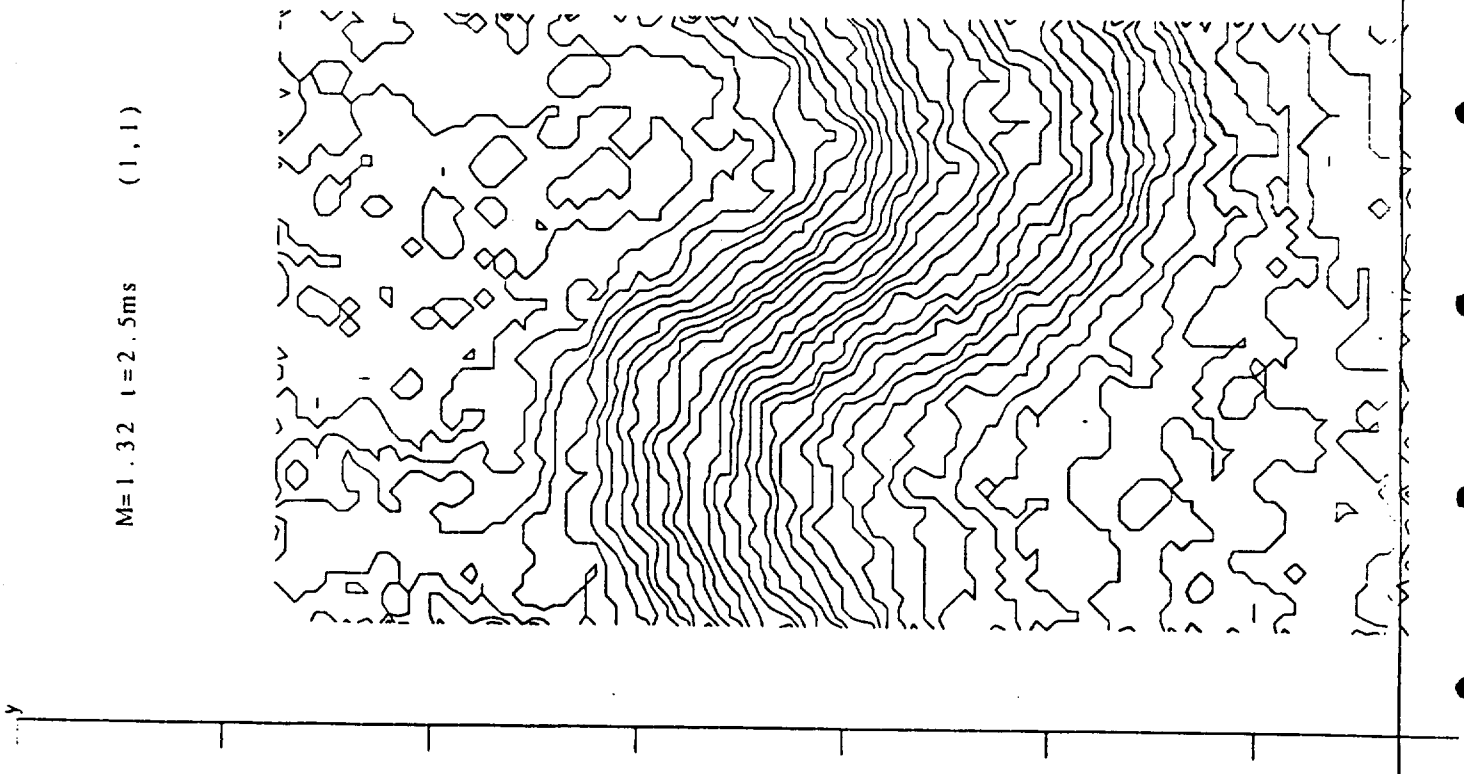

X-Ray Densitometry, Single Scale.
Carpet Plot

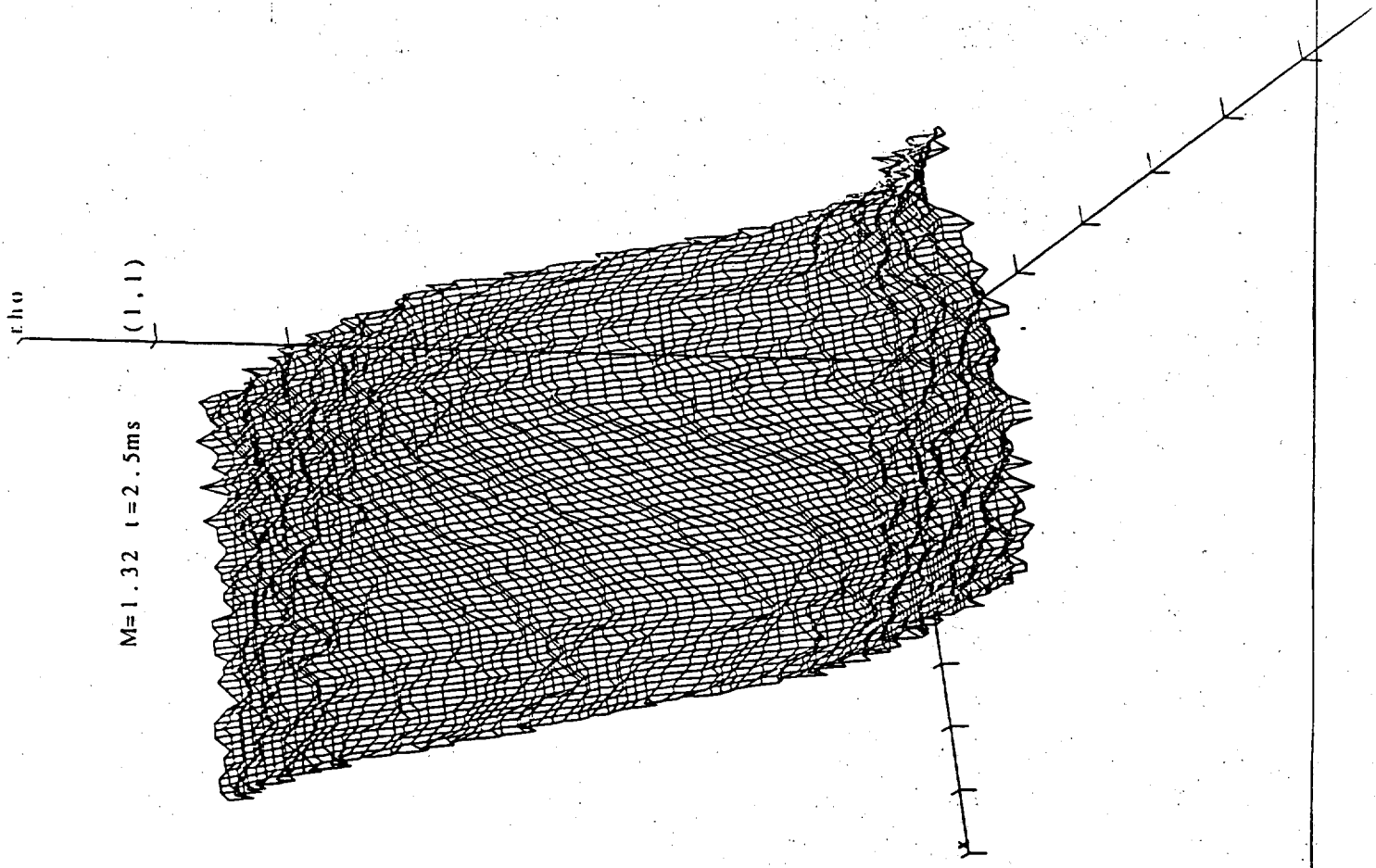

X-Ray Densitometry.
Cross Section through Shock(s), interface (I) and egg-crate (E).

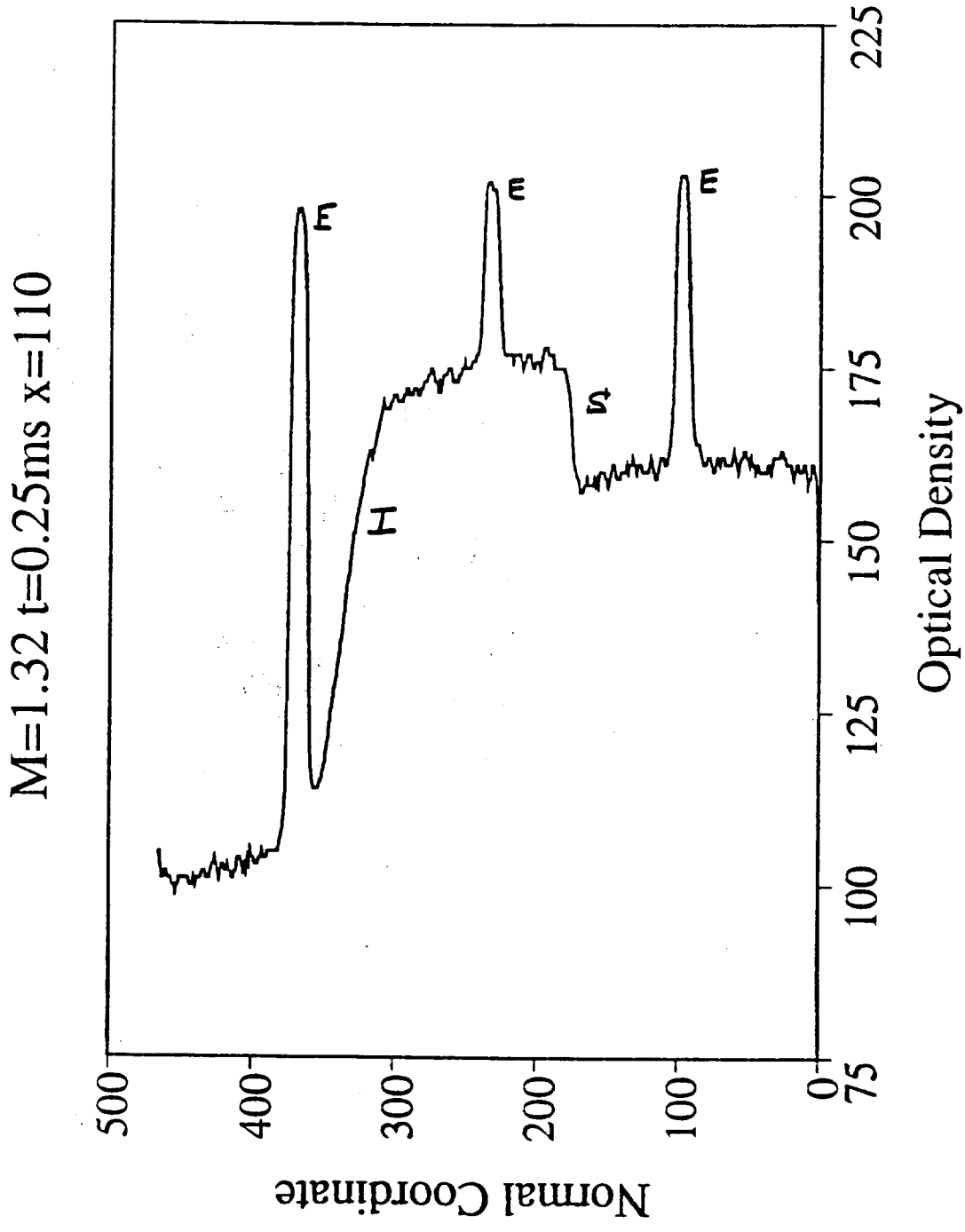

R E P O R T

RAYLEIGH - TAYLOR INSTABILITY AT THE INTERFACE BETWEEN DIFFERENT GASES IN EXPERIMENTS WITH A WEAK DECELERATING SHOCK WAVE

A.M.VASILENKO G.V.KOVALENKO
V.I.OLHOVSKAYA D.V.FINASHIN

A B S T R A C T

Developing the Rayleigh-Taylor instability of the initial plane contact interface between air/helium and air/cryptone, under the action of the decelerating shock wave with M=1.3, was investigated. It was observed developing the interface instability and still more significant development of wall gas jets in experiments with the gas configuration of air/helium.

The interface was in a stable state in experiments with the gas configuration of air/cryptone.

I. INTRODUCTION

It is known that the interface between different media is unstable, if the more dense medium is rapidly substituted by the less dense one.

The aim of this work is to investigate developing the instability of the unsteady plane contact interface between different gases under the action of a weak decelerating shock wave.

In the process of investigations, conducted earlier on shock tubes, there was studied the action of the impulsive acceleration of the shock-wave front /1,2/. In case of acting the decelerating shock wave it is possible to conduct the investigation of the combined action of the shock-wave front and the quasi-stationary acceleration, generated by the unloading wave.

The main task is to obtain the experimental information for calibrating the numerical computation techniques while considering the effect of the turbulent mixing process on the gas-dynamic flow.

The second important question which arises constantly during the experimental investigation of the instability phenomenon, is to bring out the influence of uncontrolled regular perturbations generated by the experimental installation on the studied phenomenon.

Clearing up the role of such perturbations is possible, for example, by means of comparing the results of experiments, conducted on different installations,but at similar initial conditions and identical flow patterns. It is possible that one of conditions for such comparing is the same Mach number for the flows in different installations.

2. EXPERIMENTAL SET-UP

2.1. The order of preparating and conducting the experiments

Experiments for investigating the Rayleigh-Taylor instability and the turbulent mixing were conducted while using the electromagnetic shock tube with a vacuum compartment, the description of which was given in the work /3/.

The duct of the shock tube with the internal cross-section equal to 100 mm x 100 mm was partitioned off by a flat nitrocellulose membrane, having the thickness of 0.5 ÷ 1 μm; on both sides of this membrane were located gases, having different densities. The attenuating shock wave (see Fig.2.1), incident on the interface, caused the successive effect of shock- and quasi-stationary accelerations. Experiments were conducted for two different versions of gas locations in the shock tube.

1.Air/helium - unstable configuration

In this version of the experiment conduction the discharged and measuring compartments of the shock tube were filled in with air and helium, respectively. Such configuration of gas location, relative to the action of the unloading wave following immediately by the front of the shock wave, is unstable in accordance with Taylor's criterion /4/.

2.Air/cryptone - stable configuration

In this case discharged and measuring compartments were filled in with air and cryptone, respectively. Such configuration of gases location relative to the direction of acting the acceleration, generated by the unloading wave, is unstable.

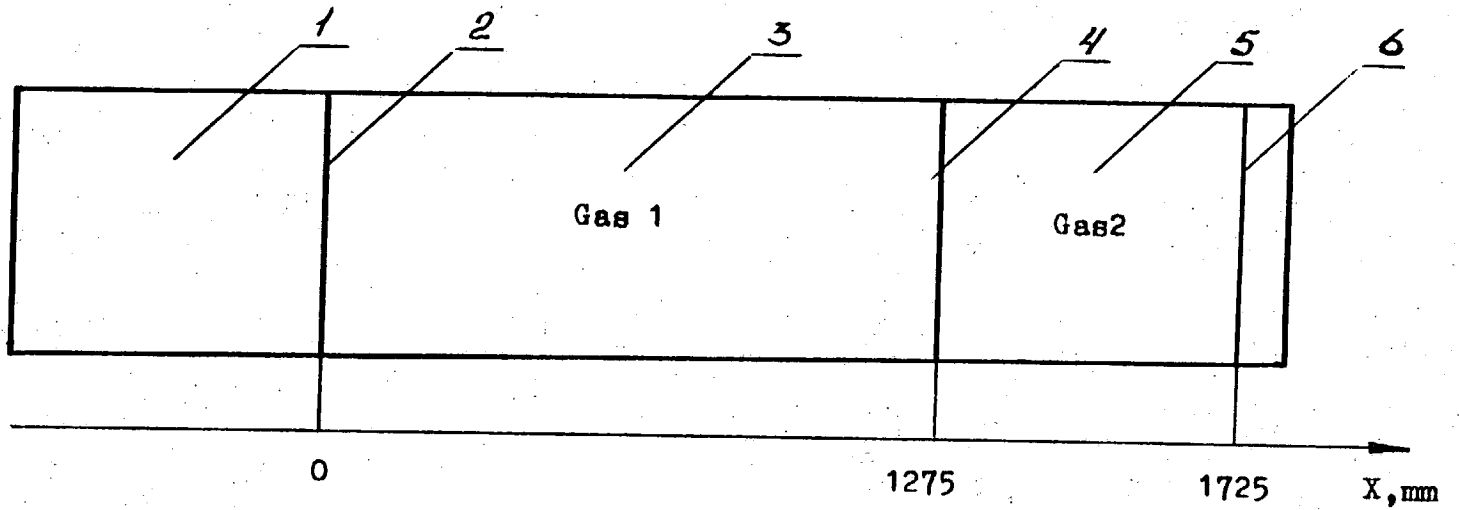

Positions of shock tube compartments in the experiments with the turbulent mixing of gases.

1 - vacuum compartment, 2 - diaphragm,
3 - discharged compartment, 4 - flat nitrocellulose membrane,
5 - measuring compartment,
6 - isolating diaphragm.

Fig. 2.1

The experiments were conducted under the standard atmospheric conditions:
P_o = 760 ± 0.5 mm of mercury (column),
T = 15 °C ± 0.3 °C

Registration of the phenomenon was carried out by means of the schlieren system of the device IAB-451, optically matched with two cameras VFU-I, carrying out simultaneous photographing the process of developing the instability both in a frame photographing variant and in a photoscan variant.

Filling in the compartments of the shock tube with gases was performed by blow-through due to displacement of atmospheric air. Filling in the discharged compartment with air was carried out by the same way, but air was dried in this case by means of silica gel.

Levelling the membrane was performed by means of the gas pressure adjustment on both sides of the membrane. The value of the membrane deflection was checked visually according to the distortion of the image of some sample, constructed by the membrane surface.

Experiments were conducted under the conditions of the subsonic gas flow behind the shock wave front. The electromagnetic shock tube for such mode of flow was put into operation while using one of three sections of capacitor bank charged to 7.2 kV and capacitance of which was equal to 200 μF.

Generation of shock wave took place under the conditions of a discharge current single pulse forming of which was carried out by means of a short-circuited spark gap.

The mode of discharge and flow in the electromagnetic shock tube was checked by the form of the discharge current and by the time of arriving the shock-wave front at piezoelectric transducers, mounted in the shock tube walls.

2.2. One-dimensional computation of flow

Computation of the flow in the shock tube was performed by analogy with the technique, described in the work /3/. The peculiarity of entering the electromagnetic shock tube into the mode of generating the shock-wave with M = 1.3 at the moment of passage X = 1275 mm is the previous computation of the flow, on the base of which there was carried out adjusting the shock tube. As usual, the calibration of the computation was made on the base of the experimental data.

One-dimensional computation was done by the program "Volna" ("Wave") /8/.

The initial condition for computations - the pressure pulse on the left air boundary, corresponding to the pressure pulse of magnetic field in the electromagnetic shock tube, was specified in the form:

$$P(t) \quad \begin{cases} 1.1 \text{ bar at } 0 < t \leq 1.146\ \mu s\ ; \\ P^* \cdot \exp\left[\frac{-2t}{\tau}\right] \cdot \sin^2 \frac{2\pi}{T} t \quad \text{at} \\ 1.146 < t < 28.64\ \mu s\ ; \\ 0 \quad \text{at} \quad t > 28.64\ \mu s\ , \end{cases}$$

where $P^* = 48.235$ bar, $\tau = 59.52\ \mu s$,

$T = 57.28\ \mu s$ - period of discharge of the capacitor bank.

The equation of state for air was used in a tabular form for one-dimensional computations on the base of the work /4/ ($\rho_{affect.} = 1.22479 \cdot 10^{-3}$ g/cm^3)

For helium and cryptone it was used the equation of state for ideal gas

($\rho_{He} = 1.69\ \ 169 \cdot 10^{-4}$ g/cm^3, $\rho_{Cr} = 3.54814 \cdot 10^{-3}$ g/cm^3).

Some results of computations, which are necessary for the analysis of experiments are given in the following.

1.The estimated moment of the shock wave output into the coordinate

X = 1640 mm, t = 3198.08 μs was used at introducing the shock tube into the given mode of the flow.

2.Unstable configuration - air/helium

After the decay of rupture at the interface between air and helium, t = 2358.38 μs, it is set the density ratio N = 7.494 which is extremely slow decreasing and after Δt = 636 μs N = 7.387.

Acceleration at the interface $g = (-1.350 \pm 0.005) \cdot 10^5 m/s^2$ during all the experiment remains constant, that is a very successful circumstance for experimental results analysis

U_o = 0.2149 mm/μs

Gas temperature is slightly increasing, that excludes the thermal desrtuction of the membrane, made of nitrocellulose.

3.Stable configuration air/cryptone

After decaying the discontinuity at the contact interface at t = 2358.39 μs it is set the density ratio N = 2.62.

Initial velocity of the interface is equal to U_o = 0.1066 mm/μs, and the acceleration $g_o = -1.036 \cdot 10^5 m/s^2$.

3. EXPERIMENTAL RESULTS AND THEIR DISCUSSION

3.1. Air/helium

The photoscan and frame photographs of the experiment N 20 are presented in Fig.3.1, and data of the time of passing the shock wave along the duct of the shock tube up to the end diaphragm, separating the internal duct of shock tube from the ambient air, are given in Table 3.1. Beginning from the third transducer the movement of the shock wave front is in agreement with the estimated mode within the error of measurements.

Table 3.1

X,t - diagram of the shock-wave front moving in the series of air/helium experiments

n - number of transducer	X, mm	t_e, μs - measuring	σ_t, μs - spread	t_c, μs - estimation
1	450	651	1.6	626.5
2	630	988	2.5	972.7
3	900	1530.2	2.6	1532.0
4	1163	2100.3	-	2107.0
5	1725	2742	7.2	2749.7

σ - spread in data is given with the confidence coefficient equal to 0.95.

Velocities of incident and passing shock waves are in agreement with estimated ones within 2.5 % error of measurements.

The picture of developing perturbations of contact interface demostrates its instability and complex structure. Along the walls of the shock tube there are developed jets(further called wall jets) which obscure the picture of developing the instability in the central part of the shock tube.

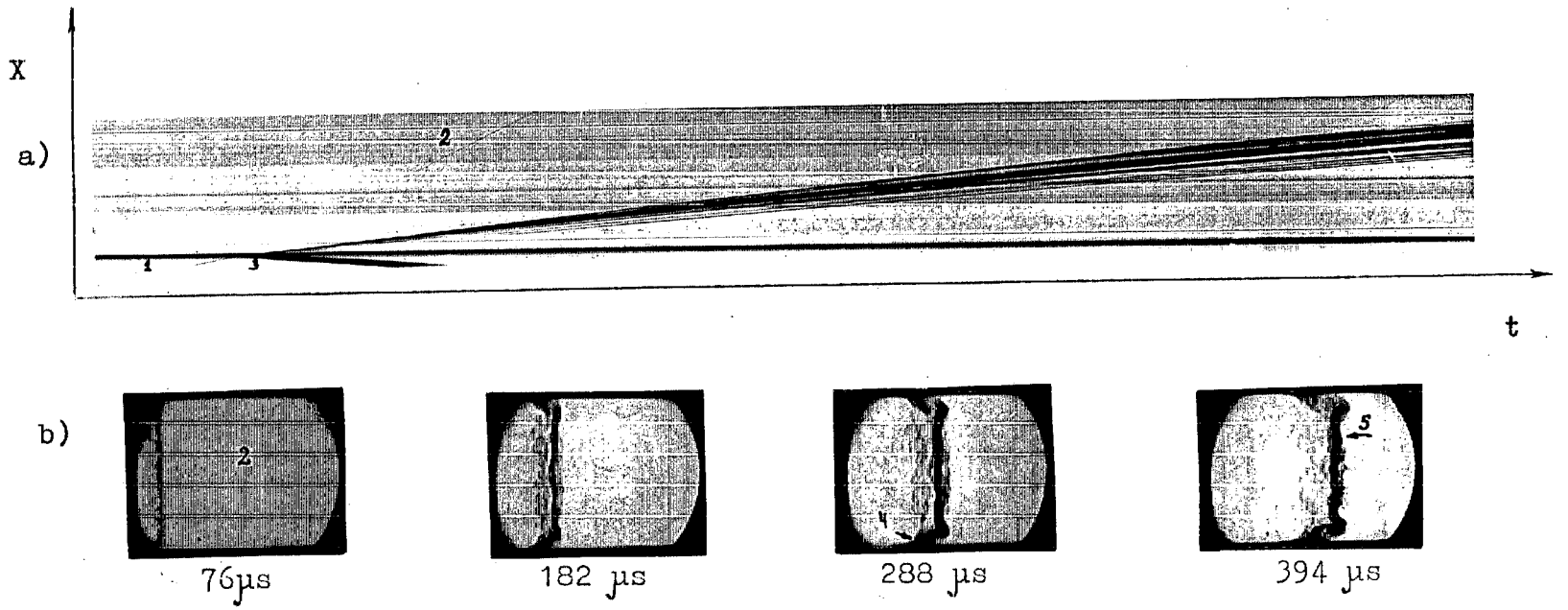

Developing perturbations on the initial plane interface between air and helium.

Experiment N 20

a)photoscan of the phenomenon
1 - incident shock-wave front
3 - discharged wave front
5 - mixing zone

b) frame images of the phenomenon
2 - passed shock-wave front
4 - wall jet

Fig. 3.1

That is why the device IAB-451 was adjusted to the minimal sensitivity (Fuko's knife was positioned at the edge of the slot while the slot width was equal to 1.5 mm), so that the wall jets did not shield the whole picture of developing the interface instabilities.

Processing of images of mixing zones was carried out by means of the microscope BMI-IZ. Coordinates of fronts of the wall jets on films of photoscans were separated out along the lines of sharp changing the density of darkening the photographic film, and namely along the lines closely fit to the regions of pure gases locations.

Processing of films with frame photograph became complicated because of obscuring the mixing zone by wall jets. In this case the opaque boundary of the image on the grey background of the wall jet image was considered as the position of the front. Position of fronts was defined according to the average value from the series bulges of the image outline. As a rule, it was observed 4-5 characteristic bulges for each front of the mixing zone.

The positions of wall jets fronts were determined by an analogous way.

Positions of the mixing zone fronts on photoscans films were not determined because of lack of true uniqueness in their identifications.

Positions of fronts for the wall jet and the passed shock wave are presented in Fig. 3.2. Good agreement is observed with the estimated trajectory of the shock-wave front.

It was noted that the front of the passed shock wave underwent the appreciable distortion, which became appearent in splitting (into two halves) the shock wave front (see Fig.3.3), this distortion, being dissapeared in $\Delta t \simeq 100$ μs, was perhaps connected with the local rupture of the membrane.

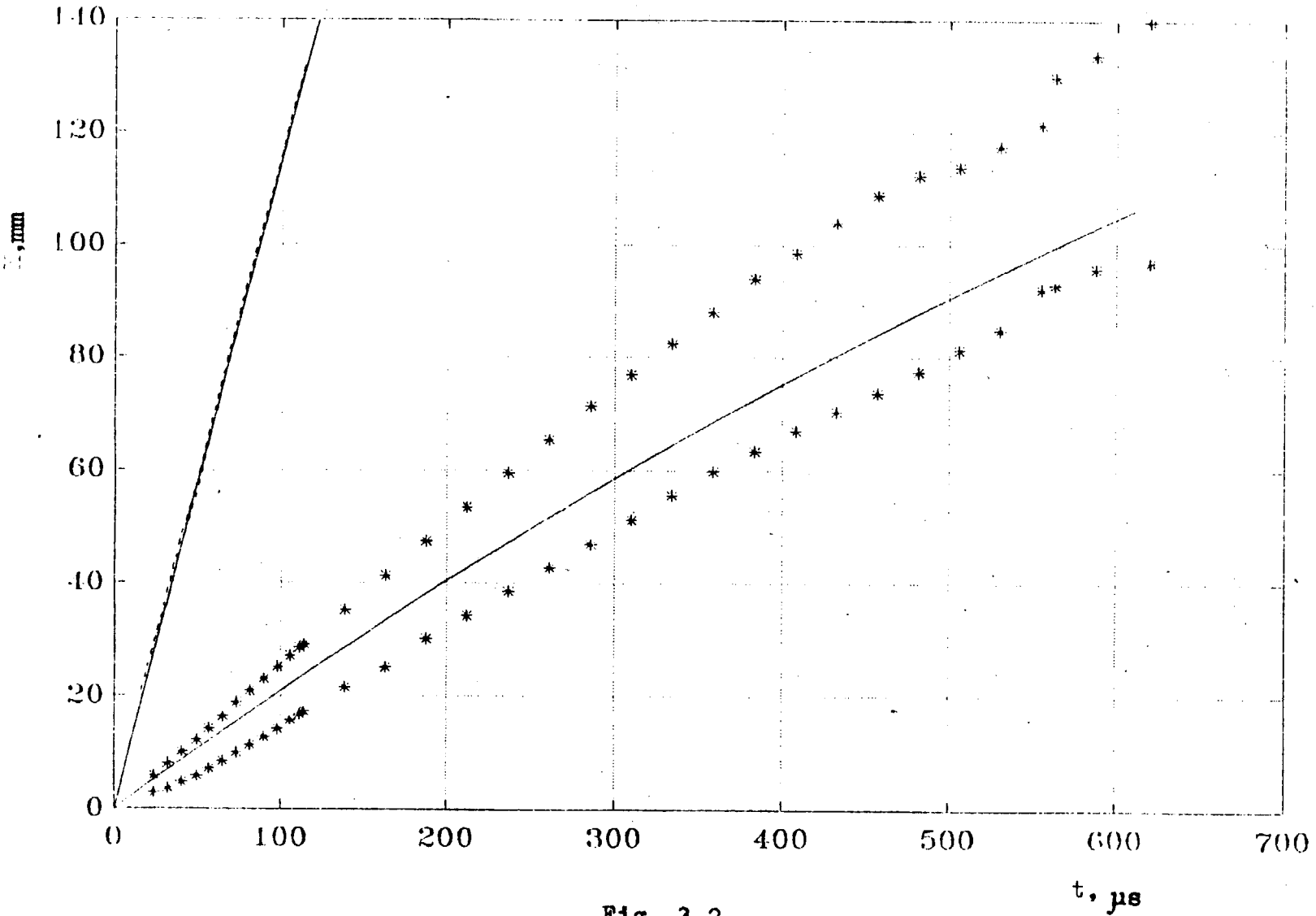

Fig. 3.2

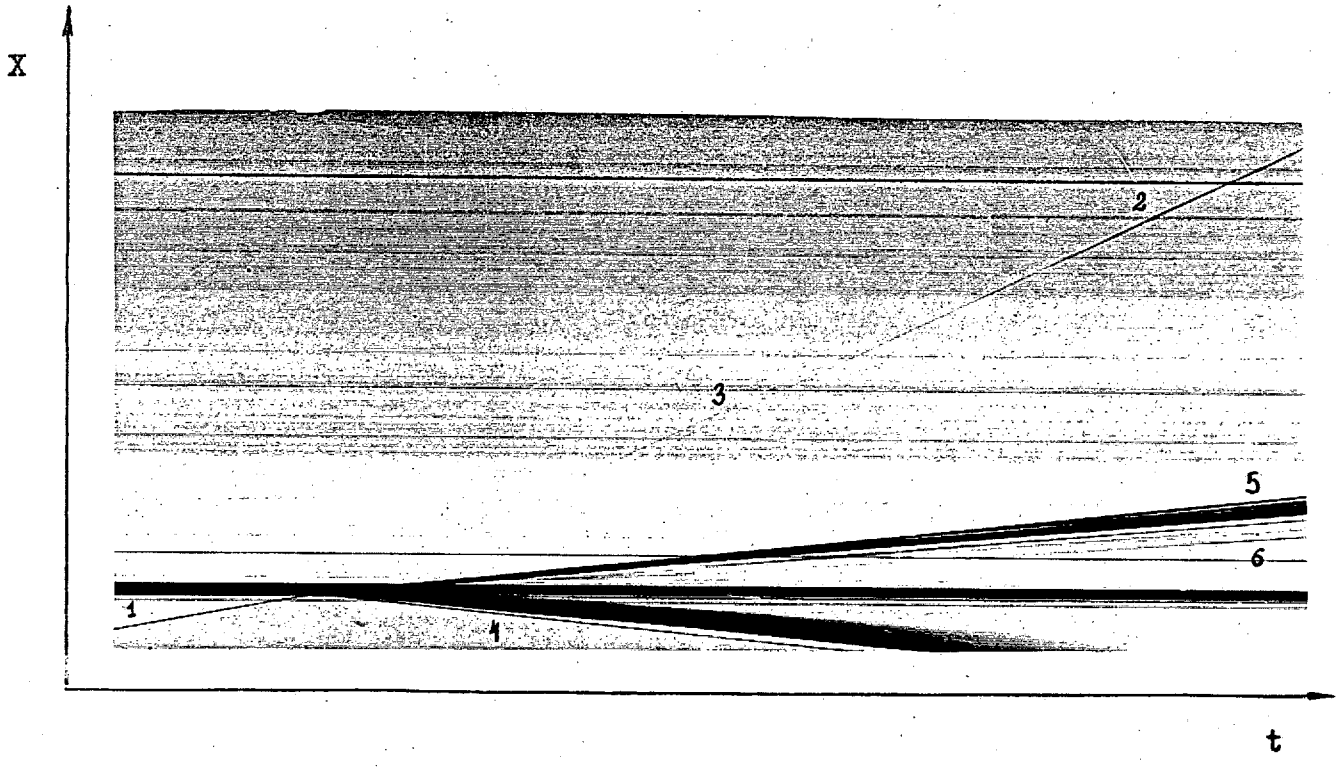

Photoscan of the process of passing the shock-wave front through the interface between air and helium.

Experiment N 20

1 - incident shock-wave front

2 - passed shock-wave front

3 - the region of splitting (into two halves) the shock-wave front

4 - unloading wave front, formed as a result of the rupture decay

5,6 - the leading and trailing fronts of wall jets

Fig.3.3

It was also noted that after conducting experiments in some cases there were discovered fragments of the membrane with the characteristic sizes being equal to 3 cm x 1.5 cm. This means that the membrane is not destructed, on the whole, but it is cut around the perimeter of the shock tube duct and it can exert the stabilizing effect on the process of the instability development.

The whole process of developing the wall jet and the mixing zone are presented in Fig.3.4. The rate of the mixing zone developing being, at average, equal to $\simeq$ 20 m/s, is rather higher than in Sturtevant's experiments /2/, conducted with the stationary shock wave.

The more intensive growth of the mixed zone as well as the growth of the wall jets is apparently explained by the dominating role of the unloading wave acceleration in comparison with the shock acceleration of the shock-wave front.

In our investigation the results of experiments on studying the developments of gravitational turbulent gas mixing were analysed on the assumption of quadratic law of dependence of the zone width on time, following from the results of works /5,6/.

The mixing zone width, L, as well as the size of the wall jet, l, as an accompanying phenomenon, were analysed on the assumption of the validity of the relationships having the form:

$$L = \alpha \cdot f(N) \cdot 2S \qquad (3.1)$$

where $S = \frac{g t^2}{2} = (U_o \hat{t} - \hat{x})$ - the path of the contact interface deceleration;

$\hat{t}$ - time relative to the shock-wave outgoing on the interface;

$\hat{x}$ - displacement of the interface relative to the initial position;

α - a constant;

$f(N)$ - function, determining the dependence on gas density ratio N.

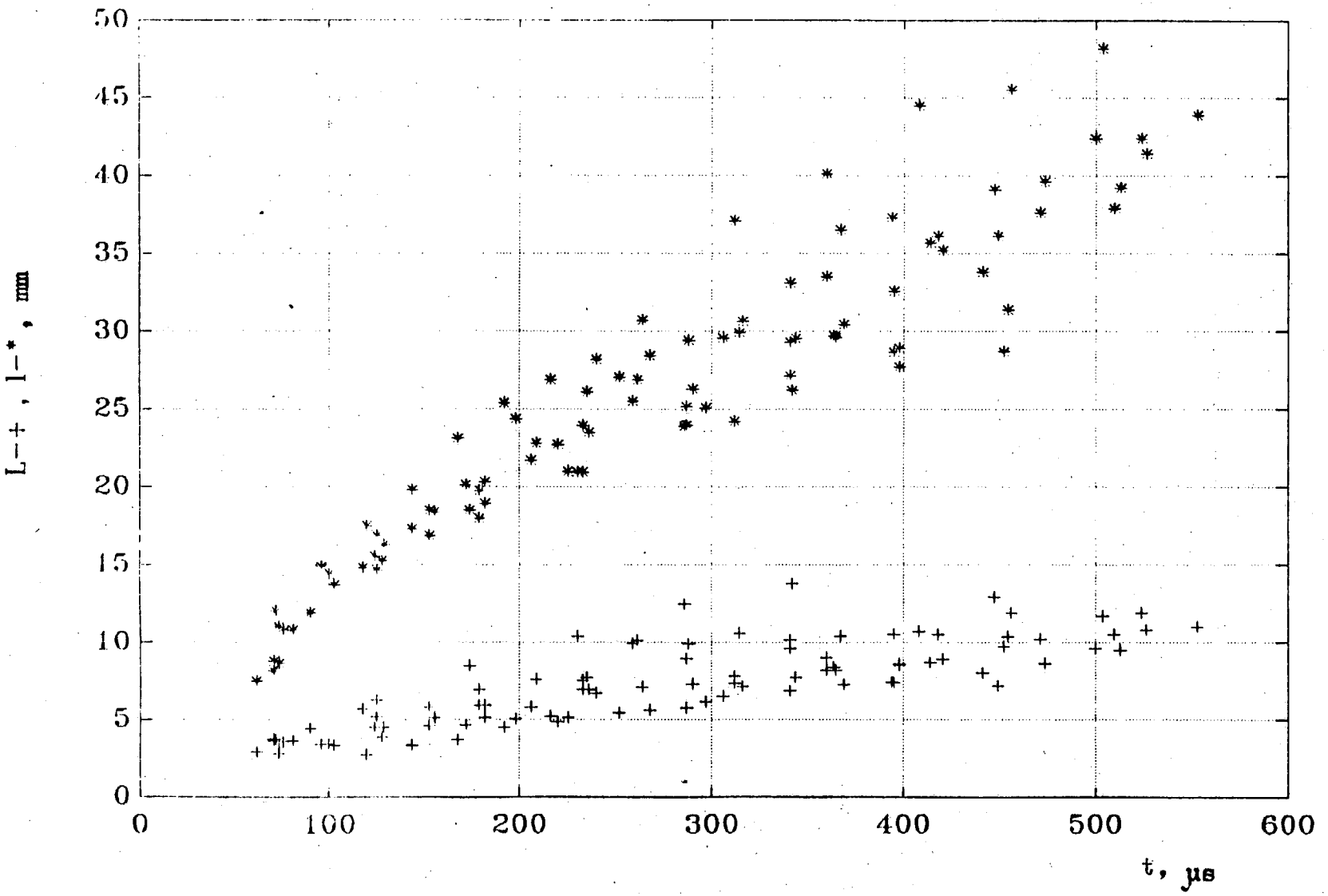

Fig. 3.4

Taking into account the influence of the initial perturbations was carried out during the data processing in the coordinate plane $\sqrt{L}$, $\sqrt{2S}$, in terms of

$$\sqrt{L} = \sqrt{L_o} + \sqrt{\mathcal{L} \cdot f \cdot 2S} \qquad (3.2)$$

suggested in the work /7/, where L_o- initial roughness.

For describing the turbulent mixing process it was introduced the notion of mixing intensity :

$$J = \frac{1}{2} \frac{d L}{d S} \qquad (3.3)$$

Data processing was made on the assumption of the random nature of acting the initial uncontrolled perturbations, realized in each particular experiment. That is why the data processing results, obtained in different experiments, were averaged and the average value was considered as the most reliable one.

Relations of $\sqrt{L}$ to $\sqrt{2S}$ as well as relations of $\sqrt{1}$ to $\sqrt{2S}$ in the first approximation are close to the linear ones (see Fig. 3.5 - 3.7) both for the set of data for each separate experiment and for results of all experiments in the whole. While comparing the average values of correlation ratio

$\overline{R(\sqrt{L}, \sqrt{2S})} = 0.897$ and $\overline{R(L, 2S)} = 0.858$

$R(\sqrt{1}, \sqrt{2S}) = 0.966$ and $R(1, 2S) = 0.936$

it is observed the tendency toward more close linear relationship of L, S (1,S) at data processing in the powered form of relations with the index being equal to 0.5.
It is necessary to note that $R(\sqrt{1}, \sqrt{2S}) > R(\sqrt{L}, \sqrt{2S})$.

Values of correlation ratios are rather close to I, that can be an objective substantiation of the adopted methods of data processing.

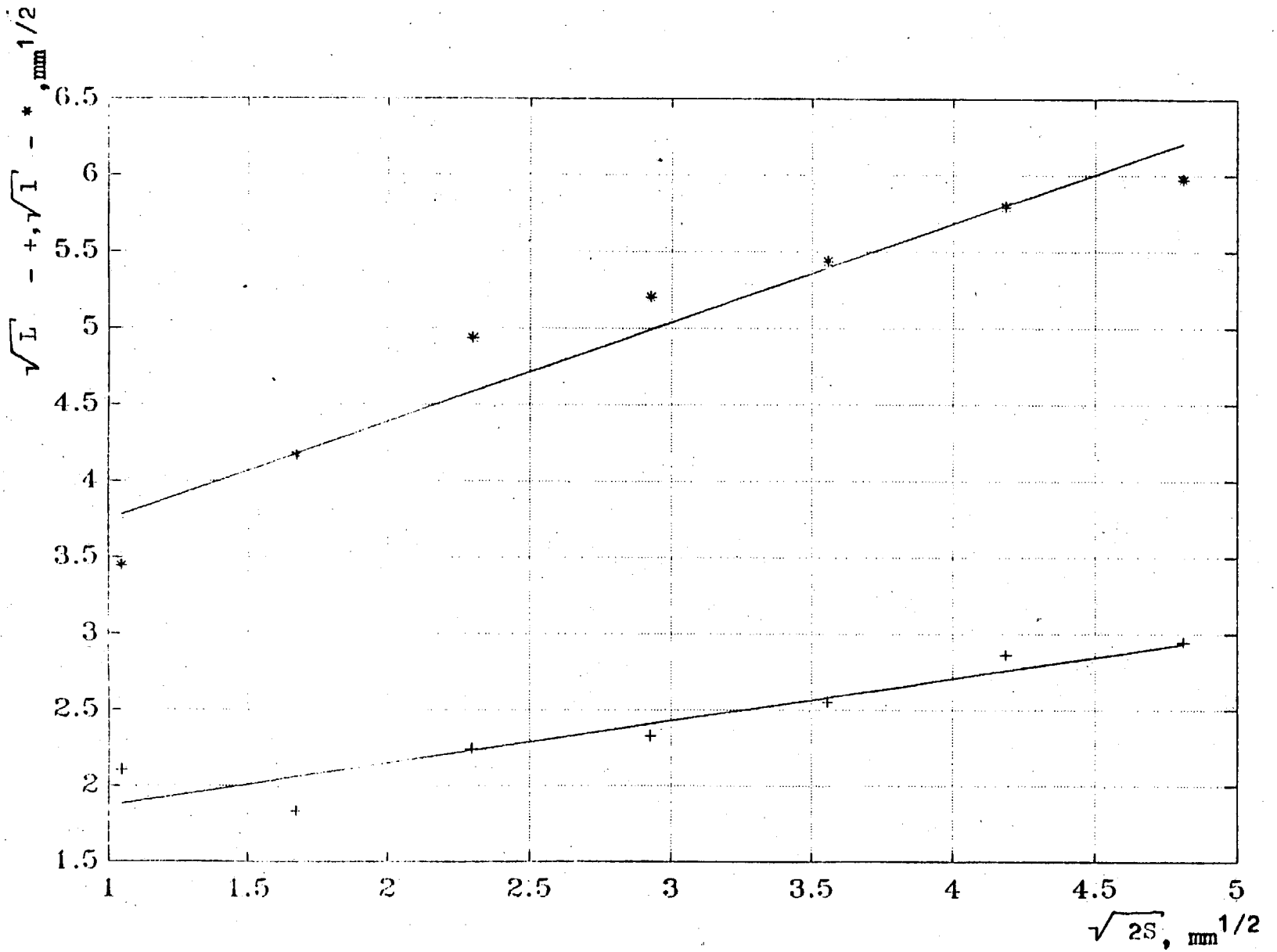
$\sqrt{L}$ - +, $\sqrt{1}$ - *, $mm^{1/2}$
6.5
6
5.5
5
4.5
4
3.5
3
2.5
2
1.5
1
1.5
2
2.5
3
3.5
4
4.5
5
$\sqrt{2S}$, $mm^{1/2}$

Fig. 3.5

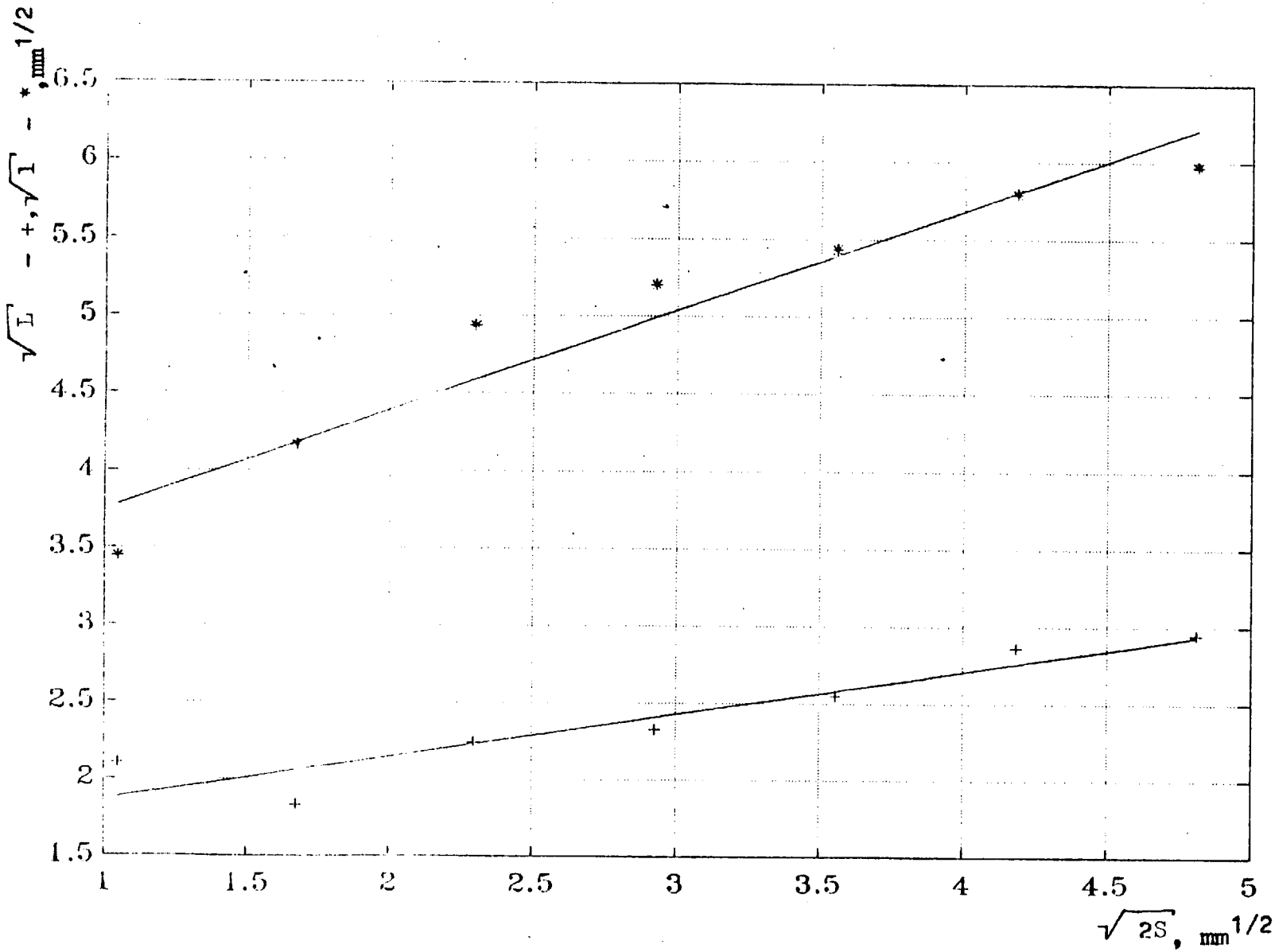
$\sqrt{L - +}, \sqrt{1 - *}$, mm$^{1/2}$
6.5
6
5.5
5
4.5
4
3.5
3
2.5
2
1.5
1
1.5
2
2.5
3
3.5
4
4.5
5
$\sqrt{2S}$, mm$^{1/2}$

Fig. 3.6

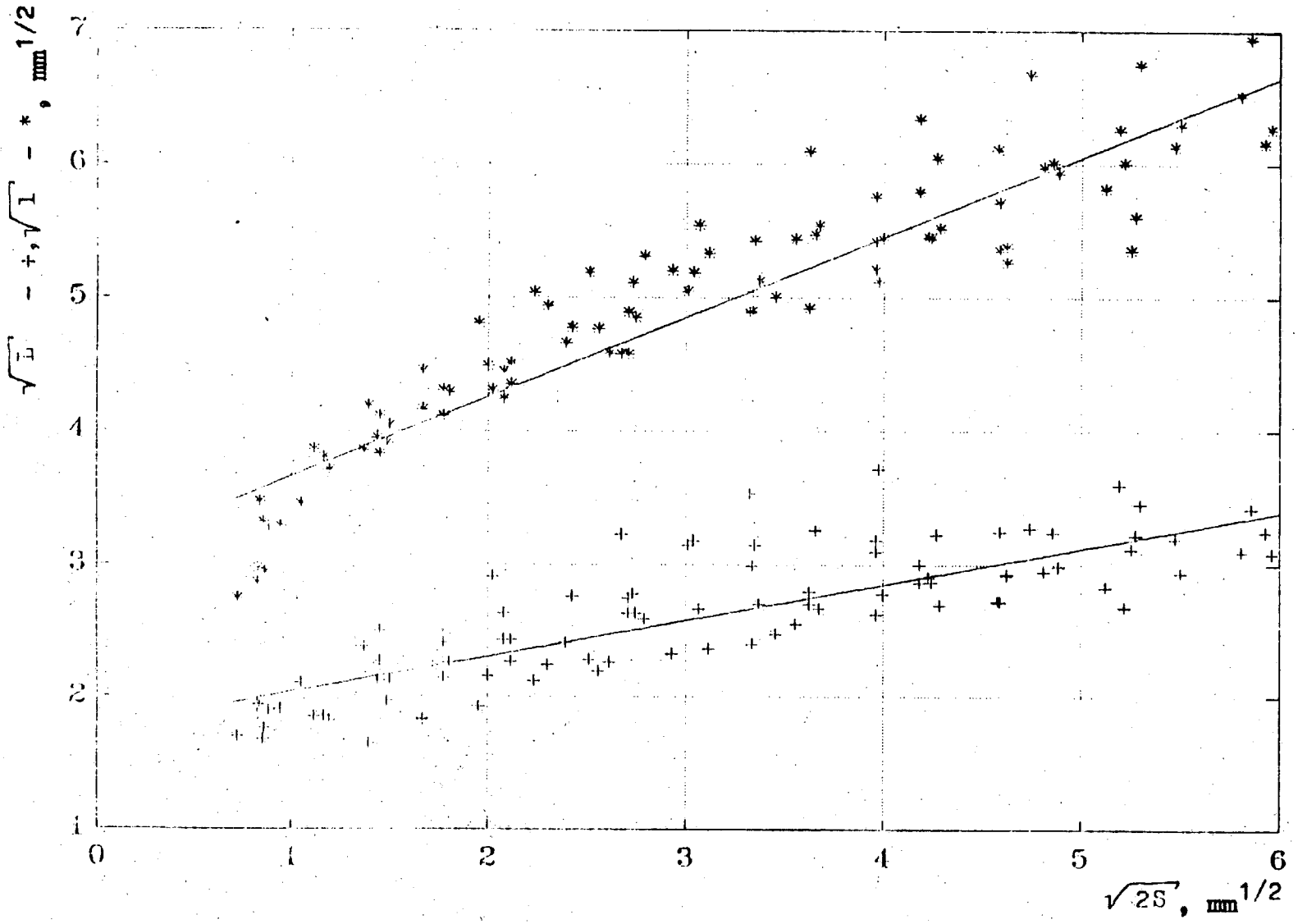

Fig. 3.7

Table 3.2

Intensity of mixing and the initial roughness in the series of air/helium experiments

N = 7.44

The number of the experiment	$\sqrt{J_L}$	$\sqrt{L_o}$	$\sqrt{J_e}$	$\sqrt{\ell_o}$
7	0.2282	1.6962	0.5670	2.9819
10	0.2777	1.6173	0.6752	2.9570
12	0.2789	1.5912	0.6454	3.1024
13	0.1255	2.1085	0.6135	2.9657
14	0.3544	1.7483	0.6212	2.7404
15	0.2362	2.1978	0.5537	2.8932
17	0.3015	1.5942	0.5168	3.0737
20	0.222	2.0431	0.5363	3.9267
21	0.3070	1.6741	0.5622	3.1308
22	0.3849	1.3401	0.6875	3.3034

Processing was carried out by the least squares fits of data $\bar{J}_L = 0.074$, $\sigma_J = 0.04$ - data spread.

$\sigma_j = 0.03$ - r.m.s. error of measuring $\bar{J}$, determined with the confidence coefficient being equal to 0.95.

$L_o = 3.1$ mm.

Data processing for the wall jets leads to the following results:

$\bar{J}_e = 0.36$, $\sigma_{J_e} = 0.07$, $\sigma_{\bar{J}e\ p=0.95} = 0.05$, $\ell_o = 9.35$mm

Data processing on the assumption of the linear character of relationships on the initial perturbations leads to the following results:

$J_L = 0.208$, $L_o = 4.6$ mm, $J_e = 0.856$, $\ell_o = 14.97$ mm

But the value of $\bar{J}_e = 0.856$ means that jets are moving with acceleration exceeding the acceleration of the interface that, generally speaking, is not possible. That is why, the results of data processing, obtained on the assumption of relations of the form (3.2), are more reliable.

Determination of the turbulent mixing constant was carried out on the assumption of validity of relation, having the form:

$$L = \alpha \frac{N - 1}{N + 1} \cdot 2S \qquad (3.4)$$

In this case

$$\alpha_L = 0.097 \pm 0.04$$

for the case of the observed zone of the turbulent mixing and

$$\alpha_e = 0.47 \pm 0.07$$

for the case where the gas mixing region is defined by the wall jets.

But the value of α_L is one-third as many as the value of constant α, obtained in experiment with the sinosoidal interface /3/. On the other hand, α_e is close to the value of 0.5 and shows the development of wall jets with acceleration close to the value of the contact interface acceleration, that, generally speaking, is possible at the slight influence of Helmholtz's instability. But the large value of initial perturbations, and especially l_o in the experiments with a flat interface, makes to suppose that the process of developing the instability is influenced by the significant boundary initial perturbations, arised as a result of shock wave - membrane interaction.

From our point of view, the destruction of the membrane occured, in general, along the perimeter of the shock tube. As the low temperature of gases excludes the thermal destruction of gases and, as it was noted, after experiments there were found fragments of membrane, it remained unbroken on the whole. This must lead to stabilization of the instability on the interface, from one hand, and to the development

of wall effects because of the obvious rupture of the membrane along the internal perimeter of the shock tube.

In addition, it can be said, that the value of the interface movement retardation, connected with involving the membrane into the motion and determined as

$$\Delta x \simeq \frac{q}{\rho_0} = 10 \text{ mm}$$

where ρ_0 - helium density, coincides with the observable value of ℓ_0 ;

q - membrane surface density.

3.2. Air/cryptone - stable configuration

There were conducted three experiments in this series of experiments, because this configuration of gases, as it was expected, was found to be stable.

Photoscans of this phenomenon and frame photographs of the second experiment are presented in Fig.3.8. Velocities of the incident and passed shock-waves, within the error of measurements, are in agreement with one-dimensional computation. But comparing the time of the shock- wave arrival at the end transducer (x=1725 mm, t = 3909 μs - computed values) is more demonstrative, t = 3861 ±3 μs, it shows that the mode of flowing in the shock tube differs in this parameter by 1.2 % from the computed one. In these experiments the possible influence of the boundary instability on the flow in the shock tube was excluded.

The slow expansion of the contact interface image was interpreted as a region of the small scale perturbations, excited by the shock wave, and, possibly, partly turbulized. The gradual expansion of this region is connected with the monotonous character of decreasing the gas densities in the unloading wave.

The size of this region to the final stage of observation (Δt = 770 μs) is equal to 4-5 mm that is considerable smaller than in experiments with the unstable gas configuration. Some distortions of the interface near the walls of the shock tube are, apparently, connected with the influence of the boundary layer.

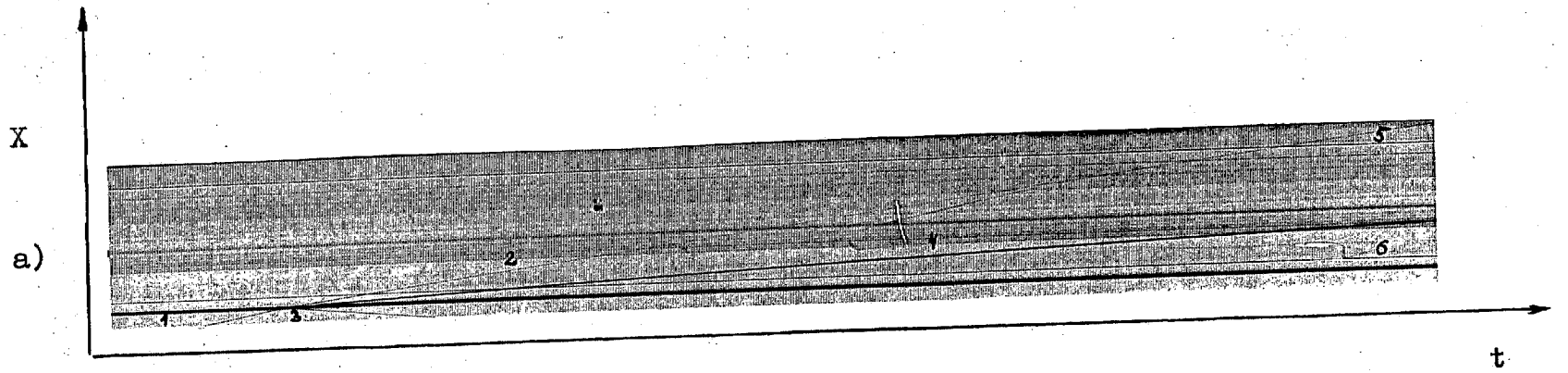

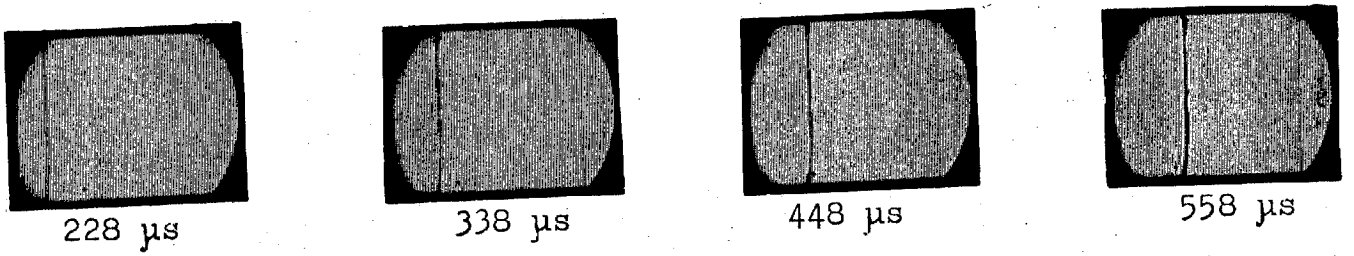

Picture of the flow in experiments with the stable configuration of gases (air/cryptone).

a) photoscan of the phenomenon
b) frame images of the phenomenon
1 - incident shock-wave front
2 - passed shock wave front
3 - reflected shock-wave front
4 - contact interface
5,6 - bank mark threads, arranged at 10 and 120 mm from the initial position of the interface

Fig. 3.8

Stability of the given gas configuration confirms experimentally the conclusion concerning the dominating role of the constant acting acceleration in comparison with the shock one at combined character of their action.

4. C O N C L U S I O N S

Investigating the stability of the plane contact interfaces between gases, having different densities, under conditions of acting the decelerating shock wave, demonstrated that the state of each particular configuration of gases was determined in relative to the direction of effect of the constant acting acceleration which played the dominating role in comparison with the shock acceleration.

The development of perturbations in the unstable configuration of gases under the subsonic conditions of flow with $M = 1.3$, exluding the thermal destruction of the membrane, displayed the essential influence of the membrane, stabilizing development of the instability, in the whole, on the interface from one hand and stimulating development of wall jets from the other hand.

In the conclusion the authors of this work express their acknowledgement to V.I.Anisimov and A.V.Polyonov for their assistance in processing the results of experiments and for helpful discussions about those results.

REFERENCES

1.V.A.Andronov, S.M. Bahrah et al.
Turbulent Mixing on the Contact Surface Accelerated by Shock Waves.
Sov.J. "Exp.& Theor. Phys.",1976,v.71, N 2(8)

2.M.Brouillette, B.Sturtevant
Growth Induced by Multiple Shock Waves Normally Incident on Plane Gaseous Interfaces.
Proceedings of CNLS Annual Conference, May 16, 1988, Elsevier, 1989

3.A.M.Vasilenko, O.V.Buryakov et al .
Experimental Investigation of Gravitational Instability and Turbulization of the Flow on the Interface of Noble Gases.
Report,Princeton, 24-27 Oct.1988

4.N.M.Kusnezov
Thermodynamic Functions and Shock Adiabats of Air at High Temperatures.
M.Mashinostroenie, 1965

5.S.Z.Belyenkii, E.S.Fradkin
Theory of Turbulent Mixing.
Transactions of Phys. Inst. Ac. Sci. by name of Lebedev, v.29,pp.207-238,1965

6.V.E.Neuvazhaev, V.G.Yakovlev
To the Theory of Turbulent Mixing.Reports of Ac.Sci (DAN) USSR,1975,v.222, N 5, pp.1053-1056

7.V.E.Neuvazhaev, V.G.Yakovlev
Relative to Mixing the Contact Boundary, Decelerated by Stationary Shock Waves. Sov.J.of Appl. Mech & Tech.Phys.,v.2,pp.85-89,1981

8.V.F.Kuropatenko
Approximate Methods for Computing the Values behind the Shock-Wave Front.Numerical Methods of Continuum Mechanics, 1970,v.1, N 6,pp.77-83

A P P E N D I X

Symbols, adopted in the appendix:

x_o - the coordinate of the shock wave front;
x_i - coordinates of the leading front (i = I) and the trailing one (i = 2) of the mixing zone;
x_i' - coordinates of the leading front (i = I) and the trailing one (i = 2) of wall jets;
L - width of the gas mixing zone
ℓ - size of wall jets

Table A.1.

X-t diagram fronts zone mixing and wall jets

Experiment № 7 q=0.077 mg/sm²

t, mks	X_1, mm	X_2, mm	L, mm	X_1', mm	X_2', mm	l, mm
81	20.06	16.44	3.62	21.75	10.98	10.77
153	37.08	32.49	4.59	40.48	23.58	16.9
225	52.48	47.37	5.11	55.87	34.89	20.98
297	68.17	62.04	6.13	72.04	46.98	25.06
369	81.83	74.58	7.25	85.9	55.48	30.42
441	95.71	87.7	8.01	101.33	67.5	33.83
513	108.3	98.8	9.5	116.18	76.98	39.2

Experiment № 10 q=0.146 mg/sm²

t	X_1	X_2	L	X_1'	X_2'	l
76	20.9	17.34	3.56	22.85	12.11	10.74
124	34.24	29.75	4.49	37.44	21.9	15.54
172	44.73	40.07	4.66	49.58	29.47	20.11
220	56.34	51.52	4.82	63.1	38.6	22.7
268	67.02	61.42	5.6	74.05	45.62	28.43
316	79.41	72.0	7.11	86.04	55.42	30.62
364	89.28	80.88	8.4	96.26	66.57	29.69

Experiment № 12 **q=0.118 mg/sm²**

t	X_1	X_2	L	X_1'	X_2'	l
90	23.89	19.47	4.42	24.07	12.2	11.87
144	34.75	31.4	3.35	38.54	21.22	17.32
198	47.14	42.12	5.02	51.9	27.52	24.38
252	57.47	52.06	5.41	63.95	36.9	27.05
306	69.47	62.97	6.5	75.69	46.13	29.56
360	80.56	72.38	8.18	85.89	52.37	33.52
414	91.16	82.48	8.68	97.1	61.42	35.68

Experiment № 13 **q=0.063 mg/sm²**

t	X_1	X_2	L	X_1'	X_2'	l
71	19.14	15.39	3.75	20.09	11.30	8.79
125	33.21	27.00	6.21	34.27	17.38	16.89
179	44.18	38.26	5.92	46.99	27.24	19.75
233	56.35	49.43	6.92	60.42	36.5	23.92
287	66.23	60.47	5.76	73.24	48.1	25.14
341	76.94	70.08	6.86	84.19	54.91	29.28
395	87.63	80.26	7.37	96.18	63.57	32.61
449	95.61	88.45	7.16	105.88	69.77	36.11

Experiment № 14 **q=0.092 mg/sm²**

t	X_1	X_2	L	X_1^i	X_2^i	l
71	18.38	14.78	3.6	18.57	10.42	8.15
125	31.9	26.76	5.14	32.91	18.27	14.64
179	44.81	37.89	6.92	46.66	28.68	17.98
233	56.38	48.85	7.53	58.76	37.81	20.95
287	68.0	59.06	8.94	70.33	46.36	23.97
341	79.82	69.68	10.14	82.36	55.23	27.13
395	88.32	77.81	10.51	91.44	62.79	28.65

Experiment № 15 **q=0.096 mg/sm²**

t	X_1	X_2	L	X_1^i	X_2^i	l
62	17.47	14.58	2.89	19.02	11.53	7.49
118	31.92	26.27	5.65	34.02	19.22	14.8
174	45.34	36.87	8.47	47.96	29.44	18.52
230	58.43	48.03	10.4	61.21	40.28	20.93
286	70.18	57.71	12.46	73.62	49.71	23.91
342	82.13	68.36	13.77	85.86	59.66	26.2
398	86.79	78.21	8.58	98.62	69.74	28.88
454	98.52	88.15	10.37	110.09	78.73	31.36
510	108.04	97.53	10.51	122.83	84.94	37.89

Experiment № 17

t	X_1	X_2	L	X_i	X_2	l
74	20.57	17.48	3.09	20.94	12.31	8.63
128	32.59	28.74	3.85	35.99	20.73	15.26
182	44.07	38.94	5.13	49.78	30.85	18.93
236	56.4	49.48	6.92	63.89	40.38	23.51
290	66.98	59.69	7.29	76.37	50.09	26.28
344	77.15	69.45	7.7	88.02	58.48	29.54
398	87.73	79.22	8.51	100.07	72.37	27.7
452	97.85	88.13	9.72	111.79	83.11	28.68

Experiment № 20 **q=0.158 mg/sm²**

t	X_1	X_2	L	X_1^i	X_2^i	l
102.5	25.4	22.1	3.3	28.0	14.3	13.7
129	31.5	27.0	4.5	33.8	17.52	16.3
155.5	37.8	32.7	5.1	40.9	22.5	18.4
182	47.3±0.9	41.4±0.8	5.9	49.9±0.9	29.6	20.3
208.5	56.1	48.5	7.6	58.5	35.7	22.8
235	56.5	48.8	7.7	61.4	35.3	26.1
261.5	63.2	53.1	10.1	67.7	40.8	26.9
288	69.9	60.0	9.9	73.9	44.5	29.4
314.5	75.3	64.7	10.6	78.8	48.9	29.9
341	81.1±2.8	71.5±0.4	9.6	84.3±1.6	51.2±2.4	33.1
367.5	84.4	74.0	10.4	90.8	54.3	36.5
394	89.0	81.6	7.4	97.0	59.7	37.3
420.5	95.8	86.9	8.9	100.9	65.7	35.2
447	104.4	91.5	12.9	110.4	71.2	39.1
473.5	105.4	96.8	8.62	111.9	72.3	39.6
500	108.0	98.4	9.6	115.6	73.2	42.4
526.5	117.2	106.4	10.8	123.3	81.9	41.4
553	121.4±.9	110.4±2.4	11	126.6±2.4	82.7±2.8	43.9

Experiment № 21 **q=0.142 mg/sm²**

t	X_1	X_2	L	X_1'	X_2'	l
73.5	18.4	15.6	2.8	21.3	10.3	11.0
100	24.7±0.5	21.3±0.5	3.4	29.6±1	15.2±2.8	14.4
153	37.7	31.9	5.8	42.6	24.1	18.5
206	49.7	43.9	5.8	55.0	33.3	21.7
259	63.0	53.1	9.9	67.2	41.7	25.5
312	71.4±2.5	63.6±0.9	7.8	78.9±2	54.7±5.8	24.2
365	80.5	72.3	8.2	88.1	58.5	29.6
418	92.8	82.3	10.5	102.3	66.2	36.1
471	101.0	90.8	10.2	110.8	73.2	37.6
524	108.7±1	96.8±2	11.9	119.1±2.5	76.7±6.6	42.4

Experiment № 22 $q=0.114$ mg/sm^2

t	X_1	X_2	L	X_1'	X_2'	l
72	20.6±0.5	16.9	3.7	21.05	9.02	12.0
96	26.6	23.2	3.4	28.8	13.9	14.9
120	31±0.2	28.3	2.7	35.7	18.15	17.5
144	37.7	34.4	3.3	42.6±0.3	23.8±1.3	19.8
168	42.9±0.4	39.2±0.5	3.7	49.5	26.3	23.1
192	49.5	45	4.5	57.0	31.6	25.4
216	54.6	49.4	5.2	62.6	35.7	26.9
240	60.7±0.5	54.0±0.5	6.7	69.2±1.4	41±1.8	28.2
264	65.8	58.7	7.1	75.1	44.4	30.7
312	67.5	60.2	7.3	78.6	41.5	37.1
360	89.1	80.1	9.0	100.6	60.5	40.1
408	100.1	89.4	10.7	111.7	67.2	44.5
456	106.5	94.6	11.9	116.4	70.9	45.5
504	$115.6^{+1.6}$	$103.9^{+2.6}$	11.7	$125.8^{+2.7}$	77.6±3.1	48.2

Table A.2.

Position of the shock-wave front and coordinates of the contact interface in the stable air/cryptone configuration

Experiment N 1 $q = 0.07$ mg/cm^2

t, μs	X_0, mm	X_1, mm	X_2, mm	L, mm
8.2	13.92			
16.4	16.38	13.08	12.08	1.00
24,5	18,98	14.00	12.97	1.03
32.7	21.51	15.13	13.80	1.33
40.9	24.06	16.23	14.66	1.57
49.1	26.53	17.32	15.43	1.89
57.2	29.00	18.17	16.34	1.83
65.4	31.68	19.36	17.44	1.92
73.6	34.10	20.23	18.36	1.87
81.8	36.66	21.44	19.28	2.16
90.0	39.17	22.40	20.03	2.37
98.1	41.71	23.42	21.20	2.22
106.3	44.24	24.17	22.05	2.12
114.5	46.70	25.25	23.04	2.21
122.7	49.28	25.91	23.60	2.31
130.9	51.68	26.93	24.50	2.43
139.0	54.22	27.60	25.57	2.03
147.2	56.74	28.72	26.44	2.28
155.4	59.17	29.41	27.32	2.09
163.6	61.70	30.41	28.12	2.29
171.8	64.26	31.41	28.74	2.67
179.9	66.65	32.15	29.69	2.46
188.1	69.30	32.50	30.30	2.20
196.3	71.70	33.59	31.28	2.31
204.5	74.15	33.93	31.90	2.03
212.6	76.62	34.39	32.31	2.08
220.8	78.97	35.12	33.14	1.98

Table A.2.

Position of the shock-wave front and coordinates of the contact interface in the stable air/cryptone configuration

Experiment N 1 $q = 0.07$ mg/cm^2

t, μs	X_0, mm	X_1, mm	X_2, mm	L, mm
8.2	13.92			
16.4	16.38	13.08	12.08	1.00
24,5	18,98	14.00	12.97	1.03
32.7	21.51	15.13	13.80	1.33
40.9	24.06	16.23	14.66	1.57
49.1	26.53	17.32	15.43	1.89
57.2	29.00	18.17	16.34	1.83
65.4	31.68	19.36	17.44	1.92
73.6	34.10	20.23	18.36	1.87
81.8	36.66	21.44	19.28	2.16
90.0	39.17	22.40	20.03	2.37
98.1	41.71	23.42	21.20	2.22
106.3	44.24	24.17	22.05	2.12
114.5	46.70	25.25	23.04	2.21
122.7	49.28	25.91	23.60	2.31
130.9	51.68	26.93	24.50	2.43
139.0	54.22	27.60	25.57	2.03
147.2	56.74	28.72	26.44	2.28
155.4	59.17	29.41	27.32	2.09
163.6	61.70	30.41	28.12	2.29
171.8	64.26	31.41	28.74	2.67
179.9	66.65	32.15	29.69	2.46
188.1	69.30	32.50	30.30	2.20
196.3	71.70	33.59	31.28	2.31
204.5	74.15	33.93	31.90	2.03
212.6	76.62	34.39	32.31	2.08
220.8	78.97	35.12	33.14	1.98

229.0	81.36	35.63	33.84	1.79
237.2	83.31	36.96	35.12	1.84
245.4	85.82	37.42	35.46	1.96
253.5	86.68	38.31	36.14	2.17
261.7	89.33	37.18	35.02	2.16
269.9	91.70	38.06	35.88	2.18
278.1	94.08	38.74	36.70	2.04
286.2	96.48	39.48	37.46	2.02
294.4	98.97	40.08	38.11	1.97
302.6	101.27	40.67	38.74	1.93
310.8	103.64	41.77	39.58	2.19
319.0	106.41	42.43	40.52	1.91
327.2	108.81	43.00	40.96	2.04
335.3	111.24	43.87	41.63	2.24
343.5	113.70	44.40	42.35	2.05
351.7		45.25	42.89	2.36
359.9		46.69	44.21	2.48
368.0		47.45	44.76	2.69
376.2		48.30	45.46	2.84
384.4		48.83	46.37	2.46
392.6		49.39	46.96	2.43
400.8		50.09	48.24	1.85
408.9		51.43	48.96	2.47
417.1		52.14	49.60	2.54
425.3		52.63	50.09	2.54
433.5		53.39	50.79	2.60
441.6		54.06	51.33	2.73
449.8		54.70	51.52	3.18
458.0		54.79	52.01	2.78
466.2		55.48	52.65	2.83

474.4		56.15	53.25	2.90	
482.6		56.66	53.97	2.69	
490.7		57.32	54.48	2.84	
498.9		57.86	55.01	2.85	
507.1		58.43	55.46	2.97	
515.3		58.80	55.94	2.86	
523.4		59.36	56.44	2.92	
531.6		59.89	56.94	2.95	
539.8		60.68	57.48	3.20	
548.0		61.28	57.97	3.31	
556.2		61.74	58.47	3.27	
564.3		62.15	59.10	3.05	
572.5		62.77	59.49	3.28	
580.7		63.32	59.98	3.34	
588.9		63.74	60.49	3.25	
597.0		64.39	60.92	3.47	
605.2		64.88	61.42	3.46	
613.4		65.28	62.05	3.23	
621.6		65.92	62.31	3.61	
629.8		66.31	62.95	3.36	
637.9		66.85	63.24	3.61	
646.1		67.25	63.73	3.52	
654.3		67.82	64.17	3.65	
662.5		68.38	64.52	3.86	
670.7		68.68	64.94	3.74	
678.8		69.19	65.35	3.84	
687.0		69.69	65.88	3.81	
695.2		70.16	66.42	3.74	
703.4		70.66	66.76	3.90	
711.6		71.05	67.25	3.80	

719.7		71.51	67.61	3.90	
727.9		72.07	68.23	3.84	
736.1		72.38	68.61	3.77	
744.3		72.82	69.01	3.81	
752.4		72.86	68.80	4.06	
760.6		73.70	69.18	4.52	
768.8		73.79	69.57	4.22	
777.0		73.94	69.22	4.72	

Experiment N 2 $q = 0.06$ mg/cm^2

t, μs	X_0, mm	X_1, mm	X_2, mm	L, mm
8.2	12.60			
16.4	15.04	11.76	10.52	1.24
24,6	17.54	12.74	11.31	1.43
32.8	20.07	13.76	12.25	1.51
41.0	22.65	14.77	13.12	1.65
49.2	23.10	15.70	14.13	1.57
57.4	27.58	16.58	15.00	1.58
65.6	30.13	17.50	15.97	1.53
73.8	32.59	18.22	16.81	1.41
82.0	35.18	19.22	17.72	1.50
90.2	37.60	19.97	18.54	1.43
98.4	40.20	20.94	19.56	1.38
106.6	42.62	21.72	20.35	1.37
114.8	45.25	22.62	21.28	1.34
123.0	47.68	23.29	22.08	1.21
131.2	50.19	24.68	22.74	1.94
139.4	51.86	25.56	23.50	2.06
147.6	54.36	25.39	23.63	1.76
155.8	56.81	26.28	24.39	1.89
164.0	59.36	27.15	25.21	1.94
172.2	61.80	27.93	26.00	1.93
180.4	64.24	28.77	26.89	1.88
188.6	66.66	29.70	27.60	2.10
196.8	69.25	30.48	28.54	1.94
205.0	70.80	31.29	29.32	1.97
213.2	73.34	31.23	29.18	2.05
221.4	72.71	31.97	30.05	1.92

229.6	75.28	29.78	27.70	2.08	
237.8	77.69	30.59	28.38	2.21	
246.0	80.17	31.18	29.37	1.81	
254.2	82.72	32.13	30.13	2.00	
262.4	85.09	32.86	30.88	1.98	
270.6	87.61	33.48	31.69	1.79	
278.8	90.17	34.38	32.33	2.05	
287.0	92.53	35.10	33.16	1.94	
295.2	95.12	35.86	34.01	1.85	
303.4	97.560	36.47	34.66	1.81	
311.6	100.04	37.44	35.29	2.15	
319.8	102.55	38.13	36.04	2.08	
328.0	105.02	38.720	36.88	1.84	
336.2	107.52	39.40	37.42	1.98	
344.4	110.05	39.98	38.14	1.84	
352.6	112.07	40.80	38.82	1.98	
360.8	114.70	41.10	39.30	1.80	
369.0	117.13	41.96	39.90	2.06	
377.2	119.53	42.69	40.58	2.11	
385.4	122.02	43.53	41.13	2.40	
393.6		44.23	42.05	2.18	
401.7		44.84	42.53	2.31	
409.9		45.51	43.44	2.07	
418.1		46.16	43.88	2.28	
426.3		46.82	44.58	2.24	
434.5		47.41	45.19	2.22	
442.7		48.19	45.82	2.37	
450.9		48.79	46.26	2.53	
459.1		49.34	47.08	2.26	
467.3		49.94	47.66	2.28	

475.5		50.50	47.87	2.63	
483.7		51.24	48.89	2.35	
491.9		51.88	49.49	2.39	
500.1		52.43	50.01	2.42	
508.3		52.73	50.12	2.61	
516.5		53.25	51.07	2.18	
524.7		53.64	51.26	2.38	
532.9		53.72	51.20	2.52	
541.1		54.18	51.74	2.44	
549.3		54.72	51.97	2.75	
557.5		55.29	52.80	2.49	
565.7		55.89	53.35	2.54	
573.9		56.42	53.98	2.44	
582.1		57.04	54.45	2.59	
590.3		57.63	55.04	2.59	
598.5		58.13	55.50	2.63	
606.7		58.80	56.04	2.76	
614.9		59.24	56.49	2.75	
623.1		60.38	56.87	3.51	
631.3		60.30	57.52	2.78	
639.5		60.78	57.93	2.85	
647.7		61.10	58.25	2.85	
655.9		61.57	58.76	2.81	
664.1		62.00	59.21	2.79	
672.3		62.47	59.62	2.85	
680.5		62.77	59.89	2.88	
688.7		63.38	60.18	3.20	
696.9		63.80	61.06	2.74	
705.1		64.65	61.34	3.31	
713.3		65.10	61.60	3.50	

721.5		65.67	61.35	4.32
729.7		65.56	62.32	3.24
737.9		65.83	62.92	2.91
746.1		67.06	64.17	2.89
754.3		67.55	64.56	2.99
762.5		67.89	64.71	3.18
770.7		68.48	65.31	3.17
778.9		68.87	65.83	3.04
787.1		69.23	66.12	3.11
795.3		69.79	66.59	3.20
803.5		70.22	67.17	3.05
811.7		70.30	67.52	2.78
819.9		71.35	67.85	3.50
828.1		71.44	67.93	3.51
836.3		71.68	68.58	3.10
844.5		72.38	68.76	3.62
852.7		72.62	69.55	3.07
860.9		73.03	69.80	3.23
869.1		73.24	70.18	3.06

Experiment N 3 $q = 0.069$ mg/cm^2

t, μs	X_0, mm	X_1, mm	X_2, mm	L, mm
8.2	12.60			
16.4	14.65	11.70	10.44	1.26
24,5	17.06	12.63	11.31	1.32
32.7	19.57	13.47	12.18	1.29
40.9	22.05	14.49	13.10	1.39
49.1	24.60	15.70	14.00	1.70
57.2	26.40	16.01	14.33	1.68
65.4	28.88	17.04	15.02	2.02
73.6	30.98	17.90	15.85	2.05
81.8	33.44	18.41	16.40	2.01
90.0	35.91	19.61	17.16	2.45
98.1	38.49	20.43	18.00	2.43
106.3	40.89	21.29	18.84	2.45
114.5	43.46	22.13	19.81	2.32
122.7	45.99	23.13	20.53	2.60
130.9	48.49	24.04	21.43	2.61
139.0	50.96	24.92	22.26	2.66
147.2	53.37	25.80	23.09	2.71
155.4	55.49	26.25	23.89	2.36
163.6	58.00	26.96	24.21	2.75
171.8	60.56	27.72	25.02	2.70
179.9	63.03	28.68	25.98	2.70
188.1	65.56	29.45	26.68	2.77
196.3	68.16	30.33	27.61	2.72
204.5	70.61	31.25	28.31	2.94
212.6	73.17	32.06	29.17	2.89
220.8	75.55	32.83	29.92	2.91

229.0	78.10	33.75	30.66	3.09
237.2	80.68	34.54	31.62	2.92
245.4	83.17	35.29	32.41	2.88
253.5	85.62	36.09	33.21	2.88
261.7	88.00	36.89	33.99	2.90
269.9	90.61	37.66	34.76	2.90
278.1	93.15	38.19	35.52	2.67
286.2	95.70	39.08	36.12	2.96
294.4	98.10	39.85	37.00	2.85
302.6	100.61	40.56	37.71	2.85
310.8	103.07	41.49	38.32	3.17
319.0	105.64	42.18	39.20	2.98
327.2	108.05	43.08	39.93	3.15
335.3	110.46	43.66	40.66	3.00
343.5	112.97	44.41	41.33	3.08
351.7	112.96	45.19	42.03	3.16
359.9	117.85	45.95	42.74	3.21
368.0	120.37	46.59	43.50	3.09
376.2	123.00	47.12	44.20	2.92
384.4	125.36	47.96	44.93	3.03
392.6	127.84	48.27	45.44	2.83
400.8		49.04	46.30	2.74
408.9		49.87	46.68	3.19
417.1		50.49	47.42	3.07
425.3		51.30	47.87	3.43
433.5		51.66	48.56	3.10
441.6		52.21	49.24	2.97
449.8		52.94	49.60	3.34
458.0		53.38	50.51	2.87
466.2		54.03	50.98	3.05

474.4		54.75	51.65	3.10	
482.6		55.00	52.15	2.85	
490.7		55.58	52.84	2.74	
498.9		56.31	53.57	2.74	
507.1		56.80	54.07	2.73	
515.3		57.57	54.65	2.92	
523.4		58.10	55.20	2.90	
531.6		58.70	55.85	2.85	
539.8		59.44	56.44	3.00	
548.0		60.06	56.89	3.17	
556.2		60.45	57.42	3.03	
564.3		61.06	58.19	2.87	
572.5		61.78	58.33	3.45	
580.7		62.45	58.96	3.49	
588.9		62.89	59.33	3.56	
597.0		63.22	60.16	3.06	
605.2		63.90	60.62	3.28	
613.4		64.57	61.15	3.42	
621.6		65.07	61.62	3.45	
629.8		65.64	62.20	3.44	
637.9		66.39	62.54	3.85	
646.1		66.86	63.10	3.76	
654.3		67.32	63.58	3.74	
662.5		67.86	64.18	3.68	
670.7		68.49	64.65	3.84	
678.8		68.96	64.73	4.23	
687.0		69.27	65.12	4.15	
695.2		69.78	65.66	4.12	
703.4		70.04	66.03	4.01	
711.6		70.54	66.42	4.12	

719.7		71.02	66.83	4.19	
727.9		71.67	67.09	4.58	
736.1		72.22	67.57	4.65	
744.3		72.75	68.06	4.69	
752.4		73.09	68.61	4.48	
760.6		73.66	69.02	4.64	
768.8		74.05	69.41	4.64	
777.0		74.51	69.84	4.67	
785.2		75.06	70.37	4.69	
793.3		75.48	70.76	4.72	
801.5		75.94	71.10	4.84	
809.7		76.39	71.47	4.92	
817.9		76.74	71.88	4.86	
826.1		77.23	72.37	4.86	
834.2		77.65	72.63	5.02	
842.4		78.02	72.92	5.10	
850.6		78.46	73.37	5.09	
858.8		79.06	73.56	5.50	
867.0		78.96	74.11	4.85	

Proceedings of the 2nd International Workshop on the Physics of Compressible Turbulent Mixing *November 1989*

Pleasanton, USA *Edited by V. Rupert*

Proceedings of the 2nd International Workshop on the Physics of Compressible Turbulent Mixing

November 1989

SHOCK PHYSICS

AWE FOULNESS

A. V. SMITH

Turbulent Mixing in Shock Tube Experimentswith a High Initial Perturbation

Pleasanton, USA

Edited by V. Rupert

SHOCK PHYSICS

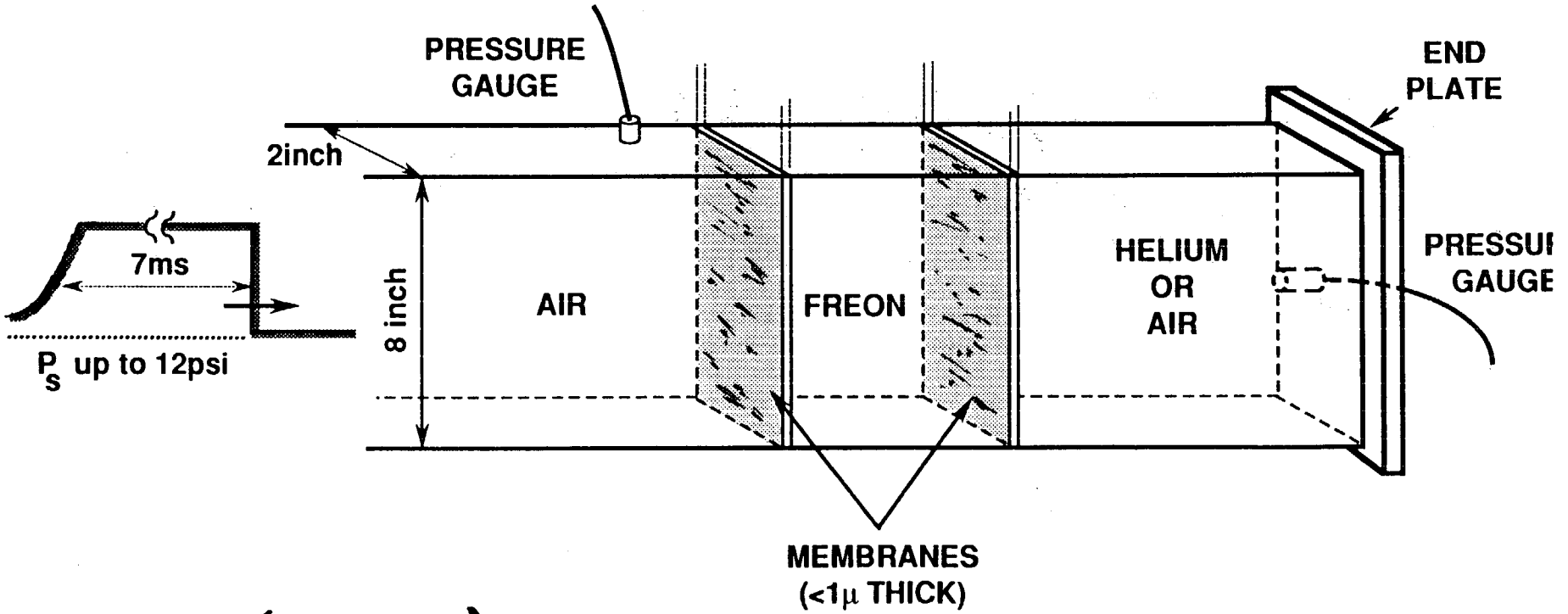

(20 x 5 cm.)

8 x 2 INCH SHOCK TUBE EXPERIMENTS

AS12

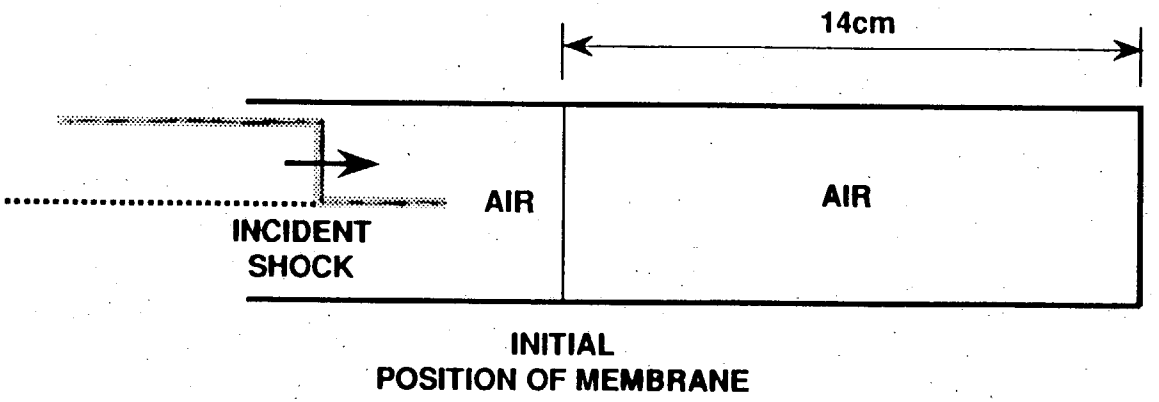
14cm
AIR
AIR
INCIDENT
SHOCK
INITIAL
POSITION OF MEMBRANE

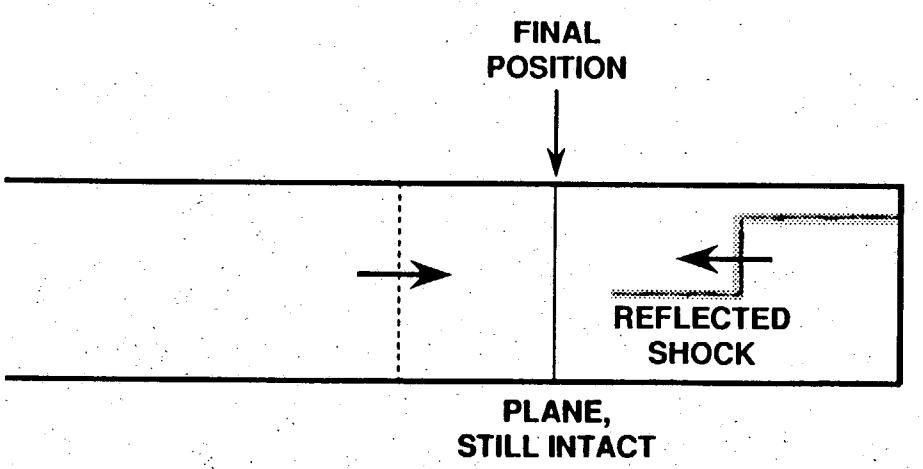
FINAL
POSITION
REFLECTED
SHOCK
PLANE,
STILL INTACT

AS 10

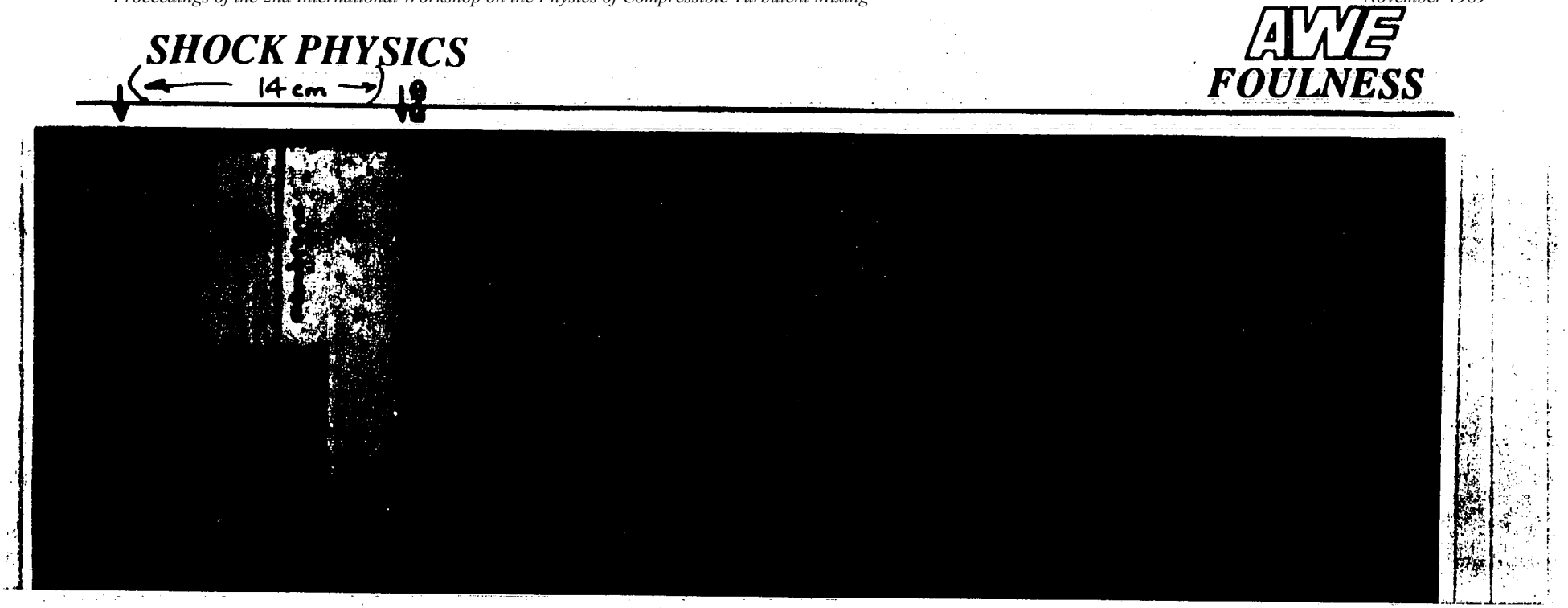
SHOCK PHYSICS
14 cm
AWE
FOULNESS

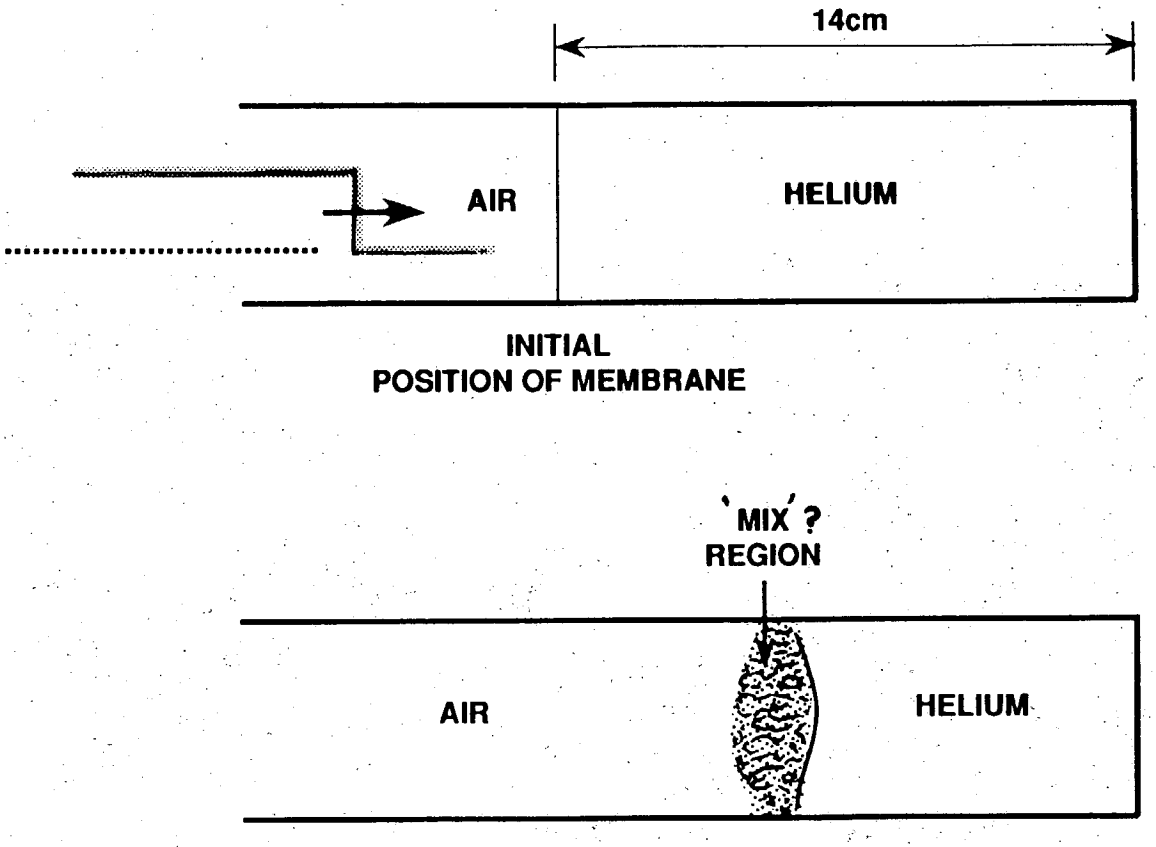
14cm
AIR
HELIUM
INITIAL
POSITION OF MEMBRANE
'MIX' ?
REGION
AIR
HELIUM

SHOCK PHYSICS

AWE FOULNESS

Pleasanton, USA *Edited by V. Rupert*

SHOCK PHYSICS

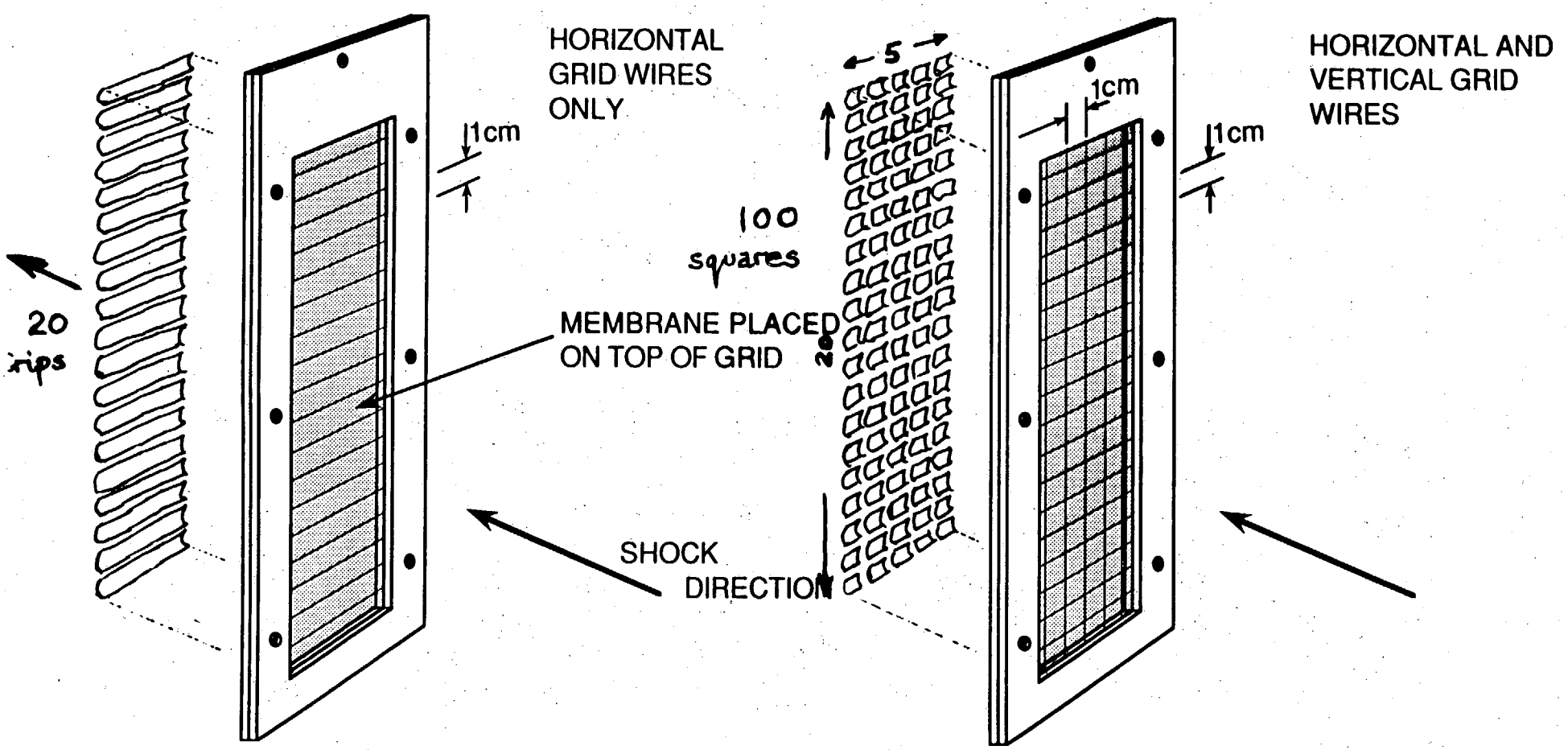

AS6

SHOCK PHYSICS

AWE
FOULNESS

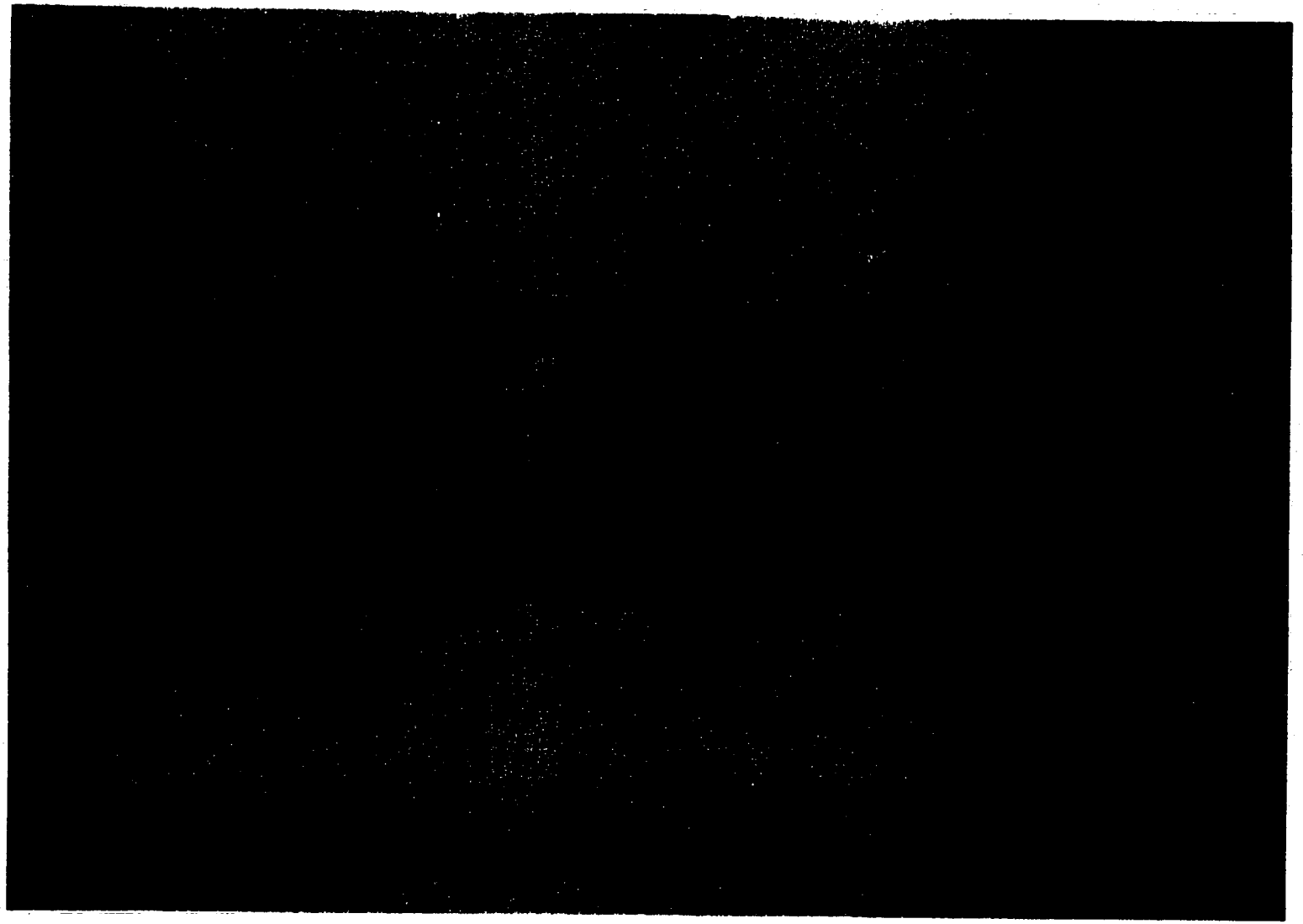

Pleasanton, USA *Edited by V. Rupert*

SHOCK PHYSICS

AWE FOULNESS

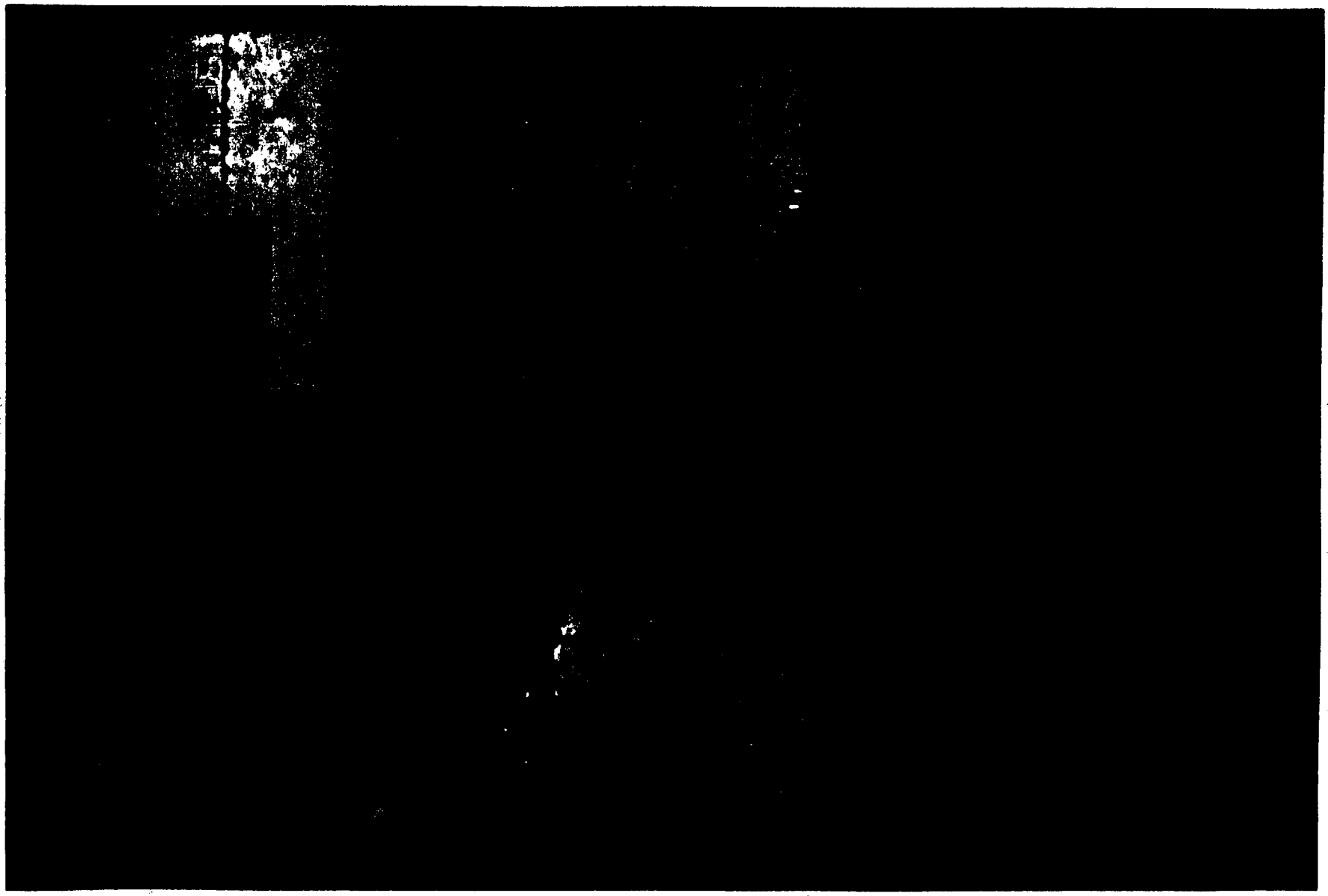

SHOCK PHYSICS

AWE
FOULNESS

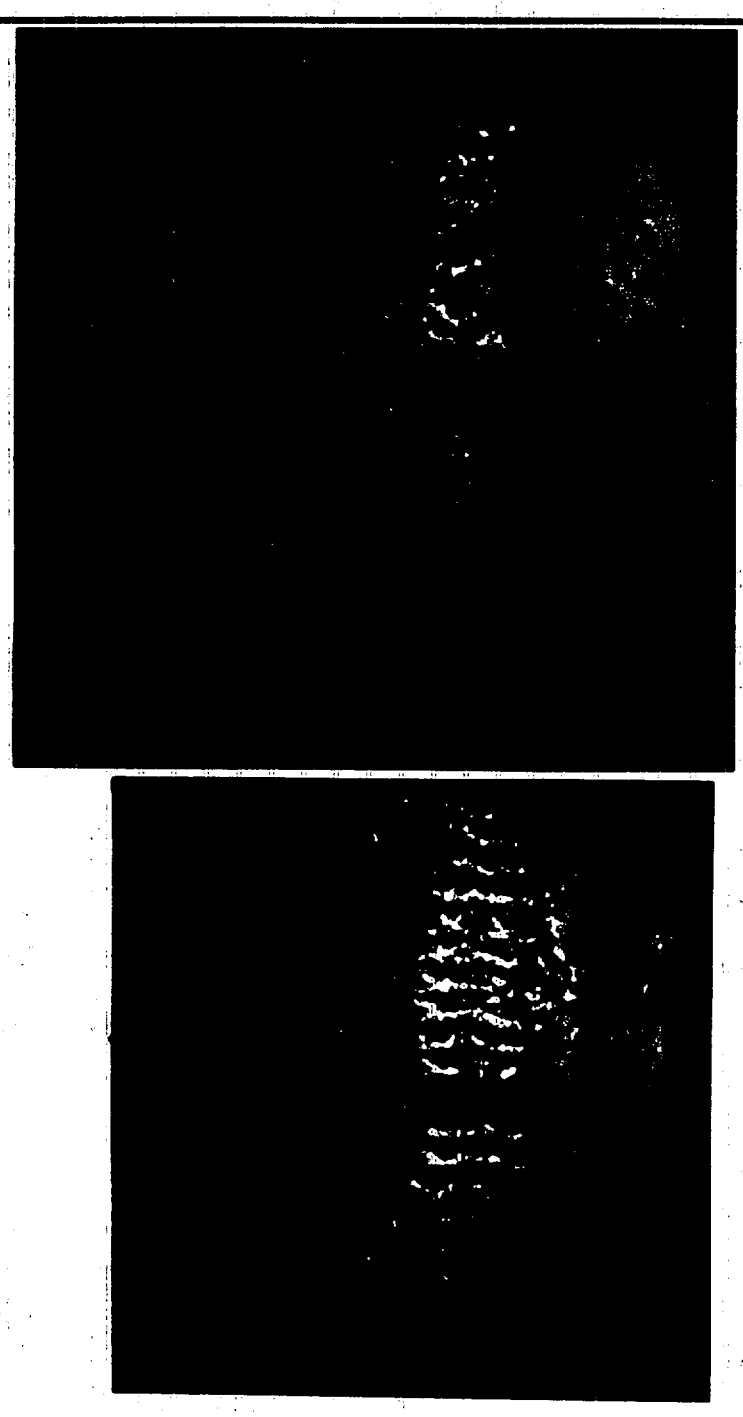

SHOCK PHYSICS

AWE FOULNESS

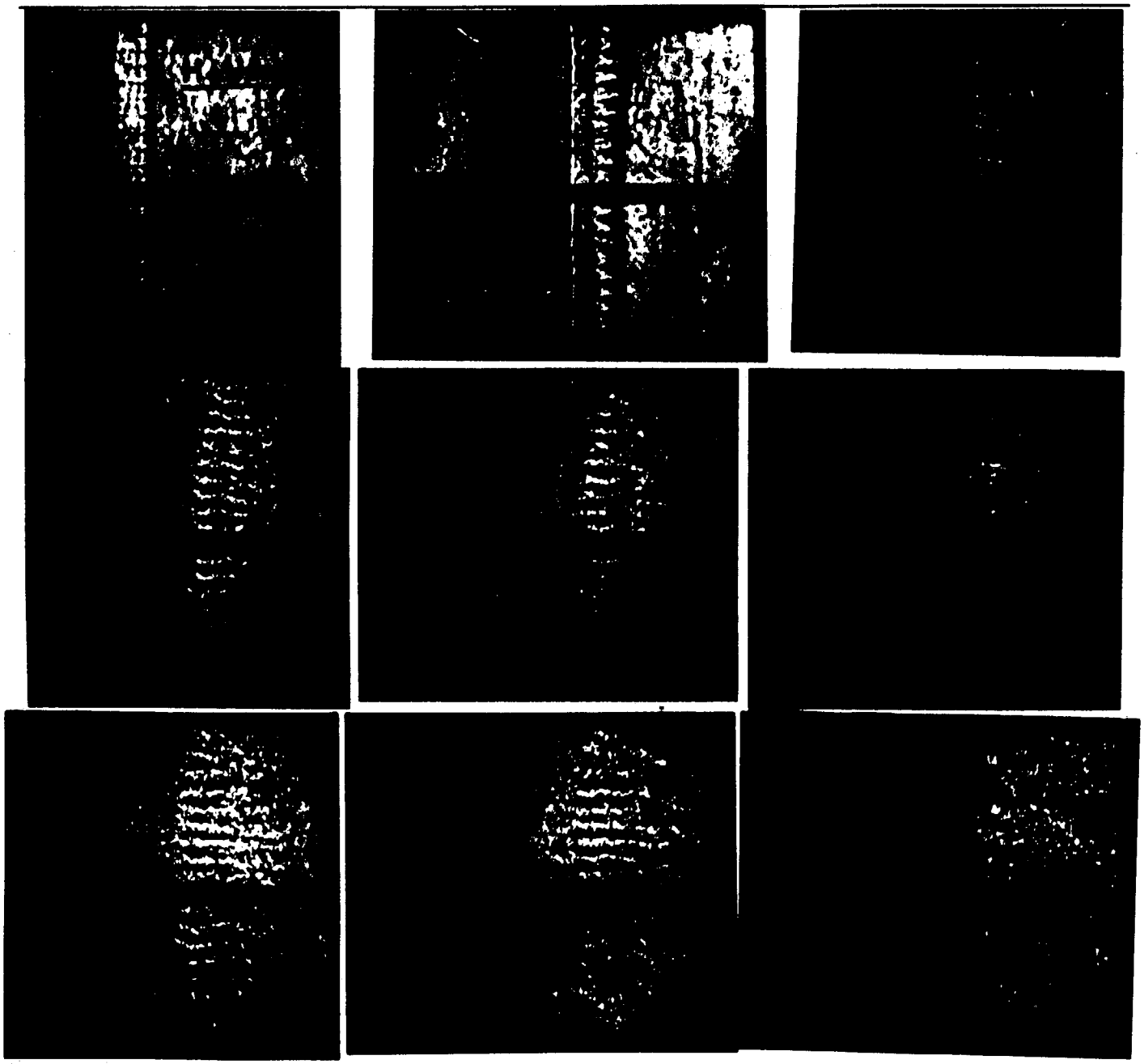

TIMES (AFTER SHOCK ARRIVAL AT MEMBRANE)

0.144, 0.298, 0,441ms

0.600, 0.750, 0.884ms

1.044, 1.348, 2.545ms

GRID WITH HORIZONTAL and VERTICAL WIRES

SHOCK PHYSICS

AWE FOULNESS

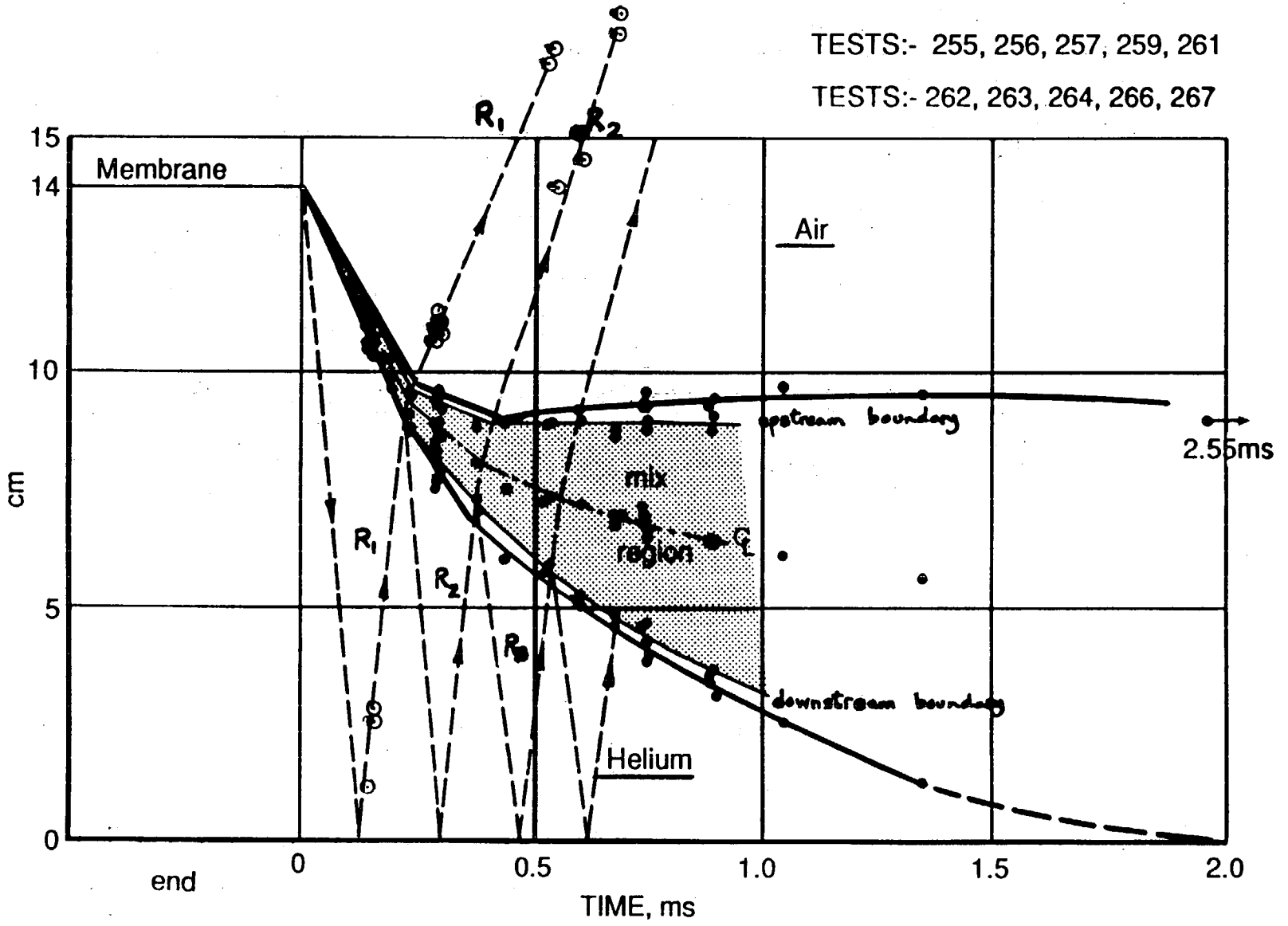

FURTHER WORK

1. Grids of different mesh size

2. Use of tandem shutter

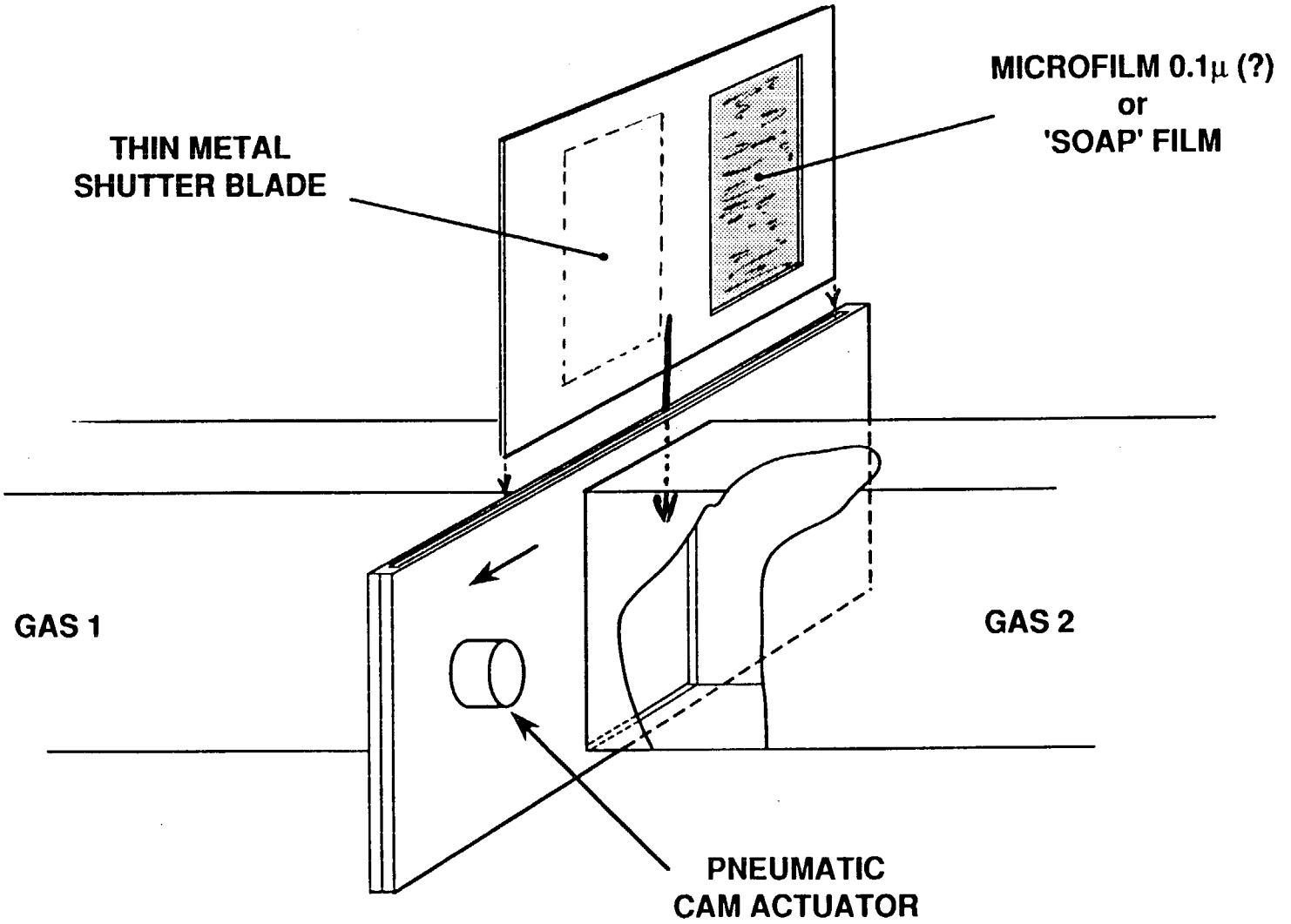

TANDEM SHUTTER DESIGN

AS 13

ABSTRACT

of the paper by E.E.Meshkov, V.V.Nikiforov, A.I.Tolshmjakov "About the Structure of Turbulent Mixing Layer at the Two-Gas Interface, Accelerated by Shock Waves"

Paper abstract for the international workshop on the inertial instabilities (Livermore, USA, November, 1989).

Structure of the turbulent mixing layer at the interface of two gases (air-helium), which is accelerated by a stationary shock wave series is experimentally investigated. The distribution of heavy das density (air) in the mixing zone was determined by light scattering in the smoke particles, mixed with the heavy gas. Between the heavy gas and a mixing layer a pronounced interface (in fact, a break in density) was established. The heavy gas penetrates into the mixing layer in the form of jets, having different scales. Characteristic jet scale grows with time. These jet fronts become indistinct due to Kelvin-Helmholtz instability. The substance density along the mixing zone (upstream) gradually decreases by pulses up to the light das density (helium).

ABOUT THE STRUCTURE OF TURBULENT MIXING LAYER AT TWO-GASES' INTERFACE, ACCELERATED BY SHOCK WAVES

E.E.Meshkov, V.V.Nikiforov, A.I.Tolshmjakov

The results of the experimental study of the structure of the turbulent mixing layer at the interface between two gases with different densities, which is accelerated by a series of stationary shock waves, are presented.

The experiments were conducted in the shock tube (ST) as it is described in ref.(1,2). The end of ST channel of 120x40 mm cross-section with transparent lateral walls consisted of the adjustable blocks, separated by an organic film of (3-4) 10^{-5} g/cm^2 specific weight. Block joints' planes were perpendicular to ST axis. Within the block volumes air, air with cigarette smoke, helium were (consequently) placed. The channel end was plugged with organic glass (a rigid wall). As in ref (1,2), the length of the block with helium was 169 mm. In such a geometry (air, air + smoke, helium, a rigid wall) the stationary shock wave with M = 1.3 accelerated the interface "air+ smoke+helium" by shocks. Then, this interface was slowed down by a series of shock waves, reflected from a rigid wall.

At a air-helium interface the turbulent mixing layer (TML) is formed. TML may be vizualized by a "light knife" method: through a transparent rigid wall in the tube end a light pulse passes from an pulsed laser with ~40 ns duration, being transformed by cylindrical lenses into a thin

"light knife". The light beam is unseen in helium region. But while the "light knife" crosses air and TML, where the smoke particles are more or less present, the light scattering in these particles forms the pattern of smoke particles' concentration distribution in the plane of a light beam.

According to the upper estimate the air motion is clearly "traced" by smoke particles in TML pulsations at scale of 0,6 mm and more.

The photoappratus with open shutter registered this picture. Thus, the only photograph was obtained for a given moment in each test.

Fig.1

Fig. I shows a photograph for one of the experiments with a "light knife" 6 mm thick at the moment t = 600 μs after the onset of the interface motion, being investigated. The TML has a rather clearly outlined edge to the left from a heavier air side and an obscure boundary to the right from light helium side. The air penetrates into the mixing layer in the form of the jets of different scales. Kelvin-Helmholtz instabilities cause the appearance of vortices at the jets' ends, mixing air and TML substance. The scattered light intensity is not homogeneous in TML - there, in average, air concentration gradually falls from the left to the right. In the layer the concentration distribution has a turbulent, pulsed character.

The film, placed originally between air and helium, is accelerated up to the velocity of an average motion at the distances of the tenths of a millimeter. At the motion onset

the film is unfolded towards the oncoming flow in the shock wave. Then, when accelerating, it is torn into pieces, and when in the motion, it is folded into balls. Their resistance to the flux becomes less, and when the environmental gas motion is slowed down, the film pieces fly out to the TML's edge and beyond its limits. In the frame we can see not only the film pieces under the light, but those, which are far away. The scattered in the smoke light makes them seen.

In the experiments conducted the initial smoke density and the registration conditions were selected so that one might neglect the scattered light absorption and the secondary scattering. So, one frame for a given moment was the result of each experiment. A frame negative of one of the experiments with "a light knife" 1.2 mm thick at moment t = 800 μs (fig.2) was photometered in a consequence along the horizontal lines (strings), which are parallel to the flux motion in a shock tube. The computer processed the data obtained. The results of photometration for each string were presented on a screen of a graphic display. The limits of string sections, corresponding the film pieces' image, may be defined by the spasmodic changes in density. One might identify the film pieces by the photography; which is marked by photometric string lines. The margins of these sections in the image were marked by moving cursors, and then the marked string section was replaced by a straight line, drawn through the marked points. Finally, after all image processing operations we obtained the scattered light intensity distribution along each photometry string. It corresponds to air density distribution in TML.

Fig 2

Fig. 3a
3б

In fig.3,a, the photometry results for string N5 (numerated according to fig.2) are given. In fig.3,b, the same string after all image processing operations is shown. Here, a concentration leap at the boundary between air and TML is clearly seen. Note, for different strings the amplitude and possition of this leap is different. In the mixing layer air concentration gradually drops by pulses up to zero the edge, adjacent to pure helium. In fig.4 density profile, $\tilde{\rho}$, of the air in TML, normalized by this value beyond the layer and averaged over 28 strings for the same experiment, is given. This profile has no concentration leap, that in the result of the averaging over the disturbances, different in scale, in the interface between air and mixing layer. Here, in fig.4, the profile of the average air density, computed in ref (2), is presented. The agreement of computation and experiment results is satisfactory.

Fig 4

Let's consider mechanism, leading to the TML development in the experiments described. At the onset of the film motion, separating gases at the interface, being investigated, is the source of the initial disturbances, which result in TML development, and thus it may notable affect the flow character. However, later, when the film goes away from the air - TML interface, in fact, it ceases to affect the TML development. The main mechanism, leading to the TML growth, is the instability (3,4). Each subsequent shock wave, arriving at the surface and reflected from a rigid wall, is a leap, accelerating jet growth of a heavy gas, penetrating

into the TML. The vortices at the jet ends spontaneously generate mixing of heavy and light gases. Simultaneously the jets of different scales are present, but, as a rule, they do not exceed the width of the TML. The characteristic scale of the jets increases with the TML growth in time.

Thus, the turbulent mixing layer structure at the surface between two gases (air-helium) , being accelerated and then slowed down by a series of stationary shock waves, was investigated. The heavy gas (air) density distribution in the mixing layer was defined by light scattering in smoke particles, mixed with air. It was found that between the heavy gas and mixing layer a clear enough interface (in fact, density break exists). The heavy gas penetrates into the mixing layer in the form of diffently scaled jets. The characteristic jet scale grows in time. Kelvin-Helmholtz instabilities cause the apperrance of vortices at the jets' ends, mixing air and TML substance. In the mixing layer the substance density drops gradually (upstream), by pulses, up to the density of light gas (helium).

REPERENCES

I. В.А.Андронов, С.М.Бахрах, Е.Е.Мешков, В.Н.Мохов, В.В.Никифоров, А.В.Певицкий, А.И.Толшмяков, ЖЭТФ, I976, т.7I, вып.2(8), стр.806-8II.

2. В.А.Андронов, С.М.Бахрах, Е.Е.Мешков, В.В.Никифоров, А.В.Певицкий, А.И. Толшмяков, ДАН СССР, I982, т.264, № I, стр.76-82.

3. R.D.Richtmyer, Comm. on Pure and Appl. Math. 1960, v.13, p.297.

4. Е.Е.Мешков, Изв. АН СССР, МЖГ, I969, № 5, стр.I5I.

Captions for paper by E.E.Meshkov, V.V.Nikiforov, A.I.Tolshmjakov.

Fig.1. Photography of TML at the interface of two gases: (air + smoke) - helium in a scattered light. Pulsed laser light as a "light Knife" (thickness; h = 6 mm) goes from right to left. At moment t = 600 μs after the onset of investigated interface motion.

Fig.2. Photography of TML at moment t = 800 μs, h = 1.2 mm. In the photography positions are marked, by which the negative photometry was done.

Fig.3. The results of photometry and of the subsequent negative processing of the experiment photograph (fig.2) along line N 5 (the image on the display screen).
a) Density profile of negative blackening D. II - the sections, corresponding the images of film pieces.
b) Scattered light intensity distribution I after the processing.

Fig.4. Averaged distribution of the relative density, $\tilde{\rho}$, of air in TML, normalized by the value beyond the TML. Distance, X, is estimated from the original position of air-helium boundary. 1 - experiment (according to fig.2), 2 - simulation (2).

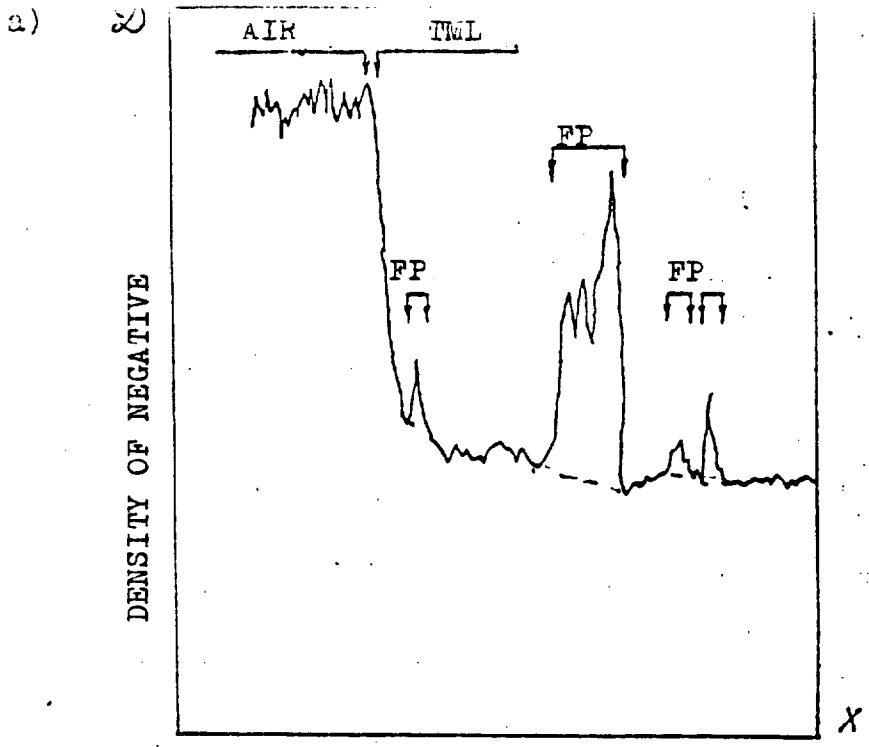
а)
D
AIR
TML
FP
FP
FP
DENSITY OF NEGATIVE
X

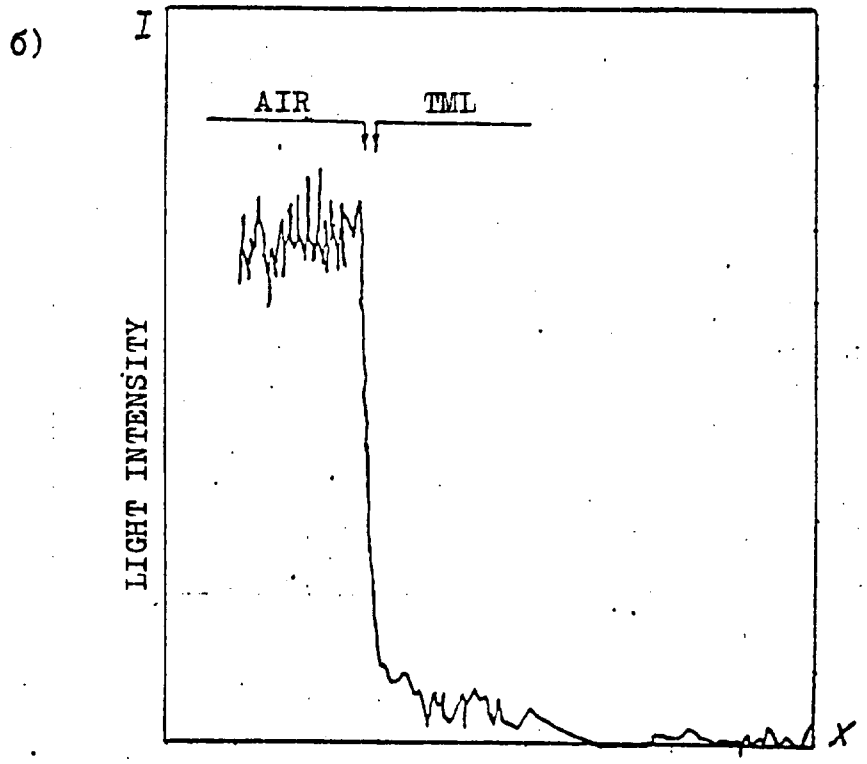
б)
I
AIR
TML
LIGHT INTENSITY
X

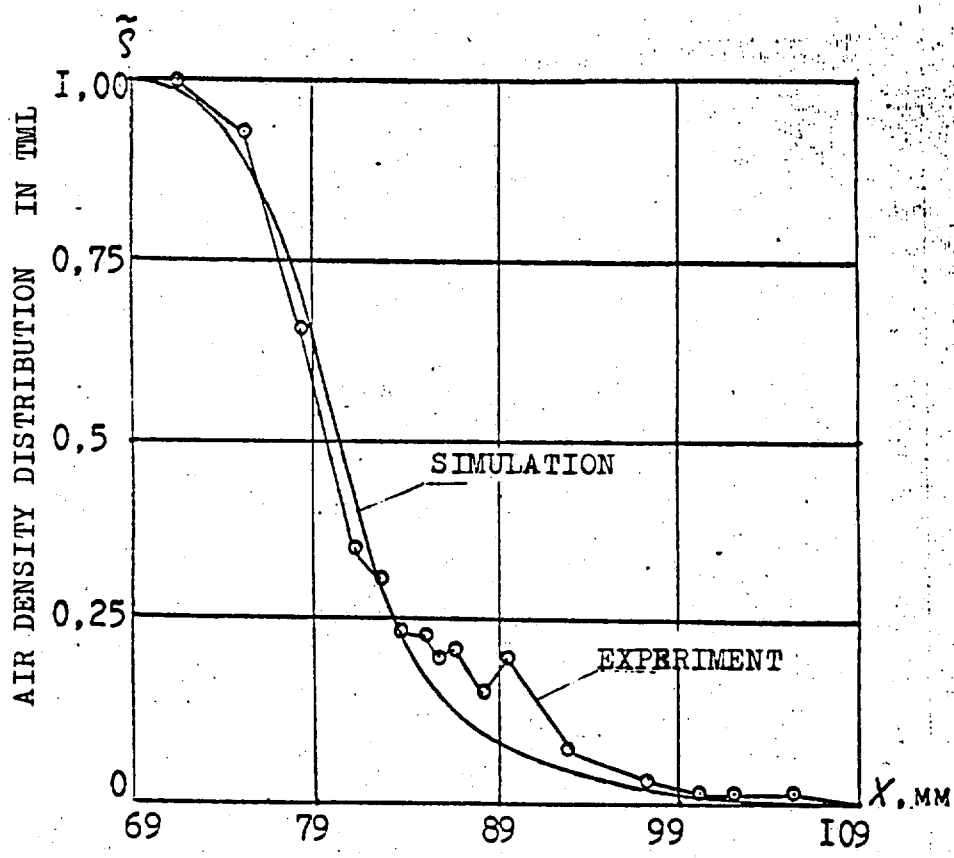

$\rho_{0_{Air}} = 1.204 \cdot 10^{-3}\ g/cm^3$

800 μsec

$\tilde{\rho} = ?$

$\frac{\text{Air mass}}{\text{Volume}}$ $\tilde{\rho} = \frac{\rho - \rho_1}{\rho_2 - \rho_1}$

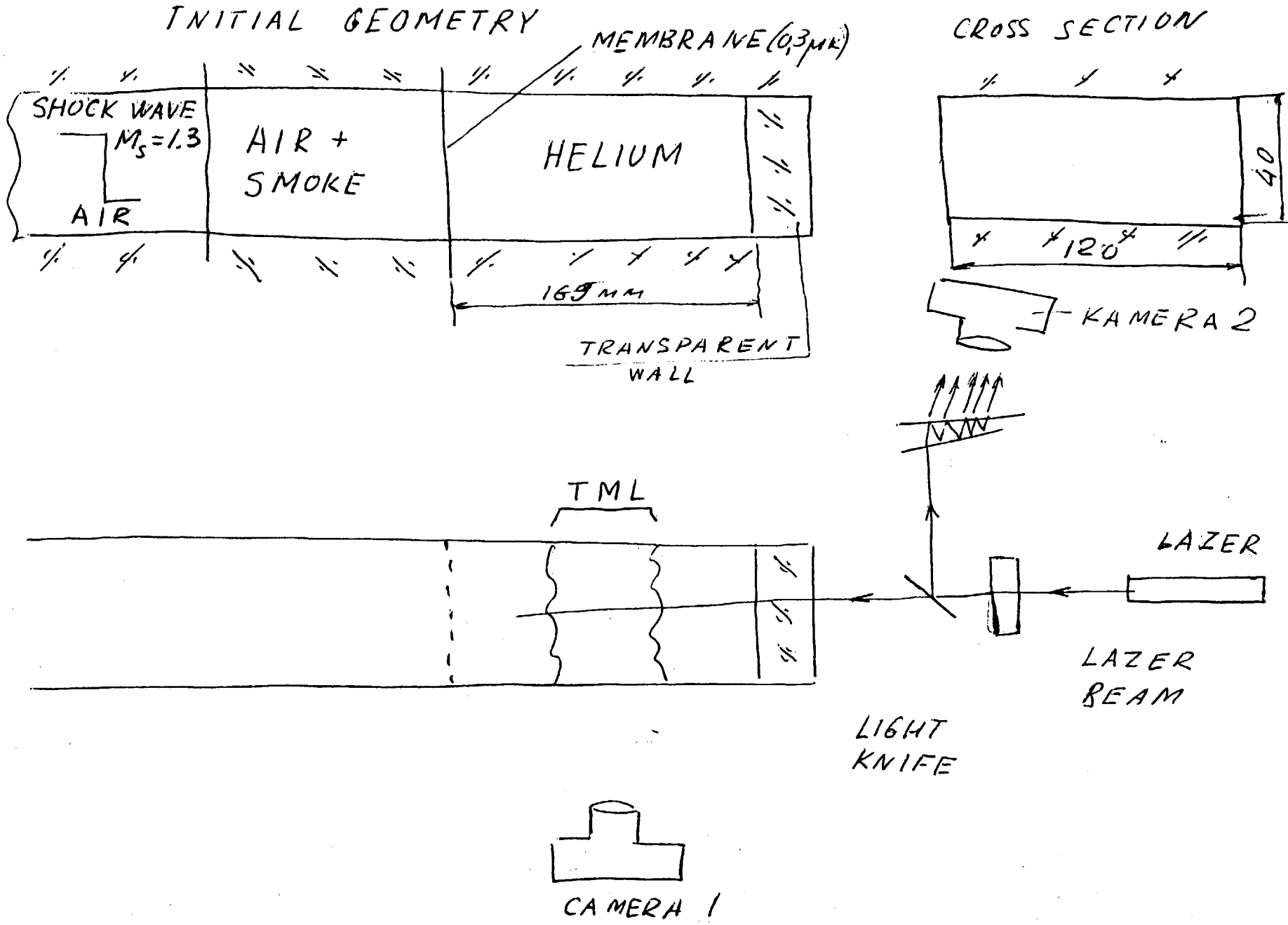

EXPERIMENTAL SET UP (TOP VIEW)


I 2 3 4 5 6 7 8 9 I0 II I2 I3 I4 I5 I6 I7 I8 I9 20 2I 22 23 24 25 26 28

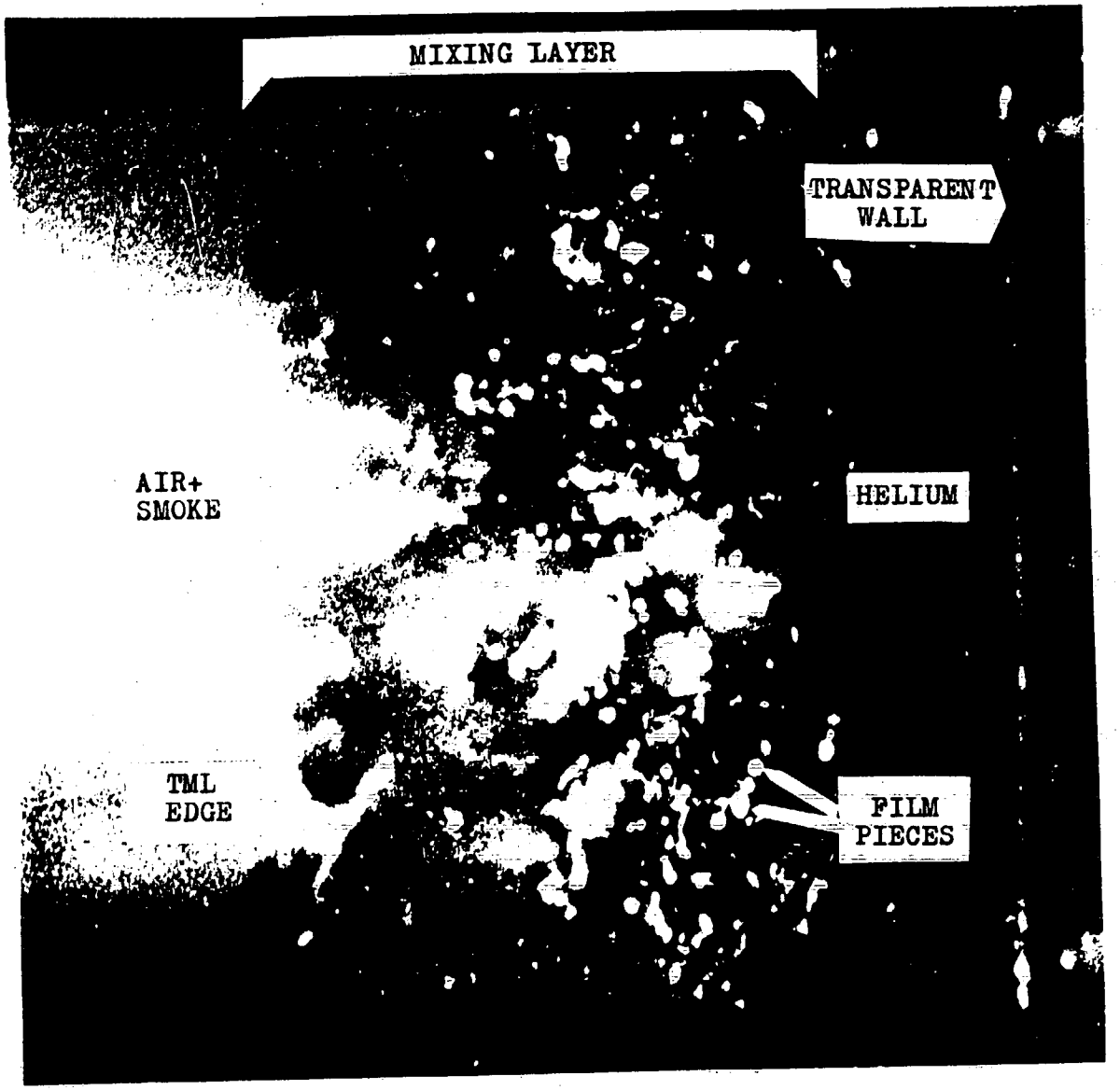
MIXING LAYER
TRANSPARENT WALL
AIR+ SMOKE
HELIUM
TML EDGE
FILM PIECES

MOLECULAR MIXING PRODUCED BY RAYLEIGH-TAYLOR INSTABILITY

P.F. Linden and J.M. Redondo
Department of Applied Mathematics & Theoretical Physics
University of Cambridge, Silver Street, Cambridge CB3 9EW, UK

This work describes the molecular mixing produced by Rayleigh-Taylor instability of two miscible fluids at low density ratios. Dense salt solution is superimposed on a layer of fresh water and the experiment is initiated by withdrawing a horizontal plate from the interface between the two layers. Gravitational instabilities causes the two layers to mix across a region whose thickness increases cuadratically with time. The flow structure is visualized using dye,shadowgraph and laser induced fluorescence and related to conductivity measurements. It is observed that at small amplitudes the fastest growing modes agree with the predictions of the linear theory. As the instabity grows to large amplitude there is an amalgamation of scales. The growing front of the mixing region is three dimensional and this is revealed by both side and plan views observations. Superimposed on these large scale features are further small scale structures generated both by secondary Rayleigh-Taylor instabilities and also by shear instabilities in the form of Kelvin-Helmholtz billows. It is found that these additional small scales are responsible for much of the mixing across the turbulent front. The molecular mixing of the two fluids is mainly produced by these small scales as pH indicator visualization techniques show. Fractal analysis of the mixing front is also used to characterise the small scale entrainment. Measurements of conductivity and of dye intensity confirm the importance of the entrainment at the sides of the larger structures formed by amalgamation of the initial instabilities.

Molecular mixing in Rayleigh-Taylor unstable flows

1. INTRODUCTION

This report describes the work carried out under this contract. The aim of the research is to determine the amount of molecular mixing that occurs during the Rayleigh-Taylor (RT) instability process, using laboratory experiments . The results are to be extrapolated to the case of laser induced implosion of glass encapsulated deuterium targets. These targets are spherical, and during the implosion process, the dense glass is accelerated towards the less dense deuterium and RT instability ensues.

The modelling approach adopted here is to use two miscible liquids, with the dense liquid accelerated by gravity towards the less dense liquid. The properties of the mixing process are examined using a range of laboratory techniques as outlined below. The density differences between the two liquids is small, particularly when compared to those encountered in the basic application, and so some assessment of the scaling effects is appropriate.

The format of this report is as follows. Section 2 summarises the main results of earlier work, both theoretical and experimental. The present laboratory set-up and the various techniques which are used are described in section 3. The results of the basic growth of the mixing layer and the appropriateness of the scaling are presented in section 4. together with some measurements of the detailed mixing process. Some

conclusions and suggestions for further work are given in the final section.

2. PREVIOUS WORK

The stability of an interface between two superposed fluids of different density was studied by Rayleigh (1900) and Taylor (1950) for the case when the dense fluid is accelerated towards the less dense fluid. A good summary of the linear theory can be found in Chandrasekhar (1961). For inviscid fluids, the interface is always unstable, with the growthrate of the unstable modes increasing as their wavelengths decrease. The instability of the short waves can be reduced by dissipative mechanisms such as surface tension or viscosity, and then linear theory predicts the maximum growthrate to occur at a finite wavelength. For the viscous two-layer case,where the upper layer (density ρ_1) is denser than the lower layer (density ρ_2), the wavelength λ_m of maximum growthrate is

$$\lambda_m \approx 4\pi \left(\frac{\nu^2 \ (\rho_1 + \rho_2)}{g \ (\rho_1 - \rho_2)} \right)^{1/3} , \qquad (2.1)$$

where ν is the mean kinematic viscosity of the two layers and g is the acceleration of gravity. The corresponding maximum growthrate is

$$n_m \approx \left(\frac{2g\pi(\rho_1 - \rho_2)}{\lambda_m(\rho_1 + \rho_2)} \right)^{1/2} . \qquad (2.2)$$

Molecular mixing in Rayleigh-Taylor unstable flows

While the linear theory for two infinite layers is well established, the development of the instability to finite amplitude is not amenable to analytic treatment. There have been a number of semi-analytical and numerical studies in recent years, but they all involve simplifying assumptions which raise serious doubts about their validity particularly when applications to mixing are sought. An overview of the subject by Sharp(1984) characterised the development of the instability through three stages before breaking up into chaotic turbulent mixing.

Stage 1: a perturbation of wavelength λ_m grows exponentially with growthrate n_m.

Stage 2: when this perturbation reaches a height of approximately $\frac{1}{2}\lambda_m$, the growthrate decreases and larger structures appear.

Stage 3: the scale of dominant structures continues to increase and memory of the initial conditions is lost; viscosity does not affect the growth of the large structures.

This latter result concerning the independence of the large amplitude structures on the initial conditions has led to the result that the width of the mixing region depends only on ρ_1, ρ_2, g and time, t. Then dimensional analysis gives

$$\delta = 2cg \frac{\rho_1 - \rho_2}{\rho_1 + \rho_2} t^2 \qquad (2.3)$$

where c is considered to be a (universal) constant.

In a series of experiments, Read and Youngs (1984) found

values of c in the range 0.030-0.035. Numerical calculations in two-dimensions have also been carried out by Youngs (1984) in which he obtained values of c = 0.020-0.025. The smaller value of c in the numerical calculations have been attributed to the absence of three-dimensional effects. Further recent experiments by Smeeton and Youngs (1988) have confirmed (2.3) with the best value of c = 0.03 for a wide range of density ratios $\frac{\rho_1}{\rho_2}$ from 2 - 600.

3.EXPERIMENTAL METHODS

The experiments were carried out in a perspex tank 500mm deep, 400 mm long and 200 mm wide. The tank had a removable aluminium sheet 1.5 mm in thickness which separated a layer of brine from a layer of fresh water below (see figure 1). The two layers of fluid were initially at rest, and the experiment was initiated by sliding the aluminium sheet horizontally through a slit in one end wall of the tank. Routine flow visualisation was either by shadowgraph or by adding dye to one of the layers. Records of the flow were made using video and still photography.

The experiments were conducted with two layers of equal depth, with a range of density differences $\frac{\rho_1-\rho_2}{\rho_1+\rho_2}$ from 1×10^{-4} to 5.0×10^{-2} . These values were chosen to enable sufficiently high Reynolds numbers to be achieved during the development of the instability, while ensuring there was sufficient time before the whole two-layer system overturned.

Quantitative measurements were made using the following techniques.

3.1 Dye visualisation

Small amounts of dye (food colouring) were added to one of the layers and the flow was observed as the instability progressed. Two main results were obtained from an analysis of these images.

(i) the maximum extent,δ, of the mixed region. This was measured directly from the video images. Anomalous regions were observed near the sides of the tank, and values quoted below were taken from the central region.

(ii) dye concentration. The values were obtained by determining the intensity of the light transmitted through the tank, using an image processing system on the digitised video frames. The values are integrated across the width of the tank.

3.2 Laser induced fluorescence

In order to resolve the detailed structure of the mixing region, the flow was also visualised by using a thin sheet of laser light to illuminate a plane perpendicular to the camera. Side, end and plan views were obtained. A 2W argon laser was used to produce a 2 mm thick sheet of high intensity light. Fluorescein dye was added to one of the layers, and this produced a brilliant green image in the laser light. The edge of the mixing region was clearly demarcated by this technique and clear

images of the small scale structures were obtained. Fractal analysis of the edge of the mixing region was carried out, using an automated procedure with the image processing system.

As with the dye measurements in 3.1, the fluorescein is only added in very small quantities so that the dye acts as a passive tracer.

3.3 Image processing

Automatic image processing has been installed using a Data Translation frame grabber and software on a IBM PC - AT compatible computer. This system allows up to 4 video images to be stored and for analysis to be carried out in order to determine light intensity measurements. Corrections of light variations in the background are made by subtracting two images, and calibrations of dye concentration with density allow quantitative estimation of mixing to be made.

3.4 Conductivity measurements

A 10 channel conductivity meter, monitoring up to 10 independent probes was used to obtain measurements of salt concentration. The output of the conductivity meter was stored on a BBC computer via a CUBAN data processing system. Maximum sampling frequencies were 50 hz, which corresponds

to the fastest time reponse of the conductivity probes. A series of tests showed that the spatial response of the probes was approximately 1 mm, Redondo(1987).

The output of the conductivity probes were calibrated against the salt concentration (and temperature) of the solutions. The response was found to be linear over the range of density differences used, and accurate to 1% of the full scale reading. The dependence on temperature was minimised by carrying out all experiments at room temperature, having let the solutions stand overnight.

The conductivity probes were arranged in a number of different configurations, as described when the results are presented. In addition, laser induced fluorescence was used in conjunction with the conductivity measurements in order to relate the measurements to the observed flow structures.

4.EXPERIMENTAL RESULTS

4.1 Plate removal time

The ideal situation, with which the experiments are designed to correspond, is the instantaneous removal of the aluminium plate between the layers with no disturbance to the planar interface. The time τ taken to remove the plate from the tank is then a compromise between two undesirable effects viz, the disturbance caused by the viscous stresses and vortex shedding from the trailing edge of the plate, and the timescale

for the onset of the instability compared with τ . The former are increased as τ decreases while the non-uniformities in the development of the interface are increased as τ increases.

Practical considerations limited the withdrawal time from 0.2 - 0.45 s. The withdrawal Reynolds number Re, based on the length of the tank, is then approximately 5×10^5. The timescale for the development of the instability is (see 2.3) .

$$t = \left(\frac{\delta(\rho_1 + \rho_2)}{2cg(\rho_1 - \rho_2)} \right)^{\frac{1}{2}} \quad . \tag{4.1}$$

For the values of ρ_1, ρ_2 quoted above the time taken for the whole box, of depth H, to overturn varied between 3 and 30 seconds. Except at the largest density differences, τ is much less than the overturning times and non-uniformities in the growth of the mixing region between the two ends of the box are small.

An estimate of the strength of the undesirable disturbances is provided by the kinetic energy, per unit area, KE imparted to the fluid due to the withdrawal of the plate. This is given by

$$KE = \rho C_D U^2 \delta_0 \quad , \tag{4.2}$$

where δ_0 is the vertical scale of the region affected by the plate, C_D is the drag coefficient and U is the average speed of the plate. We identify δ_0 as the size of the initial perturbations and is typically 1-2 cm. (see figure 6 and table 1). The speed

$U = \frac{L}{\tau}$, where L is the length of the tank and $C_D = 5 \times 10^{-3}$ is the value appropriate to the Reynolds number $Re = 5 \times 10^5$ (Hunsaker and Riatome,(1949)). This value of KE is compared to

$$PE = \frac{1}{8} \frac{g(\rho_1 - \rho_2)H^2}{(\rho_1 + \rho_2)} , \tag{4.3}$$

the amount of potential energy in the initial unstable stratification; and the results are shown on figure 2. Here and in the later figures we have defined a reduced gravity g' between the layers as

$$g' = g\frac{\Delta\rho}{\rho} = \frac{2g(\rho_1 - \rho_2)}{\rho_1 + \rho_2} . \tag{4.4}$$

Values of g' vary between $0.38 - 95\ cm\ s^{-2}$. In order to restrict the input kinetic energy to less than 10% of the initial potential energy it is necessary to use values of $g' > 10\ cms^{-2}$. Since KE increases like τ^{-2}, further decrease in the time taken to withdraw the plate further restricts the range of usable density differences.

With these considerations in mind, many of the detailed measurements were made with values of $g' \approx 20cm\ s^{-2}$.

4.2 The thickness of the mixing region

Measurements of the width, δ, of the mixing region were taken from flow visualisation experiments. Both shadowgraphs (figure 3), in which both edges of the mixing region are visible,

and dye visualizations (figure 4), in which only one edge is visible were used. There are anomalous regions near the wall where the flow accelerates due to image vortices produced by the wall boundary conditions. In the central portion of the tank the mixing region had a relatively uniform thickness and this value was recorded during the growth of the instability.

An example for one experiment is shown in figure 5. In accordance with (2.3) the data exhibit a quadratic dependence on time t. A least squares fit to the data , with $\delta^{1/2}$ plotted against t is shown, and from this we see that the line does not pass through the origin. The thickness appears to have a finite, non-zero value at t = 0, and we denote this vertical origin as δ_0. In the example shown $\delta_0 = 0.8cm$. This initial thickness is due to the disturbances generated during the withdrawal of the plate, and is consistent with the observed sizes of the vortices shed by the plate (see figures 3 and 4). The dependences of δ_0 on g' and the energy ratio KE / PE are shown on figures 6a and 6b, respectively. There is no trend with energy ratio, but the decrease in δ_0 with g' reflects the faster growth of the instability with increasing density difference.

Once the initial conditions are forgotten, the rate of growth of the mixing region $\frac{d\delta}{dt}$, depends only on δ and g' (assuming molecular effects are negligible). Dimensional analysis then gives

$$\frac{d\delta}{dt} = 2(cg'\delta)^{1/2} \quad , \tag{4.5}$$

and integration gives

$$\delta^{1/2} = \delta_0^{1/2} + (cg't^2)^{1/2} \quad , \tag{4.6}$$

where the initial condition $\delta = \delta_0$ at t = 0 has been used. When the mixing region is thick $\delta >> \delta_0$, (4.6) becomes $\delta = cg't^2$, which recovers (2.3).

Values of c are determined from the slopes of plots such as shown in figure 5. A total of 49 experiments were carried out (see table 1) and the values of c are plotted against g' in figure 7. At low values of g', the values of c are somewhat scattered, but at higher values c is approximately constant and takes the value $c = 0.035 \pm 0.005$. This value is in agreement with the values obtained at large density ratios by Read and Youngs (1984), Smeeton and Youngs (1988), and this agreement gives confidence that the present experiments are accurately modelling these earlier experiments.

4.3 Dense fluid volume fraction

Measurements of dye intensity were made which allow estimates of the dense fluid volume fraction to be made. Dye was added to the upper layer (concentration 1) while the lower layer was free of dye (concentration 0). By measuring the light

intensity, and referring it to a calibrated sample, it is possible to determine the amount of dye along any horizontal line across the tank as a function of time. Assuming that the dye acts as a passive tracer, this measurement gives a width average of the fraction of dense fluid at any point as a function of time.

Video images of the experiment were digitised providing 513 x 513 pixel frames in up to 256 intensity levels. Figure 8 shows the hardware used. Non-uniformities in background lighting were removed by subtracting the initial background from each frame. Some care was necessary with this procedure to avoid TV line phase changes. An example of a false colour image of dye intensity is shown in figure 9.

Examples of light intensity contours at different times in one experiment are shown in figure 10. The main feature to note from the figure is the rapid change in light intensity at the edge of the descending dense fluid. The thickness of the transition region is about 1 cm., and this suggests that much of the mixing is occurring at the edges of the large scale protuberances. Within the larger-scale structures the variations in concentration are relatively weak.

Vertical profiles of light intensity are shown in figures 11 and 12. These profiles show only the lower half of the tank, and are normalised so that initially the upper layer corresponds to unit concentration and lower layer to zero concentration. The advance of the mixing region is clearly shown, with a mean increase in dye concentration with height, as shown on the

averaged profiles shown in figure 11. From figure 10, and from the flow visualisation studies, we know that the dense fluid falls as semi-coherent large scale structures. Figure 12 shows the vertical profiles through one of these structures, rather than averaged along the length of the tank as in figure 11. The rapid increase in dense fluid across the base of the structure, and the relatively uniform interior is clearly visible. It also seems the case from figure 12 that the change in concentration gets sharper as the disturbance advances.

4.4 Indicator visualisation

A series of experiments have been carried out using a pH indicator to mark the points in the flow where molecular mixing is taking place. The indicator used is phenolphthalein which undergoes a marked colour change from colourless to pink in the pH range 8.3-10. The reaction for this indicator is very fast (Caldin, 1964). Acid plus indicator are added to the lower layer and base is added to the upper layer.

In order to allow quantitative measurements to be made, and to avoid any sensitivity to the detailed chemistry of phenolphthalein, the upper layer was chosen to have $pH_1 \approx 12$. The pH of the solution was measured using a pH meter accurate to 0.1. Values of the lower layer pH were chosen so that different levels of molecular mixing could be determined (Youngs, 1989).

Several experiments were made producing the change in

colour at the 50% level of mixing and at the 1% level of mixing. With a pH of 12 in the upper layer, the transition in pH is very sharp. Figure 13 shows experimental results of the final pH of a 50% mixture where the lower layer pH is indicated in abscissa and the upper layer pH is 12.

Figure 14 shows an example of the development of the mixing region as marked by the colour change at the 50% level. The regions of colour change occur mainly around the edges of the large scale structures, in agreement with the dye intensity measurements described in 4.3. Figure 15 shows the development of the mixing region when the colour change takes place at 1% mixing of the two layers, (It is symmetrical, because of exccess phenolththalein, turning red both when 1 % fluid with indicator mixes with the 12 pH upper fluid and when 99 % fluid with indicator mixes with 1 % 12 pH upper fluid) the edge of the front is seen more clearly but the structure of the inner bubbles is less clear.

4.5 Laser fluorescence and fractal analysis

The methods described above give information on the mixing process averaged across the width of the tank. In order to obtain further information on the form of the mixing structures, planes of laser light were used. In this way elevation, end and plan views were obtained in which the full three-dimensional structure of the mixing region was revealed. Examples of these images are shown in figures, 16, 17 and 18. The plan views,

in particular, show the large scale disturbances have a fully three-dimensional structure.

A range of lengthscales is observed during the RT process ranging from 5 mm to the scale of the tank. (Note this lower limit is larger than the resolution of the method which is determined by the thickness of the illuminated region. i.e. 2mm.) The behaviour was similar for all ranges of g'. Initially, small disturbances could be seen which appeared to correspond to the unstable RT modes given by equation (2.1) (see figure 19). At later times large scales structures, with horizontal scales of the order of 5-10 cm, developed. As the RT instability front advanced new small scale structures developed on the edges of the large scale stuctures (see figure 16). Some could be identified as Kelvin-Helmholtz billows, presumably generated by shear instability, and some as vortex pairs, probably caused by local gravitational instability. The large scale structues merged as the RT front advanced, leaving one or two large scale protruberances by the time the front reached the bottom of the tank. After that time a rotational overturning motion of the size of the box took over.

The fractal dimension was calculated by means of a box counting algorithm (Redondo & Linden 1989). This method divides the image into smaller and smaller boxes of dimension e, and counts the number N of the boxes through which the edge of the interface passes. The fractal dimension D_2 is given

by

$$D_2 = \frac{logN}{log(\frac{1}{e})} \quad . \tag{5.1}$$

Plots are made of log N against $log(1/e)$, and if the surface is self-similar or fractal, the points will lie on a straight line with slope D_2.

Both side and end elevations were analysed in this way and a typical result is shown on figure 20. This plot indicates roughly a self-similar behaviour, but there is a predominance of two scales (indicated by the arrows that correspond to the bubble size and the dominant KH instability on the sides.

If different regions of the fluorescein mixing front are averaged (see figure 21) the linear fit can take into account the statistical nature of the mixing processes. This shows that there is a range of scales over which the surface is statistically fractal, and in this case the fractal dimension imbedded in a 2-dimensional plane is $D_2 = 1.21$. Since this result is obtained from a projection of the surface onto a plane, the full fractal dimension of the surface in the 3-D space is believed to be D = 2.21.

The development of the full fractal structure takes approximately 2 s., for the range of densities used ($20 > g' > 10 cms^{-2}$). At earlier times only the linear RT scales and the disturbances imposed by the withdrawal of the plate are present. The fractal dimension then remains approximately constant until the influence of the bottom of the tank reduces

the dimension again. The time development of the fractal dimension is shown in figure 22 for a typical experiment. It appears then that it takes approximately 1 - 2 s. for a fully-developed turbulent flow to be established.

It should be noted that the smallest scales likely to be generated in the turbulent flow are determined by the Kolmogorov scale

$$\eta = \left(\frac{\epsilon}{\nu^2}\right)^{1/3} \quad , \tag{4.6}$$

where ϵ is the rate of dissipation. Using as an estimate for the dissipation

$$\epsilon \propto \frac{u'}{\ell} \quad , \tag{4.7}$$

where u' is a typical turbulent velocity and ℓ a turbulent scale, we estimate $\eta \approx 0.05mm$ in the present experiments. The visualisation method is restricted by the width of the laser sheet (assuming at these small scales the structure is isotropic). Thus we are unable to resolve motions on scales less than 2 mm, which exceeds the Kolmogorov scale. On the other hand, as noted earlier the smallest scales observed at the interface edge were larger than the 2 mm resolution scale suggesting that the flow is not fully developed at the edge of the mixing region.

4.6 Conductivity measurements

Molecular mixing in Rayleigh-Taylor unstable flows

(i) Single point measurements

The data collected from a single conductivity probe placed centrally 0.1 cm above the aluminium plate are useful for determining the behaviour of the system as a function of density difference. Examples at three different initial values of $g' = 7.5, 24.3$ and $64 cms^{-2}$ are shown in figure 23. These plots show the density ρ' measured by the probe, normalised by the initial density difference so that the upper layer corresponds to 1 and the lower layer to 0, as a function of time. Since the probe is in the upper layer, the reading is 1 before the plate is removed and then decreases as lower layer fluid mixes upward.

The overall behaviour is the same at all values of g', with a rapid decrease in the density being observed followed by oscillations whch eventually decay, when the probe records a density intermediate between the upper and lower values. All records show fine scale fluctuations superimposed on longer timescale oscillations. There are significant differences between the way in which this final state is reached, depending on the initial density difference. As g' increases the oscillations on both timescales decrease more rapidly. This is associated with the formation of stable stratification as the two layers overturn causing a rapid damping of the turbulent motion.

Timescales for the decay of these fluctuations are shown in figures 24 and 25. Figures 24 shows the e-folding time obtained by fitting an exponential decay to the peaks of the slow time

oscillations plotted against $\Delta\rho$. These peak values provide a measure of the mixing into the large scale structures observed in the mixing region. The timescales for the decay of these oscillations decreases with increasing initial density difference. The decay of the short timescale flucturations is shown in figure 25. These values were obtained by visual inspection of the traces, such as shown in figure 23. These values also decrease with increasing $\Delta\rho$, and the values are, in general, larger than those in figure 24.

(ii) Multiple point measurements

Time sequences of density were recorded by a number of probes positioned in the upper layer. Using this data and taking ensemble averages of the results from a number of different experiments, mean values of fluctuating concentrations were obtained.

Root-mean-square (rms) fluctuations were obtained by calculating

$$\sigma(z) = \frac{\overline{(\rho(z,t) - \bar{\rho}(z))^2}^{1/2}}{\Delta\rho} \quad , \tag{4.9}$$

where $\bar{\rho}(z)$ is the average determined as a time running mean of the density fluctuations. Figure 26 shows the raw signal and r.m.s. density values σ determined by taking running means of 0.5, 1.0, 1.5, 2.0, 2.5 and 3.0 s., respectively. The values of the maximum value of σ, σ_{max}, which corresponds to the edge of the RT turbulent front seem independent of the averaging

time in the range 1-2 seconds, figure 27, and so a value of 1.5 s. was used in the remainder of the calculations.

Figures 28 and 29 show σ plotted against time for a range of probe heights. In all cases, as the front passes the probe rises to a maximum and then decreases again. In figure 28 the probe is positioned so that a disturbance passes through the centre, while in figure 29 the probe is missed by large scale disturbances. In figures 28 b) and 29 b) the outline of the RT turbulent front is traced relatively to the probes,marked as crosses. It is clear that the behaviour is different in the two cases.

Figure 30 shows the non-dimensional density for 4 vertical probes separated 25 mm as the RT front passes through them for several experiments, all with $g' = 19cms^{-2}$. The experiments shown in figures 28 and 29 correspond to figures 30 d) and 30 a). It is seen that when a large blob transverses the probes (cases d) and e)) there is faster mixing behind the RT turbulent front.

The maximum values of $\sigma(z)$ are plotted against height in figures 31 and 32 . In figure 31 points from individual probes are shown, while in figure 32 an ensemble average, providing an equivalent average over a plane, of all runs with similar $g' \approx 20cms^{-2}$ is shown. The values of σ for $z \approx 0$ are taken from the initial sets of experiments, (see Table 1). We must take into account, however, that these density recordings are influenced by the withdrawal of the plate. This is why the

probes were positioned 4 cm away from the plate ($4cm > \delta_0$).

In figure 33 the traversing time, a) and the thickness of the initial front, b) as it passes through the probes is shown for different heights for the experiments described in figures 28 and 29. Different behaviour is also seen depending on whether the head or the side of a bubble passes trough the probes. In order to study the structure of a bubble, 5 probes were positioned parallel to the plate 25 mm apart at 10 cm from it. The variations between the initial density fluctuations as the front passes through the rack of probes indicate that the density interface is sharper near the centre of the bubble than near its sides, here KH instability produces further mixing.

5 DISCUSSION, CONCLUSIONS AND FURTHER WORK

The advance of the RT front agrees with the work of Read and Youngs(1983) and Smeeton and Youngs(1988). The initial problems with the disturbances produced by the plate are now understood, and can be controlled. Flow visualization has given considerable insight into the mixing processes inside the box.

The rms conductivity measurements show a slight overall decrease with distance from the plate, but there are distinct differences in behaviour if the probes are in an upwelling or a downwelling structure, or in what seems the most effective

mixing region, the sides of the protuberances. Further work to obtain more reliable statistical results is in progress. All of the probes of the conductivimeter will be used in further tests.

More work is still needed in order to interpret the results of the fractal analysis, but it is interesting to compare changes in the fractal dimension with other experiments such as stably stratified turbulence of flame propagation. Information about the mixing can be extracted from the thickening of the edges due to the phenolphtalein colour change, and this thickness can be now analysed with the digitizer system. For lower density runs with phenolphthalein, it was apparent that the vorticity originated by the plate increased mixing at the center of the vortices produced by it. This effect can be avoided using intermediate density differences. A variation of the colour change mixing ratio for the phenolphthalein indicator experiments is under way.

The analysis of the colour clange can be studied in time. As an example, figure 34 shows the variation of light intensity with time at 4,6.5,9,11.5,14 and 16.5 cm. from the plate, as a 1% pH indicator front advances. The step change is similar to that recorded by the conductivity probes. Both these and digitized profiles can be Fourier transformed to obtain the spectrum of fluctuations,(see figure 35 for an example).

The relation between fractal analysis and spectral analysis can be very useful to determine the evolution of scales. Presently the emerging picture of the mixing process is as

follows. Initially a pure RT instability with lengthscale λ_m appears, together with the disturbances from the plate. The growth and merging of disturbances favours the appearence of several distinct blobs, bubbles or protuberances which produce shear instabilities on their sides. These sometimes develope further secondary shear instabilities. After 2/3 of the tank (2 s) three dimensional effects have broadened the spectrum of lengthscales widely enough as to have a fractal structure in the visual range with dimensions ranging between 2.15 and 2.30.

REFERENCES

E.F. Caldin (1964), "Fast Reactions in solution", Blackwell.

S. Chandrasekhar (1961) ,"Hydrodynamic and Hydromagnetic Stability ". (Oxford Univ. Press,Oxford)

F. Hunsaker and H. Riatome (1949), "Hydrodynamics" .Ed Pergamon Press

P.F.Linden (1980), " Mixing across a density interface produced by grid turbulence" J. Fluid Mech. 100 pp 669.

D.H.Sharp (1984) "An overview of Rayleigh-Taylor Instability",Physica 12D ,3-18

V.S.Smeeton and D.L.Youngs (1988), "Experimental Investigation of Turbulent mixing by Rayleigh-Taylor instability, part 3" AWE Report O 35/87.

Rayleigh, Lord (1900), "Investigation of the character of the equilibrium of an incompressible heavy fluid of variable density", Scientific papers ii, 200-207. Cambridge, U.K.

K.I.Read (1984), "Turbulent mixing by Rayleigh-Taylor instability" AWE Report 002/84.

J.M.Redondo (1987) "Difusion turbulenta en fluidos estratificados ". Tesis Doctoral, Universidad de Barcelona.

J.M. Redondo and P.F. Linden (1989), "The fractal dimension of stratified fluids", The Physics of fluids (submitted).

K.I. Read and D.L. Youngs (1983), "Experimental Investigation of turbulent Mixing by Rayleigh-Taylor instability",AWRE Report 001/83.

G.I. Taylor (1950), "Instability of superimposed fluids", Proc. Royal Soc. London Ser. A 201, 192

J. S. Turner (1973),"Buoyancy effects in fluids",Cambridge University Press.

D.L. Youngs (1984), "Numerical similation of turbulent mixing by Rayleigh-Taylor instability ,Physica 12D ,32-44.

REFERENCES

1 - Richardson L.F. (1922) "Weather prediction by numerical process",C.U.P.

2 - Mandelbrot B.B.(1974),"Intermittent turbulence in self-similar cascades: divergence of high moments and dimension of the carrier". J.Fluid Mech. 62 ,331-358.

3 - Mandelbrot B.B. (1975), "On the geometry of homogeneous turbulence, with stress on the fractal dimension of the iso-surfaces of scalars". J.Fluid Mech. 72, part 2, 401-416 .

4 - Mandelbrot B.B. (1982) "The Fractal Geometry of Nature" W.H.Freeman.

5 - Turcotte D.L. (1988) "Fractals in Fluid Mechanics" Ann. Rev. Fluid Mech. 20 ,5-16.

6 - Lovejoy S. (1982), "Area-Perimeter relation for rain and cloud areas", Science 216, 135-186.

7- Turner,J.S. (1968), "The influence of molecular diffu-

sivity on turbulent entrainment across a density interface", J.Fluid Mech. 33 ,639-656 .

8- Crapper .P.F.& Linden P.F.(1973), "The structure of density interfaces", J.Fluid Mech. 65 ,45-63

9- Linden P.F.(1975), "The deepening of a mixed layer in a stratified fluid" , J.Fluid Mech. 71 ,385-405

10 - McDougall T.J. (1979), "Measurements of turbulence in a zero-mean-shear mixed layer", J.Fluid Mech. 94 , 409-433

11 - Hopfinger E.J. & Toly J.A.(1976), "Spatially decaying turbulence and its relation to mixing across density interfaces",J.Fluid Mech. 78 ,175-188

12 - Redondo J.M. (1987) " Effects of ground proximity on dense gas dispersion" .J . Hazardous Materials ,vol 16 , 381-393.

13 - Pearson & Linden P.F.(1983), "The final stage of decay of turbulence in stably stratified fluid", J. Fluid Mech ,vol 134 , 195-203.

14 - Hanoun I.A.,Fernando H.J.S. & List J.E.(1988) "Turbulence structure near a sharp density interface",J.Fluid Mech ,vol 189 ,189-209

15 - Hanoun I.A. & List J.E. (1988)"turbulent mixing at a shear free density interface",J. Fluid Mech.vol 189,pp 209-227

16 - Sreenivasan K.R and Meneveau C. (1986),"The fractal facets of turbulence. J. Fluid Mech.

17 Linden,P.F.(1979) "Mixing in stratified fluids", Geophys. Astrophys. Fluid Dyn. vol 13, 3-23.

18 Linden,P.F.(1980) " Mixing across a density interface produced by grid turbulence" J. Fluid Mech. 100, 691-703.

19 Taylor,G.I.(1950) "The instability of liquid surfaces when accelerated in a direction perpendicular to their planes. I", Proc. Royal Soc. A,vol. CCI, 192-196.

20 Chandrasekhar,S.(1961) "Hydrodynamic and Hydromagnetic Stability", Oxford University Press, Oxford.

21 Linden P.F, Redondo J.M. & Caulfield C.P.(1989) "Molecular mixing in Rayleigh-Taylor instability", Proceedings of 1st Conference on Compresible Turbulence and Mixing. Princeton NJ. November 1988.

22 Read,K.I. and Youngs,D.L.(1983) "Experimental Investigation of turbulent Mixing by Rayleigh-Taylor instability", AWRE Report 001/83.

23 Sharp,D.H.(1984) "An overview of Rayleigh-Taylor Instability", Physica 12D , 3-18.

24 Smeeton,V.S. and Youngs,D.L.(1988) "Experimental Investigation of Turbulent mixing by Rayleigh-Taylor instability, part 3" A.W.E. Report O 35/87.

25 J.S.Turner(1973) "Buoyancy effects in fluids", Cambridge University Press.

26 Youngs,D.L.(1984) "Numerical similation of turbulent mixing by Rayleigh-Taylor instability", Physica 12D, 32-44.

27 - Hunt J.C.R and Graham J.M.R. (1978) "Free stream turbulence near plane boundaries" ,J.Fluid Mech. 84 ,209-235

28 - Carruthers D.J. and Hunt J.C.R. (1986) ,"Turbulence

, waves and entrainment near density inversion layers " I.M.A. series Vol 15 . conference proceedings , Chester ,77-95.

29 - Lovejoy S. & Mandelbrot, B.B. (1985), "The fractal properties of rain, and a fractal model", Tellus. **37 A**, pp 209-232.

30 - Taylor G.I. (1931), "The Transport of Vorticity and Heat through Fluids in Turbulent motion", Proc. Royal Soc. **145**, pp 685-701.

31 - Hunt J.C.R.(1987), "Vorticity and Vortex Dynamics in Complex Turbulent Flows" Transactions to the CSME Vol 11 .No 1, pp 21-35

32 - Kolmogorov C.R. (1941) Acad. Nauk. U.S.S.R. 30, 301 ; 31, 538 ; 32, 16.

33 - Schertzer D. & Lovejoy S.(1987) "Physical Modelling and analysis of Rain and clouds by Anisotropic Scaling Multiplicative Processes" Jour. Geophys. Res. Vol **92** no D8 pp 9693-9714.

34 - Obukhov A.M.(1962) "Some specific features of atmospheric turbulence" and Kolmogorov A.N.(1962) "A refinement of previous hypotheses concerning the local structure of turbulence in a viscous incompressible fluid at high Reynolds number" J.Fluid Mech **3**. pp 77-85.

35 - Frisch U.,Sulem P.L. & Nelkin M.(1978) "A simple dynamical model of intermittent fully developed turbulence" J. Fluid Mech. **87** pp 719-736.

figure 27 : Variation of maximum rms density fluctuation (Occurring as the RT front passes through the probe tip) for different running means, $\bar{t}$.

figure 28 : a) Evolution of rms density fluctuations with time for each of the 5 vertically positioned probes at 4,6.5,9,11.5 and 14 cm from the plate. b) Tracings of the passage when the RT turbulent front reaches each of the first 4 probes. Times can be read of figure 30 d). In this experiment a large blob went through all the probes.

figure 29 : a) Evolution of rms density fluctuations with time for each of the 5 vertically positioned probes at 4,6.5,9,11.5 and 14 cm from the plate. b) Tracings of the passage when the RT turbulent front reaches each of the first probes. Times can be read off figure 30. a) In this experiment the probes missed a blob. c) Variation of rms density fluctuation in time and vertical space. d) variations in time of the probes at different z positions ,o - 4 cm.,x - 6.5 cm., + - 9 cm, Δ - 11.5 cm.

figure 30 : Normalized density fluctuations with time, time origin is a few seconds before pulling the plate (5-7). In experiments a),b) and c), a blob missed the vertical line of probes. In experiments d) and e) the probes intersected the center of a blob.

figure 31 : Variation of the rms density fluctuations at the RT front with height for eight experiments. For all $20 > g' > 11 cms^{-2}$.

figure 32 : Average σ for different heights as the RT turbulent front passes through the probes.

figure 33 : a) Time of passage of the initial RT front through the probes positioned at 4 , 6.5, 9 and 11.5 cm from the plate, b) Non-dimensional initial density jump as the RT front passes each probe. The symbols indicate: + - experiment shown in figure 28, when the center of a blob passes through the rack of probes. o - experiment shown in figure 29, probes near the edge of a blob.

figure 34 : Variation of the light intensity at the same heights as the probes in figure 31. As the RT front marked by 1% pH indicator , the abrupt change in light intensity corresponds to the passage of the front. 250 is light (unmixed) and 0 indicates dark (mixed) fluid.

figure 35 : Example of the spectrum of light intensity fluctuations inside the RT front.

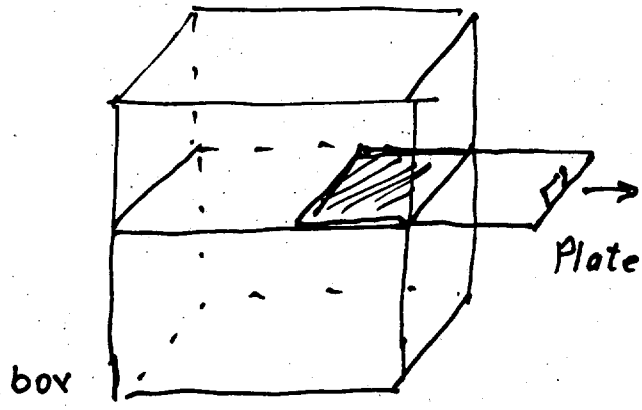

Fig 1

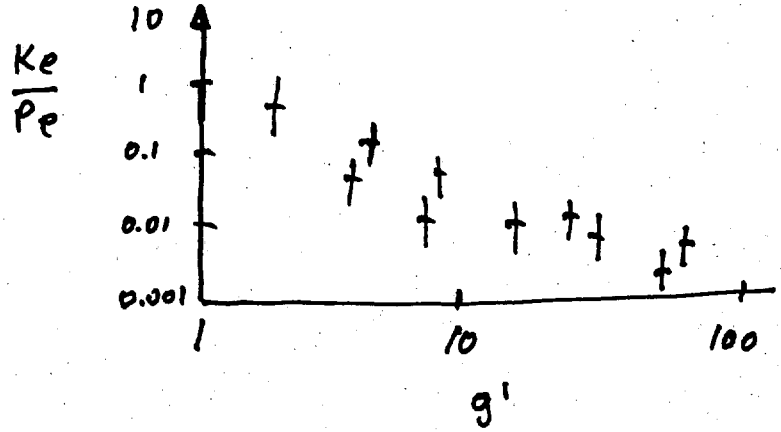

Fig 2

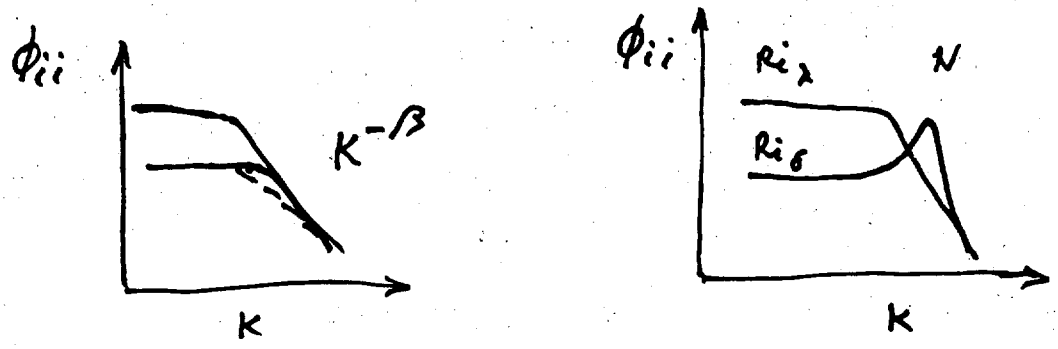

Fig 10-11

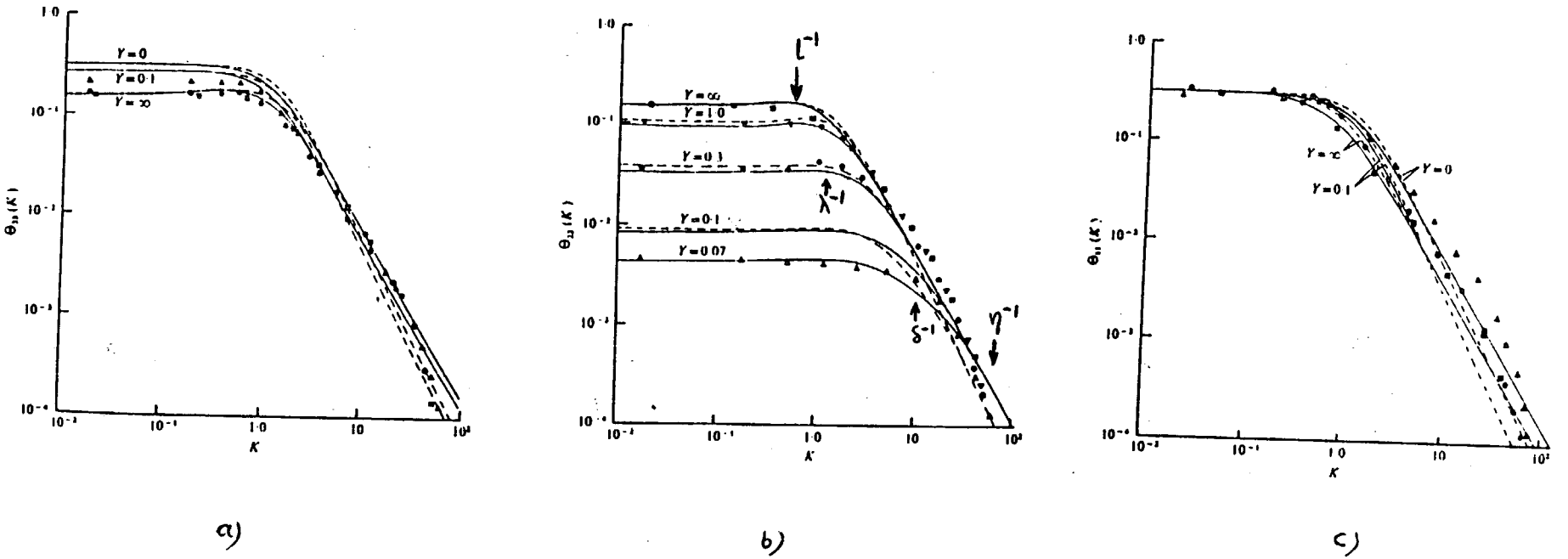

FIGURE 18: Velocity spectra calculated by Hunt & Graham [20] for turbulence near a solid boundary , Y indicates the non-dimensional distance from the boundary , a) and c) indicate horizontal velocity spectra and b) shows the vertical velocity spectrum. In figure b) , l indicates the energy containing eddies (Integral length scale of the turbulence) , and η, the Kolmogorov scale . λ and δ indicate intermediate scales which correspond to maximum vertical fluctuations at different distances from the ground (or stratifications).

$g' = 0.24\ ms^{-2}$

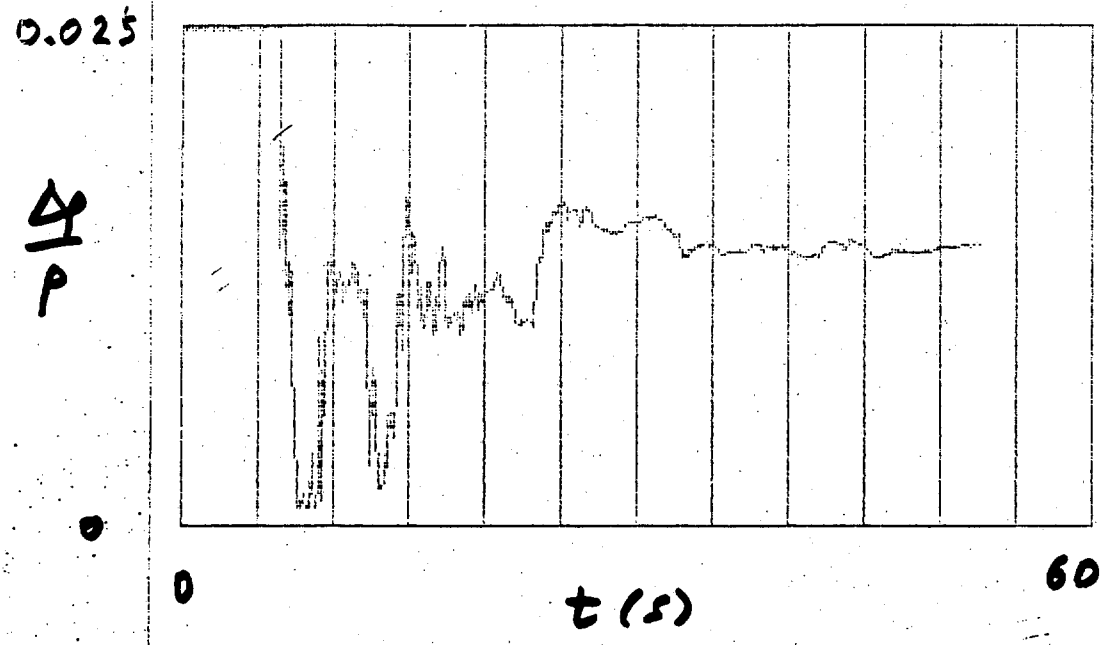

$g' = 0.17\ ms^{-2}$

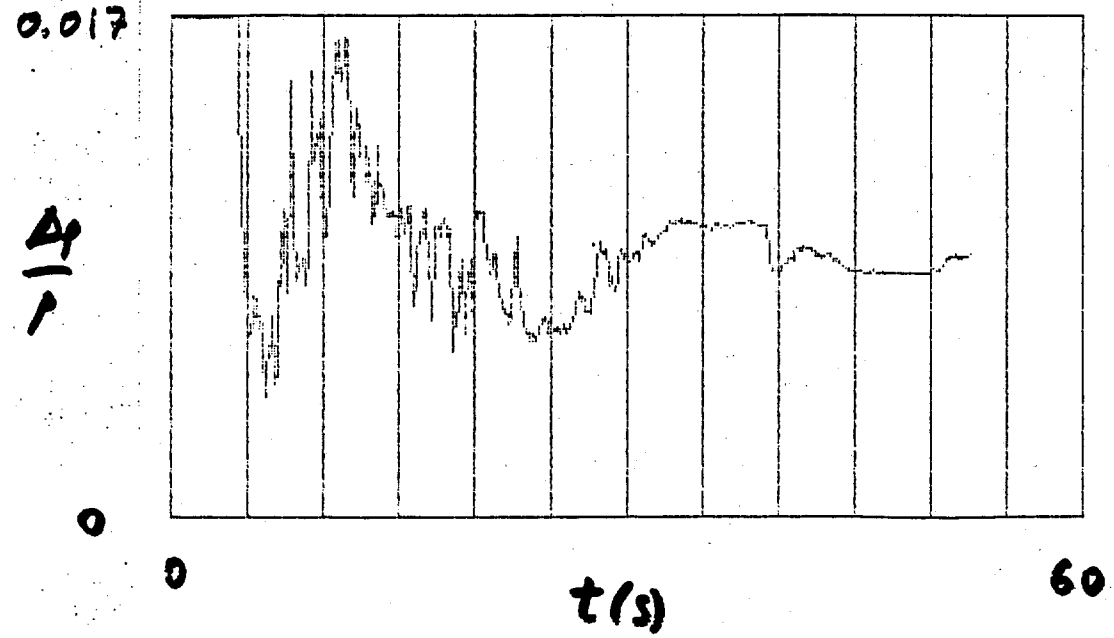

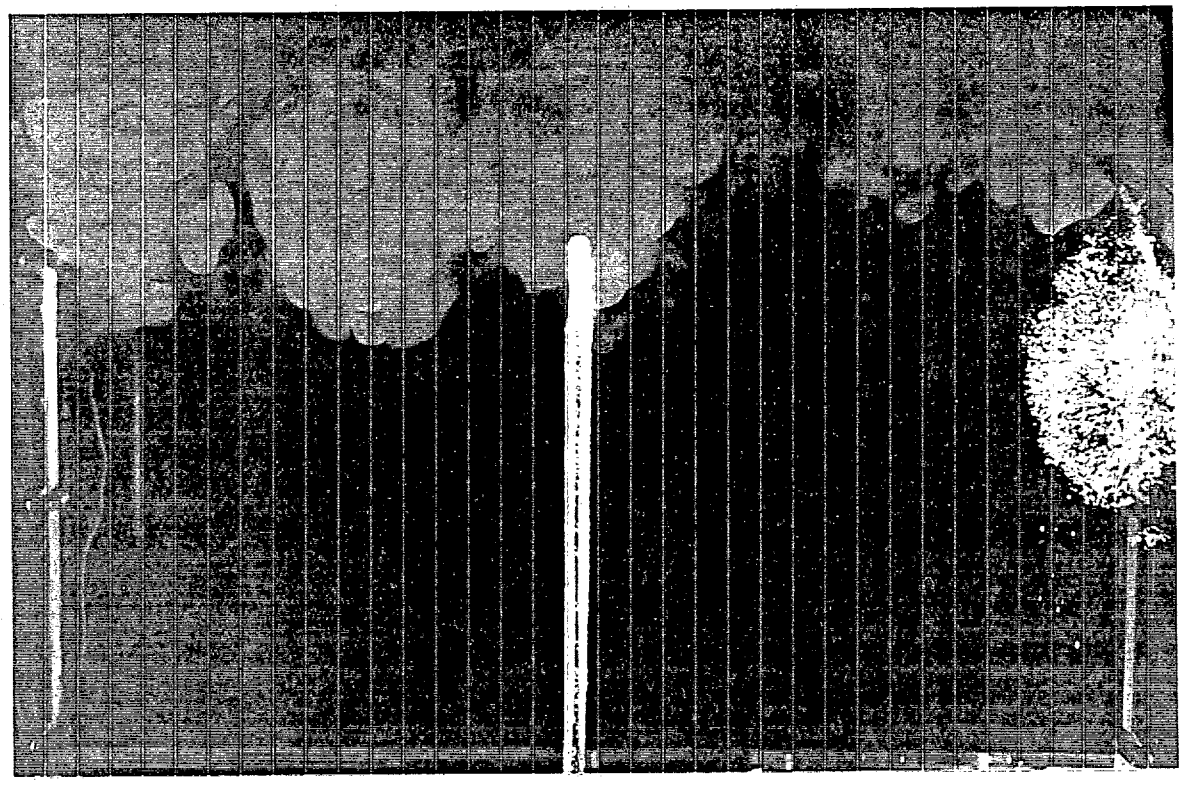

Fig 16

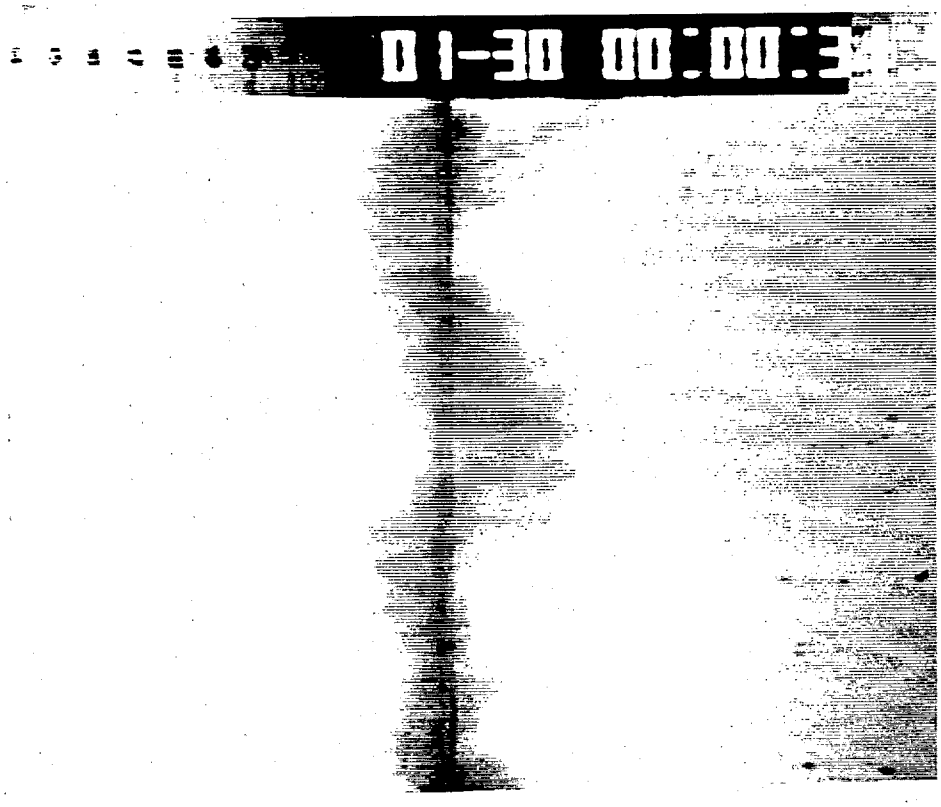

figure H: Shadowgraphs showing uniform mixing region. a),b),c),d) Evolution of the RT front for $g' = 42cms^{-2}$. e) Effect of removal of plate, f),g) Evolution of the RT front for $g' = 2cms^{-2}$.

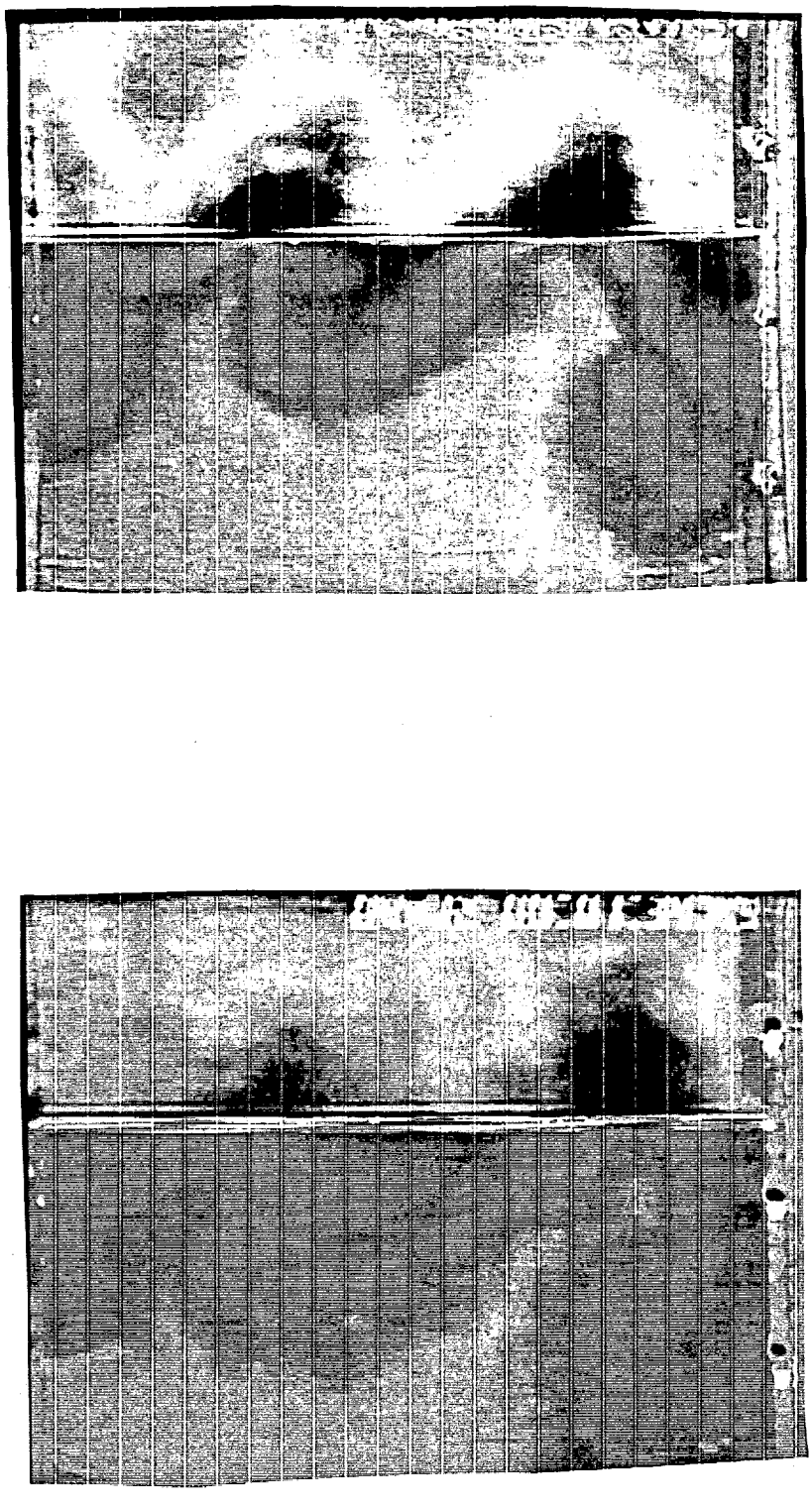

figure 10 : Dye intensities , 640 indicates no dye and 100 maximum dye integrated colour a) global view, b) detailed view of the bottom right blob. sharp contours can be seen with small scales that appear even after integration.

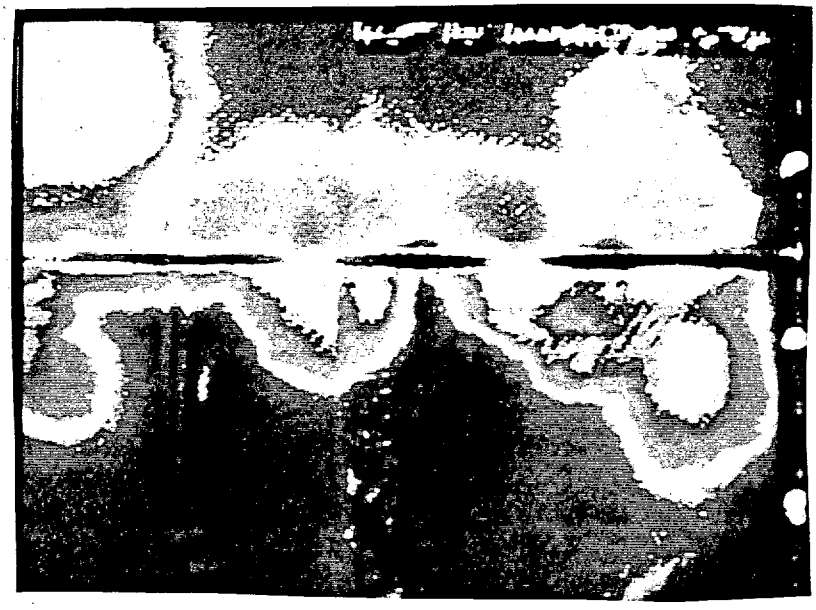

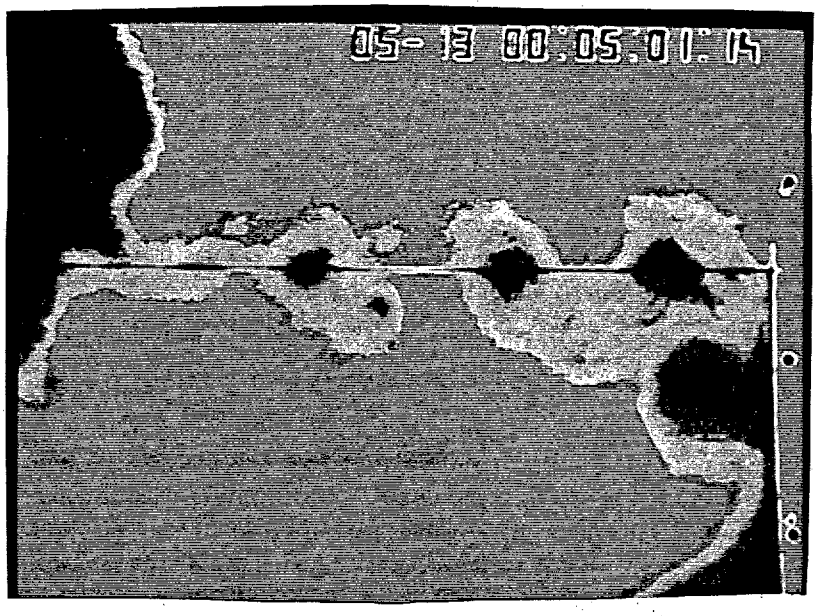
05- 13 00.05.01.15

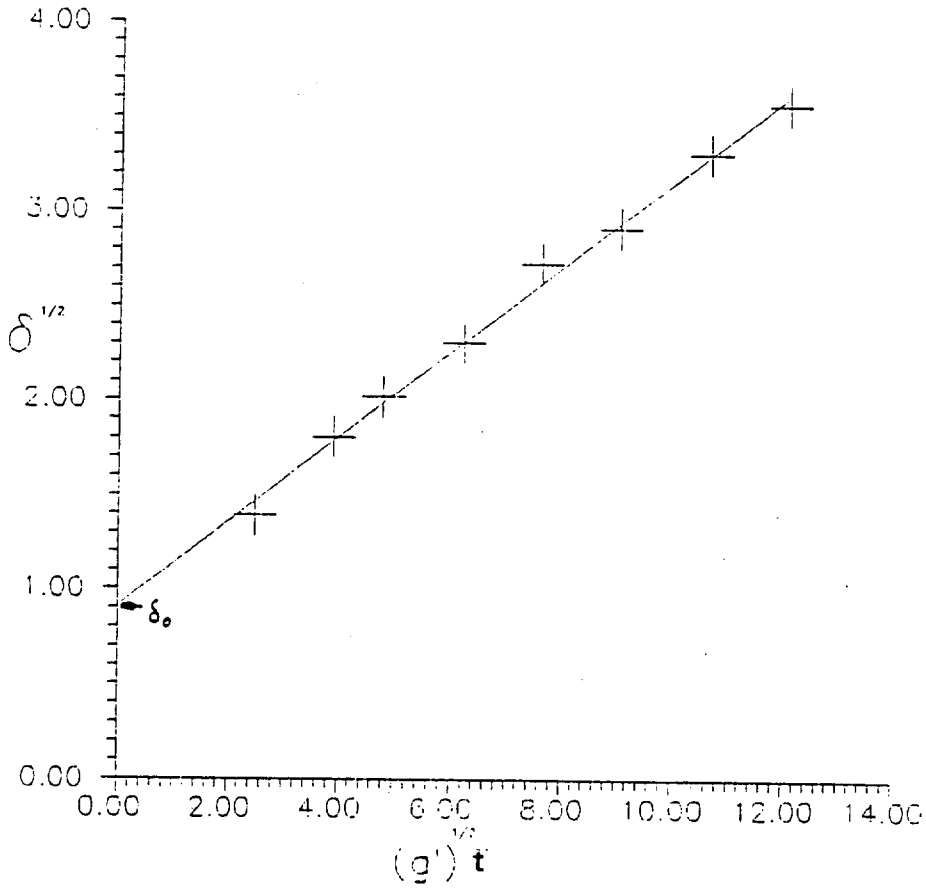

Figure 10

figure 10 : Plot of $\delta^{1/2}$ vs. time; δ_0 is the extrapolated value at t=0.

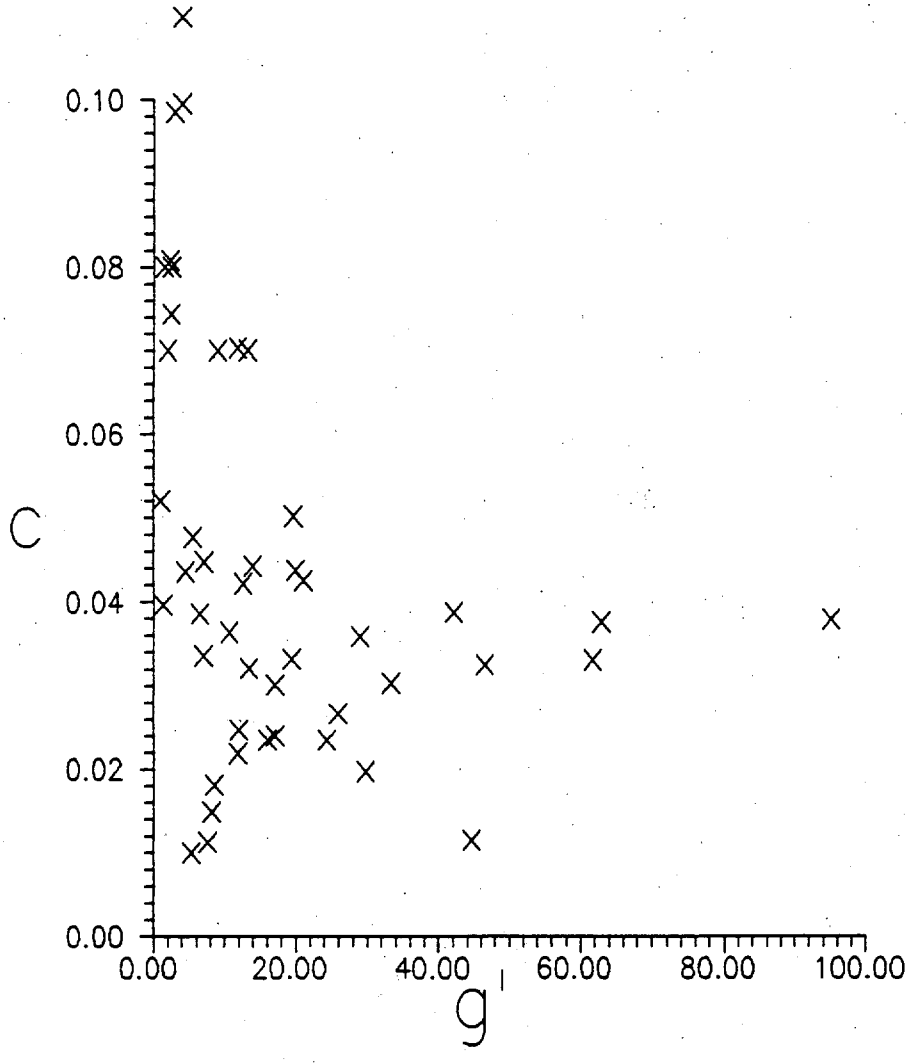

Figure 11

Figure 11: *Plot of the constant c versus* $\frac{\Delta\rho}{\rho}$.

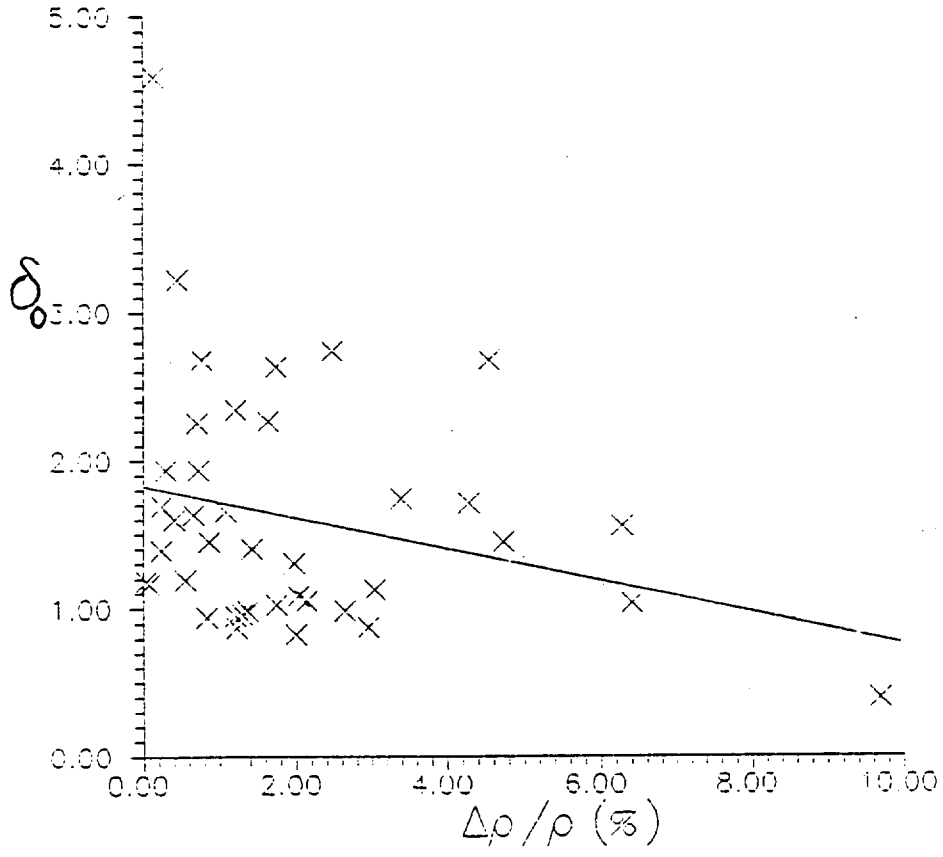

Fig 12

Figure 12: *Plot of the virtual origin, δ_0, with the initial non- dimensionalised density difference.*

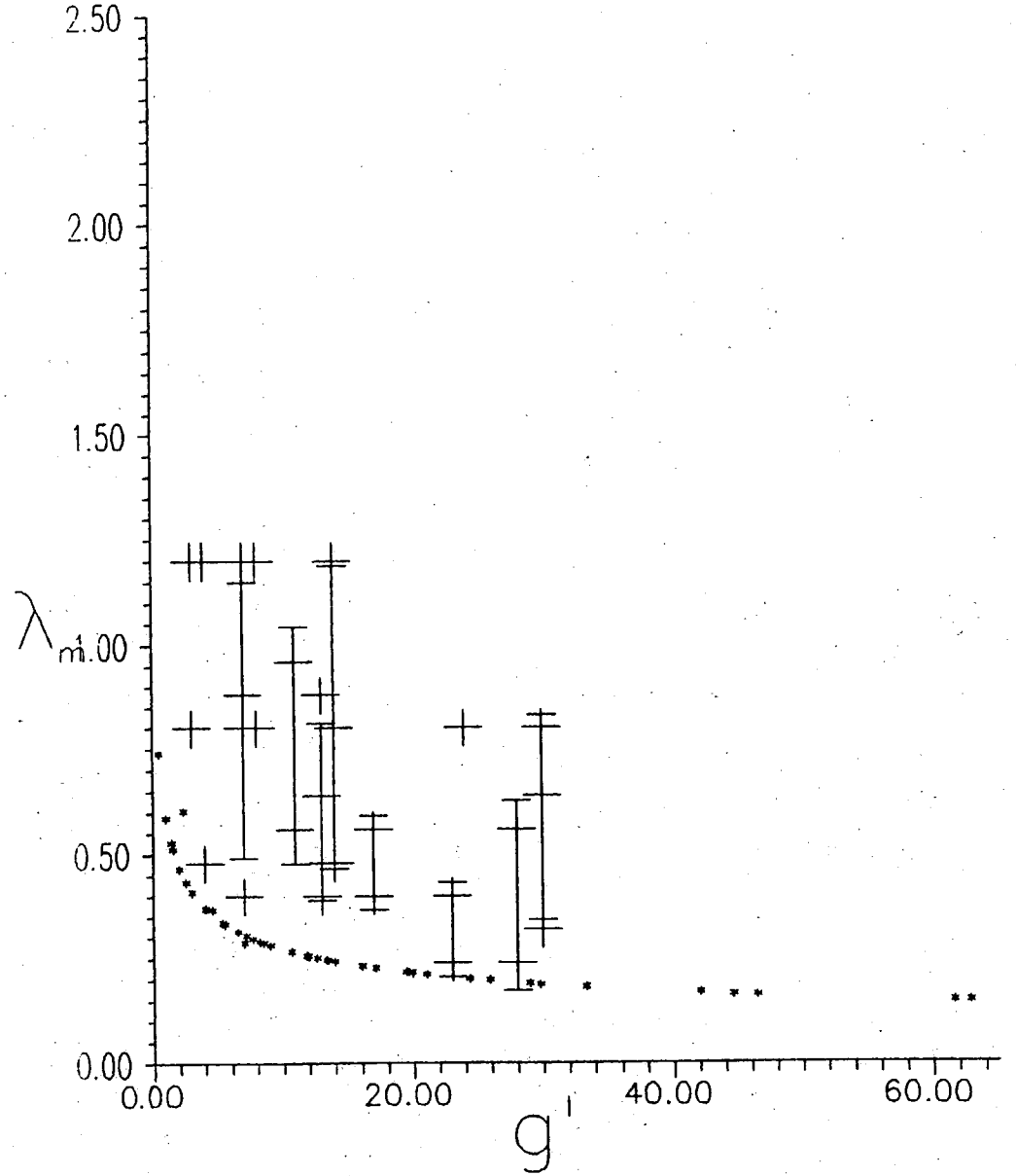

figure 13 : Observed and calculated λ_m plotted against g'. (* are theoretical points)

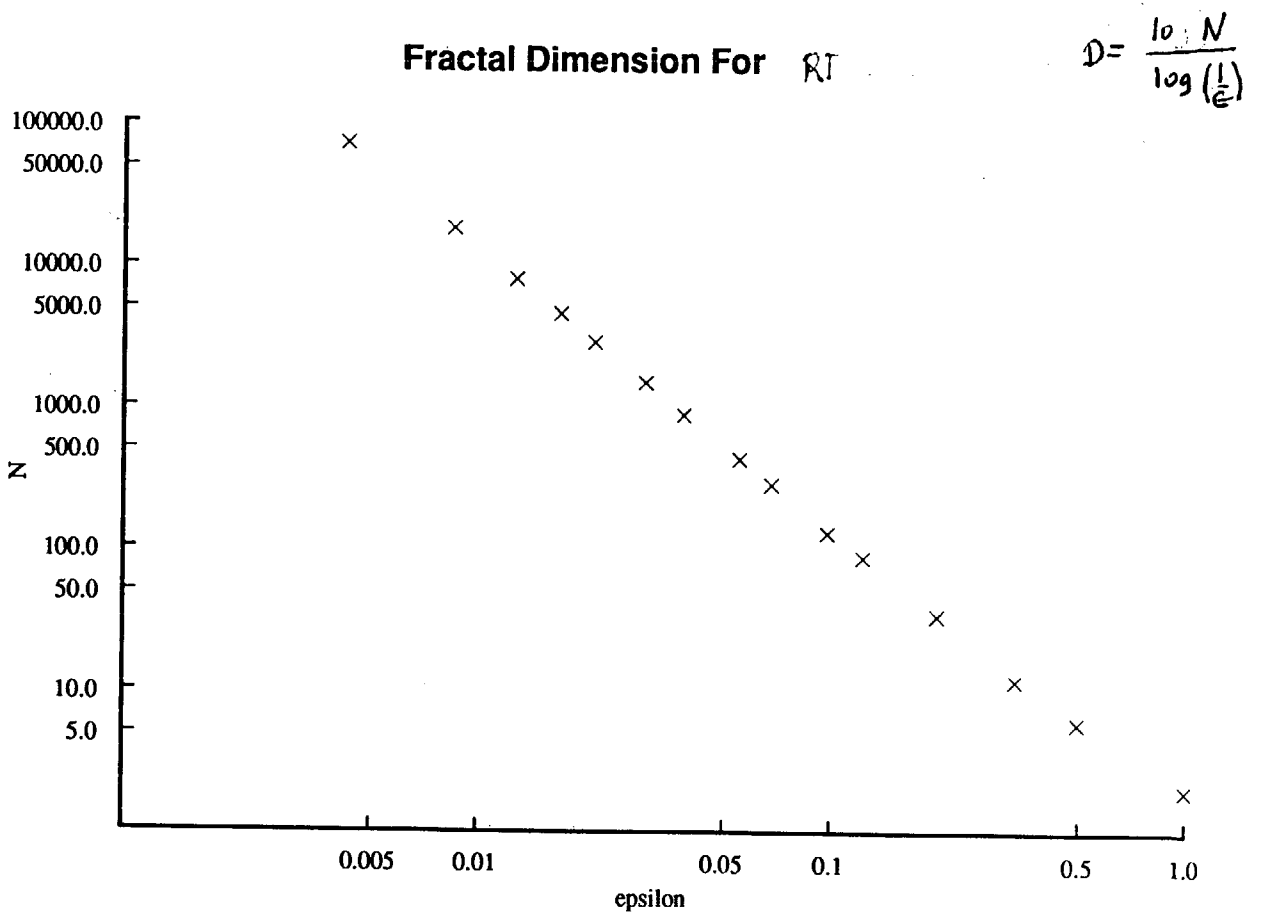
Fractal Dimension For RT
D= lo N / log (1/ε)
100000.0
50000.0
10000.0
5000.0
1000.0
500.0
100.0
50.0
10.0
5.0
N
0.005
0.01
0.05
0.1
0.5
1.0
epsilon
MenuPic:::SDFracta::Plot: 17:54 on 13/08/1989

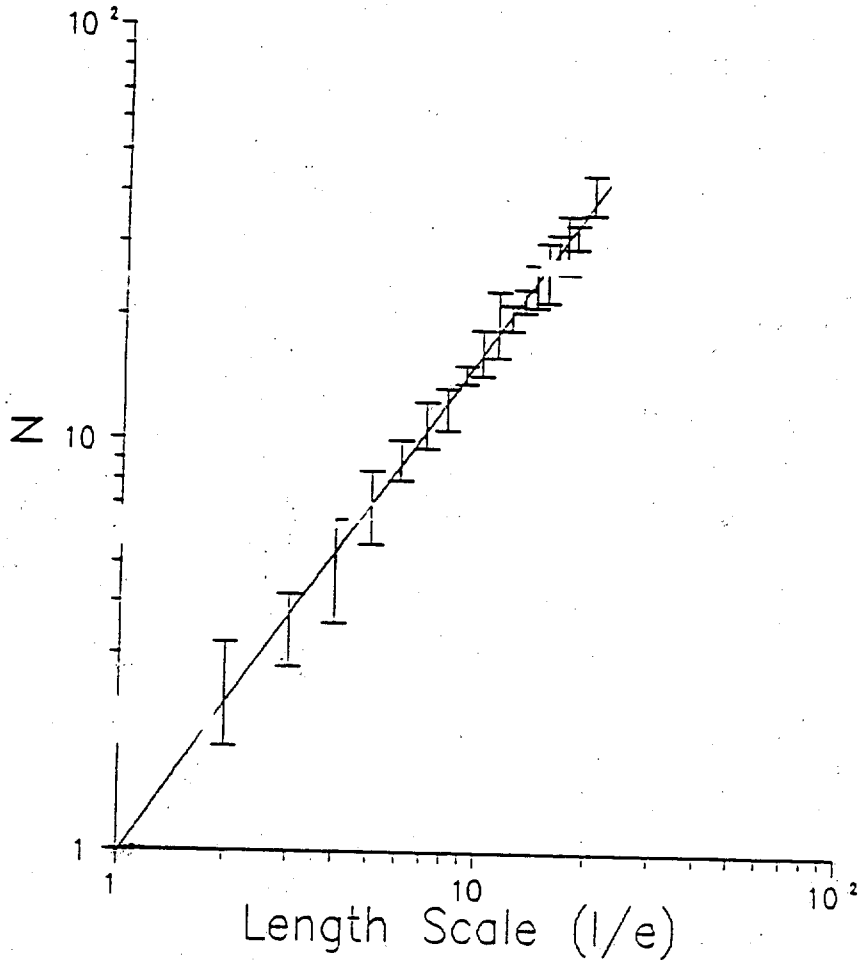

Figure 21

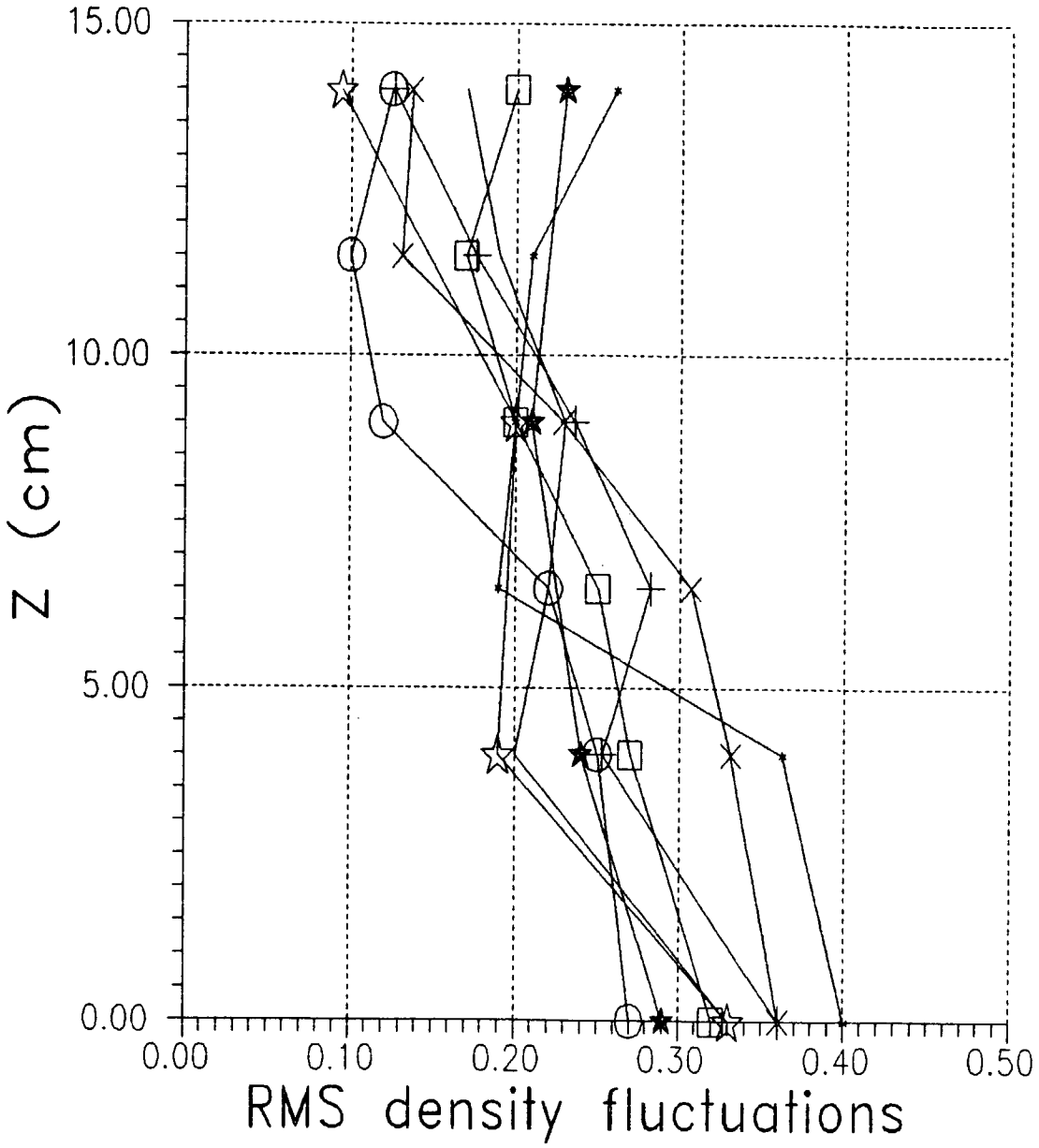
15.00
10.00
5.00
0.00
Z (cm)
0.00
0.10
0.20
0.30
0.40
0.50
RMS density fluctuations

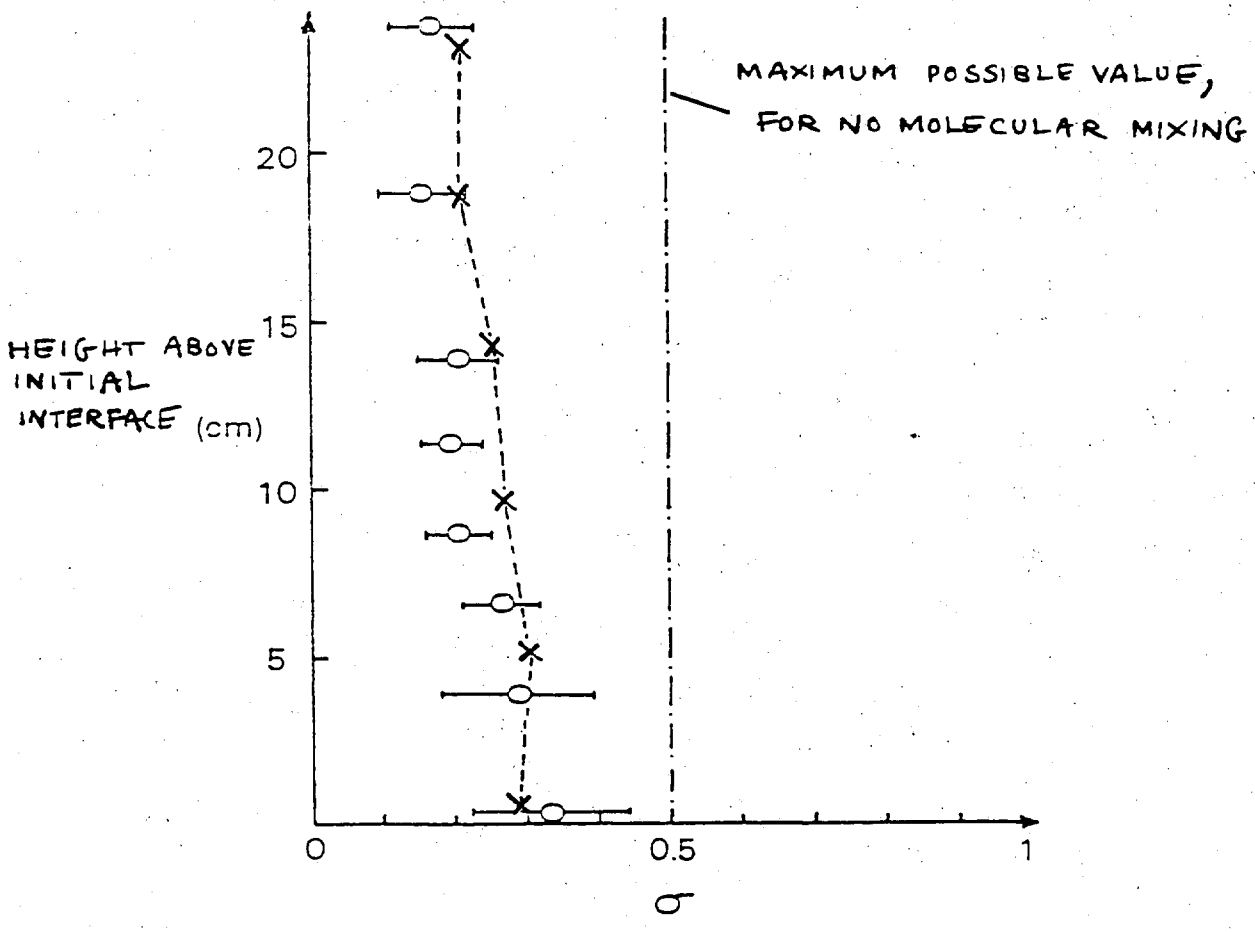

COMPARISON OF OBSERVED AND CALCULATED DENSITY FLUCTUATIONS

σ = PEAK VALUE OF $\langle(\rho-\bar{\rho})^2\rangle^{\frac{1}{2}}/(\rho_1-\rho_2)$ AT GIVEN HEIGHT

O : OBSERVED VALUES, LINDEN AND REDONDO [6]

X : VALUES CALCULATED FROM 44^3 MESH CALCULATION AT CORRESPONDING VALUE OF x/H

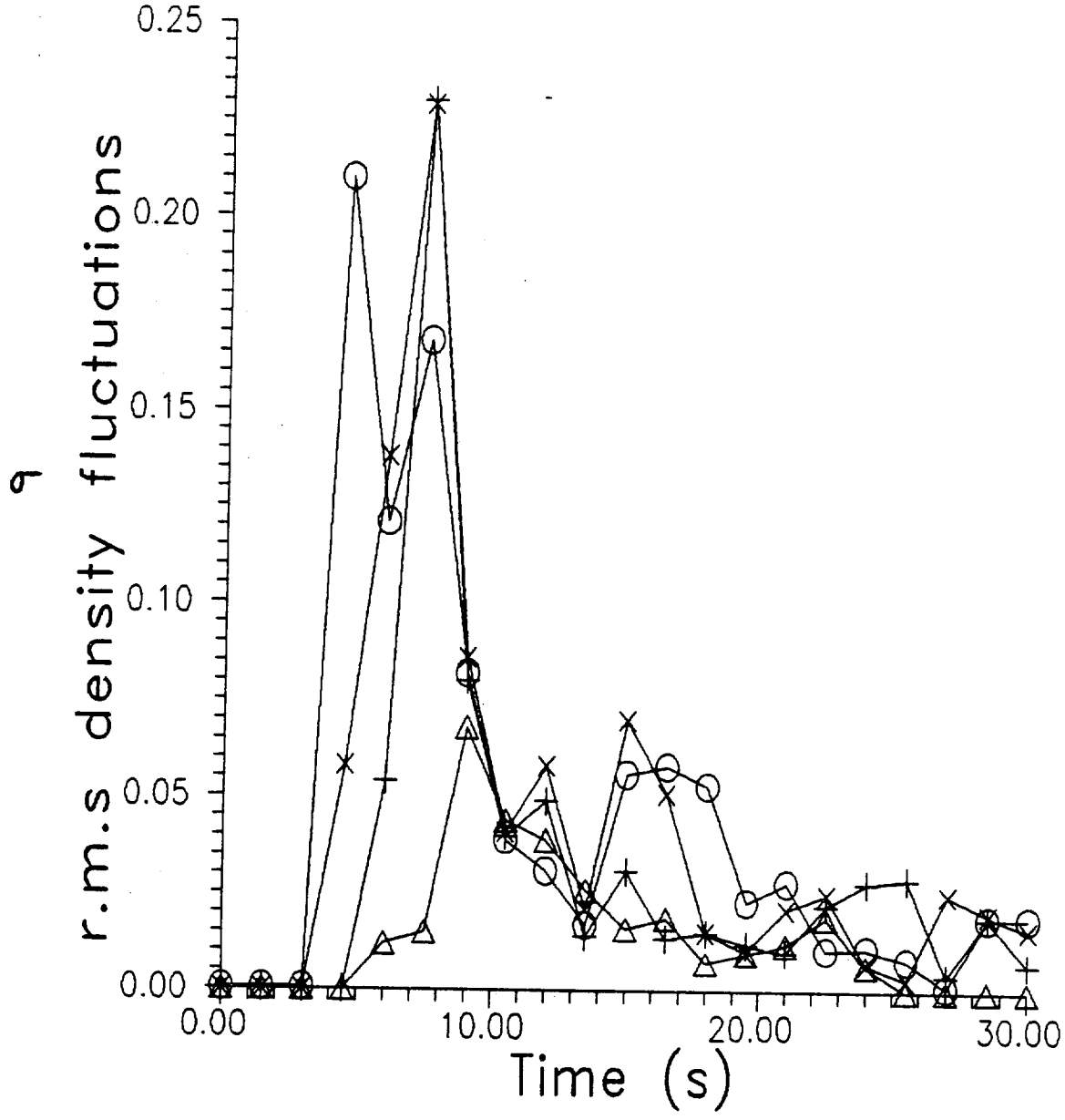
0.25
0.20
0.15
0.10
0.05
0.00
r.m.s density fluctuations
q
0.00
10.00
20.00
30.00
Time (s)

d)

Figure 29

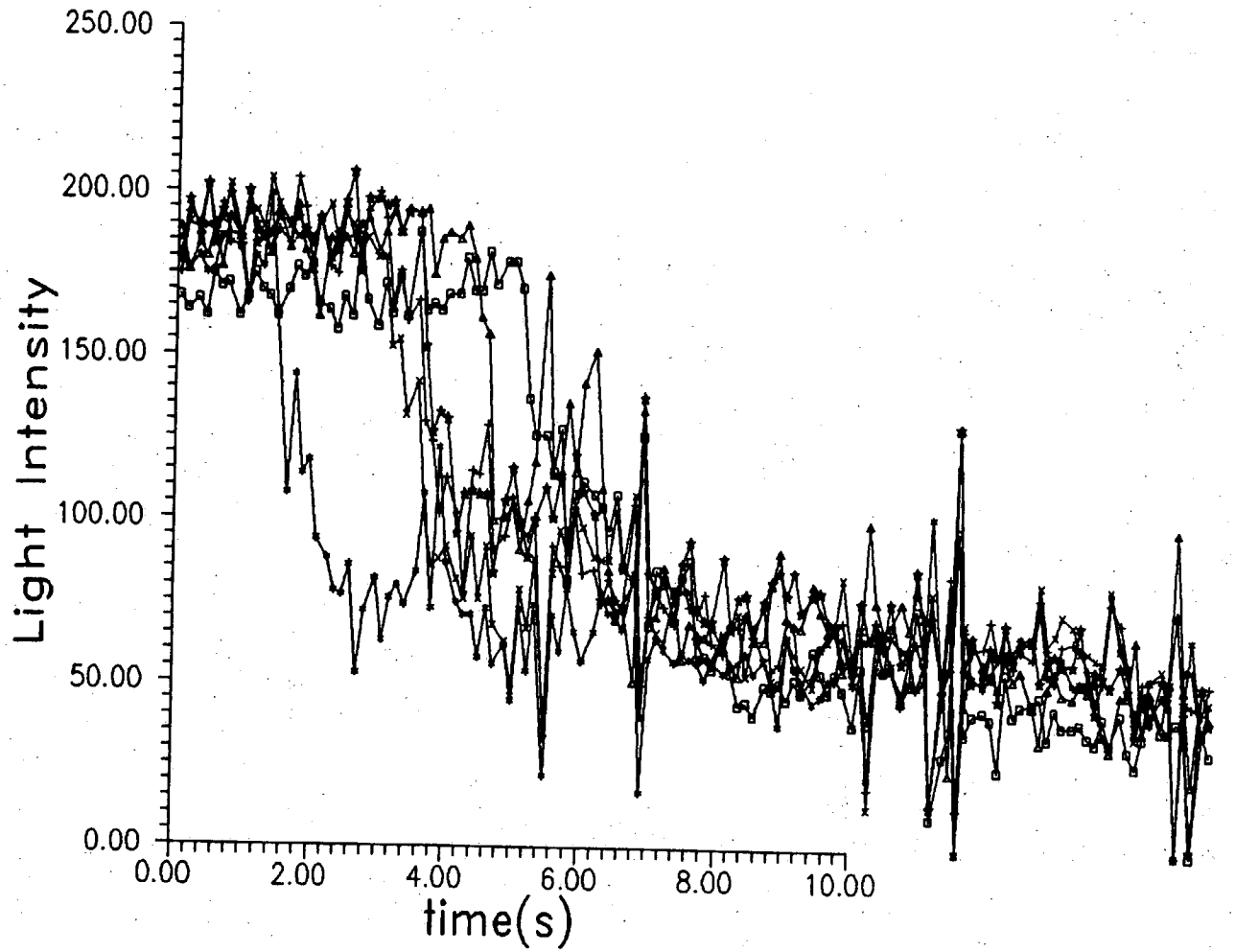
250.00
200.00
150.00
100.00
50.00
0.00
Light Intensity
0.00
2.00
4.00
6.00
8.00
10.00
time(s)

Figure 34

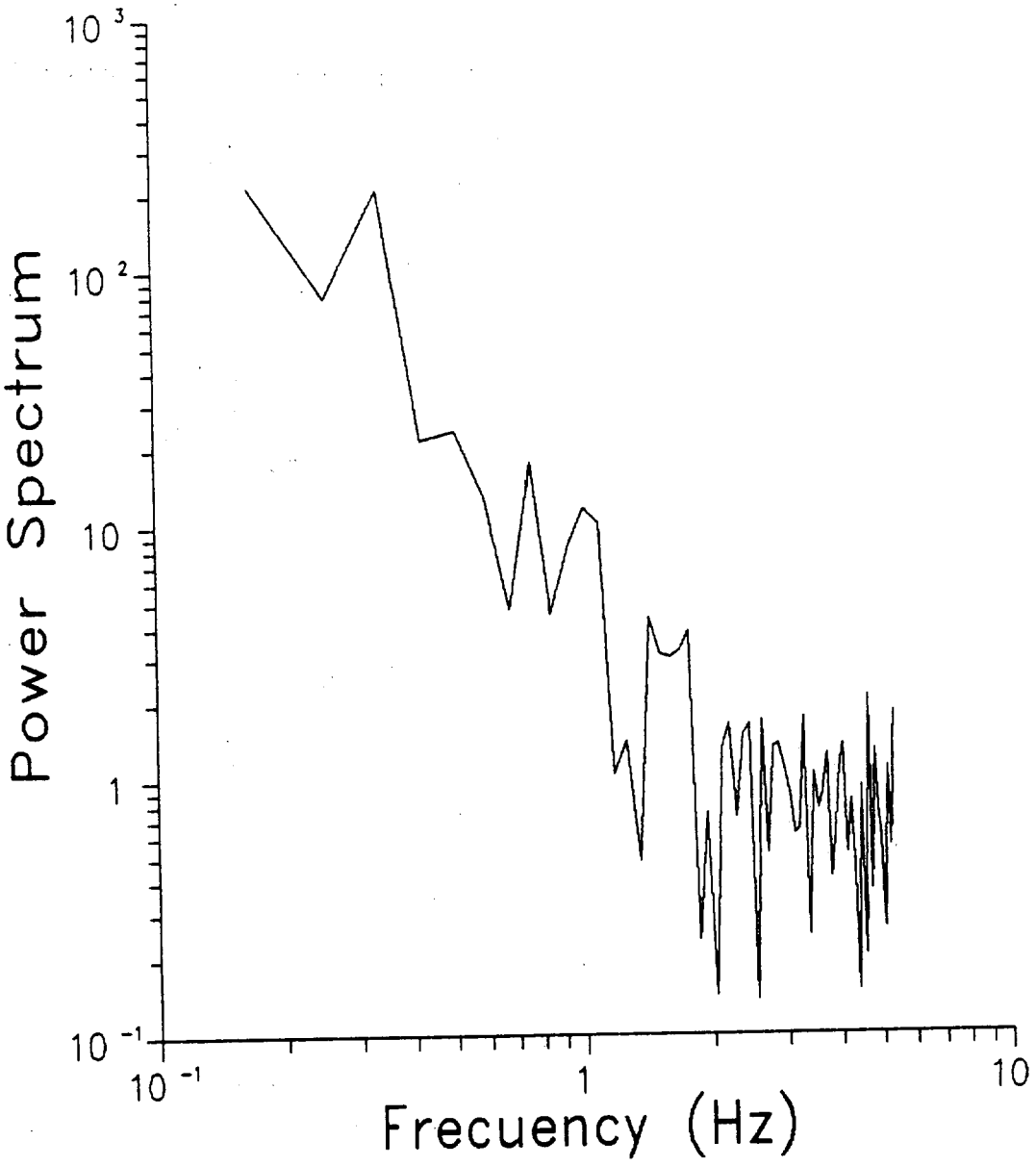

Figure 35

PLEASANTON HILTON

"Jelly" method was proposed by Dr. Rogatchev and me. Dr. Zhidov greatly contributed to the development of this method, and Mrs. Volchenko, Popov, Drs Klopov and Tolshmjakov also participated in the development.

A. Chorin / Meshkov /

20.11.89.

Reservations 1-800/HILTONS

LOCALIZED DISTURBANCES' DEVELOPMENT AT THE UNSTABLE BOUNDARY OF ACCELERATED LIQUID LAYER

Volchenko,O.I; Zhidov,I.G; Meshkov,E.E;
Rogachev,V.G.

Paper abstract for the international workshop on the inertial instabilities (Livermore,USA, November, 1989)

In the paper the investigation results of localized disturbances' dynamics, coupled with the difference in acceleration dynamics on the onset of the motion,are presented. In the investigation a new experimental method of unstationary hydrodynamic fluids modelling mith jellies was used. The developing disturbances' structure was observed in a frontal projection of an accelerating layer. Localized disturbances are shown to have a peculiarity in their development in comparison with the periodic ones, namely, an asymptotic stage is missed.

LOCALIZED DISTURBANCES DEVELOPMENT AT THE UNSTABLE BOUNDARY OF ACCELERATED LIQUID LAYER

O.I.Volchenko, I.G.Zhidov, E.E.Meshkov,
V.G.Rogachev

I. At hydrodynamic flows' realization, which leads to the energy cumulation, the instability of interfaces between substances of different densities plays a dominating role. If liquid layers are accelerated by a less dense substance, than the instabilities of Rayleigh-Taylor type (1) are being developed, which result in the adjacent substances' mixing till the accelerating layers' breakthrough. In a physical experiment a deformed interface, space heterogeneity of substance layer and of pressure at the boundary surface (difference in acceleration dynamics) may be the sources of disturbances, providing that the surface form disturbances or the difference in acceleration dynamics, as opposed to the periodic interface form disturbances, which are considered in a numerical study of Rayleigh-Taylor instability (2), may have a localized character, i.e. they might occupy a small portion of an accelerating layer surface area, compared with the periodic ones.

2. Method of unstationary hydrodynamic flows' investigation with jellies gives wide possibilities for experimental study of instabilities, accompanying liquid layers' acceleration (3). Jellies made of jelatin - water solution, are firm enough to acquire complex forms, but on the other hand, their solidity is not that high and under pressure more than 0,0-5 Atm the jelly loses it's strength and behaves as a liquid. To register a picture of the developing flow one may use optics because jellies are transparent.

3. The study conducted aimed at the observation of instability

development, which accompanies the acceleration of homogeneous liquid layer by the products after gas HE mixture explosion (GHEM) with the variation of the original surface deformations and GHEM initiation geometry, which leads to the difference in space pattern of the detonation and reflection waves' interference and, as a consequence, to the difference in acceleration dynamics.

The experiment scheme is the following: in a 4 x 4 cm square channel with transparent walls a jelly layer 1.9 cm thick was a barrier, dividing a closed camera 3.4 cm high, filled with GHEM (stechiometric mixture of oxygen and acetylen at the normal pressure) and a section of the channel, coupled with atmosphere. Dischargers are used to initiate the process. The flow pattern is registered by a high-speed camera at a frontal projection (through the liquid layer, upstream of the layer), or at a side one (through the transparent channel walls). The observation time (1 ms) exceeded by more than an order the characteristic times of pressure levelling in the closed camera. The observed motion of the upper, stable surface layer is in good agreement with the estimated in the suppusition about the adiabatic expansion of explosion products with γ=1.24 and the initial value of explosion products' pressure P_o= 13.5 atm. By the end of the observation, pressure lowered by approximately one third of it's initial value.

4. Let's consider the results of the experiments, where the disturbance source lies in the space dynamics difference at the initial acceleration stage, which is realized in the developing disturbances' structure at the lower, unstable, originally plain

surface of liquid layer.

In fig.1 the photochronograms of the certain cases of CHEM initiation in frontal projection are given: a) at one point in the center of camera bottom; b) by 8 spark gaps' chain along the camera bottom; c) at four points, placed symmetrically in the form of a square.

Fig 1

In the first frames the luminescence in the initiation points is seen. The observed structure of the developing disturbances was reproduced from test to test. The most intensive bubbles' growth at the surface of the unstable jelly-gas surface is seen in the points, corresponding to the crossing of the collision lines of the detonation waves and the non-stationary shock waves, appearing at the reflection of the detonation waves, propagating away from the initiation points.

At the initiation in one point (a) a growing bigger with time, central cavity-bubble, which form is almost spherical, is more quick to implant into the liquid layer at acceleration nearly equal the layer acceleration, in comparison with the mixing at the "plain" interface areas. The analogous picture is observed with the hemi-cylindric cavity when the initiation is by chain (b)case). In fig.2 the dependence of central bubble cross-dimension D on the layer shift X is given. The measurements show that in the case a) the depth of the bubble penetration into the layer, H, approximately equel D, i.e. $H(t) \simeq D(t)$.

Fig 2

The two stages may be distinquished: the initial one, when the cavity divelopment is determined by space difference in dynamics, and the stage, when the characteristic dimensions grow proportionally to the acceleration path. In case of a localized "point" disturbance $\frac{dH}{dx} \simeq 0.7$, i.e. a bubble "comes to surface"

at a speed, which increases with time. This dependence is limited by time, the space limitalion, i.e. the channel walls, dominates at a late stage. Almost the same picture of disturbances' development is observed, when the dominating flow disturbance is not a difference in acceleration dynamics, but a specially formed, small (at the onset) cavity on the layer surface. In the case of "chain" disturbances $\frac{dH}{dx} \simeq 0.4$, that is in agreement with the calculated results (4), obtained for interpretation of a more complex physical experiment.

Thus, a localized disturbances' development differs from the evolution of the periodic ones, characterized by a period, commensurable with a space dimension of a localized disturbance, namely, with an asymptotic stage absence, when a periodic structure of bubbles "comes to surface" into the liquid at a constant speed, $V \simeq \sqrt{\frac{g}{k}}$ (2), where g - a layer acceleration, K - a wave vector of a disturbance.

REFERENCES

1. G.I.Taylor, "The Instability of Liquid Surfaces When Accelerated in a Direction, Perpendicular to Their Planes", Proc. ROy.Soc., London, A201, 1950, p.192-196.

2. Исследование гидродинамической неустойчивости с помощью ЭВМ. Сборник научных трудов под редакцией К.И.Бабенко, М.1981, препринт ИПМ АН СССР.

3. О.И.Волченко, И.Г.Жидов, Б.А.Клопов, Е.Е.Мешков, В.В.Попов, В.Г.Рогачев, А.И.Толшмяков, "Способ моделирования нестационарных течений несжимаемой жидкости", А.с. 1026154. Бюллетень ОИПОТЗ № 24, 1983 г.

4. M.A.Sweeney, F.C.Perri, "Investigation of Shell Stability in Imploding Cylindrical Target", J.Appl. Phys. 1981, v.52, N 7, p.4487-4502.

Captions of the paper "Localized Disturbances' Development ...." by Volchenko, O.I.; Zhidov,I.G.; Meshkov,E.E; Rogachev,V.G.

Fig.1. Photochronogram frames of the experiments with the disturbances' development at an unstable interface of a liquid layer, which is accelerated by the pressure of the products after the acetylene - air mixture explosion. The process is registered in a frontal projection.

a) Explosive mixture is initiated the center at the camera bottom;

b) The initiation is realized at 8 points along the camera bottom;

c) The initiation is realized at 4 points, placed symmetrically in a form of a square.

Fig.2. Dependence of a latitudinal dimension of a central bubble on a layer displacement.

1 - initiation at one point in the center;

2 - initiation by an 8 points' chain.

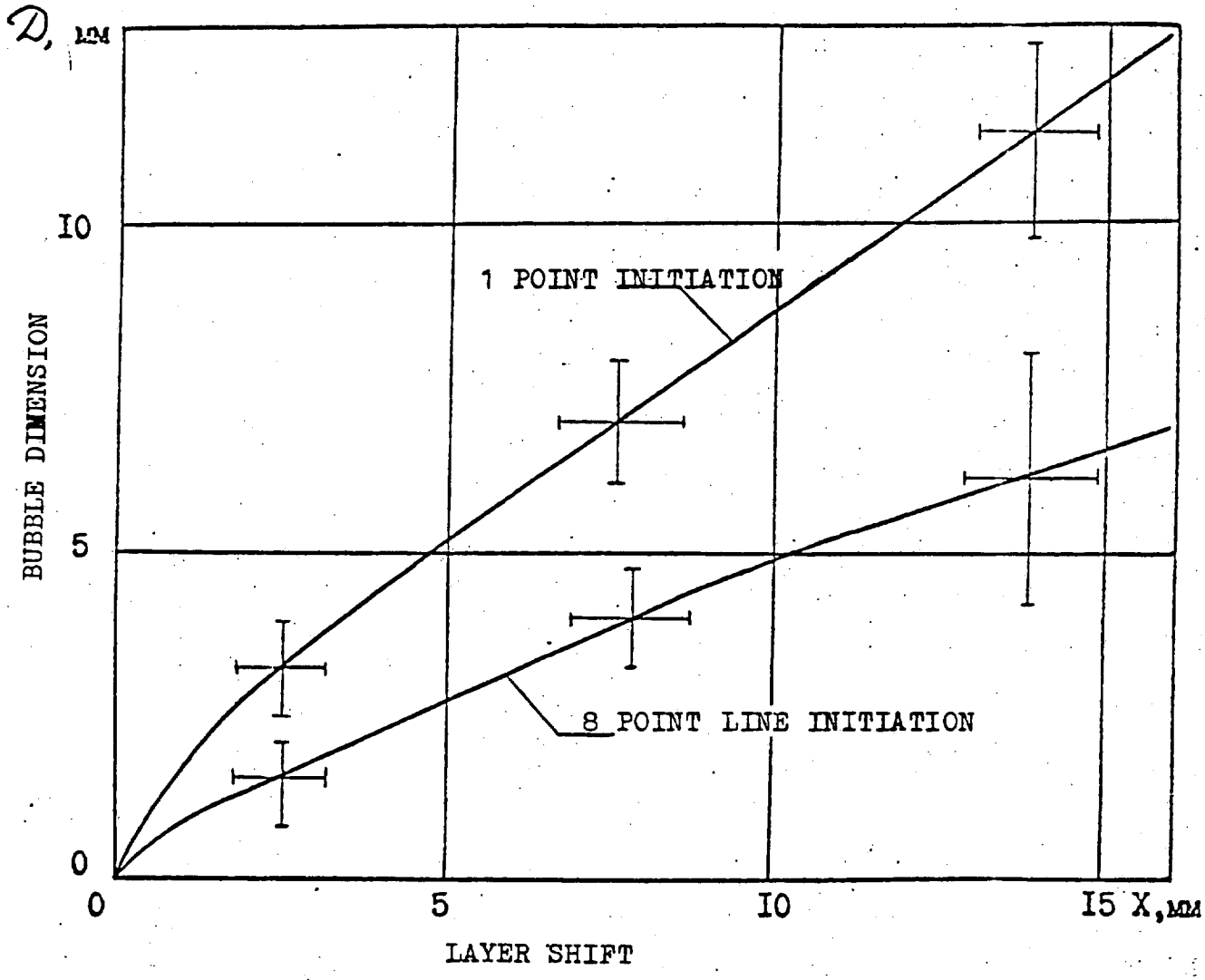
D, MM
10
5
0
0
5
10
15 X, MM
BUBBLE DIMENSION
LAYER SHIFT
1 POINT INITIATION
8 POINT LINE INITIATION

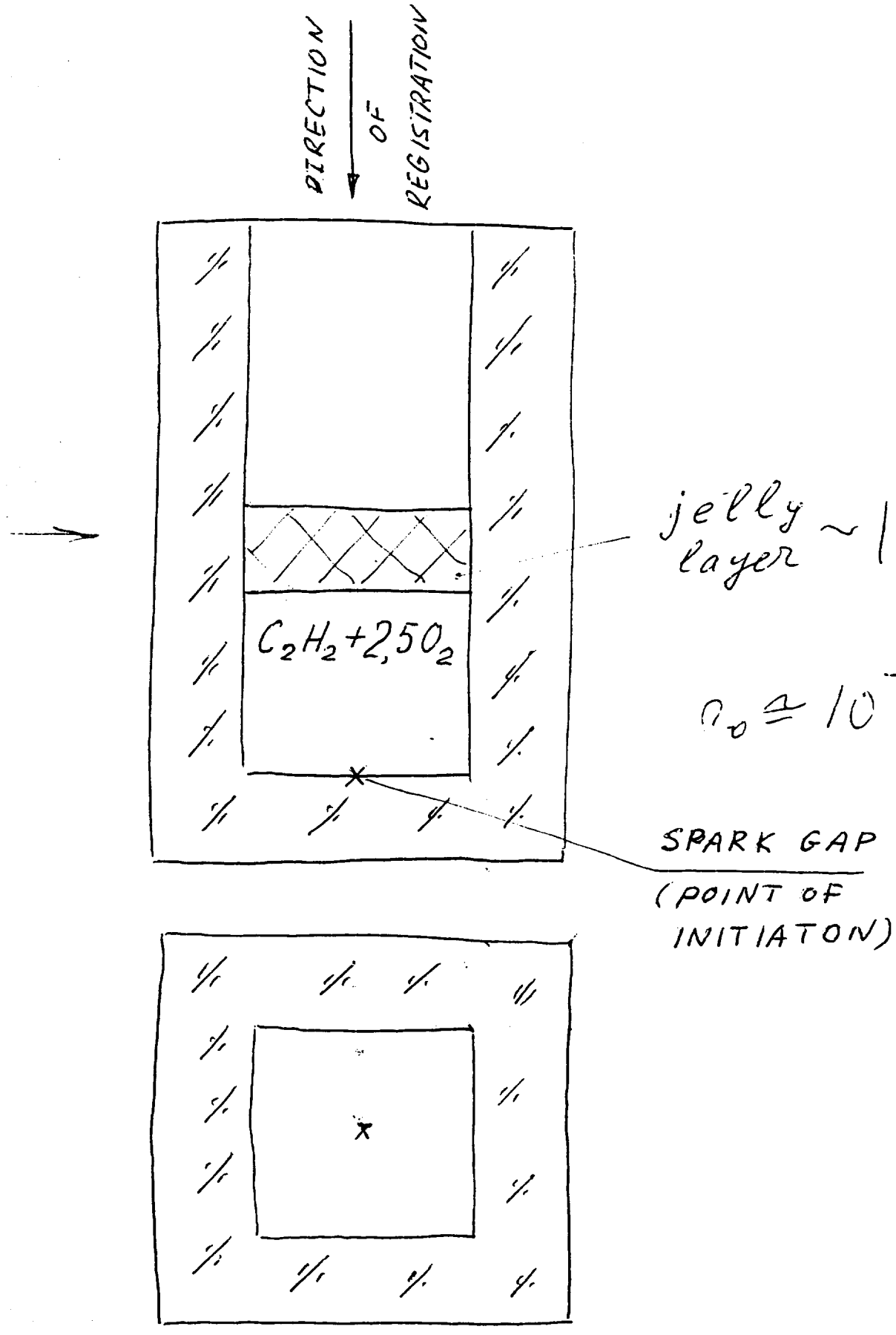

EXPERIMENTAL SET UP

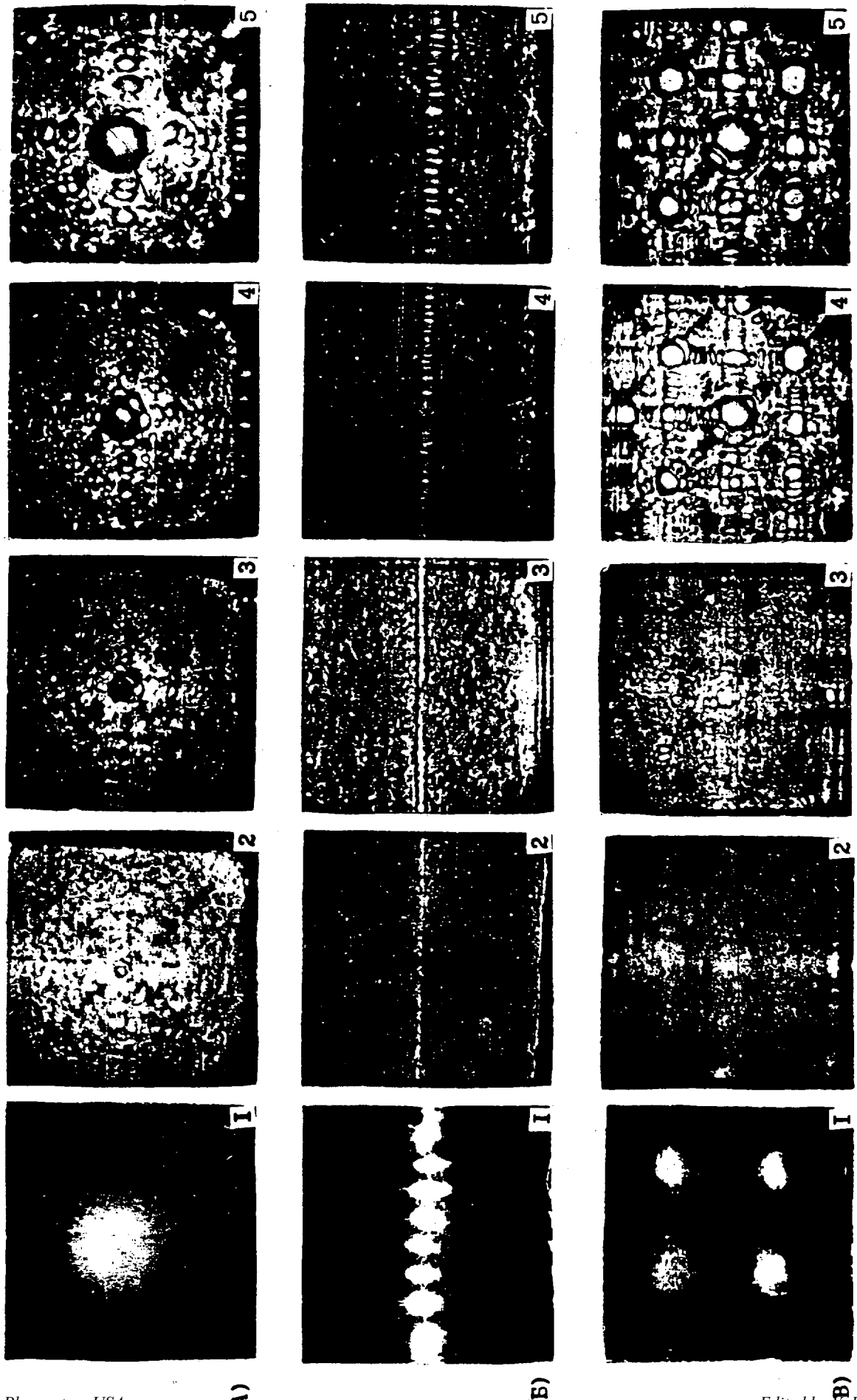
5
4
3
2
I
А)
Б)
В)

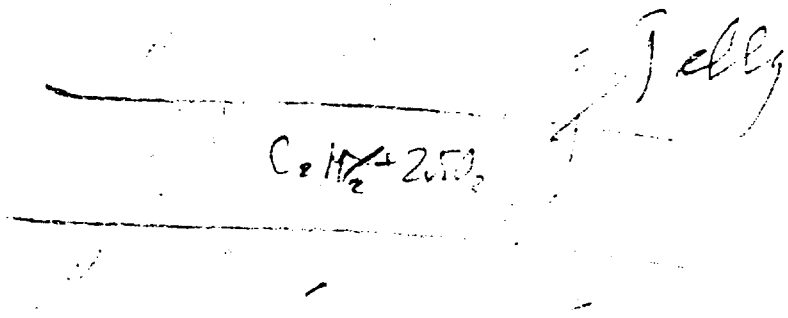

QUANTITATIVE MEASUREMENTS OF TURBULENCE INDUCED IN A PLASMA BY RAPIDLY MOVING OBJECTS

J. Grun, J. Stamper, J. Crawford*, C. Manka, T. Peyser
A. Mostovych, S. Obenschain, and B. Ripin

NAVAL RESEARCH LABORATORY
WASHINGTON D.C. 20375

*Present address: *Southwestern Texas State University*

Edited by V. Rupert

THE EXPERIMENT

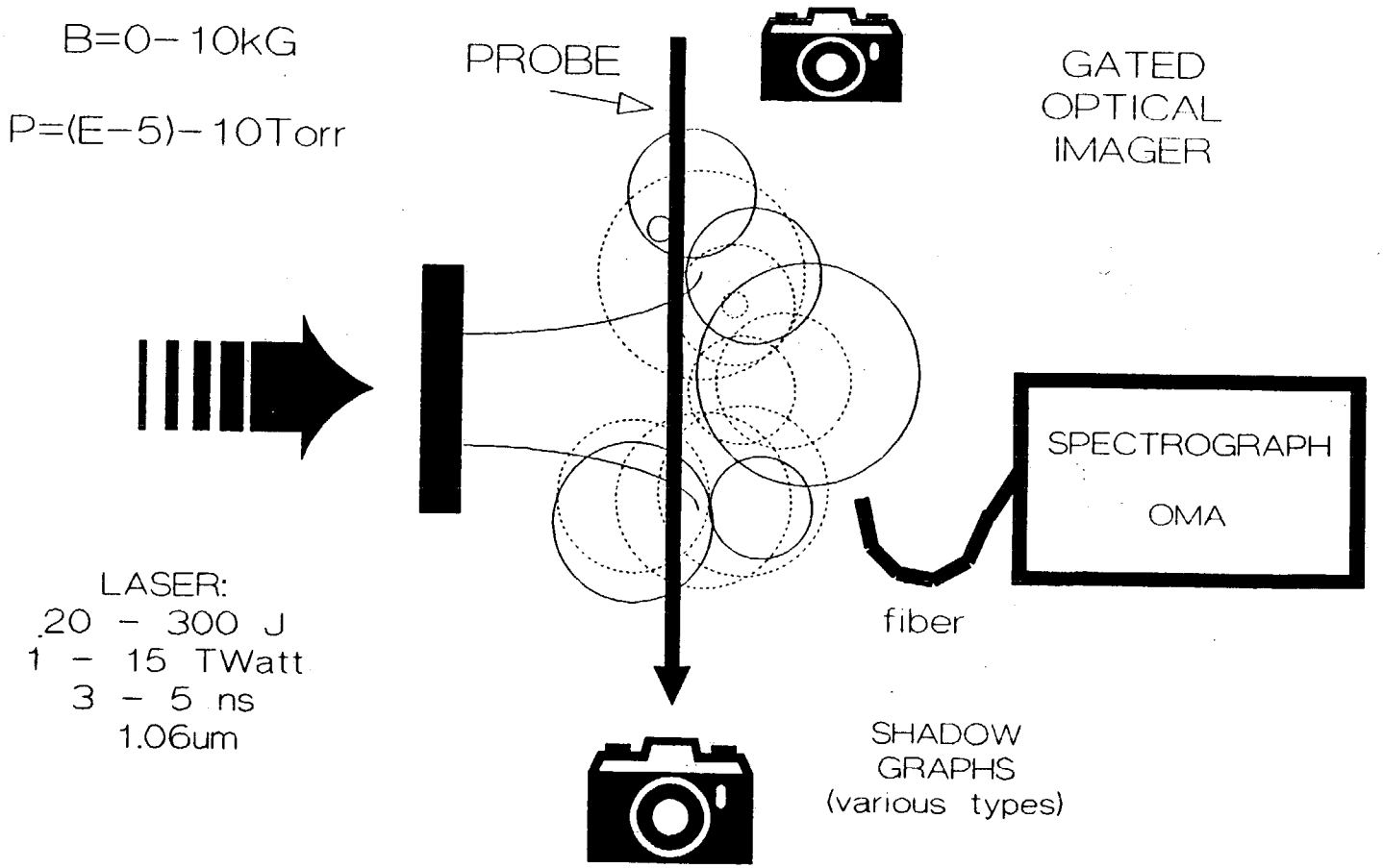

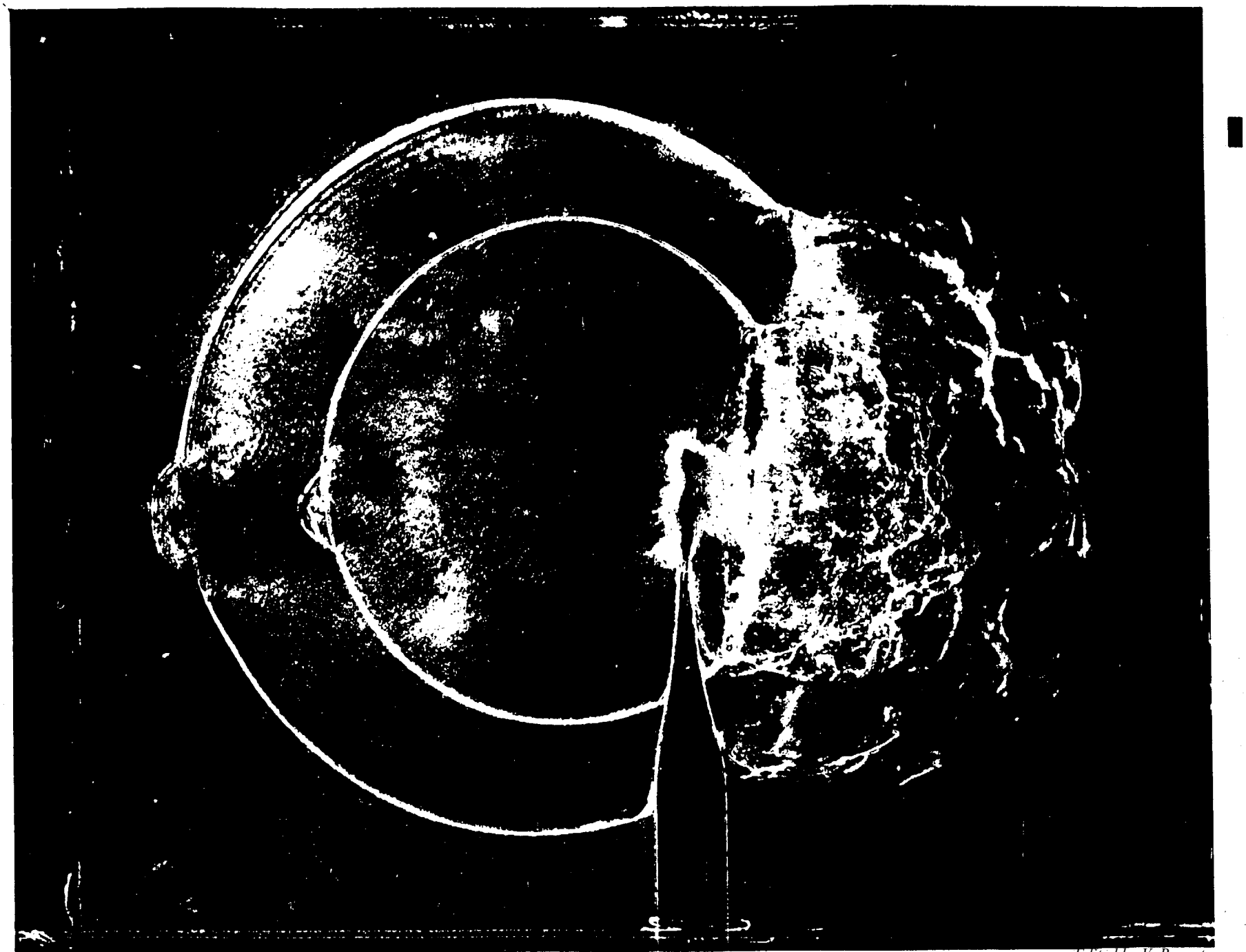

PERTURBED TARGETS ($\lambda = 100\mu m$)

14ns

43ns

81ns

FLAT TARGETS

8ns

82ns

PARAMETERS

B = 0
P = 5T N_2
E ≃ 250 Joules
τ = 3–3.5ns
9μm CH ± 1μm

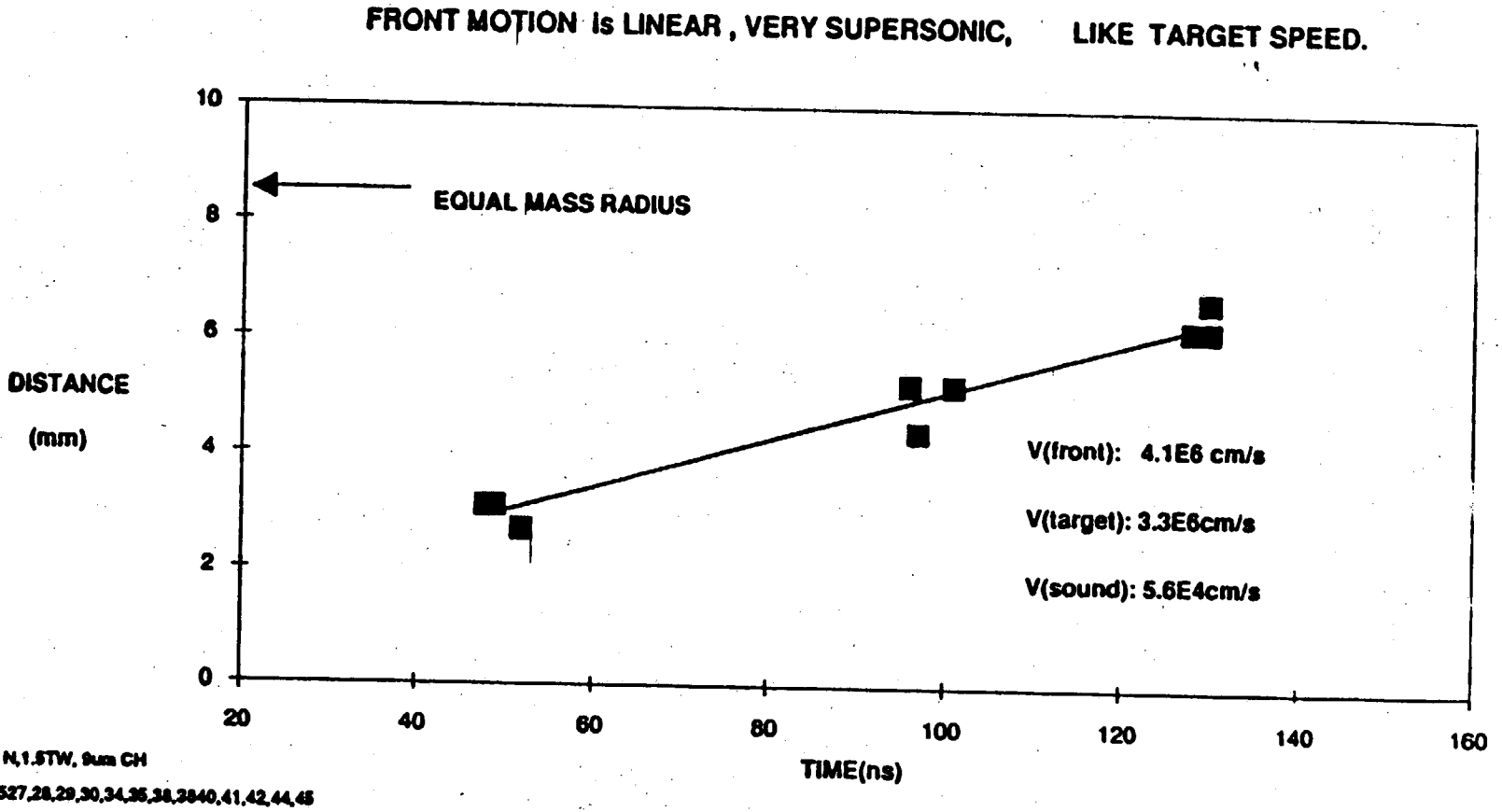
FRONT MOTION is LINEAR , VERY SUPERSONIC, LIKE TARGET SPEED.
EQUAL MASS RADIUS
DISTANCE
(mm)
10
8
6
4
2
0
20
40
60
80
100
120
140
160
TIME(ns)
V(front): 4.1E6 cm/s
V(target): 3.3E6cm/s
V(sound): 5.6E4cm/s
5 Torr N,1.5TW, 9um CH
shots:527,28,29,30,34,35,38,3940,41,42,44,45

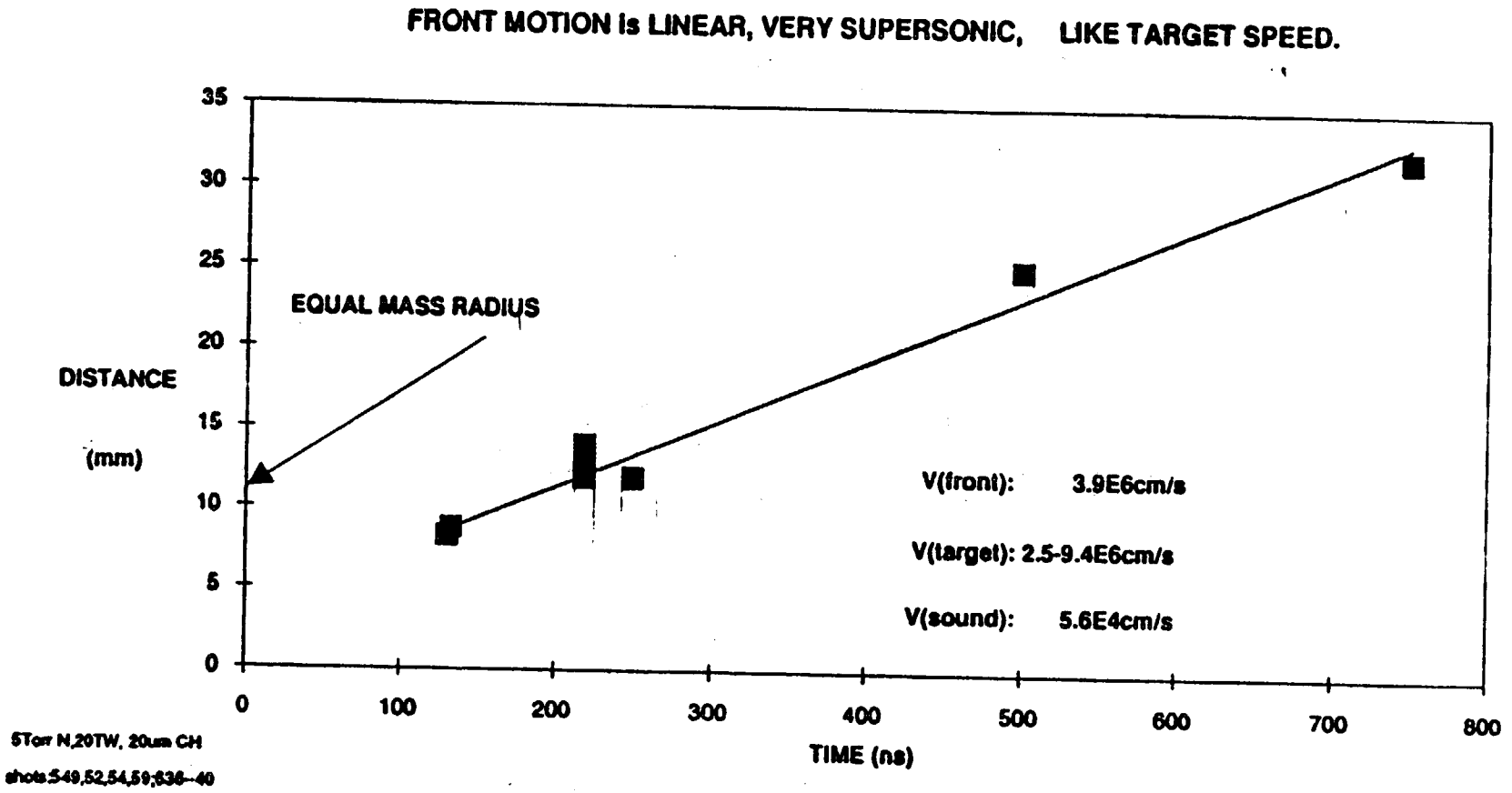
FRONT MOTION is LINEAR, VERY SUPERSONIC, LIKE TARGET SPEED.
EQUAL MASS RADIUS
DISTANCE
(mm)
TIME (ns)
V(front): 3.9E6cm/s
V(target): 2.5-9.4E6cm/s
V(sound): 5.6E4cm/s
0
5
10
15
20
25
30
35
0
100
200
300
400
500
600
700
800
5Torr N,20TW, 20um CH
shots:549,52,54,59;636--40

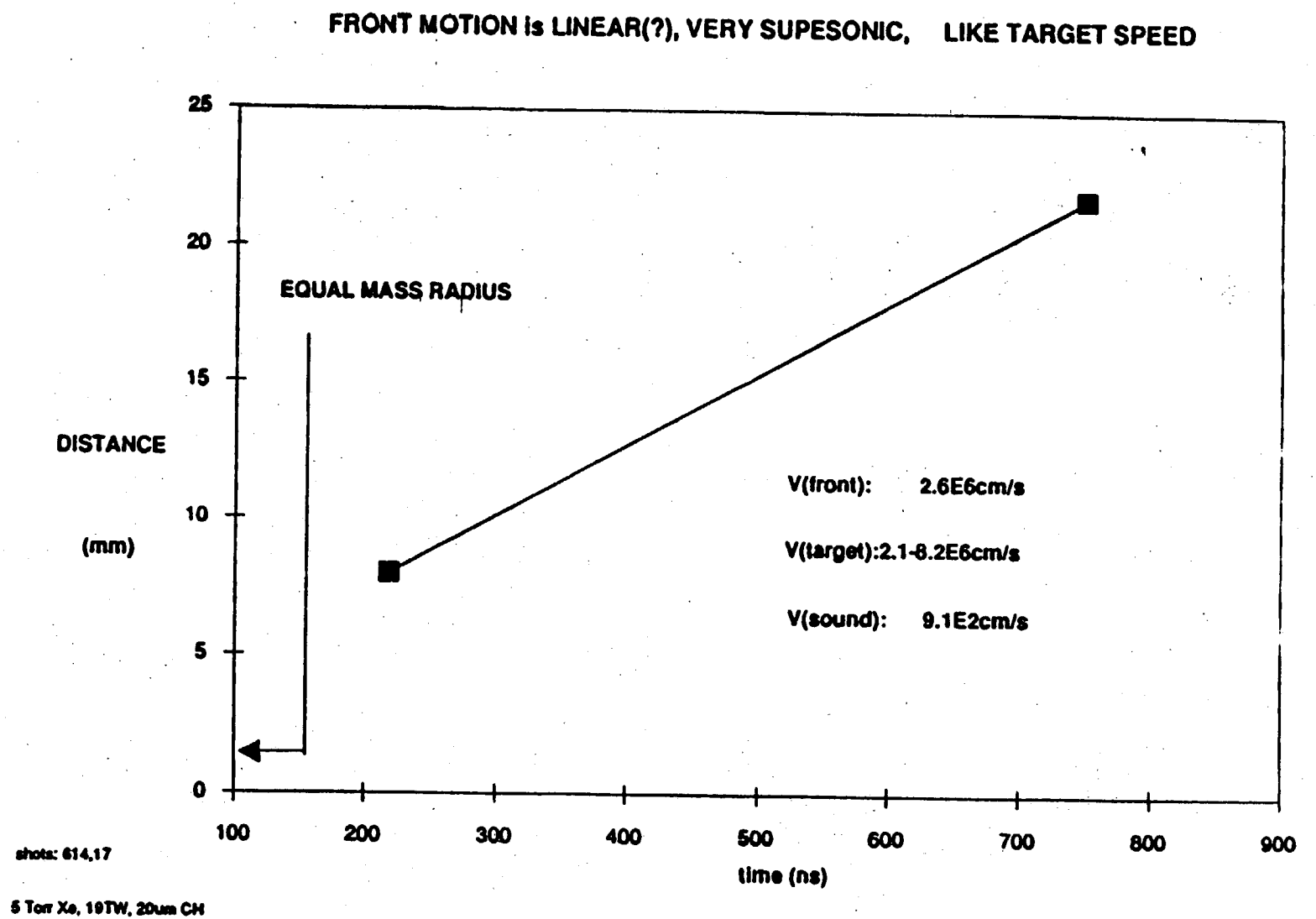
FRONT MOTION is LINEAR(?), VERY SUPESONIC, LIKE TARGET SPEED
EQUAL MASS RADIUS
DISTANCE
(mm)
V(front): 2.6E6cm/s
V(target):2.1-8.2E6cm/s
V(sound): 9.1E2cm/s
0
5
10
15
20
25
100
200
300
400
500
600
700
800
900
time (ns)
shots: 614,17
5 Torr Xe, 19TW, 20um CH

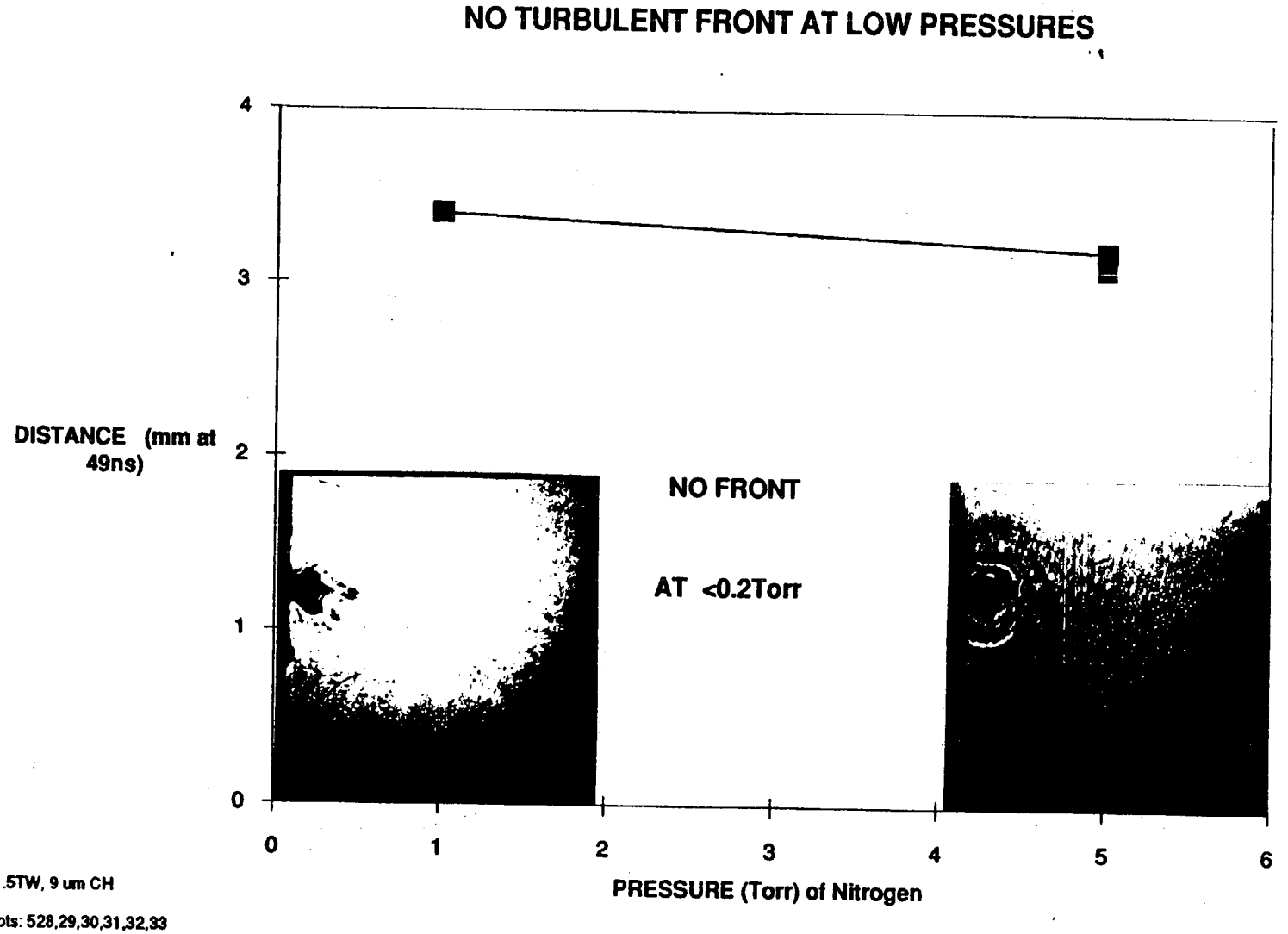
NO TURBULENT FRONT AT LOW PRESSURES
DISTANCE (mm at 49ns)
NO FRONT
AT <0.2Torr
PRESSURE (Torr) of Nitrogen
1.5TW, 9 um CH
shots: 528,29,30,31,32,33

Pleasanton, USA *Edited by V. Rupert*

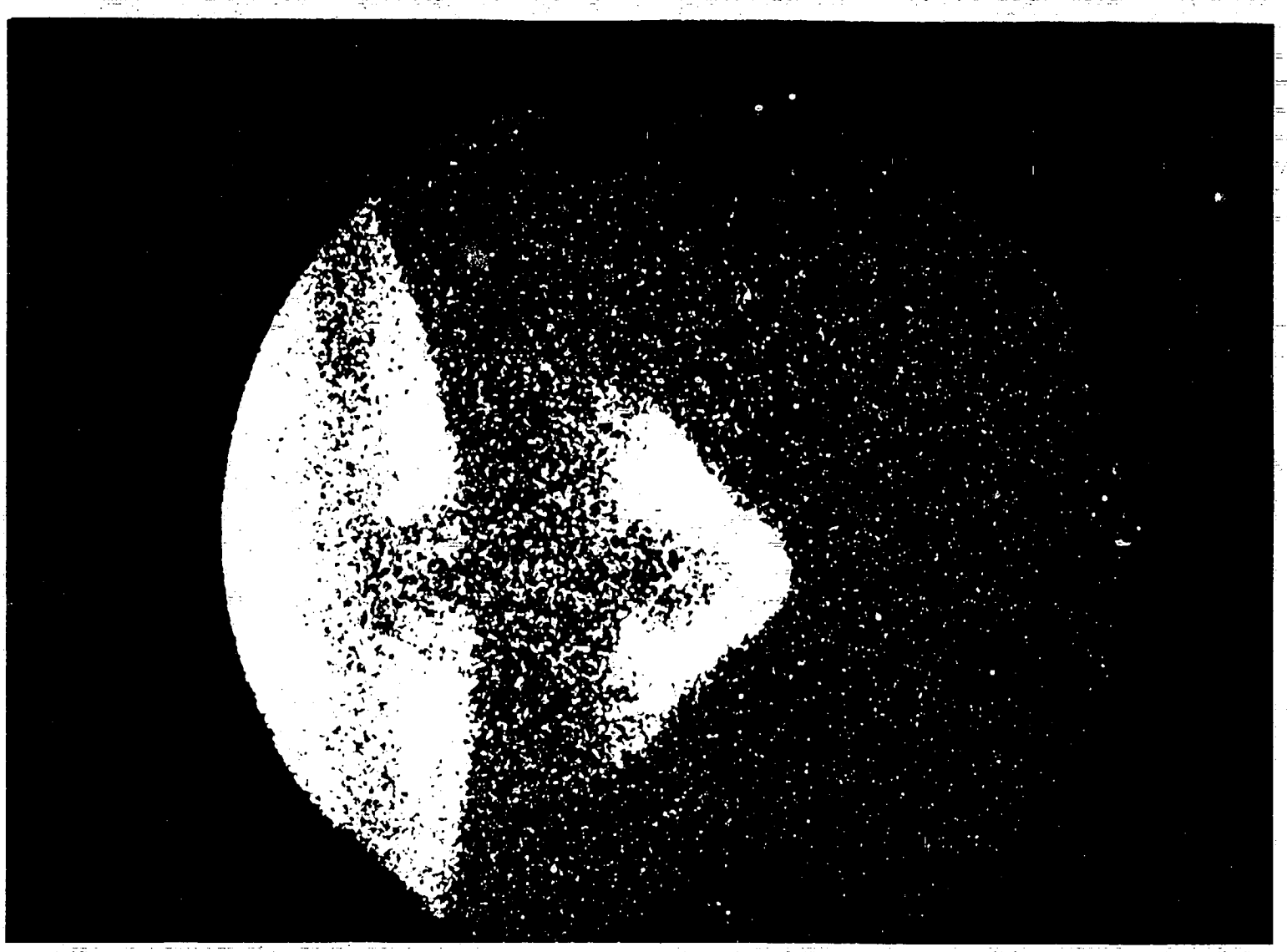

570

VII.

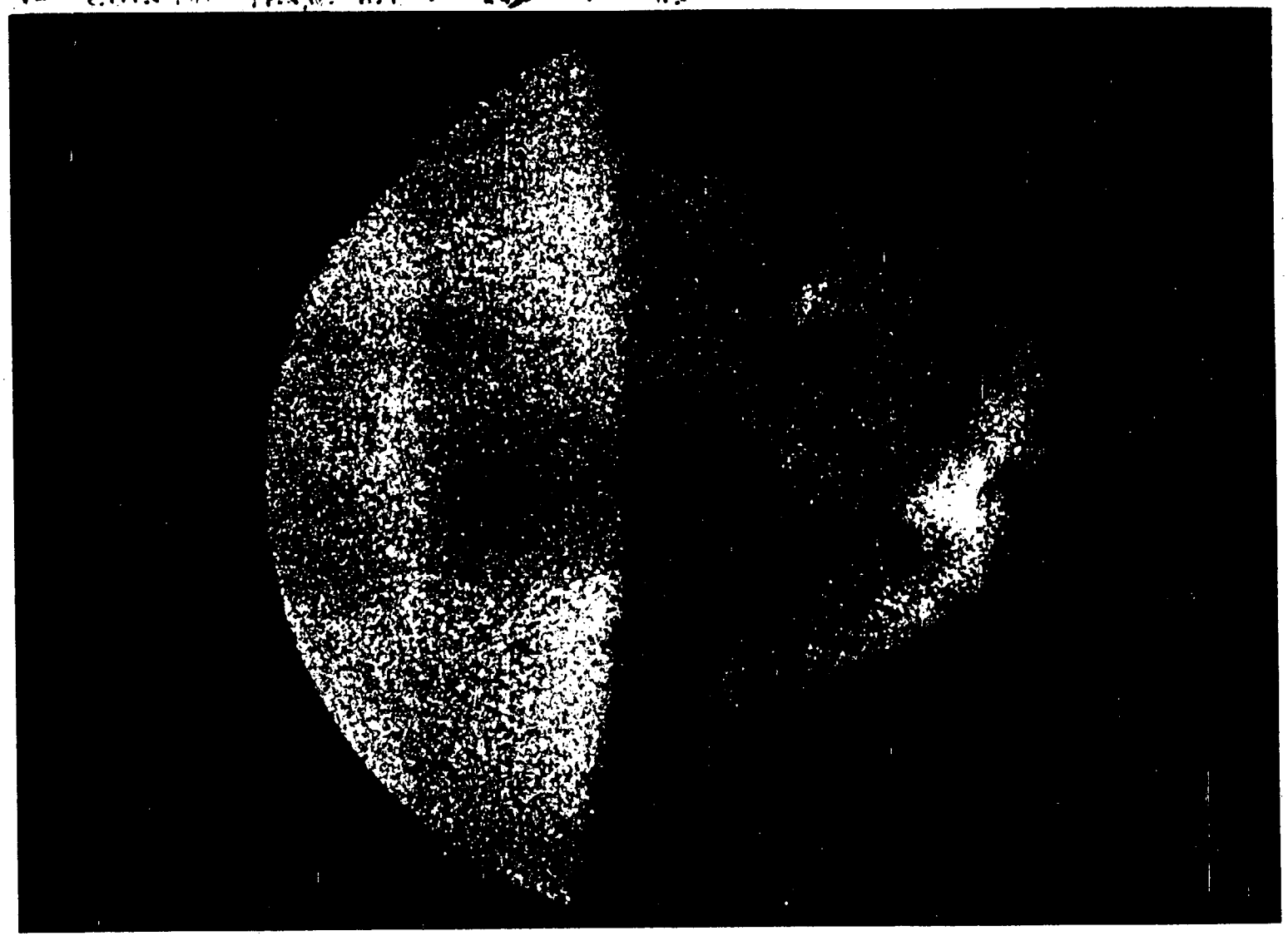

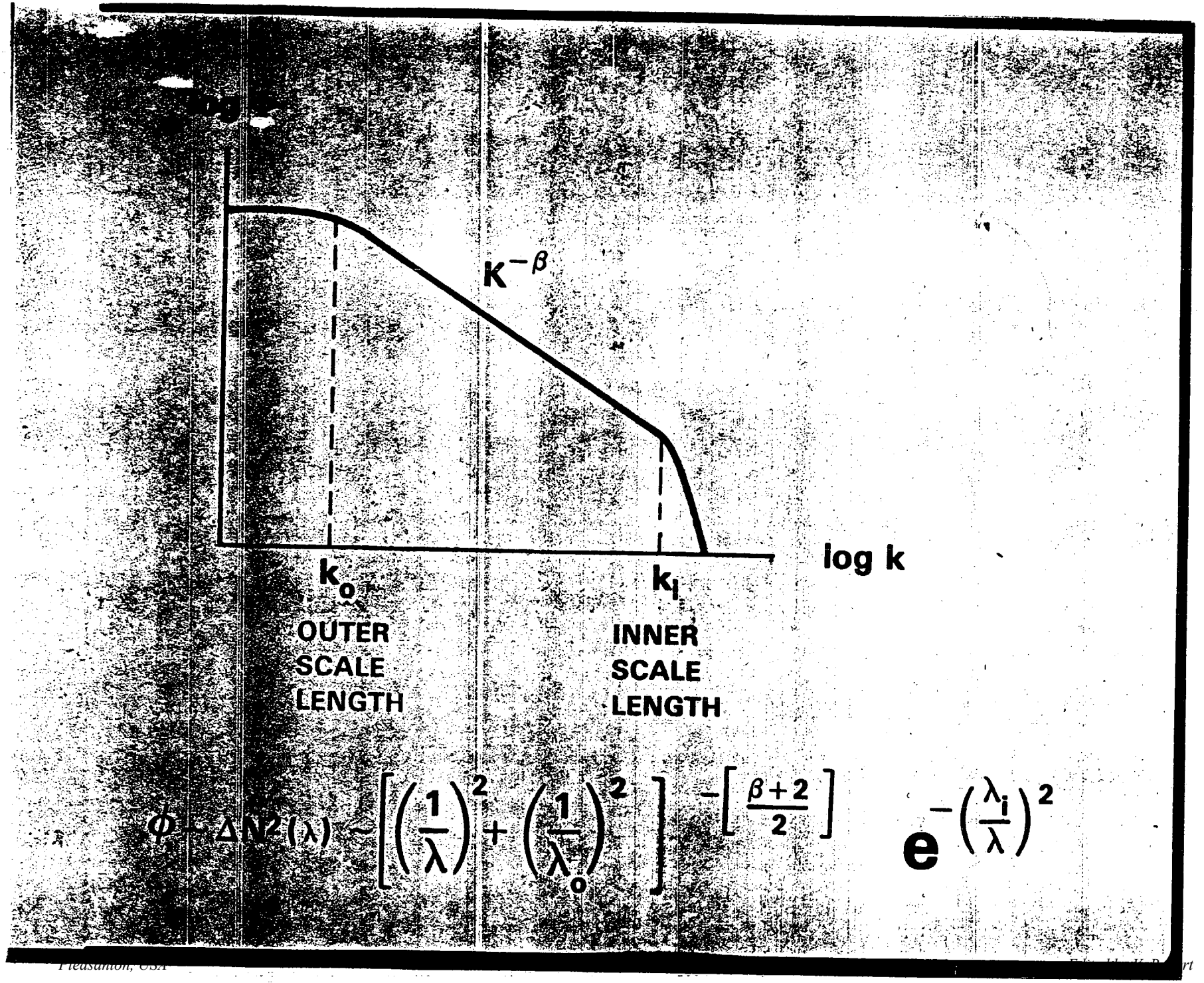
$K^{-\beta}$
log k
k_o
k_i
OUTER SCALE LENGTH
INNER SCALE LENGTH
$\Phi_{\Delta N^2}(\lambda) \sim \left[\left(\frac{1}{\lambda}\right)^2 + \left(\frac{1}{\lambda_o}\right)^2\right]^{-\left[\frac{\beta+2}{2}\right]} e^{-\left(\frac{\lambda_i}{\lambda}\right)^2}$

CONCEPT

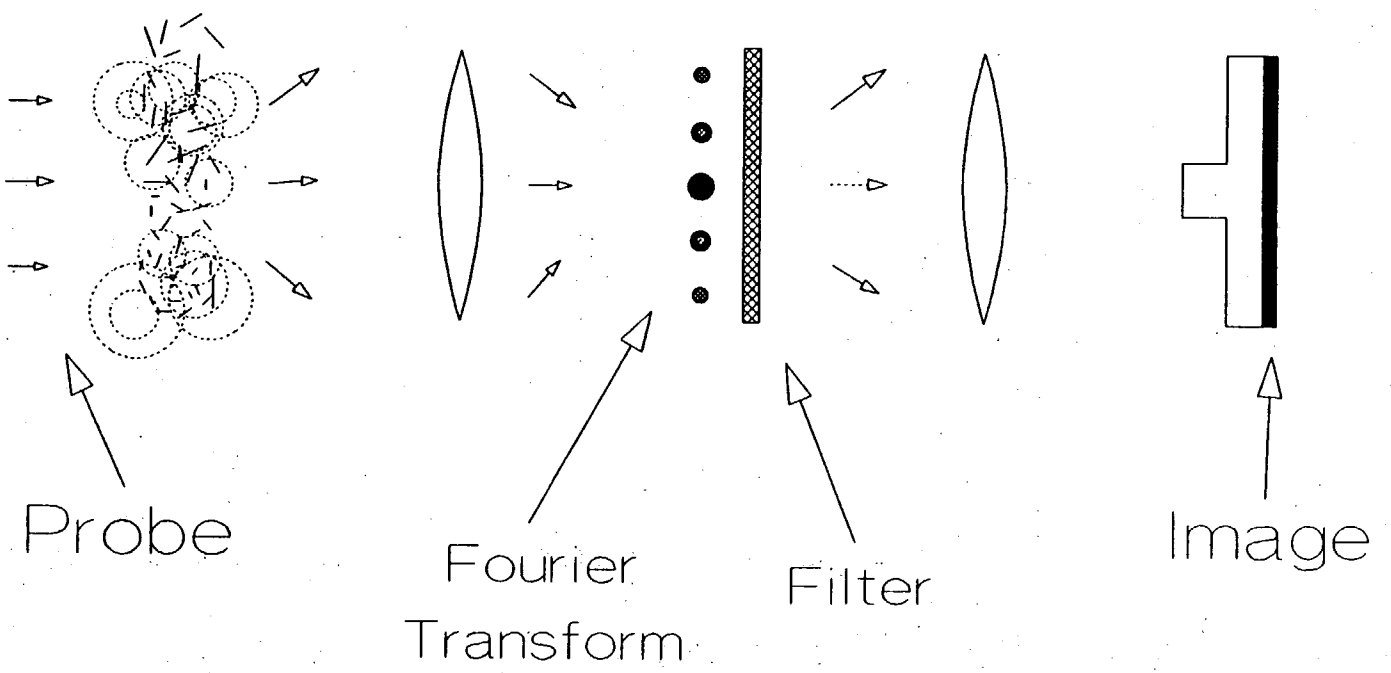

PHASE-CONTRAST METHOD

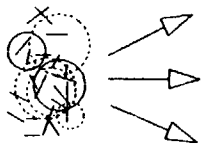

$$E=\mathcal{E}\ EXP[\iota(\varphi+\Phi(x,y))]$$
$$=\mathcal{E}\ EXP[\iota\varphi]\ \ [1+\sum_{1}(\iota\Phi)^{n}/n!]$$

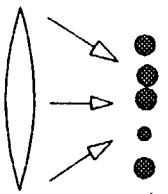

$$\mathcal{F}(E)=\mathcal{E}\ EXP[\iota\varphi]\ \ [\mathcal{F}(1)+\mathcal{F}(\sum_{1}(\iota\Phi)^{n}/n!)]$$

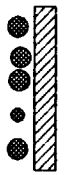

$$\mathcal{F}(1) \longrightarrow \pm\iota\mathcal{F}(1)$$

$$EE^{*}=\ \mathcal{E}\mathcal{E}^{*}[\,1\pm2\Phi+\ \ldots]$$

SETUP

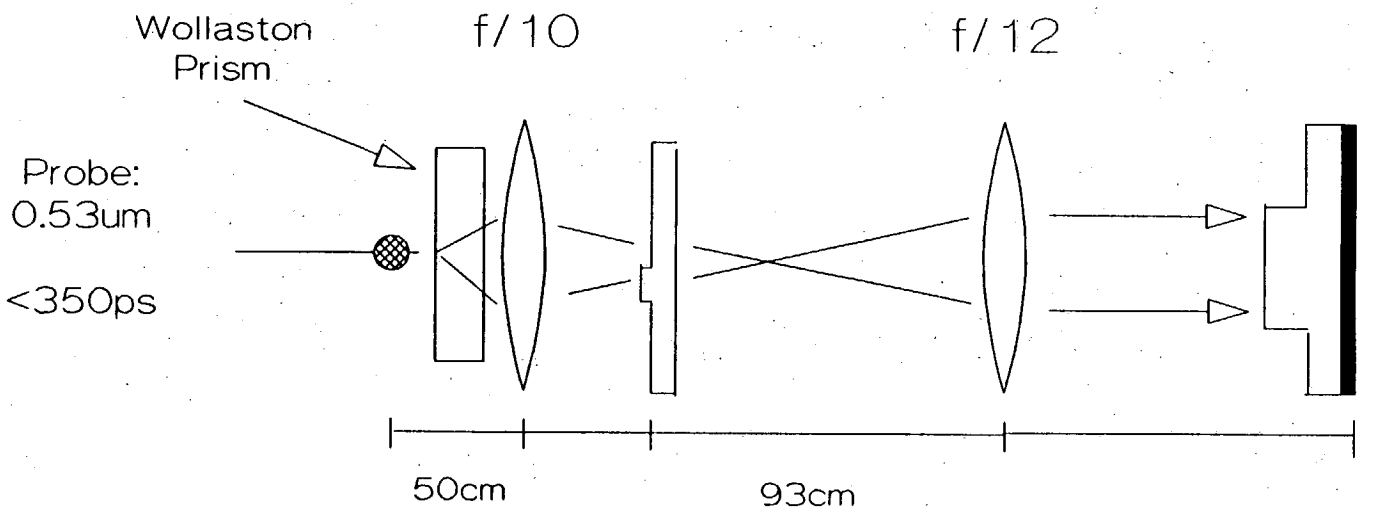

RESOLUTION : 10μm
MAGNIFICATION: 1.9

TYPICAL RESULT

NRL

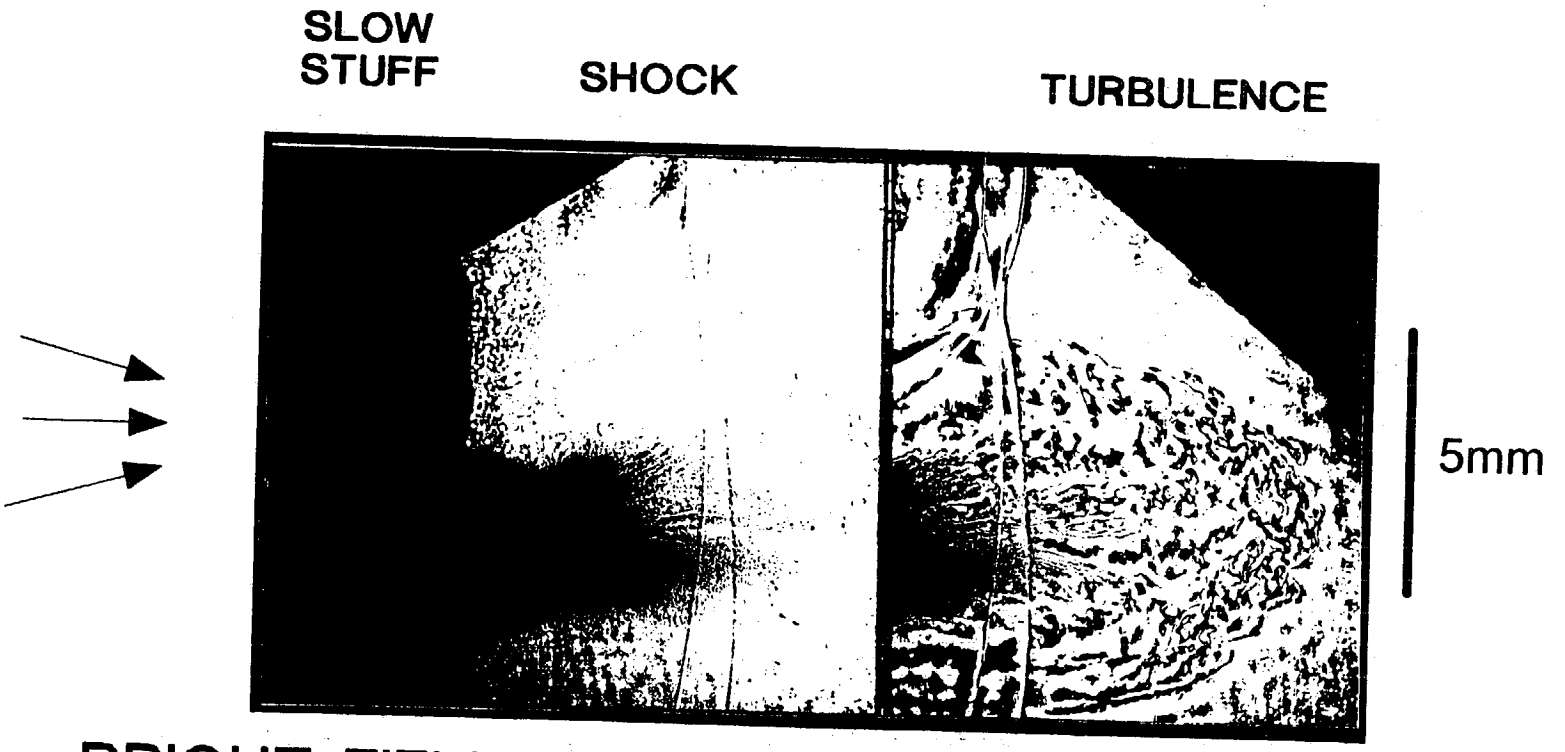

shot:568

10um Al, 4.5 TW, 219ns, 5Torr, N_2

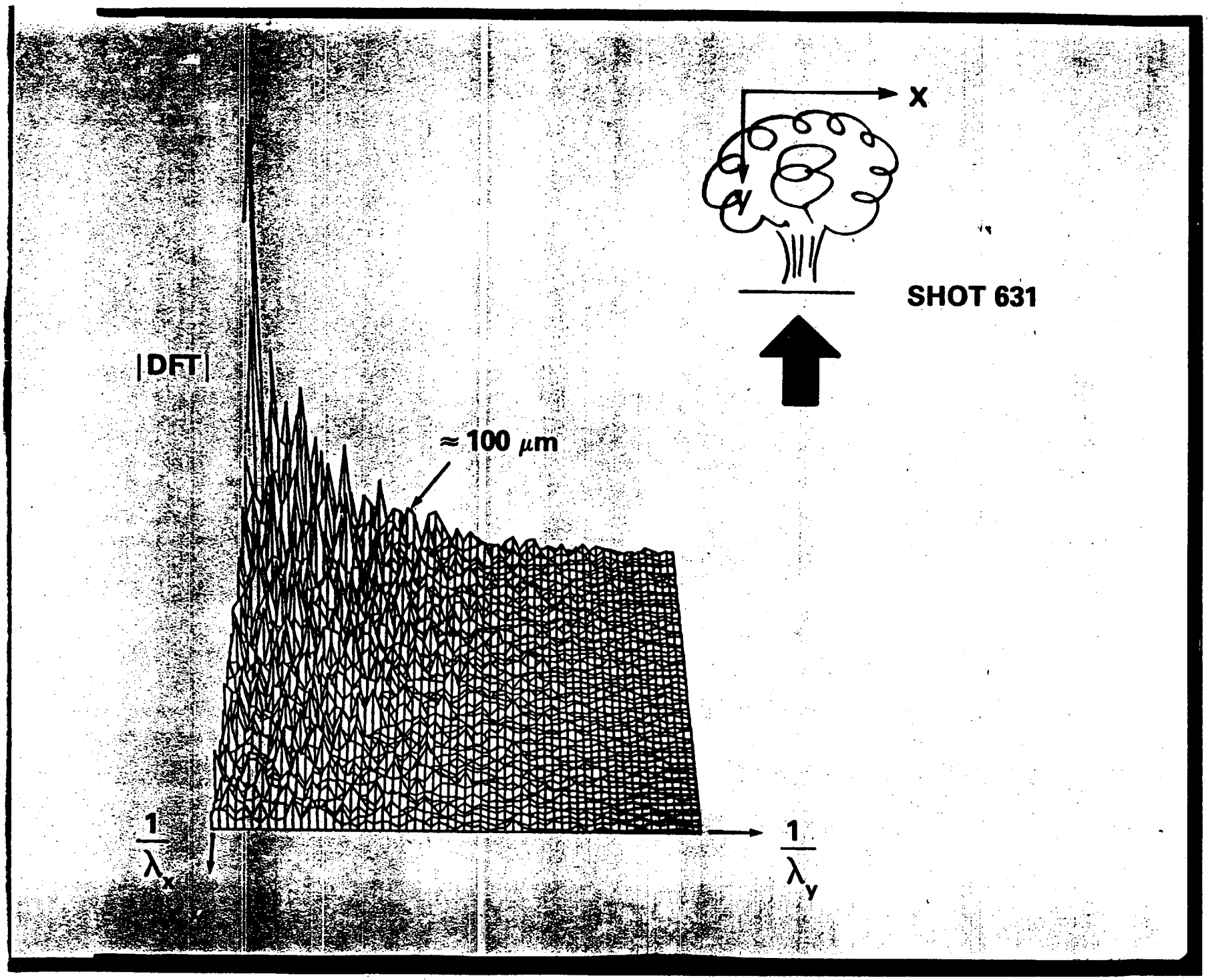
X
SHOT 631
|DFT|
≈100 μm
1/λx
1/λy

One-D Power Spectrum in K Space Shot 617

$$P(k_x,0) = \left(\mathrm{Abs}\left(\iint f(x,y)\ e^{-ik_x x}\ dx\ dy \right) \right)^2$$

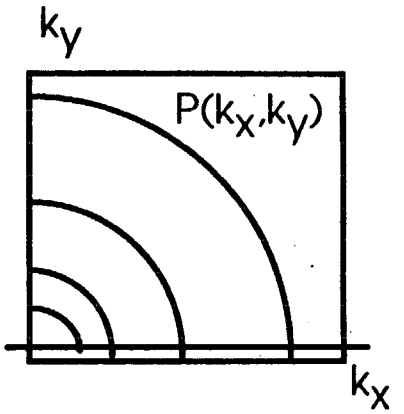

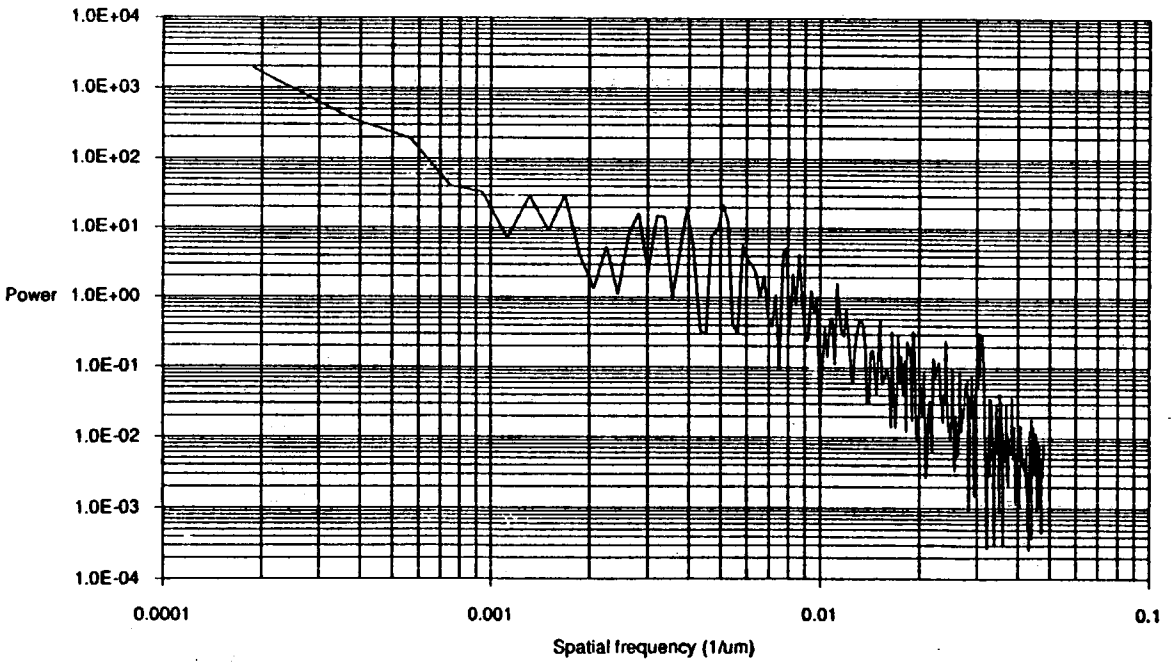

$$P(k_x,0) = k^{-3.2}$$

One-D Power Spectrum of shot 617

$$P(k_x) = \Sigma_y(\mathrm{Abs}(\int f(x,y)\, e^{-ik_x x}\, dx))^2$$

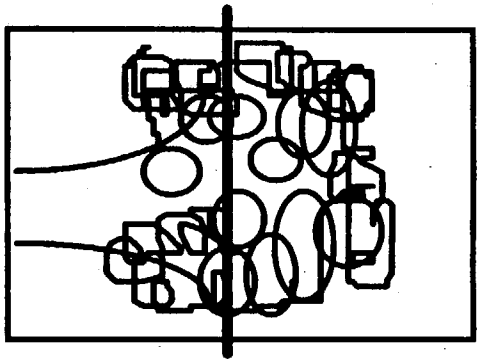

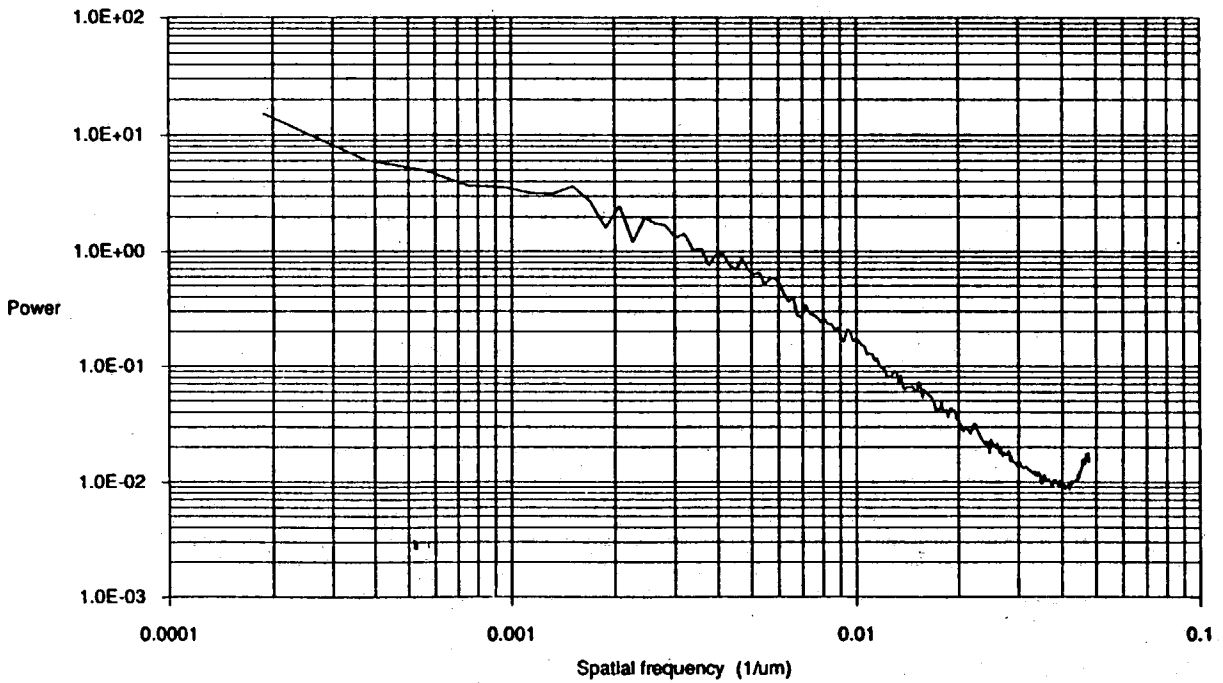

$$P(k_x) = k_x^{-2.1}$$

A Measure of Symmetry

Exponent of $k_i^{-\alpha}$ as a function of scan line

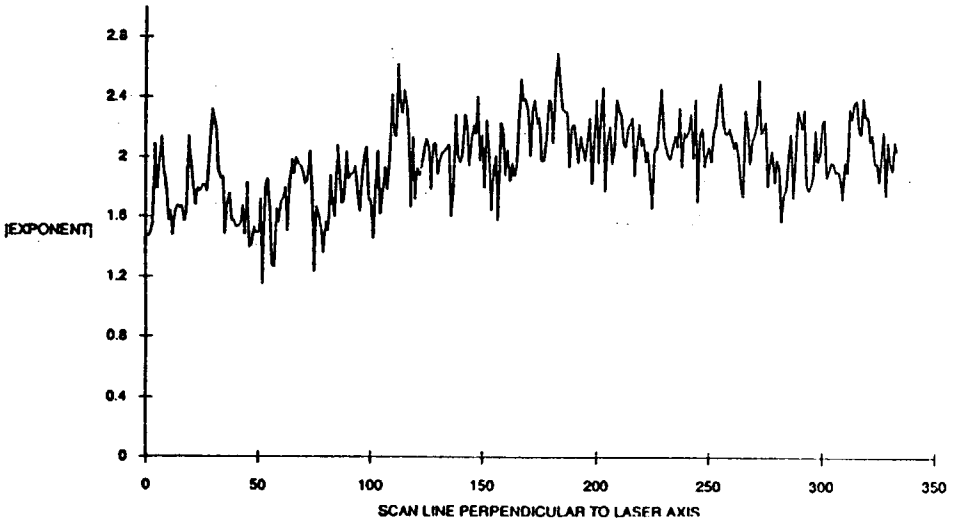

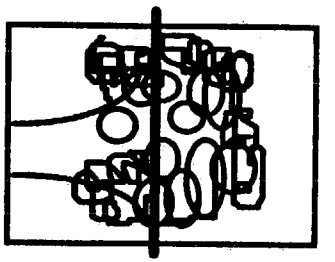

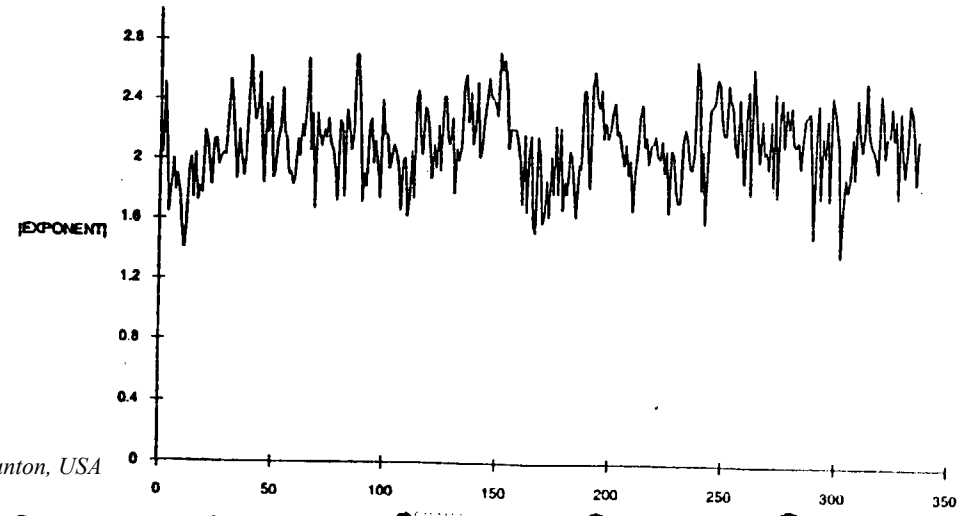

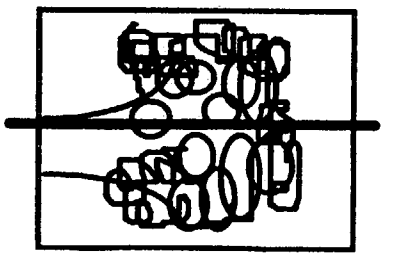

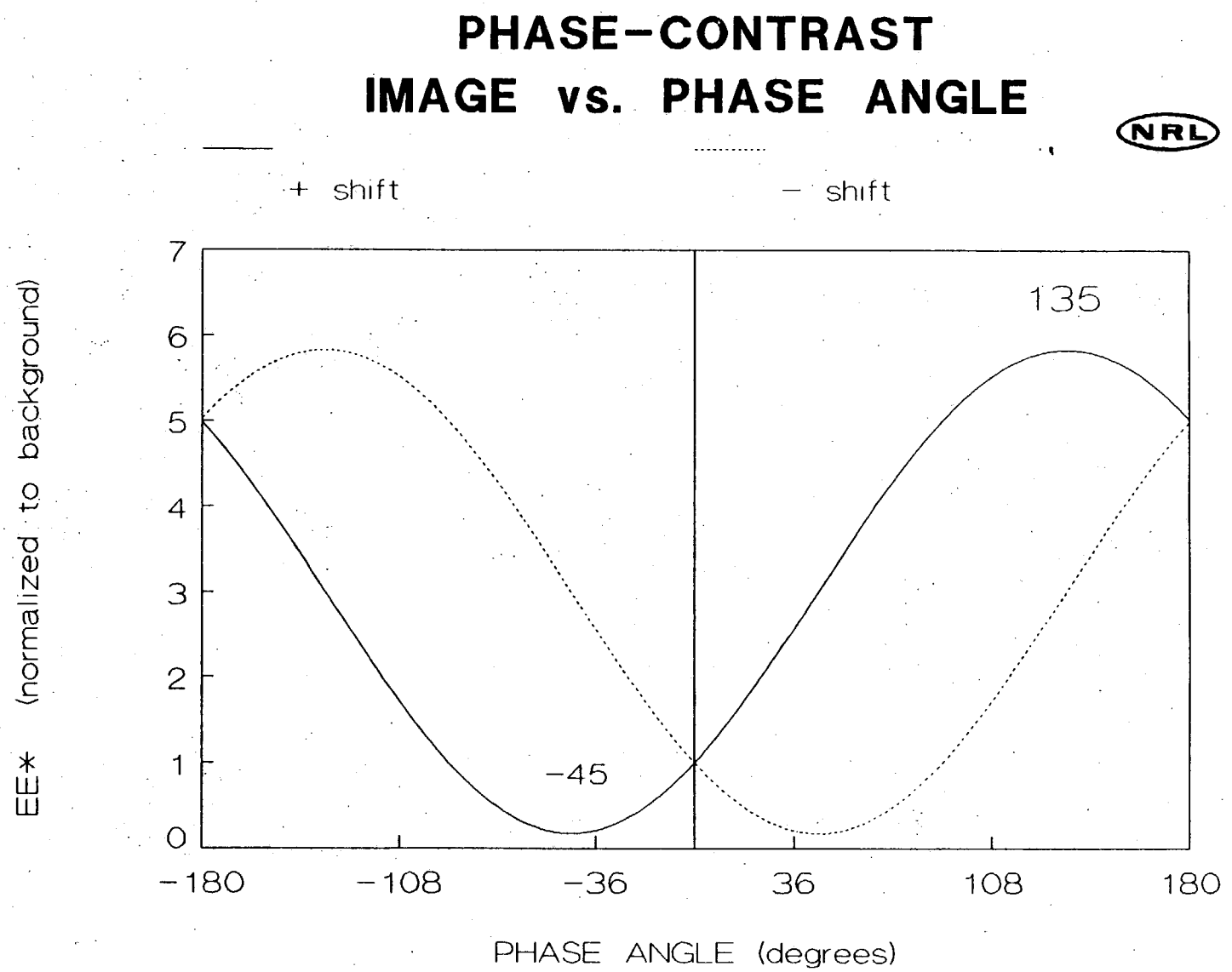
PHASE-CONTRAST
IMAGE vs. PHASE ANGLE
NRL
+ shift
− shift
EE* (normalized to background)
7
6
5
4
3
2
1
0
135
−45
−180
−108
−36
36
108
180
PHASE ANGLE (degrees)

Turbulence with Holographic Interferometry

Example with coarse fringes

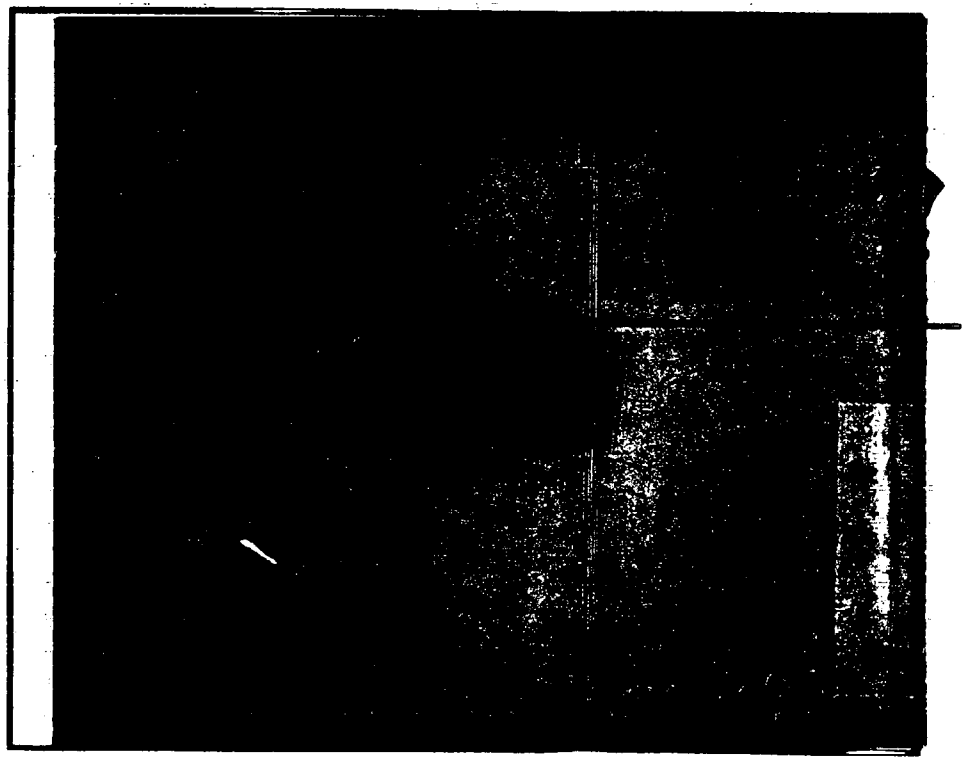

Reference Fringes (1 mm apart)

Shot 89-384, at 125ns, 10umCH foil in 5 torr Nitrogen

Pleasanton, USA

Edited by V. Rupert

Turbulence with Holographic Interferometry

Example with fine fringes

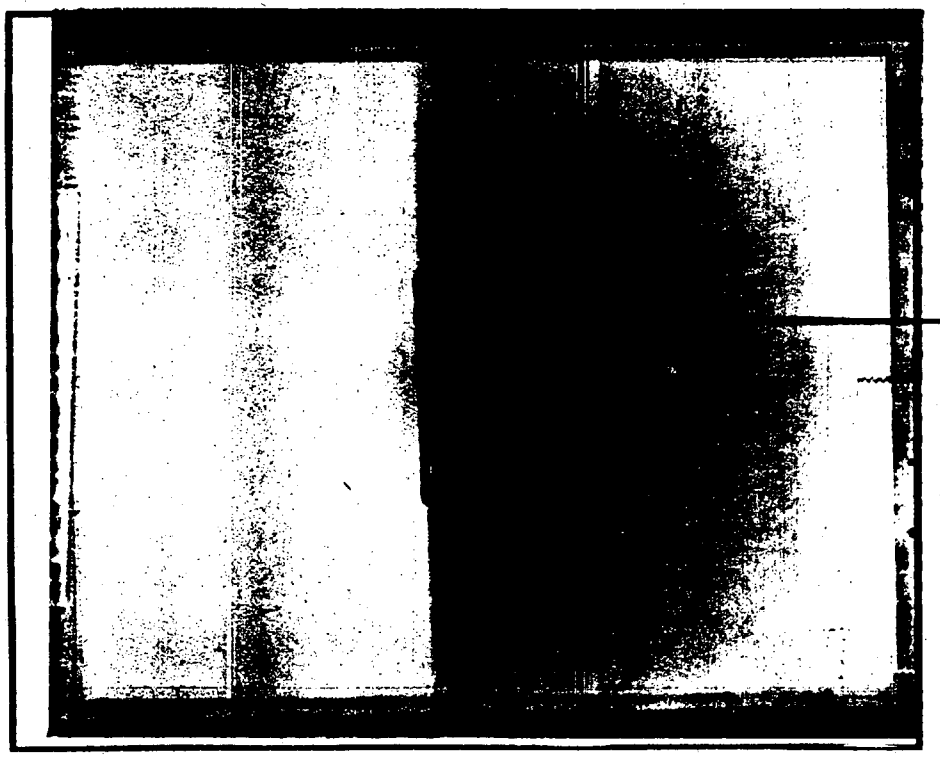

Reference Fringes (360 μm apart)

Shot 89-385, at 125ns, 10umCH foil in 5 torr Nitrogen

Turbulence with Holographic Interferometry Example with very fine (70μm) fringes

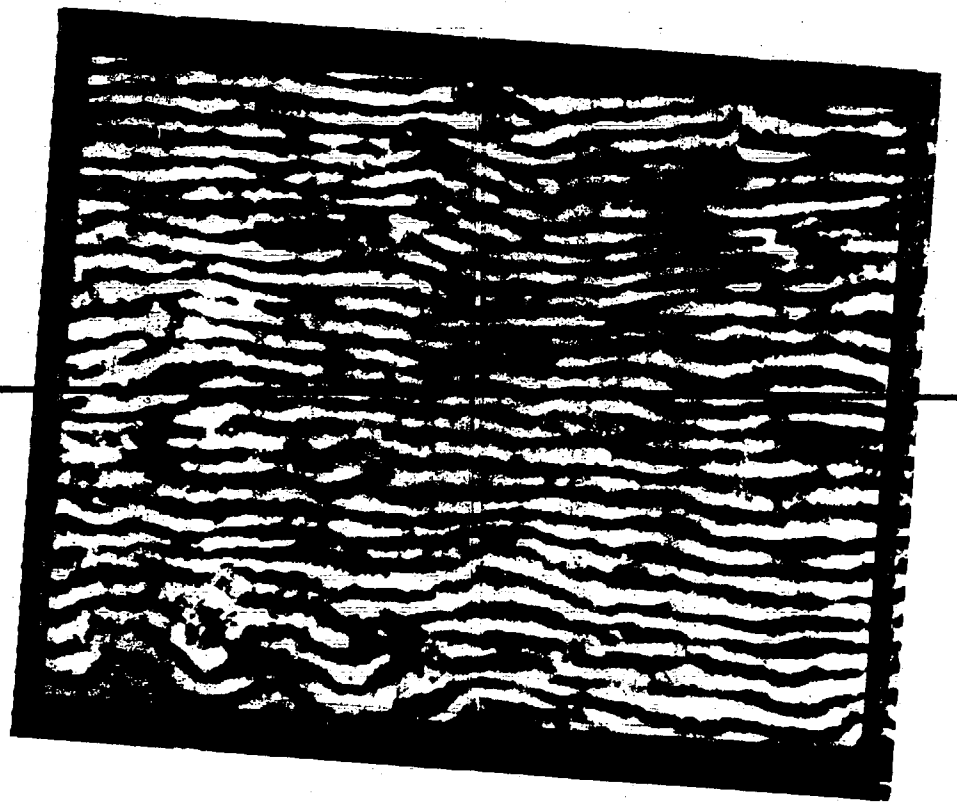

Shot 89-392, 10umCH in5 torr Nitrogen, at 125ns

NO TURBULENCE IN "BURNED THROUGH" TARGETS

NRL

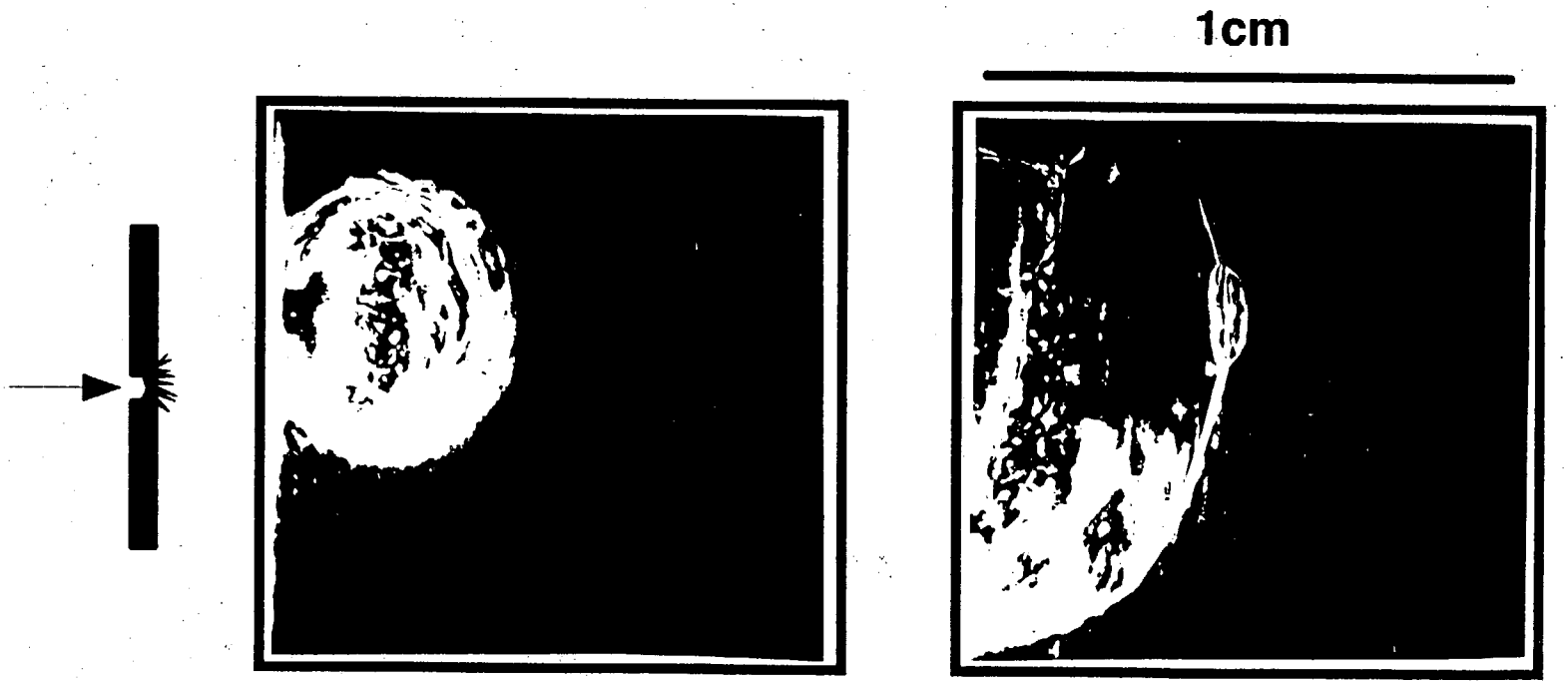

shots:515, 516
9um CH, 321 TW, Green ISI

Target Moves Through gas But Produces No Turbulence !!

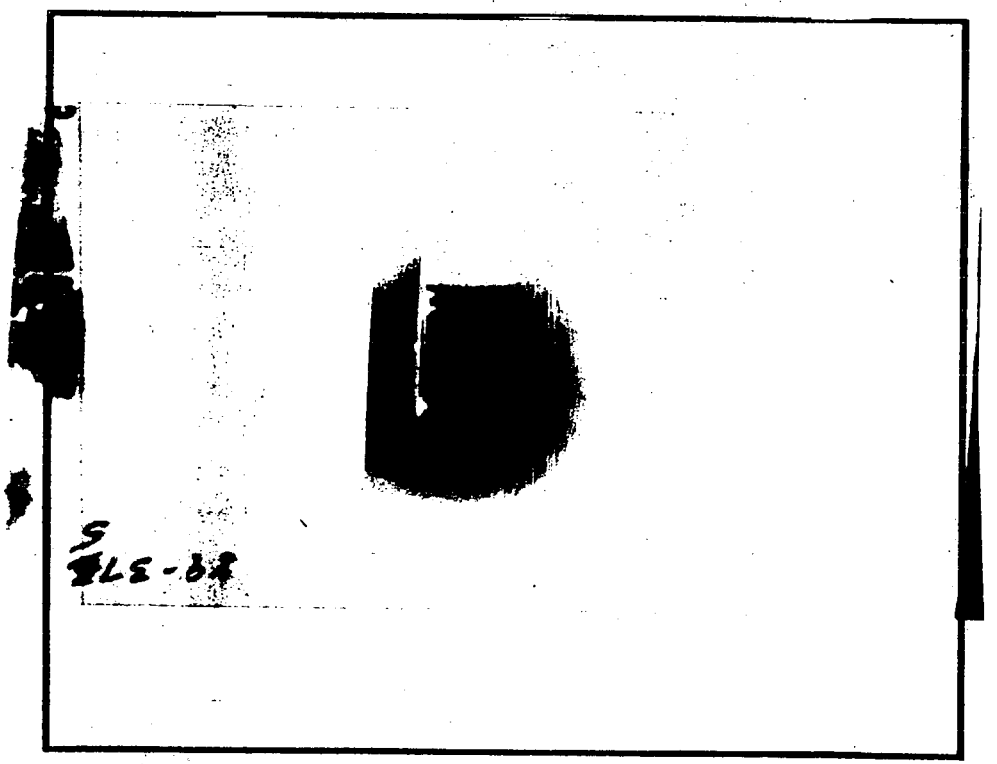

Shot 89-375, 10um CH in 5Torr Nitrogen at 125ns, ISI beam

HOLLOW-CONE TARGET (SHAPED CHARGE ANALOGUE)

NRL

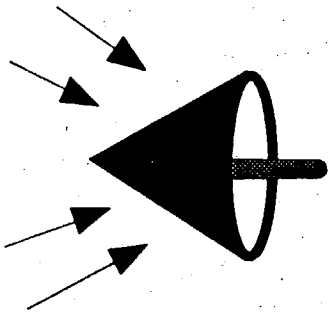

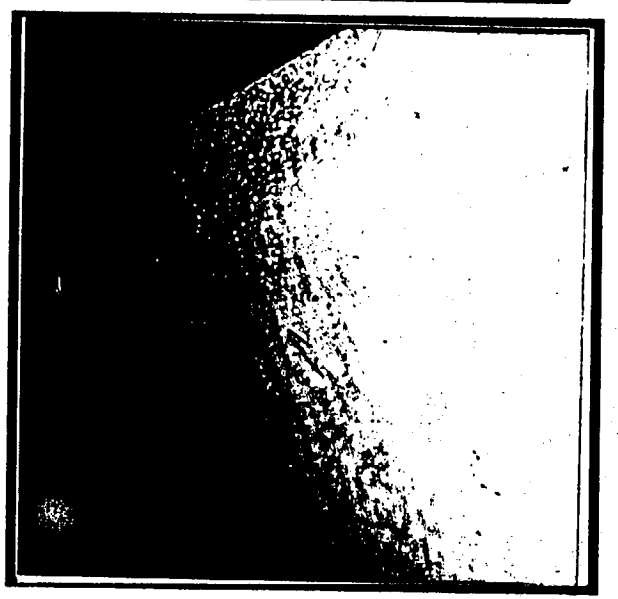

PRESHOT

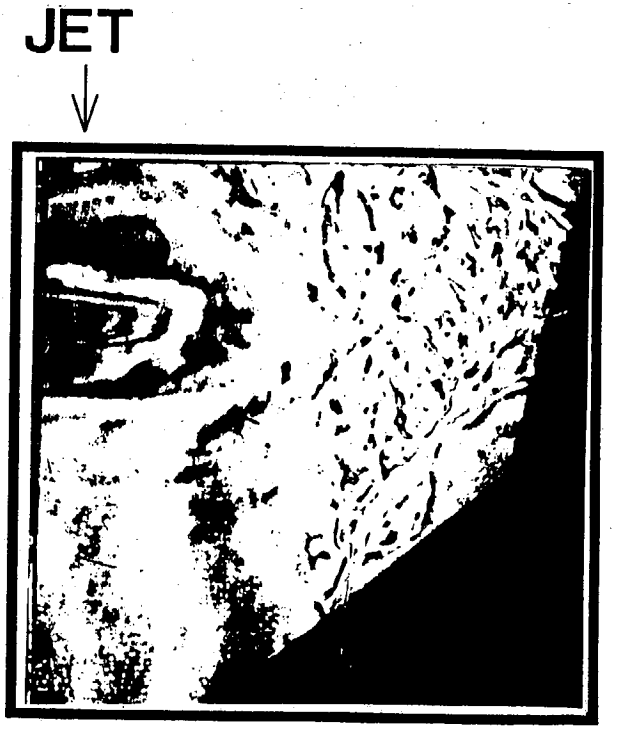

219 ns

shot:557

20um CH, 74deg. apex, 14TW

Pleasanton, USA *Edited by V. Rupert*

Summary

What we know about the turbulence

Trajectory is linear
Speed very supersonic; about same as target speed
need background gas to produce or see turbulence

Turbulence lasts very long -- 8 μs or more
Turbulence is spatially symmetric
Turbulence can be turned off

1-D K-space power spectrum varies as $K^{-3.1}$
No "inner scale" seen

RAYLEIGH TAYLOR INSTABILITY IN CYLINDRICAL CONFIGURATION

Partly unpublished results

V. FRACHET, F. GELEZNIKOFF, R. GUIX, A. HAUDUCOEUR, M. LEGRAND,
N. WILKE*, M. WULLSCHLEGER
Centre d'études de Vaujours-Moronvilliers
BP 7, 77181 Courtry, FRANCE

* Centre d'études de Limeil-Valenton
BP 27, 94190 Villeneuve-Saint-Georges, FRANCE

EXPERIMENTAL DEVICE

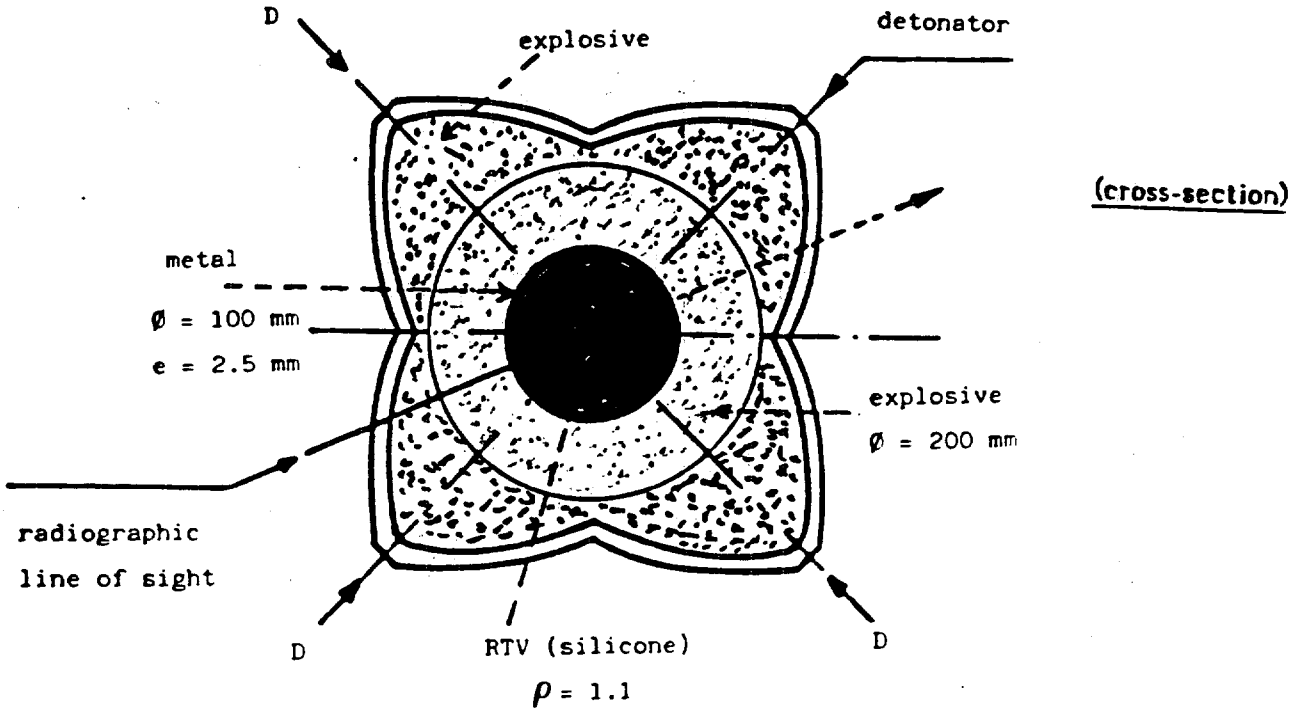

(cylinder length = 100 mm)

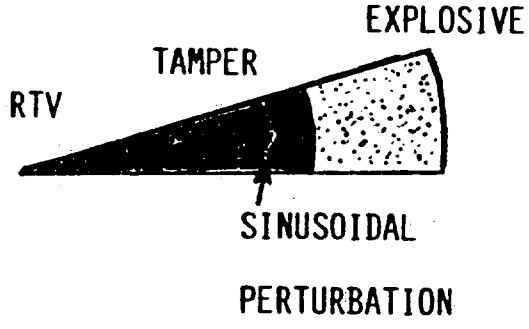

x, t diagram

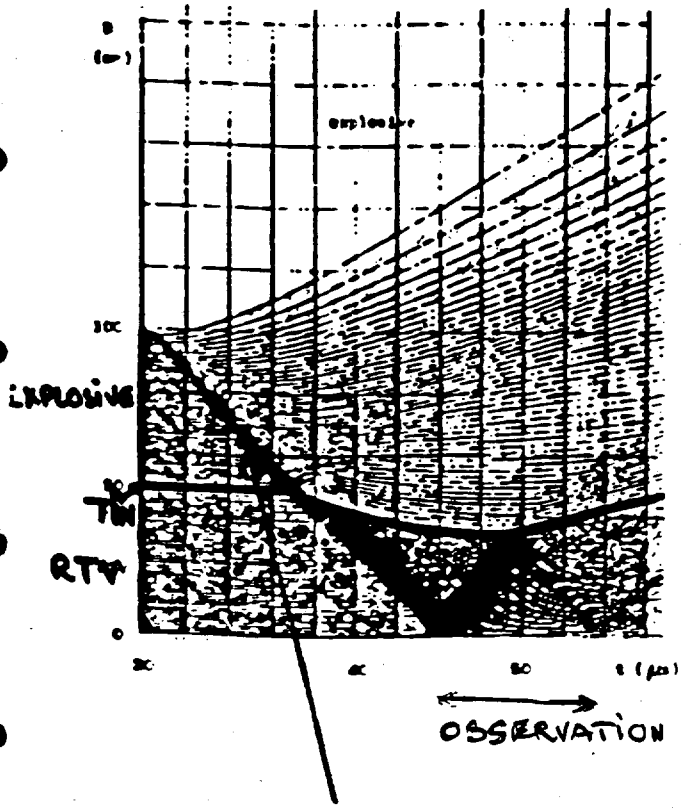

Velocity of the tin/RTV interface

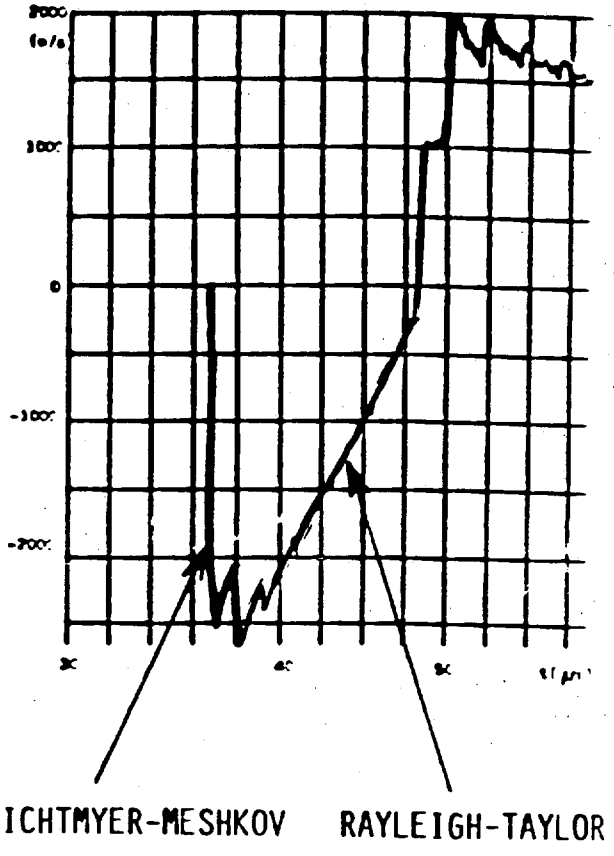

WAWE NUMBER COMBINATION

FLUID MATERIAL

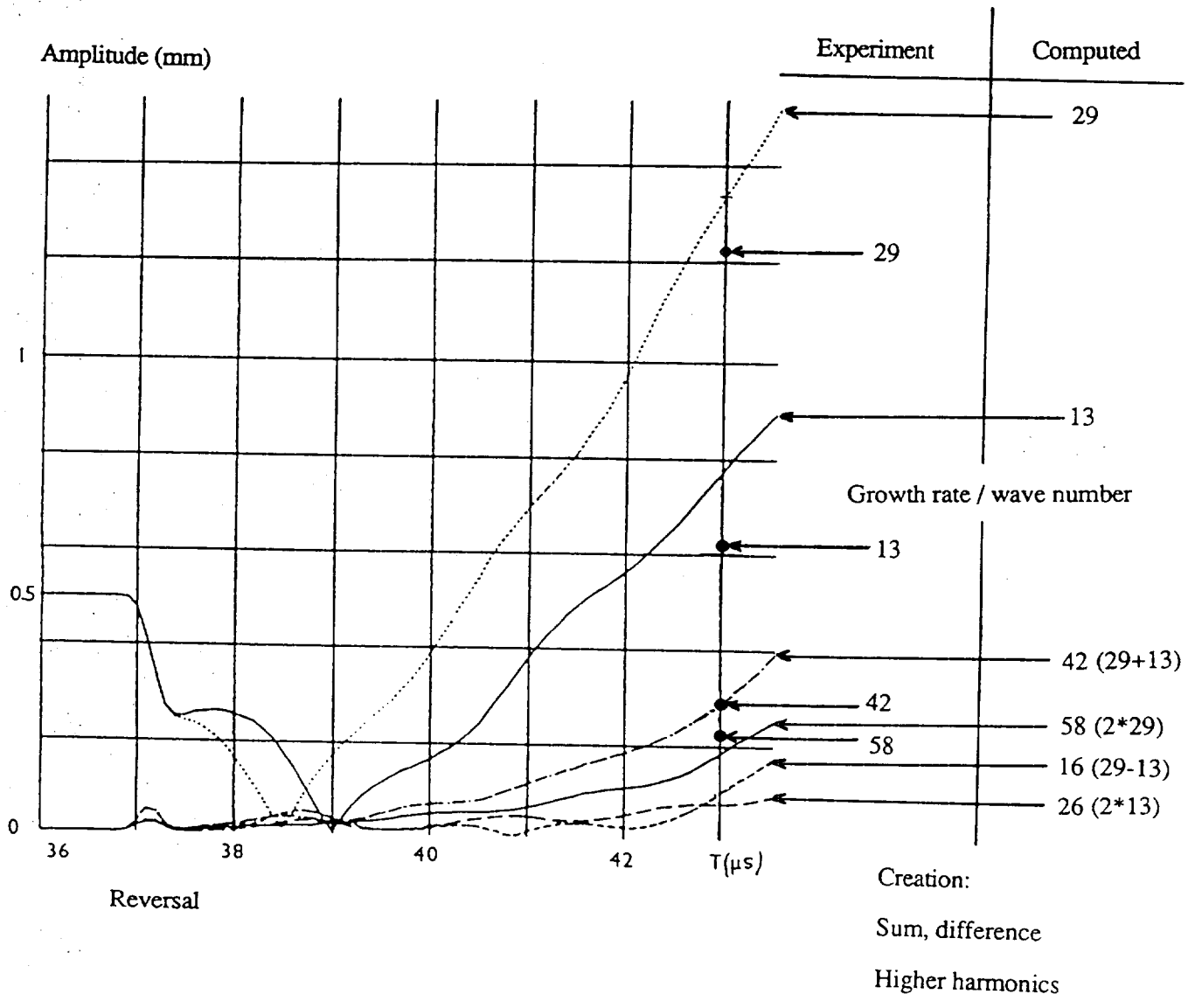

Perturbation Growth vs. time

SPECTRAL ANALYSIS OF THE INNER FACE OF THE TIN CYLINDER (EXPERIMENT)

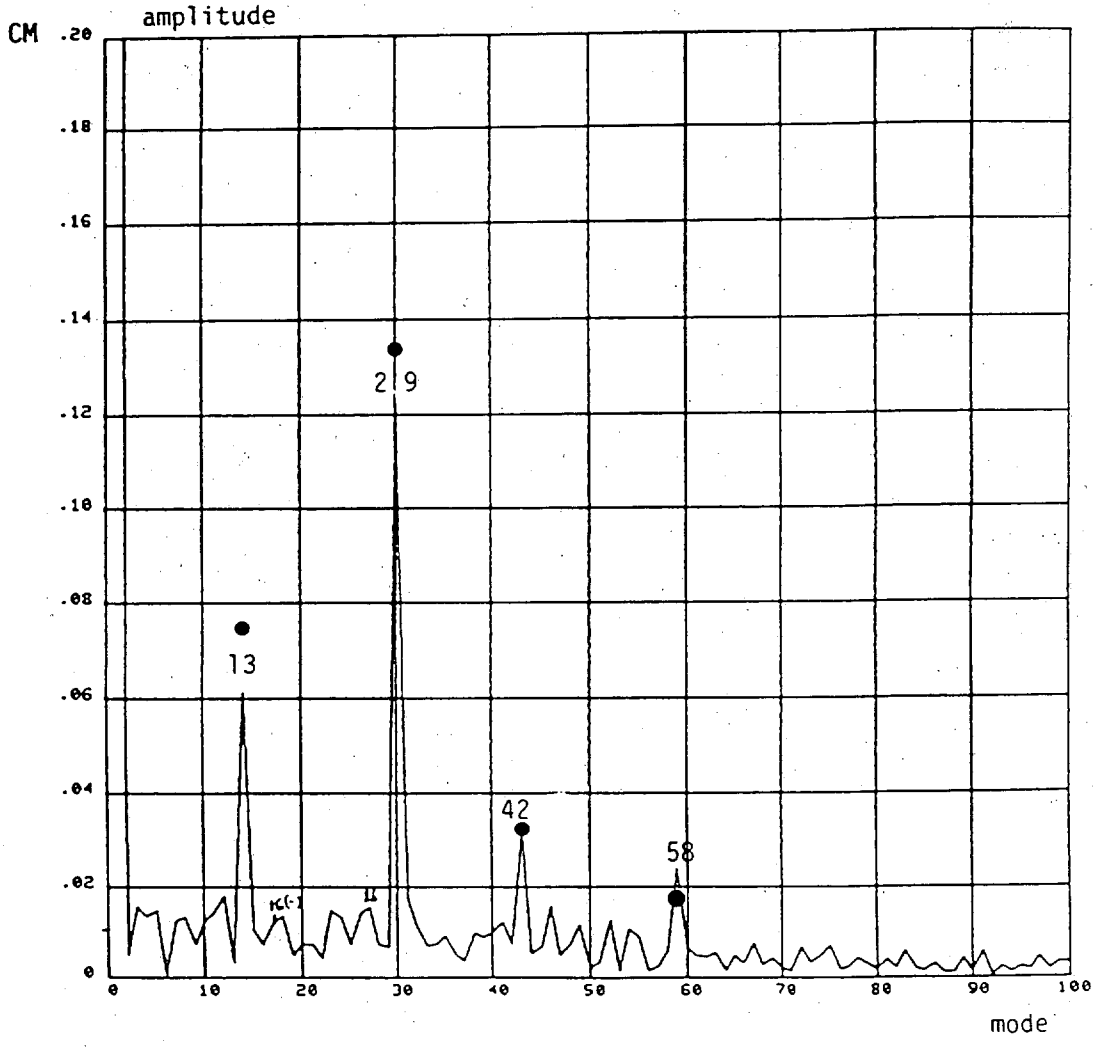

- Computed points

tin → (13 +29)

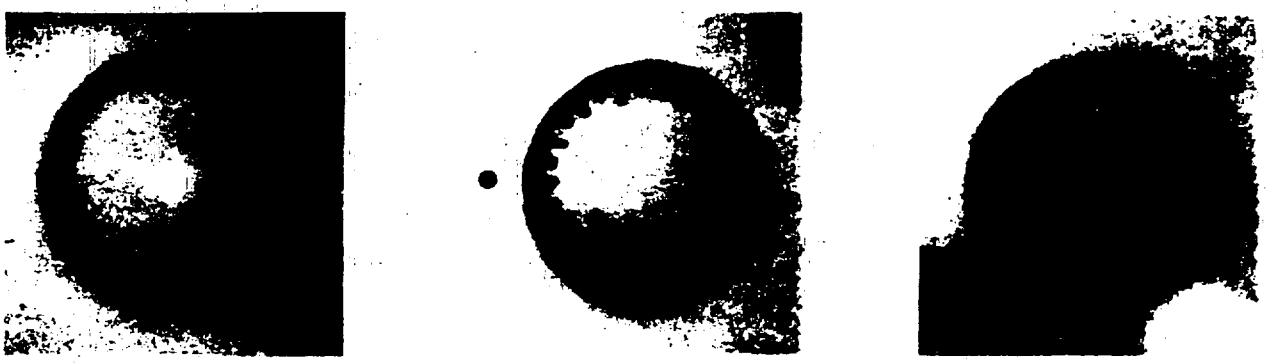

43 μs 46 μs 51 μs b)

Evolution of the tin cylinder (13, 29)

a) experiment b) simulation

SOLID MATERIAL

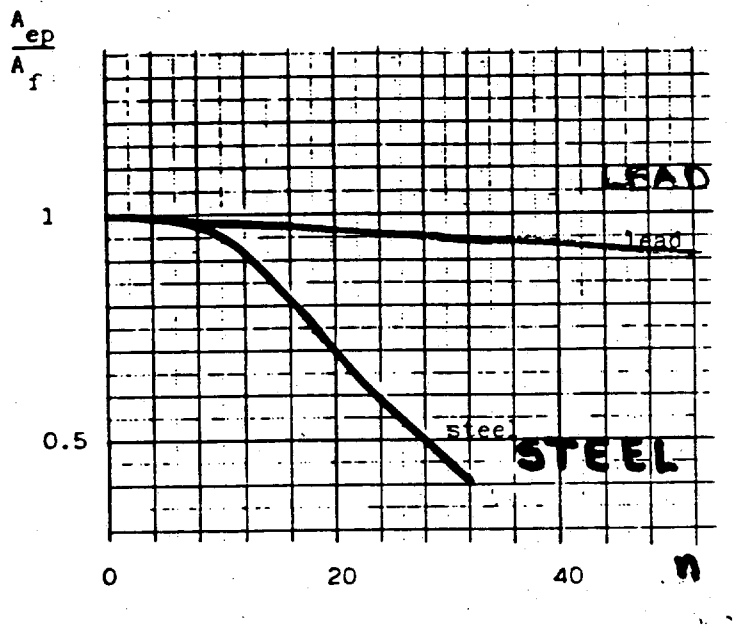

. STAINLESS STEEL (SHEAR MODULUS : 770 KBAR

YIELD STRENGH : 3,4 KBAR)

. WAVE NUMBER 24

WAVE NUMBER COMBINATION

SOLID MATERIAL (STEEL)

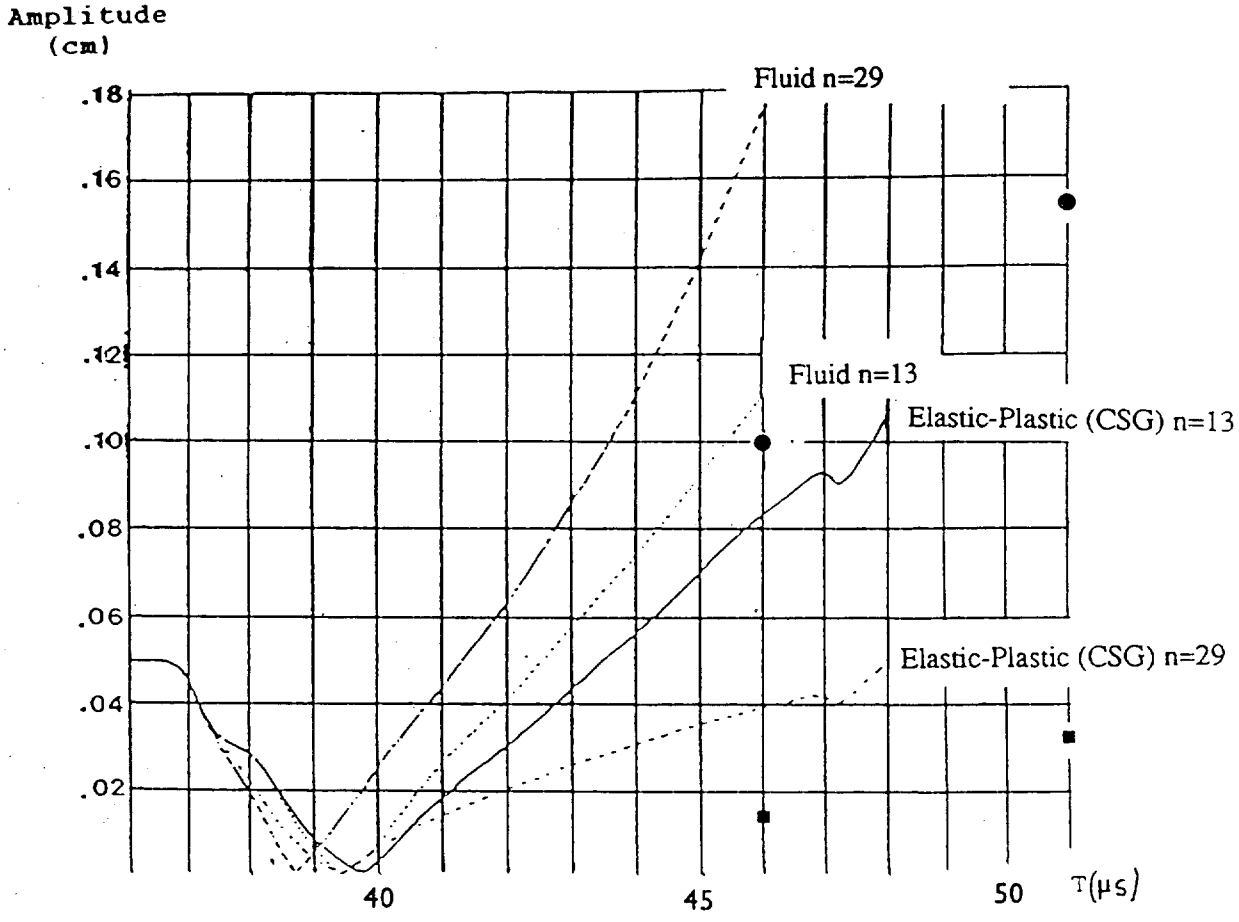

Experiment: ● n=13
■ n=29

SPECTRAL ANALYSIS OF THE INNER FACE OF THE STEEL CYLINDER (EXPERIMENT)

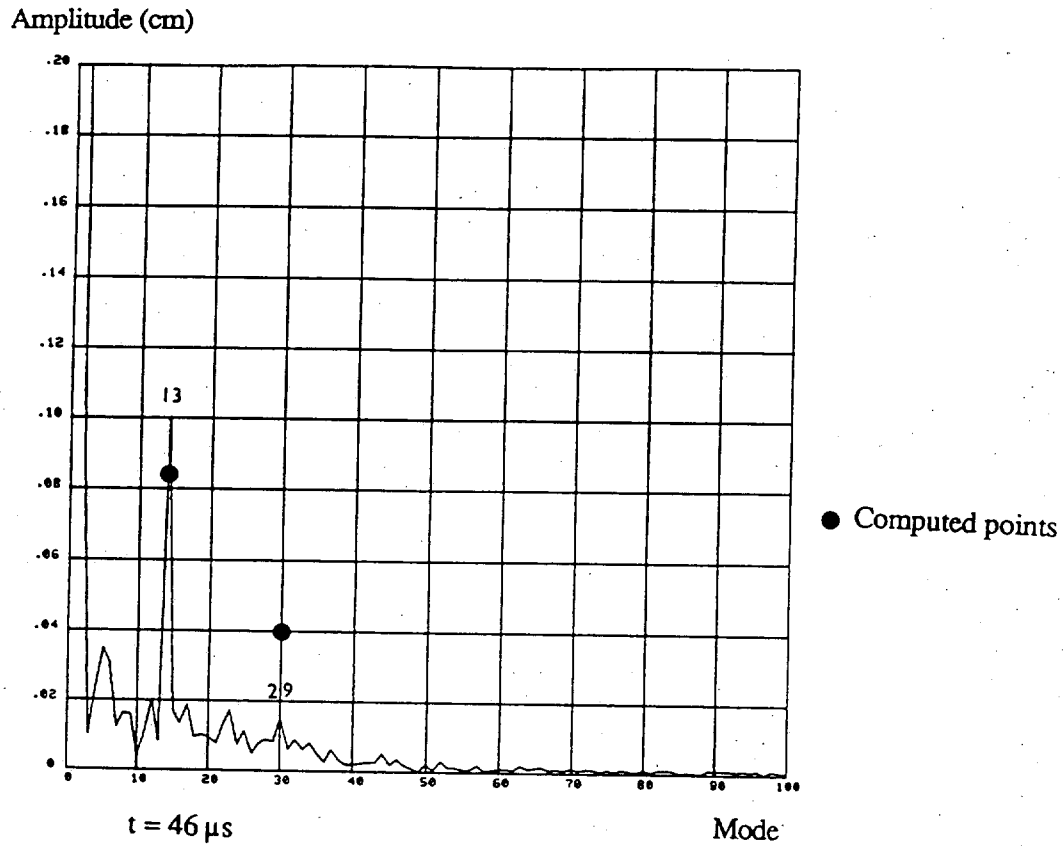

Steel → (13+29)

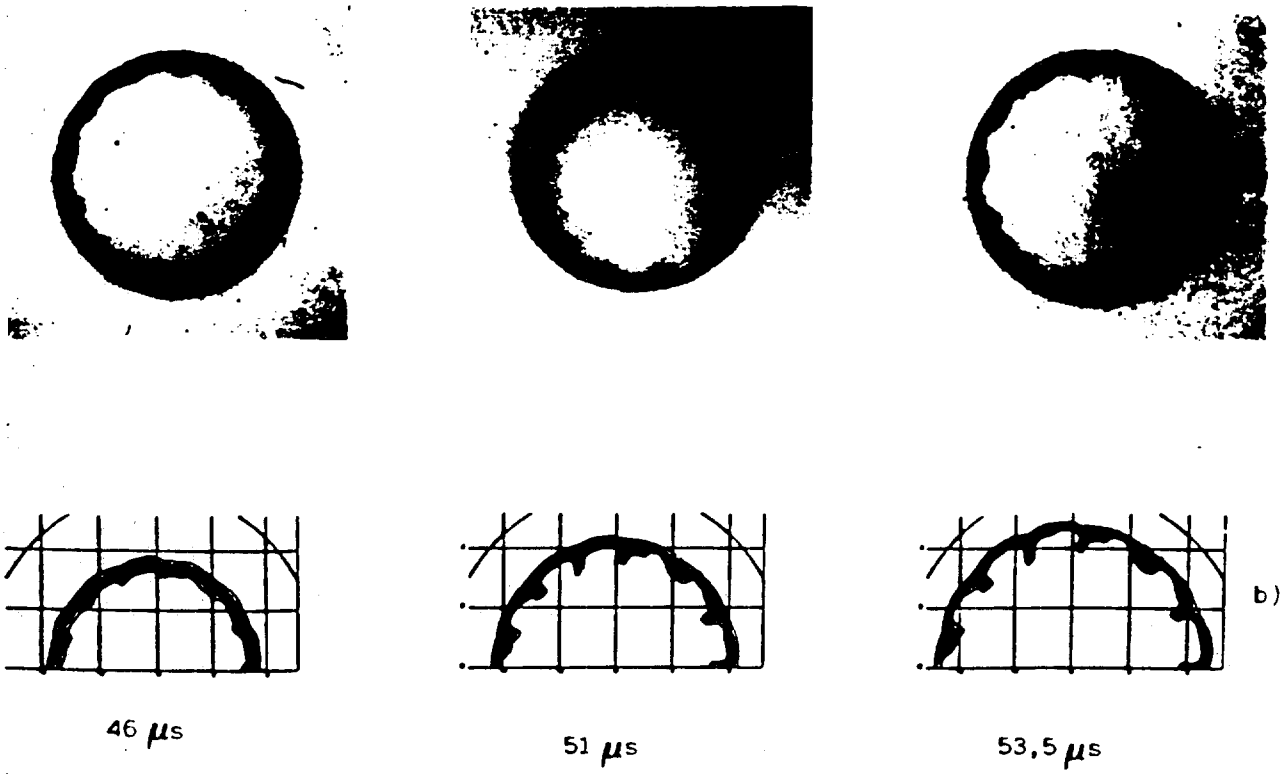

Evolution of the steel cylinder (13, 29) a) experiment ; b) evaluation

WAVE NUMBER COMBINATION

(ELASTIC PLASTIC BEHAVIOUR)

CSG Model N = 13 + 29

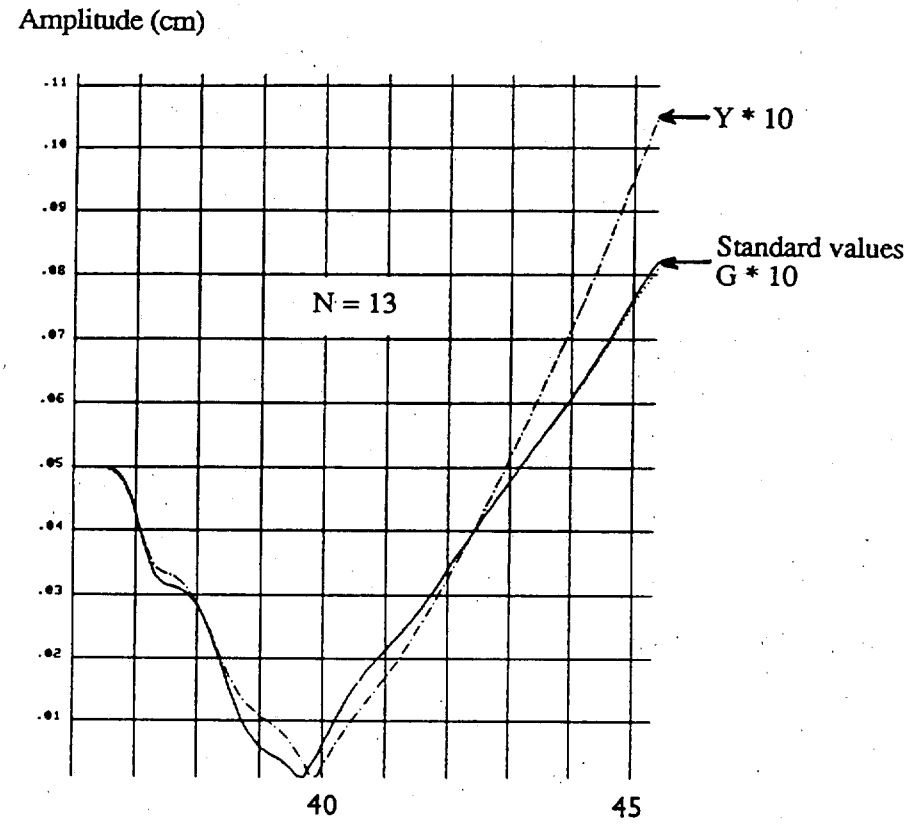

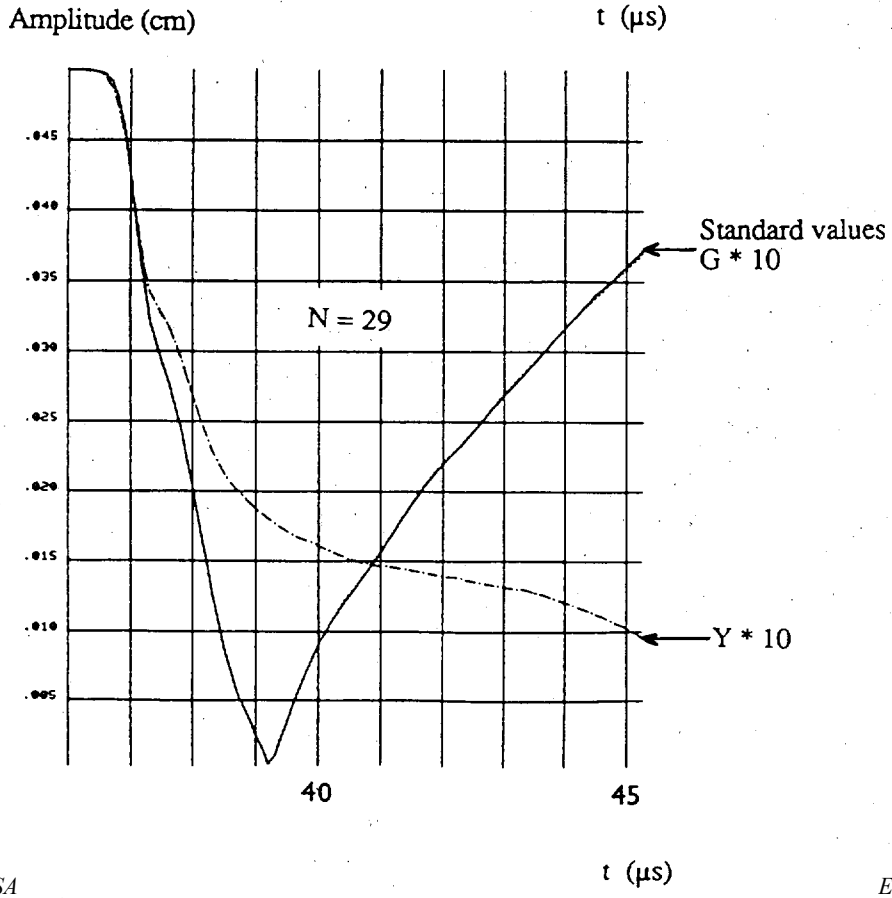

WAVE NUMBER COMBINATION

THREE MODE : 13, 21, 29

GROWTH OF THE INITIAL MODES

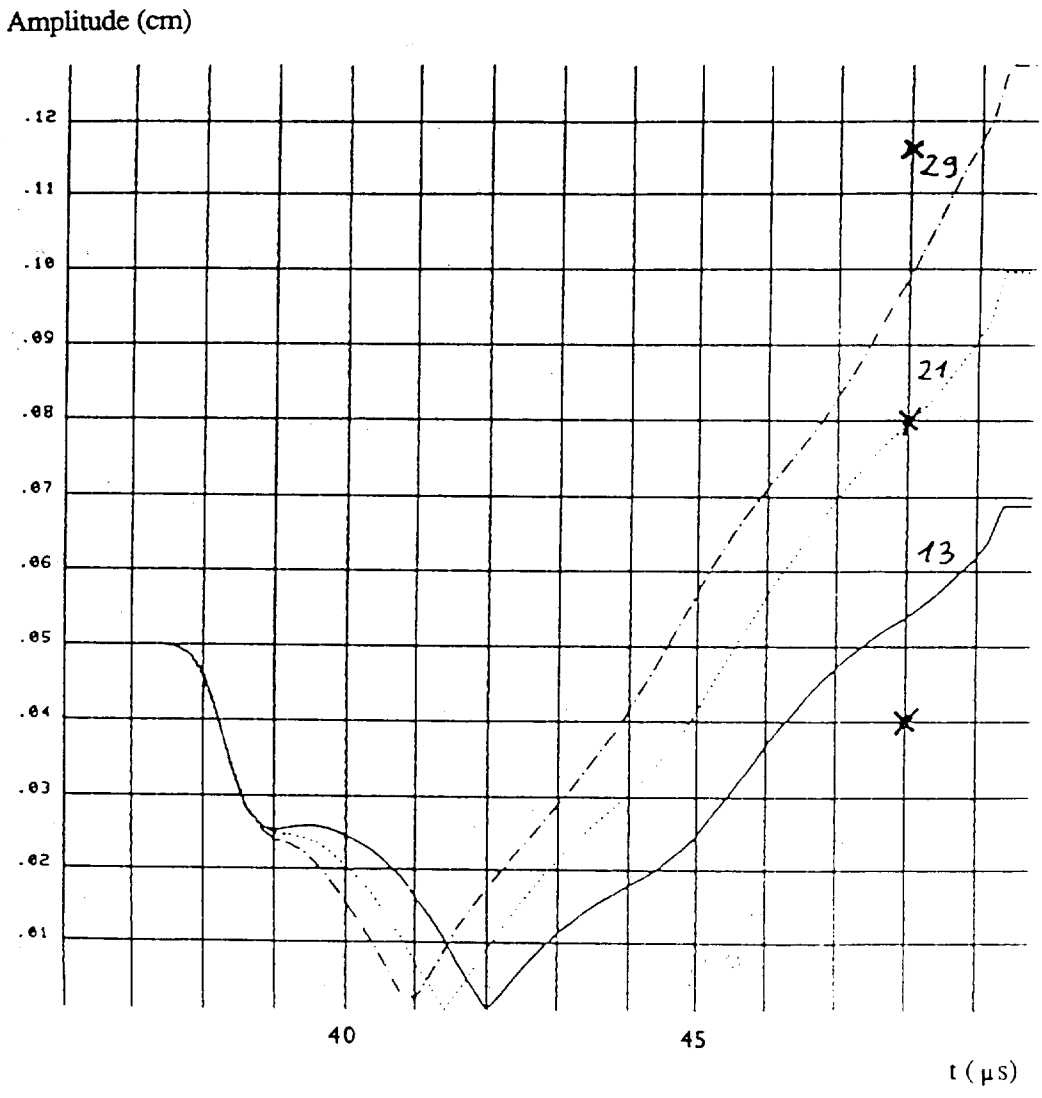

× Experimental points

SPECTRAL ANALYSIS OF THE INNER FACE OF THE TIN CYLINDER

t = 42 µs

Amplitude (cm) Computed spectrum

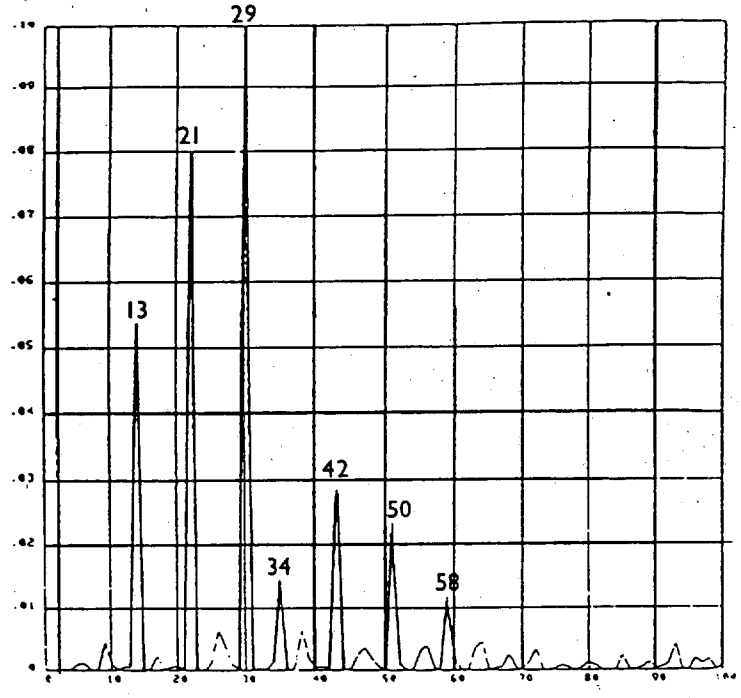

Mode

34 = 13 + 21

42 = 29 + 13 = 2 * 21

50 = 29 + 21

58 = 2 * 29

Amplitude (cm) Experimental spectrum

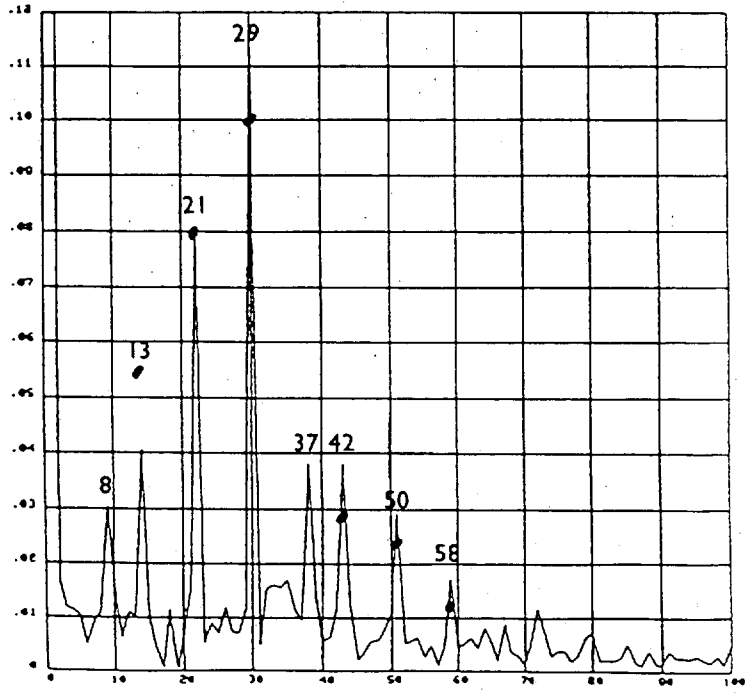

● Computed points

Mode

37 = 29 + 8

WAVENUMBER COMBINATION (TIN)

THREE MODES : 13,21,29

t = 51 μs

Experiment

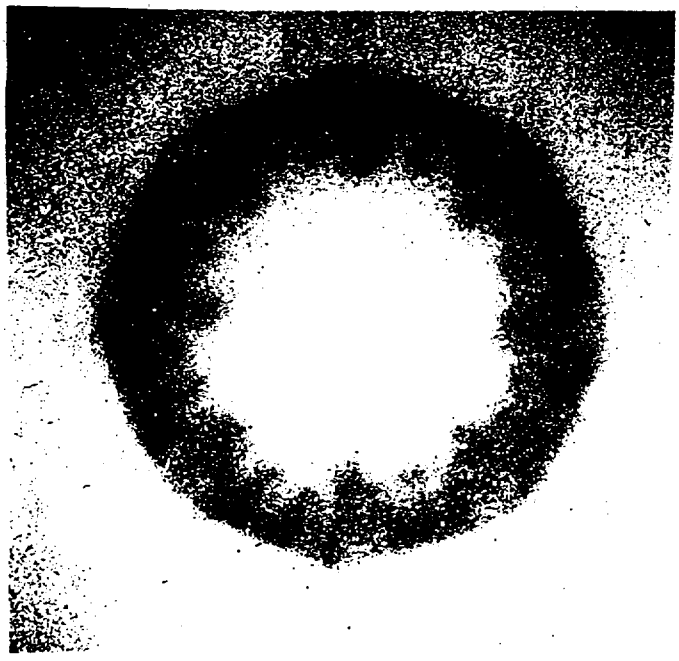

Computation